Transactions of the ASME®

Technical Editor, LEON M. KEER (1993)

The Technological Institute
Northwestern University
Evanston, IL 60201

APPLIED MECHANICS DIVISION

Chairman, MICHAEL J. FORRESTAL
Secretary, L. B. FREUND
Associate Technical Editors,
R. M. BOWEN (1994)
S. K. DATTA (1993)
G. J. DVORAK (1993)
M. E. FOURNEY (1994)
C. O. HORGAN (1992)
R. L. HUSTON (1994)
D. J. INMAN (1992)
J. T. C. LIU (1993)
R. M. McMEEKING (1994)
A. K. NOOR (1994)
J. W. RUDNICKI (1992)
W. N. SHARPE, JR. (1994)
C. F. SHIH (1993)
J. G. SIMMONDS (1992)
P. D. SPANOS (1992)
K. R. SREENIVASAN (1992)
Z. WARHAFT (1992)

BOARD ON COMMUNICATIONS
Chairman and Vice-President
R. E. NICKELL
Members-at-Large
W. BEGELL, T. F. CONRY, T. DEAR,
R. L. KASTOR, R. MATES,
E. M. PATTON, R. E. REDER,
R. D. ROCKE, A. VAN DER SLUYS,
A. J. WENNERSTROM, W. O. WINER,
B. ZIELS

President, A. E. BERGLES
Exec. Dir.
D. L. BELDEN
Treasurer, ROBERT A. BENNETT

PUBLISHING STAFF
Mng. Dir., Publ.,
CHARLES W. BEARDSLEY
Managing Editor,
CORNELIA MONAHAN
Production Editor, JUDY SIERANT
Prod. Asst., MARISOL ANDINO

Transactions of the ASME, Journal of Applied Mechanics (ISSN 0021-8936) is published quarterly (Mar., June, Sept., Dec.) for $160.00 per year by The American Society of Mechanical Engineers, 345 East 47th Street, New York, NY 10017. Second class postage paid at New York, NY and additional mailing offices. POSTMASTER: Send address changes to Transactions of the ASME, Journal of Applied Mechanics, c/o THE AMERICAN SOCIETY OF MECHANICAL ENGINEERS, 22 Law Drive, Box 2300, Fairfield, NJ 07007-2300.

CHANGES OF ADDRESS must be received at Society headquarters seven weeks before they are to be effective. Please send old label and new address.

PRICES: To members, $29.00, annually: to nonmembers, $160.00. Add $20.00 for postage to countries outside the United States and Canada.

STATEMENT from By-Laws. The Society shall not be responsible for statements or opinions advanced in papers or . . . printed in its publications (B7.1, Par. 3).

COPYRIGHT © 1990 by The American Society of Mechanical Engineers. Reprints from this publication may be made on condition that full credit be given the TRANSACTIONS OF THE ASME, JOURNAL OF APPLIED MECHANICS, and the author, and date of publication be stated.

INDEXED by Applied Mechanics Reviews and Engineering Information, Inc.

Journal of Applied Mechanics

Published Quarterly by The American Society of Mechanical Engineers

VOLUME 57 • NUMBER 3 • SEPTEMBER 1990

485 Reviewers

TECHNICAL PAPERS

488 Variational Formulation, Discrete Conservation Laws, and Path-Domain Independent Integrals for Elasto-Viscoplasticity (90-WA/APM-15)
J. C. Simo and T. Honein

498 Lode Dependences for Isotropic Pressure Sensitive Elastoplastic Materials
J. B. Bardet

507 A Fabric-Related Constitutive Model for Ganular Materials (90-WA/APM-23)
J. Jahedi, J. Mohammadi, and S. Nair

514 Swinging Wake Mechanism for Interface Wave Generation in Explosive Welding of Metals (90-WA/APM-19)
R. C. Gupta and G. S. Kainth

522 Analytical Solutions for Nonlinear Strain-Gradient Softening and Localization
H. L. Schreyer

529 Growth Instability During Nonuniform Directional Solidification of Pure Metals (90-WA/APM-33)
O. Richmond, L. G. Hector, Jr., and J. M. Fridy

537 Anisotropic Distortional Yield Model
G. Voyiadjis and M. Foroozesh

548 A Finite Deformation Theory of Viscoplasticity Based on Overstress: Part I—Constitutive Equations (90-WA/APM-9)
I. Nishiguchi, T.-L. Sham, and E. Krempl

553 A Finite Deformation Theory of Viscoplasticity Based on Overstress: Part II—Finite Element Implementation and Numerical Experiments (90-WA/APM-10)
I. Nishiguchi, T.-L. Sham, and E. Krempl

562 An Incremental Plastic Analysis of Multiphase Materials
Y. Y. Li and Y. Chen

569 Constraints on Moving Strong Discontinuity Surfaces in Dynamic Plane-Stress or Plane-Strain Deformations of Stable Elastic-Ideally Plastic Materials
Yinong Shen and W. J. Drugan

577 The Singularity Strength at the Apex of a Wedge Undergoing Finite Deformations
J. M. Duva

581 Modifications of Series Expansions for General End Conditions and Corner Singularities on the Semi-Infinite Strip (90-WA/APM-14)
Yoon Young Kim and C. R. Steele

589 A Dislocation Green's Function for the Analysis of Multiple Coplanar Cracks or Cracks With Nonuniform Crack Fronts
M. T. Hanson

596 An Arbitrary Tangential Load Underneath a Smooth Circular Punch
V. I. Fabrikant

600 A Boundary Element Method for Plane Anisotropic Elastic Media
KYU J. Lee and A. K. Mal

607 Three-Dimensional Effects Near a Crack Tip in a Ductile Three-Point Bend Specimen: Part I—A Numerical Investigation
R. Narasimhan and A. J. Rosakis

618 Three-Dimensional Effects Near a Crack Tip in a Ductile Three-Point Bend Specimen: Part II—An Experimental Investigation Using Interferometry and Caustics
A. T. Zehnder and A. J. Rosakis

627 Delamination Specimens for Orthotropic Materials
Zhigang Suo

635 Asymptotic Crack-Tip Fields for Perfectly Plastic Solids Under Plane-Stress and Mixed-Mode Loading Conditions
P. Dong and J. Pan

639 The First-Order Variation of the Displacement Field Due to Geometrical Changes in an Elliptical Crack (90-WA/APM-22)
T. Nishioka and S. N. Atluri

647 Crack Extension Force in a Piezoelectric Material
Y. E. Pak

654 Axisymmetric Stress Analysis of a Broken, Debonded Fiber (90-WA/APM-25)
U. Mbanefo and R. A. Westmann

661 Elastodynamic Scattering From Penny-Shaped and Nonplanar Cracklike Flaws With Dissipation and Restoring Forces
P. Olsson

667 An Experimental Study of the Unloading Waves in a Plucked Hyperelastic String
J. L. Wegner and J. B. Haddow

672 Elastodynamic Scattering From Inclusions Surrounded by Thin Interface Layers (90-WA/APM-12)
P. Olsson, S. K. Datta, and A. Bostrom

(Contents continued on Inside Back Cover)

Downloaded 04 May 2010 to 171.66.16.49. Redistribution subject to ASME license or copyright; see http://www.asme.org/terms/Terms_Use.cfm

677 **Axisymmetric Vibrations of Circular Plates on Tensionless Elastic Foundations**
Z. Celep and D. Turhan

682 **Inflation of an Axisymmetric Membrane: Stress Analysis** (90-WA/APM-13)
A. Sagiv

688 **Random Vibrations of Viscoelastic Laminated Plates** (90-WA/APM-20)
G. Cederbaum

694 **Measurements of Solid Spheres Bouncing Off Flat Plates** (90-WA/APM-11)
R. Sondergaard, K. Chaney, and C. E. Brennen

700 **Anisotropic Plates With Various Openings Under Uniform Loading or Pure Bending** (90-WA/APM-17)
C. Hwu

707 **Nonliner Finite Element Formulation for the Large Displacement Analysis of Plates** (90-WA/APM-26)
B. Chang and A. A. Shabana

719 **The Initial Phase of Transient Thermal Stresses Due to General Boundary Thermal Loads in Orthotropic Hollow Cylinders** (90-WA/APM-16)
G. A. Kardomateas

725 **The Rotationally Flexible Pendulum Subjected to a High Frequency Excitation**
B. A. Schmidt

731 **A Convolution Approach for the Transient Analysis of Locally Nonlinear Rotor Systems** (90-WA/APM-21)
I. F. Chiang and S. T. Noah

738 **Classical Vibration Analysis of Axially Moving Continua**
J. A. Wickert and C. D. Mote, Jr.

745 **Equations of Motion for Structures in Terms of Quasi-Coordinates**
R. D. Quinn

750 **Inverse Dynamics of Constrained Multibody Systems**
J. T. Wang

758 **Optimization of Self-Acting Gas Bearings for Maximum Static Stiffness** (90-WA/APM-18)
M. P. Robert

762 **Mixing in a Closed Room by the Action of Two Fans**
S. Lichter, A. Dagan, W. B. Underhill, and H. Ayanle

769 **The Meniscus Instability in Non-Newtonian Negative Squeeze Films**
H. Koguchi and T. Yada

BRIEF NOTES

Cumulant Neglect Closure of Nonstationary Solutions of Stochastic System
M. Pawleta and L. Socha 776

Flexural Waves in a Periodic Beam
Sen Yung Lee, Huei Yaw Ke, and Ming Jang Kao 779

The Effect of Wall Motions on the Governing Equations of Contained Fluids
R. Ohayon and C. A. Felippa 783

Steady Axial Motions of Strings
T. J. Healey and J. N. Papadopoulos 785

787 Use of Statical Indentation Laws in the Impact Analysis of Composite Laminated Plates and Shells
H. J. Lin and Y. J. Lee

789 The Effective Thermal Conductivity of a Packing of Spheres
A. Jagota and C. Y. Hui

791 Vertical Ground Motion Induced by a Blast Wave
F. R. Norwood

793 The Rolling Motion of an Expanding and Contracting Cylinder
E. V. Wilms and H. Cohen

DISCUSSION

795 ***A Note on Microbuckling in Unidirectional Fibrous Composites*** **by T. M. Minahen and W. G. Knauss—Discussion by T. W. Shield**

796 ***Discussion of Thin-Walled Open-Profile Bars*****, by M. Ojalvo—Discussion by Yoshaiki Goto, Wai-Fah Chen, and Fumio Machino**

BOOK REVIEWS

798 ***Non-Linear Oscillations,*** **2nd ed., by Peter Hagedorn . . .** Reviewed by **P. D. Spanos**

798 ***Rock Rheology,*** **by N. Cristescu . . .** Reviewed by **L. S. Costin**

ANNOUNCEMENTS AND SPECIAL NOTES

718 Change of Address Form

800 Books Received by the Office of the Technical Editor

801 Worldwide Mechanics Meetings List

513 International Conference of Nonlinear Engineering Computation

568 7th International Conference on Numerical Methods in Laminar Turbulent Flow

576 7th International Conference on Numerical Methods for Thermal Problems

588 First European Solid Mechanics Conference

(Contents continued on p. 749)

Downloaded 04 May 2010 to 171.66.16.49. Redistribution subject to ASME license or copyright; see http://www.asme.org/terms/Terms_Use.cfm

CONTENTS (CONTINUED)

617	Advances in Information Storage Systems
634	Symposium on Interfacial Phenomena in Viscoelastic Flows
638	I.U.T.A.M.—18th International Congress of Theoretical and Applied Mechanics
660	First U.S. National Congress on Computational Mechanics
681	Symbolic Computations and Their Impact on Mechanics
706	Symposium on Dynamics of Bubbles and Vortices Near a Free Surface
744	Symposium of Computational Technology for Flight Vehicles
797	International Conference on Fracture Mechanics of Concrete Structures

Downloaded 04 May 2010 to 171.66.16.49. Redistribution subject to ASME license or copyright; see http://www.asme.org/terms/Terms_Use.cfm

Variational Formulation, Discrete Conservation Laws, and Path-Domain Independent Integrals for Elasto-Viscoplasticity

J. C. Simo
Assistant Professor of Mechanical Engineering.

T. Honein
Graduate Student.

Applied Mechanics Division,
Stanford University,
Stanford, CA 94305

A discrete variational formulation of plasticity and viscoplasticity is developed based on the principle of maximum plastic dissipation. It is shown that the Euler-Lagrange equations (spatial conservation laws) emanating from the proposed discrete Lagrangian *yield the equilibrium equation, the strain-displacement relations, the stress-strain relations, the discrete flow rule and hardening law in the form of closest-point-projection algorithm, and the loading/unloading conditions in Kuhn-Tucker form. Lack of invariance of the discrete Lagrangian relative to the group of material translations precludes the classical Eshelby law from being a conservation law. However, a discrete* inhomogeneous *form of Eshelby's conservation law is derived which leads to a* path-domain independent *integral that generalizes the classical* **J***-integral to elasto-viscoplasticity. It is shown that this path-domain independent integral admits a physical interpretation analogous to Budiansky and Rice interpretation of the classical* **J***-integral.*

1 Introduction

The objective of this paper is a systematic development of the variational structure and associated spatial and material conservation laws in discrete incremental plasticity and viscoplasticity. In particular, the widely employed return mapping algorithms for plasticity and viscoplasticity with internal (hardening) variables, arise in the present context in full generality as Euler-Lagrange equations of a particular (discrete) Lagrangian. Furthermore, the counterpart of Eshelby's law along with the proper extension of the **J**-integral to elastoplasticity, emanate from the proposed discrete Lagrangian as material conservation laws. All the results carry over to the continuum case in the limit as the time step goes to zero (consistency).

Since the pioneering work of Sanders (1960) and Rice (1969), a sizable body of literature has been concerned with the formulation of conservation laws and path-independent integrals for incremental plasticity and viscoplasticity. In particular, incremental forms of the classical J-integrals have been proposed (i.e., Atluri (1982, 1984)). We refer to Nakamura, Shih and Freund (1987) and Kanninen and Popelar (1985, page 168) for a summary account, and the monograph edited by Atluri (1986) for a recent up-to-date comprehensive review.

In classical field theory, conservation laws emanate from Noether's celebrated first theorem as a result of invariance of the Lagrangian or Hamiltonian system with respect to one (or finitely-many) parameter groups of transformations (see, i.e., the comprehensive account of Olver (1986). In the context of elasticity, this is the point of view adopted by Gunther (1962), Knowles and Sternberg (1972), Fletcher (1976), and Olver (1984a, b). In particular, within this framework, one obtains the classical Eshelby law (1951) establishing the divergence-free character of the energy-momentum tensor (see also Hill (1986)). Recently, an alternative approach has been set forth by Eischen and Herrmann (1987).

Here, this classical point of view is also adopted. The corner stone in the present development is a variational formulation based on the principle of maximum plastic dissipation. This principle, often credited to von Mises and Hill ((1950, page 60)) plays a central role in the modern mathematical theory of plasticity (Duvaut and Lions (1972), Johnson (1976, 1978), Moreau (1975, 1977), and Mathies (1978)). We refer to Temam (1985) for an account of existing results. In what follows, attention is focused on the discrete problem. The main steps in the ensuing development may be outlined as follows.

(i) We discretize the time interval $[0, T] \subset \mathbb{R}_+$ of interest in nonoverlapping intervals $[0, T] = \cup_{i=0}^{i=n} [t_i, t_{i+1}]$. In a typical interval $[t_n, t_{n+1}]$, we assume the state is a given known initial data at t_n. The *total energy available* at time t_n is expressed *in terms of the state variables* at t_{n+1} as the sum of the potential

Contributed by the Applied Mechanics Division of THE AMERICAN SOCIETY OF MECHANICAL ENGINEERS for presentation at the Winter Annual Meeting, Dallas, Texas, Nov. 25–30, 1990.

Discussion on this paper should be addressed to the Technical Editor, Leon M. Keer, the Technological Institute, Northwestern University, Evanston, IL 60208, and will be accepted until two months after final publication of the paper itself in the JOURNAL OF APPLIED MECHANICS. Manuscript received by the ASME Applied Mechanics Division, Oct. 29, 1987; final revision, Oct. 13, 1988.

Paper No. 90-WA/APM-15.

Copyright © 1990 by ASME
Downloaded 03 May 2010 to 171.66.16.244. Redistribution subject to ASME license or copyright; see http://www.asme.org/terms/Terms_Use.cfm

energy at time $_{t+1}$, and the incremental dissipation in the interval $[t_n, t_{n+1}]$ computed by means of a backward Euler difference scheme. This leads to a *discrete functional* (Lagrangian) in terms of the unknown state variables at t_{n+1}.

(ii) The Euler-Lagrange equations (spatial conservation-laws) associated with this discrete Lagrangian are shown to produce the equilibrium equations, the discrete flow rule and hardening law, and the loading conditions in Kuhn-Tucker form. This latter form constitutes the classical statement of the optimality conditions for convex programming problems subjected to unilateral constraints (see, i.e., Luenberger (1984)). The discrete flow rule and hardening law, on the other hand, are the mathematical expression of the so-called closest-point-projection algorithms, first introduced in Wilkins (1964) for J_2-flow theory, and recently extended in Simo (1985), Ortiz and Popov (1985), Simo and Taylor (1986), and Simo and Hughes (1987). From a mathematical standpoint, these algorithms appear to have been first studied in Moreau (1977), who coined the expression *catching-up algorithms*.

(iii) By direct inspection, it is readily concluded that the proposed discrete Lagrangian *is not invariant* with respect to the three-parameter group of material translations. Consequently, the associated Noether quantity, i.e., the counterpart of Eshelby's energy-momentum tensor, *is not conserved in elasto-viscoplasticity*. Hence, the associated **J**-integral is not path independent. A direct calculation, however, reveals that for perfect plasticity, the divergence of the energy-momentum tensor (in the absence of body forces and hardening parameters) equals the domain term $-\sigma_{n+1}: \partial_x \epsilon_n^p$, where σ_{n+1} is the stress tensor at t_{n+1} and $\partial_x \epsilon_n^p$ the gradient of the plastic flow at time t_n. Integration by parts then leads to a *path-domain* independent integral, which is subsequently referred to as $\mathbf{J}^*$. In the absence of singularities, the $\mathbf{J}^*$ integral vanishes for any simply connected compact region $A \subset \mathbb{R}^3$ with smooth boundary ∂A, and is closely related to the discrete counterpart of the modified $\hat{J}$-integral of Kishimoto, Aoki, and Sakata (1980), and the T^*-integral of Atluri (see Atluri (1986)).

(iv) By employing an argument along the lines suggested by Budiansky and Rice (1973), it is shown that in the presence of a defect (a cavity), the $\mathbf{J}^*$-integral does in fact furnish the change in energy due to a translation of the defect. This suggests an interpretation of the $\mathbf{J}^*$-integral as an energy release rate. In this regard, three important differences with the results of Kishimoto et al. (1980), and Atluri (1986) should be noted. First, the expression given by the former authors is restricted to paths enclosing the defect which do not intersect the plastic region; the one proposed here is not, and holds in the general case. Second, the present result is given directly in algorithmic form directly amenable to numerical implementation. Last and most important, the results obtained herein are systematically derived from a discrete Lagrangian by means of invariance arguments that rely on Noether's theorem. Finally, we note that the discrete expression proposed by Atluri (1986) does not appear to match the one derived in this paper.

For completeness, a summary of the governing equations of plasticity and viscoplasticity and the role of plastic dissipation is given in Section 2.1. Details concerning the numerical implementation are discussed in Section 5.

2 Classical Plasticity and Viscoplasticity

Let $\Omega \subset \mathbb{R}^3$ be the reference configuration of the body of interest. We assume Ω open bounded with smooth boundary $\partial\Omega$ and closure denoted by $\bar{\Omega}$. Let $\mathbf{u}:\Omega \to \mathbb{R}^3$ be the displacement field and $\boldsymbol{\epsilon}(\mathbf{x}) := \partial_{\mathbf{x}}^s \mathbf{u}(\mathbf{x})$, the strain tensor at a point $\mathbf{x} \in \Omega$. We denote by $\tau \to \boldsymbol{\epsilon}(\mathbf{x}, \tau)$, where $\tau \in (-\infty, t]$, the strain history at a point $\mathbf{x} \in \Omega$ up to time $t \in \mathbb{R}_+$. Typically, we assume that this mapping is at least C^1. Often, explicit indication of the spatial argument $\mathbf{x}$ will be omitted.

2.1 Classical Rate-independent Plasticity. We assume that the elastic response is governed by a stored energy function $W(\boldsymbol{\epsilon} - \boldsymbol{\epsilon}^p)$. Plastic flow, in the other hand, is an *irreversible* process described in terms of the history of the strain tensor $\boldsymbol{\epsilon}$ and two additional variables; the *plastic strain* $\boldsymbol{\epsilon}^p$, and a suitable set of $m \geq 0$ internal plastic variables, $\mathbf{q}$, often referred to as hardening parameters. The admissible states are *constrained* to remain on or within an elastic domain, denoted by $\mathbb{K}_\sigma \subset \mathbb{R}^6$ in what follows, and defined in terms of a *yield condition* $f(\boldsymbol{\sigma}, \mathbf{q}) \leq 0$ as

$$\overline{\mathbb{K}}_\sigma := \{(\boldsymbol{\tau}, \mathbf{q}) \in \mathbb{R}^6 \times \mathbb{R}^m \mid f(\boldsymbol{\tau}, \mathbf{q}) \leq 0\}. \tag{1}$$

The notion of *irreversibility* is built into the formulation by introducing nonsmooth equations of evolution for $\boldsymbol{\epsilon}^p$ and $\mathbf{q}$ referred to as *flow rule* and *hardening law*, respectively, and summarized for convenience in Box 1. Here, $\mathbf{D} \in \mathbb{R}^m \times \mathbb{R}^m$ denotes a (constant) *symmetric positive definite* matrix. For simplicity, attention is restricted to the associative case. The consistency parameter $\dot{\gamma} \geq 0$ obeys the unilateral constraints conditions also summarized in Box 1. These are the so-called *loading/unloading* conditions stated in the form typically found in problems with unilateral constraints, i.e., Duvaut and Lions (1972), and Strang (1986). Suitable initial conditions are typically prescribed at time $t = 0$.

2.2 The Principle of Maximum Plastic Dissipation. First, attention will be focused on the case of perfect plasticity. In its local form, the principle of maximum plastic dissipation states that for *given* plastic strains $\boldsymbol{\epsilon}^p$, among all possible stresses $\boldsymbol{\tau}$ satisfying the yield criterion, the plastic dissipation given by $\mathbb{D}^p := \boldsymbol{\tau}: \dot{\boldsymbol{\epsilon}}^p$ attains its *maximum* for the *actual stress tensor* $\boldsymbol{\sigma}$. Accordingly, denoting by $\overline{\mathbb{K}}_\sigma$ the closure of the elastic range in stress space, the actual stress $\boldsymbol{\sigma} \in \overline{\mathbb{K}}_\sigma$ is the argument of the maximum principle:

$$\boldsymbol{\sigma} = \arg \left[\max_{\boldsymbol{\tau} \in \overline{\mathbb{K}}_\sigma} \{\boldsymbol{\tau}: \dot{\boldsymbol{\epsilon}}^p\}\right]. \tag{2}$$

The fundamental significance of this principle emanates from the following:

Proposition 2.1 Maximum plastic dissipation implies normality in stress space, loading/unloading conditions in Kuhn-Tucker form and convexity of the yield surface.

Proof: The proof is straightforward. Introduce the cone

$$K^p := \{\dot{\delta} \in L^2(\Omega) \mid \dot{\delta} \geq 0\}. \tag{3}$$

(i) Elastic stress-strain relations

$$\boldsymbol{\sigma} = \partial_{\boldsymbol{\epsilon}} W(\boldsymbol{\epsilon} - \boldsymbol{\epsilon}^p), \quad \text{where: } \boldsymbol{\epsilon} := \partial_{\mathbf{x}}^s \mathbf{u}$$

(ii) Associative flow rule

$$\dot{\boldsymbol{\epsilon}}^p = \dot{\gamma}\, \partial_{\boldsymbol{\sigma}} f(\boldsymbol{\sigma}, \mathbf{q})$$

(iii) Hardening law

$$\dot{\mathbf{q}} = -\dot{\gamma}\, \mathbf{D}\, \partial_{\mathbf{q}} f(\boldsymbol{\sigma}, \mathbf{q})$$

(iv) Yield and loading/unloading conditions

$$f(\boldsymbol{\sigma}, \mathbf{q}) \leq 0$$
$$\dot{\gamma} \geq 0$$
$$\dot{\gamma}\, f(\boldsymbol{\sigma}, \mathbf{q}) \equiv 0 \quad \text{and} \quad \dot{\gamma}\, \dot{f}(\boldsymbol{\sigma}, \mathbf{q}) = 0$$

Box 1 Classical infinitesimal rate-independent plasticity

Downloaded 03 May 2010 to 171.66.16.244. Redistribution subject to ASME license or copyright; see http://www.asme.org/terms/Terms_Use.cfm

The standard Kuhn-Tucker optimality conditions for problem (2) are formulated in terms of the Lagrangian functional

$$\overline{\mathbb{L}}^p(\tau,\dot{\delta};\dot{\epsilon}^p) := -\tau:\dot{\epsilon}^p + \dot{\delta} f(\tau), \tag{4}$$

where $\dot{\epsilon}^p$ is regarded as a *fixed but otherwise arbitrary parameter*. The optimal point $(\sigma, \dot{\gamma})$ is characterized by the conditions (see, e.g., Luenberger (1984, page 314), or Strang (1986, page 724)),

$$\left.\frac{\partial \overline{\mathbb{L}}^p}{\partial \tau}\right|_{\substack{\tau=\sigma \\ \delta=\gamma}} \equiv -\dot{\epsilon}^p{}_{\tau=\sigma} + \dot{\gamma}\partial_\sigma f(\sigma) = 0 \tag{5}$$

$$\dot{\gamma} \geqq 0,\ f(\sigma) \leq 0, \text{ and } \dot{\gamma} f(\sigma) \equiv 0 \text{ and } \dot{\gamma}\dot{f}(\sigma) = 0. \tag{6}$$

These conditions are the statement of normality of the flow rule and the loading/unloading conditions. Convexity of $\mathbb{K}_\sigma$ is easily proved. □

2.3 The Classical Viscoplastic Regularization. Classical viscoplastic models of the Perzyna type (Perzyna, 1966) may be considered as penalty regularizations of rate-independent plasticity. The simplest model is based on a regularized flow rule and hardening law of the form

$$\dot{\epsilon}^{vp} = \frac{\langle f(\sigma,\mathbf{q})\rangle}{\eta}\,\partial_\sigma f(\sigma,\mathbf{q})$$

$$\dot{\mathbf{q}} = -\frac{\langle f(\sigma,\mathbf{q})\rangle}{\eta}\,\mathbf{D}\partial_{\mathbf{q}} f(\sigma,\mathbf{q}), \tag{7}$$

where $\eta \in (0, \infty)$ is a fluidity parameter, and $\langle\bullet\rangle$ denotes the MacAuly bracket as $\langle x\rangle := (x + |x|)/2$.

The viscoplastic regularization of the principle of maximum plastic dissipation is constructed as follows: First, consider perfect viscoplasticity; i.e., $\mathbf{q} \equiv \mathbf{0}$. Introduce the function $\gamma^+ : \mathbb{R} \to \mathbb{R}_+$ defined as

$$\gamma^+(x) := \begin{cases} 0 & \text{iff} \quad x \leq 0 \\ \dfrac{1}{2}x^2 & \text{iff} \quad x \geq 0. \end{cases} \tag{8}$$

Observe that $\dfrac{d}{dx}\gamma^+(x) = \langle x\rangle$. These conditions ensure that γ^+ qualifies as a *penalty function*, (see Luenberger, 1984, page 366). For fixed $\dot{\epsilon}^{vp}$ define the local penalty functional $\mathbb{D}^{vp}_\eta : \mathbb{R}^6 \times \mathbb{R}^6 \to \mathbb{R}$ by

$$\mathbb{D}^{vp}_\eta(\sigma;\dot{\epsilon}^{vp}) := \sigma:\dot{\epsilon}^{vp} - \frac{1}{\eta}\gamma^+(f(\sigma)). \tag{9}$$

Clearly, $\mathbb{D}^{vp}_\eta$ represents the sum of the *viscous and plastic* dissipations. Let $\sigma_\eta \in \mathbb{R}^6$ be a solution of the *unconstrained* viscoplastic problem for a given value $\eta > 0$. It readily follows that the optimality condition for the (unconstrained) problem

$$\sigma_\eta := arg[\min_{\tau\in\mathbb{R}^6} \{-\mathbb{D}^{vp}_\eta(\tau,\dot{\epsilon}^{vp})\}], \tag{10}$$

renders the viscoplastic flow rule $(7)_1$. In addition, as $\eta \to 0$, the viscoplastic solution $\sigma_\eta \to \sigma$, where σ is the solution of the rate independent model.

2.4 Extension to Include Internal Variables. Internal (hardening) variables $\mathbf{q}$, with evolution equation given in Box 1, can be readily incorporated in the present variational framework as follows. Consider an *uncoupled* free energy function $\Psi : \mathbb{R}^6 \times \mathbb{R}^6 \times \mathbb{R}^m \to \mathbb{R}$ of the form

$$\Psi(\epsilon,\epsilon^p,\mathbf{q}) := W(\epsilon-\epsilon^p) + \frac{1}{2}\mathbf{q}\bullet\mathbf{D}^{-1}\mathbf{q}. \tag{11}$$

The dissipation function $\mathbb{D}^p : \mathbb{R}^6 \times \mathbb{R}^6 \times \mathbb{R}^m \times \mathbb{R}^6 \times \mathbb{R}^m \to \mathbb{R}$ is defined in strain space by means of the general relation

$$\mathbb{D}^p(\epsilon,\epsilon^p,\mathbf{q};\dot{\epsilon}^p,\dot{\mathbf{q}}) := -\frac{\partial\Psi(\epsilon,\epsilon^p,\mathbf{q})}{\partial\epsilon^p}:\dot{\epsilon}^p - \frac{\partial\Psi(\epsilon,\epsilon^p,\mathbf{q})}{\partial\mathbf{q}}:\dot{\mathbf{q}}. \tag{12}$$

By making use of the stress-strain relation $\sigma = \partial_\epsilon W(\epsilon - \epsilon^p)$ along with the assumed uncoupled form (11) for Ψ, the general expression (12) leads to the dissipation function $\mathbb{D}^p : \mathbb{R}^6 \times \mathbb{R}^m \times \mathbb{R}^6 \times \mathbb{R}^m \to \mathbb{R}$ in stress space, given by

$$\mathbb{D}^p(\sigma,\mathbf{q};\dot{\epsilon}^p,\dot{\mathbf{q}}) := \sigma:\dot{\epsilon}^p - \dot{\mathbf{q}}\bullet\mathbf{D}^{-1}\mathbf{q}. \tag{13}$$

The principle of maximum dissipation then characterizes the actual solution $(\sigma, \mathbf{q}) \in \mathbb{R}^6 \times \mathbb{R}^m$ for given $(\dot{\epsilon}^p, \dot{\mathbf{q}})$ as the argument of the maximum principle

$$(\sigma,\mathbf{q}) = \arg[\max_{(\tau,p)\in\overline{K}_\sigma} \{\mathbb{D}^p(\tau,\mathbf{p};\dot{\epsilon}^p,\mathbf{q})\}]. \tag{14}$$

As in Proposition 2.1, this *constrained* maximum principle is transformed into an unconstrained minimum principle by introducing the Lagrangian

$$\overline{\mathbb{L}}^p(\tau,\mathbf{p},\dot{\delta};\dot{\epsilon}^p,\dot{\mathbf{q}}) := -\mathbb{D}^p(\tau,\mathbf{p};\dot{\epsilon}^p,\mathbf{q}) + \dot{\delta} f(\tau,\mathbf{p}). \tag{15}$$

Once more, the Kuhn-Tucker optimality conditions yield the flow rule, hardening law, and loading/unloading conditions; i.e.,

$$\left.\frac{\partial \overline{\mathbb{L}}^p}{\partial \tau}\right|_{\substack{\tau=\sigma \\ \mathbf{p}=\mathbf{q} \\ \dot{\delta}=\dot{\gamma}}} \equiv -\dot{\epsilon}^p + \dot{\gamma}\partial_\sigma f(\sigma,\mathbf{q}) = 0 \tag{16a}$$

$$\left.\frac{\partial \overline{\mathbb{L}}^p}{\partial \mathbf{q}}\right|_{\substack{\tau=\sigma \\ \mathbf{p}=\mathbf{q} \\ \dot{\delta}=\dot{\gamma}}} \equiv \mathbf{D}^{-1}\dot{\mathbf{q}} + \dot{\gamma}\partial_{\mathbf{q}} f(\sigma,\mathbf{q}) = 0 \tag{16b}$$

$$\dot{\gamma} \geq 0,\ f(\sigma,\mathbf{q}) \leq 0, \text{ and } \dot{\gamma} f(\sigma,\mathbf{q}) \equiv 0 \text{ and } \dot{\gamma}\dot{f}(\sigma,\mathbf{q}) = 0. \tag{16c}$$

Remark 2.1 Inclusion of internal variables in viscoplasticity follows the same lines as above. The dissipation function (9) now becomes

$$\mathbb{D}^{vp}_\eta(\tau,\mathbf{p};\dot{\epsilon}^{vp},\dot{\mathbf{q}}) := \tau:\dot{\epsilon}^{vp} - \frac{1}{\eta}\gamma^+(f(\tau,\mathbf{p})) - \mathbf{D}^{-1}\mathbf{p}\bullet\dot{\mathbf{q}}. \tag{17}$$

The actual solution is characterized as the argument of the *unconstrained* maximum principle

$$(\sigma_\eta,\mathbf{q}_\eta) := \arg[\min_{(\tau,\mathbf{p})\in\mathbb{R}^6\times\mathbb{R}^m} \{-\mathbb{D}^{vp}_\eta(\tau,\mathbf{p};\dot{\epsilon}^{vp},\dot{\mathbf{q}})\}]. \tag{18}$$

The viscoplastic flow rule and hardening law (7) then arise as optimality conditions of (18). □

3 Discrete Variational Formulation of Elastoplasticity

In this section we develop the discrete variational formulation of plasticity and viscoplasticity.

3.1 Some Basic Notation. Let V be the space of kinematically admissible variations (virtual displacements), defined as

$$V := \{\eta:\Omega\to\mathbb{R}^N \mid \eta\in[H^1(\Omega)]^N;\eta|_{\partial_u\Omega} = \mathbf{0}\}, \tag{19}$$

where $N \leq 3$ is the spatial dimension, $H^1(\Omega)$ denotes the space of functions with derivatives bounded in energy, and $\partial_u\Omega \subset \partial\Omega$ is the part of $\partial\Omega$ (the boundary of the body $\Omega \subset \mathbb{R}^N$) where the displacement field is specified as $\mathbf{u}|_{\partial_u\Omega} = \bar{\mathbf{u}}$. We let $\partial_\sigma\Omega \subset \partial\Omega$ be the part of the boundary where the stress vector is specified as $\sigma\,\hat{\mathbf{n}}|_{\partial_\sigma\Omega} = \bar{\mathbf{t}}$.

Given a functional $\Pi : V \to \mathbb{R}$ and a point $\mathbf{u} \in V$ the *Gateaux variation* at $\mathbf{u} \in V$ in the direction $\eta \in V$ as the limit (whenever it exists)

$$\delta\Pi(\mathbf{u};\eta) := \lim_{\alpha\to 0}\frac{\Pi(\mathbf{u}+\alpha\eta)-\Pi(\mathbf{u})}{\alpha} \equiv \frac{d}{d\alpha}\Pi(\mathbf{u}+\alpha\eta)|_{\alpha=0}. \tag{20}$$

Downloaded 03 May 2010 to 171.66.16.244. Redistribution subject to ASME license or copyright; see http://www.asme.org/terms/Terms_Use.cfm

This definition generalizes the notion of directional derivative of functions in Euclidean space. The *functional derivative* of $\Pi : V \to \mathbb{R}$ at $\mathbf{u} \in V$ is the element $\dfrac{\delta \Pi}{\delta \mathbf{u}}(\mathbf{u}) \in V$ which satisfies the relation

$$\delta \Pi(\mathbf{u};\eta) =: \left\langle \frac{\delta \Pi}{\delta \mathbf{u}}(\mathbf{u}), \eta \right\rangle_V, \qquad \eta \in V, \tag{21}$$

where $\langle \cdot, \cdot \rangle_V$ is the standard L_2-pairing.[1] In applications, (21) boils down to integration by parts of the expression for the Gateaux derivative.

3.2 Discrete Lagrangian for Elastoplasticity. Let $[0, T] \subset \mathbb{R}_+$ be the time interval of interest, and denote by $t \in [0, T]$ the *current time*. We shall designate by a *subscript* ξ the value of the variable at time $\xi \in [0, t]$.

3.2.1 Energy and Dissipation Functionals. We introduce the *total energy* available at current time t, by means of the Hu-Washizu functional

$$\mathrm{I\!I}_t(\mathbf{u}_t, \epsilon_t - \epsilon^p_t, \mathbf{q}, \sigma_t) := \int_\Omega \{ \Psi(\epsilon_t - \epsilon^p_t, \mathbf{q}) + \sigma_t : (\partial^S_x \mathbf{u}_t - \epsilon_t) \} d\Omega + \mathrm{I\!I}_{\mathrm{ext}}(\mathbf{u}_t), \tag{22a}$$

where

$$\Psi(\epsilon - \epsilon^p, \mathbf{q}) := W(\epsilon - \epsilon^p) + \frac{1}{2}\, \mathbf{q} \cdot \mathbf{D}^{-1} \mathbf{q}, \tag{22b}$$

and $\mathrm{I\!I}_{\mathrm{ext}}(\mathbf{u}_t)$ is the potential energy of the external loading at current time given by

$$\mathrm{I\!I}_{\mathrm{ext}}(\mathbf{u}_t) := - \int_\Omega \rho \mathbf{b}_t \cdot \mathbf{u}_t d\Omega - \int_{\partial_\sigma \Omega} \bar{\mathbf{t}} \cdot \mathbf{u}_t d\Gamma. \tag{22c}$$

Note that in (22) we have assumed that $\{\mathbf{u}, \epsilon, \sigma\}$ are independent variables. σ_{n+1} may then be viewed as a Lagrange multiplier that enforces (weakly) the constraint $\partial^S_x \mathbf{u}_{n+1} - \epsilon_{n+1} = \mathbf{0}$.

In addition, we introduce the Lagrangian functional associated with the plastic dissipation over the entire body up to current time $t \in \mathbb{R}_+$, i.e.,

$$\mathrm{I\!L}^p_t := \int_0^t \int_\Omega [- \dot\gamma_\xi f(\partial_\epsilon W(\epsilon_\xi - \epsilon^p_\xi), \mathbf{q}_\xi) + \dot\epsilon^p_\xi : \partial_\epsilon W(\epsilon_\xi - \epsilon^p_\xi) - \dot{\mathbf{q}}_\xi \cdot \mathbf{D}^{-1} \mathbf{q}_\xi] d\Omega d\xi. \tag{23}$$

Here, $\xi \to \dot\gamma_\xi \in K^p$ is the plastic consistency parameter, K^p is the proper positive cone defined in (3), and $f(\partial_\epsilon W(\epsilon_\xi - \epsilon^p_\xi), \mathbf{q}_\xi) = 0$ defines the plastic yield surface at time $\xi \in [0, t]$. Observe that $\mathrm{I\!L}^p_t$ is formulated in terms of the strain tensor ϵ through the expression $\partial_\epsilon W(\epsilon - \epsilon^p)$, and not in terms of the stress tensor σ.

3.2.2 Discrete Lagrangian. We consider a *discrete plastic dissipation functional* obtained from its continuum counterpart defined by (23), by means of a backward-Euler differencing scheme. Explicitly, let $t = t_{n+1}$ be the current time, and let $t_{n+1} = t_n + \Delta t$, where $\Delta t > 0$ is the time step. From (23) we then have

$$\mathrm{I\!L}^p_{n+1} = \mathrm{I\!L}^p_n + \int_{t_n}^{t_{n+1}} \int_\Omega \{ \dot\epsilon^p_\xi : \partial_\epsilon W(\epsilon_\xi - \epsilon^p_\xi) - \dot\gamma_\xi f(\partial_\epsilon W(\epsilon_\xi - \epsilon^p_\xi), \mathbf{q}_\xi) - \dot{\mathbf{q}}_\xi \cdot \mathbf{D}^{-1} \mathbf{q}_\xi] d\Omega d\xi. \tag{24}$$

For convenience, we introduce the following notation

$$\chi_t := \{ \mathbf{u}_t, \epsilon_t, \sigma_t, \epsilon^p_t, \mathbf{q}_t, \gamma_t \}. \tag{25}$$

Assume that the history χ_ξ, $\xi \in [0, t_n]$, up to time t_n *is given and fixed*. Evaluation of (24) by a backward-Euler algorithm then results in

$$\mathrm{I\!L}^p(\chi_{n+1}) := - \mathrm{I\!L}^p_n + \int_\Omega [(\epsilon^p_{n+1} - \epsilon^p_n) : \partial_\epsilon W(\epsilon_{n+1} - \epsilon^p_{n+1}) - \mathbf{q}_{n+1} \cdot \mathbf{D}^{-1}(\mathbf{q}_{n+1} - \mathbf{q}_n) - \gamma_{n+1} f(\partial_\epsilon W(\epsilon_{n+1} - \epsilon^p_{n+1}), \mathbf{q}_{n+1})] d\Omega, \tag{26}$$

where interchange of spatial and time integration is allowed by the assumed smoothness of the integrand, and we have set $\gamma_{n+1} := \dot\gamma_{n+1} \Delta t$. The functional $\mathrm{I\!L}^p(\chi_{n+1})$ is the algorithmic approximation to the plastic dissipation $\mathrm{I\!L}^p_{n+1}$ up to time t_{n+1}.

As the basis for our discrete variational formulation, we consider *the total energy available at time t_n expressed in terms of χ_{n+1}, and denoted by* $\hat{\mathrm{I\!I}}_n(\chi_{n+1})$. $\hat{\mathrm{I\!I}}_n(\chi_{n+1})$ is defined as the sum of the energy $\mathrm{I\!I}_{n+1}(\chi_{n+1})$ at t_{n+1} and the incremental dissipation in $[t_n, t_{n+1}]$; i.e.,

Potential energy $|_n$ = *Potential energy* $|_{n+1}$ + *Dissipation* $|_n^{n+1}$

Accordingly, $\hat{\mathrm{I\!I}}_n(\chi_{n+1})$ is given by the relation

$$\hat{\mathrm{I\!I}}_n(\chi_{n+1}) := \mathrm{I\!I}_{n+1}(\chi_{n+1}) + [\mathrm{I\!L}^p(\chi_{n+1}) - \mathrm{I\!L}^p_n]. \tag{27a}$$

Substitution of (26) into (27) yields the explicit expression

$$\hat{\mathrm{I\!I}}_n(\chi_{n+1}) := \int_\Omega \hat{\mathrm{I\!L}}_n(\chi_{n+1}) dV + \mathrm{I\!I}_{\mathrm{ext}}(\mathbf{u}_{n+1}), \tag{27b}$$

where $\hat{\mathrm{I\!L}}_n(\chi_{n+1})$ is the *discrete Lagrangian* associated with $\hat{\mathrm{I\!I}}_n(\chi_{n+1}) - \mathrm{I\!I}_{\mathrm{ext}}(\mathbf{u}_{n+1})$ and is defined as

$$\hat{\mathrm{I\!L}}_n(\chi_{n+1}) := W(\epsilon^p_{n+1} - \epsilon_{n+1}) + \frac{1}{2}\, \mathbf{q}_{n+1} \cdot \mathbf{D}^{-1} \mathbf{q}_{n+1} + \sigma_{n+1} : [\partial^S_x \mathbf{u}_{n+1} - \epsilon_{n+1}] - \gamma_{n+1} f(\partial_\epsilon W(\epsilon_{n+1} - \epsilon^p_{n+1}), \mathbf{q}_{n+1}) + (\epsilon^p_{n+1} - \epsilon^p_n) : \partial_\epsilon W(\epsilon_{n+1} - \epsilon^p_{n+1}) - \mathbf{q}_{n+1} \cdot \mathbf{D}^{-1}(\mathbf{q}_{n+1} - \mathbf{q}_n). \tag{28}$$

In the ensuring developments we shall assume that $\mathbf{q} \in V_{\mathbf{q}} := [L_2(\Omega)]^m$, $\sigma \in V_\sigma := [L_2(\Omega)]^6$, and $\epsilon \in V_\epsilon := [L_2(\Omega)]^6$. It is known (Temam (1985)), that the latter assumption is not realistic.[2]

3.3 Euler-Lagrange Equations: Spatial Conservation Laws. We show that the Euler-Lagrange equations associated with (27) yield (i) the equilibrium equations, (ii) the strain-displacement relations, (iii) the elastic constitutive equations, (iv) the closest-point-projection algorithm, and (v) the discrete Kuhn-Tucker conditions. Explicitly, by making use of the Gateaux derivative formula one obtains the following result:

Proposition 3.1 The stationary conditions of the time-discretized functional (27) result in the following weak forms

$$\delta \hat{\mathrm{I\!I}}_n(\chi_{n+1}; \eta) = \int_\Omega [\sigma_{n+1} : \partial^S_x \eta - \rho \mathbf{b} \cdot \eta] d\Omega - \int_{\partial_\sigma \Omega} \bar{\mathbf{t}} \cdot \eta d\Gamma = 0, \tag{29a}$$

$$\delta \hat{\mathrm{I\!I}}_n(\chi_{n+1}; \tau) = \int_\Omega \tau : [\partial^S_x \mathbf{u}_{n+1} - \epsilon_{n+1}] d\Omega = 0, \tag{29b}$$

$$\delta \hat{\mathrm{I\!I}}_n(\chi_{n+1}, \xi) \int_\Omega \xi : \{ [- \sigma_{n+1} + \partial_\epsilon W(\epsilon_{n+1} - \epsilon^p_{n+1})], + \mathbf{C}_{n+1} : [\epsilon^p_{n+1} - \epsilon^p_n - \gamma_{n+1} \partial_\sigma f_{n+1}] \} d\Omega = 0, \tag{29c}$$

$$\delta \hat{\mathrm{I\!I}}_n(\chi_{n+1}; \xi^p) = - \int_\Omega \xi^p : \mathbf{C}_{n+1} : [\epsilon^p_{n+1} - \epsilon^p_n - \gamma_{n+1} \partial_\sigma f_{n+1}] d\Omega = 0, \tag{29d}$$

$$\delta \hat{\mathrm{I\!I}}_n(\chi_{n+1}; \mathbf{p}) = - \int_\Omega \mathbf{p} \cdot [\mathbf{D}^{-1}(\mathbf{q}_{n+1} - \mathbf{q}_n) + \gamma_{n+1} \partial_{\mathbf{q}} f_{n+1}] d\Omega = 0, \tag{29e}$$

[1] V is a Sobolev space, with $V = V^*$ and duality pairing defined by the L_2-inner product (i.e., $\langle \eta_1, \eta_2 \rangle := \int_\Omega \eta_1 \cdot \eta_2 \, dV$.

[2] The so-called *space of bounded deformations*, Temam and Strang (1980), is the proper setup for elastoplasticy (see Temam (1985)).

Downloaded 03 May 2010 to 171.66.16.244. Redistribution subject to ASME license or copyright; see http://www.asme.org/terms/Terms_Use.cfm

$$\delta\hat{\Pi}_n(\chi_{n+1};\lambda) = \int_\Omega f_{n+1}\lambda d\Omega = 0, \tag{29f}$$

for arbitrary $\eta \in V$, $\tau \in V_\sigma$, $\xi \in V_\epsilon$, $\xi^p \in V_\epsilon$, $\mathbf{p} \in V_q$, *and* $\lambda \in K^p$, *where* $\mathbf{C}_{n+1} := \partial_\epsilon^2 W\ (\epsilon_{n+1} - \epsilon^p_{n+1})$, *denotes the (generally nonconstant) elasticities, and* $f_{n+1} := f\ (\partial_\epsilon W\ (\epsilon_{n+1} - \epsilon^p_{n+1}), \mathbf{q}_{n+1})$.

Proof: Follows by a standard argument employing the Gateaux derivative formula along with a systematic application of the chain rule. In particular, note that

$$\frac{d}{d\alpha} f(\partial_\epsilon W(\epsilon_{n+1} - \epsilon^p_{n+1} - \alpha\xi^p), \mathbf{q})|_{\alpha=0} = -\partial_\sigma f_{n+1} : \mathbf{C}_{n+1} : \xi^p. \tag{30}$$

A similar relation is obtained for $W\ (\epsilon_{n+1} - \epsilon^p_{n+1})$. □

Corollary 3.1 The Euler-Lagrange equations associated with the discrete Lagrangian (27) *take the form*

$$-\ \mathrm{div}\ \sigma_{n+1} - \rho\ \mathbf{b} = \mathbf{0}, \tag{31a}$$

$$\sigma_{n+1}\mathbf{n} = \bar{\mathbf{t}} \text{ on } \partial_\sigma\Omega \tag{31b}$$

$$\partial_x^S \mathbf{u}_{n+1} - \epsilon_{n+1} = \mathbf{0}, \tag{31c}$$

$$\sigma_{n+1} - \partial_\epsilon W(\epsilon_{n+1} - \epsilon^p_{n+1}) = \mathbf{0}, \tag{31d}$$

$$-\epsilon^p_{n+1} + \epsilon^p_n + \gamma_{n+1}\partial_\sigma f_{n+1} = \mathbf{0}, \tag{31e}$$

$$\mathbf{D}^{-1}(\mathbf{q}_{n+1} - \mathbf{q}_n) + \gamma_{n+1}\partial_{\mathbf{q}} f_{n+1} = \mathbf{0}, \tag{31f}$$

$$f_{n+1} \le 0,\ \gamma_{n+1} \ge 0,\ \gamma_{n+1} f_{n+1} = 0. \tag{31g}$$

Proof: Follows at once from variational equations (29*a*)–(29*f*) by making use of the functional derivative formula (21). □

Remark 3.1 Assume that $\mathbf{C} := \partial_\epsilon^2 W = constant$, and $\mathbf{q} = \mathbf{0}$. Combining (31*b*) and (31*d*) one obtains

$$\begin{aligned} \sigma^{\text{trial}}_{n+1} &:= \mathbf{C}:(\epsilon_{n+1} - \epsilon_n), \\ \sigma_{n+1} &= \sigma^{\text{trial}}_{n+1} - \gamma_{n+1}\mathbf{C}:\partial_\sigma f(\sigma_{n+1}). \end{aligned} \tag{32}$$

This is the expression of the so-called *closest-point-projection* algorithm (see Simo and Hughes, 1987). According to (32), the final stress σ_{n+1} is the projection of the trial stress $\sigma^{\text{trial}}_{n+1}$ onto the elastic domain, in the energy norm defined by the elasticities $\mathbf{C}$. □

3.4 Extension to Viscoplasticity. The variational formulation of viscoplasticity follows the same lines as the rate-independent case just discussed, and is based on the viscoplastic regularization of maximum plastic dissipation considered in Section 2.3. First, since $\gamma_{n+1} \ge 0$ is no longer an independent variable, we set

$$\chi_t := \{\mathbf{u}_t, \epsilon_t, \sigma_t, \epsilon^{vp}_t, \mathbf{q}_t\}. \tag{33}$$

Next, in view of (7), the viscoplastic counterpart of the time-discretized dissipation functional (26) takes the following form

$$\begin{aligned} \mathbb{L}^{vp}_{n+1}(\chi_{n+1}) := \mathbb{L}^{vp}_n + \int_\Omega [&(\epsilon^{vp}_{n+1} - \epsilon^{vp}_n):\partial_\epsilon W(\epsilon_{n+1} - \epsilon^{vp}_{n+1}) \\ &- \mathbf{q}_{n+1}\cdot\mathbf{D}^{-1}(\mathbf{q}_{n+1} - \mathbf{q}_n) \\ &- \frac{\Delta t}{\eta}\gamma_{n+1} f(\partial_\epsilon W(\epsilon_{n+1} - \epsilon^p_{n+1}), \mathbf{q}_{n+1})]d\Omega, \end{aligned} \tag{34}$$

where $\eta > 0$, and $\gamma^+_{n+1} : \mathbb{R} \to \mathbb{R}_+$ is defined by (8). The viscoplastic counterpart of functional (27) then becomes

$$\hat{\Pi}_n(\chi_{n+1}) := \Pi_{n+1}(\chi_{n+1}) + [\mathbb{L}^{vp}_{n+1}(\chi_{n+1}) - \mathbb{L}^{vp}_n]. \tag{35}$$

Consequently, the *Lagrangian density* $\hat{\mathbb{L}}_n(\chi_{n+1})$ associated with $\hat{\Pi}_n(\chi_{n+1}) - \Pi_{\text{ext}}\ (\mathbf{u}_{n+1})$ is given in the viscoplastic case by

$$\begin{aligned} \hat{\mathbb{L}}_n(\chi_{n+1}) := W(\epsilon_{n+1} - \epsilon^{vp}_{n+1}) + \frac{1}{2}\mathbf{q}_{n+1}\cdot\mathbf{D}^{-1}\mathbf{q}_{n+1} \\ - \frac{\Delta t}{\eta}\gamma^+(f(\partial_\epsilon W(\epsilon_{n+1} - \epsilon^{vp}_{n+1}), \mathbf{q}_{n+1})) + \sigma_{n+1}:(\partial_x^S \mathbf{u}_{n+1} - \epsilon_{n+1}) \\ + (\epsilon^{vp}_{n+1} - \epsilon^{vp}_n):\partial_\epsilon W(\epsilon_{n+1} - \epsilon^{vp}_n) - \mathbf{q}_{n+1}\cdot\mathbf{D}^{-1}(\mathbf{q}_{n+1} - \mathbf{q}_n). \end{aligned} \tag{36}$$

Finally, the first four Euler-Lagrange equations remain unchanged and are given by (31*a*)–(31*d*) (or by (29*a*)–(29*c*) in weak form). The last two Euler-Lagrange equations, which are given by (31*e*), (31*f*) in the rate-independent case, are now replaced by

$$\frac{\delta\hat{\Pi}_n(\chi_{n+1})}{\delta\epsilon^{vp}_{n+1}} := -\epsilon^{vp}_{n+1} + \epsilon^{vp}_n + \frac{\Delta t\langle f_{n+1}\rangle}{\eta}\partial_\sigma f_{n+1} = \mathbf{0} \tag{37}$$

$$\frac{\delta\hat{\Pi}_n(\chi_{n+1})}{\delta\mathbf{q}_{n+1}} := -\mathbf{D}^{-1}(\mathbf{q}_{n+1} - \mathbf{q}_n) - \frac{\Delta t\langle f_{n+1}\rangle}{\eta}\partial_{\mathbf{q}} f_{n+1} = \mathbf{0}, \tag{38}$$

where $f_{n+1} := f(\partial_\epsilon W\ (\epsilon_{n+1} - \epsilon^p_{n+1}), \mathbf{q}_{n+1})$.

4 Material Conservation Laws

We are now in the position to exploit the variational structure emanating from the discrete Lagrangian (27), and derive material conservation laws by means of Noether's theorems. Recall that associated with the group of material translations, with infinitesimal generator $\partial/\partial\mathbf{x}$, there is a Noether quantity which can be recognized to be the counterpart of Eshelby's energy momentum tensor. The divergence-free character of this tensor is a conservation law that reflects the invariance of the Lagrangian relative to the group of material translations, and leads to path-independent integrals. Since this invariance is not present in plasticity and viscoplasticity, the divergence of the associated Noether quantity can no longer vanish. Application of the divergence theorem now results in a line integral plus a domain integral. The net result, then, is a path-domain independent integral with a compelling physical interpretation explored in Section 4.4. Other conserved quantities associated with classical material symmetries can be related to Eshelby's energy momentum tensor, as will be explained.

4.1 Conservation Laws and Noether's Theorem. Here we state a very restricted version of Noether's first theorem suited for our needs. We refer to Olver (1986) for a proof and a complete account. We consider a system which is governed by the Euler-Lagrange equations of a Lagrangian

$$\Pi(\chi) := \int_\Omega \mathbb{L}(\mathbf{x}, \chi, \partial_x\chi)dV, \tag{39}$$

where Ω is an open subset of $\mathbb{R}^N$, $\mathbf{x} := (x^1, x^2, \ldots, x^N)$ denotes the independent variables, while $\chi = (\chi^1, \chi^2, \ldots, \chi^m)$ designates the dependent variables. In addition, $\partial_x\chi$ is a shorthand notation for all possible first-order derivatives $\partial\chi^j/\partial x^i$. We then have

Proposition 4.1 (Olver, 1986) *A vector field* $\mathbf{v} = \xi^i(\mathbf{x}, \chi)\dfrac{\partial}{\partial x^i} + \phi^j(\mathbf{x}, \chi)\dfrac{\partial}{\partial\chi^j}$ *is an infinitesimal generator of a variational symmetry group of* Π *if and only if*

$$pr^{(1)}\mathbf{v}(\mathbb{L}) + \mathbb{L}\mathrm{Div}\xi = 0, \tag{40a}$$

where $pr^{(1)}\mathbf{v}$ *is the first prolongation of* $\mathbf{v}$ *given by*

$$pr^{(1)}\mathbf{v} = \mathbf{v} + \phi^j_i\frac{\partial}{\partial\chi^j_{,i}} \tag{40b}$$

with $\phi^j_i = D_i\phi^j - \chi^j_{,k}D_i\xi^k$. *Here* $\chi^j_{,k} := \dfrac{\partial\chi^j}{\partial x^k}$ *and* D_i *designates the total derivative with respect to* x^i. □

The version of Noether's theorem now reads:

Proposition 4.2 If $\mathbf{v}$ is the generator of a variational symmetry group of Π (χ), *then*

Downloaded 03 May 2010 to 171.66.16.244. Redistribution subject to ASME license or copyright; see http://www.asme.org/terms/Terms_Use.cfm

Table 1 Symmetry groups underlying the material conservation laws

Symmetry Group	*Infinitesimal generator*
Translations	$\dfrac{\partial}{\partial x^i}$
Rotations	$\varepsilon^{ijk}\left(x_i\dfrac{\partial}{\partial x^j}-u_i\dfrac{\partial}{\partial u^j}\right)$
Dilatation $(W(\lambda\nabla u)=\lambda^p W(\nabla u))$	$x^i\dfrac{\partial}{\partial x^i}+\dfrac{p-N}{p}u^j\dfrac{\partial}{\partial u^j}$

$$P^i=\phi^j\frac{\partial\hat{\mathbb{L}}}{\partial\chi^j_{,i}}+\xi^i\hat{\mathbb{L}}-\xi^k\chi^j_{,k}\frac{\partial\hat{\mathbb{L}}}{\partial\chi^j_{,i}} \tag{40c}$$

are the components of the conservation law: $Div\,\mathbf{P}=0$ *for the Euler-Lagrange equations.* □

Next, we apply these results to the Lagrangian formulation of viscoplasticity and plasticity derived in the preceding sections. In particular, we are concerned with the symmetries and their associated infinitesimal generators summarized in Table 1. We note that in this table p is the degree of homogeneity of W and N is the space dimension.

The Noether quantity $\mathbf{P}$ associated with the translations is given by

$$T^j_i=\hat{\mathbb{L}}\delta^j_i-u^k_{,i}\frac{\partial\hat{\mathbb{L}}}{\partial u^k_{,j}}\ \text{i.e.;}\ \mathbf{T}=\hat{\mathbb{L}}\mathbf{1}-\nabla^T\mathbf{u}\frac{\partial\hat{\mathbb{L}}}{\partial\nabla\mathbf{u}}, \tag{41a}$$

and that related to the rotations is

$$L^{ki}=\epsilon^{klj}\left(x_l T^i_j+u_l\frac{\partial\hat{\mathbb{L}}}{\partial u^j_{,i}}\right), \tag{41b}$$

while that associated with the dilatation is

$$M^i=\frac{p-N}{p}u^j\frac{\partial\hat{\mathbb{L}}}{\partial u^j_{,i}}+x^jT^i_j. \tag{41c}$$

Remarks 4.1:

(1) In the present context, invariance of the Lagrangian relative to the group generated by $\partial/\partial x^i$ means simply that $\hat{\mathbb{L}}$ does *not depend explicitly* on x^i. □

(2) For elasticity, Ω is the reference configuration, $\mathbf{x}$ are the (material) coordinates, and $\chi:\Omega\to\mathbb{R}^3$ the configurations. $\mathbf{T}$ is divergence-free for a homogeneous material and constitutes Eshelby's conservation law (see Marsden and Hughes (1983, Sec. 5.5) for a review). In addition, $\mathbf{L}$ is divergence-free for an isotropic material, and $\mathbf{M}$ is divergence-free when W is homogeneous of degree p (usually quadratic; i.e., $p=2$). The tensor $\mathbf{T}$, first introduced by Eshelby (1956), goes by the name of energy-momentum tensor. The conservations laws associated with $\mathbf{T}$, $\mathbf{L}$, and $\mathbf{M}$ were first obtained using Noether's theorem by Gunther (1962) and independently by Knowles and Sternberg (1972). □

(3) Suppose that $\mathbf{T}$ is not divergence-free; i.e., $\mathrm{div}_{\mathbf{x}}\mathbf{T}+\mathbf{f}=0$ where $\mathbf{f}\neq 0$. Consider Ω_1 and Ω_2, with $\Omega_1\subset\Omega_2$ and $A:=\Omega_2-\Omega_1$ (see Fig. 1). Application of the divergence theorem yields

$$\int_{\partial\Omega_2}\mathbf{T}\hat{\mathbf{n}}\,d\Gamma-\int_{\partial\Omega_1}\mathbf{T}\hat{\mathbf{n}}\,d\Gamma=\int_A\mathrm{div}_{\mathbf{x}}\mathbf{T}\,dV\equiv-\int_A\mathbf{f}\,dV. \tag{42a}$$

However, since $\Omega_2=\Omega_1\cup A$, it follows that

$$\mathbf{J}^*:=\int_{\partial\Omega_2}\mathbf{T}\hat{\mathbf{n}}\,d\Gamma+\int_{\Omega_2}\mathbf{f}\,dV=\int_{\partial\Omega_1}\mathbf{T}\hat{\mathbf{n}}\,d\Gamma+\int_{\Omega_1}\mathbf{f}\,dV. \tag{42b}$$

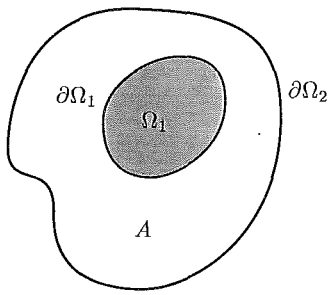


Fig. 1 Integration contours illustrating path-domain independence

Hence, $\mathbf{J}^*$ is path-domain independent. A similar argument can be advanced when $\mathbf{L}$ or $\mathbf{M}$ are not divergence-free. □

(4) The (energy-momentum) tensor $\mathbf{T}$ is nonsymmetric. The fact that $\mathbf{T}$ can be symmetrized (without changing the value of $\mathbf{J}^*$) is a standard result in classical field theory that goes back to Belinfante (1939) and Rosenfeld (1940). We refer to Soper (1976) for a detailed step-by-step account of the procedure. □

(5) In the context of elasticity, $\mathrm{div}_{\mathbf{x}}\mathbf{T}=0$ and (42*b*) reduces to the $\mathbf{J}$-integral. The presence of a singularity (a defect) inside Ω_1 gives a nonvanishing value for J_i which is interpreted as the negative of the change of the total potential energy of the system as the defect undergoes a unit translation along the x^i-axis (see Eshelby (1951, 1956)). $\mathbf{L}$ leads similarly to an integral which gives the negative of the change of the total potential energy of the system as a traction-free cavity undergoes a unit rotation while $\mathbf{M}$ leads to the same quantity when the cavity undergoes a self-similar expansion (cf., Budiansky and Rice (1973)). □

In what follows, the quantity, $\mathbf{T}$, along with the inhomogeneous term, $\mathbf{f}$, will be constructed for plasticity and viscoplasticity. Then $\mathbf{L}$ and $\mathbf{M}$ can be written down immediately.

Since the task of constructing $\mathbf{J}$, $\mathbf{M}$, $\mathbf{L}$ is straightforward for viscoplasticity, we consider this case first.

4.2 Viscoplasticity: Path-Domain Independent Integrals. For viscoplasticity, the volumetric Lagrangian density $\hat{\mathbb{L}}_n(\chi_{n+1})$ is defined by (36), to this one should add the term $-\rho\mathbf{b}_{n+1}\cdot\mathbf{u}_{n+1}$ in the presence of body forces. It follows immediately that

$$\frac{\partial\hat{\mathbb{L}}_n(\chi_{n+1})}{\partial(\partial_{\mathbf{x}}\chi_{n+1})}\equiv\frac{\partial\hat{\mathbb{L}}_n(\chi_{n+1})}{\partial(\partial_{\mathbf{x}}\mathbf{u}_{n+1})}=\sigma_{n+1}. \tag{43a}$$

Although $\hat{\mathbb{L}}_n(\chi_{n+1}(\mathbf{x}))$ does not depend explicitly on $\mathbf{x}\in\Omega$ for a homogeneous material (in the absence of body forces), the presence of $\{\epsilon^{vp}_n(\mathbf{x}),\mathbf{q}_n(\mathbf{x})\}$ destroys the invariance of $\hat{\mathbb{L}}_n(\chi_{n+1})$ relative to the group of *material translations*. The corresponding Noether quantity $\mathbf{T}^{vp}_{n+1}$ is obtained from (40) and (43*a*) as

$$\mathbf{T}^{vp}_{n+1}=\hat{\mathbb{L}}_n(\chi_{n+1})\mathbf{1}-(\partial_{\mathbf{x}}\mathbf{u}_{n+1})^T\sigma_{n+1}. \tag{43b}$$

In fact, by an explicit calculation we show below that $\mathrm{div}_{\mathbf{x}}\mathbf{T}^{vp}_{n+1}$ does not vanish. To this end, first observe that along an extremal the Euler-Lagrange equations (31*a*)–(31*f*) are *identically* satisfied. Consequently, the Lagrangian density (36) reduces to

$$\begin{aligned}\hat{\mathbb{L}}_n(\chi_{n+1})=&W(\epsilon_{n+1}-\epsilon^{vp}_{n+1})\\&+\frac{1}{2}\mathbf{q}_{n+1}\cdot\mathbf{D}^{-1}\mathbf{q}_{n+1}+\sigma_{n+1}:(\epsilon^{vp}_{n+1}-\epsilon^{vp}_n)\\&-\frac{\Delta t}{\eta}\gamma^+(f(\sigma_{n+1},\mathbf{q}_{n+1}))-\mathbf{q}_{n+1}\cdot\mathbf{D}^{-1}(\mathbf{q}_{n+1}-\mathbf{q}_n)\\&-\rho\mathbf{b}_{n+1}\cdot\mathbf{u}_{n+1}.\end{aligned} \tag{44}$$

With this expression at hand, we have the following

Proposition 4.2 The divergence of the Noether quantity

Downloaded 03 May 2010 to 171.66.16.244. Redistribution subject to ASME license or copyright; see http://www.asme.org/terms/Terms_Use.cfm

$\mathbf{T}^{vp}_{n+1}$ *associated with the group of material translations takes the value*

$$\mathrm{div}_{\mathbf{x}}\mathbf{T}^{vp}_{n+1} = -\sigma_{n+1}:\partial_{\mathbf{x}}\epsilon^{vp}_{n} + \mathbf{D}^{-1}\mathbf{q}_{n+1}\cdot\partial_{\mathbf{x}}\mathbf{q}_{n} - \mathbf{u}_{n+1}\cdot\partial_{\mathbf{x}}(\rho\mathbf{b}_{n+1}). \tag{45}$$

This result is valid for homogeneous materials.

Proof: The result follows by a direct calculation. First, from (31*c*) and the chain rule,

$$\partial_{\mathbf{x}}W(\epsilon_{n+1}-\epsilon^{vp}_{n+1}) = \sigma_{n+1}:\partial_{\mathbf{x}}(\epsilon_{n+1}-\epsilon^{vp}_{n+1}). \tag{46}$$

Second, by the product rule of differentiation,

$$\partial_{\mathbf{x}}[\sigma_{n+1}:(\epsilon^{vp}_{n+1}-\epsilon^{vp}_{n})] = \partial_{\mathbf{x}}\sigma_{n+1}:(\epsilon^{vp}_{n+1}-\epsilon^{vp}_{n}) + \sigma_{n+1}:\partial_{\mathbf{x}}(\epsilon_{n+1}-\epsilon^{vp}_{n+1}), \tag{47}$$

and, similarly,

$$\partial_{\mathbf{x}}\left[\frac{1}{2}\,\mathbf{q}_{n+1}\cdot\mathbf{D}^{-1}\mathbf{q}_{n+1} - \mathbf{q}_{n+1}\cdot\mathbf{D}^{-1}(\mathbf{q}_{n+1}-\mathbf{q}_{n})\right] = \mathbf{q}_{n+1}\cdot\mathbf{D}^{-1}\partial_{\mathbf{x}}\mathbf{q}_{n} - \partial_{\mathbf{x}}\mathbf{q}_{n+1}\cdot\mathbf{D}^{-1}(\mathbf{q}_{n+1}-\mathbf{q}_{n}). \tag{48}$$

Finally, by the chain rule,

$$\partial_{\mathbf{x}}[\gamma^{+}(f(\sigma_{n+1},\mathbf{q}_{n+1}))] = \langle f_{n+1}\rangle[\partial_{\sigma}f_{n+1}:\partial_{\mathbf{x}}\sigma_{n+1} + \partial_{\mathbf{q}}f_{n+1}\cdot\partial_{\mathbf{x}}\mathbf{q}_{n+1}. \tag{49}$$

Substitution of (46)–(49) into $\partial_{\mathbf{x}}\hat{\mathbb{L}}_{n}$, as obtained from (44), and making use of the spatial conservation laws (31) yields $\hat{\mathbb{L}}_{n}$, as obtained from (44), and making use of the spatial conservation laws (31) yields

$$\partial_{\mathbf{x}}\hat{\mathbb{L}}_{n} = \sigma_{n+1}:\partial_{\mathbf{x}}(\epsilon_{n+1}-\epsilon^{vp}_{n}) + \mathbf{D}^{-1}\mathbf{q}_{n+1}\cdot\partial_{\mathbf{x}}\mathbf{q}_{n} - \partial_{\mathbf{x}}(\rho\mathbf{b}_{n+1}\cdot\mathbf{u}_{n+1}). \tag{50}$$

However, from (43*b*) one has the result:

$$\mathrm{div}_{\mathbf{x}}\mathbf{T}^{vp}_{n+1} = \partial_{\mathbf{x}}\hat{\mathbb{L}}_{n} - (\partial_{\mathbf{x}}\mathbf{u}_{n+1})\mathrm{div}\sigma_{n+1} - \sigma_{n+1}:\partial_{\mathbf{x}}\epsilon_{n+1}. \tag{51}$$

Since div $\sigma_{n+1} = -\rho\mathbf{b}_{n+1}$, the final result follows from (50) and (51). □

Remark 4.2 Performing similar calculations, it is readily shown that the divergence of Noether quantity associated with the infinitesimal generator of infinitesimal rotations is given by

$$L^{ki}_{,i} = \epsilon^{ljk}x_{l}(-\sigma_{n+1}:\partial_{j}\epsilon^{vp}_{n} + \mathbf{D}^{-1}\mathbf{q}_{n+1}\cdot\partial_{j}\,\mathbf{q}_{n} - \mathbf{u}_{n+1}\cdot\partial_{j}(\rho\mathbf{b}_{n+1})) - \epsilon^{k}_{lj}\,\rho b^{j}_{n+1}u^{l}_{n+1}. \tag{52a}$$

This result is valid for isotropic materials.

Finally, identical arguments lead to the following expression for the divergence of the Noether quantity associated with the infinitesimal generator for dilatations

$$M^{i}_{,i} = x^{j}(-\sigma_{n+1}:\partial_{j}\,\epsilon^{vp}_{n} + \mathbf{D}^{-1}\mathbf{q}_{n+1}\cdot\partial_{j}\,\mathbf{q}_{n} - \mathbf{u}_{n+1}\cdot\partial_{j}\,\mathbf{b}_{n+1}) + N(\hat{\mathbb{L}}_{n} - W) - \frac{p-N}{p}\,\mathbf{u}_{n+1}\cdot\mathbf{b}_{n+1}. \quad \square \tag{52b}$$

Remark 4.3 Given any simply-connected compact set, $A \subset \Omega$, with smooth boundary ∂A, let $\mathbf{J}^{*}$ be defined as

$$\mathbf{J}^{*} := \int_{\partial A}\mathbf{T}^{vp}_{n+1}(\chi_{n+1})\hat{\mathbf{n}}d\Gamma + \int_{A}[\sigma_{n+1}:\partial_{\mathbf{x}}\epsilon^{vp}_{n} - \mathbf{D}^{-1}\mathbf{q}_{n+1}\cdot\partial_{\mathbf{x}}\mathbf{q}_{n} + \mathbf{u}_{n+1}\partial_{\mathbf{x}}\rho\mathbf{b}_{n+1}]dV \tag{52c}$$

where $\hat{\mathbf{n}}$ is the outer normal to ∂A. An immediate consequence of the preceding proposition is that, in the absence of singularities in A, $\mathbf{J}^{*} = \mathbf{0}$. It will be shown in Section 4.4 that $\mathbf{J}^{*}$ may in fact be interpreted as an energy release rate. One can construct similarly $\mathbf{L}^{*}$ and M^{*} □

The result in Proposition 4.2 may be related to the classical Eshelby law for elasticity as follows:

Corollary 4.1 Let $\mathbf{T}^{e}_{n+1}$ *be the classical Eshelby's energy-momentum tensor defined as*

$$\mathbf{T}^{e}_{n+1} := W(\epsilon_{n+1}-\epsilon^{vp}_{n+1})\mathbf{1} - (\partial_{\mathbf{x}}\mathbf{u}_{n+1})^{T}\sigma_{n+1}. \tag{53}$$

The conservation law (45) then implies

$$\mathrm{div}_{\mathbf{x}}\mathbf{T}^{e}_{n+1} + \sigma_{n+1}:\partial_{\mathbf{x}}\epsilon^{vp}_{n+1} = \rho\mathbf{b}_{n+1}\cdot\partial_{\mathbf{x}}\mathbf{u}_{n+1}. \tag{54}$$

Proof: From (44) and (53) it follows that

$$\mathbf{T}^{vp}_{n+1} = \mathbf{T}^{e}_{n+1} + [\sigma_{n+1}:(\epsilon^{vp}_{n+1}-\epsilon^{vp}_{n}) + \frac{1}{2}\,\mathbf{q}_{n+1}\cdot\mathbf{D}^{-1}\mathbf{q}_{n+1} - \frac{\Delta t}{\eta}\,\gamma^{+}(f(\sigma_{n+1},\mathbf{q}_{n+1})) - \mathbf{q}_{n+1}\cdot\mathbf{D}^{-1}(\mathbf{q}_{n+1}-\mathbf{q}_{n}) - \rho\mathbf{b}_{n+1}\cdot\mathbf{u}_{n+1}]\mathbf{1}. \tag{55}$$

Consequently, using the spatial balance laws (31) we find

$$\mathrm{div}_{\mathbf{x}}\mathbf{T}^{vp}_{n+1} = \mathrm{div}_{\mathbf{x}}\mathbf{T}^{e}_{n+1} + \sigma_{n+1}:\partial_{\mathbf{x}}(\epsilon^{vp}_{n+1}-\epsilon^{vp}_{n}) + \mathbf{D}^{-1}\mathbf{q}_{n+1}\cdot\partial_{\mathbf{x}}\mathbf{q}_{n} - \partial_{\mathbf{x}}(\rho\mathbf{b}_{n+1})\cdot\mathbf{u}_{n+1}, \tag{56}$$

and the result follows from the conservation law (45). □

Remark 4.4 Given any simply-connected compact set $A \subset \Omega$ with smooth boundary ∂A, it follows that $\hat{\mathbf{J}}$ defined as

$$\hat{\mathbf{J}} := \int_{\partial A}\mathbf{T}^{e}_{n+1}(\chi_{n+1})\hat{\mathbf{n}}d\Gamma + \int_{A}[\sigma_{n+1}:\partial_{\mathbf{x}}\epsilon^{vp}_{n+1} - \rho\mathbf{b}_{n+1}\cdot\partial_{\mathbf{x}}\mathbf{u}_{n+1}]dV \tag{57}$$

coincides with $\mathbf{J}^{*}$ and vanishes identically in the absence of singularities in A. This integral (in the absence of body forces) constitutes the discrete counterpart of the expression proposed in Kishimoto, Aoki and Sakata (1980). Remarkably, $\hat{\mathbf{J}}$ may not necessarily coincide with $\mathbf{J}^{*}$ in the presence of singularities. As shown in Section 4.4, $\mathbf{J}^{*}$ is the quantity which is directly amenable to interpretation as an energy release rate. □

4.3 Plasticity: Path-Domain Independent Integrals. For plasticity with internal (hardening) variables, the development of material conservation laws parallels that of viscoplasticity. Since along an extremal path the Euler-Lagrange equations are identically satisfied, the volumetric Lagrangian density $\hat{\mathbb{L}}_{n}(\chi_{n+1})$ (15) reduces to

$$\hat{\mathbb{L}}_{n}(\chi_{n+1}) := W(\epsilon_{n+1}-\epsilon^{p}_{n+1}) + \frac{1}{2}\,\mathbf{q}_{n+1}\cdot\mathbf{D}^{-1}\mathbf{q}_{n+1} + \sigma_{n+1}:(\epsilon^{p}_{n+1}-\epsilon^{p}_{n}). \tag{58}$$

Again, one should add the term $-\rho\,\mathbf{b}_{n+1}\cdot\mathbf{u}_{n+1}$ to $\hat{\mathbb{L}}_{n}(\chi_{n+1})$ if body forces are present. Then one obtains

$$\frac{\partial\hat{\mathbb{L}}_{n}(\chi_{n+1})}{\partial(\partial_{\mathbf{x}}\chi_{n+1})} \equiv \frac{\partial\hat{\mathbb{L}}_{n}(\chi_{n+1})}{\partial(\partial_{\mathbf{x}}\mathbf{u}_{n+1})} = \sigma_{n+1}. \tag{59}$$

The Noether quantity $\mathbf{T}^{p}_{n+1}$ associated with the group of *material translations* is given from (39) and (43*a*) as

$$\mathbf{T}^{p}_{n+1} = \hat{\mathbb{L}}_{n}\mathbf{1} - (\partial_{\mathbf{x}}\mathbf{u}_{n+1})^{T}\sigma_{n+1}. \tag{60}$$

Proceeding as in Proposition 2.2, by making use of the chain rule, the product rule of differentiation and the Euler-Lagrange equations (31*a*)–(31*f*) one finds

$$\partial_{\mathbf{x}}\hat{\mathbb{L}}_{n} = \sigma_{n+1}:\partial_{\mathbf{x}}(\epsilon_{n+1}-\epsilon^{p}_{n}) + \mathbf{D}^{-1}\mathbf{q}_{n+1}\cdot\partial_{\mathbf{x}}\mathbf{q}_{n} + \partial_{\mathbf{x}}\sigma_{n+1}:(\epsilon^{p}_{n+1}-\epsilon^{p}_{n}) - \partial_{\mathbf{x}}\mathbf{q}_{n+1}\cdot\mathbf{D}^{-1}(\mathbf{q}_{n+1}-\mathbf{q}_{n}) - \partial_{\mathbf{x}}(\rho\mathbf{b}_{n+1}\cdot\mathbf{u}_{n+1}). \tag{61}$$

To further simplify (61) and arrive at the counterpart of result (45), use is made of the identity recorded as follows:

Lemma 4.1 For discrete plasticity,

$$\partial_{\mathbf{x}}\sigma_{n+1}:(\epsilon^{p}_{n+1}-\epsilon^{p}_{n}) - \partial_{\mathbf{x}}\mathbf{q}_{n+1}\cdot\mathbf{D}^{-1}(\mathbf{q}_{n+1}-\mathbf{q}_{n}) \equiv \mathbf{0}. \tag{62}$$

Proof: with the help of (31*d*), (31*e*), (62) reduces to

Downloaded 03 May 2010 to 171.66.16.244. Redistribution subject to ASME license or copyright; see http://www.asme.org/terms/Terms_Use.cfm

$$\partial_{\mathbf{x}}\sigma_{n+1}:(\epsilon^p_{n+1}-\epsilon^p_n)-\partial_{\mathbf{x}}\mathbf{q}_{n+1}\cdot\mathbf{D}^{-1}(\mathbf{q}_{n+1}-\mathbf{q}_n)$$
$$=\gamma_{n+1}[\partial_\sigma f_{n+1}\partial_{\mathbf{x}}:\sigma_{n+1}+\partial_{\mathbf{q}} f_{n+1}\cdot\partial_{\mathbf{x}}\mathbf{q}_{n+1}]=\gamma_{n+1}\partial_{\mathbf{x}} f_{n+1}. \quad (63)$$

Two possible, mutually excluding, situations can now take place:

(i) For an elastic process, $f_{n+1} < 0$ and $\gamma_{n+1} = 0$. Consequently, $\gamma_{n+1}\partial_{\mathbf{x}} f_{n+1} = 0$, and the result holds for an elastic process.

(ii) For plastic loading, $\gamma_{n+1} > 0, f_{n+1} = 0$, and $\gamma_{n+1} f_{n+1} = 0$. By differentiation we obtain

$$\gamma_{n+1}\partial_{\mathbf{x}} f_{n+1}=-(\partial_{\mathbf{x}}\gamma_{n+1}) f_{n+1}=0 \quad (64)$$

since $f_{n+1} = 0$. Therefore, the result also holds in plastic loading, and the proof is completed. □

In view of this Lemma, equation (61) simplifies to yield the conservation law

$$\mathrm{div}_{\mathbf{x}}\mathbf{T}^p_{n+1}=-\sigma_{n+1}:\partial_{\mathbf{x}}\epsilon^p_n+\mathbf{D}^{-1}\mathbf{q}_{n+1}\cdot\partial_{\mathbf{x}}\mathbf{q}_n-\mathbf{u}_{n+1}\cdot\partial_{\mathbf{x}}(\rho\mathbf{b}_{n+1}). \quad (65)$$

Remarks 4.5

(1) Conservation law (65) is identical to conservation law (45) for viscoplasticity. It is easily seen that the conservation laws corresponding to $\mathbf{L}$ or $\mathbf{M}$ are also identical to those of viscoplasticity. □

(2) By applying the divergence theorem, we arrive at a path-domain independent integral $\mathbf{J}^*$ which is identical to (52). □

(3) As in Corollary 4.1, from conservation (65) one obtains the additional result

$$\mathrm{div}_{\mathbf{x}}\mathbf{T}^e_{n+1}+\sigma_{n+1}:\partial_{\mathbf{x}}\epsilon^p_{n+1}=\rho\mathbf{b}_{n+1}\cdot\partial_{\mathbf{x}}\mathbf{u}_{n+1}, \quad (66a)$$

where $\mathbf{T}^e_{n+1}$ is the classical Eshelby's energy-momentum tensor defined as

$$\mathbf{T}^e_{n+1}:=W(\epsilon_{n+1}-\epsilon^p_{n+1})\mathbf{1}-(\partial_{\mathbf{x}}\mathbf{u}_{n+1})^T\sigma_{n+1}. \quad (66b)$$

As previously remarked, given any simply-connected compact set $A \subset \Omega$ with smooth boundary ∂A, the path-domain independent integral $\hat{\mathbf{J}}$ emanating from (66) coincides with $\mathbf{J}^*$, and vanishes identically in the absence of singularities in A. However, they may not necessarily coincide in the presence of singularities. □

4.4 Energetic Interpretation as an Energy Release Rate. We consider the interpretation of the path-domain independent integral $\mathbf{J}^*$ as a discrete energy release rate. We assume that there are no body forces. Our argument is inspired by that of Budiansky and Rice (1973).

4.4.1 Energy Balance. Consider a compact region $A \subset \Omega$ with boundary Γ, which contains a cavity limited by a smooth surface C; as shown in Fig. 2. Hence, $\partial A = \Gamma \cup C$. Further, consider the following situation:

(1) At time t_n, one is given *fixed* initial data $\{\epsilon^p_n, \mathbf{q}_n\}$. We assume dead loading, with traction vector $\bar{\mathbf{t}}(\mathbf{x}) = \sigma(\mathbf{x})\hat{\mathbf{n}}(\mathbf{x})$ for $\mathbf{x} \in \Gamma$, and zero tractions on C.

(2) At time $t_{n+1} = t_n + \Delta t$ plastic flow is characterized by $\{\epsilon^p_{n+1}, \mathbf{q}^p_{n+1}\}$. In addition, $\epsilon_{n+1} = \partial^s_{\mathbf{x}}\mathbf{u}_{n+1}$, and tractions on Γ remain fixed.

Now let $\mathrm{I\!I}_n(\chi_n)$ and $\mathrm{I\!I}_{n+1}(\chi_{n+1})$ be the total energies available at times t_n and t_{n+1}, respectively. Here, as in the preceding sections, $\chi_n(\mathbf{x})$ and $\chi_{n+1}(\mathbf{x})$ denote the state variables at times t_n and t_{n+1}. In the absence of plastic dissipation, the total energy is conserved and $\mathrm{I\!I}_n = \mathrm{I\!I}_{n+1}$. If plastic flow takes place, the energy balance is given by

$$\mathrm{I\!I}_n(\chi_n)=\mathrm{I\!I}_{n+1}(\chi_{n+1})+\Delta\mathrm{I\!D}^p(\chi_n,\chi_{n+1}) \quad (67)$$

where

$$\Delta\mathrm{I\!D}^p(\chi_n,\chi_{n+1}):=\sigma_{n+1}:(\epsilon^p_{n+1}-\epsilon^p_n)-\mathbf{q}_{n+1}\cdot\mathbf{D}^{-1}(\mathbf{q}_{n+1}-\mathbf{q}_n) \quad (68)$$

is the *incremental* plastic dissipation in $[t_n, t_{n+1}]$.

3 Consider next a *homogeneous translation* of C by an amount $\eta \in \mathbb{R}^3$; that is

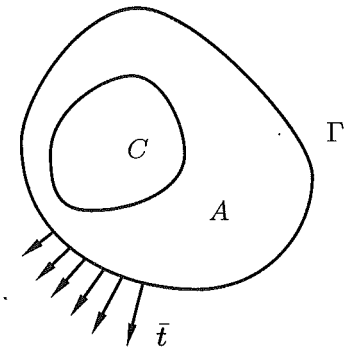


Fig. 2 Cavity with stress-free inner boundary

$$\mathbf{x}\in C\rightarrow\mathbf{x}+\alpha\eta\in\mathbb{R}^3,\ \alpha>0. \quad (69)$$

We remark that in this process, χ_n is regarded as fixed given initial data which, therefore, *remains unchanged*. Accordingly, the energy balance now reads

$$\mathrm{I\!I}_n(\chi_n)=\mathrm{I\!I}(\chi_{n+1}(\mathbf{x}+\alpha\eta))$$
$$+\Delta\mathrm{I\!D}^p(\chi_n,\chi_{n+1}(\mathbf{x}+\alpha\eta))+\mathrm{I\!F}(\chi_{n+1}(\mathbf{x}+\alpha\eta)) \quad (70)$$

where $\mathrm{I\!F}(\chi_n, \chi_{n+1})$ is the (fracture) energy released in the motion of the cavity during $[t_n, t_{n+1}]$. Recalling definition (27) of $\hat{\mathrm{I\!I}}_n$, it follows that

$$\mathrm{I\!F}(\chi_{n+1}(\mathbf{x}+\alpha\eta))=-[\hat{\mathrm{I\!I}}_n(\chi_{n+1}(\mathbf{x}+\alpha\eta))-\mathrm{I\!I}_n(\chi_n)]. \quad (71)$$

Therefore, taking the limit as $\alpha \to 0$ and using definition (21) of the functional derivative, we conclude that

$$\langle\frac{\delta\mathrm{I\!F}}{\delta\mathbf{x}},\eta\rangle_V=-\frac{d}{d\alpha}\,|_{\alpha=0}\,\hat{\mathrm{I\!I}}_n(\chi_{n+1}(\mathbf{x}+\alpha\eta)). \quad (72)$$

To summarize: The energy released in a homogeneous translation of the defect is given by the Gateaux derivative (with respect to variations in $\mathbf{x}\in\Omega$) of the total energy available at time t_n expressed in terms of the state variable χ_{n+1} at t_{n+1}.

(4) In order to examine the corresponding interpretation for $\mathbf{L}^*$ one needs to consider the transformation

$$\mathbf{x}\in C\rightarrow\mathbf{x}+\alpha\eta\times\mathbf{x}.$$

The energy release associated with this motion can also be related to Gateaux derivative and is equal to

$$\langle\frac{\delta\mathrm{I\!F}}{\delta\mathbf{x}},\eta\times\mathbf{x}\rangle_V=-\mathbf{x}\times\frac{\delta\hat{\mathrm{I\!I}}_n}{\delta\mathbf{x}}\cdot\eta.$$

4.4.2 Physical Interpretation of $\mathbf{J}^*$. The explicit calculation of (72) hinges on the *transport theorem* (see, i.e., Gurtin, 1982). Since the Lagrangian $\hat{\mathrm{I\!L}}_n$ associated with $\hat{\mathrm{I\!I}}_n(\chi_{n+1})$ is given by (58), by using Lemma 4.1 and recalling that χ_n is fixed, we obtain

$$\partial_{\mathbf{x}}\hat{\mathrm{I\!L}}_n\cdot\eta\,|_{\chi=\mathrm{const}}=\sigma_{n+1}:(\partial_{\mathbf{x}}\epsilon_{n+1}\cdot\eta). \quad (73)$$

Application of the transport theorem then yields

$$\delta\hat{\mathrm{I\!I}}_n(\chi_{n+1}(\mathbf{x});\eta)=\int_A\sigma_{n+1}:(\partial_{\mathbf{x}}\epsilon_{n+1}\cdot\eta)\,dV$$
$$-\eta\cdot\int_C\hat{\mathrm{I\!L}}_n\hat{\mathbf{n}}\,d\Gamma-\int_\Gamma\bar{\mathbf{t}}\cdot(\partial_{\mathbf{x}}\mathbf{u}_{n+1}\cdot\eta)\,d\Gamma, \quad (74)$$

where $\hat{\mathbf{n}}$ is the unit (*outward*) normal to C. Since $\partial A = \Gamma \cup C$, and $\bar{\mathbf{t}}|_\Gamma = \sigma_{n+1}\hat{\mathbf{n}}$, by using the divergence theorem and noting that C is stress-free, we obtain

$$\delta\hat{\mathrm{I\!I}}_n(\chi_{n+1}(\mathbf{x});\eta)=\int_A\{\sigma_{n+1}:(\partial_{\mathbf{x}}\epsilon_{n+1}\cdot\eta)-\partial_{\mathbf{x}}[\sigma_{n+1}(\epsilon_{n+1}\cdot\eta)]\}\,dV$$
$$-\eta\cdot\int_C[\hat{\mathrm{I\!L}}_n\mathbf{1}-(\partial_{\mathbf{x}}\mathbf{u}_{n+1})^T\sigma]\hat{\mathbf{n}}\,d\Gamma. \quad (75)$$

Downloaded 03 May 2010 to 171.66.16.244. Redistribution subject to ASME license or copyright; see http://www.asme.org/terms/Terms_Use.cfm

Since $\text{div}_{\mathbf{x}}\boldsymbol{\sigma}_{n+1} = 0$, the boundary term in (75) cancels out and one obtains

$$\delta\hat{\mathbb{I}}\hat{\Pi}_n(\chi(\mathbf{x});\boldsymbol{\eta}) = -\boldsymbol{\eta}\bullet\int_C [\hat{\mathbb{L}}_n\mathbf{1} - (\partial_{\mathbf{x}}\mathbf{u}_{n+1})^T\boldsymbol{\sigma}_{n+1}]\hat{\mathbf{n}}d\Gamma. \quad (76)$$

On the other hand, application of the divergence theorem to conservation law (60) leads to

$$\int_{\partial C}\mathbf{T}^p_{n+1}(\chi_{n+1})\hat{\mathbf{n}}d\Gamma = \int_{\partial\Gamma}\mathbf{T}^p_{n+1}(\chi_{n+1})\hat{\mathbf{n}}d\Gamma + \int_A [\boldsymbol{\sigma}_{n+1}:\partial_{\mathbf{x}}\boldsymbol{\epsilon}^p_n - \mathbf{D}^{-1}\mathbf{q}_{n+1}\bullet\partial_{\mathbf{x}}\mathbf{q}_n]dV \equiv \mathbf{J}^*. \quad (77)$$

Noting that $\mathbf{T}^p_{n+1} := [\hat{\mathbb{L}}_n\mathbf{1} - (\partial_{\mathbf{x}}\mathbf{u}_{n+1})^T\boldsymbol{\sigma}_{n+1}]$, from (71), (76), and (77), we conclude that

$$\frac{\delta\mathbb{F}}{\delta\mathbf{x}} = \mathbf{J}^*. \quad (78)$$

Remarks 4.6

(1) A physical interpretation of $\mathbf{L}^*$ as energy release rate associated with the rotation of the cavity follows similar lines, and hence is omitted. □

(2) One should carefully note that, in general, (78) *does not reduce* to the $\hat{J}$-integral defined by (57) unless the exterior path of integration Γ does not intersect the plastic zone. If this is the case, then $\mathbf{T}^p_{n+1} = \mathbf{T}^e_{n+1}$ and $\mathbf{J}^* = \hat{\mathbf{J}}$. □

5 Remarks on Numerical Implementation

A numerical implementation of the J^* integral within the framework of the finite element method may be constructed by a straightforward procedure. In a computational context, the history variables $\{\boldsymbol{\epsilon}^p_n(\mathbf{x}), \mathbf{a}_q(\mathbf{x})\}$ in a typical element, Ω_e, are kept at the *Gauss points*, $\xi_L \in \Omega_e$. Recall that the update of $\{\boldsymbol{\epsilon}^p_n, \mathbf{q}_n\}$ takes place at Gauss points through the *return mapping* algorithm (see, i.e., Simo and Taylor (1989), or Simo and Hughes (1987)). Hence, all that is needed to compute $\mathbf{J}^*$ are the gradients of $\boldsymbol{\epsilon}^p_n$ and $\mathbf{q}_n$. We proceed as follows:

Let $n \geq 2$ now denote the spatial dimension, and $\Omega \subset \mathbb{R}^N$ the reference configuration. Since $\boldsymbol{\epsilon}^p_n \in [L_2(\Omega)]^6$, and $\mathbf{q}^p_n \in [L_2(\Omega)]^m$, we may consider local interpolations *discontinuous between elements*, defined as

$$\boldsymbol{\epsilon}^p_n|_{\Omega_e} = \sum_{L=1}^{N_{\text{Gauss}}} \tilde{N}^L(\xi)\boldsymbol{\epsilon}^p_n(\xi_L)$$
$$\mathbf{q}_n|_{\Omega_e} = \sum_{L=1}^{N_{\text{Gauss}}} \tilde{N}^L(\xi)\mathbf{q}_n(\xi_L) \quad (79)$$

where $\tilde{N}^L : [-1, 1]^N \to \mathbb{R}$ are local shape functions through the Gauss point satisfying

$$\tilde{N}^L(\xi_M) = \delta^L{}_M, \quad L,M \in \{1,2, \ldots, N_{\text{Gauss}}\}, \quad (80)$$

and N_{Gauss} denotes the number of Gauss points for element Ω_e. Let $\boldsymbol{\phi} : [-1, 1]^n \to \Omega$ be the isoparametric mapping, defined as

$$\xi \in [-1, 1]^n \to \mathbf{x} = \boldsymbol{\phi}(\xi) := \sum_{A=1}^{N_{el}} N^A(\xi)\mathbf{x}_A, \quad (81)$$

where $\mathbf{x}_A$ are the nodal coordinates of Ω_e, N_{el} the number of nodal points, and N^A are the finite element shape functions (see Hughes (1987) for an introduction to this material). Denote by $\mathbf{J}(\xi) := \partial_\xi\boldsymbol{\phi}(\xi)$ the Jacobian of the isoparametric mapping. By the chain rule,

$$\partial_{\mathbf{x}}\tilde{N}^L(\mathbf{x}) = \mathbf{J}^{-1}(\xi)\partial_\xi\tilde{N}^L(\xi), \; L \in \{1,2, \ldots, N_{\text{Gauss}}\}$$
$$\partial_{\mathbf{x}}\boldsymbol{\epsilon}^p_n(\xi) = \sum_{L=1}^{N_{\text{Gauss}}} \partial_{\mathbf{x}}\tilde{N}^L(\mathbf{x})\boldsymbol{\epsilon}^p_n(\xi)_L. \quad (82)$$

Then, the domain integrals appearing in the definition of J^* may be easily computed by Gaussian quadrature in an element-by-element fashion; for instance

$$\int_{\Omega_e}\boldsymbol{\sigma}_{n+1}:\partial_{\mathbf{x}}\boldsymbol{\epsilon}^p_n dV = \sum_{L=1}^{N_{\text{Gauss}}} w(\xi_L)\det[\mathbf{J}(\xi_l)]\boldsymbol{\sigma}_{n+1}(\xi_l):\partial_{\mathbf{x}}\boldsymbol{\epsilon}^p_n(\xi_L), \quad (83)$$

where $w(\xi_L)$ is the quadrature weight. The value of the domain integral in a region $A \subset \Omega$ is then obtained by adding the contributions of all the elements $\Omega_e \subset A$. Obviously, it proves convenient to define the exterior boundary Γ of the region A enclosing the defect to coincide with element boundaries.

6 Closure

We have constructed a discrete Lagrangian whose (spatial) Euler-Lagrange equations yield the complete field equations of plasticity and viscoplasticity; in particular, the discrete form of the flow rule and hardening law in the form of general closest-point-projection algorithms. By constructing the Noether quantity associated with this Lagrangian and the group of material translations, we have obtained the corresponding material conservation law, and the proper extension of the **J** integral to discrete elasto-viscoplasticity. Similar results are obtained for the **M** and **N** integrals by considering the appropriate symmetry groups and their corresponding infinitesimal generators. The arguments employed in our derivation are straightforward in the sense that they involve a systematic use of the chain rule. Since the results are derived in discrete form, they are directly amenable to numerical implementation. Their counterpart in the continuum case follows at once by taking the limit as the time step goes to zero.

We conclude by noting that extensions to other types of inelastic behavior can be made, in particular to viscoelasticity and material response governed by irreversible thermodynamics with internal plastic variables. Numerical examples are deferred to a subsequent publication.

Acknowledgments

We thank D. Barnett, S. Govindjee, G. Herrmann, and J. Marsden for helpful discussion. We also would like to thank the reviewers for helpful suggestions. Support for this research was provided by a Grant from the National Science Foundation; the second author was supported by the Department of Energy through a contract with Stanford University. This support is gratefully acknowledged.

References

Atluri, S. N., 1982, "Path-Independent Integrals in Finite Elasticity and Inelasticity, with Body Forces, Inertia and Arbitrary Crack-Face Conditions," *Engineering Fracture Mechanics*, Vol. 16, pp. 341-364.

Atluri, S. N., 1984, "Path-Independent Integrals in Elasticity and Dynamic Fracture Mechanics," *Energetic Fracture Mechanics*, Vol. 20, pp. 209-244.

Atluri, S. N., 1986, "Engineering Approaches and Path-Independent Integrals in Fracture Mechanics," *Computational Methods in Fracture Mechanics*, S. N. Atluri, ed., Chapter 5.

Belinfante, F., 1939, "On the Current and the Density of the Electric Charge, the Energy, the Linear Momentum and the Angular Momentum of Arbitrary Fields," *Physica*, Vol. 6, pp. 887, and Vol.7, pp. 449-474.

Budiansky, B., and Rice, J. R., 1973, "Conservation Laws and Energy-Release Rates," ASME JOURNAL OF APPLIED MECHANICS, Vol. 40, pp. 201-203.

Coleman, B. D., and Gurtin, M., 1967, "Thermodynamics with Internal Variables," *J. Chem. Physics*, Vol. 47, pp. 597-613.

Duvaut, G., and Lions, J. L., 1972, *Les Inequations en Mechanique et en Physique*, Dunod, Paris.

Eischen, J. W., and Herrmann, G., 1987, "Energy Release Rates and Related Balance Laws in Linear Elastic Defect Mechanics," ASME JOURNAL OF APPLIED MECHANICS, Vol. 54, pp. 388-392.

Eshelby, J. B., 1951, "The Force on an Elastic Singularity," *Phil. Trans. Roy. Soc.*, Vol. 87, pp. 12-111.

Eshelby, J. B., 1956, "The Continuum Theory of Lattice Defects," *Solid State Physics*, F. Seitz and D. Turnbull, ed., Vol. 3, Academic Press, New York.

Downloaded 03 May 2010 to 171.66.16.244. Redistribution subject to ASME license or copyright; see http://www.asme.org/terms/Terms_Use.cfm

Fletcher, D. C., 1976, "Conservation Laws in Linear Elastodynamics," *Arch. Rat. Mech. Anal.*, Vol. 60, pp. 330–353.

Gunkther, W., 1962, "Uber einige Randintegrale der Elastomechanik," *Abhandlungen, Raunschweiger Wissenschaftliche Gesellschaft*, Vol. 14, p. 53.

Gurtin, M., 1982, *Introduction to Continuum Mechanics*, Academic Press.

Hill, R., 1950, *The Mathematical Theory of Plasticity*, (last edition, 1983), Oxford University Press, Oxford, U.K.

Hill, R., 1986, "Energy-Momentum Tensors in Elastostatics: Some Reflections on the General Theory," *J. Mech. Phys. Solids*, Vol. 34, pp. 305–317.

Hughes, T. J. R., 1987, *A Course in Linear Finite Elements*, Prentice-Hall, Englewood Cliffs, N.J.

Kanninen, M. F., and Popelar, C. H., 1985, *Advanced Fracture Mechanics*, Oxford University Press, New York.

Kishimoto, K., Aoki, S., and Sakata, M., 1980, "Dynamic Stress Intensity Factors Using $\hat{J}$-Integral and Finite Element Method," *Engineering Fracture Mechanics*, Vol. 13, pp. 387–394.

Knowles, J. K., and Sternberg, E., 1972, "On a Class of Conservation Laws in Linearized and Finite Elasticity," *Arch. Rat. Mech. Anal.*, Vol. 44, p. 187.

Johnson, C., 1976, "Existency Theorems for Plasticity Problems," *J. Math. Pures Appl.*, Vol. 55, pp. 431–444.

Johnson, C., 1978, "On Plasticity with Hardening," *J. Math. Anal. Appl.*, Vol. 62, pp. 325–336.

Luenberger, D. G., 1984, *Linear and Nonlinear Programming*, Addison-Wesley Publishing Co., Menlo Park, Calif.

Marsden, J. E., and Hughes, T. J. R., 1983, *Mathematical Foundations of Elasticity*, Prentice-Hall, Englewood Cliffs, N.J.

Matthies, H., 1987, "Problems in Plasticity and Their Finite Element Approximation," Ph.D. Thesis, Department of Mathematics, Massachusetts Institute of Technology, Cambridge, Mass.

Moreau, J. J., 1977, "Evolution Problem Associated with a Moving Convex Set in a Hilbert Space," *J. Diff. Eqn.*, Vol. 26, p. 347.

Moreau, J. J., 1976, "Application of Convex Analysis to the Treatment of Elastoplastic Systems," *Applications of Methods of Functional Analysis to Problems in Mechanics*, P. Germain and B. Nayroles, eds., Springer-Verlag, New York.

Nakamura, T., Shih, C. F., and Freund, L. B., 1987, "Computational Methods Based on an Energy Integral in Dynamic Fracture," *preprint*.

Olver, P., 1984, "Conservation Laws in Elasticity. I. General Results," *Arch. Rat. Mech. Anal.*, Vol. 85, pp. 111–129.

Olver, P., 1984, "Conservation Laws in Elasticity. II. Linear Homogeneous Isotropic Elastostatics," *Arch. Rat. Mech. Anal.*, Vol. 85, pp. 131–160.

Olver, P., 1986, *Applications of Lie Groups to Differential Equations*, Springer-Verlag, New York.

Ortiz, M., and Popov, E. P., 1985, "Accuracy and Stability of Integration Algorithms for Elastoplastic Constitutive Equations," *Int. J. Num. Meth. Engng.*, Vol. 21, pp. 1561–1576.

Perzyna, P., 1971, "Thermodynamic Theory of Viscoplasticity," *Advances in Applied Mechanics*, Vol. 11, Academic Press, New York.

Rice, J. R., 1968, "A Path-Independent Integral and the Approximate Analysis of Strain Concentrations by Notches and Cracks," ASME JOURNAL OF APPLIED MECHANICS, Vol. 35, pp. 379–386.

Rosenfeld, L., 1940, "Sur le Tenseur d'Impulsion-Energy," *Mem. Acad. R. Belg. Sci.*, Vol. 18, pp. 1–30.

Sanders, J. L., 1960, "On the Griffith-Irwin Fracture Theory," ASME JOURNAL OF APPLIED MECHANICS, Vol. 27, pp. 352–353.

Simo, J. C., 1985, "On the Computational Significance of the Intermediate Configuration and Hyperelastic Relations in Finite Deformation Plasticity," *Mechanics of Materials*, Vol. 4, pp. 439–451.

Simo, J. C., and Taylor, R. L., 1986, "A Return Mapping Algorithm for Plane Strain Elastoplasticity," *Int. J. Num. Meth. Engng.*, Vol. 22, pp. 649–670.

Simo, J. C., and Hughes, T. J. R., 1987a, "General Return Mapping Algorithms for Rate Independent Plasticity," *Constitutive Equations for Engineering Materials*, Desai, ed.

Simo, J. C., and Hughes, T. J. R., 1987b, *Elastoplasticity and Viscoplasticity, Computational Aspects*, in press.

Soper, D. E., 1976, *Classical Field Theory*, John Wiley and Sons, New York.

Strang, G., 1986, *Introduction to Applied Mathematics*, Wellesley-Cambridge Press, Wellesley, Mass.

Strang, G., Matthies, H., and Temam, R., 1980, "Mathematical and Computational Methods in Plasticity," *Variational Methods in the Mechanics of Solids*, S. Nemat-Nasser, ed., Pergamon Press.

Temam, R., and Strang, G., 1980, "Functions of Bounded Deformation," *Arch. Rat. Mech. Anal.*, Vol. 75, pp. 7–21.

Temam, R., 1985, *Mathematical Problems in Plasticity*, Gauthier-Villars, Paris, (translation of 1983 French original edition).

Wilkins, M. L., 1964, "Calculation of Elastic-Plastic Flow," *Methods of Computational Physics*, B. Alder et al., eds., Academic Press, New York.

Downloaded 03 May 2010 to 171.66.16.244. Redistribution subject to ASME license or copyright; see http://www.asme.org/terms/Terms_Use.cfm

Lode Dependences for Isotropic Pressure-Sensitive Elastoplastic Materials

J. P. Bardet
Department of Civil Engineering,
University of Southern California,
Los Angeles, CA 90089-0242

Experimental investigations indicate that the third stress invariant; Lode angle α affects significantly the behavior of pressure sensitive materials. The present communication presents a formulation to account for α in isotropic pressure-sensitive elastoplastic materials. Seven Lode dependences are reviewed. A new one, referred to as LMN, in proposed to generalize Lade and Duncan, and Matsuoka and Nakai failure surfaces. The formulation is general enough to introduce α into the isotropic elastoplastic modes which are only developed in terms of first and second-stress invariants. As an illustration, several Lode dependences are introduced into Roscoe and Burland model. The performance of the modified model is estimated by comparing experimental and analytical results in the case of true triaxial loadings on normally consolidated clay.

1 Introduction

Many conventional plasticity models for pressure-sensitive materials, such as Roscoe and Burland (1968), have been formulated in terms of the first and second-stress invariants without considering the third invariant, sometimes referred to as a Lode angle α. This simplifying assumption disregards the experimental observations made during true axial testing which indicate that the third stress invariant affects significantly the behavior of pressure sensitive soils, rocks, and concretes (Chen and Saleeb, 1982; Lade and Duncan, 1975; Matsuoka and Nakai, 1974).

The objective of the present communication is to propose a formulation which accounts for α in isotropic pressure-sensitive elastoplastic materials. The present work reviews, compares, and generalizes the past work of Argyris et al. (1974), Dafalias and Herrmann (1986), Eekelen (1980), Lade (1975), Matsuoka and Nakai (1974), William and Warnke (1975) and Zienkiewicz and Pande (1977). The formulation aims at introducing the effects of α into the isotropic elastoplastic models which are developed in terms of only first and second-stress invariants.

After reviewing the fundamental definitions of isotropic plasticity, the contribution of α on the direction and amplitude of incremental plastic strain is isolated from other plastic contributions. A particular class of yield and plastic potential functions is introduced for pressure-sensitive materials. This class of functions is illustrated by seven examples of α-dependences found in the literature and by a new one referred to as LMN dependence. LMN dependence is shown to describe the failure surfaces of Lade and Duncan (1975) and Matsuoka and Nakai (1974). The last section applies the general formulation to introduce α into the yield and plastic potential functions of the Roscoe and Burland (1968) model. The performance of the modified model is estimated by comparing experimental and analytical results in the case of true triaxial loadings on normally consolidated clay.

Contributed by the Applied Mechanics Division of THE AMERICAN SOCIETY OF MECHANICAL ENGINEERS for publication in the JOURNAL OF APPLIED MECHANICS.

Discussion on this paper should be addressed to the Technical Editor, Leon M. Keer, the Technological Institute, Northwestern University, Evanston, IL 60208, and will be accepted until two months after final publication of the paper itself in the JOURNAL OF APPLIED MECHANICS. Manuscript received by the ASME Applied Mechanics Division, Mar. 14, 1988; final revision, Oct. 25, 1988.

2 Elastoplastic Constitutive Equations

The sign convention of soil mechanics is preferred to the one of solid mechanics in order to eliminate redundant minus signs for pressure-sensitive materials that experience mostly compressive stress and strain. Hereafter, stresses and strains are assumed to be positive in compression and negative in tension.

2.1 Stress-Strain Relationships. According to one of the fundamental assumptions of the flow theory of plasticity, the strain increment is the sum of elastic and plastic strain increments:

$$d\epsilon_{ij} = d\epsilon^e_{ij} + d\epsilon^p_{ij}. \tag{1}$$

The elastic strain increment resulting from a given stress increment is generally defined by using isotropic elasticity

$$d\epsilon^e_{ij} = \frac{2G-3B}{18BG}\,\delta_{ij} d\sigma_{kk} + \frac{1}{2G}\,d\sigma_{ij}, \tag{2}$$

where the shear modulus G and the bulk modulus B may be stress or strain dependent. Adopting the conventional formulation of the flow theory of plasticity, the plastic strain increment is:

Copyright © 1990 by ASME
Downloaded 03 May 2010 to 171.66.16.244. Redistribution subject to ASME license or copyright; see http://www.asme.org/terms/Terms_Use.cfm

$$d\epsilon_{ij}^{p} = <\frac{1}{H} n_{kl} d\sigma_{kk}> m_{ij} \tag{3}$$

where the symbol $<>$ represents the following function of any scalar z:

$$<z> = \begin{cases} z & \text{if } z>0 \\ 0 & \text{if } z\le 0 \end{cases}. \tag{4}$$

m_{ij} is the normalized gradient of the plastic potential function $g(\sigma_{ij})$:

$$m_{ij} = \frac{\dfrac{\partial g}{\partial \sigma_{ij}}}{\sqrt{\dfrac{\partial g}{\partial \sigma_{kl}} \dfrac{\partial g}{\partial \sigma_{kl}}}}. \tag{5}$$

The normalized gradient n_{ij} of the yield function $f(\sigma_{ij})$ is similarly defined by using the flow function in equation (5). According to the terminology of plasticity, the flow rule is referred to as associative when n_{ij} and m_{ij} coincide. The tensors m_{ij} and n_{ij} are normalized so that they have only directional effects on the plastic flow, the amplitude of which is directly related to the plastic modulus H. The modulus H is generally calculated by enforcing the stress state to stay on the yield surface $f(\sigma_{ij}) = 0$ during plastic flow (consistency condition). The strain increment resulting from a given stress increment is obtained by adding equations (2) and (3).

$$d\epsilon_{ij} = C_{ijkl}\, d\sigma_{kl}, \tag{6}$$

where the elastoplastic constitutive matrix is

$$C_{ijkl} = \frac{2G-3G}{18BG}\, \delta_{ij}\delta_{kl} + \frac{1}{4G}\, (\delta_{ik}\delta_{jl} + \delta_{il}\delta_{jk}) + \frac{1}{H} n_{kl} m_{ij}. \tag{7}$$

2.2 Inverted Stress-Strain Relationship. In many instances, such as the displacement formulation of nonlinear finite element methods, stresses need to be computed as results of strain loading. Therefore, equation (6) must be inverted to provide the stress increments resulting from given strain increments.

$$d\sigma_{ij} = D_{ijkl}\, d\epsilon_{kl}. \tag{8}$$

It can be shown that the inverted elastoplastic constitutive matrix D_{ijkl} is

$$D_{ijkl} = E_{ijkl} - \frac{E_{ijrs} m_{rs} n_{pq} E_{pqkl}}{H + E_{abcd} n_{ab} m_{cd}} \tag{9}$$

where the inverse elastic constitutive matrix E_{ijkl} is

$$E_{ijkl} = \left(B - \frac{2}{3}G\right) \delta_{ij}\delta_{kl} + G(\delta_{ik}\delta_{jl} + \delta_{il}\delta_{jk}). \tag{10}$$

The inversion of equation (6) poses no problem as long as the denominator of equation (9) is different from zero, which is generally satisfied except for some particular stress states. Equation (9) may be rewritten in a simpler form

$$D_{ijkl} = D_{ijkl} - \frac{1}{K} M_{ij} N_{kl} \tag{11}$$

where

$$M_{ij} = E_{ijkl} m_{kl} \qquad N_{ij} = E_{ijkl} n_{kl} \tag{12}$$

$$K = H + N_{cd} m_{cd} = H + \left(B - \frac{2}{3}G\right) (n_{aa})(m_{bb}) + 2G n_{cd} m_{cd}. \tag{13}$$

M_{ij} and N_{ij} defines the direction and existence, respectively, of the stress relaxation which results from plastic strain. K is related to the amplitude of stress relaxation caused by plastic strain. In contrast to n_{ij} and m_{ij}, N_{ij} and M_{ij} are not normalized.

2.3 Istropic Elastoplastic Constitutive Relationships. The hypothesis of isotropy is a convenient assumption which simplifies the mathematical formulation of plasticity. By definition, isotropic elastoplastic models have yield and plastic potential functions which depend only on three stress invariants, instead of six independent stress components

$$f(\sigma_{ij}) = f(I, J, \alpha) \quad \text{and} \quad g(\sigma_{ij}) = g(I, J, \alpha), \tag{14}$$

where I, J, and α are the first and second-stress invariants and Lode angle, respectively,

$$\begin{cases} I = \sigma_{kk} \\ J = \sqrt{\dfrac{1}{2} s_{ij} s_{ij}} \\ \alpha = \dfrac{1}{3} \sin^{-1}\left(\dfrac{3\sqrt{3}}{2} \dfrac{S^3}{J^3}\right) \end{cases} \tag{15}$$

The deviator stress is

$$s_{ij} = \sigma_{ij} - \frac{1}{3}\, \sigma_{kk}\delta_{ij} \tag{16}$$

and the third stress invariant S is

$$S \sqrt{3}\sqrt{\frac{1}{3}\, s_{ij} s_{jk} s_{ki}}. \tag{17}$$

α is preferred to S since α can be represented in the principal stress space. According to equation (15), α varies between $\pi/6$ and $+\pi/6$. The differentials of I, J, and α with respect to stress components σ_{ij} are

$$\begin{cases} \dfrac{\partial I}{\partial \sigma_{ij}} = \delta_{ij} \\ \dfrac{\partial J}{\partial \sigma_{ij}} = \dfrac{s_{ij}}{2J} \\ \dfrac{\partial \alpha}{\partial \sigma_{ij}} = \dfrac{\sqrt{2}}{2J} S_{ij} \end{cases} \tag{18}$$

where S_{ij} is

$$S_{ij} = \frac{\sqrt{2}}{\cos 3\alpha} \left(-\frac{\sqrt{3}}{3}\, \delta_{ij} - \sin 3\alpha \frac{s_{ij}}{2J} + \sqrt{3}\, \frac{s_{ik}s_{kj}}{2J^2}\right) \tag{19}$$

and has the following properties

$$\begin{cases} S_{ij}\delta_{ij} = 0 \\ S_{ij}s_{ij} = 0 \\ S_{ij}S_{ij} = 1 \end{cases} \tag{20}$$

S_{ij} is undefined for $\alpha = \pm\pi/6$ when the gradient of α is equal to zero in (18).

By invoking the chain rule of differential calculus, the gradient of isotropic yields functions is a linear combination of f_I, f_J and f_α, the differential of the yield function with respect to I, J and α, respectively:

$$\frac{\partial f}{\partial \sigma_{ij}} = f_I \delta_{ij} + \frac{1}{2} f_J \frac{s_{ij}}{J} + \frac{\sqrt{2}}{2} \frac{f_\alpha}{J} S_{ij}. \tag{21}$$

The terms on the right-hand side of equation (21) defines the volumetric, deviatoric, and Lode contributions, respectively, on the gradient of yield function. The direction and amplitude of Lode contribution are characterized by S_{ij} and $\frac{f_\alpha}{J}$, respectively. By using equations (20) and (21), the gradient norm is

Downloaded 03 May 2010 to 171.66.16.244. Redistribution subject to ASME license or copyright; see http://www.asme.org/terms/Terms_Use.cfm

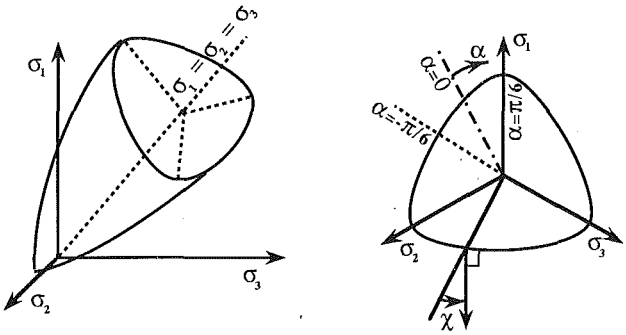


Fig. 1 Typical failure surface for isotropic pressure-sensitive material shown in principal stress space and on deviatoric plane

$$f_* = \sqrt{\frac{\partial f}{\partial \sigma_{ij}} \frac{\partial f}{\partial \sigma_{ij}}} = \sqrt{3f_I^2 + \frac{1}{2} f_J^2 + \frac{1}{2} \left(\frac{f_\alpha}{J}\right)^2} \tag{22}$$

and n_{ij} may be calculated from (5), (21), and (22). N_{ij} becomes

$$N_{ij} = 3Bf_I \delta_{ij} + Gf_J \frac{S_{ij}}{J} + \sqrt{2} G \frac{f_\alpha}{J} S_{ij}. \tag{23}$$

The definitions and results established for yield functions in (21), (22), and (23) pertain to plastic potential functions. The modulus K of (13) is related to the plastic modulus H

$$K = H + \frac{1}{f_* g_*} \left[9Bf_I g_I + Gf_J g_J + G \frac{f_\alpha g_\alpha}{J^2} \right]. \tag{24}$$

3 Lode Dependence

The following section introduces a general class of yield functions that can be used to account for α in isotropic elastoplastic materials. After reviewing the yields functions of Drucker-Prager, Tresca, and Mohr-Coulomb requirements are specified for lode dependences to give differentiable and convex yield functions. Five examples of Lode dependences are also presented.

3.1 A General Class of Yield Functions for Pressure-Sensitive Material. Figure 1 shows a principal stress view of typical yield surfaces that has been proposed for pressure-dependent soil, rock, and concrete based on true triaxial experiments (Lade and Duncan, 1975; Matsuoka and Nakai, 1974). In general, such yield functions depend only on I and the ratio J/ρ (α) where ρ is a function of α. They belong to the following class of isotropic yield functions:

$$f(I, J, \alpha) = f\left(I, \frac{J}{\rho(\alpha)}\right) \tag{25}$$

where the Lode dependence $\rho(\alpha)$ is arbitrarily set to one when $\alpha = \pi/6$. The yield surfaces $f(I, J/\rho(\alpha)) = 0$ have deviatoric sections in planes of constant I that look similar but do not necessarily coincide. The deviatoric sections are circular when the yield function does not depend on α, i.e., $\rho(\alpha) = 1$. They are not circular any longer when ρ varies with α, however, they remain periodic curves of period $2\pi/3$ since α varies between $-\pi/6$ and $\pi/6$. It can also be shown that the yield functions satisfying equation (25) give

$$f_\alpha = -J \tan\chi f_J \tag{26}$$

where $\tan\chi$ is related to ρ_α, the differential of ρ with respect to α

$$\tan\chi = \frac{\rho_\alpha}{\rho}. \tag{27}$$

As represented in Fig. 1, χ is the angle between the radial direction and the gradient of the yield function. According to (21) and (26), χ characterizes the amplitude of the Lode contribution acting in the direction of S_{ij}.

As it will be illustrated in a later section, (25) is useful to introduce the effects of α into the isotropic yield functions $f(I, J)$ that are defined only in terms of first and second invariants.

3.2 Simple Examples of Yield Function for Pressure-Sensitive Materials. Drucker-Prager, Tresca, and Mohr-Coulomb provide three examples of yield functions that satisfy (25). In the principal stress space, the Drucker-Prager surface is a cone with a circular deviatoric section centered on the hydrostatic axis

$$f_1(I, J, \alpha) = J - a_1 I - b_1 \tag{28}$$

where a_1 and b_1 are two material parameters. Since the yield function is independent of α, the Lode dependence of Drucker-Prager is

$$\rho_1(\alpha) = 1. \tag{29}$$

The extended Tresca surface is an angular cone with a regular hexagonal cross-section; its yield function depends on α:

$$f_2(I, J, \alpha) = J\cos\alpha - a_2 I - b_2 \tag{30}$$

where a_2 and b_2 are two material parameters. Its Lode dependence is

$$\rho_2(\alpha) = \frac{\sqrt{3}}{2\cos\alpha}. \tag{31}$$

According to Chen and Saleeb (1982), the yield function of Mohr-Coulomb is

$$f_3(I, J, \alpha) = J[3\cos\alpha - \sqrt{3}\sin\phi\sin\alpha] - I\sin\phi - 3c\cos\phi, \tag{32}$$

where ϕ is the friction angle and c is the cohesion. The yield function of Mohr-Coulomb can be rewritten:

$$f_3(I, J, \alpha) = \frac{\sqrt{3}\beta J}{\rho_3(\alpha)} + I(\beta - 1) - 2c\sqrt{(1 - 2\beta)(1 + \beta)}. \tag{33}$$

Therefore, its Lode dependence is

$$\rho_3(\alpha) = \frac{\sqrt{3}\beta}{(1 + \beta)\cos\alpha + \sqrt{3}(\beta - 1)\sin\alpha}, \tag{34}$$

where the coefficient β is related to the friction angle ϕ:

$$\beta = \frac{3 - \sin\phi}{3 + \sin\phi}. \tag{35}$$

When ϕ varies between 0 deg and 90 deg, β varies between 1 to 0.5. As shown in Fig. 2(*a*), the deviatoric sections of the Mohr-Coulomb surface are piecewise linear. They coincide with Tresca sections when β is equal to one and are triangular when β is equal to 0.5. The angle χ of Fig. 1 varies linearly as a function of α, but changes abruptly when α is equal to $\pm\pi/6$; the yield function of Mohr-Coulomb is not differentiable at $\alpha = \pm\pi/6$.

3.3 Requirements for Lode Dependence for Pressure-Sensitive Materials. Besides Drucker-Prager, Tresca, and Mohr-Coulomb, several types of failure surfaces have been proposed for pressure sensitive materials. They generally satisfy (25) and obey the requirements for aspect ratio, differentiability, and convexity.

3.3.1 Requirement for Aspect Ratio. The requirement on aspect ratio states that:

$$\rho\left(-\frac{\pi}{6}\right) = \beta \quad \text{and} \quad \rho\left(\frac{\pi}{6}\right) = 1 \tag{37}$$

Downloaded 03 May 2010 to 171.66.16.244. Redistribution subject to ASME license or copyright; see http://www.asme.org/terms/Terms_Use.cfm

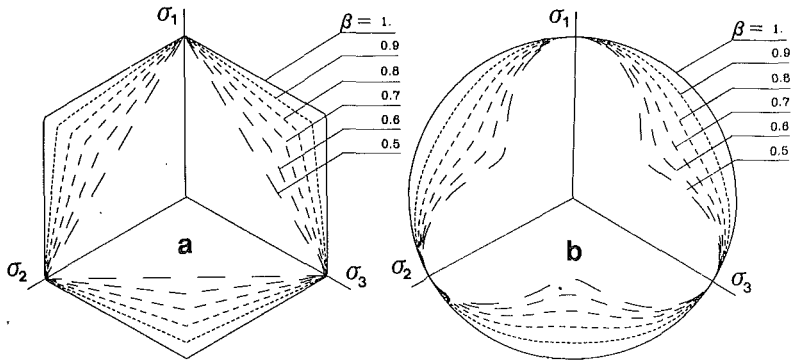


Fig. 2 Mohr-Coulomb (*a*) and cubic (*b*) dependences for various values of β

where β varies between 0.5 and 1. Equation (37) controls the general shape for the deviatoric sections of yield surfaces. This requirement comes from the experimental results (Lade and Duncan, 1975; Matsuoka and Nakai, 1974):

$$0.5 \le \frac{J(-\pi/6)}{J(\pi/6)} \le 1 \quad \text{at } I \text{ constant} \tag{36}$$

where $J(\pi/6)$ and $J(-\pi/6)$ are the values of J that correspond to failure in compression with two identical minor principal stresses and to failure in tension with two identical major principal stresses, respectively.

3.3.2 Requirement for Differentiability. The yield functions of (25) are differentiable at $\alpha = \pm\pi/6$ when

$$\rho_\alpha\left(\pm\frac{\pi}{6}\right) = 0, \tag{38}$$

provided that $\rho(\alpha)$ and $f(I, J)$ are differentiable.

3.3.3 Requirement on Convexity. The yield surfaces of (25) are convex in deviatoric planes (Lin and Bazant, 1986; Jiang and Pietruszczak, 1988) when

$$\frac{d^2\rho}{d\alpha^2} < \rho + \frac{2}{\rho}\rho_\alpha^2. \tag{39}$$

The convexity requirement is useful to satisfy the stability postulate of Drucker (1951).

The following sections present five Lode dependences which satisfy the requirement for aspect ratio and differentiability and occasionally the requirement for convexity.

3.4 Additional Examples of Lode Dependence. The first dependence is based upon a cubic polynomial that is calibrated to satisfy the requirements of (37) and (38). This cubic dependence is:

$$\rho_4(\alpha) = 1 - 2\left(\frac{3}{\pi}\right)^3 (1-\beta)\left(\frac{\pi}{6} - \alpha\right)^2 \left(\alpha + \frac{\pi}{3}\right) \tag{40}$$

Figure 2(*b*) shows $\rho_4(\alpha)$ for various values of β between 0.5 and 1. The deviatoric cross-sections are smooth but do not satisfy the convexity requirement of (39) for β smaller than 0.85, which corresponds to a friction angle $\phi = 13.8$ deg according to (35). χ varies continuously with α but not linearly as in the case of Mohr-Coulomb. Instead of a cubic dependence, William and Warnkle (1975) proposed an elliptical dependence:

$$\rho_5(\alpha) = \frac{2(1-\beta^2)\cos(\pi/6-\alpha) + (2\beta-1)\sqrt{4(1-\beta^2)\cos^2(\pi/6-\alpha) + \beta(5\beta-4)}}{4(1-\beta^2)\cos^2(\pi/6-\alpha) + (2\beta-1)^2}. \tag{41}$$

As shown in Fig. 3(*a*), the elliptical dependence provides convex cross-sections for all values of β. Due to its convexity for all values of β, William and Warnke dependence was used to account for α in modeling the elastoplastic behavior of concrete (Lin et al., 1987). When β tends to 0.5, the deviatoric section becomes triangular, as for Mohr-Coulomb. Argyris 1974) proposed a simpler expression than William and Warnke:

$$\rho_6(\alpha) = \frac{2\beta}{1+\beta+(\beta-1)\sin 3\alpha}. \tag{42}$$

However, as shown in Fig. 3(*b*), the deviatoric section becomes nonconvex when β becomes less than 7/9, which corresponds to a friction angle $\phi = 22$ deg. Argyris dependence was later generalized by Eekelen (1980) who introduced an additional parameter n:

$$\rho_7(\alpha) = \frac{1}{2^n}(1 + \beta^{1/n} + (1-\beta^{1/n})\sin 3\alpha)^n. \tag{43}$$

Equation (42) is a particular case of (43) when n is equal to -1. Eekelen dependence is plotted in Fig. 4(*a*) for the value $n = -0.299$. The surface loses its convexity for a value of β between 0.7 and 0.6.

3.5 LMN Dependence. Based on the failure surfaces of Lade and Duncan (1975) and Matsuoka and Nakai (1974), the following Lode dependence is proposed:

$$\rho_8(\alpha) = \frac{\sqrt{3}}{2}\frac{\beta}{\sqrt{\beta^2-\beta+1}}\frac{1}{\cos\theta} \tag{44}$$

where

$$\theta = \begin{cases} \dfrac{1}{6}\cos^{-1}\left(-1 + \dfrac{27}{2}\dfrac{\beta^2(1-\beta)^2}{(\beta^2-\beta+1)^3}\sin^2 3\alpha\right) & \text{if } \alpha \le 0 \\ \dfrac{\pi}{3} - \dfrac{1}{6}\cos^{-1}\left(-1 + \dfrac{27}{2}\dfrac{\beta^2(1-\beta)^2}{(\beta^2-\beta+1)^3}\sin^2 3\alpha\right) & \text{if } \alpha > 0. \end{cases} \tag{45}$$

This dependence is hereafter referred to as LMN, after the first letter of Lade, Matsuoka, and Nakai. θ varies continuously with α since (45) gives $\theta = \pi/6$ for $\alpha = 0$. The deviatoric section is shown in Fig. 4(*b*). By comparing Figs. 3(*a*) and 4(*b*), it is concluded that LMN and elliptical dependences are similar.

In summary, Lode contribution can be accounted for in isotropic elastoplastic constitutive models by using cubic,

Downloaded 03 May 2010 to 171.66.16.244. Redistribution subject to ASME license or copyright; see http://www.asme.org/terms/Terms_Use.cfm

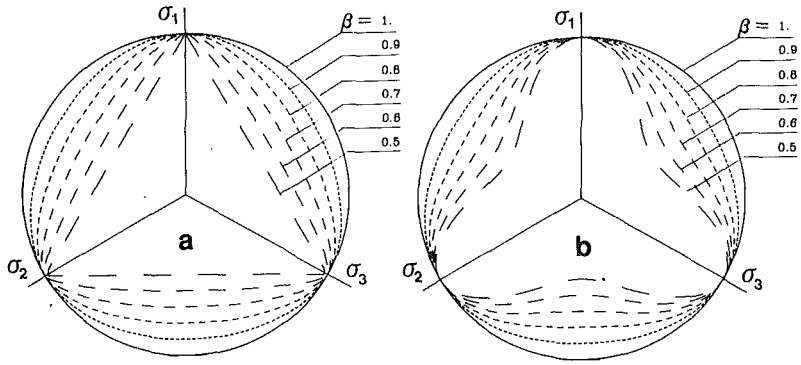


Fig. 3 Elliptical (*a*) and Argyris (*b*) dependences for various values of β

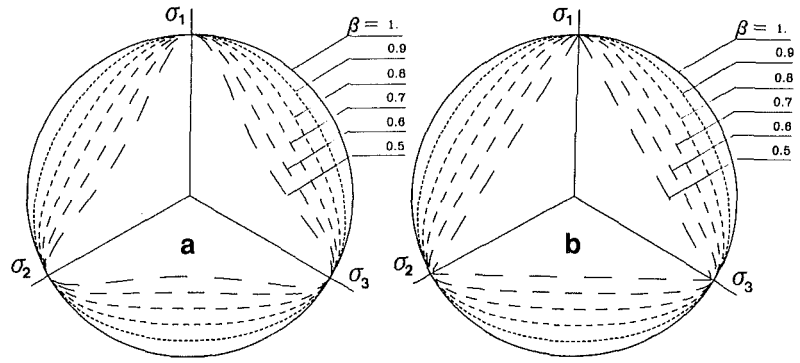


Fig. 4 Eekelen (*a*) and LMN (*b*) dependences for various values of β

Argyris, elliptical, Eekelen or LMN dependence. Cubic, Argyris, and Eekelen functions have simple mathematical expressions but lose convexity for values of parameter β, typical to frictional materials. Elliptical and LMN dependences, which have a more complicated analytical expression than the other dependences, satisfy the convexity requirement and are almost identical for all values of parameter β.

4 Application of LMN Dependence to Failure Surfaces

One of the advantages of LMN over elliptical dependence is that it describes exactly the failure surfaces of Lade-Duncan and Matsuoka-Nakai.

4.1 Application to Lade-Duncan Surface. Lade and Duncan (1975) proposed the following failure criterion:

$$I^3 - \eta_1 I_3 = 0 \tag{46}$$

where η_1 is a dimensionless material constant, I is the first stress invariant and I_3 is the third stress invariant

$$I_3 = \det(\sigma_{ij}) = \sigma_1\sigma_2\sigma_3. \tag{47}$$

σ_1, σ_2, and σ_3 are the principal stresses. Using the relation between I_3, I, J, and α:

$$I_3 = \frac{2}{3\sqrt{3}} J^3 \sin 3\alpha - \frac{1}{3} I J^2 + \frac{1}{27} I^3. \tag{48}$$

By using (46) and (48), the ratio J/I obeys the following cubic equation:

$$\frac{2\sqrt{3}}{3}\left(\frac{J}{I}\right)^3 \sin 3\alpha - \left(\frac{J}{I}\right)^2 + \left(\frac{1}{9} - \frac{3}{\eta_1}\right) = 0. \tag{49}$$

It can be shown that $J = \rho(\alpha) J_{\max}$ is the acceptable solution of (49) when $\rho(\alpha)$ is given by (44) and $J_{\max}$ is

$$J_{\max} = \frac{\sqrt{3}}{2} \frac{1-\beta^2}{1+\beta^3} I. \tag{50}$$

Lade constant η_1 is related to β through:

$$\eta_1 = \frac{1}{\frac{1}{27} - \frac{\beta^2(1+\beta)(1-\beta^2)^2}{4(1+\beta^3)^3}} = \frac{(3-\sin\phi)^3}{(1-\sin\phi)\cos^2\phi}. \tag{51}$$

ϕ is the friction angle measured during triaxial compression, i.e., for $\alpha = \pi/6$. When β tends toward one, which corresponds to $\phi = 0$ deg, η_1 is equal to 27. When β tends toward 0.5, which corresponds to $\phi = 90$ deg, η_1 is infinite. It is worth noting that Lade and Duncan give a larger value for J in tensile failure ($\alpha = -\pi/6$) than Mohr-Coulomb.

4.2 Application to Matsuoka-Nakai Surface. Based also upon experimental results, Matsuoka and Nakai (1974) proposed a failure surface that slightly differs from a Lade-Duncan surface

$$I_2 I - \eta_2 I_3 = 0, \tag{52}$$

where η_2 is a dimensionless material constant and I_2 is the second stress invariant

$$I_2 = \frac{1}{2}(I^2 - \sigma_{ij}\sigma_{ij}). \tag{53}$$

The ratio $\frac{J}{I}$ obeys the following equation:

$$\frac{2\sqrt{3}}{3}\left(\frac{J}{I}\right)^3 \sin 3\alpha - \left(1 - \frac{3}{\eta_2}\right)\left(\frac{J}{I}\right)^2 + \left(\frac{1}{9} - \frac{1}{\eta_2}\right) = 0. \tag{54}$$

Downloaded 03 May 2010 to 171.66.16.244. Redistribution subject to ASME license or copyright; see http://www.asme.org/terms/Terms_Use.cfm

It can be shown that $J=\rho(\alpha)J_{max}$ is the acceptable solution of (54) when $\rho(\alpha)$ is given by (44) and J_{max} is the same as for Mohr-Coulomb:

$$J_{max}=18\sqrt{3}\frac{\sin\phi}{3-\sin\phi}I. \tag{55}$$

The constant η_2 is related to β and ϕ through:

$$\eta_2=\frac{9\beta}{(2\beta-1)(2-\beta)}=\frac{9-\sin^2\phi}{1-\sin^2\phi}. \tag{56}$$

In summary, LMN dependence describes the failure surfaces of Lade-Duncan and Matsuoka-Nakai by using two different values of β. In contrast to the Lade-Duncan surface, the surfaces of Matsuoka-Nakai, and Mohr-Coulomb coincide at $\alpha=\pm\pi/6$.

5 Application of Lode Dependence to the Roscoe-Burland Model

One of the main applications of Lode dependence is to introduce the effects of α into isotropic elastoplastic models that are formulated only in terms of first and second-stress invariants. Following the suggestion of Dafalias and Hermann (1986), the modified yield functions $f(I, J, \alpha)$ are obtained by replacing J by $J/\rho(\alpha)$ in the yield function $f(I, J)$ as indicated in (25). The following section illustrates the introduction of α into a particular elastoplastic model.

5.1 Generalization of Stress-Strain Relationships. Among all the material models of soil mechanics, the Roscoe and Burland (1968) model is certainly the most commonly used to describe the behavior of normally and overconsolidated clays. This model was developed based upon triaxial tests. In spite of the appellation "triaxial," these latter tests apply axisymmetric stress states to the soil samples

$$\sigma_{22}=\sigma_{33}, \text{ and } \sigma_{ij}=0 \quad \text{if } i\neq j. \tag{57}$$

According to (57), stresses are described by two independent components, such as mean pressure p and deviator stress q

$$p=\frac{1}{3}(\sigma_{11}+2\sigma_{33}) \quad q=\sigma_{11}-\sigma_{33}. \tag{58}$$

When (57) applies, p and q are simply related to the stress invariants I and J

$$p=\frac{I}{3} \qquad q=\sqrt{3}J \tag{59}$$

and

$$\alpha=\begin{cases}\pi/6 & \text{if } q>0\\ -\pi/6 & \text{if } q<0.\end{cases} \tag{60}$$

Roscoe and Burland (1968) chose an elliptical yield surface

$$f(p, q, \epsilon_v^p)=\frac{q^2}{M_c^2p}+p-p_0\exp\left(\frac{1+e_0}{\lambda-\kappa}\epsilon_v^p\right)=0 \tag{61}$$

where M_c λ, and κ are three material constants. The constants p_0 and e_0 are the initial values of mean pressure and void ratio, respectively. The only internal variable of the model is the plastic volumetric strain ϵ_v^p that is referenced to the initial state characterized by p_0 and e_0. By using (35) and (59), equation (61) is generalized in terms of stress invariants

$$f(I, J, \alpha, \epsilon_v^p)=\frac{27J^2}{M_c^2\rho(\alpha)^2I}+I-I_0\exp\left(\frac{1+e_0}{\lambda-\kappa}\epsilon_v^p\right)=0 \tag{62}$$

where $I_0=3\,p_0$. The yield surface of (62) is plotted in Fig. 5 for two different values of β. The differentials of yield function with respect to I, J, and ϵ_v^p are:

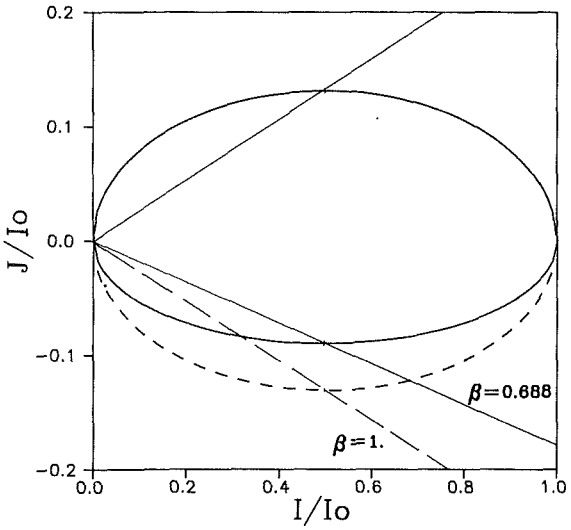


Fig. 5 Roscoe and Burland yield surface in I–J invariant stress space

$$\begin{cases} f_I=1-\dfrac{27J^2}{M_c^2\rho(\alpha)^2I^2}\\ f_J=\dfrac{54J}{M_c^2\rho(\alpha)^2I}\\ \dfrac{\partial f}{\partial\epsilon_v^p}=-\dfrac{1+e_0}{\lambda-\kappa}\left(\dfrac{27J^2}{M_c^2\rho(\alpha)^2I}+I\right)\end{cases} \tag{63}$$

Since the evolution of the yield surface during plastic flow is controlled by only one internal variable; ϵ_v^p, the consistency condition of plasticity theory implies that

$$\frac{\partial f}{\partial\sigma_{ij}}d\sigma_{ij}+\frac{\partial f}{\partial\epsilon_v^p}d\epsilon_v^p=0. \tag{64}$$

Since f is isotropic, (64) becomes

$$f_Idl+f_Jdl+f_\alpha d\alpha+\frac{\partial f}{\partial\epsilon_v^p}d\epsilon_v^p=0. \tag{65}$$

By using (3), the plastic volumetric strain is

$$d\epsilon_v^p=d\epsilon_{ii}^p=\frac{1}{H}(n_{kl}d\sigma_{kl})m_{ii}. \tag{66}$$

Therefore, the plastic strain is

$$d\epsilon_{ij}^p=\frac{-1}{3g_I\dfrac{\partial f}{\partial\epsilon_v^p}}(f_Idl+f_Jdl+f_\alpha d\alpha)\frac{\partial g}{\partial\sigma_{ij}}. \tag{67}$$

Equations (67) generalizes the incremental stress-strain relationships of Roscoe and Burland (1986) by accounting for α. The yield and plastic potential functions can be modified by selected any type of Lode dependence $\rho(\alpha)$ defined in the previous sections. Hereafter, their Lode dependences are of the same type and satisfy

$$g_I=f_I \qquad g_j=f_J. \tag{68}$$

However, g_α may be set different from f_α by selecting two different values of constants β and β_p, respectively. The flow rule is associative when β and β_p are equal. Otherwise, it is nonassociative.

5.2 Theory Versus Experiment for Loading at Constant I and α. In the case of loading at constant I and α, the second stress invariant J is gradually increased until the specimen fails:

$$I=I_0, \qquad dI=0, \qquad \text{and} \qquad d\alpha=0. \tag{69}$$

Downloaded 03 May 2010 to 171.66.16.244. Redistribution subject to ASME license or copyright; see http://www.asme.org/terms/Terms_Use.cfm

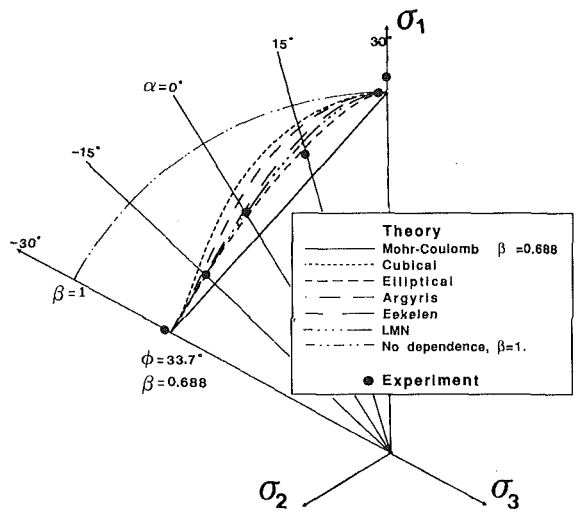


Fig. 6 Comparison between theory and experiment: failure stress in deviatoric stress plane for various true triaxial tests (experimental data after Nakai et al., 1986)

Such stress-controlled loadings were carried out in the laboratory by Nakai et al. (1986). With the mean of a true triaxial apparatus, they applied five different values of α ($\alpha=30$ deg, 15 deg, 0 deg, -15 deg, and -30 deg) to cubical material samples made of normally consolidated Fujinomori clay. Theory and experiment can be compared by examining (1) failure stress states and (2) stress-strain responses. The values of the model constants are provided by Nakai et al. (1986): $\frac{\lambda}{1+e_0}=0.0508, \frac{\kappa}{1+e_0}=0.0112, \phi=33.7$ deg and $\nu=0$. The value of $\beta=0.688$ for yield function corresponds to $\phi=33.7$ deg. The value of β_p for plastic potential function is chosen to be equal to 0.688 and 1 in the case of associative and nonassociative flow rules, respectively.

5.2.1 Comparison of Predicted and Measured Failure Stresses. The maximum value $J_{\max}$ for J corresponds to $H=0$:

$$J_{\max}=3\sqrt{3}IM_c\rho(\alpha). \tag{70}$$

Figure 6 compares the experimental and theoretical failure stresses obtained for five different values of α. LMN and elliptical dependences provide the best agreement with experimental observations. The Mohr-Coulomb dependence gives conservative failure stresses whereas cubic, elliptical, Argyris, and Eekelen dependences produce nonconservative failure stresses. The original Roscoe-Burland model that does not account for α ($\beta=1$) clearly overestimates the material strength when α is different of $\pi/6$.

5.2.2 Comparison of Predicted and Measured Stress-Strain Response. For the particular loading of (69), the elastic strain increment is

$$d\epsilon_{ij}^e=\frac{1}{2G}ds_{ij}, \tag{71}$$

where the shear modulus G is constant since I is constant (Roscoe and Burland, 1968):

$$G=\frac{1-2\nu}{2(1+\nu)}\frac{1+e_0}{\kappa}I. \tag{72}$$

The plastic strain increment is

$$d\epsilon_{ij}^p=\frac{\lambda-\kappa}{1+e_0}\frac{1}{1+\dfrac{27J^2}{M_c^2\rho^2I}}\frac{f_J}{3g_I}\frac{\partial g}{\partial\sigma_{ij}}dJ. \tag{73}$$

The incremental strain can be integrated analytically when J varies from 0 to $J_{\max}$. Since I and α are constant, the stress is a linear function of J:

$$\frac{s_{ij}}{J}=\begin{cases}\dfrac{2}{\sqrt{3}}\sin\left(i\dfrac{2\pi}{3}-\alpha\right) & \text{if } i=j=1,2,3\\ 0 & \text{if } i\neq j\end{cases} \tag{74}$$

and the direction of Lode contribution is constant:

$$S_{ij}=\begin{cases}\dfrac{\sqrt{2}}{\cos3\alpha}\left(-\dfrac{\sqrt{3}}{3}-\dfrac{1}{2}\sin3\alpha\dfrac{s_{ij}}{J}+\dfrac{\sqrt{3}}{2}\dfrac{s_{ij}^2}{J^2}\right) & \text{if } i=j=1,2,3\\ 0 & \text{if } i\neq j\end{cases} \tag{75}$$

After integrating (71) and (73), the elastic and plastic strains becomes

$$\begin{cases}\epsilon_{ij}^e=\dfrac{1}{2G}s_{ij}\\ \epsilon_{ij}^p=\dfrac{\lambda-\kappa}{1+e_0}\left[\dfrac{1}{3}\ln\left(1+\dfrac{27J^2}{M_c^2\rho^2I^2}\right)\delta_{ij}+\zeta\dfrac{s_{ij}}{J}-\sqrt{2}\zeta\tan\chi S_{ii}\right]\end{cases} \tag{76}$$

where

$$\zeta=\frac{\sqrt{3}}{M_c\rho}\left[-\tan^{-1}\left(\frac{3\sqrt{3}J}{M_c\rho I}\right)+\tanh^{-1}\left(\frac{3\sqrt{3}J}{M_c\rho I}\right)\right]. \tag{77}$$

In (76), ρ and $\tan\chi$ depend on β and β_p, respectively. The stress-strain responses of (76) have been specified for the material constants of Nakai et al. (1986) and plotted in Figs. 7, 8, and 9 for various values of α. The material responses are reported as in Nakai et al. (1986) by plotting the ratio between the major and minor principal stresses, i.e., σ_1/σ_3, versus major, intermediate, and minor principal strains, noted ϵ_1, ϵ_2, and ϵ_3, respectively. The volumetric strain $\epsilon_v=\epsilon_1+\epsilon_2+\epsilon_3$ is also plotted versus the major principal strain ϵ_1. In the triaxial compression test of Fig. 7(*a*), all Lode dependences give identical results since $\rho(\pi/6)=1$ and $\rho_\alpha(\pi/6)=0$ for any values of β and β_p. The stress-strain response is identical to the one predicted by the original Roscoe-Burland model. In the tension test of Fig. 7(*b*), all Lode dependences with $\beta=0.688$ give the same stress-strain response independently of β_p, since $\rho(-\pi/6)=\beta$ and $\rho_\alpha(-\pi/6)=0$ for any β_p. The stress-strain response of the original Roscoe and Burland model that is plotted in a dashed line in Fig. 7(*b*) largely overestimates the material strength. Similar results are obtained for the loadings corresponding to $\alpha=\pm15$ deg which are shown in Figs. 7(*c*) and 9(*d*). Figure 8 compares the associative and nonassociative responses resulting from LMN dependences during the particular loading at $\alpha=0$ deg; the intermediate principal strain ϵ_2 is simulated more accurately with a nonassociative flow rule. Figure 9 compares the responses of six different Lode dependences for $\beta=0.688$ and $\beta_p=1$. Figure 9 indicates major differences for the maximum value of σ_1/σ_3, but not for the intermediate strain ϵ_2, which is to be expected since $\rho_\alpha=0$ when $\beta_p=1$.

In summary, it is concluded that both LMN and ellipitical dependences give identical stress-strain responses and failure stresses for the generalized Roscoe and Burland model. The Mohr-Coulomb dependence gives the most conservative failure stress and the softest stress-strain response. The other Lode dependences—cubic, Argyis, and Eekelen—can be used alternatively to LMN or elliptical dependences, when the friction angle is small or when yield and plastic potential functions are not required to be convex.

Downloaded 03 May 2010 to 171.66.16.244. Redistribution subject to ASME license or copyright; see http://www.asme.org/terms/Terms_Use.cfm

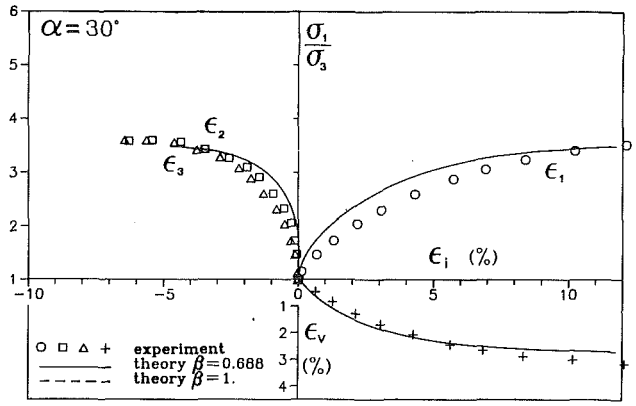


Fig. 7(a)

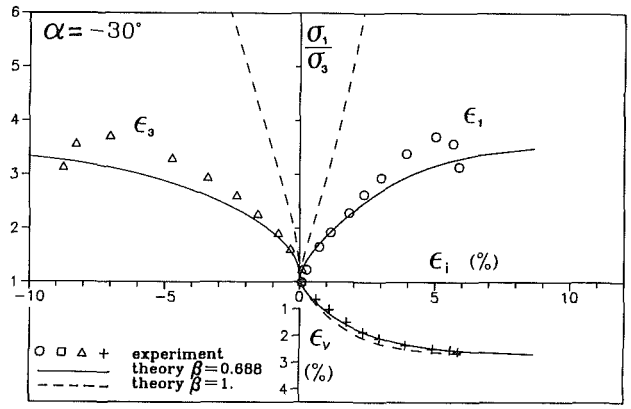


Fig. 7(b)

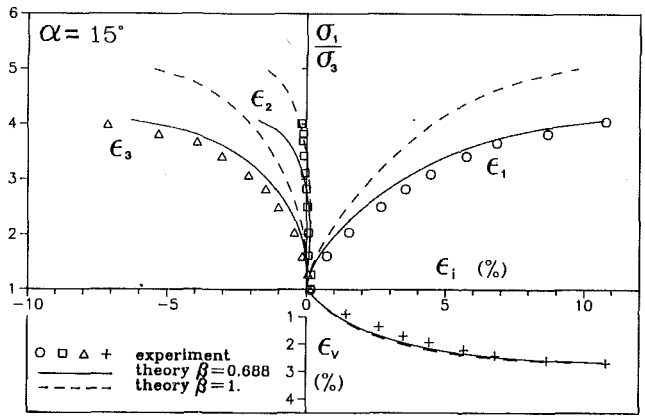


Fig. 7(c)

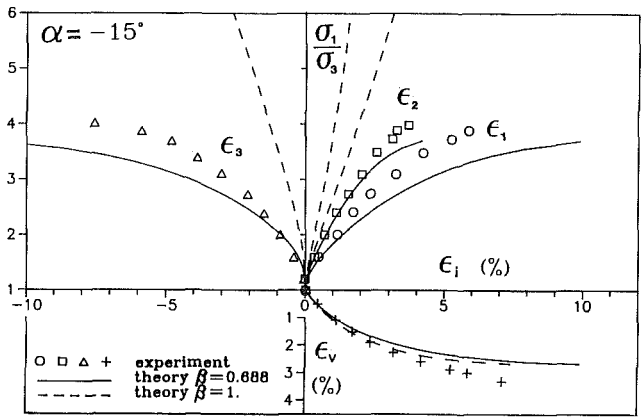


Fig. 7(d)

Fig. 7 Comparison between theory and experiment: principal strains versus principal stress ratio and volumetric strain in true triaxial tests for (*a*) $\alpha = 30$ deg, (*b*) $\alpha = -30$ deg, (*c*) $\alpha = 15$ deg, and (*d*) $\alpha = -15$ deg (experimental data after Nakai et al., 1986)

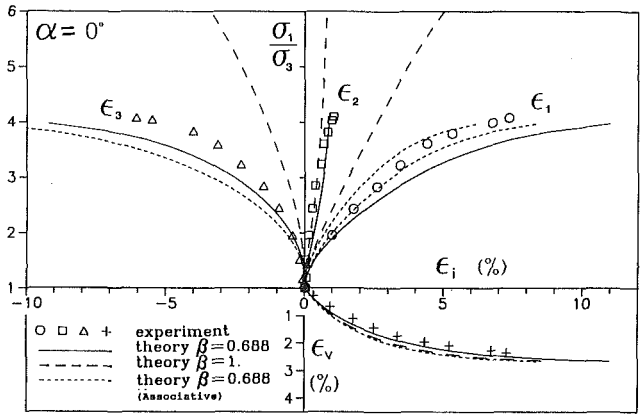


Fig. 8 Comparison between experiment and theory for associative and nonassociative flow rules: principal strains versus principal stress ratio and volumetric strain in true triaxial tests for $\alpha = 0$ deg (experimental data after Nakai et al., 1986).

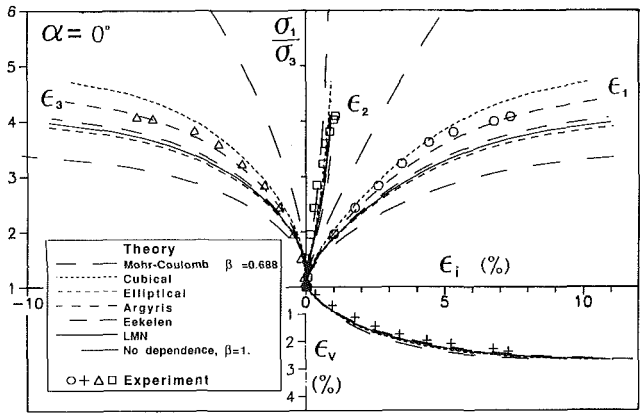


Fig. 9 Comparison between experimental and theory for six different types of lode dependence: principal strains versus principal stress ratio and volumetric strain in true triaxial tests for $\alpha = 0$ deg (experimental data after Nakai et al., 1986)

6 Conclusion

A particular class of yield and plastic potential functions has been introduced in order to account for the effects of Lode angle on isotropic pressure-sensitive materials. This class of functions is illustrated by seven Lode dependences found in the literature and by a new one, referred to as LMN, that is similar to the William and Warnke (1975) dependence. The LMN dependence gives a convex surface for all values of frictional angle and generalizes the failure surfaces of Lade and Duncan (1975) and Matsuoka and Nakai (1974). The proposed formulation has been applied to introduce the Lode angle α into the Roscoe and Burland model. The modified model is capable of reproducing the experimental observations made on true triaxial tests of clay. The formulation is general enough to introduce α into the isotropic elastoplastic models which

Downloaded 03 May 2010 to 171.66.16.244. Redistribution subject to ASME license or copyright; see http://www.asme.org/terms/Terms_Use.cfm

are only developed in terms of first and second-stress invariants.

7 Acknowledgment

The financial support of the U.S. National Science Foundation (grants CEE-8404315 and MSM 8657999) is acknowledged.

References

Argyris, J. H., et al., 1974, "Recent Development in the Finite Element Analysis of Pressure Container Reactor Vessel," *Nuclear Engineering and Design*, Vol. 28, pp. 42–75.

Chen, W. F., and Saleeb, A. F., 1982, *Constitutive Equations for Engineering Materials: Elasticity and Modeling*, John Wiley and Sons, New York.

Dafalias, Y. F., and Herrmann, L. R., 1986, "Bounding Surface Plasticity. II Application to Isotropic Cohesive Soils," *Journal of Engineering Mechanics*, Vol. 112, pp. 1263–1290.

Drucker, D. C., 1951, "A More Fundamental Approach to Plastic-Stress Strain Relations," *Proceedings 1st U.S. National Congress on Applied Mechanics*, ASME, New York, pp. 487–491.

Eekelen, H. A. M., 1980, "Isotropic Yield Surface in Three Dimensions for Use in Soil Mechanics," *Int. J. for Numerical and Analytical Methods in Geomechanics*, Vol. 4, pp. 89–101.

Gudehus, G., 1973, "Elastoplastische stoffgleichungen fur trockenen sand," *Ingenieur Archiv*, Vol. 42, pp. 151–169.

Jiang, J., and Pietruszczak, S., 1988, "Convexity of Yield Loci for Pressure Sensitive Materials," submitted to *Computers and Geotechnics*.

Lade, P. V., and Duncan, J. M., Duncan, 1975, "Elastoplastic Stress-Strain Theory for Cohesionless Soil," *J. Geotechnical Engineering Division*, ASCE, New York, Vol. 101, pp. 1037–1053.

Lin, F. B., and Bazant, Z. P., 1986, "Convexity of Smooth Yield Surface of Frictional Material," *Journal of Engineering Mechanics*, ASCE, New York, Vol. 112, pp. 1259–1262.

Lin, F. B., Bazant, Z. P., Chern, J. C., and Marchertas, A. H., 1987, "Concrete Model with Normality and Sequential Identification," *Computers and Structures*, Vol. 26, pp. 1011–1025.

Matsuoka, H., and Nakai, T., 1974, "Stress-deformation and Strength Characteristics of Soil Under Three Different Principal Stress," *Proceedings Japanese Society of Civil Engineers*, Vol. 232, pp. 59–70.

Nakai, T., Matsuoka, H., Okuno, N., and Tsuzuki, K., 1986, "True Triaxial Tests on Normally Consolidated Clay and Analysis of the Observed Shear Behavior Using Elastoplastic Constitutive Models," *Soils and Foundations*, Vol. 26, pp. 67–78.

Roscoe, K. H., and Burland, J. B., 1968, "On the Generalized Stress-Strain Behavior of Wet Clay," *Engineering Plasticity*, Cambridge Univ. Press, pp. 535–609.

William, K. J., and Warnke, E. P., 1975, "Constitutive Model for the Triaxial Behavior of Concrete," *International Association for Bridge and Structure Engineering Proceedings*, Bergamo, Italy, Vol. 19.

Yang, B. L., and Dafalias, Y. F., and Herrmann, L. R., 1985, "A Bounding Surface Plasticity Model for Concrete," *Journal of Engineering Mechanics*, ASCE, New York, Vol. 111, pp. 359–380.

Zienkiewicz, O. C., and Pande, G. N., 1977, "Some Useful Forms of Isotropic Yield Surfaces for Soil and Rock Mechanics," *Finite Elements in Geomechanics*, G. Gudehus, ed., John Wiley and Sons, New York, pp. 179–190.

Downloaded 03 May 2010 to 171.66.16.244. Redistribution subject to ASME license or copyright; see http://www.asme.org/terms/Terms_Use.cfm

J. Jahedi[1]
R. T. P. Consulting Engineers
Highland, IN

J. Mohammadi
Associate Professor,
Department of Civil Engineering.

S. Nair
Associate Professor,
Department of Mechanical and Aerospace Engineering,
Mem. ASME

Illinois Institute of Technology,
Chicago, IL 60616

A Fabric-Related Constitutive Model for Granular Materials

A new anisotropic constitutive model for granular materials is developed. This model exhibits the noncoaxiality of the principal axes of stress and strain rate as a natural consequence of a kinematic hypothesis. A fabric reconstruction parameter $\mathfrak{B}$ plays an important role in this model. The pressure sensitivity parameter, μ, and two different hardening parameters often employed in modeling granular materials, come out to be expressible in terms of this fabric reconstruction factor. The stress criterion in this model is not friction based, and therefore the rolling of granules can be taken into account through the fabric paramater. Numerical results are presented on the basis of a phenomenological trial function for $\mathfrak{B}$.

1 Introduction

In recent years, the concept of double-slip models for the granular flow has attracted considerable attention, mainly because of its capability to model the non-coaxiality of the principal axes of stress and strain rate, a known characteristic of flow of granular materials (Oda et al., 1982; Oda and Konishi, 1974; Oda 1972; Drescher and De Josselin De Jong, 1972; Drescher, 1976). Such a model, which was originally proposed by Mandel (1947) and De Josselin De Jong (1959), was put into a properly invariant plane theory for incompressible materials by Spencer (1964), and was later generalized to include the material dilatation by Mehrabadi and Cowin (1978). An excellent description of noncoaxiality in granular materials can also be found in Mandl and Fernandez (1970).

This type of noncoaxiality, however, was also achieved by other investigators using different approaches. Rudnicki and Rice (1975) added a term to their generalized deformation-type plasticity model for rocks to account for the vertex behavior of the yield surface. Nemat-Nasser et al. (1981) also added a similar term to a nonassociative, work-hardening, J_2-plasticity model which was originally proposed by Nemat-Nasser and Shokooh (1980).

Different forms of slip theory have also been extensively developed in metal plasticity (Nemat-Nasser et al., 1981; Lance et al., 1986; Asaro and Rice, 1977; Lemonds et al., 1985). A comprehensive discussion along this line and more references are given by Nemat-Nasser (1983). The present study, however, emphasizes the behavior of dry granular materials.

The primary objective of this paper is to develop a kinematic relation in such a way as to include the two most important experimentally observed characteristics of granular materials namely, *the gradual concentration of contact normals toward a unique direction and the gradual rotation of the axes of principal stresses* (see Oda et al., 1980, 1982). The methodology presented here follows the general approach employed by Mehrabadi and Cowin (1978). However, the hypothesis for deformation is conceptually different from that expressed in Mehrabadi and Cowin (1978). The basic premise of the present development is to depart from the limitations of plasticity assumptions such as: (*i*) that slip action only takes place along the characteristic laminae; and (*ii*) that the angle of dilatancy remains unchanged throughout the deformation process. The proposed model and its consequences are given in the subsequent sections.

In the discussion which follows a simplified fabric parameter is introduced (Jahedi, 1987), so that it can properly characterize the changes in the micromechnical behavior of granular materials. The significance of this model with regard to the general behavior of the material as described by other models is discussed and a kinematic hypothesis is postulated based on which the mathematical formulation is developed. The type of formulation used in Mehrabadi and Cowin (1978) is also adopted in the present study to derive the velocity equations for the behavior of grandular materials. Furthermore, a simple relation between the stresses and the fabric reconstruction parameter is introduced to complete the theory. Finally, a comparison of the new model with the existing theories is made and conclusions pertinent to these findings are presented.

2 A Simplified Model for the Fabric

The term *fabric* as used here identifies the spatial arrange-

[1]Formerly, Graduate Student, Department of Civil Engineering, Illinois Institute of Technology.

Contributed by the Applied Mechanics Division of THE AMERICAN SOCIETY OF MECHANICAL ENGINEERS for presentation at the Winter Annual Meeting, Dallas, Texas, November 25–30, 1990.

Discussion on this paper should be addressed to the Technical Editor, Leon M. Keer, The Technological Institute, Northwestern University, Evanston, Il 60208, and will be accepted until two months after final publication of the paper itself in the JOURNAL OF APPLIED MECHANICS. Manuscript received and accepted by the ASME Applied Mechanics Division, February 23, 1987.

Paper No. 90-WA/AMP-23.

Copyright © 1990 by ASME
Downloaded 03 May 2010 to 171.66.16.244. Redistribution subject to ASME license or copyright; see http://www.asme.org/terms/Terms_Use.cfm

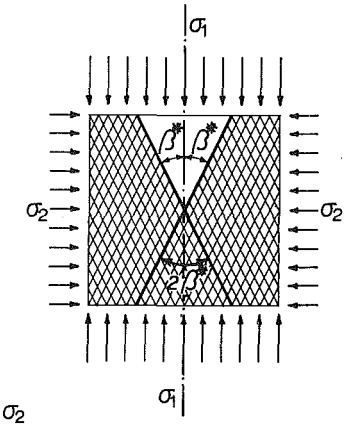


Fig. 1 An idealized representation of fabric behavior and the principal directions

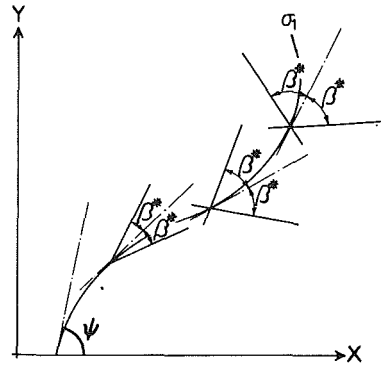


Fig. 2 Schematic representation of possible variation of β^* and ψ, the direction of principal stress

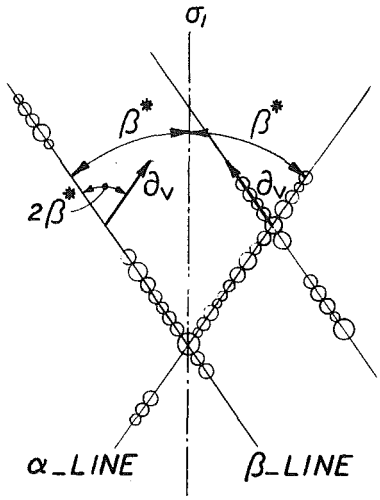


Fig. 3 Characteristic lines α and β and the relative velocity vector

ment of particles and associated voids for a macroscopically homogeneous assembly of particles (see Oda et al., 1982). This must include at least measures that identify particle orientations (fabric orientation) and measures which reflect the mutual relations of the particles (packing), (Oda and Konishi, 1974). For example, a second-order tensor is introduced by Nemat-Nasser and Mehrabadi (1983) which reflects many material components such as particle size, void ratio, contact area, as well as the orientations of the normals to the contact areas.

Considering the general microstructure of the fabric, the direction of normals to the contact area of the particles, plays a crucial role in describing the behavior of the granular material (Oda et al., 1982). For this reason, the proposed model emphasizes the average direction of these contact normals in its basic formulation of the problem. We consider a small element of the body, large enough to include a reasonably high number of contact normals. We define an angle β^* as the average of the angles which the contact normals make at each side of the principal stress direction (Jahedi, 1987). As shown in Fig. 1, the direction of the maximum compressive stress σ_1 bisects the angle $2\beta^*$. This is based on the test results that the fabric is coaxial with the principal stress direction (see Oda et al., 1980). This further implies that in an infinitesimal element we have a uniform distribution of granules, lined up along these β^*-lines, contacting each other, and, therefore transferring the overall stresses from one side of the element to the other side. Since the angle β^* is averaged over the element, any change in fabric due to stresses, such as intergrandular sliding or rolling of particles or disappearance of some contact normals and appearance of others, will only be reflected on the averaged β^*angle. This suggests that the angle β^* is continually changing during the deformation process and this angle can be considered as a dependent variable in the problem. Furthermore, the nature of the change is such that the magnitude of β^* decreases with the increase in the magnitude of the maximum compressive stress. This statement is based on the experimental observation reported by Oda et al. (1982), namely, *"the distribution of contact normals change in such a manner as to produce a greater concentration of contact normals along an orientation which parallels the direction of maximum principal compression."* The concentration of contact normals toward the direction of maximum principal compression and rotation of the principal stress direction are shown in Fig. 2.

3 Proposed Fabric Related Kinematic Hypothesis

In light of the discussion by Mehrabadi and Cowin (1978) regarding a kinematic proposal with respect to the characteristic lines, and also by virtue of the fact that in our fabric model the β^*-lines serve as the characteristic lines, we postulate that if α-lines and β-lines are two different characteristic fields, as shown in Fig. 3, any change in the velocity relative to a characteristic line α, that occurs between two of its successive points, is in the direction of the other characteristic line β. Conversely, a change in the velocity relative to β is in the direction of α. As a result of this, at any particle point each deformation consists of two such motions which are superposed on each other (see Fig. 3). This hypothesis will be expressed mathematically as velocity constraints.

3.1 Basic Assumptions. The derivation of velocity equations is similar to that of Spencer (1964), and Mehrabadi and Cowin (1978), except for the aforementioned assumption of the characteristic lines. These authors assume that the slip-lines coincide with the characteristic lines which result from a rigid perfect plasticity solution. However, they further indicate that the derivation of those velocity equations are independent of plasticity characteristic lines. In a detailed discussion, Spencer (1964), giving credit to Dr. R. Hill, explains that on any pair of curves which are bisected by the principal axis of strain at a material point, the plane deformation may in that neighborhood be regarded as the superposition of two relative velocities. In an effort to improve these models we choose two proposed β^*-lines instead of the plasticity characteristic lines to derive the respective velocity equations. Following Spencer (1964) and Mehrabadi and Cowins (1978) we introduce a rectangular coordinate system (ξ, η) which is in motion relative to the reference frame (x, y) system (see Fig. 4). On this basis, the following constraints are imposed on this model:

Downloaded 03 May 2010 to 171.66.16.244. Redistribution subject to ASME license or copyright; see http://www.asme.org/terms/Terms_Use.cfm

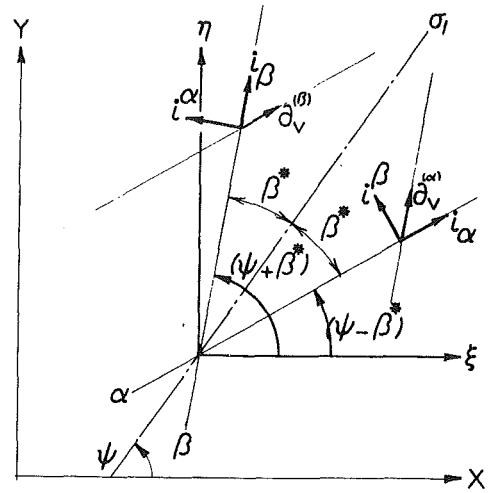


Fig. 4 The relationship among the direction of the maximum compression direction, ψ, the fabric angle β^*, and the coordinate systems attached to the characteristic lines α and β in the global coordinate system

(*a*) the origin of the (ξ,η) coordinate system always coincides with the position of the particle "Q" ;

(*b*) the (ξ,η) coordinate axes are taken to be parallel to the respective (x,y) coordinate axes at time t;

(*c*) the (ξ,η) coordinate system rotates relative to the (x,y) system about its instantaneous position "Q" in such a way that relative to (ξ,η) system the principal stress directions at "Q" are independent of time; and

(*d*) relative to the maximum principal stress direction, the α and β-lines (which are at angles of $\pm\ \beta^*$) change in such a manner that the principal stress direction always remains a bisector for the angle formed by α and β-lines, or the angle 2 β^*.

As mentioned earlier, this last constraint is imposed to incorporate the experimentally known fact that the distribution of contact normals tends to concentrate toward the direction of the maximum compressive stress (Oda et al., 1982). This differs from the model of Mehrabadi and Cowin (1978) in the following three aspects:

(*i*) Mehrabadi and Cowin (1978) assume that α and β-lines are plasticity derived characteristic lines (i.e., $\beta^* = \pi/4 + \phi/2$, in which ϕ is the internal angle of friction), whereas in our proposal, these are the average direction of force-transferring strings of granules. Although these are characteristic lines in a sense that relative velocity along these lines is zero, their property as described earlier is not derived from the classic plasticity assumption.

(*ii*) It was assumed by Mehrabadi and Cowin (1978) that the deformation is shear deformation, whereas our theory also allows the rolling of the particles as a participant of deformation mechanism.

(*iii*) A constant angle of dilatation was assumed by Mehrabadi and Cowins (1978), whereas in our basic assumption the change in β^* imposes a change in the angle of dilatancy proportional to the reconstruction of the fabric structure, (see Fig. 3).

3.2 General Formulation. We introduce $\mathbf{v}$ to denote the velocity of the particles relative to the (ξ,η) coordinate system. As shown in Fig. 4, we introduce unit vectors $\mathbf{i}_\alpha$ and $\mathbf{i}_\beta$ tangential and $\mathbf{i}^\beta$ and $\mathbf{i}^\alpha$ normal to the α and β-lines. Since the (ξ,η) coordinate as well as α-line and β-line coordinates are moving with respect to the global coordinate system, the following relations for the velocity $\mathbf{v}$ of the particle "Q" hold

$$\mathbf{v}^{(\alpha)} = \mathbf{v} - \mathbf{V} - (\psi - \beta^*)\mathbf{k} \times (s_\alpha \mathbf{i}_\alpha + s^\beta \mathbf{i}^\beta) \tag{1a}$$

$$\mathbf{v}^{(\beta)} = \mathbf{v} - \mathbf{V} - (\psi + \beta^*)\mathbf{k} \times (s_\beta \mathbf{i}_\beta + s^\alpha \mathbf{i}^\alpha) \tag{1b}$$

where $\mathbf{v}^{(\alpha)}$, $\mathbf{v}^{(\beta)}$ are velocities in α and β coordinates, respectively, V is the velocity of the origin of (ξ,η) coordinate system with respect to (x,y) coordinate system, and "s" is the length parameters along α and β coordinates. Our hypothesis may be expressed in the following way

$$\mathbf{i}^\alpha \cdot \mathbf{v}^{(\alpha)}{}_{,\alpha} = 0 \tag{2a}$$

$$\mathbf{i}^\beta \cdot \mathbf{v}^{(\beta)}{}_{,\beta} = 0. \tag{2b}$$

Substituting (1) into (2) we have

$$\mathbf{i}^\alpha \cdot [\mathbf{v}_{,\alpha} - (\psi - \beta^*)\mathbf{i}^\beta] = 0 \tag{3a}$$

$$\mathbf{i}^\beta \cdot [\mathbf{v}_{,\beta} - (\psi + \beta^*)\mathbf{i}^\alpha] = 0. \tag{3b}$$

Considering the fact that $\mathbf{i}^\alpha \cdot \mathbf{i}^\beta = \cos 2\beta^*$ we have

$$\mathbf{i}^\alpha \mathbf{v}_{,\alpha} - (\psi - \beta^*)\cos 2\beta^* = 0 \tag{4a}$$

$$\mathbf{i}^\beta \cdot_{,\beta} - (\psi + \beta^*)\cos 2\beta^* = 0. \tag{4b}$$

The transformation of coordinates to the global coordinates involves

$$\mathbf{i}^\alpha = -\sin(\psi + \beta^*)\mathbf{i} + \cos(\psi + \beta^*)\mathbf{j} \tag{5a}$$

$$\mathbf{i}^\beta = -\sin(\psi - \beta^*)\mathbf{i} + \cos(\psi - \beta^*)\mathbf{j} \tag{5b}$$

where $\mathbf{i}$ and $\mathbf{j}$ are unit vectors for the (x, y) coordinate system.

Substituting (5) into (4) and using the components v_x and v_y for the global directions of velocity, $\mathbf{v}$, we have

$$\begin{aligned}[-\sin(\psi+\beta^*)\mathbf{i} + \cos(\psi+\beta^*)\mathbf{j}] \cdot [v_{x,x}\cos(\psi-\beta^*)\mathbf{i} \\ + v_{y,x}\cos(\psi-\beta^*)\mathbf{j} + v_{x,y}\sin(\psi-\beta^*)\mathbf{i} \\ + v_{y,y}\sin(\psi-\beta^*)\mathbf{j}] - (\psi-\beta^*)\cos 2\beta^* = 0\end{aligned} \tag{6a}$$

$$\begin{aligned}[-\sin(\psi-\beta^*)\mathbf{i} + \cos(\psi-\beta^*)\mathbf{j}] \cdot [v_{x,x}\cos(\psi+\beta^*)\mathbf{i} \\ + v_{y,x}\cos(\psi+\beta^*)\mathbf{j} + v_{x,y}\sin(\psi+\beta^*)\mathbf{i} \\ + v_{y,y}\sin(\psi+\beta^*)\mathbf{j}] - (\psi+\beta^*)\cos 2\beta^* = 0.\end{aligned} \tag{6b}$$

Adding and subtracting equations (6*a*) and (6*b*) we get, respectively,

$$\begin{aligned}(v_{y,y} - v_{x,x})\sin 2\psi + v_{x,y}(\cos 2\psi - \cos 2\beta^*) \\ + v_{y,x}(\cos 2\psi + \cos 2\beta^*) - 2\dot{\psi}\cos 2\beta^* = 0\end{aligned} \tag{7a}$$

$$(v_{x,x} + v_{y,y})\sin 2\beta^* - 2\dot{\beta}^*\cos 2\beta^* = 0. \tag{7b}$$

Denoting $v_{x,x} = D_{11}$, $v_{y,y} = D_{22}$, $v_{x,y} + v_{y,x} = 2D_{12}$, and $v_{y,x} - v_{x,y} = 2\Omega_{12}$, equations (7) can be written as

$$2D_{12}\cos 2\psi + (D_{22} - D_{11})\sin 2\psi - 2(\Omega_{12} + \dot{\psi})\cos 2\beta^* = 0 \tag{8a}$$

$$(D_{11} + D_{22})\sin 2\beta^* = 2\dot{\beta}^*\cos 2\beta^*. \tag{8b}$$

The foregoing can be simplified using $\mathbf{T}$, the stress tensor and the following identities involving the stress components:

$$\tau = \left[\left(\frac{T_{11} - T_{22}}{2}\right)^2 + T_{12}^2\right]^{1/2}$$

$$\sin 2\psi = T_{12}/\tau,\ \cos 2\psi = (T_{11} - T_{22})/2\tau \tag{9}$$

$$\dot{\psi} = [(T_{11} - T_{22})\dot{T}_{12} - (\dot{T}_{11} - \dot{T}_{22})T_{12}]/4\tau^2.$$

Upon substitution of these stress identities into equations (8) and replacing the stress rate components with the Jaumann corotational rate $\mathring{T}_{ij}$, the components of the spin tensor vanishes and the final form of the velocity equations becomes

$$\begin{aligned}(D_{11} - D_{22})T_{12} - D_{12}(T_{11} - T_{22}) \\ = -\frac{\cos 2\beta^*}{2\tau}[(T_{11} - T_{22})\mathring{T}_{12} - (\mathring{T}_{11} - \mathring{T}_{22})T_{12}]\end{aligned} \tag{10a}$$

$$(D_{11} + D_{22}) = -\frac{(\cos 2\beta^*)\cos 2\beta^*}{1 - (\cos 2\beta^*)^2} \tag{10b}$$

Downloaded 03 May 2010 to 171.66.16.244. Redistribution subject to ASME license or copyright; see http://www.asme.org/terms/Terms_Use.cfm

or

$$D_{ik}T_{kj} - T_{ik}D_{kj} = -\frac{\cos 2\beta^*}{2\tau}(T_{ik}\mathring{T}_{kj} - \mathring{T}_{ik}T_{kj}) \tag{11a}$$

$$D_{ii} = -\frac{(\cos 2\beta^*)\cos 2\beta^*}{1-(\cos 2\beta^*)^2}. \tag{11b}$$

Interestingly, the only fabric parameter in the equations (11) appears in the form of cos $2\beta^*$ and its derivative. If cos $2\beta^* = 0$, (i.e., $\beta^* = \pi/4$), equation (11*b*) yields the incompressibility condition $D_{kk} = 0$, and (11*a*) yields the coaxiality of stress and strain-rate tensors. Equation (11*a*) also implies that at $\beta^* = \pi/4$, $\dot{\psi}$ can take any value and still coaxiality holds. Therefore, we conclude that β^* is a measure of geometrical anisotropy in the material and that for the specific value $\beta^* = \pi/4$, the material is isotropic. This conclusion was also made by Asaro (1979) in explaining a similar angle in metal plasticity.

Equation (11*a*), furthermore, demonstrates that in anisotropic materials (β^* not equal to $\pi/4$), the degree of noncoaxiality is also dependent on the rate of rotation of maximum compressive stress $\dot{\psi}$. When $\dot{\psi} = 0$, the coaxiality of principal stress and strain-rate axis is achieved even if the material is geometrically anisotropic (e.g., triaxial test prior to failure).

4 A Fabric-Related Stress Criterion

A rather general relation between the principal stresses and the fabric angle β^* can be expressed in the form

$$T_1/T_2 = g(\beta^*) \tag{12}$$

where g is a function of a fabric reconstruction parameter. Principal stresses are expressed in terms of the average normal and maximum shear stresses as

$$T_1, T_2 = \sigma \pm \tau \tag{13}$$

where σ is the mean stress ($\sigma = p = -T_{ii}/2$) and τ is defined before as the maximum shear stress. In this light, using equation (12), a stress criterion can be written in the familiar form of

$$\tau - \mu\sigma = 0 \tag{14}$$

and which

$$\mu = \frac{g(\beta^*) - 1}{g(\beta^*) + 1}. \tag{15}$$

Equation (14) resembles the Mohr-coulomb yield criterion. However, in this formulation the coefficient μ is not a constant but a function of the fabric reconstruction factor β^*. In the rate form, equation (14) becomes

$$\dot{\tau} - \mu\dot{\sigma} = \dot{\mu}\sigma \tag{16}$$

in which

$$\dot{\mu} = \frac{2\dot{g}(\beta^*)}{[1 + g(\beta^*)]^2}. \tag{17}$$

The right side of (16) can be viewed as a hardening function for the incremental yield surface and, as can be seen, it is dependent on the fabric reconstruction parameter and its derivative. In the indicial form equations (14) and (16) can be written as

$$\left(\frac{1}{2}T^*_{ij}T^*_{ij}\right)^{1/2} + \frac{\mu}{2}T_{ii} = 0 \tag{18}$$

$$\frac{1}{\tau}T^*_{ij}\mathring{T}_{ij} + \mu\mathring{T}_{ii} = -\dot{\mu}T_{ii} \tag{19}$$

where T^*_{ij} indicates the diviatoric components of the stress tensor. More specific possible forms of $g(\beta^*)$ will be discussed in Section 7.

5 The Complete Theory

A complete theory for the behavior of granular materials, for the case of two-dimensional deformation, is characterized by a system of equations composed of two velocity equations and one stress criterion related to the fabric reconstruction factor, two equilibrium equations, and one continuity equation. The unknowns consist of three stress components, two velocity components, and the density ρ. These equations are:

$$D_{ii} = -\frac{\dot{\mathfrak{B}}\mathfrak{B}}{1-\mathfrak{B}^2} \tag{20a}$$

$$T_{ik}D_{kj} - D_{ik}T_{kj} = -\frac{\mathfrak{B}}{2\tau}(\mathring{T}_{ik}T_{kj} - T_{ik}\mathring{T}_{kj}) \tag{20b}$$

$$\frac{1}{2\tau}T^*_{ij}\mathring{T}_{ij} + \frac{\mu}{2}\mathring{T}_{ii} = p\dot{\mu} \tag{20c}$$

$$T_{ij,i} = 0 \tag{20d}$$

$$\dot{\rho} + \rho D_{ii} = 0 \tag{20e}$$

where μ and $\dot{\mu}$ are defined by (15) and (17), respectively, and

$$\mathfrak{B} = \cos 2\beta^*, \quad \dot{\mathfrak{B}} = -2\dot{\beta}^* \sin 2\beta^*. \tag{21}$$

The fabric reconstruction factor $\mathfrak{B}$ is a time-dependent material property which can be viewed as the only hardening function which appears in this theory. Since $\mathfrak{B}$ is a meaningful parameter in terms of the laboratory experiments, different ways of determining this hardening function may be chosen:

(*i*) From the phenomenological point of view, by observing and analyzing the changes on the boundaries of the specimen, $\mathfrak{B}$ may be determined in the same way that the other hardening functions for different theories are found.

(*ii*) An alternate approach, however, is through the micromechanical study of the material in the course of deformation of the specimen. Some pioneer laboratory works have already been carried out (Oda, 1972; Drescher and De Josselin De Jong, 1976; and Oda et al., 1980, 1982). This can be viewed as a head start toward a more advanced and less costly measurement of the fabric as a material property.

6 Comparison With Existing Theories

Mehrabadi and Cowin (1980), modified the rigid-plastic yield vertex model, originally proposed by Rudnicki and Rice (1975), so that it contains their sliding deformation model, Mehrabadi and Cowin (1978), as its special case. Their final equations were of the form

$$\frac{1}{\tau}T^*_{ij}D^*_{ij} - \frac{1}{\beta_0}D_{ii} = 0 \tag{22a}$$

$$\frac{1}{h_1}(T_{ik}\mathring{T}_{kj} - \mathring{T}_{ik}T_{kj}) = D_{ik}T_{kj} - T_{ik}D_{kj},$$

$$h_1 = \tau\frac{\mu_0\beta_0 - 1}{\mu_0 - \beta_0} \tag{22b}$$

$$\frac{1}{2\tau}T^*_{ij}\mathring{T}_{ij} + \frac{\mu_0}{2}\mathring{T}_{ii} = \frac{h}{\tau}T^*_{ij}D^*_{ij} \tag{22c}$$

where D^*_{ij} are the diviatoric components of the strain-rate tensor. Equations (22) are equations (3), (18), and (20) of Mehrabadi and Cowin (1980), except that we have their μ and β replaced by μ_0 and β_0.

Downloaded 03 May 2010 to 171.66.16.244. Redistribution subject to ASME license or copyright; see http://www.asme.org/terms/Terms_Use.cfm

Comparing (22) and (20) we distinguish the nature of hardening in the two different theories. In (22*c*) a hardening parameter "h" is introduced which together with the distortional power, $T^*_{ij}D^*_{ij}$, is responsible for the hardening of the material. This type of hardening is work hardening. In (20*c*), on the other hand, the parameter "h" is not needed. Instead, the hardening is controlled by $\dot{\mu}$, a function of β^* and $\dot{\beta}^*$ which are fabric reconstruction factors and which explain a more realistic hardening procedure.

In order to express $\dot{\mu}$ in work-hardening terms, we may eliminate $\dot{\beta}^*$ from the two equations (17) and (21). This way we find the following equation

$$\dot{\mathfrak{B}} = \mathfrak{A}\dot{\mu}, \quad \mathfrak{A} = \frac{(1+g)^2 \sin 2\beta^*}{dg/d\beta^*}.$$

Using equation (20*a*) and equation (20*c*) the above relation can be written as

$$\frac{1}{2\tau} T^*_{ij} \mathring{T}_{ij} + \frac{\mu}{2} \mathring{T}_{ii} = \frac{1-\mathfrak{B}^2}{2\mathfrak{A}\mathfrak{B}} [T_{ii} D_{jj}]. \tag{23}$$

This is the rate form of the yield function in terms of the work parameters. Comparing equation (23) to that of modified vertex model (22*c*), we conclude that in the present model, the hardening function is not dependent on distortional work but on dilatational work as well as the fabric reconstruction factor. This type of hardening is also comparable to the type of hardening employed by Nemat-Nasser et al. (1980) (see their equation (4.27)) in modeling the triaxial behavior of cohesionless sands except that its distortional work hardening is inherent in the fabric hardening parameter in the new model.

Comparison of equations (22*b*) and (20*b*) shows that the second hardening parameter "h_1" is nothing but another function of fabric reconstruction factor β^*, i. e.,

$$h_1 = \frac{\tau}{\mathfrak{B}} = \frac{\tau}{\cos 2\beta^*}. \tag{24}$$

In other words, there is no need to introduce extra parameter "h_1" in the formulation. The type of noncoaxiality parameter shown in (24) is similar in form to equation (2.23) of Nemat-Nasser (1983), which was named "Mandel-Spencer noncoaxiality Modulus." Finally in comparing equations (22*a*) and (20*a*), we notice that the dependency of dilatation on an extra term ($\dot{\mathfrak{B}}$) in the new model. If $\mathfrak{B}$ is a constant, then the two equations are equivalent.

7 A Simplified Feature of the Theory

In an effort to simplify the model to tangible form, we consider the case of the triaxial test for a typical sample, and we apply equations (20*a*)–(20*c*) in order to investigate the stress-strain-volume change relations.

In the triaxial test the initial state of stress is defined by

$$T_{11} = -T_1,\ T_{22} = T_{33} = -T_2,\ T_{ij} = 0, i \neq j,\ T_1 > T_2. \tag{25}$$

Deviatoric components of the stress tensor are

$$T^*_{11} = \frac{2}{3}(T_1 - T_2),\ T^*_{22} = T^*_{33} = -\frac{1}{3}(T_1 - T_2) \tag{26}$$

and equation (9) yields

$$\tau^2 = \frac{1}{3}(T_1 - T_2)^2. \tag{27}$$

In the conventional triaxial test no rotation of the maximum principal stress, in the global coordinates, is assumed, hence $\dot{\psi} = 0$. Therefore, equation (20*b*) leads to the coaxiality of stress and strain rate and as the result of this equation we have

$$D^*_{11} = \frac{2}{3}(D_1 - D_2),\ D^*_{22} = D^*_{33} = -\frac{1}{3}(D_1 - D_2). \tag{28}$$

Substituting the above results into equations (20*a*) and (20*c*), the following equations can be derived

$$\dot{\Delta} = \frac{\dot{\mathfrak{B}}\mathfrak{B}}{1-\mathfrak{B}^2} \tag{29a}$$

$$\dot{q} - \mu\dot{p} = p\dot{\mu} \tag{29b}$$

in which the following soil mechanics conventions are used

$$\dot{\epsilon} = -D^*_{11},\ \dot{\Delta} = -(D_1 + 2D_2)$$

$$q = (T_1 - T_2) = \sqrt{3}\tau,\quad p = \frac{1}{3}(T_1 + 2T_2). \tag{30}$$

If ϵ is chosen as the time parameter, and if it is further assumed that the confining pressure is constant through the test (i.e., $\dot{p} = 0$), both equations (29*a*) and (29*b*) can be integrated to yield the following relations:

$$\Delta = \frac{1}{2}\ln(1-\mathfrak{B}^2) + C_1 \tag{31a}$$

$$\frac{q}{p} = \mu + C_2 \tag{31b}$$

where C_1 and C_2 are constants of integration and may be found by the initial conditions at $\epsilon = 0$, $\Delta = q = 0$.

It is worthwhile to depart from the subject at this point to investigate some options of the fabric function $g(\beta^*)$. Fortunately, most of the research related to the material fabric is carried out in relation to the principal stress ratio. Rowe (1962, 1964) in his investigation, and as a result of his experiments on granular materials composed of regular packing of spheres, proposed that at any stage of deformations of any ideal packing, the effective-stress relation in a triaxial test is given by

$$T_1/T_2 = \tan\alpha \tan(\phi_\mu + \beta) \tag{32}$$

in which α is the average inclination of a potential slip surface to the major principal stress axis and β is the inclination of tangents at sliding contacts to the minor principal axis. Oda and Konishi (1974) and Oda (1972), as the result of their elaborate tests, concluded that the stress ratio has a linear relation with the fabric factor which he called the fabric anisotropy factor. Oda, in discussing his results also indicated that such relation is applicable to peak stress condition as well as prepeak stress conditions. His reasoning is that "the process of fabric reconstruction is successive without any distinct change of basic mechanism during the deformation between the stage of prepeak stress and peak stress." Oda et al. (1982) expressed a second-order relation between the principal stress ratio and the fabric ratio. However, the linear part still played a dominant role in shaping their resulting curve.

It is of interest to note that a familiar form of stress ratio formulation, at failure, is common among most of the above-mentioned authors as well as other investigators, (see Lee and Seed, 1967). This formulation has the form of

$$T_1/T_2 = \tan^2(\pi/4 + \phi/2). \tag{33}$$

In the light of the foregoing discussion, and also for simplicity, it is reasonable to set the stress ratio for our theory as follows

$$T_1/T_2 = \cot^2\beta^* \tag{34}$$

where $\tan\beta^*$ is a measure of fabric ratio. As a consequence of equation (34), equation (15) can be made more specific as

$$\mu = \frac{1-\tan^2\beta^*}{1+\tan^2\beta^*} = \cos 2\beta^* = \mathfrak{B}, \tag{35}$$

Downloaded 03 May 2010 to 171.66.16.244. Redistribution subject to ASME license or copyright; see http://www.asme.org/terms/Terms_Use.cfm

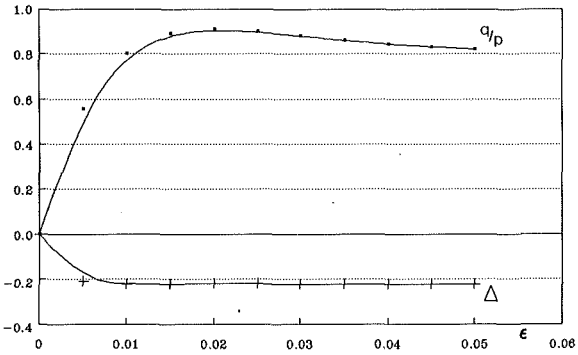


Fig. 5 Plot of the stress ratio q/p and the dilation Δ versus the strain ϵ using equations (38) when $a=0.8$, $b=80.0$, $\gamma=100.0$. (The upper curve represents q/p and the lower curve Δ.)

and finally equation (31*b*) can, in its simplest form, be written as:

$$q/p = \mathfrak{B} + C_2. \tag{36}$$

As discussed in Sections 2 and 5, the fabric reconstruction angle (i.e., β^* in this case) is an average quantity and it is a function of different physical variables, which has to be determined through experiments. Unfortunately, in the present state of knowledge, the importance of this parameter is not fully appreciated. Further investigations exploring the significance of this parameter are needed. Oda et al. (1982), Oda (1972), and Oda et al. (1980) present some preliminary examples in investigating the fabric factor.

However, like many other theories, in selecting their hardening function phenomenologically, we may also select $\mathfrak{B}$ (as a hardening function) in such a way that it reflects the variation of the material voids and the concept of the critical void ratio with respect to the derivatoric strain measure. We set

$$\mathfrak{B} = (b\epsilon - a)e^{-\gamma\epsilon} \tag{37}$$

where a, b, and γ are constants to be determined experimentally such that $\mathfrak{B}$ is always less than unity. The exponential part of equation (37) is a very common representation of loose sand and gives an asymptote at infinity. The linear term in the parenthesis, however, contributes another root for $\mathfrak{B}$ to account for the peak responses in the behavior of dense sands. By substituting $\mathfrak{B}$ into equations (31*a*) and (36), the following final equations for the response of the triaxial specimen under drained conditions are obtained:

$$\Delta = -\frac{1}{2}\ln\frac{1-\mathfrak{B}^2}{1-a^2}. \tag{38a}$$

$$\frac{q}{p} = \mathfrak{B} + a \tag{38b}$$

Equations (38) represent qualitatively the behavior of granular material over a range of loose to dense initial conditions. From equation (38*b*) it is clear that $a>0$ is nothing but the coefficient of friction of the material in the residual stress state, and can be found easily in the laboratory. Coefficient b, on the other hand, is related to the initial void ratio. If $b=0$, the model exhibits a loose sand behavior and for any values of $b>0$, it exhibits different degrees of dense behavior.

Figure 5 displays the stress-strain-volume change curves for a simple form of the model.

8 Summary and Conclusions

Based on the proposed kinematic hypothesis, two basic velocity equations are developed. One equation is responsible for the dilation in the material. The other equation, which relates the stress rates to the strain rate components, accounts for the geometrical anisotropy of the material.

A type of fabric hardening incremental stress criterion is proposed. Since this criterion is not friction-based, the rolling of the particles can also be accounted for through the β^*-parameter. The fabric reconstruction parameter, $\mathfrak{B}$, is the backbone of the theory and relates the velocity and the stress equations.

A comparison with the modified rigid plastic yield vertex model, Mehrabadi and Cowin (1980), indicates that the pressure sensitivity parameter, μ_0, the dilatancy factor, β_0, and two other hardening functions, h_1 and h, are all expressible in terms of the fabric reconstruction parameter, $\mathfrak{B}$, and this way the number of parameters is reduced.

Furthermore, material presented in Section 7 is a simplified phenomenological representation and it does not exhibit the true potential of the present theory. The capabilities of the theory may be exemplified by solving our sample problem as a field problem with prescribed boundary conditions. Employing the noncoaxiality condition of equation (20*b*) and the additional limit assumption on $\beta^*_{\min}$, together with the vertex behavior the yield function stated in other theories (see Rudnicki and Rice, 1975), may be utilized to achieve a proper softening criterion. This is expected to lead to the localization of deformation in the failure zones and to the formation of shear bands.

References

Asaro, R. J., and Rice, J. R., 1977, "Strain Localization in Ductile Single Crystals," *J. Mech. Phys. Solids*, Vol. 25, pp. 309–338.

Asaro, R. J., 1979, "Geometrical Effects in the Inhomogeneous Deformation of Ductile Single Crystals," *Acta Metallurgica*, Vol. 27, pp. 445–453.

De Josselin De Jong, G., 1959, "Statics and Kinematics in the Failable Zone of a Granular Material," *Uitgeverij*, Delft.

Drescher, A., and De Josselin De Jong, G., 1972, "Photoelastic Verification of a Mechanical Model for the Flow of a Granular Material," *J. Mech. Phys. Solids*, Vol. 20, pp. 337–351.

Drescher, A., 1976, "An Experimental Investigation of FLow Rules for Granular Materials Using Optically Sensitive Glass Particles," *Geotechnique*, Vol. 26, pp. 591–601.

Jahedi, J., 1987, "A Fabric Related Double-Slip Model For Granular Materials," Ph.D. Thesis, Illinois Institute of Technology, Chicago, Ill.

Lance, G. L., and Nemat-Nasser, S., 1986, "Slip-Induced Plastic Flow of Geomaterials and Crystals," *Mech. of Materials*, Vol. 5, pp. 1–11.

Lee, K. L., and Seed, H. B., 1967, "Drained Strength Characteristics of Sands," *J. Soil Mech. Found.*, ASCE Proc., Vol. 93, No. SM6, pp. 117–141.

Lemonds, J., Asaro, R. J., and Needleman, A., 1985, "A Numerical Study of Localized Deformation in Bi-Crystals," *Mech. of Materials*, Vol. 4, pp. 417–435.

Mandel, J., 1947, "Sur les Lignes de Glissement et le Calcul des De'placements dans la De'formation Plastique," *Comptes Rendus de l'Acaddmie des Sciences*, Vol. 225, pp. 1272–1273.

Mandl, G., and Fernandez Luque, R., 1970, "Fully Developed Plastic Shear Flow of Granular Materials," *Geotechnique*, Vol. 20, pp. 277–307.

Mehrabadi, M. M., and Cowin, S. C., 1978, "Initial Planar Deformation of Dilatant Granular Materials," *J. Mech. Phys. Solids*, Vol. 26, pp. 269–284.

Mehrabadi, M. M., and Cowin, S. C., 1980, "Prefailure and Postfailure Soil Plasticity Models," *J. Eng. Mech.*, ASCE, Vol. 106, No. EM5, pp. 991–1003.

Nemat-Nasser, S., and Shokooh, A., 1980, "On Finite Plastic Flows of Compressible Materials With Internal Friction," *Int. J. Solids Structures*, Vol. 16, No. 6, pp. 495–514.

Nemat-Nasser, S., Mehrabadi, M. M., and Iwakuma, T., 1980, "On Certain Macroscopic and Microscopic Aspects of Plastic Flow of Ductile Materials," *Three Dimentional Constitutive and Ductile Fracture*, Proc. IUTAM Symp., S. Nemat-Nasser, ed., Dourdan, France, June 2–5, 1981, North Holland, pp. 157–172.

Nemat-Nasser, S., 1983, "On Finite Plastic Flow of Crystaline Solids and Geomaterials," ASME JOURNAL OF APPLIED MECHANICS, Vol. 50, pp. 1114–1126.

Nemat-Nasser, S., and Mehrabadi, M. M., 1983, "Stress and Fabric in Granular Material Masses," *Mech. of Granular Materials*, J. T. Jenkens, ed., Elsevier, New York.

Oda, M., 1972, "Initial Fabrics and Their Relations to Mechanical Properties of Granular Material," *Soils and Foundations*, Vol. 12, pp. 17–36.

Downloaded 03 May 2010 to 171.66.16.244. Redistribution subject to ASME license or copyright; see http://www.asme.org/terms/Terms_Use.cfm

Oda, M., 1972, "The Mechanism of Fabric Changes During Compressional Deformation of Sand," *Soils and Foundations*, Vol. 12, No. 2, pp. 1–18.

Oda, M., 1972, "Deformation Mechanism of Sand in Triaxial Compression Test," *Soils and Foundations*, Vol. 12, pp. 45–63.

Oda, M., and Konishi, J., 1974, "Microscopic Deformation Mechanism of Granular Material in Simple Shear," *Soils and Foundations*, Vol. 14, pp. 25–37.

Oda, M., 1975, "On Stress-Dilatancy of Sand in Simple Shear Test," *Soils and Foundations*, Vol. 15, pp. 17–29.

Oda, M., Konishi, J., and Nemat-Nasser, S., 1980, "Some Experimentally Based Fundamental Results on the Mechanical Behavior of Granular Materials," *Geotechnique*, Vol. 30, pp. 479–495.

Oda, M., Konishi, J., and Nemat-Nasser, S., 1982, "Experimental Micromechanical Evaluation of Strength of Granular Materials: Effects of Particle Rolling," *Mech. of Materials*, Vol. 1, pp. 269–283.

Rowe, P. W., 1962, "The Stress-Dilatancy Relation for Static Equilibrium of an Assembly of Particles in Contact," *Proc. Royal Soc., London*, Vol. A269, pp. 500–527.

Rowe, P. W., 1963, "Stress-Dilatancy, Earth Pressures and Slopes," *J. Soil Mech. Found.*, Div., ASCE, Vol. 89, No. SM3, pp. 37–61.

Rudnicki, J. W., and Rice, J. R., 1975, "Conditions for the Localization of Deformation in Pressure-Sensitive Dilatant Materials," *J. Mech. Phsy. Solids*, Vol. 23, pp. 371–394.

Spencer, A. J. M., 1964, "A Theory of Kinematics of Ideal Soils Under Plane Strain Conditions," *J. Mech. Phys. Solids*, Vol. 12, pp. 337–351.

Downloaded 03 May 2010 to 171.66.16.244. Redistribution subject to ASME license or copyright; see http://www.asme.org/terms/Terms_Use.cfm

Swinging Wake Mechanism for Interface Wave Generation in Explosive Welding of Metals

R. C. Gupta
Assistant Professor,
Department of Mechanical Engineering,
Mutah University,
Mutah, Al-Karak, Jordan

G. S. Kainth
Professor,
Department of Mechanical Engineering,
Indian Institute of Technology,
Kanpur, India

A hydrodynamic model of explosive welding is considered. A swinging wake model for explosive welding is used to explain the generation of interfacial waves and to predict wave characteristics. The two plates are considered as main fluid jets divided by stagnation streamlines into a saliant jet and a reentrant jet. The model considers that the wake swings from side to side behind an imaginary obstacle bounded by the stagnation streamlines, thereby producing a wavy interface. Prediction of degree of distortion, η, and amplitude-to-wavelength ratio h/λ, by the swinging wake model show reasonable agreement with the available experimental results. The expression for the diameter of the obstacle is developed for the general situation in explosive welding.

Introduction

Explosive welding is done by oblique impact of a plate over another plate by explosive charge (Blazynski, 1983; Crossland, 1976). Explosive welding is applied to plate cladding, welding to tube plate of heat exchangers, manufacture of duplex tubing, and production of fiber-reinforced materials (Blazynski, 1983; Crossland, 1976). Explosive welding provides surface-to-surface welding which is usually not possible by other welding processes.

Explosive welding is classified into two broad categories, viz. (*a*) symmetric welding and (*b*) asymmetric welding, on the basis of whether the explosive is laid on both the plates or on one plate only. A schematic diagram for the asymmetric explosive welding is shown in Fig. 1(*a*). Flier plate is kept inclined at an angle α to the parent plate. An explosive powder/sheet is laid on the flier plate, while a buffer plate is kept in between to avoid damage to the flier plate. The explosive is ignited from one end with a detonator. Figure 1(*b*) describes the configuration of the flier plate during the process of welding.

Figure 2(*a*) shows the collision of the flier plate, moving at impact velocity, V_P, with the parent plate. Figure 2(*b*) represents a kinematically equivalent system such that the stagnation point S is considered at rest. Since the pressure encountered in explosive welding is much higher than the yield shear strength of the material (Birkhoff, 1948) and strain rates are usually higher than the critical strain rate (10^7/sec) above which the material behaves like inviscid fluid (Robinson, 1975), a hydrodynamic model of explosive welding near the impacting region, as considered by various research workers (Blazynski, 1983; Crossland, 1976; Birkhoff et al., 1948; Robinson, 1975; Bahrani et al., 1967; Hunt, 1968; Godunov, et al. 1970; Cowan, 1971; Kowalic and Hay, 1971; Reid, 1974, 1978), is justified. The flier plate is considered to impinge on

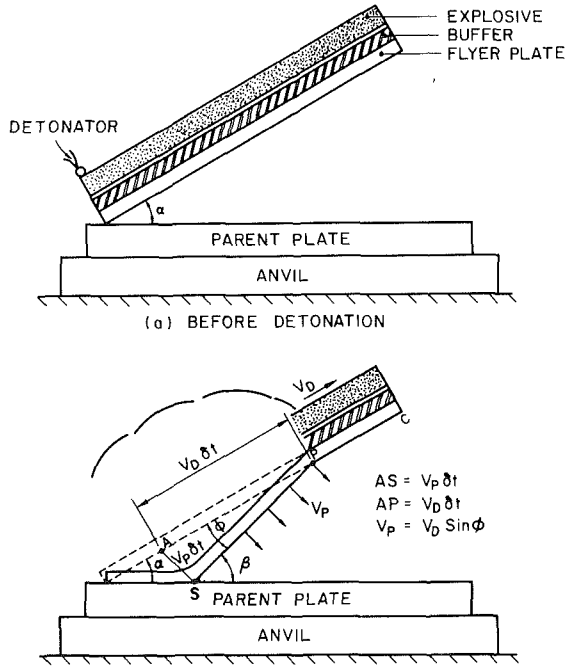


Fig. 1 Mode of collapse of flier plate

Contributed by the Applied Mechanics Division of THE AMERICAN SOCIETY OF MECHANICAL ENGINEERS for presentation at the Winter Annual Meeting, Dallas, Texas, November 25–30, 1990.

Discussion on this paper should be addressed to the Technical Editor, Leon M. Keer, The Technological Institute, Northwestern University, Evanston, IL 60208, and will be accepted until two months after final publication of the paper itself in the JOURNAL OF APPLIED MECHANICS. Manuscript received by the ASME Applied Mechanics Division, Mar. 28, 1988; final revision, Sept. 1, 1989.

Paper No. 90-WA/APM-19.

Copyright © 1990 by ASME
Downloaded 03 May 2010 to 171.66.16.244. Redistribution subject to ASME license or copyright; see http://www.asme.org/terms/Terms_Use.cfm

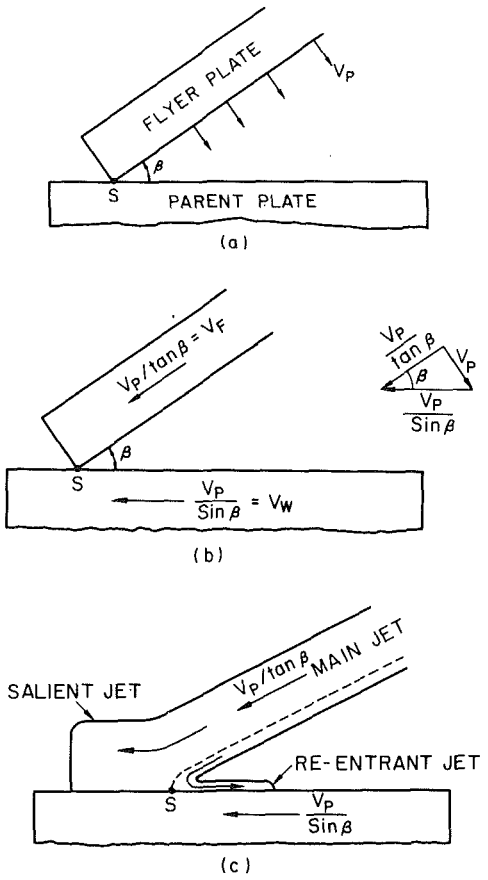


Fig. 2 The formation of the metal jet

the parent plate as a main fluid jet which divides into (*i*) saliant jet and (*ii*) reentrant jet as shown in Fig. 2(*c*).

By considering conservation of mass and momentum, expressions for the thickness of the reentrant jet, t_r, and saliant jet, t_s, are developed (Birkhoff et al., 1948) as

$$t_r = t(1-\cos\beta)/2 \tag{1}$$

$$t_s = t(1+\cos\beta)/2. \tag{2}$$

The obliquity angle β is generally given by (3)

$$\beta = \alpha + \tan^{-1}(V_P/V_D) \cong \alpha + V_P/V_D \tag{3}$$

where V_P is the plate velocity, V_D is the detonation velocity of the explosive ($V_D \gg V_P$ leads to a small angle approximation), α is the set-up angle. Equation (3) is common in the explosive welding community; however, some research workers suggest it as $\beta = \alpha + \sin^{-1}(1/2V_P/V_D)$.

The importance of the nature of the weld interface on the strength of a weld was appreciated by Bayce (1964) and Bahrani and Crossland (1966). The profile of the welded interface is, in general, wavy. Various theories (Robinson, 1975; Bahrani et al., 1967; Hunt, 1968; Godunov et al., 1970; Cowan, 1971; Kowalic and Hay, 1971; Reid, 1974, 1978) have been proposed to explain the interface-wave generation and to predict wave characteristics. Bahrani et al. (1967) proposed an indentation mechanism assuming that waves are formed by periodic indentation and hump formation ahead of the stagnation point. Hunt's (1968) analysis is based on Helmholtz instability between the reentrant jet and the parent plate. Godunov et al. (1970) envisaged that the mechanism of wave formation is due to an effect of rarefaction waves produced by the reflection of compressive shock waves. Cowan et al. (1971) and Robinson (1975) suggest that the wave formation is due to Helmholtz instability.

Klein (1965) noticed that the general appearance of the

Nomenclature

I = moment of inertia of the swinging wake
L = barrier height
N_1 = frequency of the swinging wake when moving towards a material of density ρ_1
Re = Reynolds number
U = speed of all the jets
V_D = detonation velocity of an explosive
V_{D1}, V_{D2} = detonation velocity of the two explosives
V_F = velocity of the main stream
V_{FS} = velocity of vortex street relative to fluid at infinity
V_P = plate velocity
V_{p1}, V_{p2} = velocity of plates I and II
a_1, a_2 = wavelengths of the interface wave when the wake swings toward materials of density ρ_1, ρ_2
c = amplitude-to-wavelength ratio h/λ
d = diameter of the assumed obstacle
h = height of the wake, amplitude (see Fig. 3) of the interface wave
k = fraction of total wake height occupied by the metal of density ρ_1
$2l$ = current length of the swinging wake
m = mass of the swinging wake
r = ratio of thickness of plate I to plate II, $r = t_1/t_2$
r_r = ratio of thickness of the reentrant jet to the thickness of plate II
r_s = ratio of thickness of the saliant jet to the thickness of plate II
(x_o, y_o) = coordinates of the point of intersection of the extension of the two stagnation streamlines
x_1 = abcissa of the center of the assumed obstacle
α = set-up angle (Fig. 1), 2α included angle (Fig. 5)
α_1, α_2 = inclination of the plates I and II, w.r.t. collision direction
β = obliquity angle
β_1, β_2 = obliquity angles of the plates I and II, w.r.t. collision direction
ϕ = dynamic bend angle
θ_c = collision direction w.r.t., a line bisecting the set-up angle
ϵ = V_{FS}/V_F
λ = distance between two consecutive maxima of the interface wave
ξ = distance between a maxima and the succeeding minima of the interface wave in the direction of stream
ρ_1 = density of the lighter metal
ρ_2 = density of the heavier metal
η = degree of distortion (of the wave)
ν = complex velocity
μ = viscosity of the metal jet

Downloaded 03 May 2010 to 171.66.16.244. Redistribution subject to ASME license or copyright; see http://www.asme.org/terms/Terms_Use.cfm

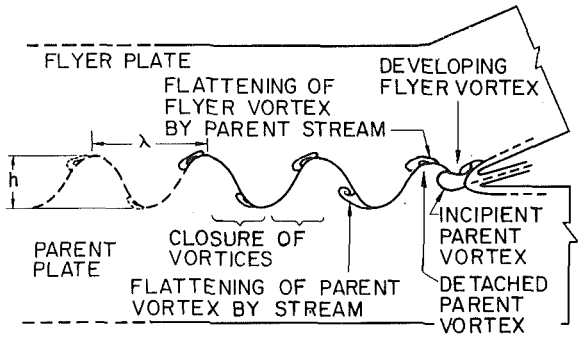


Fig. 3 Formation of wavy interface

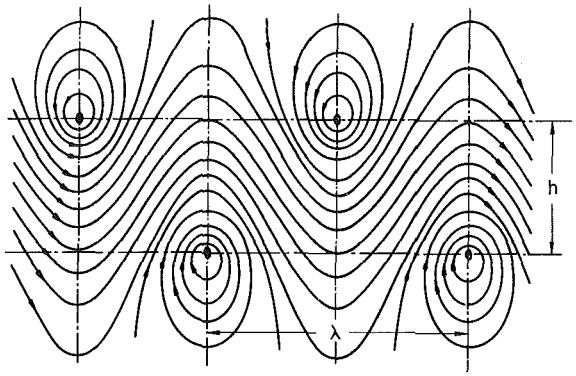


Fig. 4 Flow pattern produced by von Karman vortex street

welded interface (Fig. 3) is similar to a von Karman vortex street (Fig. 4). Klein's experimental investigation shows that the average value of amplitude-to-wavelength ratio h/λ of welded interface is 0.3, which is close to the value of the von Karman vortex street stable spacing ratio of 0.28.

Kowalic and Hay (1971) applied the vortex shedding theory to wave formation (Fig. 3) in explosive welding. They considered the collision of two plates as a fluid flow problem with the reentrant jet corresponding to an obstacle (barrier) in the flow. The flow regime behind an obstacle is governed by the Reynolds number (Re) given by

$$\mathrm{Re} = V_F L \rho / \mu \tag{4}$$

where ρ and μ are metal density and viscosity of the metal jet, V_F is the stream velocity, and L is the barrier height or the obstacle diameter. However, it is noted that in explosive welding (Kowalic and Hay, 1971), transition from laminar flow to flow causing a vortex street occurs when the Reynolds number is in the range $2 < \mathrm{Re} < 3$ and wave formation was observed up to $\mathrm{Re} \cong 10$.

An interface wave profile corresponds to a sine wave for the case of welding of similar metals; however, the wave deviates from a sine wave for the case of welding of dissimilar metals (Onzawa and Ishii, 1975). In spite of the fact that many theories have been proposed so far and that they explain wave formation, there is as yet no complete analogy available which will explain the formation of welded waves and its characteristics including distortion. In the present paper, the "Swinging Wake Model" is proposed to explain the generation of the interface wave. The model predicts wave characteristics such as amplitude, wavelength, and distortion. To cover up both (symmetric and asymmetric) cases of explosive welding and for generality, a general asymmetric case of explosive welding is considered and the proposed "swinging wake model" is applied therein.

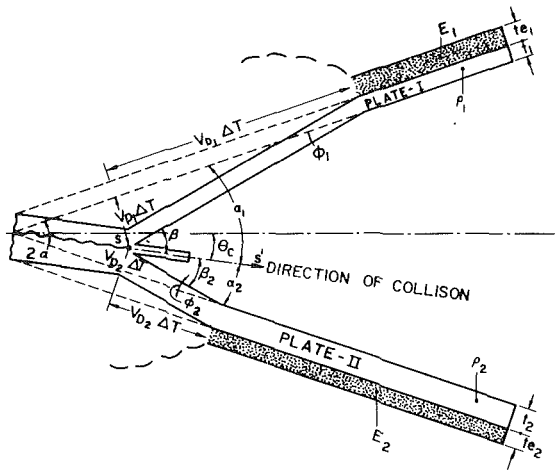


Fig. 5 Collision of plates in general-symmetric explosive welding

General Asymmetric Explosive Welding

A schematic diagram of a general asymmetric explosive welding situation is shown in Fig. 5. The plates are kept at an initial inclination of 2α. The detonation of explosive(s) imparts a velocity V_{P1} to plate I and a velocity V_{P2} to plate II.

Study of various formulae reported in the literature for plate velocity V_P, reveals that the main parameters on which V_P depends are the explosive loading and the detonation velocity of explosive. The simplest one is that given by Gurney (Birkhoff et al., 1948; Hay, 1971; Birkhoff and Zarantonello, 1948) as

$$V_P = \frac{0.612 e/m}{2 + e/m} V_D \tag{5}$$

where e/m is the explosive loading (the ratio of mass of explosive to the mass of flier plate and buffer plate) and V_D is the detonation velocity of the explosive.

A general asymmetric welding situation is defined as the case where $V_{P1} \neq V_{P2}$; and, hence, the reentrant jet does not bisect the included angle between the two plates. If the direction of collision is inclined (Fig. 5) at an angle α_1 and α_2 with plates I and II, respectively, the velocity ratio r_v, from geometry of collision and then using a small angle approximation is written (Gupta and Kainth, 1980) as

$$r_v = V_{P2}/V_{P1} = \sin\alpha_2/\sin\alpha_1 \cong \alpha_2/\alpha_1. \tag{6}$$

The included angle between the plates is thus

$$2\alpha = \alpha_1 + \alpha_2. \tag{7}$$

The angle θ_c between the direction of collision and a line bisecting the set up angle is given (Fig. 5) by $\theta_c = \alpha_1 - \alpha$ and using equations (6) and (7) for α_1, is written as

$$\theta_c = \alpha_1 - \alpha = (1 - r_v)/(1 + r_v)\alpha. \tag{8}$$

Obliquity angles β_1 and β_2, with respect to the collision direction for the two plates, are defined (using equation (3)) as

$$\beta_1 \cong \alpha_1 + V_{P1}/V_{D1} \tag{9}$$

$$\beta_2 \cong \alpha_2 + V_{P2}/V_{D2}. \tag{10}$$

The general asymmetric welding case (Fig. 5) reduces to: (*a*) asymmetric welding case (Fig. 1(*b*)) if $\beta_2 = 0$ and (*b*) symmetric welding case if $\beta_1 = \beta_2$.

Swinging Wake Model

The proposed hydrodynamic model for explosive welding of dissimilar metals is shown in Fig. 6. There are two stagnation streamlines which separate the main jets into corresponding

Downloaded 03 May 2010 to 171.66.16.244. Redistribution subject to ASME license or copyright; see http://www.asme.org/terms/Terms_Use.cfm

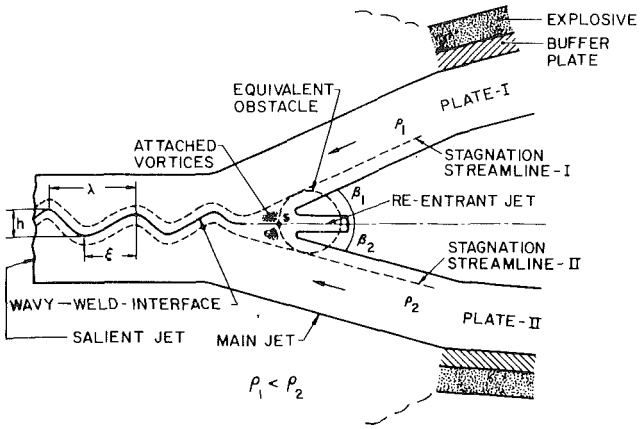


Fig. 6 Hydrodynamic model for general-symmetric explosive welding

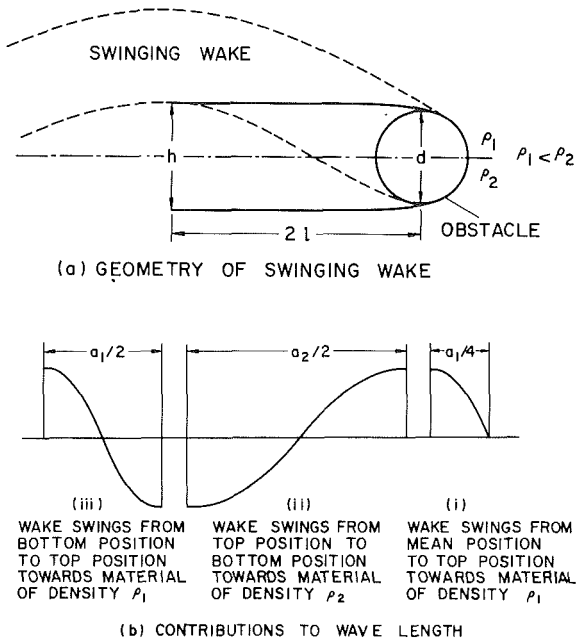


Fig. 7 Mechanism of formation of interface wave

saliant jets and reentrant jets. By considering an imaginary obstacle bounded by the two stagnation streamlines, the problem reduces to flow of two different fluids meeting at an angle over an obstacle. The velocity distribution around the stagnation streamlines is similar (Robinson, 1975) to the velocity distribution around a real obstacle in fluid flow. Hence, it is reasonable to assume an imaginary obstacle between the two stagnation streamlines.

The wake behind the obstacle swings from side to side (Fig. 6) producing a wavy interface in explosive welding which is characterized (Reid, 1974) by frequency of the swinging wake. The problem of the flow of two different fluids over an obstacle is analyzed by Gupta and Kainth (1979). The restoring force acting on the "wake," modeled as an "aerofoil," is obtained (Gupta and Kainth, 1979) by considering the flow of two different fluids meeting at an angle over an "equivalent rotating cylinder" (which is a usual way of modeling in fluid flow), as

$$F \cong 2\pi\rho^* V_F^2 l w\theta \tag{11}$$

where V_F is the fluid stream velocity, l is half the length of the swinging wake, θ is the current tilt of the wake and ρ^* is the density of the fluid from which the wake is moving away, w is the wake width.

Considering the wake oscillator model of Birkhoff (1953) and Birkhoff and Zarantonello (1948) that the wake swings from side to side, the following expression is written if the wake is moving from a fluid of density, ρ_2, into a fluid of density ρ_1 (Fig. 7(*a*)), assuming that the lift force is acting at a distance $l/2$ from the point of swing as $I\ddot{\theta}$ = restoring couple, or

$$\frac{4}{3} m l^2 \ddot{\theta} = -\pi\rho_2 V_F^2 l^2 w\theta. \tag{12}$$

The related frequency of the swinging wake is given by

$$N_1 = \frac{V_F}{2\pi}\sqrt{\frac{3\pi\rho_2 w}{4m}}. \tag{13}$$

The corresponding wavelength, a_1, is given by

$$N_1 a_1 = (V_F - V_{FS}) = V_F(1-\epsilon) \tag{14}$$

where V_{FS} is the velocity of vortex street and $\epsilon = V_{FS}/V_F$.

From equations (13) and (14)

$$a_1 = (1-\epsilon)\sqrt{\frac{16\pi m}{3\rho_2 w}}. \tag{15}$$

Considering that the wake height h is made up of two materials of densities ρ_1 and ρ_2 and k is the fraction of total wake height occupied by metal of density ρ_1, the mass of the wake (of width w) is given by

$$m = 2h[k\rho_1 + (1-k)\rho_2]lw. \tag{16}$$

It is assumed that the length of the wake "2 l" varies from 0 to $a_1/2$ giving an average value of $l = a_1/8$. Hence, from equations (15) and (16),

$$a_1 = \frac{4\pi}{3}(1-\epsilon)^2[k\rho_1 + (1-k)\rho_2]h/\rho_2. \tag{17}$$

During movement of the wake from mean position to top position in material of lower density ρ_1, the contribution to the wavelength is $a_1/4$ as shown in Fig. 7(*bi*).

Similarly, when the wake starts swinging from the top position towards material of higher density, ρ_2, it contributes a portion of the wavelength equal to $a_2/2$ as shown in Fig. 7(*bii*) such that,

$$a_2 = \frac{4\pi}{3}(1-\epsilon)^2[k\rho_1 + (1-k)\rho_2]h/\rho_1. \tag{18}$$

When the wake moves from the bottom position to the top towards material of lower density, ρ_1, it again contributes a portion of the wavelength equal to $a_1/2$, as shown in Fig. 7(*biii*).

Thus, the interface wave is formed by contributions from upward and downward movements of the wake in both materials. Combination of various portions of the wave yields the final shape of the interface wave, as represented in Fig. 6.

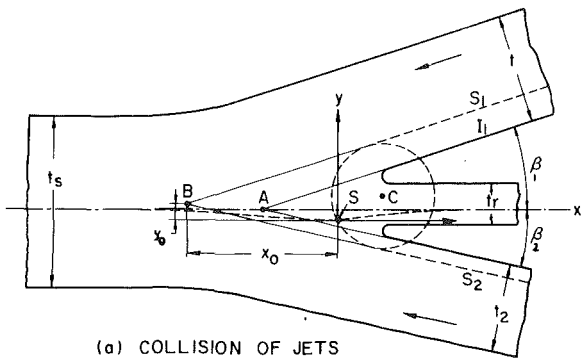
The length parameters of the interface wave (Fig. 6), i.e., λ and ξ, are defined as

$$\lambda = (a_1 + a_2)/2 \tag{19}$$

$$\xi = a_2/2. \tag{20}$$

λ is the wavelength and ξ is the contribution to the wavelength when the wake is moving from lower density to higher density material. It is seen from equations (17) and (18) that if $\rho_1 < \rho_2$, then $a_2 > a_1$ (Fig. 7), and, hence, $\xi > \lambda/2$. In other words, if the density of top plate (ρ_1) is lower than the density of bottom plate (ρ_2), then the distance (ξ) between crest and neighboring trough in the direction of stream is more than half the total wavelength. The experimental work of Onzawa and Ishii (1975) and others also show that $\xi > \lambda/2$.

Downloaded 03 May 2010 to 171.66.16.244. Redistribution subject to ASME license or copyright; see http://www.asme.org/terms/Terms_Use.cfm



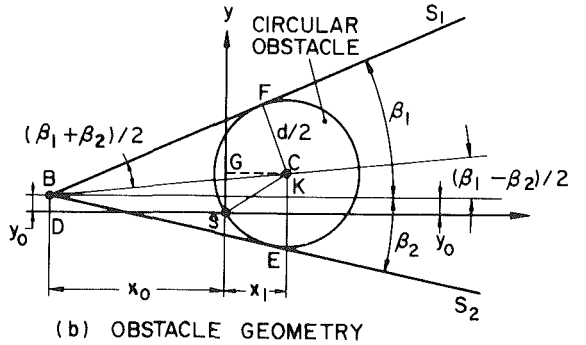
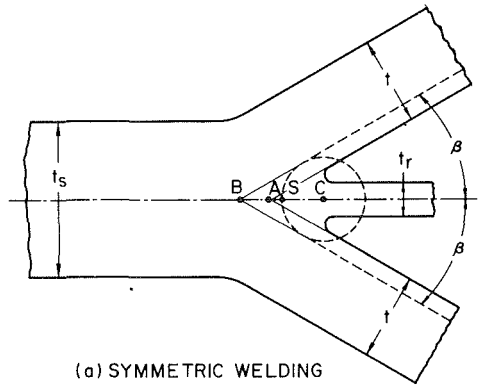


Fig. 8 Equivalent obstacle in hydrodynamic model of explosive welding



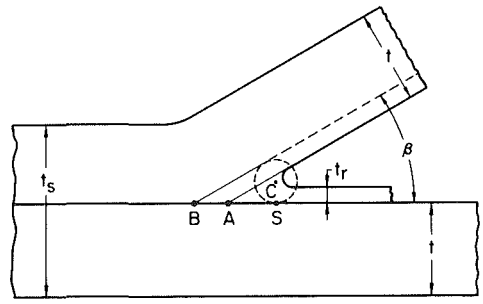


Fig. 9 Orientation of obstacle in symmetric and asymmetric welding

Interface Wave Characteristics

Degree of Distortion. The degree of distortion η is defined as $\eta = (2\xi - \lambda)/\lambda$, and using equations (19) and (20) it is given by

$$\eta = \frac{1-\rho_1/\rho_2}{1+\rho_1/\rho_2}. \tag{21}$$

Amplitude-to-Wavelength Ratio. Taking the amplitude of the interface wave equal to the height of the wake h, the amplitude-to-wavelength ratio h/λ is obtained from (17), (18), and (19) as

$$\frac{h}{\lambda} = \frac{3}{2\pi(1-\epsilon)^2} \frac{\rho_1/\rho_2}{(1+\rho_1/\rho_2)[(1-k)+k\rho_1/\rho_2]} = c. \tag{22}$$

Amplitude and Wavelength. The amplitude of the interface wave is considered equal to the total height of the wake corresponding to transverse spacing the of vortex street. From the free streamline theory, the height of wake is approximately 1.25 times the diameter, d, of the assumed obstacle; hence, wave amplitude h is given by

$$h = 1.25d. \tag{23}$$

The ratio h/λ is written as

$$h/\lambda = c. \tag{24}$$

According to the vortex shedding theory $c = 0.28$, whereas the present theory predicts a value of c given by equation (22).

From equations (23) and (24), wavelength λ is given by

$$\lambda = (1.25/c)d. \tag{25}$$

Since the value of c (equation (22)) is lower for lower values of ρ_1/ρ_2, the wavelength of a welded interface for dissimilar metals ($\rho_1/\rho_2 < 1$) will be longer than that of similar metals.

Diameter of Obstacle

Although the ratio h/λ is independent of diameter of obstacle d, the amplitude h and wavelength λ depend upon d. Thus, to estimate h and λ it is essential to know the diameter of the obstacle for the hydrodynamic model.

Considering complex velocity of jets (Milne-Thomson, 1960), Reid and Sherif (1978) developed the following expression for diameter of obstacle for symmetric welding,

$$d = 0.88t\beta, \tag{26}$$

where β is the obliquity angle and t is the thickness of each plate.

Equation (26), developed by Reid and Sherif, is for an "ideal" symmetric case where thicknesses and densities of both the plates are equal, and, hence $\beta_1 = \beta_2 = \beta$. But in actual practice the thicknesses and densities of the two plates are often different and it is therefore essential to estimate the diameter of the obstacle for a general situation. This is done as follows.

Consider an equivalent hydrodynamic model of general asymmetric welding such that the thicknesses of the incoming jets are t_1 and t_2 and that of outgoing jets are t_s and t_r (Fig. 8(*a*)). Let S be the stagnation point where all the stagnation streamlines meet and the velocity of fluid at point S is zero. The extension of the stagnation streamlines S_1 and S_2 intersect at point B. Considering the stagnation point S as the origin, coordinates of point B (x_o, y_o) can be found as shown in the Appendix.

The imaginary obstacle should be tangential to the streamlines S_1 and S_2 and it should also pass through the stagnation point S (Fig. 8(*b*)). Considering the geometry of the obstacle (triangles BFC and BCK in Fig. 8(*b*), the diameter of the obstacle is given by

$$d = 2\text{BC} \sin[(\beta_1+\beta_2)/2]$$

$$= ([x_0]+x_1)\sec(\beta_1-\beta_2)\sin[(\beta_1+\beta_2)/2] \tag{27}$$

Downloaded 03 May 2010 to 171.66.16.244. Redistribution subject to ASME license or copyright; see http://www.asme.org/terms/Terms_Use.cfm

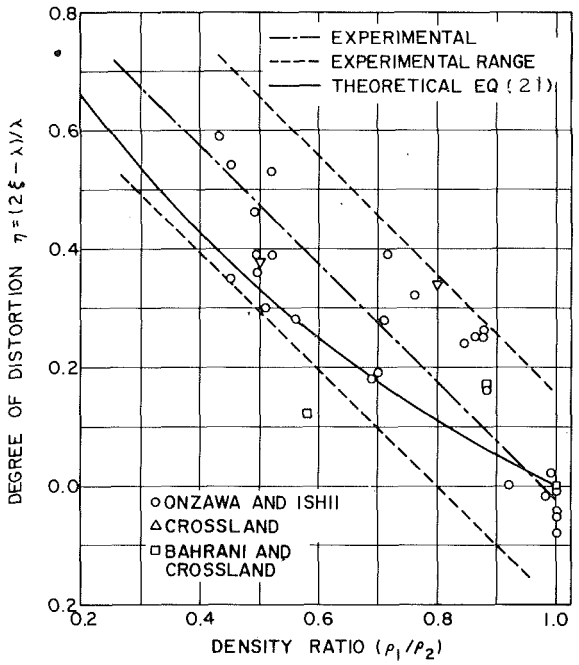


Fig. 10 Variation of of degree of distortion versus density ratio

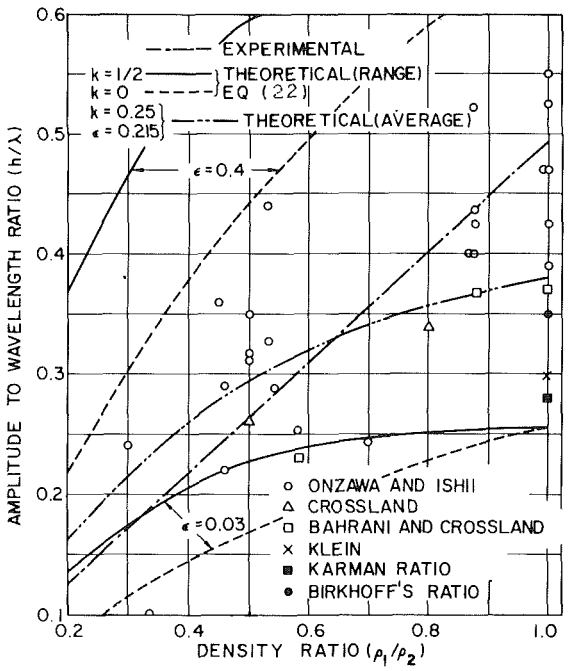


Fig. 11 Variation of amplitude to wavelength ratio versus density ratio

where the expression for x_1 can be found by considering the triangle GSC (Fig. 8(*b*)) such that

$$x_1^2+[y_0+([x_o]+x_1)\tan\{(\beta_1-\beta_2)/2\}]^2=d^2/4. \quad (28)$$

For an ideal symmetric situation, viz, $\beta_1=\beta_2=\beta$, $t_1=t_2=t$, $y_o=0$ and $x_1=d/2$ (Fig. 9(*a*)), equation (27) gives $d=0.88\,t\beta$ as was also obtained by Reid and Sherif (1978). For an asymmetric situation $\beta_2=0$, $y_o=0$, $x_1=0$ (Fig. 9(*b*)) and taking $t_1=t_2=t$ (equation (27) or (28)) in conjunction with the equations given in the Appendix (for x_o), leads to

$$d=\left[-\frac{\log_e\beta_1}{\pi}+\frac{\beta_1}{4}-0.16\right]t\beta_1. \quad (29)$$

Experimental Evidence and Discussion

The values for degree of distortion, η, and amplitude-to-wavelength ratio, h/λ, from experimental results of Onzawa and Ishii (1975) and Blazynski (1983) and Crossland (1976) are plotted in Figs. 10 and 11. Predicted values of degree of distortion η using swinging wake mechanism (equation (21)) are also plotted in Fig. 10. The results show good agreement with the experimental results. The degree of distortion decreases with increase in the ratio of the densities. The distortion is defined in a manner such that, $\eta=0$, i.e., sinusoidal wave, when the ratio of densities is unity.

In the plot of the theoretical variation of h/λ with ρ_1/ρ_2 (equation (22)), the values of ϵ and k are needed. Values of ϵ ranging from 0.03 to 0.4 have been suggested by various workers (Birkhoff, 1953). According to Onzawa and Ishii (1975), in the case of dissimilar metals most of the reentrant jet comes from the stream of lower density material. This implies that the wake would be made up, largely, of material supplied from metal of higher density. Thus, the value of k is expected to be in the range of $k=0$ to $k=1/2$ depending upon the density ratio. Predicted values of amplitude-to-wavelength ratio, h/λ, (equation (22)) are plotted for $k=0$, 1/2 and $\epsilon=0.02$, 0.4 in Fig. 11. It is observed that most of the experimental values fall within the predicted range. Average theoretical variation is also plotted for average values of $k=0.25$ and $\epsilon=0.215$.

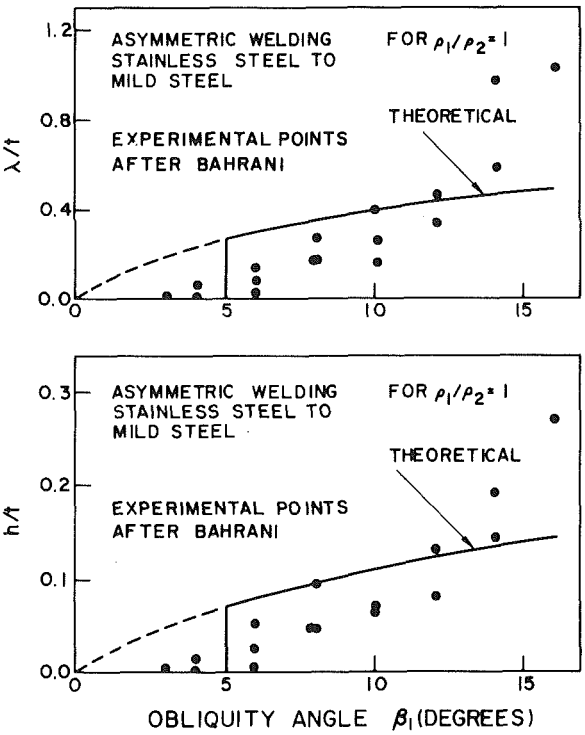


Fig. 12 Variation of amplitude and wavelength with obliquity angle

The scatter in the experimental values of h/λ is due to expected variation of k and ϵ which are likely to be affected by explosive welding parameters. The limited extent of the region within which fluidlike behavior occurs (Hunt, 1968) during explosive welding needs further investigation to establish the variation of k and ϵ with varying welding parameters. The $\epsilon=V_{FS}/V_F$ depends on the Reynolds number (Birkhoff, 1953), the value of which is difficult to determine in explosive welding. The importance of the Reynolds number is also emphazied by Kowalic and Hay (1971) while discussing the ap-

Downloaded 03 May 2010 to 171.66.16.244. Redistribution subject to ASME license or copyright; see http://www.asme.org/terms/Terms_Use.cfm

plication of a vortex street to explosive welding. However, Reid (1974) opines that "various estimates of ranges of a Reynolds number can not be interpreted too rigorously in view of the uncertainty in kinematic viscosity" of the fluidized stream of metal in explosive welding.

Consideration of the reentrant jet as barrier or obstacle in fluid flow (in explosive welding) has been advocated by various workers (Cowan, 1971; Kowalic and Hay, 1971; Reid, 1974, Klein, 1965). Although there is no real solid obstacle, the expected velocity distribution across the stagnation streamlines in explosive welding is nonuniform (Robinson, 1975) with zero velocity at the stagnation streamlines, as if the stagnation streamlines are the boundaries of a solid obstacle. Thus, the velocity distribution around it is analogous to the velocity distribution around a real obstacle in fluid flow. Also, the fluid flow on wake side consists of the saliant jet only, the reentrant jet corresponds to the obstacle in the flow. Hence, it is reasonable to imagine an obstacle between two stagnation streamlines which separate the saliant jet and the reentrant jet (Fig. 6, 8, and 9). Expression for the diameter of the obstacle for a general situation has been developed (equation (27)) which reduces to equation (26) of Reid and Sherif (1978) for an ideally symmetric case and to equation (29) for a conventional asymmetric situation.

To verify the theoretical analysis for estimation of the diameter of an obstacle, the experimental results of Bahrani (1967) are used. For asymmetric welding, theoretical variation of amplitude (equation (23)) and wavelength (equation (24)) are also plotted in Fig. 12 using the expression for the diameter of an obstacle for an asymmetric welding case taking $r=1$ and $c=0.3$ (Klein, 1965). Walsh et al. (1953) have shown that below a certain critical angle β_c, the reentrant jet is absent and hence there is no obstacle. Therefore, an interface wave is not formed, i.e., $h=0$ below a certain critical angle β_c. Taking an average value of $\beta_c=5$ deg, Fig. 12 is modified. It is seen that the values of h and λ, predicted by the theory, are of the same order of magnitude as the experimental values.

As the diameter of an obstacle is smaller in an asymmetric situation (Fig. 9(*b*)) than in a symmetric situation (Fig. 9(*a*)), waves of smaller amplitude and wavelength are likely to be produced in an asymmetric situation of explosive welding.

Conclusions

(1) The swinging wake mechanism adequately explains the generation of wave and distortion of wavy weld interface for the case of a dissimilar metal combination.

(2) Degree of distortion of a weld interface depends upon the ratio of densities of the two materials. The lower the value of ρ_1/ρ_2, the larger the deviation of wavy the interface from the sine wave.

(3) The amplitude-to-wavelength ratio of the interface wave for dissimilar metal combination is less than that for similar metal combination.

(4) The wavelength of the interface wave for dissimilar metals would be more as compared to those for similar metals.

(5) Smaller waves will be produced in an asymmetric situation as compared to a symmeric welding situation.

Acknowledgments

The authors are thankful to Messrs. R. Pandey, B.L. Arora, and S.S. Kushwaha for their assistance in typing the manuscript and in preparing the figures.

References

Bahrani, A. S., and Crossland, B., 1966, "Further Experiments on Explosive Welding and Cladding with Particular Reference to the Strength of the Bond," *Applied Mechanics Convention* (England), Vol. 180, pp. 1-16.

Bahrani, A. S., 1967, "An Experimental Investigation into Some Aspects of Explosive Welding and Cladding," Ph.D. Thesis Part Two, Queen's University, Belfast.

Bahrani, A. S. et al., 1967, "The Mechanism of Wave Formation in Explosive Welding," *Proceedings Royal Society of London*, Part (A), pp. 123-136.

Bayce, A. E., 1964, Stanford Research Institute Report,.SRI Project 4441.

Birkhoff, G., and Zarantonello, E. H., 1948, "Periodic Wakes," *Jets, Wakes and Cavities*, Academic Press, New York, pp. 290-292.

Birkhoff, G. et al., 1948, "Explosive with Lined Cavities," *Journal of Applied Physics*, Vol. 191, pp. 563-583.

Birkhoff, G., 1953, "Formation of Vortex Streets," *Journal of Applied Physics*, Vol. 24, No. 1.

Blazynski, T. J., 1983, *Explosive Welding, Forming and Compaction*, Applied Science Publishers.

Cowan, G. R. et al., 1971, "Mechanism of Bond Zone Wave Formation in Explosion-Clad Metals," *Metallurgical Trans.*, Vol. 2, pp. 3145-3155.

Crossland, B., 1976, "Review of the Present State-of-the art in Explosive Welding," *Metal Technology*, pp. 8-20.

Godunov, S. K. et al., 1970, "Hydrodynamic Effects in Colliding Solids," *Journal of Computational Physics*, pp. 517-539.

Gupta, R. C., and Kainth, G. S., 1979, "Prediction of Forces on Swinging Wake in Explosive Welding of Dissimilar Metals," *Proceedings 9th National Conference on Fluid Mechanics and Fluid Power* (India), Surat, pp. 137-141.

Gupta, R. C., and Kainth, G. S., 1980, "Asymmetries in Explosive Welding," *Proceedings 3rd I S M E Conference*, I.I.T. New Delhi, pp. 167-170.

Hay, D. R., 1971, "Explosive Welding: Applications and Techniques," *High Pressure Science and Technology*, Plenum, New York, Vol. 2, pp. 781-804.

Hunt, J. N., 1968, "Wave Formation in Explosive Welding," *Philosophical Magazine*, Vol. 17, pp. 669-680.

Klein, W., 1965, "Gefugeanderugen bein Explosivplattieven von Stahl mit Stahl einigen Nichteisenmetallein," *Z. Metallkunde*, Vol. 56, pp. 261-267.

Kowalic, J. F., and Hay, D. R., 1971, "A Mechanism of Explosive Bonding," *Metallurgical Trans.*, Vol. 2, pp. 1953-1958.

Milne-Thomson, J. M., 1960, "Jets and Currents," *Theoretical Hydrodynamics*, 4th ed. Macmillan, New York, pp. 287-290.

Onzawa, T., and Ishii, Y., 1975, "Fundamental Studies on Explosive Welding-Observation of Metal Jet and Wavy Pattern," *Trans. Japan Welding Society*, Vol. 6, No. 2, pp. 18-24.

Reid, S. R., 1974, "A Discussion of the Mechanism of Interface Wave Generation in Explosive Welding," *International Journal of Mechanical Sciences*, Vol. 16, pp. 399-413.

Reid, S. R., 1978, "Wake Instability Mechanism for Wave Formation in Explosive Welding," *International Journal of Mechanical Sciences*, Vol. 20, pp. 247-255.

Reid, S. R., and Sherif, N. H. S., 1978, Prediction of Wavelength of Interface Waves in Symmetric Explosive Welding," *Journal of Mechanical Engineering Sciences*, Vol. 18, No. 2, pp. 87-94.

Robinson, R. L., 1975, "The Mechanism of Wave Formation in Impact Welding," *Philosophical Magazine*, Vol. 131, pp. 587-597.

Walsh, J. M. et al., 1953, "Limiting Conditions for Jet Formation in High Velocity Collisions," *Journal of Applied Physics*, Vol. 24, No. 3, pp. 349-358.

APPENDIX

Consider an equivalent system of explosive welding such that the two incoming jets of thicknesses t_1 and t_2 are colliding as shown in Fig. 8(*a*). Let the outgoing jets be of thicknesses t_s and t_r. Speeds of bounding free streamlines of all the jets are U. A point (x,y) in the physical plane is denoted by $z=x+iy$, in the complex $z-$plane, and in the fluid velocity at a point which is described by the complex velocity $\nu=qe^{-\theta}$ where q is the fluid speed and θ is the direction of velocity. Stagnation point S is the origin in both the physical plane and the complex plane. The relationship between z and ν is given by Milne-Thomson (1960),

$$\pi z = U\left[\frac{t_1}{u_1}\log_e\left(1-\frac{\nu}{u_1}\right)+\frac{t_2}{u_2}\log_e\left(1-\frac{\nu}{u_2}\right)-\frac{t_s}{v_1}\log_e\left(1-\frac{\nu}{v_1}\right)-\frac{t_r}{v_2}\log_e\left(1-\frac{\nu}{v_2}\right)\right]. \quad \text{(A1)}$$

Complex velocities of incoming jets are u_1 and u_2 and those of outgoing jets are v_1 and v_2. By substituting for u_1, u_2, v_1 and v_2 as $u_1=-Ue^{-i\beta_1}$, $u_2=-Ue^{i\beta_2}$, $v_1=-U$ and $v_2=-U$, equation (A1) is written as

Downloaded 03 May 2010 to 171.66.16.244. Redistribution subject to ASME license or copyright; see http://www.asme.org/terms/Terms_Use.cfm

$$\frac{\pi z}{t_2} = -re^{i\beta_1}\log_e[1+e^{-i(\theta-\beta_1)}] - e^{i\beta_2}\log_e[1+e^{-i(\theta+\beta_2)}]$$
$$+ r_s \log_e[1+e^{-i\theta}] - r_r \log_e[1-e^{-i\theta}], \quad \text{(A2)}$$

where

$$r = t_1/t_2,\ r_s = t_s/t_2,\ r_r = t_r/t_2 \quad \text{(A3)}$$
$$t_s = 1/2[1+r+(\cos\beta_1+\cos\beta_2)]t_2 \quad \text{(A4}a\text{)}$$
$$t_r = 1/2[1+r-(\cos\beta_1+\cos\beta_2)]t_2. \quad \text{(A4}b\text{)}$$

To deduce the equation of a free streamline say, I_1 (innermost streamline of upper jet in Fig. 8), substituting $\theta \rightarrow \pi+\beta_1$ in equation (A2) and separating real and imaginary parts, we get, as follows, where $\delta \rightarrow 0$, noting that $1 = e^{-\theta/2}e^{\theta/2}$,

$$\frac{\pi}{t_2}x = r_s \log_e\left[2\sin\frac{\beta_1}{2}\right] - r_r \log_e[2\cos\beta_1/2$$
$$- r\cos\beta_1 e\delta[\pi-(\beta_1+\beta_2)]/2\sin_2$$
$$- \cos\beta_2 \log_e[2\sin 1/2(\beta_1+\beta_2)] - 1/2r\pi\sin\beta_1] \quad \text{(A5)}$$

$$\frac{\pi}{t_2}y = -r_s(\pi-\beta_1)/2 - r_r\beta_1/2 - r\sin\beta_1\log_e\delta$$
$$+ [\pi-(\beta_1+\beta_2)]/2\cos\beta_2$$
$$+ \sin\beta_2\log_e[2\sin 1/2(\beta_1+\beta_2)] + 1/2r\pi\cos\beta_1]. \quad \text{(A6)}$$

Therefore, the equation of the upper innermost streamline (I_1) is written as

$$x\sin\beta_1 - y\cos\beta_1 = \frac{t_2}{\pi}c_1, \quad \text{(A7)}$$

where c_1 is given as

$$c_1 = [r_s \log_e[2\sin\beta_1/2] - r_r \log_e[2\cos\beta_1/2$$
$$+ [\pi-(\beta_1+\beta_2)]/2\sin\beta_2$$
$$- \cos\beta_2 \log_e[2\sin(\beta_1+\beta_2)/2] - 1/2r\pi\sin\beta_1]\sin\beta_1]$$
$$- [-r_s(\pi-\beta_1)/2 - r_r\beta_1/2 - [\pi-(\beta_1-\beta_2)]/2\cos\beta_2$$
$$+ \sin\beta_2 \log_e[2\sin(\beta_1+\beta_2)/2] + 1/2r\pi\cos\beta_1]\cos\beta_1. \quad \text{(A8)}$$

Since BS_1 is parallel to AS_1 (Fig. 8(a)), equation of line BS_1 is given as

$$x\sin\beta_1 - y\cos\beta_1 = c_1\frac{t_2}{\pi} - \frac{t_{r1}}{\cos\beta_1}. \quad \text{(A9)}$$

Similarly, equation of line BS_2 is given as

$$x\sin\beta_2 + y\cos\beta_2 = c_2\frac{t_2}{\pi} - \frac{t_{r2}}{\cos\beta_2} \quad \text{(A10)}$$

where t_{r1} is the thickness of reentrant jet contributed by jet I and t_{r_2} is the thickness contributed by jet II.

Expression for c_2 is given as,

$$c_2 = [r_s \log_e[2\sin\beta_1/2] - r_r \log_e[2\cos\beta_2/2$$
$$- r[\pi-(\beta_1+\beta_2)]/2\sin\beta_1$$
$$- r\cos\beta_1 \log_e[2\sin(\beta_1+\beta_2)/2]$$
$$+ 1/2\sin\beta_2]\sin\beta_2 + [-r_s(\pi-\beta_2)/2 - r_r\beta_2/2$$
$$+ r\cos\beta_1[-(\beta_1+\beta_2)]/2$$
$$- r\sin\beta_1 \log_e[2\sin(\beta_1+\beta_2)/2] + 1/2\cos\beta_2]\cos\beta_2. \quad \text{(A11)}$$

Solving equations (A9) and (A10), and using a small angle approximation, (β_1 and β_2 are usually small), we get

$$[x_o] = \frac{t_{r1}+t_{r2}}{(\beta_1+\beta_2)} - \frac{t_2(c_1+c_2)}{\pi(\beta_1+\beta_2)} \quad \text{(A12)}$$

$$[y_o] = \frac{t_{r2}\beta_1 - t_{r1}\beta_2}{(\beta_1+\beta_2)} - \frac{t_2}{\pi}\frac{(c_2\beta_1 - c_1\beta_2)}{(\beta_1+\beta_2)}. \quad \text{(A13)}$$

The values of c_1 and c_2 (equations (A8) and (A11)) are simplified in compact form, using small angle approximations, as follows:

$$c_1 = -\beta_1\left[\log_e\frac{(\beta_1+\beta_2)^{(1+r_\beta)}}{(1+r)} - \frac{1}{\beta_1}\frac{(r\beta_1-\beta_2)}{2}\right] \quad \text{(A14)}$$

$$c_2 = -\beta_2\left[\log_e\frac{(\beta_1+\beta_2)^{(r+r/r_\beta)}}{\beta_2{}^{(1+r)}} - \frac{1}{\beta_2}\frac{(\beta_2-r\beta_1)}{2}\right] \quad \text{(A15)}$$

where $r = t_1/t_2$ and $r_\beta = \beta_2/\beta_1$.

Downloaded 03 May 2010 to 171.66.16.244. Redistribution subject to ASME license or copyright; see http://www.asme.org/terms/Terms_Use.cfm

Analytical Solutions for Nonlinear Strain-Gradient Softening and Localization

H. L. Schreyer
Department of Mechanical Engineering,
The University of New Mexico,
Albuquerque, NM 87131
Mem. ASME

Strain softening, no matter how small, is usually accompanied by localization of the softening deformation field. Inside the zone of localization, a decrease in stress is accompanied by an increase in strain; outside the zone the strain decreases. One way to describe this phenomenon is to use a nonlocal theory of plasticity in which the yield stress depends on an invariant of the gradient of plastic strain. In this paper analytical solutions to two problems are obtained for the case where the functional dependence on the invariant is quadratic. The solutions are interpreted and correlations are made between predictions of load softening and the size of the localization zone based on material parameters and experimental data. Consistency with thermodynamical restrictions is shown.

Introduction

Recently, there has been an expanding awareness of the importance of the connection between softening and localization (Read and Hegemier, 1984) as well as related computational problems (Willam, Pramono, and Sture, 1985). As pointed out by Bazant (1976), a local constitutive theory inevitably leads to a softening zone of neglible thickness and zero energy dissipation. Neither feature is supported by experimental evidence. To predict a softening zone of finite thickness, a nonlocal constitutive equation must be postulated. Nonlocal features have appeared in various forms which include the use of derivatives of strain (Aifantis, 1984; Aifantis, 1987; Triantafyllidis and Aifantis, 1986; Coleman and Hodgon, 1985; Schreyer and Chen, 1986; Chen and Schreyer, 1987), imbricated continua (Bazant, Belytschko, and Chang, 1984; Bazant, 1984), prescribed zones of localization (Bazant, 1976; Pietruszczak and Mroz, 1981), and weighted integral averages of damage (Pijaudier-Cabot and Bazant, 1987). Although each approach has an appealing feature, there are an insufficient number of analytical and numerical solutions to provide a clear consensus that any one approach should be preferred based on correlations with experimental evidence or on the ease with which analytical or numerical solutions can be obtained.

In this paper, a rate-independent plasticity model is postulated in which the yield stress is assumed to soften with respect to both strain and the gradient of strain. A particular functional form leads to analytical solutions in which the softening zone evolves in a predictive manner from zero width to a finite width at failure that may be taken as zero stress in the postpeak regime. The problems analyzed correspond to brittle specimens subjected to uniaxial tension and uniaxial compression in which shear bands appear. Ortiz (1988) has performed a bifurcation analysis of the latter problem, but here, failure is assumed to occur at the limit point. Contrary to the implicit assumption contained in Ortiz (1988) in which a large softening modulus is implied through the choice of a fracture strain, these results show that only a small amount of softening is necessary to replicate basic features displayed by experimental data. In addition to being of fundamental interest concerning possible general forms for constitutive equations, the solutions should be of value for the development and verification of computational algorithms.

Governing Equations

As a model problem, consider a homogeneous specimen loaded in tension as shown in Fig. 1. Suppose that the specimen deforms homogeneously as the specimen is loaded up to the limit stress, H_L, of the weakest point in the specimen at which time a crack is initiated. Instead of crack propagation from one edge to the other, it is assumed that the deformation is independent of the lateral coordinate and a crack process zone develops uniformly across the specimen. The specimen is fixed at one end and the displacement, δ, the other end is either prescribed or obtained as part of the solution. The uniaxial constitutive relation is taken to be linear in both the hardening and softening domains and is described by the following incremental relations (see Fig. 2):

$$\Delta\sigma = \alpha E \Delta e \quad \Delta e > 0 \qquad \Delta\sigma = E\Delta e \quad \Delta e < 0 \qquad \text{(hardening)} \quad (1)$$

$$\Delta\sigma = -\beta E \Delta e \quad \Delta e > 0 \qquad \Delta\sigma = E\Delta e \quad \Delta e < 0 \qquad \text{(softening)}. \quad (2)$$

Stress and strain are denoted by σ and e, respectively, and

Contributed by the Applied Mechanics Division of THE AMERICAN SOCIETY OF MECHANICAL ENGINEERS for publication in the JOURNAL OF APPLIED MECHANICS.

Discussion on this paper should be addressed to the Technical Editor, Prof. Leon M. Keer, The Technological Institute, Northwestern University, Evanston, 60208, and will be accepted until two months after final publication of the paper itself in the JOURNAL OF APPLIED MECHANICS. Manuscript received by the ASME Applied Mechanics Division, June 8, 1988; final revision, Oct. 10, 1989.

Copyright © 1990 by ASME
Downloaded 03 May 2010 to 171.66.16.244. Redistribution subject to ASME license or copyright; see http://www.asme.org/terms/Terms_Use.cfm

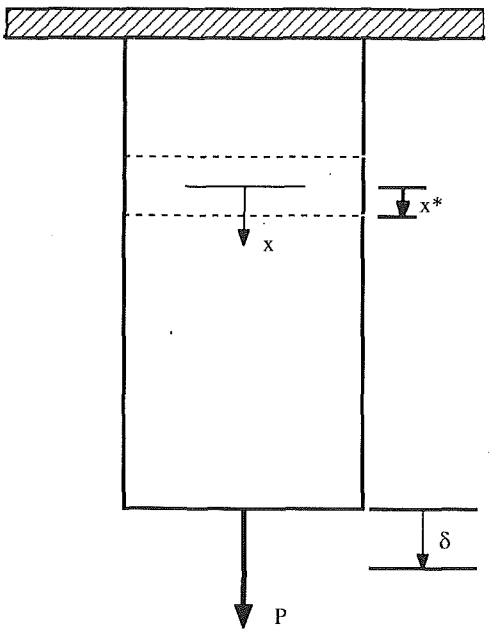


Fig. 1 Model problem and notation for a specimen in tension

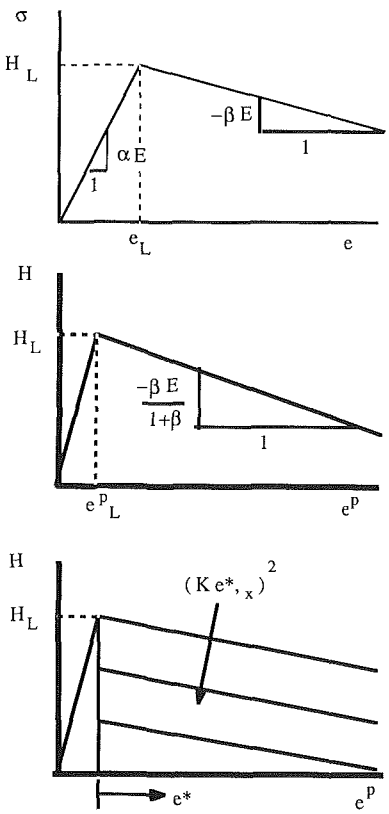


Fig. 2 Piecewise linear representation for strain hardening and softening

Young's modulus by E. The parameter, α, is restricted to the range $0<\alpha\leq 1$. Stain hardening is simulated through a value of $\alpha\neq 1$. Brittle materials are characterized by values of α close to 1; ductile materials through smaller values. The total strain is decomposed into elastic and plastic parts through the relation $e=e^e+e^p$. At the limit state these strain components attain the values:

$$e_L=H_L/\alpha \mathrm{E} \quad e_L^e=\alpha e_L \quad e_L^p=(1-\alpha)e_L. \tag{3}$$

For homogeneous softening and for positive increments in total strain, the corresponding increments in elastic and plastic strains are:

$$\Delta e^e=-\beta\Delta e \quad \Delta e^p=(1+\beta)\Delta e. \tag{4}$$

It is assumed that $0\leq\beta<\infty$. In the context of strain hardening and softening plasticity, the same information is embodied in the description of a piecewise linear yield function, H, as follows:

$$\begin{aligned} H&=H_L\frac{e^p}{e_L^p} && 0<e^p\leq e_L^p \\ H&=H_L[1-Ce^*] && 0<e^*\leq\frac{1}{C} \\ H&=0 && e^*>\frac{1}{C} \end{aligned} \tag{6}$$

where the parameters

$$e^*=e^p-e_L^p \qquad C=\frac{\beta}{1+\beta}\frac{\mathrm{E}}{H_L} \tag{7}$$

are introduced for convenience.

Now introduce a nonlocal feature into the constitutive relation by assuming that the yield function is diminished whenever there is a gradient of plastic strain. In the hardening regime this gradient is caused by spatial variations in the stress field and are insignificant in comparison with gradients that are associated with localization. Thus, it is assumed that the weakening due to the plastic strain gradient is important only in the softening regime. Let the softening function of equation (6) be replaced with the following:

$$\begin{aligned} H&=H_L[1-C\tilde{e}^*] && 0<\tilde{e}^*\leq\frac{1}{C} \\ H&=0 && \tilde{e}^*>\frac{1}{C} \end{aligned} \tag{8}$$

in which

$$\tilde{e}^*=e^*+(Ke^*{}_{,x})^2 \tag{9}$$

is a nonlocal measure of strain and K is a material parameter with the dimension of length. For the model problem under consideration, the state of strain will be homogeneous in the strain-hardening regime so all points will reach the stress, H_L. However, in the softening regime, localization is possible so alternative equilibrium paths become available and one such path is derived in the next section.

Analytical Solution

In the hardening regime, stress and strain increments are related by equation (1). For the model problem, the strain distribution is uniform up to the peak stress. The evolution of the strain field for the complete loading process is shown in Fig. 3 where the first strain distribution plotted is the uniform one associated with the peak stress. In the postpeak regime, assume that a region exists in which softening occurs, and for the remainder of the domain, the bar unloads elastically. With H given by equation (8), the softening regime is defined to be that region where $\sigma=H$, the equation which must be solved for e^* subject to the equilibrium condition $\sigma_{,x}=0$ for no surface tractions or body forces applied along the specimen. By inspection, the solution to this nonlinear differential equation is

$$e^*=\frac{1}{C}\left(1-\frac{\sigma}{H_L}\right)+gx^2 \tag{10}$$

in which g is an integration constant obtained by satisfying the homogeneous part of the differential equation. The result is

Downloaded 03 May 2010 to 171.66.16.244. Redistribution subject to ASME license or copyright; see http://www.asme.org/terms/Terms_Use.cfm

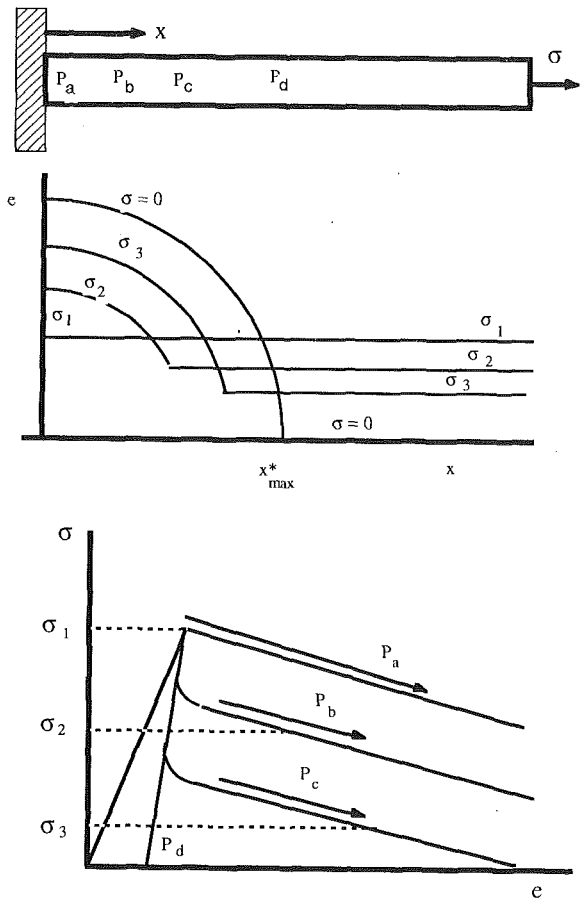


Fig. 3 Evolution of the strain field with softening

either the solution $g=0$, which is the trivial case associated with homogeneous deformation in the softening regime, or the nonlocal solution, which provides an evolving softening zone given by

$$e^* = \frac{1}{C}\left(1 - \frac{\sigma}{H_L}\right) - \frac{x^2}{4K^2}. \tag{11}$$

Since e^* must be positive, the solution of equations (10) and (11) is valid for the domain $0 \le x \le x^*$ where x^* is obtained from the criterion that $e^*(x^*) = 0$. The result is

$$x^* = \frac{2K}{\sqrt{C}}\left(1 - \frac{\sigma}{H_L}\right)^{1/2}. \tag{12}$$

For $K=0$, the theory is local and $x^*=0$ for all values of stress; otherwise, at the beginning of softening, $\sigma = H_L$ and $x^*=0$. At the end of the softening phase, $\sigma=0$ and x^* achieves its maximum value of

$$x^*_{\max} = 2K/\sqrt{C}. \tag{13}$$

An essential aspect of the theory is that for a given decrement in stress, the increment in e^* is the same as the increment in $\bar{e}^*$ since the gradient remains unchanged in the softening zone as e^* increases. The key point is that the nonlocal approach forces softening to occur over the domain $0 \le x \le x^*$, and there is an increment in the boundary, x^*, of the softening region with a decrement in stress.

As shown in Fig. 3, softening is initiated at the point $P_a(x=0)$ where the softening portion of the stress-strain curve is followed continuously. However, an adjacent point, P_b, initially unloads elastically until the plastic strain gradient causes the yield function to reduce sufficiently so that the stress point is on the yield surface. At this instant the point P_b is at x^* defined by equation (12) for the appropriate level of stress. Here, the plastic strain e^* is zero but its gradient is not zero. With continued loading, the strain-softening portion of the stress-strain curve is followed. Another point, P_c, follows the same characteristic stress-strain feature. Ultimately, P_d can be defined as the point, $x^*_{\max}$, which is on the boundary of the softening zone when the stress has reduced to zero. This point is given by equation (13) and can presumably be determined experimentally. For example, if a failed specimen has a failure zone of width, W, then the appropriate interpretation is

$$x^*_{\max} = W/2, \tag{14}$$

since the origin is located at the center of the zone. The result is one equation involving the two material parameters C and K:

$$W = 4K/\sqrt{C}. \tag{15}$$

Recall that C involves the softening modulus β which is not usually known so an additional relation is required to explicitly determine the material parameters. For this purpose attention is now focused on postpeak experimental data which are frequently available.

Load Deflection Relation

In addition to a good estimate for the width, W, of the softening zone at failure, it is assumed that load deflection or stress-average strain curves are available from experiments. To obtain estimates of β and K, an inverse procedure must be followed in which case the solution for strains in the zone of localization must be related to experimentally measured parameters. For a specimen of length L under uniaxial tension, the total deflection and average strain are:

$$\delta = \int_0^L (e^e + e^p)\,dx \qquad e_a = \delta/L. \tag{16}$$

In the hardening regime the average strain is identical to the total strain at every point in the specimen. In the softening regime, the elastic strain is everywhere equal to σ/E, while the plastic strain is $e^p_L + e^*$ with $e^*=0$ for $x > x^*$. The use of equations (10) and (11) in (16) yields

$$e_a = \frac{H_L}{\mathrm{E}}\left[\frac{\sigma}{H_L} + \frac{1-\alpha}{\alpha} + \frac{1}{3}\frac{W}{L}\frac{1+\beta}{\beta}\left(1 - \frac{\sigma}{H_L}\right)^{3/2}\right] \text{ for } e_a \ge \frac{H_L}{\alpha \mathrm{E}}. \tag{17}$$

With W known, β can be determined inversely by matching load deflection data; then C and K can be evaluated using equations (7) and (15), respectively.

The experimental data of Shah and Gopalaratnam (1985) for a concrete specimen under tension are used to illustrate the approach. They report values of $\mathrm{E} = 5 \times 10^6$ psi, $H_L = 525$ psi, $L = 3.25$ in. and $W = 3.25 \times 10^{-3}$ in. where some rounding off has been performed for convenience. The fit to the data shown in Fig. 4 is obtained with $\alpha = 0.8$ and $\beta = 7.5 \times 10^{-5}$, which indicates that an extremely small amount of softening is required. This conclusion concerning softening is at odds with the usual computational approach of assuming the fracture strain is a small multiple of the strain at the limit point. The variation of the load deflection response (stress-average strain) with alternative choices for β is shown in Fig. 5. As expected for a small value of β, the response is close to that of perfect plasticity. However, as β increases the load drops more sharply with strain and, for a large enough value, a reversal or "snapback" can theoretically occur. As described under simpler assumptions (Schreyer and Chen, 1987), snapback is the explanation for why some specimens fail unstably even under deflection controlled tests. Since β is neglible with respect to one, it is seen from equation (17) that increasing L has the same effect as increasing β and, consequently, snap-

Downloaded 03 May 2010 to 171.66.16.244. Redistribution subject to ASME license or copyright; see http://www.asme.org/terms/Terms_Use.cfm

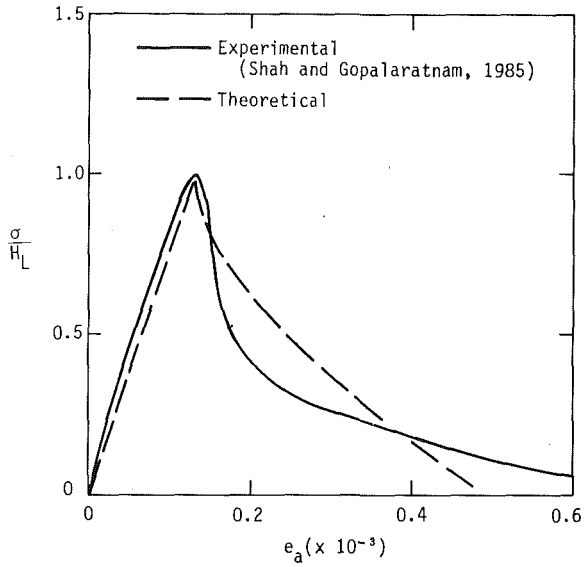


Fig. 4 Correlation of theory with experimental data for concrete in tension

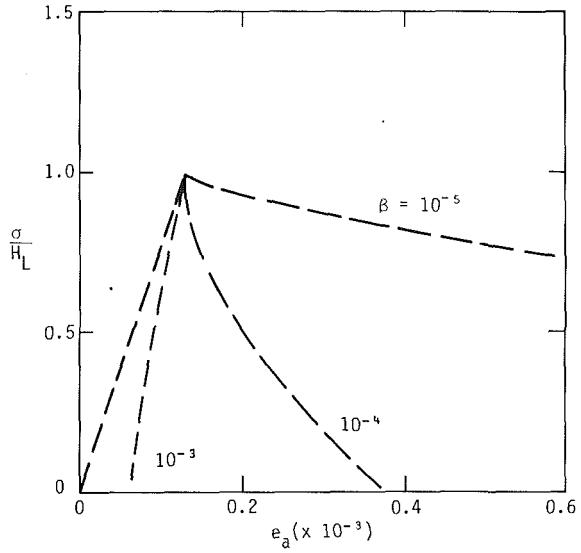


Fig. 5 The effect of the softening parameter β on the tensile response of a specimen

back can also occur if a specimen is large enough for any value of β not equal to zero.

These experimental and theoretical results provide orders of magnitude for material parameters that may be of value for other materials as well. In particular,

$$E/H_L \approx 10^4 \quad \beta \approx 10^{-4} \quad K \approx /4 \quad C \approx 1. \tag{18}$$

To conclude this section, it must be emphasized that small strains have been assumed but the strains in the localized zone are large. Thus, the analysis can only provide qualitative results and it would not make much sense to attempt to closely fit data. The essense of this theory is that the softening zone evolves from a point while the nonlocal model proposed by Coleman and Hodgon (1985), which involves a second derivative of strain, predicts that the zone contracts from infinity during the development of softening. Aifantis (1987) also uses a second derivative but obtains a shear band of finite width. Experimental observations should be able to resolve these rather interesting differences.

Localization in Shear

A similar analysis can be performed for structural elements which fail in shear. For a model problem (Sture and Ko, 1978), consider a specimen of cross-sectional area A loaded uniaxially in compression with a force P as shown in Fig. 6. The shear stress on a plane that forms an angle γ with the loaded surface is

$$\sigma_s = \frac{\sigma}{2} \sin 2\gamma \tag{19}$$

in which $\sigma = P/A$ is the uniaxial stress (positive in compression). Suppose the specimen is loaded to the limit state with the same hardening relation used previously, at which time a shear failure mode is initiated. The softening relation in shear is assumed to be analogous to equation (2). In the zone of softening, equation (10) is replaced with

$$e_s^* = \frac{1}{C_s}\left(1 - \frac{\sigma_s}{H_{LS}}\right) - \frac{x^2}{4K_s^2} \quad C_s = \frac{\beta_s}{1+\beta_s}\frac{G}{H_{LS}} \tag{20}$$

in which G denotes the elastic shear modulus and the subscript s is used to emphasize that the corresponding terms are related to shear and not axial deformation as before. As shown in Fig. 6, the local coordinate x is normal to the plane of deformation with origin at the center of the shear band. With the tensor

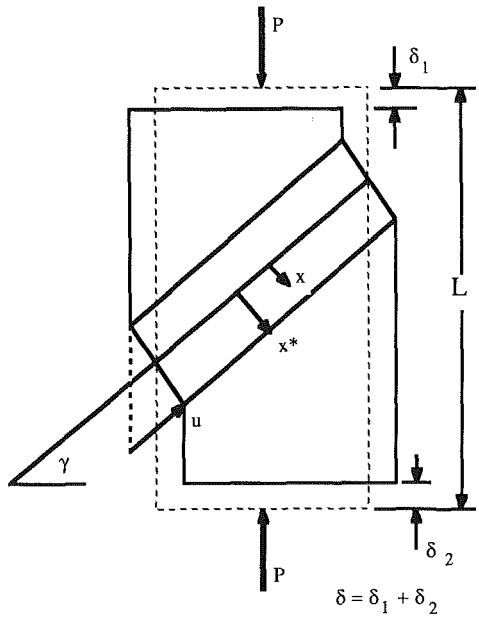


Fig. 6 Model problem and notation for a specimen in compression that fails in shear

definition of shear strain, and another factor of two because of symmetry, the relative tangential displacement across the shear band is

$$u = 4\int_0^{x^*} e_s^* dx. \tag{21}$$

Again, the expression for x^* is obtained by setting $e^*_s = 0$. The result of substituting equation (20) in (21) is

$$u = \frac{16}{3}\frac{K_s}{C_s^2}\left(1 - \frac{\sigma_s}{H_{LS}}\right)^{3/2}. \tag{22}$$

The average longitudinal strain due to the existence of the shear band is $(u \sin\gamma)/L$ so that the complete expression for the average longitudinal strain becomes

$$e_a = \frac{\sigma}{\alpha E} \quad \text{(hardening regime)}$$
$$e_a = \frac{\sigma}{E} + \frac{1-\alpha}{\alpha}\frac{H_L}{E} + \frac{u}{L}\sin\gamma \quad \text{(softening regime).} \tag{23}$$

Downloaded 03 May 2010 to 171.66.16.244. Redistribution subject to ASME license or copyright; see http://www.asme.org/terms/Terms_Use.cfm

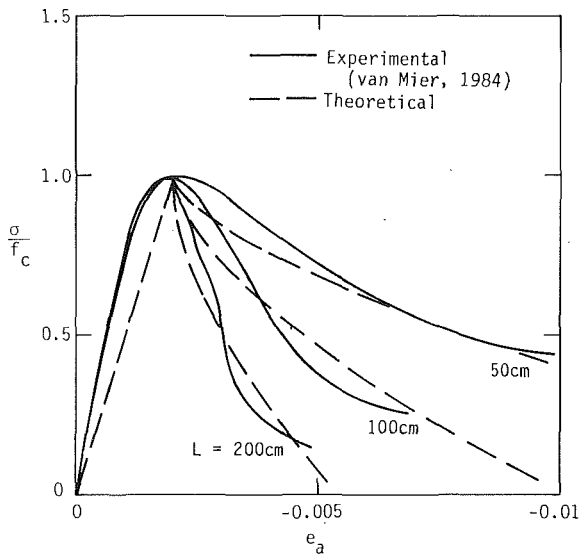


Fig. 7 Correlation of theory with experimental data for concrete in compression

Suppose that after failure, the width of the shear band is measured to be W_s. This value corresponds to twice $x^*_{\max}$, which is obtained from equation (20) with $e^*_s = 0$ and $\sigma_s = 0$. The result is

$$W_s = \frac{4K_s}{\sqrt{C_s}} \tag{24}$$

which is analogous to equation (15).

Suppose the limit stress in uniaxial compression is f_c. Then the shear band analysis is consistent only if

$$H_{LS} = \frac{f_c}{2} \sin 2\gamma. \tag{25}$$

The result of substituting equations (19), (22), (24), and (25) in (23) for the average strain in the softening regime is

$$e_a = \frac{f_c}{\mathrm{E}}\left[\frac{\sigma}{f_c} + \frac{1-\alpha}{\alpha} + \frac{\mathrm{E}}{G}\frac{W^*}{L}\left(1-\frac{\sigma}{f_c}\right)^{3/2}\right] \quad \text{for } e_a > e_L \tag{26}$$

in which f_c rather than H_{LS} is chosen as the primary parameter and

$$W^* = \frac{2}{3} W_s \frac{1+\beta_s}{\beta_s} \sin 2\gamma \sin\gamma. \tag{27}$$

For all parameters fixed in equation (26) other than γ, the maximum amount of energy will be dissipated if γ is chosen to maximize the product $\sin 2\gamma \sin\gamma$. The result is $\gamma_m = 54.8$ deg, which is approximately the angle of inclination observed in many specimens of frictional materials.

If all other material parameters are known, plots of stress versus average strain can be made with W^* adjusted to match experimental data such as those obtained by van Mier (1986) for concrete with $f_c = 42$ MPa and specimens with lengths of 50 mm, 100 mm, and 200 mm as shown in Fig. 7. In the plot, theoretical results are also shown with the parameter $\alpha = 0.65$ chosen so that the strain at the limit stress agreed with experimental data. A Young's modulus of $\mathrm{E} = 3.2 \times 10^{10}$ Pa was obtained using the initial slope of the stress-strain curve and Poisson's ratio of 0.2 was assumed to obtain G. With $\gamma = \gamma_m$, the fit to experimental data, as shown in Fig. 7, was determined by trial and error adjustments to obtain $W^* = 0.5$ m. It follows from equation (27) that $W_s \approx \beta(1m)$ so that if $W_s = 5$ mm then $\beta_s = 5 \times 10^{-3}$, both of which appear to be reasonable values.

Solution Family

The form of the yield function in the softening regime has produced a plastic strain field that varies quadratically with the coordinate x. Actually, a family of solutions are available based on yield functions that are slight variations of equation (8) as follows:

$$H = H_L[1 - C\{e^* |e^*|^{n-2} + |Ke^*{}_{,x}|^n\}]. \tag{28}$$

The solution to the equation $\sigma = H$ for e^* is

$$e^* = \left[\frac{1}{C}\left(1 - \frac{\sigma}{H_L}\right)\right]^{\frac{1}{n-1}} - \left(\frac{x}{nK}\right)^n \tag{29}$$

which provides a parameter, n, that can be chosen to match strain distributions in the softening zone. If the condition that $e^*{}_{,x}$ be finite at $x = 0$ is invoked, then n is restricted to $n > 1$ but the remaining freedom to choose n provides considerable latitude for additional investigations. The solution of equations (10) and (11) is recovered with $n = 2$.

General Considerations

If the approach described in this paper is to have general applicability, then considerations of large deformation theory, invariance of a three-dimensional formulation, and consistency with the first and second laws of thermodynamics must be addressed. Although large deformation plasticity is essential, the theory is beyond the scope of the paper which is restricted to a demonstration of the potential value of nonlocal theories for describing physical phenomena. Invariance is satisfied with a simple extension to an isotropic theory of plasticity. For example, if e^p denotes the usual path length invariant of plastic strain in three dimensions, then a suitable nonlocal parameter might be

$$\bar{e}^p = e^p + [(K\nabla e^p) \cdot (K\nabla e^p)] \tag{30}$$

in which ∇ denotes the gradient and K is a material parameter with the dimension of length. Then a nonlocal softening theory is obtained from a local theory by replacing e^p with $\bar{e}^p$ for the softening regime in the yield function.

To indicate that the proposed approach is consistent with the laws of thermodynamics, only minor modifications are necessary to the development of Simo (1989). Define a yield function in terms of the nonlocal strain invariant, $\bar{e}^p$, as follows:

$$\phi(\mathbf{s}, \bar{e}^p) \equiv f(\mathbf{s}) - (s_L - C\bar{e}^p) \tag{31}$$

in which $\mathbf{s}$ denotes the stress tensor and $\phi < 0$ defines elastic behavior. Only softening is considered so $C > 0$, and s_L is the maximum or limiting value of the stress invariant, f, defined by

$$f(\mathbf{s}) = \sqrt{(\mathbf{s}:\mathbf{A}:\mathbf{s})} \tag{32}$$

where $\mathbf{A}$ is a given symmetric, positive-definite tensor. Introduce the stress variable $\bar{s}^p$ and specify the constitutive relations

$$\mathbf{s} = \mathbf{E}:(\mathbf{e} - \mathbf{e}^p) \qquad \bar{s}^p = C\bar{e}^p \tag{33}$$

in which $\mathbf{E}$ denotes the elasticity tensor, and $\mathbf{e}$ and $\mathbf{e}^p$ the total strain and plastic strain tensors, respectively. The yield function becomes

$$\phi(\mathbf{s}, \bar{s}^p) = f(\mathbf{s}) - (s_L - \bar{s}^p). \tag{34}$$

The associated flow laws for the plastic strain and softening parameter are

$$\dot{\mathbf{e}}^p = \dot{\lambda}\frac{\partial\phi}{\partial\mathbf{s}} \qquad \dot{\bar{e}}^p = \dot{\lambda}\frac{\partial\phi}{\partial\bar{s}^p} = \dot{\lambda} \tag{35}$$

Downloaded 03 May 2010 to 171.66.16.244. Redistribution subject to ASME license or copyright; see http://www.asme.org/terms/Terms_Use.cfm

in which λ is the plasticity parameter. For elastic behavior, $\dot{\lambda}=0$, and for yielding, $\phi=0$. When $\dot{\lambda}\neq 0$, the value of $\dot{\lambda}$ is determined from the consistency condition, $\dot{\phi}=0$. Therefore, the plastic loading and unloading conditions, and the consistency condition, are described by the relations

$$\dot{\lambda}\phi=0 \qquad \dot{\lambda}\dot{\phi}=0. \tag{36}$$

With nonlocal theories of plasticity, an exact derivation of the consistency condition indicates that the plasticity parameter must satisfy an integro-differential or partial differential equation as compared with the usual algebraic equation for a local theory. This complication can lead to severe computational problems in the attempt to predict the evolution of plasticity, softening, and the zone of localization. Here, the problem is avoided by the implicit restriction to a particular solution in which the gradient of the plasticity parameter in the softening zone remains unchanged with regard to the loading parameter. The result is that the consistency condition is identical between the local theory and this nonlocal approach.

At first glance there appears to be a contradiction in the two expressions for $\dot{\lambda}$ that follow from equation (35). If equation (30) is used as the definition of the nonlocal parameter, the resulting incremental relation is $\dot{\bar{e}}^p=\dot{e}^p$ and there is no contradiction because, as mentioned previously for the softening zone, the gradient of the plastic strain invariant does not change with increments in stress. It is the domain of the softening zone and the magnitude of the plasticity parameter that change with respect to the load parameter.

For a thermodynamical formulation, let

$$W\equiv \frac{1}{2}\,(\mathbf{e}-\mathbf{e}^p):\mathbf{E}:(\mathbf{e}-\mathbf{e}^p) \tag{37}$$

be the stored energy function. Define the Helmholtz free energy by

$$\Psi = W-\frac{1}{2}\,C(\bar{e}^p)^2. \tag{38}$$

The dissipation function involves the change of free energy with respect to the internal variables $\mathbf{e}^p$ and $\bar{e}^p$:

$$D^p=-\frac{\partial\Psi}{\partial\mathbf{e}^p}:\dot{\mathbf{e}}^p-\frac{\partial\Psi}{\partial\bar{e}^p}\,\dot{\bar{e}}^p=\mathbf{s}:\dot{\mathbf{e}}^p+\bar{s}^p\dot{\bar{e}}^p. \tag{39}$$

But

$$\mathbf{s}:\dot{\mathbf{e}}^p=\mathbf{s}:\frac{\partial\phi}{\partial\mathbf{s}}\,\dot{\lambda}=\frac{\mathbf{s}:\mathbf{A}:\mathbf{s}}{\sqrt{\mathbf{s}:\mathbf{A}:\mathbf{s}}}\,\dot{\lambda}=f\dot{\lambda}, \tag{40}$$

so that

$$D^p=(f+\bar{s}^p)\dot{\lambda}. \tag{41}$$

If yielding is occurring, then $f+\bar{s}^p=s_L$ and

$$D^p=s_L\dot{\lambda}. \tag{42}$$

Since $\mathbf{s}=\partial W/\partial\mathbf{e}$, the second law for a purely mechanical formulation reduces to the inequality $D^p\geq 0$, or $\dot{\lambda}\geq 0$ because $s_L>0$.

The internal energy, U, and the entropy, G, are defined by

$$U=\Psi+G \qquad G=s_L\bar{e}^p, \tag{43}$$

Then, with the use of previous equations, the rate of change of the internal energy is

$$\begin{aligned}\dot{U}&=\dot{\Psi}+\dot{G}\\ &=\frac{\partial\Psi}{\partial\mathbf{e}}:\dot{\mathbf{e}}+\frac{\partial\Psi}{\partial\mathbf{e}^p}:\dot{\mathbf{e}}^p+\frac{\partial\Psi}{\partial\bar{e}^p}\,\dot{\bar{e}}^p+s_L\dot{\bar{e}}^p\\ &=\mathbf{s}:\dot{\mathbf{e}}-(f+\bar{s}^p-s_L)\dot{\lambda}\\ &=\mathbf{s}:\dot{\mathbf{e}}-\phi\dot{\lambda}\\ &=\mathbf{s}:\dot{\mathbf{e}}\end{aligned} \tag{44}$$

which indicates the first law of thermodynamics is satisfied.

When an attempt is made to describe softening with a local theory, plastic strains localize to a set of measure zero and the dissipation for the body becomes zero. Since rupture is associated with a finite amount of dissipation, there must be a mechanism in the theory to have dissipation distributed over a nonzero domain. The nonlocal approach provides such a domain as an evolutionary process that results from the constitutive equation.

To illustrate that a finite amount of dissipation is achieved for the one-dimensional problem, consider the solution of equation (10) which is the total plastic strain invariant if e_L^p is zero. For one-dimensional stress, $e^p=e^*=\lambda$ from which it follows that

$$\dot{\lambda}=\frac{-\dot{\sigma}}{CH_L}. \tag{45}$$

Recall that in the softening regime $\dot{\sigma}$ is negative. With $s_L=H_L$ and the use of equation (12), the total dissipation for the body is

$$\begin{aligned}D_T^p&=\int_0^L D^p\,dx=s_L\int_0^{x^*}\dot{\lambda}\,dx=\frac{-\dot{\sigma}}{C}\,x^*\\ &=\frac{-2K\dot{\sigma}}{C^{3/2}}\left(1-\frac{\sigma}{H_L}\right)^{1/2}\end{aligned} \tag{46}$$

which is not zero and automatically contains the length parameter, K. At the beginning of softening $\sigma=H_L$, and the dissipation is zero. However, as the softening zone evolves, the dissipation increases to its maximum value when $\sigma=0$, which is the point at which failure occurs.

Conclusion

Elementary solutions have been given for nonlocal softening in which the evolution of the softening band is an explicit aspect of the solution. In effect, the problem has been formulated in an inverse manner so that solutions to nonlinear ordinary differential equations are available. The use of more general hardening and softening yield functions would provide better agreement with experimental data but a numerical procedure would have to be utilized to obtain solutions. Since the purpose of this paper is to clearly show the essence of nonlocal plasticity, numerical solutions were eschewed in favor of analytical solutions to simpler formulations. Although the proposed theory is speculative, it is true nevertheless that the analytical solutions display the known features of softening and localization. To provide a more critical evaluation of the model, the distribution of strain within the zone of localization would have to be experimentally measured, a task that is currently formidable. In this context, it might be more meaningful to combine the current approach with a continuum damage mechanics model (Schreyer, 1989) which may shed more light on the actual physical mechanisms associated with localization.

The proposed theory is consistent with the laws of thermodynamics and differs from the usual local theory only to the extent that softening is enforced over a gradually expanding domain. Although the approach is elementary, the results confirm that softening can be considered a material property, provided a nonlocal theory is used. A consequence of a nonlocal approach is that the behavior of any structure is governed by one underlying theory. Furthermore, a nonlocal theory predicts softening that is rate independent, a feature which is exhibited by a number of important engineering materials.

Acknowledgment

This research was sponsored by the National Science Foun-

Downloaded 03 May 2010 to 171.66.16.244. Redistribution subject to ASME license or copyright; see http://www.asme.org/terms/Terms_Use.cfm

dation under Grant No. MSM-8411786 to the University of New Mexico. Discussions with M. Rubin were particularly enlightening.

References

Aifantis, E. C., 1984, "On the Microstructural Origin of Certain Inelastic Models," *Journal of Engineering Materials and Technology*, Vol. 106, pp. 326–330.

Aifantis, E. C., 1987, "The Physics of Plastic Deformation," *International Journal of Plasticity*, Vol. 3, pp. 211–247.

Bazant, Z. P., 1976, "Instability, Ductility, and Size Effect in Strain-Softening Concrete," *ASCE Journal of the Engineering Mechanics Division*, Vol. EM2, pp. 331–344.

Bazant, Z. B., 1984, "Imbricate Continuum and its Variational Derivation," *Journal of Engineering Mechanics*, Vol. 110, pp. 1693–1712.

Bazant, Z. B., Belytschko, T. B., and Chang, T. P., 1984, "Continuum Theory for Strain Softening," *Journal of Engineering Mechanics*, Vol. 110, pp. 1666–1692.

Chen, Z., and Schreyer, H. L., 1987, "Simulation of Soil-Concrete Interfaces with Nonlocal Constitutive Models," *Journal of Engineering Mechanics*, Vol. 113, pp. 1665–1677.

Coleman, B. D., and Hodgon, M. L., 1985, "On Shear Bands in Ductile Materials," *Archives for Rational Mechanics and Analysis*, Vol. 85, pp. 219–247.

van Mier, J. G. M., 1984, "Strain-Softening of Concrete under Multiaxial Loading Conditions," Ph.D. Dissertation, University of Eindhoven, The Netherlands.

Ortiz, M., 1989, "Extraction of Constitutive Data from Specimens Undergoing Strain Localization," *Journal of Engineering Mechanics*, Vol. 115, pp. 1748–1760.

Pietruszczak, St., and Mroz, A., 1981, "Finite Element Analysis of Deformation of Strain-Softening Materials," *International Journal of Numerical Methods in Engineering*, Vol. 17, pp. 327–334.

Pijaudier-Cabot, G. S. M., and Bazant, Z. P., 1987, "Nonlocal Damage Theory," *Journal of Engineering Mechanics*, Vol. 113, pp. 1512–1533.

Read, H. E., and Hegemier, G. A., 1984, "Strain Softening of Rock, Soil and Concrete—A Review Article," *Mechanics of Materials*, Vol. 3, pp. 271–294.

Schreyer, H. L., and Chen, Z., 1986, "One Dimensional Softening with Localization," ASME JOURNAL OF APPLIED MECHANICS, Vol. 53, pp. 791–797.

Schreyer, H. L., 1989, "Formulations for Nonlocal Softening in a Finite Zone with Anisotropic Damage," J. Mazars and Z. P. Bazant, eds., Proceedings of the France-US Workshop on "Strain Localization and Size Effect due to Cracking and Damage" held at the Laboratoire de Mecanique et Technologie, Cachan, France, Sept. 6–9, 1988, pp. 426–439.

Shah, S. P., and Gopalaratnam, V. S., 1985, "Softening Response of Plain Concrete in Direct Tension," *Journal of the American Concrete Institute*, Vol. 82, pp. 310–323.

Simo, J. C., 1989, "Some Aspects of Continuum Damage Mechanics and Strain Softening," *Cracking and Damage, Strain Localization and Size Effect*, J. Mazars and Z. P. Bazant, eds., Proceedings of the France-US Workshop on "Strain Localization and Size Effect due to Cracking and Damage" held at the Laboratoire de Mecanique et Technologie, Cachan, France, Sept. 6–9, 1988, pp. 440–461.

Sture, S., and Ko, H.-Y., 1978, "Strain-Softening of Brittle Materials," *International Journal for Numerical and Analytical Methods in Geomechanics*, Vol. 2, pp. 237–253.

Triantafyllidis, N., and Aifantis, E. C., 1986, "A Gradient Approach to Localization of Deformation: I. Hyperelastic Materials," *Journal of Elasticity*, Vol. 16, pp. 225–237.

Vermeer, P. A., 1982, "A Simple Shear-Band Analysis Using Compliances," *International Union of Theoretical and Applied Mechanics, Proceedings of the Symposium on Deformation and Failure of Granular Material*, P. A. Vermeer and H. J. Luger, eds., Delft, The Netherlands, Aug. 31–Sept. 3, 1982, A. A. Balkema, Rotterdam.

Willam, K. J., Pramono, E., and Sture, S., 1985, "Stability and Uniqueness of Strain-Softening Computations," Structural Research Series 8503, Department of Civil, Environmental and Architecture Engineering, University of Colorado, Boulder, Colo.

Downloaded 03 May 2010 to 171.66.16.244. Redistribution subject to ASME license or copyright; see http://www.asme.org/terms/Terms_Use.cfm

Growth Instability During Nonuniform Directional Solidification of Pure Metals

Owen Richmond
Corporate Fellow,
Mem. ASME.

Louis G. Hector, Jr.
Senior Research Engineer.
Mem. ASME.

Joseph M. Fridy
Mathematical Scientist.

Aluminum Company of America,
Alcoa Center, PA 15069

Solidification of a pure metal against a flat mold surface is examined using a nonuniform thermohypoelastic beam. Heat is removed with a spatially periodic heat flux superimposed onto uniform cooling, which leads to irregular growth of the casting. The associated nonuniform temperature field also produces nonuniform deformation in the casting which in time may lead to air gap nucleation along the mold/casting interface. Air gap nucleation is defined as the circumstance where the local mold/casting interface pressure falls to zero. Unstable growth occurs when such air gaps nucleate beneath thickness minima, thus further reducing heat transfer at these positions, and dramatically amplifying the existing thickness nonuniformity. The time to onset of instability depends upon material properties such as density, latent heat, thermal conductivity, elastic constants, and coefficient of thermal expansion as well as upon process parameters such as cooling rate, fluid pressure, and wavelength of the periodic heat flux.

Introduction

During nearly directional solidification of metals, the morphology of the freezing front often exhibits large cellular undulations indicating that the metal is growing with a locally nonuniform thickness and suggesting a condition of growth instability. Nonuniform growth during continuous casting can lead to a catastrophic failure known as breakout (Singh and Blazek, 1974) wherein the regions of minimum casting thickness are insufficient to oppose the pressure of the molten metal as the ingot is withdrawn from the mold, and the molten metal breaks through the thin shell leading to abortion of the process. Nonuniformity of casting thickness also can lead to nonuniformity of cast structure and to both surface and subsurface cracking due to high thermal stresses. Associated micro-air gaps at the mold surface can lead to greater surface roughness and even to surface remelting thus creating a need for scalping, wherein a layer of the surface is removed in order to render the ingot suitable for subsequent metal working operations.

A significant early model of morphological instability during solidification of metals, which has a finer scale and a different physical origin than that to be described here, was given by Rutter and Chalmers (1953). These authors noticed the formation of hexagonal cells, with projections at their centers, on the freezing front of nearly pure tin and lead crystals after the residual melt was decanted. The cellular structure was found to persist on the interior of the crystal as well. In order to examine how small amounts of impurity influenced solidification, the authors performed experiments with nearly pure lead using the radioactive tracer, antimony 124, added as an impurity. Results of these experiments indicated that segregation of small amounts of impurity occurred during solidification and that this segregation was directly related to the observed freezing front morphology. An increase of impurity concentration in tin promoted an increase in the length of the projections on the freezing front. These observations led the authors to formulate what is now known as the "constitutional supercooling" theory. As the metal solidifies the solubility of impurities decreases and the metal expels them into the liquid. The impurities thus tend to accumulate in the liquid adjacent to the freezing front forming an enriched boundary layer. Since the temperature at which solidification occurs decreases with increasing impurity content, the impurity rich liquid layer is below its equilibrium liquidus temperature and is thus considered unstable. Consequently, spontaneous solidification, which requires random nucleation with no heat extraction, occurs in the unstable zone leading to the formation of small projections on what was a planar interface.

Mullins and Sekerka (1964) developed a perturbation theory of morphological instability during directional solidification of a dilute binary alloy. A sinusoidal disturbance of infinitesimal amplitude was assumed to exist at the freezing front with no attention given to the etiology of the disturbance. The temperature and concentration fields were derived through solution of the quasi-steady heat conduction and mass diffusion equations. Instability of the freezing front was said to

Contributed by the Applied Mechanics Division of THE AMERICAN SOCIETY OF MECHANICAL ENGINEERS for presentation at the Winter Annual Meeting, Dallas, Texas, Nov. 25-30, 1990.

Discussion on this paper should be addressed to the Technical Editor, Leon M. Keer, The Technological Institute, Northwestern University, Evanston, IL 60208, and will be accepted until two months after final publication of the paper itself in the JOURNAL OF APPLIED MECHANICS. Manuscript received by the ASME Applied Mechanics Division, June 20, 1988; final revision, Jan. 16, 1990.

Paper No. 90-WA/APM-33

Copyright © 1990 by ASME
Downloaded 03 May 2010 to 171.66.16.244. Redistribution subject to ASME license or copyright; see http://www.asme.org/terms/Terms_Use.cfm

occur whenever the amplitude of the disturbance grew in time. In addition, the limiting value of the wavelength of the disturbance was determined above which the freezing front perturbation could grow in time. Sekerka (1968) discussed important theoretical differences between the constitutional supercooling and the perturbation theories. The perturbation theory provides a stability criterion which models the physics of both the growing solid and the residual liquid, while the constitutional supercooling theory is concerned solely with liquid thermodynamics. Also, the perturbation theory includes capillary effects at the freezing front which, when neglected, reveal a modified version of the constitutional supercooling theory.

Experimental studies of growth instabilities during casting often involve decanting residual molten liquid from static castings with simple geometric shapes shortly after the formation of a thin shell of metal. One of the first reported studies of this kind in metal casting is due to Neymark (1955) who designed a vacuum crystallization device to study the causes of defects on the internal and external surfaces of various steels during directional solidification. With this device molten metal was drawn at a fixed speed into a small cylindrical or rectangular mold cavity and then released after a short time, leaving a thin casting along the mold walls. In the cylindrical mold, highly alloyed steels were found to solidify with the shape of the mold while other steels were found to display undulations on their internal surfaces. In order to gain a better understanding of this behavior, a series of experiments was performed to determine the external and internal surface characteristics of tin, lead, zinc and aluminum using the vacuum crystallization device. After a thirty-second solidification time in the cylindrical mold, the lead shells displayed four to five undulations, the tin and zinc shells displayed six undulations, and the aluminum displayed eight to ten undulations. At shorter times, the number of undulations was observed to increase for each metal. When the external surfaces of the ingots were examined, air gaps were found to correspond to minima on the internal surfaces. The formation of the air gaps was attributed to deformation of the thin casting as it grew from the melt. Tests with zinc in the rectangular mold revealed similar behavior. Small nodules were formed on the internal surfaces of the zinc castings one second after the start of solidification. The nodules were found to combine into larger undulations at longer times. The external surfaces of the hollow castings were not smooth since depressions, corresponding to air gaps, were evident at locations corresponding to the depressions between the nodules. With an increase in the local thickness of the casting, the air gaps were found to grow and sometimes become cracks. Larger undulations were observed on thin plates of zinc and magnesium-modified zinc, which were formed independently by insulating two opposite sides of the rectangular mold. Air gap size was also found to increase on the external surface of the plates. The air gaps again were observed to correspond to depressions between the nodules. Cisse et al. (1971) studied freezing front asymmetries in statically cast pure aluminum and aluminum alloys. Small ingots were directionally cast in cylindrical molds. After a short time, residual fluid was decanted and freezing fronts having shapes similar to those detected by Neymark were observed. The pure aluminum ingot displayed a square freezing front (four undulations) whereas the aluminum alloys were found to display undulations identified as having lens (two undulations), triangular (three undulations), rectangular (four undulations) and pentagonal (five undulations) shapes. The mechanism behind unstable growth of the freezing front was due to air gap formation at the mold/casting interface, a concept the authors attributed, in part, to Halliday (1965). Air gaps, which were distributed along the interface as a result of irregular contraction of the casting along the mold wall, led to nonuniform heat extraction and thus freezing front instability. Highly alloyed metals, cast at low superheats, were more likely to solidify with stable freezing fronts, an observation which is in agreement with Neymark. Wray (1977, 1981) observed cellular undulation of the freezing front of lead castings. Using an apparatus similar to that of Neymark, molten lead was drawn at fixed speeds into a rectangular mold cavity of which one wall was a copper plate. The frequency of the undulations was found to increase with increased drawing speed. The undulations were attributed to uneven temperature distributions on the mold/casting interface which led to air gap formation and subsequent irregular freezing front growth. A careful examination of the external surface of the casting revealed depres-

Nomenclature

dl = differential length of beam element
$\mathbf{e}_1$ = unit vector
$\mathbf{e}_2$ = unit vector
$f(t)$ = unknown function of time
g = acceleration due to gravity
$g(t)$ = unknown function of time
k = thermal conductivity of metal
$\mathbf{n}$ = normal to freezing front
$s(x, t)$ = casting thickness
s_c = casting thickness at air gap nucleation time
t = time
$t^*(x, z)$ = layer formation time
t_c = critical time to growth instability
x = lateral spatial variable
$\bar{x}$ = x-centroid coordinate
y = longitudinal spatial variable
z = spatial variable through the casting thickness
$\bar{z}$ = z-centroid coordinate
A = amplitude of uniform cooling term
A_m = maximum allowable value of uniform cooling term
B = amplitude of spatially periodic cooling term
E = Young's modulus
$F(x, z, t)$ = equation of the freezing front
H = height of the fluid
L = latent heat
M = moment per unit length
N = lateral force per unit length
$P(x, t)$ = mold/casting interface pressure
$Q(x)$ = applied heat flux
R_1 = material property parameter controlling instability
R_2 = process parameter controlling instability
$T(x, z, t)$ = approximate temperature distribution
T_f = fusion temperature
V = shear force per unit length
α = coefficient of thermal expansion
β_i = functions in temperature approximation
δ_{ij} = Kronecker's delta
$\epsilon_{ij}(x, z, t)$ = total strain tensor
κ = thermal diffusivity
λ = wavelength of periodic disturbance
ν = Poisson's ratio
ϕ = uniform lateral strain rate
ρ = density
$\sigma_{ij}(x, z, t)$ = stress tensor
ξ = tolerance

Downloaded 03 May 2010 to 171.66.16.244. Redistribution subject to ASME license or copyright; see http://www.asme.org/terms/Terms_Use.cfm

sions which corresponded to regions of minimum growth on the freezing front. The depressions, presumably air gaps, were found to deepen as the shell grew thicker. In order to test possible meniscus effects as well as the influence of fluid motion on unstable growth, an immersion test was designed in which a copper plate was lowered into a quiescent bath of molten lead. The growth behavior of the lead shell displayed undulations similar to those found in the vertical casting. It was concluded that nonuniform growth was a result of neither meniscus behavior nor peculiar fluid motion.

In the present work, a nonuniform beam theory is used to study growth stability of pure metal castings. A casting is modeled as a thin, hypoelastic beam subjected to spatially periodic cooling. The effect of spatially periodic cooling on air gap nucleation at the mold/casting interface and consequently on the freezing front morphology is determined through calculation of the mold/casting interface pressure which is indicative of the deformation of the casting as it grows.

Assumptions

(*a*) The molten metal is pure with a single fusion temperature denoted by T_f.
(*b*) The molten metal is of finite depth H.
(*c*) Pertinent material properties are assumed to be temperature independent and are appropriate for the material near its melting point.
(*d*) The deformation in the thin casting is assumed to be governed by a hypoelastic constitutive law.
(*e*) The heat flux through the casting is due to the liberation of latent heat at the freezing front.
(*f*) The stress state at the freezing front is isostatic.
(*g*) The newly formed material at the freezing front is in a state of zero strain.
(*h*) The variation of the through-thickness stress, σ_{zz}, is not negligible.
(*i*) The boundary heat flux is strictly monotonic in time, i.e., remelting is forbidding along the mold/casting interface.
(*j*) The heat conduction and deformation models are thermomechanically uncoupled.

Assumption (*d*) asserts that casting deformation is governined by an elastic rate formulation. Assumption (*f*) is an internal boundary condition which asserts that the stress state in the molten liquid must be continuous across the freezing front. This boundary condition has been discussed by Richmond (1981) and used in one-dimensional casting models by Tien and Richmond (1982) and Heinlein, et al. (1986). Assumption (*h*) is a consequence of assumption (*f*). Assumption (*j*) renders the analysis mathematically tractable by neglecting contributions from casting deformation to the thermal field.

Heat Conduction Model

Figure 1 shows the system to be modeled which consists of a single cell of solidified metal growing nonuniformly due to spatially periodic heat extraction. The cell is assumed to be of finite width λ and infinitely long in the y-direction. The governing equation for heat transfer in this two-dimensional case is given by

$$\frac{\partial^2 T}{\partial x^2}+\frac{\partial^2 T}{\partial z^2}=\frac{1}{\kappa}\frac{\partial T}{\partial t} \qquad ;t>0,\ \forall x,z \tag{1}$$

subject to the following conditions:

$$k=\frac{\partial T}{\partial z}=Q \qquad ;z=0 \tag{2}$$

$$T=T_f \qquad ;z=s \tag{3}$$

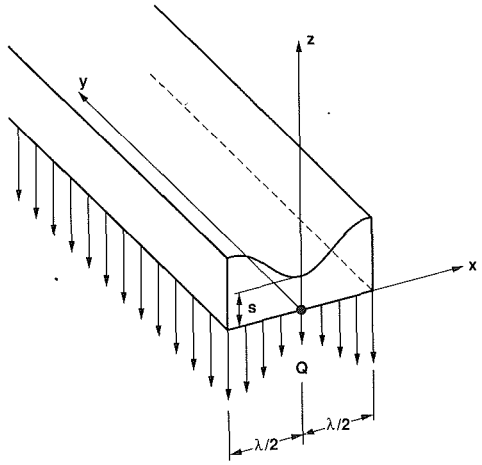


Fig. 1 Nonuniform directional solidification

$$\frac{\partial T}{\partial z}=\frac{\rho L}{k}\frac{\partial s}{\partial t} \qquad ;z=s \tag{4}$$

$$s=0 \qquad ;t=0. \tag{5}$$

The temperature distribution in the casting is denoted by $T=T(x, z, t)$, the thermal diffusivity by κ, and the thermal conductivity by k. $Q=Q(x)$ is the spatially periodic cooling profile at the mold/casting interface which is to be specified. T_f is the fusion temperature of the metal, L is the latent heat of fusion, and $s=s(x, t)$ is the local casting thickness.

Equation (1) is the transient heat conduction equation. The mold/casting interface condition, given by equation (2), indicates that latent heat is extracted from the casting with a spatially periodic heat flux. Equation (3) asserts that the freezing front is isothermal at the fusion temperature. Equation (4) is the energy balance at the freezing front which states that the speed of the freezing front is inversely proportional to the latent heat carried away from the interface (see Patel, 1968). Equation (5) states that there is no solid at initial time.

The approximate, multidimensional solution technique due to Chehl (1973) is adopted. It is a quasi-steady-state approximation in which the casting temperature distribution is assumed to be linear through the thickness of the casting and to satisfy all heat boundary conditions. Chehl's solutions for casting temperature distribution and thickness variation, which incorporate the assumption that spatial gradients of the freezing front are small, compare remarkably well with Sikarskie and Boley's (1965) embedding technique for two-dimensional melting and solidification problems.

The approximations for casting temperature and growth rate of the solid are

$$T=T_f-\frac{Qs}{k}\left(1-\frac{z}{s}\right) \tag{6}$$

$$\frac{\partial s}{\partial t}=\frac{Q}{\rho L}. \tag{7}$$

Equation (7) may be integrated to

$$s=\frac{Qt}{\rho L}. \tag{8}$$

Equation (6) is valid so long as the following condition is satisfied

$$\frac{4Qs}{\kappa\rho L}\ll 1. \tag{9}$$

The derivation of equations (6), (7), and (9) is in Appendix A.

Downloaded 03 May 2010 to 171.66.16.244. Redistribution subject to ASME license or copyright; see http://www.asme.org/terms/Terms_Use.cfm

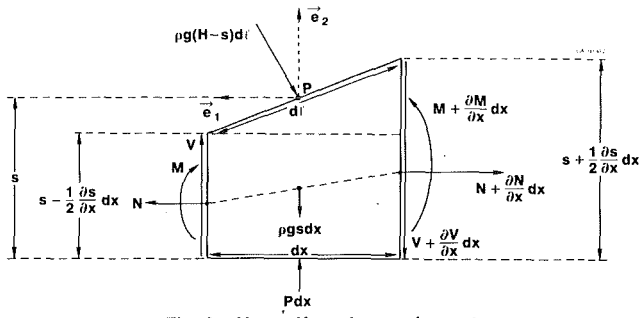


Fig. 2 Nonuniform beam element

The mold/casting interface heat flux is

$$Q = A + B\left[1 - \cos\left(\frac{2\pi x}{\lambda}\right)\right]. \tag{10}$$

The parameter A is the amplitude of the uniform cooling term, B is the amplitude of the spatially periodic term, and the wavelength of the spatial disturbance is given by λ. The symmetry of the system is such that

$$\frac{\partial T}{\partial x} = 0 \qquad ;x = \pm\frac{\lambda}{2}. \tag{11}$$

Equilibrium Equations for a Nonuniform Beam

The equilibrium relations which pertain to the nonuniform beam element shown in Fig. 2 are as follows:

$$P - \rho g H - \frac{\partial V}{\partial x} = 0 \tag{12}$$

$$\frac{\partial N}{\partial x} + \rho g (H - s)\frac{\partial s}{\partial x} = 0 \tag{13}$$

$$V + \left[\frac{N + \rho g s (H - s)}{2}\right]\frac{\partial s}{\partial x} - \frac{\partial M}{\partial x} = 0. \tag{14}$$

Combination of equations (12), (13), and (14), which involves elimination of the shear force per unit length V, leads to

$$P - \rho g H + \frac{1}{2}[N + \rho g s (H - s)]\left(\frac{\partial^2 s}{\partial x^2}\right) - \frac{\partial^2 M}{\partial x^2} = 0. \tag{15}$$

The derivation of these relations may be found in Appendix B. Equation (15) relates the mold/casting interface pressure, P, to the stress resultants per unit length denoted by N (a lateral force) and M (a moment), the casting thickness and its spatial gradient, and the fluid height, H.

The conditions which relate the lateral force, N, and the moment, M, to the lateral stress in the casting σ_{xx}, are

$$N = \int_o^s \sigma_{xx} dz \tag{16}$$

$$M = -\int_o^s \sigma_{xx}\left(z - \frac{s}{2}\right) dz. \tag{17}$$

The mold/casting interface pressure may then be written in terms of σ_{xx} as,

$$P - \rho g H + \frac{1}{2}\left[\int_o^s \sigma_{xx} dz + \rho g s (H - s)\right]\left(\frac{\partial^2 s}{\partial x^2}\right) + \frac{\partial^2}{\partial x^2}\int_o^s \sigma_{xx}\left(z - \frac{s}{2}\right) dz = 0. \tag{18}$$

Equations (13) and (18) must be satisfied by the lateral stress σ_{xx}.

Hypoelastic Constitutive Model

Deformation of a solidifying material differs from that of a standard "fixed" body. Whereas a fixed body, such as a uniformly loaded beam, is usually assumed to deform from an initial state of zero stress, a solidifying beam develops residual stresses as it grows and is never in a stress-free state. As a consequence of this very special attribute, a hypoelastic constitutive equation (see Prager, 1961), which is essentially a rate formulation of elastic behavior, is assumed to govern deformation in the casting. This equation is given by

$$\frac{\partial \epsilon_{ij}}{\partial t} = \frac{(1+\nu)}{E}\frac{\partial \sigma_{ij}}{\partial t} - \left(\frac{\nu}{E}\frac{\partial \sigma_{kk}}{\partial t} - \alpha\frac{\partial T}{\partial t}\right)\delta_{ij} \tag{19}$$

where ϵ_{ij} is the total strain, σ_{ij} is the stress, ν is Poisson's ratio, E is Young's modulus, α is the coefficient of thermal expansion, and δ_{ij} is Kronecker's delta. Equations (19) neglect the nonlinear viscoplastic portion of the constitutive law which has been used in previous models of casting deformation (see, Richmond and Tien, 1971; Tien and Richmond, 1982; Heinlein, et al., 1986). As discussed by Smelser and Richmond (1988), constitutive models which neglect inelastic deformation of the casting may still be useful for process understanding and preliminary process design.

Solidification Stresses and Strains

The solidification problem is a special initial value problem in that the "initial" conditions of zero strain and isostatic stress at the freezing front (assumptions (*f*) and (*g*)) are applied at different times for different positions in the body depending upon when the freezing front reaches those positions. After the start of solidification it is appropriate to assume that the strain history in each layer of the metal begins with its formation at a time necessarily greater than zero. Consequently, the stress distribution in the casting is determined through time integration of equations (19) such that strain accumulates within each layer of the casting starting with its formation time. Integration for the lateral stress σ_{xx} gives

$$[\sigma_{xx} - \nu(\sigma_{yy} + \sigma_{zz}) - (\sigma_{xx} - \nu\sigma_{yy} - \nu\sigma_{zz})|_{t^*} + E\alpha(T - T_f)] - E\int_{t^*}\frac{\partial \epsilon_{xx}}{\partial t} dt = 0 \tag{20}$$

where $\epsilon_{xx} = \epsilon_{xx}(x, z, t)$ is the lateral strain in the x-direction and $t^* = t^*(x, z)$ is the layer formation time which is given by

$$t^* = \frac{z\rho L}{A + B\left[1 - \cos\left(\frac{2\pi x}{\lambda}\right)\right]} \tag{21}$$

and is determined from the casting thickness. By assumption (*f*), the stress distribution at the freezing front is

$$\sigma_{xx} = \sigma_{yy} = \sigma_{zz} = -\rho g(H - z) \qquad ;z = s(x, t). \tag{22}$$

Equation (22) is an internal boundary condition which says that the stress distribution in a newly formed layer of solid metal is isostatic at the fluid pressure. By assumption (*g*), no strain accumulates at the time a new layer of solid metal is formed and thus

$$\epsilon_{xx}(x, s, t^*) = 0. \tag{23}$$

Substituting equations (22) and (23) into equation (20) gives

$$\sigma_{xx} = \nu(\sigma_{yy} + \sigma_{zz}) - \rho g(1 - 2\nu)(H - z) - E\alpha(T - T_f) - E\epsilon_{xx}. \tag{24}$$

A similar procedure for the lateral stress σ_{yy} gives

$$\sigma_{yy} = \nu(\sigma_{xx} + \sigma_{zz}) - \rho g(1 - 2\nu)(H - z) - E\alpha(T - T_f) \tag{25}$$

where

$$\epsilon_{yy}(x, z, t) = 0. \tag{26}$$

For the early stages of solidification, it may be assumed that σ_{zz} is a linear function of z, varying from the isostatic pressure

Downloaded 03 May 2010 to 171.66.16.244. Redistribution subject to ASME license or copyright; see http://www.asme.org/terms/Terms_Use.cfm

at the freezing front, given by equation (22), to the mold/casting interface pressure, P, as given by equation (18). Thus,

$$\sigma_{zz} = -\left[\left(1-\frac{z}{s}\right)P + \frac{\rho g z}{s}(H-s)\right]. \tag{27}$$

Equation (27) is substituted into equations (24) and (25) which are then solved simultaneously for the lateral stresses σ_{xx} and σ_{yy}

$$\sigma_{xx} = -\frac{1}{1-\nu}\left[\nu\left(1-\frac{z}{s}\right)P + \rho g\left\{\frac{\nu z}{s}(H-s) + (1-2\nu)H - z\right)\right\} + \mathrm{E}\alpha(T-T_f) - \frac{\mathrm{E}}{1+\nu}\epsilon_{xx}\right] \tag{28}$$

$$\sigma_{yy} = -\frac{1}{1-\nu}\left[\nu\left(1-\frac{z}{s}\right)P + \rho g\left\{\frac{\nu z}{s}(H-s) + (1-2\nu)(H-z)\right\} + \mathrm{E}\alpha(T-T_f) - \frac{\mathrm{E}\nu}{1+\nu}\epsilon_{xx}\right] \tag{29}$$

Approximations for the lateral strain ϵ_{xx} and the mold/casting interface pressure which are appropriate for small values of B are as follows:

$$\epsilon_{xx} = \phi\left(t - \frac{z\rho L}{A}\right) + \frac{BH}{kT_f}f(t)\left(1-\frac{z}{s}\right)\cos\left(\frac{2\pi x}{\lambda}\right) \tag{30}$$

$$P = \rho g H + \frac{BH}{kT_f}g(t)\cos\left(\frac{2\pi x}{\lambda}\right) \tag{31}$$

where $f(t)$ and $g(t)$ are unknown functions of time. The first term on the right-hand side of equation (30) represents the lateral strain in the casting in the absence of oscillatory behavior in Q. It is the product of the constant ϕ, which is a lateral strain rate through the casting, and the residence time which is a measure of the amount of time elapsed since the nucleation of a layer of solid metal. The second term represents a first-order perturbation about the uniform strain due to nonuniform cooling where the perturbation parameter is B. Note that the behavior of equation (30) is such that the strain vanishes at the freezing front and the gradients of strain vanish at the edges of a cell as dictated by symmetry. Similar observations can be made about equation (31). In order to determine $f(t)$ and $g(t)$, equations (30) and (31) are first substituted into equation (28), which is then substituted into equations (13) and (18). All terms multiplied by B^2 and higher powers of B are then neglected in the resulting algebraic expressions which are then solved simultaneously for $f(t)$ and $g(t)$. This procedure yields the desired forms of equations (30) and (31)

$$\epsilon_{xx} = \phi\left(t - \frac{z\rho L}{A}\right) + \frac{\alpha AB}{3k\rho^3 L^3}\left(\frac{1+\nu}{1-\nu}\right)\left(1-\frac{z}{s}\right) \times\left\{9\rho^2L^2(1-\nu)t - \frac{2\nu\pi^2A^2}{\lambda^2}t^3\right\}\cos\left(\frac{2\pi x}{\lambda}\right) \quad ;t>0 \tag{32}$$

$$P = \rho g H - \left[\frac{2\alpha\pi^2 E A^3 B}{3k\lambda^2\rho^3L^3(1-\nu)}\right]t^3\cos\left(\frac{2\pi x}{\lambda}\right) \quad ;t\geq 0. \tag{33}$$

A comparison of equation (33) for the mold/casting interface pressure with the casting thickness

$$s = \left\{A + B\left[1-\cos\left(\frac{2\pi x}{\lambda}\right)\right]\right\}\frac{t}{\rho L} \tag{34}$$

indicates that the pressure under a thickness minimum decreases from the onset of solidification. On the other hand, the pressure increases under a thickness maximum. Thus, if the pressure goes to zero, it will do so under an existing minimum and the resulting air gap will lead to unstable growth.

Instability Condition

The critical time, t_c to the onset of unstable growth is determined from equation (33) by setting P and x equal to zero. This gives

$$t_c = 0.53(R_1R_2)^{1/3} \tag{35}$$

where

$$R_1 = \frac{k\rho^4L^3(1-\nu)}{\mathrm{E}\alpha} \tag{36}$$

$$R_2 = \frac{g\lambda^2 H}{A^3 B}. \tag{37}$$

The parameter R_1 is indicative of the material property contribution to the air gap nucleation time and thus to growth instability. Materials with large thermal conductivities, densities and latent heats, and small elastic constants and coefficients of thermal expansion require longer times to air gap formation and are thus more stable. The parameter R_2 is indicative of the process parameter contribution to air gap nucleation time. Large values of wavelength in the cooling profile and of mold height and small values of the uniform and spatially periodic cooling terms lead to longer air gap nucleation times and hence greater stability.

When the critical time to air gap nucelation, t_c, is eliminated between equations (34) and (35), what results is the following expression for the casting thickness at air gap nucleation time:

$$s_c = 0.53\left[\frac{k\lambda^2\rho g H(1-\nu)}{\mathrm{E}\alpha B}\right]^{1/3}. \tag{38}$$

If the final casting thickness is less than s_c, then growth instability will not occur. Unstable growth of the freezing front can be avoided with a sufficient fluid pressure or by cooling with a long enough wavelength.

The condition given by equation (9), which establishes the validity of the approximation for the temperature distribution in the casting, places the following upper bound on the choice of uniform cooling term A which may be used in the present model

$$A_m = \frac{\kappa\rho\xi L}{4s_c} \tag{39}$$

where A_m is the maximum admissible value of the uniform cooling term, $A \gg B$ and $\xi \ll 1$ is a tolerance which must be met to satisfy equation (9). When s_c is eliminated between equations (38) and (39) what remains is the following expression which relates A_m to the casting material properties and process parameters:

$$A_m = \frac{\kappa\rho^{2/3}\xi L}{2.12}\left(\frac{\mathrm{E}\alpha B}{gk\lambda^2 H(1-\nu)}\right)^{1/3}. \tag{40}$$

Results and Discussion

The growth stability of an aluminum casting is examined with the mold/casting interface pressure given by equation (33). The material properties used in the calculation are listed in the table. These properties, which are taken from the work of Heinlein, et al. (1986), are appropriate for pure aluminum at its fusion temperature T_f. The process parameters are chosen to be

$$g = 9.8\frac{\mathrm{m}}{\mathrm{sec}^2}$$

$$A = A_m = 7.2\times 10^4\frac{\mathrm{J}}{\mathrm{m}^2\cdot\mathrm{sec}}$$

$$B = 0.1\frac{\mathrm{J}}{\mathrm{m}^2\cdot\mathrm{sec}}$$

Downloaded 03 May 2010 to 171.66.16.244. Redistribution subject to ASME license or copyright; see http://www.asme.org/terms/Terms_Use.cfm

Table 1

Properties of Pure Aluminum at the Fusion Temperature after Heinlein, et al. (1986)

Parameter	Symbol	Value at T_f
thermal conductivity	k	229.4 $\frac{J}{m \cdot sec \cdot °C}$
Young's modulus	E	6.0×10^{10} $\frac{N}{m^2}$
latent heat of fusion	L	3.9×10^5 $\frac{J}{kg}$
fusion temperature	T_f	660.0°C
coefficient of thermal expansion	α	37.8×10^{-6} $°C^{-1}$
thermal diffusivity	κ	8.2×10^{-5} $\frac{m^2}{sec}$
Poisson's ratio	ν	0.37
density	ρ	2650.0 $\frac{kg}{m^3}$

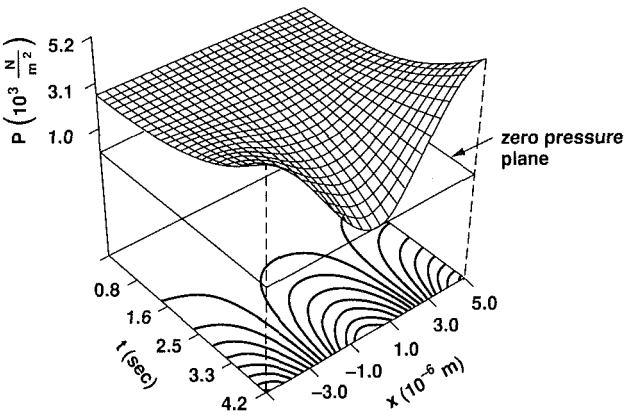


Fig. 3 Evolution of mold/casting interface pressure

$H = 0.1$ m

$\lambda = 1.0 \times 10^{-5}$m

where $\xi = 0.001$. The value chosen for A represents a fairly low cooling rate when compared to industrial aluminum casting operations in which cooling rates of the order of 10^6 $\frac{J}{m^2 \cdot sec}$ are common (Liu, 1988). By equation (35), the air gap nucleation time is $t_c = 4.2$ sec.

Figure 3 shows the evolution of the mold/casting interface pressure for a single cell of solidified material which terminates at air gap nucleation time. Contours of the pressure are shown in the lowest plane in the figure and the zero pressure plane is also noted. The pressure decreases to zero beneath a thickness minimum at $x = 0$ and builds up under the thickness maxima at $x = \pm\frac{\lambda}{2}$. The pressure response, which is indicative of the deformation of the casting as it grows, is such that heat extraction through the mold/casting interface would be significantly reduced through air gap nucleation. In addition, the improved heat extraction beneath the thickness maxima will enhance the nonuniformity in the freezing front. Figure 3 is indicative of the fact that the mold/casting interface pressure is very sensitive to spatial oscillation in the cooling profile even though the magnitude of the oscillation is very small.

An air gap between the mold and the solidifying metal can have undesirable effects on the surface and internal properties of a cast product. In continuous rod casting of aluminum alloys (de L. Davies and Westby, 1977) for example, rapid contraction of the solidifying metal from the mold, leading to an air gap with a thickness which significantly exceeds the composite surface roughness of the mold, can cause subsequent remelting of the casting surface. This remelting process is evident from surface irregularities known as liquations (Collins, 1967). The surface liquations not only ruin the aesthetic appearance of the final product but may lead to surface cracking during subsequent applications. They must therefore be removed, requiring greater production costs.

Closing Remarks

A first-order two-dimensional thermomechanical model, which predicts the location of and time to air gap nucleation, has been developed to examine growth stability during solidification of pure metal castings. In particular, the stability of an aluminum casting was examined under the assumption that the deformation of the material follows a hypoelastic constitutive law. An expression for the mold/casting interface pressure, which is indicative of the deformation of the casting as it grows from the melt, was determined through combination of a nonuniform beam theory and the hypoelastic constitutive model. Air gaps were found to nucleate beneath thickness minima on the freezing front since the mold/casting interface pressure first dropped to zero at these locations. On the other hand, the mold/casting interface pressure was found to increase under thickness maxima thereby enhancing the initial growth nonuniformity in the freezing front. The time to air gap nucleation was found to depend on pertinent material properties and process parameters.

The nonuniform beam model presented in this work is being extended to a plate model in which the strain ϵ_{yy} is nonzero. A departure from standard plate theory is necessary since the location of one boundary of the plate is constantly changing. A hypoelastoviscous constitutive model of the growth instability, which accounts for nonlinear deformation of metals at elevated temperatures, is also being developed. An improved heat conduction model, which does not require the restriction presented by equation (9), is being formulated for future instability models. An extensive experimental program is underway which will evaluate the present model and guide its improvement.

Acknowledgments

The authors gratefully acknowledge several useful interactions with Prof. J. R. Barber of the University of Michigan on the model described here including identification of a critical error in an earlier model by one of us (O.R.) and N. C. Huang of Notre Dame University. We also with to thank Mr. P. J. Wray of the Inland Steel Company for providing several of the references cited here on experimental studies and Dr. P. Anyalebechi of Alcoa Technical Center for advice on metallurgical aspects of the problem. This work was sponsored in part by Alcoa's Massena Operations and in part by the Process Tribology Program at Alcoa Technical Center.

References

Chehl, S. S., 1973, "Multidimensional Heat Conduction Problems with Change-of-Phase," Ph.D. Thesis, North Carolina State University, Raleigh, N.C.

Cisse, J. Cole, G. S., and Bolling, G. F., 1971, "Freezing Front Asymmetry During Ingot Solidification of Aluminum and its Alloys," *AFS Cast Metals Research Journal*, Vol. 7, No. 4, pp. 158–161.

Collins, D. L. W., 1967, "A New Explanation of the Surface Structures of D.C. Ingots," Vol. 76, No. 10, pp. 137–144.

de L. Davies, V., and Westby, O., 1977, "Numerical Computation of the

Downloaded 03 May 2010 to 171.66.16.244. Redistribution subject to ASME license or copyright; see http://www.asme.org/terms/Terms_Use.cfm

Solidification of Continuously Cast Aluminum Rod," *Nonferrous Wire Handbook*, Vol. 1, Chapter 8, Wire Assn. Intl., Guilford, Conn., p. 197–212.

Halliday, J. M. D., 1965, Discussion One, ISI Special Report, No. 89, p. 98.

Heinlein, M., Mukherjee, S. and Richmond, O., 1986, "A Boundary Element Method of Analysis of Temperature Fields and Stresses During Solidification," *ACTA Mechanica*, Vol. 59, pp. 59–81.

Liu, J. C., private communication to L. G. Hector, Alcoa Laboratories, Nov. 1989.

Mullins, W. W., and Sekerka, R. F., 1964, "Stability of a Planar Interface During Solidification of a Dilute Binary Alloy," *J. Appl. Phys.*, Vol. 35, pp. 444–451.

Neymark, V. Ye., 1955, "Influence of Inoculants and Crystallization Conditions on the Quality of the Skin of the Ingot," *Transactions of the First All-Union Conference on Continuous Steel Casting*, Moscow, USSR, pp. 222–240.

Özisik, M. N., 1980, *Heat Çonduction*, John Wiley and Sons, New York.

Patel, P. D., 1968, "Interface Conditions in Heat Conduction Problems with Change of Phase," *AIAA J.*, Vol. 6, p. 2454.

Prager, W., 1961, *Introduction to the Mechanics of Continųa*, Ginn and Company, New York.

Richmond, O., 1981, "Models of Stresses and Deformations in Solidifying Bodes," *Modeling of Casting and Welding Processes*, H. Brody, and D. Apelian, eds., Metallurgical Society, Warrendale, Penn., pp. 215–222.

Richmond, O., and Tien, R. H., 1971, "Theory of Thermal Stresses and Air Gap Formation During the Early Stages of Solidification in a Rectangular Mold," *J. Mech. Phys. Solids*, Vol. 19, pp. 273–284.

Rutter, J. W., and Chalmers, B., 1953, "Prismatic Substructure Formed During Solidification of Metals," *Can. J. Phys.*, Vol. 31, pp. 15–39.

Sekerka, R. F., 1968, "Morphological Instability," *J. of Crystal Growth*, Vol. 3, pp. 71–81.

Sikarskie, D. L., and Boley, B. A., 1965, "The Solution of a Class of Two Dimensional Melting and Solidification Problems," *Int. J. of Solids and Structures*, Vol. 1, pp. 201–234.

Singh, S. N., and Blazek, K. E., 1974, "Heat Transfer and Skin Formation in a Continuous-Casting Mold as a Function of Steel Carbon Content," *J. of Metals*, Oct., pp. 17–27.

Smelser, R. E., and Richmond, O., 1988, "Constitutive Model Effects on Stresses and Deformations in a Solidifying Circular Cylinder," to be published in *Proc. Fourth Conf. Modeling of Casting and Welding Processes*, Palm Coast, Fl., Apr. 17–22.

Tien, R. H., and Richmond, O., 1982, "Theory of Maximum Tensile Stresses in the Solidifying Shell of a Constrained Rectangular Casting," ASME JOURNAL OF APPLIED MECHANICS, Vol. 49, pp. 481–486.

Wray, P. J., 1977, "Nonuniform Growth of a Plate Solidifying on a Chilled Surface," presentation notes, Proceedings of the AIME Conference, Atlanta, Ga.

Wray, P. J., 1981, "Geometric Features of Chill-Cast Structures," *Metall. Trans.*, Vol. 12B, pp. 167–176.

APPENDIX A

Derivation of Equations (6), (7), and (9)

The total derivative of equation (3) is,

$$dT=\left(\frac{\partial T}{\partial x}+\frac{\partial T}{\partial z}\frac{\partial s}{\partial x}\right)dx+\left(\frac{\partial T}{\partial t}+\frac{\partial T}{\partial z}\frac{\partial s}{\partial t}\right)dt=0. \tag{A1}$$

Since x and t are independent variables, equation (A1) gives

$$\frac{\partial T}{\partial x}=-\frac{\partial T}{\partial z}\frac{\partial s}{\partial x} \tag{A2}$$

$$\frac{\partial T}{\partial t}=-\frac{\partial T}{\partial z}\frac{\partial s}{\partial t}. \tag{A3}$$

These equations relate the time and space derivatives of the casting thickness to the temperature gradients as well as the rate of temperature change. Equation (A2) may be differentiated with respect to x

$$\frac{\partial^2 T}{\partial x^2}=-\left[\frac{\partial^2 s}{\partial x^2}+\frac{\partial s}{\partial x}\frac{\partial^2 T}{\partial x\partial z}\right], \tag{A4}$$

and then differentiated with respect to z

$$\frac{\partial^2 T}{\partial z\partial x}=-\frac{\partial s}{\partial x}\frac{\partial^2 T}{\partial z^2}. \tag{A5}$$

Equation (A5) is substituted into equation (A4) which gives

$$\frac{\partial^2 T}{\partial x^2}=-\left[\frac{\partial^2 s}{\partial x^2}\frac{\partial T}{\partial z}-\left(\frac{\partial s}{\partial x}\right)^2\frac{\partial^2 T}{\partial z^2}\right]. \tag{A6}$$

Equations (A3) and (A6) are substituted in equation (1) which gives

$$\frac{\partial^2 T}{\partial z^2}+\left(\frac{1}{\kappa}\frac{\partial s}{\partial t}-\frac{\partial^2 s}{\partial x^2}\right)\frac{\partial T}{\partial z}=0. \tag{A7}$$

Equation (A7), which is the conduction equation written at the freezing front, is not rigorously valid since it lacks a heat generation term due to the liberation of latent heat (see Özisik, 1980). Nevertheless, it is assumed to be a sufficient approximation for thin castings with small freezing front gradients, since the result it provides for the temperature distribution in the casting compares favorably with the work of Sikarskie and Boley (1965) (see also Chehl, (1973)).

The temperature distribution in the casting is approximated by the following polynomial

$$T=\beta_1+\beta_2\left(\frac{z}{s}-1\right)+\beta_3\left(\frac{z}{s}-1\right)^2 \tag{A8}$$

where β_i are functions of x and t but not z. Equation (A8) is substituted into equation (3), which gives

$$\beta_1=T_f. \tag{A9}$$

Equation (A8) is substituted into equation (2) and solved for β_3 to give

$$\beta_3=\frac{1}{2}\left[\beta_2-\frac{Qs}{k}\right]. \tag{A10}$$

Equation (A8) is now written as

$$T=T_f+\frac{\beta_2}{2}\left[\left(\frac{z}{s}\right)^2-1\right]-\frac{Qs}{2k}\left[\frac{z}{s}-1\right]^2. \tag{A11}$$

In order to determine β_2, the following derivatives of equation (A11), evaluated at the freezing front, are formed:

$$\frac{\partial T}{\partial z}=\frac{\beta_2}{s} \tag{A12}$$

$$\frac{\partial^2 T}{\partial z^2}=\frac{1}{s^2}\left[\beta_2-\frac{Qs}{k}\right]. \tag{13}$$

Equation (A12) is substituted into equation (4) which gives

$$\frac{\partial s}{\partial t}=\frac{\beta_2 k}{\rho L s}. \tag{A14}$$

Finally, equations (A12), (A13), and (A14) are substituted into equation (A7) which gives

$$\beta_2{}^2+\frac{\kappa\rho L}{k}\left(1-s\frac{\partial^2 s}{\partial x^2}\right)\beta_2-\frac{\kappa\rho L s}{k^2}Q=0. \tag{A15}$$

The solutions to equation (A15) are

$$\beta_2=\frac{\kappa\rho L}{2k}\left\{-1\pm\sqrt{1+\frac{4Qs}{\kappa\rho L}}\right\} \tag{A16}$$

where

$$1-s\frac{\partial^2 s}{\partial x^2}\approx 1. \tag{A17}$$

Equation (A16) reduces to

$$\beta_2=\frac{Qs}{k} \tag{A18}$$

when

$$\frac{4Qs}{\kappa\rho L}\ll 1. \tag{A19}$$

Substitution of equation (A18) into equations (A11) and (A14) yields equations (6) and (7), respectively.

Downloaded 03 May 2010 to 171.66.16.244. Redistribution subject to ASME license or copyright; see http://www.asme.org/terms/Terms_Use.cfm

APPENDIX B

Derivation of Equations (12)–(15)

The following derivations use the quantities depicted in Fig. 2. The weight of the element acts through the element centroid. The centroid is found at the point

$$\bar{x}=\frac{1}{s}\left[\frac{s}{2}dx-\frac{dsdx}{12}\right] \tag{B1}$$

$$\bar{z}=\frac{1}{s}\left[\frac{s^2}{2}+\frac{(ds)^2}{24}\right]. \tag{B2}$$

However, we may consider the magnitudes of the following differences:

$$\frac{dx}{2}-\bar{x}=\frac{dsdx}{12s} \tag{B3}$$

$$\bar{z}-\frac{s}{2}=\frac{(ds)^2}{12s}. \tag{B4}$$

Because these differences are small, we may assume that the centroid lies at the point $\bar{x}=\frac{dx}{2}$ and $\bar{z}=\frac{ds}{2}$. The contributions to moment equilibrium due to mold pressure and the vertical component of the fluid pressure at the freezing front are thus neglected.

The equation of the freezing front at an arbitrary point (see Patel, 1968) is given by $F=F(x, z, t)=0$ where

$$F=z-s. \tag{B5}$$

The normal to the surface at this same point is

$$\mathbf{n}=\frac{\nabla F}{|\nabla F|}=\frac{-\frac{\partial s}{\partial x}\mathbf{e}_1+\mathbf{e}_2}{\sqrt{1+\left(\frac{\partial s}{\partial x}\right)^2}}. \tag{B6}$$

The condition that the net shear force V on the element must vanish is given by

$$V+Pdx=V+\frac{\partial V}{\partial x}dx+\rho gsdx+\rho g(\mathbf{e}_2\cdot\mathbf{n})(H-s)dl. \tag{B7}$$

Equation (B7) simplifies to equation (12).

The condition that the net lateral force N through the element must vanish is given by

$$N=N+\frac{\partial N}{\partial x}dx-\rho g(\mathbf{e}_1\cdot\mathbf{n})(H-s)dl. \tag{B8}$$

Equation (B8) simplifies to equation (13).

The condition that the sum of the moments about the centroid of the element must vanish is given by

$$M+\frac{\partial M}{\partial x}dx=M+Vdx+\frac{N}{2}\frac{\partial s}{\partial x}dx$$

$$-\frac{\rho g}{2}(\mathbf{e}_1\cdot\mathbf{n})(H-s)dl\frac{\partial s}{\partial x}dx+\frac{1}{2}\frac{\partial V}{\partial x}(dx)^2. \tag{B9}$$

Upon neglecting the second-order differential, equation (B9) simplifies to equation (14). Equation (14) is differentiated with respect to x and is then substituted into equation (12) for the spatial derivative of V. The result may be rearranged to equation (15).

Downloaded 03 May 2010 to 171.66.16.244. Redistribution subject to ASME license or copyright; see http://www.asme.org/terms/Terms_Use.cfm

George Z. Voyiadjis
Professor,
Mem. ASME

Mehrdad Foroozesh
Assoc. Mem., ASME

Department of Civil Engineering,
Louisiana State University,
Baton Rouge, LA 70893

Anisotropic Distortional Yield Model[1]

A yield surface model is proposed in this work which may be adapted to both small strain and large strain offset definitions of yielding. The proposed anisotropic distortional yield model is capable of translation, uniform expansion or contraction, as well as distortion of the subsequent yield surface. Two versions of the proposed model are introduced through variations in fourth-order anisotropy tensor **M** *of the yield surface. Experimental observations by Phillips and co-workers (1973, 1974, 1977, 1979, 1985), Helling et al. (1986), and Stout et al. (1985) are taken into consideration in the development of the proposed model. The corresponding fourth-order elastoplastic stiffness matrix is formulated and specific examples are given.*

Introduction

Numerous theories of plastic work-hardening materials of varying capability and complexity have been developed in the past 50 years. Most of these theories define the work-hardening of the material using two principal ideas: (1) isotropic hardening and (2) kinematic hardening. The isotropic hardening rule which assumes a uniform expansion of the yield surface in the stress space was first introduced by Hill (1950) and Hodge (1955). However, this model does not incorporate the Bauschinger effect. Ishlinskii (1954) and Prager (1956) introduced the concept of translation of the yield surface without rotation in the stress space in order to introduce the Bauschinger effect. This model is termed kinematic hardening.

In defining the kinematic hardening models, it is essential that the direction of the motion of the center of the yield surface be specified. Prager (1956) defined this direction to be normal to the yield surface at the current stress point. Shield and Ziegler (1958) and later Ziegler (1959) suggested that the motion of the center of the yield surface is in the direction of the vector connecting the center of the yield surface to the current stress point. Ziegler's model, however, does not conform to the experimental results obtained by Phillips and Lee (1979). By performing tests on specimens under combined axial and torsion loads, Phillips and Lee (1979) concluded that the direction of motion of the center of the yield surface, obtained from small offset definitions of yielding ($\epsilon \leq 3 \times 10^{-6}$), is between the normal to the yield surface and the stress rate vector with more inclination toward the direction of the stress rate vector. Phillips and Lee (1979) also confirmed the existence of a loading surface.

The more recent experiments concerned with determination of the subsequent yield surfaces, Phillips and co-workers (1973, 1974, 1977, 1979), Helling et al. (1986), and Stout et al. (1985), have shown that considerable distortion occurs during prestressing leading to anisotropy of the material. However, anisotropic distortion was first introduced mathematically in early 1950's by Hill (1950), and Edelman and Drucker (1951). Several other researchers, most notably Baltov and Sawczuk (1965), Phillips and Wang (1975), and more recently, Eisenberg and Yen (1984) and Helling and Miller (1987), introduced other distortional yield surface models. However, most of the proposed models are limited in their applicability to boundary value problems.

In this paper, an anisotropic distortional yield model is proposed. An emphasis has been placed on the practicality of the model in its use for solution of boundary value problems. The elastoplastic stiffness matrix is developed to be used in finite element programs.

Theoretical Formulation

Two-Parameter Anisotropic Distortional Yield Model. The proposed yield surface is expressed using the Hill anisotropy tensor as follows:

$$F \equiv M_{ijkl}(s_{kl} - \alpha_{kl})(s_{ij} - \alpha_{ij}) = k_0^2 \tag{1}$$

where k_0 represents the initial size of the yield surface, s_{ij} is the deviatoric component of the stress tensor σ_{ij}, and α_{ij} is the deviatoric component of the location of the center of the subsequent yield surface β_{ij}. Let

$$M_{ijkl} = \frac{1}{2}\delta_{ik}\delta_{jl} \tag{2}$$

where the tensor δ is the Kronecker delta. Substituting in equation (1) for **M** from equation (2), we obtain

$$\frac{1}{2}(s_{ij} - \alpha_{ij})(s_{ij} - \alpha_{ij}) = k_0^2. \tag{3}$$

Equation (3) is the corresponding von Mises yield surface with kinematic hardening.

---

[1] This paper was presented at the Applied Mechanics and Engineering Sciences Conference, Berkeley, Calif., June 1988.

Contributed by the Applied Mechanics Division of THE AMERICAN SOCIETY OF MECHANICAL ENGINEERS for publication in the JOURNAL OF APPLIED MECHANICS.

Discussion on this paper should be addressed to the Technical Editor, Leon M. Keer, The Technological Institute, Northwestern University, Evanston, IL 60208, and will be accepted until two months after final publication of the paper itself in the JOURNAL OF APPLIED MECHANICS. Manuscript received by the ASME Applied Mechanics Division, June 22, 1988; final revision, April 24, 1989.

Copyright © 1990 by ASME
Downloaded 03 May 2010 to 171.66.16.244. Redistribution subject to ASME license or copyright; see http://www.asme.org/terms/Terms_Use.cfm

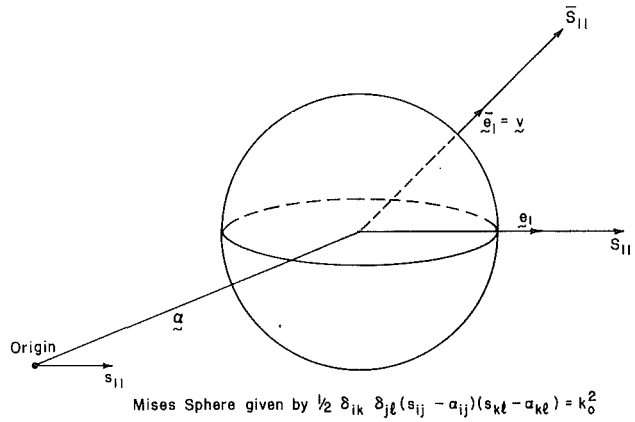


Fig. 1 Relative orientation of the local and the global coordinate axes

The experimental work of Phillips and Lee (1979), Phillips et al. (1974), Helling et al. (1986), and Stout et al. (1985) have indicated that considerable distortion occurs in the yield surfaces, obtained by small strain offset definition of yielding, during prestressing. These authors have noted that the distortion of the yield surface occurs in a particular direction. Phillips and co-workers (1974, 1979) have indicated that the direction of distortion is the same as the direction of prestressing. On the other hand, Stout et al. (1985) have suggested that the direction of distortion is coaxial with the direction of the prestrain. For the purpose of maintaining generality, we define $\mathbf{V}$ to be a tensor along the direction of distortion in the deviatoric stress space for an increment of applied load. We define a normalized tensor $\mathbf{v}$ along the same direction as $\mathbf{V}$ such that

$$\mathbf{v} = \frac{\mathbf{V}}{|\mathbf{V}|} \tag{4}$$

where $|\mathbf{V}|$ is the magnitude of the tensor $\mathbf{V}$, such that

$$|\mathbf{V}| = (V_{ij}V_{ij})^{1/2}.$$

The distortion of the surface will now be introduced through the fourth-order tensor $\mathbf{M}$ (equation (1)). The deviatoric stress space $\mathbf{S}$ where $\mathbf{S} = \mathbf{s} - \boldsymbol{\alpha}$ is considered as a nine-dimensional space which will be referred to as the global nine-space. The following nine bases define the global nine-space:

$$\mathbf{e}_1 = \begin{bmatrix} 1 \\ 0 \\ 0 \\ 0 \\ 0 \\ 0 \\ 0 \\ 0 \\ 0 \end{bmatrix}, \quad \mathbf{e}_2 = \begin{bmatrix} 0 \\ 1 \\ 0 \\ 0 \\ 0 \\ 0 \\ 0 \\ 0 \\ 0 \end{bmatrix}, \quad \ldots, \quad \mathbf{e}_9 = \begin{bmatrix} 0 \\ 0 \\ 0 \\ 0 \\ 0 \\ 0 \\ 0 \\ 0 \\ 1 \end{bmatrix} \tag{5}$$

such that $\mathbf{e}_1, \mathbf{e}_2, \mathbf{e}_3, \ldots, \mathbf{e}_9$, are bases in the directions of S_{11}, S_{12}, S_{13}, S_{21}, $\ldots$, S_{33}, axes, respectively. A local nine-space with the same origin (center of the yield surface) as the global nine-space is also introduced such that the local coordinate axis $\bar{S}_{11}$ is directed along the direction of distortion $\mathbf{v}$, while the remaining eight coordinates axes have arbitrary directions provided an orthonormal coordinate system is maintained. This is illustrated in Fig. 1. In the formulation that follows, all the quantities with a bar on top are defined with respect to this local coordinate system.

The fourth-order tensor M_{ijkl} used in equation (1) is now defined in terms of the global nine-space as follows:

$$M_{ijkl} = \frac{1}{2}\delta_{ik}\delta_{jl} + N_{ijkl}. \tag{6}$$

The fourth-order tensor $\mathbf{N}$ is used to account for all the uniform expansion, contraction, and distortion of the yield surface as loading progresses. If all the components of this tensor are zero, then the expression for the yield surface is reduced to equation (3) as described earlier. In order to better understand how distortions are introduced through the tensor $\mathbf{N}$, the development of this tensor is followed in the local coordinate system $\bar{S}_{ij}$ introduced earlier. The rate of change of the fourth-order tensor $\mathbf{N}$ of equation (6) is defined with respect to the local coordinates as follows:

$$\dot{\bar{N}}_{ijkl} = \dot{a}\delta_{ik}\delta_{jl} + \dot{b}\bar{A}_{ij}\bar{A}_{kl} \tag{7}$$

where a and b are material parameters to be determined experimentally, and they may be assumed to be functions of the plastic work κ, such that

$$\kappa = \int_0^t \sigma_{kl} e''_{kl} d\tau. \tag{8}$$

In equation (8), $\dot{e}''_{kl}$ is the plastic component of the strain rate tensor. An alternate expression for either a or b may be obtained by assuming them to be functions of the plastic strain trajectory $|e''|$, where

$$|e''| = \int_0^t \dot{e}''_{ij}\dot{e}''_{ij} dt. \tag{9}$$

The second-order tensor $\bar{\mathbf{A}}$ in equation (7) is defined with respect to the local nine-space as follows:

$$\bar{\mathbf{A}} = \begin{bmatrix} 1 & 0 & 0 \\ 0 & 0 & 0 \\ 0 & 0 & 0 \end{bmatrix}. \tag{10}$$

The first term of the right-hand side of equation (7) when used with equations (6) and (1) will cause a uniform expansion or contraction of the original Mises surface. The second term on the right-hand side of equation (7) when used with equations (6) and (1) will cause a distortion of the Mises surface in the direction of the local coordinate axis $\bar{S}_{11}$ which also coincides with the direction of distortion $\mathbf{v}$ in the global nine-space, provided that there is no previous distortions (i.e., first subsequent yield surface). For the case when previous distortions in the yield surface have occurred (i.e., after the first subsequent yield surface), use of equation (7) will result in the distortion of the yield surface in the direction of tensor $\mathbf{v}$ for radial proportional loadings only. Hence, the principal axes of the ellipsoid given by equations (1), (6), and (7) will coincide with the local coordinate system $\bar{\mathbf{S}}$ and the distortion will only be in the direction of $\bar{S}_{11}$ leaving all other principal axes of the ellipsoid unaltered. Otherwise, for a nonproportional loading, use of equations (6) and (7) in equation (1) will result in a rotation of the principal axes of the ellipsoid causing some cross effects. In this case the principal axes of the ellipsoid and the local coordinate axes will not coincide.

Equation (7) will now be expressed in terms of the global nine-space, $\mathbf{S}$. This is achieved by simply changing the bases. The bases for the local nine-space are given by $\bar{\mathbf{e}}_1, \bar{\mathbf{e}}_2, \ldots, \bar{\mathbf{e}}_9$, where

$$\bar{\mathbf{e}}_1 = \mathbf{v}. \tag{11}$$

As was previously pointed out, the remaining eight bases $\bar{\mathbf{e}}_2$, $\bar{\mathbf{e}}_3, \ldots, \bar{\mathbf{e}}_9$ may have any arbitrary direction provided an orthonormal coordinate system is maintained. The remaining eight bases $\bar{\mathbf{e}}_2, \bar{\mathbf{e}}_3, \ldots, \bar{\mathbf{e}}_9$, if required, may be generated using the Gram-Schmidt orthogonalization process. However,

Downloaded 03 May 2010 to 171.66.16.244. Redistribution subject to ASME license or copyright; see http://www.asme.org/terms/Terms_Use.cfm

for the purpose of this work, it will not be necessary to determine $\bar{\mathbf{e}}_2, \bar{\mathbf{e}}_3, \ldots, \bar{\mathbf{e}}_9$. The coordinate transformation needed to express the local bases $\bar{\mathbf{e}}$ in terms of the global bases $\mathbf{e}$ may be expressed as follows:

$$\{\bar{\mathbf{e}}\} = [\mathbf{T}]\{\mathbf{e}\} \tag{12}$$

where $\mathbf{T}$ is a nine-by-nine matrix expressed as

$$\mathbf{T} = [\{\mathbf{v}\}, \{\bar{\mathbf{e}}_2\}, \{\bar{\mathbf{e}}_3\}, \ldots, \{\bar{\mathbf{e}}_9\}]. \tag{13}$$

It must be noted that matrix $\bar{\mathbf{A}}$ is equation (10) corresponds to the basis $\bar{\mathbf{e}}_1$, and since

$$\{\bar{\mathbf{e}}_1\} = [\mathbf{T}]\{\mathbf{e}\} = \{\mathbf{v}\}, \tag{14}$$

we can conclude that tensor $\bar{\mathbf{A}}$ may be expressed as tensor $\mathbf{v}$ in terms of the global coordinates. We note that the first term of the right-hand side of equation (7), when used in equations (6) and (1), is invariant with respect to any coordinate transformation. Equation (7) may now be expressed in the global nine-space reference frame as follows:

$$\dot{N}_{ijkl} = \dot{a}\delta_{ik}\delta_{jl} + \dot{b}v_{ij}v_{kl}. \tag{15}$$

Integrating equation (15) and realizing that $\mathbf{v}$ will not change during each increment of loading, we obtain the following expression for $\mathbf{N}$ after the mth loading increment

$$N^{(m)}_{ijkl} = \sum_{n=1}^{m} \dot{a}^{(n)}\delta_{ik}\delta_{jl} + \sum_{n=1}^{m} \dot{b}^{(n)}v^{(n)}_{ij}v^{(n)}_{kl}. \tag{16}$$

Equation (16) represents the superposition of a series of distortions and expansions or contractions that have taken place during m load increments. Substituting equation (16) in equation (6), we obtain the final expression for $\mathbf{M}$ as shown here:

$$M^{(m)}_{ijkl} = \frac{1}{2}\delta_{ik}\delta_{jl} + \sum_{n=1}^{m} \dot{a}^{(n)}\delta_{ik}\delta_{jl} + \sum_{n=1}^{m} \dot{b}^{(n)}v^{(n)}_{ij}v^{(n)}_{kl}. \tag{17}$$

Equation (1) may now be expressed as follows:

$$F^{(m)} \equiv \left[\frac{1}{2}\delta_{ik}\delta_{jl} + \sum_{n=1}^{m} \dot{a}^{(n)}\delta_{ik}\delta_{jl} + \sum_{n=1}^{m} \dot{b}^{(n)}v^{(n)}_{ij}v^{(n)}_{kl}\right] \cdot (s_{ij} - \alpha_{ij})(s_{kl} - \alpha_{kl}) = k_0^2 \tag{18}$$

where $\mathbf{s}$ represents the state of stress at any point on the current yield surface. In equation (18), $F^{(m)}$ is the yield function after the mth load increment.

It must be noted that the movement and distortion of the yield surfaces obtained experimentally are sensitive and subject to the corresponding definitions of yielding (i.e., proportional limit, small strain offset, large strain offset, etc.). Phillips and Lee (1979), Phillips and Moon (1977), Phillips and Weng (1975), and Phillips et al. (1974) have shown from their experimental observations (see Fig. 2) that the yield surface changes its length in the direction of prestress such that it becomes smaller when prestressing is directed away from the origin of stress space. On the other hand, the yield surface becomes larger when prestressing is directed towards the origin of the stress space. Phillips and co-workers conducted their experiments on aluminum 1100-0, and defined yielding at the proportional limit (Phillips et al., 1974). Helling, Miller, and Stout (1986) have shown that for aluminum 1100-0, the yield surface expands rather than contracts when prestressed away from the origin. They used a small-strain offset ($\epsilon = 5 \times 10^{-6}$) to define yielding. The different experimental data obtained by Phillips et al. (1974), Helling et al. (1986), and Stout et al. (1985) may be accounted for in the proposed model (equation (18)) by evaluating the parameters a and b appropriately based on their respective experimental data.

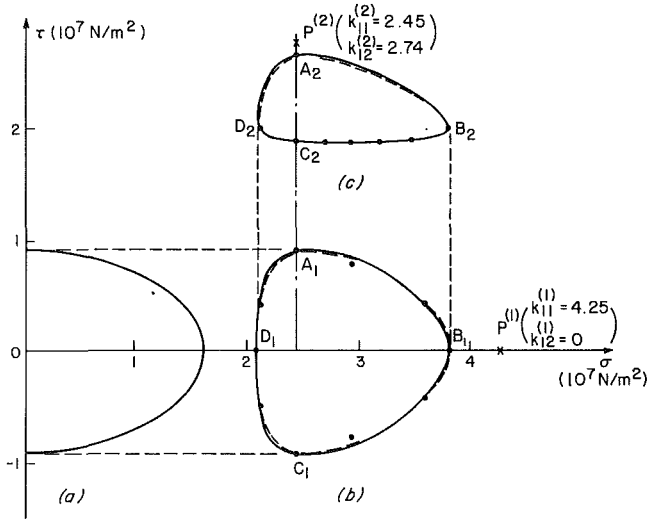
Convexity of the Two-Parameter Distortional Yield Model. The shape of the yield surface plays an important role in the theory of plasticity, and is subjected to the limitation that it must be convex. The convexity requirement was originally initiated based on the Prager's (1956) condition of irreversibility. This condition requires that because of the irreversible nature of plastic deformations, the plastic work done should be positive; that is,

$$\sigma_{ij}\dot{\epsilon}^P_{ij} > 0. \tag{19}$$

Based on this condition and the fact that it was once thought that the origin of the stress space had to be contained within the yield surface, it was shown that any radial vector from the origin to a point on the yield surface must make an acute angle with the exterior normal at that point. That is, the yield surface had to be convex. However, based on the experimental works of Phillips and co-workers (1973, 1974, 1977, 1979), Helling et al. (1986), and Stout et al. (1985), it is shown that the yield surfaces obtained based on the small offset definitions of yielding no longer have to enclose the origin. This finding is in direct contradiction with Prager's condition of irreversibility. Hence, we no longer can consider the convexity of the yield surface to be a necessary condition to satisfy expression (19). This is true because even if the yield surface is convex, expression (19) may not be satisfied when unloading is performed towards the origin.

Even if we are to ignore the condition of irreversibility, Prager's condition on consistency also requires that the yield surface be convex. This conditions states that loading from a plastic state will lead to another plastic state. Figure 3(*a*) shows that, for a convex surface, loading from a point on the yield surface leads to another plastic state. Figure 3(*b*), on the other hand, shows that loading from a yield locus which is not convex may lead to an elastic state. This violates the condition of consistency. We must therefore show that the proposed model does satisfy the condition of consistency by showing that it will remain convex as the plastic flow progresses.

The yield surface is said to be convex if a straight line connecting any two points on the yield surface does not intersect the yield surface at any third point. Referring to Fig. 4, let $\mathbf{S}^{(1)}$ and $\mathbf{S}^{(2)}$ denote the state of the stresses with respect to the global reference frame, $\mathbf{S}$, corresponding to points P_1 and P_2, respectively. In order for the yield surface to be convex, line



----- Experimentally determined
——— Analytically determined by means of our hardening law:
(a) Initial yield surface,
(b) First subsequent yield surface,
(c) Second subsequent yield surface.

Fig. 2 Comparison of yield surfaces (after Phillips and Weng, 1975)

Downloaded 03 May 2010 to 171.66.16.244. Redistribution subject to ASME license or copyright; see http://www.asme.org/terms/Terms_Use.cfm

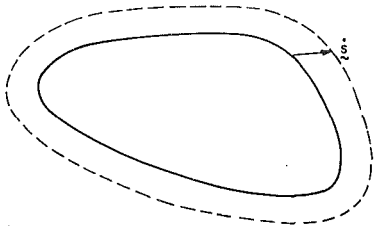


Fig. 3(*a*) Loading from a point on a yield surface which is convex leads to another plastic state

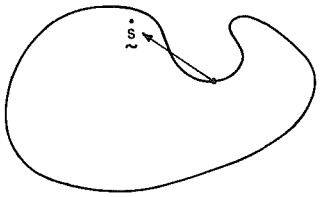


Fig. 3(*b*) Loading from a point on a yield surface which is not convex may lead to an elastic state

P_1P_2 should not intersect the curved segment along the boundary of the yield surface at any point other than points P_1 and P_2. Since P_1 and P_2 are on the boundary of the yield surface, the value of the yield function at these points will vanish, therefore:

$$F(\mathbf{S}^{(1)}) = F(\mathbf{S}^{(2)}) = 0. \tag{20}$$

Also, since the line segment P_1P_2 is fully contained within the yield surface, the value of the yield function at any third point along this line will have to be less than or equal to zero. This condition may be shown qualitatively by the following expression:

$$F(\eta\mathbf{S}^{(1)} + (1-\eta)\mathbf{S}^{(2)}) \le 0 \tag{21}$$

where

$$0 \le \eta \le 1.$$

In the inequality (21), the term contained within the brackets is a parametric representation for the state of the stress anywhere along the line segment P_1P_2. The proof of convexity of the yield surface will be complete once we show that inequality (21) is a valid expression.

Equation (1) may be expressed in terms of the global coordinate system, **S**, where $\mathbf{S} = \mathbf{s} - \boldsymbol{\alpha}$ as follows:

$$F = M_{ijkl}(S_{ij})(S_{kl}) - K_0^2. \tag{22}$$

In equation (1), $\boldsymbol{\alpha}$ represents the location of the center of the yield surface; therefore, it will not play a role in the convexity of the yield surface which almost entirely depends on the fourth-order tensor **M**. Hence, in order to simplify the proof that follows, equation (22) is used instead of equation (1).

Equation (21), which represents the value of the yield function for any point along the line P_1P_2, may be expressed as:

$$F(\eta\mathbf{S}^{(1)} + (1-\eta)\mathbf{S}^{(2)}) = M_{ijkl}[\eta S_{ij}^{(1)} + (1-\eta)S_{ij}^{(2)}][\eta S_{kl}^{(1)} + (1-\eta)S_{kl}^{(2)}] - K_0^2. \tag{23}$$

Expansion of equation (23) will result in:

$$F(\eta\mathbf{S}^{(1)} + (1-\eta)\mathbf{S}^{(2)}) = M_{ijkl}[\eta^2 S_{ij}^{(1)}S_{kl}^{(1)} + (1-\eta)^2 S_{ij}^{(2)}S_{kl}^{(2)} + \eta(1-\eta)S_{ij}^{(2)}S_{kl}^{(1)} + \eta(1-\eta)S_{ij}^{(1)}S_{kl}^{(2)}] - K_0^2. \tag{24}$$

Hence, we have:

$$F(\eta\mathbf{S}^{(1)} + (1-\eta)\mathbf{S}^{(2)}) = \eta^2 M_{ijkl}S_{ij}^{(1)}S_{kl}^{(1)} + (1-\eta)^2 M_{ijkl}S_{ij}^{(2)}S_{kl}^{(2)} + \eta(1-\eta)M_{ijkl}(S_{ij}^{(1)}S_{kl}^{(2)} + S_{ij}^{(2)}S_{kl}^{(1)}) - K_0^2. \tag{25}$$

From equation (20), we may conclude that

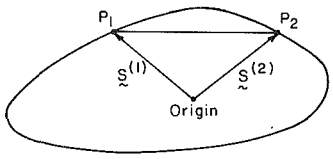


Fig. 4 For a convex surface line, P_1P_2 should not intercept the yield surface at any point other than points P_1 and P_2

$$M_{ijkl}S_{ij}^{(1)}S_{kl}^{(1)} = K_0^2 \tag{26a}$$

and

$$M_{ijkl}S_{ij}^{(2)}S_{kl}^{(2)} = K_0^2. \tag{26b}$$

Equations (26*a*) and (26*b*) are now used to simplify equation (25) as follows:

$$F(\eta\mathbf{S}^{(1)} + (1-\eta)\mathbf{S}^{(2)}) = \eta(1-\eta)[M_{ijkl}(S_{ij}^{(1)}S_{kl}^{(2)} + S_{ij}^{(2)}S_{kl}^{(1)}) - 2K_0^2]. \tag{27}$$

As expected, equation (27) will equal to zero when η is either zero or one corresponding to points P_1 and P_2 (Fig. 4), respectively. Substitution of the general expression for **M** as given by equation (17) into equation (27) results in the following:

$$F(\eta\mathbf{S}^{(1)} + (1-\eta)\mathbf{S}^{(2)}) = \eta(1-\eta)\left[\left(\frac{1}{2}\delta_{ik}\delta_{jl} + \sum_{n=1}^{m}\dot{a}^{(n)}\delta_{ik}\delta_{jl} + \sum_{n=1}^{m}\dot{b}^{(n)}v_{ij}^{(n)}v_{kl}^{(n)}\right)(S_{ij}^{(1)}S_{kl}^{(2)} + S_{ij}^{(1)}S_{kl}^{(2)}) - 2K_0^2\right] \tag{28}$$

which may be reduced to

$$F(\eta\mathbf{S}^{(1)} + (1-\eta)\mathbf{S}^{(2)}) = \eta(1-\eta)\left[\left(1 + 2\sum_{n=1}^{m}\dot{a}^{(n)}\right)S_{kl}^{(1)}S_{kl}^{(2)} + 2\sum_{n=1}^{m}\dot{b}^{(n)}(v_{ij}^{(n)}S_{ij}^{(1)})(v_{kl}^{(n)}S_{kl}^{(2)}) - 2K_0^2.\right. \tag{29}$$

We must now show that the right-hand side of equation (29) is less than or equal to zero. This is done by first substituting equation (17) for **M** in equation (26*a*) and (26*b*) in order to obtain the following expressions:

$$\left(1 + 2\sum_{n=1}^{m}\dot{a}^{(n)}\right)S_{kl}^{(1)}S_{kl}^{(1)} + 2\sum_{n=1}^{m}\dot{b}^{(n)}(v_{ij}^{(n)}S_{ij}^{(1)})^2 = 2K_0^2 \tag{30}$$

and

$$\left(1 + 2\sum_{n=1}^{m}\dot{a}^{(n)}\right)S_{kl}^{(2)}S_{kl}^{(2)} + 2\sum_{n=1}^{m}\dot{b}^{(n)}(v_{ij}^{(n)}S_{ij}^{(2)})^2 = 2K_0^2. \tag{31}$$

Now, adding both sides of equations (30) and (31) will result in:

$$\left(1 + 2\sum_{n=1}^{m}\dot{a}^{(n)}\right)(S_{kl}^{(1)}S_{kl}^{(1)} + S_{kl}^{(2)}S_{kl}^{(2)}) + 2\sum_{n=1}^{m}\dot{b}^{(n)}[(v_{ij}^{(n)}S_{ij}^{(1)})^2 + (v_{ij}^{(n)}S_{ij}^{(2)})^2] = 4K_0^2. \tag{32}$$

It is easily shown that

$$2S_{kl}^{(1)}S_{kl}^{(2)} \le (S_{kl}^{(1)}S_{kl}^{(1)} + S_{kl}^{(2)}S_{kl}^{(2)}) \tag{33}$$

and

$$2(v_{ij}^{(n)}S_{ij}^{(1)})(v_{kl}^{(n)}S_{kl}^{(2)}) \le [(v_{ij}^{(n)}S_{ij}^{(1)})^2 + (v_{ij}^{(n)}S_{ij}^{(2)})^2] \tag{34}$$

are valid inequalities. Also, since the yield surface possesses a real valued radius, we can conclude that the quantity

$$(1 + 2\sum_{n=1}^{m}\dot{a}^{(n)})$$

Downloaded 03 May 2010 to 171.66.16.244. Redistribution subject to ASME license or copyright; see http://www.asme.org/terms/Terms_Use.cfm

is always positive. It can be alternatively stated that the lower limit for the radius of the yield surface is zero. Substituting the inequalities (33) and (34) into equation (32) will result in the following expression provided that $\dot{b}^{(n)}$ for $1 \le n \le m$ is positive

$$\left(1+2\sum_{n=1}^{m}\dot{a}^{(n)}\right)(S_{kl}^{(1)}S_{kl}^{(2)}) + 2\sum_{n=1}^{m}\dot{b}^{(n)}\cdot(v_{ij}^{(n)}S_{ij}^{(1)})(v_{kl}^{(n)}S_{kl}^{(2)}) \le 2K_0^2 \tag{35}$$

Substituting inequality (35) into equation (29) will complete the proof provided that $\dot{b}^{(n)}$ is positive for every increment of loading. We must now prove the validity of inequality (35) for the case where $\dot{b}^{(n)}$ is negative for at least one loading increment. Referring to equations (30) and (31) we can conclude that the left hand side of both equations may not attain a negative value, otherwise, the yield surface turns inside out. In other words, the magnitude of the total distortions should not be greater than the radius of the yield surface for the case when the yield surface contracts. Therefore, from equations (30) and (31) we have

$$\left(1+2\sum_{n=1}^{m}\dot{a}^{(n)}\right)S_{kl}^{(1)}S_{kl}^{(1)} > -2\sum_{n=1}^{m}\dot{b}^{(n)}(v_{ij}^{(n)}S_{ij}^{(1)})^2 \tag{36}$$

and

$$\left(1+2\sum_{n=1}^{m}\dot{a}^{(n)}\right)S_{kl}^{(2)}S_{kl}^{(2)} > -2\sum_{n=1}^{m}\dot{b}^{(n)}(v_{ij}^{(n)}S_{ij}^{(2)})^2 \tag{37}$$

Since equation (32) is the sum of equations (30) and (31) we may conclude that

$$\left(1+2\sum_{n=1}^{m}\dot{a}^{(n)}\right)(S_{kl}^{(1)}S_{kl}^{(1)}+S_{kl}^{(2)}S_{kl}^{(2)}) > -2\sum_{n=1}^{m}\dot{b}^{(n)}\cdot[(v_{ij}^{(n)}S_{ij}^{(1)})^2+(v_{ij}^{(n)}S_{ij}^{(2)})^2] \tag{38}$$

is a valid inequality. The reader should also note that the difference between the right-hand side and the left-hand side of equation (33) is greater than the difference between the two sides of equation (34). This is because equation (33) involves the magnitudes of tensors $\mathbf{S}^{(1)}$ and $\mathbf{S}^{(2)}$, where as equation (34) involves the projections of $\mathbf{S}^{(1)}$ and $\mathbf{S}^{(2)}$ in the direction of the unit tensor $\mathbf{v}^{(n)}$ which may be smaller or equal to the magnitudes of vectors $\mathbf{S}^{(1)}$ and $\mathbf{S}^{(2)}$, respectively. Due to the foregoing discussion and the inequality (38), we can conclude that the reduction caused by substituting $(2S_{kl}^{(1)}S_{kl}^{(2)})$ for $(S_{kl}^{(1)}S_{kl}^{(1)}+S_{kl}^{(1)}S_{kl}^{(1)})$ in expression (32) will be greater than any increase that may be caused by substituting $2(v_{ij}^{(n)}S_{ij}^{(1)})(v_{kl}^{(n)}S_{kl}^{(2)})$ for $[(v_{ij}^{(n)}S_{ij}^{(1)})(v_{kl}^{(n)}S_{kl}^{(1)}) + (v_{ij}^{(n)}S_{ij}^{(2)})(v_{kl}^{(n)}S_{kl}^{(2)})$ when the coefficient $\dot{b}$ is negative for at least one load increment. Therefore, inequality (35) will be valid under all conditions. Substitution of inequality (35) into equation (29) results in

$$F(\eta\mathbf{S}^{(1)}+(1-\eta)\mathbf{S}^{(2)}) \le 0 \tag{39}$$

which completes the proof of the convexity of the yield surface.

Three-Parameter Anisotropic Distortional Yield Model. Both Phillips et al. (1974) and Helling et al. (1986) have shown that there is unequal distortion in the direction of prestressing with regard to the forward and rear segments of the yield surface. The rear portion of the yield surface becomes flatter, while the forward portion attains a bigger curvature. The proposed yield model as presented by equation (18) does not account for the previous experimental observations.

In general, incorporation of unequal distortions for the forward and rear portions of the yield surface would render the model impractical for numerical purposes. The three parameter model presented in this work is to introduce a methodology to account for unequal distortions for the particular case where elastic unloading does not occur. This methodology needs to be generalized to all possible types of loadings before numerical implementation of it is achieved effectively.

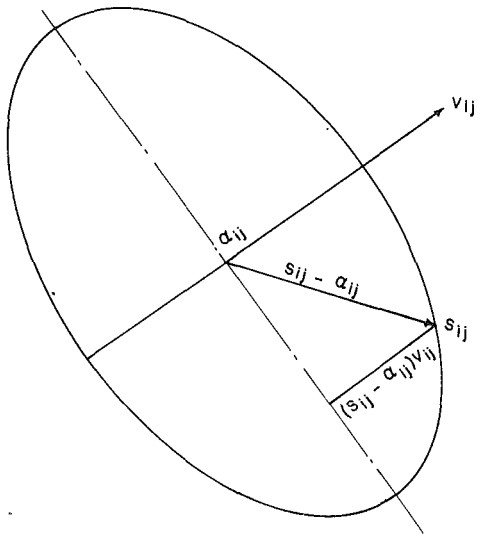


Fig. 5 Schematic representation of the hyperplane dividing the forward and the rear parts of the yield surface

In order to incorporate this unequal distorion in the direction of prestressing, $\mathbf{M}$ may be expressed as a function of $(\mathbf{s}-\boldsymbol{\alpha})$. The more general expression for $\mathbf{M}$ after the mth load increment is given by

$$M_{ijkl}^{(m)} = \frac{1}{2}\delta_{ik}\delta_{jl} + \sum_{n=1}^{m}\dot{a}^{(n)}\delta_{ik}\delta_{jl} + \sum_{n=1}^{m}v_{ij}^{(n)}v_{kl}^{(n)}[\dot{b}^{(n)}+\dot{c}^{(n)}v_{rs}^{(n)}(s_{rs}^{(n)}-\alpha_{rs}^{(n)})] \tag{40}$$

where the parameter $c^{(n)}$ is a function of either the plastic work or the effective plastic strain. The expression

$$\dot{c}^{(n)}v_{rs}^{(n)}(s_{rs}^{(n)}-\alpha_{rs}^{(n)}) \tag{41}$$

in equation (40) will be positive for the forward part of the yield surface in the direction of distortion, and negative for the corresponding rear part of the yield surface. The forward and the rear parts of the yield surface are determined by passing a plane through the yield surface such that it contains all the points of the yield surface for which expression (41) is equal to zero. This is indicated in Fig. 5. It is obvious that the three parameter expression for $\mathbf{M}$ as given by equation (40) requires more detailed experiments for its determination as opposed to the coresponding two-parameter expression given by equation (17).

Referring to Fig. 6, we can trace the movement and distortion of a series of subsequent yield surfaces obtained by prestressing in different directions. In prestressing from $\mathbf{s}^{(0)}$ state of stress to $\mathbf{s}^{(m+1)}$ without any unloading, we obtain yield surface $(m+1)$. At the state of stress $\mathbf{s}^{(m+1)}$ the fourth-order tensor $\mathbf{M}^{(m+1)}$ is given by the following expression:

$$M_{ijkl}^{(m+1)} = \frac{1}{2}\delta_{ik}\delta_{jl} + \sum_{n=1}^{m+1}\dot{a}^{(n)}\delta_{ik}\delta_{jl} + \sum_{n=1}^{m+1}v_{ij}^{(n)}v_{kl}^{(n)}[\dot{b}^{(n)}+\dot{c}^{(n)}v_{rs}^{(n)}(s_{rs}^{(n)}-\alpha_{rs}^{(n)})] \tag{42}$$

where s_{rs} relates to the state of stress on the corresponding

Downloaded 03 May 2010 to 171.66.16.244. Redistribution subject to ASME license or copyright; see http://www.asme.org/terms/Terms_Use.cfm

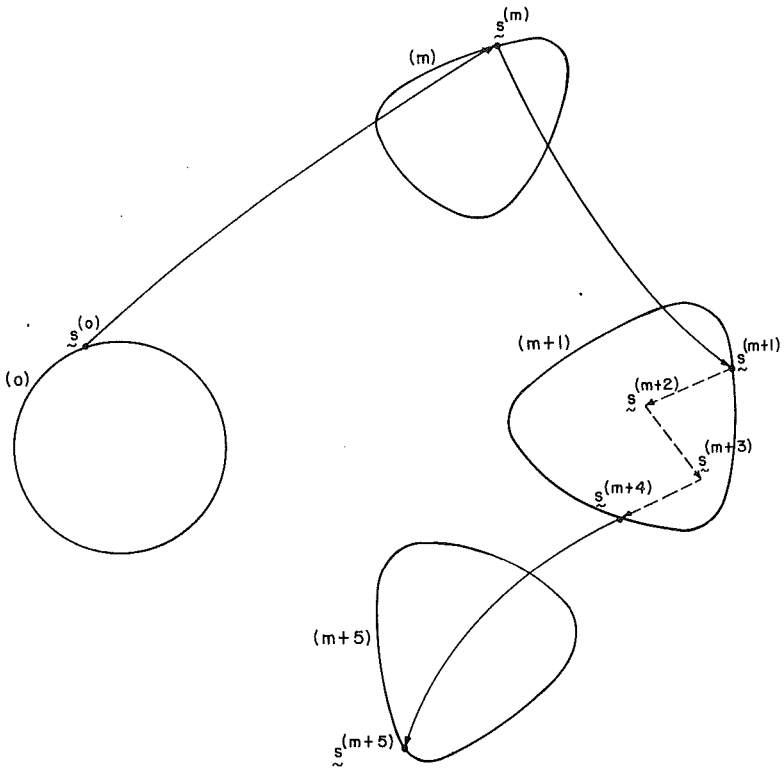


Fig. 6 Yield surfaces obtained from subsequent prestressing

yield surface. During the load increment from (m) to $(m+1)$, $\dot{M}_{ijkl}^{(m+1)}$ is given by

$$\dot{M}_{ijkl}^{(m+1)} = \dot{a}^{(m+1)}\delta_{ik}\delta_{jl} + v_{ij}^{(m+1)}v_{kl}^{(m+1)}\,[\,\dot{b}^{(m+1)} + \dot{c}^{(m+1)}v_{rs}^{(m+1)}(s_{rs}^{(m+1)} - \alpha_{rs}^{(m+1)})\,] \tag{43}$$

and the corresponding yield function is given by

$$F^{(m+1)} \equiv M_{ijkl}^{(m+1)}(s_{kl}^{(m+1)} - \alpha_{kl}^{(m+1)})(s_{ij}^{(m+1)} - \alpha_{ij}^{(m+1)}) = k_0^2. \tag{44}$$

In equations (42) through (44), $s^{(m+1)}$ relates to the state of stress at the corresponding point on the $(m+1)$ yield surface. During the subsequent load increments, the state of stress moves inside the yield surface $(m+1)$. In moving from $\mathbf{s}^{(m+1)}$ to $\mathbf{s}^{(m+4)}$ through the dotted stress path indicated in Fig. 6, the rate of change of $\mathbf{M}$ as given by equation (43) is zero. This leads to the following

$$\dot{\mathbf{M}}^{(m+2)} = \dot{\mathbf{M}}^{(m+3)} = 0 \tag{45}$$

which implies that

$$\mathbf{M}^{(m+1)} = \mathbf{M}^{(m+4)}. \tag{46}$$

Consequently, the elastic unloading will not affect the shape of the yield surface.

It is important to note that the three parameter expression for $\mathbf{M}$ given by equation (40) is of practical use provided that elastic unloading does not occur. In the case when this happens, complication will arise except in the particular case when the state of stress from the elastic region returns to the identical stress point on the yield surface prior to unloading. The complication arises, as seen from Fig. 6, when loading is continued from $\mathbf{s}^{(m+4)}$ instead of $\mathbf{s}^{(m+1)}$. In order to trace point $\mathbf{s}^{(m+4)}$ on the $(m+1)$ yield surface, it is imperative to know the previous mappings of $\mathbf{s}^{(m+4)}$ on all previous yield surfaces. For this to occur, it implies that we need to trace every point on the initial yield surface to the current yield surface. This supposition makes equation (40) practically impossible if elastic unloading occurs. As an approximation, a finite number of points on the initial yield surface may be traced to the current yield surface and all remaining points appropriately interpreted.

An approximation of equation (40) would be to set the radial tensor $(s_{rs}^{(n)} - \alpha_{rs}^{(n)})$ approximated only to its current value, that is $(s_{rs}^{(m)} - \alpha_{rs}^{(m)})$. This would imply that the additional unequal distortion is only due to the current state and is not a cummulative effect of all the previous ones. This approximation is given by equation (47):

$$M_{ijkl}^{(m)} = \frac{1}{2}\delta_{ik}\delta_{jl} + \sum_{n=1}^{m}\dot{a}^{(n)}\delta_{ik}\delta_{jl} + \sum_{n=1}^{m}\dot{b}^{(n)}v_{ij}^{(n)}v_{kl}^{(n)} + (s_{rs}^{(m)} - \alpha_{rs}^{(m)})\sum_{n=1}^{m}\dot{c}^{(n)}v_{rs}^{(n)}v_{ij}^{(n)}v_{kl}^{(n)}. \tag{47}$$

Generalized Kinematic Hardening Rule. The kinematic hardening law, describing the movement of the center of the yield surface, will be discussed next. The center of the current yield surface is assumed to be located at the center of the Mises surface which is obtained by ignoring all the distortions that may have taken place. This is shown graphically in Fig. 7. The proposed hardening rule takes into account Phillips and coworkers observations (1973, 1974, 1977, 1979, 1985), namely that the yield surface moves in the direction of the gradient to the yield surface provided that the prestressing direction is close to the gradient of the yield surface. As the angle ϕ between the prestress tensor and the gradient to the yield surface increases, the movement of the yield surface tends to become more inclinded towards the direction of prestressing. Figure 7 shows the new yield surface $(m+1)$ which is obtained from the current yield surface (m). The center of the current surface (m) translates along the unit tensor $\mathbf{u}^{(m)}$ that makes an angle $\theta^{(m)}$ with the unit normal $\mathbf{n}^{(m)}$ at $\mathbf{s}^{(m)}$. The tensor $\mathbf{u}^{(m)}$ is expressed in terms of both $\mathbf{n}^{(m)}$ and $\mathbf{l}^{(m)}$, whereas the tensor $\mathbf{l}^{(m)}$ is a normalized unit tensor along the direction of prestressing $\mathbf{s}^{(m)}$.

Downloaded 03 May 2010 to 171.66.16.244. Redistribution subject to ASME license or copyright; see http://www.asme.org/terms/Terms_Use.cfm

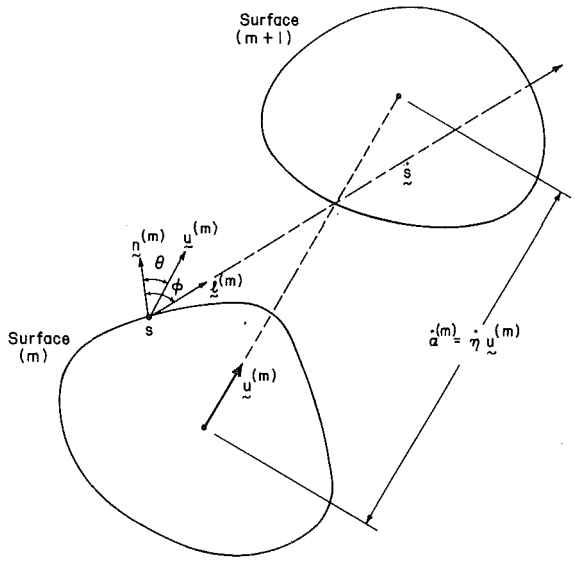


Fig. 7 Translation of the center of the yield surface

The tensor $\mathbf{u}^{(m)}$ is expressed in terms of both $\mathbf{n}^{(m)}$ and $\mathbf{l}^{(m)}$, such that

$$u_{ij}^{(m)} = \frac{dn_{ij}^{(m)} + el_{ij}^{(m)}}{[(dn_{pq}^{(m)} + el_{pq}^{(m)})(dn_{pq}^{(m)} + el_{pq}^{(m)})]^{1/2}} \tag{48}$$

where

$$u_{kl}u_{kl} = 1 \tag{49}$$

$$n_{ij} = \frac{1}{G}\frac{\partial F}{\partial \sigma_{ij}} \tag{50}$$

$$G = \left(\frac{\partial F}{\partial \sigma_{kl}}\frac{\partial F}{\partial \sigma_{kl}}\right)^{1/2} \tag{51}$$

$$n_{ij}n_{ij} = 1 \tag{52}$$

and

$$l_{ij}l_{ij} = 1. \tag{53}$$

The coefficients d and e should be chosen such that the direction of $\mathbf{u}^{(m)}$ is always closer to $\mathbf{n}^{(m)}$ than $\mathbf{l}^{(m)}$ (Phillips and Lee, 1979). In this work, following the general observations made by Phillips and co-workers (1973, 1974, 1979), d and e are set such that even if the prestressing direction $\mathbf{l}$ is along the tangent to the yield surface, the angle θ will not exceed 45 deg. Consequently, d and e are chosen such that (Voyiadjis and Kattan, 1990)

$$d = e = 1. \tag{54}$$

The movement of the center of the yield surface, as shown in Fig. 7, may be expressed as follows:

$$\dot{\alpha}_{ij} = \dot{\eta} u_{ij}^{(m)}. \tag{55}$$

$\dot{\eta}$ is positive and is obtained by assuming that the projection of $\dot{\alpha}$ on the stress gradient of the yield surface is equal to $g\dot{\mathbf{e}}''$ (Voyiadjis and Mohammad, 1988) where g is a material parameter. This results in the following expression,

$$g\dot{e}_{ij}'' = \dot{\alpha}_{cd}\frac{\dfrac{\partial F}{\partial s_{cd}}\dfrac{\partial F}{\partial s_{ij}}}{G^2} \tag{56}$$

where G is defined by equation (51). Assuming an associated flow rule

$$\dot{e}_{ij}'' = \dot{\Lambda}\frac{\partial F}{\partial s_{ij}} \tag{57}$$

where $\dot{\Lambda}$ is a scalar function and substituting equation (57) into equation (56), we obtain an expression for $\dot{\eta}$, such that

$$\dot{\eta} = \dot{\Lambda}\frac{gG^2}{u_{cd}\dfrac{\partial F}{\partial s_{cd}}}. \tag{58}$$

Substituting equation (58) into equation (55), we obtain the required expression for $\dot{\alpha}$ such that

$$\dot{\alpha}_{ij} = \dot{\Lambda}\frac{gG^2}{u_{cd}\dfrac{\partial F}{\partial s_{cd}}}u_{ij}^{(m)}. \tag{59}$$

Formulation of the Elasto-Plastic Stiffness Tensor. In the formulation that follows, wherever the summation sign Σ is not used, and scalars and tensors are referred to the current yield surface, the superscript (m) will be dropped.

The decomposition of the strain rate tensor $\dot{\mathbf{e}}$ is assumed such that

$$\dot{\mathbf{e}} = \dot{\mathbf{e}}' + \dot{\mathbf{e}}'' \tag{60}$$

where $\dot{\mathbf{e}}'$ refers to the elastic component of the strain rate tensor, and $\dot{\mathbf{e}}''$ the corresponding plastic component.

From the consistency condition of the yield surface, we have

$$\frac{\partial F}{\partial s_{kl}}\dot{s}_{kl} + \frac{\partial F}{\partial \alpha_{kl}}\dot{\alpha}_{kl} + \frac{\partial F}{\partial M_{ijkl}}\dot{M}_{ijkl} = 0. \tag{61}$$

In equation (61) $\dot{\mathbf{s}}$ represents the stress rate tensor and may be calculated from the components of the elastic strain rate tensor as follows:

$$\dot{s}_{kl} = E_{klmn}\dot{\mathbf{e}}'_{mn}. \tag{62}$$

E_{klmn} in equation (62) is the elastic stiffness tensor defined as follows:

$$E_{klmn} = \lambda\delta_{kl}\delta_{mn} + \mu(\delta_{km}\delta_{ln} + \delta_{kn}\delta_{lm}) \tag{63}$$

where λ and μ are Lame's elastic constants. Substituting for $\dot{\mathbf{e}}''$ from equation (57) into equation (60) we obtain the elastic component of the strain rate tensor such that:

$$\dot{e}'_{mn} = \dot{e}_{mn} - \dot{\Lambda}\frac{\partial F}{\partial s_{mn}}. \tag{64}$$

Making use of equation (64) together with equation (62), and multiplying both sides by $\partial F/\partial s_{kl}$, we obtain the following

$$\frac{\partial F}{\partial s_{kl}}\dot{s}_{kl} = \frac{\partial F}{\partial s_{kl}}E_{klmn}\left(\dot{e}_{mn} - \dot{\Lambda}\frac{\partial F}{\partial s_{mn}}\right). \tag{65}$$

Equation (65) represents the first term of equation (61). Making use of the three parameter expression for $\mathbf{M}$ from equation (40), we obtain $\dot{\mathbf{M}}$ as follows:

$$\dot{M}_{ijkl} = \dot{a}\delta_{ik}\delta_{jl} + v_{ij}v_{kl}[\dot{b} + \dot{c}v_{rs}(s_{rs} - \alpha_{rs})]. \tag{66}$$

Here the three parameter model is used for the purpose of maintaining generality. By allowing $\dot{c}$ to be zero in expression (66), the corresponding expression for the two-parameter model of $\mathbf{M}$ as given by equation (17) will be obtained.

Assuming a work-hardening material, a, b, and c, may be expressed in terms of the plastic work κ. The quantities $\dot{a}$, $\dot{b}$, and $\dot{c}$ may now be expressed as follows:

$$\dot{a} = \frac{\partial a}{\partial \kappa}\dot{\kappa},\ \dot{b} = \frac{\partial b}{\partial \kappa}\dot{\kappa},\ \text{and}\ \dot{c} = \frac{\partial c}{\partial \kappa}\dot{\kappa} \tag{67}$$

where $\dot{\kappa}$ is defined by equation (8). Substituting equations (8), (57), and (67) into equation (66) we obtain the following:

Downloaded 03 May 2010 to 171.66.16.244. Redistribution subject to ASME license or copyright; see http://www.asme.org/terms/Terms_Use.cfm

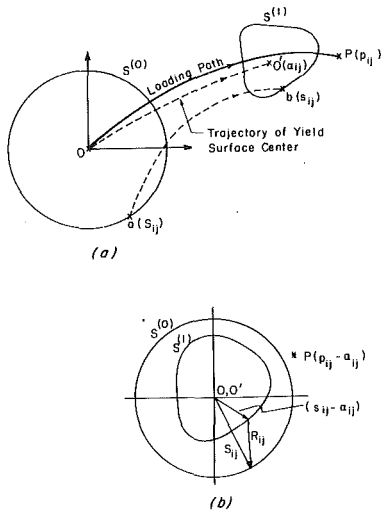


Fig. 8 Deformation and translation of the yield surface

$$\dot{M}_{ijkl}=\left\{\frac{\partial a}{\partial \kappa}\delta_{jl}\delta_{jl}+v_{ij}v_{kl}\left[\frac{\partial b}{\partial \kappa}+\frac{\partial c}{\partial \kappa}v_{rs}(s_{rs}-\alpha_{rs})\right]\right\}\sigma_{pq}\dot{\Lambda}\frac{\partial F}{\partial s_{pq}}. \tag{68}$$

Making use of equations (59), (65), and (68) together with equation (61) we obtain

$$\frac{\partial F}{\partial s_{kl}}E_{klmn}\left(\dot{e}_{mn}-\dot{\Lambda}\frac{\partial F}{\partial s_{mn}}\right)+\frac{\partial F}{\partial \alpha_{kl}}\dot{\Lambda}\frac{gG^2}{u_{cd}\dfrac{\partial F}{\partial s_{cd}}}u_{kl}+\frac{\partial F}{\partial M_{ijkl}}\left\{\frac{\partial a}{\partial \kappa}\delta_{ik}\delta_{jl}+v_{ij}v_{kl}\left[\frac{\partial b}{\partial \kappa}+\frac{\partial c}{\partial \kappa}v_{rs}(s_{rs}-\alpha_{rs})\right]\right\}\cdot s_{pq}\dot{\Lambda}\frac{\partial F}{\partial s_{pq}}. \tag{69}$$

In equation (69) we assumed the absence of plastic volumetric strains, and consequently

$$\sigma_{pq}\dot{e}''_{pq}=s_{pq}\dot{e}''_{pq}. \tag{70}$$

From equation (69), we obtain $\dot{\Lambda}$ such that:

$$\dot{\Lambda}=\frac{\dfrac{\partial F}{\partial s_{kl}}E_{klmn}\dot{e}_{mn}}{R} \tag{71}$$

where

$$R=\frac{\partial F}{\partial s_{kl}}E_{klmn}\frac{\partial F}{\partial s_{mn}}-\frac{\partial F}{\partial \alpha_{kl}}u_{kl}\frac{gG^2}{u_{cd}\dfrac{\partial F}{\partial s_{cd}}}-\frac{\partial F}{\partial M_{ijkl}}\left\{\frac{\partial a}{\partial \kappa}\delta_{ik}\delta_{jl}+v_{ij}v_{kl}\left[\frac{\partial b}{\partial \kappa}+\frac{\partial c}{\partial \kappa}v_{rs}(s_{rs}-\alpha_{rs})\right]\right\}s_{pq}\frac{\partial F}{\partial s_{pq}}. \tag{72}$$

Substituting equations (60) and (57) into equation (62), we obtain

$$\dot{s}_{rs}=E_{rsuv}\left(\dot{e}_{uv}-\dot{\Lambda}\frac{\partial F}{\partial s_{uv}}\right). \tag{73}$$

Making use of $\dot{\Lambda}$ from equation (71) and substituting it in equation (52), we obtain the incremental elastoplastic stiffness tensor **D**

$$\dot{s}_{rs}=D_{rsuv}\dot{e}_{uv} \tag{74}$$

where

$$D_{rsuv}=E_{rsmn}\left(\delta_{um}\delta_{vn}-\frac{1}{R}\frac{\partial F}{\partial s_{kl}}\frac{\partial F}{\partial s_{mn}}E_{kluv}\right). \tag{75}$$

For the special case when parameter c is set equal to zero in equation (72), we obtain the incremental stiffness matrix for the two-parameter model of the anisotropy tensor **M**, represented by equation (18).

Comparison of Proposed Models With Other Distortional Yield Models

Eisenberg and Yen (1984) and Yen and Eisenberg (1987) proposed that the subsequent yield surface may be referred back to the initial yield surface using a Lagrangian description of the yield surface such that

$$S_{ij}=s_{ij}^{(n+1)}-\alpha_{ij}^{(n+1)}+R_{ij}^{(n+1)} \tag{76}$$

where S_{ij} is the initial deviatoric yield state, $s_{ij}^{(n+1)}$ is the deviatoric component of the $(n+1)$ subsequent yield state, and $R_{ij}^{(n+1)}$ describes the deformation of the $(n+1)$ subsequent yield surfaces. This is clearly indicated in Fig. 8. $R_{ij}^{(n+1)}$ is expressed as follows:

$$R_{ij}^{(n+1)}=-L_{ijkl}^{(n+1)}(s_{kl}^{(n+1)}-\alpha_{kl}^{(n+1)}) \tag{77}$$

where the recurrence expression for $L_{ijkl}^{(n+1)}$ may be shown to be

$$L_{ijkl}^{(n+1)}=g^{(n+1)}l_{kl}^{(n+1)}l_{ij}^{(n+1)}+L_{ijkl}^{(n)}-L_{ijpq}^{(n)}g^{(n+1)}l_{pq}^{(n+1)}l_{kl}^{(n+1)}. \tag{78}$$

In equation (78) **l** is a normalized unit tensor in the direction of prestressing. Eisenberg and Yen (1984) presented $g^{(n+1)}$ to be given by

$$g^{(n+1)}=\left\{\begin{matrix}g_1^{*(n+1)}\\ g_2^{*(n+1)}\end{matrix}\right\}\text{when }(s_{ij}^{(n+1)}-\alpha_{ij}^{(n+1)})\,\mathbf{l}_{ij}\left\{\begin{matrix}\geq 0\\ <0\end{matrix}\right\} \tag{79}$$

where $g_1^{*(n+1)}$ and $g_2^{*(n+1)}$ are parameters which may be evaluated as described in the paper of Eisenberg and Yen (1984). The subsequent yield surface of Eisenberg and Yen (1984) formulation may now be expressed as follows:

$$\frac{1}{2}[s_{ij}^{(n+1)}-\alpha_{ij}^{(n+1)}-L_{ijkl}^{(n+1)}(s_{kl}^{(n+1)}-\alpha_{kl}^{(n+1)})]\cdot[s_{ij}^{(n+1)}-\alpha_{ij}^{(n+1)}-L_{ijkl}^{(n+1)}(s_{kl}^{(n+1)}-\alpha_{kl}^{(n+1)})]=k_0^2. \tag{80}$$

Due to equation (79), L_{ijkl} for the $(n+1)$ subsequent yield surface will not be a single valued function unless g_1^* is set equation to g_2^* for each subsequent yield surface. For this reason if prestressing is done in more than one direction, the yield surface, as obtained from equation (80), will be divided into more than one segment with each segment being represented by a distinctly different equation. This drawback will hinder the effective use of this model in numerical solution of problems with nonproportional loadings.

The simplified version of the Eisenberg and Yen (1984) model, where g_1^* is equal to g_2^*, will result in local concavities on the yield surface. This has been shown by Eisenberg and Yen (1984).

Downloaded 03 May 2010 to 171.66.16.244. Redistribution subject to ASME license or copyright; see http://www.asme.org/terms/Terms_Use.cfm

The model proposed in this work as presented by equation (18) represents the yield surface using a single equation and hence avoids the formation of corners, consequently making it more practical to numerical applications. This yield model also guarantees convexity.

Edelman and Drucker (1951) introduced a Mises-type criterion such that

$$F \equiv \frac{1}{2} C_{ijkl}(s_{ij} - m e''_{ij})(s_{kl} - m e''_{kl}) \tag{81}$$

where m is a material parameter and $\mathbf{C}$ is a fourth-order tensor that incorporates anisotropy to the yield surface. This is similar to that used by the authors in equation (1). Bauschinger effect is taken into account in equation (81) through the parameter m and is identical to Prager's hardening law. Unlike the present formulation, the tensor $\mathbf{C}$ used by Edelman and Drucker (1951) is considered constant throughout the plastic deformation.

Baltov and Sawczuk (1965) considered a yield function of the following form

$$F \equiv \frac{1}{2} Q_{ijkl}(s_{ij} - \alpha_{ij})(s_{ij} - \alpha_{ij}) - \frac{1}{2} = 0 \tag{82}$$

where Q_{ijkl} is considered to be a function of the total plastic strain e''_{ij} and is expressed by

$$Q_{ijkl} = I_{ijkl} + B_{ijkl}. \tag{83}$$

In equation (83), $\mathbf{I}$ is the constant isotropic fourth-order tensor for an incompressible material and $\mathbf{B}$ is expressed by

$$B_{ijkl} = \bar{B} e''_{ij} e''_{kl}. \tag{84}$$

$\bar{B}$ is a scalar function of the plastic strain invariants. This formulation is dependent on the final values of the plastic strain. Based on equation (84), distortion of the yield surface will be in the direction of the plastic component of the total strain which contradicts the experiments of Phillips and co-workers (1973, 1974, 1977, 1979, 1985) and Stout et al. (1985). We also note that the rate of change of $\mathbf{Q}$ is given by

$$\dot{Q}_{ijkl} = \dot{\bar{B}} e''_{ij} e''_{kl} + \bar{B}(\dot{e}''_{ij} e''_{kl} + e''_{ij} \dot{e}''_{kl}). \tag{85}$$

It is obvious that the second term of the right-hand side of equation (85) does not give a definite physical direction of distortion for each increment of loading. It is also noted that the uniform expansion of the yield surface expressed by $\dot{a}^{(m)} \delta_{ik} \delta_{jl}$ in equation (17) is absent in equation (85) as presented by Baltov and Sawczuk (1965).

Example

In order to better understand equation (18), let us consider evaluating the initial yield surface ($m = 0$) as well as the first subsequent yield surface ($m = 1$) for a plane stress problem where $\sigma_{13} = \sigma_{23} = \sigma_{33} = 0$. We also assume a state of principal stresses such that $\sigma_{12} = 0$. To obtain the initial yield surface ($m = 0$), the parameters $\dot{a}$, $\dot{b}$, and α which are related to the plastic strains are zero. Consequently, equation (18) may be expressed as

$$F^{(0)} \equiv \frac{1}{2} s_{ij} s_{ij} = k_0^2. \tag{86}$$

Equation (86) may be expressed in terms of the stress tensor σ as follows:

$$F^{(0)} \equiv \frac{1}{3}[\sigma_{11}^2 + \sigma_{22}^2 - \sigma_{11}\sigma_{22}] = k_0^2. \tag{87}$$

Equation (87) represents the von Mises ellipse in the σ_{11} v σ_{22} stress space as illustrated in Fig. 9.

The first subsequent yield surface is obtained from equation (18) as follows:

$$F^{(1)} \equiv \left[\frac{1}{2}\delta_{ik}\delta_{jl} + \dot{a}^{(1)}\delta_{ik}\delta_{jl} + \dot{b}^{(1)} v_{ij}^{(1)} v_{kl}^{(1)}\right] \cdot (s_{ij} - \alpha_{ij})(s_{kl} - \alpha_{kl}) = k_0^2 \tag{88}$$

where $\alpha_{ij} = \dot{\alpha}_{ij}^{(1)}$.

For the purpose of observing the distortion of the yield surface, we may assume any direction for tensor $\mathbf{v}$. As an example, let us assume that the yield surface distorts in the direction of σ_{11}. Since equation (88) is formulated in the deviatoric stress space, we must express tensor $\mathbf{v}$ in terms of the deviatoric components of the direction of distorion, hence we obtain

$$\mathbf{V}^{(1)} = \begin{bmatrix} \frac{2}{3} & 0 & 0 \\ 0 & -\frac{1}{3} & 0 \\ 0 & 0 & -\frac{1}{3} \end{bmatrix}, \tag{89}$$

and consequently,

$$\mathbf{v}^{(1)} = \frac{\mathbf{V}^{(1)}}{|\mathbf{V}|^{(1)}} = \begin{bmatrix} 0.816 & 0 & 0 \\ 0 & -0.408 & 0 \\ 0 & 0 & -0.408 \end{bmatrix}. \tag{90}$$

Substituting equation (90) into equation (88), the following expression for the first subsequent yield surface will be obtained:

$$F^{(1)} \equiv \left(\frac{1}{2} + \dot{a}^{(1)}\right)[(s_{11} - \alpha_{11})^2 + (s_{22} - \alpha_{22})^2 + (s_{33} - \alpha_{33})^2] + (0.408)^2 \dot{b}^{(1)}[4(s_{11} - \alpha_{11})^2 + (s_{22} - \alpha_{22})^2 + (s_{33} - \alpha_{33})^2] + (0.408)^2 \dot{b}^{(1)} [-4(s_{11} - \alpha_{11})(s_{22} - \alpha_{22}) - 4(s_{11} - \alpha_{11})(s_{33} - \alpha_{33}) + 2(s_{22} - \alpha_{22})(s_{33} - \alpha_{33})] = k_0^2. \tag{91}$$

Equation (91) may be expressed in terms of σ and β as follows:

$$F^{(1)} = \frac{1}{3}(1 + 2\dot{a}^{(1)})[(\sigma_{11} - \beta_{11})^2 + (\sigma_{22} - \beta_{22})^2 - (\sigma_{11} - \beta_{11})(\sigma_{22} - \beta_{22})] + (0.408)^2 \dot{b}^{(1)} [4(\sigma_{11} - \beta_{11})^2 + (\sigma_{22} - \beta_{22})^2 - 4(\sigma_{11} - \beta_{11})(\sigma_{22} - \beta_{22})] = k_0^2. \tag{92}$$

Figure 9 illustrates three possible forms for the first subsequent yield surface $F^{(1)}$ as obtained from equation (92). For the first case, $\dot{a}^{(1)}$ and β are set equal to zero whereby yield surface (i) is obtained. Note that this surface indicates a change of width in the σ_{11} direction and exhibits a zero cross-effect. In the second case where β is assumed to be in the σ_{11} direction, we obtain yield surface (ii). If $\dot{a}^{(1)}$ is not equal to zero, an expansion of the yield surface will also occur as shown by surface (iii).

We now examine the distortion of the second subsequent yield surface obtained through the use of equation (18). Figure 10 shows the second subsequent yield surface obtained for both proportional and nonproportional loadings. Surface (ii) in Fig. 10 represents the same first subsequent yield surface presented by surface (ii) in Fig. 9. For the case of proportional loadings, we may assume that the direction of distortion $\mathbf{v}^{(2)}$ and the direction of translation $\mathbf{B}^{(2)}$ will be the same as that of $\mathbf{v}^{(1)}$ and $\beta^{(1)}$, respectively, in which case surface (iii) in Fig. 10

Downloaded 03 May 2010 to 171.66.16.244. Redistribution subject to ASME license or copyright; see http://www.asme.org/terms/Terms_Use.cfm

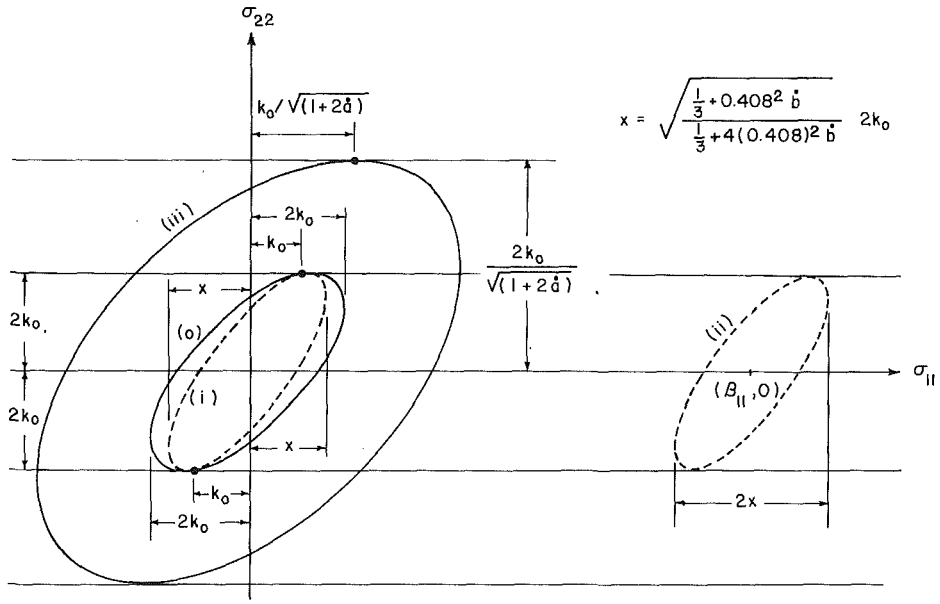


Fig. 9 Distortion and translation of first subsequent yield surface

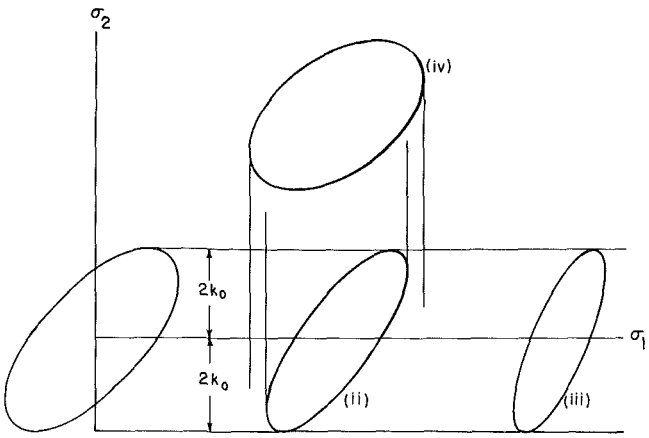


Fig. 10 Behavior of the yield surfaces obtained from the proposed model for proportional and nonproportional loadings

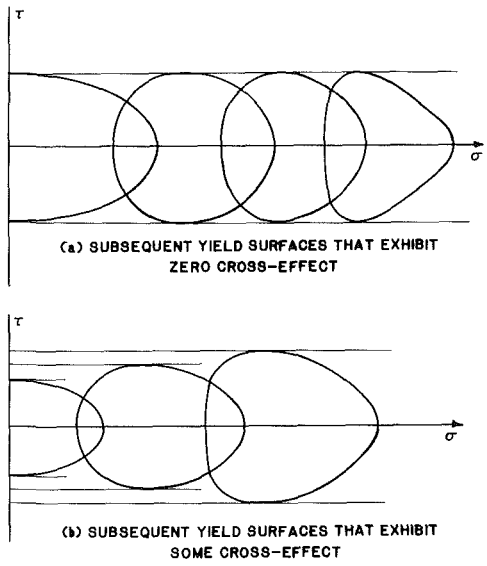


Fig. 11 Some possible experimental observations

is obtained. In this case we must note that the width of yield surface (iii) in the direction of σ_{22} remains the same as that of surface (ii). For nonproportional loadings, the direction of $\mathbf{v}^{(2)}$ and $\beta^{(2)}$ will be different than that of $\mathbf{v}^{(1)}$ and $\beta^{(1)}$. Surface (iv) is obtained by assuming $\mathbf{v}^{(2)}$ and $\beta^{(2)}$ to be in the direction of σ_{22}. It is obvious that the dimensions of surface (iv) in the directions of σ_{11} and σ_{22} are different from that of surface (ii).

The fact that for radial loadings parameter b does not cause any cross-effects is important in the experimental determination of parameters a and b. In Fig. 11(a), a series of subsequent yield surfaces similar to those obtained by Phillips and co-workers (1973, 1974, 1979) are shown for axial-torsion loading (σ v τ). These surfaces distort in the direction of σ which may be assumed to be co-directional with tensor $\mathbf{v}$. No change of width in the τ direction is observed. Hence, parameter a is set equal to zero, and parameter b may be obtained by examining the change of width of the yield surface in the σ direction and relating that to some measure of plastic work or plastic strain. Figure 11(b) shows a series of subsequent yield surfaces that exhibit cross-effects as was reported by Naghdi et al. (1965) and Ivey (1961). In this case the change in width of the yield surface in the τ direction dictates the value of a which may also be related to the plastic work or plastic strain.

Conclusions

In this work an anisotropic distortional yield model has been presented through the use of a fourth-order anisotropy tensor, $\mathbf{M}$. A two and a three-parameter model for $\mathbf{M}$ has been presented by equations (17) and (40), respectively. The two-parameter model has more practical applications in the solution of elastoplastic deformations of boundary value problems. This model will cause equal distortion for both the forward and rear parts of the yield surface with respect to the direction of distortion $\mathbf{v}$. It must be noted, however, that the direction of distortion $\mathbf{v}$ may be chosen as indicated by Phillips and co-workers (1973, 1974, 1977, 1979, 1985) to be in the direction of the increment of prestressing. However, this does not limit one to define $\mathbf{v}$ in alternate directions, such as the direction of the increment of prestraining or the final straining direction.

The elastoplastic stiffness tensor $\mathbf{D}$ is formulated for the more general model based on equation (40), although the same formulation may be used in conjunction with equation (17) by

Downloaded 03 May 2010 to 171.66.16.244. Redistribution subject to ASME license or copyright; see http://www.asme.org/terms/Terms_Use.cfm

setting c equal to zero. The evaluation of the material parameters, a, b, and c should be based on biaxial, axial-torsion tests. The detailed derivations and evaluations of these parameters will be presented by the authors in a subsequent publication.

It is also shown by the authors that the proposed model has distinct advantages over other models proposed by Eisenberg and Yen (1984), Yen and Eisenberg (1987), Edelman and Drucker (1951), and Baltov and Sawczuk (1965).

The elastoplastic stiffness matrix, as presented by equation (75) for the case of the three-parameter model, is not suitable for numerical implementation. This is because the three-parameter model cannot be used effectively when elastic unloading occurs. However, use of equation (75) for the two-parameter model for $\mathbf{M}$, as given by equation (17), could be used for numerical implementation. It should be noted that modeling distortions of yield surfaces in numerical applications can be very expensive and would require the use of supercomputers.

More work needs to be done for effective modeling of unequal distortions with respect to the forward and the rear parts of the yield surface. The three parameter model presented in this work is to introduce a methodology to account for unequal distortions for the particular case where elastic unloading does not occur. This methodology needs to be generalized to all possible types of loadings before numerical implementation of it is achieved effectively.

References

Baltov, A., and Sawczuk, A., 1965, "A Rule of Anisotropic Hardening," *Acta Mechanica*, Vol. 1, pp. 81–92.

Edelamn, F., and Drucker, D. C., 1951, "Some Extensions of Elementary Plasticity Theory," *J.F.I.*, Vol. 251, pp. 581.

Eisenberg, M. A., and Yen, C.-F., 1984, "The Anisotropic Deformation of Yield Surfaces," *ASME Journal of Engineering Materials and Technology*, Vol. 106, pp. 355–360.

Helling, D. E., and Miller, A. K., 1987, "The Incorporation of Yield Surface Distortion into a Unified Constitutive Model, Part 1: Equation Development," *Acta Mechanica*, Vol. 69, pp. 9–23.

Helling, D. E., Miller, A. K., and Stout, M. G., 1986, "An Experimental Investigation of the Yield Loci of 1100-0 Aluminum, 70:30 Brass, and an Overaged 2024 Aluminum Alloy After Various Prestrains," *ASME Journal of Engineering Materials and Technology*, Vol. 108, pp. 313–320.

Hill, R., 1950, *The Mathematical Theory of Plasticity*, Oxford University Press.

Hodge, P. G., Jr., 1955, "The Theory of Piecewise Linear Isotropic Plasticity," IUTAM Colloquium, Madrid.

Ishlinskii, A. Iu, 1954, "General Theory of Plasticity with Linear Strain hardening," *Ukr. Mat. Zh.*, Vol. 6, p. 314.

Ivey, H. J., 1961, "Plastic Stress-Strain Relations and Yield Surfaces for Aluminum Alloys," *J. Mech. Engng. Sci.*, Vol. 3, pp. 15–31.

Naghdi, P. M., Eisenberg, F., and Koff, W., 1959, "An Experimental Study of Initial and Subsequent Yield Surfaces in Plasticity," ASME JOURNAL OF APPLIED MECHANICS, Vol. 25, pp. 77–87.

Phillips, A., and Das, P. K., 1985, "Yield Surfaces and Loading Surfaces of Aluminum and Brass: An Experimental Investigation at Room and Elevated Temperatures," *International Journal of Plasticity*, Vol. 1, pp. 89–109.

Phillips, A., and Kasper, R., 1973, "On the Foundations of Thermoplasticity—An Experimental Investigation," ASME JOURNAL OF APPLIED MECHANICS, Vol. 40, pp. 891–896.

Phillips, A., and Lee, C.-W., 1979, "Yield Surfaces and Loading Surfaces. Experiments and Recommendations," *Int. J. of Solids and Structures*, Vol. 15, pp. 715–729.

Phillips, A., and Moon, H., 1977, "An Experimental Investigation Concerning Yield Surfaces and Loading Surfaces," *Acta Mechanica*, Vol. 27, pp. 91–102.

Phillips, A., Tang, J.-L., and Ricciuti, M., 1974, "Some New Observations on Yield Surfaces," *Acta Mechanica*, Vol. 20, pp. 23–39.

Phillips, A., and Weng, G. J., 1975, "An Analytical Study of an Experimentally Verified Hardening Law," ASME JOURNAL OF APPLIED MECHANICS, Vol. 42, pp. 375–378.

Prager, W., 1956, "A New Method of Analyzing Stresses and Strains in Work-Hardening Plastic Solids," JOURNAL OF APPLIED MECHANICS, Vol. 78, pp. 493.

Shield, R. T., and Ziegler, H., 1958, "On Prager's Hardening Rule," *Z. Angew. Math. Phys.*, Vol. 9, pp. 260–276.

Stout, M. G., Martin, P. L., Helling, D. E., and Canova, G. R., 1985, "Multiaxial Yield Behavior of 1100 Aluminum Following Various Magnitudes of Prestrain," *International Journal of Plasticity*, Vol. 1, pp. 163–174.

Voyiadjis, G. Z., and Kattan, P. I., 1990, "A Generalized Eulerian Two-Surface Cyclic Plasticity Model for Finite Strains," *Acta Mechanica*, 39 manuscript pages (in press).

Voyiadjis, G. Z., and Mohammad, L. N., 1988, "Rate Equations for Viscoplastic Materials Subjected to Finite Strains," *International Journal of Plasticity*, Vol. 4, No. 3, pp. 215–229.

Yen, C.-F., and Eisenberg, M. A., 1987, "The Role of a Loading Surface in Viscoplasticity Theory," *Acta Mechanica*, Vol. 69, pp. 77–96.

Ziegler, H., 1959, "A Modification of Prager's Hardening Rule," *Q. Appl. Math.*, Vol. 17, pp. 55–65.

Downloaded 03 May 2010 to 171.66.16.244. Redistribution subject to ASME license or copyright; see http://www.asme.org/terms/Terms_Use.cfm

I. Nishiguchi[1]
Mem. ASME

T.-L. Sham
Mem. ASME

E. Krempl
Fellow ASME

Department of Mechanical Engineering,
Aeronautical Engineering and Mechanics,
Rensselaer Polytechnic Institute,
Troy, NY 12180-3590

A Finite Deformation Theory of Viscoplasticity Based on Overstress: Part I—Constitutive Equations

The viscoplasticity theory based on overstress (VBO) is extended to finite deformation (FVBO). Yield surfaces and loading/unloading conditions are not part of this theory which represents creep, relaxation, and rate sensitivity in a "unified" way. Additive decomposition of the rate of deformation into the elastic and the inelastic parts is assumed. For the elastic part, the hypoelastic relation is used. For the inelastic part, the flow law of VBO is augmented by a term quadratic in the overstress together with a modified Jaumann stress rate which jointly or separately allow the modeling of second-order effects.

1 Introduction

The basic structure of the approaches to finite, rate-independent theory of plasticity, after a long history of debate, seems to have reached a consolidation (e.g., Lee and Agah-Tehrani, 1987a,b; Dafalias, 1987). The adoption of the intermediate configuration, the use of the Jaumann rate and additional constitutive assumptions for the plastic spin (Dafalias, 1987) or the rate of rotation effects (Lee and Agah-Tehrani, 1987a; Agah-Tehrani, Lee, Mallett, and Onat, 1987) are essential elements of these approaches. These theories are usually applied to simple loading conditions to illustrate their capabilities, e.g., the reproduction of the Poynting effect under monotonic loading as shown by Reed and Atluri (1985) and Lee and Agah-Tehrani (1987a). Ideally, finite deformation theories should also include the modeling of small strain effects under complicated loading histories. An example is cyclic loading behavior at small strain. In this case, the measured accumulated equivalent inelastic strain, which is usually employed to model isotropic hardening, is comparable to or greater than in monotonic loading conditions. Within the framework of the infinitesimal theory, the modeling of cyclic effects such as ratcheting, and cyclic hardening/softening under proportional and nonproportional loading, are the subject of intense current interest (Krempl and Lu, 1984; Benallal and Marquis, 1987; Burlet and Cailletaud, 1987; Chaboche, 1987; Krempl and Yao, 1987; McDowell, 1987; Tanaka, Murakami, and Ooka, 1987).

Viscoplasticity has received comparatively little attention in the study of finite deformation. The suggestion that only the rate-independent flow law of plasticity needs to be replaced by a "properly defined overstress function," Dafalias (1987), does not consider a fundamental difference between rate-independent plasticity and viscoplasticity. In rate-independent plasticity there is a unique unloaded state associated with each state of homogeneous deformation. This is no longer the case for viscoplasticity since the unloading behavior depends on the imposed boundary conditions. It is different for displacement or for stress control and depends on the unloading rate (Krempl and Kallianpur, 1985). Only if the unloading boundary conditions are specified can the unloaded state be determined. Therefore, assumptions which depend on the unique relation between the loaded and unloaded state are not valid in viscoplasticity.

In this paper a viscoplasticity theory for finite deformation is developed—the finite deformation viscoplasticity theory based on overstress, (FVBO). The current configuration is taken to be the reference configuration and the rate of deformation tensor is postulated to be the sum of the elastic rate of deformation tensor $\mathbf{D}^e$ and the inelastic rate of deformation tensor $\mathbf{D}^{in}$. Such a decomposition has been previously proposed (e.g., Lehmann, 1987), and has been used in computational approaches (Peirce, Shih, and Needleman, 1984). Within the context of FVBO an incremental constitutive equation is proposed for each rate of deformation, which are, together with the choice of an objective rate, assumptions of the theory. The hypoelastic relation (Truesdell and Noll, 1965) is the constitutive assumption for the elastic rate of deformation. For the inelastic rate of deformation the flow law of the infinitesimal theory of viscoplasticity (VBO) (Yao and

[1] On leave from the Japan Atomic Energy Research Institute, Ibaraki, Japan.

Contributed by the Applied Mechanics Division of THE AMERICAN SOCIETY OF MECHANICAL ENGINEERS for presentation at the Winter Annual Meeting, Dallas, Texas, Nov. 25–30, 1990.

Discussion on this paper should be addressed to the Technical Editor, Leon M. Kear, The Technological Institute, Northwestern University, Evanston, IL 60208, and will be accepted until two months after final publication of the paper itself in the JOURNAL OF APPLIED MECHANICS. Manuscript received by the ASME Applied Mechanics Division, Aug. 15, 1988; final revision, June 12, 1989.

Paper No. 90-WA/APM-9.

Copyright © 1990 by ASME
Downloaded 03 May 2010 to 171.66.16.244. Redistribution subject to ASME license or copyright; see http://www.asme.org/terms/Terms_Use.cfm

Krempl, 1985; Krempl, McMahon, and Yao, 1986) is augmented by a term quadratic in the overstress to allow the modeling of second-order effects independent of the objective stress rate used. In addition, growth laws for the state variables of FVBO are necessary and the simplest ones which ensure the modeling of the equivalent of isotropic and kinematic hardening are used here.

The VBO was previously developed for small strain on the basis of extensive experimental observations; first as a deformation version (Cernocky and Krempl, 1980) and then in incremental form (Yao and Krempl, 1985; Krempl, McMahon, and Yao, 1986). It is a "unified theory." It does not use yield surfaces, loading, and unloading conditions, and assumes, in accordance with experimental observations, that rate dependence is fundamental. Rate independence is modeled by making rate dependence small. (The term "unified" implies that no separate assumptions are made for rate-independent plasticity and creep; all inelastic deformations are considered rate-dependent.)

The constitutive equations of FVBO are formulated in Section 2 which is followed by a discussion. In Part II of the paper, a one-step time integration method based on the forward gradient approximation is developed and this leads to explicit expressions for the tangent operators. The FBVO is then applied to various homogeneous deformation problems.

Constitutive Equation

2.1 Rate of Deformation. The rate of deformation tensor, **D**, (the symmetric part of the velocity gradient **L**) is assumed to be the sum of an elastic part and an inelastic part, both defined on the current configuration:

$$\mathbf{D} = \mathbf{D}^e + \mathbf{D}^{in}. \tag{I.1}$$[2]

Assuming that the elastic strains are small, the elastic part $\mathbf{D}^e$ can be described by a hypoelastic constitutive relation:

$$\mathbf{d}^e = \frac{1}{2G}\hat{\mathbf{s}} = \frac{1+\nu^e}{E}\hat{\mathbf{s}}, \tag{I.2}$$

$$tr\mathbf{D}^e = \frac{1}{3K} tr\hat{\sigma} \tag{I.3}$$

where $\mathbf{d}^e$ is the deviator of $\mathbf{D}^e$, $\mathbf{s}$ the deviator of the Cauchy stress σ, $(\hat{\ })$ an objective rate, ν^e the elastic Poisson's ratio, E the Young's modulus, G the shear modulus, and K the bulk modulus. The symbol tr denotes the trace of a tensor.

The inelastic rate of deformation is assumed to be volume preserving and we may rewrite (I.1) as

$$\mathbf{D} = \mathbf{D}^e + \mathbf{d}^{in}, \tag{I.4}$$

where $\mathbf{d}^{in}$ is the deviator of $\mathbf{D}^{in}$. The tensor $\mathbf{d}^{in}$ is in general a function of $\mathbf{s}$ and other state variables. However, in accordance with the previous development of VBO, $\mathbf{d}^{in}$ is assumed to be only a function of the overstress deviator, $\mathbf{o}$,

$$\mathbf{o} = \mathbf{s} - \mathbf{g}, \tag{I.5}$$

where $\mathbf{g}$ is the deviator of the equilibrium Cauchy stress, a tensorial state variable of the theory (see Krempl, 1987). This assumption together with the use of the representation theorems for isotropic tensor-valued functions allow $\mathbf{d}^{in}$ to be represented as (e.g., Wang (1970), Gurtin (1981)):

$$\mathbf{d}^{in} = \mathbf{d}_I^{in} + \mathbf{d}_{II}^{in} \tag{I.6}$$

with

$$\mathbf{d}_I^{in} = \frac{1+\nu^{in}}{C_I}\mathbf{o}, \quad \mathbf{d}_{II}^{in} = \frac{1+\nu^{in}}{C_{II}}\mathbf{y}. \tag{I.7}$$

[2](I.xx) and (II.xx) denote equation numbers in Part I and Part II, respectively.

We refer to $\mathbf{d}_I^{in}$ as the primary inelastic rate of deformation and $\mathbf{d}_{II}^{in}$ the secondary inelastic rate of deformation. The tensor $\mathbf{y}$ is the deviator of the quadratic overstress, $\mathbf{o}\,\mathbf{o}$, and is given by

$$\mathbf{y} = \mathbf{o}\,\mathbf{o} - \frac{1}{3}(\mathbf{o}\cdot\mathbf{o})\mathbf{I} \tag{I.8}$$

where $\mathbf{I}$ is the second-order identity tensor. Here, we employ the notation $\mathbf{A}\cdot\mathbf{B}$ to denote $tr\,(\mathbf{A}^T\mathbf{B})$ for any two tensors $\mathbf{A}$, $\mathbf{B}$. The inelastic Poisson's ratio ν^{in} is assumed to be equal to 1/2. The coefficients C_I and C_{II} are selected to be functions of the invariants of $\mathbf{o}$. They are

$$J_2 = \frac{1}{2}\mathbf{o}\cdot\mathbf{o}, \quad J_3 = \frac{1}{3}(\mathbf{o}\,\mathbf{o})\cdot\mathbf{o}. \tag{I.9}$$

And we also introduce $\Gamma = \sqrt{(3/2)\mathbf{o}\cdot\mathbf{o}} = \sqrt{3J_2}$ to represent the equivalent overstress. We note that the linear and quadratic stress dependence in the inelastic part of the deformation was employed by Prager (1948) in the context of infinitesimal deformation theory of plasticity.

Introducing the primary and secondary accumulated equivalent inelastic strains, ϕ_I and ϕ_{II}, respectively, for a material point as

$$\phi_I = \int \dot{\phi}_I dt, \quad \phi_{II} = \int \dot{\phi}_{II} dt, \tag{I.10}$$

where

$$\dot{\phi}_I = \sqrt{(2/3)\mathbf{d}_I^{in}\cdot\mathbf{d}_I^{in}}, \quad \dot{\phi}_{II} = \sqrt{(2/3)\mathbf{d}_{II}^{in}\cdot\mathbf{d}_{II}^{in}}, \tag{I.11}$$

and noting $\mathbf{y}\cdot\mathbf{y} = (2/27)\Gamma^4$, $\nu^{in} = 1/2$, we find from (I.7) that

$$C_I = \frac{\Gamma}{\dot{\phi}_I}, \quad C_{II} = \omega_{II}\frac{\Gamma^2}{3\dot{\phi}_{II}} \tag{I.12}$$

where ω_{II} denotes the sign of C_{II}. Its choice will be discussed in Part II. We may now express d^{in} as

$$\mathbf{d}^{in} = \dot{\phi}_I\frac{3}{2}\frac{\mathbf{o}}{\Gamma} + \omega_{II}\dot{\phi}_{II}\frac{9}{2}\frac{\mathbf{y}}{\Gamma^2}. \tag{I.13}$$

The constitutive equations (I.2), (I.6), and (I.7) can be inverted to obtain

$$\hat{\mathbf{s}} = 2G(\mathbf{d} - \mathbf{d}^{in})$$

$$= 2G\mathbf{d} - 2G\dot{\phi}_I\frac{3}{2}\frac{\mathbf{o}}{\Gamma} - 2G\omega_{II}\dot{\phi}_{II}\frac{9}{2}\frac{\mathbf{y}}{\Gamma^2}. \tag{I.14}$$

The constitutive relations for FVBO, (I.2), (I.3), (I.4), (I.6), and (I.7), differ from those of VBO by the introduction of an objective stress rate, namely, the modified Jaumann rate to be discussed in the sequel, and $\mathbf{d}_{II}^{in}$, which depends on $\mathbf{y}$. This last term is needed to model second-order effects in the mechanical behavior (Poynting, 1909; Swift, 1974; Ronay, 1965, 1967; Freudenthal and Ronay, 1966; Wack, 1981; Han and Wack, 1987). It can also serve to represent differences in tension and compression behavior which are observed at large plastic strains (see Fig. 1 of Kocks, Stout, and Rollett, 1988). In Part II, it will be shown that the modified objective stress rate also introduces second-order effects. This objective rate and $\mathbf{d}_{II}^{in}$ are synergistic. Another objective rate may not be able to model second-order effects. Moreover, Han and Wack (1987) have shown that the use of the unmodified Jaumann rate, but without a term equivalent to $\mathbf{d}_{II}^{in}$, did not lead to a completely satisfactory modeling of second-order effects. A further reason for introducing $\mathbf{d}_{II}^{in}$ in (I.6) is the completeness of the representation of $\mathbf{d}^{in}$.

2.2 Growth Law for the Equilibrium Stress. To complete the theory a growth law for the equilibrium Cauchy stress deviator is needed. For simplicity, the growth law of the in-

Downloaded 03 May 2010 to 171.66.16.244. Redistribution subject to ASME license or copyright; see http://www.asme.org/terms/Terms_Use.cfm

finitesimal theory is generalized to finite deformation and it can be written as

$$\hat{\mathbf{g}} = \psi(\Gamma)\left(\frac{1}{1+\nu^e}\mathbf{d}^e + \frac{1}{1+\nu^{in}}\mathbf{d}^{in}\right) - \frac{r_e}{b}\frac{1}{1+\nu^{in}}\mathbf{d}^{in}. \quad \text{(I.15)}$$

This growth law is akin to the one proposed by Yao and Krempl (1985) and corrects for inconsistencies in connection with the choice of Poisson's ratio. In (I.15), $\psi(\Gamma)$ controls the shape of the stress/strain curve. It is a positive and decreasing function, with $\psi(0)$ less than and approximately equal to E (see Krempl, McMahon, and Yao, 1986).

Let r_e be the equivalent measure of the difference, $\mathbf{g}-\mathbf{f}$, given by

$$r_e = \sqrt{(3/2)(\mathbf{g}-\mathbf{f})\cdot(\mathbf{g}-\mathbf{f})}. \quad \text{(I.16)}$$

The growth law for $\mathbf{f}$, the kinematic stress or variable, is of the form

$$\hat{\mathbf{f}} = \frac{\mathrm{E}_t}{1-\mathrm{E}_t/\mathrm{E}}\frac{1}{1+\nu^{in}}\mathbf{d}^{in} \quad \text{(I.17)}$$

where E_t is the terminating slope of the uniaxial Cauchy stress versus logarithmic strain curve. If the quantity b in (I.15) is introduced as

$$b = \frac{A}{\psi-\mathrm{E}_t}\frac{\mathrm{E}-\mathrm{E}_t}{\mathrm{E}}, \quad \text{(I.18)}$$

then in any test with $\mathbf{D}=$ constant, the constitutive equations admit an asymptotic long-time solution

$$\{\hat{\mathbf{f}}\} = \{\hat{\mathbf{g}}\} = \{\hat{\mathbf{s}}\} = \frac{\mathrm{E}_t}{1-\mathrm{E}_t/\mathrm{E}}\frac{1}{1+\nu^{in}}\{\mathbf{d}^{in}\} \quad \text{(I.19)}$$

with $\{\mathbf{s}-\mathbf{g}\}=$ constant, provided that $\{r_e\}=A$. The symbol $\{\ \}$ denotes the asymptotic long-time value. When the long-time asymptotic solution (I.19) is reached, (I.2) together with (I.4) imply that $\mathbf{d}$ and $\mathbf{d}^{in}$ are collinear. The existence of an asymptotic long-time solution for VBO was proven by Cernocky and Krempl (1979) and Krempl, McMahon, and Yao (1986) (see also Sutcu and Krempl, 1989).

It is concluded from (I.19) that (I.17) can ultimately determine the stress rate. If $\mathrm{E}_t=0$, the asymptotic rates are zero in (I.19). Integration of equations derived from (I.19) suggests the schematic of Fig. 1 equivalent to that of the infinitesimal theory, (Yao and Krempl, 1985; Fig. 1). The difference $\{\mathbf{s}-\mathbf{g}\}$ is the viscous contribution to the stress and $\{\mathbf{g}-\mathbf{f}\}$ represents the rate-independent contribution. It is seen that the stress consists of a kinematic, a rate-independent (plastic), and a viscous contribution.

The equations presented so far represent cyclic neutral behavior (Yao and Krempl, 1985) and they do not allow for the modeling of isotropic hardening. To include isotropic, rate-independent hardening a growth law for the quantity A, which appears in (I.18), is necessary. Here a simple growth law is proposed:

$$\dot{A} = (B_o - C_o A)\dot{\phi} \quad \text{(I.20)}$$

where

$$\dot{\phi} = \sqrt{(2/3)\mathbf{d}^{in}\cdot\mathbf{d}^{in}} \quad \text{(I.21)}$$

and B_o and C_o are suitable constants. This growth law for A can represent cyclic hardening or softening behavior, and it reaches saturation when $A = B_o/C_o$. Such a law has been used by others (Chaboche, 1987). It cannot account for complex behaviors (see Krempl and Yao, 1987; Krempl and Lu, 1989).

For the convenience of subsequent development, we introduce parameters

$$G_\psi = \frac{\psi}{2(1+\nu^e)} \quad \text{(I.22)}$$

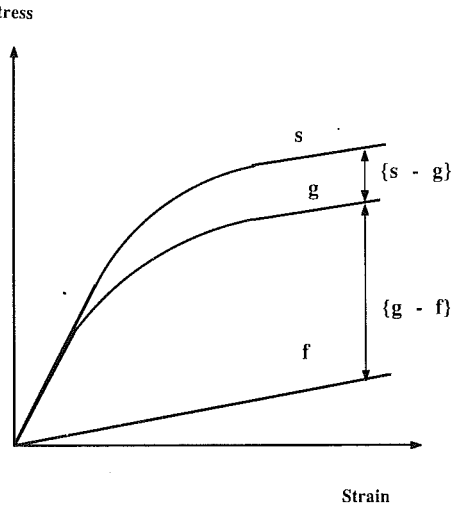


Fig. 1 Schematic showing the kinematic, rate-independent, and viscous contributions to the stress

$$G_\psi^{in} = \frac{\psi}{2(1+\nu^e)} - \frac{1}{2(1+\nu^{in})}\left[\psi - \frac{r_e}{b}\right] \quad \text{(I.23)}$$

and rewrite (I.15) as

$$\hat{\mathbf{g}} = 2G_\psi\mathbf{d} - 2G_\psi^{in}\mathbf{d}^{in}$$

$$= 2G_\psi\mathbf{d} - 2G_\psi^{in}\dot{\phi}_I\frac{3}{2}\frac{\mathbf{o}}{\Gamma} - 2G_\psi^{in}\omega_{II}\dot{\phi}_{II}\frac{9}{2}\frac{\mathbf{y}}{\Gamma^2}. \quad \text{(I.24)}$$

2.3 Modified Jaumann Rate. The objective stress rate that we have adopted for the constitutive equations described in the previous section is a modified Jaumann rate. For the case of the Cauchy stress σ this objective stress rate is defined as

$$\hat{\sigma} = \dot{\sigma} - (\mathbf{W}+\mathbf{Z})\sigma + \sigma(\mathbf{W}+\mathbf{Z}) \quad \text{(I.25)}$$

where $\dot{\sigma}$ is the material time derivative of σ. Also, $\mathbf{W}$ is the spin tensor and is given by the skew part of the velocity gradient $\mathbf{L}$. The quantity $\mathbf{Z}$ is a skew tensor which may be expressed as

$$\mathbf{Z} = z_1(\mathbf{gd}-\mathbf{dg}) + z_2(\mathbf{ggd}-\mathbf{dgg}) + z_3(\mathbf{gdgg}-\mathbf{ggdg}) \quad \text{(I.26)}$$

where $\mathbf{d}$ is the deviator of $\mathbf{D}$ and z_1, z_2, and z_3 can be functions of the invariants of $\mathbf{g}$, $\mathbf{d}$ and their joint invariants. We note that the Jaumann stress rate $\bar{\sigma}$ is given by

$$\bar{\sigma} = \dot{\sigma} - \mathbf{W}\sigma + \sigma\mathbf{W}, \quad \text{(I.27)}$$

hence, the modified Jaumann stress rate can be related to the Jaumann stress rate by

$$\hat{\sigma} = \bar{\sigma} - \mathbf{Z}\sigma + \sigma\mathbf{Z}. \quad \text{(I.28)}$$

From (I.25), we may write

$$\hat{\mathbf{s}} = \bar{\mathbf{s}} - \mathbf{Z}\mathbf{s} + \mathbf{s}\mathbf{Z}, \quad \text{(I.29)}$$

$$\mathrm{tr}\hat{\sigma} = \mathrm{tr}\bar{\sigma} = \mathrm{tr}\dot{\sigma}. \quad \text{(I.30)}$$

Similarly, the modified Jaumann rates of $\mathbf{g}$ and $\mathbf{f}$ are defined by

$$\hat{\mathbf{g}} = \dot{\mathbf{g}} - (\mathbf{W}+\mathbf{Z})\mathbf{g} + \mathbf{g}(\mathbf{W}+\mathbf{Z}), \quad \text{(I.31)}$$

$$\hat{\mathbf{f}} = \dot{\mathbf{f}} - (\mathbf{W}+\mathbf{Z})\mathbf{f} + \mathbf{f}(\mathbf{W}+\mathbf{Z}). \quad \text{(I.32)}$$

It is noteworthy that the expression for $\mathbf{Z}$ in (I.26) is deduced from a general representation of a skew tensor-valued isotropic function of $\mathbf{g}$ and $\mathbf{d}$. The general form consists of five terms (Wang, 1970) and (I.26) is obtained by choosing only the linear terms with respect to $\mathbf{d}$. Similar expressions have

Downloaded 03 May 2010 to 171.66.16.244. Redistribution subject to ASME license or copyright; see http://www.asme.org/terms/Terms_Use.cfm

been adopted by Dafalias (1983), Agah-Tehrani, Lee, Mallett, and Onat (1987), and Im and Atluri (1988) for the growth law of the back stress deviator α in the context of rate-independent plasticity. Specifically, $\mathbf{s}$ and α are used by Dafalias (1983), and Im and Atluri (1988) while $\mathbf{d}^{in}$ and α are introduced by Agah-Tehrani, Lee, Mallett, and Onat (1987) in place of $\mathbf{d}$ and $\mathbf{g}$ used here.

3 Discussion

No yield surface and no loading/unloading are used in FVBO. Aside from this fact, the major differences between the present approach and the prevailing methods for rate-independent plasticity theory at finite strains lie in the use of current configuration as the only reference configuration, the introduction of a term quadratic in the tensor variable into the viscoplastic flow law, and of the modified Jaumann rate.

Since VBO was introduced as a unified theory which is formulated in terms of strain rates, the extension to finite deformation by using the current configuration as reference, and the adoption of the additive decomposition of the rate of deformation tensor into elastic and inelastic parts, are natural. The proposed FBVO is totally incremental. Additive decomposition of the rate of deformation tensor for finite deformation has been discussed by Lehmann (1987) and used in numerical work by Peirce, Shih, and Needleman (1984), to name just a few. Agah-Tehrani, Lee, Mallett, and Onat (1987) introduced an additive decomposition of the rate of deformation tensor into modified elastic and plastic parts with both referred to the current configuration. For the special case of elastic and plastic isotropy, their formation is shown to reduce to (I.4) with $\mathbf{d}^{in}$ replaced by the plastic rate of deformation.

Although a term quadratic in the tensor variable, similar to the one introduced in (I.6), had been previously used in elasticity and plasticity (see Freudenthal and Ronay, 1966), such a term has not been included in recently proposed theories. A quadratic term in a tensor variable produces axial components when the tensor from which the square is formed has only shear components. Therefore, it was previously considered to be the sole repository for modeling second-order effects. Recently proposed theories use either the objective stress rate or constitutive assumptions equivalent to the plastic spin or both to model second-order effects. The results of Part II show the synergistic effects of the Jaumann rate, the tensor $\mathbf{Z}$, and the secondary rate of inelastic deformation. The latter is also needed for completeness of the flow law in view of representation theorems of isotropic tensor-valued functions. The Jaumann rate ensures objectivity for rigid body rotation and the tensor $\mathbf{Z}$ serves two functions. It apparently suppresses oscillatory solutions in simple shear. Material lines which instantaneously coincide with the principal axes of the rate of deformation tensor rotate with spin $\mathbf{W}$. This rotation is accounted for in the regular Jaumann rate. The effect of the rotations of other line elements is thought to be represented by the tensor $\mathbf{Z}$. All three of these elements contribute to the modeling of second-order effects as shown in Section 4.2 of Part II.

The modified Jaumann rate introduced in (I.25) is applied to all stress like quantities in this theory, see (I.31) and (I.32), as a matter of consistency. (In some theories different objective rates are used for different stress-like quantities.) As a consequence, the expressions needed for the one-step time integration method are simplified. One example is (II.10) in Part II. It may not be true if different modifications to the objective rates would be used for the Cauchy stress and the equilibrium Cauchy stress deviator.

The tensor $\mathbf{Z}$ introduced in (I.26) serves the same purpose as the plastic spin, Dafalais (1987), or as the rate of rotation terms, Agah-Tehrani, Lee, Mallett, and Onat (1987). A difference is the use of the deviatoric rate of deformation instead of the inelastic rate of deformation. The present choice makes the investigation of the influence of the modifications to the Jaumann rate possible in the case of hypoelasticity, see Section 4.1 of Part II. The use of the inelastic rate of deformation in (I.26) should be investigated in the future. In any event, the differences in the use of $\mathbf{d}$ or $\mathbf{d}^{in}$ in (I.26) have an insignificant effect when the long-time asymptotic solution is reached where $\mathbf{d}$ and $\mathbf{d}^{in}$ are collinear. If they are also collinear with $\mathbf{g}$, then (I.26) is zero for either choice as in the case of rigid body rotation.

When the two tensors used in representing the skew symmetric tensor $\mathbf{Z}$ in (I.26) are collinear, then $\mathbf{Z}=0$. This can happen with the present formulation when the long-time asymptotic solutions are reached. Then $\mathbf{s}$ and $\mathbf{g}$ are also collinear and the direction of the inelastic strain rate of the overstress theory is the same as that of a theory where $\mathbf{o}$ is replaced by $\mathbf{s}$, the stress deviator. Since the solutions of the differential equations are independent of the initial conditions and since the long-time asymptotic solutions can be rapidly attained, straining in a fixed direction does not furnish discriminating evidence. To ascertain the importance of the overstress dependence and of the influence of $\mathbf{Z}$ on the deformation behavior, changes in direction of the straining are necessary. Cyclic nonproportional loadings are ideally suited for this purpose.

In cyclic deformations leading to low-cycle fatigue, the strains are small but the accumulated equivalent plastic strain, ϕ, whose rate is defined in (I.21), can reach values exceeding ten which can be far greater than those achieved in monotonic loading. If a constitutive law for the finite deformation is to be used for small strain, then isotropic hardening determined from monotonic tests influences the behavior in cyclic test and vice versa. In cyclic nonproportional loading "extra hardening" is observed (Krempl and Lu, 1984; Tanaka, Murakami, and Ooka, 1986; Benallal and Marquis, 1987; Chaboche, 1987; McDowell, 1987). The modeling of this extra hardening takes various forms. In Krempl and Yao (1987) and Krempl and Lu (1989) terms akin to those needed to compute the tensor $\mathbf{Z}$ are introduced into a scalar measure. It increases only during nonproportional loading and represents therefore the repository for extra hardening. If the present theory was to be used to model cyclic proportional or nonproportional loading, the tensor $\mathbf{Z}$ would be different for the two cases. It could therefore serve as a partial repository for extra hardening. At the same time the growth law (I.20) will have to be modified. These questions will have to be resolved through future research.

Acknowledgment

Helpful discussions with E.H. Lee are appreciated. This work was performed while I. Nishiguchi was on a one year leave of absence from Japan Atomic Energy Research Institute. The support of the Army Research Office (T.L.S.) under Contract No. DAAL03-88-K-0041 and the Department of Energy (E.K.) under Contract No. DE-FG02-86ER13566 is gratefully acknowledged.

References

Agah-Tehrani, A., Lee, E. H., Mallett, R. L., and Onat, E. T., 1987, "The Theory of Elastic-Plastic Deformation at Finite Strain with Induced Anisotropy Modeled as Combined Isotropic-Kinematic Hardening," *Journal of the Mechanics and Physics of Solids*, Vol. 35, pp. 519–539.

Benallal, A., and Marquis, D., 1987, "Constitutive Equations Describing Non-Porportional Effects in Cyclic Plasticity," *Constitutive Laws for Engineering Materials: Theory and Applications*, C. S. Desai, E. Krempl, P. D. Kiousis, and T. Kundu, eds., Elsevier, New York, pp. 505–512.

Burlet, H., and Cailletaud, G., 1987, "Modeling of Cyclic Plasticity in Finite Element Codes," *Constitutive Laws for Engineering Materials: Theory and Ap-*

Downloaded 03 May 2010 to 171.66.16.244. Redistribution subject to ASME license or copyright; see http://www.asme.org/terms/Terms_Use.cfm

plications, C. S. Desai, E. Krempl, P. D. Kiousis, and T. Kundu, eds., Elsevier, New York, pp. 1157–1164.

Cernocky, E. P., and Krempl, E., 1979, "A Nonlinear Uniaxial Integral Constitutive Equation Incorporating Rate Effects, Creep and Relaxation," *International Journal of Nonlinear Mechanics*, Vol. 42, pp. 183–203.

Cernocky, E. P., and Krempl, E., 1980, "A Theory of Viscoplasticity Based on Infinitesimal Total Strain," *Acta Mechanica*, Vol. 36, pp. 263–289.

Chaboche, J. L., 1987, "Cyclic Plasticity Modeling and Ratchetting Effects," *Constitutive Laws for Engineering Materials: Theory and Applications*, C. S. Desai, E. Krempl, P. D. Kiousis, and T. Kundu, eds., Elsevier, New York, pp. 47–58.

Dafalias, Y. F., 1983, "Corotational Rates for Kinematic Hardening at Large Plastic Deformations," ASME JOURNAL OF APPLIED MECHANICS, Vol. 50, pp. 561–565.

Dafalias, Y. F., 1987, "Anisotropy, Reference Configuration and Residual Stresses," *Constitutive Laws for Engineering Materials: Theory and Applications*, C. S. Desai, E. Krempl, P. D. Kiousis, and T. Kundu, eds., Elsevier, New York, pp. 69–80.

Freudenthal, A. M., and Ronay M., 1966, "Second Order Effects in Dissipative Media," *Proceedings of the Royal Society of London*, Vol. A292, pp. 14–50.

Gurtin, M. E., 1981, *An Introduction Continuum Mechanics*, Academic Press, New York.

Han, S., and Wack, B., 1987, "Torsion Ratchet Associated with Mechanical Hysteresis," Transactions of the 9th International Conference on Structural Mechanics in Reactor Technology, Vol. L, Inelastic Behavior of Metals and Constitutive Equations, F. H. Wittmann, ed., A. A. Balkema, Rotterdam, pp. 421–426.

Im, S., and Atluri, S. N., 1988, "Computational Implementation of an Internal Time Constitutive Equations in Finite Deformation Plasticity," *Computational Mechanics '88*, S. N. Atluri, and G. Yagawa, eds., Springer-Verlag, New York, pp. 17.v.2–17.v.4.

Kocks, U. F., Stout, M. G., and Rollett, A. D., 1988, "The Influence of Texture on Strain Hardening," *Strength of Metals and Alloys (ICSMA 8)*, P.O. Kettunen, ed., Pergamon Press, Oxford, pp. 25–34.

Krempl, E., 1987, "Models of Viscoplasticity, Some Comments on Equilibrium (Back) Stress and Drag Stress," *Acta Mechanica*, Vol. 69, pp. 25–42.

Krempl, E., and Kallianpur, V. V., 1985, "The Uniaxial Unloading Behavior of Two Engineering Alloys at Room Temperature," ASME JOURNAL OF APPLIED MECHANICS, Vol. 52, pp. 654–658.

Krempl, E., and Lu, H., 1984, "The Hardening and Rate-Dependent Behavior of Fully Annealed AISI Type 304 Stainless Steel under Biaxial In-Phase and Out-of-Phase Strain Cycling at Room Temperature," *ASME Journal of Engineering Materials and Technology*, Vol. 106, pp. 376–382.

Krempl, E., and Lu, H., 1989, "The Path and Amplitude Dependence of Cyclic Hardening of Type 304 Stainless Steel at Room Temperature," *Biaxial and Multiaxial Fatigue*, M. W. Brown, and K. J. Miller, eds., Mechanical Engineering Publications Ltd., London, pp. 89–106.

Krempl, E., McMahon, J. J., and Yao, D., 1986, "Viscoplasticity Based on Overstress with a Differential Growth Law for the Equilibrium Stress," *Mechanics of Materials*, Vol. 5, pp. 35–48.

Krempl, E., and Yao, D., 1987, "The Viscoplasticity Theory Based on Overstress Applied to Ratchetting and Cyclic Hardening," *Low Cycle Fatigue and Elasto-Plastic Behavior of Materials*, K. T. Rie, ed., Elsevier Science Publishing Company, New York, pp. 137–148.

Lee, E. H., and Agah-Tehrani, A., 1987a, "On Elastic-Plastic Finite Deformation with Strain-Induced Anisotropy," *Constitutive Laws for Engineering Materials: Theory and Applications*, C. S. Desai, E. Krempl, P. D. Kiousis, and T. Kundu, eds., Elsevier, New York, pp. 161–172.

Lee, E. H., and Agah-Tehrani, A., 1987b, "The Structure of Constitutive Relations Involving Induced Anisotropy at Finite Strain," *Advances in Inelastic Analysis*, AMD-Vol. 88, PED-Vol. 28, ASME, New York, pp. 29–40.

Lehmann, Th., 1987, "On a Generalized Constitutive Law for Finite Deformations in Thermo-Plasticity and Thermo-Viscoplasticity," *Constitutive Laws for Engineering Materials: Theory and Applications*, C. S. Desai, E. Krempl, P. D. Kiousis, and T. Kundu, eds., Elsevier, New York, pp. 173–184.

McDowell, D. L., 1987, "An Evaluation of Recent Developments in Hardening and Flow Rules for Rate-Independent, Non-proportional Cyclic Plasticity," ASME JOURNAL OF APPLIED MECHANICS, Vol. 54, pp. 323–334.

Peirce, D., Shih, C. F., and Needleman, A., 1984, "A Tangent Modulus Method for Rate Dependent Solids," *Computers and Structures*, Vol. 18, pp. 875–887.

Poynting, J. H., 1909, "On Pressure Perpendicular to the Shear Planes in Finite Pure Shears and on the Lengthening of Loaded Wires when Twisted," *Proceedings of the Royal Society of London*, Vol. A82, pp. 546–559.

Prager, W., 1948, "The Stress-Strain Laws of the Mathematical Theory of Plasticity—A Survey of Recent Progress," ASME JOURNAL OF APPLIED MECHANICS, Vol. 15, pp. 226–233.

Reed, K. W., and Atluri, S. N., 1985, "Constitutive Modeling and Computational Implementation for Finite Strain Plasticity," *International Journal of Plasticity*, Vol. 1, pp. 63–87.

Ronay, M., 1965, "Second-Order Strain Accumulation in Cyclic Torsion," *British Journal of Applied Physics*, Vol. 16, pp. 727–728.

Ronay, M., 1967, "On Second Order Strain Accumulation in Aluminium in Reversed Cyclic Torsion at Elevated Temperature," *International Journal of Solids and Structures*, Vol. 3, pp. 167–176.

Sutcu, M., and Krempl, E., 1989, "A Stability Analysis of the Uniaxial Viscoplasticity Theory Based on Overstress," to appear in *Computational Mechanics*, Vol. 4, pp. 401–408.

Swift, H. W., 1947, "Length Changes in Materials under Torsional Overstrain," *Engineering*, Vol. 163, pp. 253–257.

Tanaka, E., Murakami, S., and Ooka, M., 1987, "Constitutive Modeling of Cyclic Plasticity in Non-Proportional Loading Conditions," *Constitutive Laws for Engineering Materials: Theory and Applications*, C. S. Desai, E. Krempl, P. D. Kiousis, and T. Kundu, eds., Elsevier, New York pp. 639–646.

Truesdell, C., and Noll, W., 1965, "The Non-Linear Field Theories of Mechanics," *Handbuch der Physik*, Band III/3, Springer Verlag, New York.

Wack, B., 1981, "Second and Third-Order Effects in the Torsion of Circular Tubes and Rods," *Journal de Mécanique*, Vol. 20, pp. 737–787.

Wang, C. C., 1970, "A New Representation Theorem for Isotropic Functions, Part 2: Vector-Valued Isotropic Functions, Symmetric Tensor-Valued Isotropic Functions and Skew-Symmetric Tensor-Valued Isotropic Functions," *Archive for Rational Mechanics and Analysis*, Vol. 36, pp. 198–223.

Yao, D., and Krempl, E., 1985, "Viscoplasticity Theory Based on Overstress: The Prediction of Monotonic and Cyclic Proportional and Nonproportional Loading Paths of an Aluminum Alloy," *International Journal of Plasticity*, Vol. 1, pp. 259–274.

Downloaded 03 May 2010 to 171.66.16.244. Redistribution subject to ASME license or copyright; see http://www.asme.org/terms/Terms_Use.cfm

I. Nishiguchi[1]
Mem. ASME

T.-L. Sham
Mem. ASME

E. Krempl
Fellow ASME

Department of Mechanical Engineering, Aeronautical Engineering, and Mechanics, Rensselaer Polytechnic Institute, Troy, NY 12180-3590

A Finite Deformation Theory of Viscoplasticity Based on Overstress: Part II—Finite Element Implementation and Numerical Experiments

A one-step time integration method is developed for the finite deformation theory of viscoplasticity based on overstress (FVBO) described in Part I. This time integration method is based on a forward gradient approximation and it leads to explicit expressions of the tangent operators suitable for finite element implementation. Numerical experiments and closed-form solutions for a hypoelastic material in homogeneous deformation states are presented. The FVBO is applied to the modeling of second-order effects in torsion. The numerical results show that a modification of the Jaumann rate and second-order terms of the inelastic rate of deformation are necessary to model the observed effects.

1 Introduction

In the previous paper, Part I, the basic equations of the finite deformation theory of viscoplasticity (FVBO) were developed. They consist of nonlinear, coupled differential equations which are stiff. This is a characteristic of all viscoplasticity models, although the "degree of stiffness" varies from model to model. Their nonlinearity makes a closed-form solution, even in a simple tensile test, unlikely. Numerical experiments are necessary for the evaluation of the theory. Various approaches for their integration have been proposed (e.g., Krieg, 1977; Shih, Delorenzi, and Miller, 1977; Argyris, Vaz, and Willam, 1978; Willam 1978; Zirin and Krempl, 1982; Peirce, Shih, and Needleman, 1984; Cordts and Kollmann, 1986; Weber, Lush, and Anand, 1988; Sham and Chow, 1989). Also, FVBO is intented for use in stress analysis using finite element methods. To accomplish both objectives, a one-step time integration method based on the forward gradient approximation is developed and this leads to explicit expressions for the tangent operators. They are implemented into a finite element program together with an incrementally objective procedure, (see Hughes and Winget, 1980; Rubinstein and Atluri, 1983; Reed and Atluri, 1983; Mallett, 1984).

The formulation of the tangent operators is given in Section 2 and the finite element implementation is outlined in Section 3. Applications of the theory to homogeneous motions of a hypoelastic material and to a material characterized by FVBO are given in Section 4.

2 Tangent Operators

As is well known, the constitutive equations of unified viscoplasticity theories are stiff. The time integration of these equations by explicit Euler method usually requires the use of very small time-step size because of numerical stability consideration. Various time integration methods, as cited in the Introduction, have been proposed to overcome such a severe restriction. For the constitutive equations proposed in Part I, we develop a one-step time integration method which is based on the so-called forward gradient approximation. The development parallels the work of Peirce, Shih, and Needleman (1984) and Sham and Chow (1989). Two measures of the inelastic strain, namely, the primary and the secondary equivalent inelastic strain rates, are chosen as the variables for the forward gradient approximation. This leads to explicit tangent operators for the constitutive equations.

Consider ϕ_I and ϕ_{II}, equation (I.10)[2] at a material particle in the current configuration. Let the increments of ϕ_I and ϕ_{II} from time t to $t+\Delta t$ be

$$\Delta\phi_I = \phi^{t+\Delta t} - \phi^t_I, \qquad \Delta\phi_{II} = \phi^{t+\Delta t}_{II} - \phi^t_{II} \tag{II.1}$$

where the superscript denotes the time at which ϕ_I and ϕ_{II} are evaluated. We now approximate the increments by a linear interpolation to obtain

[1]Presently on leave from the Japan Atomic Energy Research Institute, Ibaraki, Japan.

Contributed by the Applied Mechanics Division of THE AMERICAN SOCIETY OF MECHANICAL ENGINEERS for presentation at the Winter Annual Meeting, Dallas, Texas, Nov. 25–30, 1990.

Discussion on this paper should be addressed to the Technical Editor, Leon M. Keer, The Technological Institute, Northwestern University, Evanston, IL 60208, and will be accepted until two months after final publication of the paper itself in the JOURNAL OF APPLIED MECHANICS. Manuscript received by the ASME Applied Mechanics Division, Aug. 15, 1988; final revision, June 12, 1989.

Paper No. 90-WA/APM-10.

[2](I.xx) and (II.xx) denote equation numbers in Part I and Part II, respectively.

Copyright © 1990 by ASME
Downloaded 03 May 2010 to 171.66.16.244. Redistribution subject to ASME license or copyright; see http://www.asme.org/terms/Terms_Use.cfm

$$\Delta\phi_I = \Delta t\left((1-\theta)\dot{\phi}_I^t + \theta\dot{\phi}_I^{t+\Delta t}\right),$$

$$\Delta\phi_{II} = \Delta t\left((1-\theta)\dot{\phi}_{II}^t + \theta\dot{\phi}_{II}^{t+\Delta t}\right) \tag{II.2}$$

where

$$0 \le \theta \le 1. \tag{II.3}$$

When $\theta = 0$, the linear interpolation reduces to the explicit Euler formula, while $\theta = 1$ leads to the backward Euler formula which is an implicit method. Employing the forward gradient approximation we may write

$$\dot{\phi}_I^{t+\Delta t} = \dot{\phi}_I^t + \frac{d\dot{\phi}_I^t}{dt}\Delta t, \quad \dot{\phi}_I^{t+\Delta t} = \dot{\phi}_{II}^t + \frac{d\dot{\phi}_{II}^t}{dt}\Delta t. \tag{II.4}$$

Substituting equation (II.4) into equation (II.2) we obtain

$$\Delta\phi_I = \Delta t\dot{\phi}_I^t + \theta(\Delta t)^2\frac{d\dot{\phi}_I^t}{dt},$$

$$\Delta\phi_{II} = \Delta t\dot{\phi}_{II}^t + \theta(\Delta t)^2\frac{d\dot{\phi}_{II}^t}{dt}. \tag{II.5}$$

From equation (I.12), we find $\dot{\phi}_I = \Gamma/C_I$ and $\dot{\phi}_{II} = \Gamma^2/(3|C_{II}|)$ where C_I, C_{II} are selected to be functions of the invariants of $\mathbf{o}$. For simplicity, we assume that they only depend on the invariant Γ defined after equation (I.9), and hence we may write

$$\dot{\phi}_I = \kappa_I(\Gamma), \quad \dot{\phi}_{II} = \kappa_{II}(\Gamma). \tag{II.6}$$

These assumptions lead to

$$\frac{d\dot{\phi}_I^t}{\mathrm{dt}} = \frac{\mathrm{d}\kappa_I^t}{\mathrm{d}\Gamma}\dot{\Gamma}, \quad \frac{d\dot{\phi}_{II}^t}{dt} = \frac{d\kappa_{II}^t}{d\Gamma}\dot{\Gamma}. \tag{II.7}$$

In order to obtain an useful expression for $\dot{\Gamma}$, we first note that

$$\dot{\Gamma} = \frac{3}{2\Gamma}\,\mathbf{o}\bullet(\dot{\mathbf{s}} - \dot{\mathbf{g}}). \tag{II.8}$$

Relating the material rate $(\dot{\cdot})$ to the modified Jaumann rate $(\hat{\cdot})$ defined in equation (I.25), we find

$$\dot{\Gamma} = \frac{3}{2\Gamma}\left(\mathbf{o}\bullet(\hat{\mathbf{s}} - \hat{\mathbf{g}}) + \mathbf{o}\bullet((\mathbf{W}+\mathbf{Z})\mathbf{o}) - \mathbf{o}\bullet(\mathbf{o}(\mathbf{W}+\mathbf{Z}))\right) \tag{II.9}$$

and this leads to

$$\dot{\Gamma} = \frac{3}{2\Gamma}\,\mathbf{o}\bullet(\hat{\mathbf{s}} - \hat{\mathbf{g}}) \tag{II.10}$$

because of the symmetry of $\mathbf{o}$ and the cyclic property of the trace of products of tensors. Using the constitutive equation (I.14) and the evolution law, (I.24), and noting that $\mathbf{o}\bullet\mathbf{y} = 3J_3$, we may rewrite equation (II.10) as

$$\Delta t\dot{\Gamma} + \Delta tP(\mathbf{o}\bullet\mathbf{d}) + Q\Delta\phi_I + R\Delta\phi_{II} \tag{II.11}$$

where

$$P = \frac{3}{\Gamma}(G - G_\psi), \tag{II.12}$$

$$Q = -3(G - G_\psi^{in}), \tag{II.13}$$

$$R = -\frac{81}{2}\,\omega_{II}\frac{J_3}{\Gamma^3}(G - G_\psi^{in}). \tag{II.14}$$

Substituting equation (II.7) into equation (II.5) and using equation (II.11), we obtain the following linear algebraic equations for $\Delta\phi_I$, $\Delta\phi_{II}$:

$$\left(1 - \theta\Delta t\frac{d\kappa_I^t}{d\Gamma}Q\right)\Delta\phi_I + \left(-\theta\Delta t\frac{d\kappa_I^t}{d\Gamma}R\right)\Delta\phi_{II} = \left(\theta(\Delta t)^2\frac{d\kappa_I^t}{d\Gamma}P\right)\mathbf{o}\bullet\mathbf{d} + \Delta t\dot{\phi}_I^t \tag{II.15a}$$

$$\left(-\theta\Delta t\frac{d\kappa_{II}^t}{d\Gamma}Q\right)\Delta\phi_I + \left(1 - \theta\Delta t\frac{d\kappa_{II}^t}{d\Gamma}R\right)\Delta\phi_{II} = \left(\theta(\Delta t)^2\frac{d\kappa_{II}^t}{d\Gamma}P\right)\mathbf{o}\bullet\mathbf{d} + \Delta t\dot{\phi}_{II}^t. \tag{II.15b}$$

The solution can be expressed as

$$\Delta\phi_I = \Delta t(a_I\mathbf{o}\bullet\mathbf{d} + b_I), \ \Delta\phi_{II} = \Delta t(a_{II}\mathbf{o}\bullet\mathbf{d} + b_{II}) \tag{II.16}$$

where

$$a_I = \frac{1}{1+\zeta}\theta\Delta t\frac{d\kappa_I^t}{d\Gamma}P, \ a_{II} = \frac{1}{1+\zeta}\theta\Delta t\frac{d\kappa_{II}^t}{d\Gamma}P, \tag{II.17}$$

$$b_I = \frac{1}{1+\zeta}\left(\left(1 - \theta\Delta t\frac{d\kappa_{II}^t}{d\Gamma}R\right)\dot{\phi}_I^t + \theta\Delta t\frac{d\kappa_I^t}{d\Gamma}R\dot{\phi}_{II}^t\right),$$

$$b_{II} = \frac{1}{1+\zeta}\left(\theta\Delta t\frac{d\kappa_{II}^t}{d\Gamma}Q\dot{\phi}_I^t + \left(1 - \theta\Delta t\frac{d\kappa_I^t}{d\Gamma}Q\right)\dot{\phi}_{II}^t\right), \tag{II.18}$$

$$\zeta = -\theta\Delta t\frac{d\kappa_I^t}{d\Gamma}Q - \theta\Delta t\frac{d\kappa_{II}^t}{d\Gamma}R. \tag{II.19}$$

We now divide $\Delta\phi_I$ and $\Delta\phi_{II}$ in equation (II.16) by Δt and substitute into equation (I.13) to obtain

$$\mathbf{d}^{in} = \mathbf{\Omega}[\mathbf{d}] + b_I\frac{3}{2}\frac{\mathbf{o}}{\Gamma} + \omega_{II}b_{II}\frac{9}{2}\frac{\mathbf{y}}{\Gamma^2} \tag{II.20}$$

where

$$\mathbf{\Omega} = a_I\frac{3}{2}\frac{1}{\Gamma}\,\mathbf{o}\otimes\mathbf{o} + \omega_{II}a_{II}\frac{9}{2}\frac{1}{\Gamma^2}\,\mathbf{y}\otimes\mathbf{o}. \tag{II.21}$$

The fourth-order tensor $\mathbf{\Omega}$ is nonsymmetric due to the second term on the right of equation (II.21). The notation $\mathbf{A}[\mathbf{B}]$ denotes the operation in which the fourth-order tensor $\mathbf{A}$ transforms the second-order tensor $\mathbf{B}$ into another second-order tensor, and $\mathbf{a}\otimes\mathbf{b}$ represents the outer tensor product of second-order tensors $\mathbf{a}$, $\mathbf{b}$.

Similarly, dividing $\Delta\phi_I$ and $\Delta\phi_{II}$ by Δt and then substituting into equation (I.14) and (I.24), we arrive at the following one-step time integration formulas

$$\hat{\mathbf{s}} = 2G\mathbf{\Omega}_s^{\tan}[\mathbf{d}] - 2Gb_I\frac{3}{2}\frac{\mathbf{o}}{\Gamma} - 2G\omega_{II}b_{II}\frac{9}{2}\frac{\mathbf{y}}{\Gamma^2}, \tag{II.22}$$

$$\hat{\mathbf{g}} = 2G_\psi^{in}\mathbf{\Omega}_g^{\tan}[\mathbf{d}] - 2G_\psi^{in}b_I\frac{3}{2}\frac{\mathbf{o}}{\Gamma} - 2G_\psi^{in}\omega_{II}b_{II}\frac{9}{2}\frac{\mathbf{y}}{\Gamma^2} \tag{II.23}$$

where the tangent operators are

$$\mathbf{\Omega}_s^{\tan} = \mathbf{I} - \mathbf{\Omega}, \quad \mathbf{\Omega}_g^{\tan} = \frac{G_\psi}{G_\psi^{in}}\mathbf{I} - \mathbf{\Omega} \tag{II.24}$$

and $\mathbf{I}$ now represents the fourth-order identity tensor.

For the implementation of this one-step time integration method into existing finite element codes, it is often more convenient to obtain tangent operators which relate the Jaumann stress rates to the total rate of deformation since many of these codes adopt the Jaumann rate as the objective rate. For this purpose, we may rewrite equation (I.26) as

$$\mathbf{Z} = \mathbf{\Lambda}[\mathbf{d}] \tag{II.25}$$

where $\mathbf{\Lambda}$ is a fourth-order tensor and its Cartesian components are given by

$$\Lambda_{ijkl} = z_1[g_{ik}\delta_{lj} - \delta_{ik}g_{lj}] + z_2[(g_{ip}g_{pk})\delta_{lj} - \delta_{ik}(g_{lp}g_{pj})] + z_3[g_{ik}(g_{lp}g_{pj}) - (g_{ip}g_{pk})g_{lj}].$$

Here, δ_{ij} is the Kronecker delta. By combining equation (II.25) with equation (I.29), we find an alternative representation of equation (II.22),

Downloaded 03 May 2010 to 171.66.16.244. Redistribution subject to ASME license or copyright; see http://www.asme.org/terms/Terms_Use.cfm

$$\mathring{\bar{\mathbf{s}}} = 2G\boldsymbol{\Theta}_s^{\tan}[\mathbf{d}] - 2Gb_I \frac{3}{2}\frac{\mathbf{o}}{\Gamma} - 2G\omega_{II} b_{II} \frac{9}{2}\frac{\mathbf{y}}{\Gamma^2} \qquad \text{(II.26)}$$

where

$$\boldsymbol{\Theta}_s^{\tan} = \boldsymbol{\Omega}_s^{\tan} - \boldsymbol{\Theta} \qquad \text{(II.27)}$$

and the Cartesian components of $\boldsymbol{\Theta}$ are

$$2G\Theta_{ijlm} = s_{ik}\Lambda_{kjlm} - \Lambda_{iklm}s_{kj}. \qquad \text{(II.28)}$$

Finally, the formula

$$tr\mathring{\bar{\sigma}} = tr\mathring{\hat{\sigma}} = tr\dot{\sigma} = 3Ktr\mathbf{D} = 3Ktr\mathbf{D}^e \qquad \text{(II.29)}$$

for the hydrostatic components completes this one-step time integration method of the constitutive equations.

We note that even though the tangent operators are derived based on the assumption that ϕ_I, ϕ_{II} depend only on Γ, the one-step time integration method is applicable when ϕ_I, ϕ_{II} depend on other state variables, e.g., $\mathbf{g}$, $\mathbf{f}$, ϕ_I and ϕ_{II}. Explicit expressions for the tangent operators could also be obtained in such a generalization but we do not pursue this in the present work.

3 Finite Element Implementation

The finite element implementation of the FVBO is based on the updated Lagrangian formulation of Osias and Swedlow (1974), and McMeeking and Rice (1975). By choosing a reference configuration that is instantaneously coincident with the current configuration, the rate form of the virtual work equation, valid for arbitrary amounts of deformation and in the absence of body forces, can be expressed as

$$\int_{V_t}\left(\bar{\mathbf{s}}\cdot\delta\mathbf{d} + \frac{1}{3}(tr\bar{\sigma})\delta(tr\mathbf{D})\right)dV + \int_{V_t}\boldsymbol{\Sigma}[\mathbf{L}]\cdot\delta\mathbf{L}dV = \int_{A_t}\dot{\mathbf{T}}\cdot\delta\mathbf{v}dA \qquad \text{(II.30)}$$

where V_t is the current volume of the body, A_t its bounding surface, $\mathbf{T}$ the material rate of the nominal traction vector with respect to current areas. The symbol $\delta(\ )$ denotes the arbitary virtual variation and $\delta\mathbf{v}$ is a kinematically admissible virtual velocity field. The components of the fourth-order tensor $\boldsymbol{\Sigma}$ are

$$\Sigma_{ijkl} = \frac{1}{2}\left(\sigma_{lj}\delta_{ik} - \sigma_{ik}\delta_{lj} - (\sigma_{il}\delta_{kj} + \sigma_{kj}\delta_{il}) + 2\sigma_{ij}\delta_{kl}\right) \qquad \text{(II.31)}$$

where again, δ_{ik} is the Kronecker delta. We note that in some circumstance, e.g. J_2-flow theory of rate-independent plasticity, the rate form of the virtual work equation (II.30) is expressed in terms of the Kirchoff stress ($=\det(\mathbf{F})\boldsymbol{\sigma}$, $\mathbf{F}$ = deformation gradient) in order to arrive at a symmetric tangent stiffness matrix. However, the underlying structure of FVBO would not lead to a symmetric tangent stiffness matrix even if it is formulated with respect to the Kirchhoff stress. Since the asymmetry of the tangent stiffness matrix is an inherent feature of FVBO, we therefore employ the rate form of the virtual work equation in terms of Cauchy stress (or its deviatoric and hydrostatic components as in equation (II.30)).

Substituting the result from the one-step time integration method, equations (II.26) and (II.29), into equation (II.30) we obtain

$$\int_{V_t}\left(2G\mathbf{d} - 2G\boldsymbol{\Omega}[\mathbf{d}] - \boldsymbol{\Theta}[\mathbf{d}]\right)\cdot\delta\mathbf{d}dV + \int_{V_t}K(tr\mathbf{D})\delta(tr\mathbf{D})dV + \int_{V_t}\boldsymbol{\Sigma}[\mathbf{L}]\cdot\delta\mathbf{L}dV = \int_{A_t}\dot{\mathbf{T}}\cdot\delta\mathbf{v}dA + \int_{V_t}2G\left(b_I\frac{3}{2}\frac{\mathbf{o}}{\Gamma} + \omega_{II}b_{II}\frac{9}{2}\frac{\mathbf{y}}{\Gamma^2}\right)\cdot\delta\mathbf{d}dV. \qquad \text{(II.32)}$$

Applying the standard displacement-based finite element discretization procedure to equation (II.32), we arrive at the finite element equilibrium equation

$$[\mathbf{k}_d + \mathbf{k}_h + \mathbf{k}_g]\Delta\mathbf{u} = \Delta\mathbf{f} + \Delta\mathbf{f}_R \qquad \text{(II.33)}$$

where $\mathbf{k}_d$, $\mathbf{k}_h$, and $\mathbf{k}_g$ are, respectively, the deviatoric, hydrostatic, and geometric stiffness matrices obtained from the integrals on the left of equation (II.32), and $\Delta\mathbf{u}$ the nodal displacement increment. In addition, $\Delta\mathbf{f}$ is the nodal force increment, and $\Delta\mathbf{f}_R$ the nodal relaxation force increment, both obtained from the integrals on the right of equation (II.32). Reduced numerical integration rules are used to compute the hydrostatic stiffness matrix $\mathbf{k}_h$ in order to relieve the artificial finite element mesh constraints under nearly incompressible conditions (see Shih and Needleman (1984)).

Once the displacement increment $\Delta\mathbf{u}$ is obtained from equation (II.33), the modified Jaumann increments of $\mathbf{s}$, $\mathbf{g}$, and $\mathbf{f}$ are computed from equations (II.22), (II.23), (I.17), and (II.20). In order to evaluate the material increments of $\mathbf{s}$, $\mathbf{g}$, and $\mathbf{f}$ so that the stresses can be updated at the finite element Gauss points, we employ the incrementally objective procedure of Rubinstein and Atluri (1983) and Mallett (1984), to compute the modified rotational increments of $\mathbf{s}$, $\mathbf{g}$, and $\mathbf{f}$. Since the objective rate used in the original development of this procedure was the Jaumann rate, we need to replace the spin $\mathbf{W}$ in their alogrithm by $\mathbf{W}+\mathbf{Z}$ for our purpose.

4 Numerical Results

To investigate the behavior of the equations of FVBO and to assess its capability we considered some simple problems in which homogeneous deformation conditions were assumed. Under such conditions it would be possible to derive the relevant governing differential equations from the three-dimensional theory. Rather than directly integrating this set of ordinary, nonlinear differential equations using numerical integration packages suitable for stiff differential equations, the finite element method described earlier was used. One single eight-noded three-dimensional element was employed to model the homogeneous deformation state and appropriate constraints were imposed on the finite element to simulate the specific boundary conditions considered. For all the finite element results that will be reported, the linear interpolation parameter, θ, of the one-step integration method was set to 0.5. The time increments were prescribed throughout the loading history in each case. We note that an adaptive load incrementation scheme similar to the one employed in the infinitesimal VBO (Sham and Chow (1989)) could be implemented for the FVBO.

4.1 Second-Order Effects of a Hypoelastic Material.

When the material response is purely hypoelastic, analytical solutions can be obtained for some simple homogeneous deformation problems. These solutions provide insight into the fundamental behavior and serve also as a benchmark against which numerical results can be checked. The cases of simple shear and stress-controlled shear have been investigated for a hypoelastic material whose constitutive equations are obtained from FVBO by setting the inelastic rate of deformation to zero. In this case $\hat{\mathbf{s}}$ is approximately equal to $\hat{\mathbf{g}}$ (since $\psi(0) \approx E$), thus the constitutive equations are assumed to be

$$\mathbf{d} = \frac{1}{2G}\hat{\mathbf{s}}, \quad tr\mathbf{D} = \frac{1}{3K}tr\mathring{\hat{\sigma}} = \frac{1}{3K}tr\dot{\sigma}. \qquad \text{(II.34)}$$

The skew tensor $\mathbf{Z}$ is selected as

$$\mathbf{Z} = \left(\frac{r_{11}}{s_e} + r_{12}\right)(\mathbf{sd} - \mathbf{ds}) \qquad \text{(II.35)}$$

Downloaded 03 May 2010 to 171.66.16.244. Redistribution subject to ASME license or copyright; see http://www.asme.org/terms/Terms_Use.cfm

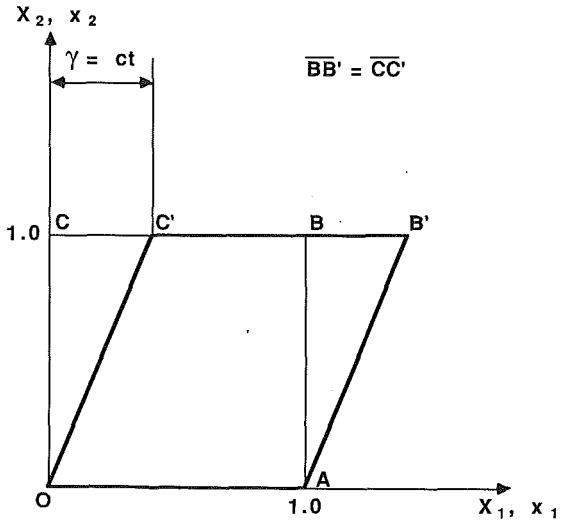


Fig. 1 Deformation field for simple shear

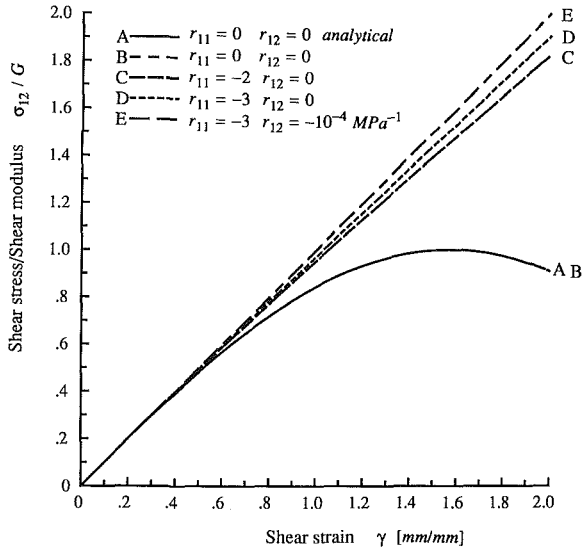


Fig. 2 Simple shear; normalized Cauchy shear stress σ_{12}/G for several values of the material constants; $E = 1.5 \times 10^5$ MPa and $\nu^e = 0.3$

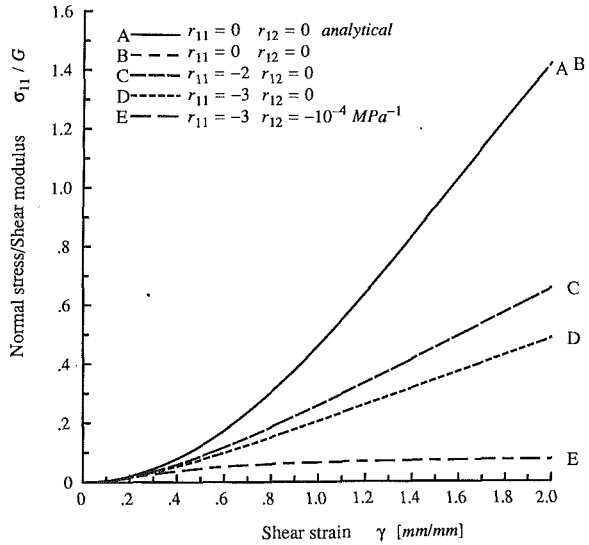


Fig. 3 Simple shear; normalized Cauchy normal stress σ_{11}/G for several values of the material constants

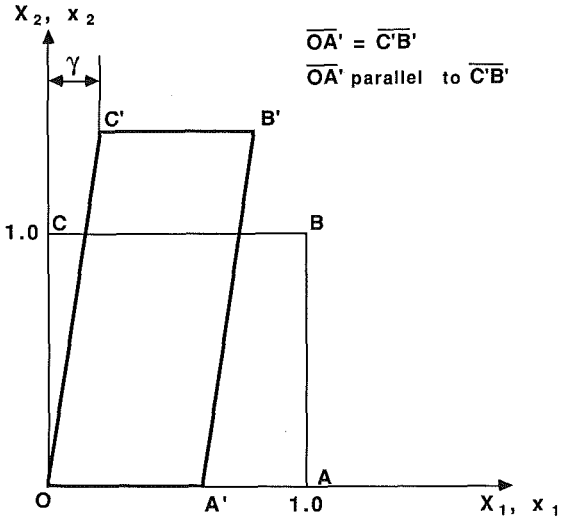


Fig. 4 Deformation field for stress-controlled shear

where $s_e = \sqrt{(3/2)\mathbf{s} \cdot \mathbf{s}}$ is the equivalent Cauchy stress. The material constants are r_{11}, which is dimensionless, and r_{12}, which as the dimension of reciprocal stress.

(*i*) *Simple Shear.* Under the simple shear assumption, the deformation field at time t can be expressed as

$$x_1 = X_1 + ctX_2, \quad x_2 = X_2, \quad x_3 = X_3 \tag{II.36}$$

where X_i, and x_i represent the coordinates of material points in the undeformed and deformed configuration, respectively, and c a constant (Fig. 1). These constraints were imposed on the finite element and finite element solutions were generated for selected values of the material constants r_{11} and r_{12}. The normalized Cauchy shear and normal stresses are plotted versus the nominal strain $\gamma = ct$ in Figs. 2 and 3, respectively. As seen from these two figures, the material constants r_{11} and r_{12} of $\mathbf{Z}$ cause the curves to increase monotonically within the range calculated. Also, the magnitude of the Cauchy normal stress can be adjusted by these constants.

When $\mathbf{Z}$ is set to zero, the objective rate adopted reduces to the Jaumann rate. The well-known analytical solution which exhibits oscillatory response for this case is (Dienes (1979)),

$$\sigma_{11} = G(1 - \cos(ct)), \quad \sigma_{22} = -G(1 - \cos(ct)), \quad \sigma_{12} = G\sin(ct). \tag{II.37}$$

The closed-form results (equation (II.37)) are also shown in Figs. 2 and 3. The agreement between the analytical solution and the finite element results is excellent in this case.

We note that for any value of $\mathbf{Z}$, the equality $\sigma_{11} + \sigma_{22} = 0$ holds. This relation does not necessarily hold for some other objective rates. An example is the Truesdell rate (see Atluri (1984)).

(*ii*) *Stress-Controlled Shear.* In this problem, the homogeneous stress field is prescribed as

$$\sigma_{12} = \sigma_{21} = ht, \quad \text{other } \sigma_{ij} = 0, \tag{II.38}$$

where h is a constant. The velocity field is assumed to be

$$v_1 = v_1(x_1, x_2, t), \quad v_2 = v_2(x_2, t), \quad v_3 = (t). \tag{II.39}$$

They are intended to approximate the stress and deformation states of a thin-walled tube under torsion.

In order to enforce the conditions (equation (II.38) and (II.39)) on the finite element, we prescribe the boundary shear traction equation (II.38)) on the finite element and constrain it to deform so that lines parallel to the horizontal axis remain

Downloaded 03 May 2010 to 171.66.16.244. Redistribution subject to ASME license or copyright; see http://www.asme.org/terms/Terms_Use.cfm

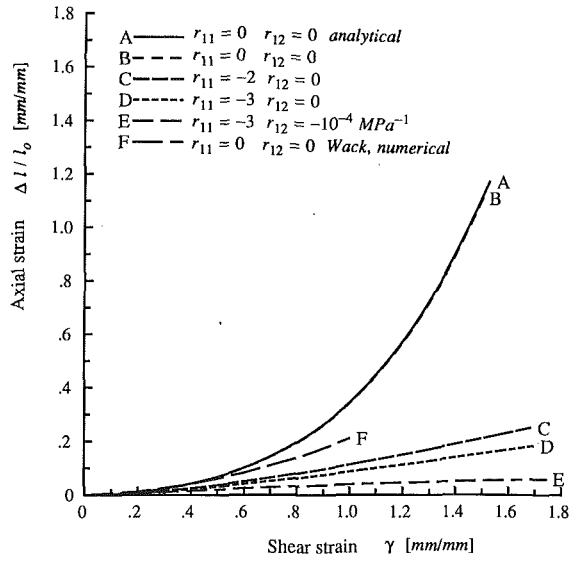


Fig. 5 Stress-controlled shear; axial elongation versus shear strain; $E=1.5\times10^5$ MPa and $\nu^e=0.3$; numerical solution by Wack (1981) is also shown

in that direction, but otherwise, the element is free to deform in the vertical direction and to change its width (Fig. 4). With such constraints imposed, finite element solutions were obtained for the same set of material constants as in the simple shear case. If we set **Z** to zero, the modified Jaumann rate reduces to the Jaumann rate. Under this special condition, an analytical solution has been derived and it is given as equation (A6) of the Appendix.

The finite element results together with the analytical solution (A6) are plotted in Fig. 5. It can be seen that the finite element solution obtained for $r_{11}=r_{12}=0$ agrees very well with equation (A6) (see curves A and B). Wack (1981) has analyzed the problem of a thin-walled tube under torsional loading and obtained a solution by solving the governing partial differential equations numerically. We have included Wack's numerical solution in Fig. 5 for comparison. We can see that treating equations (II.38) and (II.39) as an approximation of the stress and deformation states in a thin-walled tube under torsion is acceptable up to a shear strain of 0.5. At strains higher than this value the analytical and finite element solutions diverge from the numerical result of Wack (1981).

On plots of shear stress versus shear strain, none of the three solutions show any tendency for oscillatory behavior for the amount of shearing considered when the unmodified Jaumann stress rate is used. This is in contrast to the case of simple shear where oscillations develop, see Fig. 2. Also, if equation (A6) is interpreted as the approximation of the deformation field in the thin-walled tube, a decrease in the diameter and an increase in the axial length can be inferred. The modifications to the Jaumann rate reduce the axial elongation considerably. They again influence the magnitude of the second-order effect which manifests itself as axial elongation in this case.

4.2 Modeling of Second-Order Effects Using the FVBO. Numerical experiments were carried out to investigate the behavior of FVBO under various homogeneous deformation conditions, including uniaxial tension/compression, simple shear, stress-controlled shear, and strain-controlled shear. Computations for both small and large deformations were performed. The finite element solutions were compared with experimental results for cases in which they were available. Most of the loadings employed in the calculations were monotonic and the cyclic neutral version of FVBO was used for simplicity.

Table 1 Material constant and functions used in the finite element calculations. They are akin to the behavior of Type-304 Stainless Steel at room temperature.

$E = 1.95\ \text{x}10^5$ MPa	$\nu^e = 0.3$
$E_t = 2{,}955$ MPa	$A_0 = 115$ MPa
Shape function:	
$\psi(\Gamma) = c_1 + (c_2 - c_1)\exp(-c_3\Gamma)$	
$c_1 = 7.9\ \text{x}10^4$ MPa	
$c_2 = 1.825\ \text{x}10^5$ MPa	
$c_3 = 7.83\ \text{x}10^{-2}$ MPa^{-1}	
Viscosity functions:	
$k_{\text{I}}(\Gamma) = a_1^{\text{I}}\left[1+\frac{\Gamma}{a_2^{\text{I}}}\right]^{-a_3^{\text{I}}}$	$k_{\text{II}}(\Gamma) = a_1^{\text{II}}\left[1+\frac{\Gamma}{a_2^{\text{II}}}\right]^{-a_3^{\text{II}}}$
$a_1^{\text{I}} = 3.142\ \text{x}10^5\ s$	$a_1^{\text{II}} = 161.128\ s$
$a_2^{\text{I}} = 60$ MPa	$a_2^{\text{II}} = 60$ MPa
$a_3^{\text{I}} = 21.98$	$a_3^{\text{II}} = 20.98$

4.2.1 Selection of Material Functions. Formally, FVBO differs from the version for infinitesimal strain by the introduction of the secondary inelastic rate of deformation (equations (I.6) and (I.7)) and of the modified Jaumann rate, (equation (I.25)). By setting

$$C_I = Ek_I(\Gamma) > 0 \tag{II.40}$$

with k_I being the positive, decreasing viscosity function of Yao and Krempl (1985), and selecting

$$C_{II} = \frac{E^2}{3}k_{II}(\Gamma) > 0 \tag{II.41}$$

in equation (I.7), the flow law for the inelastic rate of deformation is determined. Although the representation theorems for tensor-valued functions permit other dependences, C_I and C_{II} are assumed to depend only on Γ. With this choice different behaviors in tension and compression will be represented. To further simplify the material function selection we use the same function for both k_I and k_{II} except that the constants in k_{II} are selected to be different. (Other choices are of course possible and will be investigated in the future). By this choice, $\omega_{II}=1$ in equation (I.12).

The quantity Z of equation (I.20) is selected as

$$\mathbf{z} = \left(\frac{r_{11}}{g_e} + r_{12}\right)(\mathbf{gd} - \mathbf{dg}) \tag{II.42}$$

where $g_e = \sqrt{(3/2)\mathbf{g}\cdot\mathbf{g}}$ is the equivalent equilibrium Cauchy stress, and r_{11}, r_{12} the material constants. Other material constants and functions used in the calculations are given in Table 1. They are akin to the behavior of Type-304 Stainless Steel at room temperature.

4.2.2 Uniaxial Tension/Compression. In this case the constitutive equations reduces to

$$D_{11} = \frac{\dot{\sigma}_{11}}{E} + \frac{\sigma_{11}-G_{11}}{Ek_I(\Gamma)} + \frac{(\sigma_{11}-G_{11})^2}{E^2k_{II}(\Gamma)}, \tag{II.43}$$

$$\dot{G}_{11} = \psi D_{11} - \frac{r_e}{b}D_{11}^{in}, \tag{II.44}$$

$$\dot{F}_{11} = \frac{E_t}{1-E_t/E}D_{11}^{in}, \tag{II.45}$$

Downloaded 03 May 2010 to 171.66.16.244. Redistribution subject to ASME license or copyright; see http://www.asme.org/terms/Terms_Use.cfm

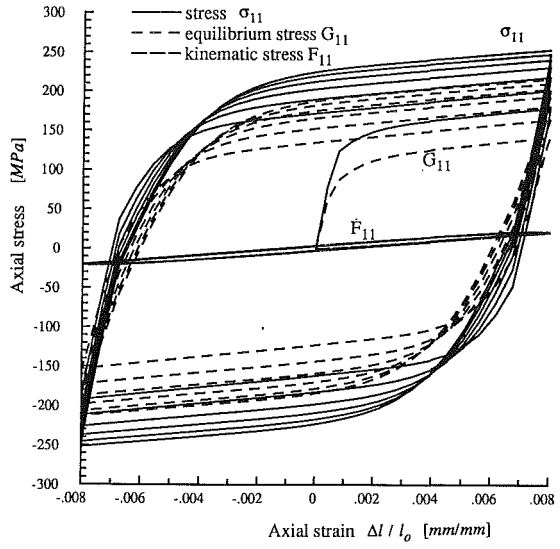


Fig. 6 Uniaxial tension/compression stress-strain curves for $D_{11} \approx |\dot{l}/l_o| = 3 \times 10^{-5}$ 1/s; the parameters B_o and C_o in equation (I.20) are equal to 2150 MPa and 10, respectively

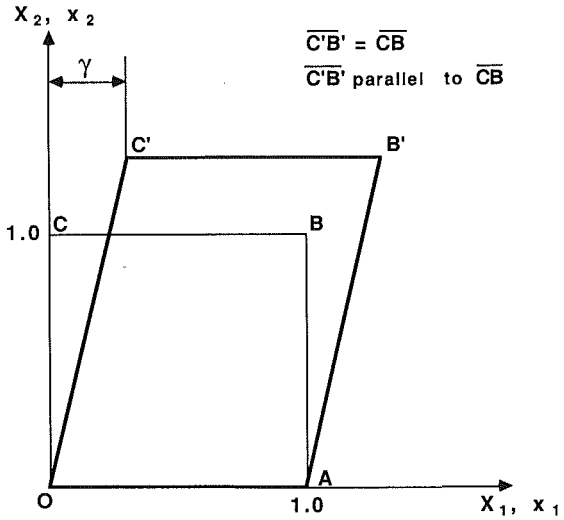


Fig. 7 Strain-controlled shear

$$\dot{A} = (B_0 - C_0 A)\dot{\phi} \tag{11.46}$$

where σ_{11} is the axial component of the Cauchy stress, and G_{11} and F_{11} are the axial components of the equilibrium Cauchy stress and the kinematic stress, respectively. These axial components are defined by $G_{11} = (3/2)g_{11}$ and $F_{11} = (3/2)f_{11}$. The symbol F_{11} used here is not related to the deformation gradient. We also note here that the material time derivative coincides with the modified Jaumann rate.

Hysteresis loops generated from the finite element solution for small strains are shown in Fig. 6. The nominal rate $D_{11} \approx \dot{l}/l_o = 3 \times 10^{-5} 1/s$ was used in the calculation. Also, the constant a_1^{II} in the material function $k_{II}(\Gamma)$ was set to $161.128s$ so that $\mathbf{d}_{II}^{in}$ becomes approximately one percent of $\mathbf{d}_I^{in}$. In addition, we employed $B_o = 2150$ MPa and $C_o = 10$ in the growth law (equation (II.46)) to represent cyclic hardening with gradual saturation. The paths for the stress, the equilibrium stress, and the kinematic stress are plotted to illustrate properties of the FVBO under cyclic loading conditions. The presence of the quadratic term in equation (II.43), which implies different behavior in tension and in compression, is not noticeable in Fig. 6. The slopes of the stress, the equilibrium stress, and the kinematic stress approach each other as the axial elongation increases and the long-time asymptotic value is nearly reached.

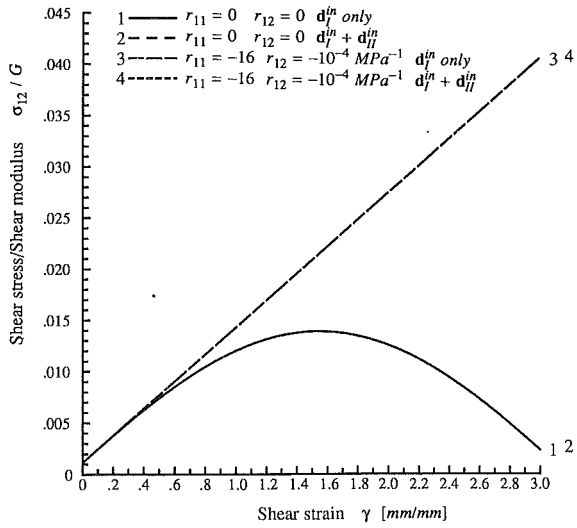


Fig. 8 Simple shear; normalized Cauchy shear stress σ_{12}/G for several values of the material constants; $\dot{\gamma} = 3 \times 10^{-5}$ 1/s

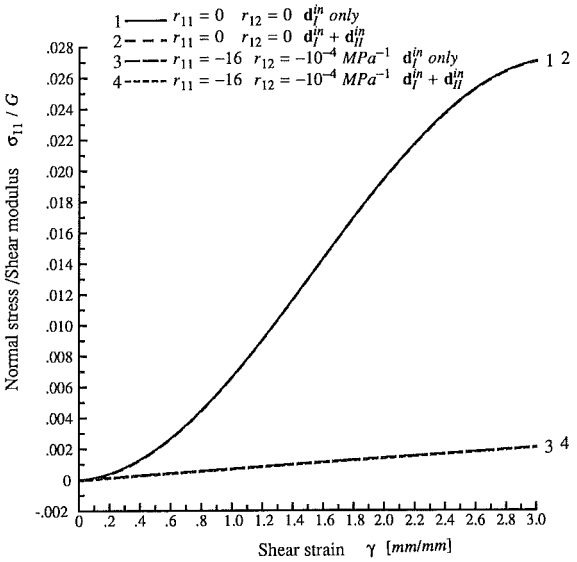


Fig. 9 Simple shear; normalized Cauchy normal stress σ_{11}/G for several values of the material constants; $\dot{\gamma} = 3 \times 10^{-5}$ 1/s

As can be seen from Fig. 6, the growth law for A causes the distance between F_{11} and G_{11} to increase to represent isotropic hardening. When E_t is set to zero the curves will ultimately be horizontal and perfectly plastic behavior is reproduced. On the other hand, a negative value of E_t would reproduce softening behavior. In regions where the stress and equilibrium stress are equal, no rate dependence of the deformation is modeled, but rather, nearly linear elastic behavior is reproduced. These regions are found around the origin and after unloading from maximum stress.

4.2.3 Shear Deformation. The properties of FVBO without isotropic hardening ($A = 0$ in (I.20)) were investigated by using the material properties given in Table 1. Of interest are the contributions of the secondary inelastic rate of deformation and of the modified Jaumann rate to the modeling of second-order effects. Comparisons with experimental results were made for small or large shear strain whenever possible. The results of the case of simple shear will be discussed first, followed by stress-controlled shear. The latter model is not very well suited to simulate experiments where the shear strain rate is imposed. For this case, the finite element constraints are modified to those shown in Fig. 7. The velocity field (equation (II.39)) still

Downloaded 03 May 2010 to 171.66.16.244. Redistribution subject to ASME license or copyright; see http://www.asme.org/terms/Terms_Use.cfm

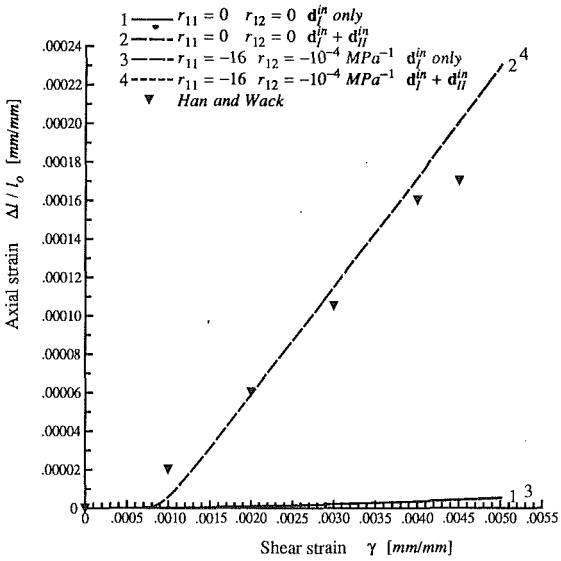


Fig. 10 Stress-controlled shear at small strains; axial elongation versus shear strain; $\dot{\sigma}_{12}=5$ MPa/s; experimental data from Han and Wack (1987) ($\dot{\gamma}=3\times10^{-5}1/s$) is also shown

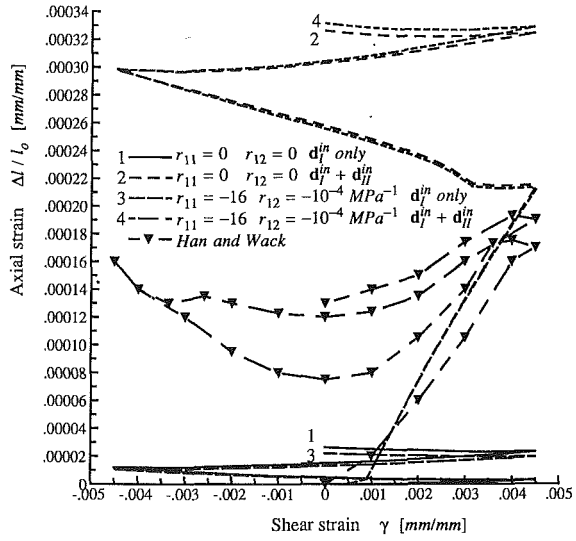


Fig. 12 Strain-controlled shear; axial elongation versus shear strain; $|\dot{\gamma}|=3\times10^{-5}1/s$; experimental data from Han and Wack (1987) ($|\dot{\gamma}|=3\times10^{-5}1/s$) is also shown

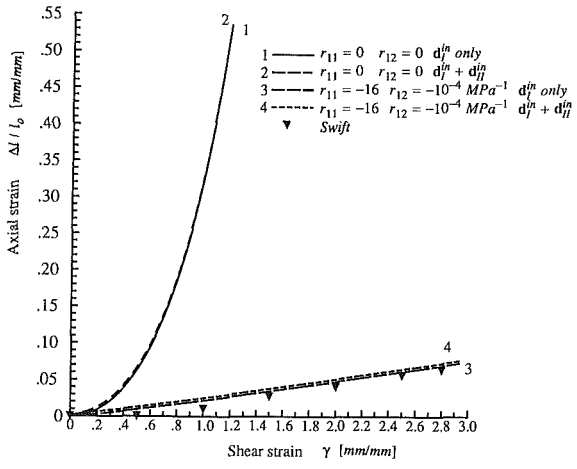


Fig. 11 Stress-controlled shear at large strains; axial elongation versus shear strain; $\dot{\sigma}_{12}=5$ MPa/s; experimental data obtained by Swift (1947) for stainless steel is also shown

applies, but with the constraints shown in Fig. 7 imposed. This model, referred to as strain-controlled shear, permits the shear strain to be prescribed in the finite element calculation for small strains.

(*i*) *Simple Shear.* The simple shear conditions described in Section 4.1 were imposed on the finite element model and a nominal strain rate $\dot{\gamma}=c=3\times10^{-5}1/s$, where c is the constant in equation (II.36), was used in the computation. The normalized Cauchy shear and normal stresses are plotted versus shear strain in Figs. 8 and 9, respectively. It is seen that the oscillation observed in the rate-independent theory (e.g., Nagetgaal and deJong (1982)) develops when the Jaumann rate is used as the objective rate whether or not $\mathbf{d}_{II}^{in}$ is included. The inclusion of the secondary inelastic rate of deformation cannot suppress the oscillation. Numerical experiments have shown that a nonzero r_{11} or r_{12} can suppress the oscillation. They also influence the magnitude of the normal stress effect. This is demonstrated for a particular value of r_{11} and r_{12}. On the graphs of Figs. 8 and 9, no influence of $\mathbf{d}_{II}^{in}$ is evident. Compared to the corresponding graphs of the hypoelastic material, Figs. 2 and 3, the magnitudes of the stresses are considerably reduced. In both cases, the modification to the Jaumann rate is responsible for the suppression of the oscillations.

(*ii*) *Stress-Controlled Shear.* Here the constraints described in equations (II.38) and (II.39) are used to simulate torsion test at small and large strains. Figure 10 shows the axial strain as a function of shear strain which does not exceed 0.5 percent. Curves 1 and 3 show that both the Jaumann rate and the modified Jaumann rate predict axial strains that are far too small compared with experiments. When the secondary inelastic rate of deformation is included, the data by Han and Wack (1987) can be reproduced. At small strains the $\mathbf{d}_{II}^{in}$-term is needed to match the data (see curves 2 and 4). At large shear strains, Fig. 11, curves 3 and 4, which contain the modified Jaumann rate, match the experimental data obtained by Swift (1947) on stainless steel. When the regular Jaumann rate is used, the axial strains predicted by the theory are much larger than those seen in experiments.

It is concluded that the secondary inelastic rate of deformation and the modifications to the Jaumann rate are necessary to match experimental data at small and large shear strains. Separate numerical experiments have been demonstrated that the variation of the constants in k_{II} and of r_{11} and r_{12} can change the magnitude of the axial strain. As an example, any curve between the curves 1, 2, and 3, 4 in Fig. 11 can be matched by the variation of these constants.

(*iii*) *Strain-Controlled Shear.* The geometric constraints of Fig. 7 were used to simulate axial strain accumulation and strain shear-cycling as reported by Han and Wack (1987). The results are shown in Fig. 12. It is seen that the curves 1 and 3 exhibit a very small axial elongation. For these curves the $\mathbf{d}_{II}^{in}$-term was omitted in the computation. Inclusion of the $\mathbf{d}_{II}^{in}$-term for curves 2 and 4 results in a reasonable agreement between experiment and theory during the *initial* loading. The results of Han and Wack (1987) exhibit a large recovery of the axial strain upon shear strain reversal which the theory cannot reproduce. For the curves obtained from the finite element calculations, no recovery occurs and this results in an overprediction of the axial elongation. Other theories, Freudenthal and Ronay (1966, Fig. 8) and Reed and Atluri (1985, p. 77), seem to have similar properties; they do not predict a large recovery of the axial strain. Other experiments should corroborate the results of Han and Wack (1987) before a serious attempt is made to reproduce the strong reversal effects.

Downloaded 03 May 2010 to 171.66.16.244. Redistribution subject to ASME license or copyright; see http://www.asme.org/terms/Terms_Use.cfm

5 Discussion

The analysis has shown that the proposed minimal modification of the infinitesimal VBO can be applied to finite deformation and to second-order effects. The numerical experiments have demonstrated that the material functions of FVBO can be adjusted to quantitatively reproducing secondary effects in the mechanical behavior of the metals and alloys. Two ingredients were necessary, the modification of the Jaumann rate and the second-order contribution to the inelastic rate of deformation, $\mathbf{d}_{II}^{in}$. It is important to note that these ingredients of finite strain theories are essential for modeling second-order effects at small and large strains. Without them no such effects can be modeled. The modification of the Jaumann rate is important for large shear strains, whereas $\mathbf{d}_{II}^{in}$ is necessary to model the observed behavior at small strains. At the present time a pure overstress dependence of the inelastic strain rate is postulated so that long-time asymptotic solutions can be achieved. Other choices are possible. As an example, $\mathbf{d}_{II}^{in}$ can be made to depend on invariants other than Γ to have significant influence at large shear strains. One possibility is the equivalent equilibrium Cauchy stress g_e used in (II.42). In this case the existence of long-time asymptotic solutions is in question. Further, the choice of the modified Jaumann rate is not unique and it is possible to choose another objective rate. Its synergisms with $\mathbf{d}_{II}^{in}$ and its use in the finite element implementation have to be investigated. If the objective rate does not introduce axial terms, then $\mathbf{d}_{II}^{in}$ will become the sole repository for modeling the second-order effects at small and large strains.

A one-step time integration method based on the forward gradient approximation has been developed and this leads to explicit expressions for the tangent operators suitable for finite element implementation. The updated Lagrangian finite element formulation of Osias and Swedlow (1974), and McMeeking and Rice (1975), was chosen for the finite element implementation since it also allows the adaptation of a small strain VBO program, Sham and Chow (1989). Also, the procedure of Rubinstein and Atluri (1983), and Mallett (1984), was employed to ensure incremental objectivity.

The single element simulation of the torsion test with axial elongation permitted has been very useful in obtaining numerical results and in studying the influence of various terms in FVBO. It facilitated the evaluation considerably. With this method global properties of the resulting set of coupled, nonlinear ordinary differential equations could not be obtained. This should be done in the future by a suitable stability analysis such as performed by Sutcu and Krempl (1989) and commonly used in analytical dynamics and nonlinear vibrations. However, the present set of equations contains nonlinear damping terms which make the usual stability analysis methods not directly applicable. It would be desirable to know, in a qualitative way, which terms in the equations cause or suppress the undesirable oscillations found in simple shear.

The experimental information on the second-order effects at small and large strains is very scarce. Additional experiments are needed to ascertain the amplitude dependence and the effect of shear strain rate or frequency on the axial strain accumulation. Of interest is also the "reversibility" of the axial strain reported by Han and Wack (1987) during torsional cycling. They are the only experiments known to the authors which report measured axial strain versus shear strain curves under cyclic loading. However, the strong reversal effects reported by Han and Wack (1987) require additional experimental corroboration before further modeling efforts be made to reproduce these effects.

Acknowledgments

Helpful discussions with E. H. Lee are appreciated. This work was performed while I. Nishiguchi was on a one-year leave of absence from Japan Atomic Energy Research Institute. The support of the Army Research Office (T.L.S.) under Contract No. DAAL03-88-K-0041 and the Department of Energy (E.K.) under Contract No. DE-FG02-86ER13566 is gratefully acknowledged.

References

Argyris, J. H., Vaz, L. E. and Willam, K. J., 1978, "Improved Solution Methods for Inelastic Rate Processes," *Computer Methods in Applied Mechanics and Engineering*, Vol. 16, pp. 231–277.

Atluri, S. N., 1984, "On Constitutive Relations at Finite Strain: Hypo-Elasticity and Elasto-Plasticity with Isotropic or Kinematic Hardening," *Computer Methods in Applied Mechanics and Engineering*, Vol. 43, pp. 137–171.

Cordts, D., and Kollmann, F. G., 1986, "An Implicit Time Integration Scheme for Inelastic Constitutive Equations With Internal State Variables," *International Journal for Numerical Methods in Engineering*, Vol. 23, pp. 533–554.

Dienes, J. K., 1979, "On the Analysis of Rotation and Stress Rate in Deforming Bodies," *Acta Mechanica*, Vol. 32, pp. 217–232.

Freudenthal, A. M., and Ronay, M., 1966, "Second Order Effects in Dissipative Media," *Proceedings of the Royal Society of London*, Vol. A292, pp. 14–50.

Han, S., and Wack, B., 1987, "Torsion Ratchet Associated with Mechanical Hysteresis," *Transactions of the 9th International Conference on Structural Mechanics in Reactor Technology, Vol. L, Inelastic Behavior of Metals and Constitutive Equations*, F. H. Wittmann, ed., A. A. Balkema, Rotterdam, pp. 421–426.

Hughes, T. J. R., and Winget, J., 1980, "Finite Rotation Effects in Numerical Integration of Rate Constitutive Equations Arising in Large-Deformation Analysis," *International Journal for Numerical Methods in Engineering*, Vol. 15, pp. 1862–1867.

Krieg, R. D., 1977, "Numerical Integration of Some New Unified Plasticity-Creep Formulations," *Transactions of the 4th International Conference on Structural Mechanics in Reactor Technology, Vol. M, Methods for Structural Analysis*, T. A. Jaeger and B. A. Boley, eds., Commission of the European Communities, Brussels, Paper No. M6/4.

Mallett, R. L., 1984, "Finite Element Formulation of the Prandtl-Reuss Constitutive Equations," *Transactions of the 2nd Army Conference on Applied Mathematics and Computing*, ARO 85-1, U.S. Army Research Office, Research Triangle Park, N.C., pp. 285–301.

McMeeking, R. M., and Rice, J. R., 1975, "Finite Element Formulations for Problems of Large Elastic-Plastic Deformation," *International Journal of Solids and Structures*, Vol. 11, pp. 606–616.

Nagetgaal, J. C. and deJong, J. E., 1982, "Some Aspects of Non-Isotropic Work-Hardening in Finite Strain Plasticity," *Plasticity of Metals at Finite Strain: Theory, Computation and Experiment*, E. H. Lee and R. L. Mallett, eds., Stanford University, Stanford, Calif., and Rensselaer Polytechnic Institute, Troy, N.Y., pp. 65–107.

Osias, J. R., and Swedlow, J. L., 1974, "Finite Elasto-Plastic Deformation—I. Theory and Numerical Examples," *International Journal of Solids and Structures*, Vol. 10, pp. 321–339.

Peirce, D., Shih, C. F., and Needleman, A. 1984, "A Tangent Modulus Method for Rate Dependent Solids," *Computers and Structures*, Vol. 18, pp. 875–887.

Reed, K. W., and Atluri, S. N., 1983, "Analysis of Large Quasistatic Deformations on Inelastic Bodies by a New Hybrid-Stress Finite Element Algorithm," *Computer Methods in Applied Mechanics and Engineering*, Vol. 39, pp. 245–295.

Reed, K. W., and Atluri, S. N., 1985, "Constitutive Modeling and Computational Implementation for Finite Strain Plasticity," *International Journal of Plasticity*, Vol. 1, pp. 63–87.

Rubinstein, R., and Atluri, S. N., 1983, "Objectivity of Incremental Constitutive Relations over Finite Time Steps in Computational Finite Deformation Analyses," *Computer Methods in Applied Mechanics and Engineering*, Vol. 36, pp. 277–290.

Sham, T.-L., and Chow, H. W., 1989, "A Finite Element Method for an Incremental Viscoplasticity Theory Based on Overstress," in *European Journal of Mechanics, A/Solids*, Vol. 8, No. 4, pp. 415–436.

Shih, C. F., Delorenzi, H. G., and Miller, A. K., 1977, "A Stable Computational Scheme for Stiff Time-Dependent Constitutive Equations," *Transactions of the 4th International Conference on Structural Mechanics in Reactor Technology, Vol. L, Inelastic Analysis of Metal Structures*, T. A. Jaeger and B. A. Boley, eds., Commission of the European Communities, Brussels, Paper No. L2/2.

Shih, C. F., and Needleman, A., 1984, "Fully Plastic Crack Problems, Part I: Solutions by a Penalty Method," ASME JOURNAL OF APPLIED MECHANICS, Vol. 51, pp. 48–56.

Sutcu, M., and Krempl, E., 1989, "A Stability Analysis of the Uniaxial Viscoplasticity Theory Based on Overstress," *Computational Mechanics*, Vol. 4, pp. 401–408.

Swift, H. W., 1947, "Length Changes in Materials under Torsional Overstrain," *Engineering*, Vol. 163, pp. 253–257.

Wack, B., 1981, "Second and Third-Order Effects in the Torsion of Circular Tubes and Rods," *Journal de Mécanique*, Vol. 20, pp. 737–787.

Downloaded 03 May 2010 to 171.66.16.244. Redistribution subject to ASME license or copyright; see http://www.asme.org/terms/Terms_Use.cfm

Weber, G., Lush, A. M., and Anand, L., 1988, "A Time Integration Procedure for a Set of Unified Elasto-Viscoplastic Constitutive Equations," *Computational Mechanics '88*, S. N. Atluri and G. Yagawa, eds., Springer-Verlag, New York, pp. 17.vi.1-17.vi.4.

Willam, K. J., 1978, "Numerical Solution of Inelastic Rate Problems," *Computers and Structures*, Vol. 8, pp. 511-531.

Yao, D., and Krempl, E., 1985, "Viscoplasticity Theory Based on Overstress: The Prediction of Monotonic and Cyclic Proportional and Nonproportional Loading Paths of an Aluminum Alloy," *International Journal of Plasticity*, Vol. 1, pp. 259-274.

Zirin, R. M., and Krempl, E., 1982, "A Finite Element Time Integration Method for the Theory of Viscoplasticity Based on Infinitesimal Total Strain," ASME *Journal of Pressure Vessel Technology*, Vol. 104, pp. 130-136.

APPENDIX

In this appendix, we shall obtain an analytical solution for the stress-controlled shearing (see Section 4.1) of a hypoelastic material using the Jaumann rate of the objective rate. This analytical solution permits us to assess the accuracy of the finite element solution obtained for this problem.

From equation (II.39), the velocity gradient is

$$\mathbf{L} = \nabla_x \mathbf{v} = \begin{bmatrix} v_{1,1} & v_{1,2} \\ 0 & v_{2,2} \end{bmatrix}. \tag{A1}$$

Using equations (II.34) and (II.38), we have

$$tr\mathbf{D} = \frac{1}{3K} tr\hat{\sigma} = \frac{1}{3k} tr\dot{\sigma} = 0. \tag{A2}$$

Since the Jaumann rate is taken as the objective rate for the special case under consideration, we can set $\mathbf{Z} = \mathbf{0}$ in equation (II.34) to obtain

$$\mathbf{D} = \mathbf{d} + \frac{1}{3}(tr\mathbf{D})\mathbf{I} = \frac{1}{2G}\hat{\sigma} = \frac{1}{2G}(\dot{\sigma} - \mathbf{W}\sigma + \sigma\mathbf{W}). \tag{A3}$$

The use of equations (II.38) and (A1) in (A3) yields

$$v_{1,1} = -\frac{h^2 t}{2G^2},\ v_{2,2} = \frac{h^2 t}{2G^2},\ v_{1,2} = \frac{h}{G}. \tag{A4}$$

Making use of $\dot{\mathbf{F}} = \mathbf{L}\mathbf{F}$, and a new variable $s = (ht)/(2G) = (\sigma_{12})/(2G)$, we find

$$\begin{bmatrix} \frac{dF_{11}}{ds} & \frac{dF_{12}}{ds} \\ \frac{dF_{21}}{ds} & \frac{dF_{22}}{ds} \end{bmatrix} = \begin{bmatrix} -2s & 2 \\ 0 & 2s \end{bmatrix} \begin{bmatrix} F_{11} & F_{12} \\ F_{21} & F_{22} \end{bmatrix}. \tag{A5}$$

The solution of equation (A5) is

$F_{11} = \exp(-s^2)$, $F_{22} = \exp(s^2)$,

$$F_{12} = 2\left(\int_0^s \exp(2x^2)dx\right)\exp(-s^2), \tag{A6}$$

with $F_{33} = 1$ and all other components of $\mathbf{F}$ being equal to zero.

Downloaded 03 May 2010 to 171.66.16.244. Redistribution subject to ASME license or copyright; see http://www.asme.org/terms/Terms_Use.cfm

An Incremental Plastic Analysis of Multiphase Materials

Y. Y. Li
Research Associate.

Y. Chen
Fellow ASME.

Department of Mechanics
and Materials Science,
Rutgers, The State University of
New Jersey,
Piscataway, NJ 08855-0909

The determination of the elastoplastic behavior of multiphase materials such as metallic alloys or steels during phase transformation is a complex problem. This incremental method is aimed at applications for composites having several phases each with different plastic behaviors and also materials undergoing phase transformation. We assume the decomposition of all strain, in the inclusion as well as in the matrix, into elastic and plastic components. Relations between various incremental stresses and strains are established through the use of the elastic moduli of the matrix and inclusions. The elastic components of the incremental stress-free strain and perturbed strain are related by an effective tangent tensor. A sample calculation was performed for a composite of epoxy matrix reinforced by silica particles. Comparisons made with experimental results existing in the literature show reasonable agreements.

1 Introduction

The determination of the elastoplastic behavior of multiphase materials such as metallic alloys or steel during phase transformation is a complex problem. Interest in the past arises from the studies of polycrystalline materials. More recently the study of composite materials has entered the domain of plastic behavior of these materials under applied load, for instance, the plastic analysis of particle-reinforced composites. Another area of interest is in the analysis of phase-transformation plasticity, which also is of recent origins.

Tandon and Weng (1988) recently gave a critical account of the mean field theories in elastoplastic analysis of multiphase materials. They pointed out that two primary lines of inquiry have been adopted in the literature; one follows the elastic constraint approach of Kröner (1961) and Budiansky and Wu (1962), and the other follows the decreasing constraint approach of Hill (1965)—both originally suggested for the study of polycrystal plasticity. At finite concentration of particles embedded in the matrix, the elastic constraint method has been developed by Tanaka and Mori (1970) and Arsenault and Taya (1987), among others. The second approach has been adopted by Hutchinson (1970) in an incremental calculation. Weng (1985) and Tandon and Weng (1988), using the secant moduli, further simplify the second approach under a monotonic proportional loading. It appears that the results of calculation of the average stress versus the average plastic strain by the elastic constraint method tend to overestimate the results as compared with the experimental data. The incremental calculation, although rigorous theoretically, is much more complex. This is due to the fact that in each incremental step an unknown anisotropic tensor needs to be be calculated by iteration. The simplified method of Tandon and Weng (1988) only applies to the case of monotonic, proportional loadings.

The basic concept of the method to be discussed in the sequel is to assume the decomposition of all strains, in the inclusions as well as in the matrix, into elastic and plastic components, and establish relations between various incremental stresses and strains through the use of the elastic moduli of the matrix and inclusions. The general method is aimed at applications to composites having several components with different plastic behavior under nonproportional or reversed loading, and also materials undergoing phase transformation.

In the next section, derivations of the basic equations will be given, followed by a numerical calculation of stress-strain curves for a two-phase material under monotonic loading to demonstrate the computational procedures. The computation for phase transformation must follow the incremental procedure, since the process progresses in time as the parent phase is gradually reduced in its volume fraction. The computation is more involved and will not be discussed here.

2 The Analysis

To begin the analysis a system of notation will be adopted. The matrix is denoted as the zeroth component, and a typical inclusion as the Nth component. All quantities associated with them will carry either a superscript or a subscript 0 for the matrix and N for the Nth inclusion, respectively. The second-rank tensors of the stress and the strain are denoted by bold characters as $\boldsymbol{\sigma}$ and $\boldsymbol{\epsilon}$. A fourth-rank tensor is represented by a capital letter. A scalar is represented by a lower case letter.

There are two types of inclusion problems. One is the transformation problem. If an inclusion which has identical elastic-

Contributed by the Applied Mechanics Division of THE AMERICAN SOCIETY OF MECHANICAL ENGINEERS for publication in the JOURNAL OF APPLIED MECHANICS.

Discussion on this paper should be addressed to the Technical Editor, Leon M. Keer, The Technological Institute, Northwestern University, Evanston, IL 60208, and will be accepted until two months after final publication of the paper itself in the JOURNAL OF APPLIED MECHANICS. Manuscript received by the ASME Applied Mechanics Division, Nov. 8, 1988; final revision, July 1, 1989.

Copyright © 1990 by ASME
Downloaded 03 May 2010 to 171.66.16.244. Redistribution subject to ASME license or copyright; see http://www.asme.org/terms/Terms_Use.cfm

plastic moduli as the matrix undergoes a stress-free strain, arising from thermal expansion, phase transformation, creep, etc., it introduces internal stresses in the inclusion and the surrounding matrix. The transformation problem is to determine the internal stresses and related quantities associated with the given stress-free strain. The second problem is the inhomogeneity problem. It is the problem in which the elastic-plastic moduli of the inclusion differ from those of the matrix, and the matrix is subjected to a uniform stress $\bar{\sigma}$ applied at a distance from the inclusion. In the homogenization procedure the inclusion is assumed to undergo a stress-free strain so that the material behavior of the inclusion is made equivalent to that of the matrix. In this latter problem if there is no applied stress, there would be no stress between the matrix and the inclusion.

In this paper all the equations are derived for the inhomogeneity problem. For the inhomogeneity problem, let a uniform traction be imposed at infinity. In the classical problem of Eshelby (1957), the inclusion is assumed to be embedded in an infinite matrix so that the perturbed stress due to the existence of the inclusion quickly dies away. The average stress in the matrix can be assumed to be the same as the applied stress. In a composite with sparsely dispersed inclusions in the matrix, the situation approaches that of the classical case. As the concentration of the inclusions increase, the average stress in the matrix, σ^0, would differ from the applied stress, $\bar{\sigma}$. This is because in the presence of inclusions the perturbed stress near the interface would not die out completely, giving rise to an average perturbed stress $\tilde{\sigma}$ in the matrix. In a multiphase material the situation is the same with reference to the influence of the concentration on the stress distribution, that is, an average perturbed stress $\tilde{\sigma}$ will be assumed to exist.

Usually a composite material is consisted of fibers or particles embedded in a matrix. For example, in a composite of epoxy and silica particles, the epoxy surrounds the silica particles even when the volume of the silica particles is larger than that of the epoxy. Therefore, physically speaking, the epoxy always serves as the matrix surrounding the particles. Also, in phase transformation the parent phase must be treated as the matrix in the same physical sense. However, in the subsequent development the model of the composite is depicted as an aggregate of M inclusions and the matrix, the volume fractions of which are denoted by c_m $(m = 0, M)$ with $\sum_0^M c_m = 1$, where M is the total number of inclusions. Also, all the subsequent summation signs Σ extend from 0 to M.

2.1 Basic Relations Based on the Elastic Moduli L_o of the Matrix—Applied $d\bar{\sigma}$. The key issue in the incremental method is to relate the various stress quantities to the elastic components of the various strain quantities through the elastic moduli L_o of the matrix and L_N of the Nth inclusion. In general, the elastic moduli are a fourth-rank tensor for anisotropic materials. For isotropic materials, the elastic moduli tensor are reduced to second-rank tensors, and can be written in the abbreviated form in terms of their hydrostatic and deviatoric components as

$$L_o = (3k_o, 2\mu_o),\ L_N = (3k_N, 2\mu_N) \tag{1}$$

where k_o and μ_o are the elastic bulk and shear moduli of the matrix, and k_N and μ_N are those of the Nth inclusion.

The incremental notation is used throughout the sequel. As explained before, the incremental average stress in the matrix $d\sigma^0$ is assumed not equal to the incremental applied stress, $d\bar{\sigma}$, but modified by an incremental average perturbed stress, $d\tilde{\sigma}$. Thus,

$$d\sigma^0 = d\bar{\sigma} + d\tilde{\sigma}. \tag{2}$$

The concept of the comparison material was introduced by Tanaka and Mori (1970) for convenience in analysis. The comparison material is assumed to have the properties of the matrix and when subjected to the incremental applied stress, $d\bar{\sigma}$, will cause an incremental strain, $d\epsilon^c$, in it, such that

$$d\epsilon^0 = d\epsilon^c + d\,\tilde{\epsilon} \tag{3}$$

where $d\,\tilde{\epsilon}$ is the incremental average perturbed strain in the matrix.

The incremental elastic component of $d\epsilon^0$ is defined as

$$d(\epsilon^0)^e = L_o^{-1} d\sigma^0 \tag{4}$$

and its plastic component as

$$d(\epsilon^0)^p = d\epsilon^0 - d(\epsilon^0)^e. \tag{5}$$

Similarly,

$$d(\tilde{\epsilon})^e = L_o^{-1} d\tilde{\sigma} \tag{6}$$

and

$$d(\tilde{\epsilon})^p = d\,\tilde{\epsilon} - d(\tilde{\epsilon})^e. \tag{7}$$

In the incremental form, we define

$$d(\epsilon^c)^e = L_o^{-1} d\bar{\sigma} \tag{8}$$

and

$$d(\epsilon^c)^p = d\epsilon^c - d(\epsilon^c)^e. \tag{9}$$

In view of equation (2),

$$L_o^{-1} d(\sigma^0) = L_o^{-1}(d\bar{\sigma} + d\tilde{\sigma}).$$

Substituting equations (4), (6), and (8) into (2), we have

$$d(\epsilon^0)^e = d(\epsilon^c)^e + d(\tilde{\epsilon})^e, \tag{10}$$

and hence

$$d(\epsilon^0)^p = d(\epsilon^c)^p + d(\tilde{\epsilon})^p. \tag{11}$$

The incremental stress and strain in the Nth component, considered as a single inclusion, are denoted by $d\sigma^N$ and $d\epsilon^N$. They each are defined by an incremental perturbed component as follows:

$$d\sigma^N = d\sigma^0 + d\sigma_N^{pt} \tag{12}$$

and

$$d\epsilon^N = d\epsilon^0 + d\epsilon_N^{pt}. \tag{13}$$

To decompose equation (13) into two equations stating the relationships between the various elastic and plastic strains, as in equations (10) and (11), one needs to proceed as follows.

The incremental stress, $d\sigma^N$, in the Nth component in terms of its elastic moduli, L_N, is given by

$$d\sigma^N = L_N[d(\epsilon^N)^e]. \tag{14}$$

Following the concept of the equivalence principle of Eshelby, we write $d\sigma^N$ in terms of the matrix elastic moduli

$$d\sigma^N = L_o[d(\epsilon^N)^e - d(\epsilon_N^*)^e], \tag{15}$$

where $d(\epsilon_N^*)^e$ is the incremental elastic component of Eshelby's equivalent stress-free strain for the Nth component. If we define

$$d\sigma_0^N = L_o d(\epsilon^N)^e, \tag{16}$$

then $d\sigma_0^N$ can be interpreted as the incremental stress in the inclusion if it were made of the matrix material under the same elastic deformation. Define next

$$d\sigma_N^* = -L_o^t d\epsilon_N^* = -L_o d(\epsilon_N^*)^e \tag{17}$$

where $d\sigma_N^*$ is the incremental stress required to restore the "transformed" inclusion under the incremental strain $d\epsilon_N^*$ back to its original shape, L_o^t being the "tangent" moduli of the matrix.

In view of equations (16) and (17), equation (15) is reduced to

$$d\sigma^N = d\sigma_0^N + d\sigma_N^*. \tag{18}$$

Downloaded 03 May 2010 to 171.66.16.244. Redistribution subject to ASME license or copyright; see http://www.asme.org/terms/Terms_Use.cfm

At the restoring stress $d\sigma_N^*$ is released, causing the perturbed incremental elastic strain $d(\epsilon_N^{pt})^e$, the perturbed stress $d\sigma_N^{pt}$ in the inclusion is the result. Therefore, the difference of these two stresses, which causes the perturbed elastic strain $d(\epsilon_N^{pt})^e$ under the constraint of the matrix, is

$$d\sigma_N^* - d\sigma_N^{pt} = -L_o d(\epsilon_N^{pt})^e. \tag{19}$$

From equation (18),

$$d\sigma_N^* = d\sigma^N - d\sigma_o^N.$$

Thus, equation (19) becomes

$$d\sigma^N - d\sigma_o^N - d\sigma_N^{pt} = -L_o d(\epsilon_N^{pt})^e,$$

but from equations (12) and (4),

$$d\sigma^N - d\sigma_N^{pt} = d\sigma^o = L_o d(\epsilon^o)^e.$$

Therefore,

$$L_o d(\epsilon^o)^e - L_o d(\epsilon^N)^e = -L_o d(\epsilon_N^{pt})^e,$$

or

$$d(\epsilon^N)^e = d(\epsilon^o)^e + d(\epsilon_N^{pt})^e. \tag{20}$$

From equation (20) it follows that

$$d(\epsilon^N)^p = d(\epsilon^o)^p + d(\epsilon_N^{pt})^p. \tag{21}$$

Thus, the intended decomposition is accomplished.

Substituting equation (20) into equation (14), the incremental stress in the Nth inclusion is expressed as

$$d\sigma^N = L_N[d(\epsilon^o)^e + d(\epsilon_N^{pt})^e]. \tag{22}$$

By the equivalence principle of Eshelby, $d\sigma^N$ can be transformed into

$$d\sigma^N = L_o[d(\epsilon^o)^e + d(\epsilon_N^{pt})^e - d(\epsilon_N^*)^e]. \tag{23}$$

Substituting equations (4) and (12) in equation (23), we obtain the relationship between the perturbed stress and strain as

$$d\sigma_N^{pt} = L_o[d(\epsilon_N^{pt})^e - d(\epsilon_N^*)^e]. \tag{24}$$

Applying Eshelby's concept to the incremental process, we note that the incremental elastic perturbed strain, $d(\epsilon_N^{pt})^e$, is related to $d(\epsilon_N^*)^e$ through the effective targent tensor, S_o.

$$d(\epsilon_N^{pt})^e = S_o^t d(\epsilon_N^*)^e \tag{25}$$

For isotropic materials, S_o^t can be decomposed into its hydrostatic and deviatoric components α_o^t and β_o^t, respectively. For a spherical inclusion in an isotropic matrix, the Eshelby's tensor of the matrix S_o^t is given by S_o^t (α_o^t, β_o^t), where

$$\alpha_o^t = \left(\frac{1}{3}\right)\left[\frac{1+\nu_o^t}{1-\nu_o^t}\right]$$

$$\beta_o^t = \left(\frac{2}{15}\right)\left[\frac{4-5\nu_o^t}{1-\nu_o^t}\right]$$

and ν_o^t is the effective Poisson's ratio of the matrix. Note that ν_o^t is calculated by iteration, i.e.,

$$\nu_o^t = \frac{1}{2} - \left(\frac{1}{2} - \nu_o\right)\frac{E_o^t}{E_o}$$

where $E_o^t = \dfrac{d(\sigma^o)^*}{d(\epsilon^o)^e + d[(\epsilon^o)^p]^*}$ and $E_o = \dfrac{d(\sigma^o)^*}{d(\epsilon^o)^e}$.

$d(\sigma^o)^*$ and $d[(\epsilon^o)^p]^*$ are the respective effective stress and plastic strain in the matrix. Also, $d(\epsilon^o)^e$ is calculated as an effective strain.

Now we will derive all stresses and strains in terms of L_o, S_o^t, $d(\epsilon_N^*)^e$, $d(\epsilon^N)^p$ and $d(\epsilon^o)^p$ in the following. From equations (21) and (25), the total incremental perturbed strain can be written as

$$d\epsilon_N^{pt} = S_o^t[d(\epsilon_N^*)^e] + [d(\epsilon^N)^p - d(\epsilon^o)^p]. \tag{26}$$

Combining equations (24) and (25) leads to

$$d\sigma_N^{pt} = L_o(S_o^t - I)d(\epsilon_N^*)^e, \tag{27}$$

where I is the unit tensor.

The incremental average stress in the composite is defined by averaging according to the linear mixture rule. Hence,

$$d\tilde{\sigma} = (d\sigma^N)_{avg} = \Sigma c_m d\sigma^m = \Sigma c_m(d\sigma^o + d\sigma_m^{pt}) = d\sigma^o + \Sigma c_m d\sigma_m^{pt}. \tag{28}$$

In view of equation (2),

$$d\tilde{\sigma} = -\Sigma c_m d\sigma_m^{pt}. \tag{29}$$

Substituting equation (27) in equation (29),

$$d\tilde{\sigma} = -L_o(S_o^t - I)\Sigma c_m d(\epsilon_m^*)^e, \tag{30}$$

since

$$d\tilde{\sigma} = L_o d(\tilde{\epsilon})^e.$$

Substituting in equation (30),

$$d(\tilde{\epsilon})^e = -(S_o^t - I)\Sigma c_m d(\epsilon_m^*)^e. \tag{31}$$

Recalling equation (2) and using equation (30) yield

$$d\sigma^o = d\tilde{\sigma} - L_o(S_o^t - I)\Sigma c_m d(\epsilon_m^*)^e \tag{32}$$

Also, from equations (12) and (27),

$$d\sigma^N = d\sigma^o + L_o(S_o^t - I)d(\epsilon_N^*)^e. \tag{33}$$

The unknown $d(\epsilon_N^*)^e$ can be solved by equating equations (22) and (23),

$$L_N[d(\epsilon^o)^e + d(\epsilon_N^{pt})^e] = L_o[d(\epsilon^o)^e + d(\epsilon_N^{pt})^e - d(\epsilon_N^*)^e]. \tag{34}$$

For isotropic materials, S_o in equation (25), L_N, and L_o in equation (34) are decomposed into their respective hydrostatic and deviatoric components. Solving equations (25) and (34) jointly, the incremental elastic components of the equivalent stress-free strain are found in terms of the elastic strains of the matrix as

$$d(\epsilon_N^*)_{kk}^e = a^* d(\epsilon_{kk}^o)^e \tag{35}$$

where

$$a^* = \frac{-1}{\alpha_o^t + \left(\dfrac{k_o}{k_N - k_o}\right)}$$

and

$$d(\epsilon_N^*)_{ij}^{e\prime} = b^* d(\epsilon_{ij}^o)^{e\prime} \tag{36}$$

where

$$b^* = \frac{-1}{\beta_o^t + \left(\dfrac{\mu_o}{\mu_N - \mu_o}\right)}.$$

To express $d(\epsilon_N^*)^e$ in terms of the stresses in the matrix, we substitute equation (4) into equations (35) and (36),

$$d(\epsilon_N^*)_{kk}^e = \frac{a^*}{3k_o} d(\sigma_{kk}^o) \tag{37}$$

and

$$d(\epsilon_N^*)_{ij}^{e\prime} = \frac{b^*}{2\mu_o} d(\sigma_{ij}^o)'. \tag{38}$$

Substituting equations (37) and (38) in equation (32) leads to the relations between $d\tilde{\sigma}$ and $d\sigma^o$,

$$d(\overline{\sigma_{kk}}) = \tilde{a}\, d(\sigma_{kk}^o), \tag{39}$$

where

$$\tilde{a} = \left[1 - \Sigma c_m \frac{(\alpha_o^t - 1)}{\alpha_o + \left(\dfrac{k_o}{k_m - k_o}\right)}\right]$$

Downloaded 03 May 2010 to 171.66.16.244. Redistribution subject to ASME license or copyright; see http://www.asme.org/terms/Terms_Use.cfm

and

$$d(\overline{\sigma_{ij}})' = \bar{b}\, d(\sigma_{ij}^o)', \tag{40}$$

where

$$\bar{b} = \left[1 - \Sigma c_m \frac{(\beta_o' - 1)}{\beta_o' + \left(\dfrac{\mu_o}{\mu_m - \mu_o}\right)} \right].$$

Substituting equations (37) and (38) in equation (33) leads to the relations between $d\boldsymbol{\sigma}^{\mathrm{N}}$ and $d\boldsymbol{\sigma}^{\mathrm{o}}$.

$$d(\sigma_{kk}^N) = a_N d(\sigma_{kk}^a) \tag{41}$$

where

$$a_N = \left[1 - \frac{(\alpha_o' - 1)}{\alpha_o' + \left(\dfrac{k_o}{k_N - k_o}\right)} \right]$$

and

$$d(\sigma_{ij}^N)' = b_N d(\sigma_{ij}^o)' \tag{42}$$

where

$$b_N = \left[1 - \frac{(\beta_o' - 1)}{\beta_o' + \left(\dfrac{\mu_o}{\mu_N - \mu_o}\right)} \right].$$

From equations (39) to (42) one can observe that the ratios of the stresses depend on the effective tangent tensor and their elastic moduli only. Therefore, when the applied stress is given, all the stresses in the matrix and the inclusions can be calculated by equations (39) to (42). Knowing the stresses, the plastic strains are calculated according to the individual stress-strain curve of the matrix and that of the inclusions.

The incremental average strain $d\bar{\boldsymbol{\epsilon}}$ of the composite can be calculated by assuming that the elastic work done by the average stress of the composite is equal to those by the local stresses of the inclusions and the matrix, i.e.,

$$W = \frac{1}{2}\int_V \overline{\sigma_{ij}(\epsilon_{ij})^e} dV = \frac{1}{2}\Sigma \int_\nu \sigma_{ij}^m (\epsilon_{ij}^m)^e d\nu \tag{43}$$

where V denotes the volume of the composite and ν, the volume of each inclusion and the matrix.

In the incremental calculations one does not, in general, need to calculate the plastic strain $d(\bar{\boldsymbol{\epsilon}})^{\mathrm{p}}$ of the composite. Occasionally, when one desires to calculate $d(\bar{\boldsymbol{\epsilon}})^{\mathrm{p}}$, even though the total average strain $d\bar{\boldsymbol{\epsilon}}$ can be calculated by the mixture rule, the same procedure cannot be used to calculate $d(\bar{\boldsymbol{\epsilon}})^{\mathrm{p}}$ due to the elastic heterogeneity (Hill, 1967).

One way to calculate $d(\bar{\boldsymbol{\epsilon}})^{\mathrm{p}}$ is based on an energy consideration as equation (43). Note that equation (43) is restricted to linear relationships between the stresses and the elastic strains since, in the incremental procedure, the incremental stresses and the incremental strains obey the linear relations. Thus, we assume that the work done during the incremental loading bears the following relationship

$$d\bar{\boldsymbol{\sigma}}\, d\bar{\boldsymbol{\epsilon}} = \Sigma c_m d\boldsymbol{\sigma}^{\mathrm{m}} d\boldsymbol{\epsilon}^{\mathrm{m}} \tag{44}$$

which can be decomposed into the hydrostatic and the deviatoric components.

$$d\overline{\sigma_{kk}} d\overline{\epsilon_u} = \Sigma c_m d\sigma_{kk}^m d\epsilon_{ll}^m \tag{45}$$

and

$$d(\overline{\sigma_{ij}})' d(\overline{\epsilon_{ij}})' = \Sigma c_m d(\sigma_{ij}^m)' d(\epsilon_{ij}^m)' \tag{46}$$

where the subscripts i and j are not summed. The relation in equation (46) shows that the work done by the average deviatoric stress $d(\overline{\sigma_{ij}})'$ in each direction is the sum of the work done by the deviatoric stresses $d(\sigma_{ij}^m)'$ of the mth constituents in the same direction. This fact is due to the proportionality between $d(\overline{\sigma_{ij}})'$ and $d(\sigma_{ij}^m)'$ as shown in equations (40) and (42). Similar relations exist between $d(\overline{\epsilon_{ij}})'$ and $d(\epsilon_{ij}^m)'$.

Then the incremental average elastic strain $d(\bar{\boldsymbol{\epsilon}})^{\mathrm{e}}$ in the composite is given by

$$d\bar{\boldsymbol{\sigma}} d(\bar{\boldsymbol{\epsilon}})^{\mathrm{e}} = \Sigma c_m d\boldsymbol{\sigma}^{\mathrm{m}} d(\boldsymbol{\epsilon}^{\mathrm{m}})^{\mathrm{e}} \tag{47}$$

or its hydrostatic and deviatoric components as

$$d\overline{\sigma_{kk}} d(\overline{\epsilon_{ll}})^e = \Sigma c_m d\sigma_{kk}^m d(\epsilon_{ll}^m)^e$$

and

$$d(\overline{\sigma_{ij}})' d(\overline{\epsilon_{ij}})^{e\prime} = \Sigma c_m d(\sigma_{ij}^m)' d(\epsilon_{ij}^m)^{e\prime}. \tag{48}$$

Subtracting equation (47) from equation (45) leads to

$$d\bar{\boldsymbol{\sigma}} d(\bar{\boldsymbol{\epsilon}})^{\mathrm{p}} = \Sigma c_m d\boldsymbol{\sigma}^{\mathrm{m}} d(\boldsymbol{\epsilon}^{\mathrm{m}})^{\mathrm{p}} \tag{49}$$

or, in its components as

$$d\overline{\sigma_{kk}} d(\overline{\epsilon_{ll}})^p = \Sigma c_m d\sigma_{kk}^m d(\epsilon_{ll}^m)^p$$

and

$$d(\overline{\sigma_{ij}})' d(\overline{\epsilon_{ij}})^{p\prime} = \Sigma c_m d(\sigma_{ij}^m)' d(\epsilon_{ij}^m)^{p\prime}. \tag{50}$$

To summarize if $d\bar{\boldsymbol{\sigma}}$ is given, one can calculate $d\boldsymbol{\sigma}^{\mathrm{o}}$ from equations (39) and (40). Knowing $d\boldsymbol{\sigma}^{\mathrm{o}}$, the following sequence of quantities can be calculated. They are: $d(\boldsymbol{\epsilon}_{\mathrm{N}}^*)^{\mathrm{e}}$ by equations (37) and (37), $d\boldsymbol{\sigma}^{\mathrm{N}}$ by equations (41) and (42), $d\boldsymbol{\sigma}_{\mathrm{N}}^{\mathrm{pt}}$ by equation (27), and $d\bar{\boldsymbol{\sigma}}$ by equation (29) or equation (30). To compute the strain components, one starts by determining $d(\boldsymbol{\epsilon}^{\mathrm{o}})^{\mathrm{p}}$ and $d(\boldsymbol{\epsilon}^{\mathrm{N}})^{\mathrm{p}}$ from their respective effective stresses and stress-strain curves. After that, a series of quantities can be computed. They are: $d\boldsymbol{\epsilon}_{\mathrm{N}}^{\mathrm{pt}}$ by equation (26), $d\boldsymbol{\epsilon}^{\mathrm{o}}$ by equations (4) and (5), $d\boldsymbol{\epsilon}^{\mathrm{N}}$ by equation (13), and $d\bar{\boldsymbol{\epsilon}}$ by equation (44). Then one can calculate the elastic and plastic average strains of the composite by equations (47) and (49), respectively.

2.2 Formulae in the Case of Applied Strain $d\bar{\boldsymbol{\epsilon}}$. Previously, the analysis was referred to an incremental applied stress $d\bar{\boldsymbol{\sigma}}$ at a large distance from the inclusion. An analysis will now be given for the case when an incremental strain $d\bar{\boldsymbol{\epsilon}}$ is applied. The incremental average stress $d\boldsymbol{\sigma}^{\mathrm{c}}$ in the comparison material caused by $d\bar{\boldsymbol{\epsilon}}$ is defined as

$$d\boldsymbol{\sigma}^{\mathrm{c}} = L_o d(\bar{\boldsymbol{\epsilon}})^{\mathrm{e}}. \tag{51}$$

Denoting the incremental stress caused by $d\boldsymbol{\epsilon}^{\mathrm{o}}$ in the matrix by $d\boldsymbol{\sigma}^{\mathrm{o}}$, the incremental average stress in the matrix can be written as

$$d\boldsymbol{\sigma}^{\mathrm{o}} = d\boldsymbol{\sigma}^{\mathrm{c}} + d\bar{\boldsymbol{\sigma}}. \tag{52}$$

The incremental strain $d\boldsymbol{\epsilon}^{\mathrm{o}}$ in the matrix is modified by the incremental average perturbed strain $d\tilde{\boldsymbol{\epsilon}}$ such that

$$d\boldsymbol{\epsilon}^{\mathrm{o}} = d\bar{\boldsymbol{\epsilon}} + d\tilde{\boldsymbol{\epsilon}}. \tag{53}$$

Substituting equations (6) and (51) in equation (52) yields

$$d\boldsymbol{\sigma}^{\mathrm{o}} = L_o[d(\bar{\boldsymbol{\epsilon}})^{\mathrm{e}} + d(\tilde{\boldsymbol{\epsilon}})^{\mathrm{e}}]. \tag{54}$$

In the case of applied strain the incremental average strain is more conveniently calculated by

$$d\bar{\boldsymbol{\epsilon}} = (d\boldsymbol{\epsilon}^{\mathrm{N}})_{\mathrm{avg}} = \Sigma c_m d\boldsymbol{\epsilon}^{\mathrm{m}} = d\boldsymbol{\epsilon}^{\mathrm{o}} + \Sigma c_m d\boldsymbol{\epsilon}_{\mathrm{m}}^{\mathrm{pt}}. \tag{55}$$

Substituting equation (53) in equation (55) and simplifying leads to

$$d\tilde{\boldsymbol{\epsilon}} = -\Sigma c_m d\boldsymbol{\epsilon}_{\mathrm{m}}^{\mathrm{pt}}. \tag{56}$$

We know equations (25), (26), (27), and (28) are applicable. By substituting equation (26), equation (56) can be reduced to

$$d\tilde{\boldsymbol{\epsilon}} = -d(\boldsymbol{\epsilon}^{\mathrm{o}})^{\mathrm{p}} - S_o' \Sigma c_m d(\boldsymbol{\epsilon}_{\mathrm{m}}^*)^{\mathrm{e}} - \Sigma c_m d(\boldsymbol{\epsilon}^{\mathrm{m}})^{\mathrm{p}}. \tag{57}$$

Downloaded 03 May 2010 to 171.66.16.244. Redistribution subject to ASME license or copyright; see http://www.asme.org/terms/Terms_Use.cfm

In this case, equations (4), (25), and (34) are applicable, and as a result the elastic components of the incremental equivalent stress-free strain $d(\epsilon_N^*)^e$ is the same as in equations (35), (36), (37), and (38).

Substituting equation (53) in equations (35) and (36), and with the aid of equation (57) yields

$$d(\epsilon_N^*)_{kk}^e = d_N d\overline{\epsilon_{kk}} - f_N \sum_{N \neq m} c_m d(\epsilon_m^*)_{kk}^e \tag{58}$$

where

$$d_N = \frac{1}{\alpha_o'(c_N - 1) - \dfrac{k_o}{k_N - k_o}}$$

$$f_N = \frac{\alpha_o'}{\alpha_o'(c_N - 1) - \dfrac{k_o}{k_N - k_o}}$$

and

$$d(\epsilon_N^*)_{ij}^{e\prime} = e_N d(\overline{\epsilon_{ij}})' - e_N \Sigma c_m d(\epsilon^m)_{ij}^p - g_N \sum_{N \neq m} c_m d(\epsilon_m^*)_{ij}^{e\prime}, \tag{59}$$

where

$$e_N = \frac{1}{\beta_o'(c_N - 1) - \dfrac{\mu_o}{\mu_N - \mu_o}}$$

$$g_N = \frac{\beta_o'}{\beta_o'(c_N - 1) - \dfrac{\mu_o}{\mu_N - \mu_o}}$$

To compute $d(\epsilon_N^*)^e$ with $d\bar{\epsilon}$ given, one can solve the system of simultaneous equations (58) and (59). One calculates $d\sigma_N^{pt}$ by equation equation (27), $d\bar{\sigma}$ by equation (28), and $d\sigma^o$ by equation (32). The plastic incremental strain $d\bar{\epsilon}^p$ of the composite can be determined as follows: The incremental average stress $d\sigma^c$ in the comparison material is obtained by the given $d\bar{\epsilon}$ from the stress-strain curve of the matrix, $d(\bar{\epsilon})^e$ is calculated by equation (47), then $d(\bar{\epsilon})^p$ is by subtracting $d(\bar{\epsilon})^e$ from $d\bar{\epsilon}$.

2.3 Stress-Strain Relations. In applying the method developed above, the stress-strain relations for each component are assumed to be given. Since the state of stress and strain for each component is usually triaxial, the effective stress σ^* and the incremental effective plastic strain $d(\epsilon^p)^*$ are related in accordance with the uniaxial σ versus ϵ^p relation. The effective stress and strain are defined in the usual way as

$$\sigma^* = \sqrt{\frac{3}{2}\sigma_{ij}'\sigma_{ij}'} \tag{60}$$

and

$$d(\epsilon^p)^* = \sqrt{\frac{2}{3} d\epsilon_{ij}^p d\epsilon_{ij}^p} \tag{61}$$

In addition, the flow rule is given by

$$d\epsilon_{ij}^p = \frac{3}{2}\frac{d(\epsilon^p)^*}{\sigma^*}\sigma_{ij}'. \tag{62}$$

For time-independent problems, the modified Ludwik equation, for example, can be used, i.e.,

$$\sigma^* = \sigma_y + h(\epsilon^{p*})^n. \tag{63}$$

In the case of time-dependent problems, it is necessary to use the incremental form of the stress-strain relation as given by

$$d\epsilon^p = d\lambda\sigma' \tag{64}$$

or

$$d(\epsilon^p)^* = \frac{2}{3} d\lambda\sigma^* \tag{65}$$

The above equations are used to represent a large class of constitutive equations, which include the classical type as well as the state variable type of viscoplastic constitutive equations.

3 A Sample Computation

To illustrate the method of analysis developed in this paper, a sample calculation was made to compare results with the experiment of Young and Beaumont (1977) as quoted in Weng (1988). This experiment was to determine the uniaxial stress-strain relation for a composite of epoxy matrix reinforced by silica particles. The silica particles are assumed to deform only elastically. Their elastic moduli are $E_1 = 73.1$ GPa and $\nu_1 = 0.18$, whereas the epoxy matrix has the elastic properties $E_o = 3.16$ GPa and $\nu_o = 0.35$. The parameters for the Ludwik equation are $\sigma_y = 75.86$ MPa, $h = 32.18$ MPa, and $n = 0.26$. Computations were performed at $c_1 = 0.0$, 0.15, 0.35, 0.42, 0.47, and 0.52, where c_1 is the fraction of the silica particles as the inclusion.

To compute the stress $\bar{\sigma}$ versus the plastic strain $\overline{\epsilon^p}$ in the composite, it is necessary to start by giving $d[(\epsilon^o)^p]^*$, the effective plastic strain of the matrix. In the computational procedure the first step is to obtain the incremental stress of the matrix $d\sigma^o$, afterwards all stresses in the composite can be calculated. To calculate the stress in the matrix from the specified $d[(\epsilon^o)^p]^*$, the deviatoric stress in the matrix is calculated first. The total effective stress $(\sigma^o)^*$ in the matrix is determined from its stress-strain curve by equations (63) or (65). Then one can obtain $d(\sigma^o)^*$ from the relation of $d(\sigma^o)^* = (\sigma^o)^* - (\sigma^o)^*_{\text{prev.}}$. Note that the ratios of the deviatoric component stresses $d(\sigma^o)'$ to the effective stress $d(\sigma^o)^*$ in the matrix, based on equation (40), are assumed to be equal to the respective ratios of $d(\bar{\sigma})'_{\text{prev.}}$ to $d(\bar{\sigma})^*_{\text{prev.}}$ of the previous step in the composite. Once the deviatoric stress components $d(\sigma^o)'$ of the matrix have been obtained, all others deviatoric quantities can be calculated by equations (38), (40), and (42) etc. Knowing the deviatoric part of the applied stress $d(\bar{\sigma})'$, the hydrostatic part of the applied stress can be calculated (for uniaxial case only). After that one can calculate all the hydrostatic stresses of the composite.

To calculate all the strains in the composite one needs first to know the plastic strain components in all the inclusions and the matrix, when the stress of the matrix $d\sigma^o$ and $d(\sigma^o)^*$ have been determined. From the stress-strain curve of the matrix the total or the incremental effective plastic strains of the matrix are obtained by equations (63) or (65), respectively, with the known total effective stress $(\sigma^o)^*$ in the matrix. The components of the plastic strain $d(\epsilon^o)^p$ in the matrix can be calculated according to the flow rule equation (62). The components of the deviatoric stress in the Nth inclusion $d(\sigma^N)'$ are calculated by equation (42) and its effective stress $d(\sigma^N)^*$ by equation (60). Then, from its stress-strain curve the total or the incremental effective plastic strains $[(\epsilon^N)^p]^*$ and $d[(\epsilon^N)^p]^*$ in the Nth inclusion follow from equation (63) or equation (65), respectively. Its components $d(\epsilon^N)^p$ are obtained using equation (62). After we have obtained $d(\epsilon_N^*)^e$, $d(\epsilon^o)^p$ and $d(\epsilon^N)^p$, the strains such as $d\epsilon_N^{pt}$ and $d\bar{\epsilon}$ can be calculated by equations (26) and (44), respectively. At this point the computational procedure has been finished.

In the following all results are pertaining to the uniaxial

Downloaded 03 May 2010 to 171.66.16.244. Redistribution subject to ASME license or copyright; see http://www.asme.org/terms/Terms_Use.cfm

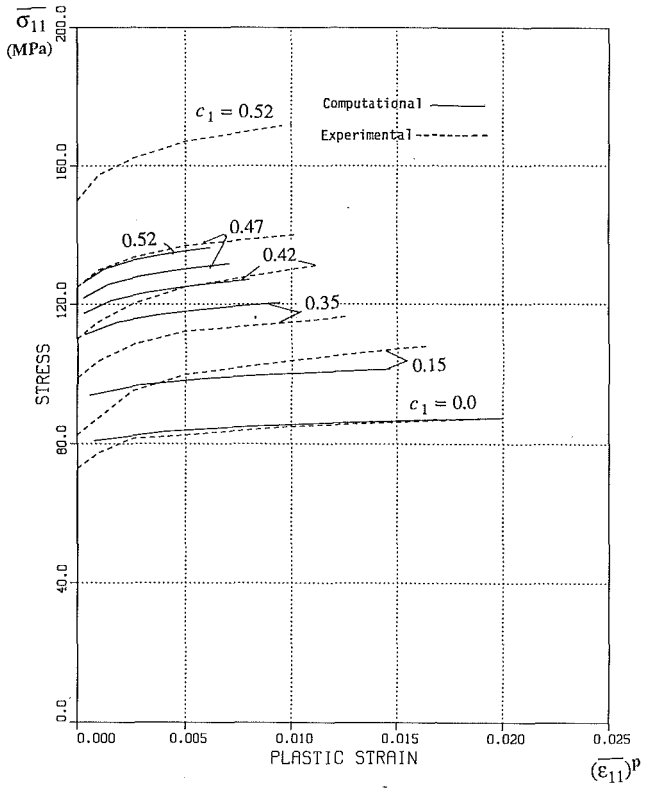


Fig. 1 Average stress versus plastic strain in composite

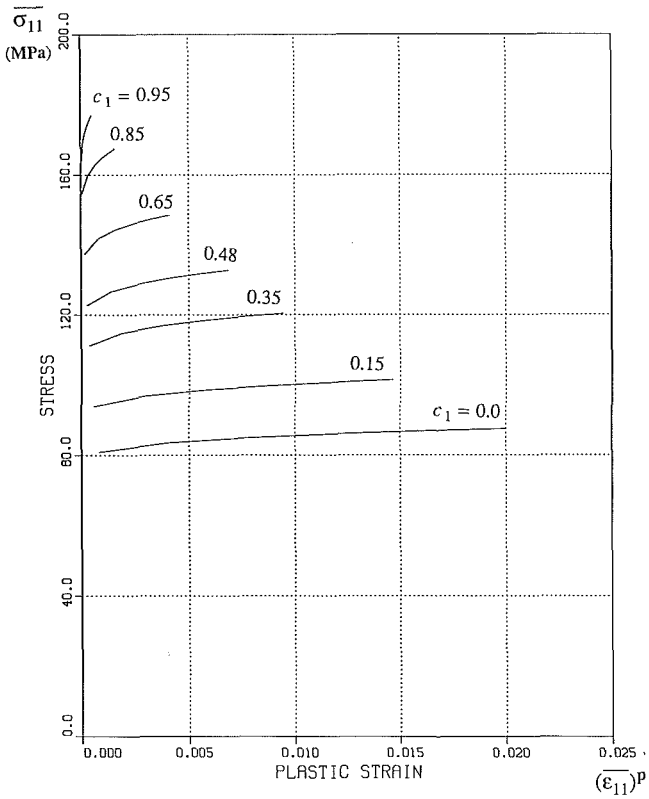


Fig. 2 Average stress versus plastic strain of silica particles/epoxy matrix composites

direction x_1. The experimental and the calculated results of the average stress and the plastic strain of the composite material are shown in Fig. 1. Dash lines are for the experimental data,

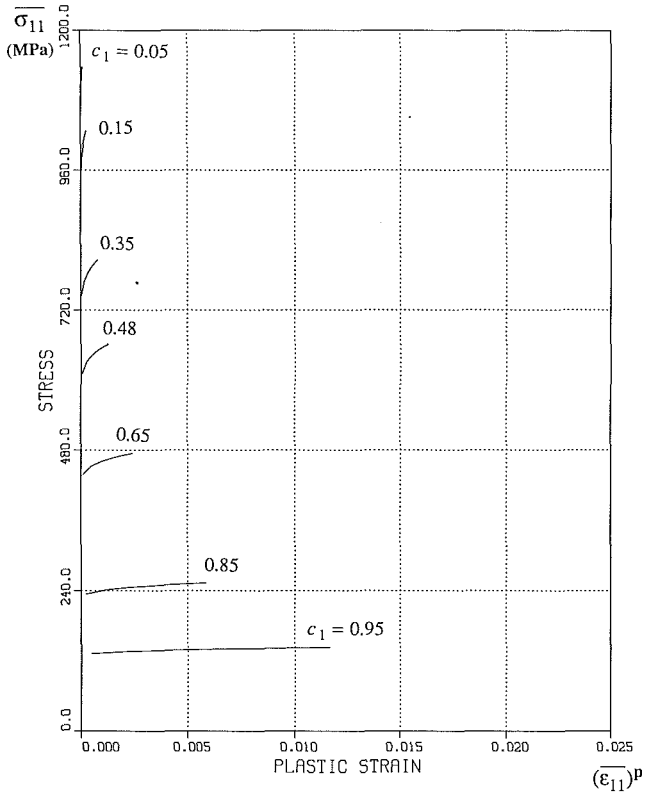


Fig. 3 Average stress versus plastic strain of epoxy particles/silica matrix composites

solid lines are for the calculated results. For the solid lines, $\tilde{\epsilon}_{11}^{p}$ is calculated by equation (49). Also, it is observed that the calculated $\overline{\sigma_{11}}$-curves of the composite appear to be lower than the experimental curves, especially for large volume fractions of the silica inclusion.

Figures 2 and 3 show the differences of the average stress and the plastic strain of the composite material for various fractions of the inclusion in two different cases. In Fig. 2 the matrix is epoxy and the inclusion is silica. In Fig. 3 we have calculated a second set of curves by reversing the roll of epoxy and silica, i.e., using silica as the matrix. As the volume fraction of silica increases, calculations show that the composite becomes stiffer and stiffer with diminishing plastic strains. It is also observed that in the same volume fraction of silica, the yield point of the composite is drastically different for the case when silica is used as the inclusion from that when it is the matrix.

4 Conclusions

A general incremental method to predict the distribution of the mean stresses and strains in a composite of several inclusions and a matrix has been developed. Good agreements were shown between the calculated results and the experimental data.

Acknowledgment

This work was partially supported by NSF DMC-84-14917. The authors wish to thank Prof. G. Weng for useful discussions during the development of this work.

Downloaded 03 May 2010 to 171.66.16.244. Redistribution subject to ASME license or copyright; see http://www.asme.org/terms/Terms_Use.cfm

References

Arsenault, R. J., and Taya, M., 1987, "Thermal Residual Stress in Metal Composite," *Acta Metallurgica*, Vol. 35, pp. 651-659.

Budiansky, B., and Wu, T. T., 1962, "Theoretical Prediction of Plastic Strains of Polycrystals," *Proceedings of the 4th U.S. National Congress of Applied Mechanics*, ASME, New York, pp. 1175-1185.

Eshelby, J. D., 1957, "The Determination of the Elastic Field of an Ellipsoidal Inclusion, and Related Problems," *Proceedings of the Royal Society, London*, Vol. A241, pp. 376-396.

Hill, R., 1965, "Continuum Micro-Mechanics of Elastoplastic Polycrystals," *J. Mech. Phys. Solids*, Vol. 13, pp. 89-101.

Hill, R., 1967, "The Essential Structure of Constitutive Laws for Metal Composites and Polycrystals," *J. Mech. Phys. Solids*, Vol. 15, pp. 79-95.

Hutchinson, J. W., 1970, "Elastic-Plastic Behavior of Polycrystalline Metals and Composites," *Proceedings of the Royal Society, London*, Vol. A319, pp. 247-272.

Kröner, E., 1961, "Zur Plastischen Verformung des Viekristalls," *Acta Metallurgica*, Vol. 9, pp. 155-161.

Tanaka, K., and Mori, T., 1970, "The Hardening of Crystlas by Non-Deforming Particles and Fibers," *Acta Metallurgica*, Vol. 18, pp. 931-941.

Tandon, G. P., and Weng, G. J., 1988, "A Theory of Particle-Reinforced Plasticity," ASME JOURNAL OF APPLIED MECHANICS, Vol. 55, pp. 126-135.

Weng, G. J., 1985, "Micromechanical Determiantion of Two-Phase Plasticity," *International Journal of Plasticity*, Vol. 1, pp. 275-287.

Weng, G. J., 1988, "Theoretical Principles for the Determination of Two Kinds of Composite Plasticity: Inclusions Plastic vs. Matrix Plastic," *Mechanics of Composite Materials*, edited by G. J. Dvorak and N. Laws, eds., AMD — Vol. 92, ASME, New York, pp. 193-208.

Young, R. J., and Beaumont, P. W. R., 1977, "Failure of Brittle Polymers to Slow Crack Growth: Part 3. Effect of Composition Upon the Fracture of Silica Particle—Filled Epoxy Resin Composites," *Journal of Materials Science*, Vol. 12, pp. 684-692.

Downloaded 03 May 2010 to 171.66.16.244. Redistribution subject to ASME license or copyright; see http://www.asme.org/terms/Terms_Use.cfm

Constraints on Moving Strong Discontinuity Surfaces in Dynamic Plane-Stress or Plane-Strain Deformations of Stable Elastic-Ideally Plastic Materials

Yinong Shen
Graduate Research Assistant.

W. J. Drugan
Associate Professor,
Assoc. Mem. ASME

Department of Engineering Mechanics,
University of Wisconsin,
Madison, WI 53706

For dynamic deformations of compressible elastic-ideally plastic materials in the practically important cases of plane stress and plane strain, we investigate the possible existence of propagating surfaces of strong discontinuity (across which components of stress, strain, or material velocity jump) within a small-displacement-gradient formulation. For each case, an explicit proof of the impossibility of such a propagating surface (except at an elastic wave speed) is achieved for isotropic materials satisfying a Huber-Mises yield condition and associated flow rule, and we show that our method of proof can be generalized to a large class of anisotropic materials. Nevertheless, we demonstrate that moving surfaces of strong discontinuity cannot be ruled out for all stable (i.e., satisfying the maximum plastic work inequality) materials, as in the case of a material whose yield surface contains a linear portion. A clear knowledge of the conditions under which dynamically propagating strong discontinuity surfaces can and cannot exist is crucial to the attainment of correct and complete solutions to such practical elastic-plastic problems as dynamic crack propagation, impact and rapidly moving load problems, high-speed forming, cutting, and other manufacturing processes.

1 Introduction

Since the monumental work of Hadamard (1903) on discontinuity surfaces in continuum mechanics, this subject has attracted the attention of many researchers in mechanics and applied mathematics. Many of the early contributions are referenced in the fine book by Courant and Friedrichs (1948), which deals mainly with nonlinear wave propagation in gas dynamics, but much of their work is also important to the study of moving strong discontinuity surfaces (i.e., shocks) in solids. Thomas (1961) and Hill (1961) extended Hadamard's (1903) work on general invariant-form compatibility conditions for discontinuity surfaces, and Hill (1961) deduced restrictions on strong discontinuities in rigid-plastic materials under quasi-static conditions. Much of the ensuing work on moving strong discontinuities in elastic-plastic solids, which usually deals with special (often one-dimensional) situations, is reviewed in Ting's (1976) paper on shock and weaker waves in elastic-plastic materials.

The significance of this knowledge about possible discontinuities lies in its necessity for constructing the solutions of boundary value problems in solid mechanics and for demonstrating the possible existence and uniqueness of such solutions. Recent interest in the moving strong discontinuity problem is partly motivated by the analysis of stress and deformation fields near a growing crack tip in elastic-ideally plastic material (see, e.g., the quasi-static crack growth analysis of Drugan and Chen (1989), and the dynamic crack growth analysis of Leighton et al. (1987)).

Drugan and Rice (1984) and Drugan (1986) developed a new direct approach for analyzing moving strong discontinuity surfaces in general three-dimensional deformations of quasi-statically deforming elastic-plastic solids. They employed a small-displacement-gradient formulation of standard weak continuum mechanical assumptions coupled with merely skeletal constitutive assumptions which are believed to describe realistically a large class of elastic-plastic materials, and which subsume many specific elastic-plastic models that are frequently employed. Among the results, they showed that the complete stress tensor must be continuous across quasi-statically moving surfaces for the general class of solids analyzed, and that jumps

Contributed by the Applied Mechanics Division of THE AMERICAN SOCIETY OF MECHANICAL ENGINEERS for publication in the JOURNAL OF APPLIED MECHANICS.

Discussion on this paper should be addressed to the Technical Editor, Leon M. Keer, The Technological Institute, Northwestern University, Evanston, IL 60208, and will be accepted until two months after final publication of the paper itself in the JOURNAL OF APPLIED MECHANICS. Manuscript received by the ASME Applied Mechanics Division, Dec. 21, 1988; final revision, July, 1, 1989.

Copyright © 1990 by ASME
Downloaded 03 May 2010 to 171.66.16.244. Redistribution subject to ASME license or copyright; see http://www.asme.org/terms/Terms_Use.cfm

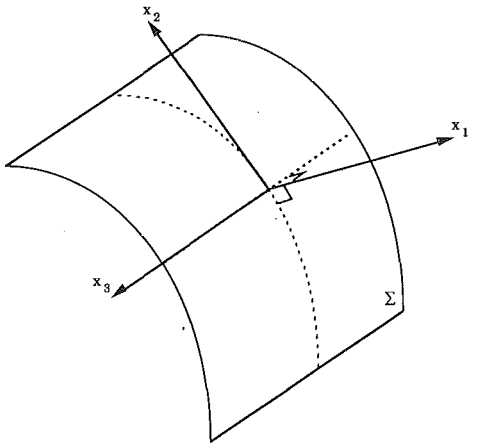


Fig. 1 Portion of a propagating strong discontinuity surface

in certain components of the strain tensor and the material velocity vector are possible only if specific conditions are met at the propagating surface. The special case of such discontinuities under quasi-static generalized plane stress was considered separately, by Pan (1982) and Narasimhan and Rosakis (1987).

Drugan and Shen (1987) deduced restrictions on *dynamically* propagating surfaces of strong discontinuity in very general elastic-plastic materials by generalizing the analyses of Drugan and Rice (1984) and Drugan (1986). In that paper, we derived one condition on jumps (termed here "Condition 1") by integrating the maximum plastic work inequality along an arbitrary portion of the deformation path across a hypothetical moving discontinuity surface, and another condition (termed here "Condition 2") by seeking nontrivial solutions of the incremental stress-strain equations across a moving discontinuity (valid for materials with smooth yield surfaces). By first analyzing shock waves that produce no plastic straining, we proved that if a shock is to propagate at a speed other than an elastic wave speed, the yield condition must be satisfied *throughout* the stress path across the shock (this requirement also applies to Condition 2). Thus, a necessary condition for the existence of an elastic-plastic shock wave (moving strong discontinuity accompanied by plastic strain variation) results by requiring that any path in stress space experienced by a material point during shock passage satisfy all the restrictions just summarized (i.e., Conditions 1 and 2, and the yield condition). In addition to deriving these general restrictions on discontinuities in arbitrary three-dimensional deformations, Drugan and Shen (1987) were able to employ Condition 1 (their Equation (3.30)) together with the yield condition to *rule out* moving strong discontinuities that propagate at speeds other than an elastic wave speed for the special cases of antiplane strain and incompressible plane-strain deformations of materials whose yield surfaces do not contain linear segments. Materials whose yield surfaces do have linear portions, such as ductile single crystals, were found to permit elastic-plastic shock waves under certain specific conditions. These results have already found practical application in the analysis of dynamic antiplane shear crack growth in elastic-ideally plastic single crystals by Nikolic and Rice (1988), who showed that a solution for the stress and deformation fields near a crack tip under such conditions must contain elastic-plastic shocks whose behavior is circumscribed by the Drugan and Shen (1987) conditions. Further confirmation of the aforementioned quasi-static and dynamic small-displacement-gradient discontinuity analyses is provided by the very recent, rigorous *finite deformation* discontinuity analysis of Drugan and Shen (1990).

Because Condition 2 (Equation (4.12) of Drugan and Shen, 1987) is not utilized in analyzing the special cases of antiplane-strain and incompressible plane-strain deformations, a natural question is whether that relation is independent of the other restrictions employed. If the answer is affirmative, that relation becomes yet another restriction on possible strong discontinuity waves, which should then allow us to rule out such waves in more general deformations.

In the present work, we apply the general discontinuity restrictions derived in Drugan and Shen (1987) to analyze the practically important cases of plane-stress and plane-strain deformations of compressible materials, within a small-displacement-gradient formulation. It is very difficult to assess the independence of these restrictions for a general material, but we do show that they are not naturally dependent on one another. We shall prove independence of these restrictions (thereby ruling out strong discontinuity surfaces moving at other than elastic wave speeds) first for isotropic materials with a Huber-Mises yield condition and associated flow rule, and then for certain classes of more general materials. We shall also further discuss the special cases of antiplane-strain and incompressible plane-strain analyzed by Drugan and Shen (1987).

With reference to Fig. 1, let Σ be a portion of a regular surface of strong discontinuity that moves with speed $V>0$ in its normal direction. A Cartesian coordinate system x_1, x_2, x_3 moves with the surface and is oriented so that x_1 is in the direction of the normal while x_3 is perpendicular to *the plane* of "plane stress" or "plane strain." $\mathbf{u}$, $\boldsymbol{\epsilon}$, and $\boldsymbol{\sigma}$ denote the tensors of displacement, strain and stress, respectively. Values of a tensorial field quantity, say $\mathbf{g}(x_1, x_2, x_3, t)$ where t is time, directly ahead of and directly behind the moving surface Σ will be denoted as $\mathbf{g}^{\pm} \equiv \lim_{\mu \downarrow 0} \mathbf{g}(x_1, x_2, x_3, t_a \mp \mu)$, respectively, where t_a is the time at which Σ arrives at a particular material point. The jump in such a field quantity across Σ will be denoted as $[\![\mathbf{g}]\!] \equiv \mathbf{g}^+ - \mathbf{g}^-$. In the sequel, components of tensors with respect to the Cartesian coordinate system of Fig. 1 are indicated either by the Roman indices i,j,k,l which have range 1,2,3 or by the Greek indices $\alpha,\beta,\gamma,\delta$ which have range 1,2 only; both types of index follow the summation convention.

2 Plane-Stress Case

The plane-stress case is very special. Because of the approximation implied in the concept of generalized plane stress, there is a possibility of "necking," i.e., a jump in u_3 and hence $[\![\epsilon_{33}]\!] = 0$ may *not* be true (Hill, 1952; Pan, 1982). By "generalized plane stress" is meant the assumptions that the field quantities $\mathbf{u}$, $\boldsymbol{\epsilon}$, $\boldsymbol{\sigma}$ represent thickness averages, and that $\sigma_{3i} \equiv 0$. For a thin sheet of material suitable for this type of description, in-plane components of stress and strain are assumed to be related by the constitutive equation

$$d\epsilon_{\alpha\beta} = d\epsilon^e_{\alpha\beta} + d\epsilon^p_{\alpha\beta} = M_{\alpha\beta\gamma\delta} d\sigma_{\gamma\delta} + d\Lambda \frac{\partial f}{\partial \sigma_{\alpha\beta}}, \tag{1}$$

where $\mathbf{M}$ is the (constant) elastic modulus tensor, assumed to be positive definite and to possess the usual symmetries, $f(\boldsymbol{\sigma}) = 0$ is the yield condition, $d\Lambda \geq 0$ is an unspecified parameter for the nonhardening materials to be considered, and superscripts e and p denote elastic and plastic part, respectively. Of course, we have assumed a smooth yield surface.

The physical requirement of finite total plastic work in any finite subregion of the body traversed by Σ demands continuity of the in-plane components of displacement, u_α. Assuming that $\partial u_\alpha / \partial x_\beta$ exist in a neighborhood of Σ and tend to finite limits as Σ is approached, a special result of Hadamard's (1903) lemma, known as Maxwell's (1873) theorem, is the compatibility requirement

$$[\![\partial u_\alpha / \partial x_2]\!] = 0. \tag{2}$$

(Recall that x_2 is the in-plane coordinate directed parallel to

Downloaded 03 May 2010 to 171.66.16.244. Redistribution subject to ASME license or copyright; see http://www.asme.org/terms/Terms_Use.cfm

Σ.) Since Σ is moving, continuity of u_α leads also to Hadamard's (1903) kinematical condition of compatibility

$$[\![v_\alpha]\!] = -V[\![\partial u_\alpha/\partial x_1]\!]. \tag{3}$$

In terms of the infinitesimal strain tensor, $\epsilon_{ij} \equiv \frac{1}{2}(\partial u_i/\partial x_j + \partial u_j/\partial x_i)$, equation (2) and equation (3) require

$$[\![v_1]\!] = -V[\![\epsilon_{11}]\!],\ [\![v_2]\!] = -2V[\![\epsilon_{12}]\!],\ [\![\epsilon_{22}]\!] = 0. \tag{4}$$

The conservation of linear and angular momentum requires (Kotchine, 1926)

$$[\![\sigma_{1\alpha}]\!] = -\rho V[\![v_\alpha]\!], \tag{5}$$

where ρ is the material density, which is treated as continuous within the small-displacement-gradient formulation, as is V, so that conservation of mass is identically satisfied. Since we employ a purely mechanical constitutive theory, the conservation of energy provides no useful additional jump restriction.

It will prove convenient to combine equations (4) and (5) as

$$[\![\epsilon_{11}]\!] = \frac{1}{\rho V^2}[\![\sigma_{11}]\!],\ [\![\epsilon_{12}]\!] = \frac{1}{2\rho V^2}[\![\sigma_{12}]\!],\ [\![\epsilon_{22}]\!] = 0. \tag{6}$$

As argued in Drugan and Shen (1987), a purely mechanical description of shock waves requires equation (6) to be true for any subdivision of the shock transition zone, which leads to

$$d\epsilon_{11} = \frac{1}{\rho V^2}d\sigma_{11},\ d\epsilon_{12} = \frac{1}{2\rho V^2}d\sigma_{12},\ d\epsilon_{22} = 0. \tag{7}$$

These equations must be satisfied throughout the stress and strain paths experienced by a material point during shock passage.

Before analyzing a shock that produces plastic straining, we first investigate the case in which the stresses remain below yield across the shock, and hence $d\Lambda = 0$. Substituting equation (7) into equation (1) in this case, we must have for nonzero $d\sigma_{\alpha\beta}$ (clearly a necessity for nonzero $[\![\sigma_{\alpha\beta}]\!]$)

$$\det\begin{bmatrix} \left(M_{1111} - \frac{1}{\rho V^2}\right) & M_{1122} & 2M_{1112} \\ M_{2211} & M_{2222} & 2M_{2212} \\ M_{1211} & M_{1222} & \left(2M_{1212} - \frac{1}{2\rho V^2}\right) \end{bmatrix} = 0 \tag{8}$$

which can be used to determine the elastic strong discontinuity wave speeds. We will show that these speeds may differ from those for the three-dimensional case, due to our assumption of plane stress.

When plastic deformation accrues during shock passage, Drugan and Shen (1987) proved that the entire stress path across the shock must remain at yield. (This is easily seen here by observing that equation (8) permits purely elastic stress changes only when V equals an elastic wave speed.) For plane stress of elastic-ideally plastic material, the yield condition has the form

$$f(\sigma_{11}, \sigma_{22}, \sigma_{12}) = 0 \tag{9}$$

(assumed to depend symmetrically on σ_{12} and σ_{21}). Combining equations (1), (7), and the yield condition (9) in differential form (Prager's consistency condition) gives

$$\begin{bmatrix} \left(M_{1111} - \frac{1}{\rho V^2}\right) & M_{1122} & 2M_{1112} & \frac{\partial f}{\partial \sigma_{11}} \\ M_{2211} & M_{2222} & 2M_{2212} & \frac{\partial f}{\partial \sigma_{22}} \\ M_{1211} & M_{1222} & \left(2M_{1212} - \frac{1}{2\rho V^2}\right) & \frac{\partial f}{\partial \sigma_{12}} \\ \frac{\partial f}{\partial \sigma_{11}} & \frac{\partial f}{\partial \sigma_{22}} & 2\frac{\partial f}{\partial \sigma_{12}} & 0 \end{bmatrix} \begin{bmatrix} d\sigma_{11} \\ d\sigma_{22} \\ d\sigma_{12} \\ d\Lambda \end{bmatrix}$$

$$\equiv [\mathbf{K}][d\mathbf{S}] = \mathbf{0}, \tag{10}$$

where this equation serves to define the matrix $\mathbf{K}$ and the vector $d\mathbf{S}$.

Thus, a necessary condition for an elastic-plastic shock to exist takes the form

$$\det(\mathbf{K}) = 0. \tag{11}$$

This equation, although it might be identified as the aforementioned Condition 2, cannot be directly deduced from equation (4.12) of Drugan and Shen (1987) because $d\epsilon_{33}$ is always required to be zero across shocks in that (general three-dimensional) derivation. As mentioned in Section 1, like the yield condition, equation (11) is to be satisfied throughout the passage of the shock since we are discussing a shock propagating at a speed V different from the elastic wave speeds. Observe that since equation (11) effectively requires an elastic-plastic shock to propagate at a plastic wave speed, the usual shock stability condition is identically satisfied.

There are two other conditions restricting the existence of elastic-plastic shock waves: one is the undifferentiated form of the yield condition, equation (9); the other is the plane-stress version of the aforementioned Condition 1. This condition is obtained by integrating the maximum plastic work inequality along any part of any admissible deformation path (one along which all governing equations are satisfied) across a hypothetical moving strong discontinuity surface:

$$\int_{\epsilon^{p+}}^{\epsilon^{p}} (\sigma_{ij} - \sigma_{ij}^o)d\epsilon_{ij}^p \geq 0. \tag{12}$$

Here, ϵ^p represents any value of the plastic strain on an admissible path between ϵ^{p+} and ϵ^{p-}, and σ^o is any fixed stress state that is at or below yield. Equation (12) can be explicitly evaluated by employing $\sigma_{3i} \equiv \sigma_{3i}^o \equiv 0$, the first equation of equation (1), the elastic part of the second equation of equation (1), and equation (7), in the manner illustrated in Drugan and Shen (1987). Doing this for the choices $\sigma^o \equiv \sigma^+$ and $\sigma^o \equiv \sigma$ (the σ – value corresponding to ϵ^p, the endpoint of integration in equation (12)), the resulting restriction is

$$<\sigma_{1\alpha}><\sigma_{1\alpha}> - \rho V^2 <\sigma_{\alpha\beta}> M_{\alpha\beta\gamma\delta} <\sigma_{\delta\gamma}> = 0 \tag{13}$$

where $<\mathbf{g}> \equiv \mathbf{g} - \mathbf{g}^+$, and here $\mathbf{g}$ represents any $\mathbf{g}$-value on an admissible path between $\mathbf{g}^+$ and $\mathbf{g}^-$.

In most cases, the stresses under restrictions of equations (9) and (11) cannot satisfy equation (13) unless $<\boldsymbol{\sigma}> = \mathbf{0}$, i.e., when there are no stress jumps. That is to say, equations (9), (11), and (13) are mutually independent except on some isolated points in $(\sigma_{11}, \sigma_{22}, \sigma_{12})$ space. Geometrically, the surfaces defined by these three equations in $(\sigma_{11}, \sigma_{22}, \sigma_{12})$ space cannot share a common intersecting curve from $\boldsymbol{\sigma}^+$ to $\boldsymbol{\sigma}^-$ that would facilitate a strong discontinuity. This independence can be explained by noting that the plastic part of equation (11) corresponds to the normality rule resulting from the maximum plastic work inequality (increments of plastic strain are normal to the yield surface), a local property of the material, while equation (13) is a result of integration along a finite path in stress space, a global property of the material during shock transition. Another form of equation (13) is $<\boldsymbol{\sigma}> : <\boldsymbol{\epsilon}^p> = 0$ which can be easily derived. Although in deriving equation

Downloaded 03 May 2010 to 171.66.16.244. Redistribution subject to ASME license or copyright; see http://www.asme.org/terms/Terms_Use.cfm

(11) we have employed the differential form of equation (13) ($d\sigma:d\epsilon^p=0$) and that of equation (9) ($df=0$), equation (11) replaces neither (9) nor (13) because neither one can be simply reverted to its original form via (10).

Actually proving the independence of equations (9), (11), and (13) is very difficult (if possible at all) for a general material. Our approach will be to prove this first for isotropic elastic-ideally plastic materials with a Huber-Mises yield condition; although this seems to be the simplest case possible, it is also very important because most theoretical solutions for the plane-stress case are for this material model. We will then show how our proof can be generalized to include certain classes of material anisotropy.

When the material is isotropic, the elastic moduli are

$$M_{ijkl}=\frac{1}{4G}(\delta_{ik}\delta_{jl}+\delta_{il}\delta_{jk})-\frac{\lambda}{2G(2G+3\lambda)}\delta_{ij}\delta_{kl} \tag{14}$$

where G and λ are the Lamé elastic constants and δ_{ij} is the Kronecker delta.

The Huber-Mises yield condition in the plane-stress case is

$$f\equiv\frac{1}{3}(\sigma_{11}^2+\sigma_{22}^2-\sigma_{11}\sigma_{22})+\frac{1}{2}(\sigma_{12}^2+\sigma_{21}^2)-k^2=0, \tag{15}$$

where k is the yield stress in shear.

When there is no plastic straining across a moving shock, equation (8) can be used to calculate the elastic shock wave speeds. For isotropic materials, two such speeds result:

$$V^2=\frac{G}{\rho},\ \text{or}\ V^2=\frac{4G(G+\lambda)}{\rho(2G+\lambda)}. \tag{16}$$

Here the dilatant shock wave speed differs from the value for general three-dimensional deformations $\left(\sqrt{(2G+\lambda)/\rho}\right)$ because of the aforementioned reason that $d\epsilon_{33}$ is allowed to be nonzero across the shock.

When the yield condition equation (15) is continuously satisfied across a moving shock (as Drugan and Shen (1987) showed it must be for a shock to propagate at any speed other than an elastic wave speed), equation (11) applies, and can be expanded to give:

$$\left(\frac{1}{G}-\frac{1}{\rho V^2}\right)\left\{\left[\frac{1}{\rho V^2}-\frac{(5G+3\lambda)}{G(2G+3\lambda)}\right]\sigma_{11}^2+\left[\frac{4}{\rho V^2}-\frac{(5G+3\lambda)}{G(2G+3\lambda)}\right]\sigma_{22}^2+\left[-\frac{4}{\rho V^2}+\frac{(8G+3\lambda)}{G(2G+3\lambda)}\right]\sigma_{11}\sigma_{22}\right\}$$
$$-\frac{36}{G(2G+3\lambda)}\left(\frac{2G+\lambda}{4G}-\frac{G+\lambda}{\rho V^2}\right)\sigma_{12}^2=0. \tag{17}$$

Another condition is equation (13), which for an isotropic material becomes

$$\left[1-\frac{\rho V^2(G+\lambda)}{G(2G+3\lambda)}\right]<\sigma_{11}>^2+\frac{\rho V^2\lambda}{G(2G+3\lambda)}<\sigma_{11}><\sigma_{22}>$$
$$-\frac{\rho V^2(G+\lambda)}{G(2G+3\lambda)}<\sigma_{22}>^2+\left(1-\frac{\rho V^2}{G}\right)<\sigma_{12}>^2=0. \tag{18}$$

In the stress space of σ_{11}, σ_{22}, and σ_{12}, as shown in Fig. 2 (for simplicity, equation (18), which depicts a cone centered at a point on (15), is not drawn in the figure), (15) represents an ellipsoid, and (17) is a cone (unless V is one of the elastic wave speeds given in (16), in which case it degenerates into a pair of planes). It can be easily proved that when the propagation speed V is smaller than the elastic wave speeds, the axis of the cone lies in the $\sigma_{11}-\sigma_{22}$ plane. (In fact, this is true as long as V is smaller than the dilatant elastic wave speed; if V is greater than that speed, equation (18) can only be satisified by zero stress jumps.) The intersection of (15) and (17) is two closed curves; we can see from these equations (or Fig. 2) that

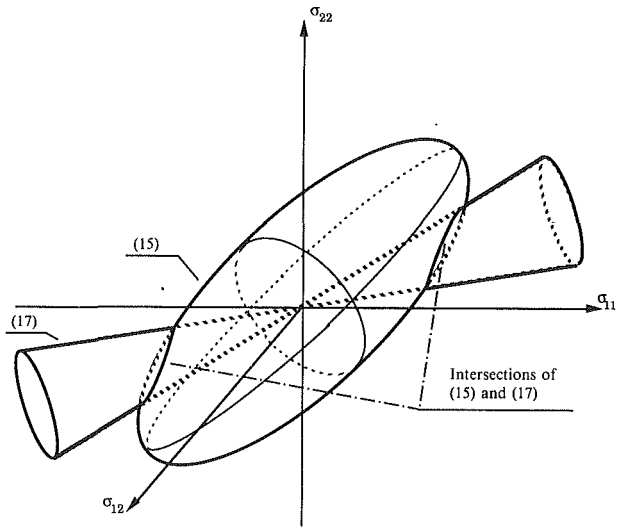


Fig. 2 Intersection of the surfaces representing two of the trans-shock stress path restrictions for the plane-stress case

if (σ_{11}, σ_{22}, σ_{12}) is on one of the curves, then (σ_{11}, σ_{22}, $-\sigma_{12}$) must fall on the same curve. Thus, if one of the curves falls on the surface described by (18), the curve should include (σ_{11}, σ_{22}, σ_{12}) and (σ_{11}, σ_{22}, $-\sigma_{12}$) simultaneously. This means that if equation (18) passes through one of these critical curves then (18), with $-\sigma_{12}$ substituted for σ_{12}, should pass through the same curve. Since both equations from (18) (with σ_{12} or $-\sigma_{12}$) pass through that curve, any linear combination of these two different versions of (18) passes through the same curve. Subtracting these two versions gives

$$\left(1-\frac{\rho V^2}{G}\right)\sigma_{12}^{+}\sigma_{12}=0, \tag{19}$$

which applies for all states σ_{12} (including $\sigma_{12}=\sigma_{12}^{+}$) on an admissible path from σ_{12}^{+} to σ_{12}^{-}.

We have already assumed $\rho V^2\neq G$; thus, for a shock to exist equation (19) requires $\sigma_{12}=0$. (If $\sigma_{12}^{+}=0$ and there is some $\sigma_{12}\neq 0$ on the path from σ^{+} to σ^{-}, we may choose that σ_{12} as a new σ_{12}^{+} and start from there to get $\sigma_{12}=0$, then $\sigma_{12}^{+}=0$ by continuity, showing $\sigma_{12}=0$ in this case as well.) That is, the curve of intersection between equations (15) and (17) must lie on the $\sigma_{11}-\sigma_{22}$ plane, which is impossible unless either the curve degenerates to a point, which means no stress changes are possible; or $\sigma_{12}\equiv\sigma_{12}^{+}\equiv 0$, which also leads to no possible stress changes because then equations (15) and (17) can only be satisfied by constant σ_{11} and σ_{22}.

Therefore, we have proved that there is no common intersecting curve for the three surfaces of equations (15), (17), (18), and hence that there is no stress path that can be followed to produce an *elastic-plastic* stress jump across a propagating surface in the material.

One question that may arise is: could equation (18) pass through a *part* of a curve of intersection of (15) and (17)? This would require that at some points (at least those points at which the curve and the surface begin to separate) the tangential direction of the curve or the normal direction of the surface or their derivatives are discontinuous. This is impossible for the nice equations (15), (17), and (18) (with the exception of the vertices of the cones, but evidently the center of (17) does not lie on (15)).

We have proved that there can be no elastic-plastic shock waves in a material satisfying the Huber-Mises yield condition and associated flow rule, but the possibility of shock waves in the plane-stress case cannot generally be ruled out. In fact, for a yield condition with a linear portion (possible for a single crystal, for example), it is easy to show that an elastic-plastic shock wave is possible. When the yield condition equation (9)

Downloaded 03 May 2010 to 171.66.16.244. Redistribution subject to ASME license or copyright; see http://www.asme.org/terms/Terms_Use.cfm

has a linear portion in (σ_{11}, σ_{22}, σ_{12}) space, (11) becomes an equation involving the coefficients of the stresses in equation (9), while equation (13) remains unchanged. In most situations, equations (9) and (13) intersect on a curve in (σ_{11}, σ_{22}, σ_{12}) space; equation (11) merely specifies the possible elastic-plastic shock speeds in terms of the coefficients in equation (9), the elastic moduli, and the material density.

It should be pointed out that for a shock wave to exist at one of the permissible speeds derived above, it is necessary that there be a jump in ϵ_{33}, i.e., necking must occur and move with the shock wave to be compatible with the plane stress requirement that $\sigma_{33} \equiv 0$. If there is no necking present, the problem becomes much easier.

When there is no necking present, in addition to the equations we have discussed ((9), (11), and (13) or their simpler forms when there is no plastic straining during shock passage), we can use restrictions involving ϵ_{33} to eliminate shock waves for most plane-stress cases. One such restriction is the plastic incompressibility condition which is true for most of the materials under discussion, and can be expressed as (Drugan and Shen, 1987)

$$<\sigma_{11}> - \rho V^2 M_{jj\gamma\delta} <\sigma_{\gamma\delta}> = 0 \tag{20}$$

where here we have only three nonzero stresses. This equation can be rewritten as

$$[1 - \rho V^2(M_{1111} + M_{2211} + M_{3311})] <\sigma_{11}> - \rho V^2 (M_{1122} + M_{2222} + M_{3322}) <\sigma_{22}> - 2\rho V^2 (M_{1112} + M_{2212} + M_{3312}) <\sigma_{12}> = 0 \tag{21}$$

which is a linear relation between σ_{11}, σ_{22}, and σ_{12}. When equation (21) is substituted into (13), the latter takes the form

$$A <\sigma_{22}>^2 + B <\sigma_{22}> <\sigma_{12}> + C <\sigma_{12}>^2 = 0 \tag{22}$$

where A, B, C are constants whose complicated forms are omitted here. Now, all the restrictions imposed by equations (13) and (21) are maintained by enforcing (22) and (21). Equation (22) requires σ_{22} to be linear in σ_{12}. As we reviewed earlier, the yield condition (equation (9)) must be satisfied throughout the shock transition. Thus, linearity of equations (21) and (22) requires that $< \boldsymbol{\sigma} > = \mathbf{0}$ unless (9) contains a straight-line segment in stress space that is representable by some combination of (21) and (22). *The conclusion is that except for this special situation, dynamic plane-stress deformation of elastic-ideally plastic solids cannot sustain propagating shocks unless they move at an elastic wave speed or they move with a neck for which equations (9), (11), and (13) happen to have a common intersection on a continuous set of points.* It should be pointed out that equation (11) does not provide an additional restriction if the yield condition is the linear surface defined by equations (21) and (22) in stress space.

3 Plane-Strain Case

The plane-strain case is more complicated. Drugan and Shen (1987) considered it for fully incompressible materials; here, we treat the more general situation involving elastic compressibility. All the restrictions derived in the general *three-dimensional* analysis of Drugan and Shen (1987) apply here, but the restrictions now involve only four nonzero stress components: σ_{11}, σ_{22}, σ_{33}, and σ_{12}, since $\sigma_{13} \equiv \sigma_{23} \equiv 0$ by assuming symmetry of the material and deformation about all planes $x_3 =$ constant. These restrictions are:

(a) yield condition:

$$f(\sigma_{11}, \sigma_{22}, \sigma_{33}, \sigma_{12}) = 0 \tag{23}$$

(assumed to depend symmetrically on σ_{12} and σ_{21});

(b) plastic incompressibility:

$$<\sigma_{11}> - \rho V^2 M_{jjkl} <\sigma_{kl}> = 0; \tag{24}$$

(c) Condition 1 (as described in Section 1):

$$<\sigma_{1i}> <\sigma_{1i}> - \rho V^2 <\sigma_{ij}> M_{ijkl} <\sigma_{kl}> = 0; \tag{25}$$

(d) Condition 2 (also described in Section 1):

$$\rho^3 (c_1^2 - V^2)(c_2^2 - V^2)(c_3^2 - V^2) - \left(\frac{\partial f}{\partial \sigma_{ij}} g_{ij}\right)^{-1} \Big\{ \eta_1 (c_2^2 - V^2)(c_3^2 - V^2) + \eta_2 (c_3^2 - V^2)(c_1^2 - V^2) + \eta_3 (c_1^2 - V^2)(c_2^2 - V^2) \Big\} = 0, \tag{26}$$

where $g_{ij} \equiv M_{ijkl}^{-1} (\partial f / \partial \sigma_{kl}) = g_{ji}$, c_i are the elastic wave speeds, and $\eta_i \equiv (q_j^{(i)} g_{j1})^2$, *where* $\mathbf{q}^{(i)}$ are the eigenvectors of M_{j1k1}^{-1} corresponding to c_i.

In most cases, the four equations (23)–(26) should be independent of one another, with possible exceptions occurring at some isolated points in (σ_{11}, σ_{22}, σ_{33}, σ_{12}) (hyper) space, and hence there can be no admissible stress path to facilitate an elastic-plastic moving strong discontinuity. The independence of these equations can be reasoned by observing that each of them describes a different aspect of the mechanical properties of the material during shock wave passage. It is very difficult mathematically to prove the independence of these equations for a general material (especially if the yield condition form is unspecified). Thus, we intend first to approach the problem for an isotropic material with a Huber-Mises yield condition. This material model is very important for many theoretical investigations. Also, the proof for one specific type of material should make it clear that these four equations are not naturally mutually dependent.

When the material is isotropic and obeys the Huber-Mises yield condition, we have

$$M_{ijkl}^{-1} = G(\delta_{ik}\delta_{jl} + \delta_{il}\delta_{jk}) + \lambda \delta_{ij}\delta_{kl} \tag{27}$$

and

$$f(\sigma_{11}, \sigma_{22}, \sigma_{33}, \sigma_{12}) \equiv \frac{1}{3}(\sigma_{11}^2 + \sigma_{22}^2 + \sigma_{33}^2 - \sigma_{11}\sigma_{22} - \sigma_{22}\sigma_{33} - \sigma_{33}\sigma_{11}) + \frac{1}{2}(\sigma_{12}^2 + \sigma_{21}^2) - k^2 = 0. \tag{28}$$

Now, the elastic wave speeds are $c_1^2 = (2G + \lambda)/\rho$ and $c_2^2 = c_3^2 = G/\rho$, so that equations (24), (25) and (26) become

$$\left(1 - \frac{\rho V^2}{2G + 3\lambda}\right) <\sigma_{11}> - \frac{\rho V^2}{2G + 3\lambda} (<\sigma_{22}> + <\sigma_{33}>) = 0, \tag{29}$$

$$<\sigma_{11}>^2 + <\sigma_{12}>^2 - \rho V^2 \left\{ \frac{1}{G(2G + 3\lambda)} [(G + \lambda)(<\sigma_{11}>^2 + <\sigma_{22}>^2 + <\sigma_{33}>^2) - \lambda(<\sigma_{11}><\sigma_{22}> + <\sigma_{22}><\sigma_{33}> + <\sigma_{33}><\sigma_{11}>)] + \frac{1}{G} <\sigma_{12}>^2 \right\} = 0, \tag{30}$$

$$(G - \rho V^2)(2G + \lambda - \rho V^2) k^2 - \frac{1}{9} G (G - \rho V^2)(4\sigma_{11}^2 - 4\sigma_{11}\sigma_{22} - 4\sigma_{11}\sigma_{33} + \sigma_{22}^2 + \sigma_{33}^2 + 2\sigma_{22}\sigma_{33}) - G(2G + \lambda - \rho V^2)\sigma_{12}^2 = 0. \tag{31}$$

Here we have four unknowns in four equations (28)–(31). It is easier to deal with only three unknowns in three equations by eliminating one of the variables. Because we can do this by linear combination and direct substitution, the properties of the possible intersecting curves do not change.

Substitution of equation (29) into (30) serves to eliminate σ_{11}:

$$\frac{\rho V^2}{G(2G + 3\lambda - \rho V^2)^2} \{ -[(\rho V^2)^2 - 3(G + \lambda)\rho V^2 + (G + \lambda) \times (2G + 3\lambda)](<\sigma_{22}>^2 + <\sigma_{33}>^2) + [-(\rho V^2)^2 + 2G\rho V^2 + \lambda(2G + 3\lambda)] <\sigma_{22}><\sigma_{33}> \} + \left(1 - \frac{\rho V^2}{G}\right) <\sigma_{12}>^2 = 0. \tag{32}$$

Downloaded 03 May 2010 to 171.66.16.244. Redistribution subject to ASME license or copyright; see http://www.asme.org/terms/Terms_Use.cfm

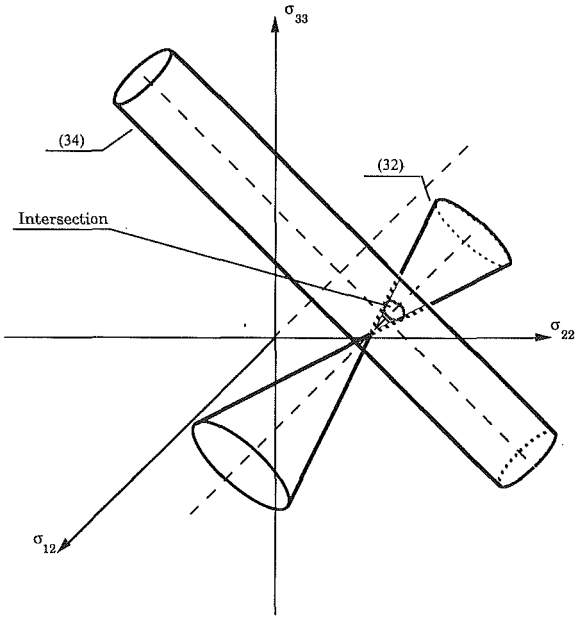


Fig. 3 Intersection of the surfaces representing two of the trans-shock stress path restrictions for the plane-strain case

Next, 3 × equation (31) + $4G(G-\rho V^2)$ × equation (28) gives another relation without σ_{11}:

$$G(G-\rho V^2)(\sigma_{22}^2+\sigma_{33}^2-2\sigma_{22}\sigma_{33})-G(2G+3\lambda+\rho V^2)\sigma_{12}^2 + (G-\rho V^2)(2G+3\lambda-3\rho V^2)k^2=0. \quad (33)$$

One more equation may be obtained by substituting equation (29) into (31) to eliminate σ_{11} and by rearranging:

$$(G-\rho V^2)(2G+\lambda-\rho V^2)k^2-\frac{1}{9}G(G-\rho V^2)\{(1-2h)(<\sigma_{22}> + <\sigma_{33}>)-[2\sigma_{11}^+-(\sigma_{22}^+ +\sigma_{33}^+)]\}^2-G(2G+\lambda-\rho V^2)\sigma_{12}^2=0 \quad (34)$$

where

$$h=\frac{\rho V^2}{2G+3\lambda-\rho V^2}. \quad (35)$$

Equations (32), (33) and (34) are the restrictions on the three variables σ_{22}, σ_{33}, and σ_{12}; by including any one of equations (28)–(31), we get four equations (e.g., (31)–(34)) that can replace equations (28)–(31) without changing the subspace defined by them. Thus, we can use equations (31)–(34) to identify the intersection problem.

Equation (32) is an elliptic cone centered at $(\sigma_{22}^+, \sigma_{33}^+, \sigma_{12}^+)$ in $(\sigma_{22}, \sigma_{33}, \sigma_{12})$ subspace; when $\rho V^2 < (2G/3)+\lambda$, the axis of the cone is parallel to the σ_{12} coordinate; when $(2G/3)+\lambda < \rho V^2 < G$ (which requires Poisson's ratio <0.125), the axis of the cone is perpendicular to the σ_{12}-coordinate and parallel to the line bisecting the σ_{22} and σ_{33} directions. Equation (34) is an elliptic cylinder whose axis lies in the $\sigma_{22}-\sigma_{33}$ plane, and perpendicular to the line bisecting the σ_{22} and σ_{33} directions (see Fig. 3, where equation (33) is not drawn).

When $\rho V^2 < (2G/3)+\lambda$, if we exchange the positions of $<\sigma_{22}>$ and $<\sigma_{33}>$, equations (32) and (34) remain unchanged. Therefore, exchanging $<\sigma_{22}>$ and $<\sigma_{33}>$ does not alter the intersecting curve of equation (32) and (34). Besides, such an exchange will remain on the same curve if there is more than one intersection, as can be seen from the geometry (also note that there are points on the intersection other than $(\sigma_{22}^+, \sigma_{33}^+, \sigma_{12}^+)$ that pass through the $\langle\sigma_{22}\rangle = \langle\sigma_{33}\rangle$ plane).

If equation (33) passes through one of the curves defined by (32) and (34), it must stay on the same curve when an exchange of $<\sigma_{22}>$ and $<\sigma_{33}>$ is made in (33).

Let us rewrite equation (33) as

$$G(G-\rho V^2)(\sigma_{22}-\sigma_{33})^2+p=0$$

where we use p to represent the last two terms of (33); the above equation can also be written as

$$G(G-\rho V^2)(<\sigma_{22}>-<\sigma_{33}>+\sigma_{22}^+-\sigma_{33}^+)^2+p=0. \quad (36)$$

When $<\sigma_{22}>$ and $<\sigma_{33}>$ are exchanged, we obtain

$$G(G-\rho V^2)(-<\sigma_{22}>+<\sigma_{33}>+\sigma_{22}^+-\sigma_{33}^+)^2+p=0. \quad (37)$$

Since both equations (36) and (37) pass through the same curve, their linear combination must include that curve as well. Subtraction of equation (37) from (36) gives

$$G(G-\rho V^2)(\sigma_{22}^+-\sigma_{33}^+)(<\sigma_{22}>-<\sigma_{33}>)=0. \quad (38)$$

Here we do not consider $\rho V^2=G$. Then equation (38) depicts a plane

$$<\sigma_{22}>-<\sigma_{33}>=0. \quad (39)$$

($\sigma_{22}^+ - \sigma_{33}^+ = 0$ will also lead to $\sigma_{22}-\sigma_{33}=0$, and hence $<\sigma_{22}>-<\sigma_{33}>=0$ by an argument similar to that adopted in the plane-stress case following equation (19)). As can be seen geometrically in Fig. 3, the curve produced by the intersection of equations (32) and (34) cannot be on such a plane. This can also be easily seen from equation (33) because $<\sigma_{22}>-<\sigma_{33}>=0$ leads to constant σ_{12}, which further leads to constant σ_{22} and σ_{33} through equations (34) and (39).

Thus, we have proved for $\rho V^2 < (2G/3)+\lambda$ that there is no common intersection curve of these equations. For $(2G/3)+\lambda \le \rho V^2 < G$, a similar scheme can be adopted by utilizing the symmetry of equations (33) and (34) with respect to the $\sigma_{22}-\sigma_{33}$ plane. Since now $\sigma_{22}=\sigma_{33}$ is the plane of symmetry of equation (33) that does not touch the hyperbolic cylinder, one can subtract versions of (32) with $\pm\sigma_{12}$ to eliminate the possibility of common intersection curves among the three equations. The overall conclusion is: The solution space consists only of discrete points, and hence (in the four-dimensional stress space) there can be no admissible stress path to produce a moving elastic-plastic stress jump.

The above proof may not be valid if a surface were to pass through only part of a curve of intersection between the other two surfaces. That would require at least two points on the curve at which either the curve or the surface has discontinuous derivatives. This can not happen for the well-behaved equations (28) through (31) or (31) through (34).

As observed earlier, the possibility of shock waves cannot generally be ruled out. With a yield condition possessing a linear portion, for example, it is easy to show that an elastic-plastic shock wave is possible. When yield condition equation (23) is linear in $(\sigma_{11}, \sigma_{22}, \sigma_{33}, \sigma_{12})$ space, (26) becomes an equation of the coefficients of the stresses in equation (23), while (24) and (25) remain unchanged. We can then substitute equation (23) into (24) and (25) to eliminate σ_{11}. In most situations, an intersection between those two surfaces in $(\sigma_{22}, \sigma_{33}, \sigma_{12})$ subspace will exist, and equation (26) will merely specify possible elastic-plastic shock wave speeds in terms of coefficients of stresses in equation (23), elastic moduli, and the material density.

4 Generalization to Anisotropic Materials

In the previous sections we have proved that in the plane-stress and plane-strain cases, there can be no propagating jumps in stresses (except at elastic wave speeds) for isotropic materials with a Huber-Mises yield surface and associated flow rule. To obtain the same conclusion for a general material seems to be too difficult mathematically, but generalizing what we have done thus far is possible.

Downloaded 03 May 2010 to 171.66.16.244. Redistribution subject to ASME license or copyright; see http://www.asme.org/terms/Terms_Use.cfm

Plane Stress. For the case of plane stress, if the yield condition can be written as

$$f \equiv g(\sigma_{11}, \sigma_{22}) + C(\sigma_{12}^2 + \sigma_{21}^2) - k^2 = 0 \tag{40}$$

where C is a constant and the equation is a closed convex surface, the same proof we applied in Section 2 is still valid *as long as the intersection of the yield condition and the new equation (17) contains* σ_{12} *and* $-\sigma_{12}$ *on the same curve.* A typical example is a yield condition of the form

$$f \equiv A(\sigma_{11}^2 + \sigma_{22}^2) + B\sigma_{11}\sigma_{22} + C(\sigma_{12}^2 + \sigma_{21}^2) - k^2 = 0 \tag{41}$$

which forms a closed (convex) surface, where A, B, C are constants. An argument similar to that in Section 2 goes through because, in this case, if we cannot prove that σ_{12} and $-\sigma_{12}$ are on the same curve, we can still use the property that when $-\sigma_{11}$ and $-\sigma_{22}$ are substituted for σ_{11} and σ_{22} simultaneously, they stay on the same curve. This facilitates the proof because equation (18) cannot be symmetrical about the σ_{12}-coordinate (except when $\sigma_{12}^+ = 0$, in which case if a jump is assumed, a $\sigma_{12} \neq 0$ on the path from σ^+ to σ^- can be chosen as a new σ_{12}^+, as discussed earlier). This strategy may also be applied to problems with elastic anisotropy, having the property that $M_{1112} = M_{2212} = 0$ (so that coupling between σ_{12} and either σ_{11} or σ_{22} is precluded in the discontinuity restrictions).

Plane Strain. For the plane-strain case, it is a special situation that our proof can go through to reduce the four-dimensional problem of independence to three dimensions without losing certain symmetry properties (interchangeability of $<\sigma_{22}>$ and $<\sigma_{33}>$ in two of the restrictions) that are crucial to our method of proof. But we still have space for some generalization. The following seems to be the most general quadratic yield condition to which our method of proof applies:

$$f \equiv A(\sigma_{11}^2 + \sigma_{22}\sigma_{33} - \sigma_{33}\sigma_{11} - \sigma_{11}\sigma_{22}) + B(\sigma_{22}^2 + \sigma_{33}^2 - 2\sigma_{22}\sigma_{33}) + C(\sigma_{12}^2 + \sigma_{21}^2) - k^2 = 0, \tag{42}$$

which forms a closed (convex) surface in stress space and satisfies plastic incompressibility, where A, B, C are constants; note that the Huber-Mises yield condition is a special case of equation (42) when $A = B = \frac{1}{3}$, $C = \frac{1}{2}$. For this form of yield condition, we can directly use equation (32) and the new equation (33); a new equation (34) is obtained by first linearly combining the new equations (28) and (31) so that the σ_{22}^2, σ_{33}^2 and $\sigma_{22}\sigma_{33}$ terms appear in the form $(\sigma_{22} + \sigma_{33})^2$, then eliminating σ_{11} through the substitution of equation (29). It can be shown that the same proof applied in Section 3 is still valid. The most obvious example is the case $A = B$, for which the proof of Section 3 applies directly.

Another possible way to prove the independence of the equations when the yield condition is quadratic (and the elastic moduli may be anisotropic) would be to reduce the problem to three quadratic equations. If two of them intersect on one curve which is not on a plane, the problem then becomes a linear independence one.

5 Discussion

Although we have not given a proof for general stable elastic-ideally plastic materials, our "plane-stress" and "plane-strain" analyses indicate that there can be no strong discontinuities traveling at speeds other than the elastic wave speeds unless there is an unusual combination of the elastic moduli and yield condition that make the aforementioned equations dependent on a continuous set of points.

In Drugan and Shen (1987), we discussed the special case of antiplane shear deformation, showing that there can be no strong discontinuity wave with speed other than one of the elastic wave speeds unless the yield condition has a linear portion in σ_{13}, σ_{23} space (equation (3.34) of Drugan and Shen, 1987). We can prove further than when the yield condition coincides with equation (3.34) of Drugan and Shen (1987), Condition 2 will be naturally satisfied. Therefore, for the antiplane shear case, Condition 2 does not provide an additional restriction when the yield surface is that linear one. But when the yield surface is nonlinear, the condition is meaningful (although redundant in the simple antiplane strain case for eliminating strong discontinuity waves); in fact, the derivation in the Appendix of Drugan and Shen (1987) makes use of all these equations.

For the incompressible plane-strain case, Drugan and Shen (1987) reached a similar conclusion that there can be no propagating (elastic-plastic) stress jumps unless the yield condition contains a special straight line segment (defined by equations (3.42) and (3.45) in Drugan and Shen, 1987). We can prove that if the yield condition is indeed a linear one that contains the line segment defined by those two equations, equation (26) here will be naturally satisfied. In fact, for all the special cases mentioned in this work, an elastic-plastic shock wave is possible whenever there is a linear portion on the yield surface. The difference is: for antiplane and incompressible plane-strain cases (and plane stress without necking), a linear portion on a yield surface is a must for existence of an elastic-plastic shock wave; whereas for plane stress and compressible plane strain, other possibilities for elastic-plastic shock waves, though not very likely, have not been eliminated.

We take this opportunity to note that equation (3.45) in Drugan and Shen (1987) was printed incorrectly; it should read:

$$\begin{aligned}(M_{1111} + M_{3333} - 2M_{1133})<s_{11}>^2 + 2(M_{1122} + M_{3333} - M_{1133} - M_{2233})<s_{11}><s_{22}> + 4(M_{1112} - M_{3312})<s_{11}><s_{12}> \\ + (M_{2222} + M_{3333} - 2M_{2233})<s_{22}>^2 + 4(M_{2212} - M_{3312}) \times <s_{22}><s_{12}> + \left(4M_{1212} - \frac{1}{\rho V^2}\right)<s_{12}>^2 = 0,\end{aligned} \tag{43}$$

or in more concise form, having employed equation (3.41) of Drugan and Shen (1987):

$$\begin{aligned}(M_{1111} - M_{1133})<s_{11}>^2 + (2M_{1122} - M_{1133} - M_{2233})<s_{11}> \times <s_{22}> + (4M_{1112} - 2M_{3312})<s_{11}><s_{12}> + (M_{2222} - M_{2233}) \\ \times <s_{22}>^2 + (4M_{2212} - 2M_{3312})<s_{22}><s_{12}> + \left(4M_{1212} - \frac{1}{\rho V^2}\right)<s_{12}>^2 = 0.\end{aligned} \tag{44}$$

Acknowledgment

Support of this research by the Mechanics Division of the Office of Naval Research under Contract N00014-86-K-0032 and Grant N00014-89-J-1206 is gratefully acknowledged.

References

Courant, R., and Friedrichs, K. O., 1948, *Supersonic Flow and Shock Waves*, 3rd printing, 1985, Springer-Verlag, New York.

Drugan, W. J., 1986, "A More Direct and General Analysis of Moving Strong Discontinuity Surfaces in Quasi-Statically Deforming Elastic-Plastic Solids," ASME JOURNAL OF APPLIED MECHANICS, Vol. 53, pp. 224–226.

Drugan, W. J., and Chen, X. Y., 1989, "Plane Strain Elastic-Ideally Plastic Crack Fields for Mode I Quasistatic Growth at Large-Scale Yielding—I. A New Family of Analytical Solutions," *Journal of the Mechanics and Physics of Solids*, Vol. 37, pp. 1–26.

Drugan, W. J., and Rice, J. R., 1984, "Restrictions on Quasi-Statically Moving Surfaces of Strong Discontinuity in Elastic-Plastic Solids," in *Mechanics of Material Behavior: The D. C. Drucker Anniversary Volume*, G. J. Dvorak and R. T. Shields, eds., Elsevier Science Publishers B.V., Amsterdam, pp. 59–73.

Drugan, W. J., and Shen, Y. N., 1987, "Restrictions on Dynamically Propagating Surfaces of Strong Discontinuity in Elastic-Plastic Solids," *Journal of the Mechanics and Physics of Solids*, Vol. 35, pp. 771–787.

Drugan, W. J., and Shen, Y. N., 1990, "Finite Deformation Analysis of Restrictions on Moving Strong Discontinuity Surfaces in Elastic-Plastic Mate-

Downloaded 03 May 2010 to 171.66.16.244. Redistribution subject to ASME license or copyright; see http://www.asme.org/terms/Terms_Use.cfm

rials: Quasi-Static and Dynamic Deformations," *Journal of the Mechanics and Physics of Solids*, Vol. 38, pp. 553–574.

Hadamard, J., 1903, *Leçons sur la Propagation des Ondes et les Equations de l'Hydrodynamique*, Hermann, Paris.

Hill, R., 1952, "On Discontinuous Plastic States, with Special Reference to Localized Necking in Thin Sheets," *Journal of the Mechanics and Physics of Solids*, Vol. 1, pp. 19–30.

Hill, R., 1961, "Discontinuity Relations in Mechanics of Solids," *Progress in Solid Mechanics*, Vol. 2, I. N. Sneddon and R. Hill, eds., North Holland, Amsterdam, pp. 247–276.

Kotchine, N. E., 1926, "Sur la Théorie des Ondes de Choc dans un Fluide," *Rend. Circ. Mat. Palermo*, Vol. 50, pp. 305–344.

Leighton, J. T., Champion, C. R., and Freund, L. B., 1987, "Asymptotic Analysis of Steady Dynamic Crack Growth in an Elastic-Plastic Material," *Journal of the Mechanics and Physics of Solids*, Vol. 35, pp. 541–563.

Maxwell, J. C., 1873, *A Treatise on Electricity and Magnetism*, Oxford, U. K.

Narasimhan, R., and Rosakis, A. J., 1987, "Reexamination of Jumps Across Quasi-Statically Propagating Surfaces under Generalized Plane Stress in Anisotropically Hardening Elastic-Plastic Solids," ASME JOURNAL OF APPLIED MECHANICS, Vol. 54, pp. 519–524.

Nikolic, R. R., and Rice, J. R., 1988, "Dynamic Growth of Anti-Plane Shear Cracks in Ideally Plastic Crystals," *Mechanics of Materials*, Vol. 7, pp. 163–174.

Pan, H., 1982, "Some Discussion on Moving Strong Discontinuity Under Plane Stress Conditions," *Mechanics of Materials*, Vol. 1, pp. 325–329.

Thomas, T. Y., 1961, *Plastic Flow and Fracture in Solids*, Academic Press, New York.

Ting, T. C. T., 1976, "Shock Waves and Weak Discontinuities in Anisotropic Elastic-Plastic Media," *Propagation of Shock Waves in Solids*, E. Varley, ed., ASME, New York, AMD Vol. 17, pp. 41–64.

Downloaded 03 May 2010 to 171.66.16.244. Redistribution subject to ASME license or copyright; see http://www.asme.org/terms/Terms_Use.cfm

The Singularity Strength at the Apex of a Wedge Undergoing Finite Deformations

J. M. Duva
Department of Applied Mathematics,
University of Virginia,
Charlottesville, VA 22903
Assoc. Mem. ASME

Herein we establish general formulae for characterizing the singular behavior at the apex of a wedge of nonlinear material of arbitrary size undergoing plane-strain finite deformation. Two sets of boundary conditions are considered: (a) both wedge flanks are clamped, and (b) one flank is clamped and the other free. The mode of deformation is obtained in one simple case for illustration.

Introduction

In previous works (Duva, 1988; Duva, 1989) the singularity strength at the apex of a square rigid wedge embedded in a nonlinear material deforming in plane strain was investigated. The aim of that work was to describe, in terms of the strength of the dominant singularity, the deformation at the (square) end of a relatively stiff, circular cylindrical fiber surrounded by plastically deforming material. Both the case in which the deforming material is perfectly bonded to the rigid wedge and the case in which the deforming material has debonded from one surface of the rigid wedge were considered. Linear strain-displacement relations were used, but a nonlinear power-law was used to relate strains and stresses. It has been made clear by Williams (1952) and Knowles and Sternberg (1975) that, with the linear strain-displacement relations, the mixed boundary conditions characterizing the debonded wedge give rise to oscillatory singularities. This undesirable feature of the solutions is not present in the special case that the deforming material is incompressible. Thus, to avoid the complication of oscillatory singularities, in the cited work by Duva incompressibility was imposed through the power-law constitutive relation.

In the present work we drop the assumption of small strains, and along with it the contradiction inherent in the model described above; namely that the strains are both small and singular at the apex of the wedge. Knowles and Sternberg (1975, 1983) have shown, for two special geometries, the oscillatory character of the asymptotically dominant singularity is an artifact of the small strain assumption, so although the assumption of incompressibility is no longer required to eliminate the oscillatory singularities, it is an aid in simplifying the analysis that we will retain. The finite deformation analysis, at least when following the pattern provided by Stephenson (1982), is simpler and more explicit than the analogous small-strain analysis. In particular, *no* numerical calculations are required to obtain the dominant singularity strength and the accompanying mode shape.

In the following section the governing equations for incompressible plane-strain deformation from the finite deformation theory will be recounted, and a family of power-law constitutive relations will be introduced. In Section 3 the governing equations will be reduced, via the assumption that the deformed position function can be written in separated form, to a nonlinear second-order ordinary differential equation. In Section 4 the solutions for the various configurations considered will be obtained and discussed.

2 Governing Equations

The wedge of deforming material originally occupies a region in two-dimensional space as shown in Fig. 1. The angular extent of the wedges we will consider is 2δ. We will consider only deformations in the plane of Fig. 1, and we will let $\mathbf{x}$ denote the position of a point in the undeformed body in this plane. The deformed position of a point originally at $\mathbf{x}$ will be given by

$$\mathbf{y} = \mathbf{x} + \mathbf{u}(\mathbf{x}). \tag{1}$$

In this equation, $\mathbf{u}$ is the displacement field associated with the deformation. The mapping defined by equation (1) is assumed to be twice continuously differentiable and invertible. Let

$$\mathbf{F}(\mathbf{x}) = \nabla \mathbf{y}(\mathbf{x}) \tag{2}$$

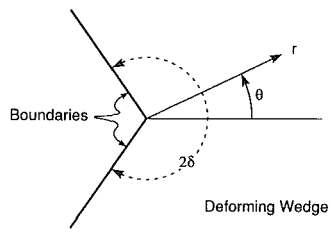


Fig. 1 Deforming wedge of material with plane polar coordinates (r, θ)

Contributed by the Applied Mechanics Division of THE AMERICAN SOCIETY OF MECHANICAL ENGINEERS for publication in the JOURNAL OF APPLIED MECHANICS.

Discussion on this paper should be addressed to the Technical Editor, Prof. Leon M. Keer, The Technological Institute, Northwestern University, Evanston, IL 60208, and will be accepted until two months after final publication of the paper itself in the JOURNAL OF APPLIED MECHANICS. Manuscript received by the ASME Applied Mechanics Division, Mar. 20, 1989; final revision, June 21, 1989.

Copyright © 1990 by ASME
Downloaded 03 May 2010 to 171.66.16.244. Redistribution subject to ASME license or copyright; see http://www.asme.org/terms/Terms_Use.cfm

be the deformation gradient field. The incompressibility condition is imposed through

$$\det \mathbf{F} = 1. \tag{3}$$

The determinant of $\mathbf{F}$ can be regarded as one of two scalar invariants of the plane deformation gradient. The other invariant, defined as

$$I = tr\,(\mathbf{F}^T\mathbf{F}), \tag{4}$$

satisfies the inequality $I \geq 2$, with equality holding only if the wedge of material undergoes a rigid motion. In equation (4) the superscript T denotes the transpose.

Let τ represent the two-dimensional Cauchy stress or *true* stress defined over the region occupied by the deformed body. In the absence of body forces,

$$div\ \tau = \mathbf{0}. \tag{5}$$

It proves advantageous in the following to introduce the *nominal* stress tensor, σ, related to the Cauchy stress through

$$\sigma\mathbf{F}^T = \tau. \tag{6}$$

No inconvenience is suffered in using the nominal stress with regard to the imposition of zero traction boundary conditions, as it can be shown that a zero true traction along an arc in the deformed body is equivalent to zero nominal traction along the pre-image of that arc in the undeformed configuration.

We will consider nonlinear elastic materials that possess an elastic potential W. For isotropic and incompressible materials, W is a function of the invariant I alone. The constitutive law can be written as

$$\sigma = 2W'(I)\mathbf{F} - p\mathbf{F}^{-T} \tag{7}$$

where W' stands for the derivative of W with respect to its argument, p is the hydrostatic pressure, and the superscript $-T$ indicates the inverse of the transpose. We will concern ourselves with a family of potentials that are characterized by the asymptotic relation

$$W(I) = AI^n + BI^{n-1} + o(I^{n-1}) \tag{8}$$

as $I \to \infty$. A, B, and n are material constants and we will take $A > 0$ and $1/2 \leq n \leq 1$.

This information is all that is required for understanding the formulation of the eigenvalue problem that describes the deformation at the apex of the wedge that is given in the next section.

3 Problem Formulation

We seek singular solutions in the vicinity of the apex of the wedge of deforming material. With r and θ taken as polar coordinates centered on the apex of the wedge, we will assume that the deformation map admits an asymptotic representation of the form

$$y_\alpha \sim r^m U_\alpha(\theta) \tag{9}$$

as $r \to 0$, where m is between 0 and 1. In general, a different exponent for r is required for each component of the deformed position $\mathbf{y}$, but Stephenson (1982) has shown that in this context the single exponent is required. This representation simplifies further upon the imposition of the incompressibility constraint. Rewriting equation (3) and using (9) yields

$$mr^{2(m-1)}[U_1\dot{U}_2 - U_2\dot{U}_1] + o(r^{2(m-1)}) = 1. \tag{10}$$

If this is to hold true as $r \to 0$ it must be that the term in brackets is zero, and, as a consequence, that

$$U_1 = a_1 U \quad U_2 = a_2 U. \tag{11}$$

Here, a_1 and a_2 are arbitrary constants, $(a_1^2 + a_2^2 \neq 0)$, and $U(\theta)$ is a smooth function on $(-\delta,\delta)$ that is not identically zero. In terms of the unknown function U, the invariant I can be written as

$$I \sim r^{2(m-1)}a^2[\dot{U}^2 + m^2U^2] \tag{12}$$

where $a^2 = a_1^2 + a_2^2$. We will assume that U does not have a multiple zero in the domain of interest so that the leading term in the expansion of I is everywhere of order $r^{2(m-1)}$.

Equation (5) can be rewritten using equations (6), (7), and (8) to yield the pair of partial differential equations

$$\frac{\partial p}{\partial r} \sim 2Aa^{2n}r^{2(m-1)n-1}mU(\theta)Z(\theta), \tag{13a}$$

$$\frac{\partial p}{\partial \theta} \sim 2Aa^{2n}r^{2(m-1)n}\dot{U}(\theta)Z(\theta), \tag{13b}$$

where

$$Z = G^{n-2}[G(\ddot{U} + m^2U) + (n-1)[\dot{G}\dot{U} + 2m(m-1)GU]] \tag{14}$$

$$G = \dot{U}^2 + m^2U^2. \tag{15}$$

Two other useful equations are obtained by integrating equation (13a) to get

$$p \sim 2Aa^{2n}r^{2(m-1)n}\frac{mUZ}{2(m-1)n} \tag{16}$$

and by cross-differentiating equations (13a) and (13b) to eliminate p and to get

$$U\dot{Z} + \left[1 + \frac{2(1-m)n}{m}\right]Z\dot{U} = 0. \tag{17}$$

Our immediate goal is to show that Z is identically zero on the domain of interest, as has been done in the related analyses by Knowles and Sternberg (1973), Stephenson (1982), and Abeyratne and Yang (1987). Then equation (14) provides a nonlinear second-order ordinary differential equation for the unknown function U. To do so requires use of the boundary conditions.

Consider first the case that the wedge of deforming material has an extent of 2δ and is clamped on both faces. Thus,

$$y_\alpha(r, \pm\delta) = a_\alpha r^m U(\pm\delta) + o(r^m) = 0 \ (\alpha = 1,2), \tag{18}$$

implying that $U(\pm\delta) = 0$ as $\mathbf{y}$ must equal $\mathbf{x}$ on these faces for all values of r. On using equations (14) and (15), this in turn implies that at $\theta = \pm\delta$

$$G = \dot{U}^2,\ Z = G^{n-2}[G\ddot{U} + (n-1)\dot{G}\dot{U}]. \tag{19}$$

Also, from equation (17), since the term in brackets is never zero for the values of m and n of interest, we deduce that

$$Z\dot{U} = 0. \tag{20}$$

But, as $\dot{U}$ cannot also vanish at $\theta = \pm\delta$, it must be that $Z(\pm\delta)$ is zero. Together with the linear (in Z) differential equation (17), these end conditions require that Z is identically zero on $-\delta \leq \theta \leq \delta$.

Next consider that the deforming wedge has an extent of 2δ and has debonded from the rigid constraint at δ and that face is traction-free. These boundary conditions can be shown to imply

$$U(\delta)\dot{U}(\delta) = 0 \quad p(\delta) \sim 2Aa^{2n}r^{2(m-1)n}G^{n-1}\dot{U}^2. \tag{21}$$

As U and $\dot{U}$ cannot be zero simultaneously and as the second of equations (21) must be consistent with equation (16), it must be that $\dot{U}(\delta)$ and $Z(\delta)$ are zero. At $\theta = -\delta$ the argument just given for the clamped boundary condition can be used to show that $Z(-\delta) = 0$. Again, these conditions and equation (17) render Z identically zero on $-\delta < \theta \leq \delta$.

We must still solve the nonlinear second-order ordinary differential equation in U arising from equation (14) when $Z = 0$, subject to the conditions $U(\pm\delta) = 0$ corresponding to the clamped-clamped boundary conditions, or $U(-\delta) = 0$ and $\dot{U}(\delta) = 0$ corresponding to the clamped-free boundary conditions. This will be done in the following section.

4 Solutions and Discussion

Noting that G is never zero, equation (14) can be rewritten as

Downloaded 03 May 2010 to 171.66.16.244. Redistribution subject to ASME license or copyright; see http://www.asme.org/terms/Terms_Use.cfm

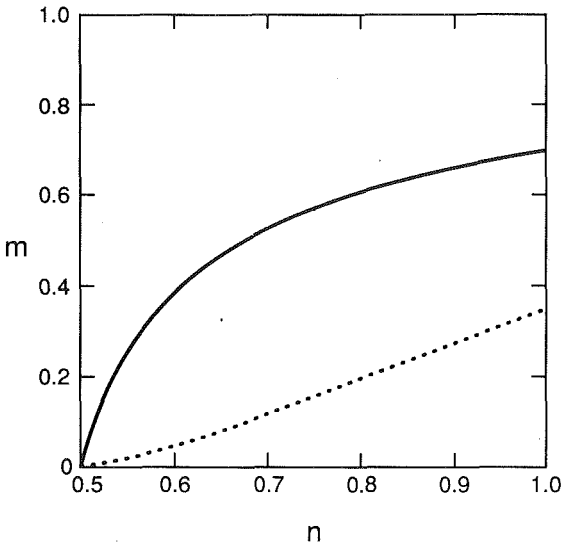


Fig. 2 Plots of m versus n for $\delta = 3\pi/4$ for clamped-clamped boundary conditions (solid) and clamped-free boundary conditions (dotted)

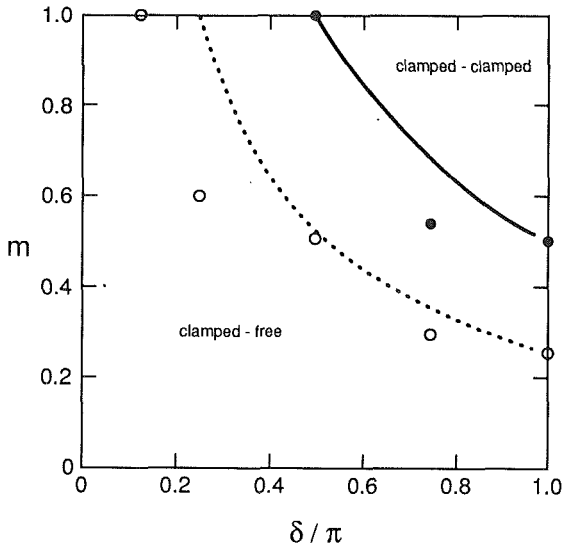


Fig. 3 Plots of m versus δ/π for $n = 1$ for the finite strain analysis (solid and dotted lines for clamped-clamped and clamped-free boundary conditions, respectively) and for the infinitesimal strain analysis (solid and open circles for clamped-clamped and clamped-free boundary conditions, respectively

$$G(\ddot{U}+m^2U)+(n-1)[\dot{G}\dot{U}+2m(m-1)GU]=0,$$
$$\delta\le\theta\le\delta. \tag{22}$$

Following Knowles and Sternberg (1973), we introduce polar coordinates (ξ, ψ) in the phase plane of U according to

$$mU=\xi(\theta)\cos\psi(\theta) \quad \dot{U}=\xi(\theta)\sin\psi(\theta), \quad -\delta\le\theta\le\delta. \tag{23}$$

Note from equations (15) and (23) that $G=\xi^2$ so ξ is never zero. Equation (23) and the compatibility relation (arising from the elimination of $\dot{U}$ in equation (23))

$$\dot{\xi}\cos\psi-\xi\dot{\psi}\sin\psi=m\xi\sin\psi \tag{24}$$

can be used to rewrite equation (22) as

$$\frac{d\psi}{d\theta}=\frac{-(1-n)-m(2n-1)-(1-n)\cos2\psi}{n+(1-n)\cos2\psi}. \tag{25}$$

Note that for $m > 0$ and $1/2 \le n \le 1$, ψ is monotonically decreasing. This monotonicity is important in choosing the limits of the integrals appearing next.

We first consider the clamped boundary condition at $\theta = -\delta$; that is, $U(-\delta) = 0$. From equation (23) we see that $\cos\psi(-\delta)$ must be zero. We choose $\psi(-\delta) = \pi/2$. Equation (25) can be recast as

$$\theta+\delta=\int_{\pi/2}^{\psi(\theta)}\frac{n+(1-n)\cos2\hat{\psi}}{-(1-n)-m(2n-1)-(1-n)\cos\hat{\psi}}\,d\hat{\psi}. \tag{26}$$

This integral can be evaluated via the substitution $\hat{\psi} = \tan^{-1}2z$ yielding

$$\theta+\delta=2\hat{\psi}+(\alpha-\beta)\left[\frac{2}{\sqrt{\beta^2-1}}\tan^{-1}\left(\sqrt{\frac{\beta-1}{\beta+1}}\tan\hat{\psi}\right)\right], \quad n\neq1 \tag{27}$$

where $\alpha = n/(1-n)$ and $\beta = 1 + m(2n-1)/(1-n)$. Note that for $n = 1$ the integrand of equation (26) simplifies with the result $\theta + \delta = \psi - \pi/2$, so equation (27) need not be used in this case. With the imposition of the boundary condition at δ, equation (27) provides a relation among δ, n, and m that can be satisfied only for specific values of m. These are the eigenvalues we seek.

Imposing the clamped condition at δ requires that $\cos\psi(\delta)=0$. As ψ is monotonic decreasing we choose $\psi(\delta) = -\pi/2$. The choice of a smaller value would lead to "more wiggly," less singular solutions. Solving for m in this instance gives

$$m=\frac{-D(1-n)-(2n-1)-\sqrt{D(2n-1)+D^2(1-n)^2}}{(D-1)(2n-1)} \tag{28}$$

where

$$D=(2\delta/\pi-1)^2. \tag{29}$$

In equation (28) the negative sign in front of the square root is chosen to give values of m in the range from 0 to 1. For $n = 1/2$ equation (28) gives $m = 1/(1-D)$. Note that for $\delta=\pi/2$, representing a deforming wedge that is a half plane, $D = 0$ and so $m = 1$ for all values of n, indicating no singular behavior as is to be expected. We are particularly interested in the case that $\delta = 3\pi/4$ as this corresponds to the motivating fiber corner configuration. Equation (28) is used to plot values of m as a function of n for this wedge angle in Fig. 2.

Imposing the free condition at δ requires that $\dot{U}(\delta) = 0$ and so for equation (23) we see that $\sin\psi(\delta) = 0$. We choose $\psi(\delta)=0$. The evaluation of equation (26) again yields an expression for m identical in form to equation (28), but in this case $D = (4\delta/\pi-1)^2$. Note that for $\delta = \pi/2$ equation (28) reduces to

$$m=1-\frac{1}{2n}. \tag{30}$$

For $n = 1$ the well-known (plane-strain) solution for the singularity strength at the corner of a rough punch in contact with an incompressible linear material is recovered. A plot of m as a function of n for $\delta = 3\pi/4$ is also given in Fig. 2. This would correspond to the fiber corner configuration immediately after debonding has occurred.

The deformation modes associated with the various values of δ and n, and the various boundary conditions, are representable by elementary functions, although in general the expressions are unwidely. As a simple example, a calculation of the deformation mode in the case that $n = 1$ and $\delta = 3\pi/4$ for the clamped-clamped boundary conditions is given next. With these values of n and δ equation (28) gives $m = 2/3$ and equation (26) becomes

$$\theta+\delta=\int_{\pi/2}^{\psi}-3/2d\hat{\psi}=-3/2\psi+3/4\pi, \tag{31}$$

implying

$$\psi=-2/3. \tag{32}$$

Downloaded 03 May 2010 to 171.66.16.244. Redistribution subject to ASME license or copyright; see http://www.asme.org/terms/Terms_Use.cfm

A differential equation for U can be obtained by combining equations (24) and (32) to get

$$\frac{dU}{U} = -\frac{2}{3}\tan(2\theta/3). \tag{33}$$

Integration gives

$$U(\theta) = \cos(2\theta/3) \tag{34}$$

where the constant of integration can be absorbed into the unknown constants a_1 and a_2. These constants depend on the conditions far from the apex of the wedge and do not influence the determination of m or the shape of U. Note that equation (34) gives the shape of *both* components of the deformed position vector, while in the infinitesimal theory each component has a different form.

Finally, we compare the values of m obtained herein using the finite strain formulation and the values obtained by Duva (1988, 1989) using an infinitesimal strain formulation. Such a comparison is not ideal because the use of different strain measures in the two theories prevents the use of identical constitutive relations. However, through an appropriate choice of material constants, the asymptotically dominant term in the constitutive relation (7) and the incompressible power-law stress-strain relation used by Duva can be made identical for simple shear deformations. Such a choice, with $n = 1$, was made to generate the values of m as a function of wedge angle δ displayed in Fig. 3. It appears that the severity of the singularity as predicted by the infinitesimal theory is always at least as great as that predicted by the finite theory, although the relative magnitudes depend on the wedge angle δ. Both theories predict some minimum wedge angle below which singular behavior fails to appear, but there is agreement on that value only for the clamped-clamped boundary conditions.

5 Conclusions

We have established general formulas for characterizing the singular behavior of a wedge of power-law material undergoing plane-strain finite deformations under two sets of boundary conditions. The boundary conditions arise in consideration of the deformation near the end of a relatively stiff fiber with a sharp corner.

Acknowledgments

The author would like to thank C. O. Horgan for the valuable advice he provided at every stage of this project.

7 References

Abeyratne, Rohan, and Yang, Jae-Sung, 1987, "Localized Shear Discontinuities Near the Tip of a Mode I Crack," *J. Elasticity*, Vol. 17, pp. 93–112.

Duva, J. M., 1988, "The Singularity at the Apex of a Rigid Wedge Embedded in a Nonlinear Material," ASME JOURNAL OF APPLIED MECHANICS, Vol. 55, pp. 361–364.

Duva, J. M., 1989, "The Singularity at the Apex of a Rigid Wedge After Partial Separation," ASME JOURNAL OF APPLIED MECHANICS, Vol. 56, pp. 977–978.

Knowles, J. K., and Sternberg, Eli, 1973, "An Asymptotic Finite-Deformation Analysis of the Elastostatic Field Near the Tip of a Crack," *J. Elasticity*, Vol. 3, pp. 67–107.

Knowles, J. K., and Sternberg, Eli, 1975, "On the Singularity Induced by Certain Mixed Boundary Conditions in Linearized and Nonlinear Elastostatics," *Int. J. Solids Structures*, Vol. 11, pp. 1173–1201.

Knowles, J. K., and Sternberg, Eli, 1983, "Large Deformations Near a Tip of An Interface-Crack Between Two Neo-Hookean Sheets," *J. Elasticity*, Vol. 13, pp. 257–293.

Stephenson, Rodney, A., 1982, "The Equilibrium Field Near the Tip of a Crack for Finite Plane Strain of Incompressible Elastic Materials," *J. Elasticity*, Vol. 12, pp. 65–99.

Williams, M. L., 1952, "Stress Singularities Arising From Various Boundary Conditions in Angular Corners of Plates in Extension," ASME JOURNAL OF APPLIED MECHANICS, Vol. 19, pp. 526–528.

Downloaded 03 May 2010 to 171.66.16.244. Redistribution subject to ASME license or copyright; see http://www.asme.org/terms/Terms_Use.cfm

Modifications of Series Expansions for General End Conditions and Corner Singularities on the Semi-Infinite Strip

Yoon Young Kim
Research Associate,
Assoc. Mem. ASME

Charles R. Steele
Professor,
Fellow ASME

Division of Applied Mechanics,
Stanford University,
Stanford, CA 94305

Modified series expansions are used to study semi-infinite isotropic elastic strip problems for general *end conditions and corner singularities. The solutions of strips with mixed lateral edges are used as the expansion sets of the end displacement and stress, and an end stiffness matrix, the relation of harmonics of the end displacement and stress, is formed. The present end stiffness matrix approach, an extension to static strip problems of the method by Kim and Steele (1989, 1990) for time-harmonic wave propagation in a semi-infinite cylinder, is effective due to the asymptotic behavior of the stiffness matrix. Also presented is a technique for handling the corner singularities, which is based on the asymptotic analysis of the expansion coefficients of the end stresses. With this, the order and strength of the singularities are determined, local oscillations are virtually suppressed, and converging solutions are obtained. Some numerical examples are given to demonstrate the effectiveness of the approach.*

1 Introduction

The number of papers on the linear isotropic elastic strip with traction-free lateral edges indicates the importance and difficulty of the problem. Several solutions are available in the literature, but it appears that satisfactory approaches for *general* end conditions have not previously been developed. The difficulty of the problem arises from the fact that there is no orthogonality relation for the components of the eigenfunctions of the strip, and that covergence of the solutions is questionable, especially when stress singularities at the corner occur for some boundary conditions.

Because of the similarities between strips and cylinders, we would like to review the available approaches for both geometries, and particularly focus on the approaches for the end effects. Most existing techniques for such problems may fall into the following category:

(1) series expansions of the bi-harmonic stress function (Gaydon and Shepherd, 1964; Balch, 1986).
(2) direct applications of the eigenfunction expansions using either bi-orthogonality (Little and Childs, 1967), or optimal weighting functions (Spence, 1983; Gerhardt and Cheng, 1981; Robert and Keer, 1987).
(3) use of singular functions to handle singular behavior of stresses at corners in addition to a complete set of series solutions (Benthem, 1963; Benthem and Minderhoud, 1972; Robert and Keer, 1987).
(4) reduction to a singular integral equation (Gupta, 1973, 1974, Adams and Bogy, 1975; Bogy 1975).
(5) the method of projection (Gregory and Gladwell, 1982).

The direct series expansion of the bi-harmonic stress function is applicable to smooth end conditions, but is not efficient for general end conditions due to the large number of linear equations to be solved. When stress singularities occur at the corner, this approach typically results in a slow covergence of the solutions with local oscillations.

It is demonstrated that the direct use of the bi-orthogonality based on the eigenfunction expansions does not guarantee the convergence of the solutions as the number of the expansion terms increases. (see Spence, 1983; Gerhardt and Cheng, 1981). As pointed out by Robert and Keer (1987), the optimal weighting function approaches give better results for stress end problems, but poor results for displacement end conditions when stress singularities occur at the corners.

For a problem where the order of the singularity is known, a function describing the corner singularity may be used in addition to complete sets of expansions. (See Benthem, 1973; Benthem and Minderhoud, 1972; Robert and Keer, 1987). As discussed by these authors, the overcompleteness of the ex-

Contributed by the Applied Mechanics Division of THE AMERICAN SOCIETY OF MECHANICAL ENGINEERS for presentation at the Winter Annual Meeting, Dallas, Texas, Nov. 25-30, 1990.

Discussion on this paper should be addressed to the Technical Editor, Leon M. Keer, The Technological Institute, Northwestern University, Evanston, IL 60208, and will be accepted until two months after final publication of the paper itself in the JOURNAL OF APPLIED MECHANICS. Manuscript received by the ASME Applied Mechanics Division, May 2, 1989; final revision, Aug. 23, 1989.

Paper No. 90-WA/APM-14.

Copyright © 1990 by ASME
Downloaded 03 May 2010 to 171.66.16.244. Redistribution subject to ASME license or copyright; see http://www.asme.org/terms/Terms_Use.cfm

pansion functions does not ensure the convergence of the solutions. Therefore, only a small number of terms in the expansions is allowed to prevent the linear dependence of the singular functions and the complete expansion sets.

Accurate results may be obtained from the singular integral equation approach (Gupta, 1973, 1974; Adams and Bogy, 1975; Bogy; 1975) which is particularly useful in handling corner singularities. However the numerical work involved appears to be substantial, and this approach would be most useful for a certain limited class of problems such as those having corner singularities.

By the method of projection (Gregory and Gladwell, 1982), the tractions at the end are expanded in terms of the displacement components of the Papkovich-Fadle eigenfunction. This technique, which is devoted mainly to problems with corner singularity, requires numerical integrations and the corresponding matrix may be poor conditioning as the size of the matrix becomes large. It appears to be difficult to extend this technique to general end problems.

In the present work, a solution procedure to handle general self-equilibrating end conditions[1] in a semi-infinite strip with traction-free lateral edges is presented. First is considered a technique to solve general end problems regardless of the presence of corner singularities. This is based on the end stiffness matrix approach which was developed by Kim and Steele (1989) for wave propagation problems in a semi-infinite cylinder. To form the stiffness matrix which is well conditioned, modified Fourier-type series are used to expand the end displacement and stress quantities. The choice of the expansion sets is crucial in the analysis, and such sets are derived from the solutions of strips with mixed lateral edge conditions.

The second part of the present approach treats the corner singularity. A technique to handle the singularity is based on the asymptotic analysis of the coefficients of the present complete expansions. This technique yields converging solutions and virtually suppresses local oscillations of the solutions. Furthermore, the order of the singularity can be estimated in the present analysis. The method described here can be generalized to more complex problems including the cases where the order of the singularity is difficult to obtain analytically.

2 Preliminaries

In a semi-infinite homogeneous isotropic elastic strip with traction-free edges, which occupies the region $|x| \le 1$, $z \ge 0$, the general symmetric solution for self-equilibrating end conditions can be written

$$\Psi(x,z) = 2\Re\left[\sum_{p=1}^{\infty} E^p \tilde{\Psi}^p(x)\exp(-\lambda^p z)\right] \tag{1}$$

where

$$[\Psi,\tilde{\Psi}^p(x)] \in \{[u_x, \tilde{u}^p_x(x)], [u_z, \tilde{u}^p_z(x)], [\sigma_{xx}, \tilde{\sigma}^p_{xz}(x)], [\sigma_{xz}, \tilde{\sigma}^p_{xz}(x)], [\sigma_{zz}, \tilde{\sigma}^p_{zz}(x)]\}.$$

The pth complex-valued expansion coefficient E^p in equation (1) is to be determined from end conditions. The eigenvalue λ^p is the solution of the equation

$$2\lambda + \sin 2\lambda = 0$$

and its asymptotic form is given in Spence (1983).[2] For the plane-strain condition, the components of the eigenfunctions (often called the Papkovich-Fadle eigenfunctions) can be written as

$$\tilde{u}^p_x(x) = \left(\lambda^p \sin\lambda^p - \frac{\alpha^2\cos\lambda^p}{1-\alpha^2}\right)\sin\lambda^p x + \lambda^p x\cos\lambda^p\cos\lambda^p x$$

$$\tilde{u}^p_z(x) = \left(\lambda^p \sin\lambda^p + \frac{\cos\lambda^p}{1-\alpha^2}\right)\cos\lambda^p x - \lambda^p x\cos\lambda^p\sin\lambda^p x$$

$$\tilde{\sigma}^p_{xx}(x) = (\lambda^p)^2(\sin\lambda^p\cos\lambda^p x - x\cos\lambda^p\sin\lambda^p x) \tag{2}$$

$$\tilde{\sigma}^p_{zz}(x) = \lambda^p[-(\lambda^p\sin\lambda^p + 2\cos\lambda^p)\cos\lambda^p x + \lambda^p\cos\lambda^p\sin\lambda^p x]$$

$$\tilde{\sigma}^p_{xz}(x) = -\lambda^p[(\lambda^p\sin\lambda^p + \cos\lambda^p)\sin\lambda^p x + \lambda^p\cos\lambda^p\cos\lambda^p x]$$

where $\alpha^2 = (1 - 2\nu)/2(1-\nu)$ and ν denotes Poisson's ratio.

In equation (2), stress σ_{ij} and displacement u_i are normalized by 2μ, twice the shear modulus, and a, half the width of the strip, respectively, The coordinates x and z are also referred to a. For the plane-stress condition, ν in (2) must be replaced by $\nu/(1+\nu)$.

A completeness proof for the Papkovich-Fadle eigenfunctions is provided by Gregory (1980). It is known that the components of the eigenfunctions are not orthogonal, and coupled linear equations need to be solved for solutions. However, there exists bi-orthogonality (see, e.g., Gregory, 1983; Johnson and Little, 1964) such that

$$\int_0^1 [\tilde{\sigma}^p_{zz}(x)\tilde{u}^q_z(x) - \tilde{u}^p_x(x)\tilde{\sigma}^q_{xz}(x)]dx = 0 \text{ for } p \ne q \tag{3}$$

and for $p = q$, a closed-form expression can be found;

$$D^p \equiv \int_0^1 [\tilde{\sigma}^p_{zz}(x)\tilde{u}^p_z(x) - \tilde{u}^p_x(x)\tilde{\sigma}^p_{xz}(x)]dx$$

$$= \frac{\sin 4\lambda^p + [8(\lambda^p)^2 + 2]\sin 2\lambda^p + 12\lambda^p\cos 2\lambda^p + 12\lambda^p}{16(\alpha^2 - 1)}.$$

3 Solutions of the Mixed Strips

Before dealing with the traction-free strip,[3] we first consider the general form of the solutions for elastic strips with mixed lateral edge conditions:

$$u_x(x,z) = \sum_{m=1}^{\infty} \sin\xi_m x\ (A_m - \frac{B_m}{1-\alpha^2} + B_m\xi_m z)\exp(-\xi_m z)$$

$$u_z(x,z) = \sum_{m=1}^{\infty} \cos\xi_m x\ (A_m + \frac{\alpha^2 B_m}{1-\alpha^2} + B_m\xi_m z)\exp(-\xi_m z)$$

$$\sigma_{xx}(x,z) = \sum_{m=1}^{\infty} \xi_m\cos\xi_m x\ (A_m - 2B_m + B_m\xi_m z)\exp(-\xi_m z) \tag{4}$$

$$\sigma_{xx}(x,z) = -\sum_{m=1}^{\infty} \xi_m\sin\xi_m x\ (A_m - B_m + B_m\xi_m z)\exp(-\xi_m z)$$

$$\sigma_{zz}(x,z) = -\sum_{m=1}^{\infty} \xi_m\cos\xi_m x\ (A_m + B_m\xi_m z)\exp(-\xi_m z).$$

Real-valued unknowns A_m and B_m must be computed from the given end conditions. For $\xi_m = m\pi\ (\equiv \beta_m)$, equation (4) satisfies the lateral condition

$$u_x|_{x=\pm 1} = 0,\ \sigma_{xz}|_{x=\pm 1} = 0 \tag{5}$$

and for $\xi_m = (2m-1)\pi/2\ (\equiv \gamma_m)$, the corresponding condition is

$$\sigma_{xx}|_{x=\pm 1} = 0,\ u_z|_{x=\pm 1} = 0. \tag{6}$$

The motivation for the study of the mixed strips is that suitable expansion sets for the traction-free strip can be found from the solutions of the mixed strips. The proper choice of the expansion sets is critical to good results, and we feel that the best expansions sets can be found from functions which

[1] End conditions with net resultants can easily be treated once self-equilibrating end conditions are handled.

[2] We only need the eigenvalues in the first quadrant of the complex plane for the present semi-infinite strip.

[3] Strips with traction-free and with mixed conditions on the lateral edges will be called "traction-free" and "mixed," respectively.

Downloaded 03 May 2010 to 171.66.16.244. Redistribution subject to ASME license or copyright; see http://www.asme.org/terms/Terms_Use.cfm

satisfy the governing equation but different lateral edge conditions.

For the elastic strips with (5) and (6), any end conditions at $z = 0$ can be expanded as

$$u_x(x,0)[\equiv U_x(x)] = \sum_{m=1}^{\infty} U_m \sin \xi_m x \tag{7a}$$

$$u_z(x,0)[\equiv U_z(x)] = \sum_{m=1}^{\infty} W_m \cos \xi_m x \tag{7b}$$

$$\sigma_{xz}(x,0)[\equiv S_x(x)] = \sum_{m=1}^{\infty} X_m \sin \xi_m x \tag{7c}$$

$$\sigma_{zz}(x,0)[\equiv S_z(x)] = \sum_{m=1}^{\infty} Z_m \cos \xi_m x. \tag{7d}$$

The corresponding end stiffness matrix which is the relation of the harmonics of the displacement and stress at the end can easily be formed:

$$\begin{Bmatrix} \mathbf{Z} \\ \mathbf{X} \end{Bmatrix} = \mathbf{K} \begin{Bmatrix} \mathbf{W} \\ \mathbf{U} \end{Bmatrix} = \begin{bmatrix} \mathbf{K11} & \mathbf{K12} \\ \mathbf{K21} & \mathbf{K22} \end{bmatrix} \begin{Bmatrix} \mathbf{W} \\ \mathbf{U} \end{Bmatrix} \tag{8}$$

where **Z**, **X**, **W**, and **U** are column vectors whose elements are Z_m, X_m, W_m, and U_m, respectively. The only nonzero elements in **K** are

$$\mathbf{K11}_{m,m} = \mathbf{K22}_{m,m} = \frac{-\xi_m}{1+\alpha^2}$$

$$\mathbf{K12}_{m,m} = \mathbf{K21}_{m,m} = \frac{-\alpha^2 \xi_m}{1+\alpha^2}.$$

4 End Stiffness Matrix Approach

For wave propagation problems in a cylinder with a traction-free cylindrical surface condition, Kim and Steele (1989, 1990) use the solutions for mixed lateral conditions as expansion sets for the traction-free problem. Similarly, we can use the expansions (7) for the end displacement and stress of the traction-free strip and construct the following end stiffness matrix **S** for the traction-free strip such that

$$\begin{Bmatrix} \mathbf{Z} \\ \mathbf{X} \end{Bmatrix} = \mathbf{S} \begin{Bmatrix} \mathbf{W} \\ \mathbf{U} \end{Bmatrix} = \begin{bmatrix} \mathbf{S11} & \mathbf{S12} \\ \mathbf{S21} & \mathbf{S22} \end{bmatrix} \begin{Bmatrix} \mathbf{W} \\ \mathbf{U} \end{Bmatrix}. \tag{9}$$

Following a procedure almost identical to that described by Kim and Steele (1989) yields the elements of the stiffness matrix **S** which are given in the appendix. It can be shown for the present case that $\mathbf{S11} = \mathbf{S11}^T$, $\mathbf{S12} = \mathbf{S21}^T$, and $\mathbf{S22} = \mathbf{S22}^T$, which are all real valued. Kim and Steele (1989, 1990) point out that their stiffness matrix **S** exhibits some crucial asymptotic behavior only if a proper choice of the expansion sets is made.

In the present formulation, we propose using two types of expansions characterized by two sets of the eigenvalues β_m and γ_m at the same time. Namely, $\xi_m = \gamma_m$ will be used for the expansions (7*a*) and (7*c*) whereas $\xi_m = \beta_m$ will be utilized for the expansions (7*b*) and (7*d*). The advantage of the present choice of the expansions over the expansions with a single set of eigenvalues, either β_m, or γ_m, is that the present expansions allow nonzero axial and transverse components of the stress and displacement; with $\xi_m = \beta_m$, $U_x(x) = S_x(x) = 0$ is imposed whereas with $\xi_m = \gamma_m$, $U_z(x) = S_z(x) = 0$ is imposed. If one expanded the bi-harmonic Papkovich-Fadle eigenfunction first and then obtained the components of the eigenfunctions as in Gaydon and Shepherd (1964) or Balch (1986), only one set of eigenvalues of the expansions could be used.

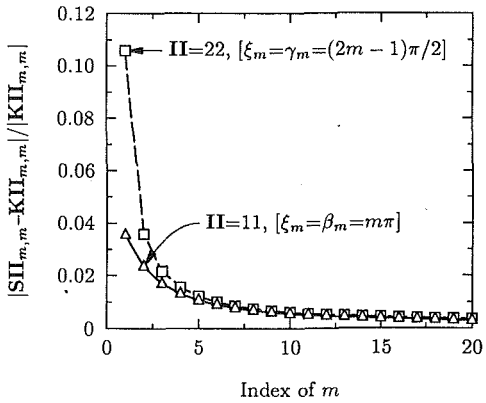


Fig. 1 Comparison of the diagonal elements of the end stiffness submatrices S11 and S22 of the traction-free strip with those of the mixed strips, K11 and K22. $\xi_m = \beta_m$ [$\equiv m\pi$], and $\xi_m = \gamma_m$ [$\equiv (2m-1)\pi/2$] are used for (K11, S11) and (K22, S22), respectively. It is seen that both $S11_{m,m}$ and $S22_{m,m}$ rapidly approach $K11_{m,m}$ and $K22_{m,m}$, respectively.

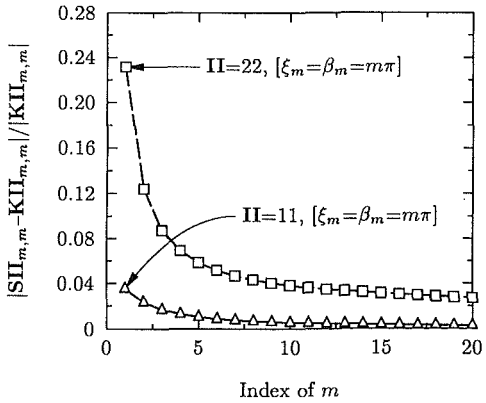


Fig. 2 $\xi_m = \beta_m = m\pi$ are used for all stiffness submatrices. It is seen that S22 does not approach K22 as rapidly as S11 approaches K11. The choice of the expansion sets affects quite significantly the asymptotic behavior of the stiffness matrix of the traction-free strip.

The advantage of the present end stiffness approach is that for large harmonic index number m: (1) the stiffness submatrices **S11** and **S22** become diagonally predominant and (2) the diagonal elements of **S11** and **S22** asymptotically approach those of **K11** and **K22**. Therefore, the stiffness matrix **S** is well conditioned and only part of **S** needs to be computed, since for large m, **S11** and **S22** can be replaced by **K11** and **K22**.

In order to demonstrate this, consider Fig. 1 which shows $|\mathbf{S11}_{m,m} - \mathbf{K11}_{m,m}| / |\mathbf{K11}_{m,m}|$ and $|\mathbf{S22}_{m,m} - \mathbf{K22}_{m,m}| / |\mathbf{K22}_{m,m}|$. It should be mentioned again that $\xi_m = \beta_m$ and $\xi_m = \gamma_m$ were used in the expansions (7) for normal and transverse components of displacement and stress, respectively, in forming the stiffness matrix shown in Fig. 1. It is obvious that the diagonal elements of **S11** and **S22** rapidly approach the counterparts of **K11** and **K22**. If we used $\xi_m = \beta_m$ for the expansions of all quantities in (7), we would obtain the results shown in Fig. 2. Comparing Fig. 1 and Fig. 2 indicates that the asymptotic behavior of the stiffness matrix is sensitive to the choice of the expansions. The present expansion sets produce better asymptotic behavior of the stiffness matrix, and this must be due to the fact that nonzero values at the lateral edges for u_x and σ_{xz} are allowed. The columnwise and rowwise diagonal dominance of the stiffness matrix **S** was also examined and strong diagonal dominance was observed.

Although the diagonal elements of **S12** do not approach those of **K12**, no substantial numerical efforts are required because only the matrices such as **S11** and **S22** need to be inverted in the present approach. In addition, the far-field

Downloaded 03 May 2010 to 171.66.16.244. Redistribution subject to ASME license or copyright; see http://www.asme.org/terms/Terms_Use.cfm

solutions requires only **S11** and **S22** as shall be explained. Kim and Steele (1989) discuss more details on the asymptotic behavior of the stiffness matrix. Kim and Steele (1990) demonstrate the end stiffness matrix approach incorporating the asymptotic behavior for localized eccentric loading of the end.

Since the end stiffness matrix gives solutions only at the end, we need a procedure to obtain the far-field solutions; namely the expansion coefficients E^p should be known. The method to determine E^p from **S** is described by Kim and Steele (1989) for time-harmonic problems in a cylinder using bi-orthogonality and we present only the results for the present problem.

$$E^p=\frac{1}{2D^p}\left[\sum_{m=1}^{n_h}\left(\sum_{l=1}^{n_h}\mathbf{S11}_{m,l}W_l\right)W^p_m - \sum_{m=1}^{n_h}\left(\sum_{l=1}^{n_h}\mathbf{S22}_{m,l}U_l\right)U^p_m\right] \tag{10}$$

In equation (10), n_h designates the number of terms in the expansion (7). Equation (10) is useful for displacement end conditions and a similar expression can be derived for stress end conditions. As equation (10) indicates, only **S11** and **S22** are needed for far-field solutions.

5 Asymptotic Analysis of Singularity at the Corner

There are some cases when stresses are singular in the domain of interest. For instance, stresses near the corner ($x = \pm 1$, $z = 0$) in an elastic strip with a clamped-free condition are singular,[4] which can be written as (see Williams (1952), Benthem (1963))

$$\sigma_{zz}(x)\sim c_z(1-x)^{-\rho},\ \sigma_{xz}(x)\sim c_x(1-x)^{-\rho} \tag{11}$$

for small $(1-x)$. The relation between the strength c_x and c_z is given by

$$c_z=\left(\frac{2\nu-3+\rho}{2\nu-\rho}\tan\frac{\rho\pi}{2}\right)c_x \tag{12}$$

and the order ρ of the singularity is the solution of

$$\cos^2\frac{\rho\pi}{2}=\frac{4(1-\nu)^2-(1-\rho)^2}{3-4\nu}. \tag{13}$$

When stress singularities occur at the corners, the convergence of solutions is usually unsatisfactory if typical expansion techniques are used. The use of singular functions (of the form (11)) as well as a complete set of expansions cannot guarantee the convergence of the solutions, either, because of overcompleteness of the expansion set. (Refer to Benthem, 1963; Benthem and Minderhoud, 1972; Robert and Keer, 1987.)

The purpose of this section is to present a technique which yields converging solutions even when stress singularities occur at the corners. The expansions (7) are used with asymptotic analysis of the expansion coefficients.

To this end, consider an expansion

$$h(x)=\sum_{m=1}^{\infty}h_m\sin\gamma_m x \text{ for } 0<x<1 \tag{14}$$

where

$$h(x)=c[(1-x)^{-\rho}-1]. \tag{15}$$

Though no difficulties occur for the analysis of the case for $\rho > 1$ or $\rho < 1$, we only focus on the case when $0 < \rho < 1$ because of its physical significance in elasticity.[5] The asymptotic expansion of the coefficients h_m may be shown to be (see Erdélyi, 1956; Lighthill, 1958; or Bleinstein and Handelsman, 1986)

$$\frac{h_m}{2c}\sim\left[\frac{(-1)^{m+1}\Gamma(1-\rho)\sin\frac{\rho\pi}{2}}{(\gamma_m)^{1-\rho}}+\sum_{l=1}^{\infty}\frac{(-1)^{l+1}\Gamma(2l-2+\rho)}{\Gamma(\rho)(\gamma_m)^{2l-1}}\right]$$

$$-\frac{1}{\gamma_m}\sim\frac{(-1)^{m+1}\Gamma(1-\rho)\sin\frac{\rho\pi}{2}}{(\gamma_m)^{1-\rho}}+O\left(\frac{1}{m^3}\right). \tag{16}$$

We introduce the operations $h^{(1)}_m$ and $h^{(2)}_m$ such that

$$h^{(1)}_m\equiv\gamma_m h_m-\gamma_{m-1}h_{m-1} \tag{17}$$

$$h^{(2)}_m\equiv\frac{h^{(1)}_m}{h^{(1)}_{m-1}}. \tag{18}$$

Substituting of equations (16) into (17) and (18) and expanding the resulting expression for large m give

$$h^{(2)}_m\sim-\frac{\gamma^\rho_m+\gamma^\rho_{m-1}}{\gamma^\rho_{m-1}+\gamma^\rho_{m-2}}\sim-\frac{2m-3+\rho}{2m-3-\rho}. \tag{19}$$

The operation (18) eliminates c so that $h^{(2)}_m$ contains only ρ and m. From equations (16) and (19),

$$\rho\sim\frac{-(2m-3)(1+h^{(2)}_m)}{1-h^{(2)}_m} \tag{20}$$

$$c\sim\frac{(-1)^{m+1}h^{(1)}_m}{2\Gamma(1-\rho)(\gamma^\rho_m+\gamma^\rho_{m-1})\sin\frac{\rho\pi}{2}}. \tag{21}$$

The useful application of the foregoing asymptotic analysis is to identify a smooth part and a singular part of the type (15) (if any) from the series expansion

$$f(x)=\sum_{m=1}^{\infty}f_m\sin\gamma_m x. \tag{22}$$

The procedure is as follows:

(1) successive application of $f^{(1)}_m$ and $f^{(2)}_m$ to f_m.

(2) successive estimation of ρ and c using (20) and (21) until convergence is met. (If ρ can be determined in advance, skip the procedure (20).)

(3) subtraction of a singular part of the type (15) from the original series.

(4) partitioning of the original series into a smooth part and a singular part.

This procedure then yields,

$$f(x)\approx\sum_{m=1}^{\infty}(f_m-h_m)\sin\gamma_m x+c[(1-x)^{-\rho}-1]. \tag{23}$$

From a numerical point of view, a series having a singularity of the type (15) converges very slowly and its truncated series usually exhibits strong local oscillations. Widely used techniques to accelerate the convergence of a truncated series, including the Cesaro sum (see, e.g., Edwards, 1979), can suppress local oscillations, but cannot capture the correct behavior of the singularity of the type (15). However, the present approach can not only suppress the local oscillations, but also estimate the nature of singularity. Numerical examples will be considered in the subsequent section.

An analogous analysis can be also carried out for the cosine expansion. Consider an expansion such that

[4]Williams (1952) treats stress singularities for various boundary conditions. The approach developed here can be equally applied to cases other than the clamped-free case.

[5]Lighthill (1958) shows that if (and only if) h_m in equation (14) is $O(m^N)$ for some N as $m\to\infty$, the series in equation (14) converges to a generalized function.

Downloaded 03 May 2010 to 171.66.16.244. Redistribution subject to ASME license or copyright; see http://www.asme.org/terms/Terms_Use.cfm

Table 1 Order and strength of shear stress σ_{xz} at the corner

	$n_h=20$	$n_h=40$	$n_h=80$	$n_h=160$	Benthem (1963)	Gregory and Gladwell (1982)
ρ	0.191	0.235	0.248	0.251	0.250 (Exact)	0.250 (Exact)
c_x	−0.243	−0.164	−0.144	−0.140	−0.145	−0.143

Table 2 Order and strength of shear stress σ_{zz} at the corner

	$n_h=20$	$n_h=40$	$n_h=80$	$n_h=160$	Benthem (1963)	Gregory and Gladwell (1982)
ρ	0.351	0.311	0.291	0.282	0.250 (Exact)	0.250 (Exact)
c_z	0.248	0.333	0.389	0.418	0.578	0.571

Table 3 Strength of corner singularity using exact order

	$n_h=20$	$n_h=40$	$n_h=80$	$n_h=160$	Benthem (1963)	Gregory and Gladwell (1982)
c_x	−0.145	−0.142	−0.142	−0.142	−0.145	−0.143
c_z	0.544	0.565	0.575	0.579	0.578	0.571

Table 4 Expansion coefficients for the end condition (33)

$p^{2.74}\|E^p\|$	$n_h=20$	$n_h=40$	$n_h=80$	$n_n=160$	Spence (1983)
$p=1$	0.8673	0.8675	0.8676	0.8676	0.8676
$p=2$	0.4784	0.4749	0.4740	0.4737	0.4735
$p=3$	0.6416	0.6241	0.6194	0.6182	0.6175
$p=4$	0.7359	0.6932	0.6818	0.6788	0.6774
$p=5$	0.7980	0.7209	0.6990	0.6934	0.6912

$$h(x)=\sum_{m=1}^{\infty} h_m \cos \beta_m x \text{ for } 0<x<1 \tag{24}$$

where

$$h(x)=c\left[(1-x)^{-\rho}-\frac{1}{1-\rho}\rho\right]. \tag{25}$$

The term $1/(1-\rho)$ in equation (25) does not necessarily need to be considered, but the form (25) is easier to work with since $\int_0^1 h(x)dx = 0$. (This is the condition for a self-equilibrating load.)

The asymptotic form of the expansion coefficient h_m is

$$\frac{h_m}{2c}\sim\frac{(-1)^m\Gamma(1-\rho)\sin\frac{\rho\pi}{2}}{(\beta_m)^{1-\rho}}+\sum_{l=1}^{\infty}\frac{(-1)^l\Gamma(2l-1+\rho)}{\Gamma(\rho)(\beta_m)^{2l}}$$

$$\sim\frac{(-1)^m\Gamma(1-\rho)\sin\frac{\rho\pi}{2}}{(\beta_m)^{1-\rho}}+O\left(\frac{1}{m^2}\right). \tag{26}$$

Defining $h_m^{(1)}$ and $h_m^{(2)}$ as

$$h_m^{(1)}\equiv\beta_m h_m-\beta_{m-1}h_{m-1} \tag{27}$$

$$h_m^{(2)}\equiv\frac{h_m^{(1)}}{h_{m-1}^{(1)}}, \tag{28}$$

we can estimate ρ and c from h_m as

$$\rho\sim\frac{-2(m-1)(1+h_m^{(2)})}{1-h_m^{(2)}} \tag{29}$$

$$c\sim\frac{(-1)^m h_m^{(1)}}{2\Gamma(1-\rho)(\beta_m^{\rho}+\beta_{m-1}^{\rho})\sin\frac{\rho\pi}{2}}. \tag{30}$$

6 Applications to Physical Problems

Consider a boundary value problem in a elastic strip with a plane stress assumption with $\nu = 0.3201398$ (Benthem, 1963)

$$\sigma_{zz}=1,\ \sigma_{xz}=0 \text{ at } z=\infty \tag{31a}$$

$$u_z=0,\ u_x=0 \text{ at } z=0 \tag{31b}$$

$$\sigma_{xz}=0,\ \sigma_{xx}=0 \text{ at } x=\pm 1. \tag{31c}$$

The traction-free lateral surface conditions is given by equation (31*c*). The end condition for end effects in a semi-infinite, traction-free strip can be written as

$$U_z(x)=0, \text{ and } U_x(x)=\nu x \text{ at } z=0 \tag{32}$$

and all physical quanitites vanish at $z\to\infty$. For $\nu = 0.3201398$, the order ρ of the stress singularity at the corner of the end at $z = 0$ is 0.25. The present solution procedure is:

Step 1 Expand the end condition (32) using equation (7).[6]

Step 2 Use the end stiffness matrix **S** in (9) to compute the expansion coefficients **Z** and **X** of the stress at $z = 0$.[7]

Step 3 Follow the procedure described in Section 4 to estimate the order and strength of singularities at the corner from **Z** and **X**.

Step 4 Partition the expansions of $S_z(x)$ and $S_x(x)$ into smooth and singular parts and then generate detailed distributions at $z = 0$.

Step 5 If interior solutions are required, use equation (10).

Following the aforementioned steps yields Table 1 listing

[6]Note that $\xi_m = \gamma_m$ for (7*a*, *c*) and $\xi_m = \beta_m$ for (7*b*, *d*).

[7]The asymptotic behavior of **S** can be used as in Kim and Steele (1989), but we have not made its use in this paper for simplicity. Note the present choice of the expansions different from that of Benthem (1963).

Downloaded 03 May 2010 to 171.66.16.244. Redistribution subject to ASME license or copyright; see http://www.asme.org/terms/Terms_Use.cfm

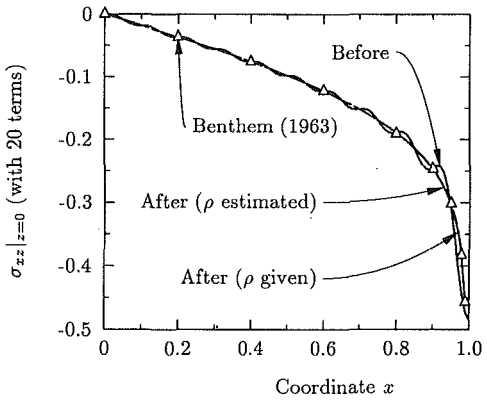


Fig. 3(*a*)

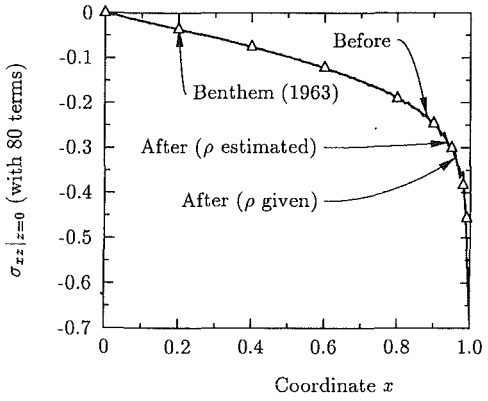


Fig. 3(*c*)

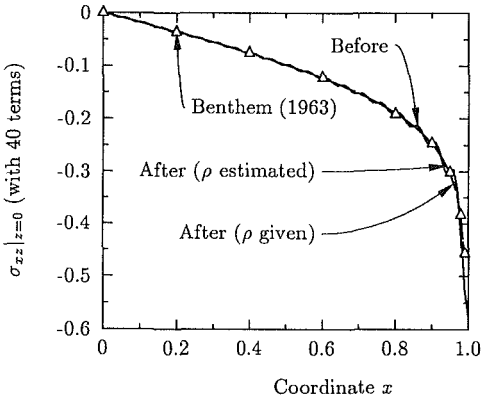


Fig. 3(*b*)

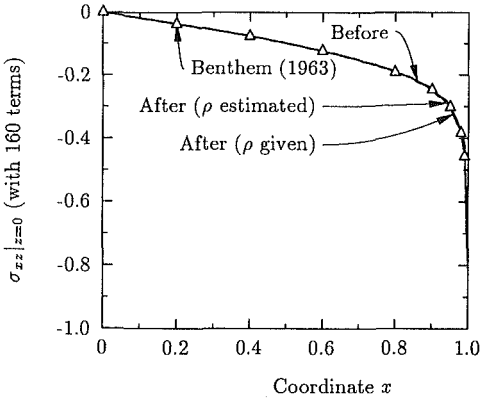


Fig. 3(*d*)

Fig. 3 The shear stress $\sigma_{xz}|_{z=0}$ in a traction-free strip of which one end ($z = 0$) is fixed and the other end ($z = \infty$) is subjected to a uniform normal stress ($\sigma_{zz} = 1$) without shear. The results obtained before (solid lines) and after separating the corner singularity are compared with Benthem's result (triangles). The oscillations before separation are reduced as the number of harmonics increases (*a*) $n_h = 20$, (*b*) $n_h = 40$, (*c*) $n_h = 80$, (*d*) $n_h = 160$. Except very near the corner ($x = 1.0$) there is little difference in the curves for ρ estimated from the series or ρ given.

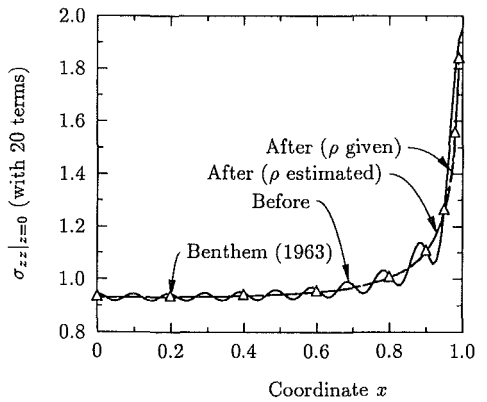


Fig. 4(*a*)

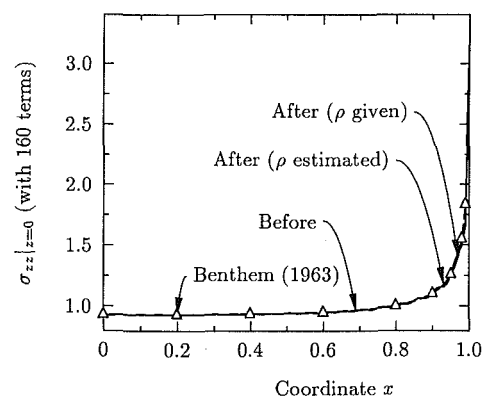


Fig. 4(*b*)

Fig. 4 The normal stress $\sigma_{zz}|_{z=0}$ in a traction-free strip of which one end ($z = 0$) is fixed and the other end ($z = \infty$) is subjected to a uniform normal stress ($\sigma_{zz} = 1$) without shear. The results obtained before (solid lines) and after separating the corner singularity are compared with Benthem's result (triangles). The oscillations before separation are reduced as the number of harmonics increases (*a*) $n_h = 20$, (*b*) $n_h = 160$. Except very near the corner ($x = 1.0$) there is little difference in the curves for ρ estimated from the series or ρ given.

the results for ρ and c_x which were computed from X_m with various n_h, the number of terms in the series expansions. The results for ρ and c_z obtained from Z_m are tabulated in Table 2. Note that we did not use the known value of ρ for Tables 1 and 2.

As Tables 1 and 2 indicate, the present approach yields converging solutions as n_h increases. Accurate results were obtained for ρ and c_x from X_m whereas Z_m produces less accurate for ρ and c_z.[8] However, ρ and c_z from Z_m tend to converge as n_h increases. From Benthem's work (see Tables 1

[8]For the problem in consideration, c_z must be $3.99c_x$ (see equation (12)).

Downloaded 03 May 2010 to 171.66.16.244. Redistribution subject to ASME license or copyright; see http://www.asme.org/terms/Terms_Use.cfm

and 2 of his paper), it may be seen that as the number of terms in his expansion increases, the magnitude of c_x tends to decrease, namely it approaches the present results with $n_h = 80$ or $n_h = 160$. Note that Gregory and Gladwell (1982) use the relation (7) in their approach, rather than compute c_x and c_z separately.

The reason for the accurate results from X_m and less accurate results from Z_m is that X_m were computed from **S22**, which is formed by means of a single set of expansions with $\beta_m = \gamma_m$ and is also strongly diagonally dominant, and that S_m were determined from **S12**, which is constructed by means of two sets of expansions and is not strongly diagonally dominant. However, good numerical results were obtained for the detailed distributions of both stresses at the end (see Figs. 3–4).

If the unknown value of ρ that is computed from equation (13) is used in the present analysis, a substantial improvement can be made. The results for the corner singularities are tabulated in Table 3 from which it may be concluded that $c_x = 0.142$. As explained before, the present approach estimates less accurate results for c_z. It should be noted that one can directly compute $c_z = 0.567$ from the converging result of $c_x = 0.142$ using equation (12) without the analysis for c_z.

Figures 3 show the shear stress $\sigma_{xz}|_{z=0}$ with different numbers of terms in the expansions with ρ either estimated from the present analysis or given from equation (13). The results are shown before (solid lines) and after (dashed lines with ρ estimated, and dot-dashed lines with ρ given) Steps 3 and 4. The results after Steps 3 and 4 agree very well with Bentham's results (triangles). As the comparison of Figs. 3(*a*) through 3(*d*) indicates, the present results even before Steps 3 and 4 predict the corner singularity by picking up larger values near $x = 1$ and converge elsewhere as n_h increases. It is apparent that local oscillations are virtually suppressed after Steps 3 and 4 without losing the singular behavior at the corner.

For the corner singularity, this method is superior to the Cesaro sum in accelerating the convergence. Even with $n_h = 20$, the results are close to those of Benthem (1963). Almost identical stress distributions are obtained except very near $x = 1$ regardless of the use of the exact order of the stress singularity.

The results for the normal stress $\sigma_{zz}|_{z=0}$ are shown in Figs. 4 with $n_h = 20$ and $n_h = 160$, respectively. Though the estimated ρ and c_z are not very accurate for a low number of terms, the distributions agree very well with Benthem's.

Finally, we consider a self-equilibrating stress end condition which was studied by Spence (1983):

$$\sigma_{zz}|_{z=0} = 1 - 3x^2 \tag{33a}$$

$$\sigma_{xz}|_{z=0} = 0. \tag{33b}$$

For this stress end condition, we use the flexibility matrix given in the Appendix. The first few expansion coefficients E^p obtained by the present stiffness approach are compared with those by Spence (1983) in Table 4.

Table 4 indicates that the present solutions converge as the number n_h of the terms in the expansions increases. Not many expansion coefficients, E^p, need to be determined in the present approach; for the solutions at the end, only the stiffness or flexibility matrices are needed, and for far-field solutions only a few number of expansion coefficients E^p need to be computed due to the exponentially decaying nature of the eigenfunctions of the traction-free strip.

7 Conclusions

The present approach is found to be effective in handling end problems and corner singularities in a semi-infinite elastic strip. The numerical examples confirm that the present technique for the corner singularity estimates accurately the order and strength of the singularity. This technique virtually suppresses the local oscillations of the stresses and yields the converging results in a clamped-free strip. It is found that only few terms in the expansions are needed for good curves of the stress distributions, and more terms are required for accurate determination of the order and strength of the singularity. Even the direct use of the present end stiffness matrix without any technique for the singularity produces converging results.

Acknowledgment

This work was partially supported by Grant MSM-8814355 from the National Science Foundation. We thank the reviewers for their comments on the earlier version of the manuscript.

References

Adams, G. G., and Bogy, D. B., 1975, "On a Paper by G. D. Gupta," ASME JOURNAL OF APPLIED MECHANICS, Vol. 42, pp. 224–225.

Balch, C. D., 1986, "End Effects in Thin-Walled Box Beams and Tubular Frame Joints," Ph.D. Thesis, Stanford University, Stanford, Calif.

Bogy, D. B., 1975, "Solutions of the Plane End Problem for a Semi-Infinite Strip," *Z.A.M.P.*, Vol. 26, pp. 749–769.

Benthem, J. P., 1963, "Laplace Transform Method for the Solution of Semi-Infinite and Finite Strip Problems in Stress Analysis," *Quart. J. Mech. Appl. Math.*, Vol. 16, pp. 413–29.

Benthem, J. P., and Minderhoud, P., 1972, "The Problem of the Solid-Cylinder Compressed between Rough Rigid Stamps," *Int. J. Solids Structures*, Vol. 8, pp. 1027–1042.

Bleistein, N., and Handelsman, R. A., 1986, *Asymptotic Expansions of Integrals*, Dover Publications, New York.

Edwards, R. E., 1979, *Fourier Series and Boundary Value Problems*, Vol. 1, 2nd ed., McGraw-Hill, New York.

Erdélyi, A., 1956, *Asymptotic Expansions*, Dover Publications, New York.

Gaydon, F. A., and Shepherd, W. M., 1964, "Generalized Plane Stress in a Semi-Infinite Strip Under Arbitrary End-Load," *Proc. Royal Soc.*, London, Vol. 281A, pp. 184–206.

Gerhardt, T. D., and Cheng, S., 1981, "A Diagonally Dominant Solution for the Cylinder End Problem," ASME JOURNAL OF APPLIED MECHANICS, Vol. 48, pp. 876–880.

Gregory, R. D., 1980, "The Traction Boundary Value Problem for the Elastostatic Semi-Infinite Strip; Existence of Solution, and Completeness of the Papkovich-Fadle Eigenfunctions," *J. Elasticity*, Vol. 10, pp. 295–327.

Gregory, R. D., 1983, "A Note on Bi-Orthogonality Relations for Elastic Cylinder of General Cross Section," *J. Elasticity*, Vol. 13, pp. 351–355.

Gregory, R. D., and Gladwell, I., 1982, "The Cantilever Beam Under Tension, Bending or Flexure at Infinity," *J. Elasticity*, Vol. 12, pp. 317–343.

Gupta, G. D., 1973, "An Integral Equation Approach to the Semi-Infinite Strip Problem," ASME JOURNAL OF APPLIED MECHANICS, Vol. 40, pp. 948–954.

Gupta, G. D., 1974, "The Analysis of the Semi-Infinite Cylinder Problem," *Int. J. Solids Structures*, Vol. 10, pp. 137–148.

Johnson, M. W., Jr., and Little, R. W., 1964, "The Semi-Infinite Elastic Strip," *Quart. Appl. Math.*, Vol. 22, pp. 335–344.

Kim, Y. Y., and Steele, C. R., 1989, "End Effects and Time-Harmonic Longitudinal Wave Propagation in a Semi-Infinite Solid Cylinder," ASME JOURNAL OF APPLIED MECHANICS, Vol. 56, pp. 334–346.

Kim, Y. Y., and Steele, C. R., 1990, "An Analytic-Asymptotic Approach for Time-Harmonic Nonsymmetric Wave Propagation in a Cylinder," *Int. J. Solids Structures*, Babcock Memorial Volume, Vol. 26, No. 9–10, pp. 1143–1158.

Lighthill, M. J., 1958, *Introduction to Fourier Analysis and Generalised Functions*, Cambridge Univ. Press, London, U.K.

Little, R. W., and Childs, S. B., 1967, "Elastostatic Boundary Region Problem in Solid Cylinder," *Quart. J. Appl. Mech.*, Vol. 25, pp. 261–274.

Robert, M., and Keer, L. M., 1987, "An Elastic Circular Cylinder with Displacement Prescribed at the Ends-Axially Symmetric Case," *Quart. J. Mech. Appl. Mech.*, Vol. 40, pp. 339–363.

Spence, D. A., 1983, "A Class of Biharmonic End-Strip Problems Arising in Elasticity and Stokes Flow," *IMA J. Appl. Math.*, Vol. 30, pp. 107–139.

Williams, M. L., 1952, "Stress Singularities Resulting From Various Boundary Conditions in Angular Corners of Plates in Extension," ASME JOURNAL OF APPLIED MECHANICS, Vol. 19, pp. 526–528.

APPENDIX

Following the procedure described by Kim and Steele (1989), the end stiffness matrix for the static strip problems can be expressed as

$$\mathbf{S11} = \mathbf{A11}^{-1},\ \mathbf{S12} = -\mathbf{S11} \cdot \mathbf{A12},\ \mathbf{S22} = \mathbf{B22}^{-1}$$

where

Downloaded 03 May 2010 to 171.66.16.244. Redistribution subject to ASME license or copyright; see http://www.asme.org/terms/Terms_Use.cfm

$$\mathbf{A11}_{l,m} = \Re\left[\sum_{p=1}^{n_e} \frac{W_l^p\, W_m^p}{D^p}\right]$$

$$\mathbf{A12}_{l,m} = -\Re\left[\sum_{p=1}^{n_e} \frac{W_l^p\, X_m^p}{D^p}\right] \qquad \text{(A1)}$$

$$\mathbf{B22}_{l,m} = \Re\left[\sum_{p=1}^{n_e} \frac{U_l^p\, U_m^p}{E^p}\right].$$

In equation (A1), W_m^p, U_m^p, and X_m^p are defined as

$$W_m^p = 2\int_0^1 \tilde{u}_z^p(x)\cos\xi_m x\, dx$$

$$U_m^p = 2\int_0^1 \tilde{u}_x^p(x)\sin\xi_m x\, dx$$

$$X_m^p = 2\int_0^1 \tilde{\sigma}_{xz}^p(x)\sin\xi_m x\, dx.$$

The flexibility matrix **F**, which is the inverse of **S**, is

$$\mathbf{F11} = \mathbf{B11}^{-1},\ \mathbf{F12} = -\mathbf{F11}\cdot\mathbf{B12},\ \mathbf{F22} = \mathbf{A22}^{-1}$$

where

$$\mathbf{B11}_{l,m} = \Re\left[\sum_{p=1}^{n_e} \frac{Z_l^p\, Z_m^p}{D^p}\right]$$

$$\mathbf{B12}_{l,m} = -\Re\left[\sum_{p=1}^{n_e} \frac{Z_l^p\, U_m^p}{D^p}\right]$$

$$\mathbf{A22}_{l,m} = \Re\left[\sum_{p=1}^{n_e} \frac{X_l^p\, X_m^p}{E^p}\right]$$

and Z_m^p is defined as

$$Z_m^p = 2\int_0^1 \tilde{\sigma}_{zz}^p(x)\cos\xi_m x\, dx.$$

Downloaded 03 May 2010 to 171.66.16.244. Redistribution subject to ASME license or copyright; see http://www.asme.org/terms/Terms_Use.cfm

A Dislocation Green's Function for the Analysis of Multiple Coplanar Cracks or Cracks With Nonuniform Crack Fronts

M. T. Hanson
Department of Engineering Mechanics,
University of Kentucky,
Lexington, KY 40506-0046

This analysis considers the interaction between a penny-shaped crack or a circular external crack and a mode I "opening" point dislocation. The dislocation is taken to lie on the plane of the crack. Symmetry considerations allow the reduction to a mixed boundary value problem for a half space which is solved by well-known methods from potential theory. Closed-form expressions are obtained for the crack opening displacement, stress on the symmetry plane, and the mode I stress intensity factor around the internal or external crack. The use of the present solution for the accurate numerical treatment of cracks with large amplitude variations in the crack front curvature as well as cases of multiple coplanar cracks is outlined.

1 Introduction

The motivation for the present work is to further develop the ability to analyze three-dimensional crack advance. This may either take the form of enlargement of a single (main) crack, or the coalesence of smaller microcracks ahead of a main crack. To study problems of this nature, a numerical formulation is generally needed since closed-form solutions for three-dimensional problems exist only for special crack geometries and loadings (Kassir and Sih, 1975). Recent work in the area of three-dimensional fracture mechanics has been the formulation of these crack problems in terms of two-dimensional singular integral equations over the crack domain which are solved numerically. Examples of this type of analysis are the surface flaw studies conducted by Murakami and Nemat-Nasser (1982, 1983) and Murakami (1985), as well as the extension by Lee et al. (1987) and Hanson et al. (1989) to include interface effects.

This type of numerical formulation involves the use of distributed point dislocation solutions to obtain an integral equation over the entire surface of the discontinuity. If a significant gradient in the crack front curvature exists (which may occur when a crack front encounters regions of higher fracture toughness), the near front crack opening displacement, and hence stress intensity factor, will also vary rapidly. Accounting for the entire crack surface in a numerical treatment leads to a loss of accuracy near the crack front where rapid variations occur. Accuracy will also be lost if multiple cracks exist since the domain of each crack must be considered.

Several investigators have addressed the two problems outlined previously. Fabrikant (1987a, 1987b) has developed a method for the analysis of multiple coplanar circular cracks in a transversely isotropic half space. A system of nonsingular integral equations was derived which related the unknown crack opening displacements and known normal stresses on the crack faces. By using the mean value theorem, an approximate solution was obtained in which the integral equations were converted to algebraic ones for the crack opening volumes (Fabrikant, 1987a). A numerical solution of the integral equations for the case of two cracks revealed that the error in the approximate solution increased rapidly as the distance between the crack contours became vanishingly small.

A recent treatment of the wavy crack front problem for a half plane crack has been conducted by Rice (1985a). He developed a perturbation solution accurate to the first order in the variation of the crack front from a straight line. This theory was applied by Rice (1988) to study crack fronts trapped by arrays of obstacles. The linear perturbation theory was extended to cracks of circular geometry by Gao and Rice (1987a, 1987b). A theory of this type eliminates the need for large numerical computation, but a first-order variation is quantitatively limited. To overcome the first-order limitations and analyze the large amplitude variation, Rice (1987) has proposed a sequence of integrations of the infinitesimal theory, although results of this type of approach have not yet been given. This theory relies on the knowledge of the weight function (Bueckner (1970), Rice (1972), Bueckner (1973, 1987)) which are only known in closed form for special crack geometries. Since it was developed specifically to investigate nonuniform crack fronts, it can not account for the presence of several cracks.

The present analysis gives the analytical treatment needed

Contributed by the Applied Mechanics Division of THE AMERICAN SOCIETY OF MECHANICAL ENGINEERS for publication in the JOURNAL OF APPLIED MECHANICS.

Discussion on this paper should be addressed to the Technical Editor, Leon M. Keer, The Technological Institute, Northwestern University, Evanston, IL 60208, and will be accepted until two months after final publication of the paper itself in the JOURNAL OF APPLIED MECHANICS. Manuscript received by the ASME Applied Mechanics Division, May 8, 1989; final revision, Aug. 4, 1989.

Copyright © 1990 by ASME
Downloaded 03 May 2010 to 171.66.16.244. Redistribution subject to ASME license or copyright; see http://www.asme.org/terms/Terms_Use.cfm

to accurately consider a numerical study of wavy planar crack fronts of large amplitude and finite size as well as the effects of multiple planar cracks. The method used here relies on the development of a dislocation interaction solution from which integral equations may be constructed. It is noted that this approach was considered first by Rice (1985b), in which an opening dislocation coplanar with a half plane crack was considered. The tensile stress on the crack dislocation plane was found in a closed form, and an integral equation given for an arbitrary opening. In a general form, Rice (1987) extended this formulation to the penny-shaped crack and off-plane dislocations of arbitrary orientation. For this general case, however, the stress field was given in terms of double integrals and no closed-form solutions were obtained. Here, the closed-form Green's function (for quantities in the plane) for a point opening dislocation is determined when the dislocation is located near a circular internal or external crack, on the plane of the crack. The crack opening displacement and the normal stress on the crack plane resulting from the interaction are found in a closed form. It is shown that knowledge of this fundamental solution, which automatically accounts for the stress-free circular surface, allows a large reduction in the crack surface that must be accounted for in a numerical treatment. For a wavy crack front, an interior circular geometry may be eliminated from numerical consideration whereas a study of microcracking ahead of a main crack will not require consideration of the main crack (as long as it is sufficiently close to a circular geometry). The analysis is not general, however, since only mode I loading is considered and the cracked surface is limited to a single plane.

2 Formulation

The full space dislocation interaction problems studied in this analysis are reduced by symmetry considerations to mixed boundary value problems for a half space. A convenient starting point for determining a solution is the potential function representation for displacements and stresses in a half space $z > 0$ given by Galin (1961) as

$$u=(1-2\nu)\int_z^\infty \frac{\partial\phi}{\partial x}\,dz - z\frac{\partial\phi}{\partial x}, \tag{1}$$

$$v=(1-2\nu)\int_z^\infty \frac{\partial\phi}{\partial y}\,dz - z\frac{\partial\phi}{\partial y}, \tag{2}$$

$$w=(1-2\nu)\phi - z\frac{\partial\phi}{\partial z}, \tag{3}$$

$$\frac{1}{2\mu}\sigma_{xx}=2\nu\frac{\partial\phi}{\partial z}+(1-2\nu)\int_z^\infty \frac{\partial^2\phi}{\partial x^2}\,dz - z\frac{\partial^2\phi}{\partial x^2}, \tag{4}$$

$$\frac{1}{2\mu}\sigma_{yy}=2\nu\frac{\partial\phi}{\partial z}+(1-2\nu)\int_z^\infty \frac{\partial^2\phi}{\partial y^2}dz - z\frac{\partial^2\phi}{\partial y^2}, \tag{5}$$

$$\frac{1}{2\mu}\sigma_{zz}=\frac{\partial\phi}{\partial z}-z\frac{\partial^2\phi}{\partial z^2}, \tag{6}$$

$$\frac{1}{2\mu}\tau_{xy}=(1-2\nu)\int_z^\infty \frac{\partial^2\phi}{\partial x\partial y}dz - z\frac{\partial^2\phi}{\partial x\partial y}, \tag{7}$$

$$\frac{1}{2\mu}\tau_{xz}=-z\frac{\partial^2\phi}{\partial x\partial z}, \tag{8}$$

$$\frac{1}{2\mu}\tau_{yz}=-z\frac{\partial^2\phi}{\partial y\partial z}, \tag{9}$$

with

$$\nabla^2\phi=0. \tag{10}$$

Equations (8) and (9) reveal that the shear stress vanishes on the half space surface while the normal displacement and stress become

$$w=2(1-\nu)\phi,\ \sigma_{zz}=2\mu\frac{\partial\phi}{\partial z},\ z=0. \tag{11}$$

For the circular geometry considered here, an appropriate solution to equation (10) is given in cylindrical coordinates as

$$\phi(r,\theta,z)=\sum_{-\infty}^{\infty}\int_0^\infty \xi C_n(\xi)e^{-\xi z}J_{|n|}(\xi r)d\xi\ e^{in\theta}. \tag{12}$$

The conditions on the surface then become

$$w=2(1-\nu)\sum_{-\infty}^{\infty}\int_0^\infty \xi C_n(\xi)J_{|n|}(\xi r)d\xi\ e^{in\theta}. \tag{13}$$

$$\sigma_{zz}=-2\mu\sum_{-\infty}^{\infty}\int_0^\infty \xi^2 C_n(\xi)J_{|n|}(\xi r)d\xi\ e^{in\theta}. \tag{14}$$

3 Point Dislocation in a Full Space

The solution for a point "opening" dislocation in a full space is determined first. This solution is well known but certain results will be of use for the more complicated interaction problems analyzed subsequently. Consider the point dislocation to be on the plane $z = 0$ of a full space $-\infty < z < \infty$, $0 < r < \infty$, $0 < \theta < 2\pi$ located at the arbitrary point (r_o, θ_o) with a z-directed opening of magnitude b. The plane $z = 0$ is then one of symmetry on which the shear stress vanishes. The normal (z-directed) displacement is zero everywhere except at the dislocation point and may be written as

$$w(r,\theta,0)=\frac{b}{2r}\delta(r-r_o)\delta(\theta-\theta_o). \tag{15}$$

Expanding equation (15) in a Fourier series and using equation (13) results in

$$\int_0^\infty \xi C_n(\xi)J_{|n|}(\xi r)d\xi=\frac{b}{2\pi(\kappa+1)r}\delta(r-r_o)e^{-in\theta o}, \tag{16}$$

where $\kappa = 3-4\nu$. The solution to this integral equation is easily found to be

$$C_n(\xi)=\frac{b}{2\pi(\kappa+1)}e^{-in\theta_o}J_{|n|}(\xi r_o). \tag{17}$$

The stress on the plane of the dislocation is the quantity of interest which can be found from equations (14) and (17). Using the relation (Watson, 1980)

$$\sum_{-\infty}^{\infty}J_{|n|}(\xi r_o)\,J_{|n|}(\xi r)\,e^{in(\theta-\theta_o)}=J_0(\xi\alpha), \tag{18}$$

where $\alpha = \sqrt{r^2+r_o^2-2rr_o\cos(\theta-\theta_o)}$ gives

$$\sigma_{zz}(r,\theta,0)=-\frac{b\mu}{\pi(\kappa+1)}\int_0^\infty \xi^2 J_0(\xi\alpha)d\xi. \tag{19}$$

The integral is formally divergent but must be interpreted as

$$\int_0^\infty \xi^2 J_0(\xi\alpha)d\xi=\lim_{z\to 0}\int_0^\infty \xi^2 e^{-\xi z}J_0(\xi\alpha)d\xi=-\frac{1}{\alpha^3}, \tag{20}$$

giving the well-known result

$$\sigma_{zz}(r,\theta,0)=\frac{b\mu}{\pi(\kappa+1)}\frac{1}{R^3}, \tag{21}$$

where R is the distance between the dislocation point (r_o, θ_o) and the field point (r, θ). Equations (17) and (21) will be of use in the following analysis.

4 Dislocation Interaction With a Penny-Shaped Crack

Attention is now focused on the problem depicted in Fig. 1. A point "opening" z-directed dislocation with magnitude b is located in the vicinity of a finite size (penny-shaped) crack.

Downloaded 03 May 2010 to 171.66.16.244. Redistribution subject to ASME license or copyright; see http://www.asme.org/terms/Terms_Use.cfm

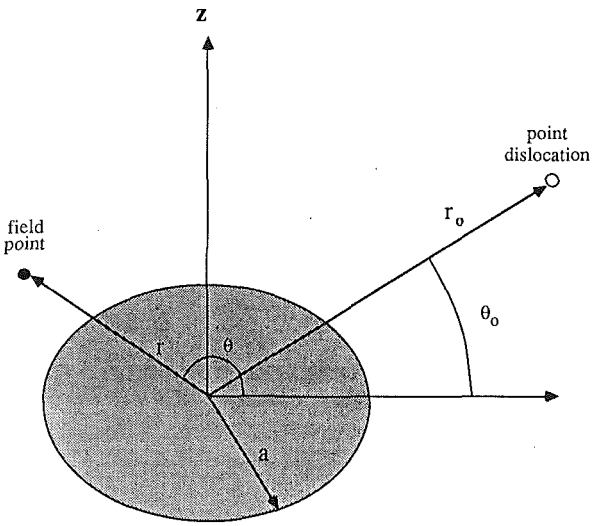


Fig. 1 Point dislocation in the vicinity of a penny-shaped crack

The crack occupies the region $z = 0, r < a$ while the dislocation is located at the point $(r_o, \theta_o, 0)$ with $r_o > a$. The problem is again reduced by symmetry to one for the half space $z > 0$ with zero shear stress on the surface along with the boundary conditions

$$\sigma_{zz}(r,\theta,0) = 0,\ r<a, \tag{22}$$

$$w(r,\theta,0) = \frac{b}{2r}\,\delta(r-r_o)\delta(\theta-\theta_o),\ r>a,\ r_o>a. \tag{23}$$

Expanding equation (23) into a Fourier series and then substituting equations (13) and (14) into equations (22) and (23), and making the following substitutions

$$r=\rho a,\ r_o=\rho_o a,\ \xi = y/a,\ yC_n\left(\frac{y}{a}\right)=\psi_n(y), \tag{24}$$

results in the dual integral equations

$$\int_0^\infty y\psi_n(y)J_{|n|}(y\rho)\,dy = 0,\ \rho<1, \tag{25}$$

$$\int_0^\infty \psi_n(y)J_{|n|}(y\rho)\,dy = f_n(\rho),\ \rho>1, \tag{26}$$

with

$$f_n(\rho) = \frac{ba}{2\pi(\kappa+1)\rho}\delta(a[\rho-\rho_o])e^{-in\theta_o}. \tag{27}$$

The solution to this pair of dual integral equations is well known (Sneddon, 1966) and is given as

$$\psi_n(y) = y^{1/2}\int_1^\infty \phi_n(t)J_{|n|+1/2}(yt)\,dt, \tag{28}$$

$$\phi_n(t) = -\frac{\sqrt{2}}{\sqrt{\pi}}\,t^{|n|+1/2}\frac{d}{dt}\int_t^\infty \frac{\rho^{1-|n|}f_n(\rho)}{\sqrt{\rho^2-t^2}}\,d\rho. \tag{29}$$

From equation (27), $\phi_n(t)$ may be given as

$$\phi_n(t) = -\frac{b}{\sqrt{2\pi}}\,\frac{1}{\pi(\kappa+1)}\,t^{|n|+3/2}\rho_o^{-|n|}e^{-in\theta_o}\,\frac{H(\rho_o-t)}{(\rho_o^2-t^2)^{3/2}}, \tag{30}$$

where $H(r)$ is the Heaviside function. Substituting equation (30) into (28) and using equation (24) results in

$$C_n(\xi) = -\frac{b}{\sqrt{2\pi\xi}}\,\frac{1}{\pi(\kappa+1)}\,r_o^{-|n|}e^{-in\theta_o}\int_a^{r_o}\frac{x^{|n|+3/2}J_{|n|+1/2}(\xi x)}{(r_o^2-x^2)^{3/2}}\,dx. \tag{31}$$

The integral is divergent at the upper limit. This is associated with the dislocation in the full space ($a=0$) and Appendix A verifies the result

$$\int_0^{r_o}\frac{x^{|n|+3/2}J_{|n|+1/2}(\xi x)}{(r_o^2-x^2)^{3/2}}\,dx = -\frac{\sqrt{\pi\xi}}{\sqrt{2}}\,r_o^{|n|}J_{|n|}(\xi r_o). \tag{32}$$

Using equation (32), equation (31) can be written as

$$C_n(\xi) = \frac{b}{2\pi(\kappa+1)}e^{-in\theta_o}\left(J_{|n|}(\xi r_o) + \frac{\sqrt{2}}{\sqrt{\pi\xi}}\,r_o^{-|n|}\int_0^a \frac{x^{|n|+3/2}J_{|n|+1/2}(\xi x)}{(r_o^2-x^2)^{3/2}}dx\right). \tag{33}$$

The first term corresponds to the point dislocation in a full space (equation (17)) while the second term is the alteration caused by the crack which vanishes for $a \to 0$.

The two quantities of interest are the crack opening displacement and the stress on the symmetry plane. The crack opening displacement is given by C.O.D. $= 2w(r, \theta, 0)$ with $w(r, \theta, 0)$ determined from equation (13). The first term of equation (33) gives a zero contribution. Inserting the second term into equation (13) and using the relations

$$\sum_{-\infty}^{\infty} t^{|n|}e^{in\alpha} = \frac{1-t^2}{1+t^2-2t\cos(\alpha)}, \tag{34}$$

$$\int_0^\infty \xi^{1/2}J_{|n|+1/2}(\xi x)J_{|n|}(\xi r)\,d\xi = \frac{\sqrt{2}}{\sqrt{\pi}}\,r^{|n|}x^{-|n|-1/2}\,\frac{H(x-r)}{\sqrt{x^2-r^2}}, \tag{35}$$

$$\int_r^a \frac{x}{(r_o^2-x^2)^{3/2}(x^2-r^2)^{1/2}}\,dx = \frac{\sqrt{a^2-r^2}}{\sqrt{r_o^2-a^2}}\,\frac{1}{(r_o^2-r^2)}, \tag{36}$$

gives the result

$$\text{C.O.D.} = \frac{b}{\pi^2}\,\frac{\sqrt{a^2-r^2}}{\sqrt{r_o^2-a^2}}\,\frac{1}{r^2+r_o^2-2rr_o\cos(\theta-\theta_o)},\ r<a, r_o>a. \tag{37}$$

The stress intensity factor can easily be found from this relation but here the stress over the entire symmetry plane will be determined. Equation (21) gives the contribution from the first term of equation (33). The effect of the crack is denoted as σ_{zz}^c and is found by substituting the second term into equation (14). Using the summation in equation (34) along with the integral

$$\int_0^\infty \xi^{3/2}J_{|n|+1/2}(\xi x)J_{|n|}(\xi r)\,d\xi = -\frac{\sqrt{2}}{\sqrt{\pi}}r^{-|n|}x^{|n|+1/2}\,\frac{H(r-x)}{(r^2-x^2)^{3/2}}, \tag{38}$$

(which has the previous interpretation) results in

$$\sigma_{zz}^c = \frac{2\mu b}{\pi^2(\kappa+1)}\int_0^a \frac{x^2(r^2r_o^2-x^4)}{(r_o^2-x^2)^{3/2}(r^2-x^2)^{3/2}[r^2r_o^2+x^4-2rr_ox^2\cos(\theta-\theta_o)]}\,dx. \tag{39}$$

This integral is evaluated in Appendix B. From this result and equation (21), the total stress is

$$\sigma_{zz}(r,\theta,0) = \frac{b\mu}{\pi(\kappa+1)}\,\frac{1}{R^3} + \frac{2\mu b}{\pi^2(\kappa+1)}\,I(r,r_o),\ r>a,\ r_o>a, \tag{40}$$

Downloaded 03 May 2010 to 171.66.16.244. Redistribution subject to ASME license or copyright; see http://www.asme.org/terms/Terms_Use.cfm

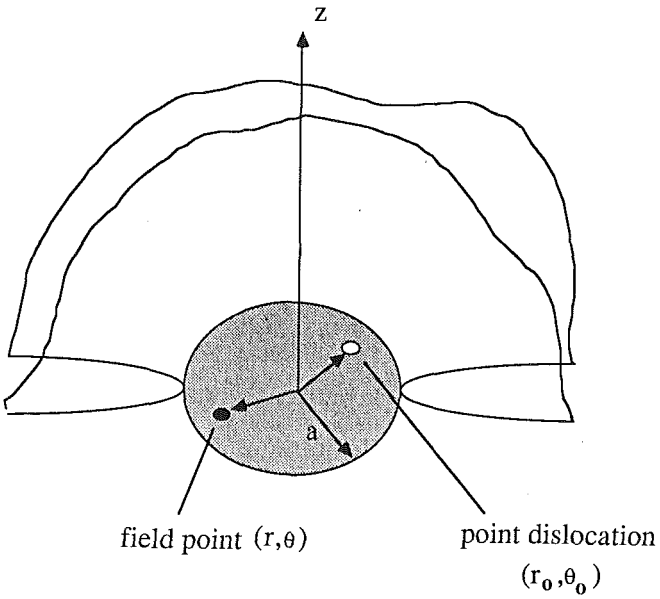


Fig. 2 Point dislocation near a circular external crack

with

$$I(r,r_o) = -\frac{1}{R^3}\tan^{-1}\left(\frac{aR}{\sqrt{r^2-a^2}\sqrt{r_o^2-a^2}}\right) + \frac{a}{R^2\sqrt{r^2-a^2}\sqrt{r_o^2-a^2}}, \tag{41}$$

and $R = \sqrt{r^2+r_o^2-2rr_o\cos(\theta-\theta_o)}$. The correction term $I(r, r_o)$ is not singular for $R \to 0$. It is singular for $r \to a^+$ and the stress intensity factor is

$$K_I = \lim_{r\to a^+}\sqrt{2\pi(r-a)}\,\sigma_{zz}(r,\theta,0) = \frac{2\mu b}{\pi^2(\kappa+1)}\frac{\sqrt{\pi a}}{\sqrt{r_o^2-a^2}(a^2+r_o^2-2ar_o\cos(\theta-\theta_o))}. \tag{42}$$

In the limit $a \to \infty$, the results of Rice (1985b) for the interaction of a point dislocation and a half plane crack are obtained.

5 Dislocation Interaction With a Circular External Crack

Having solved the internal crack problem, it is a simple matter to extend this analysis to the complementary external crack. From Fig. 2, a point dislocation with magnitude b is located in the bond region of a circular external crack. The crack occupies the domain $z = 0$, $r > a$, while the dislocation is at the point $(r_o, \theta_o, 0)$ with $r_o < a$. Along with the zero shear conditions on the plane $z = 0$, the boundary conditions are now

$$\sigma_{zz}(r,\theta,0) = 0,\ r > a, \tag{43}$$

$$w(r,\theta,0) = \frac{b}{2r}\,\delta(r-r_o)\delta(\theta-\theta_o), r<a,\ r_o<a. \tag{44}$$

Modifying equation (24) as

$$y^2 C_n\left(\frac{y}{a}\right) = \psi_n(y), \tag{45}$$

gives the dual integral equations

$$\int_0^\infty \psi_n(y)J_{|n|}(y\rho)dy = 0,\ \rho>1, \tag{46}$$

$$\int_0^\infty y^{-1}\psi_n(y)J_{|n|}(y\rho)dy = f_n(\rho),\ \rho<1, \tag{47}$$

with $f_n(\rho)$ given by equation (27).

The solution is now given as (Sneddon, 1966)

$$\psi_n(y) = y^{3/2}\int_0^1 \phi_n(t)J_{|n|-1/2}(yt)dt, \tag{48}$$

$$\phi_n(t) = \frac{\sqrt{2}}{\sqrt{\pi}}t^{-|n|+1/2}\frac{d}{dt}\int_0^t \frac{\rho^{1+|n|}f_n(\rho)}{\sqrt{t^2-\rho^2}}d\rho. \tag{49}$$

Using equation (27) results in

$$\phi_n(t) = -\frac{b}{\sqrt{2\pi}}\frac{1}{\pi(\kappa+1)}t^{-|n|+3/2}\rho_o^{|n|}e^{-in\theta_o}\frac{H(t-\rho_o)}{(t^2-\rho_o^2)^{3/2}}. \tag{50}$$

From equations (45), (48), and (50), $C_n(\xi)$ is determined as

$$C_n(\xi) = -\frac{b}{\sqrt{2\pi\xi}}\frac{1}{\pi(\kappa+1)}r_o^{|n|}\,e^{-in\theta_o}\int_{r_o}^a \frac{x^{-|n|+3/2}J_{|n|-1/2}(\xi x)}{(x^2-r_o^2)^{3/2}}dx. \tag{51}$$

The integral is now divergent at the lower limit. As with the internal crack, it can be shown by a similar procedure to the one in Appendix A that this behavior is associated with the dislocation in a full space. The final result is

$$C_n(\xi) = \frac{b}{2\pi(\kappa+1)}e^{-in\theta_o}\left(J_{|n|}(\xi r_o) + \frac{\sqrt{2}}{\sqrt{\pi\xi}}r_o^{|n|}\int_a^\infty \frac{x^{-|n|+3/2}J_{|n|-1/2}(\xi x)}{(x^2-r_o^2)^{3/2}}dx\right). \tag{52}$$

The crack opening displacement is again found by substituting equation (52) into (13) and multiplying by two. Using the integrals

$$\int_0^\infty \xi^{1/2}J_{|n|-1/2}(\xi x)J_{|n|}(\xi r)d\xi = \frac{\sqrt{2}}{\sqrt{\pi}}r^{-|n|}x^{|n|-1/2}\frac{H(r-x)}{\sqrt{r^2-x^2}}, \tag{53}$$

$$\int_a^r \frac{x}{(x^2-r_o^2)^{3/2}(r^2-x^2)^{1/2}}dx = \frac{\sqrt{r^2-a^2}}{\sqrt{a^2-r_o^2}}\frac{1}{(r^2-r_o^2)}, \tag{54}$$

along with equation (34) results in

$$\text{C.O.D.} = \frac{b}{\pi^2}\frac{\sqrt{r^2-a^2}}{\sqrt{a^2-r_o^2}}\frac{1}{r^2+r_o^2-2rr_o\cos(\theta-\theta_o)}, r>a,\ r_o<a. \tag{55}$$

The stress field in the ligament is now determined. The contribution from the first term in equation (52) is again given by equation (21), and the effect of the crack is denoted as σ_{zz}^c. Substituting the second term of equation (52) into (14) and using the integral

$$\int_0^\infty \xi^{3/2}J_{|n|-1/2}(\xi x)J_{|n|}(\xi r)d\xi = -\frac{\sqrt{2}}{\sqrt{\pi}}r^{|n|}x^{-|n|+1/2}\frac{H(x-r)}{(x^2-r^2)^{3/2}}, \tag{56}$$

and equation (34) leads to

Downloaded 03 May 2010 to 171.66.16.244. Redistribution subject to ASME license or copyright; see http://www.asme.org/terms/Terms_Use.cfm

$$\sigma_{zz}^{c}=\frac{2\mu b}{\pi^2(\kappa+1)}\int_a^\infty \frac{x^2(x^4-r^2r_o^2)}{(x^2-r_o^2)^{3/2}(x^2-r^2)^{3/2}[r^2r_o^2+x^4-2rr_ox^2\cos(\theta-\theta_o)]}dx. \quad (57)$$

Although this integral may be evaluated by the same transformation given in Appendix B, an easier approach is available. If this integral is denoted as $J(r,r_o)$, then it is easy to verify the relation

$$J(r,r_o)=\frac{a^6}{r^3r_o^3}I\left(\frac{a^2}{r},\frac{a^2}{r_o}\right), \quad (58)$$

with $I(r,r_o)$ given by equation (41). Using this result, the total stress becomes

$$\sigma_{zz}(r,\theta,0)=\frac{b\mu}{\pi(\kappa+1)}\frac{1}{R^3}+\frac{2\mu b}{\pi^2(\kappa+1)}J(r,r_o),\ r<a,\ r_o<a, \quad (59)$$

with

$$J(r,r_o)=-\frac{1}{R^3}\tan^{-1}\left(\frac{aR}{\sqrt{a^2-r^2}\sqrt{a^2-r_o^2}}\right)+\frac{a}{R^2\sqrt{a^2-r^2}\sqrt{a^2-r_o^2}}, \quad (60)$$

and $R=\sqrt{r^2+r_o^2-2rr_o\cos(\theta-\theta_o)}$. The interaction term $J(r,r_o)$ is not singular for $R\to 0$, and the stress intensity factor is

$$K_I=\lim_{r\to a^-}\sqrt{2\pi(a-r)}\,\sigma_{zz}(r,\theta,0)=\frac{2\mu b}{\pi^2(\kappa+1)}\frac{\sqrt{\pi a}}{\sqrt{a^2-r_o^2}\,(a^2+r_o^2-2ar_o\cos(\theta-\theta_o))}. \quad (61)$$

6 Integral Formulation for Multiple or Wavy Cracks

An integral formulation for multiple coplanar cracks or cracks with large amplitude variations in the crack front curvature can be obtained by distributing the fundamental solution derived here. Such a formulation was given by Rice (1985b) for an arbitrary opening ahead of a half plane crack. Rice (1987), using Bueckner's (1987) weight functions, extended this work to off-plane openings of arbitrary orientation near a half plane or circular crack. In this case, however, the fundamental solution for a point dislocation was not given in closed form but rather in terms of double integrals. In the present analysis the dislocation is less general since it is one of opening only, and limited to a single plane, but the presently derived closed-form interactions are utilized such that the resulting equations are much more attractive to consider from a numerical standpoint. To illustrate this approach, a derivation of the new integral formulation for multiple coplanar circular cracks of finite size developed by Fabrikant (1987a, 1987b) is given first. Consider a system of n coplanar circular cracks occupying the domains S_k with radius a_k and crack opening displacement b_k. Taking S_i to be the reference crack, the total crack opening of S_i can be given by the superposition

$$b_i(r,\theta)=b_i^o(r,\theta)+\frac{\sqrt{a_i^2-r^2}}{\pi^2}\sum_{\substack{k=1\\k\neq i}}^{n}\int_{S_k}\int \frac{b_k(r_o,\theta_o)r_o\,dr_o\,d\theta_o}{\sqrt{r_o^2-a_i^2}\,[r^2+r_o^2-2rr_o\cos(\theta-\theta_o)]},\ r,\theta\in S_i,\ i=1,\ldots,n. \quad (62)$$

Here, the coordinate system is taken to be centered at S_i and $b_i^o(r,\theta)$ represents the known crack opening of S_i caused solely from the applied normal stress on its faces (see equation (12) or (21) of Fabrikant (1987b) for an explicit expression). The integral terms represent the effects of the additional crack openings. The integrals in equation (62) can be written directly from equation (37) by distributing the point dislocation with a density of $b_k(r_o,\theta_o)$ over the domains S_k. Equation (62) represents a set of n simultaneous nonsingular integral equations to determine the n crack openings. Equation (62) is analogous to the integral equations given by Fabrikant (1987a) where they were derived by constructing an inverse operator to the conventional singular integral equations.

An iterative solution to these equations for the case of two equal cracks was given by Fabrikant (1987a). This method can be extended to the case of more than two cracks. Alternatively, these equations can be solved directly without any special numerical considerations since they are nonsingular. Using appropriate approximations to the crack opening displacements over elements, the integral equations can easily be converted to algebraic ones. The resulting integrals can be evaluated by standard quadrature techniques since only nonsingular integrals are involved.

A direct solution for a set of cracks by utilizing the nonsingular equations (62) still requires the consideration of each crack domain. A more general singular formulation for the presence of multiple cracks of arbitrary geometry in the vicinity of a circular crack can be obtained as follows. Let the center of coordinates be taken at the center of the circular crack (denoted as S_o) of radius "a." The regions S_k, $k=1,\ldots,n$ now represent the domains of cracks of arbitrary geometry in the vicinity of S_o. The stress on the crack plane outside of S_o caused by S_k can be written as a superposition of dislocations from equation (40) as

$$\sigma_{zz}(r,\theta)=\frac{\mu}{\pi(\kappa+1)}\sum_{k=1}^{n}\int_{S_k}\int b_k(r_o,\theta_o)\left(\frac{1}{R^3}+\frac{2}{\pi}I(r,r_o)\right)dA,\quad r>a. \quad (63)$$

Adding to this the known stress on the symmetry plane from the applied loading on the crack faces of the circular crack (denoted as $\sigma_{zz}^o(r,\theta)$, see equation (9) of Fabrikant (1987b) for an explicit form) gives the integral equations

$$\sigma_{zz}^o(r,\theta)+\frac{\mu}{\pi(\kappa+1)}\sum_{k=1}^{n}\int_{S_k}\int b_k(r_o,\theta_o)\left(\frac{1}{R^3}+\frac{2}{\pi}I(r,r_o)\right)dA=p_i(r,\theta),\ r,\theta\in S_i,\ i=1,\ldots,n \quad (64)$$

where $p_i(r,\theta)$ are the loadings on the crack faces of S_i. Equation (64) represents n integral equations to determine the n additional crack openings. Once the additional crack openings are determined, a superposition of equations (37) and (42) allows the evaluation of the additional crack opening and stress intensity factor for the circular crack. This is a more general formulation since cracks of arbitrary geometry can be considered; however, the integral equations are strongly singular.

The strong singularity (denoted as hypersingular) arises from the contribution of the point dislocation in a full space (equation (21)). The integration of this term over the cracked area results in an integral that is divergent in the ordinary Reimann sense. This singularity is also stronger than the conventional Cauchy singularity which arises in two-dimensional fracture analysis. The contribution of this term to the integral equation is as the finite part of the divergent integral. These finite part integrals have been considered previously in three-dimensional fracture studies (Murakami and Nemat-Nasser, 1982, 1983; Murakami, 1985; Lee and Keer, 1986; Lee et al., 1987; Hanson et al., 1989), and the validity of the finite part contribution for the mode I crack has been established by Ioakimidis (1982, 1987). A numerical solution to the equation (64) (or set of equations for more than one crack) follows directly the methods used by Lee et al. (1987) and Hanson et al. (1989) for the

Downloaded 03 May 2010 to 171.66.16.244. Redistribution subject to ASME license or copyright; see http://www.asme.org/terms/Terms_Use.cfm

mixed-mode analysis. The method for the evaluation of the finite part integral is given by Murakami and Nemat-Nasser (1983) and Lee and Keer (1986).

The extension to the case of multiple coplanar cracks in the bond region of a circular external crack can also be formulated from the present results. To obtain a set of integral equations similar to equation (62), both dislocation solutions of Sections 4 and 5 may be used. If the reference crack is one of the finite circular cracks in the bond region, equation (37) can be used for the superposition, and one of the domains S_k is that of the circular external crack. If the reference crack is the external crack, the origin is taken at the center of the bond region and equation (55) is utilized. In this formulation all internal cracks must be circular. If $I(r, r_o)$ in equation (64) is replaced by $J(r,r_o)$ (defined in (60)), and σ^o_{zz} is interpreted as the normal stress in the bond region from the applied stress on the external crack, equation (64) is then a set of singular integral equations for the crack openings in the bond region. This formulation has the added advantages that the internal cracks can take any shape and the infinite surface of the external crack need not be considered. The additional crack opening displacement and stress intensity for the external crack are then found by an appropriate superposition of equations (55) and (61).

An integral formulation for an internal and external crack with a nonuniform crack front can be obtained in a manner similar to the multiple crack formulation. Consider first a finite size crack of near circular geometry with a wavy crack front. Denote the total crack domain as S_t. Let S_c denote the region interior to a circle which is entirely encompassed in S_t. The crack occupying S_t can be modeled as a penny-shaped crack in S_c with distributed dislocations to account for the region $S_t - S_c$. The total stress acting on the area $S_t - S_c$ must equal the applied loading $p(r,\theta)$, which by superposition becomes

$$\sigma^o_{zz}(r,\theta) + \frac{\mu}{\pi(\kappa+1)} \int_{S_t - S_c} \int b(r_o,\theta_o) \left(\frac{1}{R^3} + \frac{2}{\pi} I(r,r_o) \right) dA = p(r,\theta),\ r,\ \theta \in S_t - S_c. \quad (65)$$

Here, $\sigma^o_{zz}(r, \theta)$ is the known stress outside of the penny-shaped crack S_c caused by the applied pressure to its faces. The integral is the contribution from the distributed dislocations. Again the kernel contains the hypersingular term, and hence the previous discussion of the finite part contribution as well as a numerical solution procedure applies here. In this case, an additional square root (integrable) singularity occurs in $I(r,r_o)$ for $r_o \to a^+$ (equation (41)), and an accurate numerical solution must also incorporate this behavior. Since a numerical solution to this equation need only consider the domain $S_t - S_c$, the advantage over considering the entire crack is evident.

A similar equation can be obtained for an external crack with a wavy front. If S_t is the domain of the total crack and S_c is that of a circular external crack encompassed in S_t, then equation (65) with I replaced by J will apply. Now $\sigma^o_{zz}(r, \theta)$ is the known stress in the bond region with the normal tractions applied to the external circular crack S_c. In this case, the infinite domain is reduced to one of finite dimensions.

7 Conclusions

This analysis has considered the interaction between a point "opening" dislocation and a circular internal or external crack. The dislocation was taken to be on the plane of the crack which allowed the reduction to a mixed boundary value problem for a half space. A closed-form solution was obtained for the crack opening displacement, stress on the symmetry plane, and hence mode I stress intensity factor around the crack front. The use of the present solution was outlined by formulating integral equations to be used in studying multiple coplanar cracks or cracks with large amplitude variations in the crack front curvature. The interaction, which automatically accounts for the stress-free circular surface, allows a large reduction in the domain which must be considered in a numerical study. The use of the present Green's function will allow a significant increase in the accuracy of future numerical calculations.

References

Bueckner, H. F., 1970, "A Novel Principle for the Computation of Stress Intensity Factors," *Z. Angew. Math. Mech.*, Vol. 50, pp. 529–546.

Bueckner, H. F., 1973, "Field Singularities and Related Integral Representations," *Mechanics of Fracture*, Vol. 1, Noordhoff, pp. 239–314.

Bueckner, H. F., 1987, "Weight Functions and Fundamental Fields for the Penny Shaped and the Half Plane Crack in Three Space," *International Journal of Solids and Structures*, Vol. 23, pp. 57–93.

Fabrikant, V. I., 1987a, "Close Interaction of Coplanar Circular Cracks in an Elastic Medium," *Acta Mechanica*, Vol. 67, pp. 39–59.

Fabrikant, V. I., 1987b, "Penny Shaped Crack Revisited: Closed Form Solutions," *Philosophical Magazine*, Vol. A56, pp. 191–207.

Galin, L. A., 1961, *Contact Problems in the Theory of Elasticity*, North Carolina State University Publications.

Gao, H., and Rice, J. R., 1987a, "Somewhat Circular Tensile Cracks," *International Journal of Fracture*, Vol. 33, pp. 155–174.

Gao, H., and Rice, J. R., 1987b, "Nearly Circular Connections of Elastic Half Spaces," ASME JOURNAL OF APPLIED MECHANICS, Vol. 54, pp. 627–634.

Gradshteyn, I. S., and Ryzhik, I. M., 1980, *Table of Integrals, Series and Products*, Academic Press, p. 81.

Hanson, M. T., Lin, W., and Keer, L. M., 1989, "Three-Dimensional Analysis of Cracking Through the Boundary of a Two Phase Material," ASME JOURNAL OF APPLIED MECHANICS, Vol. 56, pp. 850–857.

Ioakimidis, N. I., 1982, "Application of Finite-Part Integrals to the Singular Integral Equations of Crack Problems in Plane and Three-Dimensional Elasticity," *Acta Mechanica*, Vol. 45, pp. 31–47.

Ioakimidis, N. I., 1987, "Validity of the Hypersingular Integral Equation of Crack Problems in Three-Dimensional Elasticity Along the Crack Boundary," *Engineering Fracture Mechanics*, Vol. 26, pp. 783–788.

Kassir, M. K., and Sih, G. C., 1975, *Mechanics of Fracture*, Vol. 2, Noordhoff.

Lee, J. C., and Keer, L. M., 1986, "Study of a Three-Dimensional Crack Terminating at an Interface," ASME JOURNAL OF APPLIED MECHANICS, Vol. 53, pp. 311–316.

Lee, J. C., Farris, T. N., and Keer, L. M., 1987, "Stress Intensity Factors for Cracks of Arbitrary Shape Near an Interfacial Boundary," *Engineering Fracture Mechanics*, Vol. 27, pp. 27–41.

Murakami, Y., and Nemat-Nasser, S., 1982, "Interacting Dissimilar Semi-Elliptical Surface Flaws Under Tension and Bending," *Engineering Fracture Mechanics*, Vol. 16, pp. 373–386.

Murakami, Y., and Nemat-Nasser, S., 1983, "Growth and Stability of Interacting Surface Flaws of Arbitrary Shape," *Engineering Fracture Mechanics*, Vol. 17, pp. 193–210.

Murakami, Y., 1985, "Analysis of Stress Intensity Factors of Modes I, II and III for Inclined Surface Cracks of Arbitrary Shape," *Engineering Fracture Mechanics*, Vol. 22, pp. 101–114.

Rice, J. R., 1972, "Some Remarks on Elastic Crack-Tip Stress Fields," *International Journal of Solids and Structures*, Vol. 8, pp. 751–758.

Rice, J.R., 1985a, "First-Order Variation in Elastic Fields Due to Variation in Location of a Planar Crack Front," ASME JOURNAL OF APPLIED MECHANICS, Vol. 52, pp. 571–579.

Rice, J. R., 1985b, "Three-Dimensional Elastic Crack Tip Interactions with Transformation Strains and Dislocations," *International Journal of Solids and Structures*, Vol. 21, pp. 781–791.

Rice, J. R., 1987, "Weight Function Theory for Three-Dimensional Elastic Crack Analysis," *Proceedings of the 20th National Symposium on Fracture Mechanics*, ASTM-STP.

Rice, J. R., 1988, "Crack Fronts Trapped by Arrays of Obstacles: Solutions Based on Linear Perturbation Theory," *Analytical, Numerical and Experimental Aspects of Three Dimensional Fracture Processes*, ASME/AMD Vol. 91, ASME, New York, pp. 175–184.

Sneddon, I. N., 1966, *Mixed Boundary Value Problems in Potential Theory*, North-Holland, pp. 86–88.

Watson, G. N., 1980, *A Treatise on the Theory of Bessel Functions*, Cambridge University Press, pp. 358.

APPENDIX A

Here, consideration is given to the divergency that arises in the integral of equation (31). This integral results from the solution of the dual integral equations (25) and (26). It is convenient to write these in dimensional form as

$$\int_0^\infty \xi \psi_n(\xi) J_{|n|}(\xi r) d\xi = 0,\ r < a, \quad (A1)$$

$$\int_0^\infty \psi_n(\xi) J_{|n|}(\xi r) d\xi = \frac{b}{2\pi(\kappa+1)r} \delta(r - r_o) e^{-in\theta_o},\ r > a, \quad (A2)$$

Downloaded 03 May 2010 to 171.66.16.244. Redistribution subject to ASME license or copyright; see http://www.asme.org/terms/Terms_Use.cfm

where the substitution

$$\xi C_n(\xi) = \psi_n(\xi) \tag{A3}$$

has been used in place of the one in equation (24). A solution consistent with equation (28) is sought as

$$\psi_n(\xi) = \xi^{1/2} \int_a^\infty \phi_n(t) J_{|n|+1/2}(\xi t)\, dt. \tag{A4}$$

Using equation (38) reveals that equation (A1) is automatically satisfied. In the limit $a \to 0$, equation (A2) applies over the entire surface and the solution is given by equation (17). Substituting (17) into (A3) and equation (A3) to (A4) with $a = 0$ leads to

$$\frac{b}{2\pi(\kappa+1)} e^{-in\theta_o} \xi J_{|n|}(\xi r_o) = \xi^{1/2} \int_0^\infty \phi_n(t) J_{|n|+1/2}(\xi t)\, dt. \tag{A5}$$

Multiplying both sides of this equation by $\xi^{1/2} J_{|n|+1/2}(\xi s)\, ds$ and integrating from zero to infinity gives

$$\phi_n(s) = \frac{b}{2\pi(\kappa+1)} e^{-in\theta_o} s \int_0^\infty \xi^{3/2} J_{|n|+1/2}(\xi s) J_{|n|}(\xi r_o)\, d\xi, \tag{A6}$$

which by equation (38) becomes

$$\phi_n(s) = -\frac{b}{\sqrt{2\pi}} \frac{1}{\pi(\kappa+1)} s^{|n|+3/2} r_o^{-|n|} e^{-in\theta_o} \frac{H(r_o - s)}{(r_o^2 - s^2)^{3/2}}. \tag{A7}$$

Substituting this expression into equation (A5) gives the integral identity

$$\int_0^{r_o} \frac{t^{|n|+3/2} J_{|n|+1/2}(\xi t)}{(r_o^2 - t^2)^{3/2}}\, dt = -\frac{\sqrt{\pi \xi}}{\sqrt{2}} r_o^{|n|} J_{|n|}(\xi r_o), \tag{A8}$$

which is equation (32).

Since the integral is divergent, the evaluation in equation (A8) must be interpreted as the finite part. The foregoing conclusion may be proven with an integration by parts and use of some integral indentities but this is not considered further here. Although the derivation verifies equation (A8), it does not explain the presence of the divergency. This can be resolved by considering equation (A5), which is an integral representation of the function $\xi J_{|n|}(\xi r_o)$. It is easy to see that for $\xi \to 0$, both sides exhibit the same behavior for all n. For $\xi \to \infty$, the left side is 0 ($\xi^{1/2}$), which is consistent with the $\xi^{1/2}$ on the right side. However, if $\phi_n(t)$ is integrable on $0 < t < \infty$, the additional ξ in the argument of the Bessel function will give extra decay and the large ξ behavior will not be matched on both sides. Thus, $\phi_n(t)$ can not be an integrable function. In other words, an integral representation of the form (A5) does not exist for a function $\phi_n(t)$ which is integrable on $0 < t < \infty$.

APPENDIX B

To evaluate the integral in equation (39), rewrite it as

$$I = 2 \frac{d}{d\gamma_2} \int_0^a \frac{\gamma_1^2 - x^4}{\sqrt{\gamma_1^2 - \gamma_2 x^2 + x^4}\, [\gamma_1^2 - \gamma_3 x^2 + x^4]}\, dx, \tag{B1}$$

where the following substitutions have been made

$$\gamma_1 = r r_o,\ \gamma_2 = r^2 + r_o^2,\ \gamma_3 = 2 r r_o \cos(\theta - \theta_o). \tag{B2}$$

Using the transformation

$$s = \frac{(\gamma_1 - x^2)^2 (2\gamma_1 - \gamma_3)}{4\gamma_1(\gamma_1^2 - \gamma_3 x^2 + x^4)}, \tag{B3}$$

the integral becomes

$$I = -\frac{4\gamma_1}{2\gamma_1 - \gamma_3} \frac{d}{d\gamma_2} \int_{s_1}^{s_2} \frac{1}{\sqrt{ws^2 + vs + u}}\, ds, \tag{B4}$$

with

$$w = \frac{16\gamma_1^2(\gamma_3 - \gamma_2)}{(2\gamma_1 - \gamma_3)^2},\ v = \frac{4\gamma_1}{2\gamma_1 - \gamma_3},\ (-2\gamma_1 + 2\gamma_2 - \gamma_3),\ u = 2\gamma_1 - \gamma_2, \tag{B5}$$

$$s_1 = \frac{2\gamma_1 - \gamma_3}{4\gamma_1},\ s_2 = \frac{(\gamma_1 - a^2)^2 (2\gamma_1 - \gamma_3)}{4\gamma_1(\gamma_1^2 - \gamma_3 a^2 + a^4)}. \tag{B6}$$

The integral has a closed form (Gradshteyn and Ryzhik, 1980) as

$$\int \frac{1}{\sqrt{a + bx + cx^2}} dx = \frac{-1}{\sqrt{-c}} \sin^{-1}\left(\frac{2cx + b}{\sqrt{-\Delta}}\right),$$
$$\Delta = 4ac - b^2,\ c < 0,\ \Delta < 0. \tag{B7}$$

Performing the integration, using the results

$$\Delta = -16\gamma_1^2,\ \frac{2ws_1 + v}{4\gamma_1} = -1, \tag{B8}$$

and then differentiating and back substituting leads to

$$I = -\frac{1}{2R^3}\left(\frac{\pi}{2} + \tan^{-1}(A)\right) + \frac{a}{R^2\sqrt{r^2 - a^2}\sqrt{r_o^2 - a^2}}, \tag{B9}$$

$$A = \frac{a^2 R^2 - (r^2 - a^2)(r_o^2 - a^2)}{2aR\sqrt{r^2 - a^2}\sqrt{r_o^2 - a^2}}, \tag{B10}$$

$$R = \sqrt{r^2 + r_o^2 - 2 r r_o \cos(\theta - \theta_o)}, \tag{B11}$$

where the arcsine has been converted to the arctangent. From the identity

$$\frac{\pi}{2} + \tan^{-1}\left(\frac{1}{2}\left(x - \frac{1}{x}\right)\right) = 2\tan^{-1}(x), \tag{B12}$$

the integral becomes

$$I = -\frac{1}{R^3} \tan^{-1}\left(\frac{aR}{\sqrt{r^2 - a^2}\sqrt{r_o^2 - a^2}}\right) + \frac{a}{R^2\sqrt{r^2 - a^2}\sqrt{r_o^2 - a^2}}. \tag{B13}$$

Downloaded 03 May 2010 to 171.66.16.244. Redistribution subject to ASME license or copyright; see http://www.asme.org/terms/Terms_Use.cfm

An Arbitrary Tangential Load Underneath a Smooth Circular Punch

V. I. Fabrikant
Department of Mechanical Engineering,
Concordia University,
Montreal, Canada H3G 1M8

The problem of a smooth circular punch penetrating a transversely isotropic elastic half space and interacting with an arbitrarily located tangential concentrated load is considered. For the first time, a closed-form exact solution is obtained for the stress distribution under the punch as well as for the linear and angular displacements of the punch. The solution is based on the results previously obtained by the author and combined with the reciprocal theorem. A numerical example is presented as an illustration.

Introduction

The problem of interaction between a punch and an anchor load is of particular interest to geomechanics where the internal forces can be visualized as forces transmitted by anchoring regions located in the vicinity of structural foundation. Only some axisymmetric cases have been considered so far. The only nonaxisymmetric problem solved was Fabrikant et al., 1985) where the interaction of an arbitrarily located *normal* force with a smooth circular punch was considered, and where the reader can also find all the relevant references to previous work in the field. The general case of interaction between a smooth circular punch and an arbitrarily located *tangential* load is considered here for the first time. To the best of our knowledge, this problem was not considered before even for the case of isotropy. The exact closed-form solution to the problem has become possible due to the new results in potential theory obtained by the author (Fabrikant, 1989a). Numerical results are presented in order to illustrate the stress distribution under the punch due to a radial and transversal loads.

Theory

We consider a transversely isotropic elastic half space $z \geq 0$ (Fig. 1). A smooth punch of arbitrary shape penetrates its boundary, $z = 0$. The domain of contact is a circle of radius a, with its center coinciding with the coordinate system origin, $\rho = 0$. Let a horizontal point force, with the components T_x and T_y be applied at the point Q with the polar cylindrical coordinates (ρ, ϕ, z). We shall use its complex representation, namely, $T = T_x + iT_y$. We may assume, without loss of generality, that the system of external forces applied to the punch is such that eliminates the normal and angular displacements which otherwise would have been produced by the anchor load T. We need to find the normal tractions under the punch, σ, the normal force, N, and the tilting moment, M, applied to the punch in order to compensate its displacements which otherwise would have been produced by the force T.

A general solution in terms of three harmonic functions to the mixed boundary value problem for a transversely isotropic elastic half space was given in (Fabrikant, 1988). One can deduce from the results of (Fabrikant, 1989a) that the normal displacements on the plane $z = 0$ due to the force T can be defined as

$$w(\rho_0,\phi_0,0) = \frac{1}{2} H(T\bar{q} + \bar{T}q)\left[\frac{\gamma_1}{(m_1-1)R_1(R+z_1)} + \frac{\gamma_2}{(m_2-1)R_2(R_2+z_2)}\right], \quad (1)$$

where H, γ_1, γ_2, m_1, and m_2 are parameters depending on the elastic properties of the material (see Fabrikant, 1988, for detail),

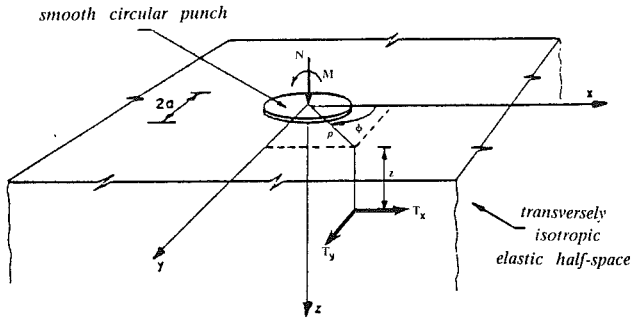


Fig. 1 Geometry and loading of a smooth punch

Contributed by the Applied Mechanics Division of THE AMERICAN SOCIETY OF MECHANICAL ENGINEERS for publication in the JOURNAL OF APPLIED MECHANICS.

Discussion on this paper should be addressed to the Technical Editor, Prof. Leon M. Keer, The Technological Institute, Northwestern University, Evanston, IL 60208, and will be accepted until two months after final publication of the paper itself in the JOURNAL OF APPLIED MECHANICS. Manuscript received by the ASME Applied Mechanics Division, May 12, 1989; final revision, Aug. 17, 1989.

Copyright © 1990 by ASME
Downloaded 03 May 2010 to 171.66.16.244. Redistribution subject to ASME license or copyright; see http://www.asme.org/terms/Terms_Use.cfm

$$q=\rho e^{i\phi}-\rho_0 e^{i\phi_0},\quad z_k=z/\gamma_k,$$

$$R_k=[\rho^2+\rho_0^2-2\rho\rho_0\cos(\phi-\phi_0)+z_k^2]^{1/2},\quad \text{for } k=1,2. \tag{2}$$

The governing integral equation, which relates the normal stress σ exerted by the punch to the displacement w defined by equation (1), is as follows:

$$\int_0^{2\pi}\int_0^a \frac{\sigma(r,\psi(rdrd\psi}{[\rho_0^2+r^2-r\rho_0\cos(\gamma_0-\psi)]^{1/2}}$$

$$=-\frac{1}{2}(T\bar{q}+\bar{T}q)\left[\frac{\gamma_1}{(m_1-1)R_1(R_1+z_1)}+\frac{\gamma_2}{(m_2-1)R_2(R_2+z_2)}\right]. \tag{3}$$

The general solution of the equation of the type equation (3) is given first in Fabrikant (1971), but it is somewhat difficult to use directly due to the complexity of the right-hand side of equation (3). We can use a shortcut instead. In addition to the point $Q(\rho,\ \phi,\ z)$, let us introduce two more points, namely, $Q_0(\rho_0,\ \phi_0,\ 0)$ and $S(r,\ \psi,\ 0)$. The following identity was established in Fabrikant et al. (1985):

$$\int_0^{2\pi}\int_0^a \frac{z}{R^3(Q,S)}\left[\frac{R(Q,S)}{h}+\tan^{-1}\left(\frac{h}{R(Q,S)}\right)\right]\frac{rdrd\psi}{R(Q_0,S)}=\frac{\pi^2}{R(Q,Q_0)}. \tag{4}$$

Here, $R(\cdot,\cdot)$ stands for the distance between two points, and

$$h=(a^2-r^2)^{1/2}(a^2-l_1^2)/a.$$

The following notation is used throughout the paper:

$$l_1(x,\rho,z)\equiv l_1(x)=\frac{1}{2}\{[(\rho+x)^2+z^2]^{1/2}-[(\rho-x)^2+z^2]^{1/2}\},$$

$$l_2(x,\rho,z)\equiv l_2(x)=\frac{1}{2}\{[(\rho+x)^2+z^2]^{1/2}+[(\rho-x)^2+z^2]^{1/2}\}. \tag{5}$$

The abbreviations l_1 and l_2 everywhere stand for $l_1(a)$ and $l_2(a)$, respectively. The notations $l_{1k}(x)$ and $l_{2k}(x)$ are understood as $l_1(x,\ \rho,\ z_k)$ and $l_2(x,\ \rho,\ z_k)$, respectively, for $k=1,2$.

We can observe that the right-hand side of equation (3) can be obtained from the right-hand side of (4) by using integration with respect to z and the consequent application of the differentiation operator Λ defined by

$$\Lambda=\frac{\partial}{\partial x}+i\frac{\partial}{\partial y}. \tag{6}$$

A similar procedure, applied to the left-hand side of equation (4), will give us the required solution. The relevant integration and differentiation is performed in Fabrikant (1989b), and the result is

$$\sigma(r,\psi)=-\Re\left\{\frac{\bar{T}}{\pi^2}\left[\frac{\gamma_1 U(z_1)}{m_1-1}+\frac{\gamma_2 U(z_2)}{m_2-1}\right]\right\}, \tag{7}$$

where $\Re$ is the real part sign, the overbar everywhere indicates the complex conjugate value, and the following notation was introduced:

$$U(z)\equiv U(\rho,\phi,z;\ r,\psi)=\frac{q_1}{R_0^3}\left[\frac{R_0}{h}+\tan^{-1}\left(\frac{h}{R_0}\right)\right]+\frac{1}{h\bar{q}_1}\left\{1-\frac{(a^2-l_1^2)^{1/2}}{a}-\frac{(a^2-l_1^2)^{1/2}}{a(\bar{\zeta}-1)^{1/2}}\left[\tan^{-1}\left(\frac{a(\bar{\zeta}-1)^{1/2}}{(a^2-l_1^2)^{1/2}}\right)-\tan^{-1}(\bar{\zeta}-1)^{1/2}\right]\right\}, \tag{8}$$

with

$$\zeta=\frac{\rho}{r}e^{i(\phi-\psi)},\quad q_1=\rho e^{i\phi}-re^{i\psi},\quad R_0=R(Q,S). \tag{9}$$

The resultant force N can be obtained by integration of σ

$$N=\int_0^{2\pi}\int_0^a \sigma(r,\psi)rdrd\psi. \tag{10}$$

Though expression (8) looks complicated, the integration in equation (11) can be performed (see Fabrikant, 1989a, for detail), and the result is rather simple:

$$N=-\Re\left\{\frac{2\bar{T}e^{i\phi}}{\pi\rho}\sum_{k=1}^{2}\left[\frac{\gamma_k[a-(a^2-l_{1k}^2)^{1/2}]}{m_k-1}\right]\right\}. \tag{11}$$

We define the tilting moment M in the complex form as follows:

$$M=M_x+iM_y=-i\int_0^{2\pi}\int_0^a \sigma(r,\psi)r^2e^{i\psi}drd\psi. \tag{12}$$

Again, the integration can be performed in elementary functions (see Fabrikant, 1989a), and the final result is

$$M=-\frac{2}{\pi}i\sum_{k=1}^{2}\left\{\frac{\gamma_k}{m_k-1}\left[T\left(z_k\sin^{-1}\left(\frac{a}{l_{2k}}\right)-(a^2-l_{1k}^2)^{1/2}\right)-\bar{T}e^{2i\phi}\frac{2a^2-(l_{1k}^2+2a^2)(a^2-l_{1k}^2)^{1/2}}{3\rho^2}\right]\right\}. \tag{13}$$

Taking into consideration the relationship between the tilting moment and the complex angle of inclination

$$\delta=\delta_x+i\delta_y=\frac{3\pi H}{4a^3}M, \tag{14}$$

we may deduce that when no tilting moment is applied, the punch will tilt, and the angle will be

$$\delta=\frac{3H}{2a^3}i\sum_{k=1}^{2}\left\{\frac{\gamma_k}{m_k-1}\left[T\left(z_k\sin^{-1}\left(\frac{a}{l_{2k}}\right)-(a^2-l_{1k}^2)^{1/2}\right)-\bar{T}e^{2i\phi}\frac{2a^3-(l_{1k}^2+2a^2)(a^2-l_{1k}^2)^{1/2}}{3\rho^2}\right]\right\}. \tag{15}$$

Formulae (7)–(9), (11), (13), and (15) are the main new results of this section.

Applications

The simplicity of the results obtained in the previous section allows us to consider various cases of distributed internal loadings. Let a uniformly distributed shear traction τ_0 be applied over the segment $\rho_1\le\rho\le\rho_2$, $\phi_1\le\phi\le\phi_2$, at the distance z from the surface. Integrating equation (11) by the method described in Fabrikant (1989a), we obtain

$$N=\Re\left\{\frac{2i}{\pi}\tau_0(e^{i\phi_2}-e^{i\phi_1})\sum_{k=1}^{2}\left[\frac{\gamma_k}{m_k-1}[V(\rho_2)-V(\rho_1)]\right]\right\}, \tag{16}$$

where

$$V(\rho)=\int[a-(a^2-l_1^2)^{1/2}]d\rho=a\rho-\frac{1}{2}\rho(a^2-l_1^2)^{1/2}-\frac{1}{2}(a^2-z^2)\sin^{-1}\left(\frac{l_1}{(a^2+z^2)^{1/2}}\right)-az\ln\frac{l_2+(\rho^2-l_1^2)^{1/2}}{(a^2+z^2)^{1/2}}. \tag{17}$$

In the case of a uniform loading over a complete annulus, formula (16) gives $N=0$ as it was expected. The value of the tilting moment can be obtained by integration of equation (13), and we present the result for the case of uniform shear loading of a circular annulus $\rho_1\le\rho\le\rho_2$

$$M=-\frac{2i}{\pi}\tau_0\sum_{k=1}^{2}\left\{\frac{\gamma_k}{m_k-1}\left[W(\rho_2)-W(\rho_1)\right]\right\}. \tag{18}$$

Downloaded 03 May 2010 to 171.66.16.244. Redistribution subject to ASME license or copyright; see http://www.asme.org/terms/Terms_Use.cfm

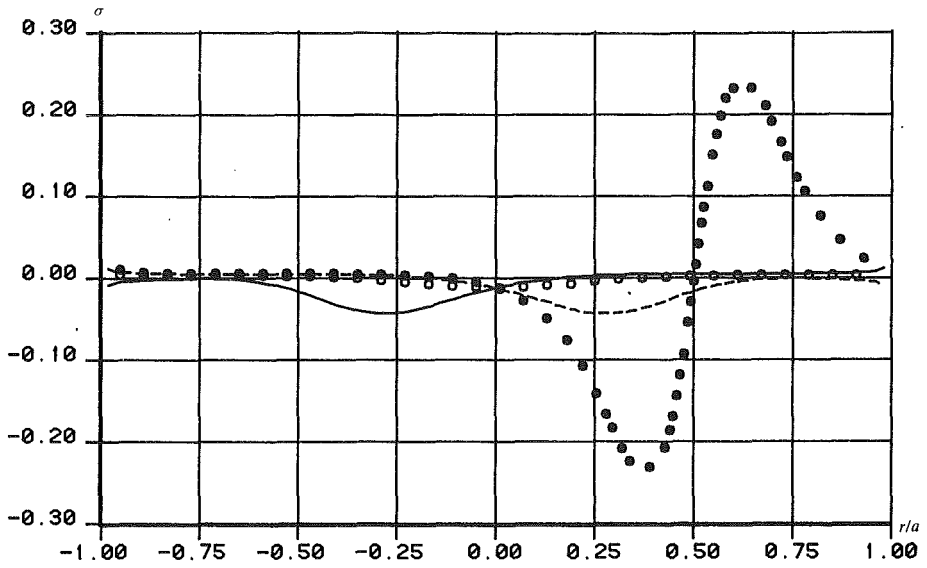


Fig. 2 Stress distribution under the punch due to a radial force

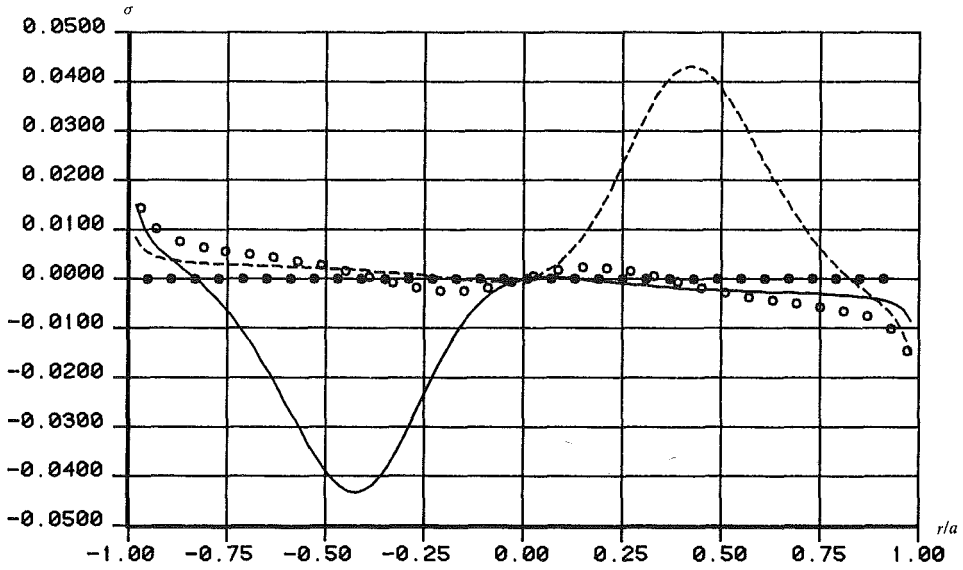


Fig. 3 Stress distribution under the punch due to a transversal force

Here,

$$W(\rho)=\int\left[z\sin^{-1}\left(\frac{a}{l_2}\right)-(a^2-l_1^2)^{1/2}\right]\rho d\rho=\frac{1}{2}z\rho^3\sin^{-1}\left(\frac{a}{l_2}\right)+\frac{z^2(2a^2-l_1^2)}{2(a^2-l_1^2)^{1/2}}-\frac{1}{3}(a^2-l_1^2)^{1/2}(3l_2^2+l_1^2-4a^2). \quad (19)$$

In the case of a torsional loading of a circular annulus, both the normal force and the tilting moment vanish.

The general solution is also valid in the case of isotropy, provided that we compute the limiting case

$$m_1=m_2=1,\ \gamma_1=\gamma_2=\gamma_3=1,\ H=\frac{1-\nu^2}{\pi E},$$

where E is the elastic modulus, and ν is Poisson coefficient.

According to the L'Hôpital rule, the following scheme should be used

$$\lim_{\gamma_1\to\gamma_2\to 1}\left[\frac{\gamma_1 f(z_1)}{m_1-1}+\frac{\gamma_2 f(z_2)}{m_2-1}\right]=-\frac{(1-2\nu)f(z)+zf'(z)}{2(1-\nu)}, \quad (20)$$

$$\lim_{\gamma_1\to\gamma_2\to 1} m_1=1,\quad \lim_{\gamma_1\to\gamma_2\to 1}\left[\frac{\partial m_1}{\partial\gamma_1}\right]=2(1-\nu), \quad (21)$$

and the symbol (′) indicates differentiation with respect to z. Formulae (7), (11), (13), and (15) in the case of isotropy will take the form

$$\sigma(r,\psi)=\Re\left\{\frac{\bar{T}}{2\pi^2(1-\nu)}[(1-2\nu)U(z)+zU'(z)]\right\}, \quad (22)$$

with $U(z)$ defined by equations (8)–(9)

$$U'(z)=\frac{\partial U}{\partial z}=-\frac{3zq}{R_0^5}\left[\frac{R_0}{h}+\tan^{-1}\left(\frac{h}{R_0}\right)\right]+\frac{z}{h(R_0^2+h^2)}\left[\frac{\rho e^{i\phi}}{l_2^2-l_1^2}+\frac{q}{R_0^2}\right]; \quad (23)$$

$$N=\Re\left\{\frac{\bar{T}e^{i\phi}}{\pi\rho(1-\nu)}\left[(1-2\nu)[a-(a^2-l_1^2)^{1/2}]-\frac{zl_1(\rho^2-l_1^2)^{1/2}}{l_2^2-l_1^2}\right]\right\}, \quad (24)$$

Downloaded 03 May 2010 to 171.66.16.244. Redistribution subject to ASME license or copyright; see http://www.asme.org/terms/Terms_Use.cfm

$$M=\frac{i}{\pi(1-\nu)}\Bigg\{(1-2\nu)\Bigg[T\left(z\sin^{-1}\left(\frac{a}{l_2}\right)-(a^2-l_1^2)^{1/2}\right)$$
$$-\bar{T}e^{2i\phi}\,\frac{2a^3-(l_1^2+2a^2)\,(a^2-l_1^2)^{1/2}}{3\rho^2}\Bigg]$$
$$+z\Bigg[T\left(\sin^{-1}\left(\frac{a}{l_2}\right)-\frac{a(l_2^2-a^2)^{1/2}}{l_2^2-l_1^2}\right)$$
$$+\bar{T}e^{2i\phi}\,\frac{al_1^2(l_2^2-a^2)^{1/2}}{l_2^2(l_2^2-l_1^2)}\Bigg]\Bigg\}, \tag{25}$$

$$\delta=\frac{3i}{8\pi\mu a^3}\Bigg\{(1-2\nu)\Bigg[T\left(z\sin^{-1}\left(\frac{a}{l_2}\right)-(a^2-l_1^2)^{1/2}\right)$$
$$-\bar{T}e^{2i\phi}\,\frac{2a^3-(l_1^2+2a^2)\,(a^2-l_1^2)^{1/2}}{3\rho^2}\Bigg]$$
$$+z\Bigg[\left(T\left(\sin^{-1}\left(\frac{a}{l_2}\right)-\frac{a(l_2^2-a^2)^{1/2}}{l_2^2-l_1^2}\right)\right.$$
$$\left.+\bar{T}e^{2i\phi}\,\frac{al_1^2(l_2^2-a^2)^{1/2}}{l_2^2(l_2^2-l_1^2)}\right]\Bigg\}. \tag{26}$$

In order to illustrate the stress distribution under the punch, computations were made due to equation (22)-(23), for $\nu = 0.3$, $\phi = 0$, $z/a = 0.25$, $\rho/a = 0.5$. The cases of a unit radial and a unit transversal loading are considered separately. The results of computations are presented in Fig. 2 and 3, respectively. The curves given by the solid dots, the dashed line, the line of circles, and the solid line correspond to the values of $\psi = 0$, $\pi/4$, $\pi/2$, $3\pi/4$, respectively. The negative values of r correspond to the argument $\psi + \pi$. It is important to emphasize that the presented results are valid only when the contact is maintained all over the circle $r \le a$. Since the normal stress is negative at the part of the domain of contact, this implies that there should be additional external loading applied to the punch, so that the results stay valid.

Discussion

There exists an alternative way to solve the problem of interaction between an external load and a circular punch. Indeed, we could use the Green's functions derived in Fabrikant (1989b) combined with the reciprocal theorem. The tangential displacements around a circular punch are defined by

$$u(\rho,\phi,z)$$
$$=\frac{1}{\pi^2}\sum_{k=1}^{2}\left\{\frac{\gamma_k}{m_k-1}\int_0^{2\pi}\int_0^a U(\rho,\phi,z_k;\,r,\psi)\omega(r,\psi)rdrd\psi\right\}. \tag{27}$$

Here, U is defined by equation (8), and ω denotes the normal displacements under the punch. We consider two systems in equilibrium, namely, a tangential force is applied at the point (ρ, ϕ, z), and a normal stress σ is applied at the domain of contact in order to eliminate the normal displacements; the second system represents a transversely isotropic half space, with a normal displacement prescribed at the point $(r, \psi, 0)$ in the form $\omega = \delta(r, \psi)$, where δ is the Dirac delta function. Application of the reciprocal theorem yields

$$\Re\{u\bar{T}\}+\int\int_S \sigma\omega dS=0. \tag{28}$$

Substitution of equation (27) in (28) and subsequent use of the properties of the delta function lead immediately to (7).

The tangential displacement around a flat circular punch, subjected to a unit normal displacement, is (Fabrikant, 1989a):

$$u=\frac{2e^{i\phi}}{\pi\rho}\sum_{k=1}^{2}\left[\frac{\gamma_k[a-(a^2-l_{1k}^2)^{1/2}]}{m_k-1}\right]. \tag{29}$$

Again, application of the reciprocal theorem yields equation (11). In order to derive equation (26), we should use the expression for tangential displacement around a flat punch inclined by the angle $\delta = \delta_x + i\delta_y$ (Fabrikant, 1989a)

$$u=\frac{2}{\pi}\,i\sum_{k=1}^{2}\left\{\frac{\gamma_k}{m_k-1}\left[\delta\left(z_k\sin^{-1}\left(\frac{a}{l_{2k}}\right)-(a^2-l_{1k}^2)^{1/2}\right)\right.\right.$$
$$\left.\left.-\bar{\delta}e^{2i\phi}\,\frac{2a^3-(l_{1k}^2+2a^2)\,(a^2-l_{1k}^2)^{1/2}}{3\rho^2}\right]\right\}. \tag{30}$$

The derivation of equation (13) from (30) is straightforward.

Acknowledgment

The reported research was sponsored by a grant from the Natural Sciences and Engineering Research Council of Canada.

References

Elliott, H. A., 1948, "Three-Dimensional Stress Distributions in Hexagonal Aeolotropic Crystals," *Proc. Cambridge Phil. Soc.*, Vol. 44, pp. 522-533.

Fabrikant, V. I., 1989a, *Applications of Potential Theory in Mechanics: Selection of New Results*. Kluwer Academic.

Fabrikant, V. I., 1989b, "Complete Solutions to Some Mixed Boundary Value Problems in Elasticity," *Advances in Applied Mechanics*, Vol. 27, pp. 153-223.

Fabrikant, V. I., 1988, "Elastic Field Around a Circular Punch," ASME Journal of Applied Mechanics, Vol. 55, pp. 604-610.

Fabrikant, V. I., Selvadurai, A. P. S., and Xistris, G. D., 1985, "Asymmetric Problem of Loading Under a Smooth Punch," ASME Journal of Applied Mechanics, Vol. 52, pp. 681-685.

Fabrikant, V. I., 1971, "Closed Form Solution of a Two-dimensional Integral Equation," *Izvestiia Vysshikh Uchebnykh Zavedenii, Matematika*, (in Russian), No. 2, pp. 102-104.

Downloaded 03 May 2010 to 171.66.16.244. Redistribution subject to ASME license or copyright; see http://www.asme.org/terms/Terms_Use.cfm

A Boundary Element Method for Plane Anisotropic Elastic Media

KYU J. Lee
Hughes Aircraft Company,
Los Angeles, CA 90009

A. K. Mal
Mechanical, Aerospace and Nuclear Engineering Department,
University of California,
Los Angeles, CA 90024
Mem. ASME

The general problem of plane anisotropic elastostatics is formulated in terms of a system of singular integral equations with Cauchy kernels by means of the classical stress function approach. The integral equations are represented over the image of the boundary in the complex plane and a numerical scheme is developed for their solution. The boundary curve is discretized and suitable polynomial approximations of the unknown functions in terms of the complex variable are introduced. This reduces the equations to a set of complex linear algebraic equations which can be inverted to yield the stresses in a straightforward manner. The major difference between the present technique and the previous ones is in the numerical formulation. The integral equations are discretized in the complex plane and not in terms of real variables which depend on arc length, resulting in improved accuracy in presence of strong boundary curvature.

Introduction

This paper is concerned with plane boundary value problems of linear elastic solids of arbitrary shape using a boundary integral method. The material is assumed to be homogeneous and anisotropic, such that the plane of elastic symmetry at each point coincides with the plane of the body.

A system of singular integral equations is derived based on the theory of complex variables. A stress function is introduced as a function of a suitable complex variable and represented by integrals of the Cauchy type. The boundary conditions are then applied to obtain a system of singular integral equations with Cauchy kernels. The present formulation is valid for traction and displacement boundary value problems in a multiply-connected region. Rizzo and Shippy (1970) as well as Benjumea and Sikareskie (1972), formulated similar problems in terms of Fredholm equations containing only real variables which described the boundary points.

A numerical scheme is developed for the solution of the integral equations in the complex domain. The boundary curve is discretized into a finite number of intervals. The unknowns are assumed to be linear functions of a complex variable in each subinterval, and the integrations are performed exactly for arbitrary curved boundaries. The singular part of the integrals are also evaluated exactly in the sense of Cauchy principal value. The integral equations are thus reduced to a set of complex linear algebraic equations which are inverted to yield the stress in a straightforward manner.

The major difference between the present technique and previous ones is that the integral equations are discretized in the complex plane and not in terms of real variables which depend on the arc length. An advantage of this approach is that the formulation is independent of the boundary curvature. Thus, the numerical solution is quite accurate, even at points where sharp changes in the slope of the boundary occur.

Formulation of the Integral Equations

The strain components ϵ_x, ϵ_y, ϵ_{xy} are related to the stress components σ_x, σ_y, σ_{xy} through the generalized Hooke's law, in the form

$$\begin{Bmatrix} \epsilon_x \\ \epsilon_y \\ 2\epsilon_{xy} \end{Bmatrix} = \begin{bmatrix} a_{11} & a_{12} & a_{16} \\ a_{12} & a_{22} & a_{26} \\ a_{16} & a_{26} & a_{66} \end{bmatrix} \begin{Bmatrix} \sigma_x \\ \sigma_y \\ \sigma_{xy} \end{Bmatrix} \tag{1}$$

where the constants a_{ij} are the elastic compliances of the material.

Following Lekhnitskii (1968), we introduce the complex variables z_1 and z_2 defined by

$$\begin{aligned} z_1 &= x + \mu_1 y \\ z_2 &= x + \mu_2 y \end{aligned} \tag{2}$$

where the complex constant μ_1 and μ_2 are the solutions of the characteristic equation,

$$a_{11}\mu^4 - 2a_{16}\mu^3 + (2a_{12} + a_{66})\mu^2 - 2a_{26}\mu + a_{22} = 0. \tag{3}$$

The stress and displacement components are expressed in terms of four analytic functions ϕ_1, ϕ_2, ψ_1, ψ_2 as

$$\begin{aligned} \sigma_x &= \mu_1^2\phi_1(z_1) + \mu_2^2\phi_2(z_2) + \overline{\mu_1^2\phi_1(z_1)} + \overline{\mu_2^2\phi_2(z_2)} \\ \sigma_y &= \phi_1(z_1) + \phi_2(z_2) + \overline{\phi_1(z_1)} + \overline{\phi_2(z_2)} \\ \sigma_{xy} &= -[\mu_1\phi_1(z_1) + \mu_2\phi(z_2) + \overline{\mu_1\phi_1(z_1)} + \overline{\mu_2\phi_2(z_2)}] \end{aligned} \tag{4}$$

$$\begin{aligned} u_x &= d_1\psi_1(z_1) + d_2\psi_2(z_2) + \overline{d_1\psi_1(z_1)} + \overline{d_2\psi_2(z_2)} - \gamma_0 y + \alpha_0 \\ u_y &= e_1\psi_1(z_1) + e_2\psi_2(z_2) + \overline{e_1\psi_1(z_1)} + \overline{e_2\psi_2(z_2)} + \gamma_0 x + \beta_0 \end{aligned} \tag{5}$$

Contributed by the Applied Mechanics Division of THE AMERICAN SOCIETY OF MECHANICAL ENGINEERS for publication in the JOURNAL OF APPLIED MECHANICS.

Discussion on this paper should be addressed to the Technical Editor, Leon M. Keer, The Technological Institute, Northwestern University, Evanston, IL 60208, and will be accepted until two months after final publication of the paper itself in the JOURNAL OF APPLIED MECHANICS. Manuscript received by the ASME Applied Mechanics Division, Aug. 23, 1988; final revision, Aug. 15, 1989.

Copyright © 1990 by ASME
Downloaded 03 May 2010 to 171.66.16.244. Redistribution subject to ASME license or copyright; see http://www.asme.org/terms/Terms_Use.cfm

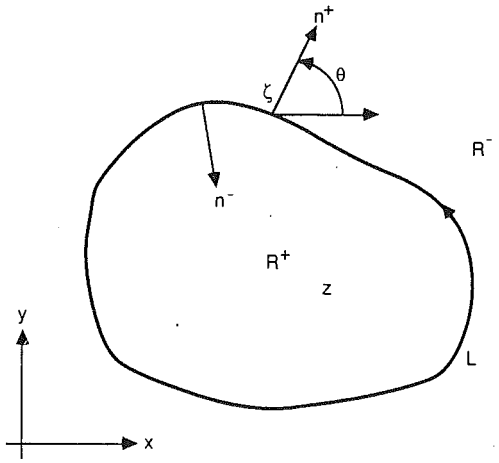


Fig. 1 Region bounded by a smooth contour L

where

$$\begin{aligned} \phi_k &= \frac{d\psi_k}{dz_k} \\ d_k &= a_{11}\mu_k^2 + a_{12} - \mu_k a_{16} \\ e_k &= \frac{a_{12}\mu_k^2 + a_{22} - a_{26}\mu_k}{\mu_k} \quad k = 1, 2. \end{aligned}$$

α_0, β_0, γ_0 are real constants associated with arbitrary rigid displacement of the body, and an overbar indicates complex conjugate.

The representations equations (4) and (5) can be used to derive a system of boundary integral equations for the unknown field variables. To this end, let R^+ be an open region in the complex plane $z = x + iy$ bounded by a smooth contour L and let R^- be the complement of $R^+ + L$, as shown in Fig. 1. The complex number ζ denotes a point on L, and s is the length of arc to ζ from an arbitrary fixed point on L. The positive direction on L will be assumed to be such that the region R^+ lies to the left of L if L is described in the direction of increasing s.

If θ be the angle between the x-axis and the n^+, normal to L at ζ (Fig. 1), then

$$\begin{aligned} \zeta(s) &= x(s) + iy(s) \\ x'(s) &= -\sin\theta = -n_y^+ = n_y^- \\ y'(s) &= \cos\theta = n_x^+ = -n_x^-. \end{aligned} \tag{6}$$

Since L is a smooth contour, it follows from equation (6) that θ is a continuous function of the arc length s.

Denoting by $T^{\pm}(\zeta)$ the values of traction on L as it is approached from the R^+ and R^- sides, respectively, it can be shown that

$$T^{\pm}(\zeta) = \mp i \sum_{K=1}^{2} \left[(1 + i\mu_k)\phi_k^{\pm} \frac{d\zeta_k}{ds} + (1 + i\,\bar{\mu}_k)\bar{\phi}_k^{\pm} \frac{\overline{d\zeta_k}}{ds} \right]. \tag{7}$$

Similarly, for displacement

$$u^{\pm}(\zeta) = \sum_{K=1}^{2} [(d_k + ie_k)\psi_k^{\pm} + (\bar{d}_k + i\,\bar{e}_k)\bar{\psi}_k^{\pm}] \tag{8}$$

where

$$\begin{aligned} T^{\pm}(\zeta) &= T_x^{\pm}(\zeta) + iT_y^{\pm}(\zeta) \\ u^{\pm}(\zeta) &= u_x^{\pm}(\zeta) + iu_y^{\pm}(\zeta), \end{aligned}$$

and we have ignored rigid body displacement.

Differentiating equation (8) with respect to the arc length s is

$$\frac{du^{\pm}}{ds} = \sum_{k=1}^{2} \left[(d_k + ie_k)\phi_k^{\pm} \frac{d\zeta_k}{ds} + (\bar{d}_k + i\,\bar{e}_k)\bar{\phi}_k^{\pm} \frac{\overline{d\zeta_k}}{ds} \right]. \tag{9}$$

Now we assume that ϕ_k can be represented as

$$\phi_k(z_k) = \frac{1}{2\pi i} \int_{Lk} \frac{w_k(\xi_k)}{\xi_k - z_k}\, d\xi_k \tag{10}$$

where L_k is obtained from L by means of the affine transformation and w_k is the density function satisfying the Holder condition on L_k (Muskhelishvili, 1953). Introducing the variable $z = x + iy$ in place of $z_k = x_k + iy_k$ in equation (10), and upon applying the Plemelj formulas, ϕ_k can be shown to have the following expression on L (Muskhelishvili, 1953).

$$\begin{aligned} \phi_k^+(\zeta_k) &= \frac{1}{2} w_k(\zeta_k) + \frac{1}{2\pi i} \int_L \frac{\lambda_k}{\xi - \zeta} d\xi \\ \phi_k^-(\zeta_k) &= -\frac{1}{2} w_k(\zeta_k) + \frac{1}{2\pi i} \int_L \frac{\lambda_k}{\xi - \zeta} d\xi \end{aligned} \tag{11}$$

where

$$\lambda_k = w_k \frac{d\xi_k}{d\xi} \frac{\xi - z}{\xi_k - z_k}.$$

The improper integrals in equation (11) must be evaluated in the sense of Cauchy principal values.

Substituting from equation (11) into (7) and (9), we have

$$T^{\pm}(\zeta) = \frac{1}{2}(G \mp H) \tag{12}$$

where

$$G = -i \sum_{k=1}^{2} \left[(1 + i\mu_k) w_k \frac{d\zeta_k}{ds} + (1 + i\,\bar{\mu}_k)\overline{w}_k \frac{\overline{d\zeta_k}}{ds} \right]$$

$$H = \frac{1}{\pi} \sum_{k=1}^{2} \left[(1 + i\mu_k) \frac{d\zeta_k}{ds} \int_L \frac{\lambda_k}{\xi - \zeta} d\xi - (1 + i\,\bar{\mu}_k) \frac{\overline{d\zeta_k}}{ds} \overline{\int_L \frac{\lambda_k}{\xi - \zeta} d\xi} \right].$$

Similarly,

$$\frac{du^{\pm}}{ds} = \frac{1}{2}[\pm M + N] \tag{13}$$

where

$$M = \sum_{k=1}^{2} \left[(d_k + ie_k) w_k \frac{d\zeta_k}{ds} + (\bar{d}_k + i\,\bar{e}_k)\overline{w}_k \frac{\overline{d\zeta_k}}{ds} \right]$$

$$N = \frac{1}{\pi i} \sum_{k=1}^{2} \left[(d_k + ie_k) \frac{d\zeta_k}{ds} \int_L \frac{\lambda_k}{\xi - \zeta_k} d\xi - (\bar{d}_k + i\bar{e}_k) \frac{\overline{d\zeta_k}}{ds} \overline{\int_L \frac{\lambda_k}{\xi - \zeta} d\xi} \right].$$

We assume that the displacement $u(\zeta)$ is continuous across L so that for each $\zeta \in L$,

$$u^+(\zeta) - u^-(\zeta) \equiv 0.$$

Consequently,

$$\frac{du^+}{ds} - \frac{du^-}{ds} = 0.$$

Now, we assume

$$T^+(\zeta) + T^-(\zeta) = w(\zeta) = p(\zeta) + iq(\zeta),$$

where $w(\zeta)$ can be interpreted as a distribution of body forces on L in an infinite medium. Then, from equations (12) and (13) we obtain

$$\begin{aligned} M &= \sum_{k=1}^{2} \left[(d_k + ie_k) w_k \frac{d\zeta_k}{ds} + (\bar{d}_k + i\,\bar{e}_k)\overline{w}_k \frac{\overline{d\zeta_k}}{ds} \right] = 0 \\ G &= -i \sum_{k=1}^{2} \left[(1 + i\mu_k) w_k \frac{d\zeta_k}{ds} + (1 + i\,\bar{\mu}_k)\overline{w}_k \frac{\overline{d\zeta_k}}{ds} \right] = w. \end{aligned} \tag{14}$$

Taking the complex conjugate of equation (14) and solving for w_k,

Downloaded 03 May 2010 to 171.66.16.244. Redistribution subject to ASME license or copyright; see http://www.asme.org/terms/Terms_Use.cfm

$$w_k(\zeta_k)=(A_k w+B_k\bar{w})\frac{ds}{d\zeta_k}=[C_k p(\zeta)-D_k q(\zeta)]\frac{ds}{d\zeta_k}, \quad (15)$$

where

$$A_k=\frac{1}{2}(C_k+iD_k), \quad B_k=\frac{1}{2}(C_k-iD_k)$$

$$C_1=\mu_1\left[(\bar{\mu}_1+\bar{\mu}_2)-\frac{a_{16}}{a_{11}}+\mu_2\left(1-\frac{a_{12}}{a_{22}}\bar{\mu}_1\bar{\mu}_2\right)\right]/\Delta_1$$

$$D_1=-\mu_1\left[\mu_2(\bar{\mu}_1+\bar{\mu}_2)-\frac{a_{12}}{a_{11}}+\bar{\mu}_1\bar{\mu}_2\left(1-\frac{a_{26}}{a_{22}}\mu_2\right)\right]/\Delta_1$$

$$C_2=\mu_2\left[(\bar{\mu}_1+\bar{\mu}_2)-\frac{a_{16}}{a_{11}}+\mu_1\left(1-\frac{a_{12}}{a_{22}}\bar{\mu}_1\bar{\mu}_2\right)\right]/\Delta_2$$

$$D_2=-\mu_2\left[\mu_1(\bar{\mu}_1+\bar{\mu}_2)-\frac{a_{12}}{a_{11}}+\bar{\mu}_1\bar{\mu}_2\left(1-\frac{a_{26}}{a_{22}}\mu_1\right)\right]/\Delta_2$$

$$\Delta_1=(\mu_1-\mu_1)(\bar{\mu}_1-\bar{\mu}_1)(\mu_2-\mu_1)$$

$$\Delta_2=-(\mu_2-\mu_1)(\bar{\mu}_1-\mu_2)(\bar{\mu}_2-\mu_2).$$

For an orthotropic solid with its symmetry axes parallel to the coordinate axis, we have

$$\bar{\mu}_1=-\mu_1,\ \bar{\mu}_2=-\mu_2 \text{ or } \bar{\mu}_1=-\mu_2,\ \bar{\mu}_2=-\mu_1 \quad (16)$$

$$a_{16}=a_{26}=0,\ \frac{a_{22}}{a_{11}}=\mu_1^2\mu_2^2.$$

Then, C_k and D_k have the following simple expressions:

$$C_1=\frac{1}{2}\left[\frac{a_{11}\mu_1^2+a_{12}}{a_{11}\mu_1(\mu_1^2-\mu_2^2)}\right],\ C_2=-\frac{1}{2}\left[\frac{a_{11}\mu_2^2+a_{12}}{a_{11}\mu_2(\mu_2^2-\mu_2^2)}\right]$$

$$D_1=-\frac{1}{2}\left[\frac{a_{11}\mu_2^2+a_{12}}{a_{11}\mu_2(\mu_1^2-\mu_2^2)}\right],\ D_2=\frac{1}{2}\left[\frac{a_{11}\mu_1^2+a_{12}}{a_{11}(\mu_1^2-\mu_2^2)}\right]. \quad (17)$$

Substituting from equation (14) into (12) we obtain the following singular integral equations with Cauchy-type kernels,

$$T(\zeta)=\frac{1}{2}w(\zeta)-\frac{1}{2\pi}\sum_{k=1}^{2}\left[(1+i\mu_k)\int_L\frac{f_k}{\xi-\zeta}d\xi-(1+i\bar{\mu}_k)\overline{\int_L\frac{f_k}{\xi-\zeta}d\xi}\right]. \quad (18a)$$

In a similar manner, we obtain from equations (8), (13), and (14),

$$u(\zeta)=\frac{1}{2\pi}\sum_{k=1}^{2}\left[(-e_k+id_k)\int_L g_k\log(\xi-\zeta)d\xi-(-\bar{e}_k+i\bar{d}_k)\overline{\int_L g_k\log(\xi-\zeta)d\xi}\right]+u_o \quad (18b)$$

where

$$f_k=[C_k p(\zeta)-D_k q(\zeta)]K_k(\xi,\zeta),\ K_k(\xi,\zeta)=\frac{\nu_k(\zeta)}{\nu(\xi)}\frac{\xi-\zeta}{\xi_k-\zeta_k} \quad (19a)$$

$$g_k=[C_k p(\zeta)-D_k q(\zeta)]J_k(\xi,\zeta),\ J_k(\xi,\zeta)=\frac{1}{\nu(\xi)}\frac{\log(\xi_k-\zeta_k)}{\log(\xi-\zeta)} \quad (19b)$$

$$\nu(\xi)=-\sin\theta(\xi)+i\cos\theta(\xi)=\frac{d\xi}{ds}$$

$$\nu_k(\xi)=-\sin\theta(\xi)+\mu_k\cos\theta(\xi)=\frac{d\xi_k}{ds}$$

$$u_o=-\gamma_o y+a_o+i(\gamma_o x+\beta_o).$$

Equation (18*a*) defines a traction boundary value problem for a region bounded by L, while equation (18*b*) corresponds to a displacement boundary value problem.

The singular operator appearing in equation (18*a*) becomes a Fredholm operator of the second kind and the integral equations gives unique solution in the admissible range of Poisson's ratios. A proof of this is given in the Appendix.

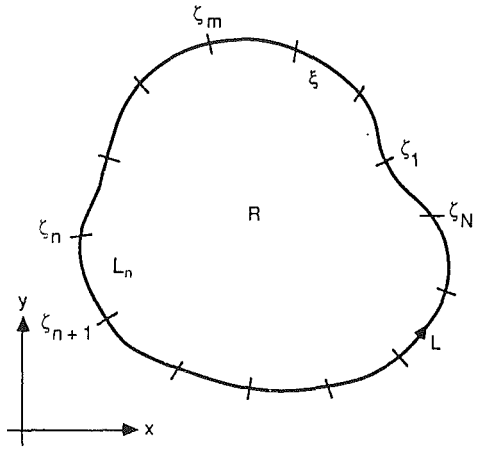


Fig. 2 Discretized boundary L

Numerical Analysis

In order to solve the integral equation numerically, the contour L is divided into N intervals L_n ($n=1, 2, \ldots, N$), (Fig. 2).

The discretized form of equation (18*a*) is

$$T(\zeta_m)=\frac{1}{2}w(\zeta_m)-\frac{1}{2\pi}\sum_{n=1}^{N}\sum_{k=1}^{2}\left[(1+i\mu_k)\int_{L_n}\frac{f_k}{\xi-\zeta_m}d\xi-(1+i\bar{\mu}_k)\overline{\int_{L_n}\frac{f_k}{\xi-\zeta_m}d\xi}\right] \quad (20)$$

where

$$L_n\epsilon[\zeta_n,\ \zeta_{n+1}].$$

The integrals in the right-hand side of equation (20) must be interpreted in the sense of Cauchy principal value.

Assuming that each L_n is small, f_1, f_2 can be expressed as polynomials in terms of the complex variable $(\xi-\zeta_m)$ within each interval. If $f_k(\xi,\zeta_m)$ is assumed to be a linear function of $(\xi-\zeta_m)$ in each subinterval,

$$f_k(\xi,\zeta_m)=a_{kn}+b_{kn}(\xi-\zeta_m),\ \xi\epsilon L_n(\zeta_n,\zeta_{n+1}), \quad (21)$$

where a_{kn}, b_{kn} are unknown constants determined from the continuity conditions across each subinterval, then the integral over L_n becomes

$$\int_{\zeta_n}^{\zeta_{n+1}}\frac{f_k}{\xi-\zeta_m}d\xi=a_{kn}\log\frac{\zeta_{n+1}-\zeta_m}{\zeta_n-\zeta_m}+b_{kn}(\zeta_{n+1}-\zeta_n). \quad (22)$$

From equation (21), we note that the continuity of f_k at $\xi=\zeta_m$ requires $a_{km}=a_{km-1}$. The singular integral on $\zeta\epsilon[\zeta_{m-1},\ \zeta_{m+1}]$ can be evaluated in the sense of Cauchy's principal value as,

$$\int_{\zeta_{m-1}}^{\zeta_{m+1}}\frac{f_k}{\xi-\zeta_m}d\xi=a_{km}\log\frac{\zeta_{m+1}-\zeta_m}{\zeta_{m-1}-\zeta_m}+b_{km-1}(\zeta_m-\zeta_{m-1})+b_{km}(\zeta_{m+1}-\zeta_m). \quad (23)$$

Note that the Cauchy Kernel, $K_k(\xi,\zeta_m)$, defined in equation (19*a*), has the limiting value

$$\lim_{\xi\to\zeta_m}K_k(\xi,\zeta_m)=1.$$

Thus,

$$a_{km}=\lim_{\xi\to\zeta_m}f_k(\xi,\zeta_m)=C_k p(\zeta_m)-D_k q(\zeta_m).$$

Finally, the singular integral in equation (23) becomes

$$\int_{\zeta_{m-1}}^{\zeta_{m+1}}\frac{f_k}{\xi-\zeta_m}d\xi=[C_k p(\zeta_m)-D_k q(\zeta_m)]\log\frac{\zeta_{m+1}-\zeta_m}{\zeta_{m-1}-\zeta_m}+b_{km-1}(\zeta_m-\zeta_{m-1})+b_{km}(\zeta_{m+1}-\zeta_m).$$

Downloaded 03 May 2010 to 171.66.16.244. Redistribution subject to ASME license or copyright; see http://www.asme.org/terms/Terms_Use.cfm

Substituting from equations (22) and (23) into (20), we obtain a system of linear algebraic equations for $p(\zeta_n)$ and $q(\zeta_n)$,

$$T(\zeta_m)=\frac{1}{2}w(\zeta_m)-\frac{1}{2\pi}\sum_{n=1}^{N}\sum_{k=1}^{2}[(1+i\mu_k)h_n(C_kp(\zeta_n) - D_kq(\zeta_n))K_k(\zeta_n,\zeta_m) - (1+i\bar{\mu}_k)\bar{h}_n(\bar{C}_kp(\zeta_n)-\bar{D}_kq(\zeta_n))\overline{K_k(\zeta_n,\zeta_m)}], \quad (24)$$

where

$$K_k(\zeta_m,\zeta_n)=\frac{\nu_k(\zeta_m)}{\nu(\zeta_n)}\frac{\zeta_n-\zeta_m}{\zeta_{kn}-\zeta_{km}}$$

$$h_n=\frac{\zeta_{n+1}-\zeta_m}{\zeta_{n+1}-\zeta_m}\log\frac{\zeta_{n+1}-\zeta_m}{\zeta_n-\zeta_m}+\frac{\zeta_m-\zeta_{n-1}}{\zeta_n-\zeta_{n-1}}\log\frac{\zeta_n-\zeta_m}{\zeta_{n-1}-\zeta_m}.$$

In particular,

$$h_m=\log\frac{\zeta_{m+1}-\zeta_m}{\zeta_{m-1}-\zeta_m}.$$

Similarly, descretization of equation (18*b*) leads to the system

$$u(\zeta_m)=\frac{1}{2\pi}\sum_{n=1}^{N}\sum_{k=1}^{2}\left[(-e_k+id_k)\int_{L_n}g_k\log(\xi-\zeta_m)d\xi - (-\bar{e}_k+i\bar{d}_k)\overline{\int_{L_n}g_k\log(\xi-\zeta_m)d\xi}\right] \quad (25)$$

where

$$L_n\epsilon[\zeta_n,\zeta_{n+1}].$$

Assuming $g_k(\xi,\zeta_m)$ to be a linear function in each interval of the form,

$$g_k(\xi,\zeta_m)=c_{kn}+d_{kn}(\xi-\zeta_m),\ \xi\epsilon L_n, \quad (26)$$

where c_{kn} and d_{kn} are determined from the continuity conditions across each subinterval, the integral over $L_n\epsilon[\zeta_n,\zeta_{n+1}]$ becomes

$$\int_{\zeta_n}^{\zeta_{n+1}}g_k\log(\xi-\zeta_m)d\xi=c_{kn}\gamma_n+d_{kn}\delta_n, \quad (27)$$

where

$$\gamma_n=\int_{\zeta_n}^{\zeta_{n+1}}\log(\xi-\zeta_m)d\xi=(\zeta_{n+1}-\zeta_m)\log(\zeta_{n+1}-\zeta_m) - (\zeta_n-\zeta_m)\log(\zeta_n-\zeta_m)-\zeta_{n+1}+\zeta_n$$

$$\delta_n=\int_{\zeta_n}^{\zeta_{n+1}}(\xi-\zeta_m)\log(\xi-\zeta_m)d\xi=\frac{1}{2}(\zeta_{n+1}-\zeta_m)^2\log(\zeta_{n+1}-\zeta_m) - \frac{1}{2}(\zeta_n-\zeta_m)^2\log(\zeta_n-\zeta_m)-\frac{1}{4}(\zeta_{n+1}-\zeta_m)^2+\frac{1}{4}(\zeta_n-\zeta_m)^2.$$

The singular integral over $[\zeta_{m-1},\zeta_{m+1}]$ is evaluated as is equation (23).

Note that $c_{km}=c_{km-1}$ from continuity of g_k at $\xi=\zeta_m$ in equation (26). Using L'Hospitals rule, we also have, from equation (19*b*),

$$\lim_{\xi\to\zeta m}J_k(\xi,\zeta_m)=1/\nu_k(\zeta).$$

Thus,

$$c_{km}=\lim_{\xi\to\zeta m}g_k(\xi,\zeta_m)=[C_kp(\zeta_m)-D_kq(\zeta_m)]/\nu_k(\zeta).$$

Evaluating the singular integral in the sense of Cauchy's principal value, we finally obtain

$$\int_{\zeta_{m-1}}^{\zeta_{m+1}}g_k\log(\xi-\zeta_m)d\xi=[C_kp(\zeta_m)-D_kq(\zeta_m)]/\nu_k(\zeta) \times[(\zeta_{m+1}-\zeta_m)\log(\zeta_{m+1}-\zeta_m) - (\zeta_{m-1}-\zeta_m)\log(\zeta_{m-1}-\zeta_m)-\zeta_{m+1}+\zeta_{m-1}]$$

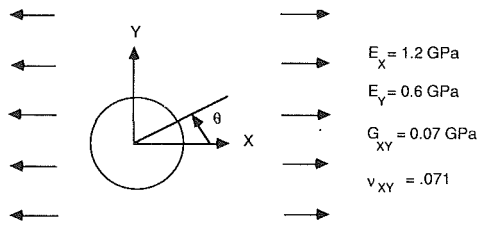


Fig. 3 An infinite plate with a circular hole under uniaxial tension

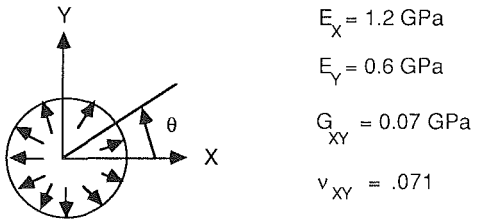


Fig. 4 An infinite plate with a circular hole under hydrostatic pressure

$$+d_{km}\left[\frac{1}{2}(\zeta_{m+1}-\zeta_m)^2\log(\zeta_{m+1}-\zeta_m)-\frac{1}{4}(\zeta_{m+1}-\zeta_m)^2\right] - d_{km-1}\left[\frac{1}{2}(\zeta_{m-1}-\zeta_m)^2\log(\zeta_{m-1}-\zeta_m)-\frac{1}{4}(\zeta_{m-1}-\zeta_m)^2\right]. \quad (28)$$

Substituting from equations (27) and (28) into (25), we obtain a system of linear algebraic equations for $p(\zeta_n)$ and $q(\zeta_n)$ as

$$u(\zeta_m)=\frac{1}{2\pi}\sum_{n=1}^{N}\sum_{k=1}^{2}(-e_k+id_k)(C_kp(\zeta_n)-D_kq(\zeta_n))v_nJ_k(\zeta_n,\zeta_m) - (-\bar{e}_k+i\bar{d}_k)(\bar{C}_kp(\zeta_n)-\bar{D}_kq(\zeta_n))\bar{v}_n\overline{J_k(\zeta_n,\zeta_m)} \quad (29)$$

where

$$v_n=\frac{(\delta_{n-1}-\gamma_{n-1}(\zeta_n-\zeta_m))}{\zeta_n-\zeta_{n-1}}+\frac{(-\delta_n+\gamma_n(\zeta_{n+1}-\zeta_m))}{\zeta_{n+1}-\zeta_n}.$$

if $n=m$,

$$v_m=[(\zeta_{m+1}-\zeta_m)\log(\zeta_{m+1}-\zeta_m) - (\zeta_{m-1}-\zeta_m)\log(\zeta_{m-1}-\zeta_m)-\frac{3}{2}\zeta_{m+1}-\zeta_{m-1}]/2.$$

Equations (24) and (29) demonstrate the major advantage of the present method over previous methods based on the use of real variables only. Further, in this method, the boundary integrations are carried out exactly along each element, and no numerical integration is necessary. Higher-order approximations can also be obtained without any difficulty. For given elastic and geometrical properties, numerical modeling can be carried out immediately using equations (24) and (29).

Numerical results are presented for traction boundary value problems only. As a first example, we consider an infinite orthotropic plate with a circular hole with two types of loading, namely, uniaxial and hydrostatic pressure as shown in Figs. 3 and 4.

To compare our results with Lekhnistskii's (1968) analytical solutions, the following elastic properties are chosen

$$E_x=1.2\text{ GPa},\ E_y=0.6\text{ GPa},\ G_{xy}=0.07\text{ GPa},\ \nu_{xy}=0.071.$$

Two types of weighting functions, constant and linear distributions, are used to study the sensitivity of the numerical procedure and the stresses are obtained at each nodal point.

Taking advantage of the symmetry properties, only a quarter circle consisting of N points is considered. A value of $N=10$ was found to be adequate for this problem. Numerical results based on this method for the two loadings are presented in

Downloaded 03 May 2010 to 171.66.16.244. Redistribution subject to ASME license or copyright; see http://www.asme.org/terms/Terms_Use.cfm

Tables 1 and 2, together with those for Lekhnistskii's analytical solutions. Agreement between the two can be seen to be excellent.

It is also interesting to note that the results for linear approximation show higher relative accuracy as the magnitude of the stress increases. Rizzo (1970) also solved the hydrostatic loading case with the same elastic properties. In his calculation, the error at $\theta = 90$ deg is 5.6 percent, while in the present method, the error is 2.9 percent using the same number of discretization points.

Next, an infinite plate with a "square" hole with rounded corners (Fig. 5) is analyzed. The hoop stresses are computed at three locations as shown in Table 3 and compared with the analytical solution.

Finally, a square plate with a circular or an elliptical hole under uniaxial tension shown in Fig. 6 is considered. To insure the integrity of the finite body solution, N is determined first using infinite body solutions which gives less than three percent error relative to the analytical solutions as shown in Table 4, while the straight boundary d is divided into $\Delta d = d/10$.

The results shown in Table 4 indicate good agreement between the solutions for finite and infinite bodies. In Fig. 6, the normalized stress distributions along the positive Y-axis are presented from which we note that the solutions are highly stable considering the magnitude of stress gradients near the hole.

In the formulations by Cruse (1969) and Rizzo (1967), numerical instabilities exist at the interior points located extremely close to the boundary caused by the high-order singularities of the kernels. Ghosh et al. (1968) modified these formulations in order to eliminate the so-called boundary layer effect. One disadvantage in Ghosh's formulation is that the tangential derivatives of the displacements are taken as boundary values rather than the displacements in the case of the second boundary value problem.

In the present formulation, the boundary layer effects are investigated using the square plate with $d = 10$ and compared

Table 1 Hoop stress around circular boundary due to uniaxial tension at infinity in Fig. 3 ($N = 10$)

θ	Numerical $\sigma_{\theta C}$	Numerical $\sigma_{\theta L}$	Analytical
0	−.705	−.706	−.707
10	−.508	−.508	−.509
20	−.184	−.184	−.185
30	.069	.069	.070
40	.286	.286	.289
50	.545	.544	.551
60	.966	.964	.975
70	1.820	1.814	1.832
80	3.650	3.656	3.662
90	5.402	5.425	5.453

$\sigma_{\theta C}$: constant distribution of weighting function
$\sigma_{\theta L}$: linear distribution of weighting function

Table 2 Hoop stress distribution around circular boundary due to hydrostatic pressure in Fig. 4 ($N = 10$)

θ	Numerical $\sigma_{\theta C}$	Numerical $\sigma_{\theta L}$	Analytical
0	2.430	2.438	2.442
10	1.855	1.858	1.862
20	.970	.968	.975
30	.412	.411	.415
40	.147	.146	.148
50	.086	.084	.086
60	.228	.226	.228
70	.710	.706	.712
80	1.869	1.873	1.874
90	3.004	3.020	3.039

$\sigma_{\theta C}$: constant distribution of weighting function
$\sigma_{\theta L}$: linear distribution of weighting function

Table 3 Hoop stress distribution of square hole due to uniaxial tension at infinity in Fig. 5 ($N = 18$)

Location	Numerical	Analytical
A	−1.115	−1.05
B	.225	.21
C	10.518	10.82
D	−.518	−.57
E	.814	.83
F	2.607	2.60

Table 4 Stress concentration factors at B in Fig. 6

d	$a=1$, $b=1$ $N=10$	$a=1$, $b=2$ $N=15$	$a=1$, $b=4$ $N=25$
Numerical			
10	5.750	11.461	26.998
20	5.524	10.283	21.287
∞	5.425	9.766	18.320
Analytical			
∞	5.453	9.906	18.812

N: no. of divisions between A and B

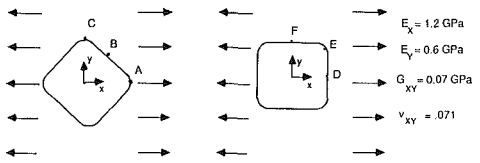


Fig. 5 Square holes under uniaxial tension at infinity

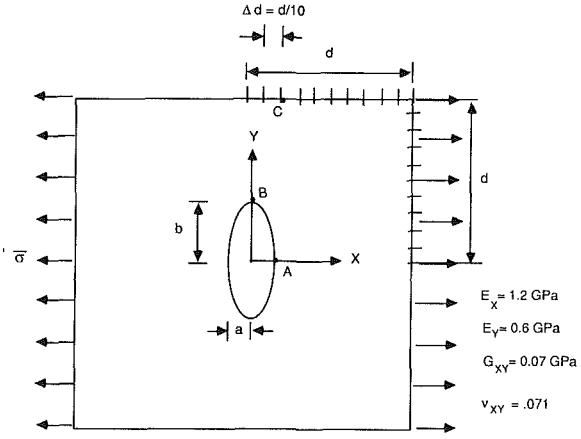


Fig. 6 Square plate with an elliptical hole under uniaxial tension

Table 5 Stress concentration factors, $\sigma_x/\bar{\sigma}$ near C in Fig. 6

Y	$a=1$, $b=1$ New	$a=1$, $b=1$ Old	$a=1/2$, $b=1$ New	$a=1/2$, $b=1$ Old	$a=1/4$, $b=1$ New	$a=1/4$, $b=1$ Old
9.99995	.974	.957	.986	.972	.992	.982
9.999995	.974	$.104\times10^6$	.986	$.1009\times10^6$	.992	$.9936\times10^5$
9.9999995	.974	$.104\times10^6$	.986	$.1009\times10^7$	.992	$.9937\times10^5$

Old results are from Ghosh (1986)

Downloaded 03 May 2010 to 171.66.16.244. Redistribution subject to ASME license or copyright; see http://www.asme.org/terms/Terms_Use.cfm

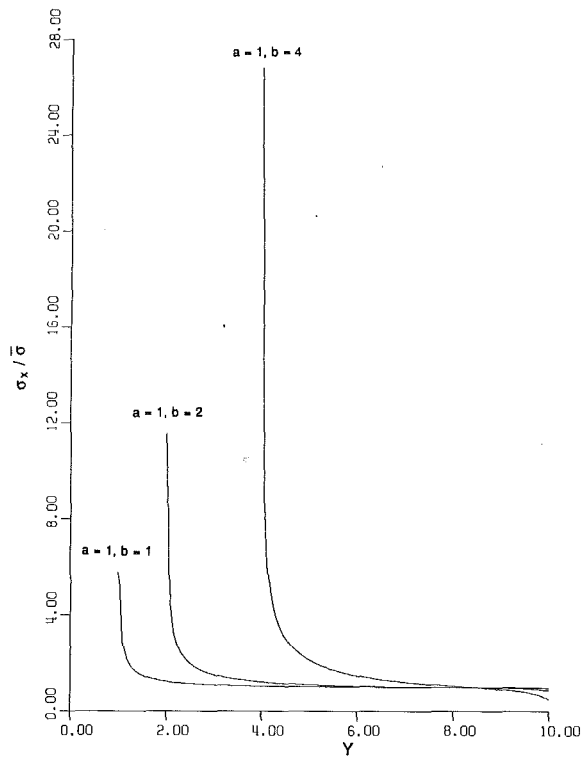


Fig. 7 Stress distribution along the positive *Y*-axis in Fig. 6

with the results given by Ghosh. As can be seen in Table 5, the boundary layer effect does not exist in this formulation.

Concluding Remarks

A system of singular integral equations is formulated and investigated numerically. The method is conceptually simple and numerically efficient. The expressions for the final system of algebraic equations are given explicitly in terms of the material properties, directions of normal vectors, and coordinates of nodal points.

Although the numerical methods for the solution of Fredholm integral equations are well known, the associated numerical procedure is usually quite complicated. In this method, the final system of algebraic equations is given explicitly in equations (24) and (29) for any specific problem. No numerical integration is necessary, and if we use complex algebra in the computer program, the simultaneous equations can be solved in a straightforward manner.

Finally, there are no boundary layer effects in this formulation and this is another advantage over the previous formulations. The stresses are obtained accurately at any interior points in contrast to previous formulations where the accuracy deteriorates near the boundary.

Acknowledgments

This research was partially supported by the Officer of Naval Research under contract N00014-87-K-035. We wish to thank Dr. Y. D. S. Rajapakse of the ONR and Mr. R. H. Jones and M. R. J. Dobbs, Managers of the Structural Mechanics Laboratory at Hughes Aircraft Company for their encouragement and support during the course of this work. It is also a pleasure to thank Ms. Jacquie Bockrath for her extraordinary skills in editing the manuscript using a MacIntosh Personal Computer.

References

Benjumea, R., and Sikareskie, D. C., 1972, "On the Solution of Plane Orthotropic Elasticity Problems by an Integral Method," ASME JOURNAL OF APPLIED MECHANICS, Vol. 39, pp. 801–808. September, 1972.

Burgess, G., and Mahajerin, E., 1984, "A Comparison of the Boundary Element and Superposition Methods," *Computers and Structures*, Vol. 19, pp. 697–705.

Copson, E. T., 1962, *Theory of Functions of a Complex Variable*, Oxford, U.K.

Cruse, T. A., 1969, "Numerical Solutions in Three-Dimensional Elastostatics," *International Journal of Solids and Structures*, Vol. 5, pp. 1259–1274.

Cruse, T. A., 1973, "Applications of the Boundary Integral Method to Three Dimensional Stress Analysis," *Computers and Structures*, Vol. 3, pp. 509–526.

Cruse, T. A., 1978, "Two-Dimensional BIE Fracture Mechanics Analysis," *Appl. Math. Modeling*, Vol. 2, pp. 287–293.

Danson, D. J., 1984, "Elasticity Problems," *Boundary Element Techniques in Computer-Aided Engineering*, C. A. Brebia, ed., (NATO ASI Series E: Applied Sciences), Martinus Nijhoff Publishers, pp. 201–238.

Ghosh, N., Rajiyah, M., Gosh, S., and Muhherjee, S., 1986, "A New Boundary Element Method Formulation for Linear Elasticity," ASME JOURNAL OF APPLIED MECHANICS, pp. 69–76, Vol. 53, pp. 69–76.

Lekhnitskii, S. C., 1968, *Anisotropic Plates*, Gordon and Breach Science Publishers, New York.

Muskhelishvili, N. I., 1953, *Singular Integral Equation*, Noordhoff, Holland.

Pape, D. A., and Banerjee, P. K., 1987, "Treatment of Body Forces in 2D Elastostatic BEM Using Particular Integrals," ASME JOURNAL OF APPLIED MECHANICS, Vol. 54, pp. 866–871.

Rizzo, F., 1967, "An Integral Equation Approach to Boundary Value Problems of Classical Elastostatics," *Quarterly of Applied Mathematics*, Vol. 25, pp. 83–95.

Rizzo, F., and Shippy, D. J., 1970, "A Method for Stress Determination in Plane Anisotropic Elastic Bodies," *J. of Composite Material*, Vol. 14, pp. 36–61.

Snyder, M. D., and Cruse, T. A., 1975, "Boundary-Integral Equation Analysis of Cracked Anisotropic Plates," *International Journal of Fractures*, Vol. 2, pp. 315–320.

APPENDIX

Equation (18*a*) can be written in the following form

$$T(\zeta)=\frac{1}{2}w(\zeta)+\frac{1}{\pi i}\int_L \frac{K_3(\zeta,\xi)p(\xi)+K_4(\zeta,\xi)q(\xi)}{\xi-\zeta}d\xi \qquad \text{(A1)}$$

where

$$K_3=\frac{1}{2}\sum_{k=1}^{2}\left[C_k(-i+\mu_k)\frac{\xi-\zeta}{\xi_k-\zeta_k}\frac{\upsilon_k(\zeta)}{\upsilon(\xi)} - \bar{C}_k(-i+i\bar{\mu}_k)\frac{\xi-\zeta}{\bar{\xi}_k-\bar{\zeta}_k}\frac{\overline{\upsilon_k(\zeta)}}{\upsilon(\xi)}\right]$$

$$K_4=\frac{1}{2}\sum_{k=1}^{2}\left[-D_k(-i+\mu_k)\frac{\xi-\zeta}{\xi_k-\zeta_k}\frac{\upsilon_k(\zeta)}{\upsilon(\xi)} + \bar{D}_k(-i+i\bar{\mu}_k)\frac{\xi-\zeta}{\bar{\xi}_k-\bar{\zeta}_k}\frac{\overline{\upsilon_k(\zeta)}}{\upsilon(\xi)}\right].$$

Equation (A1) can be expressed as the standard Cauchy singular integral equation

$$T(\zeta)=A(\zeta)w(\zeta)+\frac{1}{\pi i}\int_L \frac{K(\zeta,\xi)w(\xi)}{\xi-\zeta}d\xi \qquad \text{(A2)}$$

where

$$A(\zeta)w(\zeta)=A_{11}(\zeta)p(\zeta)+A_{12}(\zeta)q(\zeta)+i(A_{21}(\zeta)p(\zeta)+A_{22}(\zeta)q(\zeta))$$

$$K(\zeta,\xi)w(\xi)=K_{12}(\zeta,\xi)p(\xi)+K_{12}(\zeta,\xi)q(\xi)+i(K_{21}(\zeta,\xi)p(\xi)+K_{22}(\zeta,\xi)q(\xi)).$$

We define the square matrices $[A(\zeta)]$ and $[B(\zeta)]$ as

$$[A(\zeta)]=\begin{bmatrix}A_{11}(\zeta) & A_{12}(\zeta)\\ A_{21}(\zeta) & A_{22}(\zeta)\end{bmatrix} \qquad \text{(A3)}$$

$$[B(\zeta)]=[K(\zeta,\zeta)]=\begin{bmatrix}K_{11}(\zeta,\zeta) & K_{12}(\zeta,\zeta)\\ K_{21}(\zeta,\zeta) & K_{22}(\zeta,\zeta)\end{bmatrix}.$$

Then, $[A]$ and $[B]$ are readily obtained from equations (A1) and (A2) as

$$[A]=\begin{bmatrix}\frac{1}{2} & 0\\ 0 & \frac{1}{2}\end{bmatrix}$$

Downloaded 03 May 2010 to 171.66.16.244. Redistribution subject to ASME license or copyright; see http://www.asme.org/terms/Terms_Use.cfm

$$[B] = \begin{bmatrix} \frac{1}{2}(C_1\mu_1 + C_2\mu_2 - \bar{C}_1\bar{\mu}_1 - \bar{C}_2\bar{\mu}_2) & -\frac{1}{2}(D_1\mu_1 + D_2\mu_2 - \bar{D}_1\bar{\mu}_1 - \bar{D}_2\bar{\mu}_2) \\ -\frac{1}{2}(C_1 + C_2 - \bar{C}_1 - \bar{C}_2) & \frac{1}{2}(D_1 + D_2 - \bar{D} - \bar{D}_2) \end{bmatrix}.$$

Consider an orthotropic medium under generalized plane stess condition. Using equation (17), C_k and D_k can be expressed as

$$C_1 = \left(\mu_1 - \frac{\nu_{xy}}{\mu_1}\right)/\Delta,\ C_2 = -\left(\mu_2 - \frac{\nu_{xy}}{\mu_2}\right)/\Delta$$
$$D_1 = -(\mu_2^2 - \nu_{xy})/\Delta,\ D_2 = (\mu_1^2 - \nu_{xy})/\Delta \tag{A5}$$

where

$$\Delta = 2(\mu_1 + \mu_2)(\mu_1 - \mu_2).$$

We first show that the singular operator equation (A2) is a regular type operator which satisfies the following conditions (Muskhelishvili, 1953) on L,

$$S(\zeta) = \det([A(\zeta)] + [B(\zeta)] \neq 0$$
$$D(\zeta) = \det([A(\zeta)] - [B(\zeta)] \neq 0. \tag{A6}$$

Vanishing of these determinants gives

$$\nu_{xy}^2 = \frac{E_x}{G_{xy}}\sqrt{\frac{E_x}{E_y}} + \frac{E_x}{E_y}. \tag{A7}$$

We will prove that the Poisson's ratio given by equation (A7) is not admissible in physical problems.

Note that

$$\nu_{yx} = \frac{E_y}{E_x}\nu_{xy}. \tag{A8}$$

Thus,

$$\nu_{xy}\nu_{yx} = \frac{E_y}{E_x}\nu_{xy}^2. \tag{A9}$$

Substituting equation (A7) into (A9), we get

$$\nu_{xy}\nu_{yx} = \frac{E_y}{E_x}\nu_{xy}^2 = \frac{1}{G_{xy}}\sqrt{E_xE_y} + 1 > 1. \tag{A10}$$

It can be shown that the positive definiteness of strain energy function implies that $\nu_{xy}\nu_{yx} < 1$. Therefore, the regularity condition equation (A6) will always be satisfied for admissible values of the Poisson's ratio.

The index κ of the operator equation (A1) defined as (Muskhelishvili, 1953)

$$\kappa = \frac{1}{2\pi i}\left[\log\frac{D(\zeta)}{S(\zeta)}\right]_L, \tag{A11}$$

represents the increment of the function in the bracket, on one circuit of L in the positive direction.

Thus,

$$\kappa = \frac{1}{2\pi i}\left[\log\frac{D(\zeta)}{S(\zeta)}\right]_L \equiv 0, \tag{A12}$$

since $S(\zeta) = D(\zeta)$ on L. Hence, the singular operator in the right-hand side of equation (A2) is a Fredholm operator of the second kind and by Fredholm's alternative theorem, the integral equation (A2) has a unique solution for physically possible materials.

Downloaded 03 May 2010 to 171.66.16.244. Redistribution subject to ASME license or copyright; see http://www.asme.org/terms/Terms_Use.cfm

Three-Dimensional Effects Near a Crack Tip in a Ductile Three-Point Bend Specimen: Part I—A Numerical Investigation

R. Narasimhan[1]

A. J. Rosakis

Associate Professor of Aeronautics and Applied Mechanics, Assoc. Mem. ASME

Division of Engineering and Applied Science, California Institute of Technology, Pasadena, CA 92115

A simultaneous numerical and experimental investigation is undertaken to assess three-dimensional effects and HRR dominance near a crack front in a ductile 3-point bend specimen. In parallel to the three-dimensional calculations, a plane-strain and a plane-stress analysis of the same in-plane specimen geometry is performed to obtain upper and lower bounds for the three-dimensional calculation. The radial, angular, and thickness variation of the stresses and displacements are studied in great detail from contained yielding to fully plastic conditions. The results indicate that the plane-strain HRR field prevails in the interior of the specimen very near the crack front even for moderate extents of yielding. On the other hand, for distances from the crack tip exceeding about half a specimen thickness, plane-stress conditions are approached. The calculations presented here model a series of laboratory experiments involving three independent experimental techniques. Details regarding the experiments and comparisons of the experimental measurements with numerical calculations and theory are emphasized in Part II of this work.

1 Introduction

Fracture in structural components of practical dimensions, which are made of low-to-intermediate strength metals, is often accompanied by extensive plastic deformation prior to crack initiation. Hence, one is compelled to seek elastic-plastic solutions to crack problems to treat such situations. The HRR solution (Hutchinson, 1968; Rice, 1968) describes the asymptotic stress and strain variations near a monotonically loaded stationary crack tip in a material characterized by the deformation plasticity theory under two-dimensional (plane-strain, or plane-stress or antiplane shear) conditions. The J-integral (Rice, 1968), which may be interpreted as the energy release rate for a material obeying the deformation plasticity theory, also provides a measure of the intensity of the near-tip fields in the HRR solution. As emphasized by Hutchinson (1983), it is imperative that the HRR solution should dominate over a size scale which is large as compared with the region near the tip wherein finite strain effects are important. The above requirement ensures that J can be safely used to characterize the initiation of crack growth in ductile materials.

It has recently been demonstrated, on the basis of plane-strain calculations, that finite strain effects become important only for distances from the tip of the order of two or three times the crack-tip opening displacement.

The issue of J-dominance has been examined by many investigators in a variety of situations, ranging from contained yielding to fully plastic conditions under Mode I plane strain (Shih and German, 1981; McMeeking and Parks, 1979). As an outcome of these studies, it has become possible to specify proper dimensions for some commonly used specimens in fracture toughness testing, so that J-dominance could be ensured. As noted by Hutchinson (1983), analogous specifications for plane stress have not as yet been obtained. Nevertheless, the issue of HRR dominance has partly been addressed by Narasimhan and Rosakis (1988), by means of a detailed, numerical calculation which modeled Mode I, plane-stress cracks under small-scale yield conditions.

All the analyses mentioned in the foregoing section are based on the assumption of two-dimensional plane-strain or plane-stress conditions. No analytical asymptotic solution exists near three-dimensional crack fronts in elastic-plastic materials. In view of the above, it is important to examine the regions near the crack front in which the plane-stress and plane-strain HRR solutions provide a good approximation to the acutal three-dimensional fields. It is generally assumed (see, for example, Li, Shih, and Needleman, 1985) that plane-strain conditions prevail as the crack front is approached, at least in the interior of the specimen. But it appears that no

[1]Presently Assistant Professor, Department of Mechanical Engineering, Indian Institute of Technology, Powai, Bombay 40076, India.

Contributed by the Applied Mechanics Division of THE AMERICAN SOCIETY OF MECHANICAL ENGINEERS for publication in the JOURNAL OF APPLIED MECHANICS.

Discussion on this paper should be addressed to the Technical Editor, Leon M. Keer, The Technological Institute, Northwestern University, Evanston, IL 60208, and will be accepted until two months after final publication of the paper itself in the JOURNAL OF APPLIED MECHANICS. Manuscript received by the ASME Applied Mechanics Division, July 25, 1988; final revision, Sept. 22, 1989.

Copyright © 1990 by ASME

Downloaded 03 May 2010 to 171.66.16.244. Redistribution subject to ASME license or copyright; see http://www.asme.org/terms/Terms_Use.cfm

detailed investigation of the region of dominance of any singular elastic-plastic field has been carried out under three-dimensional conditions. The issue is pivotal to the definition of a local energy release rate (pointwise along the crack front) (see, for example, Li, Shih and Needleman, 1985; Nakamura, Shih, and Freund, 1986a, b) and its interpretation as an amplitude factor of the near-tip fields.

Surface integral generalizations of the line integral expression of J to three-dimensional crack problems are available in the literature (see, for example, Budiansky and Rice, 1973). Nevertheless, the definition of a local (pointwise) energy release rate and its numerical computation has been the subject of much investigation (Li, Shih, and Needleman, 1985; Shih, Moran, and Nakamura, 1986; Nakamura, Shih, and Freund, 1986a; Delorenzi and Shih, 1983; Wellman, Rolfe, and Dodds, 1987; Dodds, Carpenter, and Sorem, 1987).

In Delorenzi and Shih (1983), Wellman, Rolfe, and Dodds (1987), Dodds, Carpenter, and Sorem (1987), and Nicholas and Luxmoore (1987), fracture parameters such as J, and crack opening displacement are computed using three-dimensional numerical solutions for compact tension and three-point bend specimens and are compared with experimental results. The variation of three fracture parameters and of the stresses through the thickness are also examined in Delorenzi and Shih, (1983) Wellman, Rolfe, and Dodds (1987), Dodds, Carpenter, and Sorem, (1987), and Nicholas and Luxmoore (1987).

The purpose of the present investigation is twofold. First, numerical and experimental methods are simultaneously used to assess the effects of three dimensionality near a crack front in a ductile three-point bend specimen from contained yielding to fully plastic conditions. The experiments are based on the optical methods of caustics and interferometry and are described in detail in Part II of this investigation (Zehnder and Rosakis, 1988). Some results pertaining to the above issues and also to the variation of J and crack opening displacement will be given in Section 4.

The second issue that is addressed here (see Section 5), is the extent of regions over which plane-strain and plane-stress analyses provide a good approximation to the actual three-dimensional fields. To this end, detailed three-dimensional and two-dimensional numerical calculations have been performed (see Section 2). These calculations model the monotonic loading of a ductile three-point bend specimen from contained yielding to fully plastic conditions. The radial and angular variation of the stresses from these analyses will be compared wih the HRR solution in the spirit of Shih and German (1981), McMeeking and Parks (1979), and Narasimhan and Rosakis (1988), with the view of assessing J-dominance. An extensive collection of papers pertaining to issues similar to the ones dicussed above has recently appeared in the ASME AMD-Vol. 91 entitled "Analytical, Numerical, and Experimental Aspects of Three-Dimensional Fracture Processes." A preliminary version of the results that appear in Parts I and II of this investigation have already been discussed briefly there in the work by Narasimhan, Rosakis, and Zehnder (1988). In the same volume, the related works of Nakamura and Parks (1988) and Hom and McMeeking concentrate in detailed three-dimensional investigations of cracks in thin elastic-plastic plates performed under the idealization of small-scale yielding. In particular, the work by Hom and McMeeking emphasizes the effects of *finite deformations* on the three-dimensional nature of the near-tip region. Such effects have not been addressed in the present study.

2 Numerical Analysis

The three-point bend specimen shown in Fig. 1(*a*), was modeled using three-dimensional finite elements. The geometry of the mesh is shown in Fig. 1(*b*). Due to symmetry,

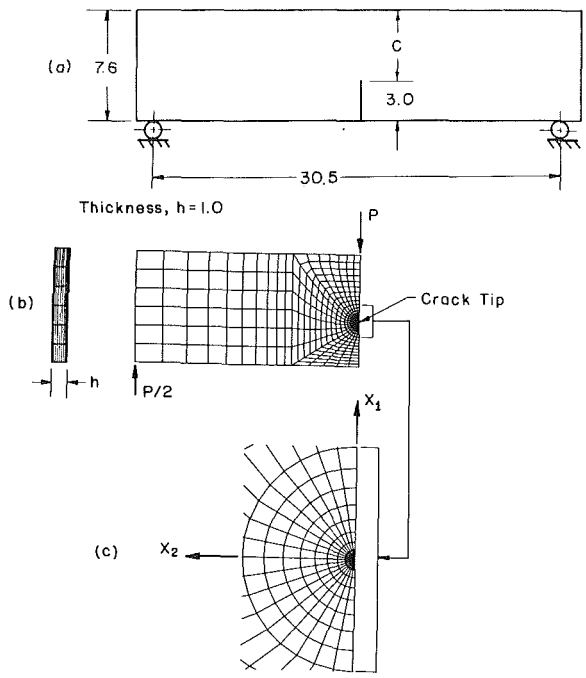


Fig. 1 (*a*) Test specimen geometry, all dimensions are in centimeters; (*b*) mesh used in finite element analysis; (c) details of in-plane mesh near the crack tip

only one quarter of the specimen was simulated, with appropriate boundary conditions imposed on the planes of symmetry. The mesh consists of five layers of elements (through *half the thickness* of the plate). Each layer is composed of 420 eight-noded brick elements. The layer interfaces are located at $x_3/h = 0$, 0.15, 0.275, 0.375, 0.45, and 0.5. It should be noted that the layers become thinner as the free surface is approached in order to model the corner singularity. The layer of elements adjoining the midsurface of the plate is three times as thick as the one near the free surface. The crack-tip elements are formed by collapsing the eight-noded brick elements to triangular prisms. The details of the *in-plane mesh* near the crack tip is shown in Fig. 1(*c*). This fine mesh is composed of a circular region whose radius is equal to the thickness of the plate. There are ten circular rings in this region, which are divided by 19 rays at equal angular intervals of 10 degrees. The radius of the innermost ring of elements (nearest to the tip) is 1/100 of the plate thickness. The detailed mesh is expected to provide sufficient resolution near the crack tip, so that a careful study of the asymptotic stress and strain variations may be performed.

Two-dimensional plane-strain and plane-stress calculations were also performed with the same in-plane mesh (Fig. 1(*b*)) to obtain upper and lower bounds for the three-dimensional calculations. A small strain, J_2-incremental plasticity theory was used. The material was assumed to be homogeneous, isotropic and to obey the Huber-Von Mises yield criterion. The response of the material in uniaxial tension was characterized by a piecewise power-hardening law of the form:

$$\frac{\epsilon}{\epsilon_0} = \begin{cases} \sigma/\sigma_0 & \sigma \le \sigma_0 \\ (\sigma/\sigma_0)^n & \sigma > \sigma_0 \end{cases} \tag{1}$$

with a hardening exponent $n = 22$ and yield stress $\sigma_0 = 1030$ Mpa. These values were chosen to match the constitutive properties of the particular heat treatment of 4340 carbon steel used in the experiments. These experiments are described in detail in Part II of this investigation.

The B-bar method proposed by Hughes (1980) and later

Downloaded 03 May 2010 to 171.66.16.244. Redistribution subject to ASME license or copyright; see http://www.asme.org/terms/Terms_Use.cfm

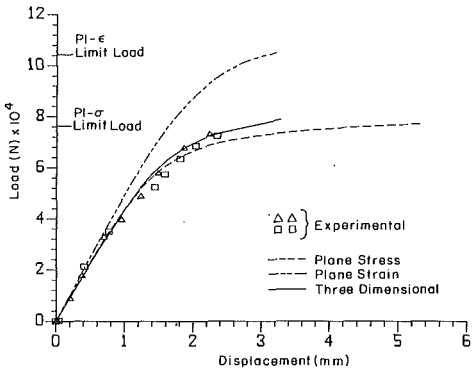


Fig. 2 Load-load displacement curve

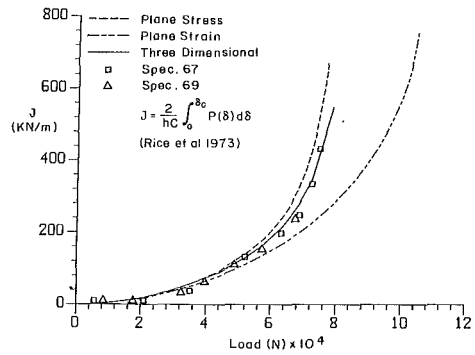


Fig. 3 J versus applied load

modified by Nakamura, Shih, and Freund (1986) was used to relieve artificial mesh locking effects that occur under nearly incompressible conditions (in the fully plastic range) under plane-strain and in three dimensions. Nakamura, Shih, and Freund (1986a, b) suggested that the B-bar method should be used with a stabilization procedure akin to Belytschko and Tsay (1983) to safeguard against a spurious pressure mode. As recommended in Nakamura, Shih, and Freund (1986), a stabilization parameter of 0.05 was used in the present calculations. The stress computations were performed using the tangential predictor-radial return method with subincrementation (see the Appendix of Narasimhan and Rosakis, 1988). The nonlinear finite element equilibrium equations were solved incrementally using a quasi-Newton method (BFGS) (Matthies and Strang, 1979). For the three-dimensional case, this method provided substantial savings as compared with the full Newton method. The convergence to an equilibrium solution was quite rapid in the early part of the load history, requiring typically three or four iterations in each load step. But it was quite slow as fully plastic conditions (given by the rigid plastic limit load) were approached. As suggested in Matthies and Strang (1979), a BFGS update was not performed whenever the condition number of the updating matrix became very large (greater than 10^5). This happened quite frequently when the limit load was approached. Also, smaller load increments were used near the limit load.

3 Description of Experiments

As described in detail in Part II, the experiments were performed on three-point bend specimens of a ductile 4340 steel with dimensions given in Fig. 1(*a*). Two specimens were tested. In both cases, the applied load and the load point displacement were measured and recorded during the experiments. In order to provide additional comparison between the numerical calculation and the experiments, a measurement of the out-of-plane displacement fields of the specimen surface was performed using Twyman-Green interferometry.

4 Results

4.1 Load-Displacement Curves. The variation of load versus load point displacement is shown in Fig. 2 from the three-dimensional and two-dimensional numerical calculations. For comparison, the experimental load-displacement records for two specimens are shown in the figure up to the point of fracture initiation. The plane-stress and plane-strain limit loads (for a rigid-perfectly plastic material) are also indicated in the figure. The curve obtained from the three-dimensional analysis lies in between the curves from plane-stress and plane-strain calculations, and is much closer to plane stress. Also, very good agreement can be seen between the experiments and the three-dimensional computation.

4.2 The *J*-Integral. The J-integral defined by Rice (1968) for a two-dimensional cracked body is path independent for a material obeying the small strain deformation theory of plasticity. Under the above conditions, this integral may be interpreted as the energy release rate and is also a characterizing parameter of the asymptotic crack-tip fields (Hutchinson, 1968, Rice and Rosengren, 1968).

For a three-dimensional crack, the J-integral is defined over a cylindrical surface (Budiansky and Rice 1973; Broberg 1987) surrounding the *entire* crack front. The numerical computation of the above surface integral in a three-dimensional finite element analysis is very difficult. However, the surface integral may also be interpreted as the energy released due to a unit (normal) virtual crack extension along the *entire* crack front. An *average* value, denoted here by J, can then be obtained by dividing the above quantity by the length of the crack front. (Nakamura, Shih, and Freund, 1986; Delorenzi and Shih, 1983). Is $\delta l(s)$ denotes the crack advance at a point s along a three-dimensional crack front (in a direction normal to it) and ds the elemental arc length along the crack front, a local quantity, $\hat{J}(x_3/h)$ has been defined by Lih, Shih, and Needleman (1985) and Shih, Moran, and Nakamura, (1986):

$$\frac{1}{h}\int_{-1/2}^{1/2} \hat{J}(x_3/h)\delta l(x_3/h)dx_3 = -\delta\Pi.$$

Here, $\delta\Pi$ is the change in potential energy of the body. It has been (heuristically) argued (see, for example, Li, Shih, and Needleman, 1985; Shih, Moran, and Nakamura, 1986) that $\hat{J}(s)$ plays a role of characterizing parameter (or amplitude factor) of the crack-tip fields provided plane-strain conditions prevail through the thickness as the crack front is approached and assuming that proportional loading is pointwise enforced. As noted earlier, this argument can be accepted only after a complete investigation of the three-dimensional near-tip fields validates the above assumptions.

A domain integral representation of J and $\hat{J}(s)$ has been discussed by Li, Shih, and Needleman (1985) Shih, Moran, and Nakamura (1986) Nakamura, Shih, and Freund (1986a, b). This method can be easily implemented in a finite element program and has also been found to give very accurate results. In particular, it is very effective in computing the near-tip value of J. This method was employed in the present analysis to calculate J from the numerical solution.

The variation of J versus the applied load is shown in Fig. 3. Also shown in the figure is the J versus applied load record calculated from the experimental results on the basis of measured load-displacement curves (see Part II). For small load levels, the three analyses show results which are not very different from each other. These values also agree very well with J calculated on the basis of small-scale yielding. Also, J from the three-dimensional analysis is close to the plane-stress

Downloaded 03 May 2010 to 171.66.16.244. Redistribution subject to ASME license or copyright; see http://www.asme.org/terms/Terms_Use.cfm

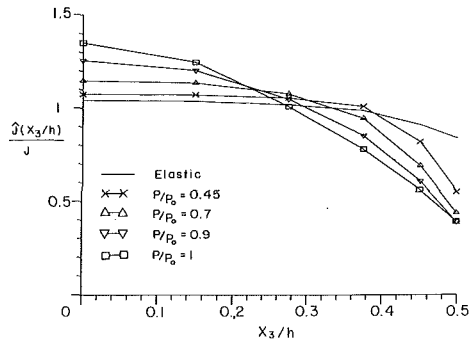


Fig. 4 Variation of $\hat{J}$ through the thickness for different load ratios; P_0 is the plane-stress limit load for a rigid-perfectly plastic material

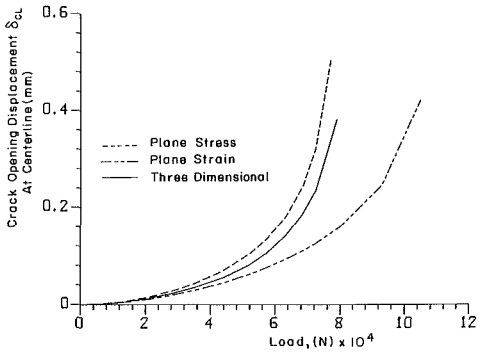


Fig. 5 Crack-tip opening displacement at centerline versus load

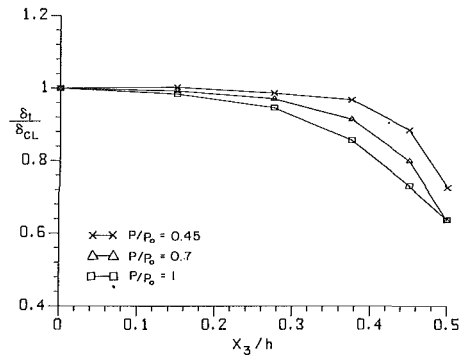


Fig. 6 Variation of the crack opening displacement along the crack front

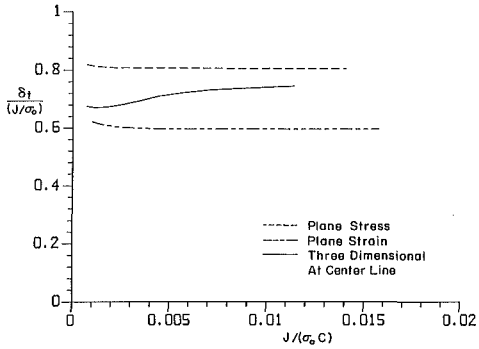


Fig. 7 Variation of the normalized centerline crack-tip opening displacement $\delta_t/(J/\sigma_0)$ from contained yielding to fully plastic conditions

solution for the entire load range, except very near the plane-stress limit load.

It is worth emphasizing here that the global three-dimensional specimen behavior such as the load displacement and the average J integral records (see Figs. 2, 3) are closer to the plane-stress rather than plane-strain approximations. This is not surprising given that the ratio of thickness to the in-plane dimensions of the specimen were relatively small. Nevertheless, as will be shown in the following section, at the vicinity of the crack tip, there is a strong variation of fields through the thickness which indicates the need for a three-dimensional analysis for the study of crack initiation. In Fig. 4, $\hat{J}$ normalized by J is plotted against normalized distance, x_3/h, along the crack front for different ratios of the applied load P to the *plane stress limit load* P_0. The variation for the elastic case is also shown in the figure. It is seen that with increasing plastic deformation, there is a considerable variation of $\hat{J}$ through the thickness with the value at the center being much higher than that at the free surface. Similar trends have been reported in Nakamura, Shih and Freund (1986a), Delorenzi and Shih (1983), and Nakamura and Parks (1988).

4.3 Crack-Tip Opening Displacement. The crack-tip opening displacement was calculated from the numerical solution using the 45 deg intercept procedure introduced by Shih (1981). The crack-tip opening displacement at the centerline of the three-dimensional specimen is plotted against the load in Fig. 5. The plane-stress and plane-strain results are also shown in the figure for comparison. As before, the three-dimensional curve is bounded by the two-dimensional analyses.

The variation of the crack-tip opening displacement along the crack front is shown in Fig. 6 for three different load ratios P/P_0. The crack-tip opening displacement δ_t has been made dimensionless by the value δ_{CL}, at the centerline of the specimen. As in the case of $\hat{J}$ in Fig. 4, there is a strong variation of the crack-tip opening with increasing plastic deformation, with the value at the centerline being very much in excess of that at the free surface. Such strong variation of crack-tip opening through the thickness was also observed in Delorenzi and Shih (1983) and Wellman, Rolfe, and Dodds (1987). This result, along with Fig. 4, suggests the possibility of a tunneling mode of fracture with the crack beginning to propagate first at the center. Indeed, some evidence of this could be seen by a post mortem examination of the fracture surface of the experimental specimen. In Fig. 7, the crack opening displacement at the center of the specimen, which is normalized by (J/σ_0) is plotted against the quantity $J/(\sigma_0 C)$. Here, C is the uncracked ligament length. The two-dimensional results are also shown in the figure. The dimensionless quantity $J/(\sigma_0 C)$ is an indication of the extend of plastic yielding (Shih, 1981; Shih and German, 1981). Small values of $J/(\sigma_0 C)$ (less than about 0.001) indicate well-contained yielding, while large values (greater than 0.01) correspond to large-scale plasticity.

The values of $\delta_t/(J/\sigma_0)$ based on the two-dimensional solutions are fairly constant over the entire range of plastic deformation. For plane stress, $\delta_t/(J/\sigma_0)$ varies from 0.82 for well-contained yielding to about 0.80 for large-scale plasticity, while for plane strain it varies from 0.62 to about 0.60. These values are somewhat smaller than the HRR solution which gives 0.95 and 0.68 for plane stress and plane strain, respectively, corresponding to $n = 22$ (Shih, 1981; Shih, 1983).

However, Narasimhan and Rosakis (1988), reported a value of $\delta_t/(J/\sigma_0)$ of 0.85 for the nonhardening case based on a finite element solution which modeled plane-stress, small-scale yielding conditions. Shih (1981) has also computed the crack opening displacement for different hardening exponents and specimen geometries based on plane-strain finite element solutions. For the Cracked Bend Bar (of perfectly plastic material), he reports a value of $\delta_t/(J/\sigma_0)$ which varies from 0.65 to 0.58 from contained yielding to fully plastic conditions. As noted in Narasimhan and Rosakis (1988), the discrepancy with the HRR solution *in the nonhardening limit*

Downloaded 03 May 2010 to 171.66.16.244. Redistribution subject to ASME license or copyright; see http://www.asme.org/terms/Terms_Use.cfm

is due to the fact that the HRR strain solution may not dominate over any finite distance near the tip. It can be seen from Fig. 7 that the normalized crack opening displacement, $\delta_t/(J/\sigma_0)$ at the centerline of the three-dimensional specimen varies from about 0.68 for contained yielding to about 0.75 for large-scale yielding. For contained yielding, this value is closer to plane strain whereas for large-scale yielding, it is closer to the plane-stress limit. A qualitatively similar trend may be noticed in the results obtained in Delorenzi and Shih (1983) for a compact tension specimen.

4.4 Stress Variation Through the Thickness. The variation of the plane-strain constraint (as given by the ratio $\sigma_{33}/(\sigma_{11}+\sigma_{22})$ through the thickness of the specimen) is shown in Fig. 8 for different load ratios P/P_0. The distribution for the elastic case is also plotted in the figure. The stresses in this plot were evaluated at the centroid of the elements *nearest* to the tip, located at $r/h=0.005$ and $\theta=0$ deg.

The first observation that can be made is that the ratio $\sigma_{33}/(\sigma_{11}+\sigma_{22})$ is uniform over most of the specimen thickness (along the crack front) and drops to zero very near the free surface. Its value in the interior of the specimen is about 0.28 for the elastic case and approaches 0.47 with increasing plastic deformation. It should be noted here that under plane-strain conditions $\sigma_{33}/(\sigma_{11}+\sigma_{22})$ is equal to the Poissons ratio (which is 0.3 in the present analysis) for the elastic case. Also this ratio is equal to 0.5 in the fully plastic limit.

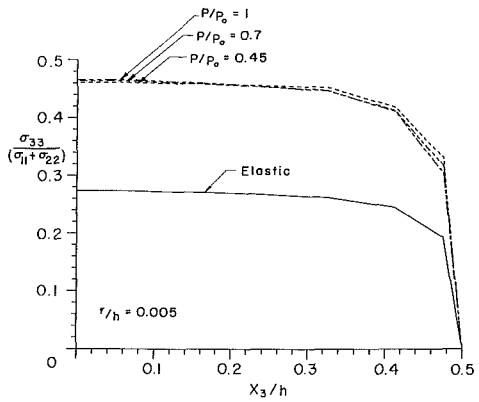


Fig. 8 Variation of the plane-strain constraint, $\sigma_{33}/(\sigma_{22}+\sigma_{22})$, along the crack front

Secondly, the numerical results indicate that even for an applied load of only 0.45 P_0 the ratio $\sigma_{33}/(\sigma_{11}+\sigma_{22})$ near the crack front is 0.46 in the interior of the specimen. The ratio shows very little variation with increase in load level. This is due to the low hardening of the material which allows very large in-plane plastic strains to accumulate near the tip even for moderate extents of yielding. This leads to a stress distribution near the crack front in the interior of the specimen which is similar to the plane-strain Prandtl field (see Rice and Rosengren, 1968; Rice, 1968; also see Section 4 and Fig. 16). The observation that $\sigma_{33}/(\sigma_{11}+\sigma_{22})$ approaches the value 0.5 near the crack front, is consistent with the expectation of a plane-strain like constraint in the center plane of the specimen.

The variation through the thickness of the cartesian stress components σ_{11}, σ_{22}, and σ_{33}, normalized by the yield stress σ_0, is shown in Figs. 9 and 10 for two different load levels ranging from contained yielding ($P=0.45P_0$) to large-scale plasticity ($P=P_0$). The stresses displayed in these figures are computed at $\theta=0$ deg and $r/h=0.005$, 0.025, 0.065, 0.125, 0.205, 0.305, 0.425, and 0.565. The arrow direction in the figures indicates increasing r/h values. The distribution through the thickness of the normalized triaxial stress $(\sigma_{11}+\sigma_{22}+\sigma_{33})/3\sigma_0$ is also shown in these figures.

It can be observed that very near the crack front (in the interior of the specimen) the stresses are highly elevated above the yield stress leading to a strongly triaxial stress field. This is characteristic of the plane-strain crack-tip fields (Rice and Rosengren, 1968; Rice, 1968). For low load levels (Fig. 9), the stress variation along the crack front is uniform over most of the specimen thickness and drops near the free surface. But in the fully plastic limit (Fig. 10) a strong variation of stresses along the crack front is noticed. This leads to a *considerable loss of triaxiality* as the free surface is approached along the crack front. This observation is important since a strongly triaxial field influences the growth and nucleation of voids.

These figures show that for $r/h>0.5$, σ_{33} is close to zero uniformly over the specimen thickness irrespective of the load level. Also, the other stress components have very little varia-

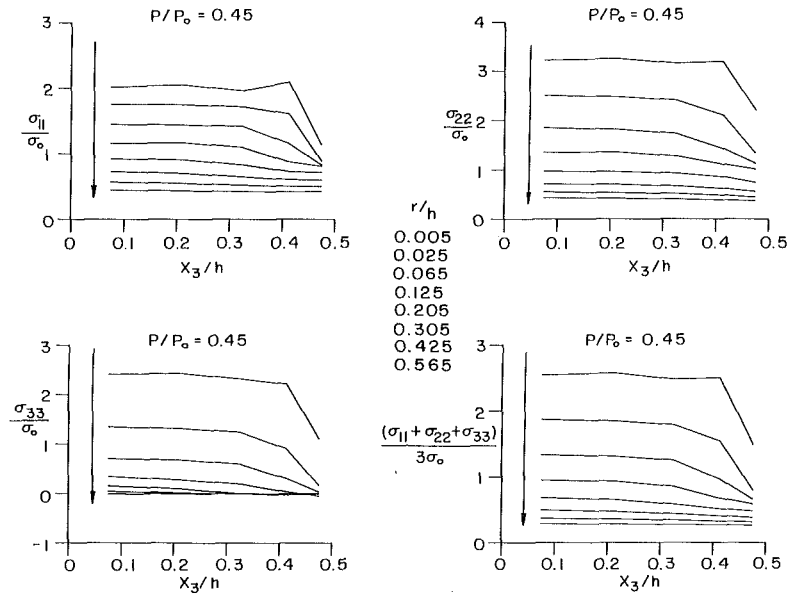


Fig. 9 Variation of normalized stress components through the thickness for load ratio $P/P_0=0.45$. The curves shown correspond to r/h – 0.005, 0.025, 0.065, 0.125, 0.205, 0.305, 0.425, and 0.565. The arrow direction indicates increasing r/h values.

Downloaded 03 May 2010 to 171.66.16.244. Redistribution subject to ASME license or copyright; see http://www.asme.org/terms/Terms_Use.cfm

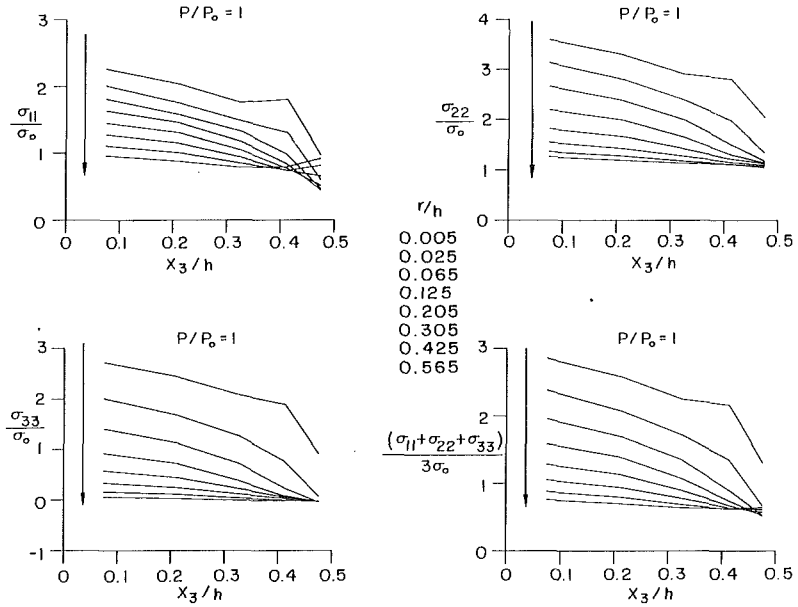


Fig. 10 Variation of normalized stress components through the thickness for load ratio $P/P_0 = 1.0$. The curves shown correspond to r/h – 0.005, 0.025, 0.065, 0.125, 0.205, 0.305, 0.425, and 0.565. The arrow direction indicates increasing r/h values.

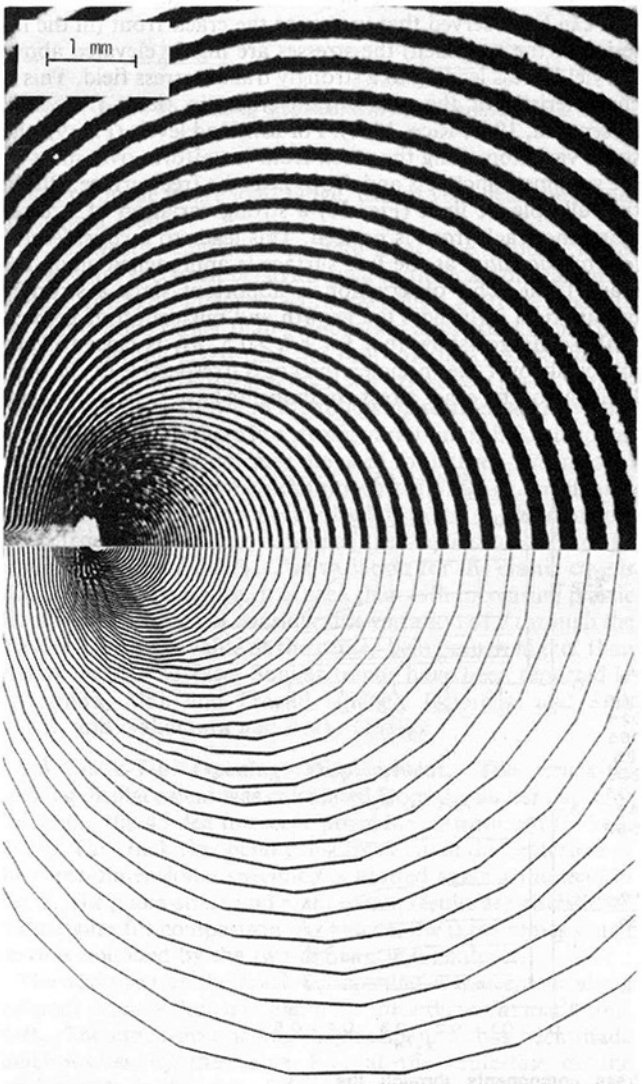


Fig. 11 Comparison of experimental and numerical interferograms, corresponding to the same load level; fringes are contours of equal out-of-plane displacement

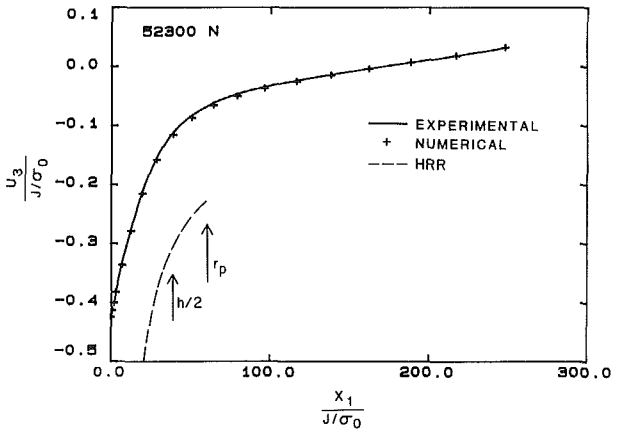


Fig. 12 Nondimensional u_3-displacement on the $\theta = 0$ line. Comparison of experimental and three-dimensional numerical results for load of 52300 N. Also shown is the HRR field within the plastic zone.

tion through the thickness for $r/h > 0.5$. This suggests that plane-stress conditions are approached for distances from the crack front in excess of half the specimen thickness (see Section 5 for further discussion).

4.5 Surface (Out-of-Plane) Displacements. The numerical simulation was used to calculate out-of-plane surface displacements and to generate numerical interferograms for comparison with the experimental results described in Part II. Figure 11 is a composite picture showing one-half of an experimental and one-half of a numerically generated interferogram. As is evident from this comparison, good qualitative agreement of experimental and synthetic interferograms is achieved. In Fig. 12, the numerical and experimental out-of-plane displacements along the ray ahead of the crack tip, $u_3(r, \theta = 0)$, are plotted against normalized distance from the tip at a load of 52300 N. The displacements have been made dimensionless by the quantity (J/σ_0). The extent of the plastic zone ahead of the tip as well as the location along the x_1-axis corresponding to half the specimen thickness are indicated for reference. The out-of-displacement corresponding to the plane-stress HRR field at the same average J value is also plotted for comparison.

Downloaded 03 May 2010 to 171.66.16.244. Redistribution subject to ASME license or copyright; see http://www.asme.org/terms/Terms_Use.cfm

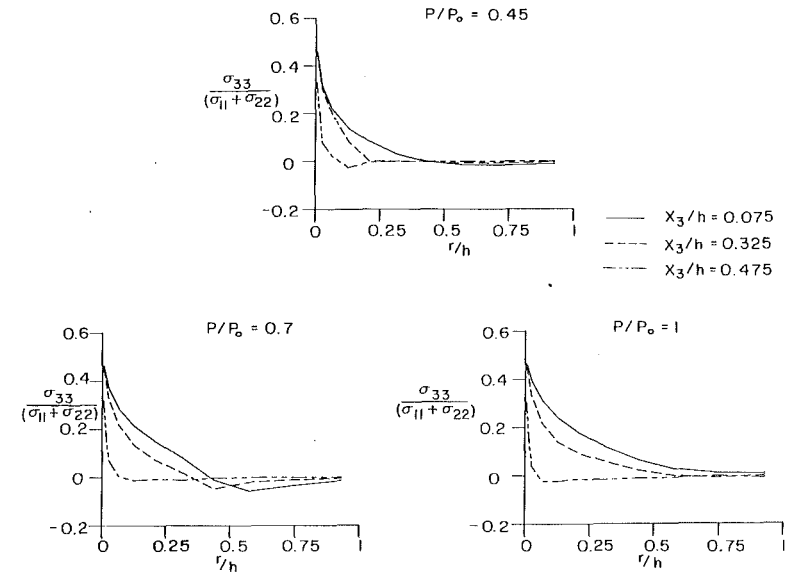


Fig. 13 Radial variation of plane-strain constraint $\sigma_{33}/(\sigma_{11}+\sigma_{22})$ along three different planes through the specimen thickness. Results are given for three different load ratios.

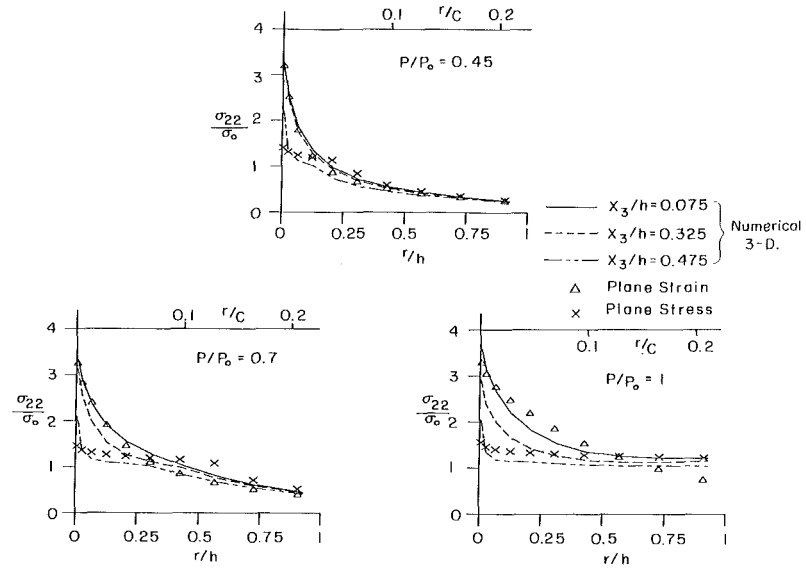


Fig. 14 Radial variation of σ_{22}/σ_0 along three different planes through the specimen thickness. Comparison between three-dimensional plane-strain and plane-stress numerical results at the same load levels.

It can be observed that there is excellent agreement between the three-dimensional numerical and experimental results, even very near the crack tip. The agreement was found to be very good over the entire range of loading (see Part II). It was found that the plane-stress HRR field did not adequately describe u_3 on the specimen surface. The above observation has also been made during previous experimental investigations using the optical method of caustics (Rosakis, Zehnder, and Narasimhan, 1987; Zehnder, 1987). In these studies, it was noticed that caustics based on plane-stress HRR fields could not always be used to accurately measure J. This discrepancy is because of three dimensionality near the crack tip and due to finite specimen dimensions that cause higher-order terms to become important away from the crack tip. Further comparisons between numerical and experimental results based on caustics and interferometry may be found in Part II.

5 Three-Dimensional Effects and HRR Dominance

5.1 Radial Stress Variation. The radial variation of the three-dimensional normalized out-of-plane stress component $\sigma_{33}/(\sigma_{11}+\sigma_{22})$ (which is an indication of the plane-strain constraint) ahead of the crack front is shown in Fig. 13 along three different planes through the specimen thickness. These planes correspond to x_3/h of 0.075 (which is near the midplane of the specimen), 0.325 (near the quarter plane) and 0.475 (near the free surface). These results have been taken from the three-dimensional solution at applied load levels of $0.45\,P_0$, $0.7P_0$, and P_0.

As noted earlier (in connection with Fig. 8), it can be seen from this figure that the ratio $\sigma_{33}/(\sigma_{11}+\sigma_{22})$ approaches a value close to 0.5 near the crack tip over most of the specimen thickness once moderate amounts of yielding take place. Also, irrespective of load level and for all planes through the

Downloaded 03 May 2010 to 171.66.16.244. Redistribution subject to ASME license or copyright; see http://www.asme.org/terms/Terms_Use.cfm

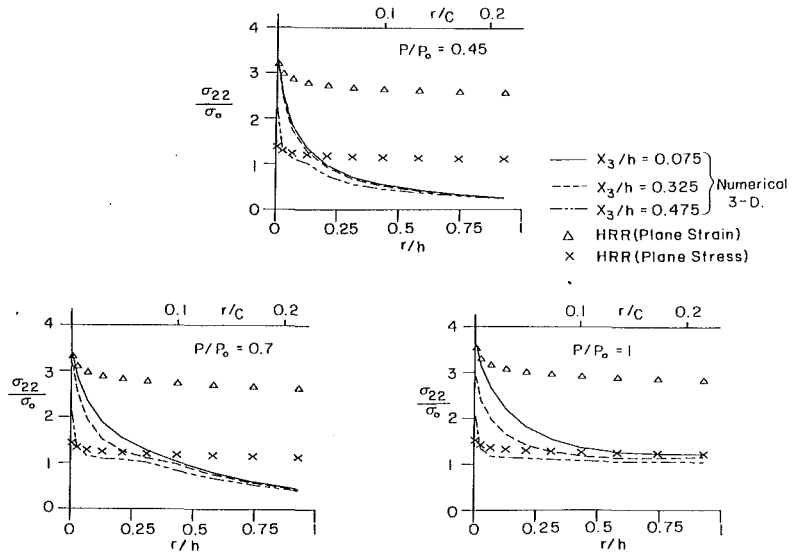


Fig. 15 Radial variation of σ_{22}/σ_0 along three different planes through the specimen thickness. Comparison between three-dimensional numerical and two-dimensional HRR solutions.

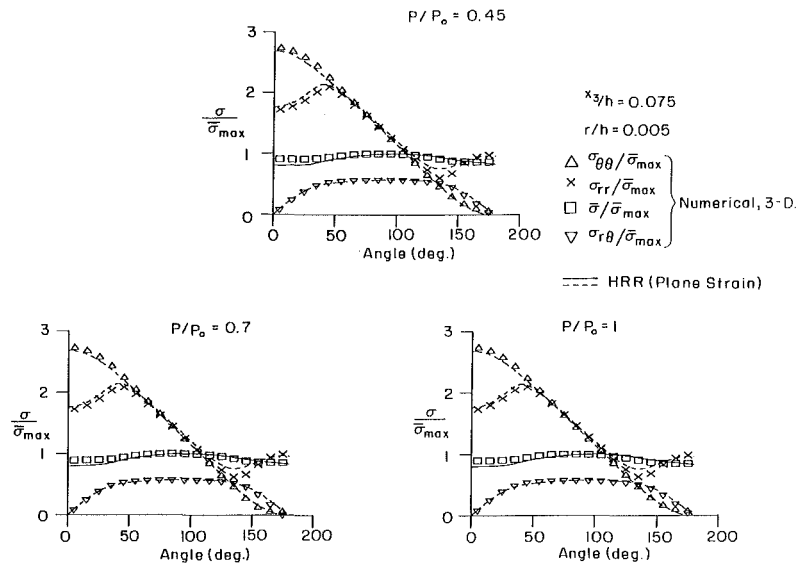


Fig. 16 Comparison between three-dimensional near-tip angular stress distribution along the plane $x_3/h = 0.075$ and HRR plane-strain solution

thickness, the above ratio becomes quite small for radial distances from the crack tip exceeding approximately half the specimen thickness ($r > 0.5h$). This observation along with Figs. 9 and 10, which show that the other stress components have negligible variation through the thickness for $r/h > 0.5$, suggests that plane-stress conditions are approached for distances from the crack tip exceeding half the specimen thickness. A similar conclusion was reached by Yang and Freund (1984) on the basis of an analytical investigation and by Parsons, Hall, and Rosakis (1986), on the basis of a numerical study of three-dimensional elastic cracked specimens. Experimental observations based on the optical method of caustics (Rosakis and Ravichandar (1984), Rosakis, Zehnder, and Narasimhan (1987)), also indicate that three-dimensional effects become important only for $r/h < 0.5$.

In order to examine the above issue further, the radial distribution of the normalized opening stress σ_{22}/σ_0 ahead of the crack front is shown along three different planes through the specimen thickness ($x_3/h = 0.075$, 0.325, and 0.475) in Fig. 14. The bottom scale in the figure gives the radial distance from the tip normalized by the specimen thickness h; while in the top scale, the normalization is done with respect to the uncracked ligament length C. For comparison, the corresponding variation based on the full-field plane-stress and the full-field plane-strain numerical solutions (at the *same load level* P) are indicated in the figure. Results are once again provided for three values of applied load.

This figure shows that for $r/h > 0.5$, the plane-stress radial stress distribution is approached over the entire specimen thickness irrespective of the load. On the other hand, the plane-strain radial stress variation provides a good approximation near the midplane of the specimen for $r/h < 0.2$. It should be noted that the σ_{22} (opening stress) distribution is highly elevated above the yield stress as the crack tip is approached in the interior of the specimen. Also, it can be seen that there is substantial variation of stresses through the

Downloaded 03 May 2010 to 171.66.16.244. Redistribution subject to ASME license or copyright; see http://www.asme.org/terms/Terms_Use.cfm

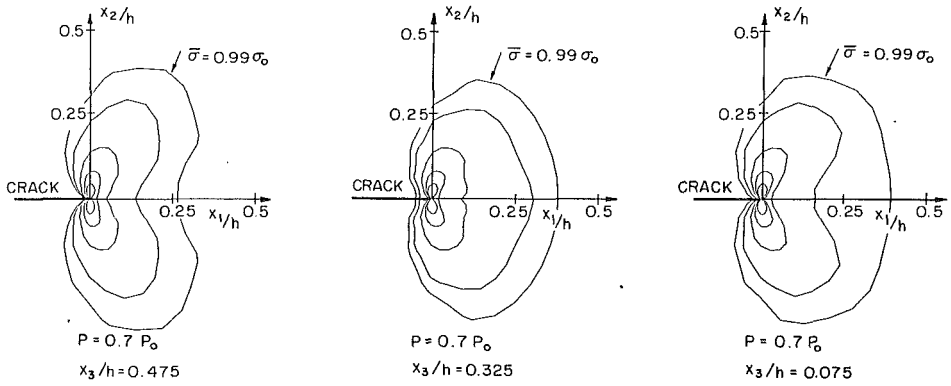


Fig. 17 Contours of equivalent stress ($\bar{\sigma}/\sigma_0 = 0.99, 1.02, 1.05, 1.08, 1.11$) for $P/P_0 = 0.7$ at $x_3/h = 0.075, 0.325, 0.475$.

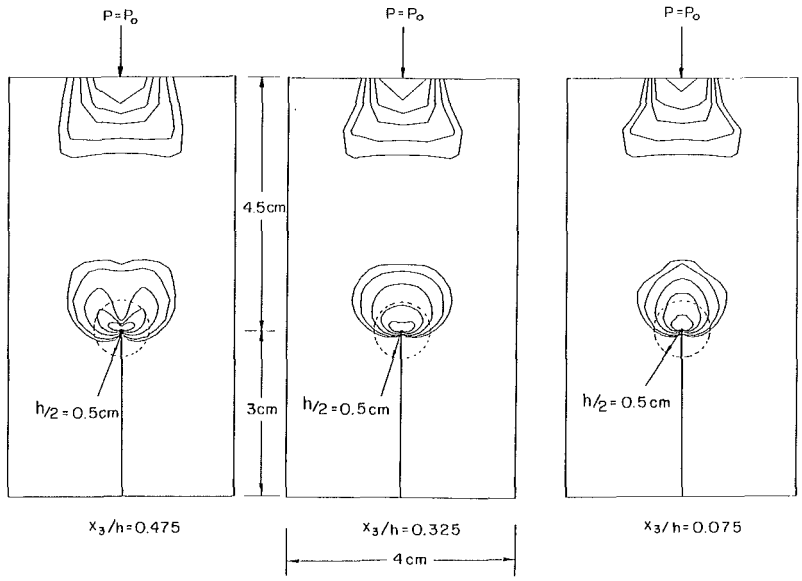


Fig. 18 Contours of equivalent stress ($\bar{\sigma}/\sigma_0 = 0.99, 1.02, 4.05, 1.08, 1.11$) for $P/P_0 = 1$ at $x_3/h = 0.075, 0.325, 0.475$.

thickness as fully plastic conditions are approached (see Fig. 10 and distribution corresponding to $P = P_0$ in Fig. 14).

In Fig. 15, the radial variation of the opening stress ahead of the crack tip is again shown in the same nondimensional scales but is now compared with the analytical asymptotic plane-stress and plane-strain HRR distributions. Th asymptotic (HRR) distributions corresponding to the same average value of J have been plotted in this figure. This figure demonstrates that very near the crack tip ($r < 0.02h$) the opening stress in the interior of the specimen tends towards the asymptotic plane-strain HRR solution. On the other hand, the plane-stress HRR solution is approached away from the crack tip within the plastic zone. This is more evident with increasing plastic yielding (see figures corresponding to $P = 0.7P_0$ and $P = P_0$).

5.2 Angular Stress Variation. In Fig. 16, the near-tip angular distribution of the normalized stresses obtained from the three-dimensional numerical solution at $x_3 = 0.075h$ (near the midplane of the specimen) and $r = 0.005h$ is shown. Results are given for three different load ratios P/P_0. The stresses in those plots have been normalized by the maximum value $\bar{\sigma}_{\max}$ of the equivalent stress $\bar{\sigma} = (3/2S_{ij}S_{ij})^{1/2}$. Also plotted in the figure is the angular stress variation given by the plane-strain HRR asymptotic solution. It is found that the three-dimensional crack-tip stresses near the midplane of the specimen agree very closely with the plane-strain HRR field.

It should be recalled that the material used in the experiments, and modeled by the numerical calculations, has a very low strain hardening ($n = 22$), and hence the angular stress variation in Fig. 16 displays all the essential features of the perfectly-plastic plane-strain Prandtl slip line field. For example, in the angular range 45 deg $< \theta <$ 135 deg, $\sigma_{rr} = \sigma_{\theta\theta}$ and $\sigma_{r\theta}$ is constant. These are characteristic of the "centered fan" region of the Prandtl field (Rice, 1968) where the plastic strains are singular as $1/r$. Also, note that the stresses are highly elevated (above $\bar{\sigma}_{\max}$) ahead of the crack tip ($\theta = 0$ deg). This result clearly demonstrates the dominance of the plane-strain HRR field along the crack front in the *interior* of the specimen.

5.3 Plastic Zones. The plastic zones corresponding to the two different load levels and three different planes through the specimen thickness ($x_3/h = 0.075$, 0.325 and 0.475) are shown in Figs. 17 and 18.

Both figures display contours of equal equivalent stress $\bar{\sigma}$. The contour further away from the crack tip (boundary of the zones) corresponds to $\bar{\sigma} = 0.99\sigma_0$. The remaining contours correspond to $\bar{\sigma} = 1.02\sigma_0$, $1.05\sigma_0$, $1.08\sigma_0$, $1.11\sigma_0$, respectively.

Downloaded 03 May 2010 to 171.66.16.244. Redistribution subject to ASME license or copyright; see http://www.asme.org/terms/Terms_Use.cfm

Figure 17 corresponds to $P=0.7P_0$. For this load level, the plastic zone has not yet interacted with the applied loads at the boundary. For all cross-sections, the maximum plastic zone site is less than half the specimen thickness and thus it lies well within the region of high near-tip three dimensionality as discussed in Section 5.1. It is somewhat surprising to note here that the plastic zone shape obtained at the specimen *surface* looks closer to the *plane-strain* plastic zone shape than its counterpart in the middle. This contradicts the popular concept of plastic zone shapes as reported in a number of books on fracture mechanics, (Hellan, 1985; Kanninen and Popelar, 1985).

It should be noted here that in the current investigation we model a specific specimen geometry where strict small-scale yielding conditions are never present in the sense that a two-dimensional plane-stress K-field is never found to dominate at any distance from the crack front at any load level. This is, for example, obvious from the experimental results presented in Fig. 9 of Part II of this work. Despite that fact, we believe that it is interesting to note that our results regarding plastic zone shapes are at least qualitatively consistent with the observations of Nakamura and Parks (1988), who studied three-dimensional plastic zone shapes under a strictly small-scale yielding idealization.

Figure 18 shows contours of $\bar{\sigma}$ for $P=P_0$. The figure clearly indicates the *interactions* of the crack-tip plastic zone with the plastic deformation at the specimen boundary due to the applied loads. In this case and for all cross-sections, the outer contour of equal $\bar{\sigma}$ reveals almost circular plastic zone shapes reminiscent of the shapes predicted by Narasimhan and Rosakis (1988), on the basis of a plane-stress analysis. This is not surprising since the elastic plastic boundary now lies well outside a circle of radius $h/2$ /(dotted line) which signifies the region outside which plane stress conditions dominate. Indeed, as shown in Fig. 13, the stress field for all load levels, approaches the plane-stress constraint for $r/h>0.5$.

6 Conclusions

A simultaneous experimental and numerical (both three-dimensional and two-dimensional) investigation has been performed to simulate the monotonic loading of a ductile 3-point bend specimen from contained to fully plastic conditions. The average J and the crack-tip opening displacement from the three-dimensional analysis are bounded by the two-dimensional (plane-stress and plane-strain) analyses. The crack-tip opening displacement and stresses exhibit a strong variation along the crack front with increasing plastic deformation. The three-dimensional numerical results clearly indicate that the plane-strain HRR field dominates very near the crack front ($r<0.02h$) in the *interior* of the specimen. The near-tip angular stress variation very close to the midsurface of the specimen displays all the essential features of the asymptotic plane-strain Prandtl field, once moderate amount of yielding has occurred. However, it should be noted here that the present small strain calculation reveals a *very small* range of dominance of the plane-strain HRR field in the specimen interior. The physical implications of this observation are that the presence of large displacement gradients near the crack front (expected to dominate over approximately a distance of $3\delta_{CL}$ from the crack front (see Hom and McMeeking, 1988) may preclude the existence of a region of plane-strain HRR dominance in a real laboratory situation. On the other hand, the plane-stress HRR field agrees well with the three-dimensional numerical results obtained on the surface layer of elements over a much larger distance from the crack front.

On the other hand, there is a considerable loss in triaxiality of the stress field as the free surface is approached along the crack front. This is particularly evident for the larger applied loads and suggests a tendency towards loss of local J dominance along the crack front as large-scale yielding conditions are approached. The radial and thickness variations of the stresses from the three-dimensional analysis suggests that for $r>0.5h$, plane-stress conditions are approached. Comparison of the results to two-dimensional analyses, whenever appropriate, and the excellent agreement between the numerical and experimental, $P-\delta$, $J-P$ and $u_3(r,\theta)$ results leave no question that the three-dimensional calculations are accurate. These comparisons also show that the calculation is sufficiently refined to model this specimen well, both in the overall behavior and in the details of the near-tip fields.

7 Acknowledgments

Support of the ONR contract N00014-85-K-0596 is gratefully acknowledged. The second author (A. J. Rosakis) also acknowledges the support of the NSF-PYI Grant MSM-8451204. The computations were performed using the Supercomputer facilities at the University of California at San Diego.

References

Belytschko, T., and Tsay, C. S., 1983, "A Stabilization Procedure for the Quadrilateral Plate Element with One-Point Quadrature," *International Journal for Numerical Methods in Engineering*, Vol. 19, pp. 405–419.

Broberg, K. B., 1987, "A Path Independent Integral for Plates," ASME JOURNAL OF APPLIED MECHANICS, Vol. 54, pp. 458–459.

Budiansky, B., and Rice, J. R., 1973, "Conservation Laws and Energy-Release Rates," ASME JOURNAL OF APPLIED MECHANICS, Vol. 40, pp. 201–203.

Delorenzi, H. G., and SHih, C. F., 1983, "Three-Dimensional Elastic Plastic Investigation of Fracture Parameters in Side-grooved Compact Specimen," *International Journal of Fracture*, Vol. 21, pp. 195–220.

Dodds, R. H., Carpenter, W. C., and Sorem, W. A., 1987, *Proceedings of the Fourth International Conference on Numerical Methods in Fracture Mechanics*, A. R. Luxmoore et al., eds., pp. 283–297.

Hellan, K., 1985, *Introduction to Fracture Mechanics*, McGraw-Hill, New York.

Hom, C. L., and McMeeking, R. M., 1988, "Crack Tip Blunting in Thin Ductile Sheets," *Analytical, Numerical, and Experimental Aspects of Three-Dimensional Fracture Processes*, A. J. Rosakis, K. Ravi-Chandar and Y. Rajapakse, eds., ASME AMD-Vol. 91.

Hughes, T. J. R., 1980, "Generalization of Selective Integration Procedures to Anisotropic and Nonlinear Media," *International Journal for Numerical Methods in Engineering*, Vol. 15, pp. 1413–1418.

Hutchinson, J. W., 1968, "Plastic Stress and Strain Fields at a Crack Tip," *Journal of Mechanics and Physics of Solids*, Vol. 16, pp. 337–347.

Hutchinson, J. W., 1983, "Fundamentals of the Phenomenological Theory of Non-linear Fracture Mechanics," ASME JOURNAL OF APPLIED MECHANICS, Vol. 50, pp. 1042–1051.

Kanninen, M. F., and Popelar, C., 1985, *Advanced Fracture Mechanics*, Oxford University Press.

Li, F. Z., Shih, C. F., and Needleman, A., 1985, "A Comparison of Methods for Calculating Energy Release Rates," *Engineering Fracture Mechanics*, Vol. 21, pp. 405–421.

Matthies, H., and Strang, G., 1979, "The Solution of Non-linear Finite Element Equations," *International Journal for Numerical Methods in Engineering*, Vol. 14, pp. 1613–1626.

McMeeking, R. M., and Parks, D. M., 1979, "On Criteria for J-dominance of Crack-tip Fields in Large-scale Yielding," *Elastic-Plastic Fracture*, ASTM-STP No. 668, pp. 175–194.

Nakamura, T., and Parks, D. M., 1988, "Conditions for J Dominance in Three-Dimensional Thin Cracked Plates," *Analytical, Numerical, and Experimental Aspects of Three-Dimensional Fracture Processes*, ASME AMD-Vol. 91, A. J. Rosakis, K. Ravi-Chandar and Y. Rajapakse, eds.

Nakamura, T., Shih, C. F., and Freund, L. B., 1986a, "Analysis of a Dynamically Loaded Three-point-bend Ductile Fracture Specimen," *Engineering Fracture Mechanics*, Vol. 25, pp. 323–339.

Nakamura, T., Shih, C. F., and Freund, L. B., 1986b, "Three-dimensional Transient Analysis of a Dynamically Loaded Three-point Bend Ductile Fracture Specimen," Brown University Report ONR 0365/3, to appear in ASTM-STP No. 995.

Narasimhan, R., and Rosakis, A. J., 1988, "A Finite Element Analysis of small-scale Yielding Near a Stationary Crack Under Plane Stress," *Journal of Mechanics and Physics of Solids*, Vol. 36, pp. 77–117.

Narasimhan, R., Rosakis, A. J., and Zehnder, A. T., 1988, "Three-dimensional Fields for a Through Crack in an Elastic-plastic Solid: Numerical Analysis and Comparison With Interferometric Measurements," *Analytical,*

Downloaded 03 May 2010 to 171.66.16.244. Redistribution subject to ASME license or copyright; see http://www.asme.org/terms/Terms_Use.cfm

Numerical and Experimental Aspects of Three-Dimensional Fracture Processes, ASME AMD-Vol. 91, A. J. Rosakis, K. Ravi-Chandar, and Y. Rajapakse, eds.

Nicholas, P. J., and Luxmoore, A. R., 1987, *Proceedings of the Fourth International Conference on Numerical Methods in Fracture Mechanics*, A. R. Luxmoore et al., eds., pp. 243–258.

Parsons, I. D., Hall, J. F., and Rosakis, A. J., 1986, "A Finite Element Investigation of the Elastostatic State Near a Three-Dimensional Edge Crack," Caltech Report No. SM 86.29.

Rice, J. R., 1968, "A Path-Independent Integral and the Approximate Analysis of Strain Concentration by Notches and Cracks," ASME JOURNAL OF APPLIED MECHANICS, Vol. 35, pp. 379–386.

Rice, J. R., and Rosengren, G. F., 1968, "Plane Strain Deformation Near a Crack Tip in a Power-law Hardening Material," *Journal of Mechanics and Physics of Solids*, Vol. 16, pp. 1–12.

Rosakis, A. J., and Ravichandar, K., 1986, "On Crack Tip Stress State: An Experimental Evaluation of Three-dimensional Effects," *International Journal of Solids and Structures*, Vol. 22, pp. 121–138.

Rosakis, A. J., Zehnder, A. T., and Narasimhan, R., 1987, "Caustics by Reflection and their Application to Elastic-plastic and Dynamic Fracture Mechanics," prepared for the SPIE Conference on Photomechanics and Speckle Metrology, San Diego, Calif., to appear in *Optical Engineering*, 1988.

Shih, C. F., 1981, "Relationships Between the *j*-integral and the Crack Opening Displacement for Stationary and Extending Cracks," *Journal of Mechanics and Physics of Solids*, Vol. 29, pp. 305–326.

Shih, C. F., 1983, "Table of HRR Singular Field Quantities," Brown University Report.

Shih, C. F., and German, M. D., 1981, "Requirements for One Parameter Characterization of Crack Tip Fields by the H.R.R. Singularity," *International Journal of Fracture*, Vol. 17, pp. 27–43.

Shih, C. F., Moran, B., and Nakamura, T., 1986, "Energy Release Rate Along a Three-dimensional Crack Front in a Thermally Stressed Body," *International Journal of Fracture*, Vol. 30, pp. 79–102.

Wellman, G. W., Rolfe, S. T., and Dodds, R. H., 1987, *Welding Research Council Bulletin*, Vol. 299, pp. 15–25.

Yang, W., and Freund, L. B., 1985, "Transverse Shear Effects for Through-Cracks in an Elastic Plate," *International Journal of Solids and Structures*, Vol. 21, pp. 977–994.

Zehnder, A. T., 1987, "Dynamic Fracture Initiation and Propagation in Metals: Experimental Results and Techniques," Ph.D. Thesis, California Institute of Technology, Pasadena, Calif.

Zehnder, A. T., and Rosakis, A. J., 1988, "Three Dimensional Effects Near a Crack Tip in a Ductile Three Point Bend Specimen: Part II—An Experimental Investigation Using Interferometry and Caustics," ASME JOURNAL OF APPLIED MECHANICS, Vol. 57, pp. 618–626.

Downloaded 03 May 2010 to 171.66.16.244. Redistribution subject to ASME license or copyright; see http://www.asme.org/terms/Terms_Use.cfm

Three-Dimensional Effects Near a Crack Tip in a Ductile Three-Point Bend Specimen: Part II—An Experimental Investigation Using Interferometry and Caustics

Alan T. Zehnder[1]
Assoc. Mem. ASME

Ares J. Rosakis[2]
Assoc. Mem. ASME

Graduate Aeronautical Laboratories,
California Institute of Technology,
Pasadena, CA 91125

An experimental investigation is undertaken to assess three-dimensional effects near a crack front in a ductile three-point bend specimen. The possibility of using the optical method of caustics for the measurement of the J-integral in the presence of large-scale yielding and three-dimensional fields is also investigated. Experiments using the optical methods of caustics by reflection and Twyman-Green interferometry are performed simultaneously on either side of the test specimen. The load and load-point displacement are also measured. The experimental results are compared with very good agreement to the results of a finite element simulation of the experiment. The caustics experiments are used to obtain a calibration relation between the value of the J-integral and the caustic diameter for load levels up to fracture initiation. It is proposed that such a calibration be used in dynamic fracture initiation experiments for the measurement of the time history of the dynamic J-integral.

1 Introduction

The J integral (Rice, 1968) is commonly used as a measure of a material's fracture toughness in ductile fracture. It is postulated that a stationary, initially sharp crack will grow when the loads are increased to a level such that a critical value of J is achieved. This critical value is assumed to be a material property. For two-dimensional, monotonically loaded, stationary cracks, the J-integral is a path-independent line integral evaluated over an open contour surrounding the crack tip, and it is also a measure of the intensity of the crack-tip strain singularity (Hutchinson, 1968; Rice and Rosengren, 1968). For three-dimensional plate specimens containing through cracks, one can define an integral evaluated over a surface surrounding the entire crack front which is equivalent to the two-dimensional J, and for monotonic loading, is independent of the choice of surface. This integral represents an average of the strength of the fields through the thickness. In addition, it can be shown that it represents the average value of the local definition of J along the crack front as given by Shih, Moran, and Nakamura, (1986), as discussed on Part I of this investigation (Narasimhan and Rosakis, 1988b).

For either two or three-dimensional problems, *dynamic* fracture initiation toughness may also be characterized by the J integral. Unfortunately, few proven experimental techniques exist for measuring J under dynamic loading conditions. Traditional load-load point displacement methods for measuring J are generally restricted to static testing. Existing dynamic techniques developed by Costin, Duffy, and Freund (1977) and analyzed by Nakamura, Shih, and Freund (1985) are based on the use of dynamic boundary value measurements interpreted on the basis of quasistatic J estimation procedures. Because of this limitation, the specimen geometries used in such experiments are highly restricted. As a result, it will be useful to develop optical methods capable of accurately estimating J directly, regardless of specimen geometry and loading rates. In this paper, the first stages of developing such a technique are described.

The optical technique chosen is the method of caustics by reflection, which has already found many useful applications in elastic dynamic fracture mechanics. This paper describes experiments designed to develop an extension of the method of

[1]Presently, Assistant Professor of Theoretical and Applied Mechanics, Cornell University, Ithaca, CA 14853-1503.

[2]Presently, Associate Professor of Aeronautics and Applied Mechanics, Division of Engineering and Applied Science, California Institute of Technology, Pasadena CA 91125.

Contributed by the Applied Mechanics Division of THE AMERICAN SOCIETY OF MECHANICAL ENGINEERS for publication in the JOURNAL OF APPLIED MECHANICS.

Discussion on this paper should be addressed to the Technical Editor, Leon M. Keer, The Technological Institute, Northwestern University, Evanston, IL 60208, and will be accepted until two months after final publication of the paper itself in the JOURNAL OF APPLIED MECHANICS. Manuscript received by the ASME Applied Mechanics Division, July 25, 1988; final revision, Sept. 22, 1989.

Copyright © 1990 by ASME
Downloaded 03 May 2010 to 171.66.16.244. Redistribution subject to ASME license or copyright; see http://www.asme.org/terms/Terms_Use.cfm

caustics to applications in elastic-plastic fracture mechanics. The application of the present results to the analysis of dynamic experiments will be described in a future paper (Zehnder, Rosakis, and Krishnaswamy, 1989).

The method of caustics was originally developed by Manogg (1964) for measuring the stress intensity factor in thin transparent elastic plates. A series of important contributions on the subject is also summarized by Theocaris (1981). The first extensions of the method of caustics to elastic-plastic fracture were made by Rosakis and Freund (1982) and by Rosakis, Ma, and Freund (1983), based on the assumption of validity of the plane-stress HRR, asymptotic crack-tip field (Hutchinson, 1968; Rice and Rosengren, 1968) and it demonstrated that under certain conditions the value of the J-integral *can* be measured with caustics. Nonetheless, the recent work of Zehnder, Rosakis, and Narasimhan (1986) showed that the two-dimensional asymptotic approach severely limits the applicability of the method. This is true because such an analysis cannot deal with either three-dimensional effects near the crack tip or with large-scale yielding effects, both characteristic of finite test specimens.

A new approach is taken here that allows for accurate measurement of thickness average of J for any planar test specimen geometry and material (Zehnder, 1987). In brief, the approach is to make a calibration of J versus the caustic diameter for a particular specimen geometry and material. It is shown that this calibration may be performed experimentally or numerically with equal accuracy. The results of simultaneous experiments that use interferometry to measure the out-of-plane surface displacements of the specimen give further insight into the limitations of previous attempts to analyze caustics through plane-stress assumptions. The interferometric measurements are also used to confirm the accuracy of the three-dimensional finite element analysis described in Part I of this investigation and to discuss the region of dominance of the plane-stress HRR field.

In the next section, the optical method of caustics is described and briefly reviewed. Subsequent sections describe experiments using the optical methods of caustics and Twyman-Green interferometry, performed simultaneously on either side of the test specimen. Load versus load-point displacement and J versus load records are also obtained experimentally. These records, as well as the out-of-plane surface displacements, measured by interferometry, are compared with their numerical counterparts obtained on the basis of the three-dimensional calculation described in Part I. Finally, the caustics experiments are used to obtain the relation between the caustic diameter, D, and the value of the J-integral for different load levels. This is found to be in excellent agreement with the equivalent relation between D and J obtained numerically by means of the three-dimensional numerical calculation of Part I.

2 Caustics By Reflection

2.1 The Mapping Equations. Consider the flat surface of an opaque plate specimen of uniform thickness h, containing a through crack. In the undeformed state, this surface, assumed to be perfectly reflective, will occupy a region in the x_1,x_2 plane at $x_3=0$. When loads are applied on the lateral boundaries of the plate, the resulting change in thickness of the plate specimen is nonuniform and the equation of the deformed specimen surface will be expressed as:

$$x_3+f(x_1,x_2)=0. \tag{1}$$

Consider further, a family of light rays parallel to the x_3-axis, incident on the reflecting surface. Upon reflection, the light rays will deviate from parallelism (see Fig. 1). If certain geometrical conditions are met by the reflecting surface, then

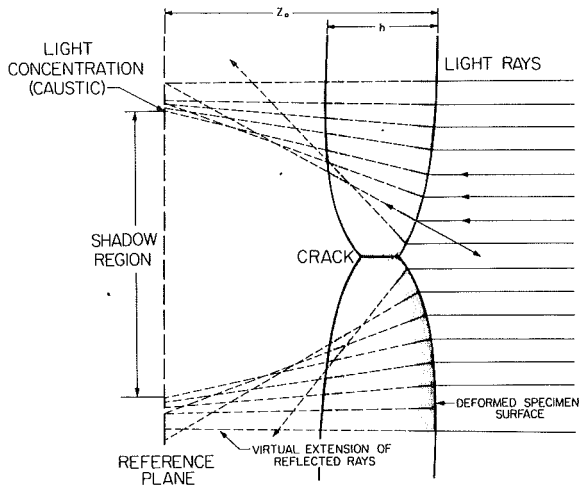


Fig. 1 Formation of caustic due to reflection of light from the polished, deformed specimen surface near the crack tip

the virtual extensions of the reflected rays (dashed lines) will form an envelope which is a three-dimensional surface in space. This surface, called the "caustic surface," is the locus of points of highest density of rays (maximum luminosity) in the virtual image space. The virtual extensions of the rays are tangent to the caustic surface. The reflected light field is recorded on a camera positioned in front of the specimen. The focal plane of this camera, which will be called the "screen," is located behind the plane $x_3=0$ (occupied by the reflector in the undeformed state) and intersects the caustic surface at the plane $x_3=-z_0$, $z_0\geq 0$. On the screen, a cross-section of the caustic surface is observed as a bright curve (the *caustic curve*), bordering a dark region (the *shadow spot*). The resulting optical pattern depends on the nature of the function $f(x_1,x_2)$ and on the focal distance z_0.

The reflection process can be viewed as a mapping of points (x_1,x_2) of the plane occupied by the reflector in the undeformed state, onto points (X_1,X_2) of the plane $x_3=-z_0$ (the *screen*). The mapping equations based on geometrical optics are given by (Rosakis and Zehnder, 1985)

$$\mathbf{X}=\mathbf{x}-2(z_0-f)\frac{\nabla f}{1-|\nabla f|^2} \tag{2}$$

where $\mathbf{X}=X_\alpha\mathbf{e}_\alpha$, $\mathbf{x}=\mathbf{x}_\alpha\mathbf{e}_\alpha$, and $\mathbf{e}_\alpha$ denote unit vectors. In the subsequent discussion, Greek subscripts have the range 1, 2.

When $z_0 \gg f$, as is usually the case in most practical applications, the above simplifies to

$$\mathbf{X}=\mathbf{x}-2z_0\nabla F. \tag{3}$$

Equation (3) are the mapping equations what will be used in the rest of this discussion.

2.2 The Initial Curve and Its Significance. Equation (2), or its approximation (3), is a mapping of the points on the reflecting surface onto points on the *screen*. If the *screen* intersects the caustic surface, then the resulting caustic curve on the *screen* is a locus of points for which the determinant of the Jacobian matrix of the mapping equations (3) must vanish or

$$I(x_1,x_2,z_0)=\det[X_{\alpha,\beta}]=\det[\delta_{\alpha,\beta}-2z_0f_{\alpha,\beta}]=0. \tag{4}$$

The above is a necessary and sufficient condition for the existence of a caustic curve. The locus of points on the reference plane $(x_1,x_2,x_3=0)$ for which the Jacobian vanishes is called the *initial curve* and its equation is given by equation (4). All points on the initial curve map onto the caustic curve. In addition, all points inside and outside this curve map *outside* the caustic. Since the light that forms the caustic curve originates from the *initial curve*, essential information conveyed by the caustic comes from that curve *only*.

Downloaded 03 May 2010 to 171.66.16.244. Redistribution subject to ASME license or copyright; see http://www.asme.org/terms/Terms_Use.cfm

Equation (4), defining the initial curve, depends parametrically on z_0. Thus, by varying z_0, the initial curve position may be varied. If z_0 is large, then the initial curve will be located far from the crack tip. If z_0 is small, then the initial curve will be close to the crack tip. Variation of z_0 can easily be achieved experimentally by simply varying the focal plane of the recording camera system. This is an essential property of the method of caustics and it can be utilized to "scan" the near-tip region to obtain information regarding the nature of deformation field at different distances from the crack tip. For the case of a crack tip surrounded by a plastic zone, varying z_0 will move the "*initial curve*" inside or outside the plastic zone, providing information on the plastic strains as well as on the surrounding elastic field.

2.3 The Interpretation of Caustics on the Basis of Plane-Stress Analyses. The discussion of the previous section is intentionally kept as general as possible, and is not restricted by the form of the function $f(x_1, x_2)$ that describes the shape of the deformed specimen surface. In general, $f(x_1,x_2)$ can be identified as the out-of-plane displacement field $u_3(x_1,x_2)$ evaluated on the surface of the plate specimen.

For a cracked plate of uniform thickness and finite, in-plane dimensions, u_3 will depend on the constitutive law of the material, on the applied load, and on the details of the specimen geometry (in-plane dimensions and thickness). Given the lack of full-field, three-dimensional analytical solutions in fracture mechanics, such information must be obtained by numerical computation. Nevertheless, there exist certain special cases where available asymptotic solutions, based on two-dimensional analyses, may provide adequate approximations for the surface out-of-plane displacement field $u_3(x_1,x_2)$. In particular, it can be argued that conditions of plane stress will dominate in thin, cracked plates provided that both the crack length and the in-plane dimensions are many times the plate thickness. In such cases, $u_3(x_1,x_2)$ can be approximated by means of available analytical solutions based on plane-stress analyses.

2.3.1 Caustics obtained on the basis of plane-stress asymptotic crack-tip fields in linear elastostatics. In linear elastic fracture mechanics, the principal application of the method of caustics is to the direct measurement of the model I and mode II stress intensity factors. By substitution of the u_3 displacements for a Mode I, plane-stress crack (Williams, 1957) into equations (3) and (4), it was shown by Manogg (1964) (see also Theocaris, 1981; Beinert and Kalthoff, 1981) that K_I is related to the maximum transverse diameter D of the caustic (width of caustic in the direction perpendicular to the crack line) by

$$K_I = \frac{ED^{5/2}}{10.7 z_0 \nu h}, \tag{5}$$

where E is the elastic modulus, ν is the Poisson's ratio, h is the specimen thickness, and K_I is the mode I stress intensity factor.

The equation for the initial curve is obtained directly from equation (4) and can be shown to be a circle of radius r_0 where

$$r_0 = 0.316D = \left(\frac{3h\nu K_I z_0}{2E\sqrt{2\pi}}\right)^{2/5}. \tag{6}$$

It should be observed here that for a given $K_I, r_0 \sim z_0^{2/5}$. A variation in z_0, the distance behind the specimen at which the camera is focussed, will result in changes in r_0.

2.3.2 Caustics Obtained on the Basis of the Asymptotic, Plane-Stress HRR Field. For stationary cracks and within the framework of small displacement gradients and proportional stress histories, the value of the J-integral can be considered as a plastic strain intensity factor. The viewpoint is adopted here that J is the scalar amplitude of the deformed shape of the surface of an elastic-plastic fracture specimen at points within the region of dominance of the *plane-stress* HRR field.

Substitution of the u_3 displacement given by the plane-stress HRR fields into equations (3) and (4) provides a relation between D and J, found by Rosakis, Ma, and Freund (1983) to be

$$J = S_n \frac{\dot{\sigma}_0^2}{E} \left(\frac{E}{\sigma_0 z_0 h}\right)^{\frac{n+1}{n}} D^{\frac{3n+2}{n}}, \tag{7}$$

where σ_0 is the yield stress, n is the hardening exponent for the Ramberg-Osgood material model and S_n is a scalar function of n tabulated by Rosakis, Ma, and Freund (1983). Unlike the elastic case, the initial curve is no longer circular; its shape depends on the hardening level of the material. It should be noted at this point that equations (5)–(7) are obtained under the assumption of the validity of particular asymptotic plane-stress fields.

2.4 Limitations of Two-Dimensional Asymptotic Analyses. The results of previous experiments and analyses by Zehnder, Rosakis, and Narasimhan (1986) show that the interpretation of caustics on the basis of plane-stress, small-scale yielding assumptions limits the applicability of the technique for practical applications in elastic-plastic fracture mechanics to small-scale yielding conditions in thin pates. Several factors combine to cause these limitations. Under small-scale yielding conditions, the region of dominance of the plane-stress HRR fields is $r < .3r_p$ where r_p is the plastic zone size ahead of the crack tip. Thus, to use equation (7) to measure J, the initial curve must satisfy $r_0 < .3r_p$. However, near the crack tip ($r < .5h$) there is a region where the deformation field is three-dimensional. Thus, unless $r_0 > .5h$, it is clear that interpetation of caustics obtained from near the crack tip and analyzed on the basis of the plane-stress HRR field will be inaccurate. In most test specimens, it is not possible to satisfy the conflicting requirements $r_0 < .3\ r_p$ and $r_0 > .5h$.

In the next section, an approach is described which will allow for the measurement of the J integral with caustics regardless of specimen dimensions and load level. In brief, this approach is a calibration of J versus the caustic diameter, D, for a particular three-dimensional specimen configuration. This calibration is performed both experimentally and numerically by means of a three-dimensional elastoplastic calculation (see Part I). The two calibrations are compared to establish agreement between the experiment and the numerical calculation. As one might think, a specimen-dependent calibration of this sort is not of particular use for static measurements of J where other techniques, based on boundary value measurements, can be used. On the other hand, such a calibration, will allow, for the first time, the interpretation of caustics obtained from a dynamic experiment by means of high speed photography.

3 Description of Experiments

The investigation described in the following sections is both experimental and numerical. Caustic curves were obtained from a particular specimen configuration at different load levels and were compared to synthetic caustics obtained by finite elements and corresponding to the same load levels. The elastic-plastic finite element analysis of Part I modeled the exact three-dimensional specimen configuration and material constitutive properties. In order to provide an additional direct comparison between the computation and the actual specimen deformation, a second experiment was performed

Downloaded 03 May 2010 to 171.66.16.244. Redistribution subject to ASME license or copyright; see http://www.asme.org/terms/Terms_Use.cfm

simultaneously with the caustics experiment. By using Twyman-Green interferometry, the out-of-plane displacement on the specimen surface was measured for load levels up to fracture initiation. These displacements were compared directly to the numerical results. In addition, the load and load-point displacement were compared to the numerical results. These experiments used three-point bend specimens (numbers 67 and 69) with a 4:1 length-to-width ratio. The specimen dimensions are given in Fig. 1 of Part I. The material used was 4340 steel, heat treated at 843°C for 1.5 hours, oil quenched, then annealed for one hour at 538°C. The material properties were yield stress $\sigma_0 = 1030$ MPa, and hardening exponent $n = 22.5$ for a fit to the piecewise power-hardening law. In uniaxial tension this is equivalent to

$$\frac{\epsilon}{\epsilon_0} = \begin{cases} \sigma/\sigma_0 & \sigma \le \sigma_0 \\ (\sigma/\sigma_0)^n & \sigma > \sigma_0 \end{cases}, \tag{8}$$

where ϵ_0 is the yield strain. For these experiments both sides of the specimen were lapped optically flat and polished to a mirror finish to allow for simultaneous caustics and interferometry measurements.

Four measurements were performed on each specimen: caustics, interferometry, load, and load-point displacement. The experiments proceeded by loading the specimen in small steps. During the loading the load cell and the load-point displacement signals were recorded. When loading was stopped at a particular step, caustics photographs and interferometric photographs (interferograms) were recorded. This process was repeated until the point-of-fracture initiation.

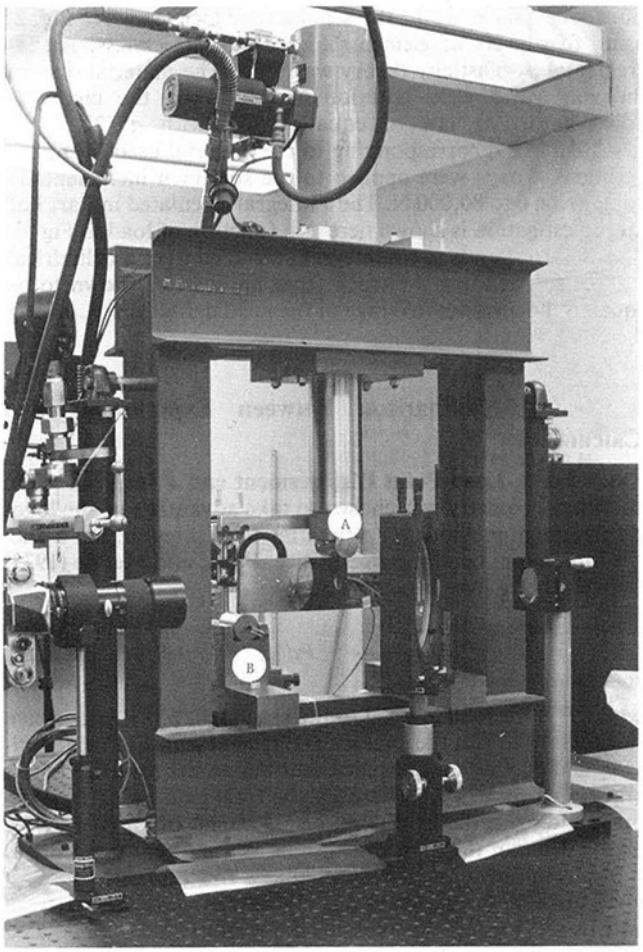


Fig. 2 Photograph of loading frame and fixtures, specimen and interferometer optics

3.1 Load and Load-Point Displacement. The load and load-point displacement were recorded with a 100,000-lb capacity load cell and a strain gage extensometer. The signals were recorded during loading by a digital oscilloscope. A photograph of the specimen and loading fixtures is shown in Fig. 2. The extensometer was attached to fixtures connected to points "A" and "B" in the figure. There exists some extraneous displacement due to compliance of the loading fixtures, and indentation of the specimen at the contacts with the rollers. This extraneous displacement was subtracted using the procedure of Robinson and Tetelman (1967). In this procedure, the support rollers are placed together, and an uncracked specimen is inserted between the support rollers and the loading roller. The entire system is then compressed and the load-load point displacement is measured. It was found that the extraneous displacement was approximately linear with load and could be approximated by $\delta/P = 4.0 \times 10^{-6}$ mm/N, where δ is the load-point displacement and P is the applied load.

3.2 Caustics. The caustics were photographed by means of the experimental arrangement shown in Fig. 3. The collimated laser light reflected from the surface of the specimen is collected by the lens, which then forms an image of the caustic on the screen. The translucent screen (made of graph paper taped over plexiglass) is then photographed with the 35-mm camera. In these experiments, z_0 was held constant. A preliminary experiment was performed to choose a suitable z_0. In the preliminary experiment, caustics were obtained for various z_0 values and load levels. At low loads the caustics were clear for all z_0's. But, as the load increased, the caustics for small z_0's become blurred and ill-defined. This is caused

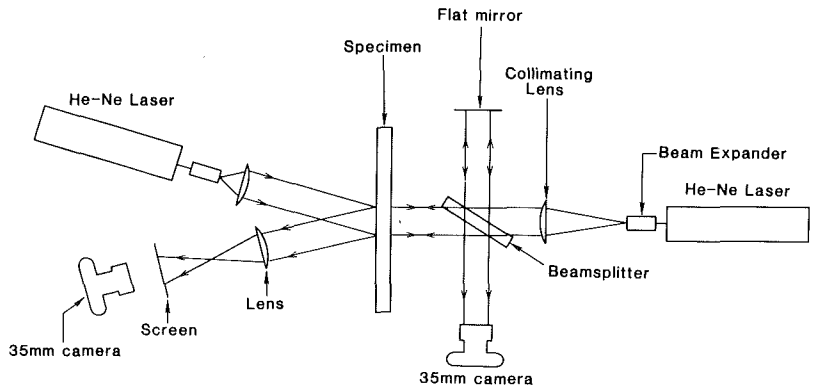


Fig. 3 Optical setup for combined caustics and interferometry experiment

Downloaded 03 May 2010 to 171.66.16.244. Redistribution subject to ASME license or copyright; see http://www.asme.org/terms/Terms_Use.cfm

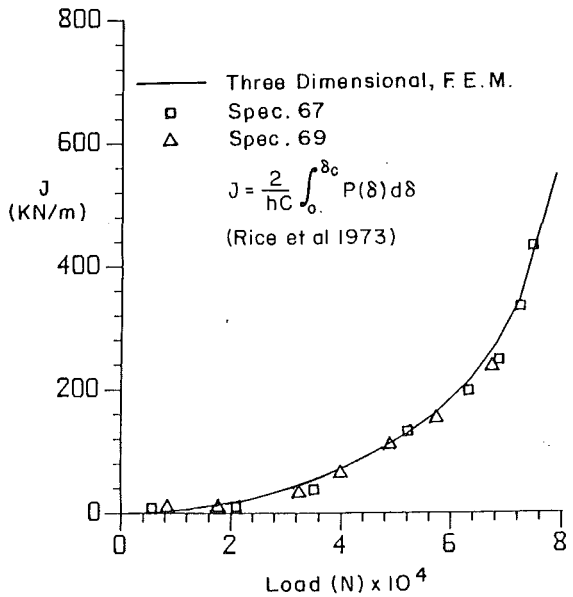


Fig. 4 *J* integral versus applied load

partially by a loss of reflectivity due to plastic deformation. On this basis it was decided to use $z_0 = 100$ cm. This choice allows caustics to be recorded without loss of definition up to the fracture initiation load.

3.3 Inteferometry. A version of the Twyman-Green interferometer (see Hecht and Zajac, 1979) was used to measure the out-of-plane surface displacement, u_3. A sketch of the optical arrangement is shown in Fig. 3. Due to the high sensitivity of interferometry, minimization of vibration of the specimen and optics is important. Thus the entire apparatus, including the loading frame, was mounted on an isolated optical table. The loading frame, optical table, camera, beam splitter, and mirror are all seen in the photograph of Fig. 2.

A 50-mm diameter, collimated laser beam split into two with a beamsplitter, was used for the interferometer. As sketched in Fig. 3, the reference beam reflects from the flat mirror back through the beamsplitter and into the camera. The object beam reflects from the specimen and then reflects from the beamsplitter into the camera. When the two beams are adjusted to fall on top of each other, any nonuniform differences in optical path length between the two beams results in light and dark fringes. For complete interference between the reference and object beams, the intensity of light from each beam must be matched. Polished steel has a reflectivity of 50 percent. Thus, to match the reference beam to the object beam, a 50 percent reflectance mirror was used. The fringe patterns were photographed with a 35-mm camera using a 200-mm f/4 (50-mm diameter) telephoto lens. The camera was located such that 50 mm of the specimen filled 25 mm on the film. Kodak Technical Pan 2415 film shot at ASA 100 and developed in Kodak D-19 was used in order to achieve high contrast and high resolution.

Destructive interference between two waves occurs when the waves are out of phase by $n\lambda/2$ where λ is the wavelength and $n = 1,3,5. \ldots$ The phase shift between the reference and object beams is equal to the difference in optical path length; thus, the change in optical path length, δS, represented by adjacent dark fringes, is $\delta S = \lambda$. For small deformations $S = 2u_3$, thus adjacent dark fringes represent a change in u_3 of $\delta u_3 = \lambda/2$. For the He-Ne laser used here, $\lambda = .632\mu$m.

Due to the angular deflection of the reflected light rays, as seen in Fig. 1, the relation $S = 2u_3$ is not completely accurate; the actual optical path is slightly larger. In addition, the angular deflection will change the location of the fringes. It was demonstrated by Zehnder (1987) that for these experiments, the maximum error in fringe location is less than 1λ and the error is less than $.01\lambda$ in the u_3 values. It is important to focus the camera on the surface of the specimen so that a large caustic will not be formed, obscuring the crack tip. By minimizing the caustic, fringes can be resolved to within approximately 2-3 crack-opening displacements. The interferograms were analyzed by making 50X enlargements and digitizing the fringes by eye on a computer digitizing pad.

4 Numerical Calculations

The numerical calculations of Part I of this investigation, (Narasimhan and Rosakis, 1988b) modeled in three dimensions, one quarter of the three-point specimen shown in Fig. 2, using five layers of elements for half the thickness. An incremental J_2-plasticity theory was used. The material obeyed the von Mises yield criterion and followed the piecewise power-hardening law of equation (8), with $n = 22.5$ and $\sigma_0 = 1030$ MPa, corresponding to the material used in the experiment. Loads were applied to the specimen incrementally going from 0 to 80,000 N. The J integral calculated in Part I of this investigation is shown here as a function of load in Fig. 4. This J corresponds to an integral evaluated over a cylindrical surface surrounding the crack front and can be shown to be equal to the thickness average of the local definition of J along the crack front.

5 Results: Comparison Between Experiments and Calculations

5.1 Load, Load-Point Displacement and *J* Integral. The specimen geometry was chosen to take advantage of the load-displacement methods for estimating the J integral. For a ductile three-point bend specimen, Rice, Paris, and Merkle (1973) showed that J may be estimated by

$$J = \frac{2}{hC}\int_0^{\delta_c} P d\delta_c, \tag{9}$$

where P is the load applied to the specimen, h is the specimen thickness, and C is the uncracked ligament length. The quantity δ_c is the load point displacement due to the presence of the crack, i.e., $\delta_c = \delta - \delta_{nc}$ where δ is the total load point displacement and δ_{nc} is the load point displacement of an uncracked, elastic beam of the same dimensions as the fracture specimen.

The resulting J integral, plotted as a function of load, P, is given in Fig. 4. Shown in the figure are J calculated from equation (9) using the experimental results and J calculated from the numerical analysis (see Part I). The agreement between the numerical and experimental results is quite good, indicating that J may be calculated accurately either way. In the following discussions, the relation between J and the applied load P shown in Fig. 4 is used.

5.2 Interferometry and u_3 Comparison. Since it is displacements that are most accurately calculated in the finite element method, these are chosen for the most direct comparison with experiments. Interferograms were recorded for load levels from 6000 N up to fracture initiation (74,700 N). At the highest load levels the quality of the interferograms deteriorates. This is due to the roughening of the surface, resulting from plastic deformation near the crack tip and also due to the high-fringe density near the crack tip. The highest load for which fringes very near the crack tip could be resolved was 57,300 N.

Typical interferograms are presented in Figs. 5 and 6. Figure 5 provides an overall picture of the out-of-plane displacement field for a region of approximately 4-cm diameter. A more detailed view of the near-tip region is shown

Downloaded 03 May 2010 to 171.66.16.244. Redistribution subject to ASME license or copyright; see http://www.asme.org/terms/Terms_Use.cfm

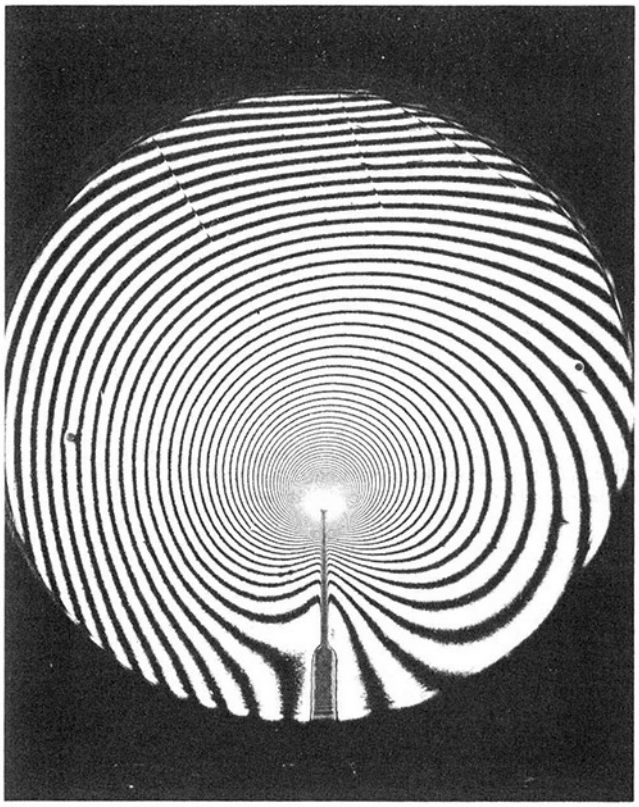


Fig. 5 Interferogram corresponding to a load of 35,000 N

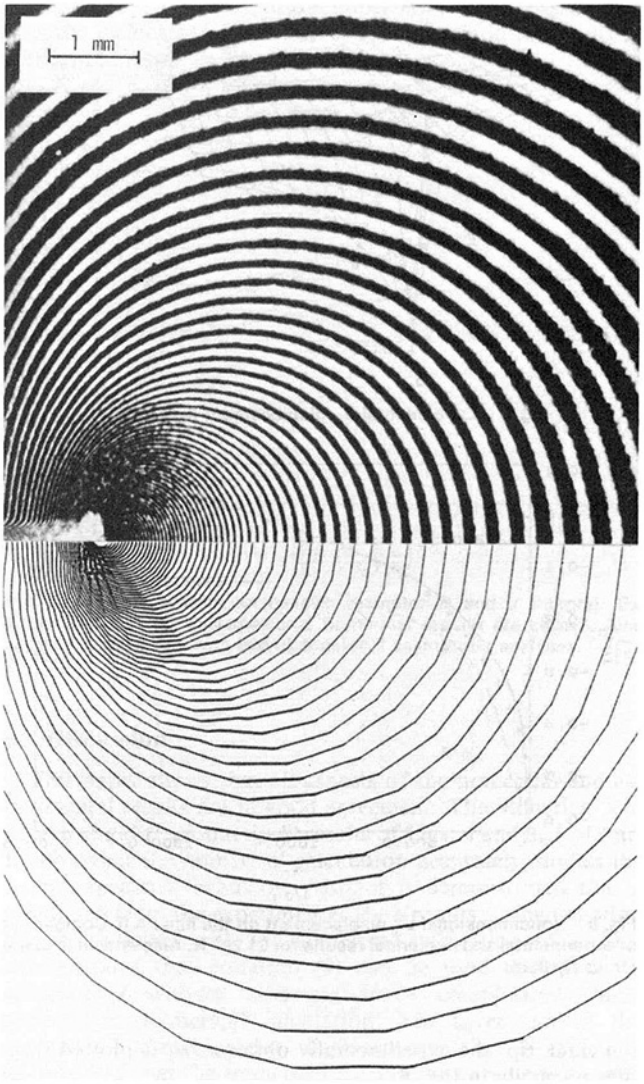


Fig. 6 Comparison of experimental and numerical interferograms; experimental interferogram is a magnification of Fig. 5

in Fig. 6. Figure 6 shows that fringes can be resolved almost all the way up to the crack tip (up to three crack-opening displacements) except for the part obscured by a small caustic. Figure 5 shows some far-field asymmetry in the fringes due to rigid body rotations of the test specimen.

Each interference fringe represents a line of constant out-of-plane displacement on the specimen surface. Thus, the interferogram is a contour map of the specimen surface. The numerical contour map on the bottom of Fig. 6 is a synthetic interferogram obtained from the out-of-plane displacements calculated from the three-dimensional numerical model in Part I. The displacement increment between the lines is the same as in the optical interferogram (.317 μm). As is evident from this comparison, good qualitative agreement of the experimental and synthetic interferograms is achieved. The interferograms represent the u_3-displacement of the specimen with respect to some plane, the plane of the reference mirror. The mirror is aligned as close to parallel to the specimen as possible. Nonetheless, it will usually deviate slightly from parallelity. This deviation can be accounted for if the displacements are known at three or more noncollinear points on the specimen. The u_3 results from the interferograms are matched to known displacements at these points. Due to the Mode I symmetry of the specimen and loading used in this experiment, the number of required points is reduced to two points not on a line parallel to the x_2-axis. The known displacements at the two points were provided by the finite element calculation. The points used ($x_1 = -1.5$ cm, $x_2 = 0$ and $x_1 = 2.1$ cm, $x_2 = 0$) are points of zero u_3-displacement.

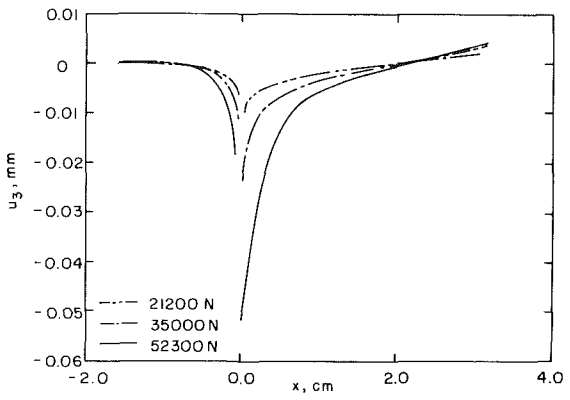


Fig. 7 Experimentally measured out-of-plane surface displacement for three different loads

The u_3-displacement along the line $\theta = 0$ is shown in Fig. 7 for three load levels. Data are shown only as close to the crack tip as fringes could be resolved. Generally, fringes could be measured to approximately 0.3 mm ahead of the crack tip and to approximately 0.5 mm behind the crack tip. Away from the crack tip u_3 is linear with x_1 as it should be for a beam. The displacement crosses zero at $x_1 = 2.1$ cm and is positive for greater x_1 values since this part of the specimen is in compression. The displacement gradients are much larger behind the crack tip than ahead of the crack tip. The plastic zone does not spread much behind the crack tip. Since most of the displacement occurs within the plastic zone, this displacement must occur over a small distance, causing the steep displacement gradients. To help visualize what the u_3 field looks like near

Downloaded 03 May 2010 to 171.66.16.244. Redistribution subject to ASME license or copyright; see http://www.asme.org/terms/Terms_Use.cfm

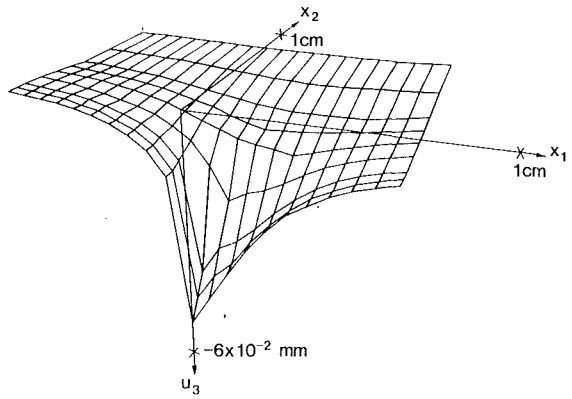


Fig. 8 Experimental u_3 displacement for 52,300 N

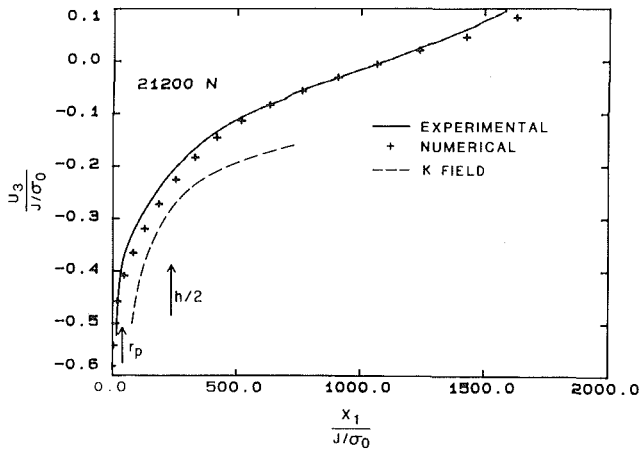


Fig. 9 Nondimensional u_3 displacement on the line $\theta = 0$. Comparison of experimental and numerical results for 21,200 N. Also shown is plane-stress K_I field.

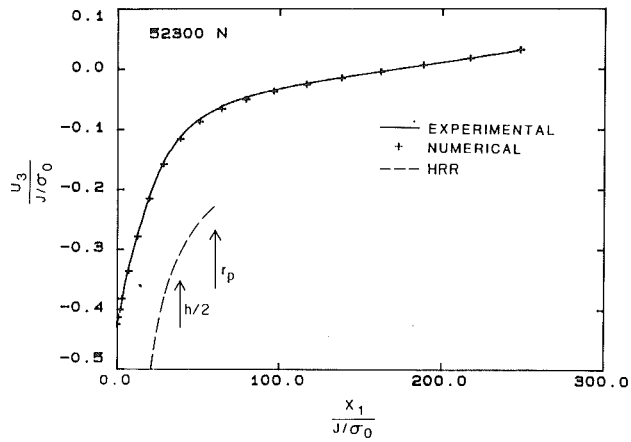


Fig. 10 Nondimensional u_3 displacement on the line $\theta = 0$. Comparison of experimental and numerical results for 52,300 N. Also shown is plane-stress K_I field and u_3 from plane-stress HRR field.

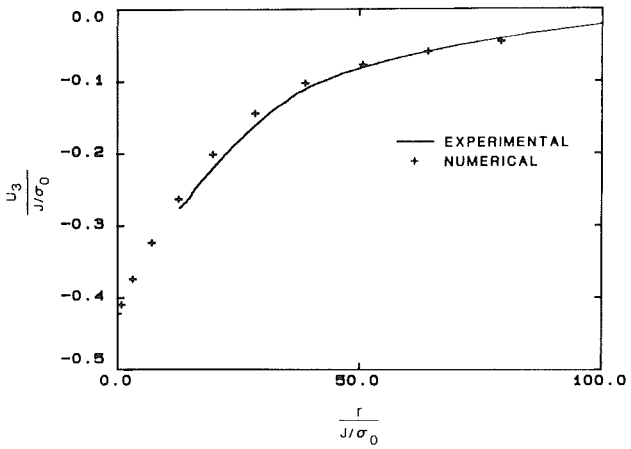


Fig. 11 Nondimensional u_3 displacement on the line $\theta = 40$ deg; comparison of experimental and numerical results for 52,300 N

the crack tip, the experimentally obtained u_3 is plotted three dimensionally in Fig. 8.

A quantitative comparison between the experimental and numerical results is given in Figs. 9–11. In these figures, the experimentally obtained out-of-plane displacement, u_3, along the line $x_2 = 0$ is plotted as a function of normalized distance x_1 from the crack tip for three load levels. Also shown are the numerical results for the displacements corresponding to the same load levels. For reference, the extent of the plastic zone ahead of the crack tip as well as the distance corresponding to one half the specimen thickness are also shown on the figures. In Fig. 9, where the plastic zone is very small, u_3 from the linear elastic plane-stress K_I field is shown for comparison. In Fig. 10, where the plastic zone is larger, u_3 from the plane-stress HRR field is given.

The first observation is the excellent agreement between the experimental and numerical results at all load levels. To show that the angular variation in displacement of the numerical results is also accurate, the numerical and experimental u_3 along the line $\theta = 40$ deg is given in Fig. 11 for a load of 52,300 N. Again, the agreement of numerical and experimental results is excellent. For all load levels (see in particular Fig. 10), it was found that there is no region where the plane-stress HRR field adequately described u_3 on the specimen surface. The asymptotic HRR field does not agree with the actual field because of three dimensionality of the near crack-tip fields and because of the limited range of dominance of the asymptotic solution. At low loads Fig. 9 shows that the plane-stress K_I field differs from the calculated u_3 by approximately 25 percent for reasons similar to the ones discussed above. However, the method of caustics as based on the K_I field could probably be used for these specimens at low loads since the experimentally obtained slope of u_3 is close to that predicted by the K_I field when $r_0 \approx .5H$. Recall that caustics depend on ∇u_3, not on the absolute value of u_3.

Recent experiments by Chiang and Hareesh (1986) on very thin, ductile specimens showed that the HRR field does predict u_3 and u_2 accurately for $r/h > 1$. In those experiments the ratio of specimen width to thickness was 30:1. In the present experiments the ratio is 7:1. The results of Chiang and Hareesh indicate that if one can make measurements in a region far enough away from the crack tip so that three-dimensional effects are negligible, but close to the crack tip compared to in-plane specimen dimensions, then the asymptotic fields will accurately describe the true fields in some finite region. The location of such a region will depend on specimen geometry and, if the material is nonlinear, on the applied load level. One puzzling result of Chiang and Hareesh is that $-u_3$ has a maximum not at the crack tip but at $r/h \approx 0.5$. This result is contradicted by both the present investigation and by results of Wu and Chiang (1986) that show that $-u_3$ has its maximum at the crack tip. Perhaps the difference has to do with the differences in specimen geometries between the different experiments.

5.3 Caustics. In the previous section we were able to demonstrate that in terms of out-of-plane displacements, the numerical results are in excellent agreement with experiment. This indicates that it should be possible to generate caustics numerically which agree well with the experimentally observed

Downloaded 03 May 2010 to 171.66.16.244. Redistribution subject to ASME license or copyright; see http://www.asme.org/terms/Terms_Use.cfm

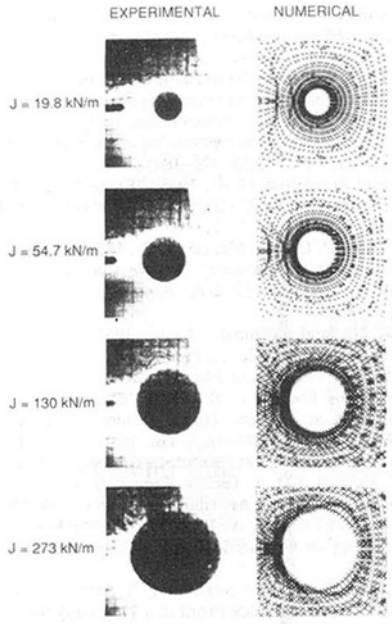


Fig. 12 Sequence of caustics for increasing loads, $z_0 = 100$ cm. Experimental results from specimen 67. Numerical results for three-dimensional numerical analysis.

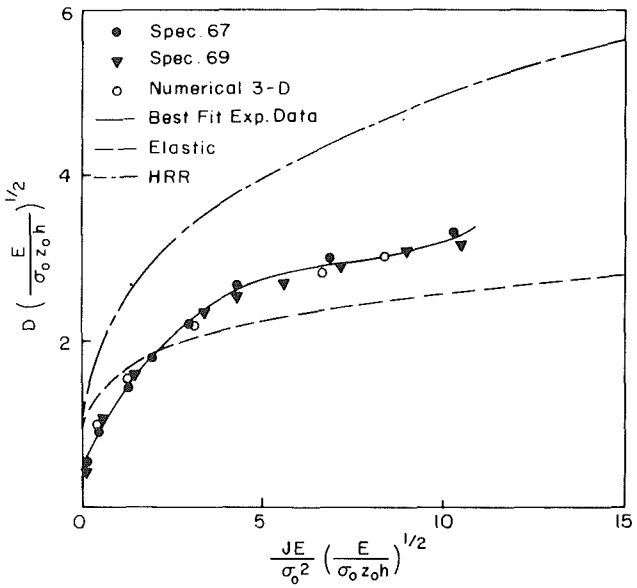


Fig. 13 Relation between caustic diameter D and J integral. Experimental and three-dimensional numerical results are shown. Also shown are relations from two-dimensional asymptotic analyses.

caustics and are useful for the measurement of the J-integral. In this section this hypothesis is tested.

Caustics are first recorded experimentally for specimens 67 and 69 using a *fixed value* of $z_0 = 100$ cm. The sequence of caustic patterns for increasing loads up to fracture initiation is shown in Fig. 12. For the same value of z_0, and the same loads, caustics are also generated numerically from the results of the three-dimensional finite element analysis. This was achieved by smoothing the u_3-displacements at the specimen surface obtained by the numerical solution using a least squares numerical scheme as described by Narasimhan and Rosakis (1988a). Caustic patterns were simulated by mapping rays point by point from this smoothed surface using equation (3). The numerically simulated caustics are also shown in Fig. 12. All of the caustic curves, both experimental and numerical are reproduced here in the same scale. The values of J shown in the figure are related to the applied load through the $J-P$ record of Fig. 4. Figure 12 shows that there is good agreement, in shapes and sizes, between the experimental and numerical, caustics.

Both experimental and numerical results were used to obtain a relation between caustic diameter D and the J integral which is shown in Fig. 13 in a nondimensional form. J was obtained from Fig. 4 and D was measured directly from the experimentally and numerically generated caustics. Also shown in the figure are the J versus D relations obtained on the basis of the plane-stress elastic analysis, equation (5), and on the basis of the plane-stress HRR field, equation (7). The solid line in Fig. 13 is a fit through the experimental and numerical data points. Note that, as is typical of the method of caustics, J is a very sensitive function of D, particularly at the highest loads.

It is seen that the experimental and numerical results are in excellent agreement. This demonstrates that such an approach can provide an accurate analysis of caustics in the form of a calibration for measuring the J integral. The best fit curve shown in Fig. 13 serves here as an empirical relationship between the caustic diameter and the J integral when the relationship based on two-dimensional asymptotic analyses are invalid. It should be emphasized here that this relationship is valid *only* for the specimen geometry and material tested here and only for $z_0 = 100$ cm.

6 Discussion

This paper shows that all aspects of the numerical and experimental results are in good agreement. The numerical and experimental $P-\delta$ and $J-P$ results of Figs. 4 and 2, 3 of Part I, show that the numerical calculation accurately models the overall specimen behavior. Also, it is demonstrated that J calculated from the experimental $P-\delta$ results, using equation (9), is consistent with the numerical calculation of J. This demonstrates that equation (9) can be used accurately to calculate J without resorting to a complicated three-dimensional numerical calculation. The agreement of the calculated and measured u_3 displacements (Figs. 9–11) leaves no question that the numerical calculations are accurate and sufficiently refined to model this specimen well, both in the overall behavior and in the details of the crack-tip fields. This provides a great deal of confidence in the numerical results and allows for the construction of accurate synthetic caustics. In addition, as evident from Fig. 13, it is demonstrated that the calibration of J versus D may be performed either experimentally or numerically with equal accuracy. In most cases, it will be more economical to perform this calibration experimentally.

The method of caustics as described in this paper is thus proposed as a technique for dynamic measurements of the J integral. A procedure is proposed as follows: Given a material to test, select a planar test specimen geometry that is adaptable to dynamic loading. Small-scale yielding conditions need not be maintained, and there is virtually no restriction on thickness of the specimen. Prepare the specimens by lapping and polishing one surface. Perform a static calibration of J versus D for different load levels and a fixed z_0. Use the same specimen geometry and material in a dynamic experiment and record the caustics (with same fixed z_0) up to crack initiation by means of a high speed camera. Then use the calibration between J and D, described above, to analyze the caustics to determine the time history of J under dynamic loading conditions. Preliminary results on the implementation of the above procedure for the dynamic measurement of J are reported by Zehnder (1987) and by Zehnder, Rosakis, and Krishnaswamy (1989).

The drawback of this procedure is that the calibration is specimen and material-dependent. However, this is made up

Downloaded 03 May 2010 to 171.66.16.244. Redistribution subject to ASME license or copyright; see http://www.asme.org/terms/Terms_Use.cfm

for by allowing for dynamic fracture toughness measurements to be performed in previously impossible situations. The advantage of this technique comes from the use of a local, near-tip measurement for estimating J. This is expected to capture the details of time variation of J near the crack tip, even for high loading rates and short times compared to stress wave transit times of the specimen. It should be noted that such an approach is expected to be most accurate in strain-rate insensitive solids. Its accuracy, when applied to highly rate sensitive materials, needs further investigation.

7 Acknowledgments

Support of the ONR contract N00014-85-K-0596 is gratefully acknowledged. The second author, (A. J. Rosakis) also acknowledges the support of the NSF-PYI Grant MSM-8451204. The computations were performed using the Supercomputer facilities at the Univesity of California at San Diego. The authors would also like to thank Mr. Richard Pfaff for assistance and advice on the interferometry part of these experiments.

References

Beinert, J., and Kalthoff, J. F., 1981, "Experimental Determination of Dynamic Stress Intensity Factors by the Method of Shadow Patterns," *Mechanics of Fracture*, Vol. VII, G. Sih, ed., Sijthoff and Noordhoff, pp. 281–320.

Chiang, F. P., and Hareesh, T. V., 1986, "Three Dimensional Crack Tip Deformation: An Experimental Study and Comparison to HRR Field," *International Journal of Fracture*, Vol. 36, 1988, pp. 243–257.

Costin, L. S., Duffy, J., and Freund, L. B., 1977, "Fracture Initiation Under Stress Wave Loading Conditions," *Fast Fracture and Crack Arrest*, ASTM-STP-627, American Society for Testing and Materials, pp. 301–318.

Hecht, E., and Zajac, A., 1979, *Optics*, Addison-Wesley Publishing Company, pp. 322–324.

Hutchinson, J. W., 1968, "Singular Behavior at the End of a Tensile Crack in a Hardening Material," *Journal of the Mechanics and Physics of Solids*, Vol. 16, pp. 13–31.

Manogg, P., 1964, "Anwendungen der Schattenoptik zur Untersuchung des Zerressvorgags von Platten," Ph.D. Thesis, Freiburg, West Germany.

Nakamura, T., Shih, C. F., and Freund, L., 1985, "Elastic-Plastic Analysis of a Dynamically Loaded Circumferentially Notched Round Bar," *Engineering Fracture Mechanics*, Vol. 22, pp. 437–452.

Narasimhan, R., and Rosakis, A. J., 1988a, "A Finite Element Analysis of Small-Scale Yielding Near a Stationary Crack Under Plane Stress," *Journal of the Mechanics and Physics of Solids*, Vol. 36, pp. 77–117.

Narasimhan, R., and Rosakis, A. J., 1988b, "Three Dimensional Effects Near a Crack Tip in a Ductile Three Point Bend Specimen: Part I—Numerical Analysis," ASME JOURNAL OF APPLIED MECHANICS, Vol. 57, pp. 607–617.

Rice, J. R., 1968, "A Path Independent Integral and the Approximate Analysis of Strain Concentration by Notches and Cracks," ASME JOURNAL OF APPLIED MECHANICS, Vol. 35, pp. 379–386.

Rice, J. R., and Rosengren, G. F., 1968, "Plane Strain Deformation Near a Crack Tip in a Power-Law Hardening Material," *Journal of the Mechanics and Physics of Solids*, Vol. 16, pp. 1–12.

Rice, J. R., Paris, P. C., and Merkel, J. G., 1973, "Some Further Results of the J-Integral Analysis and Estimtes," *Progress in Flow Growth and Fracture Toughness Testing*,' ASTM-STP-536, American Society for Testing and Materials, pp. 231–245.

Robinson, J. N., and Tetelman, A. S., 1967, "Comparison of Various Methods of Measuring K_{IC} on Small Precracked Bend Specimens that Fracture after General Yield," *Engineering Fracture Mechanics*, Vol. 8, pp. 301–313.

Rosakis, A. J., and Freund, L. B., 1982, "Optical Measurement of Plastic Strain Concentration at a Crack Tip in a Ductile Steel Plate," *Journal of Engineering Materials and Technology*, Vol. 104, pp. 115–120.

Rosakis, A. J., Ma, C. C., and Freund, L. B., 1983, "Analysis of the Optical Shadow Spot Method for a Tensile Crack in a Power-Law Hardening Material," ASME JOURNAL OF APPLIED MECHANICS, Vol. 50, pp. 777–782.

Rosakis, A. J., and Zehnder, A. T., 1985, "On the Method of Caustics: An Exact Analysis Based on Geometrical Optics," *Journal of Elasticity*, Vol. 15, pp. 347–367.

Shih, C. F., Moran, B., and Nakamura, T., 1986, "Energy Release Rate Along a Three-Dimensional Crack Front in a Thermally Stressed Body," *International Journal of Fracture*, Vol. 30, pp. 79–102.

Theocaris, P. S., 1981, "Elastic Stress Intensity Factors Evaluated by Caustics," *Mechanics of Fracture*, Vol. VII, G. Sih, ed., Sijthoff and Noordhoff, pp. 189–252.

Williams, M. L., 1957, "On the Stress Distribution at the Base of a Stationary Crack," ASME JOURNAL OF APPLIED MECHANICS, Vol. 24, pp. 109–114.

Wu, X. P., and Chiang, F. P., 1986, "Three Dimensional Crack-Tip Deformation in a Plastically Deformed Three-Point Bend Specimen," College of Engineering and Applied Sciences Technical Report No. 475, State University of New York at Stony Brook.

Zehnder, A. T., Rosakis, A. J., and Narasimhan, R., 1986, "Measurement of the J Integral with Caustics: An Experimental and Numerical Investigation," GALCIT SM Report 86-8, California Institute of Technology, to appear in ASTM-STP-995.

Zehnder, A. T., 1987, "Dynamic Fracture Initiation and Propagation in Metals: Experimental Results and Techniques," Ph.D. Thesis, California Institute of Technology.

Zehnder, A. T., Rosakis, A. J., and Krishnaswamy, S., 1989, "Dynamic Measurement of the J-Integral in Ductile Metals: Comparison of Experimental and Numerical Techniques," to appear in the *International Journal of Fracture*, special issue on nonlinear fracture mechanics *Proceedings of the IUTAM Symposium on Recent Advances on Nonlinear Fracture Mechanics*, California Institute of Technology, March 14–16, 1988, W. G. Knauss and A. J. Rosakis eds.

Downloaded 03 May 2010 to 171.66.16.244. Redistribution subject to ASME license or copyright; see http://www.asme.org/terms/Terms_Use.cfm

Delamination Specimens for Orthotropic Materials

Zhigang Suo[1]
Division of Applied Sciences,
Harvard University,
Cambridge, MA 02138

A semi-infinite crack in an infinite strip of orthotropic material is analyzed. Analytic expressions for mixed-mode stress intensity factors are derived with only parameter undetermined, which is then extracted from numerical solutions to integral equations. The results are relatively simple and complete, and provide the flexibility to simulate a wide range of practical problems, such as fracture specimens and edge delamination phenomena of woods and fiber-reinforced composites. As an illustration, specimens with transverse splitting from notches are analyzed based on the general solution. The validity of using solutions for an isotropic material to calibrate some testing geometries of orthotropic materials is discussed.

1 Introduction

Cracks in homogeneous, isotropic brittle materials tend to grow under mode I conditions. By contrast, cracks are often trapped, with *mixed-mode* local field, to geometrically particular paths such as the fiber direction of woods and uniaxial fiber reinforced composites, the interface of bimaterial systems, and the adhesive layer between bonded substrates owing to anisotropy and/or inhomogeneity in stiffness and toughness. The mixed-mode fracture problem is not only of fundamental interest, but also of significant technical importance. High apparent toughness under tension in the fiber direction for woods and composites, for example, is largely attributed to crack splitting, or fiber/matrix debonding (Ashby et al., 1985; Marshall and Evans, 1985; Budiansky et al., 1986). Experimental investigations on fracture in woods and composites appear to be initiated by Wu (1967). Recent efforts in this direction are found in Ashby et al. (1985), Marshall and Evans (1985), Prewo (1986), Michalske and Hellmann (1988), and Sbaizero et al. (1988). Research on analogous situations such as adhesive joints and bimaterial interfaces, where mixed-mode fracture is crucial, are found in Liechti and Hanson (1988), Chai (1988), Argon et al. (1989), and Wang and Suo (1990). The present work is motivated in part by the intention of using a four-point bend specimen to conduct fracture tests on fiber-reinforced composites (Sbaizero et al., 1988).

The basic problem analyzed is introduced in Fig. 1(*a*). A semi-infinite crack in an infinite strip of orthotropic material is considered. More specifically, the strip surfaces are traction-free and in the direction of a principal axis of the material. The crack is parallel to these free surfaces, and driven by the edge loads P_i and M_i, the resultant forces and moments per unit width, respectively. The material is taken to be homogeneous and linearly elastic. Both plane-stress and plane-strain deformations will be considered. The analysis provides the complete solutions for the mixed-mode stress intensity factors. The body of paper will be devoted to the representation and application of the major results. Mathematical details are grouped into three appendices, which may be of some interest in themselves.

2 Representation of Stress Intensity Factors

For generally anisotropic materials, Hooke's law can be written as

$$\epsilon_i = \sum_{j=1}^{6} s_{ij}\sigma_j, \quad i = 1, 2, 3, 4, 5, 6. \tag{1}$$

The standard correspondence is adopted, i.e., $\{\epsilon_i\} = \{\epsilon_x, \epsilon_y, \epsilon_z, \gamma_{yz}, \gamma_{zx}, \gamma_{xy}\}^T$, $\{\sigma_i\} = \{\sigma_x, \sigma_y, \sigma_z, \tau_{yz}, \tau_{zx}, \tau_{xy}\}^T$, and $[s_{ij}]$ is a six-by-six symmetric matrix, referred to as the compliance matrix, with 21 independent elements. When the material has an elastic symmetry plane normal to z-axis, the stress-strain relation for the deformation in the (x, y) plane can be reduced to (see Lekhnitskii, 1963)

$$\epsilon_i = \sum_{j=1,2,6} b_{ij}\sigma_j, \quad i = 1, 2, 6 \tag{2}$$

where

$$b_{ij} = \begin{cases} s_{ij}, & \text{for plane stress} \\ s_{ij} - s_{i3}s_{j3}/s_{33}, & \text{for plane strain} \end{cases} \qquad i, j = 1, 2, 6. \tag{3}$$

On the other hand, if the material is orthotropic with x and y-axes coincident with the principal axes of the material, there are only *four* independent elastic constants b_{11}, $b_{12} = b_{21}$, b_{22}, and b_{66}, but $b_{16} = b_{26} = 0$.

For any simply connected domain of orthotropic medium with traction prescribed on its boundary, the stresses should only depend on *two* (rather than three) nondimensional elastic parameters (see Appendix A)

[1]Current address: Department of Mechanical Engineering, University of California, Santa Barbara, CA 93106.

Contributed by the Applied Mechanics Division of THE AMERICAN SOCIETY OF MECHANICAL ENGINEERS for publication in the JOURNAL OF APPLIED MECHANICS.

Discussion on this paper should be addressed to the Technical Editor, Prof. Leon M. Keer, The Technological Institute, Northwestern University, Evanston, IL 60208, and will be accepted until two months after final publication of the paper itself in the JOURNAL OF APPLIED MECHANICS. Manuscript received by the ASME Applied Mechanics Division, Nov. 21, 1988; final revision, July 28, 1989.

Copyright © 1990 by ASME
Downloaded 03 May 2010 to 171.66.16.244. Redistribution subject to ASME license or copyright; see http://www.asme.org/terms/Terms_Use.cfm

Table 1 Values and λ and ρ for some materials

Material	$1/\lambda$	ρ
Al (FCC)	1	0.74
Cu (FCC)	1	0.03
Fe (BCC)	1	0.20
Pb (FCC)	1	0.33
Ash	10.5	1.67
Balsa	21.0	2.13
Oak	2.7	1.16
Pine	14.8	1.10
Graphite/Epoxy	9.5	3.34
GY70/Epoxy	42.0	3.36
Boron/Epoxy	14.3	4.91
Graphite/Al	5.0	1.12

$$\lambda=\frac{b_{11}}{b_{22}},\ \rho=\frac{2b_{12}+b_{66}}{2\sqrt{b_{11}b_{22}}}. \tag{4}$$

These parameters measure the anisotropy in the sense that $\lambda=1$ as the material symmetry degenerates to be transversely cubic and $\lambda=\rho=1$ as the material becomes transversely isotropic. The positive definiteness of the strain energy density requires that $\lambda>0$ and $\rho>-1$. Many nondimensional parameters for orthotropic materials other than those in equation (4) have been used in the literature, but none of them have offered the unique feature discussed in Appendix A. In Table 1, the plane-stress values of λ and ρ are listed for some single crystals, woods, and composites (no dramatic differences have been found for the corresponding plane-strain values). It appears from this list that ρ is typically somewhere in the range from 0 to 5, while λ can be significantly greater or less than 1.

The elastic stress field at the crack tip for generally anisotropic body has a square root singularity. Accordingly, stress intensity factors, K_I and K_{II}, can be defined such that the stress at a distance r ahead of the crack tip are given asymptotically by

$$\sigma_{yy}=\frac{K_I}{\sqrt{2\pi r}},\ \tau_{xy}=\frac{K_{II}}{\sqrt{2\pi r}}. \tag{5}$$

For a crack in an orthotropic body, lying in a principal plane and with its front in a principal direction, the relative crack face displacements at a distance r behind the crack tip are

$$\delta_y=8b_{11}\lambda^{-3/4}n\,K_I\sqrt{\frac{r}{2\pi}},\ \delta_x=8b_{11}\lambda^{-1/4}n\,K_{II}\sqrt{\frac{r}{2\pi}}, \tag{6}$$

where the frequently encountered constant n is defined by

$$n=\sqrt{\frac{1+\rho}{2}}. \tag{7}$$

The energy release rate, derived from equations (5) and (6), is related to the stress intensity factors by

$$G=b_{11}n(\lambda^{-3/4}K_I^2+\lambda^{-1/4}K_{II}^2). \tag{8}$$

These results are contained in the work by Sih, Paris, and Irwin (1965). The present normalization is related to theirs by $K_I=\sqrt{\pi}k_1$, $K_{II}=\sqrt{\pi}k_2$. Rearrangements have been made using the two anisotropy measures identified previously to suit our purpose.

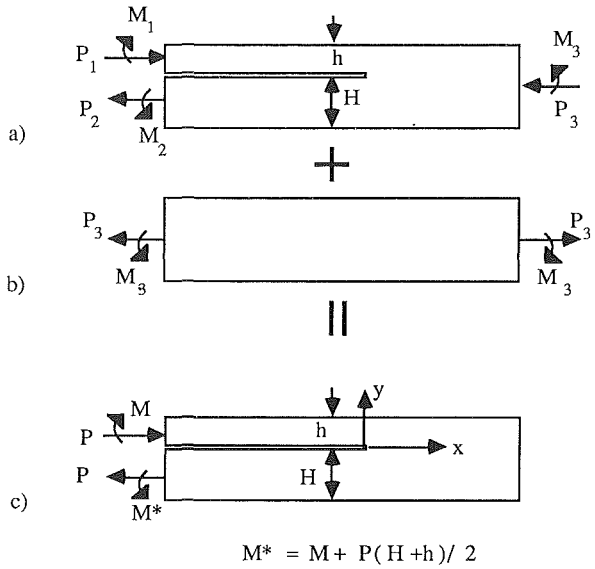


Fig. 1 Conventions and the superposition scheme

The analysis of the problem in Fig. 1(*a*) is now taken up. The aim is to solve for K_I and K_{II} as functions of the loads P's and M's, geometry specifications h and H, and anisotropy measures λ and ρ. Overall equilibrium provides two constraints among the six loads P_i and M_i. Therefore, only four of them are independent, say P_1, P_3, M_1, and M_3. Superposition of the systems in Fig. 1(*a*) and 1(*b*) gives that in Fig. 1(*c*), with P and M given by

$$P=P_1-C_1P_3-C_2M_3/h$$
$$M=M_1-C_3M_3 \tag{9}$$
$$C_1=\frac{1}{1/\eta+1},\ C_2=\frac{6/\eta}{(1/\eta+1)^3},\ C_3=\frac{1}{(1/\eta+1)^3},\ \eta=\frac{h}{H}.$$

Since no stress singularity is present in the beam in Fig. 1(*b*), the stress intensity factors must be identical for both systems in Figs. 1(*a*) and 1(*c*). We will concentrate on the reduced problem in Fig. 1(*c*). Once the latter problem is solved, the solution to the general problem in Fig. 1(*a*) can be constructed by the above relations.

The energy release rate for the system in Fig. 1(*c*) can be computed exactly by using the energy stored in the structure per unit width per unit length far behind the crack tip (e.g., Rice, 1968). The result is a positive definite quadratic in P and M which can be written as

$$G=\frac{b_{11}}{2}\left[\frac{P^2}{Ah}+\frac{M^2}{Ih^3}+2\frac{PM}{\sqrt{AIh^2}}\sin\gamma\right]. \tag{10}$$

The geometric factors are given by

$$\frac{1}{A}=1+4\eta+6\eta^2+3\eta^3,\ \frac{1}{I}=12(1+\eta^3),\ \frac{\sin\gamma}{\sqrt{AI}}=6\eta^2(1+\eta) \tag{11}$$

where the angle γ is restricted to $|\gamma|<\pi/2$ for definiteness. Without loss of generality, attention will be restricted to $h\le H$, or equivalently, $0\le\eta\le1$. The energy release rate given by equations (10) and (11) is valid even if the material is generally anisotropic.

As shown in Appendix A, for the problem in Figs. 1(*a*) and 1(*c*), the combinations $\lambda^{-3/8}K_I$ and $\lambda^{-1/8}K_{II}$ are independent of λ. It will be obvious immediately that this fact simplifies

Downloaded 03 May 2010 to 171.66.16.244. Redistribution subject to ASME license or copyright; see http://www.asme.org/terms/Terms_Use.cfm

Table 2 $\omega(\eta, \rho)$ (in degrees)

η \ ρ	−.5	0	1	2	3	4
0	51.0	51.7	52.1	52.2	52.2	52.3
0.5	50.4	50.4	50.9	51.1	51.1	51.7
1	49.1	49.1	49.1	49.1	49.1	49.1

the problem significantly. Equating the two energy release rate expressions (8) and (10), one can verify

$$\sqrt{n}\,|\lambda^{-3/8}K_I + i\lambda^{-1/8}K_{II}| = \frac{1}{\sqrt{2}}\left|\frac{P}{\sqrt{hA}} - ie^{i\gamma}\frac{M}{\sqrt{h^3 I}}\right| \tag{12}$$

where $i=\sqrt{-1}$ and $|a|$ stands for the magnitude of a complex number a. Equation (12) states that two complex quantities have the same magnitude. Consequently, they can differ only by a phase angle shift, designated as ω, namely,

$$\left(\sqrt{n}(\lambda^{-3/8}K_I + i\lambda^{-1/8}K_{II}) = \frac{e^{i\omega}}{\sqrt{2}}\frac{P}{\sqrt{hA}} - ie^{i\gamma}\frac{M}{\sqrt{h^3 I}}\right). \tag{13}$$

On dimensional grounds, ω should be nondimensional function of nondimensional quantities Ph/M, η, λ, and ρ. However, by linearity, ω should not depend on Ph/M; nor should it depend on λ, since both sides of equation (13) are independent of λ. Therefore, the angle ω depends on η and ρ only, i.e.,

$$\omega = \omega(\eta, \rho). \tag{14}$$

Rewrite equation (13) more explicitly as

$$K_I = \frac{\lambda^{3/8}}{\sqrt{2n}}\left[\frac{P}{\sqrt{hA}}\cos\omega + \frac{M}{\sqrt{h^3 I}}\sin(\omega+\gamma)\right]$$
$$K_{II} = \frac{\lambda^{1/8}}{\sqrt{2n}}\left[\frac{P}{\sqrt{hA}}\sin\omega - \frac{M}{\sqrt{h^3 I}}\cos(\omega+\gamma)\right] \tag{15}$$

so that the stress intensity factors are fully determined apart from the single dimensionless real function $\omega(\eta, \rho)$. From equation (15) one can restrict ω in the range $0<\omega<\pi/2$ to recover the positive signs of K_I and K_{II} anticipated for the special case $P>0$ but $M=0$.

Specific determination of the function $\omega(\eta, \rho)$ requires that the crack problem in Fig. 1(*c*) be solved *rigorously* for a given pair (η, ρ), for an arbitrary set of values of λ, h, P, and M. We will show next that ω is around 50 deg. Some early works on partitioning mixed-mode stress intensity factors from the energy release rate were based on unjustified symmetry arguments and contains significant errors (e.g., Tada et al., 1985, pp. 29.2, 29.4, 29.9 and Williams, 1988, Fig. 10(*a*)). In the following, an exact solution for ω is found for the case $h=H$, or $\eta=1$. Numerical solutions are presented for other cases, and a simple estimate is given for practical applications.

(i) $\omega(1, \rho)$. Exact solution can be obtained for this case by considering a special loading $P=0$, $M=1$. The geometric factors in equations (9) and (11) for $\eta=1$ are

$$A=\frac{1}{14},\ I=\frac{1}{24},\ \sin\gamma=\sqrt{\frac{3}{7}}$$
$$C_1=\frac{1}{2},\ C_2=\frac{3}{4},\ C_3=\frac{1}{8}. \tag{16}$$

Notice that $K_{II}=0$ due to the symmetry, which, when substituted into equation (15), gives $\cos(\omega+\gamma)=0$. Thus, $\omega=\cos^{-1}\sqrt{(3/7)}\approx 49.1$ deg. It is revealing that $\omega(1, \rho)$ does *not* depend on ρ. This indicates that the function $\omega(\eta, \rho)$ may vary weakly with ρ even if $\eta\neq 1$.

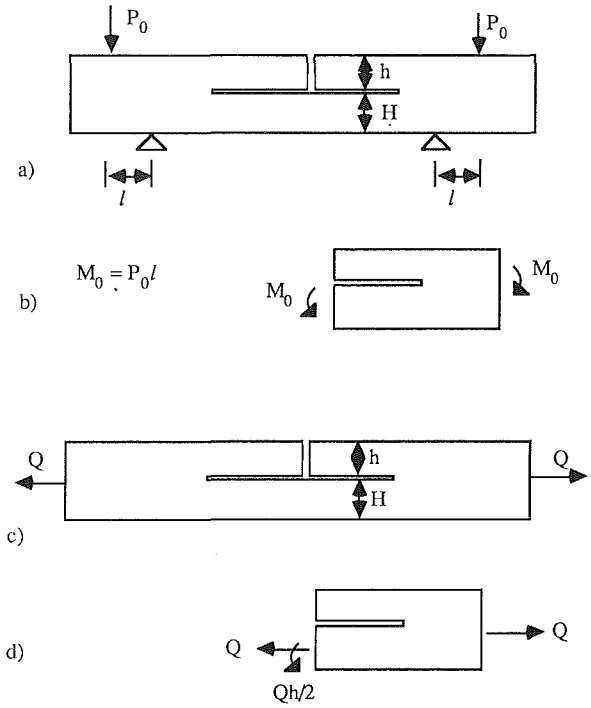


Fig. 2 Transverse splitting from notches; (*a*) four-point bend specimen, (*b*) equivalent bend moment, (*c*) delamination specimen, and (*d*) equivalent load for the delamination specimen

(ii) $\omega(\eta, 1)$. This case is equivalent to the isotropic version of the same problem, which has been solved by Suo and Hutchinson (1988a, b). For $0\leq\eta\leq 1$, an excellent approximation is

$$\omega = 52.1 - 3\eta, \quad \text{in degrees.} \tag{17}$$

(iii) $\omega(\eta, \rho)$. An integral equation is formulated and solved numerically in Appendix B for the general case. The extracted values of ω are listed in Table 2. One notes immediately that ω is a very weak function of ρ. This implies that equation (17) is an adequate estimate for a wide range of ρ for $0\leq\eta\leq 1$.

3 Fracture Specimens

3.1 A Four-Point Bend Specimen. The specimen illustrated in Fig. 2(*a*) is considered first. The beam is cut from an orthotropic material, with its principal axes coincident with the material principal axes. When the crack is long compared with h, but still lying within the central region of the specimen, the specimen can be well approximated by the system in Fig. 2(*b*). It has been shown by finite element calculations (Charalambides et al., 1989) for an analogous specimen that the crack-tip field is indifferent to the crack length if it is sufficiently long. Consequently, the structure in Fig. 2(*b*) can be imagined to be infinitely long in the crack direction. This falls into the class of the problems (Fig. 2(*a*)) analyzed in the previous section, with the special loading combination

$$P_1 = M_1 = P_3 = 0,\ M_3 = -M_0. \tag{18}$$

The equivalent loads controlling the singular field are calculated from equation (9), i.e.,

$$P = C_2 M_0/h,\ M = C_3 M_0. \tag{19}$$

The stress intensity factors are obtained when the above are substituted into equation (15), that is

Downloaded 03 May 2010 to 171.66.16.244. Redistribution subject to ASME license or copyright; see http://www.asme.org/terms/Terms_Use.cfm

$$K_I=\frac{\lambda^{3/8}}{\sqrt{2n}}M_0h^{-3/2}[C_2A^{-1/2}\cos\omega+C_3I^{-1/2}\sin(\omega+\gamma)]$$
$$K_{II}=\frac{\lambda^{1/8}}{\sqrt{2n}}M_0h^{-3/2}[C_2A^{-1/2}\sin\omega-C_3I^{-1/2}\cos(\omega+\gamma)] \quad (20)$$

where ω can be approximated by equation (17). For the special case $h=H$, or $\eta=1$, $\omega+\gamma=\pi/2$, $\cos\omega=\sqrt{(3/7)}$, $\sin\omega=\sqrt{(4/7)}$, with various geometric factors given in equation (16), equation (20) can be specialized to

$$K_I=\sqrt{3}\lambda^{3/8}n^{-1/2}M_0h^{-3/2},\ K_{II}=\frac{3}{2}\lambda^{1/8}n^{-1/2}M_0h^{-3/2}. \quad (21)$$

This is an exact solution. Notice that from equation (21),

$$\frac{K_{II}}{K_I}=\frac{\sqrt{3}}{2}\lambda^{-1/4}. \quad (21a)$$

Equation (21*a*) indicates that mode I and mode II stress intensity factors are comparable for this test arrangement.

3.2 A Tensile Specimen. Parallel results for the same geometry under tension (Fig. 2(*c*), (*d*)) are listed as follows. The stress intensity factors are given by

$$K_I=\frac{\lambda^{3/8}}{\sqrt{2n}}Qh^{-1/2}C_1A^{-1/2}\cos\omega$$
$$K_{II}=\frac{\lambda^{1/8}}{\sqrt{2n}}Qh^{-1/2}C_1A^{-1/2}\sin\omega \quad (22)$$

where, for an arbitrary value of $\eta=h/H$, C_1 and A are defined in equations (9) and (11), and ω can be approximated by equation (17). The solution for the case $h=H$, or $\eta=1$, is exact, which is

$$K_I=\frac{\sqrt{3}}{2}\lambda^{3/8}n^{-1/2}h^{-1/2}Q,\ K_{II}=\lambda^{1/2}n^{-1/2}h^{-1/2}Q, \quad (23)$$

thereby the ratio K_{II}/K_I, for the case $h=H$, is given by

$$\frac{K_{II}}{K_I}=\frac{2}{\sqrt{3}}\lambda^{-1/4}. \quad (23a)$$

Again, there is a comparable amount of stress intensity of the two modes.

3.3 More Specimens. Illustrated in Fig. 3 are geometries utilized predominantly in composite and wood fracture testing. The specimens are cut from bulk materials with principal material axes aligned with specimen axes. A common feature for all these specimens is that no specific length scale is involved in one direction. With such specimens, it has generally been the practice to use the stress intensity factors determined for the corresponding isotropic specimens (e.g., Ashby et al., 1985, Michalske and Hellmann, 1988). This can be easily justified as follows: The stress intensity factors, in general, depend on the two anisotropy measures, λ and ρ. Exploiting the rescaling technique outlined in Appendix A one can confirm that, for all configurations in Fig. 3, the stress intensity factors are independent of λ. Given the fact that ρ is typically in the range between 0 and 5, and that the solutions for analogous problems only weakly depend on ρ, one can reasonably expect that the stress intensity factors are *almost* independent of ρ. Consequently, the stress intensity factors for these geometries are nearly independent of any anisotropic factors, and thus the use of solutions for isotropic materials should be appropriate. Evidently unaware of the roles played by λ and ρ, Sweeny (1988) carried out a numerical analysis for an edge crack in an orthotropic half plane (Fig. 3(*a*)). The Table 1 in his paper can be reduced concisely as

$$K_I=Y\sigma\sqrt{\pi a},\ Y=1.12-0.011(\rho-1),\quad \text{for } 1<\rho<8. \quad (24)$$

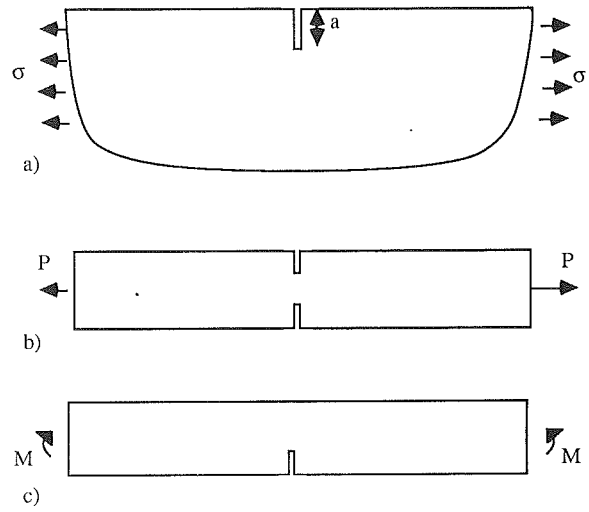


Fig. 3 Several conventional fracture specimens

The rescaling concepts have been extended to tackle specimens of finite geometries. Insights thus gained and a user-friendly catalog of most commonly used orthotropic specimens are reported in Suo et al. (1990) and Bao et al. (1990).

4 Extension to an Anisotropic Strip

Arguments leading to the stress intensity factor expression (15) have been used successfully in various contexts by Thouless et al. (1987), Hutchinson et al. (1988), Drory et al. (1988), and Suo and Hutchinson (1989a,b,c). The generality may be appreciated by considering the problem with the same configuration as Fig. 1(*c*), but with a generally anisotropic material replacing the orthotropic material considered earlier. The Sih-Paris-Irwin energy release rate expression can be rearranged as

$$G=b_{11}(n_1\lambda^{-3/4}K_I^2+n_2\lambda^{-1/4}K_{II}^2+2\sqrt{n_1n_2}\lambda^{-1/2}K_IK_{II}\sin\nu). \quad (25)$$

Here, n_1, n_2, and ν can be extracted from the work by Sih et al. (1965) as

$$n_1=-\frac{1}{2}\mathrm{Im}[t_1^{-1}+t_2^{-1}],\ n_2=\frac{1}{2}\mathrm{Im}[t_1+t_2],\ \sqrt{n_1n_2}\sin\nu=\frac{1}{2}\mathrm{Im}[t_1t_2] \quad (26)$$

and t_1 and t_2 are roots with positive imaginary parts of

$$t^4-2\rho_1t^3+2\rho t^2-2\rho_2t+1=0 \quad (27)$$

where ρ_1 and ρ_2 are defined in Appendix A. Comparing equation (25) with equation (10) one obtains

$$\left|\sqrt{n_1}\lambda^{-3/8}K_I+ie^{-i\nu}\sqrt{n_2}\lambda^{-1/8}K_{II}\right|=\frac{1}{\sqrt{2}}\left|\frac{P}{\sqrt{hA}}-ie^{i\gamma}\frac{M}{\sqrt{h^3I}}\right| \quad (28)$$

where A and I are defined by equation (11). Again one can introduce a phase angle shift $\omega=\omega(\eta,\ \rho,\ \rho_1,\ \rho_2)$, such that

$$\sqrt{n_1}\lambda^{-3/8}K_I+ie^{-i\nu}\sqrt{n_2}\lambda^{-1/8}K_{II}=\frac{e^{i\omega}}{\sqrt{2}}\left(\frac{P}{\sqrt{hA}}-ie^{i\gamma}\frac{M}{\sqrt{h^3I}}\right). \quad (29)$$

Consequently, the stress intensity factors K_I and K_{II} are fully determined apart from the function ω. One may anticipate the

Downloaded 03 May 2010 to 171.66.16.244. Redistribution subject to ASME license or copyright; see http://www.asme.org/terms/Terms_Use.cfm

approximation equation (17) to be valid for wide ranges of ρ, ρ_1, and ρ_2.

It is not a very difficult exercise to derive a formula analogous to equation (26) for an interface crack between two layers of dissimilar anisotropic materials, so that such interesting problems as bicrystal specimens (e.g., Wang, 1988) and interlaminar fracture in composites can be addressed. Helpful hints may be found in Suo and Hutchinson (1990). The corresponding relation between energy release rate and stress intensity factors can be found in Suo (1990).

Acknowledgments

The author is very grateful to A. G. Evans and J. W. Hutchinson for suggesting this problem and potential applications. This work was supported in part by DARPA University Research Initiative (Subagreement P.O. No. VB38639-0 with the University of California, Santa Barbara, ONR Prime Contract N00014-86-k-0753), by the National Science Foundation under Grant MSM-88-12779, and by the Division of Applied Sciences, Harvard University.

References

Argon, A. S., Gupta, V., Landis, H. S., and Cornie, J. A., 1989, "Intrinsic Toughness of Interfaces Between SiC Coatings and Substrates of Si or C Fibers," *J. Mater. Sci.*, Vol. 24, p. 1406–1412.

Ashby, M. F., Easterling, K. E., Harrysson, R., and Maiti, S. K., 1985, "The Fracture and Toughness of Woods," *Proc. Roy. Soc. Lond.*, Vol. A398, pp. 261–280.

Bao, G., Ho, S., Fan, B., and Suo, Z., 1990, "Orthotropy Rescaling and Fracture Specimens for Composite Materials," manuscript in preparation.

Budiansky, B., Hutchinson, J. W. and Evans, A. G., 1986, "Matrix Fracture in Fibre-reinforced Ceramics," *J. Mech. Phys. Solids*, Vol. 34, pp. 167–189.

Chai, H., 1988, "Shear Fracture," *Int. J. Fracture*, Vol. 37, pp. 137–159.

Charalambides, P. G., Lund, J., Evans, A. G., and McMeeking, R. M., 1989, "A Test Specimen for Determining the Fracture Resistance of Bimaterial Interfaces," ASME JOURNAL OF APPLIED MECHANICS, Vol. 56, pp. 77–82.

Drory, M. D., Thouless, M. D., and Evans, A. G. 1988, "The Cracking and Decohesion of Thin Films," *Acta Met.*, Vol. 36, pp. 2019–2028.

Hutchinson, J. W., Mear, M. E., and Rice, J. R., 1987, "Crack Paralleling an Interface between Dissimilar Materials," ASME JOURNAL OF APPLIED MECHANICS, Vol. 54, pp. 828–832.

Lekhnitskii, S. G., 1963, *Theory of Elasticity of an Anisotropic Body*, Holden-Day, Inc.

Liechti, K. M., and Hanson, E. C., 1988, "Nonlinear Effects in Mixed-Mode Interfacial Delamination," *Int. J. Fract.*, Vol. 36, pp. 199–217.

Marshall, D. B., and Evans, A. G., 1985, "Failure Mechanism in Ceramic-Fiber/Ceramic-Matrix Composites," *J. Am. Ceram. Soc.*, Vol. 68, pp. 225–231.

Michalske, T. A., and Hellmann, J. R., 1988, "Strength and Toughness of Continuous-Alumina-Fiber-Reinforced Glass-Matrix Composites," *J. Am. Ceram. Soc.*, Vol. 71, pp. 725–731.

Prewo, K. M., 1986, "Tension and Flexural Strength of Silicon Carbide Fiber-Reinforced Glass Ceramics," *J. Matter. Sci.*, Vol. 21, pp. 3590–3600.

Rice, J. R., 1968, "Mathematical Analysis in the Mechanics of Fracture," *Fracture, an Advanced Treatise*, Vol. 2, H. Liebowitz, ed., Academic Press, New York, pp. 191–311.

Sbaizero, O., Charalambides, P. G., and Evans, A. G., 1988, "Delamination Cracking in a Laminated Ceramic Matrix Composite," *Acta Met*, in press.

Sih, G. C., Paris, P. C., and Irwin, G. R., 1965, "On Cracks in Rectilinearly Anisotropic Bodies," *Int. J. Fracture Mech.*, Vol. 1, pp. 189–203.

Suo, Z., 1990, "Singularities, Interfaces and Cracks in Dissimilar Anistropic Media," *Proc. R. Soc. Lond.*, Vol. A427, pp. 331–358.

Suo, Z., and Hutchinson, J. W., 1990, "Interface Crack Between Two Elastic Layers," *Int. J. Fract.*, Vol. 43, pp. 1–18.

Suo, Z., and Hutchinson, J. W., 1989a, "Steady-state Cracking in Brittle Substrate beneath Adherent Films," *Int. J. Solids Structures*, Vol. 25, pp. 1337–1353.

Suo, Z., and Hutchinson, J. W., 1989b, "Sandwich Test Specimens for Measuring Interface Crack Toughness," *Mat. Sci. Eng.*, Vol. A107, pp. 135–143.

Suo, Z., Bao, G., Fan, B., and Wang, T. C., 1990, "Orthotropy Rescaling and Implications for Fracture in Composites," submitted for publication.

Sweeney, J., 1988, "The Stress Intensity for an Edge Crack in a Semi-infinite Orthotropic Body," *Int. J. Fract.*, Vol. 37, pp. 233–241.

Tada, H., Paris, P. C., and Irwin, G. R. 1985, *The Stress Analysis of Cracks Handbook*, Del Research, St. Louis, MO.

Thouless, M. D., Evans, A. G., Ashby, M. F., and Hutchinson, J. W., 1987, "The Edge Cracking and Spalling of Brittle Plates," *Acta Met.*, Vol. 35, pp. 1333–1341.

Wang, J.-S., 1988, "A New Type of Brittle Fracture in an FCC Metal Bicrystal with Intergranular Segregation," *J. Matter. Res.*, Vol. 3, pp. 16–28.

Wang, J.-S., and Suo, Z., 1990, "Experimental Determination of Interfacial Toughness Curves Using Brazil Nut Sandwiches," *Acta Met.*, in press.

Williams, J. G., 1988, "On the Calculation of Energy Release Rates for Cracked Laminates," *Int. J. Fract.*, Vol. 36, pp. 101–119.

Wu, E. M., 1967, "Application of Fracture Mechanics to Anisotropic Plates," ASME JOURNAL OF APPLIED MECHANICS, Vol. 34, pp. 967–974.

APPENDIX A

Orthotropy Rescaling

Let $U(x, y)$ by the Airy stress function, namely,

$$\sigma_x=\frac{\partial^2 U}{\partial y^2},\ \sigma_y=\frac{\partial^2 U}{\partial x^2},\ \tau_{xy}=-\frac{\partial^2 U}{\partial x\partial y}. \tag{A1}$$

The differential equation of $U(x, y)$ for rectilinearly anisotropic materials is obtained from the compatibility equation (cf. Lekhnitskii, 1963)

$$\frac{\partial^4 U}{\partial x^4}-2\rho_2\lambda^{1/4}\frac{\partial^4 U}{\partial x^3\partial y}+2\rho\lambda^{1/2}\frac{\partial^4 U}{\partial x^2\partial y^2}-2\rho_1\lambda^{3/4}\frac{\partial^4 U}{\partial x\partial y^3}+\lambda\frac{\partial^4 U}{\partial y^4}=0 \tag{A2}$$

where λ and ρ are defined in the body of the paper and $\rho_1\lambda^{3/4}=b_{16}/b_{22}$, $\rho_2\lambda^{1/4}=b_{26}/b_{22}$. Now it is obvious that for any simply connected domain of anisotropic medium with traction prescribed on its boundary, the stresses should only depend on four (rather than five) nondimensional elastic parameters. If the material is orthotropic with the principal axes in the x and y-directions, $\rho_1=\rho_2=0$, the stresses should only depend on two parameters λ and ρ. Moreover, for the problem in Fig. 2(a) with no specific length scale in x-direction, we are able to show explicitly the way in which stress intensity factors depend on λ. Rescale the x-axis by

$$\xi=\lambda^{1/4}x. \tag{A3}$$

The boundary value problem in Fig. 2(a) is then governed by the following differential equation

$$\frac{\partial^4 U}{\partial \xi^4}-2\rho_2\frac{\partial^4 U}{\partial \xi^3\partial y}+2\rho\frac{\partial^4 U}{\partial \xi^2\partial y^2}-2\rho_1\frac{\partial^4 U}{\partial \xi\partial y^3}+\frac{\partial^4 U}{\partial y^4}=0 \tag{A4}$$

and boundary conditions on (ξ, y) plane

$$\frac{\partial^2 U}{\partial y\partial \xi}=0,\ \frac{\partial^2 U}{\partial y^2}=\text{prescribed traction},\ \xi\to\pm\infty,\ -H<y<h \tag{A5}$$

$$\frac{\partial^2 U}{\partial \xi^2}=\frac{\partial^2 U}{\partial \xi\partial y}=0,\ \xi<0,\ y=0;\ -\infty<\xi<\infty,\ y=-H,\ h.$$

Clearly, $U(\xi, y)$ will not depend explicitly on λ. This has very strong implications as the stress intensity factors K_I and K_{II} are calculated

$$K_I=\lim_{x\to 0}\sqrt{2\pi x}\sigma_y(x,\ 0)=\lambda^{3/8}\lim_{\xi\to 0}\sqrt{2\pi\xi}\ \frac{\partial^2 U(\xi,\ 0)}{\partial \xi^2} \tag{A6}$$

$$K_{II}=\lim_{x\to 0}\sqrt{2\pi x}\tau_{xy}(x,\ 0)=-\lambda^{1/8}\lim_{\xi\to 0}\sqrt{2\pi\xi}\frac{\partial^2 U(\xi,\ 0)}{\partial \xi\partial y} \tag{A7}$$

so that the combinations $\lambda^{-3/8}K_I$ and $\lambda^{-1/8}K_{II}$ are independent of λ.

APPENDIX B

Integral Equation Formulation

An integral equation for the plane elasticity problem of Fig. 2(c) is formulated based on the dislocation solutions developed in Appendix C. Since only the function $\omega(\eta, \rho)$ is to be extracted from the numerical solution, one can take

$$\lambda=1,\ h=1,\ P=1,\ b_{11}=1, \tag{B1}$$

and M will be specified shortly to simplify the numerical analysis.

Downloaded 03 May 2010 to 171.66.16.244. Redistribution subject to ASME license or copyright; see http://www.asme.org/terms/Terms_Use.cfm

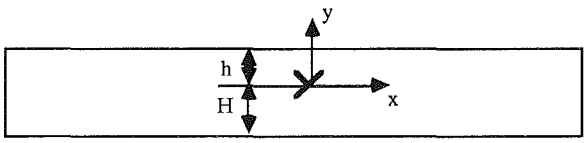


Fig. 4 An edge dislocation in an infinite strip of cubic material

The semi-infinite crack is simulated by an array of continuously distributed edge dislocations along the negative x-axis, with components $b_\alpha(\xi)$ at $x=\xi$. The traction-free condition along the crack faces results in the integral equations

$$\int_{-\infty}^{0}\frac{2B_\alpha(\xi)}{x-\xi}d\xi+\int_{-\infty}^{0}F_{\alpha\beta}(x-\xi)B_\beta(\xi)d\xi = 0, \text{ for } -\infty<x<0 \quad \text{(B2)}$$

where the first integral is in the Cauchy principal value sense, and the convention of summing up a repeated Greek suffix is adopted. Here,

$$B_\alpha(\xi)=\frac{1}{8\pi n}b_\alpha(\xi),\ n=\sqrt{\frac{\rho+1}{2}}. \quad \text{(B3)}$$

The kernel functions $F_{\alpha\beta}(\zeta)$ are given in Appendix C; they are well behaved in the whole range $-\infty<\zeta<+\infty$, with asymptotes

$$F_{\alpha\beta}(\zeta)=-\frac{2}{\zeta}\delta_{\alpha\beta}+O\left(\frac{1}{\zeta^3}\right) \quad \text{as } \zeta\to\infty. \quad \text{(B4)}$$

Noticing that by definition the Burgers vector, b_α, is related to the crack face relative displacement, δ_α, by

$$b_\alpha(x)=-\frac{\partial}{\partial x}\delta_\alpha(x), \quad \text{(B5)}$$

one can verify the following asymptotic behaviors for $B_\alpha(\xi)$

$$B_1(\xi)=(2\pi)^{-3/2}\frac{K_{II}}{\sqrt{-\xi}},\ B_2(\xi)=(2\pi)^{-3/2}\frac{K_I}{\sqrt{-\xi}} \quad \text{(B6)}$$

as $\xi\to 0^-$, and

$$B_1(\xi)=\frac{1}{8\pi n}[1+\eta(4+3\eta)-6M(1-\eta^2)],\ B_2(\xi)=\text{constant}$$

$$M=-\sqrt{\frac{I}{A}}\sin\gamma \quad \text{(B7)}$$

as $\xi\to-\infty$, where M has been chosen such that $B_2(-\infty)$ remains finite. And K_I, K_{II} and the "constant" in (B7) are not known *a priori*, but must be determined as part of the solution to the integral equations. The integral equations, together with the specified asymptotes, constitute a well-posed mathematical problem for the unknown distributions $B_\alpha(\xi)$. The details of the numerical solution procedure for analogous problems can be found in Thouless et al. (1987), and Suo and Hutchinson (1989a).

Once the $B_\alpha(\xi)$ are obtained for a given pair η and ρ, the stress intensity factors are evaluated from equation (B6). The function $\omega(\eta, \rho)$ is then extracted by specializing equation (13) with (B1), (B7) to

$$K_I+iK_{II}=\frac{\cos\gamma}{\sqrt{2nA}}e^{i(\omega+\gamma)}. \quad \text{(B8)}$$

The numerical solution yields both K_I and K_{II} and each results in a value of ω. This provides a consistency check on the accuracy of the solution. For example, knowing K_I and K_{II}, one can calculate $\cos(\omega+\gamma)$ and $\sin(\omega+\gamma)$ independently from equation (B8), and hence the check can be chosen as $[\cos^2(\omega+\gamma)+\sin^2(\omega+\gamma)]^{1/2}-1$. The results reported in Table 2 were computed with the consistency check satisfied to better than 0.1 percent. It is believed that the accuracy of ω is comparable.

APPENDIX C

An Edge Dislocation in Anisotropic Structures

In Appendix B, the solution of an edge dislocation embedded in a strip of cubic material (Fig. 4) is used as the kernel of the integral equation. This solution, together with analytic solutions to a dislocation in an infinite and semi-infinite space of generally anisotropic material, is constructed in this Appendix.

It has been shown in Lekhnitskii (1963) that the problems of plane anistropic elasticity can be conveniently formulated in terms of two analytic functions, $\phi_1(z_1)$ and $\phi_2(z_2)$ with two complex variables, $z_j=x+\mu_j y$. The parameters μ_1 and μ_2 are solved from the algebraic equation

$$b_{11}\mu^4-2b_{16}\mu^3+(2b_{12}+b_{66})\mu^2-2b_{26}\mu+b_{22}=0. \quad \text{(C1)}$$

The roots of equation (1) can never be real, and thus they occur in conjugate pairs. Here μ_1 and μ_2 are chosen to be the ones with positive imaginary parts. The stresses, resultant forces on an arc and displacements are given by

$$\begin{aligned}
\sigma_x&=2\text{Re}[\mu_1^2\phi_1'(z_1)+\mu_2^2\phi_2'(z_2)]\\
\sigma_y&=2\text{Re}[\phi_1'(z_1)+\phi_2'(z_2)]\\
\tau_{xy}&=-2\text{Re}[\mu_1\phi_1'(z_1)+\mu_2\phi_2'(z_2)]\\
f_x&=2\text{Re}[\mu_1\phi_1(z_1)+\mu_2\phi_2(z_2)] \quad \text{(C2)}\\
f_y&=-2\text{Re}[\phi_1(z_1)+\phi_2(z_2)]\\
u_x&=2\text{Re}[p_1\phi(z_1)+p_2\phi_2(z_2)]\\
u_y&=2\text{Re}[q_1\phi_1(z_1)+q_2\phi_2(z_2)]
\end{aligned}$$

where Re[ ] signifies the real part of a complex quantity, and

$$p_j=b_{11}\mu_j^2+b_{12}-b_{16}\mu_j,\ q_j=b_{22}/\mu_j+b_{12}\mu_j-b_{26}. \quad \text{(C3)}$$

(i) An Isolated Dislocation in an Infinite Body

The potentials for an edge dislocation with Burgers vector b_x and b_y at the point (x_0, y_0) in an infinite body are of the form

$$\phi_{j0}(z)=W_j\ln(z-s_j),\ s_j=x_0+\mu_j y_0 \quad \text{(C4)}$$

where the suffix 0 attached to the potentials indicates that the solution is for an *infinite body*. The complex constants W_1 and W_2 are determined from

$$\begin{cases}
\text{Im}[W_1+W_2]=0\\
\text{Im}[\mu_1W_1+\mu_2W_2]=0\\
\text{Im}[\mu_1^2W_1+\mu_2^2W_2]=-b_x/(4\pi b_{11})\\
\text{Im}[W_1/\mu_1+W_2/\mu_2]=-b_y/(4\pi b_{22})
\end{cases} \quad \text{(C5)}$$

where Im[ ] represents the imaginary part of a quantity. For the special case that the material is cubic with the principal axes along the x and y-axes, equation (C5) yields

$$W_1=\frac{1}{\mu_1-\mu_2}[-B_x+B_y/\mu_1],\ W_2=\frac{1}{\mu_1-\mu_2}[B_x-B_y/\mu_2]$$

$$B_\alpha=\frac{b_\alpha}{8\pi n b_{11}}. \quad \text{(C6)}$$

Downloaded 03 May 2010 to 171.66.16.244. Redistribution subject to ASME license or copyright; see http://www.asme.org/terms/Terms_Use.cfm

Specializing equation (C1) to a cubic material ($b_{16}=b_{26}=0$, $b_{11}=b_{22}$) gives

$$\mu_1=i(n+m),\ \mu_2=i(n-m),\quad \text{for } 1<\rho<\infty$$
$$\mu_1=in+m,\quad \mu_2=in-m,\quad \text{for } -1<\rho<1 \tag{C7}$$
$$n=\sqrt{\frac{1+\rho}{2}},\quad m=\sqrt{\left|\frac{1-\rho}{2}\right|}\ .$$

The degenerate value $\rho=1$ (corresponding to isotropic materials) can be treated as the limiting case. With the dislocation at the origin, i.e., $x_0=y_0=0$, the stresses are

$$\sigma^0_{\alpha\beta}(x,y)=f_{\alpha\beta\gamma}B_\gamma,\ f_{\alpha\beta\gamma}=\frac{1}{m}[g_{\alpha\beta\gamma}(m)-g_{\alpha\beta\gamma}(-m)] \tag{C8}$$

where

$$g_{111}(m)=-\frac{(n+m)^3y}{r^2},\ g_{112}(m)=g_{121}(m)=\frac{(n+m)x}{r^2}$$
$$g_{222}(m)=-\frac{y/(n+m)}{r^2},\ g_{221}(m)=g_{122}(m)=\frac{(n+m)y}{r^2} \tag{C9}$$
$$r^2=x^2+(n+m)^2y^2$$

for $\rho>1$, and

$$g_{111}(m)=\frac{\rho x-my}{r^2},\ g_{112}(m)=g_{121}(m)=\frac{mx+y}{r^2}$$
$$g_{222}(m)=\frac{mx-\rho y}{r^2},\ g_{221}(m)=g_{122}(m)=-\frac{x+my}{r^2} \tag{C10}$$
$$r^2=(x+my)^2+(ny)^2$$

for $-1<\rho<1$.

(ii) A Dislocation in Half Space

For a line singularity, such as a dislocation and line force, in generally anisotropic half space with traction-free boundary $y=0$, it has been shown by Suo (1990) that the potentials can be constructed with the solutions for the same singularity in an infinite body, namely,

$$\phi_1(z)=\phi_{10}(z)+\frac{1}{\mu_1-\mu_2}[(\mu_2-\bar\mu_1)\bar\phi_{10}(z)+(\mu_2-\bar\mu_2)\bar\phi_{20}(z)]$$
$$\phi_2(z)=\phi_{20}(z)+\frac{1}{\mu_1-\mu_2}[(\bar\mu_1-\mu_1)\bar\phi_{10}(z)+(\bar\mu_2-\mu_1)\bar\phi_{20}(z)]. \tag{C11}$$

(iii) A Dislocation in an Infinite Layer

A superposition scheme is used here to construct the solution for an edge dislocation embedded in an infinite strip (Fig. 4). Attention will be confined to cubic materials with a principal axis along the direction of the strip. A solution without singularity in the strip, which is represented by the Airy stress function $U(x, y)$ in Appendix A, is superposed onto the solution to an edge dislocation in an infinite body to nullify the traction on the strip boundaries. The following conventions of the Fourier-cos and -sin transforms for even and odd functions, respectively, will be adopted

$$f(x)=\int_0^{+\infty}\hat f(\theta)\cos\theta x\,d\theta,\ \hat f(\theta)=\frac{2}{\pi}\int_0^{+\infty}f(x)\cos\theta x\,dx$$
$$g(x)=\int_0^{+\infty}\hat g(\theta)\sin\theta x\,d\theta,\ \hat g(\theta)=\frac{2}{\pi}\int_0^{+\infty}g(x)\sin\theta x\,dx. \tag{C12}$$

Owing to the symmetry of the configuration, the stress function can be expressed by the Fourier integrals

$$U(x,y)=B_x\int_0^\infty\{\hat U_i(\theta,y)\}^T\{A_i(\theta)\}\frac{\cos\theta x}{\theta^2}d\theta$$
$$+B_y\int_0^\infty\{\hat U_i(\theta,y)\}^T\{C_i(\theta)\}\frac{\sin\theta x}{\theta^2}d\theta \tag{C13}$$

where $\hat U$'s are solved from

$$\left[\theta^4-2\rho\theta^2\frac{\partial^2}{\partial y^2}+\frac{\partial^4}{\partial y^4}\right]\hat U(\theta,y)=0. \tag{C14}$$

The solutions are

$$\{\hat U_i(\theta,y)\}^T=$$
$$\begin{cases}\{e^{(n+m)y\theta},\ e^{(n-m)y\theta},\ e^{(-n-m)y\theta},\ e^{(-n+m)y\theta}\},\ \rho>1\\ \{e^{ny\theta}\sin(my\theta),\ e^{ny\theta}\cos(my\theta),\ e^{-ny\theta}\sin(my\theta),\ e^{-ny\theta}\cos(my\theta)\},\\ \qquad -1<\rho<1\\ \{e^{y\theta},\ y\theta e^{y\theta},\ e^{-y\theta}y\theta,\ e^{-y\theta}\},\ \rho=1\end{cases} \tag{C15}$$

The stresses are derived from equation (A1).

$$\sigma_{yy}(x,y)=-B_x\int_0^\infty\{\hat U_i(\theta,y)\}^T\{A_i(\theta)\}\cos\theta x\,d\theta$$
$$-B_y\int_0^\infty\{\hat U_i(\theta,y)\}^T\{C_i(\theta)\}\sin\theta x\,d\theta \tag{C16a}$$

and

$$\tau_{xy}(x,y)=+B_x\int_0^\infty\{\partial\hat U_i(\theta,y)/\partial y\}^T\{A_i(\theta)\}\sin\theta x\,d\theta$$
$$-B_y\int_0^\infty\{\partial\hat U_i(\theta,y)/\partial y\}^T\{C_i(\theta)\}\cos\theta x\,d\theta. \tag{C16b}$$

The coefficients A's and C's are used to satisfy the strip boundary conditions. Written in the Fourier transform variables, these conditions become

$$\begin{bmatrix}\{\hat U_i(h)\}^T\\ \{\partial\hat U_i(h)/\partial y\}^T\\ \{\hat U_i(-H)\}^T\\ \{\partial\hat U_i(-H)/\partial y\}^T\end{bmatrix}\begin{bmatrix}A_1 & C_1\\ A_2 & C_2\\ A_3 & C_3\\ A_4 & C_4\end{bmatrix}=$$
$$\begin{bmatrix}\hat f_{221}(h) & \hat f_{222}(h)\\ -\hat f_{121}(h) & \hat f_{122}(h)\\ \hat f_{221}(-H) & \hat f_{222}(-H)\\ -\hat f_{121}(-H) & \hat f_{122}(-H)\end{bmatrix} \tag{C17}$$

where the Fourier transforms of the functions defined in equations (C8)–(C10) are

$$\hat f_{121}(y)=\frac{1}{m}[(n+m)e^{-(n+m)|y|\theta}-(n-m)e^{-(n-m)|y|\theta}]$$
$$\hat f_{222}(y)=\frac{1}{m}\left[-\frac{1}{n+m}e^{-(n+m)|y|\theta}+\frac{1}{n-m}e^{-(n-m)|y|\theta}\right] \tag{C18}$$
$$\hat f_{221}(y)=\hat f_{122}(y)=\frac{\mathrm{sgn}(y)}{m}[e^{-(n+m)|y|\theta}-e^{-(n-m)|y|\theta}]$$

for $\rho>1$, and

$$\hat f_{121}(y)=2\left[\cos(my\theta)-n\frac{\sin(m|y|\theta}{m}\right]e^{-n|y|\theta}$$
$$\hat f_{222}(y)=2\left[\cos(my\theta)+n\frac{\sin(m|y|\theta)}{m}\right]e^{-n|y|\theta} \tag{C19}$$
$$\hat f_{221}(y)=\hat f_{122}(y)=-2\left[\frac{\sin(my\theta)}{m}\right]e^{-n|y|\theta}$$

Downloaded 03 May 2010 to 171.66.16.244. Redistribution subject to ASME license or copyright; see http://www.asme.org/terms/Terms_Use.cfm

for $-1<\rho<1$. The dependence on θ has not been noted explicitly.

In the integral equation formulation in Appendix B, the stresses at x induced by the dislocation at $x=0$ are desired along the line parallel to the strip boundaries with the dislocation on it. They can be written in the form

$$\sigma_{2\alpha}(x)=\frac{2B_\alpha}{x}+F_{\alpha\beta}(x)B_\beta \tag{C20}$$

where F's are to be evaluated numerically using the Fourier integrals equation (C16) letting $y=0$. However, for the half plane problem, i.e, $H\to\infty$, analytic expressions are obtained from equation (C11). The results are

$$F_{\alpha\beta}=\left(\frac{n}{m}\right)^2[D_{\alpha\beta}(m)+D_{\alpha\beta}(-m)-2D_{\alpha\beta}(0)/n^2],\ \alpha=\beta \tag{C21}$$

$$F_{\alpha\beta}=\left(\frac{n}{m}\right)^2[D_{\alpha\beta}(m)+D_{\alpha\beta}(-m)-2D_{\alpha\beta}(0)],\ \alpha\neq\beta$$

where

$$D_{11}(m)=-\frac{(n+m)x}{nr^2},\ D_{22}(m)=-\frac{(n-m)x}{nr^2}, \tag{C22}$$

$$D_{12}(m)=-D_{21}(m)=-\frac{2(n+m)h}{nr^2},\ r^2=x^2+(n+m)^2h^2$$

for $\rho>1$, and

$$D_{11}(m)=\frac{x}{r^2},\ D_{22}(m)=\frac{x-4mh}{r^2} \tag{C23}$$

$$D_{12}(m)=-D_{21}(m)=\frac{2h}{r^2},\ r^2=(x+2mh)^2+(2nh)^2$$

for $-1<\rho<1$.

Downloaded 03 May 2010 to 171.66.16.244. Redistribution subject to ASME license or copyright; see http://www.asme.org/terms/Terms_Use.cfm

Asymptotic Crack-Tip Fields for Perfectly Plastic Solids Under Plane-Stress and Mixed-Mode Loading Conditions

P. Dong[1]

J. Pan

Department of Mechanical Engineering and Applied Mechanics, The University of Michigan, Ann Arbor, MI 48109

In this paper, we first discuss some of the properties of the crack-tip sectors for perfectly plastic materials under plane-stress conditions. Then starting with the plane-stress mixed-mode crack-tip fields suggested by Shih (1973), we assemble these sectors in a slightly different manner from those in Shih (1973). The missing governing equations needed to completely specify the crack-tip fields for both near mode I and near mode II mixed-mode loadings are derived. The mode I crack-tip field, as the limit of the near mode I cases, differs from Hutchinson's solution (1968) by the appearance of a small constant stress sector ahead of the crack tip. In addition, the relevance of the solutions of the near mode II cases to some interesting features of the mixed-mode crack-tip fields, as suggested by Budiansky and Rice (1973), is also discussed.

1 Introduction

Guided by the low-hardening crack-tip field solutions for power-law hardening Mises materials under plane-stress and mixed-mode loading conditions, Shih (1973) proposed the corresponding crack-tip fields in terms of the stress characteristics for perfectly plastic materials. These characteristic fields involve eight parameters, among which one parameter should be prescribed to vary between its mode I and mode II values. However, only six equations were realized from equilibrium considerations. Failure in finding the seventh equation left the problem unsatisfactorily resolved.

Here, we first outline and elaborate on some of the properties of the crack-tip sectors. Then, starting with the characteristic fields suggested by Shih (1973), we assemble these sectors in a slightly different manner from those in Shih (1973). The missing governing equations needed to completely specify the crack-tip fields for both near mode I and near mode II mixed-mode loadings are derived. Finally, the implications of the crack-tip fields on the crack-tip behavior of power-law hardening materials are discussed.

2 Asymptotic Crack-Tip Sectors

With the reference to the coordinate systems shown in Fig. 1, the asymptotic equation,

$$\frac{\partial(\sigma_{11}+\sigma_{22})}{\partial\theta}s_{rr}=0, \tag{1}$$

valid at the immediate vicinity of the crack tip, can be realized (Rice, 1982). s_{rr} is the radial component of the deviatoric stress tensor in the polar coordinate system. Equation (1) leads to the following forms of simple solutions near the tip:

(i) Constant Stress Sectors. Within a constant stress sector, the stresses σ_{11}, σ_{22}, and σ_{12} (referring to the Cartesian coordinates) are independent of θ, and satisfy the yield condition. The characteristic grid is generated by two nonorthogonal families of parallel lines.

(ii) Curved Fan Sectors. Within a curved fan sector, $s_{rr}=0$ corresponds to one of two families of characteristics, namely, a fan of radial lines. Along these radial lines, $\sigma_{\theta\theta}=2\sigma_{rr}$ holds. The asymptotic equilibrium equations and the yield condition are satisfied if we take

$$\sigma_{\theta\theta}=2\sigma_{rr}=\pm 2\tau_0\cos\theta_l, \tag{2}$$

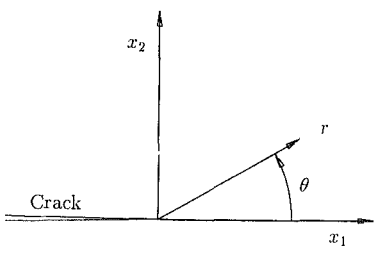


Fig. 1 Coordinate conventions

[1]Current address: Edison Welding Institute, Columbus, OH 43220.

Contributed by the Applied Mechanics Division of THE AMERICAN SOCIETY OF MECHANICAL ENGINEERS for publication in the JOURNAL OF APPLIED MECHANICS.

Discussion on this paper should be addressed to the Technical Editor, Prof. Leon M. Keer, The Technological Institute, Northwestern University, Evanston, IL 60208, and will be accepted until two months after final publication of the paper itself in the JOURNAL OF APPLIED MECHANICS. Manuscript received by the ASME Applied Mechanics Division, Dec. 6, 1988; final revision, Sept. 6, 1989.

Copyright © 1990 by ASME

Downloaded 03 May 2010 to 171.66.16.244. Redistribution subject to ASME license or copyright; see http://www.asme.org/terms/Terms_Use.cfm

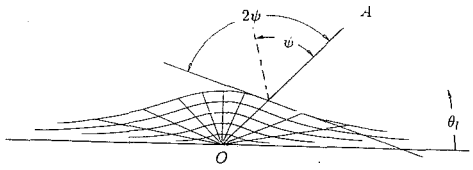


Fig. 2 A curved fan sector (fully developed)

$$\sigma_{r\theta} = \pm \tau_0 \sin\theta_l, \tag{3}$$

where θ_l is measured counterclockwise, as shown in Fig. 2, and τ_0 is the yield stress in shear.

A general curved fan sector, if fully expanded, is illustrated in Fig. 2. Evidently, the stresses are constant along the radial lines. It will be informative to examine the properties of the characteristics of the second family. In this coordinate system, 2ψ is defined as the angle made by the radial characteristic (OA) and the tangent of a curved characteristic (Fig. 2). We can write the differential equation for the curved characteristic as

$$\tan 2\psi = \frac{r(\theta_l)}{r'(\theta_l)}. \tag{4}$$

The angle 2ψ can be related to θ_l by realizing that ψ is the angle between a principal direction and the radial characteristic. It then follows that

$$\tan 2\psi = -2\tan\theta_l. \tag{5}$$

This furnishes the differental equation (4):

$$-\cot\theta_l d\theta_l = \frac{2dr}{r}. \tag{6}$$

A simple integration of both sides of equation (6) yields the equation for the curved characteristic:

$$r^2 \sin\theta_l = \text{constant}. \tag{7}$$

Apparently, equation (7) was given by Hill (1952), but in a different manner. The curved characteristics tend asymptotically to the horizontal line at $\theta_l = 0$ and π. It should be noted that equation (5) is the key to find the missing governing equations to solve the mixed-mode crack-tip fields.

3 Assembly of Crack-Tip Solutions

3.1 Near Mode I Cases. As suggested by Shih (1973), the characteristic field for near mode I mixed-mode loading under plane-stress conditions is shown in Fig. 3(a). Regions (1), (2), (4), (6), and (7) are constant stress sectors, and regions (3) and (5) are curved fan sectors. The parameters θ_1 through θ_6 are defined similarly to those in Shih (1973). δ_1 and δ are defined as the two angles between the horizontal line (crack line) and the two radial lines (oO' and oO), which would be approached asymptotically by the curved characteristics of the fan sectors, (3) and (5), respectively, if the curved characteristics were fully developed.

Along the radial lines at $\theta = \theta_1$ and $\theta = \theta_6$, σ_{rr} is assumed to be discontinuous. Its jump across the radial lines is given by requiring that the yield condition be satisfied on both sides of the lines. There are a total of eight parameters and seven regions to describe the characteristic field. The traction-free boundary conditions along the crack surfaces, in combination with the traction continuity requirement along the radial lines between two adjacent sectors, generate six independent governing equations. In the following, only the two curved fan sectors, (3) and (5), are analyzed in detail to derive the seventh governing equation.

In the curved fan sector (3), the stresses, with respect to the asymptote oO', have the same forms as equations (2) and (3). They can be expressed in terms of the θ-coordinate as

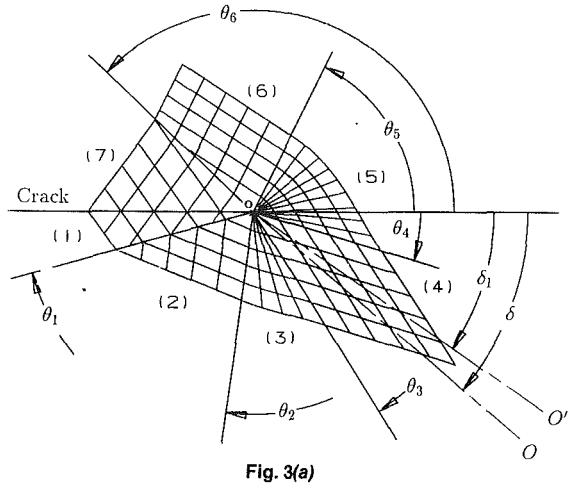


Fig. 3(a)

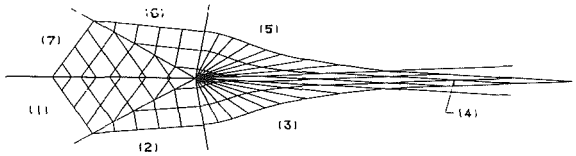


Fig. 3(b)

Fig. 3 Crack-tip stress characteristic fields: (a) near mode I mixed-mode, (b) the mode I limit

$$\sigma_{\theta\theta} = 2\sigma_{rr} = 2\tau_0 \cos(\theta + \delta_1), \tag{8}$$

$$\sigma_{r\theta} = \tau_0 \sin(\theta + \delta_1). \tag{9}$$

By the same token, for the other fan sector, (5), we have

$$\sigma_{\theta\theta} = 2\sigma_{rr} = 2\tau_0 \cos(\theta + \delta), \tag{10}$$

$$\sigma_{r\theta} = \tau_0 \sin(\theta + \delta). \tag{11}$$

The parameters θ_3, θ_4, δ_1, and δ can be related by applying equation (5) to the two fan sectors, and noting that $2\psi = \theta_4 - \theta_3$ at $\theta = \theta_3$ for fan sector (3) and $2\psi = \pi - (\theta_4 - \theta_3)$ at $\theta = \theta_4$ for fan sector (5). θ_1, θ_2, θ_3, and θ_4 are negative, since they are defined in the clockwise direction as shown in Fig. 3(a). Employing equation (5) for both fan sectors (3) and (5) gives

$$2\tan(\delta_1 + \theta_3) = -2\tan(\delta + \theta_4). \tag{12}$$

Equation (12) indicates that the bisector of the angle $\theta_4 - \theta_3$ is also the bisector of the angle $\delta - \delta_1$, i.e.,

$$\delta_1 + \delta = -\theta_3 - \theta_4. \tag{13}$$

Equation (13) is the seventh governing equation needed to completely specify the near mode I crack-tip fields.

For a characteristic field slightly perturbed from the pure mode I field, referring to Fig. 3(b), the line ahead of the crack lies within the constant stress sector (region (4)). This is in contrast to Shih's assumption (1973) that the line ahead of the crack lies within the fan sector (region (5)) for the entire mixed-mode loadings. In this case, the mixity parameter, M^p, defined by Shih (1973), cannot be expressed in a simple manner as that in Shih (1973). As the mode II component increases further, the crack line lies within the curved fan sector (region (5)) throughout the rest of the transition from mode I to mode II. The mixity parameter, M_p, then, can be conveniently expressed in terms of δ (Shih, 1973):

$$M^p = \frac{2}{\pi}\arctan\left[\lim_{r\to 0}\frac{\sigma_{\theta\theta}(r,\theta=0)}{\sigma_{r\theta}(r,\theta=0)}\right] = \frac{2}{\pi}\arctan\left[\frac{2}{\tan\delta}\right]. \tag{14}$$

Downloaded 03 May 2010 to 171.66.16.244. Redistribution subject to ASME license or copyright; see http://www.asme.org/terms/Terms_Use.cfm

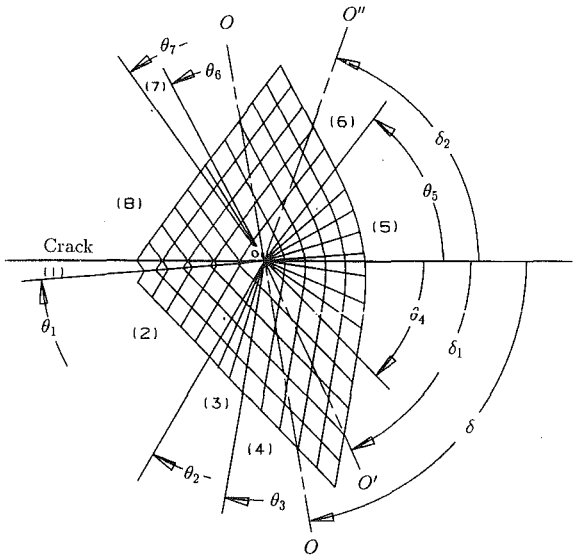


Fig. 4 Crack-tip stress characteristic field for near mode II mixed-mode loading

Since the early stage of the transition from mode I to mode II only counts for an extremely small portion of the entire mode mixture, for any practical purposes equation (14) can be used with a less than 1 percent margin of error. As δ varies from 0 deg (mode I) to 90 deg (mode II), M_p varies from 1 to 0.

For a given value of δ, a total of seven equations are solved by Newton's method (Dong, 1989). The resulting mode I characteristic field ($\delta = 0.006$ deg) is shown in Fig. 3(b). In this case, $-\theta_1 = \theta_6 = 151.24$ deg, $-\theta_2 = \theta_5 = 79.84$ deg, and $-\theta_3 = \theta_4 = 2.61$ deg. This solution differs from Hutchinson's solution (1968) by the appearance of a small constant stress sector ahead of the crack tip. In Hutchinson's solution, $\delta = 0$ (chosen to satisfy the symmetry condition for mode I), $-\theta_1 = \theta_6 = 151.4$ deg, $-\theta_2 = \theta_5 = 79.7$ deg, and $-\theta_3 = \theta_4 = 0$ deg. Although the difference in stress distributions between the two fields is not noticeable, the characteristic structures of the crack-tip fields are different. Our solution has a constant stress sector ahead of the crack tip. This is similar to the plane-strain mode I crack-tip field. As indicated in the work of Nishimura and Achenbach (1986), the same type of the characteristic field was also proposed by Thomason (1979), and a narrow constant stress sector ahead of the crack tip is more appropriate when the finite deformation of the crack tip is considered.

As the radial line of the discontinuity at $\theta = \theta_6$ approaches 125.26 deg, the magnitude of the jump in σ_{rr} at $\theta = \theta_6$ finally vanishes. At this point δ is 70.53 deg ($M^p = 0.392$) with θ_1 being 175.16 deg (note that the calculations of Shih (1973) give $\theta_1 = -177.22$ deg). This case ($M^p = 0.392$) demarcates the near mode I characteristic fields and the near mode II ones.

3.2 Near Mode II Cases. As δ deviates further from mode I, a fan sector develops between regions (6) and (7). The corresponding characteristic field is shown in Fig. 4. Ten parameters are needed to describe the field, among which δ_2 is the angle between the crack line and the asymptote (oO'') of the new fan sector, region (7). The parameters θ_7 and δ_2 can be readily determined as $\theta_7 = 125.26$ deg and $\delta_2 = 70.53$ deg (Dong, 1989).

The stresses within the curved fan sector (region (7)), with respect to θ, can be rewritten as

$$\sigma_{\theta\theta} = 2\sigma_{rr} = -2\tau_0 \cos(\theta - \delta_2), \tag{15}$$

$$\sigma_{r\theta} = -\tau_0 \sin(\theta - \delta_2). \tag{16}$$

As shown in Fig. 4, the asymptote of the fan sector (region (7)) intersects with the second asymptote of fan sector (5). A similar development to that in arriving at equation (13) results in:

$$\pi - \delta + \delta_2 = \theta_5 + \theta_6. \tag{17}$$

Again, for the near mode II cases, a total of seven equations are solved iteratively for a given value of δ using Newton's method to determine the characteristic fields (Dong, 1989).

The current solutions indicate that as δ varies from 70.53 deg to 90 deg, the transition from the near mode II mixed mode to the pure mode II is accompanied by the discontinuity in σ_{rr} until the pure mode II condition is reached. At this point the discontinuity line ($\theta = \theta_1$) merges with lower crack surface and region (1) vanishes completely. This small sector, (1), in the near mode II crack-tip fields was missed in the solutions shown in Fig. 14 in Shih (1973).

4 Concluding Remarks

Perfect-plasticity solutions of this kind bear close resemblance to the corresponding low-hardening solutions for power-law hardening materials. This suggests that the perfect-plasticity solution should be the nonhardening limits of the dominant singularity solutions. As a result, the perfect-plasticity solutions exhibit some important features of the dominant singularity solutions for power-law hardening materials.

One remarkable consequence in employing conservation intergals for cases where the strain energy density W varies inversely with the radial distance r to the tip (Budiansky and Rice, 1973) is that

$$\int_{\text{crack}} x[W_+ - W_-]dx \tag{18}$$

must be bounded, where W_+ and W_- are the strain energy densities evaluated on the upper and the lower crack surfaces, respectively. Since W depends only on $|\sigma_{rr}|$ along the crack surfaces, this implies that

$$\sigma_{rr}(\theta = \pi) = \pm \sigma_{rr}(\theta = -\pi) \tag{19}$$

must be true in all mixed-mode cases. Since $\sigma_{rr}(\pi) = \sigma_{rr}(-\pi)$ for mode I, and $\sigma_{rr}(\pi) = -\sigma_{rr}(-\pi)$ for mode II, equation (19) implies that the transition point from the positive sign to the negative sign must be at a particular mode mixture. Shih (1973) suggested that the transition from one sign to the other should be at $M^p = 1^-$ under plane-strain conditions, and at some intermediate mode under plane-stress conditions.

Interestingly enough, the current perfect-plasticity solutions for near mode II loading (see Fig. 4) suggest that the transition under plane-stress conditions should be at $M^p = 0^+$. It seems that the corresponding numerical verification (by either finite element methods or the corresponding asymptotic analysis for power-law hardening materials) is difficult in resolving the exact location of the radial stress discontinuity since it asymtotically approaches the lower crack surface as the mode II component becomes increasingly dominant.

Acknowledgment

The authors acknowledge the support of the Nuclear Regulatory Commission under grant number NRC-04-87-113. J. P. also acknowledges the partial support of this work by the National Science Foundation under grant number MSM-8613544. Helpful discussions with Prof. J. W. Hutchinson of Harvard University are greatly appreciated.

References

Budiansky, B., and Rice, J., 1973, "Conversion Laws and Energy-Release Rates," ASME Journal of Applied Mechanics, Vol. 40, pp. 201–203.

Downloaded 03 May 2010 to 171.66.16.244. Redistribution subject to ASME license or copyright; see http://www.asme.org/terms/Terms_Use.cfm

Dong, P., 1989, "Mixed-Mode Near-Tip Fields for Elastic Perfectly Plastic Solids," Ph.D. thesis, The University of Michigan, Ann Arbor, Mich.

Hill, R., 1952, "On Discontinuous Plastic States, With Special Reference to Localized Necking in Thin Sheets," *J. Mech. Phys. Solids*, Vol. 1, pp. 19–30.

Hutchinson, J. W., 1968, "Plastic Stress and Strain Fields at a Crack Tip," *J. Mech. Phys. Solids*, Vol. 16, pp. 337–347.

Nishimura, N., and Achenbach, J. D., 1986, "Finite Deformation Crack-Line Fields in a Thin Elasto-Plastic Sheet," *J. Mech. Phys. Solids*, Vol. 34, pp. 147–165.

Rice, J. R., 1982, "Elastic-Plastic Crack Growth," *Mechanics of Solids: The R. Hill 60th Anniversary Volume*, H. G. Hopkins and M. J., Sewell, eds., Pergamon Press, Oxford, pp. 539–562.

Shih, C. F., 1973, "Elastic-Plastic Analysis of Combined Mode Crack Problems," Ph.D. thesis, Harvard University, Cambridge, Mass.

Thomason, P. F., 1979, *Fracture Mechanics in Engineering Application*, G. C. Sih and S. R. Valluri, eds., Sijthoff and Noordhoff, The Netherlands, p. 43.

Downloaded 03 May 2010 to 171.66.16.244. Redistribution subject to ASME license or copyright; see http://www.asme.org/terms/Terms_Use.cfm

The First-Order Variation of the Displacement Field Due to Geometrical Changes in an Elliptical Crack

T. Nishioka
Department of Ocean Mechanical Engineering,
Kobe University of Mercantile Marine,
Kobe 658, Japan
Mem. ASME

S. N. Atluri
Center for Computational Mechanics,
Georgia Institute of Technology,
Atlanta, GA 30332-0356
Fellow, ASME

Analytical expressions are derived for the derivatives of the crack-surface displacement field, with respect to the lengths of the major and minor axes, respectively, of an elliptical crack embedded in an infinite isotropic elastic solid, when the crack faces are subjected to arbitrary tractions. These results are shown to lead, in turn, to analytical expressions for weight functions for the stress intensity factors along the fronts of elliptical-shaped embedded or part-elliptical shaped surface flaws, when a simple two-parameter characterization of the stress intensity variation along the flaw border is used. In the case of part-elliptical surface flaws, a finite-element alternating method, based on the Schwartz-Neumann superposition technique, is proposed to determine the coefficients in the analytical expressions for crack-surface displacements, and their gradients with respect to the crack dimensions.

1 Introduction

Cracks that develop in structural components due to fatigue or stress corrosion cracking are often found to be elliptical or part-elliptical in shape. To predict the crack growth rate and the critical crack size, and accurate evaluation of stress intensity factor variation along the crack front is needed. For these reasons, the elliptical or part-elliptical crack problems have been the focus of a considerable number of studies.

First, Green and Sneddon (1950) have obtained the analytical solution for an elliptical crack in an infinite solid, subject to uniform tension. Kassir and Sih (1966) have treated the cases of uniform shear loading together with the uniform normal loading on the crack face. They have also derived expressions for the singular stress field near the crack front as well as for the stress intensity factors. Shah and Kobayashi (1971) have developed the exact algebraic solution to an elliptical crack in an infinite solid subject to a cubic normal (pressure) loading.

Vijayakumar and Atluri (1981) have presented a general solution procedure for an embedded elliptical crack in an isotropic infinite solid, subject to *arbitrary* normal as well as tangential crack face tractions. Later, Nishioka and Atluri (1983) have refined and completed this solution, by deriving (*i*) alternate and more convenient forms of the linear algebraic equations relating the coefficients in the polynomials describing the prescribed crackface tractions, and the assumed potential functions in the solution, (*ii*) a general procedure for the evaluation of the required elliptic integrals and (*iii*) a systematic procedure for the evaluation of the partial derivatives of the potential functions. These derivations made it possible to extract the analytical closed-form solution for any polynomial order of crack face tractions. For later convenience, we cite this general solution altogether (Vijayakumar and Atluri, Nishioka and Atluri) as the VNA solution. The VNA solution represents a generalization, of the potential representation of Segedin (1967) and Shah and Kobayashi (1971).

The concept of weight functions for elastic crack problems dates back to the work of Bueckner (1971) and Rice (1972) (see also Bortman and Banks-Sills (1983)). The "weight function" may generally be viewed as the appropriately normalized rate of change of displacements (at the surface where tractions are applied, or in the domain where body forces are applied) due to a unit change in the crack length for a *reference state* of loading. The practical importance of the concept of the weight functions lies in the fact that, if the weight functions are evaluated from a (*perhaps simple*) *reference state of loading*, then the stress intensity factors for any arbitrary state of loading can be computed by using an integral of the worklike product between the applied tractions at a point on the surface in the arbitrary state of loading and the weight function for the reference state at the same point. Thus, the establishment of a successful weight function relies crucially on the accurate evaluation of the normalized rate of change (or the first-order variation) of displacement field in reference states, due to a unit change in the crack length.

Rice (1985) has presented results for the first-order variation

Contributed by the Applied Mechanics Division of THE AMERICAN SOCIETY OF MECHANICAL ENGINEERS for presentation at the Winter Annual Meeting, Dallas, Texas, Nov. 25-30, 1990.

Discussion on this paper should be addressed to the Technical Editor, Leon M. Keer, The Technological Institute, Northwestern University, Evanston, IL 60208, and will be accepted until two months after final publication of the paper itself in the JOURNAL OF APPLIED MECHANICS. Manuscript received and accepted by the ASME Applied Mechanics Division, Feb. 3, 1989.

Paper No. 90-WA/APM-22.

Copyright © 1990 by ASME
Downloaded 03 May 2010 to 171.66.16.244. Redistribution subject to ASME license or copyright; see http://www.asme.org/terms/Terms_Use.cfm

of an elastic displacement field associated with the arbitrary incremental planar advance of the front of a *half-plane crack* in a loaded elastic full space, discussed the relation for such results to a three-dimensional weight function theory, and derived an expression for the distribution of the Mode-I K-factor for a slightly curved crack front. Later, Gao and Rice (1986) extended this work to the mixed-mode case. Recently Bueckner (1987) has presented analytical results for three-dimensional weight functions, for a penny-shaped and a half plane crack in an elastic full space, under mixed-mode conditions. Employing these results, and Sham's (1987) variational technique, Sham and Zhou (1987) have determined the Mode I weight functions for both penny-shaped and elliptical cracks in finite bodies.

Here, our objective is to determine *analytical* expressions for crack surface weight functions for both *embedded* elliptical as well as part-elliptical *surface* cracks in finite-sized structural components. In the present paper, based on the VNA solution, analytical expressions of the first-order variation of the displacement field due to geometrical changes in the shape of an elliptical crack are derived. This analytical solution is related to the partial derivatives of the displacement field with respect to the lengths of the major and minor axes of the ellipse, respectively. As noted earlier, the VNA solution involves the generic elliptic integrals. For this reason, we need to evaluate the partial derivatives of the generic elliptic integrals with respect to the lengths of the major and minor axes of the ellipse. A systematic procedure for the evaluation of these derivatives is also developed in this paper.

In the latter part of this paper, the analytical solutions for the derivatives of displacements at the surfaces of a planar elliptical crack in a three-dimensional solid, with respect to the lengths of the major and minor axes of the ellipse, are applied to construct the weight functions for a *two-parameter model* of the elliptical, fully embedded or part-elliptical surface flaws. Simple numerical examples are given for the weighted average stress intensity factors in the sense as originally used by Besuner (1976) and Cruse and Besuner (1975). This paper also proposes a weight function method for the evaluation of the local stress intensity factors at the major and minor axes of an embedded or a surface crack of an elliptical or part-elliptical shape.

2 The VNA Solution (The General Solution for an Elliptical Crack in an Infinite Solid)

Suppose that x_1 and x_2 are Cartesian coordinates in the plane of the elliptical crack and x_3 is normal to the crack plane such that

$$(x_1/a_1)^2+(x_2/a_2)^2=1 \qquad a_1>a_2 \tag{1}$$

describes the border of the elliptical crack of aspect ratio (a_1/a_2). The necessary ellipsoidal coordinates ξ_α ($\alpha=1, 2, 3$) are defined as the roots of the cubic equation

$$\omega(s)=1-\left(\frac{x_1^2}{a_1^2+s}\right)-\left(\frac{x_2^2}{a_2^2+s}\right)-\left(\frac{x_3^2}{s}\right)=0 \tag{2}$$

where

$$\infty>\xi_3\geq 0\geq\xi_2\geq -a_2^2\geq\xi_1\geq -a_1^2$$

so that the interior of the ellipse is given $\xi_3=0$ and its boundary by $\xi_2=\xi_3=0$.

Let the tractions along the crack-surface be expressed in the form

$$\sigma_{3\alpha}^{(0)}=\sum_{i=0}^{1}\sum_{j=0}^{1}\sum_{m=0}^{M}\sum_{n=0}^{m}A_{\alpha,m-n,\,n}^{(i,j)}x_1^{2m-2n+i}\,x_2^{2n+j} \quad (\alpha=1,2,3) \tag{3}$$

so that the values of (i, j) specify the symmetries of the load with respect to the axes of the ellipse. M is an arbitrary integer which is related to the order of the polynomial. The solution corresponding to the load expressed by equation (3) can be assumed in terms of the potential functions

$$f_\alpha=\sum_{i=0}^{1}\sum_{j=0}^{1}\sum_{k=0}^{M}\sum_{l=0}^{k}C_{\alpha,k-l,l}^{(i,j)}F_{2k-2l+i,2l+j} \quad (\alpha=1,2,3) \tag{4}$$

where

$$F_{2k-2l+i,2l+j}=\frac{\partial^{2k+i+j}}{\partial x_1^{2k-2l+i}\,\partial x_2^{2l+j}}\int_{\xi_3}^{\infty}[\omega(s)]^{2k+i+j+1}\frac{ds}{\sqrt{Q(s)}} \tag{5}$$

and $Q(s)=s(s+a_1^2)(s+a_2^2)$. The components of displacement u_i and stress σ_{ij} in terms of f_α ($\alpha=1, 2, 3$) are given by

$$\begin{aligned}
u_1 &= (1-2\nu)(f_{1,3}+f_{3,1})-(3-4\nu)f_{1,3}+x_3(\nabla\cdot\hat{f})_{,1}\\
u_2 &= (1-2\nu)(f_{2,3}+f_{3,2})-(3-4\nu)f_{2,3}+x_3(\nabla\cdot\hat{f})_{,2}\\
u_3 &= -(1-2\nu)(f_{1,1}+f_{2,2})-2(1-\nu)f_{3,3}+x_3(\nabla\cdot\hat{f})_{,3}
\end{aligned} \tag{6}$$

and

$$\begin{aligned}
\sigma_{11} &= 2\mu[f_{3,11}+2\nu f_{3,22}-2f_{1,31}-2\nu f_{2,32}+x_3(\nabla\cdot\hat{f})_{,11}]\\
\sigma_{22} &= 2\mu[f_{3,22}+2\nu f_{3,11}-2f_{2,32}-2\nu f_{1,31}+x_3(\nabla\cdot\hat{f})_{,22}]\\
\sigma_{12} &= 2\mu[(1-2\nu)f_{3,12}-(1-\nu)(f_{1,23}+f_{2,13})+x_3(\nabla\cdot\hat{f})_{,12}]\\
\sigma_{33} &= 2\mu[-f_{3,33}+x_3(\nabla\cdot\hat{f})_{,33}]\\
\sigma_{31} &= 2\mu[-(1-\nu)f_{1,33}+\nu(f_{1,11}+f_{2,21})+x_3(\nabla\cdot\hat{f})_{,13}]\\
\sigma_{32} &= 2\mu[-(1-\nu)f_{2,33}+\nu(f_{1,12}+f_{2,22})+x_3(\nabla\cdot\hat{f})_{,23}]
\end{aligned} \tag{7}$$

with the notation

$$\nabla\cdot\hat{f}=f_{1,1}+f_{2,2}+f_{3,3} \tag{8}$$

where μ and ν are the shear modulus and Poisson's ratio.

By successive differentation, it can be shown from equation (5) that, since $\omega(\xi_3)=0$,

$$\begin{aligned}
F_{kl} &= \int_{\xi_3}^{\infty}\frac{\partial^{k+l}\omega^{k+l+1}}{\partial x_1^k\partial x_2^l}\frac{ds}{[Q(s)]^{1/2}}\\
&\equiv \int_{\xi_3}^{\infty}\partial_1^{k_1}\partial_2^{l_1}\partial_3^{m_1}\omega^{k+l+1}\frac{ds}{[Q(s)]^{1/2}}
\end{aligned} \tag{9}$$

wherein $(2k-2l+i)$ and $(2l+j)$ in equation (5) are replaced by k and l in equation (9) and $k_1=2k-2l+i$; $l_1=2l+j$, and $m_1=0$[1]; the notation ∂_α^l implies the jth partial derivative with respect to x_α.

We restrict our attention to the case of crack face weight functions. Since $x_3=0$ at the crack face, the crack face displacements are expressed by

$$\begin{aligned}
u_1 &= (1-2\nu)(f_{1,3}+f_{3,1})-(3-4\nu)f_{1,3}\\
u_2 &= (1-2\nu)(f_{2,3}+f_{3,2})-(3-4\nu)f_{2,3}\\
u_3 &= -(1-2\nu)(f_{1,1}+f_{2,2})-2(1-\nu)f_{3,3}
\end{aligned} \tag{10}$$

The first-order partial derivatives of F_{kl} with respect to x_β ($\beta=1, 2, 3$), which are needed in the evaluation of crack face displacements, can be expressed by

$$F_{kl,\beta}=\int_{\xi_3}^{\infty}\partial_1^{k_1}\partial_2^{l_1}\partial_3^{m_1}\omega^{k+l+1}\frac{ds}{[Q(s)]^{1/2}} \tag{11}$$

where

$$k_1=k+\delta_{1\beta} \quad l_1=l+\delta_{2\beta} \quad m_1=\delta_{3\beta} \tag{12}$$

and $\delta_{1\beta}$, etc., are the well-known Kronecker deltas.

It is now seen from equation (11) that one needs to evaluate a generic integral of the type:

[1]While $m_1=0$ in the integral on the extreme right-hand side of equation (9), such a notation is used to emphasize that this integral is a special case of a generic integral of the type given in equation (13).

Downloaded 03 May 2010 to 171.66.16.244. Redistribution subject to ASME license or copyright; see http://www.asme.org/terms/Terms_Use.cfm

$$\int_{\xi_3}^{\infty} \partial_1^{k_1}\partial_2^{l_1}\partial_3^{m_1}\omega^{k+l+1}\frac{ds}{[Q(s)]^{1/2}}. \tag{13}$$

To accomplish this, we expand ω^{k+l+1} in terms of x_α^2 and carry out the indicated differentiations term by term. Thus, we obtain:

$$\int_{\xi_3}^{\infty} \partial_1^{k_1}\partial_2^{l_1}\partial_3^{m_1}\omega^{k+l+1}\frac{ds}{[Q(s)]^{1/2}}$$
$$=(k+l+1)!\sum_{p=0}^{k+l+1}\sum_{q=0}^{p}\sum_{r=0}^{q}\frac{(-1)^p}{(k+l+1-p)!}$$
$$\times\frac{(2p-2q)!}{(p-q)!}\frac{(2q-2r)!}{(q-r)!}\frac{(2r)!}{(r)!}\frac{x_2^{2p-2q-k_1}}{(2p-2q-k_1)!}$$
$$\times\frac{x_2^{2q-2r-l_1}}{(2q-2r-l_1)!}\frac{x_3^{2r-m_1}}{(2r-m_1)!}J_{p-q,q-r,r}(\xi_3) \tag{14}$$

where

$$J_{p-q,q-r,r}(\xi_3)=\int_{\xi_3}^{\infty}\frac{ds}{(s+a_1^2)^{p-q}(s+a_2^2)^{q-r}(s+a_3^2)^r[Q(s)]^{1/2}}. \tag{15}$$

In general, the integral indicated in equation (15), for a given set of parameters p, q, r, can be evaluated in terms of incomplete elliptic integrals of the first and second kinds, and the Jacobian elliptic functions. The derivations of the closed-form expressions involves exorbitant work even for relatively lower-order components of $J_{p-q,q-r,r}$ (see Shah and Kobayashi, 1972). Therefore, the derivation of a systematic generic procedure for the evaluation of the elliptical integrals $J_{p-q,q-r,r}$ was important in the development of the VNA solution as well as its implementation in a computer program. A procedure for this has been developed by Nishioka and Atluri (1983) and is summarized as follows.

Equation (15) can be rewritten in terms of Jacobian elliptic functions as:

$$J_{p-q,q-r,r}=\frac{2}{a_1^{2p+1}}\int_0^{u_1}(sn^{2p}u)\,(nd^{2q-2r}u)(nc^{2r}u)\,du$$
$$\equiv\frac{2}{a_1^{2p+1}}L_{p,q-r,r} \tag{16}$$

for arbitrary values p, q, and r where

$$sn^2u_1=[a_1^2/(a_1^2+\xi_3)] \tag{17}$$

and (ndu) and (ncu) are defined in the following.

The following identities for Jacobian elliptic functions are used:

$$\mathrm{sn}^2u+\mathrm{cn}^2u=1 \quad k^2\mathrm{sn}^2u+\mathrm{dn}^2u=1$$
$$\mathrm{dn}^2u-k^2\mathrm{cn}^2u=k'^2 \quad k'^2\mathrm{sn}^2u+\mathrm{cn}^2u=\mathrm{dn}^2u$$
$$\mathrm{tn}u=\mathrm{sn}u/\mathrm{cn}u \quad \mathrm{dc}u=\mathrm{dn}u/\mathrm{cn}u \quad \mathrm{cd}u/\mathrm{cn}u$$
$$\mathrm{nd}u=1/\mathrm{dn}u \quad \mathrm{nc}u=1/\mathrm{cn}u \quad \mathrm{sd}u=\mathrm{sn}u/\mathrm{dn}u \tag{18a}$$

where

$$k^2=(a_1^2-a_2^2)/a_1^2 \quad k'^2=1-k^2. \tag{18b}$$

By using integration by parts in equation (16), one sees that:

$$L_{p,q-r,r}=\frac{1}{(2r-1)k'^2}\{(sn^{2p+1}u)\,(nc^{2r-1}u)\,(nd^{2q-2r-1}u)\,|_0^{u_1}$$
$$+[2(-p+r-1)+2(p-q-r+2)k^2]L_{p,q-r,r-1}$$
$$+k^2(-2p+2q-3)L_{p,q-r,r-2}\}. \tag{19}$$

Thus, one needs the starting values of $L_{p,q-r,r-1}$ and $L_{p,q-r,r-2}$ to evaluate $L_{p,q-r,r}$. The lowest-order starting values are:

$$L_{p,q,-1}=\int_0^{u_1}\mathrm{sn}^{2p}u\;\mathrm{nd}^{2q}u\;\mathrm{nc}^{-2}u\;du$$
$$L_{p,q,-2}=\int_0^{u_1}\mathrm{sn}^{2p}u\;\mathrm{nd}^{2q}u\;\mathrm{nc}^{-4}u\;du \tag{20}$$

These integrals can be reduced to the forms:

$$L_{p,q,-1}=\frac{1}{k^{2p+2}}\sum_{j=0}^{p}\sum_{\gamma=0}^{1}\frac{(-1)^{j+\gamma+1}k'^{2(1-\gamma)}p!}{(p-j)!j!(1-\gamma)!\gamma!}I_{2(q-j-\gamma)}$$
$$L_{p,q,-2}=\frac{1}{k^{2p+4}}\sum_{j=0}^{p}\sum_{\gamma=0}^{2}\frac{(-1)^{j+\gamma+2}k'^{2(2-\gamma)}p!2}{(p-j)!j!(2-\gamma)!\gamma!}I_{2(q-j-\gamma)} \tag{21}$$

where

$$I_{2m}=\int_0^{u_1}\mathrm{nd}^m u\;du \tag{22}$$

$$I_{2m+2}=\frac{2m(2-k^2)I_{2m}+(1-2m)I_{2m-2}-k^2\mathrm{sn}u_1\mathrm{cn}u_1\mathrm{nd}^{2m+1}u_1}{(2m+1)k'^2}. \tag{23}$$

For $(p-j-\gamma)<0$ in equation (21), we find $I_{-2m}=G_{2m}$, where

$$G_{2m+2}=\frac{k^2\mathrm{dn}^{2m-1}u_1\mathrm{sn}u_1\mathrm{cn}u_1+(1+2m)k'^2G_{2m-2}+2m(2-k^2)G_{2m}}{(2m+1)}. \tag{24}$$

Thus, finally we see that one needs the following starting values for evaluating the general terms of I_{2m+2} and G_{2m+2}:

$$I_0=G_0=F(u_1)=u_1$$
$$I_2=(1/k'^2)[E(u_1)-k^2\mathrm{sn}u_1\mathrm{cd}u_1]$$
$$G_2=E(u_1) \tag{25}$$

where $F(u_1)$ and $E(u_1)$ are incomplete elliptic integrals of the first and second kinds, respectively.

From the boundary conditions on the crack face ($\sigma_{3\alpha}=\sigma_{3\alpha}^o$), we can see that the potential function f_3 relates to normal loadings (mode I) and f_1 and f_2 relate to shear loadings (mixed modes of II and III).

Now, the coefficients C in the potential representation (as given in equation (4)) are related to the coefficients **A** in the prescribed crack face tractions (as given in equation (3)), by satisfying the crack face traction boundary conditions, which may be written as:

$$\sigma_{33}^{(0)}=2\mu(f_{3,11}+f_{3,22}) \tag{26a}$$
$$\sigma_{3\alpha}^{(0)}=2\mu[(1-\nu)(f_{\alpha,11}+f_{\alpha,22})+\nu(f_{1,1\alpha}+f_{2,2\alpha})];\ \alpha=1,2. \tag{26b}$$

In equation (26), $\sigma_{3\alpha}^{(0)}$ are prescribed crack face tractions as in equation (3); and fi are potential functions as given in equation (4). By comparing the coefficients of like powers in the polynomial series in the right and left-hand sides, respectively, of equation (26*a*) and (26*b*), one obtains the linear algebraic relation,

$$\mathbf{A}=\mathbf{B}\cdot\mathbf{C}$$
$$(N\times 1)(N\times N)\,(N\times 1) \tag{26c}$$

where N is the total number of coefficients in **A** or **C**.

Detailed expressions for the components of the matrix **B** are given in Nishioka and Atluri (1983) for mode I and mixed modes of II and III. A more convenient form for the mixed modes of II and III also can be found in Simon, O'Donoghue, and Atluri (1987). We rewrite the detailed expressions of equation (26*c*) for mode I for later use.

Downloaded 03 May 2010 to 171.66.16.244. Redistribution subject to ASME license or copyright; see http://www.asme.org/terms/Terms_Use.cfm

$$\sum_{i=0}^{1}\sum_{j=0}^{1}\{A^{(i,j)}_{3,m-n,n}\}$$
$$=\sum_{i=0}^{1}\sum_{j=0}^{1}\left\{2\mu\frac{(-1)^{m+i+j+1}}{(2m-2n+i)!(2n+j)!}\sum_{k=m}^{M}\sum_{l=0}^{k}(-1)^k\right.$$
$$\left.[I_1^{(i,j)}J_{L_1+1,L_2,0}(0)+I_2^{(i,j)}J_{L_1,L_2+1,0}(0)]C^{(i,j)}_{3,k-l,l}\right\}$$
$$m=0,1,\ldots,M$$
$$n=0,1,\ldots,m \tag{27}$$

where $L_1=(m-n+k-l+i)$, $L_2=n+l+j$

$$I_\alpha^{(i,j)}=\frac{(2k+i+j+1)!}{(k-m)!}\frac{(2L_1+2\delta_{1\alpha})!}{(L_1+\delta_{1\alpha})!}\frac{(2L_2+2\delta_{2\alpha})!}{(L_2+\delta_{2\alpha})!}\quad(\alpha=1,2).$$

Once the coefficients $\mathbf{C}$ are determined by solving equation (26) for given loadings on the crack surface, the stress intensity factors corresponding to these loads are computed from the following equation (Vijayakumar and Atluri, 1981):

$$K_I=8\mu\left(\frac{\pi}{a_1a_2}\right)^{1/2}a^{1/4}\sum_{i=0}^{1}\sum_{j=0}^{1}\sum_{k=0}^{M}\sum_{l=0}^{k}(-2)^{2k+i+j}(2k+i+j+1)!$$
$$\times\frac{1}{a_1a_2}\left(\frac{\cos\theta}{a_1}\right)^{2k-2l+i}\left(\frac{\sin\theta}{a_2}\right)^{2l+j}C^{(i,j)}_{3,k-l,l} \tag{28}$$

where θ is the elliptic angle and

$$a=a_1^2\sin^2\theta+a_2^2\cos^2\theta \tag{29}$$

for the mode I problem.

For the mixed-mode problem of modes II and III

$$K_{II}=8\mu\left(\frac{\pi}{a_1a_2}\right)^{1/2}a^{-1/4}\frac{1}{a_1a_2}[H_1a_2\cos\theta+H_2a_1\sin\theta] \tag{30}$$

$$K_{III}=8\mu\left(\frac{\pi}{a_1a_2}\right)^{1/2}a^{-1/4}\frac{(1-\nu)}{a_1a_2}[H_2a_2\cos\theta-H_1a_1\sin\theta], \tag{31}$$

in which

$$H_1=\sum_{i=0}^{1}\sum_{j=0}^{1}\sum_{k=0}^{M}\sum_{l=0}^{k}(-2)^{2k+i+j}(2k+i+j+1)!$$
$$\times\left(\frac{\cos\theta}{a_1}\right)^{2k-2l+i}\left(\frac{\sin\theta}{a_2}\right)^{2l+j}C^{(i,j)}_{1,k-l,l} \tag{32}$$

$$H_2=\sum_{i=0}^{1}\sum_{j=0}^{1}\sum_{k=0}^{M}\sum_{l=0}^{k}(-2)^{2k+2-i-j}(2k+3-i-j)!$$
$$\times\left(\frac{\cos\theta}{a_1}\right)^{2k-2l+1-i}\left(\frac{\sin\theta}{a_2}\right)^{2l+1-j}C^{(1-i,1-j)}_{2,k-l,l}. \tag{33}$$

The VNA solution has been implemented by Nishioka and Atluri (1981, 1983a) in a simple finite element alternating method for the solution of problems of embedded or surface flaws in complex structural geometries. The alternating method has also been successfully applied to the problem of semi-elliptical surface flaws in plates subjected to tension and bending (Nishioka and Atluri (1981, 1983a)), semi-elliptical surface flaws in the meridonal direction at the outer and inner surfaces of pressurized thick and thin cylindrical vessels (Nishioka and Atluri (1982)), quarter-elliptical surface flaws emanating from pin holes in attachment lugs (Nishioka and Atluri (1983b)), *multiple* coplanar embedded elliptical flaws in an infinite solid subject to arbitrary crack face tractions (O'Donoghue, Nishioka, and Atluri (1985)), and *multiple* semi-elliptical surface flaws in the meridonal as well as circumferential directions in cylindrical pressure vessels (O'Donoghue, Nishioka, and Atluri (1984a, 1984b)).

3 Detailed Expressions for the Crack Face Displacements

For simplicity, we treat here only the mode I case. Then, the crack face displacement, u_3, due to the mode I normal loading, can be expressed as follows:

$$u_3=-2(1-\nu)f_{3,3}$$
$$=-2(1-\nu)\sum_{i=0}^{1}\sum_{j=0}^{1}\sum_{k=0}^{M}\sum_{l=0}^{k}C^{(i,j)}_{3,k-l,l}(F_{2k-2l+i,2l+j}),_3$$
$$\equiv\mathbf{U}^T\cdot\mathbf{C} \tag{34}$$

Each component in the vector $\mathbf{U}$ can be evaluated by equations (11) and (14) using $k_1=2k-2l+i$, $l_1=2l+j, m_1=1$. This can be expressed by

$$U_n=-2(1-\nu)(2k+i+j+1)!$$
$$\times\sum_{p=0}^{2k+i+j+1}\sum_{q=0}^{p}\sum_{r=1}^{q}\frac{(-1)^p}{(2k+i+j+1-p)!}$$
$$\times\frac{(2p-2q)!}{(p-q)!}\frac{(2q-2r)!}{(q-r)!}\frac{(2r)!}{(r)!}\frac{x_1^{2(p-q-k+l)-i}}{\{2(p-q-k+l)-i\}!}$$
$$\times\frac{x_2^{2(q-r-l)-j}}{\{2((q-r-l)-j)\}!}\frac{x_3^{2r-1}}{(2r-1)!}J_{p-q,q-r,r}(0) \tag{35}$$

where

$$n=1,2,3,\ldots,N;\quad l=0,1,\ldots k;$$
$$k=0,1,\ldots,M\ ;\quad j=0,1\ \ ;\quad i=0,1.$$

Note that the term with $r=0$ was eliminated in equation (35), since $\partial x_3^0/\partial x_3=0$.

Because of the singular nature of $J_{p-q,q-r,r}(0)$ when $r\geq 1$, special care should be exercised in the evaluation of $x_3^{2r-1}J_{p-q,q-r,r}(0)$. To this end, the following relations (Green and Sneddon, 1950) may be utilized:

$$x_3=(\xi_1\xi_2\xi_3)^{1/2}/(a_1a_2) \tag{36}$$

$$\xi_1\xi_2=a_1^2a_2^2\left(1-\frac{x_1^2}{a_1^2}-\frac{x_2^2}{a_2^2}\right). \tag{37}$$

Using equations (36) and (37) and (16)-(19) in $x_3^{2r-1}J_{p-q,q-r,r}(0)$, and taking the limits as $\xi_3\to 0$, the displacement functions given by equation (35) can be rewritten as

$$U_n=-2(1-\nu)(2k+i+j+1)!$$
$$\sum_{p=0}^{2k+i+j+1}\sum_{q=0}^{p}\sum_{r=1}^{q}\frac{(-1)^p}{(2k+i+j+1-p)!}$$
$$\times\frac{(2p-2q)!}{(p-q)!}\frac{(2q-2r)!}{(q-r)!}\frac{(2r)!}{(r)!}\frac{x_1^{2p-2q-2k+2l-i}}{(2p-2q-2k+2l-i)!}$$
$$\times\frac{x_2^{2q-2r-2l-j}}{(2q-2r-2l-j)!}\frac{1}{(2r-1)!}\frac{2}{(2r-1)}a_1^{p_1}a_2^{p_2}$$
$$\times\left(1-\frac{x_1^2}{a_1^2}-\frac{x_2^2}{a_2^2}\right)^{r-(1/2)} \tag{38}$$

where

$$p_1=-2p+2q-1\ \text{ and }\ p_2=-2q+2r-1. \tag{39}$$

If the coefficients $\mathbf{C}$ are determined by solving equation (26) for given loadings on the crack surface, the crack face displacement can be evaluated by the following equation:

$$U_3=-2(1-\nu)\sum_{i=0}^{1}\sum_{j=0}^{1}\sum_{k=0}^{M}\sum_{l=0}^{k}C^{(i,j)}_{3,k-l,l}(2k+i+j+1)!$$
$$\sum_{p=0}^{2k+i+j+1}\sum_{q=0}^{p}\sum_{r=1}^{q}\frac{(-1)^p}{(2k+i+j+1-p)!}\frac{(2p-2q)!}{(p-q)!}$$

Downloaded 03 May 2010 to 171.66.16.244. Redistribution subject to ASME license or copyright; see http://www.asme.org/terms/Terms_Use.cfm

$$\times\frac{(2q-2r)!}{(q-r)!}\frac{(2r)!}{(r)!}\frac{x_1^{2p-2q-2k+2l-i}}{(2p-2q-2k+2l-i)!}\frac{x_2^{2q-2r-2l-j}}{(2q-2r-2l-j)!}$$
$$\times\frac{1}{(2r-1)!}\frac{2}{(2r-1)}a_1^{p1}a_2^{p2}\left(1-\frac{x_1^2}{a_1^2}-\frac{x_2^2}{a_2^2}\right)^{r-(1/2)}. \quad (40)$$

4 The First-Order Variation of Crack Face Displacement Field Due to Geometrical Changes in the Shape of an Elliptical Crack

Here we consider two specific types of geometrical variations in the shape of an elliptical crack as shown in Fig. 1. Thus, the shapes of the crack after these variations are also elliptical, such that

$$x_1^2/(a_1+\delta_{1\alpha}\delta a_1)^2+x_2^2/(a_2+\delta_{2\alpha}\delta a_2)^2=1 \quad (\alpha=1,2) \quad (41)$$

where δa_α is the variation in the length of the major axis ($\alpha = 1$) or minor axis ($\alpha = 2$). The first-order variation of u_3 due to the variation of δa_α is given by

$$\delta_\alpha u_3=\frac{\partial u_3}{\partial a_\alpha}\delta a_\alpha \ (\alpha=1,2\text{: no sum on }\alpha). \quad (42)$$

Therefore, to evaluate the first-order variation $\delta_\alpha u_3$, we need to evaluate $\partial u_3/\partial a_\alpha$. However, it should be noted that not only $\mathbf{U}^T$ but also $\mathbf{C}$ are functions of a_α ($\alpha = 1, 2$).

Differentiating both sides of equation (34), with respect to a_α ($\alpha = 1, 2$), we have

$$\frac{\partial u_3}{\partial a_\alpha}=\frac{\partial U^T}{\partial a_\alpha}\bullet\mathbf{C}+\mathbf{U}^T\bullet\frac{\partial\mathbf{C}}{\partial a_\alpha} \ (\alpha=1,2). \quad (43)$$

For any *given* polynomial loading expressed in terms of the coefficients $\mathbf{A}$ as given in equation (3), the coefficients $\mathbf{C}$ for the potential functions which lead to analytical solution are determined by solving the linear equations (27). Differentiating both sides of equation (26), with respect to a_α ($\alpha = 1, 2$), we have[2]

$$\frac{\partial\mathbf{B}}{\partial a_\alpha}\bullet\mathbf{C}+\mathbf{B}\bullet\frac{\partial\mathbf{C}}{\partial a_\alpha}=\frac{\partial\mathbf{A}}{\partial a_\alpha}\equiv 0 \ (\alpha=1,2). \quad (44)$$

Therefore, $\partial\mathbf{C}/\partial_{a_\alpha}$ can be expressed by

$$\frac{\partial\mathbf{C}}{\partial a_\alpha}=-\mathbf{B}^{-1}\bullet\frac{\partial\mathbf{B}}{\partial a_\alpha}\bullet\mathbf{C} \ (\alpha=1,2). \quad (45)$$

Substituting equation (45) into equation (43), we obtain the following expression:

$$\frac{\partial u_3}{\partial a_\alpha}=\left(\frac{\partial\mathbf{U}^T}{\partial a_\alpha}-\mathbf{U}^T\mathbf{B}^{-1}\frac{\partial\mathbf{B}}{\partial a_\alpha}\right)\mathbf{C} \ (\alpha=1,2). \quad (46)$$

Now, we need to evaluate $\partial\mathbf{U}^T/\partial a_\alpha$ and $\partial\mathbf{B}/\partial a_\alpha$. Each component of $\partial\mathbf{U}^T/\partial a_\alpha$ can be obtained by directly differentiating equation (38), as

$$\frac{\partial U_n}{\partial a_\alpha}=-2(1-\nu)(2k+i+j+1)!\sum_{p=0}^{2k+i+j+1}\sum_{q=0}^{p}\sum_{r=1}^{q}$$
$$\times\frac{(-1)^p}{(2k+i+j+1-p)!}\frac{(2p-2q)!}{(p-q)!}\frac{(2q-2r)!}{(q-r)!}\frac{(2r)!}{(r)!}$$
$$\times\frac{x_1^{2p-2q-2k+2l-i}}{(2p-2q-2k+2l-i)!}\frac{x_2^{2q-2r-2l-j}}{(2q-2r-2l-j)!}\frac{1}{(2r-1)!}$$
$$\times\frac{2}{(2r-1)}a_1^{p1}a_2^{p2}\left(1-\frac{x_1^2}{a_1^2}-\frac{x_2^2}{a_2^2}\right)^{r-(1/2)}\frac{p_\alpha}{a_\alpha}$$
$$\times\left\{1+\frac{x_\alpha^2(2r-1)}{a_\alpha^2 p_\alpha}\Big/\left(1-\frac{x_1^2}{a_1^2}-\frac{x_2^2}{a_2^2}\right)\right\}. \quad (47)$$

From equation (27) it is seen that the components of $\partial\mathbf{B}/\partial a_\alpha$ involve the evaluation of $\partial\{J_{L_1+1,L_2,0}(0)\}/\partial a_\alpha$ and $\partial\{J_{L_1,L_2+1,0}(0)\}/\partial a_\alpha$. Therefore, to evaluate equation (46) it is crucial to develop a systematic general procedure for the evaluation of the partial derivatives of the generic elliptic integrals with respect to a_α, i.e., $\partial\{J_{p-q,q-r,r}(0)\}/\partial a_\alpha$.

[2]Note that the crack face loading is held fixed while the crack shape undergoes a virtual change.

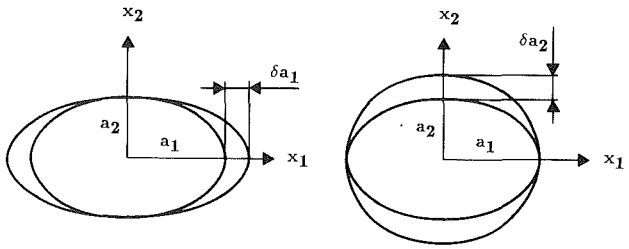


Fig. 1 Geometrical variations of an elliptical crack due to the major or minor axis variations

5 A Systematic Procedure for the Evaluation of the Partial Derivatives of the Elliptic Integrals with Respect to a_α ($\alpha = 1,2$)

Although the partial derivatives of $J_{p-q,q-r,r}$ with respect to a_α can be obtained through a term-by-term differentiation of equations (16)–(25), this involves an exorbitant manipulation of elliptic integrals. Therefore, we attempt here to derive simpler formulae.

By direct differentiation of the original expression of the generic elliptic integrals, equation (15), with respect to a_α ($\alpha = 1, 2$), we have

$$\frac{\partial\{J_{p-q,q-r,r}(\xi_3)\}}{\partial a_\alpha}$$
$$=\frac{\partial}{\partial a_\alpha}\int_{\xi_3}^{\infty}\frac{ds}{(s+a_1^2)^{p-q}(s+a_2^2)^{q-r}(s+a_3^2)^r\sqrt{Q(s)}}$$
$$=p_\alpha a_\alpha\int_{\xi_3}^{\infty}\frac{ds}{(s+a_1^2)^{p-q+\delta 1\alpha}(s+a_2^2)^{q-r+\delta 2\alpha}(s+a_3^2)^r\sqrt{Q(s)}}$$
$$-\left[\frac{1}{(s+a_1^2)^{p-q}(s+a_2^2)^{q-r}(s+a_3^2)^r\sqrt{Q(s)}}\right]_{s=\xi_3}\frac{\partial\xi_3}{\partial a_\alpha}. \quad (48)$$

In equation (48), the integral in the first term on the right-hand side can be simply expressed in terms of the generic elliptic integral, as $J_{p-q+\delta 1\alpha,q-r+\delta 2\alpha,r}$.

The partial derivatives of ξ_β ($\beta = 1, 2, 3$), with respect to a_α ($\alpha = 1, 2$), are obtained from equation (2) as follows:

$$\frac{\partial\omega(\xi_\beta)}{\partial a_\alpha}=\frac{2a_\alpha x_\alpha^2}{(a_\alpha^2+\xi_\beta)^2}+\left[\frac{\partial\omega(s)}{\partial s}\right]_{s=\xi_\beta}\frac{\partial\xi_\beta}{\partial a_\alpha}=0. \quad (49)$$

The expression for $\omega(s)$ in equation (2) may be written in the alternate form:

$$\omega(s)=P(s)/Q(s) \quad (50)$$

where

$$P(s)=(s-\xi_1)(s-\xi_2)(s-\xi_3) \text{ and } Q(s)=s(s+a_1^2)(s+a_2^2). \quad (51)$$

Using equation (50), we have

$$\left[\frac{\partial\omega(s)}{\partial s}\right]_{s=\xi_\beta}=\frac{P'(\xi_\beta)}{Q(\xi_\beta)}. \quad (52)$$

Thus, substituting equation (52) into equation (49), one obtains the following relations:

$$\frac{\partial\xi_\beta}{\partial a_\alpha}=-\frac{2a_\alpha x_\alpha^2 Q(\xi_\beta)}{(a_\alpha^2+\xi_\beta)^2P'(\xi_\beta)}. \quad (53)$$

Using equation (53) for $\beta = 3$, equation (48) reduces to

Downloaded 03 May 2010 to 171.66.16.244. Redistribution subject to ASME license or copyright; see http://www.asme.org/terms/Terms_Use.cfm

$$\frac{\partial\{J_{p-q,q-r,r}(\xi_3)\}}{\partial a_\alpha} = p_\alpha a_\alpha J_{p-q+\delta_{1\alpha},q-r+\delta_{2\alpha},r}(\xi_3)$$

$$+\frac{2a_\alpha x_\alpha^2\sqrt{Q(\xi_3)}}{(a_1^2+\xi_3)^{p-q+2\delta_{1\alpha}}(a_2^2+\xi_3)^{q-r+2\delta_{2\alpha}}(a_3^2+\xi_3)^r P'(\xi_3)}. \quad (54)$$

Along the crack surface $\xi_3 = 0$, i.e., the region inside the ellipse (1) in the plane $x_3 = 0$, the second term on the r.h.s. in equation (54) vanishes when $r = 0$, since $\sqrt{Q(0)} = 0$. Thus, one obtains

$$\frac{\partial\{J_{p-q,q,0}(0)\}}{\partial a_\alpha} = a_\alpha p_\alpha J_{p-q+\delta_{1\alpha},q+\delta_{2,0}}(0). \quad (55)$$

Therefore, the derivatives of the generic elliptic integrals, required for the evaluation of $\partial\mathbf{B}/\partial a_\alpha$, can be simply evaluated through the same procedures as given by equations (16)–(25), using parameters that are higher by one order.

6 A Weight Function Method for Elliptical Crack Problems (a Two-Parameter Model)

Here we consider, for simplicity, only mode I problems of planar cracks in three-dimensional isotropic elastic solids. Suppose that the cracked solid is subjected to a reference loading[3] with tractions t_i^R at S_t and body forces f_i^R in V; S_t is the surface where tractions are applied and V is the volume of the solid. The stress intensity factor variation along the crack front Γ_c is denoted by K_I^R under this reference loading.

For any arbitrary loading with t_i on S_t and f_i in V, Rice (1972) has derived the relation

$$\int_{\Gamma_c}\frac{2}{H}[K_I K_I^R \delta l]d\Gamma = \int_{S_t} t_i \delta_l u_i^R dS + \int_V f_i \delta_l u_i^R dV \quad (56)$$

where K_I is the stress intensity factor variation along Γ_c under the loading of t_i and f_i; H is an appropriate elastic modulus ($H = E/(1-\nu^2)$ for plane strain). δl is a smooth function along Γ_c denoting the infinitesmal advance of the crack in a direction locally normal to the crack front contour Γ_c in the plane of the crack; $\delta_l u_i^R$ will denoted the first-order variation in u_i^R due to a geometrical change in the crack front.

Here our objective is to discuss *crack face* weight functions for embedded or surface cracks of the elliptical geometry, i.e., we treat S_t to be the crack face S_c in equation (56) and ignore the body forces. For surface or corner flaws of semi- or quarter-elliptical geometry, respectively, engineering theories of fatigue crack growth are often based on the consideration of K factors at the major and minor axis locations (i.e., at $x_1 = a_1$, $x_2 = 0$ and at $x_1 = 0$, $x_2 = a_2$), respectively. (See points (1) and (2) in Fig. 2.)

Thus, one often thinks of a two-parameter characterization of the K-factor variation along the crack front, for the given arbitrary loading. In this case, equation (56) reduces to

$$\frac{2}{H}\int_{\Gamma_c}[K_I K_I^R \delta l_\alpha(\theta)]d\Gamma = \int_{S_c}\sigma_{33}\delta_\alpha u_3^R dS \ (\alpha = 1,2) \quad (57)$$

where $\delta l_\alpha(\theta)$ $(\alpha = 1,2)$, for the presently considered variations in the lengths of the major and minor axes of the ellipse as shown in Fig. 1, are given by

$$\delta l_\alpha(\theta) = \delta a_\alpha f_\alpha(\theta) \quad (58a)$$

and

$$f_1(\theta) = a_2\cos^2\theta/(a_1^2\sin^2\theta + a_2^2\cos^2\theta)^{1/2}. \quad (58b)$$

$$f_2(\theta) = a_1\sin^2\theta/(a_1^2\sin^2\theta + a_2^2\cos^2\theta)^{1/2}. \quad (58c)$$

[3]Without loss of generality, we may consider S_t to be the crack surface alone. Even when the loading is at the far-field, one may use the principle of superposition to reduce the problem to a complementary one involving crack face loading alone.

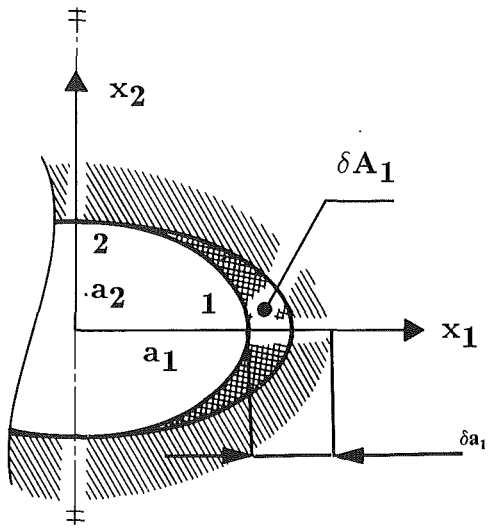


Fig. 2(*a*) Embedded crack; two parameter crack model and definitions of stress intensity factors. The shaded area δA_1, is the change in crack surface area due to a change in the length of major axis of magnitude δa_1. Likewise, δA_2 corresponds to a change in crack surface area due to a change δa_2 in the length of the minor axis.

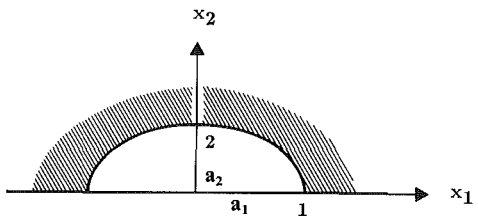


Fig. 2(*b*) Surface crack

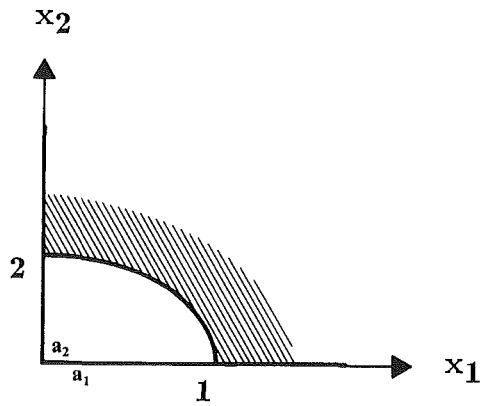


Fig. 2(*c*) Corner crack

The crack surface S_c can be partitioned into the upper and lower crack surfaces ($S_c = S_c^+ + S_c^-$). If only the upper surface is used, using equations (42) and (58), equation (57) reduces to

$$\frac{1}{H}\int_{I_c}[K_I K_I^R f_\alpha(\theta)]d\Gamma = \int_{S_c^+}\sigma_{33}\frac{\partial u_3^R}{\partial a_\alpha}dS \ (\alpha = 1,2). \quad (59)$$

The aforementioned two-parameter model is considered to be the simplest worthwhile approximation of a three-dimensional crack problem, since it does permit some change of crack shape during its propagation and promises a relative ease of application.

There are two alternative approaches for the two-parameter characterization. The alternatives are illustrated in Fig. 2 as being "local" involving the stress intensity factor magnitudes K_{I1} and K_{I2} at the location of the major and minor axis end

Downloaded 03 May 2010 to 171.66.16.244. Redistribution subject to ASME license or copyright; see http://www.asme.org/terms/Terms_Use.cfm

points of the elliptical or part elliptical flaw, or as being "local weighted average," involving averaged values of the stress intensity factors along specified portions of the crack front, $\bar{K}_1$ and $\bar{K}_2$. (See Fig. 2 for definitions of $\bar{K}_1$ and $\bar{K}_2$.) The weight functions for weighted average stress intensity factors have been defined by Besuner (1976), and used for residual life estimates of complex structures (Besuner, 1976; and Cruse and Besuner, 1975).

The weight function approach for the "weighted average" stress intensity factors can be shown (Besuner (1976)) to lead to:

$$\bar{K}_\alpha = \int_{S_c^+} \sigma_{33} \bar{h}_\alpha dS \ (\alpha = 1,2) \tag{60}$$

where the weight functions are given by

$$\bar{h}_\alpha = \frac{H}{\bar{K}_\alpha^R} \frac{4a_\alpha}{\pi a_1 a_2} \frac{\partial u_3^R}{\partial a_\alpha} \ (\alpha = 1,2) \tag{61}$$

and $\bar{K}_\alpha^R$ are the average stress intensity factors for the reference loading. The definitions of $\bar{K}_\alpha$ are also given in Fig. 2.

As seen from equation (61) the weight functions are easily evaluated by knowing $\partial u_3^R/\partial a_\alpha$ ($\alpha = 1, 2$), the analytical expressions for which are given in the previous sections.

So far to our knowledge, no attempts have been made to extract the weight functions for the local stress intensity factors at point 1 and 2. This will be given in the following.

For this purpose we introduce a trial function for the normalized stress intensity factor, $F_I(\theta)[= K_I(\theta)/K_I^R(\theta)]$, written in terms of its values at points 1 and 2, and denoted as

$$F_I(\theta) = F_{I1} N_1(\theta) + F_{I2} N_2(\theta) \tag{62}$$

where $N_\alpha(\theta)$ ($\alpha = 1, 2$) are some assumed shape functions which have a unit value at point α ($\alpha = 1$ or 2) and zero at the other point, and θ is the elliptic angle ($\theta = 0$ at point 1 and $\theta = \frac{\pi}{2}$ at point 2).

Introducing equation (62) into (59), one obtains the following linear equations:

$$W_{\alpha\beta} F_{I\beta} = R_\alpha \ (\alpha,\beta = 1,2) \tag{63}$$

where

$$W_{\alpha\beta} = \frac{1}{H} \int_{\Gamma_c} (K_I^R)^2 f_\alpha(\theta) N_\beta(\theta) d\Gamma \ (\alpha,\beta = 1,2) \tag{64}$$

$$R_\alpha = \int_{S_c^+} \sigma_{33} \frac{\partial u_3^R}{\partial a_\alpha} dS \ (\alpha = 1,2). \tag{65}$$

Equation (63) can be solved for $F_{I\beta}$. Noting that ($F_{I\beta} = K_{I\beta}/K_{I\beta}^R$; $\beta = 1, 2$), one has

$$K_{I\alpha} = \int_{S_c^+} \sigma_{33} \, h_{I\alpha} dS \ (\alpha = 1,2). \tag{66}$$

where $h_{I\alpha}$ ($\alpha = 1, 2$) are the weight functions for the local stress intensity factor at point α ($\alpha = 1, 2$). The weight functions are given by

$$\begin{aligned} h_{I1} &= \frac{K_{I1}^R}{|W_{\alpha\beta}|} \left(W_{22} \frac{\partial u_3^R}{\partial a_1} - W_{12} \frac{\partial u_3^R}{\partial a_2} \right) \\ h_{I2} &= \frac{K_{I2}^R}{|W_{\alpha\beta}|} \left(W_{11} \frac{\partial u_3^R}{\partial a_2} - W_{21} \frac{\partial u_3^R}{\partial a_1} \right) \end{aligned} \tag{67a}$$

and

$$|W_{\alpha\beta}| = W_{11} W_{22} - W_{12} W_{21}. \tag{68}$$

7 Numerical Examples

The analytical solutions for the derivatives of the crack face displacements with respect to the lengths of the major and minor axes of elliptical crack were implemented in a computer program to construct the weight functions of the weighted averages of stress intensity factors, as given in equation (61). To check the validity of the present solution procedure and the computer program, a simple numerical test was conducted. We consider an elliptical crack ($a_1 = 2.0$, $a_2 = 1.0$) in an infinite solid (Young's modulus $E = 1.0$, Poisson's ratio $\nu = 0.3$). The crack faces are subjected to normal stresses of the type (*i*) $\sigma_{33}^{(0)} = -p_o$ and (*ii*) $\sigma_{33}^{(0)} = -p_o x_1$. The constant pressure loading on the crack faces was also chosen as the reference loading for the weight function method. For the reference load of constant crack face pressure, $\partial u_3^R/\partial a_\alpha$ at S_c^+ was evaluated as per details given in Sections 4 and 5.

Table 1 Numerical results obtained by the ordinary Gaussian quadrature, for the problem (*i*) $\sigma_{33}^{(0)} = -p_o$

	8×8 Gauss	10×10 Gauss	15×15 Gauss	20×20 Gauss
$\bar{K}_1$	1.1349 (−3.7)	1.1431 (−3.0)	1.1543 (−2.0)	1.1600 (−1.5)
$\bar{K}_2$	1.3106 (−5.3)	1.3246 (−4.3)	1.3438 (−2.9)	1.3536 (−2.2)

( ): error percent
$\bar{K}_1$ (exact) = 1.7179
$\bar{K}_2$ (exact) = 1.3840

Table 2 Numerical results obtained by a singular quadrature (8×8 integration points)

	Problem (*i*) $\sigma_{33}^{(0)} = -p_o$	Problem (*ii*) $\sigma_{33}^{(0)} = -p_o x_1$
$\bar{K}_1$ (W.F.M.) (% Error)	1.1779 (0.0)	1.5844 (1.4)
$\bar{K}_2$ (W.F.M.) (% Error)	1.3840 (0.0)	1.0380 (1.1)
$\bar{K}_1$ (exact)	1.1779	1.5624
$\bar{K}_2$ (exact)	1.3840	1.0264

The "average" K-factors for the two considered load cases were computed by numerically evaluating the integral in equation (60). The numerical results obtained by using ordinary Gaussian quadrature for evaluating the integral in equation (60), for the problem (*i*) are listed in Table 1. Due to the singularity in the weight functions along the crack border (see equation (47)), somewhat large numerical errors were found in the results obtained through lower-order quadrature. The accuracy improved with increasing integration order.

To account for the singularity in the weight functions along the crack border, a singular quadrature based on appropriate coordinate transformations was developed. Numerical results obtained by this singular quadrature with 8 × 8 integration points are listed in Table 2. Fairly good results were obtained even with a small number of integration points.

We briefly comment on the application of the present methodology to surface flaws. Suppose S_c represents the area of a part-elliptical crack near the surface of a structure. The weight functions would be evaluated from a reference state of loading, say constant pressure, on the crack face. The finite element *alternating* method (Nishioka and Atluri (1983)), based on a superposition of (*i*) the VNA analytical solution for an embedded crack (subjected to arbitrary tractions) in an infinite solid (Sections 2 and 3) and (*ii*) a finite element solution of the *uncracked* solid subjected to varying residual tractions at the boundaries of the finite solid, is used *iteratively* to solve for the surface flaw problem until convergence is achieved. The end result of the finite element–alternating method is the *converged solution*[4] for parameters C in the displacement field,

[4]For a detailed discussion of the properties of convergence, and accuracy of the alternating method for surface flaws, the reader is referenced to Atluri (1986).

Downloaded 03 May 2010 to 171.66.16.244. Redistribution subject to ASME license or copyright; see http://www.asme.org/terms/Terms_Use.cfm

equation (40), for the surface flaw under the reference loading. Using these results for **C** in equation (46), (61), and (67), the weight functions for a two-parameter model of the surface flaw can be determined.

Acknowledgment

This work was supported by ONR, with Dr. Y. Rajapakse as the program official. The authors also thank Ms. Deanna Winkler and Ms. Brenda Bruce for their assistance.

References

Atluri, S. N., ed., 1986, *Computational Methods in the Mechanics of Fracture*, North-Holland Publishing Co.

Besuner, P. M., 1976, "Residual Life Estimates for Structures with Partial Thickness Cracks," *Mechanics of Crack Growth*, ASTM-STP-590, pp. 403–419.

Bortmas, Y., and Banks-Sills, L., 1983, "An Extended Weight Function Method for Mixed-Mode Elastic Crack Analysis," ASME JOURNAL OF APPLIED MECHANICS, Vol. 50, pp. 907–909.

Bueckner, H. F., 1971, "Weight Functions for a Notched Bar," *Z. Anqeq. Mathem. a Mech.*, Vol. 51, pp. 97–107.

Bueckner, H. F., 1987, "Weight Functions and Fundamental Fields for Penny-Shaped and the Half-Plane Crack in Three-Space," *Int. Jrl. Solids and Structures*, Vol. 23, pp. 57–93.

Cruse, T., and Besuner, P. M. 1975, "Residual Life Prediction for Surface Cracks in Complex Structural Details," *J. Aircraft*, Vol. 12, pp. 369–375.

Gao, H., and Rice, J. R., 1986, "Shear Stress Intensity Factors for a Planar Crack with Slightly Curved Crack-Front," ASME JOURNAL OF APPLIED MECHANICS, Vol. 53, pp. 774–778.

Green, A. E., and Sneddon, J. N., 1950, "The Distribution of Stress in the Neighborhood of a Flat Elliptical Crack in an Elastic Solid," *Philosophical Society*, Vol. 46, pp. 159–164.

Kassir, M. K., and Sih,G. C., 1966, "Three-Dimensional Stress Distribution Around an Elliptical Crack Under Arbitrary Loadings," ASME JOURNAL OF APPLIED MECHANICS, Vol. 33, pp. 601–611.

Nishioka, T., and Atluri, S. N., 1981, "A Major Development Towards a Cost-Effective Alternating Method for Fracture Analysis of Steel Reactor Pressure Vessels," *Trans. 67th Int. Conf. on Structural Mechanics in Reactor Technology*, Paper No. G-1/2, Paris.

Nishioka, T., and Aluri, S. N., 1982, "Analysis of Surface Flaws in Pressure Vessels by a New 3-Dimensional Alternating Method," ASME *Journal of Vessel Technology*, Vol. 104, pp. 229–307.

Nishioka, T., and Atluri, S. N., 1983a, "Analytical Solution for Embedded Elliptical Cracks, and Finite Element Alternating Method for Elliptical Surface Cracks, Subjected to Arbitrary Loadings," Engng. Fracture Mech., Vol. 17, pp. 247–268.

Nishioka, T., and Atluri, S. N., 1983b, "An Alternating Method for Analysis of Surface Flawed Aircraft Structural Components," *AIAA Journal*, Vol. 21, pp. 749–757.

O'Donoghue, P. E., Nishioka, T., and Atluri, S. N., 1984a, "Multiple Surface Flaws in Pressure Vessels," *Engng. Fracture Mechanics*, Vol. 20, pp. 545–560.

O'Donoghue, P. E., Nishioka, T., and Atluri, S. N., 1984b, "Analysis of Interaction Behavior of Surface Flaws in Pressure Vessels," *Computational Fracture Mechanics—Nonlinear and 3-D Problems*, PVP Vol. 85, AMD Vol. 6, P. D. Hilton and L. N. Gifford, eds., ASME, New York, pp. 77–92.

O'Donoghue, P. E., Nishioka, T., and Atluri, S. N., 1985, "Multiple Coplanar Embedded Elliptical Cracks in an Infinite Solid Subject to Arbitrary Crack Tractions", *Int. J. Numer. Meth. in Engng.*, Vol. 21, pp. 437–449.

Rice, J. R., 1972, "Some Comments on Elastic Crack-Tip Fields," *Int. J. Solids Struct.*, Vol. 8, pp. 751–758.

Rice, J. R., 1985, "First Order Variations in Elastic Fields Due to Variations in Location of a Planar Crack Front," Vol. 52, pp. 571–579.

Segedin, C. M., 1967, "Some Three-Dimensional Mixed Boundary-Value Problems in Elasticity," Report 67-3, Department of Aeronautics and Astronautics, University of Washington.

Shah, R. C., and Kobayashi, A. S., 1971, "Stress Intensity Factor for an Elliptical Crack Under Arbirtrary Normal Loading," *Engineering Fracture Mechanics*, Vol. 3, pp. 71–96.

Shah, R. C., and Kobayashi, A. S., 1972, "On the Surface Flow Problem," *The Surface Crack: Physical Problems and Computational Solution*, J. L. Swedlow, ed., The ASME, New York, pp. 79–124.

Sham, T. L., 1987, "A Unified Finite Element Method for Determining Weight-Functions in Two and Three-Dimensions," *Int. Journal Solids and Structures*, Vol. 23, pp. 1357–1372.

Sham, T. L., and Zhou, Y., 1988, "Computation of Three-Dimensional Weight Functions for Circular and Elliptical Cracks," *Int. Jrl. of Fract.*, submitted for publication.

Simon, H. L., O'Donoghue, P. E., and Atluri, S. N., 1987, "A Finite-Element Alternating Technique for Evaluating Mixed Modes Stress Intensity Factors for Part-Elliptical Surface Flaws," *Int. J. for Num. Meth. in Engng.*, Vol. 24, pp. 689–709.

Vijayakumar, K., and Atluri, S. N., 1981, "An Embedded Elliptical Flaw in an Infinite Solid, Subject to Arbitrary Crack-Face Tractions," ASME JOURNAL OF APPLIED MECHANICS, Vol. 48, pp. 88–96.

Downloaded 03 May 2010 to 171.66.16.244. Redistribution subject to ASME license or copyright; see http://www.asme.org/terms/Terms_Use.cfm

Crack Extension Force in a Piezoelectric Material

Y. Eugene Pak
Grumman Corporate Research Center,
Bethpage, NY 11714
Mem. ASME

A conservation law that leads to a path-independent integral of fracture mechanics is derived along with the governing equations and boundary conditions for linear piezoelectric materials. A closed-form solution to the antiplane fracture problem is obtained for an unbounded piezoelectric medium. The path-independent integral is evaluated at the crack tip to obtain the energy release rate for a mode III fracture problem. For a fixed value of the mechanical load, it is shown that the crack growth can be either enhanced or retarded depending on the magnitude, the direction, and the type of the applied electrical load. It is also shown that, for certain ratios of the applied electrical load to mechanical load, crack arrestment can be observed.

Introduction

It is well known that piezoelectric materials produce an electric field when deformed and undergo deformation when subjected to an electric field. Due to this intrinsic coupling phenomenon, piezoelectric materials are used widely in technology such as high power sonar transducers, electromechanical actuators, and piezoelectric power supplies. When subjected to mechanical and electrical stresses in service, these piezoelectric materials can fail prematurely due to the propagation of flaws or defects produced during their manufacturing process. Therefore, it is important that the fracture processes in piezoelectric materials be understood and analyzed so that reliable service lifetime predictions of the components can be made. This paper attempts to provide a better understanding of the mechanics of piezoelectric materials in the presence of defects such as cracks. Although extensive studies have been made in wave propagation and plate vibrations of piezoelectric materials, relatively few studies have been made in defect mechanics of such materials. Parton (1976) has considered the problem of a finite crack at the interface of a piezoelectric material and a conductor subjected to a far-field uniform tension. More general defect mechanics of piezoelectric material was considered by Deeg (1980) using Green's function method and modeling the defect with a collinear dislocation and charge dipole line. Sosa and Pak (1990) have considered a three-dimensional eigenfunction analysis of a semi-infinite crack in a piezoelectric material. Due to the anisotropic nature of piezoelectric materials and the coupling of an additional field variable in the governing equations, piezoelectric boundary value problems generally pose serious mathematical difficulty. When a defect such as a crack is introduced, the problem becomes even more difficult. The antiplane crack problem considered in this paper offers a simplification that makes it possible to find a closed-form solution readily. Once the solution is obtained for the mode III crack problem, the effects of the electrical fields on the crack propagation in piezoelectric materials are studied within the framework of macroscopic linear elastic fracture mechanics.

Governing Equations

The three-dimensional formulation of linear piezoelectricity that was presented by Tiersten (1969) is briefly summarized here. The variational formulation for a static linear piezoelectric material occupying region V bounded by surface S can be derived from Hamilton's principle as follows:

$$\delta\int_V (-H)dV+\int_S (T_i\delta u_i - q\delta\phi)dS=0, \tag{1}$$

where H is the electric enthalpy density, T_i is the applied surface traction, u_i is the displacement, q is the applied surface charge, and ϕ is the electric potential whose negative of the gradient is the electric field, i.e.,

$$E_k=-\phi_{,k}. \tag{2}$$

In this formulation, the displacement and the electric potential are taken to be the independent field variables. For linear piezoelectric materials, the electric enthalpy density is expressed as

$$H(\varepsilon_{ij},E_i)=\frac{1}{2}C_{ijkl}\varepsilon_{ij}\varepsilon_{kl}-\frac{1}{2}\epsilon_{ij}E_iE_j-e_{ikl}\varepsilon_{kl}E_i, \tag{3}$$

where C_{ijkl} are the elastic moduli measured in a constant electric field, ϵ_{ij} are the dielectric constants measured at constant strain, e_{ikl} are the piezoelectric constants, and ε_{ij} is the strain tensor,

$$\varepsilon_{ij}=\frac{1}{2}(u_{i,j}+u_{j,i}). \tag{4}$$

The first term of equation (3) is the energy stored in the deformation, the second term is the energy stored in the electric fields, and the last term is the interaction energy. Valid symmetry conditions for the material constants are

Contributed by the Applied Mechanics Division of THE AMERICAN SOCIETY OF MECHANICAL ENGINEERS for publication in the JOURNAL OF APPLIED MECHANICS.

Discussion on this paper should be addressed to the Technical Editor, Leon M. Keer, The Technological Institute, Northwestern University, Evanston, IL 60208, and will be accepted until two months after final publication of the paper itself in the JOURNAL OF APPLIED MECHANICS. Manuscript received by the ASME Applied Mechanics Division, May 20, 1987; final revision, July 13, 1989.

Copyright © 1990 by ASME
Downloaded 03 May 2010 to 171.66.16.244. Redistribution subject to ASME license or copyright; see http://www.asme.org/terms/Terms_Use.cfm

$$C_{ijkl} = C_{jikl} = C_{jilk} = C_{klij},\ e_{kij} = e_{kji},\ \epsilon_{ij} = \epsilon_{ji}. \tag{5}$$

With these symmetry relations, $_{ij}$ in (3) can be replaced by $u_{i,j}$.

The variational formulation for the piezoelectric continuum provides the following results.

Governing field equations:

$$\begin{aligned} \sigma_{ij,j} &= 0 \\ D_{i,i} &= 0. \end{aligned} \tag{6}$$

Boundary conditions:

$$\begin{aligned} \sigma_{ij} n_j &= T_i \\ D_i n_i &= -q. \end{aligned} \tag{7}$$

Constitutive equations:

$$\begin{aligned} \sigma_{ij} &= \frac{\partial H}{\partial\ _{ij}} = C_{ijkl}\ _{kl} - e_{kij} E_k \\ D_i &= -\frac{\partial H}{\partial E_i} = e_{ikl}\ _{kl} + \epsilon_{ik} E_k. \end{aligned} \tag{8}$$

In these equations, σ_{ij} is the stress tensor, n_i is the unit normal vector, and D_i is the electric displacement vector.

Path-Independent Integral

Conservation laws that lead to path-independent integrals can be derived in various ways. A familiar one, involving use of the Lagrangian for the system under consideration, consists of allowing a larger class of variations and imposing the invariance conditions on the corresponding action integral. An alternate direct procedure was shown by Eshelby (1970) for a static elastic continuum. It involves the Lagrangian density only and consists of differentiating it with respect to the independent variables. The terms are grouped in such a way that the use of the equation of motion can be made. The method can be demonstrated by taking electric enthalpy density to be the Lagrangian density and simply differentiating it with respect to the spatial coordinate, x_k. This operation leads to

$$\frac{\partial}{\partial x_k} H(x_i;\ u_{i,j},\ E_i) = \left(\frac{\partial H}{\partial x_k}\right)_{\exp} + \frac{\partial H}{\partial u_{i,j}} u_{i,jk} + \frac{\partial H}{\partial \phi_{,i}} E_{i,k} \tag{9}$$

where $(\partial H/\partial x_k)_{\exp}$ denotes explicit dependence of H on x_k with the other dependent and independent variables held constant, i.e.,

$$\left(\frac{\partial H}{\partial x_k}\right)_{\exp} = \frac{\partial}{\partial x_k} H(x_i;\ u_{i,j},\ E_i)\Big|_{\{u_{i,j}, E_i; x_i, i \neq k\} = \text{const.}}. \tag{10}$$

With the use of the field equations (6) and the constitutive relations (8), equation (9) becomes

$$\left(\frac{\partial H}{\partial x_k}\right)_{\exp} = [H\delta_{ik} - \sigma_{ij} u_{i,k} + D_j E_k]_{,j}. \tag{11}$$

If the material is homogeneous and is free of any defects so that the electric enthalpy density does not depend explicitly on the coordinates, then $(\partial H/\partial x_k)_{\exp} = 0$, and equation (11) becomes a statement of the conservation law

$$[H\delta_{jk} - \sigma_{ij} u_{i,k} + D_j E_k]_{,j} = 0. \tag{12}$$

The quantity in the bracket is called the "material momentum tensor." Integrating the divergence of the material momentum tensor over the volume and applying the divergence theorem, the conservation law (12) can be put into the surface integral form

$$F_k = \int_S [H\delta_{jk} - \sigma_{ij} u_{i,k} + D_j E_k] n_j dS, \tag{13}$$

where F_k denotes the kth component of the conservation integral and δ_{ij} is Kronecker delta. This expression becomes a conservation law in any part of the piezoelectric material where no defect or inhomogeneity is present. It is this fact, that the surface integral above vanishes when it surrounds a perfect material, that guarantees the path-independence of the integral. Therefore, equation (13) can be called the path-independent integral for linear piezoelectric materials. This expression is identical to the one derived by Pak and Herrmann (1986) for a linear elastic dielectric material interacting with an external electric field with H taking the place of stored energy function for dielectric materials. They have shown that this expression is physically meaningful in that its value, when evaluated on a surface enclosing a defect, is the total potential energy release rate per infinitesimal translation of the defect in the x_k-direction. If all the electrical field quantities are made to vanish, then (13) reduces to

$$F_k = \int_S [W\delta_{jk} - \sigma_{ij} u_{i,k}] n_j dS, \tag{14}$$

whose x-component is the J-integral of fracture mechanics in which W is the strain energy density.

Anti-plane Crack Problem

For a special case of a piezoelectric material representing a transversely isotropic medium belonging to a hexagonal crystal class 6 mm, the constitutive relations (8) are of the form (Berlincourt, Curran, and Jaffe, 1964)

$$\begin{Bmatrix} \sigma_{xx} \\ \sigma_{yy} \\ \sigma_{zz} \\ \sigma_{zy} \\ \sigma_{zx} \\ \sigma_{xy} \end{Bmatrix} = \begin{bmatrix} c_{11} & c_{12} & c_{13} & 0 & 0 & 0 \\ c_{12} & c_{11} & c_{13} & 0 & 0 & 0 \\ c_{13} & c_{13} & c_{33} & 0 & 0 & 0 \\ 0 & 0 & 0 & c_{44} & 0 & 0 \\ 0 & 0 & 0 & 0 & c_{44} & 0 \\ 0 & 0 & 0 & 0 & 0 & \frac{1}{2}(c_{11} - c_{12}) \end{bmatrix} \begin{Bmatrix} \\ \\ \\ 2\ _{zy} \\ 2\ _{zx} \\ 2\ _{xy} \end{Bmatrix} - \begin{bmatrix} 0 & 0 & e_{31} \\ 0 & 0 & e_{31} \\ 0 & 0 & e_{33} \\ 0 & e_{15} & 0 \\ e_{15} & 0 & 0 \\ 0 & 0 & 0 \end{bmatrix} \begin{Bmatrix} E_x \\ E_y \\ E_z \end{Bmatrix} \tag{15}$$

$$\begin{Bmatrix} D_x \\ D_y \\ D_z \end{Bmatrix} = \begin{bmatrix} 0 & 0 & 0 & 0 & e_{15} & 0 \\ 0 & 0 & 0 & e_{15} & 0 & 0 \\ e_{31} & e_{31} & e_{33} & 0 & 0 & 0 \end{bmatrix} \begin{Bmatrix} \epsilon_{xx} \\ \epsilon_{yy} \\ \epsilon_{zz} \\ 2\epsilon_{zy} \\ 2\epsilon_{zx} \\ 2\epsilon_{xy} \end{Bmatrix} + \begin{bmatrix} \epsilon_{11} & 0 & 0 \\ 0 & \epsilon_{11} & 0 \\ 0 & 0 & \epsilon_{33} \end{bmatrix} \begin{Bmatrix} E_x \\ E_y \\ E_z \end{Bmatrix}. \tag{16}$$

Downloaded 03 May 2010 to 171.66.16.244. Redistribution subject to ASME license or copyright; see http://www.asme.org/terms/Terms_Use.cfm

As mentioned previously, the piezoelectric boundary value problem simplifies considerably if we consider only the out-of-plane displacement and the in-plane electric fields such that

$$u_x = u_y = 0, \quad u_z = u_z(x,y), \tag{17}$$

$$E_x = E_x(x,y), \quad E_y = E_y(x,y), \quad E_z = 0. \tag{18}$$

In this case the governing equations (6) simplify to

$$\begin{aligned} c_{44}\nabla^2 u_z + e_{15}\nabla^2\phi &= 0 \\ e_{15}\nabla^2 u_z - \epsilon_{11}\nabla^2\phi &= 0, \end{aligned} \tag{19}$$

where ∇^2 is the two-dimensional Laplacian operator

$$\nabla^2 \equiv \frac{\partial^2}{\partial x^2} + \frac{\partial^2}{\partial y^2}. \tag{20}$$

The constitutive relations (8) become

$$\begin{aligned} \sigma_{zx} &= c_{44}\frac{\partial u_z}{\partial x} + e_{15}\frac{\partial \phi}{\partial x} \\ \sigma_{zy} &= c_{44}\frac{\partial u_z}{\partial y} + e_{15}\frac{\partial \phi}{\partial y} \\ D_x &= e_{15}\frac{\partial u_z}{\partial x} - \epsilon_{11}\frac{\partial \phi}{\partial x} \\ D_y &= e_{15}\frac{\partial u_z}{\partial y} - \epsilon_{11}\frac{\partial \phi}{\partial y}. \end{aligned} \tag{21}$$

Consider a mode III fracture problem for which a finite crack of length $2a$ is embedded in an infinite piezoelectric medium subjected to far-field mechanical and electrical loads (Fig. 1). We will consider four possible cases of boundary conditions at infinity. The first case is a uniform shear traction, $\sigma_{zy} = \tau_\infty$, applied with a uniform electric displacement, $D_y = D_\infty$; the second is a uniform shear strain, $\gamma_{zy} = \gamma_\infty$, with a uniform electric field, $E_y = E_\infty$; the third is a uniform shear traction with a uniform electric field; and the fourth is a uniform shear strain with a uniform electric displacement. Applying a uniform electric displacement in the y-direction is equivalent to distributing a uniform surface charge on the boundary whose normal is in the y-direction, as can be seen from the boundary condition (7). A uniform electric field can be produced by having an electrode with a constant electric potential at the surface of the piezoelectric material. This condition can be achieved in the laboratory more readily than an electric displacement boundary condition.

The boundary conditions on the upper and the lower surfaces of the crack are to be free of the surface traction and the surface charge for all cases of far-field loading conditions, i.e.,

$$\sigma_{zy} = 0, \quad D_y = 0 \quad |x| < a, \quad |y| = 0. \tag{22}$$

Some of the assumptions made in applying these boundary conditions are discussed in the Appendix.

Examination of equation (19) reveals that the field equations are satisfied if u_z and ϕ are harmonic functions. This can be achieved by letting u_z and ϕ be the imaginary part of some analytic functions such that

$$\begin{aligned} u_z &= \mathrm{Im}U(z) \\ \phi &= \mathrm{Im}\Phi(z). \end{aligned} \tag{23}$$

The stresses and the electric displacements can then be obtained from these functions:

$$\begin{aligned} \sigma_{zx} &= \mathrm{Im}[c_{44}U'(z) + e_{15}\Phi'(z)] \\ \sigma_{zy} &= \mathrm{Re}[c_{44}U'(z) + e_{15}\Phi'(z)] \\ D_x &= \mathrm{Im}[e_{15}U'(z) - \epsilon_{11}\Phi'(z)] \\ D_y &= \mathrm{Re}[e_{15}U'(z) - \epsilon_{11}\Phi'(z)], \end{aligned} \tag{24}$$

where Re is the real part of the complex function and the prime indicates differentiation with respect to the complex variable $z = x + iy$. Taking a semi-inverse approach by assuming $U(z)$ and $\Phi(z)$ to be

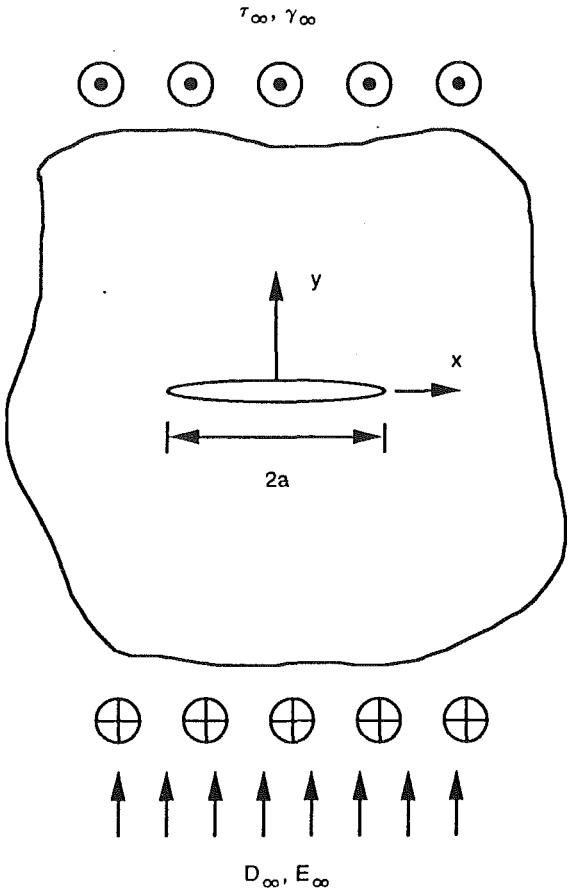


Fig. 1 Far-field mechanical and electrical loads

$$\begin{aligned} U(z) &= A(z^2 - a^2)^{1/2} \\ \Phi(z) &= -B(z^2 - a^2)^{1/2}, \end{aligned} \tag{25}$$

we see that the governing equations (19) and the boundary conditions (22) are satisfied. In these equations, A and B are real constants, which will be determined from the far-field loading conditions. Substituting (25) into (23) and (24), we arrive at

$$\begin{aligned} u_z &= A\sqrt{r_1 r_2}\sin\left(\frac{\theta_1 + \theta_2}{2}\right) \\ \phi &= -B\sqrt{r_1 r_2}\sin\left(\frac{\theta_1 + \theta_2}{2}\right) \\ \sigma_{zx} &= (c_{44}A - e_{15}B)\frac{r}{\sqrt{r_1 r_2}}\sin\left(\theta - \frac{\theta_1 + \theta_2}{2}\right) \\ \sigma_{zy} &= (c_{44}A - e_{15}B)\frac{r}{\sqrt{r_1 r_2}}\cos\left(\theta - \frac{\theta_1 + \theta_2}{2}\right) \\ D_x &= (e_{15}A + \epsilon_{11}B)\frac{r}{\sqrt{r_1 r_2}}\sin\left(\theta - \frac{\theta_1 + \theta_2}{2}\right) \\ D_y &= (e_{15}A + \epsilon_{11}B)\frac{r}{\sqrt{r_1 r_2}}\cos\left(\theta - \frac{\theta_1 + \theta_2}{2}\right), \end{aligned} \tag{26}$$

where r and θ are coordinates defined in Fig. 2. By applying the far-field loading conditions, the constants A and B are evaluated as follows:

Downloaded 03 May 2010 to 171.66.16.244. Redistribution subject to ASME license or copyright; see http://www.asme.org/terms/Terms_Use.cfm

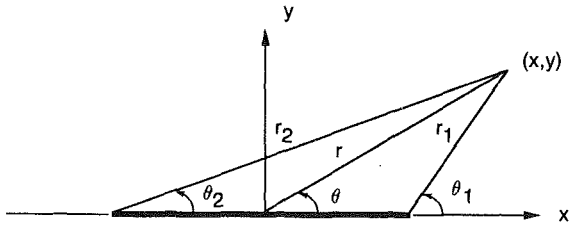


Fig. 2 Coordinates used to express solution

Case 1, $\sigma_{zy}=\tau_\infty$ and $D_y=D_\infty$ as $x^2+y^2\to\infty$

$$A=\frac{\epsilon_{11}\tau_\infty+e_{15}D_\infty}{c_{44}\epsilon_{11}+e_{15}^2}$$
$$B=\frac{c_{44}D_\infty-e_{15}\tau_\infty}{c_{44}\epsilon_{11}+e_{15}^2}. \tag{27}$$

Case 2, $\gamma_{zy}=\gamma_\infty$ and $E_y=E_\infty$ as $x^2+y^2\to\infty$

$$A=\gamma_\infty$$
$$B=E_\infty. \tag{28}$$

Case 3, $\sigma_{zy}=\tau_\infty$ and $E_y=E_\infty$ as $x^2+y^2\to\infty$

$$A=\frac{\tau_\infty+e_{15}E_\infty}{c_{44}}$$
$$B=E_\infty. \tag{29}$$

Case 4, $\gamma_{zy}=\gamma_\infty$ and $D_y=D_\infty$ as $x^2+y^2\to\infty$

$$A=\gamma_\infty$$
$$B=\frac{D_\infty-e_{15}\gamma_\infty}{\epsilon_{11}}. \tag{30}$$

Evaluating the solution (26) near the right crack tip and extending the traditional concept of stress intensity factors to other field variables, we have

$$E_x=-\frac{K^E}{\sqrt{2\pi r_1}}\sin\frac{\theta_1}{2} \qquad \gamma_{zx}=-\frac{K^S}{\sqrt{2\pi r_1}}\sin\frac{\theta_1}{2}$$
$$E_y=\frac{K^E}{\sqrt{2\pi r_1}}\cos\frac{\theta_1}{2} \qquad \gamma_{zy}=\frac{K^S}{\sqrt{2\pi r_1}}\cos\frac{\theta_1}{2}$$
$$\sigma_{zx}=-\frac{K^T}{\sqrt{2\pi r_1}}\sin\frac{\theta_1}{2} \qquad D_x=-\frac{K^D}{\sqrt{2\pi r_1}}\sin\frac{\theta_1}{2} \tag{31}$$
$$\sigma_{zy}=\frac{K^T}{\sqrt{2\pi r_1}}\cos\frac{\theta_1}{2} \qquad D_y=\frac{K^D}{\sqrt{2\pi r_1}}\cos\frac{\theta_1}{2},$$

where K^E is the "electric field intensity factor," K^S the "strain intensity factor," K^T the stress intensity factor, and K^D the "electric displacement intensity factor." These field intensity factors are defined here as

$$K^E=B\sqrt{\pi a}$$
$$K^S=A\sqrt{\pi a}$$
$$K^T=c_{44}K^S-e_{15}K^E \tag{32}$$
$$K^D=e_{15}K^S+\epsilon_{11}K^E.$$

For this particular piezoelectric fracture problem, all the field variables have the same crack-tip behavior as the classical mode III fracture problem. If all the electrical quantities are made to vanish, the piezoelectric solution reduces to the purely elastic mode III solution in which c_{44} becomes the shear modulus μ. Crack-tip singular behaviors of all the field variables normalized to their respective intensity factors are plotted in Figs. 3 and 4. Contours of constant electric potential around the crack are plotted in Fig. 5. It is interesting to

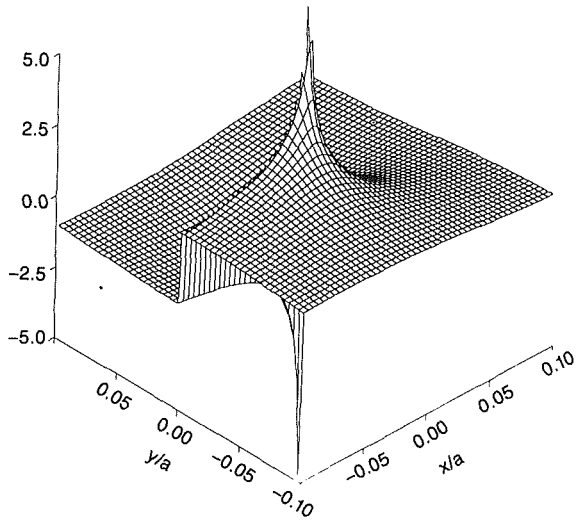


Fig. 3 Normalized field variables E_x/K^E, D_x/K^D, γ_{zx}/K^S, τ_{zx}/K^T near a crack tip

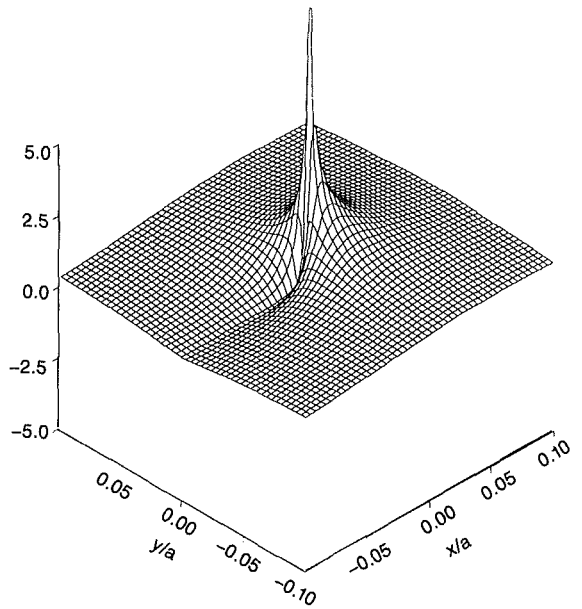


Fig. 4 Normalized field variables E_y/K^E, D_y/K^D, γ_{zy}/K^S, τ_{zy}/K^T near a crack tip

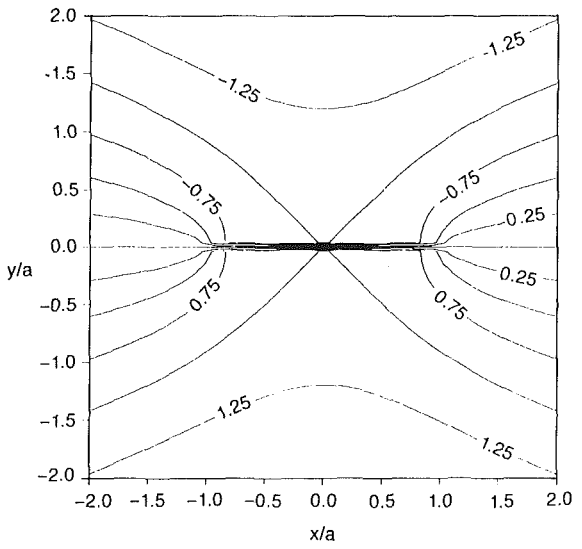


Fig. 5 Contours of constant electric potential near the crack

Downloaded 03 May 2010 to 171.66.16.244. Redistribution subject to ASME license or copyright; see http://www.asme.org/terms/Terms_Use.cfm

note that, in all cases, the field intensity factors corresponding to the field variables applied at infinity become independent of the material constants and the other respective loading parameter;

$$\begin{aligned} &\text{Case 1,} \quad K^T=\tau_\infty\sqrt{\pi a},\ K^D=D_\infty\sqrt{\pi a},\\ &\text{Case 2,} \quad K^S=\gamma_\infty\sqrt{\pi a},\ K^E=E_\infty\sqrt{\pi a},\\ &\text{Case 3,} \quad K^T=\tau_\infty\sqrt{\pi a},\ K^E=E_\infty\sqrt{\pi a},\\ &\text{Case 4,} \quad K^S=\gamma_\infty\sqrt{\pi a},\ K^D=D_\infty\sqrt{\pi a}. \end{aligned} \tag{33}$$

When there is an electrical load in addition to a mechanical load, it is not clear that these "field intensity factors" would have the same significance as the stress intensity factors in the purely elastic case. Therefore, we will consider the energy release rate concept in characterizing defects subjected to more than one field loading.

Energy-Release Rate

The path-independent integral derived earlier can now be evaluated to obtain the energy release rate for the mode III piezoelectric fracture problem under consideration. Denoting J to be the x component of the conservation integral F_k, the path-independent integral takes the form

$$J=F_x=\int_S (Hn_x-T_iu_{i,x}+D_in_iE_x)dS. \tag{34}$$

Using the solution obtained previously, evaluating this integral on a vanishingly small contour at a crack tip results in

$$J=\frac{K^TK^S-K^DK^E}{2}. \tag{35}$$

This result can also be obtained by considering the work done in closing the crack tip over an infinitesimal distance Δx (Fig. 6), which can be calculated by

$$\Delta W=2\int_0^{\Delta x}\frac{1}{2}\sigma_{zy}u_z dx+2\int_0^{\Delta x}\frac{1}{2}D_y\phi dx. \tag{36}$$

The crack extension force, G, can then be calculated as the energy released in propagating the crack an infinitesimal distance, i.e.,

$$G=\lim_{\Delta x\to 0}\frac{\Delta W}{\Delta x}=\frac{K^TK^S-K^DK^E}{2}. \tag{37}$$

This result is the same as that obtained by evaluating the path-independent integral (34) on a contour enclosing a crack tip. Therefore, for linear piezoelectric materials, as in the purely elastic case, the value of J is identical to the crack extension force, G:

$$J=G. \tag{38}$$

Writing the energy release rate expression in terms of the material constants and the far-field mechanical and electrical loads, we obtain

$$J=\begin{cases} \dfrac{\pi a}{2}\left[\dfrac{\epsilon_{11}\tau_\infty^2+2e_{15}D_\infty\tau_\infty-c_{44}D_\infty^2}{\epsilon_{11}c_{44}+e_{15}^2}\right], & \text{Case 1,}\\ \dfrac{\pi a}{2}\left[c_{44}\gamma_\infty^2-2e_{15}E_\infty\gamma_\infty-\epsilon_{11}E_\infty^2\right], & \text{Case 2,}\\ \dfrac{\pi a}{2}\left[\dfrac{\tau_\infty^2-(\epsilon_{11}c_{44}+e_{15}^2)E_\infty^2}{c_{44}}\right], & \text{Case 3,}\\ \dfrac{\pi a}{2}\left[\dfrac{(\epsilon_{11}c_{44}+e_{15}^2)\gamma_\infty^2-D_\infty^2}{\epsilon_{11}}\right], & \text{Case 4.} \end{cases} \tag{39}$$

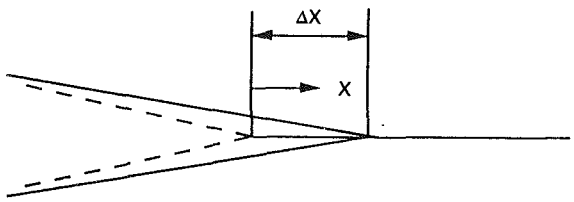


Fig. 6 Closing of the crack tip over an infinitesimal distance, Δx

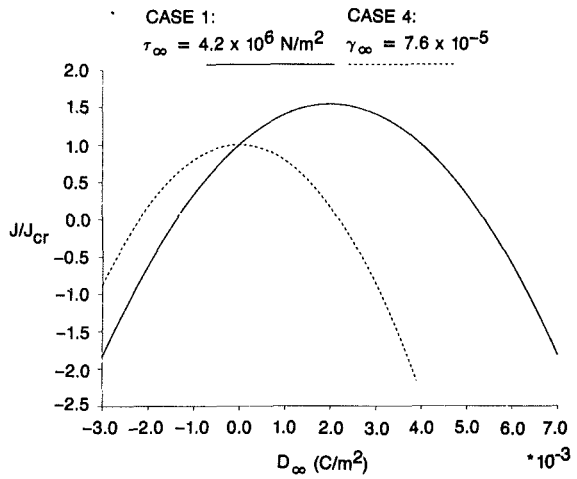


Fig. 7 Crack extension force in PZT material for Cases 1 and 4

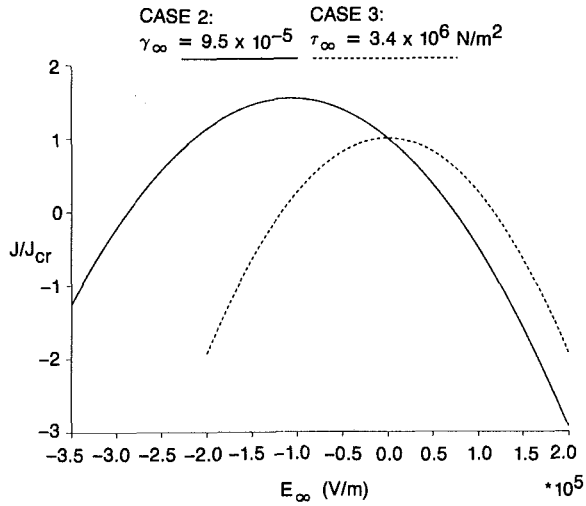


Fig. 8 Crack extension force in PZT material for Cases 2 and 3

Examining equations (39) one can see that the energy release rate can have negative values depending on the direction, the magnitude, and the type of the electrical loads. Solving the roots of the quadratic equations in (39), the crack extension force can be shown to be positive when

$$\begin{aligned} &\text{Case 1,} \quad -\frac{\sqrt{e_{15}^2+\epsilon_{11}c_{44}}-e_{15}}{c_{44}}<\frac{D_\infty}{\tau_\infty}<\frac{\sqrt{e_{15}^2+\epsilon_{11}c_{44}}+e_{15}}{c_{44}},\\ &\text{Case 2,} \quad -\frac{\sqrt{e_{15}^2+\epsilon_{11}c_{44}}+e_{15}}{\epsilon_{11}}<\frac{E_\infty}{\gamma_\infty}<\frac{\sqrt{e_{15}^2+\epsilon_{11}c_{44}}-e_{15}}{\epsilon_{11}}\\ &\text{Case 3,} \quad -\frac{1}{\sqrt{e_{15}^2+\epsilon_{11}c_{44}}}<\frac{E_\infty}{\tau_\infty}<\frac{1}{\sqrt{e_{15}^2+\epsilon_{11}c_{44}}},\\ &\text{Case 4,} \quad -\sqrt{e_{15}^2+\epsilon_{11}c_{44}}<\frac{D_\infty}{\gamma_\infty}<\sqrt{e_{15}^2+\epsilon_{11}c_{44}}. \end{aligned} \tag{40}$$

The negative ratio implies the case in which the direction of

Downloaded 03 May 2010 to 171.66.16.244. Redistribution subject to ASME license or copyright; see http://www.asme.org/terms/Terms_Use.cfm

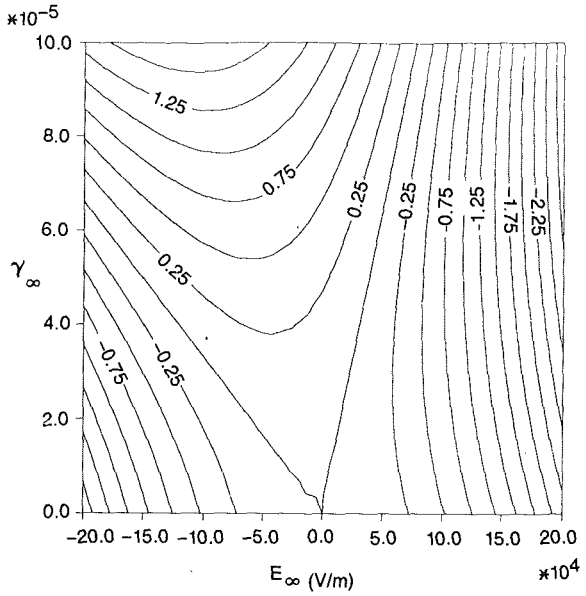


Fig. 9 Contours of constant J/J_{cr} for Case 2

one of the loads is reversed. This shows that, at certain ratios of the electrical load to the mechanical load, crack arrestment can be observed. It is also interesting to note that in the absence of the mechanical loads, i.e., when τ_∞ or γ_∞ is zero, the crack extension force is always negative, indicating that a crack would not propagate under these conditions. These observations agree with those of Deeg (1980) who hypothesized and showed that crack arrestment can be made by adjusting the electrical load to yield a crack extension force, G, less than the critical value or even less than zero.

As an example, lead zirconate titante (PZT-5H) piezoceramic is considered; its material properties are given by (Deeg, 1980; Pohanka and Smith, 1988):

$$c_{44} = 3.53 \times 10^{10} \frac{N}{m^2}$$

$$e_{15} = 17.0 \frac{C}{m^2}$$

$$\epsilon_{11} = 151 \times 10^{-10} \frac{C}{Vm} \tag{41}$$

$$J_{cr} = 5.0 \frac{N}{m},$$

where N is the force in Newtons, C is the charge in coulombs, V is the electric potential in volts, m is the length in meters, and J_{cr} is the critical crack extension force. The crack extension forces for PZT material with a crack of length $2a = .02$ m are plotted in Figs. 7 and 8 as a function of the electrical loads, with the mechanical loads fixed such that $J = J_{cr}$ at zero electrical loads. The maximum crack extension force can be found by differentiating J with respect to the electrical loads. For this particular problem, they occur at

$$\text{Case 1,} \quad D_\infty = \frac{e_{15}}{c_{44}} \tau_\infty = 2.0 \times 10^{-3} \frac{C}{m^2},$$

$$\text{Case 2,} \quad E_\infty = -\frac{e_{15}}{\epsilon_{11}} \gamma_\infty = -1.1 \times 10^5 \frac{V}{m}, \tag{42}$$

$$\text{Case 3,} \quad E_\infty = 0 \frac{V}{m},$$

$$\text{Case 4,} \quad D_\infty = 0 \frac{C}{m^2}.$$

As can be seen from Figs. 7 and 8, the crack extension force can be made negative by making the electrical loads such that they are outside the ranges, $-1.4 \times 10^{-3} < D_\infty < 5.4 \times 10^{-3}$ C/m^2, $-2.9 \times 10^5 < E_\infty < 7.3 \times 10^4$ V/m, $|E_\infty| < 1.2 \times 10^5$ V/m, and $|D_\infty| < 2.2 \times 10^{-3}$ C/m^2, for Cases 1, 2, 3, and 4, respectively. In the first two cases, as the magnitude of electrical load is increased from zero, J can be made either to increase or to decrease depending on the directions of the load. But, once the maximum J is reached, further increase in the electrical load will monotonically decrease J. In the third and the fourth cases, the presence of the electrical field always decreases J, inducing retardation in the crack growth. As an example, contours of constant J/J_{cr} are plotted in Fig. 9 for the second loading case. The experimental works by McHenry and Koepke (1983) and Koepke et al. (1986) on the mode I fracture of poled PZT ceramics report that the electric field enhances the crack growth and induces the mixed-mode fracture resulting in crack skewing. One should, however, perform a controlled experiment on mode III fracture to confirm some of the fracture behavior predicted by this analysis.

Concluding Remarks

A mode III piezoelectric fracture problem was formulated, and the solution is obtained by the semi-inverse method for the case of out-of-plane deformation and in-plane electrical loads. The classical mode III crack-tip singular behavior was observed for all the field variables. Eshelby's method of deriving conservation laws was used to obtain the path-independent integral which provides the energy release rate that can be used to characterize defects in piezoelectric materials subjected to both mechanical and electrical loads. By applying this path-independent integral to the mode III fracture problem at hand, it was found that the crack extension force is always negative in the absence of the mechanical load. It was shown that crack arrestment can be induced at certain ratios of the electrical to mechanical load. The analysis also showed that, at a given mechanical load, presence of electrical load can either promote or retard crack growth, depending on the magnitude, the direction, and the type of the electrical load. This phenomenon, observed for the mode III problem, is expected to be observed for the in-plane mode I and II problems for which the closed-form solutions remain to be found.

Acknowledgment

This work was supported by Advanced Development Program at Grumman Aircraft Systems.

References

Berlincourt, D. a., Curran, D. R., and Jaffe, H., 1964, "Piezoelectric and Piezomagnetic Materials and Their Function in Transducers," *Physical Acoustics*, Vol. 1A, W. P. Mason, ed., Academic Press, New York, p. 177.

Deeg, W. F., 1980, "The Analysis of Dislocation, Crack, and Inclusion Problems in Piezoelectric Solids," Ph.D. Thesis, Stanford University, Stanford, Calif.

Eshelby, J. D., 1970, "Energy Relations and the Energy-Momentum Tensor in Continuum Mechanics," *Inelastic Behavior of Solids*, M. F. Kanninen et al., eds., McGraw-Hill, New York, pp. 77-113.

Jackson, J. D., 1975, *Classical Electrodynamics*, John Wiley and Sons, New York, p. 149.

Koepke, B. G., McHenry, K. D., Seifried, L. M., and Stokes, R. J., 1986, "Mechanical Integrity of Piezoelectric and Dielectric Ceramics," *IEEE Ultrasonic Symposium*, Nov. 19, Williamsburg, VA.

Landau, L. M., and Lifschitz, E. M., 1960, *Electrodynamics of Continuous Media*, Pergamon Press, Oxford, U.K., p. 40.

McHenry, K. D., and Koepke, B. G., 1983, "Electric Field Effects on Subcritical Crack Growth in PZT," *Fracture Mechanics of Ceramic*, Vol. 5, R. C. Bradt et al., Plenum Press, New York, p. 337.

Pak, Y. E., and Herrmann, G., 1986, "Conservation Laws and the Material Momentum Tensor for the Elastic Dielectric," *Int. J. Engng. Sci.*, Vol. 24, pp. 1365-1374.

Downloaded 03 May 2010 to 171.66.16.244. Redistribution subject to ASME license or copyright; see http://www.asme.org/terms/Terms_Use.cfm

Parton, V. Z., 1976, "Fracture Mechanics of Piezoelectric Materials," *Acta Astronautica*, Vol. 3, pp. 671-683.

Pohanka, R. C., and Smith, P. L., 1988, "Recent Advances in Piezoelectric Ceramics," *Electronic Ceramics*, L. M. Levinson, ed., Marcel Dekker, New York.

Sosa, H. A., and Pak, Y. E., 1990, "Three-Dimensional Eigenfunction Analysis of a Crack in a Piezoelectric Material," *Int. J. Solids Structures*, Vol. 26, No. 1, pp. 1-15.

Tieresten, H. F., 1969, *Linear Piezoelectric Plate Vibrations*, Plenum Press, New York.

Toupin, R. A., 1956, "The Elastic Dielectric," *J. Rat. Mech. Anal.*, Vol. 5, p. 849.

APPENDIX

Boundary Conditions on the Piezoelectric Crack Face

In analyzing the piezoelectric crack problem, we have assumed that the crack contains a small but finite volume that is filled with vacuum (or air). Of course, in mathematical idealization the crack is modeled as a slit with only a length parameter. However, proper physical boundary conditions must be prescribed at the crack faces taking into account the interactions that take place at the interface between the piezoelectric material and the void inside the crack. To be formal, one must solve a two-domain problem with the appropriate governing equations and the boundary conditions for each domain, namely:

Governing equations;

$$\begin{aligned} &\sigma_{ij,j}=0 \\ &D_{i,i}=0 \quad \text{in piezoelectric material,} \end{aligned} \tag{A1}$$

$$\nabla^2\phi^{(c)}=0 \quad \text{in void inside the crack.} \tag{A2}$$

Boundary and continuity conditions

$$\begin{aligned} \sigma_{ij}n_j&=0 \quad \text{traction-free,} \\ (D_i^{(p)}-D_i^{(c)})n_i&=0 \quad \text{charge-free,} \\ \mathbf{n}\times(\nabla\phi^{(p)}-\nabla\phi^{(c)})&=0 \quad \text{irrotationality of electric fields.} \end{aligned} \tag{A3, A4, A5}$$

Since the electric field is determined by the gradient of the scalar potential ϕ, the continuity condition on the tangential component of the electric field given in equation (A5) can be replaced by (Toupin, 1956)

$$\phi^{(p)}=\phi^{(c)} \tag{A6}$$

at the interface without loss of generality. In the previous equations the superscripts (p) and (c) refer to the quantities in the piezoelectric material and in the void inside the crack, respectively.

In light of the fact that piezoelectric materials have strong electro-elastic coupling and have very high dielectric constants, one can make certain assumptions regarding the interface phenomena and decouple the domains to make a self-contained, single domain, boundary value problem. For the problem at hand, our main interest is in the behavior of the fields inside the piezoelectric material.

If we now consider the anti-plane piezoelectric crack problem, the boundary condition (A3) becomes

$$c_{44}\ \varepsilon_{zy}-e_{15}E_y^{(p)}=0. \tag{A7}$$

The continuity condition of the electric displacement, equation (A4), becomes

$$e_{15}\ \varepsilon_{zy}+\epsilon_{11}E_y^{(p)}=\epsilon_0E_y^{(c)}, \tag{A8}$$

where ϵ_0 is the permittivity of free space. From the traction-free boundary condition (A7), we obtain

$$\varepsilon_{zy}=\frac{e_{15}}{c_{44}}E_y^{(p)}. \tag{A9}$$

Substituting this expression into the electric displacement continuity condition (A8), we arrive at

$$\frac{E_y^{(p)}}{E_y^{(c)}}=\frac{\epsilon_0}{(e_{15}^2/c_{44}+\epsilon_{11})}. \tag{A10}$$

This expression shows the relative magnitude of the normal components of the electric field just inside and outside the piezoelectric crack face as a function of the relative magnitude of the material constants. In examining the actual values of these material constants used in the analysis, one can easily see that the ratio e_{15}^2/c_{44} is of the same order of magnitude as the dielectric constant of the piezoelectric material, ϵ_{11}, which in turn is three orders of magnitude greater than the dielectric constant of the vacuum, ϵ_0. Since the ratio of the material constants is very small, i.e.,

$$\frac{\epsilon_0}{(e_{15}^2/c_{44}+\epsilon_{11})}\ll 1, \tag{A11}$$

one can simplify the problem by assuming that the ratio of the electric fields, $E_y^{(p)}/E_y^{(c)}$, approaches zero at the piezoelectric-vacuum interface. At this limit, $E_y^{(p)}$ must approach zero if $E_y^{(c)}$ is to remain finite. Physically, we are assuming here that the piezoelectric material is so highly polarizable that the depolarizing field reduces the electric field to a small value just inside the piezoelectric material at the interface. Of course, the only true case of the electric field being absolutely zero would be in the case of a conductor that can be regarded as a body of infinite dielectric permeability (Landau and Lifshitz, 1960; Jackson, 1975).

It is interesting to note that, in examining the expression given in (A10), the ratio of the fields is small, independent of the relative magnitude of the dielectric constants ϵ_0/ϵ_{11}, for e_{15}^2/c_{44} is also much greater than ϵ_0. This indicates that, for piezoelectric materials, there are two independent reasons for the electric field to be small at the boundary. This becomes clearer in looking at the traction-free boundary condition (A7), which indicates that in order for the strain to be zero at the boundary the electric field has to vanish.

Therefore, one can set $E_y^{(p)}=0$ at the boundary of the piezoelectric material and decouple the domains by ignoring the field inside the crack. The field exists inside the crack, which in fact is greater than that just inside the piezoelectric material. However, we will not be concerned with this field or the Maxwell stress it produces since the stresses and strains produced by the piezoelectric effects are much larger than those due to the Maxwell stress or the electrostriction. Once we impose $E_y^{(p)}=0$, it follows from (A7) that $\varepsilon_{zy}=0$. Indeed, the complex potentials for the independent variables u_z and ϕ used in the analysis satisfy these conditions identically. However, well-posed piezoelectric boundary value problems require the traction, $\sigma_{ij}n_j=T_i$, and the extrinsic surface charge, $D_in_i=q$, to be prescribed at the boundary. Therefore, once the domains are decoupled, the conditions resulting from the assumptions are equivalently satisfied by

$$\begin{aligned} \sigma_{zy}&=0 \quad \text{traction-free,} \\ D_y&=0 \quad \text{charge-free.} \end{aligned} \tag{A12}$$

The validity of this simplification is subjected to the condition that the crack is filled with a vacuum or a nonconducting gas (i.e., the crack faces are not in perfect contact with each other). In most realistic cases, this assumption is valid especially when a far-field crack-opening mechanical load is present.

Downloaded 03 May 2010 to 171.66.16.244. Redistribution subject to ASME license or copyright; see http://www.asme.org/terms/Terms_Use.cfm

U. Mbanefo[1]
Applied Mechanics Department,
AiResearch Los Angeles Division,
Allied-Signal Aerospace Company,
Torrance, CA 90509

R. A. Westmann
Mechanical, Aerospace, and Nuclear
Engineering Department,
University of California,
Los Angeles, CA 90024
Mem. ASME

Axisymmetric Stress Analysis of a Broken, Debonded Fiber

The study of a single broken fiber embedded in an infinite elastic matrix subjected to a uniform far-field strain is presented. The solution, which accounts for the presence of interface debonding in the neighborhood of the fiber fracture, is carried out within the framework of classical elastostatics. The boundary value problem is reduced first to a pair of dual integral equations, and then to a Cauchy singular integral equation which is solved numercially. Results are presented illustrating the dependence of the fiber axial force and the interface shear stress upon the geometrical and material parameters.

I Introduction

The widespread and increasing structural application of fiber-reinforced materials has generated theoretical and experimental interest in the mechanics of such composites. Interest has risen especially in the mechanics of the redistribution of forces following the fracture of one or more of the fibers. Upon fracture of one such fiber, force transmission occurs through the surrounding matrix to adjacent fibers, resulting in increased force in those neighboring reinforcements. The matrix stresses and the fiber-matrix interface shear stresses become very large in the neighborhood of the fracture. If the fiber-matrix bond strength is low enough, debonding of the fiber from the matrix will follow, and should the fiber force concentrations be sufficiently high, additional fibers may break. Ultimately, tearing of the matrix and crack propagation through adjacent fibers leads to catastrophic overall failure of the composite.

A basic understanding of the mechanics of such failure must address such questions as these attendant force concentrations and their dependence on the relative fiber-matrix flexibility and the extent of fiber debonding. Other independent variables include matrix tearing, the number and spacing of adjacent fibers, and the nature and region of influence of a single fiber fracture.

A number of investigators have previously studied allied problems of axial load diffusion from a broken fiber to the surrounding matrix. Among these works, three are of particular relevance to the present study. Muki and Sternberg (1971) employed, as does the present study, an approximate one-dimensional model of the fiber to examine the longitudinal distribution of the fiber force and its interaction with the bond forces along the fiber-matrix interface. Their results show that the efficiency of the fiber force absorption by the surrounding matrix is a diminishing function of the fiber-matrix stiffness ratio, and that the gradient of the fiber force tends to infinity at the fracture plane. A subsequent effort by Ford (1973) relaxed the one-dimensional approximation of the fiber, modeling both the fiber and the matrix as three-dimensional axisymmetric solids. Although Ford obtained the same general results as those reported by Muki and Sternberg (1971), he differed in two important details. First, his axial force gradients with respect to stiffness ratio E_2/E_1 assume both negative and positive values for values of the axial coordinate less than one fiber radius. Secondly, the axial forces for all $E_2/E_1 > 1$ are consistently higher than those reported by Muki and Sternberg. In both the studies by Muki and Sternberg (1971) and Ford (1973) only a single fiber is considered, and interface debonding in the neighborhood of the fiber fracture is not permitted.

Most recently Wiley (1983) studied, among other cases, finite-fiber models in single and multiple-fiber arrays, and showed that the fiber-matrix debond length has pronounced effects on the fiber axial force and interface shear stress distributions.

The purpose of this paper is to solve the problem of the fiber fracture in the presence of fiber-matrix interface debonding. Such a solution may be viewed as an extension of the studies reported by Muki and Sternberg (1971) and Ford (1973) wherein the debond length is zero. The fiber is modeled as a one-dimensional continuum, while the matrix is treated as a three-dimensional axisymmetric solid; the study is carried out entirely within the framework of classical elastostatics. The fiber fracture is presumed to be opened by a far-field strain ϵ_∞ uniformly imposed on both the fiber and the matrix in a direction parallel to the axis of the fiber (see Fig. 1). The objective of the study is the determination of the general stress distribution, in particular the fiber-matrix interface shear stress and the resulting fiber-axial force distribution, and their dependence on the fiber-matrix flexibility and debond length.

[1]Presently at Structures Research Department, Northrop Aircraft Division, Hawthorne, CA 90250.

Contributed by the Applied Mechanics Division of THE AMERICAN SOCIETY OF MECHANICAL ENGINEERS for presentation at the Winter Annual Meeting, Dallas, Texas, Nov. 25–30, 1990.

Discussion on this paper should be addressed to the Technical Editor, Leon M. Keer, The Technological Institute, Northwestern University, Evanston, IL 60208, and will be accepted until two months after final publication of the paper itself in the JOURNAL OF APPLIED MECHANICS. Manuscript received by the ASME Applied Mechanics Division, March 16, 1989; final revision, Aug. 10, 1989.

Paper No. 90-WA/APM-25.

Copyright © 1990 by ASME
Downloaded 03 May 2010 to 171.66.16.244. Redistribution subject to ASME license or copyright; see http://www.asme.org/terms/Terms_Use.cfm

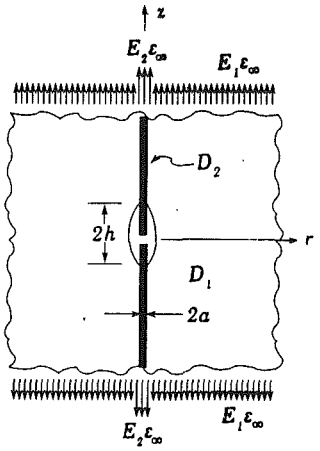


Fig. 1 Fiber-matrix geometry

In the following, Section II presents a detailed statement of the model and the associated boundary value problem, and reduces the solution to a consideration of a pair of dual integral equations (DIEs). Section III further reduces the DIEs to a Cauchy singular integral equation (CSIE) with an appropriate constraint condition; in Section IV, use is made of the Erdogan-Gupta method to solve the CSIE. Numerical results are presented in Section V.

II Problem Formulation

A circular cylindrical coordinate system (r, θ, z) is employed with the axis $(r = 0)$ coinciding with the center line of the fiber (Fig. 1). The matrix and fiber occupy regions D_1 and D_2, respectively, where

$$\left.\begin{aligned} D_1 &= \{(r,\theta,z)\ \epsilon(a,\infty)\times[0,2\pi)\times(-\infty,\infty)\}, \quad a>0 \\ D_2 &= \{(r,\theta,z)\ \epsilon[0,a)\times[0,2\pi)\times(-\infty,\infty)\} \end{aligned}\right\}. \tag{1}$$

$$\left.\begin{aligned} (\rho,\zeta) &= (r/a,\ z/a) \\ (u_\rho,u_\zeta) &= (U_r/a,\ U_z/a) \\ (\sigma_{\rho\rho},\ \sigma_{\theta\theta},\ \sigma_{\zeta\zeta},\ \sigma_{\rho\zeta}) &= (\tau_{rr},\ \tau_{\theta\theta},\ \tau_{zz},\ \tau_{rz})/\sigma_\infty,\ \sigma_\infty = E_1\epsilon_\infty \end{aligned}\right\}. \tag{2}$$

The dimensionless equations of classical elasticity for the matrix, in the absence of body forces, may then be stated in terms of the Navier displacement equations of equilibrium:

$$\left.\begin{aligned} \frac{1}{1-2\nu}\frac{\partial e}{\partial\rho}+\nabla^2 u_\rho-\rho^{-2}u_\rho &= 0 \\ \frac{1}{1-2\nu}\frac{\partial e}{\partial\zeta}+\nabla^2 u_\zeta &= 0 \end{aligned}\right\} \tag{3}$$

where

$$e=\frac{1}{\rho}\frac{\partial}{\partial\rho}(\rho\, u_\rho)+\frac{\partial u_\zeta}{\partial\zeta}.$$

The fiber is modeled as a one-dimensional filament, with the cross-sectional averaged extensional stress and displacement components being taken as the important unknowns. If the components of the fiber displacement and normal stress in the axial direction are taken to be $(u_f,\ \sigma_f)$, then their dimensionless counterparts are defined by

$$(u,\sigma)=\left(\frac{u_f}{a},\ \frac{\sigma_f}{\sigma_\infty}\right). \tag{4}$$

Assuming that the radius of the fiber does not change during deformation (i.e., Poisson's ratio of the fiber vanishes), and enforcing the stress-strain and strain-displacement relations, results in the following equation between u and σ:

$$u_{,\zeta}=\frac{E_1}{E_2}\epsilon_\infty\sigma. \tag{5}$$

Equilibrium of a differential length ds of the fiber is readily determined to be satisfied if

$$\sigma_{,\zeta}+2\sigma_{\rho\zeta}(1,\zeta)=0 \tag{6}$$

where $\sigma_{\rho\zeta}(1,\ \zeta)$ is the interface shear stress in the matrix.

The side conditions for this problem are stated as follows:

(*i*) far-field:

$$\left.\begin{aligned} &\sigma_{\zeta\zeta}=1,\sigma_{\rho\zeta}=0 && \rho\epsilon[1,c],\ \zeta\to\infty \\ &\sigma_{\rho\rho}=\sigma_{\rho\zeta}=0 && \zeta\epsilon[0,c],\ \rho\to\infty \\ &\sigma=E_2/E_1 && \zeta\to\infty \end{aligned}\right\} \quad c \text{ finite} \tag{7}$$

(*ii*) interface:

$$\left.\begin{aligned} u\zeta(1+,\zeta)&=u(\zeta) \\ u_\rho(1+,\zeta)&=0 \end{aligned}\right\} \quad |\zeta|>h/a\equiv\alpha_0 \tag{8}$$

(*iii*) debond zone:

$$\left.\begin{aligned} \sigma_{\rho\zeta}(1+,\zeta)&=0 \\ u_\rho(1+,\zeta)&=0 \end{aligned}\right\} \quad |\zeta|<\alpha_0 \tag{9}$$

(*iv*) broken-fiber surface:

$$\sigma(0\pm)=0. \tag{10}$$

The matrix material is assumed to be homogeneous, isotropic, and linearly elastic, with elastic constants E_1, ν. The fiber is also composed of a homogeneous, isotropic, and linearly elastic material with extensional modulus E_2. The fiber and matrix are assumed to be perfectly bonded together along their common boundary except for the interface $\{(r, \theta, z): r = a, (\theta, z) \epsilon [0, 2\pi) \times [-h, h]\}$ where only frictionless contact is maintained. The fiber is broken in the plane $z = 0$, so the fiber surfaces $z = 0\pm$ are traction free. The fiber-matrix assemblage is subjected to a uniform strain ϵ_∞ in z-direction as $r^2 + z^2 \to \infty$; the resulting three-dimensional torsionless response is axisymmetric.

Dimensionless coordinates and dimensionless components of the matrix displacement and stress fields are introduced as follows:

It is convenient to express the solution to this problem as the sum of the fields for the matrix and *unbroken* fiber and the perturbation stress and displacement fields associated with the broken fiber. One may readily verify that the solution for the stress and displacement components for the unbroken fiber problem is given by

$$\left.\begin{aligned} (u_\rho,u_\zeta) &= \epsilon_\infty\left\{\nu\left(\frac{1-\rho^2}{\rho}\right),\zeta\right\} \\ (\sigma_{\rho\rho},\sigma_{\theta\theta},\sigma_{\zeta\zeta},\sigma_{\rho\zeta}) &= \frac{\nu}{1+\nu}\left\{\frac{-1}{\rho^2},\frac{1}{\rho^2},\frac{1+\nu}{\nu},0\right\} && \rho,\zeta\epsilon D_1 \\ (u,\ \sigma) &= \epsilon_\infty\zeta,\ \frac{E_2}{E_1} && \rho,\zeta\epsilon D_2. \end{aligned}\right\} \tag{11}$$

Downloaded 03 May 2010 to 171.66.16.244. Redistribution subject to ASME license or copyright; see http://www.asme.org/terms/Terms_Use.cfm

The side conditions for the perturbation field are given by equations (7)–(10) except that (7) are replaced by their homogeneous counterparts while (10) becomes

$$\sigma(0\pm) = -\frac{E_2}{E_1}.$$

The perturbation solution is readily obtained by employing Love's stress function (Love, 1944), $\Phi = \Phi(\rho,\zeta)$. An integral representation appropriate for this biharmonic function is given by

$$\Phi(\rho,\zeta) = \int_0^\infty [\bar{A}(\xi)K_0(\rho\xi) + \bar{B}(\xi)\rho\xi K_1(\rho\xi)]\sin(\zeta\xi)d\xi, \quad \rho > 1 \tag{12}$$

where $\bar{A}$, $\bar{B}$ are coefficients to be determined and K_m ($m = 0, 1$) are the modified Bessel functions of the second kind of order m.

Enforcement of the interface condition

$$u_\rho(1+,\zeta) = 0, \quad |\zeta| < \infty$$

permits the expression of $\bar{A}(\xi)$ in terms of $\bar{B}(\xi)$. Determination of the stress and displacement field from equation (12) and combining with (11) then provides the following expressions for the total stress and displacement components in the matrix.

$$u_\rho(\rho,\zeta) = (\rho^{-1} - \rho)\nu\epsilon_\infty + (1+\nu)\epsilon_\infty \int_0^\infty \frac{B(\xi)}{\xi} R_1(\rho,\xi)\{\rho\xi R(\rho\xi) - \xi R(\xi)\}\cos(\zeta\xi)d\xi$$

$$u_\zeta(\rho,\zeta) = \zeta\epsilon_\infty - (1+\nu)\epsilon_\infty \int_0^\infty \frac{B(\xi)}{\xi} R_1(\rho,\xi)\{[4(1-\nu) + \xi R(\xi)]R(\rho\xi) - \rho\xi\}\sin(\zeta\xi)d\xi$$

$$\sigma_{\rho\rho}(\rho,\zeta) = -\left(\frac{\nu}{1+\nu}\right)\rho^{-2} + \int_0^\infty B(\xi)R_1(\rho,\xi)\{[1-2\nu+\xi R(\xi)]R(\rho\xi) + \frac{R(\xi)}{\rho} - \rho\xi\}\cos(\zeta\xi)d\xi \tag{13}$$

$$\sigma_{\theta\theta}(\rho,\zeta) = \left(\frac{\nu}{1+\nu}\right)\rho^{-2} + \int_0^\infty B(\xi)R_1(\rho,\xi)\left\{(1-2\nu)R(\rho\xi) - \frac{R(\xi)}{\rho}\right\}\cos(\zeta\xi)d\xi$$

$$\sigma_{\zeta\zeta}(\rho,\zeta) = 1 - \int_0^\infty B(\xi)R_1(\rho,\xi)\{[4-2\nu + \xi R(\xi)]R(\rho\xi) - \rho\xi\}\cos(\zeta\xi)d\xi$$

$$\sigma_{\rho\zeta}(\rho,\zeta) = \int_0^\infty B(\xi)R_1(\rho,\xi)\{2-2\nu+\xi R(\xi) - \rho\xi R(\rho\xi)\}\sin(\zeta\xi)d\xi$$

where $R(\xi) = K_0(\xi)K(\xi)^{-1}$ and $R_1(\rho,\xi) = K_1(\rho\xi)K(\xi)^{-1}$ and $B(\xi)$ is a function to be determined.

It remains to satisfy equations (5), (6) and to determine $B(\xi)$ so that the interface conditions

$$u_\zeta(1+,\zeta) = u(\zeta) \quad |\zeta| > \alpha_0$$
$$\sigma_{\rho\zeta}(1+,\zeta) = 0 \quad |\zeta| < \alpha_0$$

are satisfied subject to the constraint requirement

$$\int_{\alpha_0}^\infty \sigma_{\rho\zeta}\, d\zeta + \frac{1}{2}\frac{E_2}{E_1} = 0. \tag{14}$$

This latter condition is simply a statement that the fiber be in global equilibrium.

Upon integrating the fiber equilibrium equation (6) over (ζ, ∞), $\zeta \geq \alpha_0$, and enforcing equation (5), there results

$$\int_\zeta^\infty \left[\frac{d\sigma}{dt} + 2\sigma_{\rho\zeta}(1,t)\right]dt = \int_\zeta^\infty \left[\frac{E_2}{\epsilon_\infty E_1}u_{,tt} + 2\sigma_{\rho\zeta}(1,t)\right]dt = \frac{E_2}{E_1\epsilon_\infty}[u_{,\zeta}(\infty) - u_{,\zeta}(\zeta)] + 2\int_\zeta^\infty \sigma_{\rho\zeta}(1,t)dt = 0.$$

Finally, applying the first of the interface conditions (8) and using the representation for $u_\zeta(1,\zeta)$, equation (13) leads to the result

$$\frac{E_2}{E_1}(1+\nu)\int_0^\infty B(\xi)M(\xi)\cos(\zeta\xi)d\xi + 2\int_\zeta^\infty \sigma_{\rho\zeta}(1,t)dt = 0 \quad \zeta \geq \alpha_0$$

where

$$M(\xi) = [4(1-\nu) + \xi R(\xi)]R(\xi) - \xi \sim \begin{cases} -\beta_0\xi\log\xi + \xi^3\log^2\xi - \xi, & \xi \to 0 \\ \sum_{n=0}^\infty C_n\xi^{-n}, & \xi \to \infty \end{cases} \tag{15}$$

and

$$\{C_n\}_{n=0}^\infty = \{(\beta_0 - 1), \frac{1}{2}(\beta_0 - 2), \frac{3}{8}(\beta_0 - 3), -\frac{3}{8}(\beta_0 - 4), \ldots\}, \quad \beta_0 = 4(1-\nu).$$

This result, together with the debond-zone condition, first of equations (9), leads to the following pair of dual integral equations

$$\int_0^\infty B(\xi)\sin(\zeta\xi)d\xi = 0 \qquad \zeta < \alpha_0 \tag{16a}$$

$$\int_0^\infty B(\xi)M(\xi)\cos(\zeta\xi)d\xi + k\int_\zeta^\infty \sigma_{\rho\zeta}(1,t)dt = 0, \quad \zeta \geq \alpha_0, \qquad k = \frac{2}{1+\nu}\frac{E_1}{E_2}. \tag{16b}$$

These equations are subject to the constraint condition, equation (14).

III Reduction to a Cauchy Singular Integral Equation

To reduce equations (16) to a Cauchy singular integral equation, an explicit expression for the interface shear stress $\sigma_{\rho\zeta}(1, t)$ is developed. To this end define a new function $\phi(\zeta)$, $|\zeta| < \alpha_0$, as

$$\phi(\zeta) \equiv \int_0^\infty B(\xi)M(\xi)\cos(\zeta\xi)d\xi + k\int_{\max(\alpha_o,\zeta)}^\infty \sigma_{\rho\zeta}(1,t)dt. \tag{17}$$

The physical meaning of $\phi(\zeta)$ is readily seen from the derivation of equation (15) showing that it is proportional to $\{[u(\zeta) - u_\zeta(1,\zeta)],_\zeta\}$, i.e., proportional to the discontinuity in $\epsilon_{\zeta\zeta}$ across the debonded interface. Accordingly it follows that $\phi(\zeta) = 0$ for $|\zeta| > \alpha_0$ and $\phi(\zeta)$ is a symmetric function with respect to $\zeta = 0$.

Applying the inverse Fourier cosine transform[2] to both sides of equation (17) leads to the following expression for $B(\xi)$

$$\frac{\pi}{2}B(\xi)M(\xi) = \int_0^\infty \left[\phi(\zeta) - k\int_{\max(\alpha_o,\zeta)}^\infty \sigma_{\rho\zeta}(1,t)dt\right]\cos(\zeta\xi)d\zeta = \int_0^{\alpha 0} \phi(\zeta)\cos(\zeta\xi)d\zeta - \frac{k}{\xi}\int_{\alpha_o}^\infty \sigma_{\rho\zeta}(1,t)\sin(\xi t)dt \tag{18}$$

which satisfies the second dual integral equation (16*b*). Another expression for $B(\xi)$ may be established by applying the inverse

[2]Justification of the mathematical operations in deriving the solution are not presented. Validity of all the mathematical details and operations have been established and presented elsewhere (Mbanefo, 1987).

Downloaded 03 May 2010 to 171.66.16.244. Redistribution subject to ASME license or copyright; see http://www.asme.org/terms/Terms_Use.cfm

Fourier sine transform to the integral representation for $\sigma_{\rho\zeta}(1, \zeta)$ (equation (13)) and enforcing the first dual integral equation (16*a*). It results then that

$$2(1-\nu)\frac{\pi}{2}B(\xi)=\int_{\alpha_o}^{\infty}\sigma_{\rho\zeta}(1,t)\sin(\xi t)dt. \tag{19}$$

Combining equations (18) and (19) and eliminating the infinite integral gives the desired relation between $B(\xi)$ and $\phi(\zeta)$

$$\frac{\pi}{2}B(\xi)=\frac{\xi}{[2(1-\nu)k+\xi M(\xi)]}\int_0^{\alpha_o}\phi(\zeta)\cos(\zeta\xi)d\zeta. \tag{20}$$

Substituting from equation (20) into the right-hand side of the integral representation of $\sigma_{\rho\zeta}(1, \zeta)$ (equation (13)) then leads to the desired expression for the interface shear stress in terms of $\phi(\zeta)$

$$\sigma_{\rho\zeta}(1,\zeta)=\frac{2}{\pi}2(1-\nu)\int_0^{\infty}\left[\frac{\xi}{2(1-\nu)k+\xi M(\xi)}\times\int_0^{\alpha_o}\phi(t)\cos(\xi t)dt\right]\sin(\zeta\xi)d\xi. \tag{21}$$

It remains to determine $\phi(t)$ so that equation (16*a*) is satisfied. For this purpose define $I(\zeta)$ to be the integral of the left-hand side of equation (16*a*) over $(0, \zeta)$, i.e.,

$$I(\zeta)=\int_0^{\zeta}\left[\int_0^{\infty}B(t)\sin(\xi t)dt\right]d\xi=\int_0^{\infty}B(t)\frac{[1-\cos(\zeta t)]dt}{t}. \tag{22}$$

Provided $\zeta\epsilon[0, \alpha_0)$, $I(\zeta) = 0$.

Substituting the expression for $B(\xi)$, equation (20), into (22), exchanging the order of integration, and simplifying somewhat leads to the following

$$C_0 I(\zeta)=\int_0^{\alpha_o}\phi(\xi)\left\{\log\left|\frac{\xi^2-\zeta^2}{\xi^2}\right|+2\int_0^{\infty}\left[\frac{C_0 t}{tM(t)+\beta}-1\right]\left[\frac{1-\cos(\zeta t)}{t}\right]\cos(\xi t)dt\right\}d\xi=0,$$

$$\zeta\epsilon[0,\alpha_0),\quad C_0=3-4\nu,\quad \beta=\frac{4(1-\nu)}{(1+\nu)}\frac{E_1}{E_2}.$$

Differentiating $I(\zeta)$, invoking the symmetry of $\phi(t)$, and evaluating one of the integrals results in the final singular integral equation for the unknown $\phi(\xi)$

$$\int_{-\alpha_o}^{\alpha_o}\frac{\phi(\xi)}{\zeta-\xi}d\xi+\int_{-\alpha_o}^{\alpha_o}G(\zeta,\xi)\phi(\xi)d\xi=0 \tag{23}$$

where $G(\zeta, \xi)$ is a bounded continuous function given by

$$G(\zeta,\xi)=-\beta\int_0^{\infty}\frac{\sin[(\zeta-\xi)t]dt}{[(3-4\nu)t+\beta]}+\int_0^{\infty}\frac{(3-4\nu)[(3-4\nu)-M(t)]t^2\sin[(\zeta-\xi)t]dt}{[tM(t)+\beta][(3-4\nu)t+\beta]}. \tag{24}$$

The first integral in equation (24) can be expressed in terms of cosine and sine integrals while the second integral is readily evaluated numerically.

A simple transformation

$$\xi=\alpha_0 y,\ \zeta=\alpha_0 x,\ \phi(\alpha_0 y)=\Phi(y)$$

converts equation (23) to a standard Cauchy singular integral equation of the first kind

$$\int_{-1}^{1}\frac{\Phi(y)\,dy}{x-y}+\int_{-1}^{1}K(x,y)\Phi(y)dy=0,\quad x\epsilon(-1,1) \tag{25}$$

where $K(x, y) = \alpha_0 G(\alpha_0 x, \alpha_0 y)$. The associated constraint condition (14) then assumes the form

$$\int_1^{\infty}\sigma_{\rho\zeta}(1+,\alpha_0 x)dx+\frac{1}{2\alpha_0}\frac{E_2}{E_1}=0. \tag{26}$$

Solution (numerical) of equations (25) and (26) for $\phi(\xi)$ and substitution into (20) determines the unknown $B(\xi)$. The solution for the stress and displacement fields follows from equations (13) upon numerical integration.

IV Numerical Solution

Normally, an interface crack between two dissimilar materials has a crack-tip stress field with an oscillatory singularity (Williams, 1959) of the form

$$\sigma\sim r^{-1/2}e^{i\Theta\log(r)}$$

where Θ measures the discontinuity in the elastic constants of the two materials. In this particular problem the oscillatory behavior is not present (see Wiley, 1983) due to the model of the fiber and the interface debonding.

The solution to equation (25) possesses the well-known square root singularity at the end points (7) and may be represented in the form

$$\Phi(x)=\frac{F(x)}{\sqrt{1-x^2}}=\sum_{n=0}^{N-1}\frac{B_{2n}T_{2n}(x)}{\sqrt{1-x^2}}. \tag{27}$$

In Equation (27) it is assumed that $F(x)$ is sufficiently smooth so that it may be adequately approximated by polynomials. As the procedure of Erdogan and Gupta (1972) is to be employed, Chebyshev polynomials $T_n(x)$ are used and only the even powers are retained in view of the symmetry of $\Phi(x)$.

In anticipation of enforcing the constraint condition (26), the interface shear stress is first expressed in terms of the solution form (27). From equation (27) it follows that

$$\int_0^1\Phi(x)\cos(\alpha_0\xi x)dx=\sum_{n=0}^{N=1}B_{2n}\int_0^1\frac{T_{2n}(x)\cos(\alpha_0\xi x)dx}{\sqrt{1-x^2}}=\sum_{n=0}^{N-2}\frac{\pi}{2}B_{2n}(-1)^n J_{2n}(\alpha_0\xi) \tag{28}$$

upon using the definition of the Chebyshev polynomials and an integral representation, Abramowitz and Stegun (1987), for the Bessel functions $J_{2n}(x)$.

The unknown constants B_{2n} are expressed in terms of $F(x)$ by the following procedure. Multiply both sides of equation (27) by $T_{2m}(x)$, integrate between the limits of $(-1, 1)$, and employ the orthogonality properties of $T_{2m}(x)$. Then

$$\int_{-1}^{1}\frac{T_{2m}(x)\,F(x)\,dx}{\sqrt{1-x^2}}=\sum_{n=0}^{N-1}\left[\int_{-1}^{1}\frac{T_{2m}(x)\,T_{2n}(x)\,dx}{\sqrt{1-x^2}}\right]B_{2n}$$

$$=\pi B_0,\qquad m=0$$

$$=\frac{\pi}{2}B_{2m},\quad m=n\neq 0. \tag{29}$$

The integral in equation (29) involving $F(x)$ is readily evaluated by the Gaussian integration scheme appropriate for Chebyshev polynomials to obtain

$$B_{2n}=\frac{\gamma_n}{N}\sum_{m=1}^{N}T_{2n}(x_m)\,F(x_m) \tag{30}$$

where $\gamma_0 = 1$, $\gamma_n = 2$ $(n > 0)$, and $x_m = \cos\{[(2m - 1)/(2N)]\pi\}$.

Substituting from equation (30) into (28) and in turn into (21) leads to the following expression for the interface shear stress

Downloaded 03 May 2010 to 171.66.16.244. Redistribution subject to ASME license or copyright; see http://www.asme.org/terms/Terms_Use.cfm

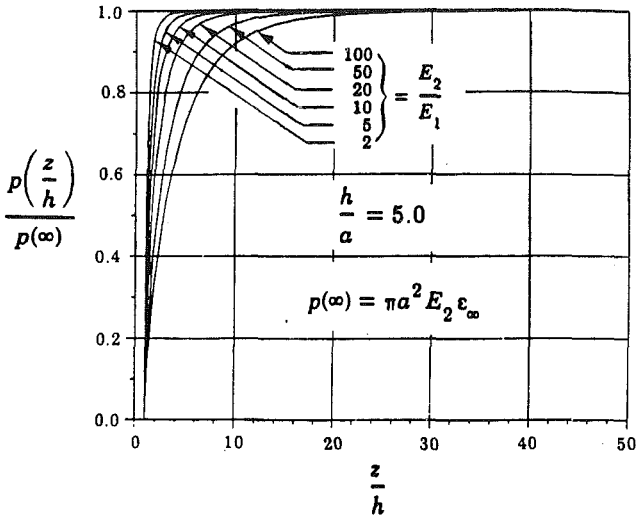


Fig. 2 Fiber axial force distribution, $h/a = 5$

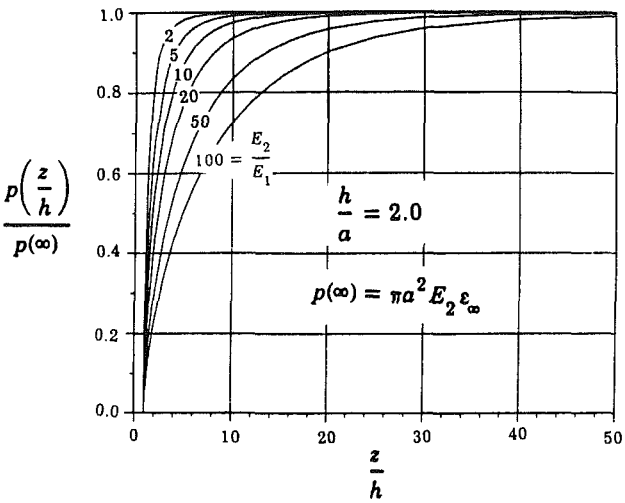


Fig. 3 Fiber axial force distribution, $h/a = 2$

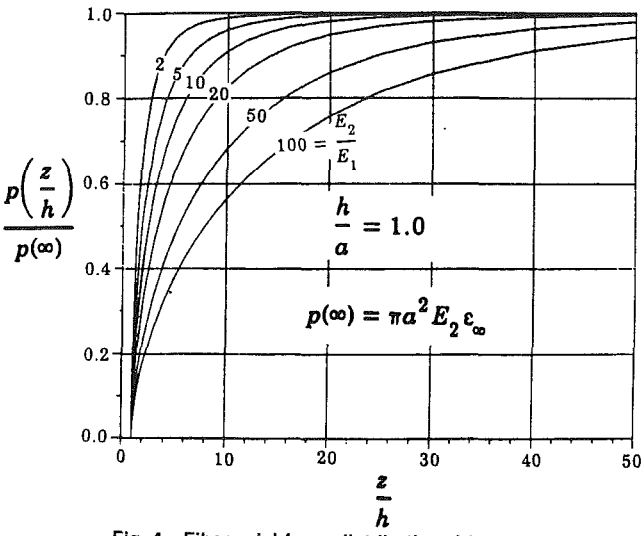


Fig. 4 Fiber axial force distribution, $h/a = 1$

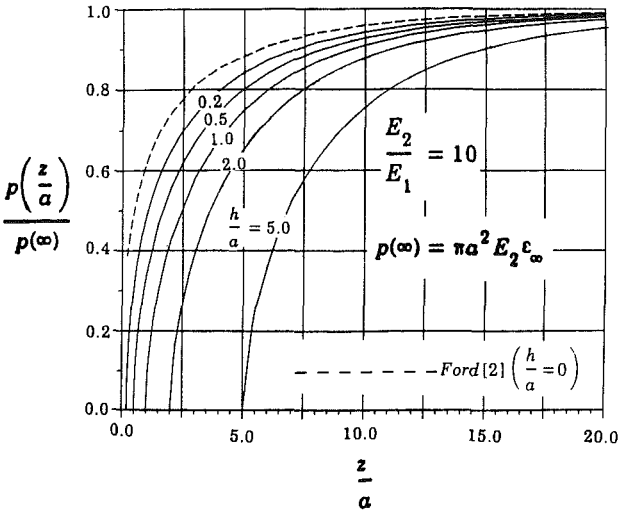


Fig. 5 Fiber axial force distribution, $E_2/E_1 = 10$

$$\sigma_{\rho\zeta}(1,\zeta) = 2(1-\nu)\alpha_0 \sum_{n=0}^{N-1} (-1)^n \times \left[\frac{\gamma_n}{N} \sum_{m=1}^{N} T_{2n}(x_m)\, F(x_m)\right] x \int_0^\infty \left[\frac{\xi}{2(1-\nu)k + \xi M(\xi)}\right] \times J_{2n}(\alpha_0 \xi)\, \sin(\zeta\xi) d\xi. \quad (31)$$

With equation (31) the constraint condition can now be satisfied. Substituting from equation (31) into (26) leads to the final desired result

$$\sum_{m=1}^{N} p_m F(x_m) = -\frac{1}{2\alpha_0} \frac{E_2}{E_1} \quad (32)$$

where

$$p_m = \frac{2(1-\nu)}{N} \alpha_0 \sum_{n=0}^{N-1} T_{2n}(x_m) Z_{2n}$$

$$Z_{2n} = (-1)^n \gamma_n \sum_{1}^{\infty} \left\{ \int_0^\infty \left[\frac{\xi}{2(1-\nu)k + \xi M(\xi)}\right] \times J_{2n}(\alpha_0 \xi) \sin(\alpha_0 x \xi) d\xi \right\} dx.$$

The Cauchy singular integral equation (25) is treated by the standard Erdogan, Gupta (1972) method which in this case reduces to

$$\frac{\pi}{N} \sum_{m=1}^{N} \left[\frac{1}{y_n - x_m} + K(y_n, x_m)\right] F(x_m) = 0, \; n = 1,2, \ldots, N-1 \quad (33)$$

where

$$x_m = \cos\left[\frac{(2m-1)\pi}{2N}\right], \; y_n = \cos\left(\frac{n\pi}{N}\right).$$

Solution of equations (32) and (33) for $F(x_m)$ gives $\Phi(x_m)$ and B_{2m}. From this the stress and displacement fields are evaluated in a manner analogous to the development of the expression for $\sigma_{\rho\zeta}$ (equation (31)). These numerical details have been completed for the case $\nu = 1/4$ and several results of interest are presented and discussed in the next section.

V Discussion

Figures 2 through 4 present the axial force distributions for a range of E_2/E_1 and values of $a/h = 0.2, 0.5, 1.0$. These results show how a higher modulus fiber attains its far-field value more slowly than a lower modulus fiber. In a similar

Downloaded 03 May 2010 to 171.66.16.244. Redistribution subject to ASME license or copyright; see http://www.asme.org/terms/Terms_Use.cfm

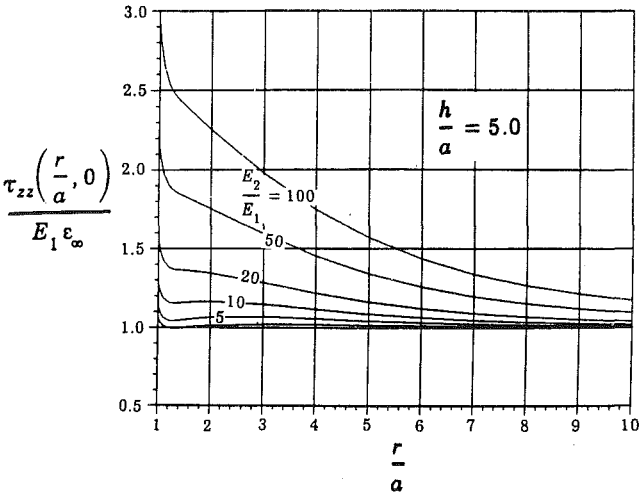


Fig. 6 Normal stress distributions in matrix-fiber fracture plane

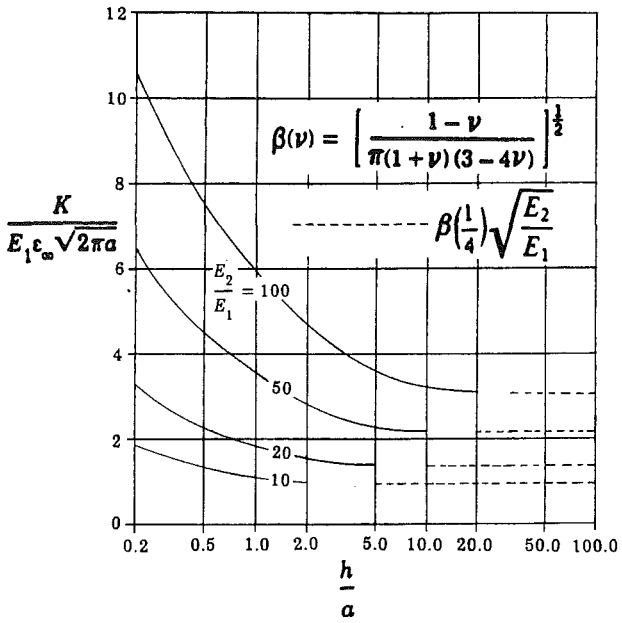


Fig. 7 Debond tip stress intensity factors

way these figures illustrate the role of decreasing a/h. As the fiber radius decreases (with respect to debond length), the fiber becomes increasingly compliant and reaches its far-field limit for smaller values of z/h.

In Fig. 5 the axial force distribution is presented for $E_2/E_1 = 10$ and decreasing values of h/a. This figure shows how the fiber force increases more slowly with increasing z/a for larger values of debonding. This means that a fiber with greater interface debonding performs (locally) as a more compliant fiber with a shorter debond length.

The results due to Ford (1973) are recorded in Fig. 5 for comparison. In the Ford results, debonding was not considered ($h/a = 0$) and the fiber was treated as a three-dimensional continuum. While it is not possible to let h/a vanish in the present formulation, the results for decreasing values of h/a appear to be approaching the Ford curve.

The normal stress τ_{zz} $(r/a, 0)$ on the fiber fracture plane is presented in Fig. 6 for a range of E_2/E_1. This shows that for the case where the debond length is five times the fiber radius, the stress concentration (in plane $z=0$) increases from 1.05 to 2.9 as the fiber stiffness increases. While not presented, other results for different values of h/a show that this stress concentration increases significantly as the debond length decreases (with respect to fiber radius). This demonstrates how the matrix is more likely to fracture if extensive debonding does not occur.

As pointed out in Section IV, the matrix stress field in the neighborhood of the tip of the debond zone is singular. The intensity of this singularity may be measured by the debond tip stress intensity factor K defined by

$$\tau_{rz}(a+,z)=\frac{K}{\sqrt{2\pi(z-h)}}+0(1), \quad z-h\to 0+. \tag{34}$$

Figure 7 presents this stress intensity factor for a range of values of E_2/E_1 and h/a. It is observed that the debond tip stress intensity factor decreases with increasing h/a indicating that interface debonding is a stable process for this range of h/a.

Knowledge of the debond tip stress intensity factor and the relative debond displacement $[U_z(a, z) - u_f(z)]$ of the matrix with respect to the fiber permits the calculation of the strain energy release rate, G. The strain energy release rate (energy released/unit debond extension) for the axisymmetric case considered here is related to the debond intensity factor by the expression

$$G=\frac{1-\nu}{(3-4\nu)(1+\nu)}\frac{K^2}{8E_1}. \tag{35}$$

It may be readily shown for $h/a \gg 1$ that $G = E_2\epsilon_\infty^2$ $(a/4)$ and from equation (35) it results that

$$\frac{K}{E_1\epsilon_\infty\sqrt{2\pi a}}=\left[\frac{1-\nu}{\pi(3-4\nu)(1+\nu)}\right]^{1/2}\left(\frac{E_2}{E_1}\right)^{1/2}. \tag{36}$$

Equation (36) provides an asymptotic limit as $h/a \to \infty$ and is shown in Fig. 7.

Let K^* denote the *critical* debond tip intensity factor (an interface material property) at which debond growth occurs. It follows from equation (36) that if the applied far-field stress $E_1\epsilon_\infty$ exceeds the value

$$(E_1\epsilon_\infty)^*=\frac{K^*}{\sqrt{2\pi a}}\left[\frac{\pi(3-4\nu)(1+\nu)}{1-\nu}\right]^{1/2}\left(\frac{E_1}{E_2}\right)^{1/2}, \tag{37}$$

then debonding will continue indefinitely rendering the reinforcing fiber useless. From this one finds that the bound on complete debonding failure is proportional to $(E_1/E_2a)^{1/2}$.

Results for the interface shear stress are not presented. Upon noting that the axial fiber force $P(z)$ may be expressed in terms of $\tau_{rz}(a+,z)$,

$$P(z)=\int_a^z \tau_{rz}(a+,\xi)2\pi a d\xi, \tag{38}$$

then it follows that $\tau_{rz}(a+,z)$ is proportional to the slope of the curves in Figs. 2 through 4.

The mechanics model for the fiber (equations (5), (6)) places certain restrictions on the range of parameters for which the results presented here are valid. A plane stress/plane strain analog of the present three-dimensional problem was considered by Mbanefo (1987) and the fiber treated as a two-dimensional elastic continuum. It resulted that as $h/a \to \infty$, the formulation reduced to a pair of dual integral equations corresponding to those for a one-dimensional fiber. The results presented (Mbanefo, 1987) show that the fiber approximations used herein are strictly valid only for larger values of h/a. In Figs. 6 and 7, results are presented for $h/a < 1$. While the curves for lower values of h/a are mathematically correct, their representation of the three-dimensional elasticity problem is suspect.

The model of the interface debond zone used in this paper assumes that adjacent debond surfaces remain in normal con-

Downloaded 03 May 2010 to 171.66.16.244. Redistribution subject to ASME license or copyright; see http://www.asme.org/terms/Terms_Use.cfm

tact. Calculation of the interface normal stress $\tau_{rr}(a+,z)$, in the debond zone ($z\epsilon[0,h)$) shows this particular stress component to be compressive (for far-field loading used herein). Thus, the model of the debond zone employed is accurate provided the debond surfaces are smooth and the interface friction zero.

The mathematical solution and subsequent numerical treatment presented have been checked as follows. The same procedures were employed to solve the analogous two-dimensional plane stress/plane strain problem. These two-dimensional results were compared with solutions obtained by an entirely different method (Vardanyan, 1988) and excellent agreement was observed.

VI Acknowledgments

The authors express their gratitude to Mr. V. Vardanyan for sharing results from his unpublished research, thereby permitting partial validation of the methods and conclusions presented here. Further, the authors thank Prof. J. E. Marsden (Mathematics Department, University of California, Berkeley) who was Co-chairman of the thesis research, Mbanefo (1987), upon which this paper is based.

References

Abramowitz, M., and Stegun, I. A., eds., 1987, *Handbook of Mathematical Functions*, Dover.

Erdogan, F., and Gupta, G. D., 1972, "On the Numerical Solution of Singular Integral Equations," *Quarterly of Appl. Maths.*, p. 525.

Ford, E. F., 1973, "Stress Analysis of a Broken Fiber Imbedded in an Elastic Medium," D.E.A.P., Harvard University, Tech. Report No. 1.

Love, A. E. H., 1944, *A Treatise on the Mathematical Theory of Elasticity*, Dover, pp. 274–276.

Mbanefo, U., 1987, "Mixed Boundary-Value Problems of Stress Singularities in the Neighborhood of a Fractured and Debonded Fiber Embedded in an Infinite Elastic Matrix," Ph.D. Thesis, University of California, Berkeley, Calif.

Muki, R., and Sternberg, E., 1971, "Load-absorption by a Discontinuous Filament in a Fiber-Reinforced Composite," *Z. Ange. Math. Physik*, Vol. 22, p. 809.

Muskhelishvilli, N. I., 1953, *Singular Integral Equations*, P. Noordhoff Ltd.

Vardanyan, V., 1988, private communication.

Wiley, D. S., 1983, "Single and Multiple Fiber Models for Fracture of Fibrous Composites," Ph.D. Thesis, University of California, Los Angeles, Calif.

Williams, M. L., 1959, "The Stresses Around a Fault or Crack in Dissimilar Media," *Bulletin of the Seismological Society of America*, Vol. 49, p. 199.

Downloaded 03 May 2010 to 171.66.16.244. Redistribution subject to ASME license or copyright; see http://www.asme.org/terms/Terms_Use.cfm

Elastodynamic Scattering From Penny-Shaped and Nonplanar Cracklike Flaws With Dissipation and Restoring Forces

Peter Olsson
Division of Mechanics,
Chalmers University of Technology,
Goteborg, Sweden S-412 96

Scattering from penny-shaped and nonplanar cracklike flaws, with a type of boundary condition which incorporates dissipation and restoring forces, is studied. Scattering cross-sections and energy absorption cross-sections are computed, and comparisons with open cracks are performed. A partially debonded inclusion, with the debonding in the form of a cracklike flaw, is also discussed. The method employed is a modified null field approach, incorporating some ideas previously used for treating scattering from nonplanar open or fluid-filled cracks. In the present context, the boundary conditions lead to great simplifications in the implementation of the method, in that part of the relevant matrices can be computed analytically.

Introduction

The elastodynamic scattering problem for cracks is one which has received much attention, particularly due to its importance in ultrasonic nondestructive evaluation of materials. It is not possible here to give any review of the vast literature on the subject. We give only a few references to papers of a more or less immediate connection to the present study. The papers by Krenk and Schmidt (1982) and Martin and Wickham (1983) treat the scattering by penny-shaped cracks. The latter reference also contains many references to earlier literature. Peterson (1988) has used the results of Krenk and Schmidt to compute multiple scattering from two penny-shaped cracks. Recently, Budreck and Achenbach (1988) treated the case of planar noncircular cracks by the boundary integral equation method. On the scattering from nonplanar cracks, Boström and Olsson (1987) and Olsson (1986) give null-field solutions for open, i.e., traction-free, and fluid-filled, i.e., "perfectly lubricated," cracks.

In the present paper we treat the problem of scattering from a type of cracklike flaws with boundary conditions incorporating the effects of an "imperfect" adhesion between the "faces" of the flaw. The adhesion is modeled as a linear but frequency-dependent restoring force and a viscous damping of the relative motion of the faces. The boundary conditions employed are, apart from the particular frequency dependence and the damping, essentially the boundary conditions of Jones and Whittier (1967) and Aboudi (1988). In these papers the boundary conditions are used as a model for the imperfect bonding between two layers in a laminated composite. Similar boundary conditions have also been studied by a number of authors. Mal and Bose (1974) determined the dynamic elastic moduli for a solid containing a random distribution of spherical inclusions with boundary conditions where the tangential stresses across the boundary of the particles are proportional to the amount of tangential slip.

Nayfeh and Nassar (1978), in a study of the dynamic influence of bonding materials in laminated composites, derived a set of related, though slightly more complicated, boundary conditions which essentially relate discontinuities of the displacements and the traction across the bonding layer to the displacements and tractions themselves. Chatterjee et al. (1980) studied the dynamic elastic moduli of a solid with a distribution of penny-shaped cracks, where the boundary conditions incorporate viscous damping. Other studies which should be mentioned are: (1) the paper by Plarsky and Rose (1988) where the problem of determining the possible weakness of bonding layer in a laminated composite is studied and (2) the paper by Mal (1988). The latter paper is a study of guided waves in a laminated composite with imperfect bonding.

In the present study the boundary conditions of continuous traction and the normal and tangential traction being proportional to the normal and tangential crack opening displacement, respectively, are used as the simplest linear model for an imperfectly lubricated crack, with restoring forces as well as damping. As has been noted in the references given previously, the boundary conditions in question contain both the open and the fluid-filled crack as limiting cases, and they provide models for a number of very thin flaws of practical interest. It is, therefore, of interest to study the scattering properties of these boundary conditions, as well as the numerical behavior

Contributed by the Applied Mechanics Division of THE AMERICAN SOCIETY OF MECHANICAL Engineers for publication in the JOURNAL OF APPLIED MECHANICS. Discussion on this paper should be addressed to the Technical Editor, Leon M. Keer, The Technological Institute, Northwestern University, Evanston, IL 60208, and will be accepted until two months after final publication of the paper itself in the JOURNAL OF APPLIED MECHANICS. Manuscript received by the ASME Applied Mechanics Division, Jan. 3, 1989; final revision, Aug. 20, 1989.

Copyright © 1990 by ASME
Downloaded 03 May 2010 to 171.66.16.244. Redistribution subject to ASME license or copyright; see http://www.asme.org/terms/Terms_Use.cfm

of the particular method of solution presented here. Ultimately the interest, of course, lies in trying to determine the properties of such a thin inclusion or crackline flaw from the scattering data, but it seems clear that before that inverse problem can be studied with any hope of success, the direct scattering problem must be solved in an effective manner (c.f., Pilarsky and Rose, 1988).

The method of solution employed here for the direct problem of a finite scatterer allows us to treat both penny-shaped and even nonplanar, cap-shaped, cracklike flaws. Analytical and numerical results are given for both these types of flaws.

The case when the cracklike flaw forms part of the boundary of an otherwise welded elastic inclusion is also solved, though no numerical results are presented here for the latter case.

The Scattering Problem

Let us consider a cracklike flaw on an oriented open surface S inside a linear, homogeneous, and isotropic elastic solid. The surface may be planar or nonplanar. In addition S could, in principle, consist of several disjoint parts (cf., Boström and Olsson, 1987), though we will not pursue that possibility in the present paper. The positive unit normal of S we denote by $\hat{n}$, and we assume that S is sufficiently smooth for $\hat{n}$ to vary continuously over S. By subscripts + and −, we will denote limits taken from the positive and negative side of S, respectively.

On S we assume the boundary conditions

$$\mathbf{t}_+ = \mathbf{t}_- \qquad \text{on } S \tag{1}$$

$$\mathbf{u}_+ - \mathbf{u}_- = \frac{1}{\mu k_s}(\alpha \hat{n}\hat{n}\cdot\mathbf{t}_- + \beta(\mathbf{t}_-)_{\tan}) \qquad \text{on } S \tag{2}$$

for the displacement $\mathbf{u}$ and the traction $\mathbf{t}$. Here, α and β are dimensionless complex constants, and μk_s is introduced for dimensional reasons. λ and μ are the Lamé constants of the solid, k_p and k_s are the P and S wave numbers corresponding to the frequency ω, $\hat{n}\cdot\mathbf{t}_-$ denotes the scalar product between the unit normal and $\mathbf{t}_-$, and $(\cdot)_{\tan}$ denotes the tangential part of a vector. In principle, α and β could be frequency dependent, but for reasons that will be discussed they are here assumed to be constant.

It should be noted that for $\alpha=\beta=0$, this is simply the boundary conditions of welded contact; i.e., no scatterer, and if we let $|\alpha|\to\infty$, $|\beta|\to\infty$, we get the boundary conditions of an open crack. Similarly, if we let $\alpha=0$, $|\beta|\to\infty$, we get a perfectly lubricated crack (see Aboudi, 1988). Since we assume α and β to be constants independent of the frequency, positive imaginary parts correspond to viscous damping forces, while the real parts correspond to restoring forces—the spring constants of which increase with increasing frequency.

The motivation for including the frequency dependency (the factor k_s^{-1}) in the spring constants, while keeping α and β constant, is twofold. First, we want to have "local" boundary conditions, in the sense that they should be independent of the overall geometry of the flaw. We are not assuming any specific thickness for the flaw, so the only parameters of dimension length then available to us are k_s^{-1} and k_p^{-1}. For dimensional reasons a linear relation between $\mathbf{u}_+ - \mathbf{u}_-$ and $\mathbf{t}_-$ must contain a parameter of dimension length, leading to equation (2). Secondly, as we shall see in the next section, this choice leads to results for the scattering cross-section which already for comparatively small α and β lie rather close to the results for open cracks.

The direct scattering problem for the cracklike flaw at S which we consider is the following: Given an incident displacement field $\mathbf{u}^i$ (which the time factor $e^{-i\omega t}$ suppressed), the presence of the flaw produces a scattered field $\mathbf{u}^s$. For a given $\mathbf{u}^i$, we want to compute $\mathbf{u}^s$. To accomplish this we append to S another, fictitious, surface S_0, thus forming the closed surface $S+S_0$. (See Fig. 1.) The outward pointing unit normal on all of $S+S_0$ we denote by $\hat{n}$. ($\hat{n}$ on S is in this way extended to a closed surface of which S forms only a part.) Inside $S+S_0$ we choose an origin O, and denoting by $r_{\min}$ and $r_{\max}$ the minimum and maximum distances from O to $S+S_0$, respectively, we can expand $\mathbf{u}^i$ and $\mathbf{u}^s$ as

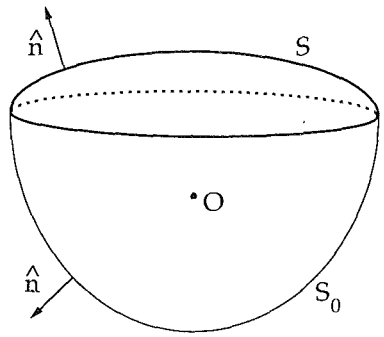


Fig. 1 The open surface S of the flaw and a fictitious surface S_0

$$\mathbf{u}^i = \sum_n a_n \mathrm{Re}\psi_n, \quad r<r_{\min} \tag{3}$$

$$\mathbf{u}^s = \sum_n f_n \psi_n, \quad r>r_{\max}. \tag{4}$$

Here, $\mathrm{Re}\psi_n$ and ψ_n are regular and outgoing spherical vector waves with respect to O, defined in the same manner as in, e.g., Boström (1980), and we assume that sources of $\mathbf{u}^i$ lie outside the finite volume bounded by $S+S_0$. The expansion in equation (3) in fact converges at least out to the nearest source of the incident field, thus in particular in the region $r<r_{\min}$ indicated. The sources of the scattered field all lie on S, and as the expansion in equation (4) converges outside the smallest closed ball containing all the sources of the scattered field, in particular it converges in the region $r>r_{\max}$ as indicated.

To compute the expansion coefficients of the scattered field in terms of the incident field, we employ the null-field approach (cf., Boström and Olsson, 1987 for further references on this method). On S_0 we have the boundary conditions of welded contact, and on S we have the boundary conditions (1) and (2). The expansion coefficients are expressed as (cf., e.g., Boström, 1980)

$$a_n = -\frac{ik_s}{\mu}\int_{S+S_0}[\mathbf{u}_-\cdot\mathbf{t}(\psi_n) - \mathbf{t}_-\cdot\psi_n]\,dS$$
$$-\frac{i}{\mu^2}\int_S \mathbf{t}_-\cdot((\alpha-\beta)\hat{n}\hat{n}+\beta\vec{I})\cdot\mathbf{t}(\psi_n)dS \tag{5}$$

$$f_n = \frac{ik_s}{\mu}\int_{S+S_0}[\mathbf{u}_-\cdot\mathbf{t}(\mathrm{Re}\psi_n) - \mathbf{t}_-\cdot\mathrm{Re}\psi_n]\,dS$$
$$+\frac{i}{\mu^2}\int_S \mathbf{t}_-\cdot((\alpha-\beta)\hat{n}\hat{n}+\beta\vec{I})\cdot\mathbf{t}(\mathrm{Re}\psi_n)dS \tag{6}$$

where subscripts + and − now denote limits with respect to $S+S_0$. $\mathbf{t}(\cdot)$ is the surface traction operator, $\mathbf{t}_+$ and $\mathbf{t}_-$ are the limits of $\mathbf{t}(\mathbf{u})$, and $\vec{I}$ is the unit dyadic. Approximating the surface displacement field on the inside of $S+S_0$ as

$$\mathbf{u}_- = \sum_n \gamma_n \mathrm{Re}\psi_n \tag{7}$$

we know (see Pao, 1978) that the surface traction is given by

$$\mathbf{t}_- = \sum_n \gamma_n \mathbf{t}(\mathrm{Re}\psi_n). \tag{8}$$

Downloaded 03 May 2010 to 171.66.16.244. Redistribution subject to ASME license or copyright; see http://www.asme.org/terms/Terms_Use.cfm

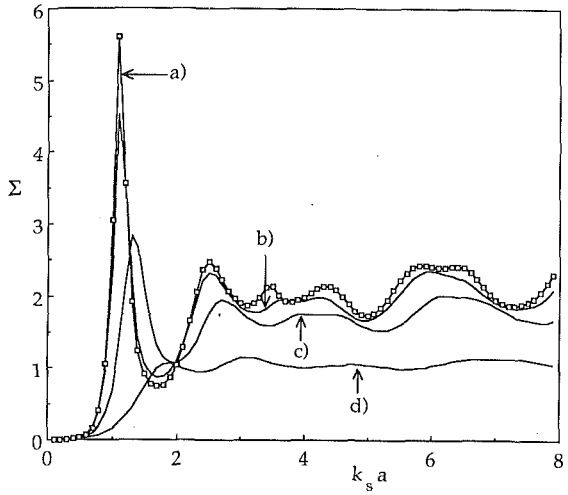


Fig. 2 The normalized total scattering cross-section Σ for a cap-shaped hemispherical flaw, and a plane *S* wave incident along the symmetry axis: (*a*) open crack, (*b*) flaw with $\alpha^{-1}=\beta^{-1}=0.1$, (*c*) $\alpha^{-1}=\beta^{-1}=0.2$, (*d*) $\alpha^{-1}=\beta^{-1}=0.5$

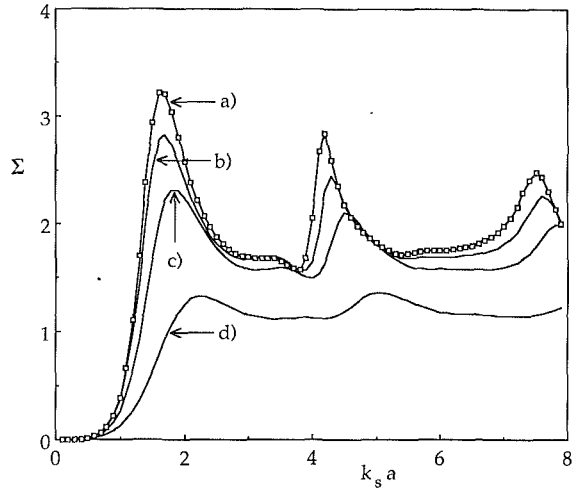


Fig. 3 Same as Fig. 2 but for plane *P* wave incident along the symmetry axis

Inserting this into equations (5) and (6) we can perform the integration over $S+S_0$ analytically by means of Betti identities (Pao (1978)), obtaining the relations

$$a=-i\,Q\,\gamma \tag{9}$$

$$f=i\,\mathrm{Re}Q\,\gamma \tag{10}$$

in obvious matrix notation, where the elements of the matrices Q and ReQ are

$$Q_{nn'}=i\delta_{nn'}+\frac{1}{\mu^2}\int_S \mathbf{t}(\mathrm{Re}\psi_{n'})\cdot[(\alpha-\beta)\hat{n}\hat{n}+\beta\vec{I}]\cdot\mathbf{t}(\psi_n)dS \tag{11}$$

$$\mathrm{Re}Q_{nn'}=\frac{1}{\mu^2}\int_S \mathbf{t}(\mathrm{Re}\psi_{n'})\cdot[(\alpha-\beta)\hat{n}\hat{n}+\beta\vec{I}]\cdot\mathbf{t}(\mathrm{Re}\psi_n)dS. \tag{12}$$

Eliminating γ, we obtain

$$f=Ta \tag{13}$$

where

$$T=-(\mathrm{Re}Q)Q^{-1} \tag{14}$$

is the transition matrix of the cracklike flaw. It should be noted that if losses in the flaw are included, i.e., α and β have imaginary parts, Re$Q_{nn'}$ is not the real part of $Q_{nn'}$.

Having obtained the transition matrix of the cracklike flaw as in equation (14) above, we have solved the scattering problem, at least formally. The transition matrix in a sense contains all information about the scattering properties of the flaw. Combined with the information about the incident field, given by the coefficients a_n, the scattered field can be obtained by means of equations (13) and (4). In practice, the transition matrix can, of course, only be computed up to a certain truncation and the numerical stability of the results, with respect to an increase in the truncation, must be checked (cf. the next section).

An interesting feature of the expressions for Q and ReQ above, is that they are independent of our choice of S_0. That the resulting T matrix should not depend on S_0 is obvious, but the Q and ReQ matrices relate the surface field on all of $S+S_0$ to the incident and scattered fields, respectively, and it is not at all obvious that these matrices should be independent of the choice of S_0. Indeed, similar expressions for the Q-matrices of open or fluid-filled nonplanar cracks do contain a dependence on a corresponding fictitious surface (Boström and Olsson, 1987; Olsson, 1986).

It should be noted that the solution to the scattering problem above could easily be extended to the case of a cracklike flaw over part of the boundary of an elastic inclusion. The Q and ReQ matrices obtained for this case are

$$Q_{nn'}=Q^{\mathrm{incl}}_{nn'}+\frac{1}{\mu^2}\int_S \mathbf{t}^1(\mathrm{Re}\psi^1_{n'})\cdot[(\alpha-\beta)\hat{n}\hat{n}+\beta\vec{I}]\cdot\mathbf{t}(\psi_n)dS \tag{15}$$

$$\mathrm{Re}Q_{nn'}=\mathrm{Re}Q^{\mathrm{incl}}_{nn'}+\frac{1}{\mu^2}\int_S \mathbf{t}^1(\mathrm{Re}\psi^1_{n'})\cdot[(\alpha-\beta)\hat{n}\hat{n}+\beta\vec{I}]\cdot\mathbf{t}(\mathrm{Re}\psi_n)dS \tag{16}$$

where

$$Q^{\mathrm{incl}}_{nn'}=\frac{k_s}{\mu}\int_{S+S_0}[\mathrm{Re}\psi^1_{n'}\cdot\mathbf{t}(\psi_n)-\mathbf{t}^1(\mathrm{Re}\psi^1_{n'})\cdot\psi_n]\,dS \tag{17}$$

$$\mathrm{Re}Q^{\mathrm{incl}}_{nn'}=\frac{k_s}{\mu}\int_{S+S_0}[\mathrm{Re}\psi^1_{n'}\cdot\mathbf{t}(\mathrm{Re}\psi_n)-\mathbf{t}^1(\mathrm{Re}\psi^1_{n'})\cdot\mathrm{Re}\psi_n]\,dS \tag{18}$$

are Q and ReQ matrices for a perfectly bonded elastic inclusion. Wave functions and traction operators with a superscript 1 have the material parameters appropriate for the medium of the elastic inclusion. In this case S_0 can not be chosen arbitrarily. It must be taken as that part of the boundary of the inclusion where the inclusion is in welded contact with the matrix medium.

Numerical Results

In the present section we will consider some numerical results, both for penny-shaped and nonplanar rotationally symmetric cracklike flaws obeying the boundary conditions (1), (2). Starting with some comparisons with open cracks, we have in Figs. 2 and 3 the total scattering cross-section for S and P wave incidence against a hemispherical surface on which we take $\alpha=\beta$. The direction of incidence is along the axis of symmetry, and scattering cross-section is normalized by dividing by πa^2, where a is the radius of the crack edge. This normalization is used in all of the following. The Poisson ratio is in all cases 0.25.

Downloaded 03 May 2010 to 171.66.16.244. Redistribution subject to ASME license or copyright; see http://www.asme.org/terms/Terms_Use.cfm

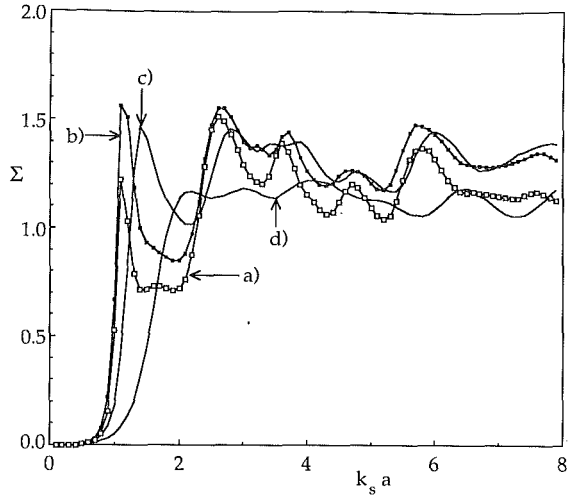


Fig. 4 Same as Fig. 2 but for plane *P* wave incident perpendicularly to the symmetry axis

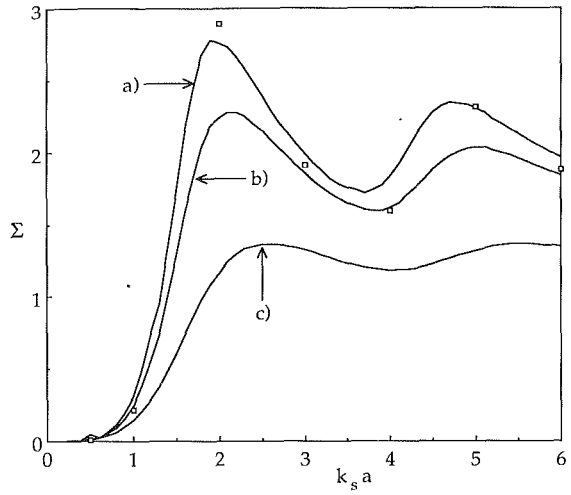


Fig. 6 Same as Fig. 5 but for plane *P* wave incident along the symmetry axis

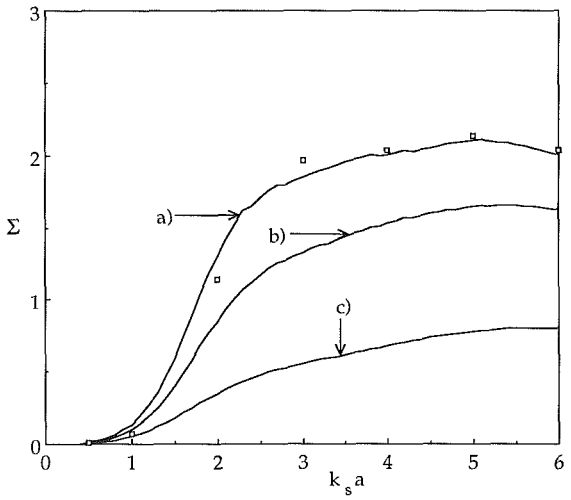


Fig. 5 The normalized total scattering cross-section Σ for a penny-shaped flaw, and a plane *S* wave incident along the symmetry axis: (*a*) $\alpha^{-1} = \beta^{-1} = 0.1 - i0.01$, (*b*) $\alpha^{-1} = \beta^{-1} = 0.2 - i0.02$, (*c*) $\alpha^{-1} = \beta^{-1} = 0.5 - i0.05$; □ denotes data points from Krenk and Schmidt (1982) (though see text)

Table 1 Convergence of the scattering cross-section for *SV* wave incident at 90 deg to the symmetry axis of a penny-shaped, cracklike flaw of radius *a* with $\alpha = \beta$. $m_{max} = 8$ at $k_s a = 3$, and $m_{max} = 13$ at $k_s a = 6$.

$\frac{1}{\beta} = 0.5 - i0.05$				$\frac{1}{\beta} = 0.1 - i0.01$			
$k_s a = 3$		$k_s a = 6$		$k_s a = 3$		$k_s a = 6$	
l_{max}	Σ	l_{max}	Σ	l_{max}	Σ	l_{max}	Σ
8	0.1813	16	0.3470	12	0.5588	16	1.392
10	0.2130	18	0.3118	14	0.5690	18	0.706
12	0.2049	20	0.3156	16	0.5781	20	0.803
14	0.2047	22	0.3176	18	0.5806	22	0.813
16	0.2046	24	0.3176	20	0.5805	24	0.818

We can see that as we increase $|\alpha|$ and $|\beta|$, the scattering cross-section of the cracklike flaw approaches the cross-section of the open crack. The scattering cross-section of the open cap-shaped crack has been computed by means of the method of Boström and Olsson (1987). We have in fact also tried to put $|\alpha| = |\beta| = \infty$, in equations (11) and (12), by dividing out $\alpha = \beta$ before taking the limit. However, the resulting *Q*-matrix is numerically almost singular, and the results thus very unstable. Apparently this limit is a singular limit.

In Fig. 4 we see the total scattering cross-section for a *P* wave incident at right angles to the symmetry axis of the hemispherical flaw. This plot clearly shows that the scattering cross-section of the cracklike flaw (with $|\alpha|$, $|\beta| < \infty$) sometimes is greater than that of the open crack.

Turning now to a penny-shaped flaw we have, in Figs. 5 and 6, the scattering cross-sections for *S* and *P* waves incident along the symmetry axis. Here a small amount of dissipation has been added, primarily to enhance the convergence. With the present method, the penny-shaped flaw is a more awkward case numerically than the cap-shaped flaw. The present calculations have been performed with a program allowing a maximum trunction of $l_{max} = 24$ for the degree *l* of the Legendre functions in the spherical vector waves. For the cap-shaped flaw, this suffices well for the interval $0 < k_s a < 8$, but as can be seen from Table 1, it is slightly too small at the upper limit of the frequency interval $0 < k_s a < 6$ for the "worst" penny-shaped flaw, i.e., that of the greater value of $|\alpha| = |\beta|$.

In connection with Table 1, we may note that the convergence is influenced by our choice of origin for the spherical waves. Here we have simply chosen to take the origin on the symmetry axis at a distance from the penny-shaped surface equal to the radius of the penny. However, if we take this distance to be 30 percent greater, we need to take $l_{max} = 24$ to get within 0.1 percent of the value 0.2046 at $k_s a = 3$ in Table 1. No systematic study has been performed here to find the optimal distance of the origin from the flaw surface.

Comparing the values of Table 1 to the results of Krenk and Schmidt (1982) (or rather the corrected values available from Dr Krenk: 0.737 at $k_s a = 3$, and 1.042 at $k_s a = 6$), we see that higher values of $|\alpha| = |\beta|$ are needed to get as close to the scattering cross-section of the penny-shaped open crack, as in the case of 0-deg incidence in Figs. 5 and 6. However, for a *P* wave incident at 90 deg to the symmetry axis, the cross-sections are rather close to those of an open crack for the highest $|\alpha| = |\beta|$ considered here, as can be seen in Fig. 7.

The dissipation added in the cases of penny-shaped flaws studied so far is given by $|\text{Im } \beta^{-1}| = 0.1 \text{ Re } \beta^{-1}$. As stated previously, this slightly enhances the convergence, which is desirable for the higher frequencies and the higher values of $|\alpha| = |\beta|$. However, we can see from computations for cap-shaped flaws that this small amount of dissipation changes the

Downloaded 03 May 2010 to 171.66.16.244. Redistribution subject to ASME license or copyright; see http://www.asme.org/terms/Terms_Use.cfm

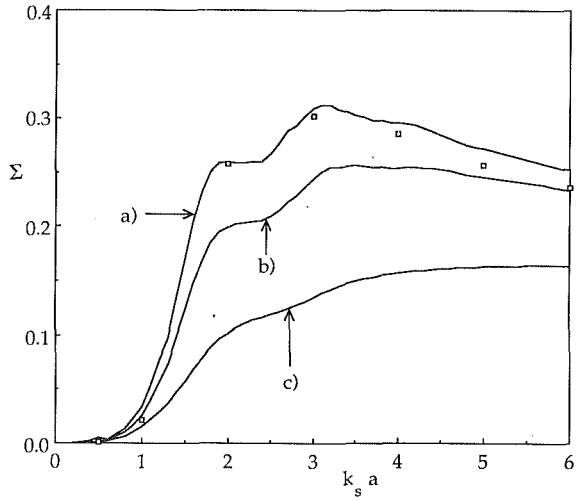


Fig. 7 Same as Fig. 5 but for plane *P* wave incident perpendicularly to the symmetry axis

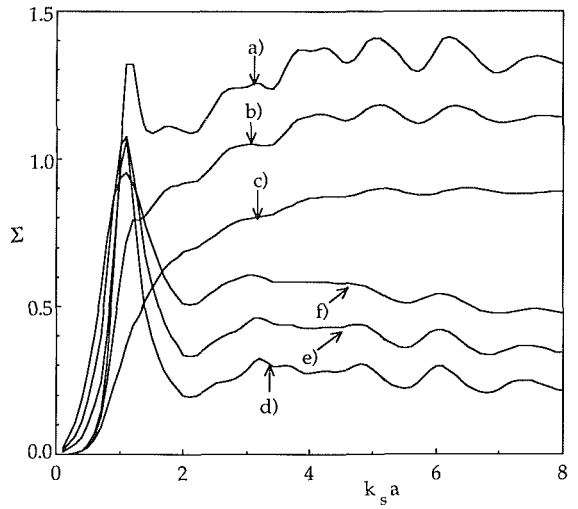


Fig. 8 The normalized total scattering and absorption cross-sections for a cap-shaped hemispherical flaw, and a plane *SV* wave incident perpendicularly to the symmetry axis; scattering cross-sections: (*a*) $\alpha^{-1}=\beta^{-1}=0.1-i0.05$, (*b*) $\alpha^{-1}=\beta^{-1}=0.1-i0.1$, (*c*) $\alpha^{-1}=\beta^{-1}=0.1-i0.2$, absorption cross-sections: (*d*) $\alpha^{-1}=\beta^{-1}=0.1-i0.05$, (*e*) $\alpha^{-1}=\beta^{-1}=0.1-i0.1$, (*f*) $\alpha^{-1}=\beta^{-1}=0.1-i0.2$

scattering cross-section very little, and the absorption cross-section (defined next) is just a few percent of the scattering cross-section. For example, at $k_s a=4$, a change from $\alpha^{-1}=\beta^{-1}=0.1$ to $\alpha^{-1}=\beta^{-1}=0.1-i\,0.01$, changes the scattering cross-section for the case in Fig. 4 by only 3 percent, and the absorption cross-section goes from zero to 3 percent of the scattering cross-section.

In Figs. 8–11 we study the effect of increasing the absorption. Both the total scattering cross-section and the absorption cross-section are plotted. The absorption cross-section, referred to above, is defined as the power dissipated in the scatterer, divided by the power per unit area in the incident plane wave passing through a plane normal to its direction of propagation. It is normalized by dividing by πa^2, exactly as for the scattering cross-section. The absorption cross-section is here computed essentially by means of the elastodynamic version of the optical theorem (cf., Varatharajulu, 1977).

Figures 8 and 9 show results for a hemispherical cap-shaped flaw. These plots should be compared to the corresponding curves in Figs. 2 and 3 of Boström and Olsson (1987). Figure 9 can also be compared to Fig. 4 of the present paper. We see that the additional absorption smoothens out the peak in the

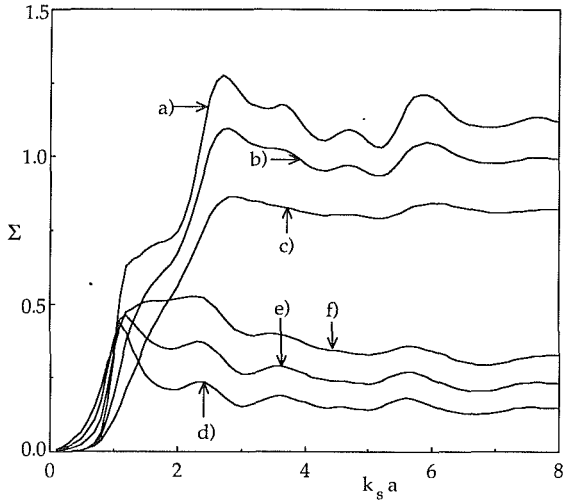


Fig. 9 Same as Fig. 8, but for plane *P* wave

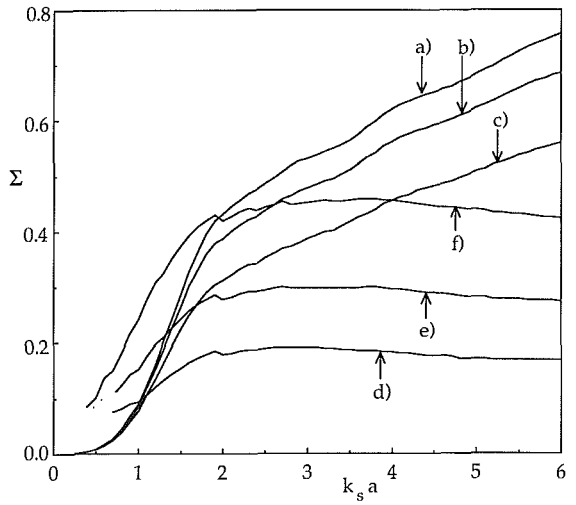


Fig. 10 Same as Fig. 8, but for a penny-shaped flaw and a plane *SV* wave

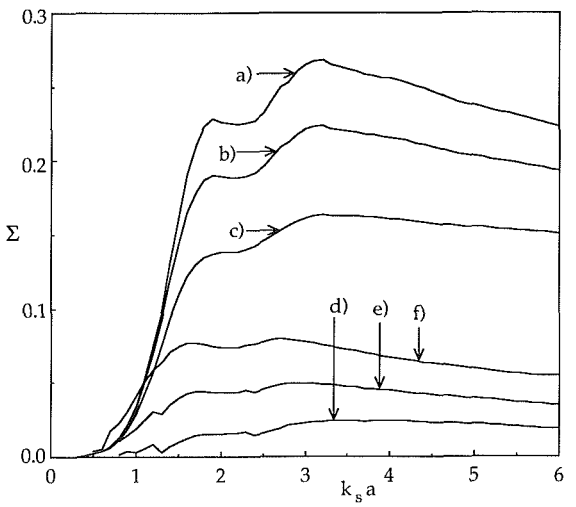


Fig. 11 Same as Fig. 8, but for a penny-shaped flaw and a plane *P* wave

scattering cross-section of the open crack around $k_s a=1.1$ for the *P* wave, while some trace of it remains for the *SV* wave for the smaller value of $|\mathrm{Im}\,\beta^{-1}|$. However, in both the *P* and *SV* cases, except for the greater value of $|\mathrm{Im}\,\beta^{-1}|$, the absorption cross-section shows a peak at that frequency.

Downloaded 03 May 2010 to 171.66.16.244. Redistribution subject to ASME license or copyright; see http://www.asme.org/terms/Terms_Use.cfm

In Figs. 10 and 11 we have the same scattering situation as in Figs. 8 and 9, but now for a penny-shaped flaw. For the SV case, the absorption cross-section is larger than for the P wave case. This can be seen also in Figs. 8 and 9, but is more pronounced for the penny-shaped flaw. We note also that, except for the scale, Figs. 9 and 11 are rather similar in appearance.

The reason why the curves for the absorption cross-sections in Figs. 10 and 11 start at a higher frequency than do the curves for the scattering cross-sections, is that the computed values here become unstable for lower frequencies. Why this is so for the present calculation, we can not yet give any explanation. For the absorption cross-section to be of roughly the same magnitude as the scattering cross-section in the frequency intervals considered, the imaginary parts of α^{-1} and β^{-1} should apparently be of the same order of magnitude as the real parts. This indicates at least approximately the relative importance of the viscous damping terms and the springlike terms in equation (2).

Concluding Remarks

In the present article it has been shown how the null-field approach can be adapted to treat a class of planar and nonplanar cracklike flaws, with boundary conditions incorporating both damping and restoring forces between the faces of the flaw. While only numerical results for such flaws in an otherwise homogeneous matrix have been presented here, the formal solution for a flaw over part of the boundary of an elastic inclusion has also been given.

In the numerical examples we have considered the case $\alpha=\beta$. Cases where $\alpha\neq\beta$ are, of course, also of interest, in particular perhaps the case $\alpha=0$, $\beta\neq 0$, corresponding to a crack which remains closed but can slide in the tangential directions under damping and restoring forces. In principle, α and β could be frequency dependent (cf., the references given in the Introduction), but another dimensional constant would then have to be introduced. Other interesting cases for future study are cases of multiple scattering by cracklike flaws. Apart from the possibility of using the multiple scattering T matrix method (Boström, 1980), the case of, e.g., two closely situated cracklike faws could be handled directly by the present method. The surface S is then simply taken as two disjoint parts corresponding to the two flaws (cf., Boström and Olsson, 1987). Cracklike flaws in a half space or in an elastic plate can be handled by methods found in Boström and Kristensson (1980) and Boström and Karlsson (1985).

Acknowledgments

The work reported in this paper was carried out in the course of research supported by the Swedish Board for Technical Development, and this support is gratefully acknowledged. I also wish to thank the (anonymous) reviewers for bringing several of the references now included in the Introduction to my attention.

References

Aboudi, J., 1988, "Wave propagation in damaged composite materials," *International Journal of Solids and Structures*, Vol. 24, pp. 117–138.

Boström, A., 1980, "Multiple scattering of elastic waves by bounded obstacles," *Journal of the Acoustical Society of America*, Vol. 67, pp. 399–413.

Boström, A., and Karlsson, A., 1985, "Point force excitation of an elastic plate with an embedded cavity," ASME JOURNAL OF APPLIED MECHANICS, Vol. 52, pp. 937–942.

Boström, A., and Kristensson, G., 1980, "Elastic wave scattering by a three-dimensional inhomogeneity in an elastic half space," *Wave Motion*, Vol. 2, pp. 937–942.

Boström, A., and Olsson, P., 1987, "Scattering of elastic waves by non-planar cracks," *Wave Motion*, Vol. 9, pp. 61–76.

Budreck, D. E., and Achenbach, J. D., 1988, "Scattering for three-dimensional planar cracks by the boundary integral equation method," ASME JOURNAL OF APPLIED MECHANICS, Vol. 55, pp. 405–412.

Chatterjee, A. K., Mal, A. K., Knopoff, L., and Hudson, J. A., 1980, "Attenuation of elastic waves in a cracked, fluid-saturated solid," *Mathematical Proceedings of the Cambridge Philosophical Society*, Vol. 88, pp. 547–561.

Jones, J. P., and Whittier, J. S., 1967, "Waves at a flexibly bonded interface," ASME JOURNAL OF APPLIED MECHANICS, Vol. 34, pp. 905–909.

Krenk, S., and Schmidt, W., 1982, "Elastic wave scattering by a circular crack," *Philosophical Transactions of the Royal Society, London*, Vol. A308, pp. 167–198.

Mal, A. K., 1988, "Guided waves in layered solids with interface zones," *International Journal of Engineering Science*, Vol. 26, pp. 873–881.

Mal, A. K., and Bose, S. K., 1974, "Dynamic elastic moduli of a suspension imperfectly bonded spheres," *Proceedings of the Cambridge Philosophical Society*, Vol. 76, pp. 587–600.

Martin, P. A., and Wickham, G. R., 1983, "Diffraction of elastic waves by a penny-shaped crack: Analytical and numerical results," *Proceedings of the Royal Society, London*, Vol. A390, pp. 91–129.

Nayfeh, A. H., and Nassar, E. A.-A.M., 1978, "Simulation of the influence of bonding materials on the dynamic behavior of laminated composites," ASME JOURNAL OF APPLIED MECHANICS, Vol. 45, pp. 822–828.

Olsson, P., 1986, "Elastodynamic scattering by fluid-filled nonplanar cracks," *Journal of Nondestructive Evaluation*, Vol. 5, pp. 161–168.

Pao, Y.-H., 1978, "Betti's identity and transition matrix for elastic waves," *Journal of the Acoustical Society of America*, Vol. 64, pp. 302–310.

Peterson, L., 1988, "Elastic wave scattering by two penny-shaped cracks," Report 88-6, Institute of Theoretical Physics, S-412 96 Göteborg, Sweden.

Pilarski, A., and Rose, J. L., 1988, "A Transverse-wave ultrasonic oblique-incidence technique for interfacial weakness detection in adhesive bonds," *Journal of Applied Physics*, Vol. 63, pp. 300–307.

Varatharajulu, V., 1977, "Reciprocity relations and forward amplitude theorems for elastic waves," *Journal of Mathematical Physics*, Vol. 18, pp. 537–543.

Downloaded 03 May 2010 to 171.66.16.244. Redistribution subject to ASME license or copyright; see http://www.asme.org/terms/Terms_Use.cfm

J. L. Wegner
Assoc. Mem. ASME

J. B. Haddow
Mem. ASME

Department of Mechanical Engineering,
University of Victoria,
Victoria, BC Canada W8W 2Y2

An Experimental Study of the Unloading Waves in a Plucked Hyperelastic String

This paper is concerned with the unloading response of symmetrically plucked hyperelastic strings and presents some results of an experimental study. The validity of certain similarity solutions due to Wegner et al. (1989) is investigated and the experimental results are in acceptable agreement with the predictions of these solutions. A small extension of the similarity solutions to consider the response of a string after the first reflection is presented along with some experimental verification.

1 Introduction

In a recent paper (Wegner et al., 1989), henceforth referred to as WHT, the authors present similarity solutions, obtained by the method of characteristics, for unloading waves in a symmetrically plucked hyperelastic string. These solutions are valid until the first reflections occur at the fixed ends and predict that the string occupies a configuration of the form shown in Fig. 1, after the string is released. In this paper, we describe experimental work on the plucked string problem. Deformed configurations of strings, before and after the first reflection, are obtained experimentally and the configurations before the first reflection are compared with the predictions of the similarity solutions given in WHT. The relation between stretch and nominal stress in simple tension for the specimens used in the experiments is closely approximated by that for a special case of the Mooney-Rivlin strain energy function. The similarity solutions given in WHT, for the problem with a Mooney-Rivlin material, involve a longitudinal shock and a transverse shock so that, in general, there are three constant state regions in the characteristic plane, except for the special case when the longitudinal and transverse shocks coincide, then there are two constant state regions.

Analysis of the response after the first reflection by the method of characteristics is, in general, very complicated because of multiple interactions and reflections of the longitudinal and transverse waves. A solution for the response between the time of the first reflection and the arrival of the reflected wave at the midpoint has been obtained for the special case when the transverse and longitudinal shocks coincide before the first reflection. Results from this solution are compared with experimental results. When the similarity solution consists of three constant state regions in the characteristic plane and the longitudinal shock speed is greater than the transverse shock speed, a partial solution is easily obtained for the time interval between the first reflection of the longitudinal wave at a fixed end and the interaction of the reflected longitudinal wave and the incident transverse wave. These partial solutions indicate that the reflected longitudinal wave is compressive for certain initial conditions. Since the string is assumed to be perfectly flexible and incapable of sustaining an axial compressive stress, the characteristic solution is then no longer valid after the first reflection. The experimental studies show that buckling of the string can occur after the first reflection and this is predicted by the theoretical solutions.

2 Theoretical Preliminaries

We refer to results obtained in WHT for a string whose strain energy function for simple tension is a special case,

$$W = \frac{\mu}{2}\{0.6(\lambda^2 + 2\lambda^{-1} - 3) + 0.4(\lambda^{-2} + 2\lambda - 3)\}, \quad (1)$$

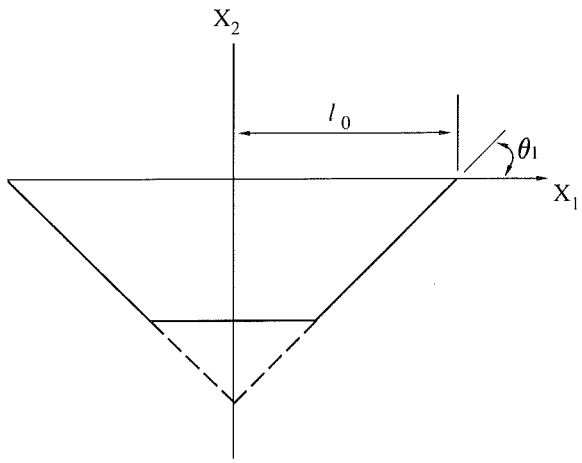


Fig. 1 Deformed configuration after release and before first reflection. Dotted line indicates deformed configuration before release.

Contributed by the Applied Mechanics Division of THE AMERICAN SOCIETY OF MECHANICAL ENGINEERS for publication in the JOURNAL OF APPLIED MECHANICS.

Discussion on this paper should be addressed to the Technical Editor, Leon M. Keer, The Technological Institute, Northwestern University, Evanston, IL 60208, and will be accepted until two months after final publication of the paper itself in the JOURNAL OF APPLIED MECHANICS. Manuscript received by the ASME Applied Mechanics Division, Feb. 16, 1989; final revision, July 7, 1989.

Copyright © 1990 by ASME
Downloaded 03 May 2010 to 171.66.16.244. Redistribution subject to ASME license or copyright; see http://www.asme.org/terms/Terms_Use.cfm

of the Mooney-Rivlin strain energy function, where μ is the infinitesimal shear modulus and λ is the stretch. The relation,

$$P = \mu(0.6 + 0.4\lambda^{-1})(\lambda - \lambda^{-2}), \tag{2}$$

where P is the nominal tensile stress, is obtained from equation (1). Results of simple tension tests performed on the rubber strings used in the experiments are in very close agreement with equation (2) for stretches up to about 3 and this stretch was not exceeded in the plucking experiments.

It is convenient to give a brief formulation of the problem before discussing the theory and more details can be obtained in WHT.

A perfectly flexible uniform hyperelastic string of natural length $2L$ is fixed at points $\pm l_0$ of the x_1-axis of a system of rectangular Cartesian axes. The reference configuration is taken as an unstressed configuration occupying the interval $[-L,L]$ of the x_1-axis, and at time t, the particle whose coordinate is $X \in [-L,L]$ in the reference configuration is at place $x_\alpha(X,t)$, $\alpha \in \{1,2\}$, since plane motion in the Ox_1x_2 plane is assumed. At time $t = 0$ the string is released from the symmetrically deformed configuration given by

$$x_1(X,0) = \lambda_0 X,\ x_2 = -\lambda_0(L - X)\tan\theta_1,\ X \in [0,L], \tag{3}$$

where $\lambda_0 = l_0/L$ and θ_1 is the angle the string makes with the x_1-axis as indicated in Fig. 1. The stretch λ_1 at $t = 0$ is given by

$$\lambda_0 = \lambda_1\cos\theta_1. \tag{4}$$

If $0 \le \lambda_0 < 1$, the string is slack before the deformation equation (3) is applied and λ_0 does not denote a stretch unless $l_0 \ge L$.

The governing equations and jump relations are given in WHT and are not repeated here. The nondimensionalization scheme used in WHT is adopted; that is, quantities with the dimension of length, stress, velocity, and time are nondimensionalized by dividing by $L, 3\mu, c_0$ and L/c_0, respectively, where $c_0 = \{3\mu/\rho\}^{1/2}$ is the longitudinal wave speed for propagation into an undeformed region and ρ is the density. Henceforth, nondimensional quantities are used except when otherwise indicated. As in WHT, the x_1 and x_2 components of particle velocity are denoted by u and v, respectively. The longitudinal and transverse Lagrangian wave speeds are obtained from the stress-stretch relation equation (2), and are

$$c_L = \left\{\frac{\partial P}{\partial \lambda}\right\}^{\frac{1}{2}} \text{ and } c_T = \left\{\frac{P}{\lambda}\right\}^{\frac{1}{2}}, \tag{5}$$

respectively. We denote longitudinal and transverse Lagrangian shock velocities by

$$V_L = \pm\left\{\frac{[P]}{[\lambda]}\right\}^{\frac{1}{2}} \text{ and } V_T = \pm\left\{\frac{P}{\lambda}\right\}^{\frac{1}{2}}, \tag{6}$$

respectively, where the square brackets indicate the jump across the shock of the enclosed quantity and the $+(-)$ sign refers to a shock travelling in the $+(-)$ x_1-direction. The first similarity solution we are concerned with is valid for $\lambda_1 < \lambda_c$ or $\lambda_1 > \lambda_c$ and $\lambda_2 < \lambda_*$ where $\lambda_c = 2.473$ is the value of λ for which $c_T = c_L$, $\lambda_* < \lambda_c$ is the value of λ for which $c_T(\lambda_*) = c_T(\lambda_1)$ as indicated in Fig. 2, and λ_2 is the unloaded stretch behind the longitudinal shock. This similarity solution consists of three constant state regions in the (X,t) plane as indicated in Fig. 3 and the details are as follows:

$$\begin{aligned}
&\text{Region 1:} && X/t > V_L;\\
&&& u = v = 0,\ \lambda = \lambda_1,\ \theta = \theta_1,\\
&\text{Region 2:} && V_L > X/t > V_T;\\
&&& u = u_2,\ v = v_2,\ \lambda = \lambda_2,\ \theta = \theta_2 = \theta_1,\\
&&& v_2 = u_2\tan\theta_1,\\
&\text{Region 3:} && V_T > X/t > 0;\\
&&& v = v_3,\ u = 0,\ \lambda = \lambda_3 = \lambda_2,\ \theta = 0,
\end{aligned} \tag{7}$$

$$V_L = \left\{\frac{P(\lambda_2) - P(\lambda_1)}{\lambda_2 - \lambda_1}\right\}^{\frac{1}{2}},\ V_T = \left\{\frac{P(\lambda_2)}{\lambda_2}\right\}^{\frac{1}{2}}. \tag{8}$$

If θ_1 and λ_0 are given, λ_1 is obtained from equation (4) and u_2 and λ_2 from

$$u_2 = -V_L(\lambda_2 - \lambda_1)\cos\theta_1,\ u_2 = V_T\lambda_2(1 - \cos\theta_1) \tag{9}$$

and equation (8), then v_2 and v_3 are obtained from equation (7) and

$$v_3 = V_T\lambda_2\sin\theta_1 + v_2, \tag{10}$$

respectively. Equations (9) and (10) follow from the jump relations given in WHT.

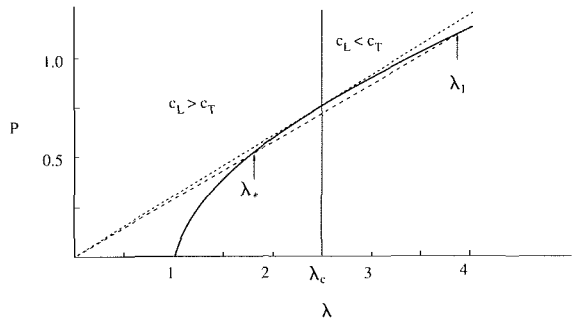


Fig. 2 Nondimensional relation between P and λ given by equation (2)

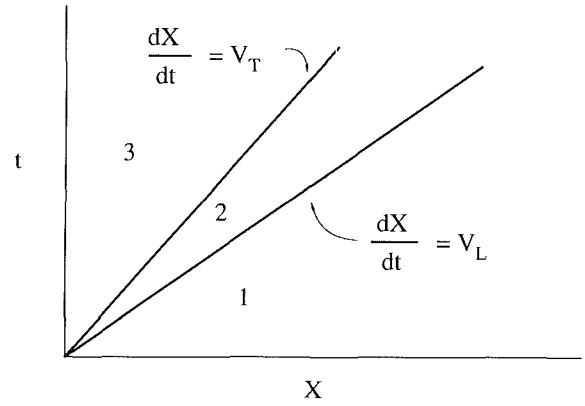


Fig. 3 Schematic form of similarity solution for $\lambda_1 < \lambda_c$ or $\lambda_1 > \lambda_c$ and $\lambda_2 < \lambda_*$

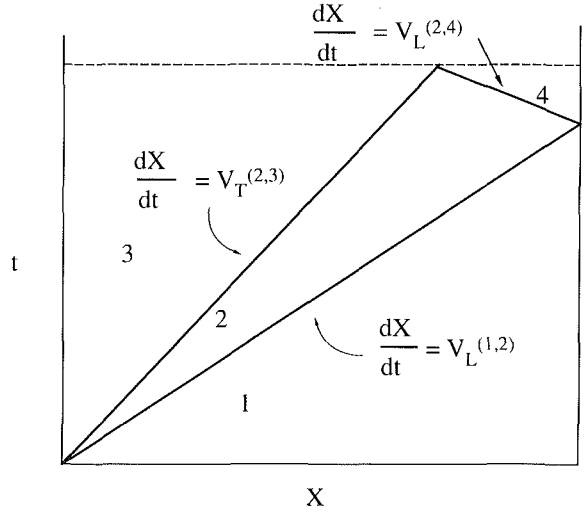


Fig. 4 Schematic form of solution for $\lambda_1 < \lambda_c$ or $\lambda_1 > \lambda_c$ and $\lambda_2 = \lambda_*$ valid until interaction between reflected longitudinal wave and incident transverse wave

Downloaded 03 May 2010 to 171.66.16.244. Redistribution subject to ASME license or copyright; see http://www.asme.org/terms/Terms_Use.cfm

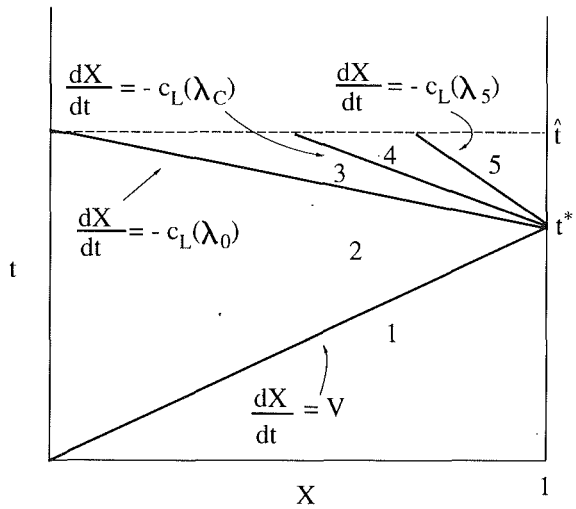


Fig. 5 Schematic form of solution for the special case $\lambda_1 < \lambda_c$ and $\lambda_2 = \lambda_* = \lambda_0$, valid until reflected wave reaches $X = 0$

We now consider the reflection of the incident longitudinal wave at $X = 1$ and obtain a solution—valid until the reflected longitudinal wave interacts with the incident transverse wave as indicated in Fig. 4. Referring to Fig. 4, we are concerned with the solution for region 4, which is as follows,

$$u_4 = \nu_4 = 0, \ \lambda = \lambda_4, \ \theta = \theta_1,$$

with λ_4 obtained from

$$u_2 = -\left\{\frac{P(\lambda_4) - P(\lambda_2)}{\lambda_4 - \lambda_2}\right\}^{\frac{1}{2}} (\lambda_4 - \lambda_2)\cos\theta_1, \qquad (11)$$

which follows from the jump relation equation $(15)_1^*$. Henceforth, bracketed numbers with an asterisk ()* refer to equations in WHT and the notation used in WHT is also used in this section. In equation (11), u_2 and λ_2 are already known from the similarity solution. If equation (11) gives $\lambda_4 < 1$, the string buckles after the first reflection and the characteristic solution is no longer valid. We later present experimental results which show buckling just after the first reflection and these results are predicted by the theory.

The second similarity solution we are concerned with is the special case when $\lambda_1 > \lambda_c$ and $\lambda_2 = \lambda_*$. This solution consists of two constant state regions in the (X, t) plane separated by a transverse shock which coincides with a longitudinal shock. Referring to Fig. 5, the constant state regions are regions 1 and 2. A simple solution for the response during the interval between the first reflection and the arrival of the reflected wave at $X = 0$ can be obtained as an extension of this similarity solution. The similarity solution is as follows:

Region 1: $X/t > V$;
$u = \nu = 0, \ \lambda = \lambda_1, \ \theta = \theta_1,$

Region 2: $V > X/t > 0$;
$u = 0, \ \nu = \nu_2, \ \lambda = \lambda_2 = \lambda_*, \ \theta = 0,$

where

$$V = \left\{\frac{P(\lambda_1)}{\lambda_1}\right\}^{\frac{1}{2}} = \left\{\frac{P(\lambda_*)}{\lambda_*}\right\}^{\frac{1}{2}} = \left\{\frac{P(\lambda_1) - P(\lambda_*)}{\lambda_1 - \lambda_*}\right\}^{\frac{1}{2}}. \qquad (12)$$

Only one of λ_0, λ_1, and θ_1 can be prescribed independently. It follows from equation (4) and

$$\lambda_* = \lambda_1\cos\theta_1,$$

which is obtained from the jump relation equation $(22)_1^*$, that $\lambda_0 = \lambda_* = \lambda_2$. The relation between λ_0 and λ_1 is given by equation (12) so that if either λ_1 or λ_0 is prescribed, the other can be obtained and θ_1 is then obtained from equation (4) and ν_2 from

$$\nu_2 = V\lambda_1\sin\theta_1,$$

which is obtained from jump relation equation $(22)_2^*$.

At nondimensional time $t^* = 1/V$ where V is given by equation (12), that is, at the instant the incident wave reaches $X = 1$,

$$u = 0, \lambda = \lambda_0 = \lambda_* \ \forall \ X \in [0,1] \text{ and } \nu = \nu_2 \ \forall \ X \in [0,1),$$

$$\nu = 0 \text{ for } X = 1.$$

If we superimpose velocity $\nu = -\nu_2$ on the system at time $1/V$, we have essentially a particular case of the transverse impact problem discussed by Beatty and Haddow (1985) and Wegner et al. (1989). The similarity solution for this transverse impact problem can be used to determine the solution for $t^* < t < \hat{t} = 1/V + 1/c_L(\lambda_0)$. Referring to Fig. 5, this solution is as follows,

Region 2: $(1 - X)/(t - t^*) \geq c_L(\lambda_0)$
$u = 0, \ \nu = \nu_2, \ \lambda = \lambda_2 = \lambda_0, \ \theta = 0$

Region 3: $c_L(\lambda_0) \geq (1 - X)/(t - t^*) > c_T(\lambda_c)$
$(1 - X)/(t - t^*) = c_L(\lambda), \ u = \int_{\lambda_0}^{\lambda} c_L(\eta)d\eta,$
$\nu = \nu_2 = \nu_3, \ \theta = 0$

Region 4: $c_T(\lambda_c) > (1 - X)/(t - t^*) \geq c_L(\lambda_5)$
$\theta = \theta_4, \ (1 - X)/(t - t^*) = c_L(\lambda),$
$u = u_4 = u_4^- + \int_{\lambda_0}^{\lambda} c_L(\eta)d\eta\cos\theta_4$
$\nu = \nu_4 = \nu_4^- + \int_{\lambda_c}^{\lambda} c_L(\eta)d\eta\sin\theta_4$

Region 5: $c_L(\lambda_5) \geq (1 - X)/(t - t^*) \geq 0$
$\lambda = \lambda_5, \ \theta = \theta_4 = \theta_5,$
$u = u_5 = 0, \ \nu = \nu_5 = 0.$

It follows from jump relation equations (16)* and (17)* that

$$V_T^{(3,4)}\lambda_c(\cos\theta_4 - 1) = -\left(u_4^- - \int_{\lambda_0}^{\lambda_c} c_L(\lambda)d\lambda\right) \qquad (13)$$

$$V_T^{(3,4)}\lambda_c\sin\theta_4 = -(\nu_4^- - \nu_2) \qquad (14)$$

where

$$V_T^{(3,4)} = -c_T(\lambda_c) = -\left\{\frac{P(\lambda_c)}{\lambda_c}\right\}^{\frac{1}{2}}.$$

Also, since $u_5 = \nu_5 = 0$,

$$u_4^- = -\int_{\lambda_c}^{\lambda_5} c_L(\lambda)d\lambda\cos\theta_4, \ \nu_4^- = -\int_{\lambda_c}^{\lambda_5} c_L(\lambda)d\lambda\sin\theta_4. \qquad (15)$$

The four unknowns λ_5, θ_4, u_4^-, and ν_4^- can be obtained from equations (13), (14), and (15).

The experimental results are obtained for $\theta_1 = 45$ deg; consequently, we now present results for a special case of the solution indicated in Fig. 5:

$$\theta_1 = 45 \text{ deg}, \ \lambda_0 = \lambda_* = \lambda_2 = 2.125,$$

$$\lambda_1 = 3.005, \ \nu_2 = 1.031,$$

$$c_T(\lambda_0) = 0.485, \ c_T(\lambda_c) = 0.487,$$

$$\theta_4 = \theta_5 = -44.998 \text{ deg}, \ \lambda_5 = 3.0055.$$

It is interesting to note that $-\theta_5 \cong \theta_1$, $\lambda_1 \cong \lambda_5$ and the deformed configuration for $t^* < t < t$ is similar to that for $0 < t < t^*$. However, we were unable to reproduce this reflected deformed configuration experimentally and the experimental results indicate that a double kink develops after the first reflection.

Downloaded 03 May 2010 to 171.66.16.244. Redistribution subject to ASME license or copyright; see http://www.asme.org/terms/Terms_Use.cfm

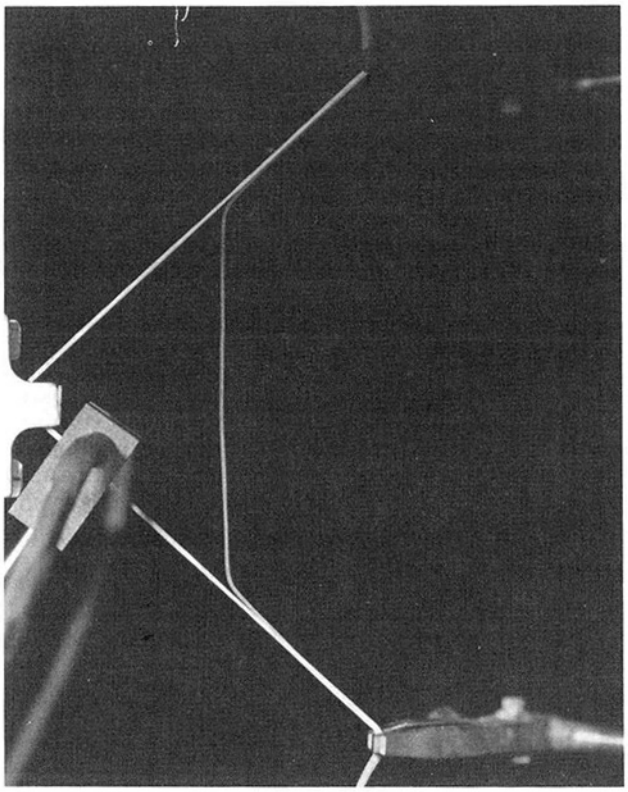


Fig. 6 Deformed configurations before release at $t = 0$ and after release, but before first reflection

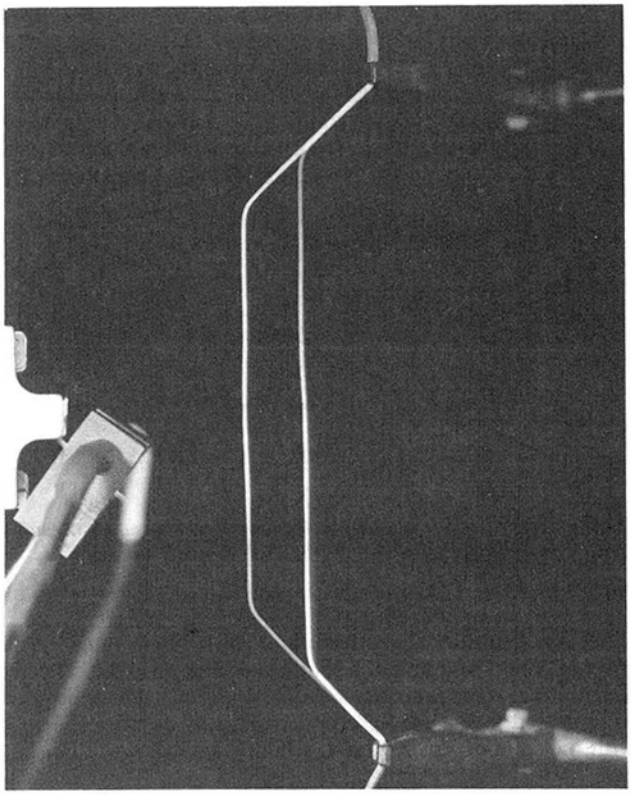


Fig. 7 Double exposure showing deformed configurations before first reflection, $\theta_1 = 45$ deg, $\lambda_0 = 2$

3 Experimental Procedure

The strings used in the experimental work are carefully selected rubber bands of cross-section 1.69 × 1.15 mm and density $\rho = 1020$ kg/m^{-3}. Nominal stress-stretch relations obtained from tensile tests on these bands are in close agreement with equation (2) for λ up to 3 and good reproducibility was noted. It was determined from the tensile tests that,

$$E = \left(\frac{d\,P}{d\lambda}\right)_{\lambda=1} = 1570 \text{ kPa},$$

where E is Young's modulus for infinitesimal deformation from the natural reference state. Since compressibility of the bands is neglected, we take $E = 3\mu$.

It follows that the longitudinal wave speed for propagation into an undeformed region is $c_0 = 39.23$ m/s. It is reasonable to assume that the influence of viscoelastic effects on the experimental results is negligible since an increase in stretch of only 3 percent was observed when a band was stretched initially to $\lambda = 7$ and held under constant tensile load for 20 hours.

An elastic string, with the desired initial stretch λ_0, is held vertically between two clamps 128 mm apart and is then further deformed to the configuration given by equation (3) and clamped as its midpoint by a modified telephone relay as indicated in Fig. 6. The room is then darkened and the relay is opened so that the string is released. It passes a photo detector which triggers a delay generator sending a pulse to a stroboscopic light source. After the delay, the stroboscopic light flashes and an exposure is taken. The camera shutter is held open until the flash has occurred.

Double exposures, as shown in Fig. 7, are used to determine the velocity of the central straight part of the string after it has been released. A second delay generator and strobe light are required. When the string passes through the photo detector, the signal triggers both of the delay generators which are set to different delays and time between flashes is the difference between the two delays. The velocity is obtained by determining, from the photograph, the distance the central straight part of the string has travelled in the time between exposures.

Experiments were performed with $\theta_1 = 45$ deg and various values of λ_0.

4 Experimental Results

Figure 6 shows the deformed configuration before release at $t = 0$ and also the configuration after release and before the first reflection. This figure provides experimental verification of the configuration predicted by the similarity solutions as indicated in Fig. 1, except for a slight rounding of the predicted θ discontinuity, probably due to the imperfect flexibility of the string.

Experimental results are presented for $\theta_1 = 45$ deg and $\lambda_0 = 1$, 2 and 2.125. The similarity solution indicated in Fig. 3 holds for $\theta_1 = 45$ deg and $\lambda_0 = 1$ and 2. When $\theta_1 = 45$ deg and $\lambda_0 = 2.125$, the characteristic solution indicated in Fig. 5 is obtained; however, experimental verification of this solution after the first reflection indicates that θ_4 is approximately -42 deg rather than $\theta_4 \cong -\theta_1$.

Figure 7 is for a string with $\theta_1 = 45$ deg and $\lambda_0 = 2$. The similarity solution predicts that v_3, the nondimensional velocity of the central straight part of the string, is 0.972, which is equivalent to 38.13 m/s if the measured values $3\mu = 1570$ kPa and $\rho = 1020$ kg/m^{-3} are assumed. Experimental values of the dimensional v_3 were obtained from double exposure photographs as shown in Fig. 7. These experimental values ranged from 38.22 to 39.60 m/s with a mean value of 39.10 m/s. Figures 8 and 9 show the configuration after the first reflection and before the wave front reaches $X = 0$. There is an indication in Fig. 9 that a double kink develops after the first reflection.

Figure 10 is for $\theta_1 = 45$ deg and $\lambda_0 = 1$. According to the similarity solution,

Downloaded 03 May 2010 to 171.66.16.244. Redistribution subject to ASME license or copyright; see http://www.asme.org/terms/Terms_Use.cfm

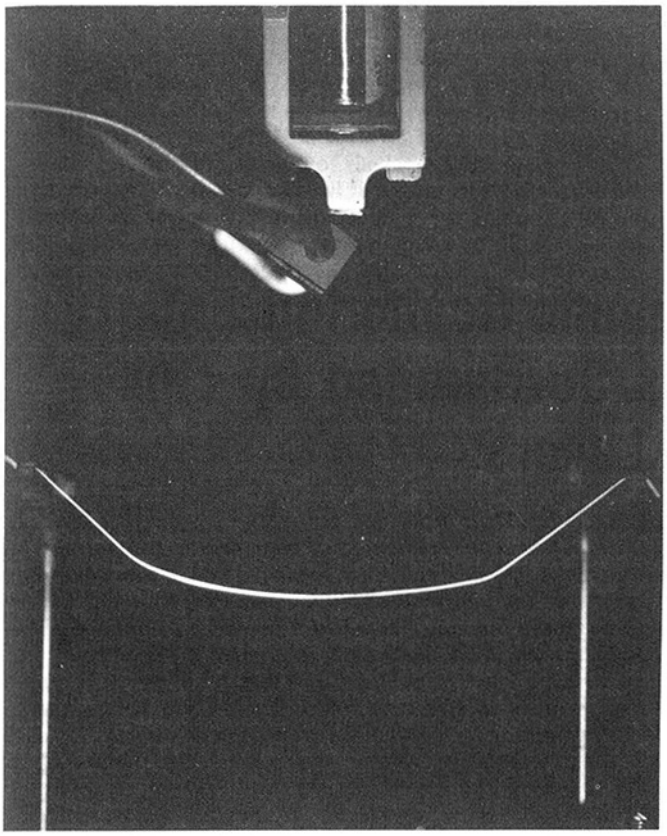


Fig. 8 Deformed configuration after first reflection, but before reflected wave reaches $X = 0$, $\theta_1 = 45$, $\lambda_0 = 2.125$

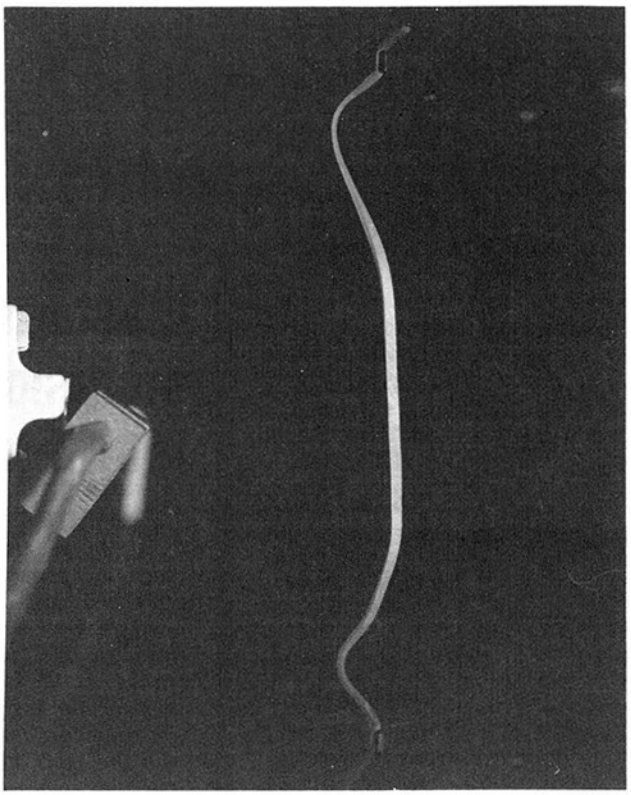


Fig. 10 Buckled deformed configuration at $t = 3.9$ ms, $\theta = 45$ deg, $\lambda = 1.0$

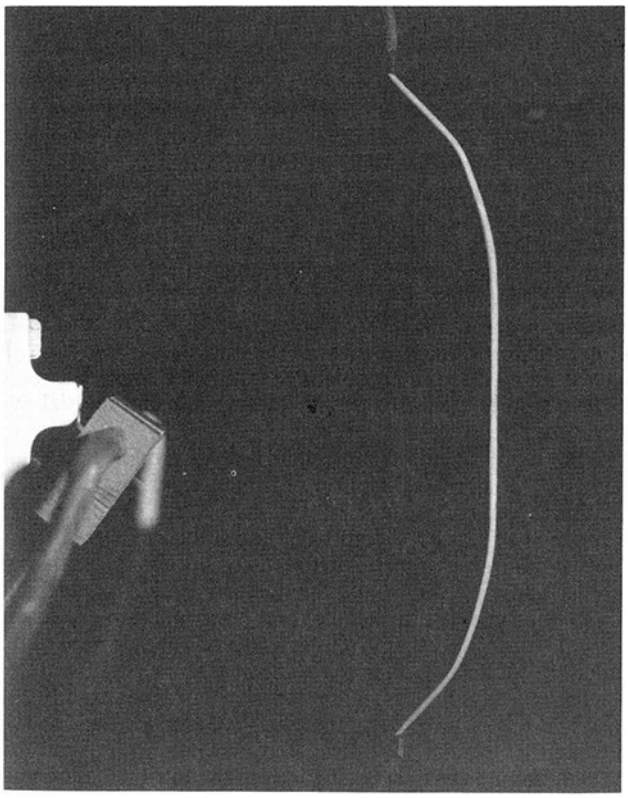


Fig. 9 Deformed configuration after first reflection but before reflected wave front reaches $X = 0$, $\theta_1 = 45$, $\lambda_0 = 2$

$$\lambda_1 = \sqrt{2},\ \lambda_2 = 1.179,\ \nu_3 = 0.413$$
$$V_L = 0.729,\ V_T = 0.350.$$

The longitudinal shock reaches $X = 1$ at nondimensional time $t = 1/V_L$, and referring to Fig. 4, the analysis for the reflected longitudinal shock gives $\lambda_4 = 0.623$ with a corresponding nondimensional stress $P/(3\mu) = -0.81$, so that the string buckles and the characteristic solution is no longer valid. An experimental verification of this is shown in Fig. 10. Using the experimentally determined properties, the dimensional Lagrangian longitudinal shock velocity is $0.792\ c_0 = 28.6$ m/s so that the arrival time of the incident longitudinal shock is 2.24 ms. Figure 10 was taken at 3.9 ms, that is after the arrival of the incident longitudinal shock.

According to the similarity solution, the dimensional velocity of the straight central part of the string is $\nu_3 c_0 = 16.21$ m/s for the measured values of the material properties. This value of $\nu_3 c_0$ is valid after the first reflection, and until the reflected wave reaches $X = 0$. Referring to Fig. 10, the measured time of 3.9 ms and the measurements taken from the photograph give $\nu_3 c_0 = 16.41$ m/s, which is in acceptable agreement with the theoretical result.

Acknowledgment

The authors would like to acknowledge the help given with the photography by Mr. B. Faulkner of the Department of Mechanical Engineering, University of Alberta.

References

Beatty, M. F., and Haddow, J. B., 1985, "Transverse Impact of a Stretched String," ASME Journal of Applied Mechanics, Vol. 52, pp. 137–143.

Wegner, J., and Haddow, J. B., and Tait, R. J., 1989, "Unloading Waves in a Plucked Hyperelastic String," ASME Journal Of Applied Mechanics, Vol. 56, pp. 459–465.

Wegner, J. L., and Haddow, J. B., and Tait, R. J., 1989, "Finite Amplitude Wave Propagation in a Stretched Elastic String," *Elastic Wave Propagation*, M. F McCarthy, M. A. Hayes, ed. Elsevier Science Publishers B. V., North-Holland, pp. 161–166.

Downloaded 03 May 2010 to 171.66.16.244. Redistribution subject to ASME license or copyright; see http://www.asme.org/terms/Terms_Use.cfm

P. Olsson
Division of Mechanics,
Chalmers University of Technology,
Göteborg, Sweden

S. K. Datta
Department of Mechanical Engineering and
CIRES,
University of Colorado,
Boulder, CO 80309
Fellow ASME

A. Bostrom
Division of Mechanics,
Chalmers University of Technology,
Göteborg, Sweden

Elastodynamic Scattering From Inclusions Surrounded by Thin Interface Layers

The scattering of elastic waves by elastic inclusions surrounded by interface layers is a problem of interest for nondestructive evaluation of interfaces in composites. In the present paper the scattering by a single elastic inclusion is studied. The scattering problem is solved by means of the null field approach and the properties of the interface layer enters through the boundary conditions on the inclusion. Various ways of doing this have been tried, from the simpler approach of just keeping the inertia of the layer, to using a membrane type of approximation or a more sophisticated method that includes all effects to first order in the layer thickness. The results obtained by using these different methods are compared numerically and with the exact solution for a layered sphere and with some recent results for a spheroid obtained using a hybrid finite element and wave function expansion technique. The numerical results show significant dependence on parameters containing the thickness and stiffness of the interface layer.

1 Introduction

Three-dimensional scattering of elastic waves by inclusions has been the subject of investigation since the turn of the last century. Early studies were concerned only with spherical inclusions. A comprehensive review of these was published by Pao and Mow (1973). Elastodynamic scattering by inclusions of arbitrary shape is not amenable to exact solutions and only in recent years it has been possible to obtain numerical and approximate asymptotic solutions for scattering by spheroidal inclusions. The approximate solutions presented by Datta and Sangster (1974), Datta (1977), Gubernatis (1979), and Willis (1980) are valid at low frequenies. On the other hand, numerical solutions valid at arbitrary frequencies have been reported by Varadan and Varadan (1979), Boström (1980), Opsal and Visscher (1985), Olsson (1985), and others. In all these reported studies it has been assumed that the inclusion is perfectly bonded with the surrounding elastic matrix.

In composites, particularly metal-matrix composites reinforced by fibers or particles, it is often the case that there is an interface layer surrounding the particles (or fibers) induced by processing conditions. The strength and fracture behavior of the composite is significantly influenced by this interface layer. It is, however, difficult to characterize this layer nondestructively. The purpose of this paper is to analyze the effect of an interface layer on the scattering cross-section of a spheroidal inclusion. It is hoped that this study will help in assessing the feasibility of determining interface characteristics by ultrasonic means. In an earlier study Mal and Bose (1974) considered the effect of thin viscous layers on long wavelength scattering by spherical inclusions. More recently, Datta et al. (1988) have studied scattering by spherical inclusions surrounded by thin elastic interface layers. In both these studies it is assumed that the tractions are continuous across the layer, whereas the displacements satisfy jump conditions that are linear in the thickness of the layer. It may be noted that the approximate boundary conditions used in these studies are based on the assumption that inertial and curvature effects are negligible.

In the present study the interface layer is modeled as a thin shell, the equations of motion of which enter the boundary conditions on the surface of the inclusion. The scattering problem is solved by the null field approach and results for some simple shell approximations are compared with one another and with the results obtained by Paskaramoorthy et al. (1988) using a finite element and eigenfunction expansion method. It is found that if all the terms of $0(h)$ are kept in the boundary conditions, then the results agree very well with the calculations based on modeling the interface layer exactly as a third phase. It is also found that the shell approximations give meaningful results at low frequencies, but tend to underestimate the scattering cross-section at moderate frequencies.

2 The Null Field Approach

Consider an elastic inclusion surrounded by a thin interface layer in an otherwise homogeneous elastic matrix. The matrix

Contributed by the Applied Mechanics Division of THE AMERICAN SOCIETY OF MECHANICAL ENGINEERS for presentation at the Winter Annual Meeting, Dallas, Texas, Nov. 25–30, 1990.

Discussion on this paper should be addressed to the Technical Editor, Leon M. Keer, The Technological Institute, Northwestern University, Evanston, IL 60208, and will be accepted until two months after final publication of the paper itself in the JOURNAL OF APPLIED MECHANICS. Manuscript received and accepted by the ASME Applied Mechanics Division, Feb. 20, 1989.

Paper No. 90-WA/APM-12.

Copyright © 1990 by ASME
Downloaded 03 May 2010 to 171.66.16.244. Redistribution subject to ASME license or copyright; see http://www.asme.org/terms/Terms_Use.cfm

has density ρ, Lamé parameters, λ and μ, and wave numbers, k_p and k_s (the time factor $\exp(-i\omega t)$ is assumed throughout). The corresponding quantities in the inclusion and layer are ρ_1, λ_1, μ_1, k_{p1}, k_s, and ρ_0, λ_0, μ_0, k_{p0}, k_{so}, respectively. The thickness h of the layer is assumed to be small. The surface of the inclusion is denoted S_0 and its outward-pointing unit normal $\hat{n}$. The outer surface of the layer is denoted S_h.

In the null field approach all pertinent fields are expanded in spherical vector waves (Boström, 1980; Olsson, 1985). In the matrix the regular waves are denoted $\mathrm{Re}\psi_n$ and the outgoing ones are denoted ψ_n, where n is a quadruple index. The corresponding regular waves in the inclusion are $\mathrm{Re}\psi_n^1$. The incoming and scattered displacement fields are then expanded as

$$\mathbf{u}^{in} = \sum_{Ii} a_n \mathrm{Re}\psi_n \tag{1}$$

$$\mathbf{u}^{s} = \sum_{n} f_n \psi_n. \tag{2}$$

Here, a_n is assumed known and f_n is to be determined, i.e., the problem is to determine the transition matrix, $T_{nn'}$ that gives the linear relationship between a_n and f_n:

$$f_n = \sum_{n'} T_{nn'} a_{n'}. \tag{3}$$

Following the usual procedure in the null field approach, the outer integral representation gives relation between a_n, f_n, and the surface displacement $\mathbf{u}_+$ and traction $\mathbf{t}_+$:

$$a_n = -ik_s/\mu \int_{S_h} [\mathbf{u}_+ \cdot \mathbf{t}(\psi_n) - \mathbf{t}_+ \cdot \psi_n]\, dS \tag{4}$$

$$f_n = ik_s/\mu \int_{S_h} [\mathbf{u}_+ \cdot \mathbf{t}(\mathrm{Re}\psi_n) - \mathbf{t}_+ \cdot \mathrm{Re}\psi_n]\, dS. \tag{5}$$

The index + denotes the limit from the outside and $\mathbf{t}(\cdot)$ is the traction operator. The surface field on the inclusion is expanded in the regular spherical waves within the inclusion

$$\mathbf{u}_- = \sum_{n} \alpha_n \mathrm{Re}\psi_n^1 \tag{6}$$

and the inner integral representation then gives an expansion of the surface traction on the inclusion as

$$\mathbf{t}_- = \sum_{n} \alpha_n \mathbf{t}^1(\mathrm{Re}\psi_n^1) \tag{7}$$

where $\mathbf{t}^1(\cdot)$ is the traction operator for the inclusion.

The question is now how to relate $\mathbf{u}_+$ and $\mathbf{t}_+$ on S_h appearing in equations (4) and (5) to $\mathbf{u}_-$ and $\mathbf{t}_-$ on S_o appearing in equations (6) and (7). One way to proceed would be to use the null field approach for a layered medium (Boström, 1980), but in the present context with a thin layer one would then violate the requirement that the circumscribing sphere of the inner surface should not intersect the outer surface (Boström, 1984). Instead the assumed smallness of h is used to expand the right-hand sides of equation (4) to (5) to order h and it must then be remembered that the surface, the surface fields, and the partial waves all depend on the location of the outer surface. Thus, one gets

$$a_n = ik_s/\mu \int_{S_o} [\mathbf{u}_- \cdot \mathbf{t}(\psi_n) - \mathbf{t}_- \cdot \psi_n]\, dS$$

$$-ik_s/\mu \int_{S_o} h\left[\frac{\partial \mathbf{u}}{\partial n} \cdot \mathbf{t}(\psi_n) - \frac{\partial \mathbf{t}}{\partial n} \cdot \psi_n\right] dS$$

$$-ik_s/\mu \int_{S_o} h\left[\mathbf{u}_- \cdot \frac{\partial}{\partial n}\mathbf{t}(\psi_n) - \mathbf{t}_- \cdot \frac{\partial}{\partial n}\psi_n\right] dS$$

$$-ik_s/\mu \int_{S_o} [\mathbf{u}_- \cdot \mathbf{t}(\psi_n) - \mathbf{t}_- \cdot \psi_n]\, h \frac{\partial}{\partial n} dS \tag{8}$$

and similarly for f_n. The first integral is what one gets if there were no interface layer, the second will reflect the properties of the layer as will be presented, and the third and fourth are geometrical terms which arise because S_o and S_h are different surfaces.

The normal derivatives of the displacement and traction in the second integral in equation (8) must now be expressed in terms of $\mathbf{u}_-$ and $\mathbf{t}_-$. This is done by using the properties of the interface layer and a consistent approach is to start with the three-dimensional constitutive equation and equations of motion and extract the desired quantities with the normal derivatives present. For a rotationally symmetric inclusion when the azimuthal unit vector $\hat{\Phi}$ and the unit vector $\hat{\tau} = \hat{\Phi} x \hat{n}$ are tangential to S_o this leads to

$$\left(\frac{\partial \mathbf{u}}{\partial n}\right)_{\tan} = [(\mathbf{t}_-)_{\tan}/\mu_o - \hat{n} x (\nabla_s x \mathbf{u}_-)] \tag{9}$$

$$\hat{n} \cdot \frac{\partial \mathbf{u}}{\partial n} = \frac{1}{(\lambda_o + 2\mu_o)} [\hat{n} \cdot \mathbf{t}_- - \lambda_o \nabla_s \cdot \mathbf{u}_-] \tag{10}$$

and

$$\frac{\partial \mathbf{t}}{\partial n} = \mathbf{B}(\mathbf{u}_-, \mathbf{t}_-) \tag{11}$$

where

$$\mathbf{B}(\mathbf{u}, \mathbf{t}) = -[\rho_o \omega^2 \mathbf{u} + \nabla_s \cdot \sigma^s(\mathbf{u}) + \hat{n} \nabla_s \cdot \mathbf{t} + \mathbf{t}_{\tan} \nabla_s \cdot \hat{n} + \tau \cdot \mathbf{t} \frac{\partial \hat{n}}{\partial \tau} + \hat{\phi} \cdot \mathbf{t}(\hat{\phi} \cdot \nabla)\hat{n} + \nabla_s \cdot \left\{(\hat{\tau}\hat{\tau} + \hat{\phi}\hat{\phi}) \frac{\lambda_o}{\lambda_o + 2\mu_o} (\hat{n} \cdot \hat{t} - \lambda_o \nabla_s \cdot \mathbf{u})\right\}. \tag{12}$$

The tangential stress tensor in the layer is

$$\sigma^s_{\tau\tau}(\mathbf{u}) = \lambda_o \nabla_s \cdot \mathbf{u} + 2\mu_o \hat{\tau} \cdot \frac{\partial \mathbf{u}}{\partial \tau} \tag{13}$$

$$\sigma^s_{\phi\phi}(\mathbf{u}) = \lambda_o \nabla_s \cdot \mathbf{u} + 2\mu_o \hat{\phi} \cdot (\hat{\phi} \cdot \nabla)\mathbf{u} \tag{14}$$

$$\sigma^s_{\tau\phi}(\mathbf{u}) = \mu_o \left[\hat{\phi} \cdot \frac{\partial \mathbf{u}}{\partial \tau} + \hat{\tau} \cdot (\hat{\phi} \cdot \nabla)\mathbf{u}\right] \tag{15}$$

In the foregoing formulas, $\nabla_s \cdot$ and $\nabla_s x$ are the surface divergence and curl, respectively. It should be noted that earlier investigations of problems of the present type (see Datta et al. (1988) for a recent example) have usually assumed the traction to be continuous across the layer; i.e., it has been assumed that $\mathbf{B} = 0$. Moreover, curvature effects have usually been neglected so that the last terms in equations (9) and (10) are dropped.

A straightforward collection of all the previous formulas now determines the transition matrix as

$$T_{nn'} = -\sum_{n''} \mathrm{Re}Q_{nn''}(Q^{-1})_{n''n'} \tag{16}$$

with

$$Q_{nn'} = k_s/\mu \int_{S_o} [\mathbf{t}(\psi_n) \cdot \mathrm{Re}\psi_{n'} - \psi_n \cdot \mathbf{t}^1(\mathrm{Re}\psi^1_{n'})]\, dS$$

$$+ k_s/\mu \int_{S_o} h\, [\mathbf{t}(\psi_n) \cdot \mathbf{B}(\mathrm{Re}\psi^1_n, \mathbf{t}^1(\mathrm{Re}\psi^1_{n'}))$$

Downloaded 03 May 2010 to 171.66.16.244. Redistribution subject to ASME license or copyright; see http://www.asme.org/terms/Terms_Use.cfm

$$-\psi_n \cdot \mathbf{C}(\mathrm{Re}\psi^1_n, \mathbf{t}^1(\mathrm{Re}\psi^1_{n'}))]\,dS$$

$$+k_s/\mu \int_{S_o} h[\mathrm{Re}\psi^1_{n'} \cdot \frac{\partial}{\partial n}\mathbf{t}(\psi_n)$$

$$-\mathbf{t}^1(\mathrm{Re}\psi^1_{n'}) \cdot \frac{\partial}{\partial n}\psi_n]\,dS + k_s/\mu \int_{S_o} [\mathbf{t}(\psi_n) \cdot \mathrm{Re}\psi^1_{n'}$$

$$-\psi_n \cdot \mathbf{t}^1(\mathrm{Re}\psi^1_{n'})]h\frac{\partial}{\partial n}dS \tag{17}$$

where

$$\mathbf{C}(\mathbf{u}, \mathbf{t}) = \frac{\hat{n}}{\lambda_o + 2\mu_o}(\hat{n} \cdot \mathbf{t} - \lambda_o \nabla_s \cdot \mathbf{u}) - \mathbf{t}_{\tan}/\mu_o$$

$$-\hat{n}x(\nabla_s x\mathbf{u}) \tag{18}$$

and $\mathrm{Re}Q_{nn'}$ contains $\mathrm{Re}\psi_n$ instead of ψ_n in all places. For some details concerning the computation of $\partial/\partial n\, dS$ and $\partial/\partial n\, \mathbf{t}(\psi_1)$, see the Appendix.

The exact order h expressions given previously are hideously complicated to use in actual computations and there are, therefore, good reasons to look for simplified theories that might contain the most important effects. One way is to use a membrane shell type of approximation, i.e., to skip the last two integrals, the operator **C** and all of **B** except the first term in equation (17). This has been shown earlier to lead to meaningful results (Olsson et al., 1988). In fact, one could also skip the second term in **B** and only keep the first inertial term, and this actually captures the main effects of the interface layer at low frequencies. As mentioned previously, another approach is to put $\mathbf{B} = 0$ and to skip the second and fourth terms in **C** in equation (18).

3 Numerical Results and Discussion

The present section contains some examples of computations performed by means of the approach developed in the previous section. The total scattering cross-sections for S and P wave scattering from spherical and spheroidal inclusions have been computed. The normalization chosen is with respect to the square of the radius of the sphere circumscribing the inclusion inside the layer. The main emphasis is on checking, by comparing the results from other methods, that the approximate boundary conditions derived in the previous section indeed yield meaningful results.

Table 1 Material parameters for the SiC inclusion in *A*1

Matrix	$\rho = 2.706$ kg m^{-3}, $(\lambda + 2\mu\ ,\ \mu) = (1.105\ ,\ 0.267) \times 10^{11}$ Pa
Inclusion	$\rho_1 = 3.181$ kg m^{-3}, $(\lambda_1 + 2\mu_1\ ,\ \mu_1) = (4.742\ ,\ 1.881) \times 10^{11}$ Pa
Layer	$\rho_0 = (\rho + \rho_1)/2\ ,\ \lambda_0 = (\lambda + \lambda_1)/2\ ,\ \mu_0 = (\mu + \mu_1)/2$

The inclusion is taken to be a SiC inclusion used by Paskaramoorthy, Datta, and Shah (1988). The properties are given in Table 1.

To check the null field computer program, various tests have been performed. One is that of taking the center of a spherical inclusion to be displaced from the origin of the spherical coordinate system employed. For an incident P wave at $k_s a = 2$, where a is the radius of the sphere, and thickness $h = 0.1a$, the results from calculations for a sphere displaced by $0.5a$ differ by less than 5×10^{-6} from those for a sphere centered at the origin. This should be compared to the value of the scattering cross-section, which is roughly 1.5.

In Table 2 a comparison is made between the results of the various approximations for a thin layer on a spherical inclusion, and the exact analytical results. A conclusion from the table is that in the frequency interval considered the results of including only the jump in the displacement to order h (and no geometrical effects, etc.) are inferior to the full-order h results, as well as to the membrane and inertial approximations described in Section 2. The importance of the geometrical terms is also borne out in the table. Only the full-order h column contains the effects of including the last two terms, the geometrical ones, in equation (17). Note that the last two columns contain values which are actually below the values for a sphere without a surrounding layer. The corresponding boundary conditions thus represent a kind of smoothing of the contrast between the inclusion and the matrix.

Turning now to the plots, in Figs. 1 and 2 are found results for scattering from spherical inclusions. The full-order h results are here compared to the results from exact separation of variables calculations. A good agreement is found between the exact results and those of the order h theory in the frequency range considered, but it can be noted that the P wave results are in close agreement over a larger interval than are the S wave results. This is only to be expected from the difference in wavelength between P and S waves, $k_s h$ being roughly twice as large as $k_p h$. Note also that the S wave curve peaks at $k_s a \approx 4.5$, while the P wave curve does not peak in the interval considered. For larger frequencies the curves are of course expected to approach a constant value. The great effect of the interface layer on the cross-section can be clearly seen in these and the following plots, since results for inclusions without a layer are also included.

Figure 3 contains results for the total scattering cross-section for an SV wave incident at 45 deg angle to the symmetry axis on an 1:2 oblate spheriod. For comparison, data points from the FEM calculations of Paskaramoorthy, Datta, and Shah (1988) are included for scatterers with and without interface layers. The agreement between the results is in this case very good. (It should be noted that the frequency variable and the normalization used here differs from that of the previous reference. The difference only matters for

Table 2 Comparison of analytical and numerical results for the total scattering cross-section for a plane P wave incident on a coated SiC sphere in *A*1.$h = a/10$

$k_s a$	Analytical	Full order h	Membrane	Inertial	Only jump in u	Order h without geometrical effects
0.1	4.232×10^{-5}	4.211×10^{-5}	3.880×10^{-5}	3.741×10^{-5}	2.346×10^{-5}	2.414×10^{-5}
0.5	2.212×10^{-2}	2.201×10^{-2}	2.142×10^{-2}	2.067×10^{-2}	1.264×10^{-2}	1.313×10^{-2}
1.0	0.2339	0.2328	0.2443	0.2355	0.1408	0.1482
1.5	0.7504	0.7469	0.7559	0.7234	0.4675	0.4874
2.0	1.5574	1.5474	1.4113	1.3379	0.9831	1.0029

Downloaded 03 May 2010 to 171.66.16.244. Redistribution subject to ASME license or copyright; see http://www.asme.org/terms/Terms_Use.cfm

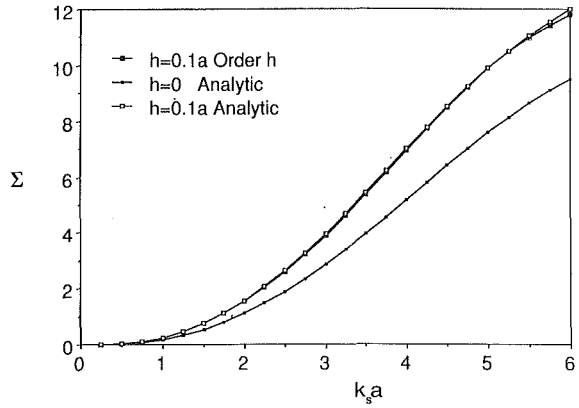


Fig. 1 The total scattering cross-section normalized by a^2 for P wave scattering from a sphere of radius a

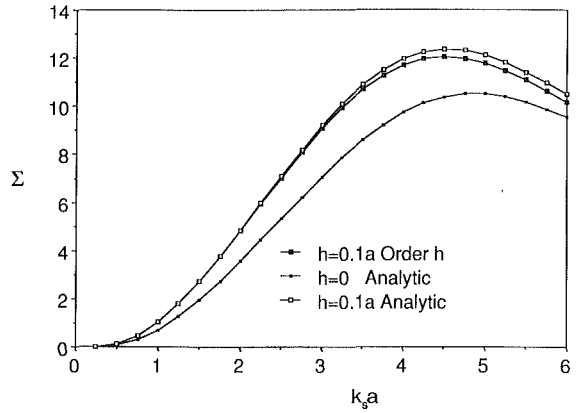


Fig. 2 Same as Fig. 1 but for S wave scattering

nonspherical bodies.) The discrepancy is not appreciably larger for the inclusion with a layer than for the one without a layer.

A less good agreement with FEM is found in the next plot, Fig. 4, which shows the scattering cross-section for SV incidence at 45 deg on a prolate 2:1 spheriod. However, we again find that the disagreement is roughly the same for the cases $h = 0.1a$ and $h = 0$. In the latter case, the case of an inclusion without a layer, the present method reduces to the ordinary (well-tested) null field approach. The discrepancy is possibly due to discretization errors in the FEM calculation. Curiously, the largest differences occur at an intermediate frequency.

Similar remarks can be made concerning Fig. 5, which contains results for P wave scattering from a coated 1:2 oblate spheroid, except that here the largest differences occur at the highest frequency compared. Note also that while the curves in Fig. 3 seem to be approaching a peak just outside the frequency interval plotted, the curves in Fig. 5 have just reached at most an inflection point. As for the sphere, this is a result of the different wavelengths of P and S waves.

4 Conclusion

The main conclusions of the present study are the following. First, the results of using approximate boundary conditions coupled with the null field method are in agreement with those obtained by Paskaramoorthy et al. (1988), who used a hybrid finite element (FE) and eigenfunction expansions technique to take into account the interface layer properties in an exact manner. These results indicate that the effect of an interface layer is to significantly increase the scattering cross-section. Second, the results of the simpler membrane shell and

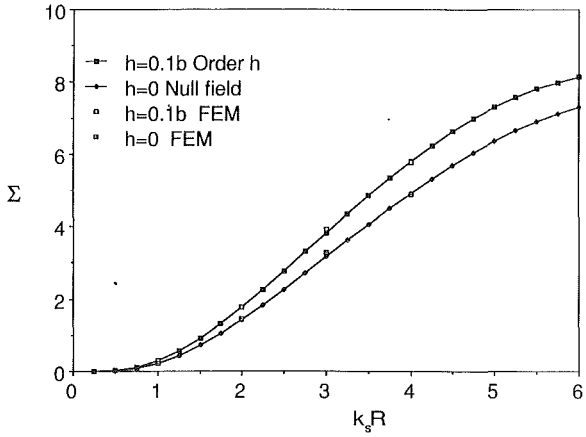


Fig. 3 The total scattering cross-section normalized by R^2 for SV wave scattering from an oblate spheroid; major axis $a = R$, minor axis $b = a/2$; angle of incidence 45 deg from axis of symmetry

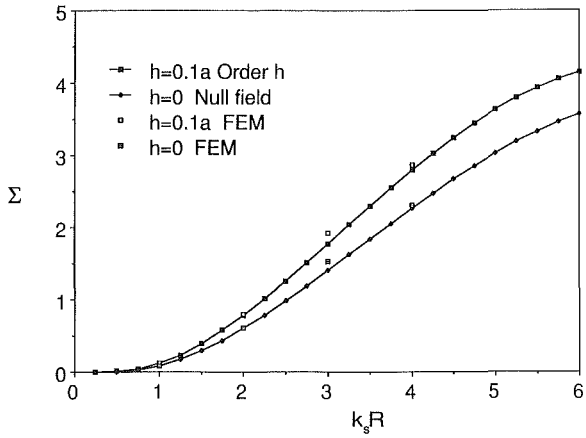


Fig. 4 The total scattering cross-section normalized by R^2 for SV wave scattering from a prolate spheroid; major axis $b = R$, minor axis $a = b/2$; angle of incidence 45 deg from axis of symmetry

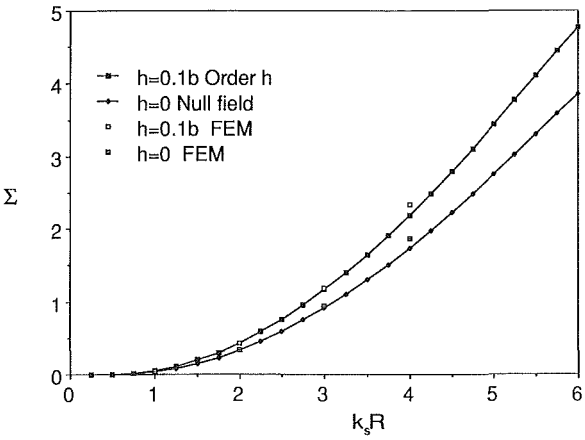


Fig. 5 Same as Fig. 3 but for P wave scattering

"phenomenological" approaches presented here and by Olsson et al. (1988) are in close agreement at low frequencies ($k_sR = 2$) with the exact calculations for the sphere and with the hybrid FE results for spheroids. As seen from Table 2, the usual approximation of considering the jump in u without the geometrical effects underestimates the scattering cross-sections considerably. Third, the full $O(h)$ calculations in-

Downloaded 03 May 2010 to 171.66.16.244. Redistribution subject to ASME license or copyright; see http://www.asme.org/terms/Terms_Use.cfm

cluding the geometrical effects presented in this study are found to agree quite well with the exact results for the sphere even at moderately high frequencies ($k_sR=6$). Thus, it may be concluded that the "phenomemological" approach is meaningful at low frequencies in describing the effect of interface thin layers in composite materials with arbitrarily shaped inclusions. At higher frequencies, however, one needs to take into account all terms of $O(h)$ in the boundary conditions.

Although only a single scattering problem is considered here, the results obtained in this case can be used to study dispersion and attenuation of plane waves in the presence of a distribution of inclusions. We plan to present these results in a future communication.

In the case of the "phenomenological" approach of taking $\mathbf{t}_+ - \mathbf{t}_-$ proportional to $\mathbf{u}_-$, we have here simply taken the constant of proportionality to be the same as that of the inertial term of (11). To achieve better results, one could possible vary this constant, and even have different constants for the normal and tangential components, respectively. We hope to pursue these possibilities further in the future.

Acknowledgment

The work of SKD was supported in part by a grant from the Office of Naval Research (No. N00014-86-K0280; Program Manager: Dr. Y. Rajapakse) and in part by grants from the National Science Foundation (INT-8521422 and INT-8610487). The work of PO and AB was sponsored by the National Swedish Board for Technical Development.

References

Boström, A., 1980, "Multiple Scattering of Elastic Waves by Bounded Obstacles," *Journal of the Acoustical Society of America*, Vol. 67, pp. 399–413.

Datta, S. K., 1977, "Diffraction of Plane Elastic Waves by Ellipsoidal Inclusions," *Journal of the Acoustical Society of America*, Vol. 61, pp. 1432–1437.

Datta, S. K., Ledbetter, H. M., Shindo, Y., and Shah, A. H., 1988, "Phase Velocity and Attenuation of Plane Elastic Waves in a Particle-Reinforced Composite Medium," *Wave Motion*, Vol. 10, pp. 171–182.

Datta, S. K., and Sangster, J. D., 1974, "Response of a Rigid Spherodial Inclusion to an Incident Plane Longitudinal Wave," *SIAM Journal of Applied Mathematics*, Vol. 26, pp. 350–369.

Gubernatis, J. E., 1979, "Long Wave Approximation for the Scattering of Elastic Waves from Flaws with Applications to Ellipsoidal Voids and Inclusion," *Journal of Applied Physics*, Vol. 50, pp. 4046–4058.

Mal, A. K., and Bose, S. K., 1974, "Dynamic Elastic Moduli of a Suspension of Imperfectly Bonded Spheres," *Proceedings of the Cambridge Philosophical Society*, Vol. 76, pp. 587–600.

Olsson, P., 1985, "The Rigid Movable Inclusion in Elastostatics and Elastodynamics," *Wave Motion*, Vol. 7, pp. 421–445.

Olsson, P., Datta, S. K., and Boström, A., 1988, "Scattering of Elastic Waves by Inclusions Surrounded by Thin Interface Layers," Proceedings of the IUTAM Symposium on Elastic Wave Propagation, Galway, Ireland.

Opsal, J. L., and Visscher, W. M., 1985, "Theory of Elastic Wave Scattering: Applications of the Method of Optimum Truncation," *Journal of Applied Physics*, Vol. 58, pp. 1102–1115.

Pao, Y. H., and Mow, C. C., 1973, *Diffraction of Elastic Waves and Dynamic Stress Concentration*, Crane and Russak, New York.

Paskaramoorthy, R., Datta, S. K., and Shah, A. H., 1988, "Effect of Interface Layers on Scattering of Elastic Waves," ASME JOURNAL OF APPLIED MECHANICS, Vol. 55, pp. 871–878.

Varadan, V. V., and Varadan, V. K., 1979, "Scattering Matrix for Elastic Waves. III. Application to Spheroids," *Journal of the Acoustical Society of America*, Vol. 65, pp. 896–905.

Willis, J. R., 1980, "A Polarization Approach to the Scattering of Elastic Waves—I. Scattering by a Single Inclusion," *Journal of the Mechanics and Physics of Solids*, Vol. 28, pp. 287–305.

APPENDIX

Consider a family of surfaces S_ϵ, $0 \le \epsilon \le h$, given by the parametrization

$$\gamma = \gamma_\epsilon(\theta, \phi) \equiv \gamma_o(\theta, \phi) + \epsilon \hat{n}_o(\theta, \phi)$$

where $\gamma = \gamma_o(\theta, \phi)$ is a parametrization of S_o, and $\hat{n}_o$ is the outward pointing unit normal of S_o.

The normal derivative of the surface element at S_o can then be computed as

$$\frac{\partial}{\partial n} dS = \left\{ \frac{\partial}{\partial \epsilon} \left| \frac{\partial \gamma_\epsilon}{\partial \theta} \times \frac{\partial \gamma_\epsilon}{\partial \phi} \right| \right\} \Big|_{\epsilon=0} d\theta d\phi .$$

Quantities like the normal derivative of the unit normal at S_o can similarly be computed as

$$\frac{\partial \hat{n}}{\partial n} = \frac{\partial}{\partial \epsilon} \hat{n}_\epsilon \Big|_{\epsilon=0}$$

where

$$\hat{n}_\epsilon = \frac{\dfrac{\partial \gamma_\epsilon}{\partial \theta} \times \dfrac{\partial \gamma_\epsilon}{\partial \phi}}{\left| \dfrac{\partial \gamma_\epsilon}{\partial \theta} \times \dfrac{\partial \gamma_\epsilon}{\partial \phi} \right|}$$

defines the unit normal of S_ϵ. Incidentally, $\partial \hat{n}/\partial n$ turns out to be zero.

Thus,

$$\frac{\partial}{\partial n} \mathbf{t}(\mathbf{u}) = \hat{n} \cdot \frac{\partial}{\partial n} \sigma(\mathbf{u})$$

where σ is the stress tensor.

Downloaded 03 May 2010 to 171.66.16.244. Redistribution subject to ASME license or copyright; see http://www.asme.org/terms/Terms_Use.cfm

Axisymmetric Vibrations of Circular Plates on Tensionless Elastic Foundations

Zekai Celep
Professor,
Faculty of Civil Engineering,
Technical University,
80626 Maslak,
Istanbul, Turkey

Doğan Turhan
Professor,
Department of Mechanical Engineering,
Karadeniz Technical University,
61080 Trabzon, Turkey

The present study deals with the axisymmetric vibrations of a circular plate subjected to a concentrated dynamic load at its center. The plate is assumed to be supported on an elastic foundation that reacts in compression only. At first the static solution is obtained and contact radius is determined. Later, this is used as an initial configuration of the forced vibrations. The forced vibrations are assumed to be due to the time dependency of the load. The solution is carried out by Galerkin's method and by using modal functions of the completely free plate. Numerical results are illustrated in figures for stepwise change of the loading.

Introduction

The Winkler hypothesis, that the foundation pressure at any point is proportional to the deflection at that point, has been widely used for determining the behavior of structures supported on foundations. However, one of its shortcomings is its assumption that the foundation acts in tension as well as in compression. Although extensive studies exist in the analysis of beams and plates on a conventional Winkler foundation, there are many fewer investigations concerned with foundations that react in compression only. Many of these studies deal with beams.

Weitsman (1970) considered a weightless plate of infinite extent supported on a tensionless foundation. The plate is assumed to be subjected to a concentrated load. An unexpected result of the study was that the radius of the contact circle does not depend on the level of the loading, but only on the relative flexural rigidity of the plate with respect to the foundation modulus. Kamiya (1977) investigated the circular plate with a clamped edge by using the Berger method. He attempted to clarify the behavior of the foundation on the nonlinear deformations of the plate. Recently, a rectangular weightless plate on a tensionless foundation has been studied by Villaggio (1983). The plate is assumed to be subjected to a concentrated load at its center.

The difficulty of this type of problem is that the boundary of the contact region is not known in advance and must be determined by requiring that the deflection of the plate vanishes along the contact curve. Thus, the problem becomes nonlinear. In a dynamical treatment of such a problem, the contact boundary becomes a function of time, and the problem appears as a moving boundary value problem. The authors are not aware of any dynamic analysis of plates on a tensionless Winkler foundation.

In this paper an attempt is made to investigate the behavior of a circular plate on a tensionless foundation, subjected to a dynamical concentrated load at its center.

Analysis

Consider a circular thin elastic plate of radius, a, and stiffness, D, supported on a tensionless Winkler type of foundation having modulus, k, (Fig. 1). The plate is assumed to be subjected to a dynamical concentrated load, $P(t)$, applied at the center. Since the geometrical and loading configurations of the problem are axially symmetric, the deflection of the plate is assumed to be axially symmetric as well, i.e., $w = w(r, t)$. The oscillations of the plate are governed by the differential equation (Timoshenko and Woinowsky-Krieger, 1959)

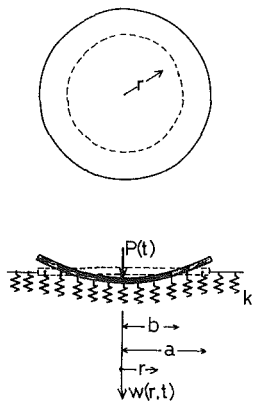


Fig. 1 Circular plate on a tensionless foundation

Contributed by the Applied Mechanics Division of THE AMERICAN SOCIETY OF MECHANICAL ENGINEERS for publication in the JOURNAL OF APPLIED MECHANICS.

Discussion on this paper should be addressed to the Technical Editor, Leon M. Keer, The Technological Institute, Northwestern University, Evanston, IL 60208, and will be accepted until two months after final publication of the paper itself in the JOURNAL OF APPLIED MECHANICS. Manuscript received by the ASME Applied Mechanics Division, November 3, 1986; final revision, February 10, 1988.

Copyright © 1990 by ASME
Downloaded 03 May 2010 to 171.66.16.244. Redistribution subject to ASME license or copyright; see http://www.asme.org/terms/Terms_Use.cfm

$$D\Delta\Delta w = -m\ddot{w} + \frac{P\delta(r)}{2\pi r} - kH(r)w \tag{1}$$

where m is the mass of the plate per unit area, $\delta(r)$ is the Dirac delta function,

$$\Delta = \frac{d^2}{dr^2} + \frac{1}{r}\frac{dr}{d}, \tag{2}$$

and $H(r)$ is an auxiliary function defined as

$$H(r) = 1 \quad \text{for} \quad 0 \le r \le b,$$

$$H(r) = 0 \quad \text{for} \quad b < r \le a. \tag{3}$$

The plate is assumed to be in contact with the foundation within a circle of radius b as shown in Fig. 1. Being aware of the difficulty of a closed-form solution of the problem, Galerkin's approximation is adapted here. The deflection of the plate is assumed to be a linear combination of the axially symmetric, free vibration mode shapes of the completely free plate, $R_n(r)$, by including an additional term for a rigid translation as follows:

$$w(r, t) = a\sum_{n=1}^{\infty} R_n(r)T_n(t) + aT_o(t), \tag{4}$$

where (Leissa, 1969; McLachlan, 1955),

$$R_n(r) = J_o(s_n r/a) + A_n I_o(s_n r/a) \quad \text{for} \quad n \ge 1, \tag{5}$$

and J_o, I_o denotes Bessel functions of the first kind. By requiring that the mode shapes satisfy the boundary conditions of the plate one obtains the following equations for the nondimensional free vibration frequencies, s_n^2, and the constants, A_n,

$$\frac{J_1(s_n)}{I_1(s_n)} = \frac{(1-\nu)J_1(s_n) - s_n J_o(s_n)}{(1-\nu)I_1(s_n) - s_n I_o(s_n)}, \tag{6}$$

$$A_n = -J_1(s_n)/I_1(s_n), \tag{7}$$

where ν denotes the Poisson's ratio. Defining $R_o(r) = 1$, the deflection of the plate given by equation (4) can be rewritten as

$$w(r, t) = a\sum_{n=0}^{\infty} R_n(r)T_n(t). \tag{8}$$

Employing Galerkin's procedure, substituting the deflection function (8) into the governing equation (1), and requiring that the error be orthogonal to each mode shape within the region of definition of the problem, the following system of differential equations is obtained

$$\mathbf{A}\ddot{\mathbf{T}} + \mathbf{B}\mathbf{T} = \mathbf{C}, \tag{9}$$

where

$$T = [T_0, T_1, T_2, \ldots, T_n]^T, \tag{10}$$

$$\mathbf{A} = \text{diag}\,[0.5, F_1\, F_2, \ldots, F_n], \tag{11}$$

$$\mathbf{B} = \begin{bmatrix} B_{00} & B_{01} & B_{02} & \ldots & B_{0n} \\ & B_{11} & B_{12} & \ldots & B_{1n} \\ & & B_{22} & \ldots & B_{2n} \\ \text{symmetric} & & & \ldots & \\ & & & & B_{nn} \end{bmatrix}, \tag{12}$$

$$B_{ij} = k^* E_{ij} + \delta_{ij} s_i^4 F_i \quad \text{for} \quad i \ge 0, j \ge 0, \tag{13}$$

$$E_{ij}(\bar{r}_b) = \int_0^{\bar{r}_b} R_i(\bar{r})R_j(\bar{r})\bar{r}d\bar{r}, \qquad \bar{r} = r/a, \tag{14}$$

$$F_i = \int_0^1 R_i^2(\bar{r})\bar{r}d\bar{r}, \qquad \bar{r}_b = b/a, \tag{15}$$

$$C_1 = P^*/2\pi, \quad C_{i+1} = (1 + A_i)P^*/2\pi \text{ for } i \ge 1, \tag{16}$$

$$\delta_{ij} = \text{Kronecker's delta}, \; P^* = Pa/D, \; k^* = ka^4/D. \tag{17}$$

The differentiations in equation (9) are with respect to the nondimensional time, τ, is defined as

$$\tau = t\sqrt{D/m}/a^2. \tag{18}$$

In the derivation of the governing equation (9), the orthogonality of the mode shapes, including the rigid translation, is used; the coupling of the system, however, is due to the partial contact between the plate and the foundation. When full contact is present, the matrix **B** becomes a diagonal one and the coupling will vanish. The introduction of the mode shapes into previous expressions leads to the following relations:

$$E_{00} = \bar{r}_b/2, \tag{19}$$

$$E_{n0} = E_{0n} = \bar{r}_b[J_1(s_n\bar{r}_b) + A_n I_1(s_n\bar{r}_b)]/s_n, \tag{20}$$

$$E_{nn} = 0.5\bar{r}_b^2[J_0^2(s_n\bar{r}_b) + J_1^2(s_n\bar{r}_b)] + \bar{r}_b A_n[J_o(s_n\bar{r}_b)I_1(s_n\bar{r}_b) + I_0(s_n\bar{r}_b)J_1(s_n\bar{r}_b)]/s_n + 0.5\bar{r}_b^2 A_n^2[I_0^2(s_n\bar{r}_b) - I_1^2(s_n\bar{r}_b)] \tag{21}$$

$$E_{mn} = \bar{r}_b[s_m J_0(s_n\bar{r}_b)J_1(s_m\bar{r}_b) - s_n J_0(s_m\bar{r}_b)J_1(s_n\bar{r}_b)]/(s_m^2 - s_n^2) + \bar{r}_b A_n[s_n J_0(s_m\bar{r}_b)I_1(s_n\bar{r}_b) + s_m I_0(s_n\bar{r}_b)J_1(s_m\bar{r}_b)]/(s_m^2 + s_n^2) + \bar{r}_b A_m[s_m J_0(s_n\bar{r}_b)I_1(s_m\bar{r}_b) + s_n I_o(s_m\bar{r}_b)J_1(s_n\bar{r}_b)]/(s_m^2 + s_n^2) + \bar{r}_b A_m A_n[s_m I_0(s_n\bar{r}_b)I_1(s_m\bar{r}_b) - s_m I_0(s_m\bar{r}_b)I_1(s_m\bar{r}_b)]/(s_m^2 - s_n^2)$$

$$\text{for } m \ne n, \; m \ge 1, \; n \ge 1 \tag{22}$$

$$F_n = 0.5[J_0^2(s_n) + J_1^2(s_n)] + A_n[J_0(s_n)I_1(s_n) + I_0(s_n)J_1(s_n)]/s_n + 0.5A_n^2[I_n^2(s_n) - I_1^2(s_n)]. \tag{23}$$

The radius of the contact is obtained at the point where the deflection vanishes, i.e.,

$$w(\bar{r} = \bar{r}_b, t) = 0, \tag{24}$$

which indicates that $\bar{r}_b = \bar{r}_b(t)$. However, the relation can be used for $0 < \bar{r}_b < 1$, since for $\bar{r}_b = 0$ the plate will be just touching the foundation or it will be separated completely from the foundation depending on whether the deflection of the center, $w_o(t) = w(\bar{r} = 0, t)$, is zero or negative, respectively. The complete contact will appear for $\bar{r}_b = 1$; then the deflection of the edge of the plate, $w_a(t) = w(\bar{r} = 1, t)$, will be zero or take positive values. Although the system of differential equations (9) looks like a linear one, the problem is highly nonlinear, since the radius of the contact depends on time and it appears in the matrix **B**. This fact indicates that the numerical solution has to be an iterative one. Finally, it is noted that the static solution of the problem can also be obtained from the governing equation (9) by assuming that $\mathbf{T} = \text{constant}$.

Numerical Examples and Discussion

The series-type solution obtained is quite suitable for computer programming, depending only upon the existence of the appropriate Bessel function subroutines. The numerical calculations are carried out at the Computer Center of King Saud University, Riyadh. In order to investigate the rate of convergence of the series, several test cases are calculated and their results are compared. It is found that a rather acceptable accuracy can be obtained for graphical representation by taking into account four mode shapes in addition to the rigid

Downloaded 03 May 2010 to 171.66.16.244. Redistribution subject to ASME license or copyright; see http://www.asme.org/terms/Terms_Use.cfm

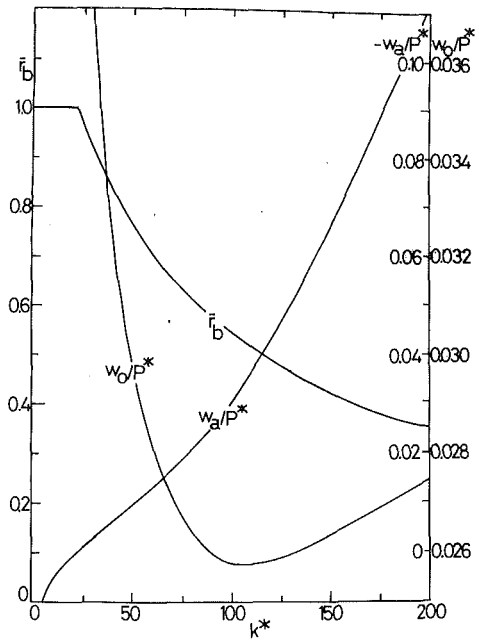


Fig. 2 Radius of contact, $\bar{r}_b$, deflections of the center, w_o, and the edge, w_a, of the plate versus stiffness of the foundation, k^*, for static case

translation. In all of the numerical calculations, $\nu = 0.33$ is assumed.

Fig. 2 shows the results corresponding to the static loading. By assuming $\mathbf{T}$ = constant, the unknown factors of the mode shapes can be obtained from equation (9) as $\mathbf{T} = \mathbf{C}\mathbf{B}^{-1}$. Since the contact circle is not known in advance, the solution requires an iterative scheme. The numerical results yield that the radius of the contact circle, $\bar{r}_b$, does not depend on the loading level, and the deflection of the center, w_o, and the edge, w_a, of the plate depend linearly on the loading; this fact has also been noted by Weitsman (1970) and Villaggio (1983). However, it is a nonincreasing function of the relative foundation modulus with respect to the flexural rigidity of the plate, k^*. As shown in Fig. 2 the plate lifts off the foundation, except for rather low foundation moduli where complete contact develops. The deflection of the center displays a rather low foundation moduli where complete contact develops. The deflection of the center displays a rather unexpected variation by showing a minimum value for a certain foundation modulus, whereas the deflection of the edge increases continuously. As the foundation gets stiffer, the contact radius and the deflection of the center decrease for a constant load to establish the vertical equilibrium. However, after a certain foundation modulus the contact radius decreases monotonically at a decreasing rate, and the deflection of the center increases to satisfy the equilibrium condition. The vertical equilibrium requires that

$$P = 2\pi \int_0^b kwrdr, \tag{25}$$

which can be written in nondimensional form as follows:

$$P = 2\pi k^* \left[0.5\, \bar{r}_b^2 T_0 + \sum_{n=1}^{\infty} T_n E_{0n} \right]. \tag{26}$$

Athough it can not be seen explicitly in the last term, the right-hand side of equation (26) depends on the square of $\bar{r}_b$, and it is geometrically equal to the product of the deflected foundation volume by the foundation modulus.

The solution of equation (9), which governs the oscillations of the plate, is obtained by using the Runge-Kutta method (Collatz 1966). Although the analysis and the corresponding computer program does not have any restriction on the variation of the load, $P(t)$, a stepwise change is considered in the following results. To this end, the static solution of the plate is found, as explained previously, by assuming that it is subjected to a specific load, P^*; then the external load is changed to βP^* suddenly, and this level of the load is kept constant. Due to this change in the loading, the plate experiences oscillatory motion. The case $\beta > 1$ denotes an increase in the loading of the plates whereas $0 < \beta < 1$ and $\beta = 0$ indicate partial and total unloadings, respectively. Since the differential equation (9) is solved step-by-step starting from the initial condition, a general method requires the solution of equation (24) for $\bar{r}_b$ and the evaluation of $E_{ij}(\bar{r}_b)$ at every time step, because the contact radius depends on time. However, this kind of solution scheme requires a rather lengthy computer time; hence, the following incremental solution is adapted here. It is assumed that the contact radius $\bar{r}_b = \bar{r}_{b1}$ is known for $\tau = \tau_1$ which means

$$\sum_{n=0} R_n(\bar{r}_{b1}) T_n(\tau_1) = 0. \tag{27}$$

For $\tau = \tau_2 = \tau_1 + \Delta\tau$ the radius will be $\bar{r}_b = \bar{r}_{b2} = \bar{r}_{b1} + \Delta\bar{r}_b$ and

$$\sum_{n=0} R_n(\bar{r}_{b2}) T_n(\tau_2) = 0, \tag{28}$$

will be satisfied. The increment of the contact radius can be obtained by expanding R_n into Taylor series and taking into account the linear term only:

$$\Delta\bar{r}_b = -\sum_{n=0} R_n(\bar{r}_{b1})[T_n(\tau_2) - T_n(\tau_1)] /$$

$$\sum_{n=1} R_n'(\bar{r}_{b1}) T_n(\tau_1), \tag{29}$$

where

$$R_n'(\bar{r}_b) = -s_n[J_1(s_n\bar{r}_b) - A_n I_1(s_n\bar{r}_b)]. \tag{30}$$

Thus, an iteration at each step can be avoided. The approximation can be checked by determining the deflection of the contact circle $w(\bar{r} = \bar{r}_b, t)$, which must vanish. When the approximation becomes unacceptable, then the solution for $\bar{r}_b$ can be updated by solving equation (24) iteratively. A similar approach can also be implemented in the evaluation of $E_{ij}(\bar{r}_b)$ as follows:

$$E_{ij}(\bar{r}_{b1} + \Delta\bar{r}_b) = E_{ij}(\bar{r}_{b1}) + \Delta E_{ij}(\bar{r}_{b1}, \Delta\bar{r}_b), \tag{31}$$

where

$$\Delta E_{00} = \bar{r}_{b1}\Delta\bar{r}_b \tag{32}$$

$$\Delta E_{0i} = \Delta E_{i0} = [J_0(s_i\bar{r}_{b1}) + A_i I_0(s_i\bar{r}_{b1})]\Delta\bar{r}_b \quad \text{for } i \geq 1 \tag{33}$$

and

$$\Delta E_{ij} = [J_0(s_i\bar{r}_{b1}) + A_i I_0(s_i\bar{r}_{b1})][J_0(s_j\bar{r}_{b1}) + A_j I_0(s_j\bar{r}_{b1})]\bar{r}_{b1}\Delta\bar{r}_b$$

$$\text{for } i \geq 1\ ,\ j \geq 1. \tag{34}$$

Figure 3 shows the variations of the contact radius and the deflections of the center and the edge of the plate with respect to nondimensional time $\tau_1 = s_1^2\tau/2\pi$, where s_1^2 is the first nondimensional circular frequency of free vibrations of the completely free plate and it equals to 9.084 for $\nu = 0.33$. The dynamic load factor, β, is assumed to be equal to 0.5, which means that the plate in static equilibrium at P^* is unloaded suddenly. The oscillations take place under $0.5P^*$. Although

Downloaded 03 May 2010 to 171.66.16.244. Redistribution subject to ASME license or copyright; see http://www.asme.org/terms/Terms_Use.cfm

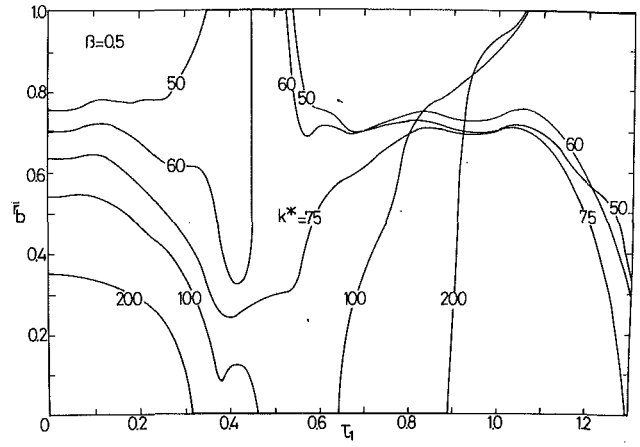


Fig. 3(a)

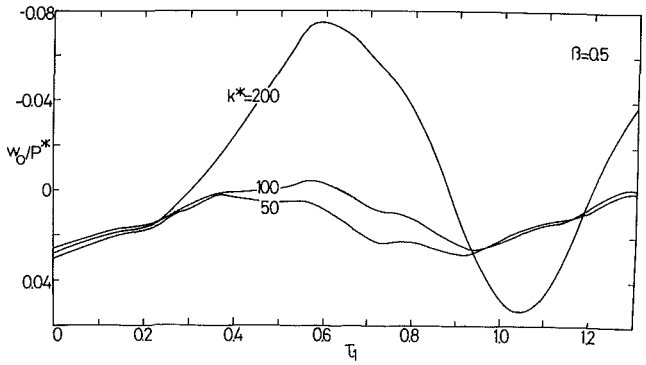


Fig. 3(b)

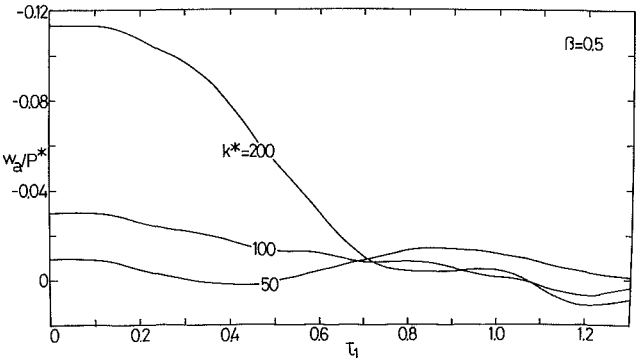


Fig. 3(c)

Fig. 3 (a) Radius of contact, $\bar{r}_b$, deflections of (b) the center, w_o, and (c) the edge, w_a, of the plate versus time for constant unloading parameter, β, and various foundation moduli, k^*

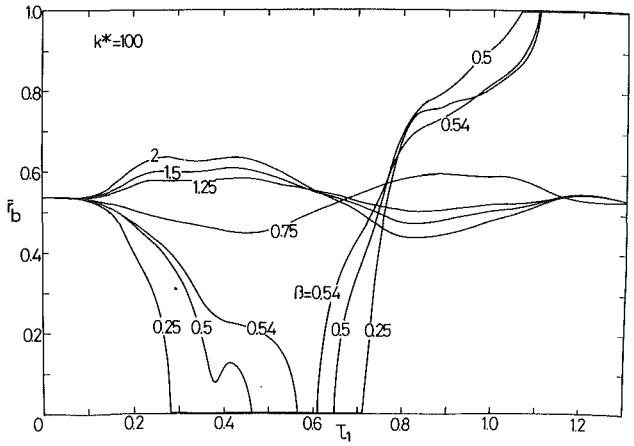


Fig. 4(a)

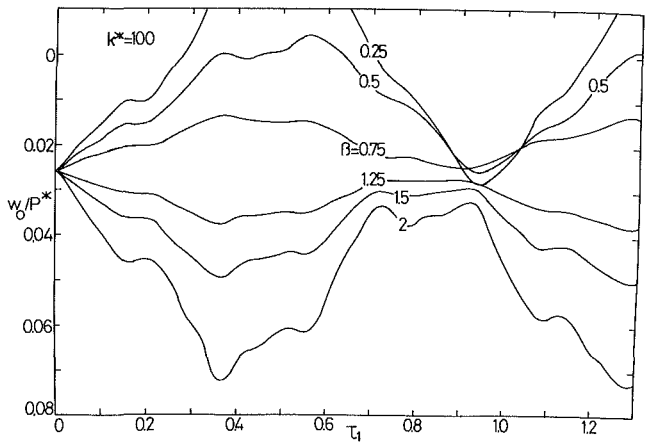


Fig. 4(b)

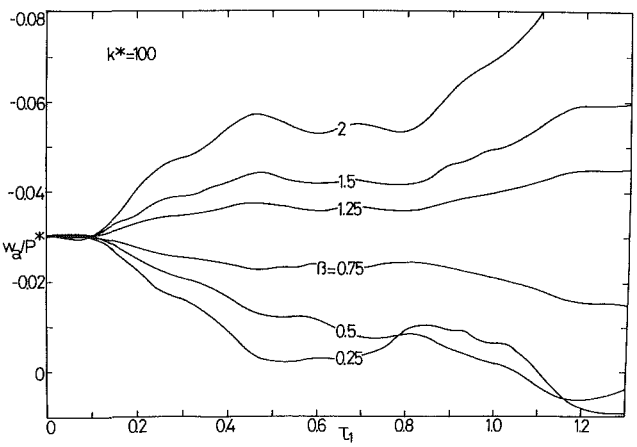


Fig. 4(c)

Fig. 4 (a) Radius of contact, $\bar{r}_b$, deflections of (b) the center, w_o, and (c) the edge, w_a, of the plate versus time for constant foundation modulus, k^*, and various loading/unloading parameters, β

the center and the edge of the plate experience common nonlinear oscillations, the behavior of the contact radius is quite different, and it displays different curves depending on the foundation modulus. For a low foundation modulus the plate loses contact with the foundation completely ($\bar{r}_b = 0$) and subsequently returns to the foundation. However, its behavior is quite different when the foundation modulus is high; the contact regions increases and the complete contact ($\bar{r}_b = 1$) develops and stays for some time; but later, after a partial contact between the foundation and the plate, the plate loses contact completely. An unexpected property of the solution is that the contact radius does not depend on the initial loading level either as it is the case in the static solution. However, as expected, the deflections are linear functions of the load.

Figure 4 illustrates the dependency of the variations of $\bar{r}_b$, w_o, and w_a on β. When β is close to one, then oscillations are relatively small; furthermore, the variations resemble the linear oscillations, as expected, and their nondimensional relative periods, with respect to that of the completely free plate, are smaller than one due to the presence of the elastic foundation. For the loading cases ($\beta > 1$), the variation of the contact radius is again of an oscillatory type, however, for unloading cases ($\beta < 1$), the behavior of the contact radius becomes quite different as β gets smaller; the plate completely loses the contact with the foundation, but later the contact is established, at first partially, then completely, and so on.

As it is stated in the static solution, the dynamic solution is

Downloaded 03 May 2010 to 171.66.16.244. Redistribution subject to ASME license or copyright; see http://www.asme.org/terms/Terms_Use.cfm

also carried out by taking four mode shapes of the completely free plate and a rigid translation into account. Moreover, some test cases are carried out by considering fewer mode shapes and their results are compared. It is interesting to note that the number of the mode shapes has a less significant effect on the contact radius than on the deflections. On the other hand, its effect on the deflections is quite different. In fact, it is found out that a relatively good overall accuracy could be obtained by taking a smaller number of mode shapes into account. If one considers more mode shapes, the overall accuracy changes very little; oscillations having small amplitudes, but high frequencies, appear in the solution.

Conclusion

The formulation and some numerical solutions were presented to clarify the behavior of the circular plate resting on a tensionless foundation. Since the contact region changes as the plate experiences oscillations, the problem is a nonlinear one, although the linear theory of plates is used. Numerical results are presented in the figures to show the behavior of the plate. It is found that the dynamic deflections of the plate depend linearly on the initial loading, whereas the contact radius of the plate does not depend on it. However, they display rather complicated variations as time increases.

References

Collatz, L., 1966, *Numerical Treatment of Differential Equations*, Springer-Verlag, Berlin.

Kamiya, N., 1977, "Circular Plates Resting on Bimodulus and No-Tension Foundations," *ASCE Journal of the Engineering Mechanics*, Vol. 103, pp. 1161–1164.

Leissa, A. W., 1969, "Vibration of Plates," NASA SP-160.

McLachlan, N. W., 1955, *Bessel Functions for Engineers*, Clarendon Press, Oxford.

Timoshenko, S. P., and Woinowsky-Krieger, S., 1959, *Theory of Plates and Shells*, McGraw-Hill, New York.

Villaggio, P., 1983, "A Free Boundary Value Problem in Plate Theory," ASME Journal of Applied Mechanics, Vol. 50, pp. 297–302.

Weitsman, Y., 1970, "On Foundations That React in Compression Only," Journal of Applied Mechanics, Vol. 37, pp. 1019–1030.

Downloaded 03 May 2010 to 171.66.16.244. Redistribution subject to ASME license or copyright; see http://www.asme.org/terms/Terms_Use.cfm

Inflation of an Axisymmetric Membrane: Stress Analysis

A. Sagiv
RAFAEL-Armament Development Authority,
Haifa 31021, Israel

An analysis of the stresses and deformations of an inflated axisymmetric membrane was obtained. Large deformations of Mooney material were assumed. The development of the governing differential equations is an extension of the Adkins-Rivlin equations. The extension is for a general form of undeformed profiles with symmetry of revolution. The equations obtained, when reduced identically to the special cases treated in the literature of flat, spherical, and half-ellipsoid undeformed shapes, are fully compatible. A family of axisymmetric ellipsoid curves were used as an example of undeformed shapes for numerical demonstration. A fourth-order Runge-Kutta method was applied to integrate the equations. The results show relations between the nondimensional parameters governing the deformed membrane, such as pressure, membrane height, undeformed profiles, stresses, and deformations. An analysis of a very large deformation was carried out. It was found that in this case the membrane surface approaches a spherical shape except near the support, regardless of its undeformed profile.

Introduction

Experiments in thin circular membranes were first carried out by Treloar (1944). His results were used to confirm theoretical analyses of inflated membranes (Adkins and Rivlin, 1952; Hart-Smith and Crisp, 1967; Vishwanath and Glockner, 1973; Haines and Wilson, 1979). Special interest was given to thin circular membranes by which values of elastic parameters of rubberlike materials were obtained (Klingbeil and Shield, 1964; Hart-Smith, 1966; James et al., 1975; Haines and Wilson, 1979; Miller et al., 1979; Blaedel et al., 1985). In the biomedical field, Miller et al., (1979) have studied the problem of human fetal membranes. Another application may be found in using biomedical material to produce balloon pumps as heart-assist devices (Darowski et al., 1976; Kao and Ohley, 1982; Miya et al., 1986). Rand (1964) has studied the stress required to rupture a red-cell membrane. Crisp and Hart-Smith (1971) have examined the stability of multilobed inflated membranes. Their study may be applied to investigate the mechanical behavior of alveolar cells of lungs.

A feature common to all of these studies is the substantial change of the membrane form, due to relatively low pressure. So far the study of a membrane inflation started with either flat, hemispherical, or half-elliptical undeformed shapes (Adkins and Rivlin, 1952; Hart-Smith, 1966; Crisp and Hart-Smith, 1971, Feng and Huang, 1974; Miller et al., 1979).

This review shows that in most applications the undeformed membranes have more complex shapes which are found especially in the biomedical field such as balloon pump, alveolar, and blood cells. Thus, it is interesting to examine the effect of more practical shapes of an undeformed membrane.

The purpose of this work is to relate analytically the deformed membrane shape to an undeformed shape. These relationships may be used to design devices which include membranes of various shapes. Such a relationship may also be used to predict pressure and elastic parameters of membranes which can be treated only through observations on their shapes such as red blood cells.

Formulation of Membrane Equations

An exact formulation of the problem was obtained under the following conditions:

(1) The undeformed membranes should be a surface of revolution.

(2) Its profile may have any continuous shape. More specifically, it should have first and second derivatives of a cross-section radius R, $R'(s)$, $R''(s)$, respectively (Fig. 1).

(3) The membrane equilibrium equations are used with its assumptions.

(4) The material is incompressible.

Geometric Relations

All variables in this analysis are nondimensional. The geometric variables described in Figs. 1 and 2 are expressed in R_o units—the clamped radius of the membrane. The independent variable of the analysis is the curve length s ($s = \bar{s}/R_o$) of the undeformed membrane, and the derivatives of variables with respect to s are indicated as

Contributed by the Applied Mechanics Division of THE AMERICAN SOCIETY OF MECHANICAL ENGINEERS for presentation at the Winter Annual Meeting, Dallas, Texas, November 25-30, 1990.

Discussion on this paper should be addressed to the Technical Editor, Leon M. Keer, The Technological Institute, Northwestern University, Evanston, IL 60208, and will be accepted until two months after final publication of the paper itself in the JOURNAL OF APPLIED MECHANICS. Manuscript received by the ASME Applied Mechanics Division, Nov. 18, 1988; final revision, July 19, 1989.

Paper No. 90-WA/APM-13.

Copyright © 1990 by ASME
Downloaded 03 May 2010 to 171.66.16.244. Redistribution subject to ASME license or copyright; see http://www.asme.org/terms/Terms_Use.cfm

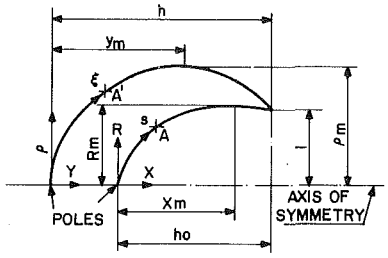


Fig. 1 Undeformed and deformed membrane profiles; axis and geometric variables definitions

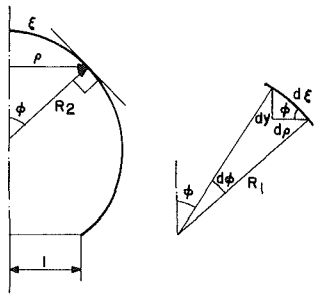


Fig. 2 Deformed membrane-radii of curvature

$$d(\ )/ds = (\ )'. \tag{1}$$

The extension ratios along the meridian λ_1, on a line of latitude λ_2, and along the membrane thickness λ_3 are given by the following geometric relations:

$$\lambda_1 = \xi',\ \lambda_2 = \rho/R,\ \lambda_3 = 1/(\lambda_1\lambda_2), \tag{2}$$

where ξ is the meridian curve length measured from the pole of the inflated membrane, ρ and R are radii of deformed and undeformed membranes, respectively.

Let us denote the nondimensional curvatures (Fig. 2) by:

$$k_1 = R_o/R_1,\ k_2 = R_o/R_2, \tag{3}$$

where R_1 and R_2 are the radii of curvatures in the meridian and latitude directions, respectively.

From Fig. 2 we obtain expressions for the curvatures:

$$k_2 = [1-(\rho'/\lambda_1)^2]^{1/2}/\rho,\ k_1 = (k_2/\rho)'/\rho' \tag{4}$$

and

$$y' = k_2\rho\lambda_1,\ y' = (\lambda_1 - \rho'^2)^{1/2}. \tag{5}$$

Differentiating ρ from equation (2) twice, we obtain

$$\rho' = \lambda_2' R + \lambda_2 R';\ \rho'' = \lambda_2'' R + 2\lambda_2' R' + \lambda_2 R''. \tag{6}$$

Differentiation of y' from equation (5) and substitution for equations (5) and (6) into k_1 in equation (4) lead to

$$k_1 = \frac{\lambda_1'}{y'\rho'} - \left(\frac{\lambda_2'' R + 2\lambda_2' R' + \lambda_2 R''}{y'\lambda_1}\right) - \frac{\lambda_1'\rho k_2}{\rho'\lambda_1}. \tag{7}$$

Constitutive and Equilibrium Equations

The Cauchy principal stress components T_1 and T_2 (forces/unit length), developed by Rivlin and Saunders (1951), for a pure, homogeneous strain of a thin rubber sheet and of thickness, t_o, are:

$$T_1 = 2t_o\lambda_3(\lambda_1^2 - \lambda_3^2)\left(\frac{\partial W}{\partial I_1} + \lambda_2^2\frac{\partial W}{\partial I_2}\right) \tag{8}$$

$$T_2 = 2t_o\lambda_3(\lambda_2^2 - \lambda_3^2)\left(\frac{\partial W}{\partial I_1} + \lambda_1^2\frac{\partial W}{\partial I_2}\right) \tag{9}$$

where W is the Rivlin-type strain energy function, namely

$$W = \sum_{i,j=0}^{\infty} C_{ij}(I_1-3)^i(I_2-3)^j. \tag{10}$$

I_1 and I_2 are strain invariants expressed in terms of principal extension ratios.

$$I_1 = \lambda_1^2 + \lambda_2^2 + \lambda_3^2,\ I_2 = 1/\lambda_1^2 + 1/\lambda_2^2 + 1/\lambda_3^2 \tag{11}$$

C_{ij} are material constants. $C_{oo} = 0$ to meet the condition that $W = 0$ in the unstrained state.

The simplest form of W, that includes the two invariants I_1 and I_2, is the equivalent form of Mooney (1940) type

$$W = C_{10}(I_1-3) + C_{01}(I_2-3). \tag{12}$$

Equation (12) is known as the Mooney-Rivlin model for strain energy density (Rigbi and Hiram, 1981; Keppel and Dadeppo, 1988). This equation is widely used to describe the behavior of membrane inflation made of rubberlike materials (Adkins and Rivlin, 1952; Hart-Smith, 1966; Yang and Feng, 1970; James et al., 1975; Haines and Wilson, 1979; Miller et al. 1979; Tang, 1982).

From the practical point of view, there is often little to choose between various strain energy functions (Rigbi and Hiram, 1981). This conclusion follows from production limitations, exposure of membranes to oil, humidity, and temperature. The simpler the equation, the easier it will be to draw conclusions related to membrane behavior. Therefore, the Mooney-Rivlin material equation (12) is used for further analysis.

Equations (8), (9), and (12) give the nondimensional form of the stresses t_1 and t_2

$$t_1 = \frac{T_1}{2Ct_o} = \lambda_3\ (\lambda_1^2 - \lambda_3^2)(1+\alpha\lambda_2^2) \tag{13}$$

$$t_2 = \frac{T_2}{2Ct_o} = \lambda_3\ (\lambda_2^2 - \lambda_3^2)(1+\alpha\lambda_1^2) \tag{14}$$

where $\alpha = C_{01}/C_{10}$ and $C = C_{10}$.

The nondimensional equilibrium equations of the deformed membrane are

$$(t_1\rho)' = t_2\rho' \tag{15}$$

$$k_1 t_1 + k_2 t_2 = p \tag{16}$$

where $p = PR_o/(2Ct_o)$ is the nondimensional inflation pressure.

Substitution of k_1 from equation (7) into equation (16) provides the expression for the second derivative of λ_2

$$\lambda_2'' = \frac{\lambda_1}{R}\left[\frac{\lambda_1'}{\rho} - \frac{1}{\lambda_1}(2\lambda_2' R' + \lambda_1 R'') + \frac{y'}{t_1}(k_2 t_2 - p) - \frac{y'\lambda_1'\rho k_2}{\rho'\lambda_1}\right]. \tag{17}$$

An expression for λ_1' is obtained by differentiating t_1 (equation (13)) and manipulating equations (14) and (15)

$$\lambda_1' = \frac{\rho'(t_2 - t_1)/\lambda_3 - \rho\lambda_2'[3\lambda_3^2 - \lambda_1^2 + (\lambda_1^2 + \lambda_3^2)\alpha\lambda_2^2]/\lambda_2}{\rho(\lambda_1^2 + 3\lambda_3^2)(1+\alpha\lambda_2^2)/\lambda_1} \tag{18}$$

Integration of y'—from equation (5), λ_1' and λ_2'' from equations (18) and (17), respectively, provides the relationship between the undeformed and deformed profiles at any point over the membrane surface. However, at the pole ($s = 0$), equations (17) and (18) are undefined. Therefore, a special treatment is needed at this point.

Boundary Conditions at $s = 0$

The condition of axisymmetry provides the following relations at the pole

Downloaded 03 May 2010 to 171.66.16.244. Redistribution subject to ASME license or copyright; see http://www.asme.org/terms/Terms_Use.cfm

$$k_1(o)=k_2(o)=k,\ \lambda_1(o)=\lambda_2(o)=\lambda$$
$$\rho(o)=R(o)=\rho''(o)=R''(o)=0 \tag{19}$$
$$\rho'(o)=\lambda,\ R'(o)=1,\ y'(o)=\lambda_1'(o)=\lambda_2'(o)=0.$$

Using equations (19) the stress and pressure equations are, respectively,

$$t_1(o)=t_2(o)=t=(1-1/\lambda^6)(1+\alpha\lambda^2),\ p=2kt. \tag{20}$$

In order to perform a numerical integration of y', λ_1' and λ_2'' using the Runge-Kutta method, a second approximation is used to estimate the values of λ_1, λ_2, and y at the first step. This estimation is of the form,

$$\lambda_1(\Delta s)\simeq\lambda+\lambda_1''(o)(\Delta s)^2/2. \tag{21}$$

Now it is necessary to develop expressions for the second derivatives of λ_1, λ_2, and y at $s=0$.

A combination of equations (2) and (4) provides

$$\lambda_1''(o)=3\lambda_2''(o)+\lambda(\lambda^2k^2+R'''(o)). \tag{22}$$

From equations (13) to (15), and (22) it follows that

$$\lambda_2''(o)=\frac{-\lambda(\lambda^2k^2+R'''(o))[2+3/\lambda^6+\alpha\lambda^2(1+4/\lambda^6)]}{4(1+3/\lambda^6)(1+\alpha\lambda^2)}. \tag{23}$$

Differentiation of equation (5) at $s=0$ leads to

$$y''(o)=k\lambda^2. \tag{24}$$

A special case of the above equations are the Adkin's and Rivlin's (1952) equations for flat, undeformed membranes. This can be accomplished by substituting $R=s$, $R'=1$, and $R''=R'''=0$ into equations (1) to (24).

The Undeformed Profile

Equations (1) to (24) include $R(s)$, $R'(s)$, and $R''(s)$. Therefore, necessary and sufficient conditions for specific solution of equations (1) to (24) is that the undeformed profile should satisfy the following conditions:

(1) For a given profile $R(s)$, the derivatives $R'(s)$ and $R''(s)$ should exist when $s\geq 0$.

(2) The profile should be axisymmetric.

Within these limitations, one can choose any undeformed profile through which one can get an exact solution of equations (1) to (24) to get a suitable deformed profile.

A family of revolutional ellipsoids of the form

$$R^2=(c_o-a_oX)X,\ c_o=(1+a_oh_o^2)/h_o,\ o\leq X\leq h_o \tag{25}$$

is attractive, since it includes the following three special cases discussed in the literature.

(1) Flat membrane—It interested many researchers because of the ability of comparing their theories with Treloar's (1944) experimental data (Adkins and Rivlin, 1952; Klingbeil and Shield, 1964; Hart-Smith and Crisp, 1967; Yang and Feng, 1970; Feng and Huang, 1974; James et al., 1975; Haines and Wilson, 1979; Miller et al., 1979; Blaedel, 1985).

(2) Spherical membranes—(Adkins and Rivlin, 1952; Yang and Feng, 1970; Crisp and Hart-Smith, 1971; Vishwanath and Glockner, 1973; Akkas, 1978).

(3) Half-ellipsoidal membranes—Feng (1976) discussed viscoelastic half-ellipsoidal axisymmetric membranes. He used the neo-Hookean elastic material as the elastic part of the viscoelastic material employed in his analysis.

In equation (25), the height h_o and $X(s)$ axis is illustrated in Fig. 1. This equation is used to carry out the numerical solution.

Equation (25) satisfies the conditions of undeformed profiles and the boundary conditions

$$R(o)=X'(o)=0,\ R'(o)=1 \text{ and } R=1 \text{ at } X=h_o. \tag{26}$$

The maximum value of R, R_m, at $X=X_m$ is

$$X_m=c_o/2a_o \text{ and } R_m^2=a_oX_m^2. \tag{27}$$

From equation (27) it is seen that a_o is the shape factor of the undeformed membrane.

The relationship of R' and X' is derived from Fig. 1,

$$X'^2+R'^2=1. \tag{28}$$

A combination of equation (25), its derivative, and equation (28) provides

$$X'=2R/(4R^2+U^2)^{1/2},\ U=c_o-2a_oX \tag{29}$$

$$R'=UX'/2R,\ R''=-\frac{2UX'(R'U-RU')}{R'(4R^2+U^2)^{3/2}}. \tag{30}$$

Notice that R' in equation (30) reduces to the case of flat membrane as $\lim R'(s)=1$ when h_o tends to zero.

An undeformed ellipsoidal curve described in equation (25) is determined by a specific pair of values a_o and h_o. It also determines whether R_m will be inside or outside the undeformed membrane, or coincide with the clamped radius ($h_o>X_m$, $h_o<X_m$ and $h_o=X_m$, respectively).

Again, for numerical integration purposes, it is necessary to estimate the X value of the first step

$$X(\Delta s)\simeq X''(o)(\Delta s)^2/2. \tag{31}$$

Differentiation of X' in equations (29) and (28) provides

$$X''(o)=2/c_o \text{ and } R'''(o)=-4/c_o^2. \tag{32}$$

If the initial profile differs from that in equation (25) and produced analytically, one should reformulate this section accordingly. When the initial profile is taken numerically from a table of $R(s)$, then, using finite differences, one should calculate $R'(s)$, $R''(s)$ and $R'''(o)$.

Numerical Calculation Order

(1) Definition of the initial profile parameters: In the case of ellipsoidal curve R_o, h_o and a_o should be given.

(2) Initial profile calculations: Integration of X' in equation (29) using equation (25), to find $X(s)$ in N steps, calculation of $R'(s)$ and $R''(s)$ according to equation (30), and $R'''(o)$ from equation (32).

(3) Introduce c, α, t_o, and λ. Guess k.

(4) Calculation of variables at the pole ($s=0$): y, y', y'', λ_1, λ_2, t, p, λ_2'' and λ_1''.

(5) Evaluation of the first integration step of λ_1, λ_2, λ_2', and y.

(6) For each step, from the second one until $\lambda_2\leq 1$, do the following steps.

(6.1) Calculate ρ, ρ', k_2, y', λ_3, t_1, t_2, λ_2', λ_1' and λ_2''.

(6.2) Recalculate the variables in 6.1 for $\lambda_2=1$ at the clamped point for the last step M.

(6.3) If $M=N$, then print the results. Else, guess another value of k and return to stages 4 to 6.

Numerical Examples

A computer program was written following stages 1 to 6, and using fourth-order Runge-Kutta method of integration. Several effects were studied for material constant $\alpha=0.1$.

(1) Initial profile effects; Figure 3 illustrates the effect of initial height, h_o, initial shape factor, a_o, and crown deformation, λ, on the inflation pressure. The values of pressure at $h_o=0$ are for a flat membrane. When $h_o\leq 0.5$, the effect of the membrane shape on the pressure is negligible. The pressure needed to achieve a certain value of λ decreases with initial membrane height. Longer membranes ($a_o<1$) need higher pressure to attain certain λ than shorter membranes ($a_o\geq 1$).

Downloaded 03 May 2010 to 171.66.16.244. Redistribution subject to ASME license or copyright; see http://www.asme.org/terms/Terms_Use.cfm

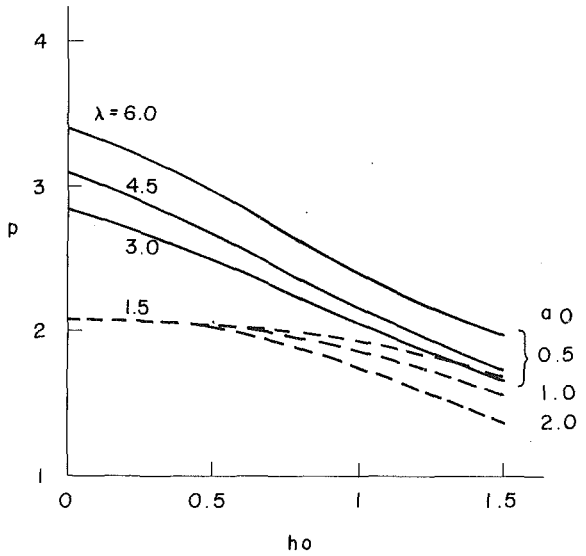


Fig. 3 Pressure change as a function of initial profile and pole extension ratios (α = 0.1)

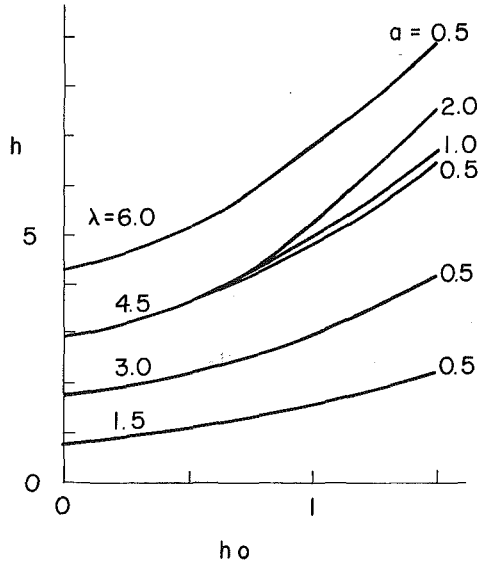


Fig. 4 Deformed membrane height as a function of initial profile and pole extension ratios (α = 0.1)

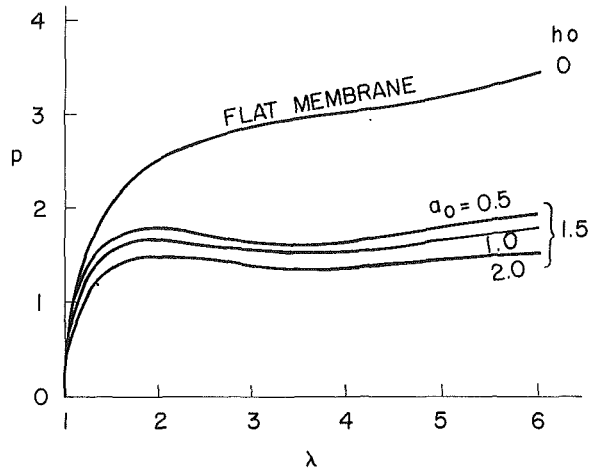


Fig. 5 Pressure change with initial profile and extension ratio (h_o = 0 and 1.5, α = 0.1)

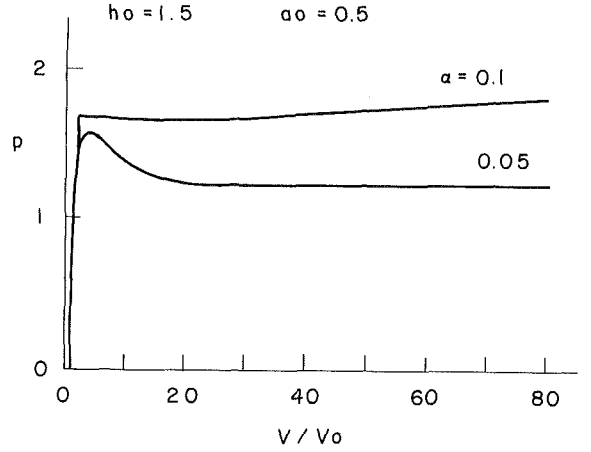


Fig. 6 Pressure versus volume graph with two different material constants (a_o = 0.5, h_o = 1.5)

The higher the initial profile, the smaller the differences between pressure values for various λ.

Figure 4 shows effects of initial height h_o on the deformed height h. Similar effects were found for ρ_{max}, $y(\rho_{max})$ and radii of curvature, so this figure represents the effects of initial geometry on the deformed geometry. Again, a membrane shape affects the deformed dimensions for $h_o > 0.5$. It is easier to inflate (lower pressure) flattened membranes than elongated membranes. It is also shown in Fig. 4 that the higher h_o and λ, the greater the deformed membrane height and height differences between the membranes.

(2) Pressure effects on a deformed membrane: Adkins and Rivlin (1952), and Akkas (1978) have shown statistically and dynamically a snap-out phenomenon of a spherical membrane at certain values of either pressure or deformation. A similar phenomenon was experimentally observed during an inflation of a plane circular viscoelastic membrane (Blaedel et al., 1985). Figure 5 shows a similar phenomenon of a negative pressure slope with deformation for various initial shapes, elongated, spherical, and shortened membranes. An interesting result is shown in Fig. 5. Within this variation of membrane shapes the λ values for the peak pressure is practically independent of an initial membrane shape. This result may accelerate the numerical solution by putting $k = \beta/\lambda$ as an initial guess where $\beta = 1/a$ for a spherical shape of radius a. In the case of an elongated or shortened shape, β will be smaller or greater than $1/a$, respectively. When the membrane is flat ($h_o = 0$) and $\alpha = 0.1$, its inflation is stable (Fig. 5).

A p-v graph is presented in Fig. 6. In this figure, pressure, p, is shown versus volume ratio, V/V_o, where V is the inflated and V_o is the initial volume of the membrane. Its initial shape is determined by $a_o = 0.5$ and $h_o = 1.5$. As in Fig. 5, a negative pressure slope is shown after a peak pressure of 1.7 for $\alpha = 0.1$. The lower the α, the lower the pressure and the steeper the negative slope after the peak pressure. Similar negative pressure slopes were obtained in graphs of p versus membrane area and p versus ρ_{max}. These results imply that there is an instability zone of a membrane geometry inflation made of Mooney material.

(3) Distribution of variables along the meridional curve s. Figure 7 illustrates the distribution of stresses along s. The calculations were made for $a_o = 0.5$, $h_o = 1.5$ and $\lambda = 1.5$. An interesting result from the engineering point of view is the maximum stress in the membrane t_1, which exists at the clamped end. The stresses t_1 and t_2 are rather constant along the meridian. Only toward the clamped end they changed to their maximum and minimum values, respectively. Similar behavior exists for flat membranes (Adkins and Rivlin, 1952).

Downloaded 03 May 2010 to 171.66.16.244. Redistribution subject to ASME license or copyright; see http://www.asme.org/terms/Terms_Use.cfm

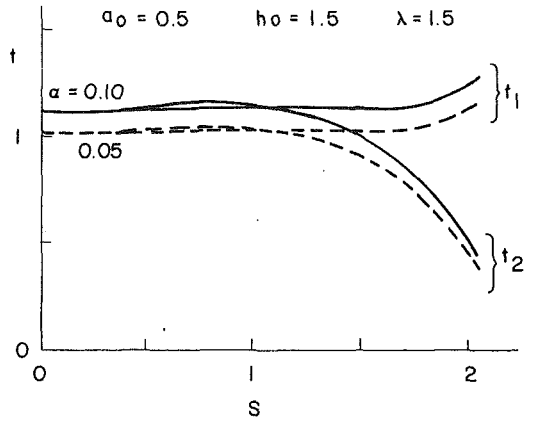


Fig. 7 Stress distribution along the meridian with two different material constants (a_o = 0.5, h_o = 1.5, λ = 1.5)

Very Large Deformations

To complete the discussion on the effect of an undeformed meridional shape of a membrane on its deformed shape, one should discuss the limit case of very large deformations. Wu (1972) showed that the inflated shape of an initially spherelike or tubelike membrane tends to a spherical surface asymptotically as $p \to \infty$. Wu assumed a Mooney material.

Yu and Valanis (1970) defined very large deformations as $\lambda_1 = \lambda_2 \geq 2$. Using these assumptions together with a neo-Hookean material, they found that when the inflation pressure is uniform, the deformed shape is spherical.

These results, as well as other investigations on very large deformations, suggest that the surface of an inflated membrane tends to become a sphere regardless of its undeformed shape. As the present investigation deals with a general undeformed meridional shape of axisymmetric membranes, it will be useful to validate it at this range of deformations.

For each λ there exists

$$\lambda \geq \lambda_2 \geq 1. \tag{33}$$

$\lambda_2 = 1$ at the clamped end and equals to λ at the pole.

The value of λ_1 is of an order of the ratio between lengths of the deformed and undeformed meridional curves of the membrane.

Therefore,

$$\lambda_1 = 0(\lambda). \tag{34}$$

Large deformations defined as

$$\epsilon \equiv 1/\lambda,\ \epsilon^2 << 1 \text{ (say } \epsilon < 0.2 \text{ or } \lambda > 5) \tag{35}$$

From equations (13), (14), and (33)–(35) it follows that

$$1 \geq t_2/t_1 > \alpha/(1+\alpha). \tag{36}$$

The stress ratio in equation (36) tends to $\alpha/(1+\alpha)$ at the clamped end, and equals 1 at the pole. This equation implies that the membrane surface may be spherical elsewhere except near the clamped end.

The pressure drop is estimated by using Adkins and Rivlins's (1952) expression for pressure drop of a spherical membrane and equations (35).

$$\frac{dp}{d\lambda} \simeq \frac{2\alpha}{a} = 0(\epsilon) \tag{37}$$

where $a = \tilde{a}/R_o = 0(\lambda)$ is the nondimensional radius of the sphere.

For large deformations,

$$k \simeq \frac{1}{a}. \tag{38}$$

Substitution of equations (38) into (20) provides

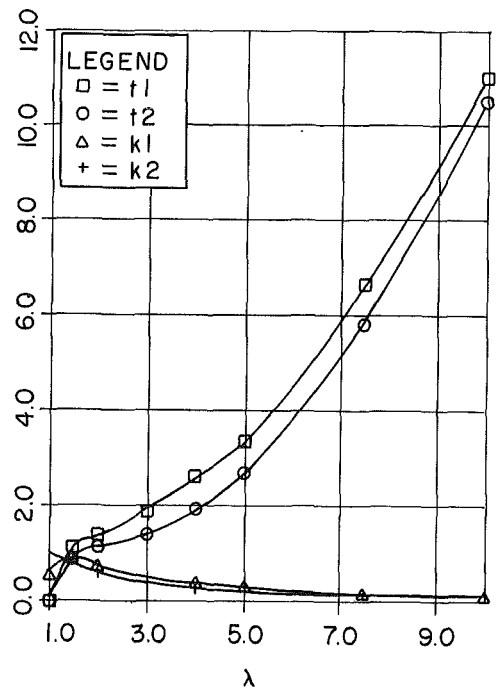


Fig. 8 Stresses t_1, t_2 and curvatures k_1 and k_2 versus λ at s = 1.45 (s_{max} = 2); undeformed profile parameters a_o = 0.5, h_o = 1.5

$$p \simeq \frac{2}{a}(1+\alpha\lambda^2). \tag{39}$$

The implication that stems from equations (37) and (39) is that the pressure growth with λ is rather slow and it depends on the value of α.

The following numerical example will illustrate the relations in equations (37) to (39):

Given λ = 10 and α = 0.1, then
$k = 0.119$, $p = 2.63$, $1/a = 0.1195 \simeq k$, $dp/d\lambda = 0.02$.

The curvature k_2, at very large deformations, is obtained from Fig. 2,

$$k_2 \rho = \sin\phi. \tag{40}$$

Substitution of equations (20), (35), and (39) into (40) provides

$$k_2 = 0\left(\frac{1}{a}\right). \tag{41}$$

The limit value of k_1 is obtained by a substitution of equations (35), (36), (39), and (41) into equation (16)

$$0 \leq k_1 - k_2 < \alpha\lambda - 1. \tag{42}$$

Near the clamped end, $k_1 - k_2 = 0(\alpha\lambda - 1)$. Elsewhere, $k_1 - k_2$ tends to zero.

Equation (42) implies that from the curvature point of view, an axisymmetric membrane tends to have a spherical shape at very large deformations, with the exception of the clamped end and its vicinity. The same implication is valid for the stresses. Figure 8 illustrates this trend of the curvatures and stresses toward relations typical to the sphere. Namely, $k_1 \simeq k_2$ and $t_1 \simeq t_2$ at very high value of λ.

The k and t data were taken at the point s = 1.45 (s_{max} = 2). The initial profile was determined by a_o = 0.5 and h_o = 1.5. This point was chosen as the limit point (for a given material and undeformed profile) which is affected by the clamped end. For s < 1.45 the data were typical to those of a sphere when λ ≥ 5.

Downloaded 03 May 2010 to 171.66.16.244. Redistribution subject to ASME license or copyright; see http://www.asme.org/terms/Terms_Use.cfm

Discussion

The effect of initially given axisymmetric undeformed profile on a deformed profile of a membrane has been discussed. It was shown that any axisymmetric continuous profile $R(s)$ may be used to predict its deformed dimensions and stresses (for given material constants). The necessary continuity conditions are the existence of $R'(s)$ and $R''(s)$. For numerical example, a family of ellipsoids were selected. Special cases of these curves, flat, spherical, and half-ellipsoid, were discussed in the literature. The approach of this study to these cases gave identical results.

When the height of the initial profile $h_0 < 0.5$, the effect of the initial shape is negligible. For higher values of h_o, the more shortened the initial profile, the greater its deformed dimensions, and vice versa for initially elongated membranes. The higher the undeformed membrane, the lower the pressure required for a given deformation.

The stress distribution was tested. Maximum stress was obtained for t_1 at the clamped end. Apart from the vicinity of the clamped end, both the stresses and deformations are approximately constant. Membrane thickness distribution is similar to the t_1 distribution. Namely, the maximum thickness is at the clamped end.

For extension-ratios $\lambda > 2$, it was obtained (Fig. 6) that

$$\partial P/\partial V,\ \partial P/\partial A,\ \partial P/\partial \rho_m \simeq 0 \tag{43}$$

where A is the membrane area. Therefore, the inflation energy is approximately

$$\int_o^{\Delta V} pdv \simeq p(\lambda \simeq 1.5)\ \Delta V. \tag{44}$$

A limit case analysis for very large deformations proved equation (43), since equation (37) shows that $dP/d\lambda = 0(\epsilon)$

$$\frac{\partial P}{\partial(V,A,\rho m)} = (dP/d\lambda)/[(d(V,A,\rho m)/d\lambda] = 0(\epsilon). \tag{45}$$

Equation (45) implies that for practical range of λ, equations (43) and (44) are valid for a very large λ. At this range of λ it was also found that the membrane surface approaches a spherical shape except near the clamped end.

An interesting implication of this study is its use to investigate the mechanical behavior and material properties of practical membranes in biomedical field, such as red blood cells, balloon pumps, and alveolar cells of lungs.

References

Adkins, J. E., and Rivlin, R. S., 1952, "Large Elastic Deformations of Isotropic Materials, IX. The Deformation of Thin Shells, *Trans. Roy. Soc. Lond.*, Vol. 244A, pp. 505–531.

Akkas, N., 1978, "On the Dynamic Snap-Out Instability of Inflated Non-Linear Spherical Membranes," *Int. J. Non-Linear Mechanics*, Vol. 13, pp. 177–183.

Blaedel, K. L., Radewan, C. H., and Feng, W. W., 1985, "Controlling Biaxial Strain in an Inflated Elastomeric Membrane," *Experimental Techniques*, Nov., pp. 29–32.

Crisp, J. D. C., and Hart-Smith, L. J., 1971, "Multi-Lobed Inflated Membranes: Their Stability Under Finite Deformation," *Int. J. Solids Structures*, Vol. 7, pp. 843–861.

Darowski, M., Gorczynska, K., Grodzicki, K., Szurmak, Z., and Wanski, Z., 1976, "Some Examples of Fluidics Applications in the Medical Field," *Engineering in Medicine, I Mech E*, Vol. 5, pp. 13–18.

Feng, W. W., 1976, "Inflation of a Viscoelastic Ellipsoidal Neo-Hookean Membrane," *AIAA Journal*, Vol. 14, pp. 672–675.

Feng, W. W., and Huang, P., 1974, "On the Inflation of a Plane Nonlinear Membrane," ASME JOURNAL OF APPLIED MECHANICS, Vol. 41, pp. 767–771.

Haines, D. W., and Wilson, W. D., 1979, "Strain-Energy Density Function for Rubber-Like Materials," *J. Mech. Phys. Solids*, Vol. 27, pp. 345–360.

Hart-Smith, L. J., 1966, "Elasticity Parameters for Finite Deformations of Rubber-Like Materials," *ZAMP*, Vol. 17, No. 39, pp. 608–625.

Hart-Smith, L. J., and Crisp, J. D., 1967, "Large Elastic Deformations of Thin Rubber Membranes," *Int. J. Engng. Sci.*, Vol. 5, pp. 1–24.

Isaacson, E., 1965, "The Shape of a Balloon," *Comm. Pure Math.*, Vol. 18, pp. 163–166.

James, A. G., Green, A., and Simpson, G. M., 1975, "Strain Energy Functions of Rubber. I. Characterization of Gum Vulcanizates," *Journal of Applied Polymer Science*, Vol. 19, pp. 2033–2058.

Kao, C., and Ohley, W. J., 1982, "Influence of Vascular Parameters on the Effectiveness of Intra-Aortic Balloon Pumping: A Model Study," *Medical and Biological Engineering and Computing*, Vol. 20, pp. 529–538.

Keppel, W. J., and DaDeppo, D. A., 1988, "Finite Axisymmetric Deformation of Rubber-Like Shells of Revolution," ASME JOURNAL OF APPLIED MECHANICS, Vol. 55, pp. 332–340.

Klingbeil, W. W., and Shield, R. T., 1964, "Some Numerical Investigations on Empirical Strain Energy Functions in Large Axi-Symmetric Extensions of Rubber Membranes," *ZAMP*, Vol. 15, No. 39, pp. 608–629.

Miller, C. E., Lavery, J. P., and Donnelly, T. A., 1979, "Determination of Elastic Parameters for Human Fetal Membranes," *Journal of Rheology*, Vol. 23, pp. 57–78.

Miya, J., Maeta, H. A., Sakura, T., and Hori, M., 1986, "Experimental Evaluation of Extrapulmonary Arterial Balloon Pumping (EPABP) for Right Heart Failure of Diverse Etiologies," *Trans. Am. Soc. Artif. Intern. Organs*, Vol. 32, pp. 211–216.

Rand, R. P., 1964, "Mechanical Properties of the Red Cell Membrane, II. Viscoelastic Breakdown of the Membrane," *Biophysical Journal*, Vol. 4, pp. 303–316.

Rigbi, Z., and Hiram, Y., 1981, "An Approximate Method for the Study of Large Deformations of Membranes," *Int. J. Mech. Sci.*, Vol. 23, pp. 1–10.

Rivlin, R. S., and Saunders, D. W., 1951, "Large Elastic Deformations of Isotropic Materials," *Phil. Trans.*, Part 7, pp. 243–251.

Tang, S. c., 1982, "Large Strain Analysis of an Inflating Membrane," *Computers and Structures*, Vol. 15, pp. 71–78.

Treloar, L. R. G., 1944, "Strains in an Inflated Rubber Sheet and the Mechanism of Bursting," *Inst. Rubber Ind. Trans.*, Vol. 19, pp. 201–212.

Vishwanath, T., and Glockner, P. G., 1973, "Effect of Axisymmetric Loads on Inflated Non-Linear Membranes," *Int. J. Non-Linear Mechanics*, Vol. 8, pp. 345–369.

Wu, C. H., 1972, "Spherelike Deformations of a Balloon," *Quarterly of Applied Mathematics*, pp. 183–194.

Yang, W. H., and Feng, W. W., 1970, "On Axisymmetrical Deformations of Nonlinear Membranes," ASME JOURNAL OF APPLIED MECHANICS, Vol. 37, pp. 1002–1011.

Yu, L. K., and Valanis, K. C., 1970, "The Inflation of Axially Symmetric Membranes by Linearily Varying Hydrostatic Pressure," *Transactions of the Society of Rheology*, Vol. 14, pp. 1593–183.

Downloaded 03 May 2010 to 171.66.16.244. Redistribution subject to ASME license or copyright; see http://www.asme.org/terms/Terms_Use.cfm

Random Vibrations of Viscoelastic Laminated Plates

G. Cederbaum
Department of Solid Mechanics, Materials, and Structures,
Tel-Aviv University,
Ramat-Aviv, 69978, Israel

The response of viscoelastic laminated plates subjected to random excitation is investigated. The Fourier transform of the Boltzmann representation of the viscoelastic phases is incorporated into a micromechanical analysis, which establish the five frequency-dependent functions, characterizing the effective behavior of unidirectional fiber composites. This enables to express the governing equation, using the first-order shear deformation theory, in the frequency domain. The inversion of the response function into the time domain is performed by the Fast Fourier Transform algorithm. Two stationary random fields are considered: (i) ideal white noise, and (ii) band-limited white noise. In both cases analytical expressions for the mean squares are derived. Furthermore, the complex eigenvalues are investigated and the ratio between the imaginary part and the real one, η, is shown to relate to the damping ratio. The influence of the temperature, length-to-thickness ratio, and the fibers' orientation on η is studied.

1 Introduction

Polymeric matrices, when used in unidirectional laminates, are expected to exhibit strong viscoelastic effects. A comprehensive review and analysis of viscoelastic composite materials was given by Schapery (1974). It appears that the determination of the five time-dependent functions, which characterize the effective transversely isotropic behavior of unidirectional fiber composites, is very difficult. On the other hand, these five time-dependent functions can be readily obtained by a micromechanical analysis of the composite which takes into account the interaction between fibers and matrix.

A micromechanical analytical model for the prediction of the effective elastic moduli of fiber-reinforced materials was developed by Aboudi (1984, 1987). The theory is based on the analysis of a periodic array of square fibers imbedded regularly in the matrix. Once the overall properties of the composite are extracted from the model, a transformation is employed which provides the effective transversely-isotropic behavior of the unidirectional fiber composite. It should be mentioned that this micromechanics theory provides, in a closed-form manner, all the five independent effective elastic properties of the unidirectional composite from the knowledge of the fiber and matrix constants and the reinforcement volume ratio.

In a viscoelastic composite, the phases are viscoelastic materials possessing time-dependent properties. In a previous work by Aboudi and Cederbaum (1988), the behavior of viscoelastic laminated plates subjected to quasi-static loads was analyzed. The single unidirectional lamina was composed of a viscoelastic matrix (epoxy), reinforced by perfectly elastic fibers (graphite). The five time-dependent functions were determined from the above micromechanics analysis and the correspondence principle. The inversion of the Laplace transform yielded the required functions in the time domain.

The dynamic response of viscoelastic laminated plates was investigated by Cederbaum and Aboudi (1988). The Boltzmann representation of the viscoelastic phases was given in the frequency domain by application of the Fourier transform. By utilizing the aforementioned micromechanics analysis, the Fourier transform of the five time-dependent functions were obtained, and it enables us to express the governing equations of the plate in the frequency domain. The inversion of the response function into the time domain was performed by using the Fast Fourier Transform algorithm.

In the present paper the response of viscoelastic laminated plates to random excitation is derived, based on the method described for the dynamic problem. Square, simply-supported, orthotropic and angle-ply plates are analyzed by using the First-Order Shear Deformation Theory (FSDT) (Whitney and Pegano, 1970). Two stationary random fields are considered: (i) ideal white noise, and (ii) band-limited white noise, and analytical expressions for the mean-squares displacements are obtained.

Furthermore, the complex eigenvalues were investigated, and it was found that the real part is asymptotic to the elastic natural frequency, and that the ratio between the imaginary part and the real one, η, can be regarded as the damping ratio (see also Christensen, 1982).

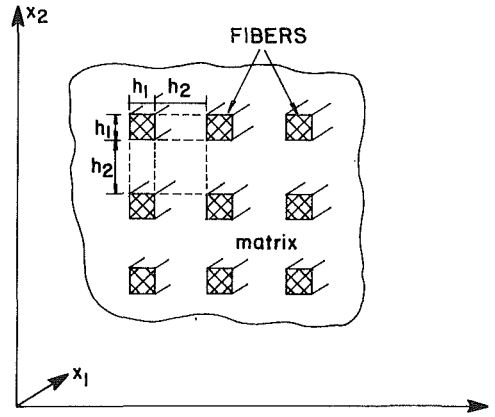
The dependence of η on various parameters like temperature, length-to-thickness ratio, and the direction of the fibers in angle-ply laminates is studied. The results enlighten the important problem of damping in laminated composite plates.

Contributed by the Applied Mechanics Division of THE AMERICAN SOCIETY OF MECHANICAL ENGINEERS for presentation at the Winter Annual Meeting, Dallas, Tex., November 25-30, 1990.

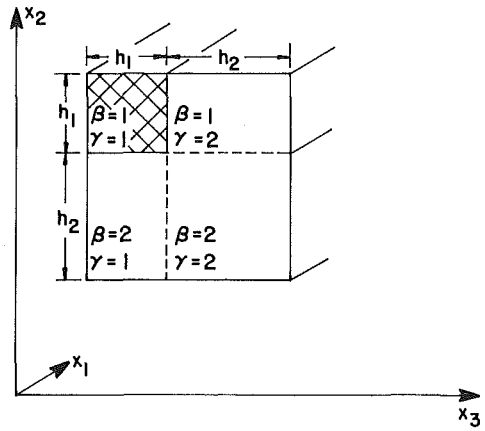
Discussion on this paper should be addressed to the Technical Editor, Leon M. Keer, The Technological Institute, Northwestern Unversity, Evanston, IL 60208, and will be accepted until two months after final publication of the paper itself in the JOURNAL OF APPLIED MECHANICS. Manuscript received and accepted by the ASME Applied Mechanics Division, Oct. 31, 1988.

Paper No. 90-WA/APM-20.

Copyright © 1990 by ASME
Downloaded 03 May 2010 to 171.66.16.244. Redistribution subject to ASME license or copyright; see http://www.asme.org/terms/Terms_Use.cfm



(a)



(b)

Fig. 1(*a*) A composite with a doubly periodic array of square fibers extending in the x_1 direction; (*b*) a representative cell

2 Composite Elastic Constants

Let (x_1, x_2, x_3) denote a Cartesian system of coordinates with x_1 oriented in fiber direction of a unidirectional, fiber-reinforced elastic composite. The constitutive law for the effective transversely-isotropic behavior of such composite is given by (Aboudi, 1987)

$$\bar{\sigma} = \mathbf{E}\bar{\epsilon} \tag{1}$$

$$\bar{\sigma} = (\bar{\sigma}_{11},\ \bar{\sigma}_{22},\ \bar{\sigma}_{33},\ \bar{\sigma}_{12},\ \bar{\sigma}_{13},\ \bar{\sigma}_{23})$$

is the average stress,

$$\bar{\epsilon} = (\bar{\epsilon}_{11},\ \bar{\epsilon}_{22},\ \bar{\epsilon}_{33},\ 2\bar{\epsilon}_{12},\ 2\bar{\epsilon}_{13},\ 2\bar{\epsilon}_{23})$$

is the average strain, and

$$\mathbf{E} = \begin{bmatrix} e_{11} & e_{12} & e_{13} & 0 & 0 & 0 \\ & e_{22} & e_{23} & 0 & 0 & 0 \\ & & e_{22} & 0 & 0 & 0 \\ & & & e_{44} & 0 & 0 \\ \text{symmetric} & & & & e_{44} & 0 \\ & & & & & \tfrac{1}{2}(e_{22}-e_{23}) \end{bmatrix} \tag{2}$$

where e_{ij} are the effective elastic constant. Their explicit expressions in terms of the fibers and matrix properties and the reinforcement volume ratio can be found in Aboudi (1987).

The equations (1) and (2) were derived from a micromechanical analysis in which the fibers of square cross-section, h_1^2, are arranged in the matrix phase is a doubly periodic array at distances h_2 apart, (see Fig. 1(*a*)). A representative cell of this arrangement is shown in Fig. 1(*b*). It contains four subcells $\beta, \gamma = 1, 2$, where the first one with $\beta = \gamma = 1$ is occupied by the fiber region, while the remaining subcells $\beta + \gamma \neq 2$ are occupied by the matrix region.

3 Composite Viscoelastic Representation

With $\mathbf{E}$ in (1) represents the five independent elastic constants of the equivalent transversely-isotropic material which represent the unidirectional composite, it is possible to obtain the five-time dependent functions which characterize the viscoelastic composite whose phases are viscoelastic materials. Each phase is represented by the Boltzmann's superposition principle (Christensen, 1982) which, in tensorial notation, is given by

$$\sigma_{ij}^{(\beta\gamma)}(t) = \int_{-\infty}^{t} C_{ijkl}^{(\beta\gamma)}(t-\tau)\,\dot{\epsilon}_{kl}^{(\beta\gamma)}(\tau)\,d\tau, \tag{3}$$

where $C_{ijkl}^{(\beta\gamma)}(t)$ are the relaxation functions of the phase. These functions can be represented in the following form (Aboudi, 1972)

$$C_{ijkl}^{(\beta\gamma)}(t) = C_{ijkl}^{(\beta\gamma)}(0)[1 - \psi_{ijkl}^{(\beta\gamma)}(t), \tag{4}$$

in which

$$C_{ijkl}^{(\beta\gamma)}(0) \equiv C_{ijkl}^{(\beta\gamma)}(t=0)$$

and $\psi_{ijkl}^{(\beta\gamma)}(t)$ are zero for $t \leq 0$. It should be noted that in the case of an elastic phase, $\psi_{ijkl}^{(\beta\gamma)}(t) \equiv 0$.

Substituting equations (4) into (3) yields

$$\sigma_{ij}^{(\beta\gamma)}(t) = C_{ijkl}^{(\beta\gamma)}(0)\epsilon_{kl}^{(\beta\gamma)}(t) - C_{ijkl}^{(\beta\gamma)}(0)\int_{-\infty}^{t}\psi_{ijkl}^{(\beta\gamma)}(t-\tau)\,\dot{\epsilon}_{kl}^{(\beta\gamma)}(\tau)\,d\tau. \tag{5}$$

Integrating by parts the convolution integral provides

$$\sigma_{ij}^{(\beta\gamma)}(t) = C_{ijkl}^{(\beta\gamma)}(0)\epsilon_{kl}^{(\beta\gamma)}(t) - C_{ijkl}^{(\beta\gamma)}(0) \int_{-\infty}^{t}\dot{\psi}_{ijkl}^{(\beta\gamma)}(t-\tau)\epsilon_{kl}^{(\beta\gamma)}(\tau)\,d\tau$$

and, by defining $\xi = t - \tau$ we get

$$\sigma_{ij}^{(\beta\gamma)}(t) = C_{ijkl}^{(\beta\gamma)}(0)\epsilon_{kl}^{(\beta\gamma)}(t) - C_{ijkl}^{(\beta\gamma)}(0) \int_{o}^{\infty}\dot{\psi}_{ijkl}^{(\beta\gamma)}(\xi)\epsilon_{kl}^{(\beta\gamma)}(t-\xi)\,d\xi. \tag{6}$$

The lower limit of integration can be extended to $-\infty$. Applying the Fourier transform to equation (6) and using the convolution theorem, we get

$$F[\sigma_{ij}^{(\beta\gamma)}(t)] = C_{ijkl}^{(\beta\gamma)}(0)\{1 - F[\dot{\psi}_{ijkl}^{(\beta\gamma)}(t)]\}F[\epsilon_{kl}^{(\beta\gamma)}(t)]. \tag{7}$$

Thus, the use of equation (7) in the micromechanics analysis (instead of $C_{ijkl}^{(\beta\gamma)}$ in the elastic case) provides the Fourier transform of the effective time-dependent viscoelastic properties, $F[\mathbf{E}(t)]$, of the composite. These enable us to express the governing equations of the laminated viscoelastic plates in the frequency domain. To this end, the imposed dynamic load is incorporated in these equations in its Fourier transform form.

4 Application to Laminated Plates

In a previous work by Aboudi and Cederbaum (1988) it was shown that the viscoelastic effects predicted by using the FSDT for the analysis of laminated plates subjected to quasi-static loadings are significant when compared with those predicted by the classical plate theory-CPT (Whitney, 1987), even for relatively high length-to-thickness aspect ratio (e.g., 50). It was also shown, by Cederbaum and Aboudi (1988), that the dynamic response as predicted by using the FSDT and two refined shear deformation theories developed by Reddy (1984) and Librescu et al. (1988) are almost the same. For these reasons

Downloaded 03 May 2010 to 171.66.16.244. Redistribution subject to ASME license or copyright; see http://www.asme.org/terms/Terms_Use.cfm

we will use in the present investigation the FSDT mainly, and the CPT for a matter of comparison only.

Within FSDT, the following displacement field across the plate thickness is considered:

$$U_1(x, y, z, t) = U(x, y, t) + z\psi_x(x, y, t)$$
$$U_2(x, y, z, t) = V(x, y, t) + z\psi_y(x, y, t) \quad (8)$$
$$U_3(x, y, t) = W(x, y, t)$$

where U_1, U_2, and U_3 are the components of the three-dimensional displacement vector in the x, y, and z directions, respectively, U, V, and W denote the displacements of a point (x, y) on the midplane, while ψ_x and ψ_y are the rotations of the normals to the midplane about the y and x-axes, respectively. The governing equations are written as:

$$\begin{aligned}
&A_{11}U_{,xx} + 2A_{16}U_{,xy} + A_{66}U_{,yy} + A_{16}V_{,xx} \\
&\quad + (A_{12} + A_{66})V_{,xy} + A_{16}V_{,yy} + B_{11}\psi_{x,xx} \\
&\quad + 2B_{16}\psi_{x,xy} + B_{66}\psi_{x,yy} + B_{16}\psi_{y,xx} \\
&\quad + (B_{12} + B_{66})\psi_{y,xy} + B_{26}\psi_{y,yy} = I_1\ddot{U} + I_2\ddot{\psi}_x, \\
&A_{16}U_{,xx} + (A_{12} + A_{66})U_{,xy} + A_{26}U_{,yy} + A_{66}V_{,xx} \\
&\quad + 2A_{26}V_{,xy} + A_{22}V_{,yy} + B_{16}\psi_{x,xx} \\
&\quad + (B_{12} + B_{66})B\psi_{x,xy} + B_{26}\psi_{x,yy} + B_{66}\psi_{y,xx} \\
&\quad + 2\psi_{26}\psi_{y,xy} + B_{22}\psi_{y,yy} = I_1\ddot{V} + I_2\ddot{\psi}_y, \\
&A_{55}(\psi_{x,x} + W_{,xx}) + A_{45}(\psi_{x,y} + \psi_{y,x} + 2W_{,xy}) \\
&\quad + A_{44}(\psi_{y,y} + W_{,yy}) + P_3 = I_1\ddot{W}, \\
&B_{11}U_{,xx} + 2B_{16}U_{,xy} + B_{66}U_{,yy} + B_{16}V_{,xx} + (B_{12} + B_{66})V_{,xy} \\
&\quad + B_{26}V_{,yy} + D_{11}\psi_{x,xx} + 2D_{16}\psi_{x,xy} \\
&\quad + D_{66}\psi_{x,yy} + D_{16}\psi_{y,xx} + (D_{12} + D_{66})\psi_{y,xy} \\
&\quad + D_{26}\psi_{y,yy} - A_{55}(\psi_x + W_{,x}) - A_{45}(\psi_y + W_{,y}) = I_2\ddot{U} + I_3\ddot{\psi}_x, \\
&B_{16}U_{,xx} + (B_{12} + B_{66})U_{,xy} + B_{26}U_{,yy} + B_{66}V_{,xx} \\
&\quad + 2B_{26}V_{,xy} + B_{22}V_{,yy} + D_{16}\psi_{x,xx} \\
&\quad + (D_{12} + D_{66})\psi_{x,xy} + D_{26}\psi_{x,yy} + D_{66}\psi_{y,xx} + 2B_{26}\psi_{y,xy} \\
&\quad + D_{22}\psi_{y,yy} - A_{45}(\psi_x - W_{,x}) - A_{44}(\psi_y + W_{,y}) = I_2\ddot{V} + I_3\ddot{\psi}_y, \quad (9)
\end{aligned}$$

where

$$(A_{ij}, B_{ij}, D_{ij}) = \int_{-h/2}^{h/2} Q_{ij}(1, z, z^2)dz \qquad i, j = 1,2,6$$
$$A_{ij} = \int_{-h/2}^{h/2} kC_{ij}dz \qquad i, j = 4,5$$
$$(I_1, I_2, I_3) = \int_{-h/2}^{h/2} \rho(1, z, z^2)dz$$

and C_{ij} are the components of the stiffness matrix, Q_{ij} are the reduced components of the elastic tensor, ρ denotes the mass density, k is the shear correction factor, and $p_3 \equiv p_3(x, y, t)$ describes the applied transverse load.

5 Dynamic Response

The previous theory for the viscoelastic representation of unidirectional fiber composites is applied here to investigate the dynamic response of viscoelastic laminated plates.

5.1 Dynamic Response of a Square Orthotropic Plate. For the case of a symmetric orthotropic plate $U = V = 0$, $B_{ij} = 0$, $A_{16} = A_{26} = D_{16} = D_{26} = 0$ and the five governing equations (9) are reduced to the last three ones with ψ_x, ψ_y, and W being the unknowns. The elastic counterpart of this problem was considered by Dobyns (1981).

The square plate occupies the region $0 \le x \le a$, $0 \le y \le a$ and is simply-supported all around. The solution functions and the transverse loading function are given, using the separation of variables, as the product of a spacewise and a frequency-dependent functions

$$\psi_x(x, y, \omega) = \sum_{m,n} \hat{X}_{mn}\cos\alpha x \sin\beta y\, T_{mn}(\omega) \equiv \sum_{m,n} X_{mn}T_{mn}(\omega),$$
$$\psi_y(x, y, \omega) = \sum_{m,n} \hat{Y}_{mn}\sin\alpha x \cos\beta y\, T_{mn}(\omega) \equiv \sum_{m,n} Y_{mn}T_{mn}(\omega),$$
$$W(x, y, \omega) = \sum_{m,n} \hat{W}_{mn}\sin\alpha x \sin\beta y\, T_{mn}(\omega) \equiv \sum_{m,n} W_{mn}T_{mn}(\omega),$$

and

$$P_3(x, y, \omega) = \sum_{m,n} q_{mn}\sin\alpha\, x \sin\beta y\, F_{mn}(\omega) \quad (10)$$

where $\alpha = m\pi/a$, $\beta = n\pi/a$, $\hat{X}$, $\hat{Y}$, and $\hat{W}$ are the coefficients of the mode shapes associated with the free vibration problem, $T_{mn}(\omega)$ denote the generalized coordinates, q_{mn} are Fourier coefficients, and $F_{mn}(\omega)$ is the Fourier transform of the time-dependent generalized force. Substituting (10) into (9) and setting $F_{mn}(\omega) \equiv 0$, the free vibration equation is obtained as

$$[[K(\omega)]_{mn} - \lambda_{mn}^2(\omega)[M]]\{\Delta\}_{mn} = \{0\} \quad (11)$$

where $\{\Delta\}_{mn}^T = \{\hat{X}_{mn}, \hat{Y}_{mn}, \hat{W}_{mn}\}$, and $[K(\omega)]$, $[M]$ are the rigidities and the inertia matrices.

In the forced vibration problem, the following expression for $T_{mn}(\omega)$ is obtained by using the modal analysis technique, in conjunction with the orthogonality condition (e.g., Meirovitch, 1980):

$$-\omega^2 T_{mn}(\omega) + \lambda_{mn}^2(\omega)T_{mn}(\omega) = \frac{P(\omega)\int_o^a\int_o^a \left[P_3(x, y)W_{mn}(x, y)\right]dxdy}{\int_o^a\int_o^a \left[I_1 W_{mn}^2(x, y)\right]dxdy} \equiv \frac{Q_{mn}(\omega)}{J_{mn}} \quad (12)$$

from which

$$T_{mn}(\omega) = \frac{1}{J_{mn}}\frac{Q_{mn}(\omega)}{-\omega^2 + \lambda_{mn}^2} \equiv \frac{1}{J_{mn}}\frac{Q_{mn}(\omega)}{L_{mn}(\omega)}. \quad (13)$$

Substituting (13) into equation (10), one obtains the final solution of the frequency-dependent transverse displacement

$$W(x,y,\omega) = \sum_{m,n} W_{mn}\frac{1}{J_{mn}}\frac{Q_{mn}(\omega)}{L_{mn}(\omega)}. \quad (14)$$

5.2 Dynamic Response of a Square Antisymmetric Angle-Ply Laminate. For this case the governing equations within the FSDT are obtained by setting in (9) $A_{16} = A_{26} = A_{45} = D_{16} = D_{26} = 0$, and $B_{11} = B_{22} = B_{12} = B_{66} = 0$. The expression for J_{mn} is

$$J_{mn} = \int_0^a\int_0^a I_1(U_{mn}^2 + W_{mn}^2 + W_{mn}^2) + 2I_2(U_{mn}X_{mn} + V_{mn}Y_{mn}) + I_3(X_{mn}^2 + Y_{mn}^2)]dydx. \quad (15)$$

The final solution is derived by following the steps in 5.1.

Downloaded 03 May 2010 to 171.66.16.244. Redistribution subject to ASME license or copyright; see http://www.asme.org/terms/Terms_Use.cfm

6 Random Vibrations

The cross-spectral density function of the transverse displacement W can be put in the form

$$S_w(x_1, y_1, x_2, y_2, \omega) = \sum_{m,n} W_{mn}(x_1, y_1) W_{mn}(x_2, y_2) \frac{1}{J_{mn}^2 |L_{mn}^{(\omega)}|^2} S_{mn}^{(\omega)} + \sum_{\substack{m,n \\ m \neq p}} \sum_{\substack{p,q \\ p \neq n}} W_{mn}(x_1, y_1) W_{pq}(x_2, y_2) \frac{1}{J_{mn} J_{pq} L_{mn}^{*(\omega)} L_{pq}^{(\omega)}} S_{mnpq}^{(\omega)} \tag{16}$$

where

$$S_{mn}^{(\omega)} = \int_{A_1} \int_{A_2} S_p(x_1, y_1, x_2, y_2, \omega) \times W_{mn}(x_1, y_1) W_{mn}(x_2, y_2) dA_2 dA_1$$

and

$$S_{mnpq}^{(\omega)} = \int_{A_1} \int_{A_2} S_p(x_1, y_1, x_2, y_2, \omega) \times W_{mn}(x_1, y_1) W_{pq}(x_2, y_2) dA_2 dA_1.$$

The first sum in (16) is associated with the modal autocorrelation and the second with the cross-correlations.

For the case where the system is driven by a point load at $(\bar{x}, \bar{y})$, the load is expressed as

$$p(x, y, \omega) = p(\omega) \delta(x - \bar{x}) \delta(y - \bar{y}), \tag{17}$$

and for $\bar{x} = \frac{a}{2}$, $y = \frac{a}{2}$ (the midpoint of the plate), the cross-spectral density at the same point is

$$S_w\left(\frac{a}{2}, \frac{a}{2}, \omega\right) = \sum_{m,n} \frac{1}{J_{mn}^2} \sin^2\left(\frac{m\pi}{2}\right) \sin^2\left(\frac{n\pi}{2}\right) \frac{S(\omega)}{|L_{mn}^{(\omega)}|^2} + \sum_{m,n} \sum_{p,q} \frac{1}{J_{mn} J_{pq}} \sin\left(\frac{m\pi}{2}\right) \sin\left(\frac{n\pi}{2}\right) \sin\left(\frac{p\pi}{2}\right) \sin\left(\frac{q\pi}{2}\right) \frac{S(\omega)}{L_{mn}^{*(\omega)} L_{pq}^{(\omega)}}$$

$$= \sum_{m,n} \frac{1}{J_{mn}^2} \frac{S(\omega)}{|L_{mn}^{(\omega)}|^2} + \sum_{m,n} \sum_{p,q} \frac{1}{J_{mn} J_{pq}} \times \left[(-1)^{\frac{m-1}{2}} (-1)^{\frac{n-1}{2}} (-1)^{\frac{p-1}{2}} (-1)^{\frac{q-1}{2}} \right] \frac{S(\omega)}{L_{mn}^{*(\omega)} L_{pq}^{(\omega)}(\omega)}$$

$$\equiv S_w(\omega) \qquad m,n,p,q = 1,3,5\ldots \tag{18}$$

However, if the eigenvalues λ_{mn} are well separated, and for the case of light damping, the cross-terms can be omitted, following the condition (Elishakoff (1977)):

$$|\omega_{mn}^2 - \omega_{pq}^2| \gg \mu \max(\omega_{mn}^2, \omega_{pq}^2) \tag{19}$$

where μ is the hysteretic damping factor.

Assuming this case, it is necessary then to express the term $|L_{mn}^{(\omega)}|^2$ explicitly. For each m,n we may write

$$|L(\omega)|^2 = [\lambda^2(\omega) - \omega^2][\lambda^{*2}(\omega) - \omega^2]. \tag{20}$$

The complex eigenvalue can be written as

$$\lambda = \omega' + i\omega'' \tag{21}$$

so that

$$|L(\omega)|^2 = [(\omega' + i\omega'')^2 - \omega^2][(\omega' - i\omega'')^2 - \omega^2] = (\tilde{\omega}^2 - \omega^2)^2 + 4\omega'\omega'' \tag{22}$$

where

$$\tilde{\omega}^2 = (\omega')^2 - (\omega'')^2.$$

6.1 Band-Limited White Noise. For this case

$$S_p(\omega) = \begin{cases} S_0, & |\omega| \leq \omega_c \\ 0, & \text{otherwise} \end{cases}$$

so that the cross-spectral density function of W is

$$S_w(\omega) = \sum_{m,n} \frac{1}{J_{mn}^2} \frac{S_0}{|L_{mn}^{(\omega)}|^2}, \qquad |\omega| \leq \omega_c \tag{23}$$

and zero otherwise. The autocorrelation function is

$$R_w(\tau) = \sum_{m,n} \frac{S_0}{J_{mn}^2} \int_{-\omega_c}^{\omega_c} \frac{e^{i\omega\tau} d\omega}{|L_{mn}^{(\omega)}|^2}, \tag{24}$$

and it is derived by using the Fast Fourier Transform (FFT) algorithm (IMSL, 1984). The mean-square response is given as

$$E[W^2] \equiv R_w(o) = S_0 \sum_{m,n} \frac{1}{J_{mn}^2} \int_{-\omega_c}^{\omega_c} \frac{d\omega}{[\tilde{\omega}_{mn}^2 - \omega^2]^2 + 4\omega'_{mn}\omega''_{mn}}. \tag{25}$$

Using the method of undetermined coefficients, the integrand is represented, for each m,n as

$$\frac{1}{[\tilde{\omega}^2 - \omega^2]^2 + 4\omega'\omega''} = \frac{M_1\omega + N_1}{\omega^2 + \tilde{\omega}^2 - 2\omega\omega'} + \frac{M_2\omega + N_2}{\omega^2 + \tilde{\omega}^2 + 2\omega\omega'}, \tag{26}$$

where

$$M_1 = -M_2 = -\frac{1}{2\omega'\tilde{\omega}^2} \qquad ; N_1 = N_2 = \frac{1}{\tilde{\omega}^2}$$

and

$$\tilde{\omega}^2 = (\omega')^2 + (\omega'')^2.$$

The mean square is then

$$E[W^2] = S_0 \sum_{m,n} \frac{1}{J_{mn}^2 \tilde{\omega}_{mn}^2} \int_{-\omega_c}^{\omega_c} \left[\frac{-\frac{\omega}{2\omega'_{mn}} + 1}{(\omega - \omega'_{mn})^2 + (\omega''_{mn})^2} + \frac{\frac{\omega}{2\omega'_{mn}} + 1}{(\omega + \omega'_{mn})^2 + (\omega''_{mn})^2} \right] d\omega \tag{27}$$

and its final expression is

$$E[W^2] = S_0 \sum_{m,n} \frac{1}{J_{mn}^2 \tilde{\omega}_{mn}^2} \left\{ \frac{1}{2\omega'_{mn}} \ln \frac{(\omega_c + \omega'_{mn})^2 + (\omega''_{mn})^2}{(\omega_c - \omega'_{mn})^2 + (\omega''_{mn})^2} + \frac{1}{\omega''_{mn}} \left[\tan^{-1}\left(\frac{\omega_c - \omega'_{mn}}{\omega''_{mn}}\right) + \tan^{-1}\left(\frac{\omega_c + \omega'_{mn}}{\omega''_{mn}}\right) \right] \right\}$$

$$= \sum_{m,n} \frac{S_0 \pi}{J_{mn}^2 2\omega''_{mn} \tilde{\omega}_{mn}^2} I\left(\frac{\omega_c}{\omega'_{mn}}; \eta_{mn}\right) \tag{28}$$

where

$\eta_{mn} \equiv \frac{\omega''_{mn}}{\omega'_{mn}}$ is the damping ratio, and

$$I\left(\frac{\omega_c}{\omega'_{mn}}; \eta_{mn}\right) = \frac{\eta_{mn}}{\pi} \ln \left\{ \frac{\left(\frac{\omega_c}{\omega'_{mn}} + 1\right)^2 + \eta_{mn}^2}{\left(\frac{\omega_c}{\omega'_{mn}} - 1\right)^2 + \eta_{mn}^2} + \frac{2}{\pi} \left[\tan^{-1}\left(\frac{\frac{\omega_c}{\omega'_{mn}} - 1}{\eta}\right) + \tan^{-1}\left(\frac{\frac{\omega_c}{\omega'_{mn}} + 1}{\eta}\right) \right] \right\}.$$

Downloaded 03 May 2010 to 171.66.16.244. Redistribution subject to ASME license or copyright; see http://www.asme.org/terms/Terms_Use.cfm

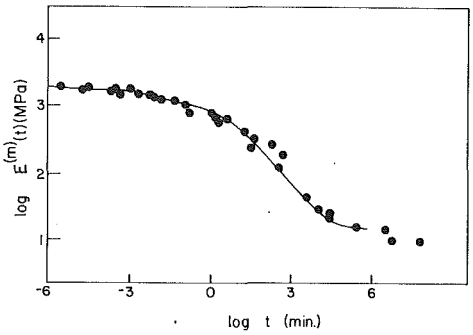


Fig. 2 Measured data (Moehlenpah et al., 1971) of epoxy matrix at 50°C. The solid line is its representation by cubic splines.

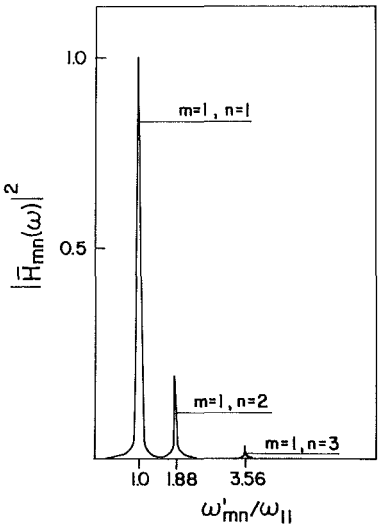


Fig. 3 Normalized frequency response function—Case 5.1, $a = b = 20h$.

6.2 Ideal White-Noise. The results for this case are obtained from those of band-limited white noise when $\omega_c \to \infty$. The autocorrelation becomes

$$R_w(\tau) = \sum_{m,n} \frac{S_0}{f_{mn}^2} \int_{-\infty}^{\infty} \frac{e^{i\omega\tau}}{[\tilde{\omega}_{mn}^2 - \omega^2]^2 + 4\omega'_{mn}\omega''_{mn}} d\omega$$

$$= \sum_{m,n} \frac{S_0}{f_{mn}^2} \frac{1}{\omega''_{mn}\tilde{\omega}_{mn}^2} \int_{-\infty}^{\infty} \frac{2\omega''_{mn}\tilde{\omega}_{mn}^2}{\tilde{\omega}_{mn}^4 + 2[(\omega''_{mn})^2 - (\omega'_{mn})^2]\omega^2 + \omega^4} e^{i\omega\tau} d\omega$$

$$= \sum_{m,n} \frac{S_0}{f_{mn}^2} \frac{\pi}{2\omega''_{mn}\tilde{\omega}_{mn}^2} \left\{ e^{-\omega''_{mn}|\tau|} [\cos(\omega'_{mn}\tau) + \eta_{mn} \sin(\omega'_{mn}|\tau|)] \right\}, \tag{29}$$

and the mean square is, therefore,

$$E[W^2] = \sum_{m,n} \frac{S_0}{f_{mn}^2} \frac{\pi}{2\omega''_{mn}\tilde{\omega}_{mn}^2}. \tag{30}$$

Using the expression for η in equation (28), the condition for not including the cross-correlation terms is written as

$$\left| 1 - \frac{(\omega'_{mn})^2}{(\omega'_{pq})^2} \right| \gg \max(\eta_{mn}, \eta_{pq}). \tag{31}$$

7 Results and Discussions

Results are given for a viscoelastic isotropic epoxy matrix whose measured time-dependent Young's modulus was reported by Moehlenpah et al. (1971) at 50°C as shown in Fig. 2. Cubic splines were fitted to these measured data in the region $0 \le t \le 10^6$ min.

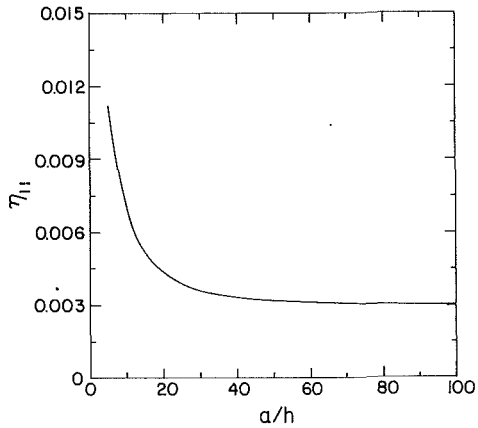


Fig. 4 Variation of η_{11} versus a/h – Case 5.1

The correspondence between the measured values and the cubic splines representation, as shown in Fig. 2, is excellent. The Poisson's ratio of the matrix was assumed to be constant $\nu_m = 0.38$ (Schapery, 1974). T-300 graphite elastic fibers were taken to reinforce the epoxy matrix with 60 percent volume ratio. The engineering constants of the transversely-isotropic graphite fibers are $E_A = 220$ GPa, $\nu_A = 0.3$, $E_T = 22$ GPa, $\nu_T = 0.35$, and $G_A = 22$ GPa. Here, E_A and ν_A denote the axial Young's modulus and Poisson's ratio, E_T and ν_T are the transverse Young's modulus and Poisson's ratio, and G_A is the axial shear modulus. These values are related to the $C_{ijkl}^{(\beta\gamma)}$ of the phases by the standard relationships.

Results at a temperature other than the reference one (50°C) can be obtained from Moehlenpah et al. (1971) by determining first the value of a shift factor a_T at the desired temperature

$$\log a_T = -0.1049 - 0.2071(T-50) - 1.243 \cdot 10^{-3}(T-50)^2 + 4.013 \cdot 10^{-5}(T-50)^3 \tag{32}$$

and then the abssisa $\log t$ of the master curve of Fig. 2 is shifted by $\log a_T$ resulting a new abssisa $\log t^*$:

$$\log t^* = \log t - \log a_T. \tag{33}$$

We consider first a square orthotropic plate. The length of the plate is $20h$, the shear correction factor is 5/6, and $T = 78$°C.

The function $|H_{mn}(\omega)|^2 \equiv |L_{mn}(\omega)|^{-2}$, normalized to its maximum value, is shown in Fig. 3 versus the ratio $\omega'_{mn}/\omega'_{11}$. Two conclusions can be made from this figure: (*i*) that the eigenvalues are well separated, and (*ii*) that practically the mean-square response can be derived within the first mode only.

The behavior of η is studied next. Figure 4 displays the variation of η_{11} versus the length-to-thickness ratio. Apart from the relatively flat part at the region of $50 \le a/h \le 100$, η_{11} is rapidly increasing as a/h decreases. The relation of this value and its counterpart obtained by using the CPT, $\bar{\eta}$, is shown in Fig. 5, from which it can be seen that even at $a/h = 50$ the two theories defer by 7.2 percent.

The influence of the temperature on η is studied for the case of constant ratio $a/h = 20$. Figure 6 shows the variation of $\log(\eta_{11})$ versus T for $50°C \le T \le 78°C$. At relatively low temperatures in the range, η is small. It should be noted here that for very small η, $E[W^2] \to \infty$, like in the undamped elastic case.

Angle-ply laminates $[\theta, -\theta, \theta, -\theta]$, with $a/h = 20$ and $T = 78$ deg are considered next. The variation of η_{11} versus θ is shown in Fig. 7, where the maximum value is obtained at $\theta = 7$ deg. The ratio between this value and the minimum one (at $\theta = 45$ deg) is 1.535. The influence of this behavior on the mean-

Downloaded 03 May 2010 to 171.66.16.244. Redistribution subject to ASME license or copyright; see http://www.asme.org/terms/Terms_Use.cfm

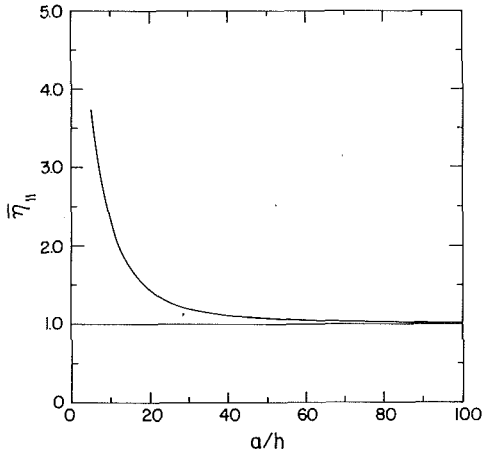


Fig. 5 Relative (to CPT) η_{11} versus a/h – Case 5.1

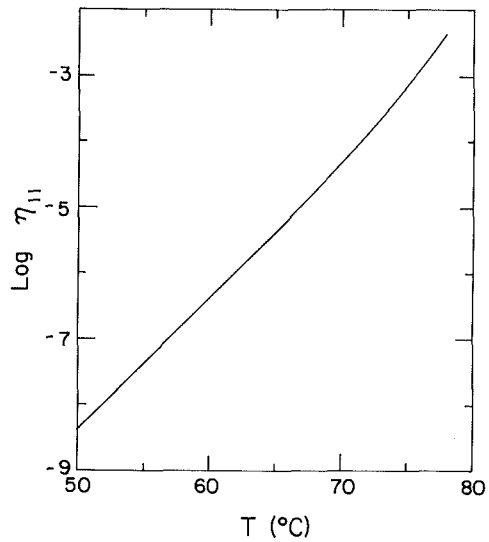


Fig. 6 Log (η_{11}) versus T – Case 5.1

square response is shown in Fig. 8, where the results, normalized to the one obtained at $\theta = 0$ deg, are found to be continuously decreasing despite the reduction in the value of η.

Referring to the last two figures, it is for the designer to decide if a laminate with a low mean-square and small damping, high mean-square with high damping, or something in between in preferred.

Acknowledgments

The author would like to thank Prof. J. Aboudi of the Tel-Aviv University and Prof. I. Elishakoff of the Technion—I.I.T. for their helpful discussions.

References

Aboudi, J., 1984, "Effective Behavior of Inelastic Fiber-Reinforced Composites," *International Journal of Engineering Science*, Vol. 22, pp. 439–449.

Aboudi, J., 1987, "Closed Form Constitutive Equations for Metal Matrix Composites," *International Journal of Engineering Science*, Vol. 25, pp. 1229–1240.

Aboudi, J., and Cederbaum, G., 1989, "Analysis of Viscoelastic Composite Laminated Plates," *Composite Structures*, Vol. 12, pp. 243–256.

Aboudi, J., 1972, "Propagation of Transient Pulses From a Spherical Cavity in a Viscoelastic Medium," *International Journal of Numerical Methods in Engineering*, Vol. 4, pp. 289–299.

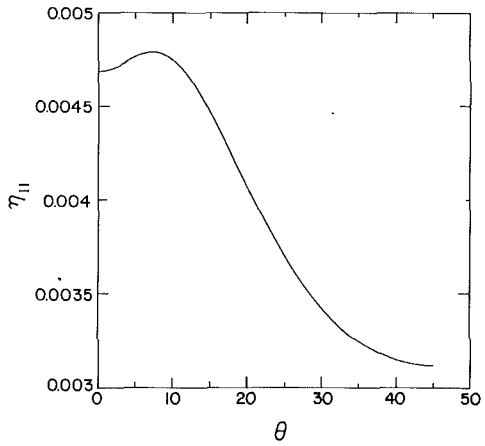


Fig. 7 Variation of η_{11} versus θ – Case 5.2

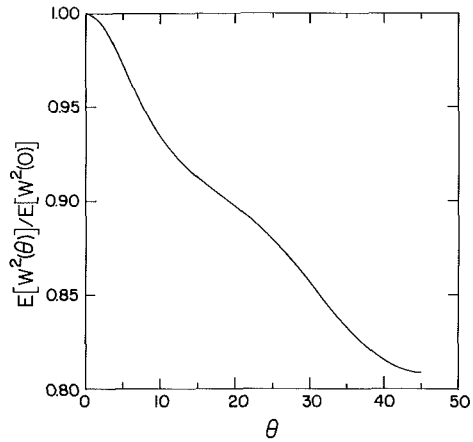


Fig. 8 Relative (to the value at $\theta = 0$) mean-square displacement versus θ – Case 5.2

Cederbaum, G., and Aboudi, J., 1989, "Dynamic Response of Viscoelastic Laminated Plates," *Journal of Sound and Vibration*, Vol. 133(2), pp. 225–238.

Cederbaum, G., Librescu, L., and Elishokoff, I., 1988, "Random Response of Laminated Composite Plates Using High-Order Shear Deformation Theory," *Journal of the Acoustical Society of America*, Vol. 84(2), pp. 660–666.

Cederbaum, G., Elishahoff, I., and Librescu, L., 1987, "Random Vibrations of Laminated Plates Modulled Within the First-Order Shear Deformation Theory," *Composite Structures*, Vol. 12, pp. 47–111.

Christensen, R. M., 1982, *Theory of Viscoelasticity*, Academic Press, New York.

Dobynes, A. L., 1981, "Analysis of Simply-Supported Orthotropic Plates Subjected to Static and Dynamic Loads," *AIAA Journal*, Vol. 19, pp. 642–650.

Elishakoff, I., 1977, "On the Role of Cross-Correlations in the Random Vibrations of Shells," *Journal of Sound and Vibration*, Vol. 50, pp. 239–252.

Elishakoff, I., 1983, *Probabilistic Methods in the Theory of Structures*, John Wiley and Sons, New York.

IMSL, Programs Package, 1984, Tel-Aviv University.

Meirovitch, L., 1980, *Computational Methods in Structural Dynamics*, Sijthoff and Noordhoff.

Moehlenpah, A. E., Ishai, O., and DiBenedetto, A. T., 1971, "The Effect of Time and Temperature on the Mechanical Behavior of Epoxy Composites," *Journal of Polymer Engineering Science*, Vol. 11, pp. 129–138.

Reddy, J. N., 1984, "A Simple Higher-Order Theory for Laminated Composite Plates," ASME JOURNAL OF APPLIED MECHANICS, Vol. 51, pp. 745–751.

Whitney, J. M., and Pagano, N. J., 1970, "Shear Deformation in Heterogeneous Anisotropic Plates," ASME JOURNAL OF APPLIED MECHANICS, Vol. 37, pp. 1031–1036.

Whitney, J. M., 1987, *Structural Analysis of Laminated Anisotropic Plates*, Technomic.

Schapery, R. A., 1974, "Viscoelastic Behavior and Analysis of Composite Materials," *Composite Materials*, Vol. 2, G. P. Sendeckyj, ed., Academic Press, New York.

Downloaded 03 May 2010 to 171.66.16.244. Redistribution subject to ASME license or copyright; see http://www.asme.org/terms/Terms_Use.cfm

R. Sondergaard

K. Chaney

C. E. Brennen

California Institute of Technology,
Pasadena, Ca 91125

Measurements of Solid Spheres Bouncing Off Flat Plates

1 Introduction

Recent years have seen a substantial increase of interest in the flows of granular materials whose rheology is dominated by the physical contact between particles and between particles and the containing walls. Considerable advances in the theoretical understanding of rapid granular material flows have been made by the application of the statistical methods of molecular gas dynamics (e.g., Jenkins and Savage (1983), Lun et al. (1984)) and by the use of computers simulations of these flows (e.g., Campbell and Brennen (1985), Walton (1984)). Experimental studies aimed at measurements of the fundamental rheology properties are much less numerous and are understandably limited by the great difficulties involved in trying to measure velocity profiles, solid fraction profiles, and fluctuating velocities within a flowing granular material. Nevertheless, it has become clear that one of the most severe problems encountered when trying to compare experimental data with the theoretical models is the uncertainty in the material properties governing particle/particle or particle/wall collisions. Many of the theoretical models and computer simulations assume a constant coefficient of restitution (and, in some cases, a coefficient of friction).

The purpose of the present project was to provide some documentation for particle/wall collisions by means of a set of relatively simple experiments in which solid spheres of various diameters and materials were bounced off plates of various thickness and material. The objective was to provide the kind of information on individual particle/wall collisions needed for the theoretical rheological models and computer simulations of granular material flows: in particular, to help resolve some of the issues associated with the boundary condition at a solid wall. For discussion of the complex issues associated with dynamic elastic or inelastic impact, reference is made to Goldsmith (1960) and the recent text by Johnson (1985).

Contributed by the Applied Mechanics Division of THE AMERICAN SOCIETY OF MECHANICAL ENGINEERS for presentation at the Winter Annual Meeting, Dallas, Texas, Nov. 25–30, 1990.

Discussion on this paper should be addressed to the Technical Editor, Leon M. Keer, The Technological Institute, Northwestern University, Evanston, IL 60208, and will be accepted until two months after final publication of the paper itself in the JOURNAL OF APPLIED MECHANICS. Manuscript received by the ASME Applied Mechanics Division, Feb. 3, 1989; final revision, May 30, 1989.

Paper No. 90-WA/APM-11.

2 Normal Impact Between Spheres and Uniform Plates

Most of the literature (e.g., Goldsmith (1960), Johnson (1985)) concentrates on the impact of a sphere with large blocks. Yet the walls of most containers of granular material flows are plates which can often be thinner than one particle diameter. Hence, the first set of tests was carried out to determine the influence of the ratio of the particle diameter to the plate thickness on the coefficient of restitution resulting from a normal impact. The solid spheres used were precision ball bearings (steel or bronze) and glass spheres ranging in diameter from 0.317 to 2.54 cm. These were dropped from various heights onto plates of lucite or aluminum (ranging in thickness from 0.317 to 3.81 cm). Prior to release the spheres were suspended at the end of a tube by means of a small vacuum applied to the tube. A quick opening valve relieved this vacuum and released the particle in a precise and repeatable manner and without any significant rotational velocity.

The sphere trajectories and the height of the rebound were determined from multiple exposure photographs made using stroboscopic light; the strobe frequency was adjusted to achieve maximum resolution which occurred when each image of the sphere was separated by a maximum of one or two sphere diameters. Aerodynamic forces were determined to be small (at least outside the immediate moment of impact). Hence, for example, in the case of normal impacts, the coefficients of restitution were calculated from the ratio of the release height to the maximum height achieved after the first (or subsequent) rebounds.

The first question which arose concerned the effect of the structure supporting the plates upon the results. Two sides of the rectangular plates were solidly clamped to a relatively rigid support structure. By dropping the sphere to impact the plate at various distances from either of the clamped edges, it was determined that the coefficient of restitution decreased with distance of the impact point from the clamped edge until, at a certain critical distance, it became independent of the distance from the support. An example of this dependence is shown in Fig. 1 in which data for steel ball bearings impacting a 1.27-cm thick lucite plate are presented.

The critical distance was a linear function of the ball diameter but was independent of the plate thickness at least for the two thicknesses investigated. As seen in Fig. 2, the

Copyright © 1990 by ASME
Downloaded 03 May 2010 to 171.66.16.244. Redistribution subject to ASME license or copyright; see http://www.asme.org/terms/Terms_Use.cfm

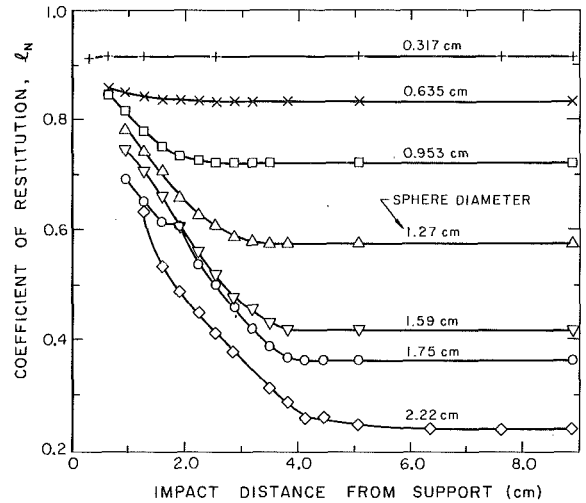


Fig. 1 Coefficient of restitution as a function of the distance of the impact point from the clamping support for various steel spheres impacting a 1.27-cm thick lucite plate from a drop height of 63.5 cm

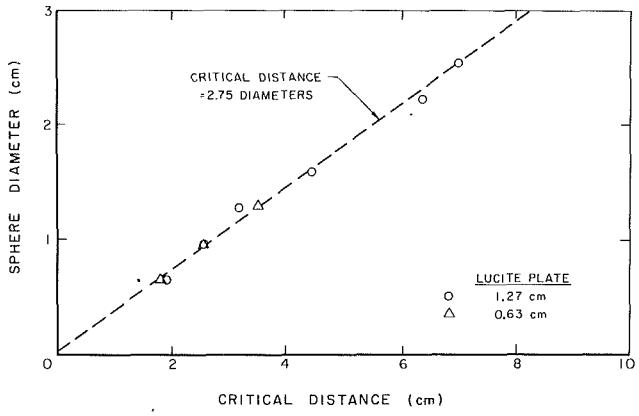


Fig. 2 Critical distance from support plotted versus sphere diameter for the steel sphere/lucite plate experiments

critical distance was 2.75 sphere diameters for the steel ball/lucite plate system. In theory, the rebound of the sphere can only be affected by the proximity of a plate support if there is sufficient time during contact for a wave to travel through the plate from the point of impact to the support and return to the impact region. Dilational, shear, and Rayleigh surface waves will be generated by impact, their speeds being given by

$$c = k[E_p/\rho_p]^{1/2} \tag{1}$$

where, assuming Poisson's ratio for the plate material to be 0.3, k is roughly 1.16, 0.62, and 0.57 for the three types of wave, respectively. The plate modulus of elasticity is E_p and its density is ρ_p; for lucite (polymethyl methacrylate) we assume a value of E of 2.6×10^9 kg/m sec^2 and a specific gravity of 1.18, though the former can only be considered quite approximate.

The Hertzian contact time, T_c, for a sphere on a semi-infinite block will be used to estimate the contact time with a finite plate and is given (Goldsmith (1960)) by

$$T_c = 3.21[(1-\nu_s^2)+(1-\nu_p^2)E_s/E_p]^{2/5} a/\left(\frac{E_s}{\rho_s}\right)^{2/5} (v_{N1})^{1/5} \tag{2}$$

where a is the sphere radius, v_{N1} is its impact velocity, E_s, ρ_s, ν_s are the modulus of elasticity, the density and Poisson's ratio for the sphere material, and ν_p is Poisson's ratio for the plate. The following values are assumed for the steel sphere/lucite plate system: $\nu_p = 0.3$, $\nu_s = 0.208$, $E_s = 2\times10^{11}$ kg/m sec^2. Moreover, due to the fifth power, the dependence on v_{N1} is not very strong and we assume a drop height of 60 cm so that $v_{N1} = 28.7$ cm/sec. Consequently, for each of the three types of wave the critical distance from the impact point to the support (for the steel sphere/lucite plate system) should be

$$\frac{cT_c}{2} = 11.14\ k\ a. \tag{3}$$

Note that the linear dependence of the critical distance on the sphere size is reproduced by the present experiments. Furthermore, the critical distance predicted by the theory would be 6.46, 3.45, or 3.18 sphere diameters for the dilational, shear, and Rayleigh waves, respectively. The difference between this and the observed critical distance of 2.75 sphere diameters may be due to inaccuracies in the lucite material properties. The agreement between theory and observation may be as good as could be expected and suggests that it is the reflection of the shear or Rayleigh waves rather than the dilational wave which creates the effect of the supporting system.

As a result of the foregoing investigation, the effect of the plate support system could be eliminated by ensuring that for each sphere/plate system, the impact point occurred beyond the critical distance from the support. Under these conditions, coefficients of restitution for normal impacts, e_N, were obtained for a wide range of sphere diameters, plate thicknesses ($2b$), and impact velocities (drop heights). Leaving aside, for the moment, the issue of the dependence on impact velocity, it was immediately apparent that the coefficient of restitution was almost solely a function of the ratio of the sphere diameter, $2a$, to the plate thickness, $2b$, irrespective of the separate values of these dimensions. This almost universal functional dependence is demonstrated in Fig. 3 for the steel sphere/lucite plate system and in Fig. 4 for experiments with Pyrex glass spheres and lucite plates. Data for the entire range of sphere diameters and plate thicknesses are presented in both figures.

It is important to emphasize that the decrease in e_N with increasing a/b does not necessarily imply an increased loss in kinetic energy of the whole system. Instead, with decreasing plate thickness, an increasing amount of kinetic energy is transferred to the kinetic energy of the plate at the instant of departure. Zener (1941) (see also Goldsmith (1960)) has analyzed the normal impact of spheres with flat plates and obtained an expression for the kinetic energy imparted to the plate upon departure. This is then converted to yield an "effective" coefficient of restitution for the sphere assuming no loss in the total kinetic energy. The result is a coefficient of restitution which is a function only of the impact parameter, λ, defined as

$$\lambda = \left(\frac{\Pi\rho_s}{\rho_p}\right)^{3/5} \frac{1}{4\sqrt{3}} \left(\frac{a}{b}\right)^2 \left[\frac{v_{N1}^2\rho_p(1-\nu_p^2)}{E_p}\right]^{1/10} \times \left[1+\frac{E_p(1-\nu_s^2)}{E_s(1-\nu_p^2)}\right]^{-2/5}. \tag{4}$$

Note that consistent with our experiments, it follows that e_N is a function only of a/b for given materials. Zener's results are included in Figs. 3 and 4 assuming the previously quoted values for ν and the material properties of steel and lucite; for glass the values $\nu = 0.22$, $E = 6.2\times10^{10}$ kg/m sec^2 and $\rho = 2.24$ gm/cm^3 were employed. The theory and experiments agree very well. The slightly lower experimental values of e_N can be ascribed to other energy loss mechanisms not included in the theory, in particular, to the energy required for plastic deformation. It follows that although the effective coefficient of restitution is quite small, most of the apparent loss of kinetic

Downloaded 03 May 2010 to 171.66.16.244. Redistribution subject to ASME license or copyright; see http://www.asme.org/terms/Terms_Use.cfm

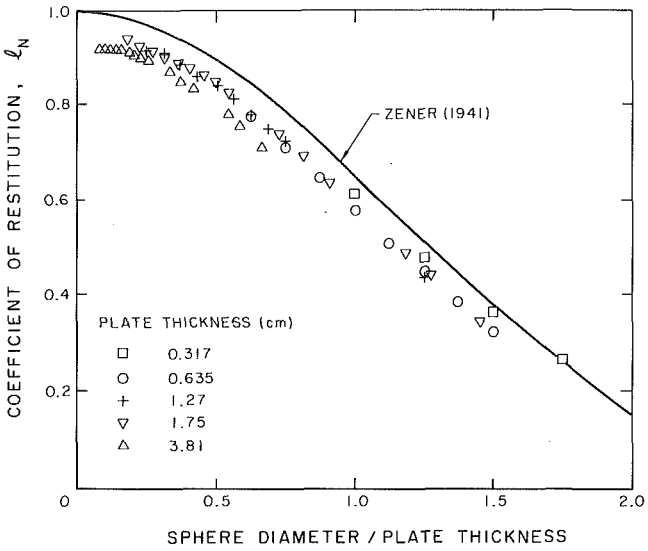


Fig. 3 Coefficients of restitution for normal collisions of steel spheres (diameters varying from 0.317 to 2.54 cm) impacting lucite plates of various thicknesses as indicated. Also shown is the theoretical result of Zener (1941).

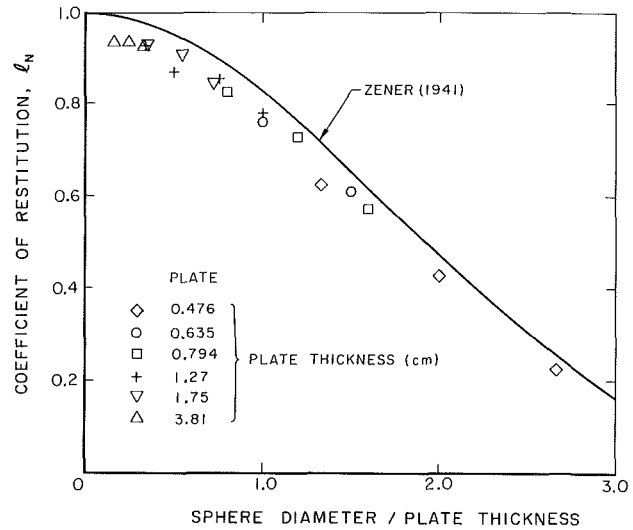


Fig. 4 Coefficients of restitution for normal collisions of Pyrex glass spheres (diameters varying from 0.635 to 1.27 cm) impacting lucite place of various thicknesses as indicated. Also shown is the theoretical result of Zener (1941).

energy is converted into motion of the plate and in a granular material flow could be subsequently recovered by a subsequent collision of a particle with the wall. Indeed, the comparisons in Figs. 3 and 4 suggest that the actual energy loss may even be smaller for larger a/b than for small a/b.

Finally, we should comment on the influence of impact velocity. Previous experiments and theory (Johnson (1985)) on the impact of spheres with large blocks of material have shown that the coefficient of restitution is essentially unity until the critical impact velocity causing plastic deformation is exceeded. This critical velocity is very small for most materials and is exceeded in all the circumstances of the present experiments. At significantly higher velocities fully plastic deformation occurs, and when this is reached, experiment and theory indicate a coefficient of restitution which decreases like $(v_{N1})^{-1/4}$ with increasing impact velocity, v_{N1}. In Fig. 5, the results for one specific system, one plate thickness, and two sizes of sphere are plotted against v_{N1} for velocities ranging from 1.7 to 3.8

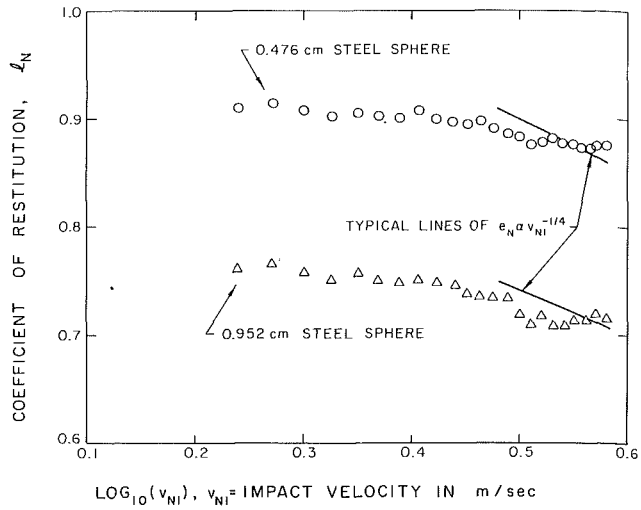


Fig. 5 Variation of coefficient of resitution with normal incident velocity for steel spheres impacting a 1.27-cm lucite plate

m/sec. Clearly the impacts lie between the critical velocity for plastic deformation and the fully plastic deformation velocity. The dependence on impact velocity is weak at the lower velocities; at higher velocities it may be approaching the $(v_{N1})^{-1/4}$ dependence. Some granular material flows will involve impact velocities substantially smaller than 1.7 m/sec; however, it was difficult to obtain accurate data at the very small drop heights involved.

It may be useful to observe that the phenomena described provides a full explanation of a demonstration which Profs. D. Shield and J. K. Knowles brought to our attention. This demonstration involves ball bearings of several sizes and lucite plates of several thicknesses which are supported by two wooden bars. When the balls are dropped on the thicker plate, the largest ball exhibits a substantial rebound while the smallest ball hardly bounces at all. On the other hand, when they are dropped onto the thinner plate the reverse is observed. This occurs because of two competing effects, one of which dominates with the thinner plates and the other with the thicker plates. The first effect is that the larger the ball bearing the closer it is to the support in terms of ball diameters and therefore the larger the coefficient of restitution. This first effect dominates for the larger plates because (as seen in Fig. 3) the coefficient of restitution only depends weakly on the plate thickness when the ratio of the ball diameter to plate thickness is small. The other effect is that the effective coefficient of restitution decreases quite rapidly with increasing ball diameter to plate thickness once the latter ratio exceeds about 0.5. Hence, for the thinner plates this effect overwhelms the support proximity effect and causes the smaller ball bearings to have a larger rebound.

One other result which follows from the present measurements and is essentially a restatement of the Shield-Knowles demonstration is that a plot of the coefficient of restitution against the sphere diameter for a plate of a given thickness, with supports a fixed distance apart, would exhibit a minimum. We initially produced such plots and were puzzled by their form until the effect of the support became clear. It is interesting to note that Koller and Busenhart (1986) observed a minimum in the coefficients of restitution for spheres impacting spherical shells. Those authors emphasize that a spherical shell will tend to rebound whereas a flat plate will not (their supports are well beyond any critical distance). In this respect a spherical shell may be phenomenologically similar to a flat plate with supports at less than the critical distance from the impact point.

Downloaded 03 May 2010 to 171.66.16.244. Redistribution subject to ASME license or copyright; see http://www.asme.org/terms/Terms_Use.cfm

3 Oblique Impact Between Solid Spheres and Uniform Plates

As Johnson (1985) indicates in his review, oblique collisions with plastic deformation and the possibility of microslip at the contact surfaces involve complicated mechanics at the microscale. This makes prediction of appropriate macroscopic collision characteristics quite difficult. Most of the theoretical or computational models of granular material flow assume (1) a "normal" condition consisting of a coefficient of restitution, e_N, relating the normal component of the departure velocity to the normal component of the approach velocity and (2) a "tangential" condition. Several asympotic or simplified "tangential" conditions have been employed in theoretical and computational models. One possibility is to assume that slip exists between the contact surfaces during the entire collision process; one might then relate the normal and tangential impulses by a friction coefficient. Alternatively, slip may cease during contact in which case an appropriate tangential condition would be to equate the departure tangential velocities of the two contacting surfaces.

Further discussion of these possibilities and the variation with incidence angle is given in the recent review by Brach (1988). Brach also provides a most useful summary of the existing data on oblique impact. The present experiments were carried out to obtain further information on the appropriate tangential condition.

The present oblique experiments used a 0.317-cm aluminum plate set at a series of angles, θ, to the horizontal (up to 70 deg in increments of 5 deg). Thus, θ is the angle of the trajectory to a target surface normal. Glass and steel balls of different sizes were dropped from various heights to impact the plate obliquely. The entire trajectory was photographed, and both components of the impact and departure velocities of the center of the spheres were ascertained from these trajectories. These velocities were used to calculate a "normal coefficient of restitution," e_N, defined as $-v_{N2}/v_{N1}$, where v_{N1} and v_{N2} are the components of the approach and departure velocities normal to the plate (positive into plate), and a "tangential coefficient of restitution," e_T, defined as v_{T2}/v_{T1} where v_{T1} and v_{T2} are the corresponding components tangential to the plate. Note that these are all translational velocities of the center of the spheres: The rotational velocities of the spheres before impact were zero and this fact is used later in discussing velocities of the contact point.

An alternative way to present this data is to plot the total coefficient of restitution e which represents the total loss of translational kinetic energy where

$$e=[e_N^2\cos^2\theta+e_T^2\sin^2\theta]^{1/2} \tag{5}$$

and a coefficient f, defined as the ratio of tangential to normal impulse of the collision so that

$$f=(1-e_T)\tan\theta/(1+e_N). \tag{6}$$

Following Brach (1988) the quantity f is termed the impulse ratio. The normal and tangential impulses acting through the contact point are denoted by J and K, respectively, so that

$$J=m(v_{n1}-v_{n2});\ K=m(v_{T1}-v_{T2}). \tag{7}$$

Furthermore,

$$Ka=mk^2(w_1-w_2) \tag{8}$$

where κ is the radius of gyration of the sphere and w_1, w_2 are the rotational velocities before and after impact. Also note, for future purposes, that the tangential velocity of the contact point upon departure, v_{Tc2}, is given by $v_{Tc2}=v_{T2}+aw_2$, and it follows that since $k^2/a^2=2/5$ for a sphere, and since $w_1=0$ in the present experiments then

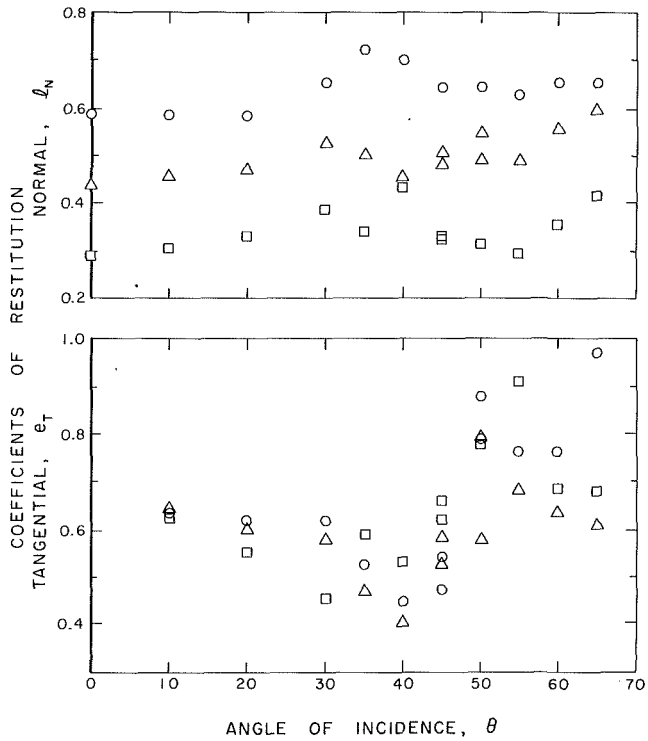


Fig. 6 Normal and tangential coefficients of restitution, e_N and e_T, for Pyrex glass spheres obliquely impacting a 0.317-cm thick aluminum plate: ○ = 0.635-cm sphere, ▽ = 0.953-cm sphere, □ = 1.27-cm sphere

$$\frac{v_{Tc2}}{v_{N1}}=\tan\theta\left\{\frac{7}{2}\frac{v_{T2}}{v_{T1}}-\frac{5}{2}\right\}=\tan\theta\left\{\frac{7}{2}e_T-\frac{5}{2}\right\}. \tag{9}$$

Consider first the simple theory described by Brach (1988) in which tangential deformations are neglected. Then for incidence angles, θ, less than a certain critical value, θ_c, slip will cease prior to departure so that $v_{Tc2}=0$ and from the relations (6) and (9).

$$e_T=5/7 \text{ and } f=\frac{2\tan\theta}{7(1+e_N)} \tag{10}$$

On the other hand, for $\theta>\theta_c$, slip will continue throughout contact and the ratio f should be equal to a Coulombic friction coefficient, μ, so that

$$e_T=1-\mu(1+e_N)\cot\theta \quad \text{and} \quad f=\mu. \tag{11}$$

Thus, as θ increases, f should first increase from 0 according to equation (10) until the critical value of $\theta_c\approx\arctan(7(1+e_N)\mu/2)$ is reached. For larger values of θ, f should remain relatively constant or, as Brach observes, may decrease due to a decrease in μ with increasing slip velocity. In the context of the present tests, experiments were carried out to measure the Coulombic coefficient of friction between the glass spheres and the aluminum plates. An average value of $\mu=0.23$ resulted when the target was clean and polished. Values as high as $\mu=0.3$ resulted when the aluminum surface was dirtier. Since e_N varied from 0.3 to 0.7 (see Fig. 6), the corresponding critical values, θ_c, were in the range of 45 deg to 55 deg.

A more detailed analysis should include the deformations and velocities associated with the elasticity of both surfaces. Then, in the case when slip has ceased during contact, the velocity of the contact point is no longer zero upon departure, but is equal to the time rate of change of the tangential deformation. Maw, Barber, and Fawcett (1976 and 1981) have analyzed this problem and shown both theoretically and experimentally that the appropriate tangential condition

Downloaded 03 May 2010 to 171.66.16.244. Redistribution subject to ASME license or copyright; see http://www.asme.org/terms/Terms_Use.cfm

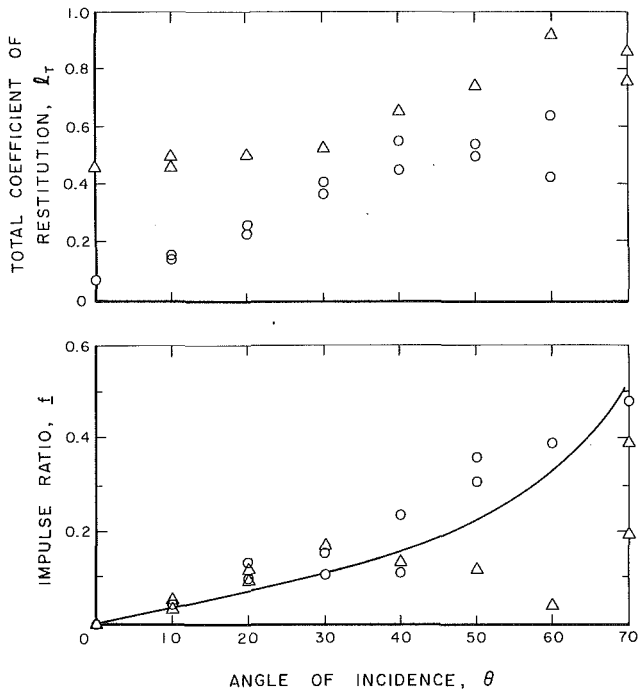


Fig. 7 Normal and tangential coefficients of restitution, e_N and e_T, for steel spheres obliquely impacting a 0.317-cm thick aluminum plate: △ = 0.317-cm sphere, ○ = 0.953-cm sphere

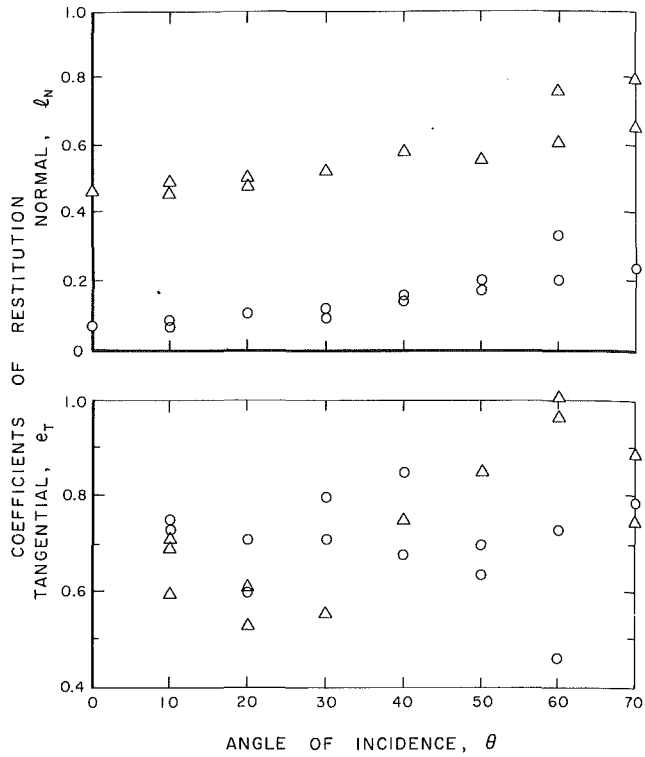


Fig. 8 Total coefficient of resitution and impulse ratio, f, corresponding to the data of Fig. 6.

depends on the material properties (including a Coulomb friction coefficient, μ, at the contact interface and a parameter, κ, which is a ratio of elastic moduli of the two materials) and on the incidence angle. Specifically they demonstrate that the phenomenon is controlled by a nondimensional incidence angle $(\kappa/\mu)\tan\theta$ where θ is the angle of the trajectory of the contact point to a normal to the surface. When $(\kappa/\mu)\tan\theta$ is less than a value of the order of 4 to 6, tangential elasticity causes the tangential relative velocity of the contact point upon departure to be negative (opposite direction to the incident tangential velocity). One must exceed this critical value of 4 to 6 for the departure tangential velocity to become positive. When κ is of order unity, the critical angles resulting from the Maw, Barber, and Fawcett analysis do not differ greatly from those of the simpler analysis described previously.

In the present investigation, preliminary experiments revealed that although the data for e_N was quite consistent and repeatable, the data for e_T was very scattered. This scatter was reduced but not eliminated by carefully cleaning all the surfaces with acetone prior to every test. We concluded that the scatter was at least in part caused by lack of repeatability in the frictional conditions existing at the contact surface. Data for 0.635-cm, 0.953-cm, and 1.27-cm glass spheres and for 0.317-cm and 0.953-cm steel spheres are presented in Figs. 6 and 7, respectively. The variation of the normal coefficient, e_N, with incidence angle is not great in any of this data. In general, however, e_N does appear to increase a little with incidence angle. In the case of the glass spheres, there is a slight local maxima at an incidence angle of 30 deg – 40 deg. The data for the steel spheres displayed a substantial increase in scatter at the larger incidence angles.

The corresponding data for the tangential coefficient, e_T, is shown in Figs. 6 and 7. The data for the glass spheres shows more variation with incidence angle than occurred with the normal coefficient. It is also striking that the scatter in the data increases markedly above an incidence angle of about 40 deg. The same was true of the data for the steel spheres which showed substantial increase in the scatter above about 50 deg.

The data of Figs. 6 and 7 was also used to produce the

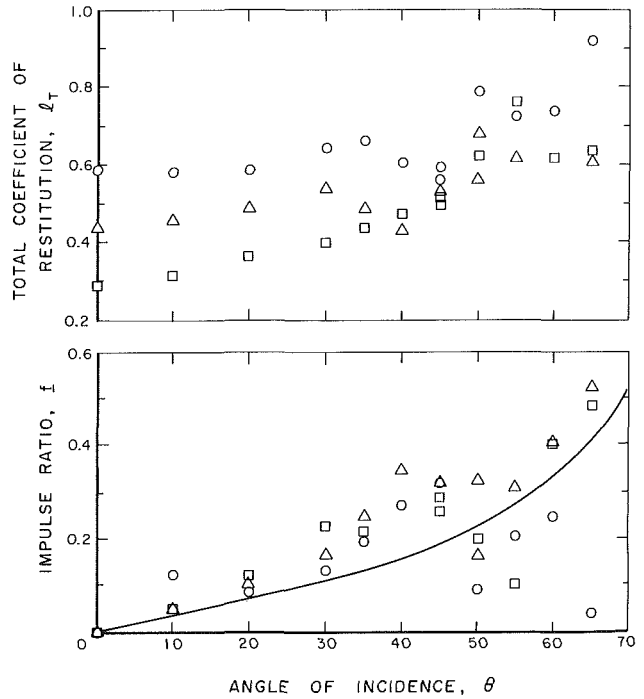


Fig. 9 Total coefficient of restitution and impulse ratio corresponding to the data of Fig. 7.

graphs of total coefficient of restitution, e, and impulse ratio, f, included as Figs. 8 and 9. Both sets of data show a consistent increase in e with increasing incidence angle, a trend which appears consistent with previous data (Brach, 1988). The data for the impulse ratio show that f increases systematically with θ until an incidence angle of about 45 deg (Fig. 8) or about 35 deg (Fig. 9) is reached. These values are

Downloaded 03 May 2010 to 171.66.16.244. Redistribution subject to ASME license or copyright; see http://www.asme.org/terms/Terms_Use.cfm

roughly consistent with the critical angles for complete slip estimated earlier as being in the range 45 deg to 55 deg. Furthermore, the data for angles less than the critical values are quite consistent and roughly follow the aniticipated form $f=2\tan\theta/7(1+e_N)$ as is illustrated by the solid lines in Figs. 8 and 9 which are for $e_N=0.6$. Thus, the data on the impulse ratio are in general agreement with the form of the previous data obtained by Ratner and Styller (1981) and by Hutchings (1974).

It should, however, also be noted that the data above the critical incidence angles of about 45 deg and about 35 deg is very scattered and inconsistent. Because of this scatter it is not possible to say whether it corresponds to a constant value of $f=\mu$ or not. Indeed, the data do suggest that collisions at angles greater than the critical may be very sensitive to variations in the effective friction of the surfaces in the vicinity of the contact points.

In the case of the glass spheres (Figs. 6 and 8), the critical incidence angle is particularly evident in the data of e_T (Fig. 6). Note that for subcritical incidence angles of less than about 45 deg, e_T is smaller than the value of 5/7 (0.71) which would occur if $v_{cT2}=0$. Values of e_T less than 5/7 imply a negative v_{cT2} and therefore indicate that the tangential elasticity played a significant role in determining the rebound conditions for subcritical incidence angles. Some of the data for the steel spheres (Fig. 7) show a similar trend, but the evidence is less conclusive in that case.

4 Acknowledgments

The authors wish to express their thanks to James Helgren who participated in setting up the experiments described here and to Hojin Ahn and Professors Knowles and Sabersky for their interest and encouragement.

References

Campbell, C. S., and Brennen, C. E., 1985, "Computer Simulation of Granular Shear Flows," *J. Fluid Mech.*, Vol. 151, p. 167.

Goldsmith, W., 1960, *Impact: The Theory and Physical Behavior of Colliding Solids*, Edward Arnold, London.

Hutchings, I. M., 1974, "The Erosion of Ductile Metals by Solid Particles," Ph.D. Thesis, Univ. of Cambridge, Cambridge, U.K.

Jenkins, J. T., and Savage S. B., 1983, "A Theory for the Rapid Flow of Identical, Smooth, Nearly Elastic Particles," *J. Fluid Mech.*, Vol. 130, p. 187.

Johnson, K. L., 1985, *Contact Mechanics*, Cambridge Univ. Press, U.K.

Lun, C. K. K., Savage, S. B., Jeffrey, D. J., and Chepurniy, N., 1984, "Kinetic Theories for Granular Flow: Inelastic Particles in Couette Flow and Slightly Inelastic Particles in a General Flowfield," *J. Fluid Mech.*, Vol. 140, p. 223.

Maw, N., Barber, J. R., and Fawcett, J. N., 1976, "The Oblique Impact of Elastic Spheres," *Wear*, Vol. 38, p. 101.

Maw, N., Barber, J. R., and Fawcett, J. N., 1981, "The Role of Tangential Compliance in Oblique Impact," *ASME J. Lub. Tech.*, Series F, Vol. 103, p. 74.

Walton, O. R., 1984, "Computer Simulation of Particulate Flow," *Energy and Tech. Review*, Lawrence Livermore Laboratory, May 1984, p. 24.

Zener, C., 1941, "The Intrinsic Inelasticity of Large Plates," *Phys. Rev.*, Vol. 59, p. 669.

Ratner, S. B., and Styller, E. E., 1981, "Characteristics of Impact Friction and Wear of Polymeric Materials," *Wear*, Vol. 73, p. 213.

Downloaded 03 May 2010 to 171.66.16.244. Redistribution subject to ASME license or copyright; see http://www.asme.org/terms/Terms_Use.cfm

Anisotropic Plates With Various Openings Under Uniform Loading or Pure Bending

Chyanbin Hwu
Associate Professor,
Institute of Aeronautics and Astronautics,
National Cheng Kung University,
Tainan, Taiwan 70101

In the case when an anisotropic plate contains a triangular, oval, or square opening, the only solution available in the literature is an approximate solution for orthotropic plates with openings, which was obtained by Lekhnitskii using the complex variable formulation. Solutions for any kind of anisotropic plates with various openings are presented in this paper by applying the Stroh formalism and using the technique of conformal mapping. Unlike the former results, which have different orders of approximation for different openings, the solutions presented here have only one simple unified expression for various openings such as the ellipse, circle, crack, triangle, oval, and square. Two special loading conditions are considered: one is uniform loading, the other is pure bending. Through the use of identities developed in the literature, the hoop stress along the opening boundary is obtained in real form. The results show that the effect of anisotropy on the stress concentration is totally determined through the fundamental elasticity matrices N_1 and N_3 introduced by Stroh.

1 Introduction

The problem of determining stress distributions induced by openings has aroused considerable interest for almost half a century. Of various openings, the elliptic shape and its geometric limits, such as circles and cracks, have evoked the most interest among researchers. If the stress concentration is of more concern, optimization in a class of hole shapes (Durelli and Rajaiah, 1979; Dhir, 1981) has shown that the optimized hole is not necessary an ellipse. In the literature, however, there are very few works dealing with openings differing from an ellipse. Evan-Iwanoski (1956) used the complex variable approach developed by Muskhelishvili (1953) to derive the stress solutions for an infinite isotropic plate with a triangular inlay. A similar approach has been applied to the problem of an isotropic plate with rigid rectangular inclusions by Yu (1952) and Chang and Conway (1968). For orthotropic plates with rectangular openings, work has been done by Jong (1981), Rajaiah and Naik (1983). Their studies were based on the solutions given by Lekhnitskii (1968), which are only approximate solutions due to the mathematical difficulties involved.

In Lekhnitskii's approach (1968), the state of generalized plane stress or plane strain is the restrictive condition. This implies that at each point of the anisotropic plate there is a plane of elastic symmetry which is parallel to the middle plane of a thin plate, or normal to the generator of a long cylinder. Therefore, the solutions obtained by using this approach are valid only for monoclinic materials, and in-plane loading will not induce antiplane displacement or transverse shear. Furthermore, a special treatment is also required for degenerate anisotropic elastic materials. However, for the general anisotropic materials it is not always possible to treat the in-plane and antiplane deformations independently, and this approach cannot be applied.

In my recent work (Hwu and Ting, 1989), an analytical solution for the anisotropic plate with an elliptic inclusion subjected to the uniform loadings at infinity has been obtained by using the Stroh formalism (Eshelby et al., 1953; Stroh, 1958; Barnett and Lothe, 1973 and 1975; Chadwick and Smith, 1977; Ting, 1986) instead of the classical formulation (Lekhnitskii, 1963 and 1968). The results are valid for any kind of anisotropic materials including monoclinic materials and degenerate materials such as isotropic materials. In the case when the anisotropic plate contains a triangular, oval, or square opening, the exact solution has not yet been found. The only analytical solution available in the literature is an approximate solution for orthotropic plates (Lekhnitskii, 1968). To find solutions valid for general anisotropic plates, the Stroh formalism has been applied. In order to obtain an exact solution for various openings, we use the technique of conformal mapping. Instead of considering the opening to be slightly different from an ellipse and introducing a small parameter which will characterize the deviation of the opening from an ellipse, we treat the opening as itself. In the former case, the stress function is approximated by using that of the elliptic opening due to the difficulties of finding the exact and explicit form. In the

Contributed by the Applied Mechanics Division of THE AMERICAN SOCIETY OF MECHANICAL ENGINEERS for presentation at the Winter Annual Meeting, Dallas, Texas, Nov. 25-30,1990.

Discussion on this paper should be addressed to the Technical Editor, Leon M. Keer, The Technological Institute, Northwestern University, Evanston, IL 60208, and will be accepted until two months after final publication of the paper itself in the JOURNAL OF APPLIED MECHANICS. Manuscript received by the ASME Applied Mechanics Division, February 13, 1989; final revision, August 5, 1989.
Paper No. 90-WA/APM-17.

Copyright © 1990 by ASME
Downloaded 03 May 2010 to 171.66.16.244. Redistribution subject to ASME license or copyright; see http://www.asme.org/terms/Terms_Use.cfm

latter, an implicit stress function has been used to avoid the possible mathematical difficulties. Explicit solutions are obtained for the stresses along the opening boundary through the use of some relations derived in this paper. In some cases the requirement of conformal mapping cannot be satisfied, the solutions for those cases are therefore not exact, but approximate (Hwu, 1990).

Utilizing the identities developed in the literature (Ting, 1986; Hwu and Ting, 1989), which enables us to convert the complex form solution into a real form, the hoop stresses along the opening are then expressed in real form. Two different loading conditions are considered in this study. One is uniform loading, the other is pure bending. Since the openings of the ellipse, circle, triangle, oval, square, . . . , etc. can be represented by using one expression, the final result has only one simple unified expression for each loading condition. The comparison of this general unified result with special cases given in the literature shows that the solutions presented here are accurate. The effect of anisotropy, the opening shape, the loading direction, and the location on the stress concentration along the opening can then be studied through this unified expression. For the opening subjected to the unidirectional tension (or compression) parallel to the x_1-axis, the stress concentration at the end points of the major axis of the opening is found to be independent of the shape of the opening. This same phenomenon has been found for the special case of the elliptic opening (Hwu and Ting, 1989). After simplifying the solutions for isotropic materials, the stress concentration along the opening is obtained in a simple form, and is independent of the material constants.

2 Basic Equations for Two-Dimensional Anisotropic Elasticity

In a fixed cartesian coordinate system x_i, $i = 1, 2, 3$, let u_i, σ_{ij}, ϵ_{ij} be, respectively, the displacement, stress, and strain. The strain-displacement equations, the stress-strain laws, and the equations of equilibrium are

$$\epsilon_{ij} = \frac{1}{2}(u_{i,j} + u_{j,i}), \tag{1}$$

$$\sigma_{ij} = C_{ijks}\epsilon_{ks}, \tag{2}$$

$$C_{ijks}u_{k,sj} = 0, \tag{3}$$

where repeated indices imply summation, a comma stands for differentiation, and C_{ijks} are the elastic constants which are assumed to be fully symmetric and positive definite. For two-dimensional problems, u_i can be assumed to depend on x_1 and x_2 only. Based on this assumption and the basic equations (1) to (3), the general solutions for u_i and σ_{ij} can then be obtained (Hwu and Ting, 1989). Following Stroh's formulation (Stroh, 1958; Ting, 1986), we first find the eigenvalues p and eigenvectors ξ of the following eigenrelation

$$\mathbf{N}(\omega)\xi = p(\omega)\xi, \tag{4}$$

$$\mathbf{N}(\omega) = \begin{bmatrix} \mathbf{N}_1(\omega) & \mathbf{N}_2(\omega) \\ \mathbf{N}_3(\omega) & \mathbf{N}_1^T(\omega) \end{bmatrix}, \quad \xi = \begin{bmatrix} \mathbf{a} \\ \mathbf{b} \end{bmatrix}, \tag{5}$$

$$\begin{aligned} \mathbf{N}_1(\omega) &= -\mathbf{T}^{-1}(\omega)\mathbf{R}^T(\omega), \\ \mathbf{N}_2(\omega) &= \mathbf{T}^{-1}(\omega) = \mathbf{N}_2^T(\omega), \\ \mathbf{N}_3(\omega) &= \mathbf{R}(\omega)T^{-1}(\omega)\mathbf{R}^T(\omega) - \mathbf{Q}(\omega) = \mathbf{N}_3^T(\omega), \end{aligned} \tag{6}$$

where the superscript T stands for the transpose, the 3×3 real matrices $\mathbf{Q}$, $\mathbf{R}$, $\mathbf{T}$ are

$$\begin{aligned} Q_{ik}(\omega) &= C_{ijks}n_j n_s \quad , \\ R_{ik}(\omega) &= C_{ijks}n_j m_s \quad , \\ T_{ik}(\omega) &= C_{ijks}m_j m_s \quad , \end{aligned} \tag{7}$$

$$\begin{aligned} \mathbf{n}(\omega) &= (\cos\omega, \sin\omega, 0) \quad , \\ \mathbf{m}(\omega) &= (-\sin\omega, \cos\omega, 0) \quad , \end{aligned} \tag{8}$$

and ω is an arbitrary real parameter. There are six eigenvalues $p_\alpha(\omega)$, $\alpha = 1, 2, \ldots, 6$, which come in three pairs of complex conjugates (Eshelby et al., 1953). We let

$$p_{\alpha+3}(\omega) = \bar{p}_\alpha(\omega), \; Imp_\alpha(\omega) > 0, \; \alpha = 1, 2, 3,$$

in which Im stands for the imaginary part and the overbar denotes the complex conjugate. We then have

$$\xi_{\alpha+3} = \bar{\xi}_\alpha, \; \alpha = 1, 2, 3.$$

Assuming that $p_\alpha(\omega)$ are distinct, it can be shown that the 6-vector ξ_α, and hence its 3-vectors $\mathbf{a}_\alpha$, $\mathbf{b}_\alpha$, are independent of ω. We now introduce the 3×3 matrices

$$\mathbf{A} = [\mathbf{a}_1 \; \mathbf{a}_2 \; \mathbf{a}_3], \; \mathbf{B} = [\mathbf{b}_1 \; \mathbf{b}_2 \; \mathbf{b}_3], \tag{9}$$

and the diagonal matrices

$$\mathbf{F}(\mathbf{Z}) = \mathrm{diag}[f_1(z_1), f_2(z_2), f_3(z_3)], \tag{10}$$

$$z_\alpha = x_1 + p_\alpha(0)x_2, \tag{11}$$

where f_1, f_2, f_3 are arbitrary functions of their arguments. The general solutions for equations (1) to (3) can then be written as

$$\mathbf{u} = 2Re\{\mathbf{AF(Z)q}\}, \; \boldsymbol{\phi} = 2Re\{\mathbf{BF(Z)q}\}, \tag{12}$$

$$\sigma_{i1} = -\phi_{i,2}, \; \sigma_{i2} = \phi_{i,1}, \tag{13}$$

in which Re stands for the real part, $\mathbf{q}$ is an arbitrary complex constant, and $\boldsymbol{\phi}$ is the stress function. The stress and strain can then be calculated from equations (13) and (1). More generally, if $\mathbf{t}$ is the surface traction at a point on a curved boundary,

$$\mathbf{t} = \partial\boldsymbol{\phi}/\partial s, \tag{14}$$

where s is the arclength measured along the curved boundary in the direction such that, when one faces the direction of increasing s, the material is located on the right-hand side (Stroh, 1958). We see that equations (13) are special cases of equation (14) when the boundary is a plane parallel to the x_2-axis or the x_1-axis.

To consider the problem subjected to loadings at infinity, the general solution can also be modified as

$$\begin{aligned} \mathbf{u} &= \mathbf{u}^\infty + 2Re\{\mathbf{AF(Z)q}\}, \\ \boldsymbol{\phi} &= \boldsymbol{\phi}^\infty + 2Re\{\mathbf{BF(Z)q}\}, \end{aligned} \tag{15}$$

where $\mathbf{u}^\infty$, $\boldsymbol{\phi}^\infty$ represent the displacement and stress function of the plate without any disturbances such as inclusions or openings, which is subjected to given external loadings at infinity. From equation (11) and the fact that $\mathbf{A}$, $\mathbf{B}$ are independent of ω, we should notice that the general solution (equation (15)) depends on $\omega = 0$ only, and we could here set the arbitrary parameter $\omega = 0$ in equations (4) through (8). However, in the latter derivation we need $\mathbf{N}(\omega)$ and $p(\omega)$ for $\omega \neq 0$. It can be shown that $\mathbf{N}(\omega)$ is periodic in ω with periodicity π and $p(\omega)$, $p(0)$ are related by (Ting, 1982)

$$p(\omega) = \frac{p(0)\cos\omega - \sin\omega}{p(0)\sin\omega + \cos\omega}. \tag{16}$$

The general solution in equation (15) is valid for any anisotropic material whose eigenvalues p_α are distinct. For degenerate materials such as isotropic materials which have a repeated eigenvalue, a modified solution has been found by Ting (1982) and Ting and Hwu (1988). We hasten to add that real form solutions presented in this paper do not contain the eigenvalues p_α and the eigenvectors ξ_α. Therefore, those solutions are valid for degenerate materials.

Due to the orthogonality relation among the eigenvectors ξ_α derived by Stroh (1958), three real matrices has been introduced as

$$\begin{aligned} \mathbf{S} &= i(2\mathbf{AB}^T - \mathbf{I}) \\ \mathbf{H} &= 2i\mathbf{AA}^T, \; \mathbf{L} = -2i\mathbf{BB}^T, \end{aligned} \tag{17}$$

Downloaded 03 May 2010 to 171.66.16.244. Redistribution subject to ASME license or copyright; see http://www.asme.org/terms/Terms_Use.cfm

in which $\mathbf{I}$ is the unit matrix. $\mathbf{H}$ and $\mathbf{L}$ are symmetric and positive definite and $\mathbf{SH}$, $\mathbf{LS}$, $\mathbf{H}^{-1}\mathbf{S}$, $\mathbf{SL}^{-1}$ are antisymmetric. We can also prove that

$$\mathbf{HL}-\mathbf{SS}=\mathbf{I}. \tag{18}$$

An integral formalism to determine $\mathbf{S}$, $\mathbf{H}$, $\mathbf{L}$ directly from C_{ijks} has been introduced by Barnett and Lothe (1973) as

$$\mathbf{S}=\frac{1}{\pi}\int_0^{\pi}\mathbf{N}_1(\omega)d\omega\,,$$
$$\mathbf{H}=\frac{1}{\pi}\int_0^{\pi}\mathbf{N}_2(\omega)d\omega\,,\quad \mathbf{L}=\frac{-1}{\pi}\int_0^{\pi}\mathbf{N}_3(\omega)d\omega. \tag{19}$$

In equation (19), the need of determining the eigenvalues p and eigenvectors ξ is circumvented, and hence equation (19) applies regardless of whether p is repeated or not. We list next the expression for $\mathbf{N}_i(\omega)$, $i = 1, 2, 3$ and $\mathbf{H}$, $\mathbf{L}$, $\mathbf{S}$ for isotropic materials:

$$\mathbf{N}_1(\omega)=\frac{1}{2(1-\nu)}\begin{bmatrix}\sin 2\omega & -(1-2\nu)-\cos 2\omega & 0\\ 1-2\nu-\cos 2\omega & -\sin 2\,\omega & 0\\ 0 & 0 & 0\end{bmatrix},$$

$$\mathbf{N}_2(\omega)=\frac{1}{4\mu(1-\nu)}\begin{bmatrix}3-4\nu+\cos 2\omega & \sin 2\omega & 0\\ \sin 2\omega & 3-4\nu-\cos 2\omega & 0\\ 0 & 0 & 4(1-\nu)\end{bmatrix}, \tag{20a}$$

$$\mathbf{N}_3(\omega)=\frac{-\mu}{1-\nu}\begin{bmatrix}1+\cos 2\omega & \sin 2\omega & 0\\ \sin 2\omega & 1-\cos 2\omega & 0\\ 0 & 0 & 1-\nu\end{bmatrix}, \tag{20a}$$

and

$$\mathbf{S}=\frac{1-2\nu}{2(1-\nu)}\begin{bmatrix}0 & -1 & 0\\ 1 & 0 & 0\\ 0 & 0 & 0\end{bmatrix},$$

$$\mathbf{H}=\frac{1}{4(1-\nu)\mu}\begin{bmatrix}3-4\nu & 0 & 0\\ 0 & 3-4\nu & 0\\ 0 & 0 & 4(1-\nu)\end{bmatrix}, \tag{20b}$$

$$\mathbf{L}=\frac{\mu}{1-\nu}\begin{bmatrix}1 & 0 & 0\\ 0 & 1 & 0\\ 0 & 0 & 1-\nu\end{bmatrix},$$

where μ, ν are, respectively, the shear modulus and Poisson's ratio. For anisotropic materials, the general expression of $\mathbf{N}_i(\omega)$, $\mathbf{S}$, $\mathbf{H}$, $\mathbf{L}$ can be obtained from equations (6)–(8) and (19).

3 An Anisotropic Plate With a Special Kind of Opening

In this section various special kind of openings such as the ellipse, circle, crack, triangle, oval, and square are represented by a unified equation. Using this unified contour expression, the final results can then be written in one equation. Consider an opening, the contour of which is represented by

$$\left.\begin{aligned}x_1&=a(\cos\psi+\epsilon\cos k\psi)\\ x_2&=a(c\sin\psi-\epsilon\sin k\psi)\end{aligned}\right\}, \tag{21}$$

where $0 < c \le 1$, and k is an integer. When $\epsilon = 0$, we obtain an ellipse with semiaxes a and ac. In the case of $\epsilon = 0$, $c = 1$ and $\epsilon = 0$, $c \to 0$, the contour represents, respectively, a circle and a crack. When $c = 1$ and $k = 2$ the opening has three symmetry axes. With an appropriate selection of the parameter ϵ, the opening will differ from an equilateral triangle with rounded corners. When $c = 1$ and $k = 3$ there are four symmetry axes, and at some values of ϵ, the opening will differ little from a square with rounded corners. When $c < 1$ and $k = 3$ we will obtain ovals of a special type. Example is given in Fig. 1 for $c = 1$, $k = 4$, and $\epsilon = 0.1$, which is a pentagon.

An infinite plane with an opening represented by equation (21) is transformed to the ζ-plane with an opening in the shape of a unit circle $|\zeta| = 1$. The transformation function can be assumed as

$$z_\alpha=a\left[a_1\zeta+a_2\frac{1}{\zeta}+a_3\zeta^k+a_4\frac{1}{\zeta^k}\right]. \tag{22}$$

In order to make the transformation single-valued and conformal, it is necessary that all the roots of the equation

$$\frac{dz_\alpha(\zeta)}{d\zeta}=0 \tag{23}$$

be located inside the unit circle $|\zeta| = 1$. The ζ-plane is chosen so that the boundary of the opening corresponds to the unit circle $|\zeta| = 1$, and $|\zeta| \to \infty$ when $|z_\alpha| \to \infty$. Substituting equations (11) and (21) into equation (22) for the boundary, we obtain

$$a_1=\frac{1}{2}(1-ip_\alpha c),\quad a_2=\frac{1}{2}(1+ip_\alpha c),$$
$$a_3=\frac{\epsilon}{2}(1+ip_\alpha),\quad a_4=\frac{\epsilon}{2}(1-ip_\alpha). \tag{24}$$

Here, p_α has been used to substitute for $p_\alpha(0)$ because the general solution depends on $\omega = 0$ only, and we could omit the argument to simplify the formulation. Under the requirement that in any point outside the opening, the derivative of the transformation function is different from zero; $z_\alpha = z_\alpha(\zeta)$ will then have a single-valued inverse, that is, $\zeta = \zeta(z_\alpha)$.

Consider the plate subjected to uniform loading or pure bending at infinity, the technique of conformal transformation tells us that $\mathbf{F(Z)}$ may be chosen as

$$\mathbf{F}(\mathbf{Z})=\mathbf{F}^*(\zeta), \tag{25}$$

where F^* can be expressed as a polynomial. We now present the solutions for these two simple loading cases. For any other loading conditions, similar approaches can be applied.

3.1 Uniform Loading. A unidirectional tension (or compression) σ^∞, which makes an angle α with the positive x_1-axis (Fig. 1), is applied at infinity on the anisotropic plate with an opening represented by equation (21). The displacement $\mathbf{u}^\infty$ and stress function $\boldsymbol{\phi}^\infty$ shown in equation (15), which produce the given constant stresses σ_{ij}^∞ and strains ϵ_{ij}^∞, can be written as (Ting, 1988)

$$\mathbf{u}^\infty=x_1\boldsymbol{\epsilon}_1^\infty+x_2\boldsymbol{\epsilon}_2^\infty\,,$$
$$\boldsymbol{\phi}^\infty=x_1\mathbf{t}_2^\infty-x_2\mathbf{t}_1^\infty\,, \tag{26}$$

where

$$\boldsymbol{\epsilon}_1^\infty=\begin{Bmatrix}\epsilon_{11}^\infty\\ \epsilon_{12}^\infty\\ 2\epsilon_{13}^\infty\end{Bmatrix},\ \boldsymbol{\epsilon}_2^\infty=\begin{Bmatrix}\epsilon_{21}^\infty\\ \epsilon_{22}^\infty\\ 2\epsilon_{23}^\infty\end{Bmatrix},$$

$$\mathbf{t}_1^\infty=\begin{Bmatrix}\sigma_{11}^\infty\\ \sigma_{12}^\infty\\ \sigma_{13}^\infty\end{Bmatrix}=\begin{Bmatrix}\sigma^\infty\cos^2\alpha\\ \sigma^\infty\sin\alpha\cos\alpha\\ 0\end{Bmatrix}=\sigma^\infty\cos\alpha\mathbf{n}(\alpha), \tag{27}$$

Downloaded 03 May 2010 to 171.66.16.244. Redistribution subject to ASME license or copyright; see http://www.asme.org/terms/Terms_Use.cfm

$$\mathbf{t}_2^\infty = \begin{Bmatrix} \sigma_{21}^\infty \\ \sigma_{22}^\infty \\ \sigma_{23}^\infty \end{Bmatrix} = \begin{Bmatrix} \sigma^\infty \sin\alpha \cos\alpha \\ \sigma^\infty \sin^2\alpha \\ 0 \end{Bmatrix} = \sigma^\infty \sin\alpha\, \mathbf{n}(\alpha).$$

In equation (27) the strains ϵ_{ij}^∞ are determined from

$$\epsilon_{ij}^\infty = S_{ijks}\sigma_{ks}^\infty, \tag{28}$$

where S_{ijks} are the elastic compliances. We note that, for arbitrary uniform loading, σ_{ij}^∞ have to be prescribed in such a way that $\epsilon_{33}^\infty = 0$, which is the requirement of Stroh formalism. Furthermore, the rigid body translation and rotation have been neglected in equation (26).

The boundary conditions along the opening and at infinity can be satisfied if

$$\left.\begin{array}{ll} \boldsymbol{\phi} = \mathbf{0} & \text{along the opening boundary} \\ \boldsymbol{\phi} \to \boldsymbol{\phi}^\infty & \text{at infinity} \end{array}\right\}. \tag{29}$$

Here equations (14) and (15) have been used. To satisfy equation $(29)_2$, the polynomial $\mathbf{F}^*(\zeta)$ shown in equation (25) should have a negative power which can make the last term of equation $(15)_2$ vanish. Along the opening boundary (x_1, x_2) can be represented by equation (21), and $\zeta = e^{i\psi}$. Substituting this contour expression and equations (25), (26) into the general solution of equation (15), the traction-free boundary condition (equation $(29)_1$) along the opening suggests that the arbitrary function $\mathbf{F}(\mathbf{Z})$ be chosen as the combination of ζ^{-1} and ζ^{-k}. Therefore, the general solution for the plate subjected to uniform loading can now be written as

$$\begin{aligned} \mathbf{u} &= x_1\boldsymbol{\epsilon}_1^\infty + x_2\boldsymbol{\epsilon}_2^\infty + 2\sum_{l=1,k} Re\{\mathbf{A}\mathbf{F}_l(\mathbf{Z})\mathbf{q}_l\}\ , \\ \boldsymbol{\phi} &= x_1\mathbf{t}_2^\infty - x_2\mathbf{t}_1^\infty + 2\sum_{l=1,k} Re\{\mathbf{B}\mathbf{F}_l(\mathbf{Z})\mathbf{q}_l\}\ , \end{aligned} \tag{30}$$

where k is the shape parameter which has been described at the beginning of this section. $\mathbf{F}_l(\mathbf{Z})$ is taken as

$$\mathbf{F}_l(\mathbf{Z}) = \mathrm{diag}[\zeta_1^{-l}, \zeta_2^{-l}, \zeta_3^{-l}],\ l = 1,\ k. \tag{31}$$

Along the boundary of the opening of equation (21),

$$\begin{aligned} \zeta_\alpha &= \cos\psi + i\sin\psi,\ \alpha = 1,\ 2,\ 3, \\ \mathbf{F}_l(\mathbf{Z}) &= (\cos l\psi - i\sin l\psi)\mathbf{I},\ l = 1,\ k. \end{aligned} \tag{32}$$

We now replace the complex constant $\mathbf{q}_l$ by

$$\mathbf{q}_l = \mathbf{A}^T\mathbf{g}_l + \mathbf{B}^T\mathbf{h}_l,\ l = 1,\ k, \tag{32}$$

where $\mathbf{g}_l$ and $\mathbf{h}_l$ are real. Since $|\zeta| \to \infty$ when $|z| \to \infty$, the boundary condition at infinity, equation $(29)_2$, is satisfied. To determine the unknown constants $\mathbf{g}_l$ and $\mathbf{h}_l$, we apply equation $(29)_1$. By substituting equations (21), (32), (33), into $(30)_2$ and using equation (17), the traction-free boundary condition along the opening gives us

$$\begin{aligned} &\mathbf{g}_1 = -a\mathbf{t}_2^\infty,\ \mathbf{g}_k = -a\epsilon\mathbf{t}_2^\infty, \\ &\mathbf{h}_i = a\mathbf{L}^{-1}(c\mathbf{t}_1^\infty - \mathbf{S}^T\mathbf{t}_2^\infty),\ \mathbf{h}_k = -a\epsilon\mathbf{L}^{-1}(\mathbf{t}_1^\infty + \mathbf{S}^T\mathbf{t}_2^\infty). \end{aligned} \tag{34}$$

3.2 Pure Bending. We now consider the plate subjected to pure bending M in a direction at an angle α with the positive x_1-axis (Fig. 1). The stress function $\boldsymbol{\phi}^\infty$ can be written as

$$\begin{aligned} \boldsymbol{\phi}^\infty &= -\frac{M}{2I}x_2^{*2}\mathbf{n}(\alpha) \\ &= -\frac{M}{2I}(x_1\sin\alpha - x_2\cos\alpha)^2\mathbf{n}(\alpha), \end{aligned} \tag{35}$$

where I is the moment inertia of the plate cross-section normal to the loaded axis. The displacement function $\mathbf{u}^\infty$ can then be determined by using equations (13), (28), and (1). The boundary conditions can also be expressed by using equation (29). Similar to the procedure we used in the case of uniform loading,

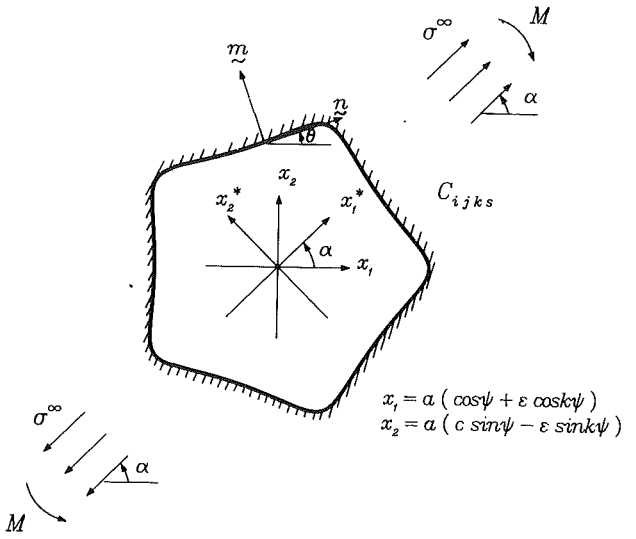


Fig. 1 Loading and geometry ($a = 1$, $c = 1$, $\epsilon = 0.1$, $k = 4$)

the general solution for the plate under pure bending can be written as

$$\begin{aligned} \mathbf{u} &= \mathbf{u}^\infty + 2\sum_{\substack{l=0,2,k-1 \\ k+1,2k}} Re\{\mathbf{A}\mathbf{F}_l(\mathbf{Z})\mathbf{q}_l\}, \\ \boldsymbol{\phi} &= \boldsymbol{\phi}^\infty + 2\sum_{\substack{l=0,2,k-1 \\ k+1,2k}} Re\{\mathbf{B}\mathbf{F}_l(\mathbf{Z})\mathbf{q}_l\}, \end{aligned} \tag{36}$$

where $\mathbf{F}_l(\mathbf{Z})$, $\mathbf{q}_l$ are the same as equations (31) and (33), except l is now extended to 0, 2, $k-1$, $k+1$ and $2k$. By substituting equations (21), (32), (33), (35) into $(36)_2$ and using (17), $(29)_1$, the unknown constants $\mathbf{g}_l$ and $\mathbf{h}_l$ can be determined as

$$\left.\begin{aligned} \mathbf{g}_l &= \frac{Ma^2}{2I}c_l\mathbf{n}(\alpha) \\ \mathbf{h}_l &= \frac{Ma^2}{2I}\mathbf{L}^{-1}(s_l\mathbf{I} + c_l\mathbf{S}^T)\mathbf{n}(\alpha) \end{aligned}\right\} l = 2,\ k-1,\ k+1,\ 2k, \tag{37}$$

where

$$\begin{aligned} c_2 &= \frac{1}{4}[1 - c^2 - (1+c^2)\cos 2\alpha], & s_2 &= \frac{-c}{2}\sin 2\alpha\ , \\ c_{k-1} &= \frac{\epsilon}{2}[(1-c) - (1+\epsilon)\cos 2\alpha], & s_{k-1} &= \frac{\epsilon}{2}(1+c)\sin 2\alpha\ , \\ c_{k+1} &= \frac{\epsilon}{2}[(1+c) - (1-c)\cos 2\alpha], & s_{k+1} &= \frac{\epsilon}{2}(1-c)\sin 2\alpha\ , \\ c_{2k} &= \frac{-\epsilon^2}{2}\cos 2\alpha, & s_{2k} &= \frac{\epsilon^2}{2}\sin 2\alpha\ . \end{aligned} \tag{38}$$

In the foregoing equations we omit the solution corresponding to $\mathbf{g}_0$ and $\mathbf{h}_0$, because the constant stress function $\boldsymbol{\phi}$ does not produce stress.

4 Stresses Along the Boundary of the Opening

Let $\mathbf{n}(\theta)$, $\mathbf{m}(\theta)$ given in equation (8) be, respectively, the unit vector tangent and normal to the opening boundary (Fig. 1). The angle θ is directed counterclockwise from the positive x_1-axis to the direction of $\mathbf{n}(\theta)$. For any point along the opening boundary, the unit tangent $\mathbf{n}(\theta)$ can also be expressed by $-d\mathbf{x}$ where $\mathbf{x}$ is given in equation (21). Therefore, we have

Downloaded 03 May 2010 to 171.66.16.244. Redistribution subject to ASME license or copyright; see http://www.asme.org/terms/Terms_Use.cfm

$$\left.\begin{aligned}\frac{-dx_1}{\rho d\psi} &= \frac{a}{\rho}(\sin\psi + k\epsilon\sin k\psi) = \cos\theta \\ \frac{-dx_2}{\rho d\psi} &= \frac{-a}{\rho}(c\cos\psi - k\epsilon\cos k\psi) = \sin\theta\end{aligned}\right\}, \tag{39}$$

where

$$\rho^2 = a^2\{k^2\epsilon^2 + \sin^2\psi + c^2\cos^2\psi + 2k\epsilon\sin\psi\sin k\psi - 2ck\epsilon\cos\psi\cos k\psi\}. \tag{40}$$

If $\mathbf{t}_m$ is the surface traction at a point along the opening boundary of which the normal is $\mathbf{m}$ we have, by equations (14) and (8),

$$\mathbf{t}_m = \boldsymbol{\phi}_{,n} = \cos\theta\boldsymbol{\phi}_{,1} + \sin\theta\boldsymbol{\phi}_{,2}. \tag{41}$$

The normal stresses σ_{mm} and the shear stresses σ_{mn} and σ_{m3} along the boundary are

$$\sigma_{mm} = \mathbf{m}^T(\theta)\mathbf{t}_m,\ \sigma_{mn} = \mathbf{n}^T(\theta)\mathbf{t}_m,\ \sigma_{m3} = (\mathbf{t}_m)_3. \tag{42}$$

Similarly, for the traction $\mathbf{t}_n$ on the surface of which the normal is $\mathbf{n}$,

$$\mathbf{t}_n = -\boldsymbol{\phi}_{,m} = \sin\theta\boldsymbol{\phi}_{,1} - \cos\theta\boldsymbol{\phi}_{,2}. \tag{43}$$

The normal stress (or the hoop stress) σ_{nn} and the shear stresses σ_{nm}, σ_{n3} are determined from

$$\sigma_{nn} = \mathbf{n}^T(\theta)\mathbf{t}_n,\ \sigma_{nm} = \mathbf{m}^T(\theta)\mathbf{t}_n,\ \sigma_{n3} = (\mathbf{t}_n)_3, \tag{44}$$

where σ_{nm} can be proved to be equal to σ_{mn} shown in equation (42).

Using the solutions shown in equations (30) and (34) for uniform loading and equations (36) and (37) for pure bending, we can calculate the stresses along the opening boundary by applying equations (41)–(44). In the following, we will present a real-form solution for the hoop stress σ_{nn} along the opening boundary. All the other stress components can be obtained by using a similar approach. To obtain the real form solution of σ_{nn}, it is necessary to calculate $\mathbf{F}_{l,m}(\mathbf{Z})$. We first notice that

$$\frac{\partial}{\partial x_1}f(z_\alpha) = \frac{df}{dz_\alpha},\ \frac{\partial}{\partial x_2}f(z_\alpha) = p_\alpha(0)\frac{df}{dz_\alpha},\ \alpha \text{ not summed.}$$

Hence,

$$\frac{\partial}{\partial m}f(z_\alpha) = p_\alpha(\theta)[p_\alpha(0)\sin\theta + \cos\theta]\frac{df}{dz_\alpha}; \tag{45}$$

in equation (45), equation (16) has been used. Differentiating both sides of equation (11), and evaluating the results along the opening by using equation (39), we have

$$dz_\alpha = -\rho[\cos\theta + p_\alpha(0)\sin\theta]d\psi. \tag{46}$$

From equation (32), we know that along the opening boundary,

$$d\zeta_\alpha = (-\sin\psi + i\cos\psi)d\psi. \tag{47}$$

Using equations (45)–(47), we obtain

$$\frac{\partial\zeta_\alpha^{-l}}{\partial m} = \frac{l}{\rho}(\sin l\psi + i\cos l\psi)p_\alpha(\theta). \tag{48}$$

Therefore, from equations (31) and (48), along the opening boundary we have

$$\mathbf{F}_{l,m}(Z) = \frac{l}{\rho}(\sin l\psi + i\cos l\psi)\mathbf{P}(\theta), \tag{49}$$

where $\mathbf{P}(\theta)$ is defined as

$$\mathbf{P}(\theta) = \mathrm{diag}[p_1(\theta), p_2(\theta), p_3(\theta)]. \tag{50}$$

In order to convert the complex form into a real form, we introduce the identities (Hwu and Ting, 1989)

$$\begin{aligned}2\mathbf{B}\mathbf{P}(\theta)\mathbf{A}^T &= \mathbf{N}_1^T(\theta) - i[\mathbf{N}_1^T(\theta)\mathbf{S}^T + \mathbf{N}_3(\theta)\mathbf{H}], \\ 2\mathbf{B}\mathbf{P}(\theta)\mathbf{B}^T &= \mathbf{N}_3(\theta) - i[\mathbf{N}_3(\theta)\mathbf{S} - \mathbf{N}_1^T(\theta)\mathbf{L}].\end{aligned} \tag{51}$$

We are now ready to express σ_{nn} in a real form not containing the eigenvalues p_α and eigenvectors ξ_α.

4.1 Uniform Loading. For the plate subjected to uniform loading, the stress function $\boldsymbol{\phi}$ is given in equations (30), (33), and (34). The hoop stress σ_{nn} can then be obtained from equations (43) and $(44)_1$. By applying equations (49) and (51), one should be able to obtain the real form solution of σ_{nn}. Through the use of equation (18) and the relation between θ and ψ given in equation (39), the final simplified result is

$$\begin{aligned}\mathbf{t}_n &= \cos\theta\,\mathbf{t}_1^\infty + \sin\theta\mathbf{t}_2^\infty \\ &\quad + \frac{1}{\rho}\mathbf{N}_3(\theta)\mathbf{L}^{-1}\{[\rho\cos\theta - (1+c)a\sin\psi]\mathbf{t}_1^\infty + [\rho\sin\theta \\ &\quad + (1+c)a\cos\psi]\mathbf{t}_2^\infty\} \\ &\quad + [\mathbf{N}_1^T(\theta) - \mathbf{N}_3(\theta)\mathbf{S}\mathbf{L}^{-1}]\{-\sin\theta\mathbf{t}_1^\infty + \cos\theta\mathbf{t}_2^\infty\}, \\ \sigma_{nn} &= \mathbf{n}^T(\theta)\mathbf{t}_n.\end{aligned} \tag{52}$$

For the plate under a unidirectional tension (or compression) σ^∞ directed at an angle α with the positive x_1-axis, by substituting $\mathbf{t}_1^\infty$ and $\mathbf{t}_2^\infty$ given in equation (27) into equation (52), we obtain

$$\begin{aligned}\sigma_{nn}/\sigma^\infty &= \cos^2(\theta-\alpha) \\ &\quad + \left[\cos(\theta-\alpha) - \frac{(1+c)a}{\rho}\sin(\psi-\alpha)\right]\mathbf{n}^T(\theta)\mathbf{N}_3(\theta)\mathbf{L}^{-1}\mathbf{n}(\alpha) \\ &\quad - \sin(\theta-\alpha)\mathbf{n}^T(\theta)[\mathbf{N}_1^T(\theta) - \mathbf{N}_3(\theta)\mathbf{S}\mathbf{L}^{-1}]\mathbf{n}(\alpha).\end{aligned} \tag{53}$$

The result of equation (53) is valid for any kind of anisotropic material. The shape of the opening can be an ellipse, circle, crack, triangle, oval, square, . . . , etc., which satisfies equation (21). The single-valued requirement stated in equation (32) should be satisfied in order to have an exact solution. Otherwise, the solutions are only approximate due to nonconformal transformation (Hwu, 1990). In this solution, the material properties are represented by $\mathbf{N}_1$, $\mathbf{N}_3$, $\mathbf{S}$ and $\mathbf{L}$. However, equation (19) shows that $\mathbf{S}$ and $\mathbf{L}$ can be obtained by the integrals of $\mathbf{N}_1$ and $\mathbf{N}_3$. Therefore, the effect of anisotropy on the hoop stress σ_{nn} is totally determined through the fundamental elasticity matrices $\mathbf{N}_1$ and $\mathbf{N}_3$. The shape of the opening can be distinguished by c, ρ, and ψ. The effect of the loading direction is then reflected by α. To find the location of maximum or minimum hoop stress, all we have to do is to differentiate σ_{nn} with respect to θ and set the result to zero. Note that ψ and ρ are functions of θ, which can be seen in equations (39) and (40).

At the point when $\psi = \alpha + n\pi$ the hoop stress depends only upon θ and α, where θ can be determined by the shape parameters a, c, k, ϵ and the position variable ψ through the use of equation (39). However, when $\sin\psi = \sin k\psi = 0$, i.e., $\psi = m\pi$, θ will be independent of the shape parameters and equal to $\pm\pi/2$. In other words, when the unidirectional tension (or compression) is parallel to the x_1-axis ($\alpha = 0$), the hoop stress at the point where $\theta = \pm\pi/2$ is independent of the shape of the opening. This same phenomenon has been found for the special case of the elliptic opening (Hwu and Ting, 1989).

For isotropic materials, by using equation (20) we have

$$\begin{aligned}\mathbf{n}^T(\theta)\mathbf{N}_3(\theta)\mathbf{L}^{-1}\mathbf{n}(\alpha) &= -2\cos(\theta-\alpha), \\ \mathbf{n}^T(\theta)[\mathbf{N}_1^T(\theta) - \mathbf{N}_3(\theta)\mathbf{S}\mathbf{L}^{-1}]\mathbf{n}(\alpha) &= \sin(\theta-\alpha).\end{aligned} \tag{54}$$

Downloaded 03 May 2010 to 171.66.16.244. Redistribution subject to ASME license or copyright; see http://www.asme.org/terms/Terms_Use.cfm

Hence, equation (53) can now be reduced to

$$\sigma_{nn}=\sigma^{\infty}\left\{-1+\frac{2(1+c)a}{\rho}\sin(\psi-\alpha)\cos(\theta-\alpha)\right\}. \quad (55)$$

For the opening subjected to a uniform tensile stress perpendicular to x_1-axis, $\alpha = \pi/2$, the stress concentration at the end points of the major axis of the opening, $\psi = 0, \pi$, (or $\theta = \pm\pi/2$) equals

$$\sigma_{nn}/\sigma^{\infty}=-1\pm\frac{2(1+c)a}{\rho},\ \rho=a|c\pm k\epsilon|,$$

where the $\pm$ sign depends on the shape of the opening and the position of the point and can easily be determined by equations (40) and (55). For elliptic opening $\epsilon = 0$, and the plus sign has been determined for both of the end points, so

$$\sigma_{nn}/\sigma^{\infty}=1+\frac{2}{c},$$

which is a well-known result for isotropic plates (Timoshenko and Goodier, 1970).

4.2 Pure Bending. For the plate under pure bending, the stress function ϕ is given in equations (36), (31)–(33), (35), (37), and (38). Following the same procedure as the case of uniform loading, the final simplified result can now be written as

$$\sigma_{nn}/\left(\frac{Ma}{I}\right)=s_0^*\cos^2(\theta-\alpha)+\frac{ac^*}{2\rho}\mathbf{n}^T(\theta)\mathbf{N}_3(\theta)\mathbf{L}^{-1}\mathbf{n}(\alpha)$$
$$+\frac{as^*}{2\rho}\mathbf{n}^T(\theta)[\mathbf{N}_1^T(\theta)-\mathbf{N}_3(\theta)\mathbf{S}\mathbf{L}^{-1}]\mathbf{n}(\alpha), \quad (56)$$

where

$$s_0^*=\sin(\psi-\alpha)-\epsilon\sin(k\psi+\alpha)-(1-c)\cos\alpha\sin\psi,$$
$$s^*=-\sum_{\substack{l=2,k-1\\k+1,2k}}l(c_l\sin l\psi+s_l\cos l\psi)$$
$$c^*=-\sum_{\substack{l=2,k-1\\k+1,2k}}l(s_l\sin l\psi+c_l\cos l\psi). \quad (57)$$

The results for equations (56) and (57) can be further simplified for any special kind of opening. For example, $\epsilon = 0$, $ac = b$ for an elliptic opening; $\epsilon = 0$, $c = 1$ for a circular hole; $\epsilon = 0$, $c \to 0$ for a crack; $c = 1$, $k = 2$ for a triangular opening; $c = 1$, $k = 3$ for a square opening; $0 < c < 1$, $k = 3$ for an oval opening. For isotropic materials, by applying equation (54), the hoop stress shown in equation (56) can be reduced to

$$\sigma_{nn}=\frac{Ma}{I}\{s_0^*\cos^2(\theta-\alpha)$$
$$+\frac{a}{2\rho}[s^*\sin(\theta-\alpha)-2c^*\cos(\theta-\alpha)]\}. \quad (58)$$

5 Concluding Remarks

We have obtained in this paper solutions to the problem of a special kind of opening in an infinite anisotropic medium subjected to uniform loading or pure bending. The hoop stress along the opening boundary is obtained in real form. Several analytical solutions for various special cases have been given in the literature, for example, the exact solutions for the isotropic or orthotropic plates with elliptic openings (Muskhelishvili, 1953; Lekhnitskii, 1968), the approximate solutions for the orthotropic plates with triangular, square, or oval openings (Lekhnitskii, 1968), and the solutions for the plates containing cracks (Berezhnitskii and Onyshko, 1981). Comparison with the above solutions show that the solutions presented here are accurate as well as simple, unified, and general. The optimized hole can then be obtained through this unified expression. Discussions for the case when the opening degenerates to a crack have been given in (Hwu and Ting, 1989).

The results for the hoop stress show that the effect of anisotropy on the stress concentration along the opening boundary is totally determined through the fundamental elasticity matrices $\mathbf{N}_1$ and $\mathbf{N}_3$ introduced by Stroh. By a numerical calculation, we can find the location of maximum or minimum hoop stress, which is not necessarily the same as when the material is isotropic. Finally, by using the same approach presented in this paper, the problem for a rigid inclusion with a special kind of shape can be solved. The only difference is the boundary conditions which is replaced by $\mathbf{u} = \mathbf{0}$.

Acknowledgments

The author would like to thank Prof. T. C. T. Ting for many helpful discussions. The work presented here has been supported by the National Science Council, Republic of China, through Grant No. NSC 78-0401-E006-31.

References

Barnett, D. M., and Lothe, J., 1973, "Synthesis of the Sextic and the Integral Formalism for Dislocation, Green's Function, and Surface Waves in Anisotropic Elastic Solids," *Phys. Norv.*, Vol. 7, pp. 13–19.

Barnett, D. M., and Lothe, J., 1975, "Line Force Loadings on Anisotropic Half-Spaces and Wedges," *Phys. Norv.*, Vol. 8, pp. 13–22.

Berezhnitskii, L. T., and Onyshko, L. I., 1981, "Fundamental Solutions for an Anisotropic Plate with a Crack," *Sov. Mat. Sci.*, Vol. 17, No. 1, pp. 69–73.

Chadwick, P., and Smith, G. D., 1977, "Foundations of the Theory of Surface Waves in Anisotropic Elastic Materials," *Adv. Appl. Mech.*, Vol. 17, pp. 303–376.

Chang, C. S., and Conway, H. D., 1968, "A Parametric Study of a Complex Variable Method for Analyzing the Stress in an Infinite Plate Containing a Rigid Rectangular Inclusion," *Int. J. Solids Structures*, Vol. 4, pp. 1057–1066.

Dhir, S. K., 1981, "Optimization in a Class of Hole Shapes in Plate Structures," ASME Journal of Applied Mechanics, Vol. 48, pp. 905–908.

Durelli, A. J., and Rajaiah, K., 1979, "Optimum Hole Shapes in Finite Plates Under Uniaxial Load," ASME Journal of Applied Mechanics, Vol. 46, pp. 691–695.

Eshelby, J. D., Read, W. T., and Shockley, W., 1953, "Anisotropic Elasticity with Applications to Dislocation Theory," *Act. Met.*, Vol. 1, pp. 251–259.

Evan-Iwanowski, R. M., 1956, "Stress Solutions for an Infinite Plate with Triangular Inlay," ASME Journal of Applied Mechanics, Vol. 23, pp. 336–338.

Hwu, C., and Ting, T. C. T., "Solutions for the Anisotropic Elastic Wedge at Critical Wedge Angles," to appear in *J. Elasticity*.

Hwu, C., and Ting, T. C. T., 1989, "Two-Dimensional Problems of the Anisotropic Elastic Solid with an Elliptic Inclusion," *Q. J. Mech. Appl. Math*, Vol. 42, pt. 4, pp. 553–572.

Hwu, C., 1990, "Composite Laminates With Various Cutouts Under Inplane Loading," National Science Council, R.O.C., Report No. NSC-78-0401-E006-31.

Jong, T. D., 1981, "Stresses Around Rectangular Holes in Orthotropic Plates," *J. Comp. Mat.*, Vol. 15, pp. 311–328.

Lekhnitskii, S. G., 1963, *Theory of Elasticity of an Anisotropic Body*, Holden-Day, San Francisco, Calif.

Lekhnitskii, S. G., 1968, *Anisotropic Plates*, Gordon and Breach.

Muskhelishvili, N. I., 1953, *Some Basic Problems of the Mathematical Theory of Elasticity*, Noordhoff Pub., Groningen.

Rajaiah, K., and Naik, N. K., 1983, "Optimum Quasi-Rectangular Holes in

Downloaded 03 May 2010 to 171.66.16.244. Redistribution subject to ASME license or copyright; see http://www.asme.org/terms/Terms_Use.cfm

Infinite Orthotropic Plates Under Inplane Loadings," ASME JOURNAL OF APPLIED MECHANICS, Vol. 50, pp. 891–892.

Stroh, A. N., 1958, "Dislocations and Cracks in Anisotropic Elasticity," *Phil. Mag.*, Vol. 7, pp. 625–646.

Timoshenko, S. P., and Goodier, J. N., 1970, *Theory of Elasticity*, McGraw-Hill, New York.

Ting, T. C. T., 1982, "Effects of Change of Reference Coordinates on the Stress Analyses of Anisotropic Elastic Materials," *Int. J. Solids Structures*, Vol. 18, pp. 139–152.

Ting, T. C. T., 1986, "Explicit Solution and Invariance of the Singularities at an Interface Crack in Anisotropic Composites," *Int. J. Solids Structures*, Vol. 22, pp. 965–983.

Ting, T. C. T., 1988, "Some Identities and the Structures of N_i the Stroh Formalism of Anisotropic Elasticity," *Q. Appl. Math.*, Vol. 46, pp. 109–120.

Ting, T. C. T., and Hwu, C., 1988, "Sextic Formalism in Anisotropic Elasticity for Almost Non-Semisimple Matrix N," *Int. J. Solids Structures*, Vol. 24, pp. 65–76.

Yu, Y. Y., 1952, "Solutions for Exterior of General Ovaloid Under Arbitrary Loading and Its Application to Square Rigid Core Problems," *Proceedings of the First National Congress of Applied Mechanics*, pp. 227–236.

Downloaded 03 May 2010 to 171.66.16.244. Redistribution subject to ASME license or copyright; see http://www.asme.org/terms/Terms_Use.cfm

Nonlinear Finite Element Formulation for the Large Displacement Analysis of Plates

Bilin Chang
Assoc. Mem. ASME

A. A. Shabana
Mem. ASME

Department of Mechanical Engineering,
University of Illinois at Chicago,
Chicago, IL 60680

In this investigation a nonlinear total Lagrangian finite element formulation is developed for the dynamic analysis of plates that undergo large rigid body displacements. In this formulation shape functions are required to include rigid body modes that describe only large translational displacements. This does not represent any limitation on the technique presented in this study, since most of commonly used shape functions satisfy this requirement. For each finite plate element an intermediate element coordinate system, whose axes are initially parallel to the axes of the element coordinate system, is introduced. This intermediate element coordinate system, which has an origin which is rigidly attached to the origin of the deformable body, is used for the convenience of describing the configuration of the element with respect to the deformable body coordinate system in the undeformed state. The nonlinear dynamic equations developed in this investigation for the large rigid body displacement and small elastic deformation analysis of the rectangular plates are expressed in terms of a unique set of time invariant element matrices that depend on the assumed displacement field. The invariants of motion of the deformable body discretized using the plate elements are obtained by assembling the invariants of its elements using a standard finite element procedure.

1 Introduction

The use of the finite element method in the static and dynamic analysis of plates and shells has increased in recent years since their application in practice has widened considerably. In fact the interest in the plate bendings came at a very early stage in the history of the finite element method. A finite element formulation based on the linear theory of elasticity may be developed for plate problems by using either the Kirchhoff (Zienkiewicz, 1977) or Mindlin (Hinton et al., 1975) plate theory. In the classical theory (Kirchhoff's assumptions), shear deformations are ignored by assuming that the normals to the midsurface remain normal after deformation.

At the early stage of the history of the finite element analysis, a number of plate elements were proposed (Adini and Clough, 1960; Tocher, 1962; Clough and Tocher, 1965). Many rectangular elements with different characteristics have been developed for the plate bending analysis. Some of these elements proposed by Melosh (1961) violate certain continuity conditions at the interface between adjacent elements. On the other hand, some other elements which achieve the compatibility conditions (Papenfuss, 1959) have the disadvantage that some of the basic bending modes are not accounted for. The inter-element continuity was sought for both the transverse displacements and slopes at the element boundaries. Higher-order elements (Veubeke, 1968; Smith and Duncan, 1970) are better at satisfying the continuity conditions and representing bending modes. These elements, however, use more degrees-of-freedom at the nodal points.

The conformity of plates in bending has been examined by Popplewell and McDonald (1971) who proposed a high-order conforming, rectangular finite element for the analysis of the free vibrations of a plate in bending while Gopalacharyulu (1973) re-examined the problem of generation of shape functions for conforming rectangular elements and also proposed a new higher-order compatible rectangular element for plate bending. An improved rectangular element for plate bending analysis was presented by Armanios and Negm (1983) in which three interpolation functions corresponding to the normal deflections and tangential slopes at the nodal points were written in parametric form. Hrabok and Hrudey (1984) presented an extensive review of the researches and the developments on the finite element for thin plate in bending and also pointed out that this area for which the element selection was particularly difficult was that of plate bending where the number of available elements was large and no one particular element had emerged as the so-called "best" element. Yang and Bhatti (1985) suggested the shape functions used in the finite element formulation for plate problem be required to ensure C^1 con-

Contributed by the Applied Mechanics Division of THE AMERICAN SOCIETY OF MECHANICAL ENGINEERS for presentation at the Winter Annual Meeting, Dallas, Texas, Nov. 25-30, 1990.

Discussion on this paper should be addressed to the Technical Editor, Leon M. Keer, The Technological Institute, Northwestern University, Evanston, IL 60208, and will be accepted until two months after final publication of the paper itself in the JOURNAL OF APPLIED MECHANICS. Manuscript received by the ASME Applied Mechanics Division, Aug. 17, 1989; final revision, Nov. 13, 1989.

Paper No. 90-WA/APM-26.

Copyright © 1990 by ASME
Downloaded 03 May 2010 to 171.66.16.244. Redistribution subject to ASME license or copyright; see http://www.asme.org/terms/Terms_Use.cfm

tinuity, or otherwise a nonconforming formulation must be adopted. They also examined the geometric nonlinearity for several plate elements by using updated Lagrangian formulation which, in general, had been considered efficient compared to the Eulerian formulation. Torres et al. (1986) presented a C^1 finite element family for Kirchhoff plate bending using triangular elements. These elements were applied to simple cases in order to assess their computational efficiency.

The conformity of plate elements were not, in general, easy to achieve without using higher-order elements which were found to be stiff. Consequently, there was considerable skepticism about the need to meet the C^1 continuity requirement and many researchers sought alternate formulations. Recently, Ortiz and Morris (1988) presented a method which was based on an alternative formulation of Kirchhoff's equations which was amenable to a standard C^0 finite element discretization. Bogner et al. (1965) proposed a deflection function that insured both the deflection and slope compatibility on an adjacent element in which the deflections were expressed by means of the Hermitian interpolation formula for two dimensions. Using this conforming deflection function, Przemieniecki (1966) presented, explicitly, the mass matrix for rectangular plate in bending by neglecting the rotary inertia effects, while Chang (1989) presented the same mass matrix including the effect of the rotary inertia.

A literature survey reveals that most of the finite element formulations developed for plates are only suitable when the rigid body rotation of the element is assumed to be small. This assumption represents a serious limitation on the use of these formulation when plates undergo finite rotations. It is, therefore, the objective of this investigation to develop a total Lagrangian finite element formulation for the dynamic analysis of plates that undergo large rigid body displacements and small elastic deformations. The configuration of each plate element on the deformable body is identified using four coordinate systems: element, body, intermediate element, and global coordinate systems (Shabana and Wehage, 1983; Shabana, 1989). Using these coordinate systems, the configuration of the plate element can be identified in the global frame of reference in terms of a coupled set of body reference and elastic nodal coordinates. The formulation presented in this investigation leads to a nonlinear mass matrix for the plate element expressed in terms of a set of invariants that depend on the assumed displacement field. The invariants of the deformable body can be obtained by assembling the invariants of the elements by using a standard finite element procedure. The dynamic formulation presented in this investigation is applied to the dynamic analysis of constrained multibody systems consisting of interconnected rigid and deformable bodies that undergo large rigid body displacements.

2 Assumed Displacement Field

In this investigation a 20 degree-of-freedom plate element is used. The degrees-of-freedom represent the displacements and slopes of the four nodal points of the rectangular plate element. The assumed displacement field of the plate element j on the body i can be written compactly as

$$\bar{\mathbf{u}}^{ij} = \mathbf{S}^{ij}\mathbf{q}^{ij} \tag{1}$$

where

$$\bar{\mathbf{u}}^{ij} = [u^{ij}\ v^{ij}\ w^{ij}]^{\mathrm{T}} \tag{2}$$

in which u^{ij}, v^{ij}, and w^{ij} are, respectively, the components of the displacement vector $\bar{\mathbf{u}}^{ij}$ of an arbitrary point on the mid-surface of the rectangular plate element ij and $\mathbf{q}^{ij}$ is the total vector of nodal coordinates of the rectangular plate element given by

$$\mathbf{q}^{ij} = [\mathbf{q}_1^{ij\mathrm{T}}\ \mathbf{q}_2^{ij\mathrm{T}}\ \mathbf{q}_3^{ij\mathrm{T}}\ \mathbf{q}_4^{ij\mathrm{T}}]^{\mathrm{T}} \tag{3}$$

in which superscript T indicates the transpose of a vector or a matrix and $\mathbf{q}_k^{ij}$ is the vector of coordinates of node k given by

$$\mathbf{q}_k^{ij} = [u_k^{ij}\ v_k^{ij}\ w_k^{ij}\ \theta_{xk}^{ij}\ \theta_{yk}^{ij}\ \theta_{zk}^{ij}]^{\mathrm{T}}, \quad k = 1, 2, 3, 4. \tag{4}$$

The components u_k^{ij}, v_k^{ij}, and w_k^{ij} ($k = 1, 2, 3, 4$) are, respectively, the nodal coordinates of the kth node in the directions of the **X**, **Y**, and **Z** axes, while θ_{xk}^{ij}, θ_{yk}^{ij}, and θ_{zk}^{ij} are the rotations of the kth node about the **X**, **Y**, and **Z** axes, respectively. If rotation of the plate about the **Z** axis as the result of deformation is not considered, the vector of nodal coordinates of the kth node of the plate element reduces to

$$\mathbf{q}_k^{ij} = [u_k^{ij}\ v_k^{ij}\ w_k^{ij}\ \theta_{xk}^{ij}\ \theta_{yk}^{ij}]^{\mathrm{T}}, \quad k = 1, 2, 3, 4. \tag{5}$$

The plate element shape function $\mathbf{S}^{ij}$ of equation (1) used in this investigation is given by

$$\mathbf{S}^{ij} = \begin{bmatrix} (1-\zeta)(1-\eta) & 0 & 0 \\ 0 & (1-\zeta)(1-\eta) & 0 \\ 0 & 0 & (1+2\zeta)(1-\zeta)^2(1+2\eta)(1-\eta)^2 \\ 0 & 0 & (1+2\zeta)(1-\zeta)^2\eta(1-\eta)^2 b \\ 0 & 0 & -\zeta(1-\zeta)^2(1+2\eta)(1-\eta)^2 a \\ (1-\zeta)\eta & 0 & 0 \\ 0 & (1-\zeta)\eta & 0 \\ 0 & 0 & (1+2\zeta)(1-\zeta)^2(3-2\eta)\eta^2 \\ 0 & 0 & -(1+2\zeta)(1-\zeta)^2(1-\eta)\eta^2 b \\ 0 & 0 & -\zeta(1-\zeta)^2(3-2\eta)\eta^2 a \\ \zeta\eta & 0 & 0 \\ 0 & \zeta\eta & 0 \\ 0 & 0 & (3-2\zeta)\zeta^2(3-2\eta)\eta^2 \\ 0 & 0 & -(3-2\zeta)\zeta^2(1-\eta)\eta^2 b \\ 0 & 0 & (1-\zeta)\zeta^2(3-2\eta)\eta^2 a \\ \zeta(1-\eta) & 0 & 0 \\ 0 & \zeta(1-\eta) & 0 \\ 0 & 0 & (3-2\zeta)\zeta^2(1+2\eta)(1-\eta)^2 \\ 0 & 0 & (3-2\zeta)\zeta^2\eta(1-\eta)^2 b \\ 0 & 0 & (1-\zeta)\zeta^2(1+2\eta)(1-\eta)^2 a \end{bmatrix}^{ij\mathrm{T}}_{20\times 3} \tag{6}$$

in which $\zeta = x/a$ and $\eta = y/b$ where a and b are, respectively, the dimensions of the rectangular plate element ij in the **X** and **Y** directions as shown in Fig. 1.

Although several other shape functions for plate elements with different number of degrees-of-freedom are reported in the literature, the shape function of equation (6) is used in this investigation since the case of the two-dimensional rectangular plate element that undergoes large displacement can easily be obtained as a special case in which only the extension of the plate is considered.

Downloaded 03 May 2010 to 171.66.16.244. Redistribution subject to ASME license or copyright; see http://www.asme.org/terms/Terms_Use.cfm

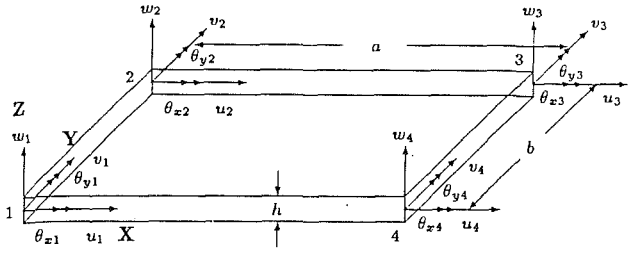


Fig. 1 Nodal coordinates of the plate element

3 Background

If the plate moves as a rigid body, there are six possible rigid body modes; translations in the **X**, **Y**, and **Z** directions and rotations about the **X**, **Y**, and **Z** axes These rigid body modes are examined in this section and the conclusions drawn from this study are used as the basis for developing the nonlinear finite element formulation presented in the following sections.

Rigid Body Translation. If the plate element undergoes a rigid body translation dx in the **X** direction, the values of the nodal coordinates are given by

$$\mathbf{q}^{ij} = [dx\ 0\ 0\ 0\ 0\ dx\ b\ 0\ 0\ 0\ (a+dx)\ b\ 0\ 0\ 0\ (a+dx)\ 0\ 0\ 0\ 0]^{ij\mathrm{T}}.$$

Substituting this vector and $\mathbf{S}^{ij}$ of equation (6) into equation (1), one may obtain the displacement of an arbitrary point on the midsurface of the plate element as

$$\bar{\mathbf{u}}^{ij} = \mathbf{S}^{ij}\mathbf{q}^{ij} = [(dx + a\xi)\ b\eta\ 0]^{ij\mathrm{T}} = [(dx+x)\ y\ 0]^{ij\mathrm{T}} = \bar{\mathbf{u}}_0^{ij} + d\mathbf{x}^{ij}$$

where $\bar{\mathbf{u}}_0^{ij} = [x\ y\ 0]^{ij\mathrm{T}}$ is the position vector of the arbitrary point on the plate element before displacement and $d\mathbf{x}^{ij} = [dx\ 0\ 0]^{ij\mathrm{T}}$ is the rigid body displacement of the plate element. Clearly, every point on the midsurface of the plate element is translated by the same amount of displacement dx in the **X**-direction; and accordingly, the assumed shape function can be used to describe a rigid body translation in the **X**-direction. By using a similar argument, one can show that the assumed shape function can also be used to describe large rigid body translation along the **Y** and **Z** directions.

Finite Rigid Body Rotation. If the plate element rotates a finite rotation ϕ about the **X**-axis, the transformation matrix from the plate element coordinate system to the fixed coordinate system is defined by (Shabana, 1990)

$$\mathbf{A}_x^{ij} = \begin{bmatrix} 1 & 0 & 0 \\ 0 & \cos\phi & -\sin\phi \\ 0 & \sin\phi & \cos\phi \end{bmatrix}^{ij}.$$

Using this transformation, the new positions of the nodal coordinates of the rectangular plate element are, respectively, (0, 0, 0), (0, $b\cos\phi$, $b\sin\phi$), (a, $b\cos\phi$, $b\sin\phi$), and (a, 0, 0). Substituting these values for the nodal coordinates and $\mathbf{S}^{ij}$ of equations (6) into equation (1) yields

$$\bar{\mathbf{u}}^{ij} = \mathbf{S}^{ij}\mathbf{q}^{ij} = [xy\ \cos\phi y(3\eta - 2\eta^2)\sin\phi]^{ij\mathrm{T}}.$$

That is, $\bar{\mathbf{u}}^{ij} \neq A_x^{ij}\,\bar{\mathbf{u}}_0^{ij}$, which indicates that the assumed shape function can not be used to describe a finite rotation about the **X**-axis. Observe that in order to arrive at this conclusion, the slopes at the nodal points are assumed to be equal to zero, that is, the slopes are defined to be the rotation of the sections of the plate from its midsurface. One may, however, suggest using the mathematical definition of the slope. For instance, as the result of this finite rotation, one has

$$\bar{\mathbf{u}}^{ij} = \begin{bmatrix} u^{ij} \\ v^{ij} \\ w^{ij} \end{bmatrix} = \begin{bmatrix} 1 & 0 & 0 \\ 0 & \cos\phi & -\sin\phi \\ 0 & \sin\phi & \cos\phi \end{bmatrix}^{ij} \begin{bmatrix} x \\ y \\ 0 \end{bmatrix}^{ij} = \begin{bmatrix} x \\ y\cos\phi \\ y\sin\phi \end{bmatrix}^{ij}. \tag{7}$$

By using this equation, the mathematical definition of the slopes is

$$\theta_x^{ij} = \frac{\partial w^{ij}}{\partial y} = \sin\phi \tag{8}$$

$$\theta_y^{ij} = -\frac{\partial w^{ij}}{\partial x} = 0 \tag{9}$$

Observe that the slope in equation (8) is equal to $\sin\phi$ instead of $\tan\phi$, since the spatial coordinates are defined in the element coordinate system.

One may suggest using equations (8) and (9) to define the slopes at the nodal points as the result of the finite rotation. In this case the vector of nodal coordinates is given by

$$\mathbf{q}^{ij} = [0\ 0\ 0\ \sin\phi\ 0\ 0\ b\cos\phi\ b\sin\phi\ \sin\phi\ 0\ a\ b\cos\phi\ b\sin\phi\ \sin\phi\ 0\ a\ 0\ 0\ \sin\phi\ 0]^{ij\mathrm{T}}.$$

Using this vector and the shape function of equation (6), one obtains

$$\bar{\mathbf{u}}^{ij} = \mathbf{S}^{ij}\mathbf{q}^{ij} = \begin{bmatrix} x \\ y\cos\phi \\ y\sin\phi \end{bmatrix}^{ij} \tag{10}$$

which is the same result obtained in equation (7). The nodal coordinates, however, can *not* be defined using equation (7) by trigonometric functions, since this will introduce many technical problems in connecting the elements as well as transforming the coordinates. Therefore, equation (8) can be used only when the rotation is small, that is

$$\theta_x^{ij} \approx \phi.$$

Clearly, with this definition of the slope, the shape function can be used to describe only infinitesimal rotations. Similar comments apply to the case of rotations about the **Y**-axis. Consequently, any use of the nodal coordinates to describe the finite rotations, even in an updated Lagrangian formulation, leads to a subtle linearization of the resulting kinematic and dynamic equations. It can be shown, however, that the assumed displacement field can be used to describe finite rigid body rotations about the **Z**-axis.

From the analysis presented in this section, it is clear that the assumed displacement field of equation (1) can be used to describe the large translations in the three directions along the axes of the plate element coordinate system. This assumed displacement field, however, can not be used to describe general finite rotations about the axes in the plane of the midsurface of the plate element. In the following sections a nonlinear total Lagrangian formulation is presented wherein the large displacement of the plate element is defined in a global inertial frame of reference. This formulation leads to a nonlinear mass matrix even in the cases where lumped mass techniques are used. This mass matrix, however, is expressed in terms of invariants that depend on the assumed displacement field of the plate element.

Downloaded 03 May 2010 to 171.66.16.244. Redistribution subject to ASME license or copyright; see http://www.asme.org/terms/Terms_Use.cfm

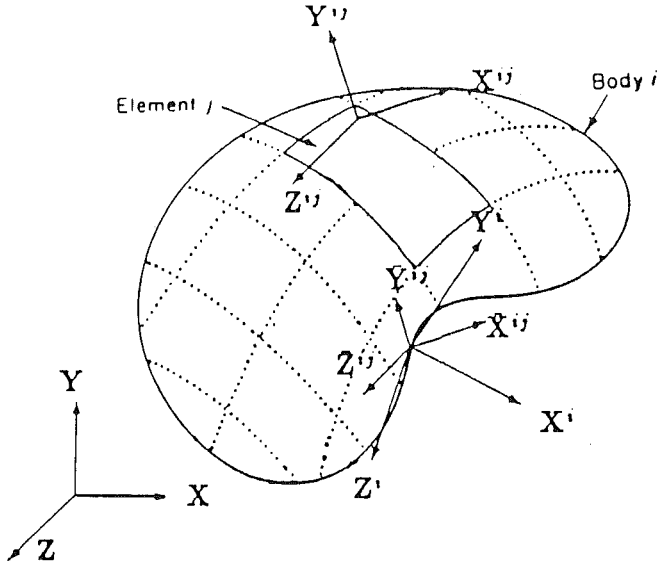


Fig. 2 Finite element coordinate systems

4 Coordinate Systems

In order to describe the large displacement of the plate element, four coordinate systems are used. For each rectangular plate element j on the deformable body i, an element coordinate system denoted as $\mathbf{X}^{ij}\ \mathbf{Y}^{ij}\ \mathbf{Z}^{ij}$ is selected. A body coordinate system is also assigned for the deformable body i which represents a unique reference for the elements of this body. This body coordinate system is denoted as $\mathbf{X}^i\ \mathbf{Y}^i\ \mathbf{Z}^i$. Since the assumed displacement field can be used to describe the large translation, an intermediate element coordinate system $\bar{\mathbf{X}}^{ij}\ \bar{\mathbf{Y}}^{ij}\ \bar{\mathbf{Z}}^{ij}$ shown in Fig. 2 is introduced (Shabana and Wehage, 1983). This coordinate system has an origin which is rigidly attached to the origin of the body coordinate system. Therefore, the intermediate element coordinate system translates and rotates with the coordinate system of the deformable body i and accordingly it shares its rigid body motion. The axes of the intermediate element coordinate system, however, are assumed to be initially parallel to the axes of the plate element coordinate system in the undeformed state. The three coordinate systems $\mathbf{X}^{ij}\ \mathbf{Y}^{ij}\ \mathbf{Z}^{ij}$, $\bar{\mathbf{X}}^{ij}\ \bar{\mathbf{Y}}^{ij}\ \bar{\mathbf{Z}}^{ij}$ and $\mathbf{X}^i\ \mathbf{Y}^i\ \mathbf{Z}^i$ are used to define the configuration of the element with respect to the global coordinate system $\mathbf{X}\ \mathbf{Y}\ \mathbf{Z}$ which is fixed in time and serves as a unique reference for the entire assembly of bodies.

Displacement Field in the Intermediate Element Coordinate System. In the undeformed state, the assumed displacement field of equation (1) can be used to define the initial configuration of the plate element with respect to the intermediate element coordinate system as

$$\bar{\mathbf{u}}_{0i}^{ij} = \mathbf{S}^{ij}\mathbf{q}_{0i}^{ij} \tag{11}$$

where $\mathbf{q}_{0i}^{ij}$ is the vector of nodal coordinates of the plate element in the undeformed state defined in the intermediate element coordinate system $\bar{\mathbf{X}}^{ij}\ \bar{\mathbf{Y}}^{ij}\ \bar{\mathbf{Z}}^{ij}$. That is, the vector $\bar{\mathbf{u}}_{0i}^{ij}$ represents the position vector of an arbitrary point on the midsurface of the plate element in the undeformed state, with respect to the intermediate element coordinate system $\bar{\mathbf{X}}^{ij}\ \bar{\mathbf{Y}}^{ij}\ \bar{\mathbf{Z}}^{ij}$ as the result of the pure translation of the plate element.

The deformation of the plate element can also be described in the intermediate element coordinate system by the vector $\bar{\mathbf{u}}_{fi}^{ij}$ as

$$\bar{\mathbf{u}}_{fi}^{ij} = \mathbf{S}^{ij}\mathbf{q}_{fi}^{ij} \tag{12}$$

where $\mathbf{q}_{fi}^{ij}$ is the vector of elastic nodal coordinates defined in the intermediate element coordinate system. Therefore, equations (11) and (12) can be used to define, in the intermediate element coordinate system, the displacement field of the plate element after deformation as

$$\bar{\mathbf{u}}_i^{ij} = \bar{\mathbf{u}}_{0i}^{ij} + \bar{\mathbf{u}}_{fi}^{ij} \tag{13}$$

which can also be written as

$$\bar{\mathbf{u}}_i^{ij} = \mathbf{S}^{ij}(\mathbf{q}_{0i}^{ij} + \mathbf{q}_{fi}^{ij}) \tag{14}$$

Displacement Field in the Body Coordinate System. Since the intermediate element coordinate system $\bar{\mathbf{X}}^{ij}\ \bar{\mathbf{Y}}^{ij}\ \bar{\mathbf{Z}}^{ij}$ has a constant orientation with respect to the body coordinate system $\mathbf{X}^i\ \mathbf{Y}^i\ \mathbf{Z}^i$, the displacement vector $\bar{\mathbf{u}}^{ij}$ can be defined in the body coordinate system as

$$\bar{\mathbf{u}}^{ij} = \mathbf{C}^{ij}\bar{\mathbf{u}}_i^{ij} = \mathbf{C}^{ij}\mathbf{S}^{ij}(\mathbf{q}_{0i}^{ij} + \mathbf{q}_{fi}^{ij}) \tag{15}$$

where $\mathbf{C}^{ij}$ is a constant transformation matrix from the intermediate element coordinate system to the body coordinate system. This transformation matrix can be obtained by defining the direction cosines between the axes of the intermediate element coordinate system and the body coordinate system.

Connectivity Between the Elements. In order to define the connectivity between the plate elements, the element nodal coordinates must be defined in the body coordinate system $\mathbf{X}^i\mathbf{Y}^i\mathbf{Z}^i$. Since the intermediate element coordinate system has a constant orientation with respect to the body coordinate system, one has

$$\mathbf{q}_{0i}^{ij} = \bar{\mathbf{C}}^{ij}\mathbf{q}_0^{ij} \tag{16}$$

and

$$\mathbf{q}_{fi}^{ij} = \bar{\mathbf{C}}^{ij}\mathbf{q}_f^{ij} \tag{17}$$

where $\mathbf{q}_0^{ij}$ and $\mathbf{q}_f^{ij}$ are, respectively, the vector of the nodal coordinates of the element in the undeformed state, and the vector of elastic nodal coordinates defined in the body coordinate system and $\bar{\mathbf{C}}^{ij}$ is an appropriate constant transformation matrix between the intermediate element coordinate system and the body coordinate system.

The connectivity between the plate elements can be described using a constant Boolean matrix $\mathbf{B}_1^{ij}$ as

$$\mathbf{q}_0^{ij} = \mathbf{B}_1^{ij}\mathbf{q}_0^i \tag{18}$$

$$\mathbf{q}_f^{ij} = \mathbf{B}_1^{ij}\bar{\mathbf{q}}_f^i \tag{19}$$

where

$$\mathbf{q}_0^i = [\mathbf{q}_0^{i1\mathrm{T}}\ \mathbf{q}_0^{i2\mathrm{T}}\ \ldots\ \mathbf{q}_0^{in_e\mathrm{T}}]^{\mathrm{T}}$$
$$\bar{\mathbf{q}}_f^i = [\bar{\mathbf{q}}_f^{i1\mathrm{T}}\ \bar{\mathbf{q}}_f^{i2\mathrm{T}}\ \ldots\ \bar{\mathbf{q}}_f^{in_e\mathrm{T}}]^{\mathrm{T}}$$

in which n_e is the total number of the plate elements on the deformable body i. Substituting equations (16)–(19) into equation (15) yields

$$\bar{\mathbf{u}}^{ij} = \mathbf{C}^{ij}\mathbf{S}^{ij}\bar{\mathbf{C}}^{ij}\mathbf{B}_1^{ij}(\mathbf{q}_0^i + \bar{\mathbf{q}}_f^i). \tag{20}$$

5 Unique Displacement Field

It is clear from the discussion presented in Section 3 that the assumed shape function $\mathbf{S}^{ij}$ of equation (20) contains the rigid body modes. Furthermore, in the special case in which the plate element undergoes rigid body motion, equation (20) can not be used to describe a general finite rotation in the dynamic formulation.

In this investigation, the large translations and the finite rotations of the rectangular plate element are described using a set of absolute coordinates that define the location and orientation of the body coordinate system $\mathbf{X}^i\mathbf{Y}^i\mathbf{Z}^i$. In order to define a unique displacement field, the rigid body modes of the element shape function must be eliminated using a set of

Downloaded 03 May 2010 to 171.66.16.244. Redistribution subject to ASME license or copyright; see http://www.asme.org/terms/Terms_Use.cfm

reference conditions. These reference conditions can be expressed as (Shabana, 1989)

$$\tilde{\mathbf{q}}_f^i = \mathbf{B}_r^i \mathbf{q}_f^i \tag{21}$$

where $\mathbf{q}_f^i$ is the vector of independent elastic coordinates of body i and $\mathbf{B}_r^i$ is the matrix of the reference conditions which eliminates the rigid body modes of the plate element shape function.

Substituting equation (21) into (20), one obtains

$$\tilde{\mathbf{u}}^{ij} = \mathbf{C}^{ij}\mathbf{S}^{ij}\tilde{\mathbf{C}}^{ij}\mathbf{B}_1^{ij}(\mathbf{q}_0^i + \mathbf{B}_r^i \mathbf{q}_f^i), \tag{22}$$

which can be written compactly as

$$\tilde{\mathbf{u}}^{ij} = \tilde{\mathbf{u}}_0^{ij} + \tilde{\mathbf{u}}_f^{ij} = \mathbf{N}^{ij}(\mathbf{q}_0^i + \mathbf{B}_r^i \mathbf{q}_f^i) = \mathbf{N}^{ij}\mathbf{q}_n^i, \tag{23}$$

where

$$\mathbf{N}^{ij} = \mathbf{C}^{ij}\mathbf{S}^{ij}\tilde{\mathbf{C}}^{ij}\mathbf{B}_1^{ij} \tag{24}$$

$$\mathbf{q}_n^i = \mathbf{q}_0^i + \mathbf{B}_r^i \mathbf{q}_f^i \tag{25}$$

$$\tilde{\mathbf{u}}_0^{ij} = \mathbf{N}^{ij}\mathbf{q}_0^i \tag{26}$$

$$\tilde{\mathbf{u}}_f^{ij} = \tilde{\mathbf{N}}^{ij}\mathbf{q}_f^i \tag{27}$$

$$\tilde{\mathbf{N}}^{ij} = \mathbf{N}^{ij}\mathbf{B}_r^i, \tag{28}$$

in which $\mathbf{q}_n^i$ is the total vector of nodal coordinates of body i resulting from the finite element discretization, $\tilde{\mathbf{u}}_0^{ij}$ is the displacement field of the plate element ij in the undeformed state, defined in the body coordinate system, and $\tilde{\mathbf{u}}_f^{ij}$ is the deformation vector of the plate element defined in the body coordinate system $\mathbf{X}^i\mathbf{Y}^i\mathbf{Z}^i$.

6 Large Displacement of the Plate Element

The large displacement of the plate element can be described using the following reference coordinates

$$\mathbf{q}_r^i = [\mathbf{R}^{iT}\ \theta^{iT}]^T \tag{29}$$

which describe the location of the origin and the orientation of the ith body reference. Therefore, the position vector $\mathbf{r}^{ij}$ of an arbitrary point on the plate element j of body i is given by

$$\mathbf{r}^{ij} = \mathbf{R}^i + \mathbf{A}^i \tilde{\mathbf{u}}^{ij} \tag{30}$$

where $\mathbf{R}^i$ is the location of the origin of the body reference with respect to the global frame of reference and $\mathbf{A}^i$ is the transformation matrix from the body reference to the global system defined as (Shabana, 1989)

$$\mathbf{A}^i = \left[\mathbf{I}_3 + \tilde{\mathbf{v}}^i \sin\theta^i + 2(\tilde{\mathbf{v}}^i)^2 \sin^2\left(\frac{\theta^i}{2}\right)\right] \tag{31}$$

where $\mathbf{I}_3$ is the 3×3 identity matrix, θ^i is the rotation angle about the axis of rotation, and $\tilde{\mathbf{v}}^i$ is the skew symmetric matrix defined as

$$\tilde{\mathbf{v}}^i = \begin{bmatrix} 0 & -v_Z^i & v_Y^i \\ v_Z^i & 0 & -v_X^i \\ -v_Y^i & v_X^i & 0 \end{bmatrix} \tag{32}$$

in which v_X^i, v_Y^i, and v_Z^i are the components of the vector $\mathbf{v}^i$ and $\mathbf{v}^i$ is a unit vector along the axis of rotation defined in the global system. With the use of equation (23), (30) can be written as

$$\begin{aligned} \mathbf{r}^{ij} &= \mathbf{R}^i + \mathbf{A}^i \tilde{\mathbf{u}}^{ij} \\ &= \mathbf{R}^i + \mathbf{A}^i \mathbf{N}^{ij}(\mathbf{q}_0^i + \mathbf{B}_r^i \mathbf{q}_f^i). \end{aligned} \tag{33}$$

Differentiating equation (33) with respect to time and introducing Euler parameters for the description of the orientation of the deformable body i yields the velocity vector (Shabana, 1989)

$$\dot{\mathbf{r}}^{ij} = [\mathbf{I}_3 - \mathbf{A}^i \tilde{\mathbf{u}}^{ij} \tilde{\mathbf{G}}^i \ \mathbf{A}^i \mathbf{N}^{ij} \mathbf{B}_r^i] \begin{bmatrix} \dot{\mathbf{R}}^i \\ \dot{\theta}^i \\ \dot{\mathbf{q}}_f^i \end{bmatrix} \tag{34}$$

where

$$\tilde{\tilde{\mathbf{u}}}^{ij} = \begin{bmatrix} 0 & -\bar{u}_z^{ij} & \bar{u}_y^{ij} \\ \bar{u}_z^{ij} & 0 & -\bar{u}_x^{ij} \\ -\bar{u}_y^{ij} & \bar{u}_x^{ij} & 0 \end{bmatrix} \tag{35}$$

$$\mathbf{A}^i = \begin{bmatrix} 1-2\theta_2^{i2}-2\theta_3^{i2} & 2(\theta_1^i\theta_2^i - \theta_0^i\theta_3^i) & 2(\theta_1^i\theta_3^i + \theta_0^i\theta_2^i) \\ 2(\theta_1^i\theta_2^i + \theta_0^i\theta_3^i) & 1-2\theta_1^{i2}-2\theta_3^{i2} & 2(\theta_2^i\theta_3^i - \theta_0^i\theta_1^i) \\ 2(\theta_1^i\theta_3^i - \theta_0^i\theta_2^i) & 2(\theta_2^i\theta_3^i + \theta_0^i\theta_1^i) & 1-2\theta_1^{i2}-2\theta_2^{i2} \end{bmatrix} \tag{36}$$

and

$$\tilde{\mathbf{G}}^i = 2\begin{bmatrix} -\theta_1^i & \theta_0^i & \theta_3^i & -\theta_2^i \\ -\theta_2^i & -\theta_3^i & \theta_0^i & \theta_1^i \\ -\theta_3^i & \theta_2^i & -\theta_1^i & \theta_0^i \end{bmatrix} \tag{37}$$

in which θ_k^i ($k = 0, 1, 2, 3$) are the four Euler parameters (Goldstein, 1980) of body i defined as

$$\begin{aligned} \theta_0^i &= \cos\frac{\theta^i}{2} \\ \theta_1^i &= v_X^i \sin\frac{\theta^i}{2} \\ \theta_2^i &= v_Y^i \sin\frac{\theta^i}{2} \\ \theta_3^i &= v_Z^i \sin\frac{\theta^i}{2} \end{aligned} \tag{38}$$

where θ^i is the angle of rotation of body i about the axis of rotation $\mathbf{v}^i$.

7 Nonlinear Mass Matrix of the Plate Element

The kinetic energy of the plate element j of the body i can be defined as

$$T^{ij} = \frac{1}{2}\int_{V^{ij}} \rho^{ij} \dot{\mathbf{r}}^{ijT} \dot{\mathbf{r}}^{ij} dV^{ij} \tag{39}$$

where ρ^{ij} and V^{ij} are, respectively, the mass density and the volume of the plate element ij. Substituting equation (34) into (39), one obtains

$$T^{ij} = \frac{1}{2}\dot{\mathbf{q}}^{iT}\mathbf{M}^{ij}\dot{\mathbf{q}}^i \tag{40}$$

where $\mathbf{q}^i$ is the total vector of the generalized coordinates of body i defined as

$$\mathbf{q}^i = [\mathbf{R}^{iT}\ \theta^{iT}\ \mathbf{q}_f^{iT}]^T = [\mathbf{q}_R^{iT}\ \mathbf{q}_\theta^{iT}\ \mathbf{q}_f^{iT}]^T \tag{41}$$

and $\mathbf{M}^{ij}$ is the mass matrix of the plate element ij which can be written according to the partition of equation (41) as

$$\mathbf{M}^{ij} = \int_{V^{ij}} \rho^{ij} \begin{bmatrix} \mathbf{I}_3 & -\mathbf{A}^i\tilde{\tilde{\mathbf{u}}}^{ij}\tilde{\mathbf{G}}^i & \mathbf{A}^i\mathbf{N}^{ij}\mathbf{B}_r^i \\ & \tilde{\mathbf{G}}^{iT}\tilde{\tilde{\mathbf{u}}}^{ijT}\tilde{\tilde{\mathbf{u}}}^{ij}\tilde{\mathbf{G}}^i & \tilde{\mathbf{G}}^{iT}\tilde{\tilde{\mathbf{u}}}^{ij}\mathbf{N}^{ij}\mathbf{B}_r^i \\ \text{sym.} & & \mathbf{B}_r^{iT}\mathbf{N}^{ijT}\mathbf{N}^{ij}\mathbf{B}_r^i \end{bmatrix} dV^{ij}, \tag{42}$$

where the orthogonality of the transformation matrix $\mathbf{A}^i$ has been utilized. The mass matrix can be written in a more simplified form as

Downloaded 03 May 2010 to 171.66.16.244. Redistribution subject to ASME license or copyright; see http://www.asme.org/terms/Terms_Use.cfm

$$\mathbf{M}^{ij} = \begin{bmatrix} \mathbf{M}^{ij}_{RR} & \mathbf{M}^{ij}_{R\theta} & \mathbf{M}^{ij}_{Rf} \\ & \mathbf{M}^{ij}_{\theta\theta} & \mathbf{M}^{ij}_{\theta f} \\ \text{sym.} & & \mathbf{M}^{ij}_{ff} \end{bmatrix}. \tag{43}$$

The submatrix $\mathbf{M}^{ij}_{RR}$ of equation (43) can be defined as

$$\mathbf{M}^{ij}_{RR} = \int_{V^{ij}} \rho^{ij}\, \mathbf{I}_3\, dV^{ij} = \begin{bmatrix} m^{ij} & 0 & 0 \\ 0 & m^{ij} & 0 \\ 0 & 0 & m^{ij} \end{bmatrix} \tag{44}$$

in which m^{ij} is the mass of the plate element ij. One may observe that the submatrix $\mathbf{M}^{ij}_{RR}$ is diagonal and time invariant.

Coupling Between Translation and Rotation. The submatrix $\mathbf{M}^{ij}_{R\theta}$, which represents the inertia coupling between the translation and rotation of the body reference, is defined as

$$\mathbf{M}^{ij}_{R\theta} = -\int_{V^{ij}} \rho^{ij} \mathbf{A}^i \tilde{\mathbf{u}}^{ij} \bar{\mathbf{G}}^i dV^{ij} = -\mathbf{A}^i \tilde{\bar{\mathbf{S}}}^{ij}_f \bar{\mathbf{G}}^i \tag{45}$$

where the skew symmetric matrix $\tilde{\bar{\mathbf{S}}}^{ij}_f$ is defined according to

$$\tilde{\bar{\mathbf{S}}}^{ij}_f = \int_{V^{ij}} \rho^{ij} \tilde{\mathbf{u}}^{ij} dV^{ij} \tag{46}$$

or in a vector form as

$$\bar{\mathbf{S}}^{ij}_f = \int_{V^{ij}} \rho^{ij} \bar{\mathbf{u}}^{ij} dV^{ij} \tag{47}$$

Using the definition of $\bar{\mathbf{u}}^{ij}$ of equation (22) and the definition of the skew symmetric matrix $\tilde{\bar{\mathbf{u}}}^{ij}$ of equation (35), one may easily verify that the following integration is required in order to evaluate the matrix $\mathbf{M}^{ij}_{R\theta}$ of equation (45)

$$\bar{\mathbf{S}}^{ij} = \mathbf{C}^{ij} \left[\int_{V^{ij}} \rho^{ij} \mathbf{S}^{ij} dV^{ij} \right] \bar{\mathbf{C}}^{ij} \mathbf{B}^{ij}_1 \tag{48}$$

which can be written as

$$\bar{\mathbf{S}}^{ij} = \mathbf{C}^{ij} \mathbf{I}^{ij} \bar{\mathbf{C}}^{ij} \mathbf{B}^{ij}_1 \tag{49}$$

where

$$\mathbf{I}^{ij} = \int_{V^{ij}} \rho^{ij} \mathbf{S}^{ij} dV^{ij}. \tag{50}$$

The matrix $\mathbf{I}^{ij}$, which depends on the assumed displacement field within the plate element, is constant. Using the assumed displacement field of equation (1), the matrix $\mathbf{I}^{ij}$ that appears in (50) is given by

$$\mathbf{I}^{ij} = \frac{m^{ij}}{24} \begin{bmatrix} 6 & 0 & 0 & 0 & 0 & 6 & 0 & 0 & 0 & 0 & 6 & 0 & 0 & 0 & 0 & 6 & 0 & 0 & 0 & 0 \\ 0 & 6 & 0 & 0 & 0 & 0 & 6 & 0 & 0 & 0 & 0 & 6 & 0 & 0 & 0 & 0 & 6 & 0 & 0 & 0 \\ 0 & 0 & 6 & b & -a & 0 & 0 & 6 & -b & -a & 0 & 0 & 6 & -b & a & 0 & 0 & 6 & b & a \end{bmatrix}.$$

Coupling Between Translation and Deformation. One can also show that the matrix $\mathbf{I}^{ij}$ is also required for evaluating the submatrix $\mathbf{M}^{ij}_{Rf}$ which represents the inertia coupling between the translation of the body reference and the elastic deformation of the plate element ij. In order to see this, we write $\mathbf{M}^{ij}_{Rf}$ as follows:

$$\mathbf{M}^{ij}_{Rf} = \int_{V^{ij}} \rho^{ij} \mathbf{A}^i \mathbf{N}^{ij} \mathbf{B}^i_f dV^{ij} = \mathbf{A}^i \left[\int_{V^{ij}} \rho^{ij} \mathbf{N}^{ij} dV^{ij} \right] \mathbf{B}^i_f \tag{51}$$

Using the definition of $\mathbf{N}^{ij}$ of equation (24) and the fact that the matrices $\mathbf{C}^{ij}$, $\bar{\mathbf{C}}^{ij}$, and $\mathbf{B}^{ij}_1$ are constant matrices, one can write (51) as

$$\mathbf{M}^{ij}_{Rf} = \mathbf{A}^i \mathbf{C}^{ij} \left[\int_{V^{ij}} \rho^{ij} \mathbf{S}^{ij} dV^{ij} \right] \bar{\mathbf{C}}^{ij} \mathbf{B}^{ij}_1 \mathbf{B}^i_f. \tag{52}$$

Using the definition of the matrix $\bar{\mathbf{S}}^{ij}$ of equation (49), the matrix $\mathbf{M}^{ij}_{Rf}$ can be written compactly as

$$\mathbf{M}^{ij}_{Rf} = \mathbf{A}^i \bar{\mathbf{S}}^{ij} \mathbf{B}^i_f. \tag{53}$$

Inertia Tensor of the Plate Element. The central term in the matrix of equation (43) can be written as

$$\begin{aligned} \mathbf{M}^{ij}_{\theta\theta} &= \int_{V^{ij}} \rho^{ij} \bar{\mathbf{G}}^{iT} \tilde{\mathbf{u}}^{ijT} \tilde{\mathbf{u}}^{ij} \bar{\mathbf{G}}^i dV^{ij} \\ &= \bar{\mathbf{G}}^{iT} \left[\int_{V^{ij}} \rho^{ij} \tilde{\mathbf{u}}^{ijT} \tilde{\mathbf{u}}^{ij} dV^{ij} \right] \bar{\mathbf{G}}^i. \\ &= \bar{\mathbf{G}}^{iT} \mathbf{J}^{ij} \bar{\mathbf{G}}^i \end{aligned} \tag{54}$$

Thus, $\mathbf{M}^{ij}_{\theta\theta}$ depends on both the rotation of body reference and the elastic deformation. The matrix $\mathbf{J}^{ij}$ is the inertia tensor of the ijth plate element defined in the body reference. The inertia tensor is then defined as

$$\mathbf{J}^{ij} = \int_{V^{ij}} \rho^{ij} \tilde{\mathbf{u}}^{ijT} \tilde{\mathbf{u}}^{ij} dV^{ij}. \tag{55}$$

One may observe that the inertia tensor of the plate element is symmetric. This inertia tensor, however, depends on the elastic generalized coordinates of the plate element. Furthermore, if we let $\mathbf{S}^{ij}_1$, $\mathbf{S}^{ij}_2$, and $\mathbf{S}^{ij}_3$ be the rows of the assumed shape function of plate element ij, that is

$$\mathbf{S}^{ij} = \begin{bmatrix} \mathbf{S}^{ij}_1 \\ \mathbf{S}^{ij}_2 \\ \mathbf{S}^{ij}_3 \end{bmatrix}, \tag{56}$$

and recall that $\mathbf{N}^{ij}$ was given in equation (24), one can easily verify that the following six-time invariant element matrices, $\bar{\mathbf{S}}^{ij}_{kl}$, are required in order to evaluate the inertia tensor of the plate element (Shabana, 1989).

$$\bar{\mathbf{S}}^{ij}_{kl} = \int_{V^{ij}} \rho^{ij} \mathbf{N}^{ijT}_k \mathbf{N}^{ij}_l dV^{ij} = \mathbf{B}^{ijT}_1 \bar{\mathbf{C}}^{ijT} \left[\int_{V^{ij}} \rho^{ij} \mathbf{S}^{ijT}_k \mathbf{S}^{ij}_l dV^{ij} \right] \bar{\mathbf{C}}^{ij} \mathbf{B}^{ij}_1, \quad k, l = 1, 2, 3 \tag{57}$$

Equation (57) can be written compactly as

$$\bar{\mathbf{S}}^{ij}_{kl} = \mathbf{B}^{ijT}_1 \bar{\mathbf{C}}^{ijT} \mathbf{I}^{ij}_{kl} \bar{\mathbf{C}}^{ij} \mathbf{B}^{ij}_1, \quad k, l = 1, 2, 3 \tag{58}$$

where

$$\mathbf{I}^{ij}_{kl} = \int_{V^{ij}} \rho^{ij} \mathbf{S}^{ijT}_k \mathbf{S}^{ij}_l dV^{ij}. \tag{59}$$

Using the shape function of equation (6), the invariants of (59) can be evaluated (Chang, 1989). The explicit forms of these invariants are given in the Appendix.

Coupling Between Rotation and Deformation. The six constant matrices of equation (59), which depend on the assumed displacement field, are also needed to evaluate the submatrix $\mathbf{M}^{ij}_{\theta f}$ of equation (43), which describes the inertia coupling between the rotation of the body reference and the deformation of the plate element. This can be demonstrated by writing $\mathbf{M}^{ij}_{\theta f}$ as:

Downloaded 03 May 2010 to 171.66.16.244. Redistribution subject to ASME license or copyright; see http://www.asme.org/terms/Terms_Use.cfm

Table 1 Data for RSSR mechanism

Links		Cranker	Coupler	Rocker
Dimensions (M)		.1016×.02×.01	.381×.1905×.004	(.254+2×.1016)×.02×.01
Mass (Kg)		0.1585	2.2645	0.3962
Locations of Body Reference (M)	x	0.0254	0.1778	0.3048
	y	0.0440	0.1229	0.0789
	z	0.0000	0.1376	0.1757
Orientations of Body Reference in Euler Angles (Rad)	ϕ	1.0470	0.2680	1.5708
	θ	0.0000	−1.5708	1.5708
	ψ	0.0000	−0.8074	0.9007
Mass Moments of Inertia of Bodies (Kg-M^2)	I_{xx}	6.60×10^{-6}	6.85×10^{-3}	4.52×10^{-3}
	I_{yy}	1.38×10^{-4}	2.74×10^{-2}	1.09×10^{-2}
	I_{zz}	1.42×10^{-4}	3.42×10^{-2}	6.41×10^{-3}
Material Properties		$E = 0.2\times10^{12}\ N/M^2$, $\rho = 7800\ Kg/M^3$, $\nu = 0.3$		

$$\mathbf{M}_{\theta f}^{ij} = \int_{V^{ij}} \rho^{ij} \bar{\mathbf{G}}^{i^{\mathrm{T}}} \tilde{\mathbf{u}}^{ij} \mathbf{N}^{ij}\, \mathbf{B}_r^i\, dV^{ij}$$

$$= \bar{\mathbf{G}}^{i^{\mathrm{T}}} \left[\int_{V^{ij}} \rho^{ij} \tilde{\mathbf{u}}^{ij} \mathbf{N}^{ij} dV^{ij} \right] \mathbf{B}_r^i = \bar{\mathbf{G}}^{i^{\mathrm{T}}} \bar{\mathbf{I}}_{\theta f}^{ij}\, \mathbf{B}_r^i \tag{60}$$

where $\bar{\mathbf{I}}_{\theta f}^{ij}$ is defined as

$$\bar{\mathbf{I}}_{\theta f}^{ij} = \int_{V^{ij}} \rho^{ij} \tilde{\mathbf{u}}^{ij} \mathbf{N}^{ij} dV^{ij}. \tag{61}$$

Clearly, $\bar{\mathbf{I}}_{\theta f}^{ij}$ can be expressed in terms of the following skew symmetric matrices which can be expressed in terms of the invariants of equation (57) as

$$\tilde{\mathbf{N}}_{kl}^{ij} = \bar{\mathbf{S}}_{kl}^{ij} - \bar{\mathbf{S}}_{kl}^{ij^{\mathrm{T}}} = \int_{V^{ij}} \rho^{ij} (\mathbf{N}_k^{ij^{\mathrm{T}}} \mathbf{N}_l^{ij} - \mathbf{N}_l^{ij^{\mathrm{T}}} \mathbf{N}_k^{ij}) dV^{ij},$$

$$k, l = 1, 2, 3. \tag{62}$$

Finally, the last terms in the mass matrix of equation (43) can be expressed in terms of the invariants of (57) as

$$\mathbf{M}_{ff}^{ij} = \int_{V^{ij}} \rho^{ij} \mathbf{B}_r^{i^{\mathrm{T}}} \mathbf{N}^{ij^{\mathrm{T}}} \mathbf{N}^{ij} \mathbf{B}_r^i dV^{ij}$$

$$= \mathbf{B}_r^{i^{\mathrm{T}}} \left[\int_{V^{ij}} \rho^{ij} \mathbf{N}^{ij^{\mathrm{T}}} \mathbf{N}^{ij} dV^{ij} \right] \mathbf{B}_r^i \tag{63}$$

$$= \mathbf{B}_r^{i^{\mathrm{T}}} [\bar{\mathbf{S}}_{11}^{ij} + \bar{\mathbf{S}}_{22}^{ij} + \bar{\mathbf{S}}_{33}^{ij}] \mathbf{B}_r^i$$

where $\bar{\mathbf{S}}_{kk}^{ij}$, $k = 1, 2, 3$, are given by (58).

Mass Matrix of the Deformable Body. The mass matrix of the deformable body i discretized using the plate elements can be obtained by assembling the element matrices. One can show that the deformable body nonlinear mass matrix $\mathbf{M}^i$ can be expressed in terms of time invariant matrices which can be obtained by assembling the invariants of the plate elements using a standard finite element procedure. These invariants are defined as

$$\bar{\mathbf{S}}^i = \sum_{j=1}^{n_e} \bar{\mathbf{S}}^{ij} \tag{64}$$

$$\bar{\mathbf{S}}_{kl}^i = \sum_{j=1}^{n_e} \bar{\mathbf{S}}_{kl}^{ij} \quad k, l = 1, 2, 3 \tag{65}$$

where n_e is the total number of plate elements. Using the expressions for the strain energy, the stiffness matrix of the deformable body can be developed by using the procedure described by Chang (1989). The differential equations of motion can then be developed using Lagrange's equation or the principle of virtual work in dynamics (Shabana, 1989).

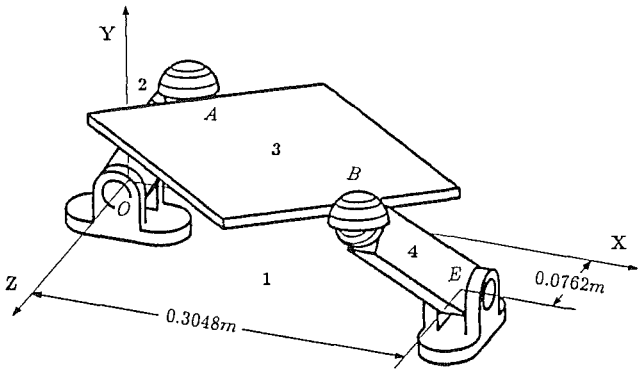


Fig. 3 The RSSR mechanism

8 Numerical Example

In this section a numerical example is presented in order to demonstrate the use of the finite element formulation presented in this investigation. To this end we consider the spatial RSSR (revolute-spherical-spherical-revolute) mechanism shown in Fig. 3. The mechanism consists of four links; the fixed link denoted as body one, the crank shaft denoted as body two, the coupler denoted as body three, and the rocker denoted as body four. The crankshaft is connected to the ground (fixed link) by a revolute joint at O and to the coupler by a spherical joint at A. The rocker is connected to the coupler by a spherical joint at B and to the fixed link by a revolute joint at E. Since the joint has one degree-of-freedom and the spherical joint has three degrees-of-freedom, by applying Kutzbach criterion (Shigley, 1980) in order to determine the mobility of this mechanism one can show that in the special case in which the mechanism consists of rigid members, the system has two degrees-of-freedom. Clearly, one of these degrees of freedom is the idle freedom of the coupler to spin about its own axis AB. This idle freedom, however, does not affect the input-output relationships. The dimensions, inertia properties, and initial configuration of the mechanism are shown in Table 1. In order to demonstrate the application of the dynamic formulation presented in this paper, the coupler is assumed to be a flexible body discretized using a finite number of rectangular plate elements. In this case, the total number of degrees-of-freedom

Downloaded 03 May 2010 to 171.66.16.244. Redistribution subject to ASME license or copyright; see http://www.asme.org/terms/Terms_Use.cfm

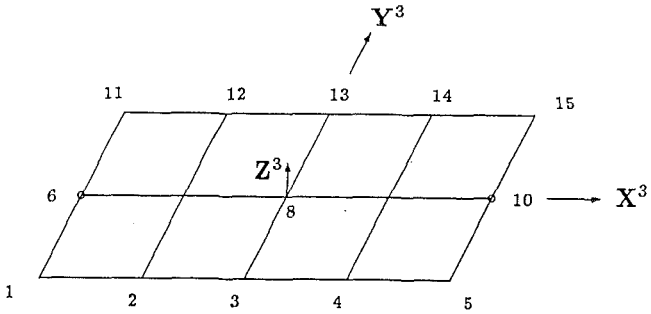


Fig. 4 Finite element discretization of the coupler

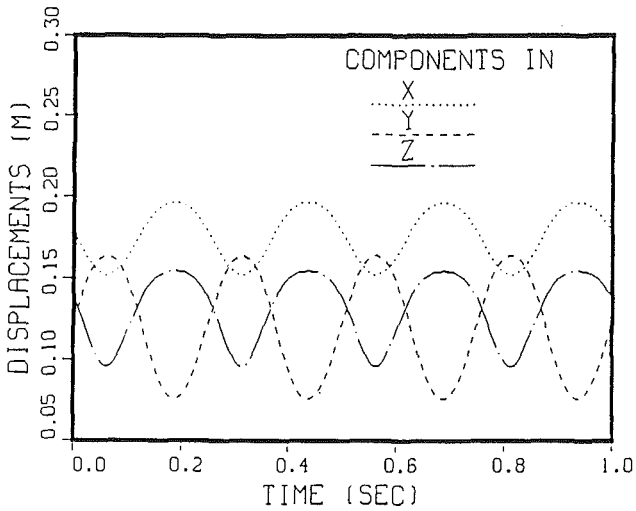


Fig. 5 Displacement of the origin of the coupler coordinate system

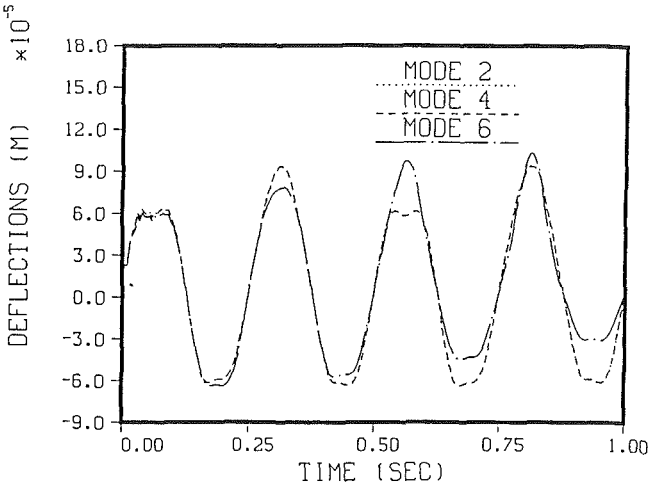


Fig. 6 The transverse elastic displacement at node 8

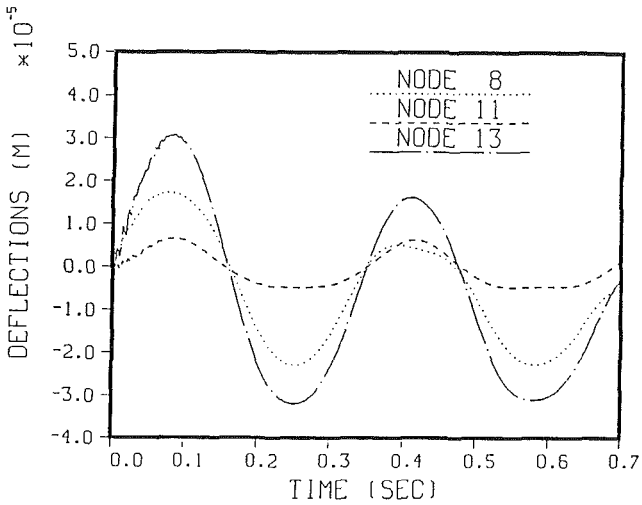


Fig. 7 The transverse elastic displacement at nodes 8, 11, and 13

of the mechanism is equal to two plus the number of elastic coordinates of the plate. The crankshaft is assumed to rotate with the following angular velocity

$$\omega^2 = \frac{4\pi}{3}\,\pi\cos(8\,\pi t)$$

where ω^2 is the angular velocity of the crankshaft (body 2) and t is time. In the numerical investigation presented in this paper the coupler is divided into eight rectangular plate elements as shown in Fig. 4. The origin of the body reference of the coupler is assumed to initially coincide with node 8 as shown in the figure. The number of elastic coordinates are reduced by using component mode synthesis techniques (Shabana, 1989). A modal damping coefficient of 0.03 is used for all modes. In this investigation, six modes of vibrations are considered (Chang, 1989). Figure 5 shows the rigid body motion of the coupler as described by the components of the position vector of the origin of the coupler reference. Figure 6 shows the effect of using different number of modes on the deflection of the midpoint of the coupler, while Fig. 7 shows the transverse displacements at the selected nodes of the coupler with six modes.

9 Conclusions

In this investigation a total Lagrangian finite element formulation is presented for the rectangular plate elements that undergo large translational and rotational displacements. The configuration of each rectangular plate element on the deformable body is identified using four coordinate systems. The first coordinate system is a global inertial frame of reference which is fixed in time and serves as a unique reference for the entire assembly of bodies. Kinematic constraint equations between different bodies in the system are formulated in this global coordinate system. The second coordinate system is the deformable body reference which serves as a unique reference for the finite plate elements of the body. Connectivity between plate elements on this body are defined using a constant Boolean matrix. The large translational and rotational displacements of this reference are described using a coupled set of Cartesian and rotational coordinates that define the location and orientation of the body reference with respect to the inertial frame. The third coordinate system is the element coordinate system which translates and rotates with the plate element. The fourth coordinate system is an intermediate element coordinate system whose origin is rigidly attached to the origin of the body coordinate system. Therefore, this coordinate system translates and rotates with the body. This coordinate system is also selected such that its axes are initially parallel to the plate element coordinate system in the undeformed state.

By using these coordinate systems, the configuration of the rectangular plate element can be identified in the global coordinate system in terms of a coupled set of body reference and elastic nodal coordinates. The kinetic energy of each element is then defined and the element mass matrix is identified.

Downloaded 03 May 2010 to 171.66.16.244. Redistribution subject to ASME license or copyright; see http://www.asme.org/terms/Terms_Use.cfm

It is shown that the mass matrix of the rectangular plate element can be expressed in terms of a set of element invariants that depend on the assumed displacement field. The invariants of the deformable body can be obtained by assembling the invariants of the elements using a standard finite element procedure. While the use of the updated Lagrangian formulation leads only to the definition of the mass matrix that appears in linear structural systems, the use of the total Lagrangian formulation presented in this investigation leads to seven time-invariant matrices that have to be evaluated in advance for the dynamic analysis. Furthermore, the use of the lumped mass techniques in the total Lagrangian formulation does not lead to a diagonal mass matrix as in the case of the updated Lagrangian formulation. It can be shown (Shabana, 1989) that when lumped mass techniques are used, the structure of the dynamic equations remains the same; one only needs to generate the invariants of motion using the lumped mass techniques.

Acknowledgment

This research was supported, in part, by the U.S. Army Research Office, Research Triangle Park, N.C.

References

Adini, A., and Clough, R. W., 1960, "Analysis of Plate Bending by the Finite Element Method," report submitted to the National Science Foundation (Grant No. G7337), Washington, D.C.

Armanios, E. A., and Negm, H. M., 1983, "An Improved Rectangular Element for Plate Bending Analysis," *Computers and Structures*, Vol. 16, pp. 677–686.

Bogner, F. K., Fox, R. L., and Schmit, L. A., 1965, "The Generation of Inter-Element Compatible Stiffness and Mass Matrices by Use of Interpolation Formulas," *Proc. 1st Conf. on Matrix Methods in Structural Mech.*, Ohio, pp. 397–443.

Chang, B., 1989, "A Nonlinear Finite Element Formulation for the Large Displacement Analysis of Plates," Ph.D. Thesis, Department of Mechanical Engineering, University of Illinois at Chicago.

Clough, R. W., and Tocher, J. L., 1965, "Finite Element Stiffness Matrices for the Analysis of Plate Bending," *Proc. 1st Conf. on Matrix Methods in Structural Mech.*, Ohio, pp. 515–545.

Dym, C. L., and Shames, I. H., 1973, *Solid Mechanics, A Variational Approach*, McGraw-Hill, New York.

Goldstein, H., 1980, *Classical Mechanics*, 2nd ed., Addison-Wesley.

Gopalacharyulu, S., 1973, "A Higher Order Conforming, Rectangular Plate Element," *Journal of Sound and Vibrations*, Vol. 6, No. 2, pp. 305–308.

Hinton, E., Razzaque, A., Zienkiewicz, O. C., and Davies, J. D., 1975, "A Simple Finite Element Solution for Plates of Homogeneous Sandwich and Cellular Construction," *Proceedings*, Part 2, Vol. 59, Institute of Civil Engineers, pp. 43–65.

Hrabok, M. M., and Hrudey, T. M., 1984, "A Review and Catalogue of Plate Bending Finite Elements," *Computers and Structures*, Vol. 3, pp. 479–495.

Melosh, R. J., 1961, "A Stiffness Matrix for the Analysis of the Thin Plate in Bending," *J. Aeronaut. Sci.*, Vol. 28, No. 1, pp. 34–42.

Ortiz, M., and Morris, G. R., 1988, "C^0 Finite Element Discretization of Kirchhoff's Equations of Thin Plate Bending," *International Journal for Numerical Methods in Engineering*, Vol. 26, pp. 1551–1566.

Papenfuss, B. W., 1959, "Lateral Plate Deflection by Stiffness Matrix Methods with Application to a Marquee," M.Sc. Thesis, Department of Civil Engineering, University of Washington, Seattle, Wash.

Popplewell, N., and McDonald, H., 1971, "Conforming Rectangular and Triangular Plate-Bending Elements," *Journal of Sound and Vibrations*, Vol. 19, No. 3, pp. 333–347.

Przemieniecki, J. S., 1966, "Equivalent Mass Matrices for Rectangular Plates in Bending," *AIAA*, Vol. 4, No. 5, pp. 949–950.

Przemieniecki, J. S., 1968, *Theory of Matrix Structural Analysis*, McGraw-Hill, New York.

Shabana, A., and Wehage, R. A., 1983, "A Coordinate Reduction Technique for Transient Analysis of Spatial Substructure with Large Angular Rotations," *Journal of Structural Mechanics*, Vol. 11, No. 3, pp. 401–431.

Shabana, A. A., 1989, *Dynamics of Multibody Systems*, John Wiley and Sons, New York.

Shabana, A. A., 1990, *Theory of Vibration, Vol. II, Discrete and Continuous Systems*, Springer-Verlag, New York.

Shigley, J. E., and Uicker, J. J., 1980, *Theory of Machines and Mechanisms*, McGraw-Hill, New York.

Smith, I. M., and Duncan, W., 1970, "The Effectiveness of Nodal Continuities in Finite Element Analysis of Thin Rectangular and Skew Plates in Bending," *International Journal for Numerical Methods in Engineering*, Vol. 2, pp. 253–258.

Tocher, J. L., 1962, "Analysis of Plate Bending Using Triangular Elements," Ph.D. Thesis, Department of Civil Engineering, University of California, Berkeley, Calif.

Torres, J., Samartin, A., Arroyo, V., and Valle, J. D., 1986, "A C^1 Finite Element Family for Kirchhoff Plate Bending," *International Journal for Numerical Methods in Engineering*, Vol. 23, pp. 2005–2029.

Veubeke, F., 1968, "A Conforming Finite Element Approach to Plate Bending," *IJSS*, Vol. 4, pp. 95–108.

Yang, R. J., and Bhatti, M. A., 1985, "Nonlinear Static and Dynamic Analysis of Plates," *Journal of Engineering Mechanics*, Vol. 111, pp. 175–187.

Zienkiewicz, O. C., 1977, *The Finite Element Method in Engineering Science*, 3rd ed., McGraw-Hill, New York.

APPENDIX

Using the shape function of the plate element of equation (6), the invariants of motion of the element of (59) are given by

$$I_{11}^{ij} = \frac{m^{ij}}{36}$$

$$\begin{bmatrix}
4&0&0&0&0&2&0&0&0&0&1&0&0&0&0&2&0&0&0&0\\
0&0&0&0&0&0&0&0&0&0&0&0&0&0&0&0&0&0&0&0\\
0&0&0&0&0&0&0&0&0&0&0&0&0&0&0&0&0&0&0&0\\
0&0&0&0&0&0&0&0&0&0&0&0&0&0&0&0&0&0&0&0\\
0&0&0&0&0&0&0&0&0&0&0&0&0&0&0&0&0&0&0&0\\
2&0&0&0&0&4&0&0&0&0&2&0&0&0&0&1&0&0&0&0\\
0&0&0&0&0&0&0&0&0&0&0&0&0&0&0&0&0&0&0&0\\
0&0&0&0&0&0&0&0&0&0&0&0&0&0&0&0&0&0&0&0\\
0&0&0&0&0&0&0&0&0&0&0&0&0&0&0&0&0&0&0&0\\
0&0&0&0&0&0&0&0&0&0&0&0&0&0&0&0&0&0&0&0\\
1&0&0&0&0&2&0&0&0&0&4&0&0&0&0&2&0&0&0&0\\
0&0&0&0&0&0&0&0&0&0&0&0&0&0&0&0&0&0&0&0\\
0&0&0&0&0&0&0&0&0&0&0&0&0&0&0&0&0&0&0&0\\
0&0&0&0&0&0&0&0&0&0&0&0&0&0&0&0&0&0&0&0\\
0&0&0&0&0&0&0&0&0&0&0&0&0&0&0&0&0&0&0&0\\
2&0&0&0&0&1&0&0&0&0&2&0&0&0&0&4&0&0&0&0\\
0&0&0&0&0&0&0&0&0&0&0&0&0&0&0&0&0&0&0&0\\
0&0&0&0&0&0&0&0&0&0&0&0&0&0&0&0&0&0&0&0\\
0&0&0&0&0&0&0&0&0&0&0&0&0&0&0&0&0&0&0&0\\
0&0&0&0&0&0&0&0&0&0&0&0&0&0&0&0&0&0&0&0
\end{bmatrix}_{20\times 20}$$

$$I_{22}^{ij} = \frac{m^{ij}}{36}$$

$$\begin{bmatrix}
0&0&0&0&0&0&0&0&0&0&0&0&0&0&0&0&0&0&0&0\\
0&4&0&0&0&0&2&0&0&0&0&1&0&0&0&0&2&0&0&0\\
0&0&0&0&0&0&0&0&0&0&0&0&0&0&0&0&0&0&0&0\\
0&0&0&0&0&0&0&0&0&0&0&0&0&0&0&0&0&0&0&0\\
0&0&0&0&0&0&0&0&0&0&0&0&0&0&0&0&0&0&0&0\\
0&0&0&0&0&0&0&0&0&0&0&0&0&0&0&0&0&0&0&0\\
0&2&0&0&0&0&4&0&0&0&0&2&0&0&0&0&1&0&0&0\\
0&0&0&0&0&0&0&0&0&0&0&0&0&0&0&0&0&0&0&0\\
0&0&0&0&0&0&0&0&0&0&0&0&0&0&0&0&0&0&0&0\\
0&0&0&0&0&0&0&0&0&0&0&0&0&0&0&0&0&0&0&0\\
0&0&0&0&0&0&0&0&0&0&0&0&0&0&0&0&0&0&0&0\\
0&1&0&0&0&0&2&0&0&0&0&4&0&0&0&0&2&0&0&0\\
0&0&0&0&0&0&0&0&0&0&0&0&0&0&0&0&0&0&0&0\\
0&0&0&0&0&0&0&0&0&0&0&0&0&0&0&0&0&0&0&0\\
0&0&0&0&0&0&0&0&0&0&0&0&0&0&0&0&0&0&0&0\\
0&0&0&0&0&0&0&0&0&0&0&0&0&0&0&0&0&0&0&0\\
0&2&0&0&0&0&1&0&0&0&0&2&0&0&0&0&4&0&0&0\\
0&0&0&0&0&0&0&0&0&0&0&0&0&0&0&0&0&0&0&0\\
0&0&0&0&0&0&0&0&0&0&0&0&0&0&0&0&0&0&0&0\\
0&0&0&0&0&0&0&0&0&0&0&0&0&0&0&0&0&0&0&0
\end{bmatrix}_{20\times 20}$$

Downloaded 03 May 2010 to 171.66.16.244. Redistribution subject to ASME license or copyright; see http://www.asme.org/terms/Terms_Use.cfm

$$I_{33}^{ij} = \frac{m^{ij}}{176400}$$

$$\begin{bmatrix}
0 & 0 & 0 & 0 & 0 & 0 & 0 & 0 & 0 & 0 & 0 \\
0 & 0 & 0 & 0 & 0 & 0 & 0 & 0 & 0 & 0 & 0 \\
0 & 0 & 24336 & 3432b & -3432a & 0 & 0 & 8424 & -2028b & -1188a & 0 \\
0 & 0 & 3432b & 624b^2 & -484ab & 0 & 0 & 2028b & -468b^2 & -286ab & 0 \\
0 & 0 & -3432a & -484ab & 624a^2 & 0 & 0 & -1188a & 286ab & 216a^2 & 0 \\
0 & 0 & 0 & 0 & 0 & 0 & 0 & 0 & 0 & 0 & 0 \\
0 & 0 & 0 & 0 & 0 & 0 & 0 & 0 & 0 & 0 & 0 \\
0 & 0 & 8424 & 2028b & -1188a & 0 & 0 & 24336 & -3432b & -3432a & 0 \\
0 & 0 & -2028b & -468b^2 & 286ab & 0 & 0 & -3432b & 624b^2 & 484ab & 0 \\
0 & 0 & -1188a & -286ab & 216a^2 & 0 & 0 & -3432a & 484ab & 624a^2 & 0 \\
0 & 0 & 0 & 0 & 0 & 0 & 0 & 0 & 0 & 0 & 0 \\
0 & 0 & 0 & 0 & 0 & 0 & 0 & 0 & 0 & 0 & 0 \\
0 & 0 & 2916 & 702b & -702a & 0 & 0 & 8424 & -1188b & -2028a & 0 \\
0 & 0 & -702b & -162b^2 & 169ab & 0 & 0 & -1188b & 216b^2 & 286ab & 0 \\
0 & 0 & 702a & 169ab & -162a^2 & 0 & 0 & 2028a & -286ab & -468a^2 & 0 \\
0 & 0 & 0 & 0 & 0 & 0 & 0 & 0 & 0 & 0 & 0 \\
0 & 0 & 0 & 0 & 0 & 0 & 0 & 0 & 0 & 0 & 0 \\
0 & 0 & 8424 & 1188b & -2028a & 0 & 0 & 2916 & -702b & -702a & 0 \\
0 & 0 & 1188b & 216b^2 & -286ab & 0 & 0 & 702b & -162b^2 & -169ab & 0 \\
0 & 0 & 2028a & 286ab & -468a^2 & 0 & 0 & 702a & -169ab & -162a^2 & 0
\end{bmatrix}$$

$$\begin{bmatrix}
0 & 0 & 0 & 0 & 0 & 0 & 0 & 0 & 0 \\
0 & 0 & 0 & 0 & 0 & 0 & 0 & 0 & 0 \\
0 & 2916 & -702b & 702a & 0 & 0 & 8424 & 1188b & 2028a \\
0 & 702b & -162b^2 & 169ab & 0 & 0 & 1188b & 216b^2 & 286ab \\
0 & -702a & 169ab & -162a^2 & 0 & 0 & -2028a & -286ab & -468a^2 \\
0 & 0 & 0 & 0 & 0 & 0 & 0 & 0 & 0 \\
0 & 0 & 0 & 0 & 0 & 0 & 0 & 0 & 0 \\
0 & 8424 & -1188b & 2028a & 0 & 0 & 2916 & 702b & 702a \\
0 & -1188b & 216b^2 & -286ab & 0 & 0 & -702b & -162b^2 & -169ab \\
0 & -2028a & 286ab & -468a^2 & 0 & 0 & -702a & -169ab & -162a^2 \\
0 & 0 & 0 & 0 & 0 & 0 & 0 & 0 & 0 \\
0 & 0 & 0 & 0 & 0 & 0 & 0 & 0 & 0 \\
0 & 24336 & -3432b & 3432a & 0 & 0 & 8424 & 2028b & 1188a \\
0 & -3432b & 624b^2 & -484ab & 0 & 0 & -2028b & -468b^2 & -286ab \\
0 & 3432a & -484ab & 624a^2 & 0 & 0 & 1188a & 286ab & 216a^2 \\
0 & 0 & 0 & 0 & 0 & 0 & 0 & 0 & 0 \\
0 & 0 & 0 & 0 & 0 & 0 & 0 & 0 & 0 \\
0 & 8424 & -2028b & 1188a & 0 & 0 & 24336 & 3432b & 3432a \\
0 & 2028b & -468b^2 & 286ab & 0 & 0 & 3432b & 624b^2 & 484ab \\
0 & 1188a & -286ab & 216a^2 & 0 & 0 & 3432a & 484ab & 624a^2
\end{bmatrix}_{20\times 20}$$

$$I_{12}^{ij} = \frac{m^{ij}}{36}$$

$$\begin{bmatrix}
0 & 4 & 0 & 0 & 0 & 0 & 2 & 0 & 0 & 0 & 0 & 1 & 0 & 0 & 0 & 0 & 2 & 0 & 0 & 0 \\
0 & 0 & 0 & 0 & 0 & 0 & 0 & 0 & 0 & 0 & 0 & 0 & 0 & 0 & 0 & 0 & 0 & 0 & 0 & 0 \\
0 & 0 & 0 & 0 & 0 & 0 & 0 & 0 & 0 & 0 & 0 & 0 & 0 & 0 & 0 & 0 & 0 & 0 & 0 & 0 \\
0 & 0 & 0 & 0 & 0 & 0 & 0 & 0 & 0 & 0 & 0 & 0 & 0 & 0 & 0 & 0 & 0 & 0 & 0 & 0 \\
0 & 0 & 0 & 0 & 0 & 0 & 0 & 0 & 0 & 0 & 0 & 0 & 0 & 0 & 0 & 0 & 0 & 0 & 0 & 0 \\
0 & 2 & 0 & 0 & 0 & 0 & 4 & 0 & 0 & 0 & 0 & 2 & 0 & 0 & 0 & 0 & 1 & 0 & 0 & 0 \\
0 & 0 & 0 & 0 & 0 & 0 & 0 & 0 & 0 & 0 & 0 & 0 & 0 & 0 & 0 & 0 & 0 & 0 & 0 & 0 \\
0 & 0 & 0 & 0 & 0 & 0 & 0 & 0 & 0 & 0 & 0 & 0 & 0 & 0 & 0 & 0 & 0 & 0 & 0 & 0 \\
0 & 0 & 0 & 0 & 0 & 0 & 0 & 0 & 0 & 0 & 0 & 0 & 0 & 0 & 0 & 0 & 0 & 0 & 0 & 0 \\
0 & 0 & 0 & 0 & 0 & 0 & 0 & 0 & 0 & 0 & 0 & 0 & 0 & 0 & 0 & 0 & 0 & 0 & 0 & 0 \\
0 & 1 & 0 & 0 & 0 & 0 & 2 & 0 & 0 & 0 & 0 & 4 & 0 & 0 & 0 & 0 & 2 & 0 & 0 & 0 \\
0 & 0 & 0 & 0 & 0 & 0 & 0 & 0 & 0 & 0 & 0 & 0 & 0 & 0 & 0 & 0 & 0 & 0 & 0 & 0 \\
0 & 0 & 0 & 0 & 0 & 0 & 0 & 0 & 0 & 0 & 0 & 0 & 0 & 0 & 0 & 0 & 0 & 0 & 0 & 0 \\
0 & 0 & 0 & 0 & 0 & 0 & 0 & 0 & 0 & 0 & 0 & 0 & 0 & 0 & 0 & 0 & 0 & 0 & 0 & 0 \\
0 & 0 & 0 & 0 & 0 & 0 & 0 & 0 & 0 & 0 & 0 & 0 & 0 & 0 & 0 & 0 & 0 & 0 & 0 & 0 \\
0 & 2 & 0 & 0 & 0 & 0 & 1 & 0 & 0 & 0 & 0 & 2 & 0 & 0 & 0 & 0 & 4 & 0 & 0 & 0 \\
0 & 0 & 0 & 0 & 0 & 0 & 0 & 0 & 0 & 0 & 0 & 0 & 0 & 0 & 0 & 0 & 0 & 0 & 0 & 0 \\
0 & 0 & 0 & 0 & 0 & 0 & 0 & 0 & 0 & 0 & 0 & 0 & 0 & 0 & 0 & 0 & 0 & 0 & 0 & 0 \\
0 & 0 & 0 & 0 & 0 & 0 & 0 & 0 & 0 & 0 & 0 & 0 & 0 & 0 & 0 & 0 & 0 & 0 & 0 & 0 \\
0 & 0 & 0 & 0 & 0 & 0 & 0 & 0 & 0 & 0 & 0 & 0 & 0 & 0 & 0 & 0 & 0 & 0 & 0 & 0
\end{bmatrix}_{20\times 20}$$

Downloaded 03 May 2010 to 171.66.16.244. Redistribution subject to ASME license or copyright; see http://www.asme.org/terms/Terms_Use.cfm

$$I_{13}^{ij} = \frac{m^{ij}}{1200}$$

$$\begin{bmatrix}
0 & 0 & 147 & 21b & -21a & 0 & 0 & 63 & -14b & -9a & 0 \\
0 & 0 & 0 & 0 & 0 & 0 & 0 & 0 & 0 & 0 & 0 \\
0 & 0 & 0 & 0 & 0 & 0 & 0 & 0 & 0 & 0 & 0 \\
0 & 0 & 0 & 0 & 0 & 0 & 0 & 0 & 0 & 0 & 0 \\
0 & 0 & 0 & 0 & 0 & 0 & 0 & 0 & 0 & 0 & 0 \\
0 & 0 & 63 & 14b & -9a & 0 & 0 & 147 & -21b & -21a & 0 \\
0 & 0 & 0 & 0 & 0 & 0 & 0 & 0 & 0 & 0 & 0 \\
0 & 0 & 0 & 0 & 0 & 0 & 0 & 0 & 0 & 0 & 0 \\
0 & 0 & 0 & 0 & 0 & 0 & 0 & 0 & 0 & 0 & 0 \\
0 & 0 & 0 & 0 & 0 & 0 & 0 & 0 & 0 & 0 & 0 \\
0 & 0 & 27 & 6b & -6a & 0 & 0 & 63 & -9b & -14a & 0 \\
0 & 0 & 0 & 0 & 0 & 0 & 0 & 0 & 0 & 0 & 0 \\
0 & 0 & 0 & 0 & 0 & 0 & 0 & 0 & 0 & 0 & 0 \\
0 & 0 & 0 & 0 & 0 & 0 & 0 & 0 & 0 & 0 & 0 \\
0 & 0 & 0 & 0 & 0 & 0 & 0 & 0 & 0 & 0 & 0 \\
0 & 0 & 63 & 9b & -14a & 0 & 0 & 27 & -6b & -6a & 0 \\
0 & 0 & 0 & 0 & 0 & 0 & 0 & 0 & 0 & 0 & 0 \\
0 & 0 & 0 & 0 & 0 & 0 & 0 & 0 & 0 & 0 & 0 \\
0 & 0 & 0 & 0 & 0 & 0 & 0 & 0 & 0 & 0 & 0 \\
0 & 0 & 0 & 0 & 0 & 0 & 0 & 0 & 0 & 0 & 0
\end{bmatrix}$$

$$\begin{bmatrix}
0 & 27 & -6b & 6a & 0 & 0 & 63 & 9b & 14a \\
0 & 0 & 0 & 0 & 0 & 0 & 0 & 0 & 0 \\
0 & 0 & 0 & 0 & 0 & 0 & 0 & 0 & 0 \\
0 & 0 & 0 & 0 & 0 & 0 & 0 & 0 & 0 \\
0 & 0 & 0 & 0 & 0 & 0 & 0 & 0 & 0 \\
0 & 63 & -9b & 14a & 0 & 0 & 27 & 6b & 6a \\
0 & 0 & 0 & 0 & 0 & 0 & 0 & 0 & 0 \\
0 & 0 & 0 & 0 & 0 & 0 & 0 & 0 & 0 \\
0 & 0 & 0 & 0 & 0 & 0 & 0 & 0 & 0 \\
0 & 0 & 0 & 0 & 0 & 0 & 0 & 0 & 0 \\
0 & 147 & -21b & 21a & 0 & 0 & 63 & 14b & 9a \\
0 & 0 & 0 & 0 & 0 & 0 & 0 & 0 & 0 \\
0 & 0 & 0 & 0 & 0 & 0 & 0 & 0 & 0 \\
0 & 0 & 0 & 0 & 0 & 0 & 0 & 0 & 0 \\
0 & 0 & 0 & 0 & 0 & 0 & 0 & 0 & 0 \\
0 & 63 & -14b & 9a & 0 & 0 & 147 & 21b & 21a \\
0 & 0 & 0 & 0 & 0 & 0 & 0 & 0 & 0 \\
0 & 0 & 0 & 0 & 0 & 0 & 0 & 0 & 0 \\
0 & 0 & 0 & 0 & 0 & 0 & 0 & 0 & 0 \\
0 & 0 & 0 & 0 & 0 & 0 & 0 & 0 & 0
\end{bmatrix}_{20\times 20}$$

and

$$I_{23}^{ij} = \frac{m^{ij}}{1200}$$

$$\begin{bmatrix}
0 & 0 & 0 & 0 & 0 & 0 & 0 & 0 & 0 & 0 & 0 \\
0 & 0 & 147 & 21b & -21a & 0 & 0 & 63 & -14b & -9a & 0 \\
0 & 0 & 0 & 0 & 0 & 0 & 0 & 0 & 0 & 0 & 0 \\
0 & 0 & 0 & 0 & 0 & 0 & 0 & 0 & 0 & 0 & 0 \\
0 & 0 & 0 & 0 & 0 & 0 & 0 & 0 & 0 & 0 & 0 \\
0 & 0 & 0 & 0 & 0 & 0 & 0 & 0 & 0 & 0 & 0 \\
0 & 0 & 63 & 14b & -9a & 0 & 0 & 147 & -21b & -21a & 0 \\
0 & 0 & 0 & 0 & 0 & 0 & 0 & 0 & 0 & 0 & 0 \\
0 & 0 & 0 & 0 & 0 & 0 & 0 & 0 & 0 & 0 & 0 \\
0 & 0 & 0 & 0 & 0 & 0 & 0 & 0 & 0 & 0 & 0 \\
0 & 0 & 0 & 0 & 0 & 0 & 0 & 0 & 0 & 0 & 0 \\
0 & 0 & 27 & 6b & -6a & 0 & 0 & 63 & -9b & -14a & 0 \\
0 & 0 & 0 & 0 & 0 & 0 & 0 & 0 & 0 & 0 & 0 \\
0 & 0 & 0 & 0 & 0 & 0 & 0 & 0 & 0 & 0 & 0 \\
0 & 0 & 0 & 0 & 0 & 0 & 0 & 0 & 0 & 0 & 0 \\
0 & 0 & 0 & 0 & 0 & 0 & 0 & 0 & 0 & 0 & 0 \\
0 & 0 & 63 & 9b & -14a & 0 & 0 & 27 & -6b & -6a & 0 \\
0 & 0 & 0 & 0 & 0 & 0 & 0 & 0 & 0 & 0 & 0 \\
0 & 0 & 0 & 0 & 0 & 0 & 0 & 0 & 0 & 0 & 0 \\
0 & 0 & 0 & 0 & 0 & 0 & 0 & 0 & 0 & 0 & 0
\end{bmatrix}$$

Downloaded 03 May 2010 to 171.66.16.244. Redistribution subject to ASME license or copyright; see http://www.asme.org/terms/Terms_Use.cfm

$$
\begin{bmatrix}
0 & 0 & 0 & 0 & 0 & 0 & 0 & 0 & 0 \\
0 & 27 & -6b & 6a & 0 & 0 & 63 & 9b & 14a \\
0 & 0 & 0 & 0 & 0 & 0 & 0 & 0 & 0 \\
0 & 0 & 0 & 0 & 0 & 0 & 0 & 0 & 0 \\
0 & 0 & 0 & 0 & 0 & 0 & 0 & 0 & 0 \\
0 & 0 & 0 & 0 & 0 & 0 & 0 & 0 & 0 \\
0 & 63 & -9b & 14a & 0 & 0 & 27 & 6b & 6a \\
0 & 0 & 0 & 0 & 0 & 0 & 0 & 0 & 0 \\
0 & 0 & 0 & 0 & 0 & 0 & 0 & 0 & 0 \\
0 & 0 & 0 & 0 & 0 & 0 & 0 & 0 & 0 \\
0 & 0 & 0 & 0 & 0 & 0 & 0 & 0 & 0 \\
0 & 147 & -21b & 21a & 0 & 0 & 63 & 14b & 9a \\
0 & 0 & 0 & 0 & 0 & 0 & 0 & 0 & 0 \\
0 & 0 & 0 & 0 & 0 & 0 & 0 & 0 & 0 \\
0 & 0 & 0 & 0 & 0 & 0 & 0 & 0 & 0 \\
0 & 0 & 0 & 0 & 0 & 0 & 0 & 0 & 0 \\
0 & 63 & -14b & 9a & 0 & 0 & 147 & 21b & 21a \\
0 & 0 & 0 & 0 & 0 & 0 & 0 & 0 & 0 \\
0 & 0 & 0 & 0 & 0 & 0 & 0 & 0 & 0 \\
0 & 0 & 0 & 0 & 0 & 0 & 0 & 0 & 0
\end{bmatrix}_{20\times 20}.
$$

Downloaded 03 May 2010 to 171.66.16.244. Redistribution subject to ASME license or copyright; see http://www.asme.org/terms/Terms_Use.cfm

The Initial Phase of Transient Thermal Stresses due to General Boundary Thermal Loads in Orthotropic Hollow Cylinders

G. A. Kardomateas
Assistant Professor,
School of Aerospace Engineering,
Georgia Institute of Technology,
Atlanta, GA 30332-0150
Mem. ASME

The stresses and displacements in the initial phase of applying a thermal load on the bounding surfaces of an orthotropic hollow circular cylinder are obtained using the Hankel asymptotic expansions for the Bessel functions of the first and second kind. Such a load may be constant temperature, constant heat flux, zero heat flux, or heat convection to a different medium at either surface. The material properties are assumed to be independent of temperature. A constant applied temperature at the one surface and convection into a medium at a different temperature at the other surface is used to illustrate the variation of stresses with time and through the thickness in the initial transient phase.

Introduction

Meeting the need for materials which can function usefully at different temperature levels is one of the most challenging problems facing our technology. The difficulty is compounded by the fact that operating conditions involve not only elevated temperature levels but frequently also severe temperature gradients. Such temperature differentials may produce thermal stresses significant enough to limit the material life. Some of the more important applications of fiber-reinforced composites involve the configuration of a hollow cylinder, typically produced by filament winding on a cylindrical mandrel. For example, composite tubes of considerable thickness could be used in such parts as automotive suspension components. The manufacturing stage includes a thermal treatment phase, during which thermal stresses of considerable magnitude may be generated. Other applications may be for launch tubes or landing gears.

Relevant work on understanding the thermally-induced stresses in such configurations was done by Kalam and Tauchert (1978), Hyer and Cooper (1986), and Avery and Herakovich (1986). These studies dealt with the steady-state problem. A solution to the transient thermal stress problem was derived by Kardomateas (1989). This solution involved a series expansion of Bessel functions of the first and second kind and it is valid only beyond a certain time value. This is because the series expansions cannot be used for large arguments; small time values require including an increasing number of terms and therefore large arguments. This paper gives the solution for this case of the very beginning of applying the thermal loads (the initial phase of transient thermal stresses). The analysis is limited to orthotropic tubes, (for example, composite tubes with the fibers aligned circumferentially). The material properties are assumed to be independent of temperature, the stresses not to vary along the generators and that there are no body forces.

In this paper the body is assumed to be subjected to any kind of thermal load such as constant temperature, constant heat flux, zero heat flux, or heat convection to a different medium at either surface; in this respect this paper also extends the work by Kardomateas (1989), which was done for the specific case of a constant temperature on the one surface of the cylinder and heat convection to a different medium at the other. We shall present an example for the distribution of stresses and displacements in the initial phase of transient stresses, where it is assumed that one surface of the cylinder is at a constant temperature and at the other there is heat convection into a medium at the reference temperature.

Derivation of the Governing Equations

Consider a circular cylindrical shell $r_1 \le r \le r_2$ whose axis coincides with the axis of z. The initial (reference) temperature is assumed to be zero. The thermal problem consists of the heat conduction equation

$$K\left(\frac{\partial^2 T(r,t)}{\partial r^2} + \frac{1}{r}\frac{\partial T(r,t)}{\partial r}\right) = \frac{\partial T(r,t)}{\partial t} \quad (r_1 < r < r_2, t > 0), \tag{1a}$$

Contributed by the Applied Mechanics Division of THE AMERICAN SOCIETY OF MECHANICAL ENGINEERS for presentation at the Winter Annual Meeting, Dallas, Texas, Nov. 25-30, 1990.

Discussion on this paper should be addressed to the Technical Editor, Leon M. Keer, The Technological Institute, Northwestern University, Evanston, IL 60208, and will be accepted until two months after final publication of the paper itself in the JOURNAL OF APPLIED MECHANICS. Manuscript received by the ASME Applied Mechanics Division, Feb. 2, 1989; final revision, June 21, 1989.

Paper No. 90-WA/APM-16.

Copyright © 1990 by ASME
Downloaded 03 May 2010 to 171.66.16.244. Redistribution subject to ASME license or copyright; see http://www.asme.org/terms/Terms_Use.cfm

where K is the thermal diffusivity of the composite in the r direction, and the initial and boundary conditions

$$T(r,t=0)=0 \text{ at } r_1 \le r \le r_2, \tag{1b}$$

$$h_1 \frac{\partial T(r,t)}{\partial r}\Big|_{r=r_1} - h_2 T(r_1,t) = h_3 (t>0), \tag{1c}$$

$$h_1^* \frac{\partial T(r,t)}{\partial r}\Big|_{r=r_2} + h_2^* T(r_2,t) = h_3^* (t>0), \tag{1d}$$

where h_1, h_2, h_1^*, h_2^* are constants which may be positive or zero (provided h_1 and h_2, or h_1^* and h_2^* do not both vanish) and h_3 and h_3^* are constants. By choice of these constants the general results include all combinations of constant temperature, constant heat flux, zero heat flux, or heat convection to a different medium at either surface. A solution for the temperature field is given by Carslaw and Jaeger (1959) in terms of the Bessel functions of the first and second kind J_n and Y_n, as follows

$$T(r,t) = d_1 + d_2 \ln(r/r_1) + d_3 \ln(r/r_2) + \sum_{n=1}^{\infty} e^{-Ka_n^2 t}[d_{4n} J_0(ra_n) + d_{5n} Y_0(ra_n)], \tag{2}$$

where $\pm a_n$ are the roots (all real and simple) of:

$$[h_1 x J_1(r_1 x) + h_2 J_0(r_1 x)][h_1^* x Y_1(r_2 x) - h_2^* Y_0(r_2 x)] - [h_1 x Y_1(r_1 x) + h_2 Y_0(r_1 x)][h_1^* x J_1(r_2 x) - h_2^* J_0(r_2 x)]. \tag{3}$$

The constants d_i are given in Appendix A.

In cylindrical coordinates (r, θ, z), the constitutive equations for the orthotropic body are given in terms of the elastic constants C_{ij} and the thermal expansion coefficients, α_i:

$$\begin{bmatrix} \sigma_{rr} \\ \sigma_{\theta\theta} \\ \sigma_{zz} \\ \tau_{\theta z} \\ \tau_{rz} \\ \tau_{r\theta} \end{bmatrix} = \begin{bmatrix} C_{11} & C_{12} & C_{13} & 0 & 0 & 0 \\ C_{12} & C_{22} & C_{23} & 0 & 0 & 0 \\ C_{13} & C_{23} & C_{33} & 0 & 0 & 0 \\ 0 & 0 & 0 & C_{44} & 0 & 0 \\ 0 & 0 & 0 & 0 & C_{55} & 0 \\ 0 & 0 & 0 & 0 & 0 & C_{66} \end{bmatrix} \begin{bmatrix} \epsilon_{rr} - \alpha_r \Delta T \\ \epsilon_{\theta\theta} - \alpha_\theta \Delta T \\ \epsilon_{zz} - \alpha_z \Delta T \\ \gamma_{\theta z} \\ \gamma_{rz} \\ \gamma_{r\theta} \end{bmatrix}. \tag{4}$$

Since the temperature field is independent of the angular and axial coordinates, the stresses and strains will be a function of r and t only.

Following the analysis by Kardomateas (1989), the strain field for this class of problems is expressed in terms of the radial displacement $U(r, t)$:

$$\epsilon_{rr} = \frac{\partial U(r,t)}{\partial r};\ \epsilon_{\theta\theta} = \frac{U(r,t)}{r};\ \epsilon_{zz} = C(t), \tag{5a}$$

$$\gamma_{\theta z} = \gamma_{rz} = \gamma_{r\theta} = 0. \tag{5b}$$

There remain one equilibrium equation for the nonvanishing stresses:

$$\frac{\partial \sigma_{rr}(r,t)}{\partial r} + \frac{\sigma_{rr}(r,t) - \sigma_{\theta\theta}(r,t)}{r} = 0. \tag{6}$$

Define

$$q_1 = C_{11}\alpha_r + C_{12}\alpha_\theta + C_{13}\alpha_z, \tag{7a}$$

$$q_2 = (C_{11} - C_{12})\alpha_r + (C_{12} - C_{22})\alpha_\theta + (C_{13} - C_{23})\alpha_z, \tag{7b}$$

$$q_3 = C_{13}\alpha_r + C_{23}\alpha_\theta + C_{33}\alpha_z. \tag{7c}$$

Set

$$U(r,t) = U_0(r) + \sum_{n=1}^{\infty} e^{-Ka_n^2 t} R_n(r), \tag{8}$$

and express the parameter $C(t)$ in the form

$$C(t) = c_0 + \sum_{n=1}^{\infty} c_n e^{-Ka_n^2 t}. \tag{9}$$

Substituting equations (4), (5) into (6) and using the definitions (7), (8), and (9) results in the following differential equations:

$$C_{11}\left(U_0''(r) + \frac{U_0'(r)}{r}\right) - \frac{C_{22}}{r^2} U_0(r) = \frac{q_1(d_2+d_3) + q_2 d_1 + (C_{23} - C_{13})c_0}{r} + q_2 d_2 \frac{\ln(r/r_1)}{r} + q_2 d_3 \frac{\ln(r/r_2)}{r}, \tag{10}$$

$$C_{11}\left(R_n''(r) + \frac{R_n'(r)}{r}\right) - \frac{C_{22}}{r^2} R_n(r) = \frac{(C_{23} - C_{13})c_n}{r} + d_{4n}\left[\frac{J_0(ra_n)}{r} - q_1 a_n J_1(ra_n)\right] + d_{5n}\left[\frac{Y_0(ra_n)}{r} - q_1 a_n Y_1(ra_n)\right] \quad n = 1, \ldots \infty. \tag{11}$$

Solution

Define

$$\lambda_{1,2} = \pm\sqrt{C_{22}/C_{11}}. \tag{12}$$

For $C_{11} \neq C_{22}$, the solution of (10) for $U_0(r)$ is

$$U_0(r) = G_{10} r^{\lambda_1} + G_{20} r^{\lambda_2} + \frac{C_{23} - C_{13}}{C_{11} - C_{22}} c_0 r + U_0^*(r), \tag{13a}$$

$$U_0^*(r) = \frac{q_2}{C_{11} - C_{22}}[d_2 r \ln(r/r_1) + d_3 r \ln(r/r_2)] + \left[\frac{q_2(d_2+d_3) + q_2 d_1}{C_{11} - C_{22}} - \frac{2C_{11} q_2 (d_2+d_3)}{(C_{11} - C_{22})^2}\right] r. \tag{13b}$$

For $C_{11} = C_{22}$, the corresponding solution is

$$U_0(r) = G_{10} r + \frac{G_{20}}{r} + \frac{(C_{23} - C_{13})}{2C_{11}} c_0 r \ln(r/r_2) + U_0^*(r), \tag{14a}$$

$$U_0^*(r) = \frac{q_2}{4C_{11}}[d_2 r \ln^2(r/r_1) + d_3 r \ln^2(r/r_2)] + \frac{(2q_1 - q_2)(d_2+d_3) + 2q_2 d_1}{4C_{11}} r \ln(r/r_2), \tag{14b}$$

where G_i are constants, yet unknown, which, together with the constants c_i, are found later from the boundary conditions.

To solve equation (11) for large arguments, we use the Hankel asymptotic expansions of the Bessel functions of the first and second kind. For $C_{11} \neq C_{22}$, the solution for R_n is expressed

Downloaded 03 May 2010 to 171.66.16.244. Redistribution subject to ASME license or copyright; see http://www.asme.org/terms/Terms_Use.cfm

$$R_n(r) = G_{1n} r^{\lambda 1} + G_{2n} r^{\lambda 2} + \frac{C_{23} - C_{13}}{C_{11} - C_{22}} c_n r + R_n^*(r), \quad (15a)$$

and for $C_{11} = C_{22}$, the solution for R_n is

$$R_n(r) = G_{1n} r + \frac{G_{2n}}{r} + \frac{C_{23} - C_{13}}{2C_{11}} c_n r \ln(r/r_2) + R_n^*(r). \quad (15b)$$

The function $R_n^*(r)$ is the particular solution of the equation that results from equation (11) if the right-hand side includes only the Bessel functions terms. For small values of the argument the function $R_n^*(r)$ was given in Kardomateas (1989) (although a specific thermal load was considered in that work, the expression holds true for the general thermal load considered here).

For large arguments, we use the Hankel asymptotic expansions of the Bessel functions of the first and second kind (see Appendix B). Employing the substitution

$$\rho = r a_n;\ R_n^*(r) = R_n^{**}(\rho), \quad (16)$$

gives the following equation for $R_n^{**}(\rho)$

$$C_{11} a_n^2 \left(R_n^{**\prime\prime}(\rho) + \frac{R_n^{**\prime}(\rho)}{\rho} \right) - C_{22} a_n^2 \frac{R_n^{**}(\rho)}{\rho^2}$$

$$= \sum_{k=0}^{\infty} \frac{(-1)^k a_n \psi_1(k)}{(2k)!(8\rho)^{2k} \rho \sqrt{\pi\rho}}$$

$$\times \{ (d_{4n} + d_{5n}) (\sin\rho - a_{1,k}\rho \cos\rho + a_{2,k}\rho^2 \sin\rho) +$$

$$+ (d_{4n} - d_{5n}) (\cos\rho + a_{1,k}\rho \sin\rho + a_{2,k}\rho^2 \cos\rho) \}, \quad (17)$$

where

$$a_{1,k} = q_1 \frac{4k+1}{4k-1} - \frac{16k}{(4k-1)^2};\ a_{2,k} = \frac{16kq_1}{(4k-1)(4k-3)}. \quad (18)$$

and $\psi_1(k)$ is defined in Appendix B.

The solution of equation (17) for the function $R_n^{**}(\rho)$ is found to be

$$R_n^{**}(\rho) = \sum_{n=0}^{\infty} p_{k,1}^n \rho^{-2k-1/2} \cos\rho + s_{k,1}^n \rho^{-2k-1/2} \sin\rho +$$

$$+ p_{k,2}^n \rho^{-2k-3/2} \cos\rho + s_{k,2}^n \rho^{-2k-3/2} \sin\rho. \quad (19)$$

The coefficients $p_{k,1}^n$, $s_{k,1}^n$, $p_{k,2}^n$, $s_{k,2}^n$ are determined by considering the terms in the sum (18) that contribute to the terms $\rho^{-2k-1/2} \cos\rho$, $\rho^{-2k-1/2} \sin\rho$, $\rho^{-2k-3/2} \cos\rho$, $\rho^{-2k-3/2} \sin\rho$ in the right-hand side of equation (17a). We obtain the following recursive formulas for $p_{k,1}^n$, $s_{k,1}^n$,

$$p_{k,1}^n C_{11} = p_{k-1,1}^n [C_{11}(-2k+3/2)^2 - C_{22}] + s_{k-1,2}^n C_{11} 2(-2k+1)$$

$$+ \frac{(-1)^k \psi_1(k) a_{1,k}}{(2k)! 8^{2k} a_n \sqrt{\pi}} (d_{4n} + d_{5n}), \quad (20a)$$

$$s_{k,1}^n C_{11} = s_{k-1,1}^n [C_{11}(-2k+3/2)^2 - C_{22}] - p_{k-1,2}^n C_{11} 2(-2k+1)$$

$$+ \frac{(-1)^{k+1} \psi_1(k) a_{1,k}}{(2k)! 8^{2k} a_n \sqrt{\pi}} (d_{4n} - d_{5n}), \quad (20b)$$

and for $p_{k,2}^n$, $s_{k,2}^n$,

$$p_{k,2}^n C_{11} = p_{k-1,2}^n [C_{11}(-2k+1/2)^2 - C_{22}] - s_{k,1}^n C_{11} 4k$$

$$+ \left\{ \frac{(-1)^{k+1} \psi_1(k)}{(2k)! 8^{2k} a_n \sqrt{\pi}} + \frac{(-1)^k \psi_1(k+1) a_{2,k+1}}{[2(k+1)]! 8^{2(k+1)} a_n \sqrt{\pi}} \right\} (d_{4n} - d_{5n}), \quad (20c)$$

$$s_{k,2}^n C_{11} = s_{k-1,2}^n [C_{11}(-2k+1/2)^2 - C_{22}] + p_{k,1}^n C_{11} 4k$$

$$+ \left\{ \frac{(-1)^{k+1} \psi_1(k)}{(2k)! 8^{2k} a_n \sqrt{\pi}} + \frac{(-1)^k \psi_1(k+1) a_{2,k+1}}{[2(k+1)]! 8^{2(k+1)} a_n \sqrt{\pi}} \right\} (d_{4n} + d_{5n}). \quad (20d)$$

The process starts from $k = 1$ and the starting values for $k = 0$ are from equations (17) and (18) as follows:

$$p_{0,1} = -\frac{q_1 (d_{4n} + d_{5n})}{a_n \sqrt{\pi}};\ s_{0,1} = \frac{q_1 (d_{4n} - d_{5n})}{a_n \sqrt{\pi}}, \quad (21a)$$

$$p_{0,2} = (-8 + .3q_1) \frac{(d_{4n} - d_{5n})}{8 a_n \sqrt{\pi}};\ s_{0,2} \quad (21b)$$

$$= (-8 + 3q_1) \frac{(d_{4n} + d_{5n})}{8 a_n \sqrt{\pi}}. \quad (21b)$$

A fine point of the analysis will be addressed now. The solution (19) is a particular solution of equation (17). It was derived based on the Hankel asymptotic expansions of the Bessel functions for values of the argument $\rho = r a_n \geq \rho_{tr} = 18.0$ (see Appendix B). A corresponding solution, $R_{nS}^*(r)$, for values of the argument $\rho \leq \rho_{tr}$ had been derived by Kardomateas (1989), based on a series expansion for the Bessel functions. Since, for a given root a_n the argument ρ ranges from $r_1 a_n$ to $r_2 a_n$, there may be a transition point from one solution to the other for $R_n^*(r)$ in the expression (15). Both solutions are particular ones and may be different. Therefore, at that transition point a homogeneous solution term should be added to (19) so that

$$R_{nL}^{**}(\rho) = d_{6n} \rho^{\lambda 1} + d_{7n} \rho^{\lambda 2} + R_n^{**}(\rho);\ R_n^*(r) = R_{nL}^{**}(\rho), \quad (22a)$$

where d_{6n} and d_{7n} are determined from the condition of equal value and slope at the transition point

$$R_{nL}^{**}(\rho_{tr}) = R_{nS}^*(\rho_{tr}/a_n);\ R_{nL}^{**\prime}(\rho_{tr}) a_n = R_{nS}^{*\prime}(\rho_{tr}/a_n). \quad (22b)$$

The unknown constants c_j, G_{ij} are found from the conditions of zero external traction and zero resultant force. These are modified from Kardomateas (1989) to include the general thermal load case. The traction-free condition, $\sigma_{rr}(r_i, t) = 0$, gives the following two linear equations in G_{10}, G_{20}, c_0.

$$(C_{11}\lambda_1 + C_{12}) r_i^{\lambda 1 - 1} G_{10} + (C_{11}\lambda_2 + C_{12}) r_i^{\lambda 2 - 1} G_{20} + A_0 c_0 =$$

$$= -C_{11} U_0^{*\prime}(r_i) - C_{12} \frac{U_0^*(r_i)}{r_i} + q_1 [d_1 + d_2 \ln(r_i/r_1)$$

$$+ d_3 \ln(r_i/r_2)]\ i = 1,2, \quad (23a)$$

where

$$A_0 = \frac{C_{11} + C_{12}}{C_{11} - C_{22}} (C_{23} - C_{13}) + C_{13} \text{ for } C_{11} \neq C_{22}$$

$$= \frac{C_{23} - C_{13}}{2C_{11}} [C_{11} + (C_{11} + C_{12}) \ln(r_i/r_2)] + C_{13} \text{ for } C_{11} = C_{22} \quad (23b)$$

and two linear equations for G_{1n}, G_{2n}, c_n, $n = 1, \infty$,

$$(C_{11}\lambda_1 + C_{12}) r_i^{\lambda 1 - 1} G_{1n} + (C_{11}\lambda_2 + C_{12}) r_i^{\lambda 2 - 1} G_{2n} + A_0 c_n =$$

$$= -C_{11} a_n R_{nL}^{**\prime}(r_i a_n) - C_{12} \frac{R_{nL}^{**}(r_i a_n)}{r_i} + q_1 [d_{4n} J_0(r_i a_n)$$

$$+ d_{5n} Y_0(r_i a_n)]\ i = 1,2. \quad (23c)$$

The condition of zero resultant axial force, $P_z = \int_{r_1}^{r_2} \sigma_{zz}(r, t) 2\pi r\, dr = 0$, gives the last set of equations that are needed to determine the constants G_i, c_i. For $C_{11} \neq C_{22}$

$$\left(C_{13} + \frac{C_{23} - C_{13}}{\lambda_1 + 1} \right) (r_2^{\lambda 1 + 1} - r_1^{\lambda 1 + 1}) G_{10} + A_1 G_{20} + A_2 c_0 =$$

Downloaded 03 May 2010 to 171.66.16.244. Redistribution subject to ASME license or copyright; see http://www.asme.org/terms/Terms_Use.cfm

$$= -E_0(r_1,r_2) + \frac{q_3}{2}\left[\frac{(r_2^2-r_1^2)}{2}(2d_1-d_2-d_3) + (d_2r_2^2+d_3r_1^2)\ln(r_2/r_1)\right], \quad (24a)$$

and for $n = 1, \infty$,

$$\left(C_{13}+\frac{C_{23}-C_{13}}{\lambda_1+1}\right)(r_2^{\lambda_1+1}-r_1^{\lambda_1+1})G_{1n}+A_1G_{2n}+A_2c_n =$$

$$= -E_n(r_1,r_2) + (q_3/a_n)\sum_{i=1}^{2}(-1)^i[d_{4n}r_iJ_1(r_ia_n)+d_{5n}r_iY_1(r_ia_n)], \quad (24b)$$

where $E_0(r_2, r_1)$ and $E_n(r_1, r_2)$ are defined in Appendix C. The coefficients A_1, A_2 are defined as:

$$A_1 = \left(C_{13}+\frac{C_{23}-C_{13}}{\lambda_2+1}\right)(r_2^{\lambda_2+1}-r_1^{\lambda_2+1}) \text{ for } C_{11}\neq C_{22}$$

$$= C_{13}+(C_{23}-C_{13})\ln(r_2/r_1) \text{ for } C_{11}=C_{22} \quad (24c)$$

$$A_2 = \frac{r_2^2-r_1^2}{2}\left(C_{33}+\frac{C_{23}^2-C_{13}^2}{C_{11}-C_{22}}\right) \text{ for } C_{11}\neq C_{22}$$

$$= \frac{(r_2^2-r_1^2)}{8C_{11}}[4C_{33}C_{11}-(C_{23}-C_{13})^2] + \frac{C_{23}^2-C_{13}^2}{4C_{11}}r_1^2\ln(r_2/r_1) \text{ for } C_{11}=C_{22}. \quad (24d)$$

After the displacements have been determined, the stresses are found by substituting in equations (5) and (4).

Discussion

As an example, consider a glass/epoxy circular cylindrical shell of inner radius $r_1 = 20$ mm and outer radius $r_2 = 36$ mm, with circumferential fibers. The moduli in GN/m^2 and Poisson's ratios for this material are listed next, where 1 is the radial (r), 2 is the circumferential (θ), and 3 the axial (z) direction:

$$E_1 = 13.7,\ E_2 = 55.9,\ E_3 = 13.7,\ G_{12} = 5.6,\ G_{23} = 5.6,$$
$$G_{31} = 4.9,\ \nu_{12} = 0.068,\ \nu_{23} = 0.277,\ \nu_{31} = 0.4.$$

The thermal expansion coefficients are: $\alpha_r = 40 \times 10^{-6}/°C$, $\alpha_\theta = 10 \times 10^{-6}/°C$, $\alpha_z = 40 \times 10^{-6}/°$ C. For this material,

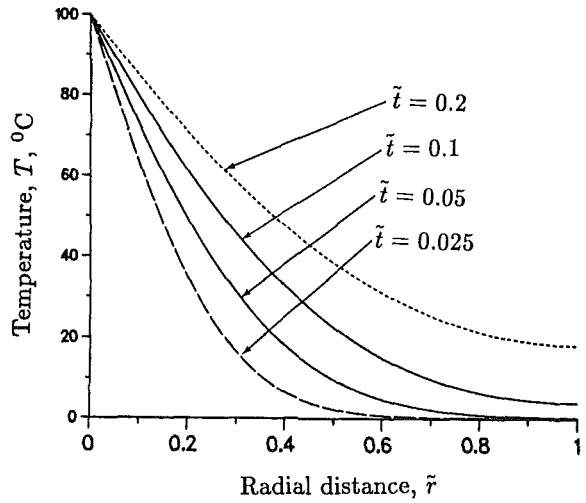


Fig. 1 Temperature T at different times for constant applied temperature $T_0 = 100°C$ at the inner surface and heat convection at the outer surface. The nondimensional time is defined by $\tilde{t} = Kt/(r_2 - r_1)^2$.

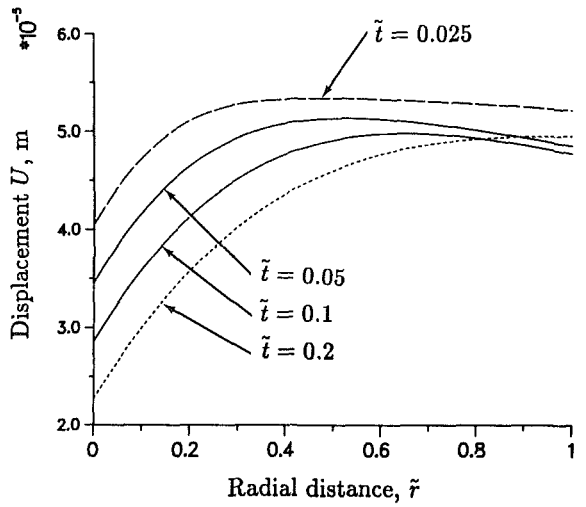


Fig. 2 Through the thickness distribution of the radial displacement U

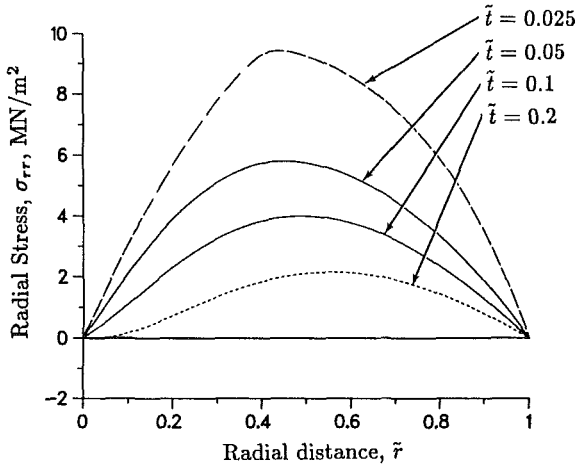


Fig. 3 Radial stress σ_{rr} versus normalized radial distance

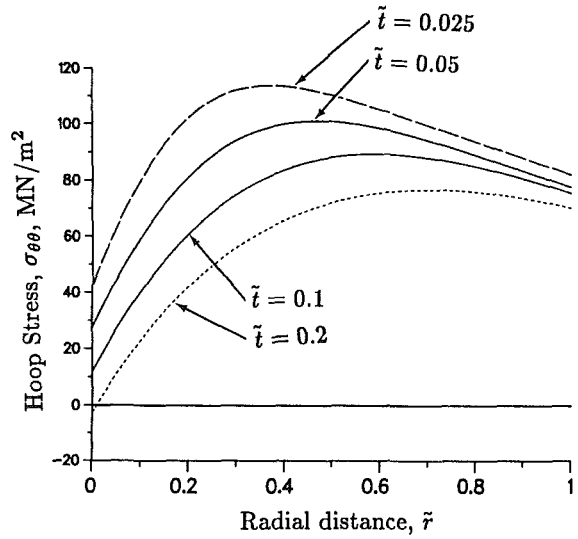


Fig. 4 Hoop stress $\sigma_{\theta\theta}$ versus normalized radial distance

Downloaded 03 May 2010 to 171.66.16.244. Redistribution subject to ASME license or copyright; see http://www.asme.org/terms/Terms_Use.cfm

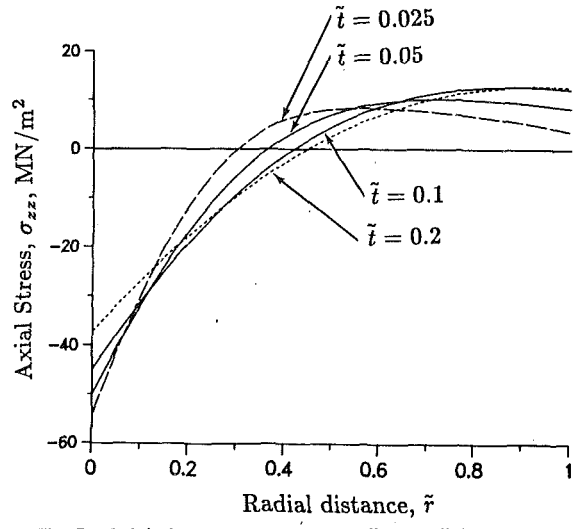


Fig. 5 Axial stress σ_{zz} versus normalized radial distance

the thermal diffusivity in the radial direction is $K = 0.112 \times 10^{-5}$ m^2/sec. Let us assume that a temperature of $T_0 = 100°C$ above the reference one is applied at $r = r_1$ while there is heat convection to the surrounding air at $r = r_2$. In this case $h_1 = h_3^* = 0$, $h_1^* = h_2 = 1$, $h_3 = -T_0$, $h_2^* = h$ where h is the ratio of the convective heat-transfer coefficient between the composite tube and the surrounding medium at $r = r_2$ and the thermal conductivity of the tube in the radial direction. A typical value of this parameter for heat convection to the air is $h = 0.15$ m^{-1}. As was mentioned by Kardomateas (1989), although the reference temperature is taken equal to zero, the analysis is the same for any initial temperature other than zero, in which case T_0 is the applied temperature above this reference value.

In presenting the results, the nondimensional radial distance (i.e., through the thickness) is used, defined by

$$\tilde{r} = \frac{r - r_1}{r_2 - r_1}.$$

Figure 1 shows the temperature and Fig. 2 the displacement distribution for time values $\tilde{t} = 0.20$, 0.10, 0.05, and 0.025. Temperature gradients are steeper for small time values. The corresponding distribution of stresses σ_{rr}, $\sigma_{\theta\theta}$, and σ_{zz} are shown in Figs. 3, 4, and 5. The biggest of those is the hoop stress $\sigma_{\theta\theta}$ and its maximum value is seen to be larger for $\tilde{t} = 0.025$ than for $\tilde{t} = 0.20$ by a factor of about 1.8 (Fig. 4). The location of the maximum stress also changes with time. The radial stress σ_{rr} is tensile and its maximum value at $\tilde{t} = 0.025$ is 2.75 times that at $\tilde{t} = 0.20$ (Fig. 3). For the same example case, Kardomateas (1989) found that under steady-state conditions, the radial stress is compressive throughout and the steady-state hoop stress is compressive if $\tilde{r} < 0.45$. This underlines the strong dependence of the stress distribution on the time scale. The axial stress σ_{zz} has a maximum compressive value at the inner surface; at $\tilde{t} = 0.025$, its magnitude is 1.4 times that at $\tilde{t} = 0.20$ (Fig. 5). The axial component is important because the material is normally weaker in the directions perpendicular to the fibers.

Table 1 shows the number of terms $N_{\max}$ for the summation over n in the solution (8) that are required for convergence at different times. Convergence is defined here so as the successive last three terms are decreasing by at least an order of magnitude and the ratio of the last term over the first one for the stresses, temperature, and displacement is less than 10^{-5}. Only three of the roots, a_n, are in the "small argument" region; the rest are in the "large argument" (Hankel asymptotic expansion) region. In fact, in this initial phase of transient thermal stresses the roots in the "large argument" region are dominant and more terms are required for smaller time values.

Table 1 Number of terms $N_{\max}$ of the solution (8) required for convergence*. Only three of the roots a_n are in the "small argument" region; the rest are in the "large argument" (Hankel asymptotic expansions) region.

$\tilde{t}$	$N_{\max}$
0.200	4
0.100	5
0.050	6
0.025	8
0.010	11

*Convergence is defined here so as the successive last three terms are decreasing by at least an order of magnitude and the ratio of the last term over the first one on the stresses, temperature, and displacement is less than 10^{-5}.

References

Abramowitz, M., and Stegun, I. A., eds., 1970, "Handbook of Mathematical Functions With Formulas, Graphs, and Mathematical Tables," National Bureau of Standards Applied Mathematics Series No. 55, 9th printing, Washington, D.C.

Avery, W. B., and Herakovich, C. T., 1986, "Effect of Fiber Anisotropy on Thermal Stresses in Fibrous Composites," ASME JOURNAL OF APPLIED MECHANICS, Vol. 53, pp. 751–756.

Carslaw, H. S., and Jaeger, J. C., 1959, *Conduction of Heat in Solids*, 2nd ed., Oxford at the Clarendon Press, U.K.

Hyer, M. W., and Cooper, D. E., 1986, "Stresses and Deformations in Composite Tubes Due to a Circumferential Temperature Gradient," ASME JOURNAL OF APPLIED MECHANICS, Vol. 53, pp. 757–764.

Kalam, M.A., and Tauchert, T. R., 1978, "Stresses in an Orthotropic Elastic Cylinder due to a Plane Temperature Distribution $T(r, \theta)$," *Journal of Thermal Stresses*, Vol. 1, pp. 13–24.

Kardomateas, G. A., 1989, "Transient Thermal Stresses in Cylindrically Orthotropic Composite Tubes," ASME JOURNAL OF APPLIED MECHANICS, Vol. 56, pp. 411–417.

APPENDIX A

The constants d_1, d_2, d_3 are expressed in terms of

$$Q = r_1 h_2 h_1^* + r_2 h_1 h_2^* + r_1 r_2 h_2 h_2^* \ln(r_2/r_1), \tag{A1a}$$

as follows:

$$d_1 = (r_2 h_3^* h_1 - r_1 h_3 h_1^*)/Q, \tag{A1b}$$

$$d_2 = r_1 r_2 h_3^* h_2/Q;\ d_3 = r_1 r_2 h_3 h_2^*/Q. \tag{A1c}$$

The constants d_{4n}, d_{5n} are given in terms of

$$F_1(a_n) = [h_1^* a_n J_1(r_2 a_n) - h_2^* J_0(r_2 a_n)] \times \{h_3[h_1^* a_n J_1(r_2 a_n) - h_2^* J_0(r_2 a_n)] - h_3^*[h_1 a_n J_1(r_1 a_n) + h_2 J_0(r_1 a_n)]\}, \tag{A2a}$$

$$F_2(a_n) = (h_1^{*2} a_n^2 + h_2^{*2})[h_1 a_n J_1(r_1 a_n) + h_2 J_0(r_1 a_n)]^2 - (h_1^2 a_n^2 + h_2^2)[h_1^* a_n J_1(r_2 a_n) - h_2^* J_0(r_2 a_n)]^2, \tag{A2b}$$

as follows:

$$d_{4n} = -\pi \frac{F_1(a_n)}{F_2(a_n)} [h_1 a_n Y_1(r_1 a_n) + h_2 Y_0(r_1 a_n)], \tag{A3a}$$

$$d_{5n} = \pi \frac{F_1(a_n)}{F_2(a_n)} [h_1 a_n J_1(r_1 a_n) + h_2 J_0(r_1 a_n)]. \tag{A3b}$$

Finally, it should be noted that the case of $h_2 = h_2^* = 0$ is excluded (although it can be treated along the same lines).

APPENDIX B

For large arguments, we can use the Hankel asymptotic expansions for the Bessel functions (see, e.g., Abramowitz and Stegun, 1970) to obtain the following expressions

Downloaded 03 May 2010 to 171.66.16.244. Redistribution subject to ASME license or copyright; see http://www.asme.org/terms/Terms_Use.cfm

$$J_0(x) = A_0(x)\sin x + B_0(x)\cos x;\ J_1(x) = B_1(x)\sin x - A_1(x)\cos x, \quad \text{(B1}a\text{)}$$

$$Y_0(x) = B_0(x)\sin x - A_0(x)\cos x;\ Y_1(x) = -A_1(x)\sin x - B_1(x)\cos x. \quad \text{(B1}b\text{)}$$

The functions $A_0(x)$, $A_1(x)$, $B_0(x)$, $B_1(x)$ are given in terms of

$$\psi_1(k) = 1^2.3^2.5^2 \ldots (4k-1)^2,\ k = 1,\infty;\ \psi_1(0) = 1, \quad \text{(B2)}$$

as follows:

$$(\pi x)^{1/2}A_0(x) = \sum_{k=0}^{\infty} \frac{(-1)^k\psi_1(k)}{(2k)!(8x)^{2k}}\left[1 - \frac{16kx}{(4k-1)^2}\right], \quad \text{(B3}a\text{)}$$

$$(\pi x)^{1/2}A_1(x) = \sum_{k=0}^{\infty} \frac{(-1)^{k+1}\psi_1(k)(4k+1)}{(2k)!(8x)^{2k}(4k-1)}\left[1 - \frac{16kx}{(4k-3)(4k+1)}\right], \quad \text{(B3}b\text{)}$$

$$(\pi x)^{1/2}B_0(x) = \sum_{k=0}^{\infty} \frac{(-1)^k\psi_1(k)}{(2k)!(8x)^{2k}}\left[1 + \frac{16kx}{(4k-1)^2}\right], \quad \text{(B3}c\text{)}$$

$$(\pi x)^{1/2}B_1(x) = \sum_{k=0}^{\infty} \frac{(-1)^{k+1}\psi_1(k)(4k+1)}{(2k)!(8x)^{2k}(4k-1)}\left[1 + \frac{16kx}{(4k-3)(4k+1)}\right]. \quad \text{(B3}d\text{)}$$

In the numerical calculations of the foregoing series, the summation process is terminated at the point where the term becomes less than a specified small number, which is taken here to be 10^{-16}. In this way, the above series of the Hankel asymptotic expansion can be used to calculate the Bessel functions for values of the argument $x \geq 18$. The series converges rapidly and the number of terms required in the summation over k is at most 13 at $x = 18.0$, being smaller for larger values of the argument.

APPENDIX C

For $C_{11} \neq C_{22}$, the expression for E_0 in equation (24a), is:

$$E_0(r_1,r_2) = \frac{q_2(r_2^2d_2 + r_1^2d_3)}{2(C_{11}-C_{22})}(C_{23}+C_{13})\ln(r_2/r_1) + \frac{(r_2^2-r_1^2)}{4(C_{11}-C_{22})} \times \left\{(C_{13}-C_{23})q_2(d_2+d_3) + 2(C_{13}+C_{23})\left[q_1(d_2+d_3) + q_2d_1 - \frac{2C_{11}q_2(d_2+d_3)}{C_{11}-C_{22}}\right]\right\}. \quad \text{(C1}a\text{)}$$

For $C_{11} = C_{22}$, the expression for E_0 is

$$E_0(r_1,r_2) = \frac{q_2(r_2^2d_2 - r_1^2d_3)}{8C_{11}}(C_{23}+C_{13})\ln^2(r_2/r_1) + \frac{\ln(r_2/r_1)}{8C_{11}}\{(r_2^2d_2 + r_1^2d_3)(C_{13}-C_{23})q_2 + r_1^2(C_{13} + C_{23})[(2q_1 - q_2)(d_2+d_3) + 2q_2d_1]\} + \frac{(r_2^2-r_1^2)}{8C_{11}}(C_{23}-C_{13})[(q_2-q_1)(d_2+d_3) - q_2d_1], \quad \text{(C1}b\text{)}$$

and the expressions for E_n, $n = 1, \infty$ in equation (27), (they involve an integration of $R_{nL}^{**}(\rho)$) are for the case of large arguments

$$E_n = C_{13}[r_2R_{nL}^{**}(r_2a_n) - r_1R_{nL}^{**}(r_1a_n)] + (C_{23} - C_{13})a_n^{-1}\sum_{i=1}^{2}(-1)^i\left[\frac{d_{6n}(r_ia_n)^{\lambda_1+1}}{\lambda_1+1} + d_{7n}F_i\right] + (C_{23}-C_{13})a_n^{-1}\sum_{k=0}^{\infty}\left\{\left(p_{k,1}^n + \frac{s_{k,2}^n}{2k+1/2}\right)A_k^n + \left(s_{k,1}^n - \frac{p_{k,2}^n}{2k+1/2}\right)B_k^n + \sum_{i=1}^{2}\frac{(-1)^{i+1}}{2k+1/2}\left[p_{k,2}^n(r_ia_n)^{-2k-1/2}\cos(r_ia_n) + s_{k,2}^n(r_ia_n)^{-2k-1/2}\sin(r_ia_n)\right]\right\}. \quad \text{(C2}a\text{)}$$

The constant A_k^n and B_k^n are defined by the recursive formulas

$$A_k^n = -\frac{1}{(2k-1/2)(2k-3/2)}A_{k-1}^n + \sum_{i=1}^{2}(-1)^i\left\{\frac{(r_ia_n)^{-2k+3/2}\sin(r_ia_n)}{(2k-1/2)(2k-3/2)} - \frac{(r_ia_n)^{-2k+1/2}\cos(r_ia_n)}{2k-1/2}\right\}, \quad \text{(C2}b\text{)}$$

$$B_k^n = -\frac{1}{(2k-1/2)(2k-3/2)}B_{k-1}^n + \sum_{i=1}^{2}(-1)^{i+1}\left\{\frac{(r_ia_n)^{-2k+3/2}\cos(r_ia_n)}{(2k-1/2)(2k-3/2)} + \frac{(r_ia_n)^{-2k+1/2}\sin(r_ia_n)}{2k-1/2}\right\}. \quad \text{(C2}c\text{)}$$

The initial values are

$$A_0^n = \int_{r_1a_n}^{r_2a_n}\rho^{-1/2}\cos\rho d\rho;\ B_0^n = \int_{r_1a_n}^{r_2a_n}\rho^{-1/2}\sin\rho d\rho. \quad \text{(C3)}$$

The constants F_i, $i = 1, 2$ in equation (C2a) are defined

$$F_i = \frac{(r_ia_n)^{\lambda_2+1}}{\lambda_2+1} \text{ for } C_{11} \neq C_{22} = \ln(r_ia_n) \text{ for } C_{11} = C_{22}. \quad \text{(C4)}$$

The expressions of E_n for small arguments were given by Kardomateas (1989) and are the same for this case of general thermal loading.

Downloaded 03 May 2010 to 171.66.16.244. Redistribution subject to ASME license or copyright; see http://www.asme.org/terms/Terms_Use.cfm

Bertram A. Schmidt
Department of Mathematics,
Central Michigan University,
Mount Pleasant, MI 48859

The Rotationally Flexible Pendulum Subjected to a High Frequency Excitation

A high frequency harmonic excitation is applied to the pivot of a rotationally flexible pendulum. It is found that various equilibrium positions occur depending on the stiffness of the flexible parts.

1 Introduction

Pendulums with oscillating base motions have been studied by many investigators. Stephenson (1907) considered the pendulum subjected to a vertical oscillation. He pointed out that this pendulum was stable in the inverted position. He stated characteristics for the equilibrium positions if the imposed oscillation was not vertical. The imposed oscillations were of small amplitude and high frequency. He noted that the spherical pendulum could stand in the inverted position. Lowenstern (1932) investigated several devices with imposed high frequency, small amplitude oscillations. He showed the spherical pendulum is stable in the inverted position and that the double pendulum can be made to be stable in the inverted position. Phelps and Hunter (1965) presented a thorough study of the plane pendulum with an imposed harmonic vertical oscillation of the base. In this they used the linear approximation of the equations of motion near the inverted position. The frequency of the imposed oscillation was not restricted. Sethna and Hemp (1964) studied the gyroscopic pendulum with a vertical oscillation applied to the pivot. This pendulum was a spherical pendulum with a spinning wheel. The frequency of the oscillation was not restricted. Motions near steady precession motions were found. Howe (1974) described a theory of the stabilization of the inverted position by imposed random oscillations in the vertical direction. Bogdanoff and Citron (1965) presented experimental results which verify the stability of the inverted position of a pendulum subjected to random parametric excitation in the vertical direction. Mitchell (1972) used the method of averaging to investigate the inverted position of the plane pendulum subjected to small amplitude, high frequency oscillations. Sinusoidal and almost periodic oscillations were considered. Stability boundaries were established. Ryland and Meirovitch (1977) investigated a flexible pendulum with a vertical oscillation at an unrestricted frequency. The mass of the pendulum was allowed to move radially under the influence of a spring. Conditions for stability in the downward and upward vertical positions were established. Schmidt (1980) analyzed a pendulum with a mass free to move radially along a weightless rod. A horizontal, small amplitude, high frequency oscillation was applied to the pivot. For this pendulum equilibrium was found to be: the angle was downward and the radius was some positive number. The imposed oscillation caused inertia forces which kept the mass from sliding off the rod. Schmidt (1981) studied a spherical pendulum with a mass flexibility attached to the rod. A rotational oscillation was applied to the pivot. The oscillation and the flexibility caused new stable equilibrium positions: the upward vertical position and two downward nonvertical positions. Schmidt (1983) investigated a pendulum that was flexible in the radial direction. A small amplitude, high frequency harmonic oscillation was applied to the pivot. The imposed oscillation and the flexibility caused new stable equilibrium in the upward vertical position and in downward nonvertical positions.

In this paper, we consider a plane pendulum whose mass can rotate under the influenced of a spring. The pendulum is shown in Fig. 1. The pendulum is made up of a mass, a spring, and a weightless rod. The mass is allowed to rotate with respect to the rod about an axis perpendicular to the plane of the motion of the pendulum. This rotation is restrained by the spring. A small amplitude harmonic excitation is applied to the pivot in the vertical direction. The frequency of the excitation is large with respect to the natural frequency of the swinging motion of the pendulum. The frequency of the excitation is not large with respect to the natural frequency of the rotary motion of the mass with respect to the rod.

The intention of this investigation is to find approximate stable equilibrium positions and to find motions near these stable equilibrium positions. In Section II, the equations of motions are expressed in terms of motions are expressed in terms of dimensionless variables and parameters. The equations of motion are transformed into a form which can be easily transformed into the standard form for the method of averaging (see Bogoliuboff and Mitropolskiy, 1962). The transformation is made and the averaging process is applied. The average equations are examined to find stable equilibrium solutions. These, along with the transformations, yield the approximate equilibrium positions for the original variables. After this, the improved first approximation of the method of av-

Contributed by the Applied Mechanics Division of THE AMERICAN SOCIETY OF MECHANICAL ENGINEERS for publication in the JOURNAL OF APPLIED MECHANICS.

Discussion on this paper should be addressed to the Technical Editor, Leon M. Keer, The Technological Institute, Northwestern University, Evanston, IL 60208, and will be accepted until two months after final publication of the paper itself in the JOURNAL OF APPLIED MECHANICS. Manuscript received by the ASME Applied Mechanics Division, July 29, 1988; final revision, July 15, 1989.

Copyright © 1990 by ASME
Downloaded 03 May 2010 to 171.66.16.244. Redistribution subject to ASME license or copyright; see http://www.asme.org/terms/Terms_Use.cfm

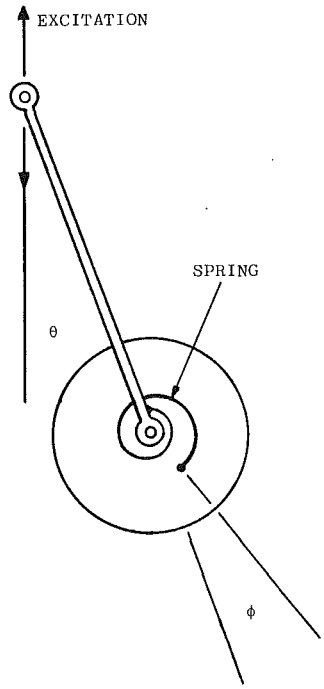


Fig. 1 The pendulum

eraging is found. From this we obtain approximate solutions near the equilibrium positions.

II The Analysis

The angle between the pendulum and the vertical line is θ. The angular position of the mass with respect to the rod is ϕ. The equations of motion are

$$mr^2\ddot{\theta} - K\phi + cr^2\dot{\theta} + mrg\sin\theta + mrA\nu^2\sin\theta\cos\nu t = 0$$

$$I(\ddot{\theta} + \ddot{\phi}) + K\phi = 0,$$

where m is the mass, I is the moment of inertia of the mass with respect to its center, r is the distance from the pivot to the center of the mass, g is the gravitational constant, A and ν are the amplitude and frequency of the excitation, respectively, K is the spring constant, c is the damping coefficient, t is time and the dot indicates differentiation with respect to time. The joint between the mass and the rod is frictionless. The system is damped by the damping moment in the first equation.

For this problem, ν is large. We introduce a small dimensionless parameter, ϵ, such that ϵ is of order $(gr^{-1})^{1/2}\nu^{-1}$. We establish other dimensionless variables and parameters. Let $\tau = \nu t$, $\epsilon^2\delta = g(r\nu^2)^{-1}$, $\epsilon\gamma = Ar^{-1}$, $k^2 = K(I\nu^2)^{-1}$, $\mu = I(mr^2)^{-1}$, $\epsilon a = c(m\nu)^{-1}$, and let the prime indicate differentiation with respect to τ. The equations of motion become

$$\theta'' - \mu k^2\phi + \epsilon a\theta' + \epsilon^2\delta\sin\theta + \epsilon\gamma\sin\theta\cos\tau = 0$$

$$\theta'' + \phi'' + k^2\phi = 0. \qquad (1a, b)$$

The parameters μ, k^2, a, and δ are positive and independent of ϵ. γ is non-negative and independent of ϵ. Further restrictions are made: k^2 is not near zero or $(1+\mu)^{-1}$, i.e., k^2 and $k^2 - (1+\mu)^{-1}$ are independent of ϵ. Also, $\phi(0)$ and $\phi'(0)$ are of order ϵ.

To change the equations of motion (1) into four equations in the standard form for the method of averaging, the following two-step process is applied. In the first step, three things are done, first, equation (1*a*) is subtracted from (1*b*), and second (1*a*) is added to (1*b*) multiplied by μ, and third, a new variable ψ is introduced so that θ can be replaced by

$$\theta = \psi - \mu(1+\mu)^{-1}\phi. \qquad (2)$$

This gives

$$\phi'' + \lambda^2\phi = \epsilon a\psi' - \epsilon a\mu(1+\mu)^{-1}\phi' + \epsilon^2\delta\sin(\psi - \mu(1+\mu)^{-1}\phi) + \epsilon\gamma\sin(\psi - \mu(1+\mu)^{-1}\phi)\cos\tau$$

$$\psi'' = \epsilon(1+\mu)^{-1}[-\gamma\sin(\psi - \mu(1+\mu)^{-1}\phi)\cos\tau - a(\psi' - \mu(1+\mu)^{-1}\phi') - \epsilon\delta\sin(\psi - \mu(1+\mu)^{-1}\phi)], \qquad (3a, b)$$

where $\lambda^2 = (1+\mu)k^2$. Equations (3) are in a form suitable for transformation into the standard form for the method of averaging. The second step, then, is to apply the transformation

$$\phi = \epsilon u\sin\lambda\tau + \epsilon v\cos\lambda\tau + (\lambda^2 - 1)^{-1}\epsilon\gamma\sin\psi\cos\tau$$

$$\phi' = \epsilon\lambda u\cos\lambda\tau - \epsilon\lambda\sin\lambda\tau + \epsilon(\lambda^2-1)^{-1}\gamma\psi'\cos\psi\cos\tau - \epsilon(\lambda^2-1)^{-1}\gamma\sin\psi\sin\tau$$

$$\psi' = \epsilon\omega - \epsilon(1+\mu)^{-1}\gamma\sin\psi\sin\tau. \qquad (4a, b, c)$$

Transformation equations (4) removes ϕ from (3) and introduces the new variables u, v, ω. This gives four equations in the standard form for the method of averaging which involve the variables u, v, ψ, and ω. They are

$$\begin{aligned}
u' = {} & \epsilon\lambda^{-1}[\gamma^2(\lambda^2-1)^{-1}(1+\mu)^{-1}\sin\psi\cos\psi\cos^2\tau \\
& + 2(\lambda^2-1)^{-1}\gamma(\omega - (1+\mu)^{-1}\gamma\sin\psi\sin\tau)\cos\psi\sin\tau \\
& - \gamma\mu(1+\mu)^{-1}(u\sin\lambda\tau \\
& + v\cos\lambda\tau + (\lambda^2-1)^{-1}\gamma\sin\psi\cos\tau)\cos\psi\cos\tau \\
& + a\omega - a\gamma(1+\mu)^{-1}\sin\psi\sin\tau + \delta\sin\psi \\
& - a\mu(1+\mu)^{-1}(\lambda u\cos\lambda\tau - \lambda v\sin\lambda\tau \\
& - \gamma(\lambda^2-1)^{-1}\sin\psi\sin\tau)]\cos\lambda\tau \\
v' = {} & -\epsilon\lambda^{-1}[\gamma^2(\lambda^2-1)^{-1}(1+\mu)^{-1}\sin\psi\cos\psi\cos^2\tau \\
& + 2(\lambda^2-1)^{-1}\gamma(\omega - (1+\mu)^{-1}\gamma\sin\psi\sin\tau)\cos\psi\sin\tau \\
& - \gamma\mu(1+\mu)^{-1}(u\sin\lambda\tau \\
& + v\cos\lambda\tau + (\lambda^2-1)^{-1}\gamma\sin\psi\cos\tau)\cos\psi\cos\tau \\
& + a\omega - a\gamma(1+\mu)^{-1}\sin\psi\sin\tau + \delta\sin\psi \\
& - a\mu(1+\mu)^{-1}(\lambda u\cos\lambda\tau - \lambda v\sin\lambda\tau \\
& - \gamma(\lambda^2-1)^{-1}\sin\psi\sin\tau)]\sin\lambda\tau \\
\psi' = {} & \epsilon[\omega - (1+\mu)^{-1}\gamma\sin\psi\sin\tau] \\
\omega' = {} & \epsilon[\gamma(1+\mu)^{-1}(\omega - (1+\mu)^{-1}\gamma\sin\psi\sin\tau)\cos\psi\sin\tau \\
& + a\mu(1+\mu)^{-2}(\lambda u\cos\lambda\tau - \lambda v\sin\lambda\tau - (\lambda^2-1)^{-1}\gamma\sin\psi\sin\tau) \\
& - a(1+\mu)^{-1}(\omega - (1-\mu)^{-1}\gamma\sin\psi\sin\tau) \\
& - \delta(1+\mu)^{-1}\sin\psi \\
& + \gamma\mu(1+\mu)^{-2}(u\sin\lambda\tau \\
& + v\cos\lambda\tau + (\lambda^2-1)^{-1}\gamma\sin\psi\cos\tau)\cos\psi\cos\tau].
\end{aligned} \qquad (5a, b, c, d)$$

In equations (5), terms of order ϵ^2 have been discarded. The first approximation of the method of averaging is to be found, i.e., the averaging operator is applied to the right-hand sides of equations (5) and the variables u, v, ψ, and ω are replaced by their approximations U, V, Ψ, and Ω. This gives

Downloaded 03 May 2010 to 171.66.16.244. Redistribution subject to ASME license or copyright; see http://www.asme.org/terms/Terms_Use.cfm

$$U' = -\epsilon \frac{1}{2} a\mu(1+\mu)^{-1}U$$

$$V' = -\epsilon \frac{1}{2} a\mu(1+\mu)^{-1}V \qquad (6a, b, c, d)$$

$$\Psi' = \epsilon\Omega$$

$$\Omega' = \epsilon[-B\sin\Psi - C\sin 2\Psi - a(1+\mu)^{-1}\Omega],$$

where $B = \delta(1+\mu)^{-1}$ and $C = \frac{1}{4}\gamma^2 (1+\mu)^{-1} (k^2-1)[(1+\mu)k^2-1]^{-1}$.

In this investigation, stable equilibrium solutions of equations (6) are found. In considering these equilibrium solutions, it is helpful to refer to a theorem of Balachandra and Sethna 1975). This theorem pertains to the first approximation of the method of averaging for more general hypotheses than are needed in this problem. By means of this theorem, we can state that there exists a solution to equation (5) which approaches an equilibrium solution of (6) as $\epsilon \to 0$ for all τ. We present the equilibrium solutions of equations (6) as approximations of certain solutions of (5) by this theorem.

We will find stable equilibrium values for U, V, Ψ, and Ω. These are denoted with the subscript e. Equations (6a) and (6b) can be solved. The stable equilibrium values are

$$U_e = 0. \qquad (7a, b)$$
$$V_e = 0.$$

From equations (6c), (6d), we obtain equilibrium equations for Ψ and Ω,

$$\Omega_e = 0 \qquad (8a, b)$$

$$(B + 2C\cos\Psi_e)\sin\Psi_e = 0,$$

and the variation equation

$$\alpha'' + \epsilon a(1+\mu)^{-1}\alpha' + \epsilon^2(B\cos\Psi_e + 2C\cos 2\Psi_e)\alpha - \epsilon^2\frac{1}{2}(B\sin\Psi_e + 4C\sin 2\Psi_e)\alpha^2 - \epsilon^2\frac{1}{6}(B\cos\Psi_e + 8C\cos 2\Psi_e)\alpha^3 = 0, \qquad (9)$$

where $\alpha = \Psi - \Psi_e$.

Examination of the equilibrium equation (8b) and the variation equation (9), reveals stable equilibrium values for Ψ. Ψ_e takes on the value 0 if $C/B \geq -\frac{1}{2}$. Ψ_e takes on the value π if $C/B > \frac{1}{2}$. Ψ_e takes on a value between 0 and $\pi/2$ and another value between $\frac{3}{2}\pi$ and 2π if $C/B < -\frac{1}{2}$. These last two equilibrium values are located symmetrically about the vertical line. We describe next how the stable equilibrium values depend on the parameters γ, δ, μ, and k^2.

The stable equilibrium value $\Psi_e = 0$ occurs if

a, $k^2 \geq 1$ or $k^2 < (1+\mu)^{-1}$ or if

b, $(1+\mu)^{-1} < k^2 < 1$

and $\gamma^2 \leq 2\delta(1+\mu)[k^2-(1+\mu)^{-1}](1-k^2)^{-1}$.

The stable equilibrium value $\Psi_e = \pi$ occurs if

$k^2 > 1$ or $k^2 < (1+\mu)^{-1}$ when $\gamma^2 > 2\delta(1+\mu)[k^2-(1+\mu)^{-1}](k^2-1)^{-1}$.

Stable equilibrium values in the first and fourth quadrants occur if

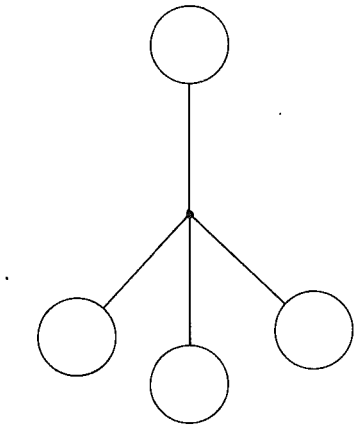


Fig. 2 The equilibrium positions

$(1+\mu)^{-1} < k^2 < 1$ when $\gamma^2 > 2\delta(1+\mu)[k^2-(1+\mu)^{-1}](1-k^2)^{-1}$.

The equilibrium values in the first and fourth quadrants move nearer to $\frac{1}{2}\pi$ or $\frac{3}{2}\pi$ if γ is made larger or if k^2 is made nearer to $(1+\mu)^{-1}$.

Replacing u, v, and ψ by their equilibrium values and combining equations (2), (4a), and discarding terms of order ϵ, we obtain approximate solutions for ϕ and θ. They are

$$\phi_a = 0 \qquad (10a, b)$$

$$\theta_a = \Psi_e,$$

where Ψ_e are the equilibrium values previously described. The error is of order ϵ.

We could obtain slow motions near the equilibrium solutions (10). This is not done here. We can also find fast motions near the equilibrium solutions. We do this next. We will call this the first-order solution. The error in the first-order solution is of order ϵ^2. Finding the first order solution involves the improved first approximation of the method of averaging. The theorem of Balachandia and Sethna does not pertain to the improved first approximation so the validity it attaches to the first approximation is not useful here. However, the improved first approximation more fully satisfies the differential equations than does the first approximation. To form the first-order solution, we are interested in only the improved first approximation for ψ. It is

$$\psi = \Psi_e + \epsilon(1+\mu)^{-1}\gamma\sin\Psi_e\cos\tau. \qquad (11)$$

The second term in equation (11) is obtained by these three steps: (a) ω is removed from equation (5c); (b) equation (5c) is integrated while holding ψ constant; and (c) ψ is replaced by Ψ_e. Then, replacing u, v, and ω by their equilibrium values and combining equations (11), (4a), (7a), (7b), and (2), and recognizing $\lambda^2 = (1+\mu)k^2$, we obtain solutions which include fast motions near the equilibrium solutions. They are

$$\phi_a = \epsilon\gamma[(1+\mu)k^2-1]^{-1}\sin\Psi_e\cos\tau$$

and

$$\theta_a = \Psi_e + \epsilon\gamma(k^2-1)[(1+\mu)k^2-1]^{-1}\sin\Psi_e\cos\tau, \qquad (12a, b)$$

where Ψ_e are the equilibrium values described above. The error is of order ϵ^2.

Figure 3 is helpful in showing the values of the parameters for which the stable equilibrium positions occur. The curves X, Y, and Z indicate regions in the k^2, γ^2/δ plane which allow the stable equilibrium positions. For these curves, μ was chosen to be .05, .16, .36, and .64. Referring to Fig. 3, we can indicate these regions this way:

Downloaded 03 May 2010 to 171.66.16.244. Redistribution subject to ASME license or copyright; see http://www.asme.org/terms/Terms_Use.cfm

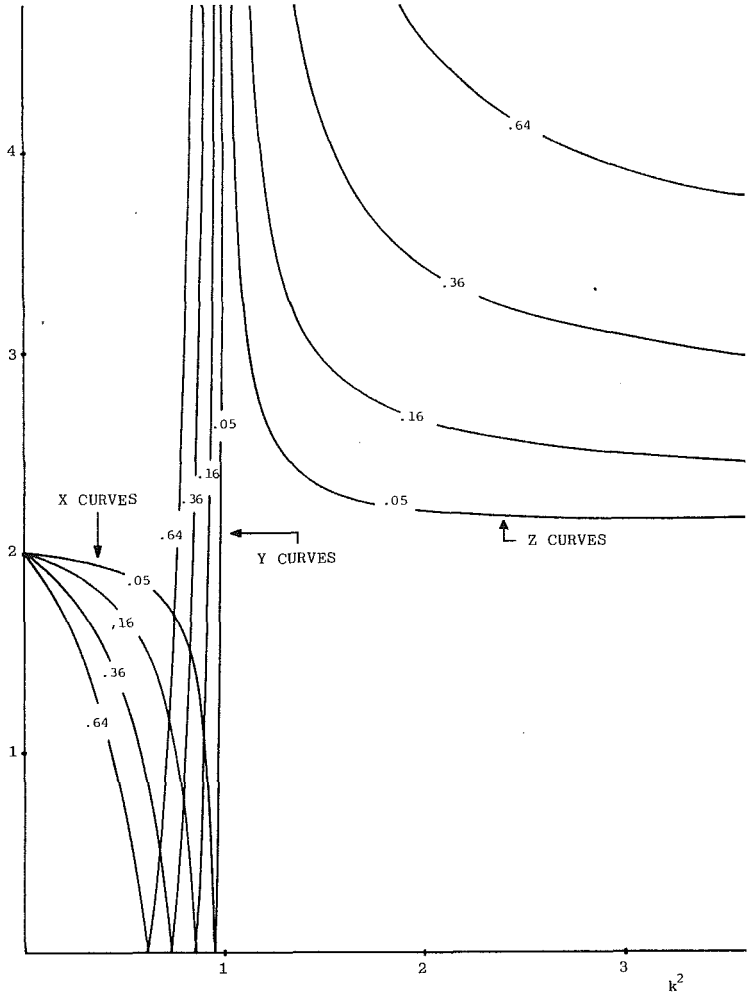


Fig. 3 Boundaries for the stable equilibrium positions

(1) For a given μ, $\Psi_e = 0$ is a stable equilibrium value for all points on or vertically above or vertically below the X and Z curves. Also, $\Psi_e = 0$ is a stable equilibrium value for all points on or vertically below the Y curve.

(2) For a given μ, $\Psi_e = \pi$ is a stable equilibrium value for all points vertically above the X and Z curves.

(3) For a given μ, Ψ_e is a first or fourth quadrant angle for any point vertically above the Y curve. These angles are described by $\cos \Psi_e = (2\delta/\gamma^2)((1+\mu)k^2 - 1)(1-k^2)^{-1}$.

Figure 4 shows the regions in the k^2, γ^2/δ plane for $\mu = .16$.

It's worth noting that if k^2 is large, there are only two stable equilibrium values. These are $\Psi_e = 0, \pi$. For large k^2 the condition for stability in the inverted position is approximated by $\gamma^2 > 2\delta(1+\mu)$. For the special case the concentrated mass ($I = 0$), this becomes $\gamma^2 > 2\delta$. This agrees with the previously established condition for the inverted pendulum with a concentrated mass. This is shown in Bogoliuboff and Mitropolskiy (1962). Also, if k^2 is small, the requirement for stability in the inverted position is again approximated by $\gamma^2 > 2\delta$. This coincides with the stability boundary for the inverted pendulum with a concentrated mass. This is to be expected, since if $k^2 = 0$, the pendulum should behave as if there were a concentrated mass.

A numerical example is presented. Equations (1) were solved numerically. Fourth-order Runge-Kutta with a step size of .1 was used. The numerical solution is compared to the solution given by equation (12). For this example the parameters were chosen so that the motion is a small oscillatory motion near a first quadrant angle. The parameters were chosen in this way: $\epsilon = .01$, $\gamma = 9.00$, $k^2 = .95$, $\mu = .16$, $a = 1.00$, and $\delta = 19.62$. For this example, equations (12) become

Table 1

τ	ϕ(M.Av.)	ϕ(Num.)	θ(M.Av)	θ(Num.)
0	.13477	.13477	.14660	.14660
4	-.08809	-.08798	.16105	.15775
8	-.01961	-.01965	.15432	.15468
12	.11373	.11336	.14765	.14693
16	-.12906	-.12833	.15980	.15883
20	.05500	.05447	.15059	.14968
24	.05717	.05685	.15048	.14926
28	-.12973	-.12859	.15983	.15840
32	.11243	.11121	.14772	.14632
36	-.01725	-.01689	.15420	.15259
40	-.08988	-.08895	.15784	.15616
44	.13475	.13296	.14660	.14482
48	-.08627	-.08482	.15766	.15558
52	-.02197	-.02184	.15444	.15248
56	.11499	.11305	.14759	.14538
60	-.12836	-.12585	.15976	.15709
64	.05281	.05170	.15070	.14823

$$\phi_a = .13477 \cos\tau,$$

and

$$\theta_a = .15334 - .00674 \cos\tau. \qquad (13a, b)$$

The Runge-Kutta solution and solutions (13) are shown in Table 1. These approximate solutions are given for more than ten cycles of $\cos\tau$. All values are measured in radians. For these values of τ, the differences in the two solutions is less than .003.

Downloaded 03 May 2010 to 171.66.16.244. Redistribution subject to ASME license or copyright; see http://www.asme.org/terms/Terms_Use.cfm

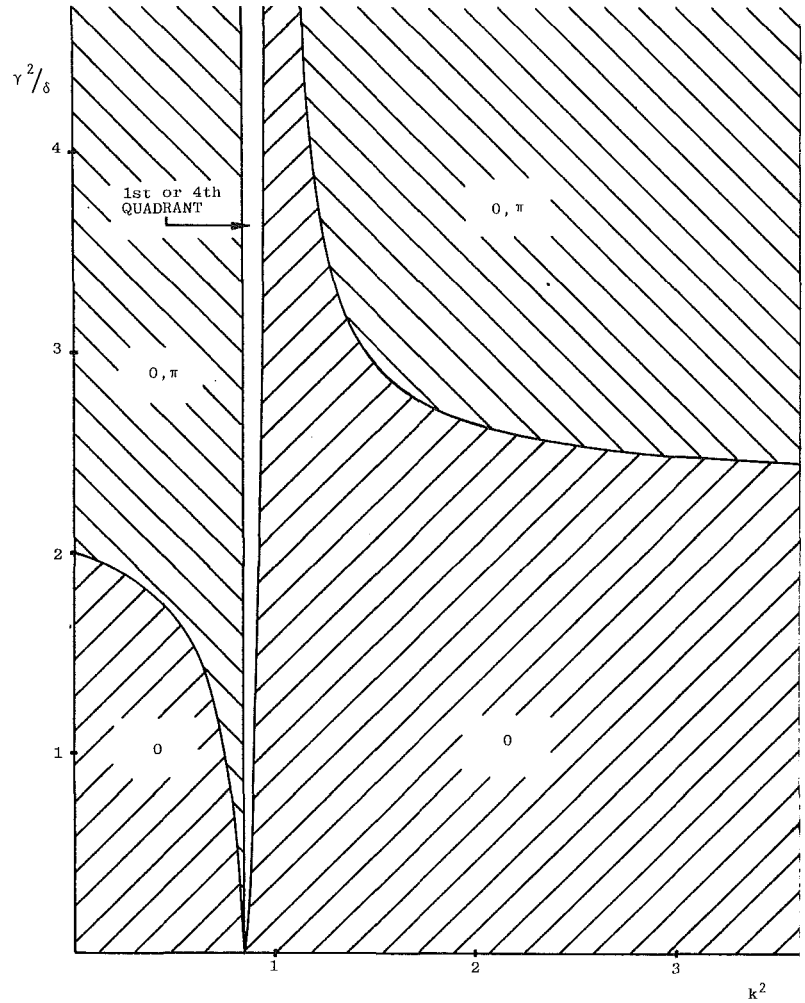


Fig. 4 Regions of stable equilibrium for $\mu = .16$

For this example, ϵ was chosen modestly. For a smaller ϵ, the error in solutions (12) would be smaller.

III Summary and Remarks

We have investigated the motions of a pendulum with a vertical, small amplitude, high frequency oscillation applied to the pivot. The pendulum is constructed with an additional degree-of-freedom, i.e., the mass is allowed to rotate on the rod of the pendulum under the influence of a spring. We have found that the imposed oscillation and the flexibility cause additional stable equilibrium positions. These are the upward vertical position and two downward nonvertical positions. The expected downward vertical position also occurs.

In Section II, we stated the regions of stability for these equilibrium positions in terms of the parameters γ, δ, k^2, and μ. We now state our results in terms of the original parameters A and ν (the amplitude and frequency of the imposed oscillation), I (moment of inertia), r (length of the pendulum), K (spring constant), and m (mass). The regions of stability are described by:

The downward vertical position is stable if

(a) $K/I\nu^2 < (1+I/mr^2)^{-1}$ or $K/I\nu^2 \geq 1$ or if

(b) $(1+I/mr^2)^{-1} < K/I\nu^2 < 1$

and $A^2\nu^2/gr \leq 2[(1+I/mr^2)K/I\nu^2 - 1](1-K/I\nu^2)^{-1}$.

The upward vertical position is stable if

$K/I\nu^2 > 1$ or $K/I\nu^2 < (1+I/mr^2)^{-1}$

when $A^2\nu^3/gr > 2[(1+I/mr^2)K/I\nu^2 - 1](K/I\nu^2 - 1)^{-1}$.

Two downward nonvertical positions are stable if

$(1+I/mr^2)^{-1} < K/I\nu^2 < 1$

when $A^2\nu^2/gr > 2[(1+I/mr^2)K/I\nu^2 - 1](1-K/I\nu^2)^{-1}$.

These equilibrium positions are described by

$$\cos\theta_e = \frac{2gr}{A^2\nu^2}\,[(K/I\nu^2)(1+I/mr^2) - 1](1-K/I\nu^2)^{-1}.$$

It is suitable to note the effect of the flexible connection between the mass and the rod of the pendulum. This flexibility introduces an additional degree-of-freedom. Without this, the pendulum would merely be a pendulum with an oscillation applied to the pivot and it would have a stable equilibrium position at $\theta = 0$ and another stable equilibrium position at $\theta = \pi$ (if the amplitude and frequency of the oscillation were large enough). The additional degree-of-freedom introduces new equilibrium positions.

We make a few remarks to provide an understanding of why these extra equilibrium positions occur. The imposed oscillation can cause an oscillating θ motion. This motion along with the acceleration of the imposed oscillation causes an average inertia moment which tends to cause stable equilibrium in the two vertical positions or in the two horizontal positions. The term $C \sin 2\Psi$ in equation (6*d*) shows this average moment. If $K/I\nu^2 < (1+I/mr^2)^{-1}$ or if $K/I\nu^2 > 1$, the oscillatory θ mo-

Downloaded 03 May 2010 to 171.66.16.244. Redistribution subject to ASME license or copyright; see http://www.asme.org/terms/Terms_Use.cfm

tion is in phase with the acceleration of the imposed oscillation and the average moment tends to cause stable equilibrium in the two vertical positions. C in equation (6*d*) is positive for these values of $K/I\nu^2$. If $(1+I/mr^2)^{-1}<K/I\nu^2<1$, the θ oscillation is 180 deg out of phase with the acceleration of the imposed oscillation. The average moment tends to cause stable equilibrium in the two horizontal positions. The average moment eliminates the upward vertical equilibrium position and tends to eliminate the downward vertical equilibrium position. If the amplitude or frequency of the imposed oscillation is large enough, the downward vertical equilibrium position is eliminated and the stable equilibrium positions in the first and fourth quadrants are formed. C in equation (6*d*) is negative for these values of $K/I\nu^2$.

Additional equilibrium positions caused by flexible members is exhibited in other vibrated pendulum problems. In Schmidt (1983), the pendulum is flexible in the sense that the mass is allowed to move (restrained by a spring) in the radial direction. Because of this flexibility, the imposed oscillation causes new stable equilibrium positions to be formed (for large enough amplitude and frequency of the imposed oscillation) in the upward vertical position and in two downward nonvertical positions. In Schmidt (1981), a spherical pendulum is given a rotational oscillation at the pivot. The oscillation is rotational about a vertical axis. The mass is allowed to rotate on the rod about the axis of the rod. It is restrained by a spring. Because of the flexible connection between the rod and the mass, the imposed oscillation causes new stable equilibrium positions in the inverted position and in two downward nonvertical positions.

Acknowledgment

We would like to express appreciation for the assistance given by Professor David G. McDowell in some important points in the analysis.

References

Balachandra, M., and Sethna, P. R., 1975, "A Generalization of the Method of Averaging for Systems with Two Time Scales," *Archive for Rational Mechanics and Analysis*, Vol. 58, pp. 261–283.

Bogdanoff, J. L., and Citron, S. J., 1965, "Experiments With an Inverted Pendulum Subject to Random Parametric Excitation," *Journal of the Acoustical Society of America*, Vol. 38, pp. 447–452.

Bogoliuboff, N. M., and Mitropolskiy, Yu, A., 1962, *Asymptotic Methods in the Theory of Nonlinear Oscillations*, Gordon and Breach.

Howe, M. S., 1974, "The Mean Square Stability of an Inverted Pendulum Subject to Random Parametric Excitation," *Journal of Sound and Vibration*, Vol. 32, pp. 407–421.

Lowenstern, E. R., 1932, "The Stabilizing Effect of Imposed Oscillations of High Frequency on a Dynamical System," *Philosophical Magazine*, Vol. 13, pp. 458–486.

Mitchell, R., 1972, "Stability of the Inverted Pendulum Subjected to Almost Periodic and Stochasitc Base Motion—An Application of the Method of Averaging," *International Journal of Non Linear Mechanics*, Vol. 7, pp. 101–123.

Phelps, F. M., III, Hunter, J. H., Jr., 1965, "An Analytical Solution of the Inverted Pendulum," *American Journal of Physics*, Vol. 33, pp. 285–295.

Ryland, G., II, and Meirovitch, I., 1977, "Stability Boundaries of a Swinging Spring With Oscillatory Support," *Journal of Sound and Vibration*, Vol. 51, pp. 547–560.

Schmidt, B. A., 1980, "Vibrated Pendulum With a Mass Free to Move Radially," ASME JOURNAL OF APPLIED MECHANICS, Vol. 47, pp. 428–430.

Schmidt, B. A., 1981, "Pendulum With a Rotational Vibration," ASME JOURNAL OF APPLIED MECHANICS, Vol. 48, pp. 200–203.

Schmidt, B. A., 1983, "The Radially Flexible Pendulum Subjected to a High-Frequency Excitation," ASME JOURNAL OF APPLIED MECHANICS, Vol. 50, pp. 443–448.

Sethna, P. R., and Hemp, G. W., 1964, "Nonlinear Oscillation of a Gyroscopic Pendulum With an Oscillatory Point of Suspension," *Proc. Colloq. International du Center National de la Recherche Scientifique*, N-148, Les Vibrations Forcees dans les Systems Non-Lineares, pp. 375–392.

Stephenson, A., 1907, "On a New Type of Dynamical Stability," *Memoirs and Proceedings of the Manchester Literary and Philosophical Society*, Vol. 52, pp. 1–10.

Downloaded 03 May 2010 to 171.66.16.244. Redistribution subject to ASME license or copyright; see http://www.asme.org/terms/Terms_Use.cfm

A Convolution Approach for the Transient Analysis of Locally Nonlinear Rotor Systems

I. F. Chiang
Graduate Student.

S. T. Noah
Associate Professor.
Mem. ASME.

Mechanical Engineering Department,
Texas A&M University,
College Station, TX 77843

A computationally efficient convolution method, based on discretized impulse response and transition matrix integral formulations, is developed for the transient analysis of complex linear structures interacting through strong local nonlinearities. In the formulation, the coupling forces due to the nonlinearities are treated as external forces acting on the coupled subsystems. Iteration is utilized to determine their magnitudes at each time increment. The method is applied to a generic rotor-housing model representing a turbopump of a space shuttle main engine (SSME). In that model, the local nonlinearity is due to clearances between the rotor bearing outer races and the carrier attached to the housing. As compared to the fourth-order Runge-Kutta numerical integration methods, the convolution approach proved more efficient and robust for the same accuracy requirement. This is due to the closed-form formulation of the convolution approach which allows for the use of relatively larger time increments and for a reduction in the roundoff errors.

Introduction

The use of a direct numerical integration for determining the transient response of coupled nonlinear rotor-flexible housing systems may require excessive computational time and involve unacceptable computational roundoff errors. To remedy these problems, different procedures have been developed by analysts to determine the transient response of large order rotor systems. The procedures can be recognized as falling under one of two basic approaches: those using physical or modal coordinates of the complete system and those using the coordinates of the individuals components of the system. The methods also differ in the numerical integration methods selected for the analysis.

Rouch and Kao (1980) employed Guyan (static) reduction method to arrive at a reduced size model in terms of the remaining physical coordinates. Accuracy of the results could be expected to be acceptable, since the rotor is basically a train of mass-stiffness subsystems. Nordmann (1975) attempted to minimize the inaccuracy of static condensation by applying the static reduction technique to an arbitrarily substructured rotor system and then assembling the reduced substructures to form a reduced system. The procedure is very laborious and no guarantees of accuracy are apparent.

Childs (1978) utilized free-interface modes of the various system components to represent the assembled turbopumps of a space shuttle main engine (SSME). The method, using fourth-order Runge-Kutta integration, does not allow for size reduction of the housing model while maintaining sufficient modal coordinates for accurate representation of the housing. Nelson et al. (1982), on the other hand, uses fixed-interface complex component modes to assemble a reduced size model. For systems with a large number of coupling points among the components, the approach suffers from an introduction of higher frequencies resulting from an excessive number of constraints imposed at the coupling (or boundary) points. In a transient analysis, this will necessitate employing much smaller time increments and consequently will lead to excessive computational time.

Only a few analysts have presented techniques for the general transient analysis of large nonlinear rotor systems. Adams (1980) used a normal mode representation for the rotor in terms of its undamped, free symmetric modes and treated gyroscopic and nonlinear terms as pseudo-external loads. The method presented by Childs (1978) makes use of a similar procedure to couple the rotor to its flexible housing. Nelson et al. (1982) developed a general computer code for the transient analysis of large rotor systems. The user may utilize time-step integration in the constrained-rotor (fixed-interface) modal space. Again, all connection points, including those at the nonlinearities, must be constrained, leading to the same shortcomings described previously.

Spanos et al. (1988) considered linear systems analyzed as decoupled subsystems. The accelerations at the interface are predicted at the beginning of each time step. The accelerations of the interface and interior nodes are then calculated and

Contributed by the Applied Mechanics Division of THE AMERICAN SOCIETY OF MECHANICAL ENGINEERS for presentation at the Winter Annual Meeting, Dallas, Texas, Nov. 25–30, 1990.

Discussion on this paper should be addressed to the Technical Editor, Leon M. Keer, The Technological Institute, Northwestern University, Evanston, IL 60208, and will be accepted until two months after final publication of the paper itself in the JOURNAL OF APPLIED MECHANICS. Manuscript received by the ASME Applied Mechanics Division, Oct. 10, 1988; final revision, Sept. 27, 1989.

Paper No. 90-WA/APM-21.

Copyright © 1990 by ASME
Downloaded 03 May 2010 to 171.66.16.244. Redistribution subject to ASME license or copyright; see http://www.asme.org/terms/Terms_Use.cfm

corrected through iterations. The decoupling makes the modeling of the assembled system more efficient. Hagedorn (1988) proposed a method for the analysis of a large linear subsystem coupled to one or more nonlinear subsystems. The dynamics of the system is represented by an integral equation of the convolution type containing the transfer matrix of the linear subsystem, and by the functional relation describing the nonlinearities. It appears that since no iterative technique was used, the method would require a very small integration step.

A method which proves to be highly efficient in determining the transient response of linear systems under specified general excitations is to utilize the convolution integral, or the transition matrix (Meirovitch, 1980) of the system. Von Pragenau (1981) utilized the transition matrix, stating that it offers the simplicity of the Euler method without requiring small steps. Von Pragenau maintained that for systems with constant coefficients, the stability and accuracy of the method are acquired through the closed-form solution of the transition matrix.

In the present study, the convolution methods (impulse response and transition integrals) are shown to be very effective when extended for application to linear systems with *local nonlinearities*. The forces at the nonlinear locations are treated as the external forces on the systems or subsystems and iteration is used at each time increment to determine the magnitude of the forces for subsequent increments.

The technique presented in this paper can also be applied in terms of the modes of subsystems calculated separately. However, system equations of motion will be formed as in a component mode synthesis approach. The response of each substructure is solved separately by treating the interface forces of the system as external forces to the subsystems. The convolution approach can also be applied to the generalized second-order system equations developed from component mode synthesis. In contrast to the convolution approach, if local nonlinearities occur at the interface, standard free interface, component mode synthesis methods fail.

The convolution approach is applied to a general rotor-housing system with rotor imbalance during startup or shutdown. In the present work, eigencoordinates are used to represent both housing and rotor. The local nonlinearities were taken as deadband clearances at the rolling element bearings which support the rotor in its housing. The integral formulation of the rotor motion is represented by its transition matrix and that of the housing by a convolution integral (based on the housing's impulse response).

The convoluted impulse response can only be applied to a system of uncoupled equations while the transition matrix formulation, in addition, can be applied to coupled equations. The transition matrix can therefore be applied to coupled dynamical systems represented by their physical coordinates or, in case of rotors, coupled by the gyroscopic terms in otherwise decoupled modal representation. Kubomura (1985) used a convolution integration method to achieve dynamic condensation of a substructure to its coupling points to other structures. Convolution was also used by Tongue and Dowell (1983), and Clough and Wilson (1979) to reduce system coordinates to that at the nonlinearities.

Modeling of a Rotor-Housing System

A representative complex rotor system with a flexible housing is shown in Fig. 1. The particular model shown in which the present method can be readily applied, represents the high pressure oxygen turbopump (HPOTP) of the SSME. The interaction forces between rotor and housing include various seal, impeller, turbine tip clearance, bearing clearance, and fluid side forces.

(a) Rotor. The equations of small transverse motion, (Noah, 1986), $\{S\}$ of the rotor under transient external and imbalance forces may be written as

$$[M]_R\{\ddot{S}\} - \dot{\phi}[G]\{\dot{S}\} + [K]_R\{S\} = \{F_I\}_R + \{F_E\}_R. \quad (1)$$

In equation (1), $\{S\}$ represents the translational and rotational displacements and only includes those displacements which are associated with masses and rotary inertias. Other displacements are reduced out using static condensation. The spinning speed of the rotor is denoted by $\dot{\phi}$, $[G]$ is the gyroscopic matrix corresponding to the attached disks, $\{F\}_R$ represents the coupling forces on the rotor due to coupling to the housing while $\{F_E\}_R$ represents the external forces including the imbalance forces. Let

$$\{S\} = [\Phi]_R\{q\}_R \quad (2)$$

in which $[\Phi]_R$ is the modal matrix, normalized with respect to the mass matrix of the nonspinning rotor and $\{q\}_R$ are the associated modal coordinates.

Nomenclature

$[\backslash C \backslash]$ = structural damping matrix
$[C]_I$ = coupling damping matrix
$[CM]$ = convergent matrix
$[D]$ = generalized damping matrix of rotor model
e = imbalance of disk
$\{F\}$ = physical force
$[G]$ = gyroscopic matrix
$\{H\}$ = physical coordinates of housing
$[\backslash I \backslash]$ = identity matrix
$[K]$ = structural stiffness matrix
$[K]_I$ = coupling stiffness matrix
$[M]$ = mass matrix
$\{P\}$ = generalized force (modal force)
$\{q\}$ = generalized displacement (modal displacement)
$[Q]$ = transition matrix
S = physical displacement of rotor in bearing
$\{S\}$ = physical coordinates of rotor
t = time
T = time increment
t_i = time at iT
$\{u\} = \begin{pmatrix} q \\ \dot{q} \end{pmatrix}$, generalized coordinates of rotor
ω_n, ω_d = natural and damped natural frequencies
$[0]$ = null matrix
$[\alpha]$ = the rotor state matrix
$[\backslash \Lambda \backslash]$ = diagonal eigenvalue matrix
$\dot{\phi}$ = spinning speed of rotor
$[\Phi]$ = normalized modal matrix
ζ = damping ratio

Brackets and Symbols

$[\ ]$ = square matrix
$[\backslash\ \backslash]$ = diagonal matrix
$\{\ \}$ = column matrix
$[\ ]^{-1}$ = inverse of a matrix
$[\ ]^T$ = transpose of a matrix

Subscripts

R = rotor
H = housing
E = external
I = coupling
X, Y, Z = X, Y, Z direction
i = ith time increment

Downloaded 03 May 2010 to 171.66.16.244. Redistribution subject to ASME license or copyright; see http://www.asme.org/terms/Terms_Use.cfm

Using the modal transformation (2), equation (1) is written in the form

$$\{\ddot{q}\}_R - [\Phi]_R^T \dot{\phi} [G]_R [\Phi]_R \{\dot{q}\}_R + [\Lambda]_R \{q\}_R = [\Phi]_R^T (\{F_I\}_R + \{F_E\}_R) \quad (3)$$

where

$$[\Lambda]_R = [\omega_n^2]_R.$$

ω_n is the natural frequency of the nonspinning of the rotor. Adding a modal damping matrix $[C]$ to equation (3) yields

$$\{\ddot{q}\}_R + [D]_R \{\dot{q}\}_R + [\Lambda]_R \{q\}_R = [\Phi]_R^T (\{F_I\}_R + \{F_E\}_R) \quad (4)$$

where

$$[D]_R = [C]_R - [\Phi]_R^T \dot{\phi} [G]_R [\Phi]_R \quad (5)$$

$$[C]_R = [2\zeta\omega_n]_R. \quad (6)$$

(b) Housing. The equation of motion of the housing may be expressed as

$$[M]_H \{\ddot{H}\} + [K]_H \{H\} = \{F_I\}_H + \{F_E\}_H \quad (7)$$

where $\{H\}$ represents the transverse displacement in the Y and Z-directions. In terms of the modal coordinates of the housing while uncoupled to the rotor, equation (7) takes the form (after adding a modal damping matrix)

$$\{\ddot{q}\}_H + [D]_H \{\dot{q}\}_H + [\Lambda]_H \{q\}_H = [\Phi]_H^T (\{F_I\}_H + \{F_E\}_H) \quad (8)$$

where

$$[D]_H = [C]_H = [2\zeta\omega_n]_H \quad (9)$$

and

$$[\Lambda]_H = [\omega_n^2]_H. \quad (10)$$

(c) Coupling Forces. Forces due to linear coupling between rotor and housing may include the direct and cross-coupling forces due to seals, impeller, and turbine forces. The nonlinear coupling forces are taken as those due to the clearance between the rolling element bearing outer race and the housing. Figure 2 shows a model for the gap at each of the loosely supported bearings.

The bearing force acting on the housing in the Y-direction is

$$(F_G)_Y = K_G (R - \delta) \frac{S_Y - H_Y}{R} + C_G (\dot{S}_Y - \dot{H}_Y) \quad R \geq \delta$$

$$(F_G)_Y = C_G (\dot{S}_Y - \dot{H}_Y) \quad R \leq \delta$$

where the bearing support stiffness, K_G, is shown in Fig. 3 and C_G is the damping in bearing. Analogous equations hold for the Z-direction, and

$$R = \sqrt{(S_Y - H_Y)^2 + (S_Z - H_Z)^2}$$

where

S_Y, S_Z are the physical displacements of rotor in the Y and Z directions, respectively, at the bearing location.

H_Y, H_Z are the physical displacements of housing in the Y and Z directions, respectively, at the bearing location.

The bearing forces can further be written as

$$(F_G)_Y = \bar{K}_G (S_Y - H_Y) + C_G (\dot{S}_Y - \dot{H}_Y) \quad (11)$$

$$(F_G)_Z = \bar{K}_G (S_Z - H_Z) + C_G (\dot{S}_Z - \dot{H}_Z) \quad (12)$$

where

$$\bar{K}_G = K_G \left(1 - \frac{\delta}{R}\right) \quad R \geq \delta \quad (13)$$

$$\bar{K}_G = 0 \quad R \leq \delta. \quad (14)$$

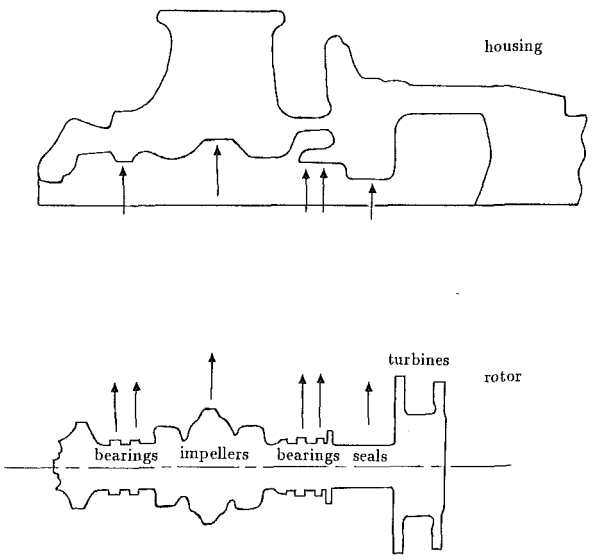


Fig. 1 Complex rotor system with flexible housing

Method of Analysis

A hybrid convolution method proposed by Noah et al., (1986) and (1988), is utilized here for the analysis of the coupled rotor-housing system. The displacements of the housing are best represented by a convolution integral due to its accuracy advantage over the transition matrix formulation. Due to the presence of the unsymmetric gyroscopic terms, the equations of motion for the rotor are transformed to first order. The displacements of the rotor are expressed in terms of transition matrix for the motion of the rotor.

The restriction of an impulse response convolution integral is that the equations of motion have to be decoupled. For a coupled subsystem, such as rotor with gyroscopic moments at the left-hand side of its equations, a transition matrix formulation has to be employed. However, the convolution integral is more computationally efficient than transition matrix formulation.

Transition Matrix for the Rotor. The equations of motion of the rotor, equation (4), are cast in first-order form,

$$\{\dot{u}\}_R = [\alpha]_R \{u\}_R + \{P\}_R \quad (15)$$

where

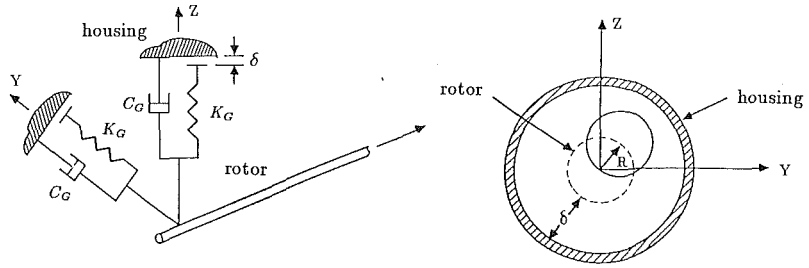


Fig. 2 Rotor and housing displacements at bearing location

Downloaded 03 May 2010 to 171.66.16.244. Redistribution subject to ASME license or copyright; see http://www.asme.org/terms/Terms_Use.cfm

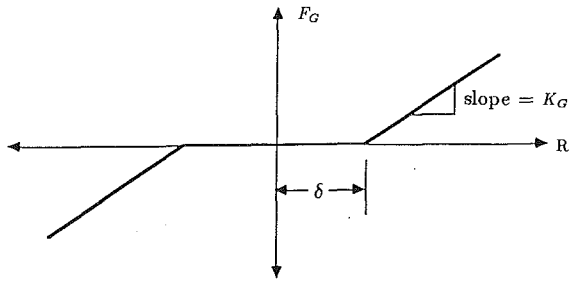


Fig. 3 Nonlinear bearing force, F_G, due to K_G

$$[\alpha]_R = \begin{pmatrix} [0] & [\backslash I \backslash] \\ -[\backslash \Lambda \backslash]_R - [D]_R & \end{pmatrix} \tag{16}$$

$$\{P\}_R = \begin{pmatrix} 0 \\ [\Phi]_R^T(\{F_I\}_R + \{F_E\}_R) \end{pmatrix}. \tag{17}$$

If the spinning speed is a function of time, the gyroscopic term of equation (5) can be moved to the right-hand side of equation (4) to avoid solving a new eigenproblem at each time step. In this case, the coefficient matrices, given by equations (16) and (17), are replaced by

$$[\alpha]_R = \begin{pmatrix} [0] & [\backslash I \backslash] \\ -[\backslash \Lambda \backslash]_R - [\backslash C \backslash]_R & \end{pmatrix} \tag{16'}$$

$$\{P\}_R = \begin{pmatrix} 0 \\ [\Phi]_R^T(\{F_I\}_R + \{F_E\}_R) \end{pmatrix} + \begin{pmatrix} 0 \\ [\Phi]_R^T \dot{\phi}[G]_R[\Phi]_R\{\dot{q}\}_R \end{pmatrix}. \tag{17'}$$

In this case, the equations of motion of the rotor becomes decoupled, and a convolution integral becomes a better selection because it is more efficient than the transition matrix method.

The solution of equation (15) can be written as

$$\{u(t)\}_R = e^{t[\alpha]_R}\{u_0\} + \int_0^t e^{(t-\tau)[\alpha]_R}\{P(\tau)\}_R d\tau \tag{18}$$

where

$$e^{t[\alpha]_R} = \sum_{k=0}^{\infty} \frac{t^k[\alpha]_R^k}{k!}. \tag{19}$$

Equation (19) is transition matrix and $\{u_0\}$ is the initial generalized coordinates.

Equation (18) can be cast in a discretized form in which the generalized forces, $\{P\}_R$, are taken as varying linearly between time t_i and t_{i+1} so that

$$\{P(t)\} = \{P(t_i\} + \frac{t-t_i}{T}(\{P(t_{i+1})\} - \{P(t_i)\}) \quad t_i \le t \le t_{i+1}$$

where $t_{i+1} = t_i + T$ and T is a small increment in time. The discretized form of equation (18) can then be shown to take the form

$$\{u(t_{i+1})\}_R = [Q(T)]\{u(t_i)\}_R + ([Q(T)] - [\backslash I \backslash])[\alpha]_R^{-1}\left(\{P(t_i)\}_R + [\alpha]_R^{-1} \times \frac{\{P(t_{i+1})\}_R - \{P(t_i)\}_R}{T}\right) - [\alpha]_R^{-1}(\{P(t_{i+1})\}_R - \{P(t_i)\}_R) \tag{20}$$

where

$$[Q(T)] = e^{T[\alpha]_R}. \tag{21}$$

Convolution Integral for Housing. The decoupled form of the equations of motion of the housing allows expressing the nodal displacements of the housing by an integral. The integral formulation has the advantage of providing a closed-form expression as opposed to conventional numerical integration schemes. Also this representation allows dealing directly with diagonal modal matrices as opposed to coupled, first-order modal equations used with the Runge-Kutta method of the convolutional formulation matrices. This results in higher computational speed and accuracy of the convolution formulation.

Based on equation (8), the housing generalized coordinates can be expressed as

$$\{q(t)\}_H = [\backslash e^{-\zeta\omega_n t}\cos\omega_d t \backslash]\{q(0)\}_H + \left[\backslash \frac{1}{\omega_d} e^{-\zeta\omega_n t}\sin\omega_d t \backslash\right](\{\dot{q}(0)\}_H + \zeta\omega_n\{q(0)\}_H) + \int_0^t \left[\backslash \frac{1}{\omega_d} e^{-\zeta\omega_n(t-\tau)}\sin\omega_d(t-\tau)\backslash\right]\{P(\tau)\}_H d\tau \tag{22}$$

where $\{q(0)\}$, $\{\dot{q}(0)\}$ are initial solutions, ω_n, ω_d are undamped and damped natural frequencies of housing, ζ is damping ratio of housing, $\{P\}_H = [\Phi]_H^T(\{F_I\}_H + \{F_E\}_H)$, the generalized forces act on housing.

The expression (22) is next written in discretized form, with the generalized forces taken as before as varying linearly within each time step, or

$$\{q(t_{i+1})\}_H = [\backslash e^{-at_{i+1}}\cos bt_{i+1}\backslash]\{q(0)\}_H + \left[\backslash \frac{1}{b} e^{-at_{i+1}}\sin bt_{i+1}\backslash\right](\{\dot{q}(0)\}_H + a\{q(0)\}_H) + \left\{\frac{\sin bt_{i+1}}{b(a^2+b^2)} EA_{i+1} - \frac{\cos bt_{i+1}}{b(a^2+b^2)} EB_{i+1}\right\} \tag{23}$$

$$\{\dot{q}(t_{i+1})\}_H = [\backslash -e^{-at_{i+1}}(a\cos bt_{i+1} + b\sin bt_{i+1})\backslash]\{q(0)\}_H + \left[\backslash e^{-at_{i+1}}\left(-\frac{a}{b}\sin bt_{i+1} + \cos bt_{i+1}\right)\backslash\right](\{\dot{q}(0)\}_H + a\{q(0)\}_H) + \left\{\frac{-a\sin bt_{i+1} + b\cos bt_{i+1}}{b(a^2+b^2)} EA_{i+1} + \frac{a\cos bt_{i+1} + b\sin bt_{i+1}}{b(a^2+b^2)} EB_{i+1}\right\} \tag{24}$$

where

$$a = \zeta\omega_n \tag{25}$$

$$b = \omega_d \tag{26}$$

$$EA_{i+1} = e^{-aT}EA_i + A_{i+1} \tag{27}$$

$$EB_{i+1} = e^{-aT}EB_i + B_{i+1} \tag{28}$$

$$EA_i = e^{-at_{i-1}}A_1 + e^{-at_{i-2}}A_2 + \ldots + A_i \tag{29}$$

$$EB_i = e^{-at_{i-1}}B_1 + e^{-at_{i-2}}B_2 + \ldots + B_i \tag{30}$$

$$A_{i+1} = P_{i+1}(a\cos bt_{i+1} + b\sin bt_{i+1}) - \frac{P_{i+1}-P_i}{T(a^2+b^2)}(a^2\cos bt_{i+1} + 2ab\sin bt_{i+1} - b^2\cos bt_{i+1}) + \frac{P_{i+1}-P_i}{T(a^2+b^2)} e^{-aT}(a^2\cos bt_i + 2ab\sin bt_i - b^2\cos bt_i) - P_i e^{-aT}(a\cos bt_i + b\sin bt_i) \tag{31}$$

Downloaded 03 May 2010 to 171.66.16.244. Redistribution subject to ASME license or copyright; see http://www.asme.org/terms/Terms_Use.cfm

$$B_{i+1}=P_{i+1}(a\sin bt_{i+1}-b\cos bt_{i+1})$$
$$-\frac{P_{i+1}-P_i}{T(a^2+b^2)}(a^2\sin bt_{i+1}-2ab\cos bt_{i+1}-b^2\sin bt_{i+1})$$
$$+\frac{P_{i+1}-P_i}{T(a^2+b^2)}e^{-aT}(a^2\sin bt_i-2ab\cos bt_i-b^2\sin bt_i)$$
$$-P_i e^{-aT}(a\sin bt_i-b\cos bt_i) \quad (32)$$

P is element of vector $\{P\}$.

The Coupling Forces. The coupling forces acting on the housing are given by

$$\{F_I\}_H=[K]_I(\{S\}-\{H\})+[C]_I(\{\dot S\}-\{\dot H\}) \quad (33)$$

and those on the rotor are

$$\{F_I\}_R=-\{F_I\}_H$$

where $[K]_I$ and $[C]_I$ are the coupling stiffness and damping matrices, respectively. The coupling stiffness matrix includes the updated bilinear bearing stiffness at each iteration.

The Computational Procedure. For the responses at time $t=t_{i+1}$, the coupling forces between the housing and rotor are unknown. An iterative technique is used to calculate these forces. The following iterative loop is used in both the hybrid and Runge-Kutta methods:

If the responses at $t=t_i$ are known and responses at $t=t_{i+1}$ are desired, then:

(a) Set $\{F_I(t_{i+1})\}=\{F_I(t_i)\}$.

(b) Calculate $\{P\}_R$ and $\{P\}_H$.

(c) Solve $\{u(t_{i+1})\}_R$ and $\{q(t_{i+1})\}_H$, $\{\dot q(t_{i+1})\}_H$ by the hybrid method (or the Runge-Kutta method). Calculate the Euclidean norm of $\{u(t_{i+1})\}_R$ and $\{q(t_{i+1})\}_H$.

(d) Transfer $\{u(t_{i+1})\}_R$ and $\{q(t_{i+1})\}_H$, $\{\dot q(t_{i+1})\}_H$ back to physical coordinates, then a new connection force $\{F_I(t_{i+1})\}$ can be calculated.

(e) If the Euclidean norms of two consecutive iterations of both rotor and housing are close enough then stop the iteration and go to step (f), otherwise go to (b).

(f) Move a time increment and go to (a) until t reaches a specified time for terminating the run.

The Convergence of Hybrid Method. Rewrite the coupling forces as the function of the generalized coordinates, equations (20), (23), and (24) can be arranged as the following form:

$$\begin{pmatrix} u(t_{i+1})^{(k)} \\ \cdots \\ q(t_{i+1})^{(k)} \\ \dot q(t_{i+1})^{(k)} \end{pmatrix} = [CM]\times \begin{pmatrix} u(t_{i+1})^{(k-1)} \\ \cdots \\ q(t_{i+1})^{(k-1)} \\ \dot q(t_{i+1})^{(k-1)} \end{pmatrix} + \{c\} \quad (34)$$

where k stands for kth iteration at a given time t_{i+1}, $[CM]$ is the convergent matrix (Isaacson and Keller, 1966), $\{c\}$ is vector with known values, and

$$[CM]=\begin{pmatrix} [S1] & [S2] \\ [S3] & [S4] \end{pmatrix} \quad (35)$$

where

$$[S1]=[T1]\times\begin{pmatrix} 0 & 0 \\ -[\Phi]_R^T[K]_I[\Phi]_R & -[\Phi]_R^T[C]_I[\Phi]_R \end{pmatrix}$$

$$[S2]=[T1]\times\begin{pmatrix} 0 & 0 \\ [\Phi]_R^T[K]_I[\Phi]_H & [\Phi]_R^T[C]_I[\Phi]_H \end{pmatrix}$$

$$[S3]=\begin{pmatrix} [T2][\Phi]_H^T[K]_I[\Phi]_R & [T2][\Phi]_H^T[C]_I[\Phi]_R \\ [T3][\Phi]_H^T[K]_I[\Phi]_R & [T3][\Phi]_H^T[C]_I[\Phi]_R \end{pmatrix}$$

$$[S4]=\begin{pmatrix} -[T2][\Phi]_H^T[K]_I[\Phi]_H & -[T2][\Phi]_H^T[C]_I[\Phi]_H \\ -[T3][\Phi]_H^T[K]_I[\Phi]_H & -[T3][\Phi]_H^T[C]_I[\Phi]_H \end{pmatrix}$$

and

$$[T1]=[\alpha]_R^{-1}\left(([Q(T)]-[\Lambda])\frac{[\alpha]_R^{-1}}{T}-[\Lambda]\right)$$

$$[T2]=\left[\frac{\sin bt_{i+1}}{b(a^2+b^2)}AC-\frac{\cos bt_{i+1}}{b(a^2+b^2)}AS\right]$$

$$[T3]=\left[\frac{-a\sin bt_{i+1}+b\cos bt_{i+1}}{b(a^2+b^2)}AC+\frac{a\cos bt_{i+1}+b\sin bt_{i+1}}{b(a^2+b^2)}AS\right]$$

where

$$AC=a\cos bt_{i+1}+b\sin bt_{i+1}$$
$$-\frac{1}{T(a^2+b^2)}(a^2\cos bt_{i+1}+2ab\sin bt_{i+1}-b^2\cos bt_{i+1})$$
$$+\frac{e^{-aT}}{T(a^2+b^2)}(a^2\cos bt_i+2ab\sin bt_i-b^2\cos bt_i)$$
$$AS=a\sin bt_{i+1}-b\cos bt_{i+1}$$
$$-\frac{1}{T(a^2+b^2)}(a^2\sin bt_{i+1}-2ab\cos bt_{i+1}-b^2\sin bt_{i+1})$$
$$+\frac{e^{-aT}}{T(a^2+b^2)}(a^2\sin bt_i-2ab\cos bt_i-b^2\sin bt_i).$$

Equation (34) is in the form of the Jacobi iterative method (simultaneous iterations), see (Isaacson and Keller, 1966). The convergent matrix, $[CM]$ may not be fixed at a given time $t=t_{i+1}$ as in an ordinary linear system because matrix $[K]_I$ may change during the iteration if the switch between two slope areas in Fig. 3 exists. $[K]_I$ will be updated because the nonlinear bearing stiffness, K_G, changes. In this case, there are two convergence rates during the iteration at that given time.

Equation (34) will converge if and only if all eigenvalues of $[CM]$ are less than one in absolute value. An alternative way to check the convergence is that the iterative method will converge if, for any matrix norm (Euclidean, maximum, etc.), $\|[CM]\|<1$. Uncommon cases occur where convergence criteria are met within one region in Fig. 3 and not the other. In that case, overall convergence at a given time t_{i+1} might occur depending on the pattern of movement from one region to the other. In any case, the convergence rate and size of the increment T will determine the outcome for acceptable accuracy.

The rate of convergence, CR, is defined as the following:

$$CR\equiv-\log\rho([CM])$$

where $\rho([CM])$ is the spectral radius of $[CM]$ defined by

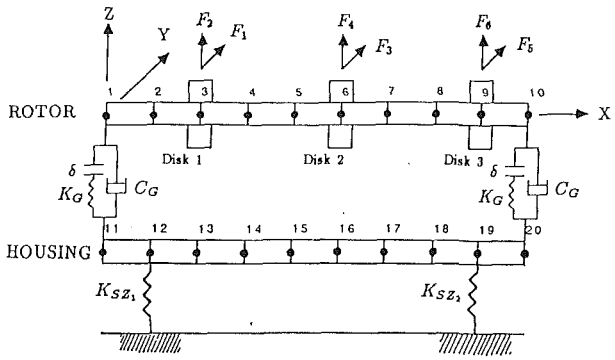
$$\rho([CM])\equiv\max|\lambda_i|$$

where λ_i are the eigenvalues of $[CM]$.

Let the initial error be defined as the norm of the vector of the difference between the exact solution and an initial guess at the beginning of iteration. The number of iterations, ν, required to reduce the initial error by the factor 10^{-m} is inversely proportional to CR and is defined as

$$\nu\geq\frac{m}{CR}.$$

Downloaded 03 May 2010 to 171.66.16.244. Redistribution subject to ASME license or copyright; see http://www.asme.org/terms/Terms_Use.cfm



ROTOR: Shaft dismeter: OD = $7.26 \times 10^{-2}m$, ID = $0.0m$
Material: $E = 2.0684 \times 10^{10} N/m^2$
Joint length= $7.26 \times 10^{-2}m$
Rotor length= $6.858 \times 10^{-1}m$

HOUSING: Housing/rotor weight ratio = 6/1

$(EI)_R = 8.6947 \times 10^3 Nm^3$
$(EI)_H = 1.7494 \times 10^4 Nm^3$

$F_1(t) = m_1 e\dot{\phi}^2 cos\dot{\phi}t$ $K_{SZ_1} = 7.005 \times 10^6 N/m$ $C_G = 0.0$
$F_2(t) = m_1 e\dot{\phi}^2 sin\dot{\phi}t$ $K_{SY_1} = 8.7563 \times 10^6 N/m$
$F_3(t) = m_2 e\dot{\phi}^2 cos\dot{\phi}t$ $K_{SZ_2} = 8.7563 \times 10^6 N/m$
$F_4(t) = m_2 e\dot{\phi}^2 sin\dot{\phi}t$ $K_{SY_2} = 2.6269 \times 10^7 N/m$
$F_5(t) = m_3 e\dot{\phi}^2 cos\dot{\phi}t$ $K_G = 8.7563 \times 10^7 N/m$
$F_6(t) = m_3 e\dot{\phi}^2 sin\dot{\phi}t$ $\delta = 0.0127mm$

Fig. 4 The generic model

Application and Discussion

The present convolution method is applied to a modified version of a rotor model proposed by Davis et al. (1984). The model was proposed to represent a simplified generic model of the SSME turbopumps. The parameters and coefficients of the present generic model (shown in Fig. 4) are given in Tables 1 and 2. The imbalance forces are taken as shown on Fig. 4.

Response of the generic rotor-housing model at the bearing location is determined for the hypothetical startup-shutdown case shown in Fig. 5. For various time increments, Δt, a comparison is made of the errors and computer CPU time (on a VAX 8650) between the results obtained using Runge-Kutta fourth-order method and those using the present convolution method.

Comparisons of the CPU time, are made with comparable errors of the results of using both methods. The errors is measured at time $t = 0.01$ seconds and defined as the following

$$\text{Error} = \frac{\|V_{ex} - V\|}{\|V_{ex}\|}$$

where V_{ex} is the exact solution of the rotor and housing displacements in vector form and V represents the displacements of rotor and housing at the corresponding time in vector form.

The "exact" solution is calculated using the hybrid convolution method with a very small time increment, 2×10^{-7} seconds and tolerance $= 1 \times 10^{-12}$. The tolerance is the absolute value of the difference of the displacement and velocity norms of rotor and housing described in step (e) of the computational procedure.

As shown in Figs. 6 and 7, with the tolerance equals to 1×10^{-8} seconds, the hybrid convolution method is faster and more accurate. For more meaningful comparison, the accuracies of the Runge-Kutta and convolution methods are made closer by reducing the allowable tolerance for the Runge-Kutta to 1×10^{-12} seconds and 1×10^{-14} seconds. The CPU time for the Runge-Kutta increases quickly from 1.42 times of the hybrid method's CPU to 4.23 times (with a time increment of 2×10^{-5}). For the closest accuracies, the CPU time of the Runge-Kutta is 4.23 times that of the hybrid method. The hybrid convolution method is also more robust than the Runge-Kutta method. The Runge-Kutta algorithm failed to converge for time increments greater than 2×10^{-5} seconds. However, the hybrid method will diverge when the increment used is larger than 3.3×10^{-5} seconds.

Table 1 Parameters of the generic model

Disk	Mass (Kg)	Imbalance (mm)	Moment of inertia ($Kg.m^2$) Polar	Diametrical
1	4.5358	0.0508	3.1635×10^{-3}	1.7964×10^{-3}
2	6.8124	0.0508	2.1806×10^{-2}	1.1411×10^{-2}
3	9.0175	0.0508	1.1363×10^{-1}	5.7373×10^{-2}

Table 2 Coefficients of the generic model

Disk	K_{YY}, K_{ZZ} (N/m)	K_{XY}, K_{YX} (N/m)	C_{YY}, C_{ZZ} (N sec/m)
1	1.7513×10^7	2.6269×10^6	1.1033×10^4
2	-1.5586×10^6	-7.0050×10^5	1.7513×10^2
3	1.5236×10^6	3.3274×10^5	4.0279×10^2

Disk	Side force (N) Y-direction	Z-direction
1	$2.2019 \times 10^{-5}\ \dot{\phi}^2$	$-1.2482 \times 10^{-4}\ \dot{\phi}^2$
2	$2.7210 \times 10^{-4}\ \dot{\phi}^2$	$3.2387 \times 10^{-4}\ \dot{\phi}^2$
3	$1.0582 \times 10^{-4}\ \dot{\phi}^2$	0

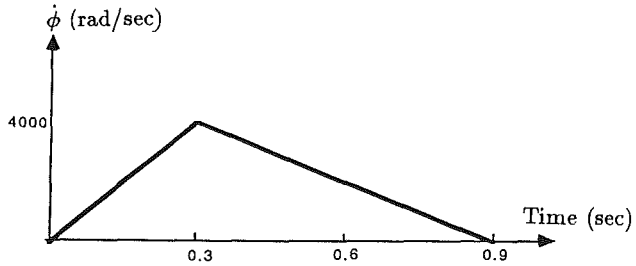


Fig. 5 Running speed of rotor

Concluding Remarks

The convolution integral and transition matrix methods are represented in closed form. They generate less roundoff errors and require less numerical computation time in comparison with the Runge-Kutta fourth-order method. Moreover, they are more robust than the Runge-Kutta method since they will converge for larger time-step size.

The hybrid convolution approach developed in this study is shown to provide an efficient and accurate closed-form integral formulation for determining the transient response of linear systems coupled through local nonlinearities. A typical application in which the present method proved quite effective is the determination of the transient response of a generic model of the high pressure oxygen turbopump (HPOTP) of a space shuttle main engine (SSME) in presence of bearing clearances, constituting the local nonlinearities. Substantial savings in computation time were achieved as compared with direct numerical integration techniques.

The use of the transition matrix allows the representation of rotors involving skew-symmetric matrices of gyroscopic loads or other nonconservative systems with general velocity coefficient matrices. A convolution integral would represent quite effectively other systems with classical modes, such as

Downloaded 03 May 2010 to 171.66.16.244. Redistribution subject to ASME license or copyright; see http://www.asme.org/terms/Terms_Use.cfm

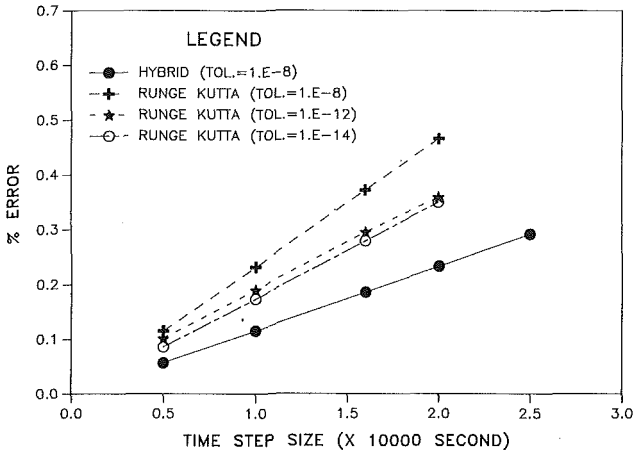


Fig. 6 Accuracy of hybrid method and Runge-Kutta methods

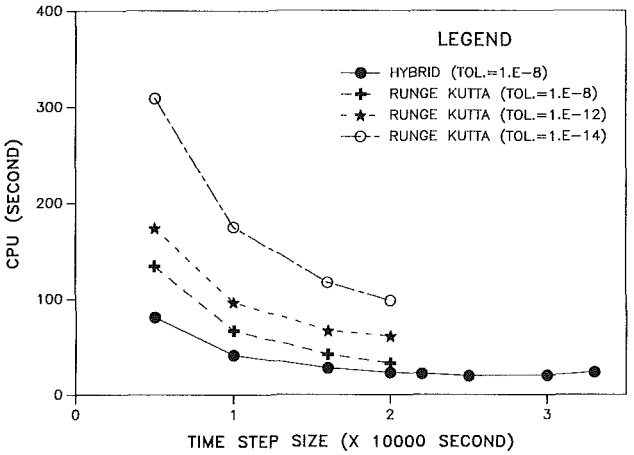


Fig. 7 CPU time of hybrid method and Runge-Kutta methods

the housing of the HPOTP or other nonrotating, proportionally damped structures. The convolution formulation allows accommodating with ease changes in the nonlinear or linear coupling parameters among the various linear subsystems involved.

Possible improvement of the method could be achieved through other alternative or optimization for the iteration procedure utilized in this study. The methods described in this study is believed to be capable of handling any type of local nonlinearity. For an impact case at the bearing, for example, iteration over the contact force could be replaced by iteration to establish contact/no-contact at each increment and then reverse the impact velocity. Applications of the present method to systems with various types of local nonlinearities could be worthwhile.

Acknowledgment

This work was carried out as part of a research project supported by NASA, Marshall Flight Center, under contract No. NAS8-36293. The authors are grateful to Thomas Fox, the technical monitor, for his enthusiastic support and interest.

References

Adams, M. L., 1980, "Non-linear Dynamics of Flexible Multi-Bearing Rotors," *Journal of Sound and Vibration*, Vol. 71, pp. 129–144.

Childs, D. W., 1978, "The Space Shuttle Main Engine High Pressure Fuel Turbopump-Rotordynamic Instability Problem," *ASME Journal of Engineering for Power*, Vol. 100, pp. 48–51.

Clough, R. W., and Wilson, E. L., 1979, "Dynamic Analysis of Large Structural Systems With Local Nonlinearities," *Computer Methods in Applied Mechanics and Engineering*, Vol. 17 18, pp. 107–129.

Davis, L. B., Wolfe, E. A., and Beatty, R. F., 1984, "Housing Flexibility Effects on Rotor Stability," MSFC Advanced High Pressure O_2/H_2 Technology Conference Proceedings, G. Marshall Space Flight Center, Huntsville, Ala.

Hagedorn, P., Schramm, W., 1988, "On the Dynamics of Large Systems With Localized Nonlinearities," ASME JOURNAL OF APPLIED MECHANICS, Vol. 55, pp. 946–951.

Isaacson, E., and Keller, H. B., 1966, *Analysis of Numerical Methods*, John Wiley and Sons, New York.

Kubomura, K., 1985, "Transient Loads Analysis by Dynamic Condensation," ASME JOURNAL OF APPLIED MECHANICS, Vol. 52, pp. 559–564.

Meirovitch, L., 1980, *Computational Methods in Structural Dynamics*, Sijthoff and Noordhoff.

Nelson, H. D., Meacham, W. L., Fleming, D. P., and Kascak, A. F., 1982, "Nonlinear Analysis of Rotor Bearing Systems Using Component Mode Synthesis, ASME Paper No. 82-GT-303.

Noah, S. T., 1986, "Hybrid Methods for Rotordynamic Analysis," Final NASA Report, G. C. Marshall Space Flight Center, Ala., under Contract No. NAS8-36182, Dec. 1986.

Noah, S. T., Chiang, I. F., and Kim, Y. B., 1988, "Dynamic Analysis of Nonlinear Rotor/Housing Systems," MSFC Advanced High Pressure O_2/H_2 Technology Conference Proceedings, G. Marshall Space Flight Center, Huntsville, Ala.

Noah, S. T., Fan, U. J., Choi, Y.-S., and Fox, T., 1986, "Efficient Transient Analysis Methods for the Space Shuttle Main Engine Turbopumps," NASA Conference on Advanced Earth-to-Orbits Propulsion Tech., G. Marshall Space Flight Center, Huntsville, Ala., May 13–15.

Nordmann, R., 1975, "Eigenvalues and Resonance Frequency Forms of Turborotors with Sleeve Bearings Crank Excitation, External, and Internal Damping," Machine Dynamics Group, Technical University Darmstadt, F.R.G.

Rouch, K. E., and Kao, J. S., 1980, "Dynamic Reduction in Rotor Dynamics by the Finite Element Method," ASME JOURNAL OF MECHANICAL DESIGN, Vol. 102, pp. 360–368.

Spanos, P. D., Cao, T. T., Jacobson, C. A., Jr., and Nelson, D. A. R., Jr., 1988, "Decoupled Dynamic Analysis of Combined Systems by Iterative Determination of Interface Accelerations," *Earthquake Engineering and Structural Dynamics*, Vol. 16, pp. 491–500.

Tongue, B. H., and Dowell, E. H., 1983, "Component Mode Analysis of Nonlinear, Nonconservative Systems," ASME JOURNAL OF APPLIED MECHANICS, Vol. 50, pp. 204–209.

Von Pragenau, G. L., 1981, "Large Step Integration for Linear Dynamic Systems," Conference Proc. IEEE Southeastern '81, reprint Apr.

Downloaded 03 May 2010 to 171.66.16.244. Redistribution subject to ASME license or copyright; see http://www.asme.org/terms/Terms_Use.cfm

Classical Vibration Analysis of Axially Moving Continua

J. A. Wickert
Research Assistant,
Assoc. Mem. ASME

C. D. Mote, Jr.
Professor and Chairman,
Fellow ASME

Department of Mechanical Engineering,
University of California,
Berkeley, CA 94720

Axially moving continua, such as high-speed magnetic tapes and band saw blades, experience a Coriolis acceleration component which renders such systems gyroscopic. The equations of motion for the traveling string and the traveling beam, the most common models of axially moving materials, are each cast in a canonical state space form defined by one symmetric and one skew-symmetric differential operator. When an equation of motion is represented in this form, the eigenfunctions are orthogonal with respect to each operator. Following this formulation, a classical vibration theory, comprised of a modal analysis and a Green's function method, is derived for the class of axially moving continua. The analysis is applied to the representative traveling string and beam models, and exact closed-form expressions for their responses to arbitrary excitation and initial conditions result. In addition, the critical transport speed at which divergence instability occurs is determined explicitly from a sufficient condition for positive definiteness of the symmetric operator.

1 Introduction

The class of axially moving continua encompasses such apparently diverse mechanical systems as high-speed magnetic and paper tapes, aerial cable tramways, band saws, pipes that contain flowing fluid, and power transmission chains and belts (Wickert and Mote, 1988; Paidoussis, 1987). Characterization of the vibration and dynamic stability of such systems and prediction of the response to general excitation is requisite for the analysis and optimal design of a broad class of technological devices.

The traveling flexible string and the traveling, tensioned Euler-Bernoulli beam are the most common models of axially moving continua. Previous studies of these second and fourth-order models focus on aspects of free vibration including the nature of wave propagation is moving media (Swope and Ames, 1963) and the effects of axial motion on the frequency spectrum and eigenfunctions (Archibald and Emslie, 1958; Simpson, 1973). The natural frequency of each mode decreases with the transport speed, and at sufficiently high speed, the traveling string and beam each experience divergence instability. A convective acceleration component in the equations of motion results in complex, speed-dependent modes, and the corresponding free motion is of nonconstant phase.

Despite the apparent simplicity of the traveling string and beam models, the response of either model to general excitation and initial conditions cannot be analytically predicted using previous methods for axially moving materials, which date to the nineteenth century (Skutch, 1987). Calculation of the eigenfunctions notwithstanding, orthogonality relations among the eigenfunctions have not been heretofore derived. Accordingly, the generalized coordinates in an eigenfunction expansion remain coupled, and the classical modal analysis and Green's function methods, which are applied to the non-translating string and beam models, are not applicable to axially moving continua. Response predictions are available when the excitation assumes special forms, such as a constant transverse point force (Chonan, 1986) or harmonic support motion (Miranker, 1960), but the understanding of the general response of axially moving materials is limited.

In the present study, the equations of motion for the traveling string and beam models are each cast in a canonical, first-order form that is defined by one symmetric and one skew-symmetric matrix differential operator. When an equation of motion is represented in this form, the eigenfunctions are orthogonal with respect to each operator. Following this formulation, the response of axially moving materials to arbitrary excitation and initial conditions is represented by two closed-form solutions: a modal analysis and a Green's function method. These response predictions are then specialized to the traveling string and beam models, and the associated critical speeds are determined explicitly.

2 Canonical Form of the Equations of Motion

2.1 Second-Order Model. Consider a uniform, flexible, axially moving string of linear density ρ, tension P, and transport speed V that travels between two fixed eyelets which are separated by distance L. The transverse displacement is $U(X,T)$, and the string is excited by the distributed loading $F(X,T)$ as shown in Fig. 1. For $U_X^2 \ll 1$, the transverse velocity of a material particle on the string is $U_T + VU_X$, and the

Contributed by the Applied Mechanics Division of THE AMERICAN SOCIETY OF MECHANICAL ENGINEERS for publication in the JOURNAL OF APPLIED MECHANICS.

Discussion on this paper should be addressed to the Technical Editor, Prof. Leon M. Keer, The Technological Institute, Northwestern University, Evanston, IL 60208, and will be accepted until two months after final publication of the paper itself in the JOURNAL OF APPLIED MECHANICS. Manuscript received by the ASME Applied Mechanics Division, Mar. 10, 1988; final revision, Mar. 23, 1989.

Copyright © 1990 by ASME
Downloaded 03 May 2010 to 171.66.16.244. Redistribution subject to ASME license or copyright; see http://www.asme.org/terms/Terms_Use.cfm

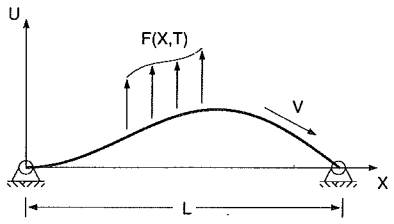


Fig. 1 Schematic of an externally excited, axially moving string. The collection of material particles that constitutes the portion of the string between the eyelets changes with time.

velocity in the axial direction is approximately V. The equation of motion is derived using either Newtonian mechanics (Swope and Ames, 1963) or Hamilton's principle as extended to traveling media (Archibald and Emslie, 1958; Benjamin, 1961), and each technique yields the hyperbolic equation

$$\rho(U_{TT}+2VU_{XT}+V^2U_{XX})-PU_{XX}=F. \tag{1}$$

Measured by a stationary observer, a material particle on the traveling string experience the local, Coriolis, and centripetal acceleration components U_{TT}, $2VU_{XT}$, and V^2U_{XX}, respectively.

The equation of motion is nondimensionalized using the definitions

$$x=X/L \quad u=U/L \quad t=T(P/\rho L^2)^{1/2} \quad f=FL/P$$
$$v=V(\rho/P)^{1/2}. \tag{2}$$

The transport speed parameter v is the ratio of the physical transport speed and the wave speed in the stationary string. With the introduction of the mass, gyral, and second-order stiffness operators,

$$M=I \quad G=2v\frac{\partial}{\partial x} \quad K=-(1-v^2)\frac{\partial^2}{\partial x^2}, \tag{3}$$

where I is the identity operator. Equation (1) is written in the dimensionless symbolic form

$$Mu_{tt}+Gu_t+Ku=f. \tag{4}$$

2.2 Fourth-Order Model. The inhomogeneous equation of transverse motion of a traveling, tensioned Euler-Bernoulli beam is (Mote, 1965)

$$\rho(U_{TT}+2VU_{XT}+V^2U_{XX})-PU_{XX}+EIU_{XXXX}=F. \tag{5}$$

Here, EI is the flexural stiffness, and the remaining terms are as defined in equation (1). Equation (5) is cast in dimensionless form using

$$x=X/L \quad u=U/L \quad t=T(EI/\rho L^4)^{1/2} \quad f=FL^3/EI \tag{6}$$
$$v=V(\rho L^2/EI)^{1/2} \quad \mu^2=PL^2/EI,$$

where the transport speed is nondimensionalized with respect to the speed of a disturbance of wavelength L in a stationary and tensionless beam. The differential operators for the fourth-order problem are identified

$$M=I \quad G=2v\frac{\partial}{\partial x} \quad K=-(\mu^2-v^2)\frac{\partial^2}{\partial x^2}+\frac{\partial^4}{\partial x^4}, \tag{7}$$

and with these definitions, the governing equation for the traveling beam assumes the form (4).

2.3 State Space Representation. The equation of motion (4), which represents each model, is cast in first-order form. With the state and excitation vectors

$$\mathbf{w}(x,t)=\begin{Bmatrix} u_t \\ u \end{Bmatrix} \qquad \mathbf{q}(x,t)=\begin{Bmatrix} f \\ 0 \end{Bmatrix} \tag{8a}$$

and the matrix differential operators

$$\mathbf{A}=\begin{bmatrix} M & 0 \\ 0 & K \end{bmatrix} \qquad \mathbf{B}=\begin{bmatrix} G & K \\ -K & 0 \end{bmatrix}, \tag{8b}$$

equation (4) becomes

$$\mathbf{A}\mathbf{w}_t+\mathbf{B}\mathbf{w}=\mathbf{q}. \tag{8c}$$

Equation (8c) is the canonical form of the equation of motion, and its solution satisfies the initial condition

$$\mathbf{w}(x,t=0)=\mathbf{w}_0=\begin{Bmatrix} b(x) \\ a(x) \end{Bmatrix} \tag{9}$$

and appropriate boundary conditions. For the second-order model, the state vector $\mathbf{w}$ is an element of the function space S containing all complex two-dimensional vectors with components that are of class C^0 and satisfy the fixed-end conditions

$$\mathbf{w}=0 \text{ at } x=0 \text{ and } x=1. \tag{10a}$$

Similarly, for the fourth-order model, the elements of S are of class C^1 and satisfy either

simple supports: $\mathbf{w}=\mathbf{w}_{xx}=0$ at $x=0$ and $x=1$ or

fixed supports: $\mathbf{w}=\mathbf{w}_x=0$ at $x=0$ and $x=1$. (10b)

The inner product of two vectors $\mathbf{w}_1$ and $\mathbf{w}_2$ in S is defined as

$$<\mathbf{w}_1,\mathbf{w}_2>=\int_0^1 \mathbf{w}_1^T\bar{\mathbf{w}}_2\,dx, \tag{11}$$

where the overbar denotes complex conjugation. With respect to this inner product, the operators $\mathbf{A}$ and $\mathbf{B}$ enjoy several properties which are the cornerstones of the subsequent analyses. First, operator $\mathbf{A}$ is symmetric, and $\mathbf{B}$ is skew symmetric; namely,

$$<\mathbf{A}\mathbf{w}_1,\mathbf{w}_2>=<\mathbf{w}_1,\mathbf{A}\mathbf{w}_2>$$
$$<\mathbf{B}\mathbf{w}_1,\mathbf{w}_2>=-<\mathbf{w}_1,\mathbf{B}\mathbf{w}_2>. \tag{12}$$

Dynamic systems described by one symmetric and one skew-symmetric operator are termed gyroscopic, and in particular, axially moving continua are rendered gyroscopic by the operator G which derives from the Coriolis acceleration component. Second, operator $\mathbf{A}$ is positive definite for sufficiently low transport speed. As shown in the Appendix, each of the aforementioned models suffers divergence instability at the critical speed $v=v_c$, and a sufficient condition for positive definiteness of $\mathbf{A}$ is $v<v_c$. For the second-order model, $v_c=1$ is easily shown, and the critical speed for the fourth-order model depends on the end conditions (10b)

$$\text{simple supports:} \quad v_c=\sqrt{\mu^2+\pi^2}$$
$$\text{fixed supports:} \quad v_c=\sqrt{\mu^2+4\pi^2}. \tag{13}$$

For sufficiently high tension, these conditions reduce to $v_c\approx\mu$, a result which is consistent with the criterion for the second-order model. In the sequel, subcritical transport speed is specified.

3 Modal Analysis

With the equations of motion cast in the structured form (8), the vibration and stability of axially moving materials are studied in the context of gyroscopic dynamic systems. Meirovitch (1974; 1975) studied the matrix eigenvalue problem for discrete gyroscopic systems and derived a corresponding modal analysis; a contact transformation in the generalized coordinates and momenta decouples the discrete equations of motion. Subsequently, D'Eleuterio and Hughes (1984; 1986)

Downloaded 03 May 2010 to 171.66.16.244. Redistribution subject to ASME license or copyright; see http://www.asme.org/terms/Terms_Use.cfm

extended the modal analysis to continuous structures with a specified distribution of angular momentum that is independent of the mass distribution.

The general solution to equation (8*c*) is represented as an eigenfunction expansion, and the response to arbitrary excitation and initial conditions is obtained in closed form. The separable solution

$$\mathbf{w}(x,t) = \mathrm{Re}\{\phi(x)e^{\lambda t}\} \tag{14a}$$

leads to the eigenvalue problem

$$\lambda \mathbf{A}\boldsymbol{\phi} + \mathbf{B}\boldsymbol{\phi} = 0, \tag{14b}$$

where λ and $\boldsymbol{\phi} \in S$ are complex. The eigensolutions satisfy several properties (Meirovitch, 1974). First, the eigenvalues are imaginary; namely, $\lambda_n = i\omega_n$ where ω_n is the real oscillation frequency, and $i = \sqrt{-1}$. Second, in light of equations (8*a*) and (14*a*), the complex $\boldsymbol{\phi}_n$ have the structure

$$\phi_n(x) = \boldsymbol{\phi}_n^R(x) + i\boldsymbol{\phi}_n^I(x) \tag{15}$$

$$\boldsymbol{\phi}_n^R(x) = \begin{Bmatrix} -\omega_n \psi_n^I(x) \\ \psi_n^R(x) \end{Bmatrix} \qquad \boldsymbol{\phi}_n^I(x) = \begin{Bmatrix} \omega_n \psi_n^R(x) \\ \psi_n^I(x) \end{Bmatrix}.$$

Here, $\psi_n(x) = \psi_n^R(x) + i\psi_n^I(x)$ is the normalized scalar eigenfunction associated with the displacement field u, and its components ψ_n^R and ψ_n^I are real. Third, the $\boldsymbol{\phi}_n$ satisfy the orthonormality relations

$$\begin{aligned} &<\mathbf{A}\boldsymbol{\phi}_n^R, \boldsymbol{\phi}_m^R> = \delta_{nm} \qquad <\mathbf{A}\boldsymbol{\phi}_n^I, \boldsymbol{\phi}_m^I> = \delta_{nm} \qquad <\mathbf{A}\boldsymbol{\phi}_n^R, \boldsymbol{\phi}_m^I> = 0 \\ &<\mathbf{B}\boldsymbol{\phi}_n^R, \boldsymbol{\phi}_m^R> = 0 \qquad <\mathbf{B}\boldsymbol{\phi}_n^I, \boldsymbol{\phi}_m^I> = 0 \qquad <\mathbf{B}\boldsymbol{\phi}_n^R, \boldsymbol{\phi}_m^I> = \omega_n \delta_{nm}. \end{aligned} \tag{16}$$

Both the amplitude and shape of the complex eigenfunction ψ_n depend on the normalization. Denote the nonnormalize eigenfunction and state vector by $\hat{\psi}_n$ and $\hat{\phi}_n$, respectively, and let $\theta = \alpha + i\beta$ be the normalization constant. The components of $\psi_n = \theta\hat{\psi}_n$ are

$$\psi_n^R = \alpha\hat{\psi}_n^R - \beta\hat{\psi}_n^I \qquad \psi_n^I = \beta\hat{\psi}_n^R + \alpha\hat{\psi}_n^I, \tag{17}$$

and $\boldsymbol{\phi}_n$ is found using equation (15). Imposition of the normalization requirements and use of the identity

$$<\mathbf{A}\hat{\boldsymbol{\phi}}_n^R, \hat{\boldsymbol{\phi}}_n^R> = <\mathbf{A}\hat{\boldsymbol{\phi}}_n^I, \hat{\boldsymbol{\phi}}_n^I> = r^2 \tag{18}$$

lead to the single requirement $|\theta| = \sqrt{\alpha^2 + \beta^2} = 1/r$. Although the modulus of θ is determined, its argument is arbitrary, and the construction of ψ_n^R and ψ_n^I using equation (17) is not unique. For example, both θ and $i\theta$ are admissible normalization constants, but each results in a different realization of the eigenfunction. In the sequel, the constraint $\beta = 0$ is imposed.

Consider the expansion

$$\mathbf{w}(x,t) = \sum_{n=1}^{\infty} \xi_n^R(t)\boldsymbol{\phi}_n^R(x) + \xi_n^I(t)\boldsymbol{\phi}_n^I(x) \tag{19}$$

as the solution of equation (8*c*). The components $\xi_n^R(t)$ and $\xi_n^I(t)$ of the generalized coordinates are real, and it is assumed that the expansion is complete. Substitution into the field equation, satisfaction of the initial condition, and use of the orthonormality conditions yield the modal coordinates (Meirovitch, 1975)

$$\begin{aligned} \xi_n^R(t) &= \int_0^t (f_n^R(s)\cos[\omega_n(t-s)] \\ &+ f_n^I(s)\sin[\omega_n(t-s)])ds + \xi_n^R(0)\cos(\omega_n t) + \xi_n^I(0)\sin(\omega_n t) \\ \xi_n^I(t) &= \int_0^t (f_n^I(s)\cos[\omega_n(t-s)] - f_n^R(s)\sin[\omega_n(t-s)])ds \\ &+ \xi_n^I(0)\cos(\omega_n t) - \xi_n^R(0)\sin(\omega_n t). \end{aligned} \tag{20}$$

The generalized forces are defined

$$\begin{aligned} f_n^R(t) &= <\mathbf{q}, \boldsymbol{\phi}_n^R> = -\omega_n \int_0^1 \psi_n^I(x) f(x,t)dx \\ f_n^I(t) &= <\mathbf{q}, \boldsymbol{\phi}_n^I> = \omega_n \int_0^1 \psi_n^R(x) f(x,t)dx, \end{aligned} \tag{21a}$$

and the initial values of the modal coordinates are

$$\xi_n^R(0) = <\mathbf{A}\mathbf{w}_0, \boldsymbol{\phi}_n^R> \qquad \xi_n^I(0) = <\mathbf{A}\mathbf{w}_0, \boldsymbol{\phi}_n^I>. \tag{21b}$$

Following the definition (8*a*), the field variable expansion becomes

$$u(x,t) = \sum_{n=1}^{\infty} \xi_n^R(t)\psi_n^R(x) + \xi_n^I(t)\psi_n^I(x). \tag{22}$$

The complex eigenfunctions render the response of nonconstant phase, and unlike nongyroscopic linear systems, the material particles comprising axially moving continua do not pass through equilibrium simultaneously.

4 Green's Function Method

For the class of gyroscopic systems (8), an integral representation of the solution to the initial value problem is derived in terms of the scalar Green's function $g(x,\zeta;t-\tau)$. Following Roach (1982), the state vector $\mathbf{g} = \{g_\tau\ g\}^T$ is the solution of the inhomogeneous adjoint problem. Consider the auxiliary field equation $\mathbf{A}\mathbf{w}_\tau + \mathbf{B}\mathbf{w} = \mathbf{q}$ which is defined over $0 < \xi < 1$ and $0 < \tau < t$ for $\mathbf{w} = \{u_\tau(\zeta,\tau)\ u(\zeta,\tau)\}^T$ and $\mathbf{q} = \{f(\zeta,\tau)\ 0\}^T$. Here, $\mathbf{A}$ and $\mathbf{B}$ are differential operators with respect to the spatial variable ζ and have the structure as in equation (8*b*). The inner product of the auxiliary equation with $\mathbf{g}$ over the product domain of ζ and τ is

$$\int_0^t <\mathbf{g}, \mathbf{A}\mathbf{w}_\tau> + <\mathbf{g}, \mathbf{B}\mathbf{w}> d\tau = \int_0^t <\mathbf{g}, \mathbf{q}> d\tau. \tag{23}$$

Integration by parts and use of the operator symmetry properties yield

$$\int_0^t <\mathbf{A}\mathbf{g}_\tau + \mathbf{B}\mathbf{g}, \mathbf{w}> d\tau = -\int_0^t <\mathbf{g}, \mathbf{q}> d\tau + <\mathbf{A}\mathbf{g}, \mathbf{w}>|_{\tau=0}^{\tau=t}. \tag{24}$$

Accordingly, the state vector of the Green's function satisfies

$$\mathbf{A}\mathbf{g}_\tau + \mathbf{B}\mathbf{g} = \begin{Bmatrix} \delta(\zeta - x)\delta(\tau - t) \\ 0 \end{Bmatrix}, \tag{25}$$

where $\delta(\bullet)$ is the Dirac function, $\mathbf{g}(x,\zeta;0) = 0$, and $\mathbf{g}$ is subject to the same homogeneous boundary conditions as $\mathbf{w}$. Following equation (4), the identity $g_\tau = -g_t$ and the initial condition, equation (24) defines the inverse integral operator for gyroscopic systems, including axially moving continua. The corresponding representation of the solution is

$$\begin{aligned} u(x,t) &= \int_0^1 b(\zeta)Mg(x,\zeta;t) + a(\zeta)(Mg_t(x,\zeta;t) - Gg(x,\zeta;t))d\zeta \\ &+ \int_0^t \int_0^1 g(x,\zeta;t-\tau)f(\zeta,\tau)d\zeta d\tau, \end{aligned} \tag{26a}$$

where M and G are the differential operators with respect of ζ

Downloaded 03 May 2010 to 171.66.16.244. Redistribution subject to ASME license or copyright; see http://www.asme.org/terms/Terms_Use.cfm

contained in **A** and **B**. The Green's function is expressed formally as the bilinear series

$$g(x,\zeta;t-\tau)=H(t-\tau)\sum_{n=1}^{\infty}\omega_n(\sin[\omega_n(t-\tau)](\psi_n^R(\zeta)\psi_n^R(x)+\psi_n^I(\zeta)\psi_n^I(x))-\cos[\omega_n(t-\tau)](\psi_n^I(\zeta)\psi_n^R(x)-\psi_n^R(\zeta)\psi_n^I(x))), \tag{26b}$$

where $H(t-\tau)$ is the Heaviside function.

5 Discussion and Application

5.1 Second-Order Model. The modal analysis is specialized to the second-order model with operators (3) and boundary conditions (10*a*). The natural frequency of the *n*th mode is

$$\omega_n=n\pi(1-v^2), \tag{27a}$$

and the components of the orthonormal eigenfunctions are

$$\psi_n^R(x)=\frac{1}{n\pi}\sqrt{\frac{2}{1-v^2}}\sin(n\pi x)\cos(n\pi vx)$$

$$\psi_n^I(x)=\frac{1}{n\pi}\sqrt{\frac{2}{1-v^2}}\sin(n\pi x)\sin(n\pi vx). \tag{27b}$$

At the critical transport speed $v_c=1$, V equals the transverse wave speed in the stationary string, and the frequency of each mode vanishes. Figure 2 illustrates the first three modes at $v=1/2$. Although the nodal points are the same as those of the stationary string eigenfunctions, axial motion significantly distorts the shapes. The components in equation (27*b*) can be combined in accordance with equation (17) to form equivalent orthonormal eigenfunctions.

Following equation (22), the displacement field is

$$u(x,t)=\sum_{n=1}^{\infty}\frac{1}{n\pi}\sqrt{\frac{2}{1-v^2}}(\xi_n^R(t)\sin(n\pi x)\cos(n\pi vx)+\xi_n^I(t)\sin(n\pi x)\sin(n\pi vx)), \tag{28}$$

and the generalized coordinates are calculated from equation (20) using

$$f_n^R(t)=-\sqrt{2(1-v^2)}\int_0^1 f(x,t)\sin(n\pi x)\sin(n\pi vx)dx$$

$$f_n^I(t)=\sqrt{2(1-v^2)}\int_0^1 f(x,t)\sin(n\pi x)\cos(n\pi vx)dx \tag{29a}$$

$$\xi_n{}^R(0)=n\pi\sqrt{2(1-v^2)}\int_0^1 a(x)((1+v^2)\sin(n\propto\pi x)\cos(n\pi vx)+2v\cos(n\pi x)\sin(n\pi vx))dx-\sqrt{2(1-v^2)}\int_0^1 b(x)\sin(n\pi x)\sin(n\pi vx)dx \tag{29b}$$

$$\xi_n^I(0)=n\pi\sqrt{2(1-v^2)}\int_0^1 a(x)((1+v^2)\sin(n\pi x)\sin(n\pi vx)-2v\cos(n\pi x)\cos(n\pi vx))dx+\sqrt{2(1-v^2)}\int_0^1 b(x)\sin(n\pi x)\cos(n\pi vx)dx.$$

The Green's function and the integral representation of u are obtained in closed form. Specialization of equation (26*a*) gives the general response of an axially moving string

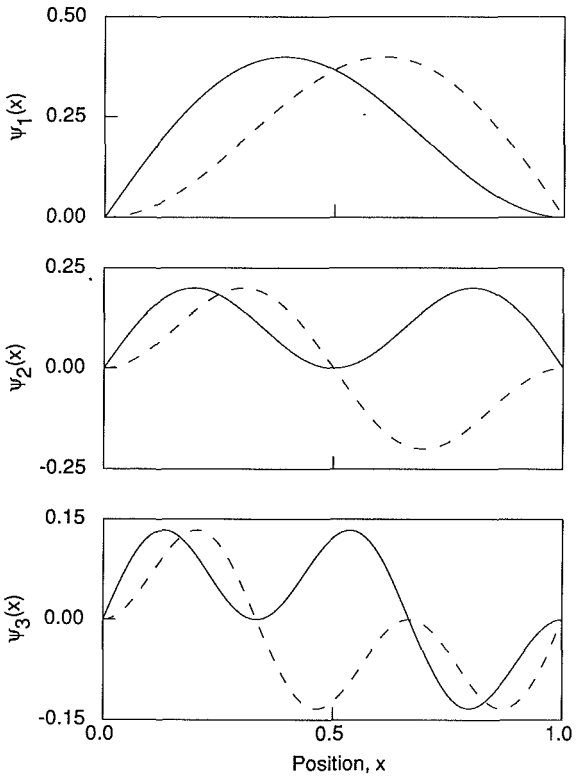


Fig. 2 First three complex, orthonormal eigenfunctions of an axially moving string at $v=1/2$: real component (solid), imaginary component (dashed), $\omega_1=2.356$, $\omega_2=4.712$, $\omega_3=7.069$. The nodal points of a traveling string are the same as those of a stationary string.

$$u(x,t)=\int_0^1 b(\zeta)g(x,\zeta;t)+a(\zeta)(g_t(x,\zeta;t)-2vg_\zeta(x,\zeta;t))d\zeta+\int_0^t\int_0^1 g(x,\zeta;t-\tau)f(\zeta,\tau)d\zeta d\tau, \tag{30a}$$

where the Green's function is given by the pointwise-convergent series

$$g(x,\zeta;t-\tau)=H(t-\tau)\sum_{n=1}^{\infty}\frac{2}{n\pi}\sin[n\pi(1-v^2)(t-\tau)+n\pi v(x-\zeta)]\sin(n\pi x)\sin(n\pi\zeta). \tag{30b}$$

For illustration, the solution is applied to a simple model of a monocable aerial tramway that transports a single inertial payload (Schneigert, 1966). If the transverse acceleration of the cable is sufficiently small, the interaction force between the payload and cable is approximately equal to the payload weight (Fryba, 1972). Accordingly, the tramway system is modeled as a traveling string that is excited by $f(x,t)=-p\delta(x-vt)$. The response of the moving string/moving force system is found using either the modal analysis or the Green's function method. With homogeneous initial conditions, the response becomes

$$u(x,t)=\sum_{n=1}^{\infty}\frac{p}{n^2\pi^2(1-v^2)}((1-v)\sin[n\pi v(x-(1+v)t)]-(1+v)\sin[n\pi v(x+(1-v)t)]+2v\sin[n\pi(vx+(1-v^2)t)])\sin(n\pi x) \tag{31}$$

over one transit period of the payload, namely $0\le t\le 1/v$. Figure 3 illustrates the response at speed $v=1/2$, and three traveling-wave components with different phase speeds are

Downloaded 03 May 2010 to 171.66.16.244. Redistribution subject to ASME license or copyright; see http://www.asme.org/terms/Terms_Use.cfm

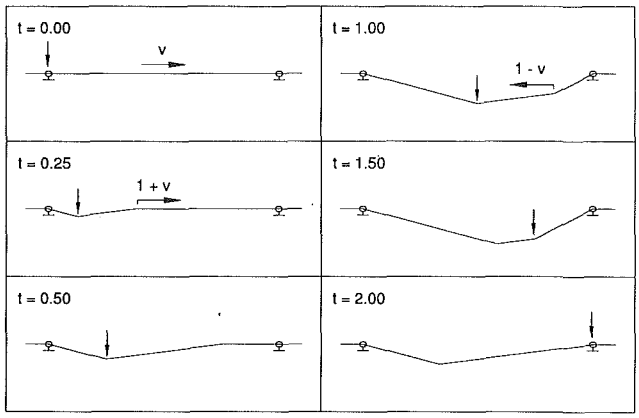


Fig. 3 Exact response (31) of a moving string/moving force system at $\nu = 1/2$. The force and associated slope discontinuity travel downstream at speed ν, and at time $t = 1/(1+\nu)$, the forward wave with speed $1+\nu$ is reflected from the right support with phase speed $1-\nu$.

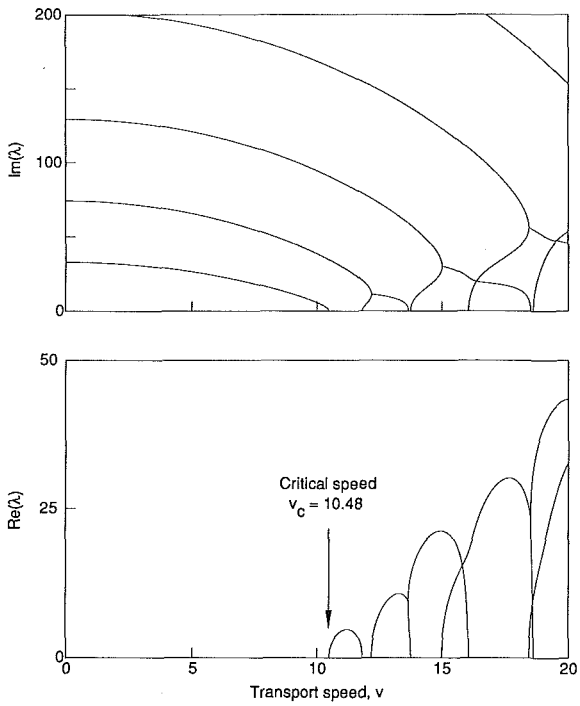


Fig. 4 Frequency spectrum of a simply-supported traveling beam with $\mu^2 = 100$. First mode divergence instability occurs at the critical speed $\nu_c = 10.48$. All eigenvalues are imaginary for $\nu < \nu_c$, and both divergence and flutter instabilities occur at supercritical speeds.

identified. The point force and associated slope discontinuity travel downstream at the transport speed ν. A forward wave with speed $1+\nu$ propagates downstream ahead of the force and is reflected with phase speed $1-\nu$ from the right support.

5.2 Fourth-Order Model. Solutions of the eigenvalue problem for the fourth-order model are found numerically through solution of a complex transcendental equation. Each eigenfunction is a linear combination of terms $ce^{i\gamma x}$, and nontrivial solutions of the homogeneous field equation satisfy the dispersion relation

$$\gamma^4 + (\mu^2 - \nu^2)\gamma^2 + 2i\nu\lambda\gamma + \lambda^2 = 0. \tag{32}$$

Satisfaction of the boundary conditions (10*b*) requires that the four roots γ_k of equation (32) are related by the auxiliary condition

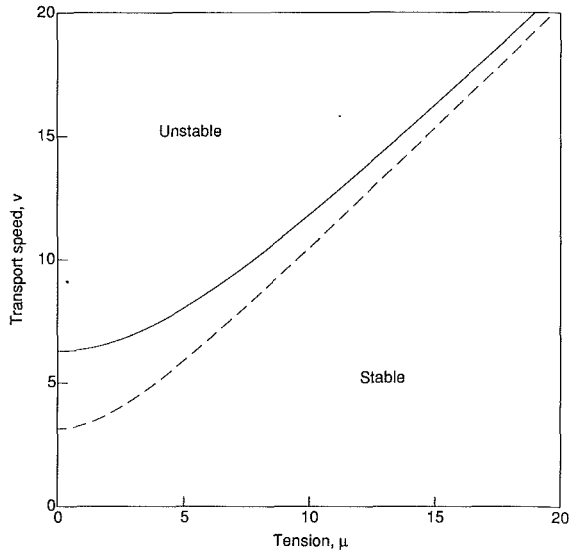


Fig. 5 Sufficient conditions (13) for stability of a tensioned, axially moving beam: fixed supports (solid), simple supports (dashed). The criteria divide the parameter plane into guaranteed stable and possibly unstable regions, and first-mode divergence instability occurs on the demarcation line.

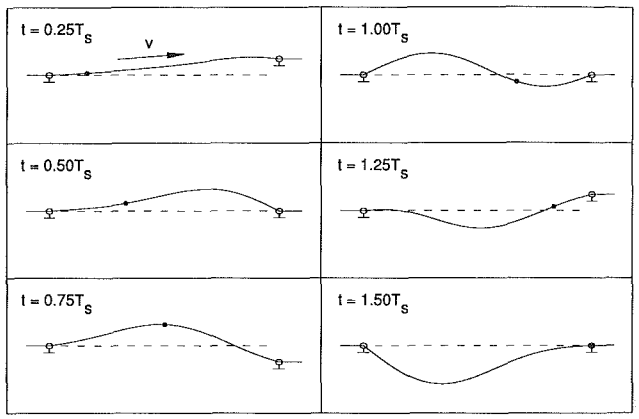


Fig. 6 Transient response of a simply-supported traveling beam with rest initial conditions and harmonic support motion: $\nu = 5.0 < \nu_c$, $\mu^2 = 100$, $e_0 = 0.1$, and $\Omega_s = 47.1$. The response is shown over 1.5 periods T_s of the support motion. A specific material particle on the beam is highlighted to aid in the description of the axial motion.

$$(\Gamma_1 - \Gamma_2)(\Gamma_4 - \Gamma_3)(e^{i(\gamma_1+\gamma_2)} + e^{i(\gamma_3+\gamma_4)})$$
$$+ (\Gamma_2 - \Gamma_3)(\Gamma_4 - \Gamma_1)(e^{i(\gamma_2+\gamma_3)} + e^{i(\gamma_1+\gamma_4)})$$
$$+ (\Gamma_1 - \Gamma_3)(\Gamma_2 - \Gamma_4)(e^{i(\gamma_1+\gamma_3)} + e^{i(\gamma_2+\gamma_4)}) = 0, \tag{33}$$

where $\Gamma_k = \gamma_k^2$ for simple supports (Mote, 1965) or $\Gamma_k = \gamma_k$ for fixed supports (Simpson, 1973). Characteristic values of λ which satisfy both equations (32) and (33) are found using an available routine for nonlinear equations. The eigenfunctions are normalized and become

$$\psi(x) = \sum_{k=1}^{4} c_k e^{i\gamma_k x}.$$

With the spectrum and complex modes so determined, the general response is calculated subsequently using either the formal modal analysis or the inverse operator.

In Fig. 4, the frequency spectrum of a simply-supported, axially moving beam with tension $\mu^2 = 100$ is shown. As

Downloaded 03 May 2010 to 171.66.16.244. Redistribution subject to ASME license or copyright; see http://www.asme.org/terms/Terms_Use.cfm

calculated from equation (13), the first mode frequency vanishes at the critical speed $v_c = 10.48$. In the speed regimes $v < v_c$ and $11.81 < v < 12.18$, all eigenvalues are imaginary, and for supercritical transport speed, both flutter and divergence instabilities exist. In Fig. 5, the positive definiteness criteria for simple and fixed supports define the loci in the $\mu - v$ parameter space at which first mode divergence instability occurs. The loci divide the space into guaranteed stable and possibly unstable regions.

The solution techniques are illustrated by application to an axially moving beam that is excited by prescribed transverse support motion. The traveling beam satisfies the homogeneous equation of motion (4) with operators (7), rest initial conditions, and the inhomogeneous boundary conditions $u(x=0,t)=0$, $u(x=1,t)=e(t)$, and $u_{xx}=0$ at $x=0$ and 1. The rigid body rotation of the beam is suppressed by the transformation

$$\tilde{u}(x,t) = u(x,t) - xe(t). \tag{34}$$

Accordingly, $\tilde{u}$ satisfies homogeneous, simple-support end conditions and equation (4) with $f(x,t) = -xe_{tt} - 2ve_t$. The solution is found using the Green's function method, and Fig. 6 illustrates the transient response u for the case $e(t) = e_0 \sin(\Omega_s t)$.

6 Conclusion

The equations of motion of continuous systems other than axially moving continua, such as rotating plates and shafts, can be transformed into the canonical form (8) with one symmetric and one skew-symmetric differential operator. For this class of systems, the response to arbitrary excitation and initial conditions is represented as a superposition of orthonormal eigenfunctions and as a convolution with the Green's function. The expressions for the modal response, Green's function, and inverse integral operator reduce to the classical results for nongyroscopic continua when the operator G is deleted.

Axially moving continua are inherently gyroscopic. With the equations of motion cast in first-order form, the vibration and stability of axially moving materials are readily studied within the broader framework of gyroscopic systems. The orthonormality relations among the complex eigenfunctions are the key to the utility of this formulation. Although the eigenfunctions of axially moving continua were calculated in previous studies, their orthogonality properties were not recognized, and accordingly, decoupling of the generalized coordinates was not achieved.

The contribution of nonlinear terms in the equations of motion of axially moving continua increases with the transport speed (Mote, 1966; Thurman and Mote, 1969). In many applications, the response at speeds near or above v_c is of interest, but linear analyses cannot accurately predict response in this high speed regime. Analytical studies of nonlinear models can use to advantage the present modal representation of the linear response as the fundamental solution in perturbation analyses.

The present results can also improve the accuracy of discretized models of complicated structures such as traveling elastic cables and curved, elastically restrained pipes that convey fluid. In global discretizations of these systems, the eigenfunctions of the stationary string or beam are typically chosen as expansion functions. At high transport speed, these constant phase solutions are poor approximations to the actual motion of the traveling system, and many expansion terms are required for suitable accuracy. Because the orthonormal eigenfunctions of the traveling string and beam models adapt with increasing transport speed, they are expected to constitute superior bases of admissible functions.

Acknowledgment

This material is based upon work supported by the National Science Foundation and partially by the University of California Forest Products Laboratory and the authors' group of industrial sponsors.

References

Archibald, F. R., and Emslie, A. G., 1958, "The Vibration of a String Having a Uniform Motion Along Its Length," ASME JOURNAL OF APPLIED MECHANICS, Vol. 25, pp. 347–348.

Benjamin, T. B., 1961, "Dynamics of a System of Articulated Pipes Conveying Fluids: Theory," *Proc. Roy. Soc. London*, Vol. 261A, pp. 457–486.

Chonan, S., 1986, "Steady State Response of an Axially Moving Strip Subjected to a Stationary Lateral Load," *J. Sound Vib.*, Vol. 107, pp. 155–165.

D'Eleuterio, G. M., and Hughes, P. C., 1984, "Dynamics of Gyroelastic Continua," ASME JOURNAL OF APPLIED MECHANICS, Vol. 51, pp. 415–422.

Dym, C. L., 1974, *Stability Theory and Its Applications to Structural Mechanics*, Noordhoff International, Leyden.

Fryba, L., 1972, *Vibration of Solids and Structures Under Moving Loads*, Noordhoff International, Groningen.

Hardy, G. H., Littlewood, J. E., and Polya, G., 1952, *Inequalities*, Cambridge University Press.

Hughes, P. C., and D'Eleuterio, G. M., 1986, "Modal Parameter Analysis of Gyroelastic Continua," ASME JOURNAL OF APPLIED MECHANICS, Vol. 53, pp. 919–924.

Meirovitch, L., 1974, "A New Method of Solution of the Eigenvalue Problem for Gyroscopic Systems," *AIAA J.*, Vol. 12, pp. 1337–1342.

Meirovitch, L., 1975, "A Modal Analysis for the Response of Linear Gyroscopic Systems," ASME JOURNAL OF APPLIED MECHANICS, Vol. 42, No. 2, pp. 446–450.

Miranker, W. L., 1960, "The Wave Equation in a Medium in Motion," *IBM J. R&D*, Vol. 4, pp. 36–42.

Mote, Jr., C. D., 1965, "A Study of Band Saw Vibrations," *J. Franklin Inst.*, Vol. 279, pp. 430–444.

Mote, Jr., C. D., 1966, "On the Nonlinear Oscillation of an Axially Moving String," ASME JOURNAL OF APPLIED MECHANICS, Vol. 33, pp. 463–464.

Paidoussis, M. P., 1987, "Flow-Induced Instabilities of Cylindrical Structures," *Appl. Mech. Rev.*, Vol. 40, ASME, New York, pp. 163–175.

Roach, G. F., 1982, *Green's Functions*, Cambridge University Press.

Schneigert, Z., 1966, *Aerial Tramways and Funicular Railways*, Pergamon Press.

Simpson, A., 1973, "Transverse Modes and Frequencies of Beams Translating Between Fixed End Supports," *J. Mech. Eng. Sci.*, Vol. 15, pp. 159–164.

Skutch, R., 1897, "Uber die Bewegung Eines Gespannten Fadens, Weicher Gezwungen ist, Durch Zwei Feste Punkte, mit Einer Constanten Geschwindigkeit zu gehen, und Zwischen denselben in Transversal-Schwingungen von gerlinger Amplitude Versetzt Wird," *Annalen der Physik und Chemie*, Vol. 61, pp. 190–195.

Swope, R. D., and Ames, W. F., 1963, "Vibrations of a Moving Threadline," *J. Franklin Inst.*, Vol. 275, pp. 36–55.

Thurman, A. L., and Mote, Jr., C. D., 1969, "Free, Periodic, Nonlinear Oscillation of an Axially Moving String," ASME JOURNAL OF APPLIED MECHANICS, Vol. 36, pp. 83–91.

Wickert, J. A., and Mote, Jr., C. D., 1988, "Current Research on the Vibration and Stability of Axially Moving Materials," *Shock Vib. Dig.*, Vol. 20, pp. 3–13.

APPENDIX

Derivation of the Critical Transport Speed

1 Second-Order Model. In equation (27*a*), each natural frequency of a traveling string vanishes when $v = 1$. In addition, when $v < 1$, both the stiffness operator and **A** are positive definite. Accordingly, the critical speed is $v_c = 1$.

2 Fourth-Order Model. When the response of an axially moving beam is independent of time, u satisfies

$$u_{xxxx} + (v^2 - \mu^2)u_{xx} = 0 \tag{A1}$$

and appropriate boundary conditions. Nontrivial solutions exist when $v^2 - \mu^2 = (n\pi)^2$ for simple supports or when $v^2 - \mu^2 = (2n\pi)^2$ for fixed supports; here n is an integer. The critical speed is the lowest speed at which such divergent solu-

Downloaded 03 May 2010 to 171.66.16.244. Redistribution subject to ASME license or copyright; see http://www.asme.org/terms/Terms_Use.cfm

tions exist, and the values with $n=1$ for each set of end conditions are given in equation (13).

Operator K in equation (7) is positive definite if

$$<u,Ku> = \int_0^1 (\mu^2 - \nu^2)\,|u_x|^2 + |u_{xx}|^2 dx > 0 \qquad \text{(A2)}$$

for nonzero admissible u. The lower bound for this functional depends on the boundary conditions and is derived using appropriate variational inequalities (Hardy et al., 1952; Dym, 1974):

simple supports: $<u,Ku> \geq \pi^2 \int_0^1 (\mu^2 - \nu^2 + \pi^2)\,|u|^2 dx$ and

fixed supports: $<u,Ku> \geq \pi^2 \int_0^1 (\mu^2 - \nu^2 + 4\pi^2)\,|u|^2 dx.$

(A3)

The strict equality holds when u is the eigenfuction of equation (A1) corresponding to $n=1$. Therefore, with the critical speed of a traveling beam so defined, operator **A** is positive definite for $\nu < \nu_c$.

Downloaded 03 May 2010 to 171.66.16.244. Redistribution subject to ASME license or copyright; see http://www.asme.org/terms/Terms_Use.cfm

Equations of Motion for Structures in Terms of Quasi-Coordinates

Roger D. Quinn
General Motors Assistant Professor,
Mechanical and Aerospace Engineering,
Case Western Reserve University,
Cleveland, Ohio 44106
Assoc. Mem. ASME

A form of Lagrange's equations in terms of quasi-coordinates (Boltzmann/Hamel equations) is presented. Identities are introduced which permit a straightforward method for formulating the equations of motion for structures for which the kinetic and potential energies are explicit functions of angular orientation. This formulation may be utilized once the energies are expressed in matrix form as functions of angular velocities and coordinate transformation matrices. This method is particularly useful for a large class of problems in the dynamics of structures including spacecraft, robots, ground vehicles, and aircraft.

1 Introduction

The purpose of this paper is to present a form of Lagrange's equations in terms of quasi-coordinates (Boltzmann/Hamel equations). This form is specific to a large class of problems in the dynamics of structures including spacecraft, robots, ground vehicles, and aircraft where the angular velocities of the structure can be considered to be time derivatives of quasi-coordinates. Identities are introduced which permit a straightforward method of formulating the equations of motion when the kinetic and potential energies are explicit functions of angular orientation. The formulation may be utilized once the kinetic and potential energies are expressed in matrix form as functions of angular velocities and coordinate transformation matrices.

The concept of quasi-coordinates is not new. According to Whittaker (1944) and Neimark and Fufaev (1967), Lagrange and Euler used quasi-coordinates to study rigid body motion and the so-called Lagrange's equation for quasi-coordinates were developed by Boltzmann and Hamel at the beginning of the twentieth century. Hence, some dynamicists choose to call this Lagrangian formalism the Boltmann/Hamel equations. Advanced texts in dynamics such as those by Whittaker (1944) and Meirovitch (1970) include a section on the subject; and this method of equation development has been recently used by Passeron et al. (1986), Huston and Passerello (1980), and Oz et al. (1980). However, the treatment in dynamics texts is usually of a general nature and, as such, a simplification which enhances the utility of the method does not appear in the literature.

Lagrange's equations are popular among dynamicists because they provide (*i*) a straightforward and orderly method which produces (*ii*) form-invariant equations of motion in which (*iii*) holonomic constraint forces can be eliminated, included or retrieved, as desired, and (*iv*) natural symmetry is preserved. According to Neimark and Fufaev (1967), Lagrange' equations for quasi-coordinates were developed as a form which was uniformly valid for all dynamic systems with or without constraints for true or quasi-coordinates. In practical terms, Lagrange's equations for quasi-coordinates permit a most efficient formulation of the equations of motion of some systems. Perhaps the clearest (and earliest) example is that of a structure undergoing finite rotations in three-dimensional space. If true, generalized coordinates are chosen to represent these rotations; the derivation of the equations of motion using Lagrange's equations becomes quite tedious. In the quasi-coordinate formulation, the angular velocity vector components are the time derivatives of a set of quasi-coordinates rather than true coordinates; these quasi-coordinates are defined only in terms of their differentials. This approach is based on the observation that the kinetic energy of a body can be represented in its most compact form in terms of these angular velocity components or quasi-velocities.

It is important to note that the validity of the equations of motion of a dynamic system depends on the system model used in their development, not on the particular method of formulation, as there are many theoretically equivalent methods (all based on Lagrange's principle of virtual work) as discussed by Likins (1974, 1975). However, the form of the resulting equations may be different and considerable mathematical manipulations may be necessary for comparisons. The best method of equation of motion development for a particular dynamic system produces the simplest and most useful (e.g., symmetry preservation) form of the equations in an orderly fashion. It is for this reason of formulation efficiency that the Boltzmann/Hamel equations have been examined.

General forms of Lagrange's equations in quasi-coordinate form appear ungainly. It is when special cases are examined that these equations appear most promising. An important special case is that mentioned earlier where a structure undergoes finite rotations and the kinetic and potential energies are not functions of the angular orientation. The purpose of this paper is to present simplifying identities which

Contributed by the Applied Mechanics Division of THE AMERICAN SOCIETY OF MECHANICAL ENGINEERS for publication in the JOURNAL OF APPLIED MECHANICS.

Discussion on this paper should be addressed to the Technical Editor, Leon M. Keer, The Technological Institute, Northwestern University, Evanston, IL 60208, and will be accepted until two months after final publication of the paper itself in the JOURNAL OF APPLIED MECHANICS. Manuscript received by the ASME Applied Mechanics Division, September 12, 1988; final revision, April 30, 1989.

Copyright © 1990 by ASME
Downloaded 03 May 2010 to 171.66.16.244. Redistribution subject to ASME license or copyright; see http://www.asme.org/terms/Terms_Use.cfm

enhance the usefulness of this approach in cases where the energies are explicit functions of the angular orientation.

In the kinematic analysis of a structure, it is often convenient to express different velocity and position vectors in different reference frames rather than all in the same frame. Hence, when the energies are expressed in matrix form, coordinate transformation matrices must be introduced. These coordinate transformation matrices and, hence, the energies are functions of the relative angular orientation of the reference frames. For this reason, a quasi-coordinate form of Lagrange's equations which can easily account for terms involving angular orientation is valuable.

This formulation of Lagrange's equations for quasi-coordinates is clearly useful for the dynamic analysis of robots, spacecraft, ground vehicles, and aircraft. The equations governing the rotational motion of a maneuvering flexible spacecraft are developed using this approach. The purpose of this example is to demonstrate this method of dynamic analysis for a problem of current interest, the solution of which has been published previously, for comparison.

2 General Form of Lagrange's Equations for Quasi-Coordinates

Lagrange's equations of motion for holonomic systems in terms of true generalized coordinates can be expressed in the matrix form

$$\frac{d}{dt}\left(\frac{\partial T}{\partial \dot{\mathbf{q}}}\right)-\frac{\partial T}{\partial \mathbf{q}}+\frac{\partial V}{\partial \mathbf{q}}=\mathbf{Q} \tag{1}$$

where $\mathbf{q}$ is a set of n true independent generalized coordinates, T and V are the kinetic and potential energies where $T=T(\mathbf{q}, \dot{\mathbf{q}})$, $V=V(\mathbf{q})$, and $\mathbf{Q}$ is a set of generalized forces which are defined in terms of the virtual work expression,

$$\delta W=\mathbf{Q}^T\delta\mathbf{q}. \tag{2}$$

Lagrange's equations in the form of equation (1) provide a straightforward method of deriving reactionless equations of motion for dynamic systems. However, when a structure is free to undergo finite rotations, derivation of the equations governing the rigid-body orientation in this manner can become tedious. For this reason other forms of Lagrange's equations have been developed.

The most compact form of the kinetic energy of a structure undergoing finite rotations is expressed in terms of the inertial angular velocity vector. Hence, we might conclude that the most efficient derivation of the equations of motion must also be in terms of these angular velocities. For this reason a concept was developed where the angular velocity vector is considered to be the time derivative of so-called quasi-coordinates, which are of themselves undefined.

That part of equation (1) which governs the orientation of a structure can be expressed as

$$\frac{d}{dt}\left(\frac{\partial T}{\partial \dot{\boldsymbol{\alpha}}}\right)-\frac{\partial T}{\partial \boldsymbol{\alpha}}+\frac{\partial V}{\partial \boldsymbol{\alpha}}=\mathbf{Q}_\alpha \tag{3}$$

where $\boldsymbol{\alpha}$ is a set of three true coordinates such as Euler angles, and $\mathbf{Q}_\alpha$ is a set of corresponding moments. The angular velocity vector can be expressed as a function of the true coordinates and their time derivatives, or in matrix form

$$\omega=D(\boldsymbol{\alpha})\dot{\boldsymbol{\alpha}}, \tag{4}$$

where $D(\boldsymbol{\alpha})$ is a 3×3 matrix which is a nonlinear function of $\boldsymbol{\alpha}$. The kinetic energy can then be expressed as an explicit function of ω and $\boldsymbol{\alpha}$, or $\bar{T}(\omega, \boldsymbol{\alpha})$. The introduction of the inverse of equation (4) into equation (3) permits Lagrange's equations to be represented in terms of ω. In this manner Lagrange's equations of motion for rigid body rotations can be expressed as

$$D^T\frac{d}{dt}\left(\frac{\partial \bar{T}}{\partial \omega}\right)+\dot{D}^T\left(\frac{\partial \bar{T}}{\partial \omega}\right)-\omega^TD^{-T}\frac{\partial D^T}{\partial \boldsymbol{\alpha}}\frac{\partial \bar{T}}{\partial \omega}-\frac{\partial \bar{T}}{\partial \boldsymbol{\alpha}}+\frac{\partial V}{\partial \boldsymbol{\alpha}}=\mathbf{Q}_\alpha \tag{5}$$

where the following matrix notation has been used:

$$\omega^TD^{-T}\frac{\partial D^T}{\partial \boldsymbol{\alpha}}=\left[\omega^TD^{-T}\left[\frac{\partial D^T}{\partial \alpha_1}\right]\ \omega^TD^{-T}\left[\frac{\partial D^T}{\partial \alpha_2}\right]\omega^TD^{-T}\left[\frac{\partial D^T}{\partial \alpha_3}\right]\right]^T \tag{6}$$

and $D^{-T}=(D^T)^{-1}$.

Premultiplying equation (5) by D^{-T}, Lagrange's equations for quasi-coordinates can be expressed as

$$\frac{d}{dt}\left(\frac{\partial \bar{T}}{\partial \omega}\right)+D^{-T}\left[\dot{D}^T-\omega^TD^{-T}\frac{D^T}{\partial \boldsymbol{\alpha}}\right]\frac{\partial \bar{T}}{\partial \omega}+D^{-T}\left(\frac{\partial V}{\partial \boldsymbol{\alpha}}-\frac{\partial \bar{T}}{\partial \boldsymbol{\alpha}}\right)=D^{-T}\mathbf{Q}_\alpha. \tag{7}$$

This form of Lagrange's equations appears in Whittaker (1944) (in indicial notation), Meirovitch (1970), and Likins (1975). Although, in the development of equation (7), rotating structures have been discussed, the resulting equations are of general utility in that the symbols $\boldsymbol{\alpha}$ and ω could take other meanings. Equation (7) is actually more complex than equation (3) and, in practice, can be rather cumbersome to apply. Fortunately, for the class of problems considered in this paper, equation (7) can be simplified greatly.

Rotating Structures

In the case of structures undergoing finite rotations in three-dimensional space, the angular velocites can be further related to the D matrix to simplify equation (7).

Let the matrix $C(\boldsymbol{\alpha})$ denote the orthogonal rotational transformation of a structure from the inertial reference frame to a body-fixed reference frame. The time rate of change of the C matrix can be expressed as

$$\dot{C}=\tilde{\omega}C \tag{8a}$$

where $\tilde{\omega}$ is a skew symmetric matrix defined as

$$\tilde{\omega}=\begin{bmatrix}0 & \omega_z & -\omega_y\\ -\omega_z & 0 & \omega_x\\ \omega_y & -\omega_x & 0\end{bmatrix}. \tag{8b}$$

Solving equation (8a) for $\tilde{\omega}$, we have

$$\tilde{\omega}=\dot{C}C^T=\left[\frac{\partial C}{\partial \boldsymbol{\alpha}}\dot{\boldsymbol{\alpha}}\right]C^T \tag{9a}$$

where

$$\left[\frac{\partial C}{\partial \boldsymbol{\alpha}}\dot{\boldsymbol{\alpha}}\right]=\left[\sum_{i=1}^{3}\frac{\partial C}{\partial \alpha_i}\dot{\alpha}_i\right]. \tag{9b}$$

The introduction of equation (4) into equation (9a) produces an explicit relationship between the matrices C and D. This permits the proof of the following identity, which is implicit in Meirovitch (1970):

$$\tilde{\omega}^T=D^{-T}\left[\dot{D}^T-\omega^TD^{-T}\frac{\partial D^T}{\partial \boldsymbol{\alpha}}\right]. \tag{10}$$

Introducing equation (10) into equation (7), Lagrange's equations for quasi-coordinates take the form

$$\frac{d}{dt}\left(\frac{\partial \bar{T}}{\partial \omega}\right)+\tilde{\omega}^T\frac{\partial \bar{T}}{\partial \omega}+D^{-T}\left(\frac{\partial V}{\partial \boldsymbol{\alpha}}-\frac{\partial \bar{T}}{\partial \boldsymbol{\alpha}}\right)=\mathbf{M} \tag{11}$$

Downloaded 03 May 2010 to 171.66.16.244. Redistribution subject to ASME license or copyright; see http://www.asme.org/terms/Terms_Use.cfm

where

$$\mathbf{M} = D^{-T}\mathbf{Q}_\alpha \tag{12a}$$

is the moment which can be defined in terms of virtual work as

$$\delta W = \mathbf{M}^T \delta\beta \tag{12b}$$

where β is the set of quasi-coordinates which are defined in differential form as $\omega = d\beta/dt$. In the literature, attention is focused on cases where $\bar{T}$ and V are not functions of the orientation α so that the last term on the left side of equation (11) is null. In this case, the result is the familiar set of equations that are often derived from angular momentum principles. On the other hand, if the last term is not null, the utilization of equation (11) remains rather cumbersome.

In general, the potential and kinetic energies are functions of the angular orientation of the structure. In matrix form, $\bar{T}$ and V contain rotational transformation matrices which depend explicitly on angular orientation. A term of the kinetic energy might take the matrix form

$$\bar{T}^* = \mathbf{a}^T C \mathbf{b} \tag{13}$$

where **a** and **b** are vectors represented in the body-fixed and inertial reference frames, respectively. In this case, the last term on the left side of equation (11) involving $\bar{T}^*$ can be expressed as

$$D^{-T}\frac{\partial \bar{T}^*}{\partial \alpha} = D^{-T}\left\{\mathbf{a}^T \frac{\partial C}{\partial \alpha}\mathbf{b}\right\} \tag{14}$$

where the notation of equation (6) has been used to define the terms on the right-hand side of equation (14). Moreover, it can be shown that

$$D^{-T}\left\{\mathbf{a}^T \frac{\partial C}{\partial \alpha}\mathbf{b}\right\} = \tilde{a}^T C \mathbf{b}. \tag{15}$$

To show this, equation (15) is multiplied by $\dot{\alpha}^T D^T$ and equation (4) is introduced into the result producing the expression

$$\dot{\alpha}^T\left\{\mathbf{a}^T \frac{\partial C}{\partial \alpha}\mathbf{b}\right\} = \mathbf{a}^T \tilde{\omega} C \mathbf{b}. \tag{16}$$

Introducing equation (9*a*) into equation (16) results in the expression

$$\dot{\alpha}^T\left\{\mathbf{a}^T \frac{\partial C}{\partial \alpha}\mathbf{b}\right\} = \mathbf{a}^T\left[\frac{\partial C}{\partial \alpha}\dot{\alpha}\right]\mathbf{b} \tag{17}$$

which, considering equation (9*b*), is an identity. Introducing another useful symbolic notation, equation (14) can then be expressed as

$$\frac{\partial \bar{T}^*}{\partial C} = D^{-T}\frac{\partial \bar{T}^*}{\partial \alpha} = \tilde{\mathbf{a}}^T C \mathbf{b}. \tag{18a}$$

Then Lagrange's equations for quasi-coordinates can be expressed as

$$\frac{d}{dt}\left[\frac{\partial \bar{T}}{\partial \omega}\right] + \tilde{\omega}^T \frac{\partial \bar{T}}{\partial \omega} - \frac{\partial \bar{T}}{\partial C} + \frac{\partial \bar{V}}{\partial C} = \mathbf{M} \tag{18b}$$

where the kinematic and potential energies are expressd in matrix form in terms of angular velocity vectors and rotational transformation matrices or $T(\omega, C)$ and $\bar{V}(C)$. Equations can be used along with equation (13) to permit a straightforward and efficient method of deriving the equations of motion of complex structures.

4 Example

As an example of the application of Lagrange's equations for quasi-coordinates, consider a flexible spacecraft orbiting the earth. The spacecraft of Fig. 1 consists of the shuttle, which will be assumed to be relatively rigid, and a flexible appendage extending from the shuttle cargo bay. Considering Fig. 1 and let the position of the origin 0 of the body-fixed reference frame $x_0y_0z_0$ be represented by the vector **R**, the

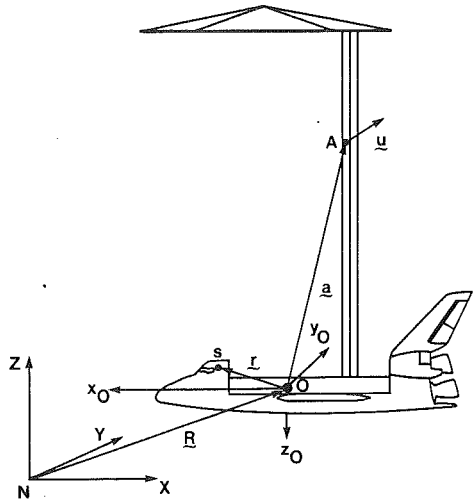


Fig. 1 Shuttle with antenna appendage

position of a point S on the shuttle relative to 0 by **r**, and the position of a point A on the appendage relative to 0 by **a**. Moreover, the elastic displacement vector of point A is defined as **u**. The position of S and A relative to the inertial frame XYZ is $\mathbf{R}_S = \mathbf{R} + \mathbf{r}$ and $\mathbf{R}_A = \mathbf{R} + \mathbf{a} + \mathbf{u}$, respectively. The velocities of points S and A on the spacecraft are $\dot{\mathbf{R}}_S = \dot{\mathbf{R}} + \omega x \mathbf{r}$ and $\dot{\mathbf{R}}_A = \dot{\mathbf{R}} + \omega x(\mathbf{a} + \mathbf{u}) + \dot{\mathbf{u}}$, respectively, where $\dot{\mathbf{R}}$ is the translational velocity and ω is the angular velocity of the frame $x_0y_0z_0$ with respect to the inertial frame. Hence, the kinetic energy of the spacecraft is

$$T = \frac{1}{2}\int_{m_S} |\dot{\mathbf{R}}_S|^2 dm_S + \frac{1}{2}\int_{m_A} |\dot{\mathbf{R}}_A|^2 dm_A. \tag{19}$$

In order to discretize the system in space, we express the elastic displacement vector in the form

$$\mathbf{u}(x, t) = \Phi(x)\mathbf{q}(t) \tag{20}$$

where Φ is a matrix of space-dependent admissible functions and **q** is a vector of time-dependent generalized coordinates. Introducing equation (20) into (19), the kinetic energy can be expressed in the matrix form

$$T = \frac{1}{2} m\dot{\mathbf{R}}^T\dot{\mathbf{R}} + \frac{1}{2}\omega^T I_0 \omega + \dot{\mathbf{R}}^T C^T \tilde{\mathbf{S}}_0 \omega + \frac{1}{2}\dot{\mathbf{q}}^T M_A \dot{\mathbf{q}}$$
$$+ \dot{\mathbf{R}}^T C^T \tilde{\Phi}\dot{\mathbf{q}} + \dot{\mathbf{R}}^T C^T \tilde{\omega}^T \tilde{\Phi}\mathbf{q} + \dot{\mathbf{q}}^T \tilde{\Phi}^T \omega + \omega^T \int_{m_A} \tilde{a}^T \tilde{\omega}^T \Phi dm_A \mathbf{q}$$
$$- \frac{1}{2}\mathbf{q}^T \tilde{L}_A(\omega)\mathbf{q} + \dot{\mathbf{q}}^T L_A(\omega)\mathbf{q} \tag{21}$$

where

$$\tilde{\Phi} = \int_{m_A} \Phi dm_A \tag{22a}$$

$$\tilde{\Phi}^T = \int_{m_A} \Phi^T \tilde{a} dm_A \tag{22b}$$

$$\tilde{L}_A(\omega) = \int_{m_A} \Phi^T \tilde{\omega}^T \Phi dm_A \tag{22c}$$

$$\bar{L}_A(\omega) = \int_{m_A} \Phi^T \tilde{\omega}^2 \Phi dm_A \tag{22d}$$

$$M_A = \int_{m_A} \Phi^T \Phi dm_A \tag{22e}$$

$$\mathbf{S}_0 = \int_{m_S} \mathbf{r} dm_s + \int_{m_A} \mathbf{a} dm_A. \tag{22f}$$

Also, m is the mass and I_0 is the mass moment of inertia

Downloaded 03 May 2010 to 171.66.16.244. Redistribution subject to ASME license or copyright; see http://www.asme.org/terms/Terms_Use.cfm

matrix about point 0 of the spacecraft. The matrix M_A is the mass matrix of the appendage. The matrix C represents a rotational transformation from the inertial frame to the body-fixed frame.

Assuming the origin of the inertial coordinate system coincides with the center of the gravitational field, the gravitational potential energy can be expressed as

$$V_g = -Gm_e\left(\int_{m_S} |\mathbf{R}+\mathbf{r}|^{-1}dm_S + \int_{m_A} |\mathbf{R}+\mathbf{a}+\mathbf{u}|^{-1}dm_A\right) \tag{23}$$

where m_e is the mass of the earth and G is the gravitational constant. The strain energy can be expressed as an energy inner product denoted by [,] as in Meirovitch (1980). The total potential energy then becomes

$$V = \frac{1}{2}[\mathbf{u}, \mathbf{u}] + V_g \tag{24}$$

where [**u**, **u**] includes the potential energy due to centrifugal and gravitational stiffening effects.

Recognizing that the magnitude of **R** is large in comparison with the magnitude of the other vectors in equation (23) and ignoring higher-order terms, a binomial expansion permits us to write

$$V_g \cong -Gm_e\left\{m|\mathbf{R}|^{-1} - \mathbf{R}^T\left(\mathbf{S}_0 + \int_{m_A}\mathbf{u}dm_A\right)|\mathbf{R}|^{-3} + \frac{1}{2}|\mathbf{R}|^{-3}\left[\int_{m_S}(3\mathbf{r}^TC\hat{\mathbf{R}}\hat{\mathbf{R}}^TC^T\mathbf{r} - \mathbf{r}^T\mathbf{r})dm_s + \int_{m_A}(3\mathbf{a}^TC\mathbf{R}\mathbf{R}^TC^T\mathbf{a} - \mathbf{a}^T\mathbf{a})dm_A\right]\right\}. \tag{25}$$

Introducing equation (25) into equation (24) and considering equation (20), the potential energy can be written in the matrix form

$$V \cong \frac{1}{2}\mathbf{q}^TK_A\mathbf{q} - Gm_e\left\{\frac{m}{|\mathbf{R}|} - \frac{1}{|\mathbf{R}|^2}\hat{\mathbf{R}}^TC^T(\mathbf{S}_0+\Phi\mathbf{q}) + \frac{1}{2|\mathbf{R}|^3}\left[3\hat{\mathbf{R}}^TC^T\bar{J}C\hat{\mathbf{R}} - \left(\int_{m_S}\mathbf{r}^T\mathbf{r}dm_S + \int_{m_A}\mathbf{a}^T\mathbf{a}dm_A\right)\right]\right\} \tag{26}$$

where

$$K_A = [\Phi, \Phi] \tag{27a}$$

$$\hat{\mathbf{R}} = \frac{\mathbf{R}}{|\mathbf{R}|} \tag{27b}$$

$$\bar{J} = \int_{m_S}\mathbf{r}\mathbf{r}^Tdm_S + \int_{m_A}\mathbf{a}\mathbf{a}^Tdm_A \tag{27c}$$

are the stiffness matrix of the appendage, a unit vector in the direction of **R**, and a matrix of inertia integrals, respectively. Because the control forces are most conveniently expressed in the body-fixed frame, the transformation matrix C must be employed in expressing the virtual work as follows:

$$\delta W = \mathbf{F}^TC\delta\mathbf{R} + \mathbf{M}^T\delta\mathbf{B} + \mathbf{Q}^T\delta\mathbf{q} \tag{28}$$

where **F**, **M**, and **Q** are generalized force vectors in terms of components about x_o, y_o, and z_o.

Lagrange's equations which govern the translation and elastic vibration of the spacecraft can be written in the symbolic form

$$\frac{d}{dt}\left(\frac{\partial T}{\partial\dot{\mathbf{R}}}\right) + \frac{\partial V}{\partial\mathbf{R}} = C^T\mathbf{F} \tag{29a}$$

$$\frac{d}{dt}\left(\frac{\partial T}{\partial\dot{\mathbf{q}}}\right) - \frac{\partial T}{\partial\mathbf{q}} + \frac{\partial V}{\partial\mathbf{q}} = Q \tag{29b}$$

whereas equation (18*b*) governs the rotational motion of the structure. The equations of motion are expressed in detail by Meirovitch and Quinn (1987). The purpose of this example is to demonstrate the use of equations (18*a*,*b*) in producing the equations which govern the rotational motion of the structure.

For convenience we shall consider the ten terms of equation (21) describing the kinetic energy of the structure separately, or

$$T = \sum_{i=1}^{10} T_i \tag{30}$$

where the individual T_i terms are defined by the order of equation (21). Considering (18*b*), the terms of Lagrange's equations involving derivatives with respect to angular velocity can be expressed as follows:

$$N_1(T_2) = I_0\dot{\omega} + \tilde{\omega}^TI_0\omega \tag{31a}$$

$$N_1(T_3) = \tilde{S}_0^TC\ddot{\mathbf{R}} + \tilde{S}_0^T\tilde{\omega}C\dot{\mathbf{R}} + \tilde{\omega}^TS_0^TC\dot{\mathbf{R}} \tag{31b}$$

$$N_1(T_6) = \tilde{\omega}^T\tilde{b}^TC\dot{\mathbf{R}} + \dot{\tilde{b}}^TC\dot{\mathbf{R}} + \tilde{b}^T\tilde{\omega}C\dot{R} + \tilde{b}^TC\ddot{R} \tag{31c}$$

$$N_1(T_7) = \tilde{\Phi}\ddot{\mathbf{q}} + \tilde{\omega}^T\tilde{\Phi}\dot{\mathbf{q}} \tag{31d}$$

$$N_1(T_8) = \dot{J}\mathbf{q} + J\dot{\mathbf{q}} + \tilde{\omega}^TJ\mathbf{q} \tag{31e}$$

where

$$N_1(T_i) = \frac{d}{dt}\left(\frac{\partial T_i}{\partial\omega}\right) + \tilde{\omega}^T\frac{\partial T_i}{\partial\omega} \tag{32a}$$

$$\mathbf{b} = \tilde{\Phi}\mathbf{q}. \tag{32b}$$

$$J = J(\omega) = \int_{m_A}(\tilde{a}\tilde{\omega} + [\tilde{\tilde{a}}\omega])\Phi dm_A. \tag{32c}$$

The tilde over a matrix-vector product in brackets as in equation (32*c*) denotes a skew symmetric matrix formed from the vector product. Next, considering equation (18*a*), the terms of the kinetic and potential energies, as expressed by equations (21), (26), and (30), involving derivatives with respect to angular orientation can be expressed as follows:

$$N_2(T_3) = [\tilde{\tilde{S}}\omega]^TC\dot{\mathbf{R}} \tag{33a}$$

$$N_2(T_5) = \dot{\tilde{b}}^TC\dot{\mathbf{R}} \tag{33b}$$

$$N_2(T_6) = [\tilde{\tilde{b}}\omega]^TC\dot{\mathbf{R}} \tag{33c}$$

$$N_2(V) = \frac{Gm_e}{|\mathbf{R}|^3}[\tilde{C}\mathbf{R}]\left(\mathbf{S}_0 - \frac{3\bar{J}C\hat{\mathbf{R}}}{|\mathbf{R}|} + \mathbf{b}\right) \tag{33d}$$

where the differential operator is defined as

$$N_2(T_i) = \frac{\partial T_i}{\partial C}. \tag{34}$$

The equations governing the rotational motion of the spacecraft can be found by summing equations (31) and (33*d*) and subtracting equations (33*a*)–(33*c*). These equations can be simplified with the introduction of the following identity involving skew symmetric matrices:

$$\tilde{a}\tilde{b} + \tilde{b}^T\tilde{a} + [\tilde{\tilde{a}}\omega]] = [0]. \tag{35}$$

Lagrange's equations governing the rotational motion of the spacecraft can then be expressed as

$$I_0\dot{\omega} + \tilde{\omega}^TI_0\omega + \tilde{S}_0^TC\ddot{\mathbf{R}} + \tilde{\Phi}\ddot{\mathbf{q}} + \left[[\tilde{C}\ddot{\mathbf{R}}]\tilde{\Phi} + J(\dot{\omega}) + \tilde{\omega}^TJ(\omega) + \frac{Gm_e}{|\mathbf{R}|^3}[\tilde{C}\mathbf{R}]\tilde{\Phi}\right]\mathbf{q} + [\tilde{\omega}^T\tilde{\Phi} + J(\omega)]\dot{\mathbf{q}}$$

Downloaded 03 May 2010 to 171.66.16.244. Redistribution subject to ASME license or copyright; see http://www.asme.org/terms/Terms_Use.cfm

$$+\frac{Gm_e}{|\mathbf{R}|^3}[\tilde{C}\mathbf{R}]\left(\mathbf{S}_0+3\tilde{J}C\frac{\hat{\mathbf{R}}}{|\mathbf{R}|}\right)=\mathbf{M}. \tag{36}$$

Equation (35) is also helpful in simplifying the equations of motion governing translation and elastic vibration which have been presented in simplified form by Meirovitch and Quinn (1987).

5 Conclusions

A form of Lagrange's (Boltzmann/Hamel) equations for quasi-coordinates has been presented which provides a straightforward method of formulating the equations of motion of structures when the energy expressions are explicit functions of angular orientation. A simplifying identity, equation (18*a*), has been introduced which may be utilized if the energies are expressed in matrix form as functions of angular velocities and coordinate transformations matrices. This method applies to a large class of problems in the dynamics of structures including spacecraft, robot, ground vehicles, and aircraft. The derivation of the equations of motion of a maneuvering flexible spacecraft was shown to be relatively straightforward using this method. A second simplifying identity, equation (35), was introduced which permits the recognition and cancellation of some like terms which appear in the Lagrangian formulation. The formulation and method, including the simplifying identity are suitable for symbolic computation. This permits the dynamic analysis of relatively complex systems.

References

Huston, R. L., and Passerello, C. E., 1980, "Multibody Structural Dynamics Including Translation Between the Bodies," *Computers and Structures*, Vol. 12, pp. 713–720.

Likins, P. W., 1974, "Analytical Dynamics and Nonrigid Spacecraft Simulation," Technical Report 32-1593, July 15, Jet Propulsion Lab, Pasadena, Calif.

Linkins, P. W., 1975, "Quasicoordinate Equations for Flexible Spacecraft," *AIAA Journal*, Vol. 13, No. 4, pp. 524–526.

Meirovitch, L., 1970, *Method of Analytical Dynamics*, McGraw-Hill, New York, pp. 157–162.

Meirovitch, L., 1980, *Computational Methods in Structural Dynamics*, Sijthoff and, Noordhoff, The Netherlands, pp. 242–252.

Meirovitch, L., and Quinn, R. D., 1987, "Equations of Motion for Maneuvering Flexible Spacecraft," *Journal of Guidance and Control*, Vol. 10, pp. 453–465.

Neimark, Ju. I., and Fufaev, N. A., 1972, *Dynamics of Nonholonomic Systems*, American Mathematical Society, Providence, R.I., (translated from Russian, 1967).

Oz, H., Meirovitch, L., and Montgomery, R. C., 1980, "On Maneuvering Large Flexible Spacecraft Using an Annular Momentum Control Device," AIAA and AAS, Astrodynamics Conference, Danvers Mass., Aug. 11–13.

Passeron, L., Garnier, Ch., and Sevennec, B., 1986, "Dynamic Modeling and Optimal Control Design for Large Flexible Space Structures," *Mechanical Qualification of Large Flexible Spacecraft Structures*, AGARD, Paris, France, pp. 3–1 to 3–13.

Whittaker, E. T., 1944, *Analytical Dynamics of Particles and Rigid Bodies*, Dover Publications, New York, pp. 41–44.

Downloaded 03 May 2010 to 171.66.16.244. Redistribution subject to ASME license or copyright; see http://www.asme.org/terms/Terms_Use.cfm

Inverse Dynamics of Constrained Multibody Systems

J. T. Wang
Senior Research Engineer,
Engineering Mechanics Department,
General Motors Research Laboratories,
Warren, MI 48090-9055
Mem. ASME

A method for analyzing constrained multibody systems is presented. The method is applicable to a class of problems in which the multibody system is subjected to both force and kinematic constraints. This class of problems cannot be solved by using the classical methods. The method is based upon the concept of partial velocity and generalized forces of Kane's method to permit the choice of constraint forces for fulfilling both kinematic and force constraints. Thus, the constraint forces or moments at convenient points or bodies may be specified in any desired form. For many applications, the method also allows analysts to choose a constant coefficient matrix for the undetermined force term to greatly reduce the burden of repeatedly computing its orthogonal complement matrix in solving the differential algebraic dynamic equations. Two examples illustrating the concepts are presented.

1 Introduction

During the past two decades dynamics of multibody systems has been the subject of extensive research. A multibody system is simply a collection of bodies with a given connection configuration. Multibody systems have been used to model vehicles, linkages, robots, human bodies, spacecrafts, etc. Of particular interest recently, is the analysis of nonholonomic systems, such as multibody systems with specified or restricted motion. This is an inverse dynamics problem. Namely, given a desired motion, the system response and constraint forces to fulfill nonholonomic constraints must be determined.

Many methods of dynamics analysis for nonholonomic systems have been developed for obtaining the governing equations (Whittaker, 1973; Goldstein, 1980; Haug et al., 1981; Hemani and Weimer, 1981; Passerello and Huston, 1973; Kamman and Huston, 1984; Kane, 1961; Kane and Levinson, 1980, 1985; Mani et al., 1985; Singh and Likins, 1985; Wampler et al. 1985). Broadly, these methods are based upon either of the three classical mechanics forms: Newton-Euler's, Lagrange's, or d'Alembert's. Of these, perhaps the best known method for nonholonomic systems is that of Lagrange multipliers (Whittaker, 1973; Goldstein, 1980). In this method, the system is essentially treated as holonomic and constraint forces are introduced via the undetermined multipliers. That is, the constraint forces and moments at the points and bodies where their kinematics are specified by the constraint equations are introduced through a product of undetermined multipliers and a coefficient matrix of the constraint equations. Lagrange's equations are then applicable and the equations of motion are obtained but with the complexity of computing scalar energy functions and their derivatives. This leads to a relatively large system of differential and algebraic equations with a sparse coefficient matrix for the generalized acceleration term.

In a different approach, Kane (1961) developed a method based upon the concept of partial velocity and d'Alembert's principle to analyze nonholonomic systems. One of the advantages of using Kane's method is that a set of predetermined generalized speeds (including quasi-coordinate derivatives) is readily accommodated to obtain a relatively small and compact system of differential equations without the presence of constraint force components. However, since the generalized speeds must be determined before analysis proceeds, analysts need to foresee the outcome of analysis due to a set of chosen generalized speeds which can be a difficult job. Besides, when a different set of generalized speeds is selected for a previously solved problem, whole dynamics analysis must be repeated to accommodate the new generalized speeds. This can be cumbersome and inefficient.

Alternatively, Wang and Huston (1987, 1988) have introduced a method based upon both Kane's method and the concept of Lagrange multipliers, called Kane's equations with undetermined multipliers. This method has been shown to possess the advantages of both Kane's method and the Lagrange multiplier method. Particularly, it enables analysts to perform dynamics analysis to result in a large system of differential and algebraic equations first and then a set of post determined generalized speeds can be used to eliminate the multipliers from the equations to form a compact system of equations, such as the one obtained by using Kane's method. That is, this method has rearranged the procedure of Kane's method to avoid the difficulty in predetermining the generalized speeds for analysis. It also suggests the equivalence of Kane's equations and Lagrange multiplier formulation.

While all the classical methods possess their own unique procedures, the resulted dynamic equations are virtually all equivalent. However, there is a class of problems which cannot

Contributed by the Applied Mechanics Division of THE AMERICAN SOCIETY OF MECHANICAL ENGINEERS for publication in the JOURNAL OF APPLIED MECHANICS.

Discussion on this paper should be addressed to the Technical Editor, Leon M. Keer, The Technological Institute, Northwestern University, Evanston, IL 60208, and will be accepted until two months after final publication of the paper itself in the JOURNAL OF APPLIED MECHANICS. Manuscript received by the ASME Applied Mechanics Division, Feb. 28, 1989; final revision, June 21, 1989.

Copyright © 1990 by ASME
Downloaded 03 May 2010 to 171.66.16.244. Redistribution subject to ASME license or copyright; see http://www.asme.org/terms/Terms_Use.cfm

be solved by using these classical methods. For example, when constraint forces and moments are needed to be applied at some specific places, or to have a specific form, such that the vector space spanned by these forces and moments are different from the vector space spanned by the coefficient of the constraint equations, it is not always possible to transfer the constraint forces and moments in the form of undetermined multipliers to the desired places. Thus, the attempt to solve this problem by using the classical methods may fail. Therefore, there is a need to have a more general method for evaluating the constraint force components and the corresponding system response, independently of the vector space of the constraint equations.

In this paper we present such a method. Instead of adopting the classical method of Lagrange multipliers, it is based upon a similar procedure used with Kane's equations—the concept of partial velocity and generalized forces. Thus, the constraint forces or moments at convenient points or bodies may be specified in any desired form.

The paper is divided into four parts. The first part contains some preliminary concepts useful in the analysis. The second part presents the details of the method. The third part provides two illustrations of applications of the method: a biomechanical problem and a redundant manipulator problem. Concluding remarks are given in the final part.

2 Preliminary Considerations

2.1 Coordinates and Kinematics. Consider a typical multibody system S. Let R be an inertial reference frame in which S moves. If S contains N bodies, it may have as many as $6N$ degrees-of-freedom. If the system is restrained by being constrained by joints, by having closed loops, or by having specified motion, it will have fewer degrees-of-freedom.

For the purpose of the analysis herein, consider first a multibody system S connected with joints which are all the same and such that no closed loops are formed. Let S have n degrees-of-freedom described by n generalized coordinates x_l ($l = 1,\ldots, n$). For such a system, it has been shown that the angular velocities of the bodies and the velocities of the mass centers of the bodies, relative to R, may be written in the form (Huston, et al., 1978, 1979):

$$\omega_k = \omega_{klm} y_l \mathbf{n}_m \text{ and } \mathbf{v}_k = v_{klm} y_l \mathbf{n}_m \tag{1}$$

where the subscript k refers to a typical body B_k and its mass center G_k. The y_l ($l = 1,\ldots,n$) are generalized speeds, which are linear combinations of the generalized coordinate derivatives $\dot{x}_l$. The $\mathbf{n}_m$ ($m = 1, 2, 3$) are unit vectors fixed in R. The coefficients ω_{klm} and v_{klm} are scalar components of the "partial angular velocity" and "partial velocity" vectors of S as used by Kane and Levinson (1980, 1985). These coefficients are functions of the x_l and time t, but not the y_l. Finally, regarding notation in equation (1), there is a sum for repeated indices over the range of the index.

The partial angular velocity and the partial velocity vectors may be defined as the derivatives $\partial\omega_k/\partial y_l$ and $\partial\mathbf{v}_k/\partial y_l$. Efficient algorithms have been written for the numerical evaluation of their components and their derivatives (Huston et al., 1978, 1979).

By taking the time derivatives of ω_k and $\mathbf{v}_k$, we see from equation (1) that the angular acceleration of B_k and the acceleration of G_k, in R, may be written in the forms:

$$\alpha_k = (\dot{\omega}_{klm} y_l + \omega_{klm}\dot{y}_l)\mathbf{n}_m \text{ and } \mathbf{a}_k = (\dot{v}_{klm} y_l + v_{klm}\dot{y}_l)\mathbf{n}_m. \tag{2}$$

2.2 Generalized Forces. Let the inertia forces on S be represented on a typical body B_k by a single force $\mathbf{F}_k^*$ passing through G_k together with a couple with torque $\mathbf{M}_k^*$. Then the generalized inertia force corresponding to the generalized speed y_l is defined as:

$$F_l^* = \mathbf{F}_k^* \cdot (\partial\mathbf{v}_k/\partial y_l) + \mathbf{M}_k^* \cdot (\partial\omega_k/\partial y_l) = F_{km}^* v_{klm} + M_{km}^* \omega_{klm} \tag{3}$$

where F_{km}^* and M_{km}^* are the $\mathbf{n}_m$ components of $\mathbf{F}_k^*$ and $\mathbf{M}_k^*$. $\mathbf{F}_k^*$ and $\mathbf{M}_k^*$ may be written in the forms (Kane and Levinson, 1985):

$$\mathbf{F}_k^* = -m_k\mathbf{a}_k \text{ and } \mathbf{M}_k^* = -\mathbf{I}_k \cdot \alpha_k - \omega_k \times (\mathbf{I}_k \cdot \omega_k) \tag{4}$$

where m_k is the mass of B_k and $\mathbf{I}_k$ is the central inertia dyadic of B_k. (In this case, there is no sum on k).

Now, let S be subjected to two general force fields, active forces and constraint forces. On a typical body B_k of S, let the active force field be represented by a single force $\mathbf{F}_k$ passing through G_k together with a couple with torque $\mathbf{M}_k$. Then, the generalized active force F_l corresponding to the generalized speed y_l is defined as

$$F_l = \mathbf{F}_k \cdot (\partial\mathbf{v}_k/\partial y_l) + \mathbf{M}_k \cdot (\partial\omega_k/\partial y_l) = F_{km} v_{klm} + M_{km}\omega_{klm} \tag{5}$$

where F_{km} and M_{km} are the $\mathbf{n}_m$ components of $\mathbf{F}_k$ and $\mathbf{M}_k$. As before, there is a sum over repeated indices.

Suppose now that additional constraints are placed on the system. For example, suppose the system has new joints or closed loops or specified motion of some of its points or bodies. Such constraints will lead to equations of the form:

$$B_{rp} y_p = g_r (r = 1,\ldots,m) \tag{6}$$

where $m < n$, and B_{rp} and g_r are functions of the x_l and time t.

Let the constraint forces and moments associated with the constraint equations (6) be represented by a series of forces $\mathbf{F}_i'$ applied at points P_i, $i = 1, \ldots, N'$, together with a series of couples with moments $\mathbf{M}_j'$ applied to bodies B_j, $j = 1, \ldots, M'$. (Observe that the $\mathbf{F}_i'$ and $\mathbf{M}_j'$ may each have as many as three constraining components. Hence, there may be as many as $3(N' + M')$ constraint equations. In the analysis which follows, m is taken as $3(N' + M')$. Similar procedures apply if m is less than $3(N' + M')$.) Then the generalized constraint forces associated with these constraint forces and moments are (Wang and Huston, 1987)

$$F_l' = \sum_{r=1}^{m} \lambda_r B_{lr}. \tag{7}$$

2.3 Dynamics and Governing Equations. By using Kane's method as exposited by Kane et al. (1961, 1980, 1983, 1985) and d'Alembert's principle, Wang and Huston (1987) have shown that the equations of motion for S may be obtained by setting the sum of the generalized inertia, active, and constraint forces equal to zero. That is

$$F_l^* + F_l + F_l' = 0 \ (l = 1,\ldots,n). \tag{8}$$

By substituting from equations (7) to (8), these equations may be written in the explicit form

$$F_l^* + F_l + \sum_{r=1}^{m} \lambda_r B_{lr} = 0 \tag{9}$$

or

$$A_{lp}\dot{y}_p = f_l + \sum_{r=1}^{m} \lambda_r B_{lr}, \tag{10}$$

where the A_{lp} and f_l are

$$A_{lp} = m_k v_{klm} v_{kpm} + I_{ksm}\omega_{kls}\omega_{kpm} \tag{11}$$

and

$$f_l = F_l - (m_k v_{klm}\dot{v}_{kpm} y_p + I_{ksm}\omega_{kls}\dot{\omega}_{kpm} y_p + e_{tsm} I_{ksr}\omega_{kpt}\omega_{klm} y_p y_q) \tag{12}$$

Downloaded 03 May 2010 to 171.66.16.244. Redistribution subject to ASME license or copyright; see http://www.asme.org/terms/Terms_Use.cfm

where e_{tsm} is the permutation symbol.

Equations (6) through (10) may be written in the matrix forms:

$$By = g, \tag{13}$$

$$F' = B^T\lambda, \tag{14}$$

$$F^* + F + F' = 0, \tag{15}$$

$$F^* + F + B^T\lambda = 0 \tag{16}$$

and

$$A\dot{y} = f + B^T\lambda. \tag{17}$$

where the matrices A and B and the arrays y, f, g, and λ are defined by inspection of equations (6) through (10). Equation (16) is called "Kane's equations with undetermined multipliers" (Wang and Huston, 1987). Taken together with the constraint equation (13) they constitute a set of $n + m$ equations for the n y_p and the m λ_r.

While Kane's equations with undetermined multipliers provide a unique procedure to efficiently formulate the dynamical equations for constrained multibody systems, the equivalence of the formulation and those obtained by using other classical methods such as Lagrange multipliers, Kane's equations, etc., can be easily shown. For example, the undetermined multipliers may be eliminated from equation (16) to result in the equations equivalent to the standard form of Kane's equations for constrained systems (Wang and Huston, 1987).

Several questions which arise are: (1) Is it absolutely necessary to restrict the constraint forces to the form of undetermined multipliers? (2) Can constraint forces be applied to the system S at arbitrary points or bodies? (3) What is the general form of dynamical equations for constrained multibody systems such that the constraint forces will not be restricted to the undetermined multipliers only? These questions are addressed in the following sections.

3 Analysis

3.1 Configuration Constraints and Motion Constraints. Consider again the constrained multibody system S. Let the kinematic constraints be separated into two parts consisting of: (1) the configuration constraints due to joints or closed loops, in the form of

$$B_1 y = g_1 \tag{18}$$

and (2) the motion constraints due to specified motions, in the form of

$$B_2 y = g_2 \tag{19}$$

where the $q \times n$ matrix B_1, the $(m-q) \times n$ matrix B_2, the array y, the $q \times 1$ array g_1 and the $(m-q) \times 1$ array g_2 are defined by inspection of equations (13), (18), and (19). That is

$$B = \begin{pmatrix} B_1 \\ \hline B_2 \end{pmatrix} \tag{20}$$

and

$$g = \begin{pmatrix} g_1 \\ \hline g_2 \end{pmatrix}. \tag{21}$$

Let the constraint forces associated with these constraints be designated by F_1' and F_2'. Then Kane's equations with undetermined multipliers are

$$F^* + F + F_1' + F_2' = 0 \text{ or } F^* + F + B_1^T\lambda_1 + B_2^T\lambda_2 = 0. \tag{22}$$

The constraint forces due to configuration constraints are reaction forces or moments at the points or bodies with specified kinematics. The Lagrange multipliers provide direct solutions for these quantities. The use of Lagrange multipliers for configuration constraints is well justified.

The constraint forces associated with those motion constraints may be considered as active forces which are needed to be supplied to the system at appropriate places. Since there are infinite number of ways to choose these places, the corresponding constraint forces are not necessary to be unique nor equivalent. In this case an infinite number of system kinematics due to the different constraint forces correspond to the same motion constraints. This suggests that the use of those methods based upon the classical mechanics (for example, Kane's method, Lagrange multipliers, etc., which will always result in one and only one unique solution for a motion constraint) for analyzing multibody systems with motion constraints can be misleading. Indeed, one may choose a number of sets $(m-q)$ or more than $(m-q)$ points or bodies is S for applying constraint forces or moments to fulfill the motion constraints. When the constraint forces and moments at some specific places with a specific form are chosen, such that the vector space spanned by these forces and moments are different from the vector space spanned by the coefficient of the constraint equations, Lagrange multiplier method, or any other equivalent method may fail. In what follows, we present a more general method for evaluating the corresponding system response and the constraint force components independently of the vector space of the constraint equations.

3.2 Undetermined Constraint Forces and Force Constraints. Assume that a set of s ($s \geq (m-q)$) points or bodies are chosen for applying constraint forces or moments. From kinematic analysis, the velocities and angular velocities of these points and bodies may be written in matrix form:

$$v_c = \hat{H}y \tag{23}$$

where $\hat{H}$ is an $s \times n$ matrix. By definition the partial velocity of v_c is

$$\frac{\partial v_c}{\partial y} = \hat{H}^T, \tag{24}$$

and the generalized constraint forces are

$$\hat{F}_2' = \hat{H}^T\hat{\mu} \tag{25}$$

where the $\hat{\mu}$ is an $s \times 1$ array representing the corresponding constraint forces and moments at those chosen points and bodies. Since, theoretically, for $(m-q)$ motion constraints it is necessary to supply only $(m - q)$ independent constraint forces, the size of the $\hat{\mu}$ array needs to be reduced to exactly $(m-q) \times 1$. This implies that additional $s - (m - q)$ constraints among these constraint forces $\hat{\mu}$ must be introduced into the analysis.

Let these *force constraints* be in the form of

$$\hat{Q}\hat{\mu} = \hat{b} \tag{26}$$

where the $(s - (m - q)) \times s$ matrix $\hat{Q}$ and the $(s - (m - q)) \times 1$ array $\hat{b}$ are functions of the x_l and time t. Observe the similarity between the force and kinematic constraint equations.

Now, let the $(m - q) \times 1$ array μ be the independent undetermined forces. The force constraints then may be rewritten to the form of

$$\hat{\mu} = Q\mu + b \tag{27}$$

where the $s \times (m - q)$ matrix Q and the $s \times 1$ array b are functions of the x_l and time t, and the following expressions are automatically satisfied:

$$\hat{Q}Q = 0 \text{ and } \hat{Q}b = \hat{b}. \tag{28}$$

The matrix Q is the orthogonal complement of the matrix $\hat{Q}$. Substituting from equations (27) into (25) yields

$$\hat{F}_2' = \hat{H}^T(Q\mu + b) = H^T\mu + \hat{H}^T b \tag{29}$$

where H is an $(m - q) \times n$ matrix and

$$H^T = \hat{H}^T Q. \tag{30}$$

Downloaded 03 May 2010 to 171.66.16.244. Redistribution subject to ASME license or copyright; see http://www.asme.org/terms/Terms_Use.cfm

Observe that the array μ consists of $(m - q)$ independent undetermined forces, but not the Lagrange multipliers.

3.3 Dynamical Equations With Undetermined Forces. In view of the foregoing analysis, the dynamical equations with both configuration and motion constraint forces may be written in the form of

$$F^* + F + B_1^T \lambda_1 + \hat{H}^T \hat{\mu} = 0. \tag{31}$$

Equations (13), (26), and (31) form $m + s - (m - q) + n$ equations for the n y_p, the q λ_r, and the s $\hat{\mu}_t$.

By substituting from equations (11) and (29) to (31), these equations may be written in the explicit form

$$F^* + F + B_1^T \lambda_1 + H^T \mu + \hat{H}^T b = 0 \text{ or } A\dot{y} = f + \hat{H}^T b + (B_1^T | H^T) \begin{pmatrix} \lambda_1 \\ \mu \end{pmatrix}. \tag{32}$$

These expressions can be called "Kane's equations with undetermined *forces*." Taken together with the constraint equations (13), they constitute a set of $(n + m)$ equations for the n y_p, the q λ_r, and the $(m - q)$ μ_s. These equations provide additional freedom for preplanning the application location and relative relations of constraint forces and moments before the dynamics analysis is carried out. In the sequel, this method will be referred to as "undetermined force method" to distinguish it from the undetermined multiplier method.

At this point, it is helpful to make several observations and remarks: First, the introduction of force constraints in the form of equation (26) into dynamics analysis is a new concept and Kane's equations with undetermined forces are not just another form of the undetermined multipliers formulation, i.e., equation (32) is not always equivalent to equation (22). A unique set of solutions, including both kinematics and constraint force components, will be obtained for a unique set of force constraints by using the undetermined force method. Recall that whenever the vector space spanned by the constraint force components is different from the vector space spanned by the coefficient of the constraint equations, a set of unique solutions exists which may be different from the one obtained from using the method of Lagrange multipliers or any other equivalent method by ignoring the force constraints.

Second, observe the differences between the force constraints and the constraint forces. The "force constraints" regulate the applying places and forms of the constraint forces, while the "constraint forces" ensure that the kinematic constraints will be fulfilled. Also observe the similarity between the forms of force constraints and kinematic constraints. The properties possessed by the kinematic constraint equation (6) also apply for the force constraint equation (26). For example, an orthogonal complement matrix (Kamman and Huston, 1984; Wang and Huston, 1987) also exists for the coefficient matrix of the force constraint equations. As will be shown in the next section, this orthogonal matrix may be used to eliminate the undetermined forces from equation (32) to result in a smaller system of pure differential equations.

Third, for many applications the places and/or the forms of the constraint forces need not to be restrained. In these cases, analysts may take the advantage of the new formulation to choose a convenient set of force constraint equations to make the numerical analysis more efficient. For example, a set of force constraint equations, which will result in a constraint force vector in the form consisting of constant elements for its coefficient matrix, may be chosen to eliminate the burden of repeatedly updating the orthogonal complement matrix for each integration time-step. We will illustrate this idea in Section 4 and further discuss it in Section 5.

One final observation: Equation (22) may be seen as a special case of equation (32) in which the motion constraints are treated as configuration constraints such that the constraint forces or moments are placed at the points or bodies with the specified kinematics. In this context, we see that the undetermined force method is more general than the undetermined multiplier method.

3.4 Solution Procedures. A general solution procedure used for solving the undetermined multiplier formulation (Wang and Huston, 1987, 1988) can also be used for the undetermined force formulation. That is, equation (32) may be reduced from a set of differential and algebraic equations to a set of differential equations by premultiplying it by an orthogonal complement matrix of the coefficient matrix of the undetermined force term. After solving this reduced set of differential equations, the undetermined forces may then be computed by back substitution. The details of this procedure are presented as follows.

Suppose an $n \times (n - m)$ matrix C can be found such that

$$\begin{pmatrix} B_1 \\ H \end{pmatrix} C = 0 \text{ or } C^T [B_1^T | H^T] = 0. \tag{33}$$

Then, by premultiplying the matrix form of equation (32) by C^T we obtain

$$C^T F^* + C^T F + C^T \hat{H}^T b = 0 \text{ or } C^T A \dot{y} = C^T f + C^T \hat{H}^T b. \tag{34}$$

Equation (34) together with equation (13) then represent a set of $(n - m) + m$ equations for the n y_p. These equations may be written in the partitioned matrix form:

$$\begin{pmatrix} C^T A \\ B \end{pmatrix} \dot{y} = \begin{pmatrix} C^T f + C^T \hat{H}^T b \\ \dot{g} - \dot{B} y \end{pmatrix}. \tag{35}$$

Observe that the undetermined forces have been eliminated from the analysis. This equation is equivalent to the standard form of Kane's equations for constrained systems, if and only if the matrix $\hat{H}$ is identical to the matrix B_2. However, for the class of problems studied in this paper, this is not the case.

Once the y_p and the generalized coordinates are determined, the λ_r and the μ_t may be determined by back substitution in equation (32). We have

$$\begin{pmatrix} \lambda_1 \\ \mu \end{pmatrix} = \left(\begin{pmatrix} B_1 \\ H \end{pmatrix} [B_1^T | H^T] \right)^{-1} (A\dot{y} - f - \hat{H}^T b). \tag{36}$$

The real constraint forces $\hat{\mu}$ then may be computed by using equation (27).

The matrix C, an "orthogonal complement" of

$$\begin{pmatrix} B_1 \\ H \end{pmatrix} \tag{37}$$

may be found in several ways: One is by inspection, another is by matrix manipulation (Passarello and Huston, 1973). These methods are useful for small systems. For large systems, many methods have been proposed. For example, we can use the zero-eigenvalues (Walton and Steeves, 1969; Kamman and Huston, 1984) or singular value decomposition methods (Lawson and Hanson, 1974) to obtain the desired orthogonal complement matrix C.

3.5 Singularity Problems. In the above analysis it was assumed that the coefficient matrix of equation (35),

$$\begin{pmatrix} C^T A \\ B \end{pmatrix},$$

is nonsingular. In practice, it may happen that the motion constraint forces defined in equation (29) are chosen such that the coefficient matrix becomes singular at all times and then the numerical integrations of equation (35) will fail.

Singularity is simply due to the fact that repeated roots occur for certain system configurations. These repeated roots may be seen as an intersection of paths of plural solutions of equation systems. If an instruction to guide the computation to

Downloaded 03 May 2010 to 171.66.16.244. Redistribution subject to ASME license or copyright; see http://www.asme.org/terms/Terms_Use.cfm

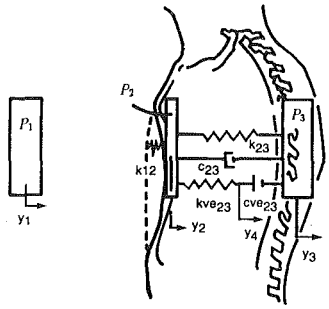


Fig. 1 An impactor—thorax system

follow one of these paths is given at the singular configuration, the singularity is then not a problem.

Much research has been done in this area. For example, two algorithms described in (Gear and Petzold, 1984) may be used to rewrite equation (35) in a form which can be solved numerically. Both algorithms start from premultiplying equation (35) by a nonsingular matrix P to zero out a maximal number of rows of the coefficient matrix and permute the zero rows to the bottom. Then the singularity may be removed either by differentiating the bottom half of the equation system to obtain a new system or by using the "algebraic" constraints to solve for some variables in terms of the remaining variables, and thus reducing the size of the system.

4 Examples

4.1 An Impactor-Thorax System. To illustrate the use of the undetermined force method we consider an impactor-thorax system as depicted in Fig. 1. The system consists of a rigid impactor and a lumped-mass thoracic model, known as Lobdell's thorax model (Lobdell, 1973). Let m_1, m_2, and m_3 designate the masses of bodies P_1, P_2, and P_3, respectively. The Lobdell model is known to represent the response of the human cadaver thorax under blunt frontal impacts. Since it is a one-dimensional model with no joints and closed loops, the system is free from configuration constraints.

A padding system is needed to be designed and placed between the impactor and the thoracic model (i.e., between bodies P_1 and P_2) to reduce the injury risk of the thorax. The $(VC)_{\max}$ criterion (Viano and Lau, 1988) defined as the peak value of the product of the thorax compression velocity and deformation, will be used as an index to indicate the level of injury risk. In a recent study, however, the value of VC is found to be proportional to the energy storing rate of the thorax (Wang, 1989). Thus, a possible constraint is to prescribe an energy storing rate time history which is composed of values less than the threshold of the $(VC)_{\max}$ criterion. The above argument may be written in the mathematical form

$$(0 \quad y_{23} \quad -y_{23}) \begin{pmatrix} \dot{y}_1 \\ \dot{y}_2 \\ \dot{y}_3 \end{pmatrix} = g \tag{38}$$

where

$$y_{23} = y_2 - y_3 \tag{39}$$

and g is the prescribed energy storing rate which is a function of time. Equation (38) is a motion constraint in the form of equation (19) and we observe that

$$B_2 = (0 \quad y_{23} \quad -y_{23}). \tag{40}$$

Differentiating equation (38) with respect to time yields

$$(0 \quad y_{23} \quad -y_{23}) \begin{pmatrix} \ddot{y}_1 \\ \ddot{y}_2 \\ \ddot{y}_3 \end{pmatrix} = (g' - \dot{y}_2^2 + 2\dot{y}_2\dot{y}_3 - \dot{y}_3^2). \tag{41}$$

Following the procedure presented in Section 2, the equations of motion with undetermined multipliers can be obtained in the form of

$$\begin{pmatrix} m_1 & 0 & 0 \\ 0 & m_2 & 0 \\ 0 & 0 & m_3 \end{pmatrix} \begin{pmatrix} \ddot{y}_1 \\ \ddot{y}_2 \\ \ddot{y}_3 \end{pmatrix} = \begin{pmatrix} 0 \\ -c_{23}\dot{y}_{23} - k_{23}y_{23} - kve_{23}y_{24} \\ c_{23}\dot{y}_{23} + k_{23}y_{23} + kve_{23}y_{24} \end{pmatrix} + \begin{pmatrix} 0 \\ y_{23} \\ -y_{23} \end{pmatrix} (\lambda) \tag{42}$$

where

$$y_{24} = y_2 - y_4 \tag{43}$$

and

$$\dot{y}_{23} = \dot{y}_2 - \dot{y}_3. \tag{44}$$

Moreover, to account for the Maxwell spring-damper element in the Lobdell's model, the following equation must be appended to equation (42):

$$-cve_{23}(\dot{y}_3 - \dot{y}_4) = kve_{23}y_{24} \tag{45}$$

or

$$\dot{y}_4 = \dot{y}_3 + \frac{kve_{23}}{cve_{23}} y_{24}. \tag{46}$$

Equation (42) indicates that a constraint force must be applied to both P_2 and P_3 in opposite directions. Clearly, if our attempt is to apply constraint force between P_1 and P_2 which is where the padding system is located, the attempt to study the padding effect has failed. Since the equivalence among all classical methods, it can be easily shown that the other classical methods will not be applicable for this problem, either. In what follows we will show that the undetermined force method can be used to solve the problem.

Let the constraint forces acting on the mass centers of bodies P_1, P_2, and P_3 be F'_{P1}, F'_{P2}, and F'_{P3}, respectively. The force constraint due to the padding system may then be expressed as

$$(1 \ 1 \ 0) \begin{pmatrix} F'_{P1} \\ F'_{P2} \\ F'_{P3} \end{pmatrix} = 0. \tag{47}$$

Comparing equation (47) with equations (25) and (26), we have

$$\hat{H}^T = \begin{pmatrix} 1 & 0 & 0 \\ 0 & 1 & 0 \\ 0 & 0 & 1 \end{pmatrix}, \tag{48}$$

$$\hat{\mu} = \begin{pmatrix} F'_{P1} \\ F'_{P2} \\ F'_{P3} \end{pmatrix}, \tag{49}$$

$$\hat{Q} = (1 \ 1 \ 0), \tag{50}$$

and

$$\hat{b} = 0. \tag{51}$$

Now, by satisfying equation (28), we obtain

$$Q = \begin{pmatrix} -1 \\ 1 \\ 0 \end{pmatrix} \text{ and } b = 0. \tag{52}$$

Matrix H may be obtained by using equations (30), (48), and (52):

Downloaded 03 May 2010 to 171.66.16.244. Redistribution subject to ASME license or copyright; see http://www.asme.org/terms/Terms_Use.cfm

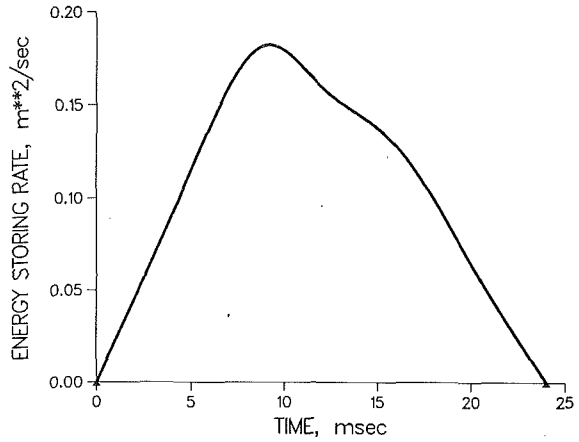


Fig. 2 The desired energy storing rate time history

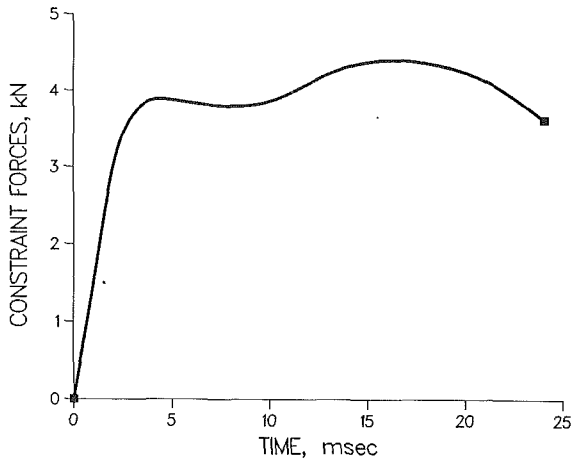


Fig. 3 The constraint force between the impactor and the thorax

$$H^T = \hat{H}^T Q = (-1\ 1\ 0). \tag{53}$$

The equations of motion can then be written based on the undetermined force method:

$$\begin{pmatrix} m_1 & 0 & 0 \\ 0 & m_2 & 0 \\ 0 & 0 & m_3 \end{pmatrix} \begin{pmatrix} \ddot{y}_1 \\ \ddot{y}_2 \\ \ddot{y}_3 \end{pmatrix} = \begin{pmatrix} 0 \\ -c_{23}\dot{y}_{23} - k_{23}y_{23} - kve_{23}y_{24} \\ c_{23}\dot{y}_{23} + k_{23}y_{23} + kve_{23}y_{24} \end{pmatrix} + \begin{pmatrix} -1 \\ 1 \\ 0 \end{pmatrix} (\mu). \tag{54}$$

Equations (41), (45), and (54) form 1 + 1 + 3 differential-algebraic equations for 5 unknowns, y_1, y_2, y_3, y_4, and μ. The matrix C defined in equation (33) may then be obtained by inspection:

$$C = \begin{pmatrix} 1 & 0 \\ 1 & 0 \\ 0 & 1 \end{pmatrix}. \tag{55}$$

It can be easily verified that $C^T H^T = 0$. Premultiplying equation (54) with C^T yields the reduced dynamic equations:

$$\begin{pmatrix} m_1 & m_2 & 0 \\ 0 & 0 & m_2 \end{pmatrix} \begin{pmatrix} \ddot{y}_1 \\ \ddot{y}_2 \\ \ddot{y}_3 \end{pmatrix} = \begin{pmatrix} -c_{23}\dot{y}_{23} - k_{23}y_{23} - kve_{23}y_{24} \\ c_{23}\dot{y}_{23} + k_{23}y_{23} + kve_{23}y_{24} \end{pmatrix}. \tag{56}$$

Equations (41), (45), and (56) form 1 + 1 + 2 ordinary differential equations for 4 unknowns, y_1, y_2, y_3, and y_4. The constraint forces μ may be determined by back substitution in equation (54). We have

$$\mu = \frac{1}{2}(-m_1\ddot{y}_1 + m_2\ddot{y}_2 + c_{23}\dot{y}_{23} + k_{23}y_{23} + kve_{23}y_{24}). \tag{57}$$

Observe that coincidentally the elements of the coefficient matrix H^T are all constant, and hence the corresponding orthogonal complement matrix C is also composed of constant elements as shown in equation (55). As indicated in Section 3.3, indeed this will greatly reduce the computation burden in evaluating the orthogonal complement matrix for each integration step.

Making use of the above analysis, we studied a case in which the impactor mass is 4.35 kg with a 15 m/sec initial impact velocity. The desired energy storing rate, which is used as a motion constraint, is given in Fig. 2. The motion constraint forces between the impactor and the thorax are obtained and shown in Fig. 3. This information can be used to design the padding system. About how to design the padding system, however, it is beyond the scope of this paper.

4.2 A Redundant Manipulator

As a second example, consider a planar redundant manipulator.It consists of three identical 1 m, 1 kg, pin-connected rods. The left end is fixed. A 10 kg payload is attached to the right end of the manipulator. The manipulator possesses three degrees of freedom in the inertial reference frame R. Now, the right end is given an upward acceleration from time zero to 0.1 seconds.

$$\ddot{X}_{re} = 0 \text{ and } \ddot{Y}_{re} = 1419.6 - 28392t \text{ m/sec}^2. \tag{58}$$

They are essentially the motion constraint equations for the system. The system is kinematically redundant, since only two motion constraint equations are given for this three degrees of freedom system. Additionally, we imposed a force constraint on the system such that the torque at joint 3 must always equal to one-half of the torque at joint 2. The objective of the problem is to determine the system response such that both motion and force constraints will be fulfilled.

Let absolute angular velocities be generalized speeds. This essentially eliminates the need to evaluate the configuration constraint forces at joints. That is, equation (58) is the only kinematic constraint needed to be considered in the analysis. From kinematic analysis, we obtain motion constraints:

$$l \begin{pmatrix} -s_1 & -s_2 & -s_3 \\ c_1 & c_2 & c_3 \end{pmatrix} \begin{pmatrix} \dot{\theta}_1 \\ \dot{\theta}_2 \\ \dot{\theta}_3 \end{pmatrix} = \begin{pmatrix} \dot{X}_{re} \\ \dot{Y}_{re} \end{pmatrix} \tag{59}$$

where $s_i = \sin\theta_i$, $c_i = \cos\theta_i$ and θ_i $(i = 1, 2, 3)$ are the absolute angular displacements in R, and l is the length of each rod. The constraint forces corresponding to undetermined multipliers method as defined in equation (22) are

$$F_2' = l \begin{pmatrix} -s_1 & c_1 \\ -s_2 & c_2 \\ -s_3 & c_3 \end{pmatrix} \begin{pmatrix} \lambda_{21} \\ \lambda_{22} \end{pmatrix}. \tag{60}$$

Obviously, the torque at joint 3 would not always be equal to one-half of the torque at joint 2, if this force expression is to be used in the equations of motion. Again, we have shown that this class of problems cannot be solved by using the Lagrange multiplier method or any other equivalent method.

In the undetermined force method, the constraint forces may be chosen independently of the motion constraint equations, and force constraints may be applied to the system. We will

Downloaded 03 May 2010 to 171.66.16.244. Redistribution subject to ASME license or copyright; see http://www.asme.org/terms/Terms_Use.cfm

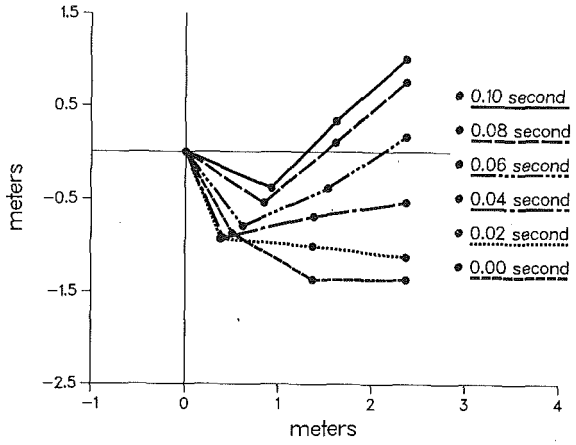


Fig. 4 The selected instantaneous configurations of a redundant manipulator

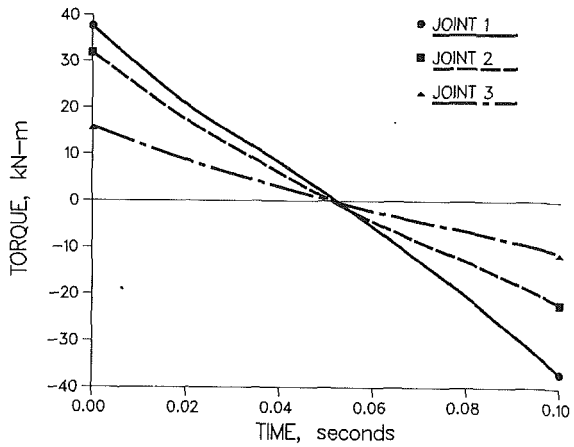


Fig. 5 The constraint torques at joints

show that the desired torques can be obtained by using this method.

Let $\hat{\theta}_i$ $(i = 1, 2, 3)$ be the set of relative angular velocities. Then, the absolute angular velocities may be written in matrix form as:

$$\begin{pmatrix} \dot{\theta}_1 \\ \dot{\theta}_2 \\ \dot{\theta}_3 \end{pmatrix} = \begin{pmatrix} 1 & 0 & 0 \\ 1 & 1 & 0 \\ 1 & 1 & 1 \end{pmatrix} \begin{pmatrix} \dot{\hat{\theta}}_1 \\ \dot{\hat{\theta}}_2 \\ \dot{\hat{\theta}}_3 \end{pmatrix}. \tag{61}$$

Inversely, we have

$$\begin{pmatrix} \dot{\hat{\theta}}_1 \\ \dot{\hat{\theta}}_2 \\ \dot{\hat{\theta}}_3 \end{pmatrix} = \begin{pmatrix} 1 & 0 & 0 \\ -1 & 1 & 0 \\ 0 & -1 & 1 \end{pmatrix} \begin{pmatrix} \dot{\theta}_1 \\ \dot{\theta}_2 \\ \dot{\theta}_3 \end{pmatrix}. \tag{62}$$

The partial velocity corresponding to the relative velocities at the joints as defined in equation (24) are

$$\frac{\partial \dot{\theta}}{\partial \dot{\theta}} = \begin{pmatrix} 1 & -1 & 0 \\ 0 & 1 & -1 \\ 0 & 0 & 1 \end{pmatrix}. \tag{63}$$

Now, let T_i and $\hat{T}_i$ $(i = 1, 2, 3)$ be the torques at the joints corresponding to the absolute angular displacements and relative angular displacements, respectively. We have the generalized constraint forces in the form corresponding to equation (25):

$$\begin{pmatrix} T_1 \\ T_2 \\ T_3 \end{pmatrix} = \begin{pmatrix} 1 & -1 & 0 \\ 0 & 1 & -1 \\ 0 & 0 & 1 \end{pmatrix} \begin{pmatrix} \hat{T}_1 \\ \hat{T}_2 \\ \hat{T}_3 \end{pmatrix}. \tag{64}$$

Recall that the desired torques must satisfy the given force constraint as stated in equations (26) and (27):

$$\hat{T}_3 = \frac{1}{2}\hat{T}_2 \text{ or } \begin{pmatrix} \hat{T}_1 \\ \hat{T}_2 \\ \hat{T}_3 \end{pmatrix} = \begin{pmatrix} 1 & 0 \\ 0 & 1 \\ 0 & \tfrac{1}{2} \end{pmatrix} \begin{pmatrix} \hat{T}_1 \\ \hat{T}_2 \end{pmatrix}. \tag{65}$$

By substituting into equation (64) we obtain the desired constraint torque expressions:

$$\begin{pmatrix} T_1 \\ T_2 \\ T_3 \end{pmatrix} = \begin{pmatrix} 1 & -1 & 0 \\ 0 & 1 & -1 \\ 0 & 0 & 1 \end{pmatrix} \begin{pmatrix} 1 & 0 \\ 0 & 1 \\ 0 & \tfrac{1}{2} \end{pmatrix} \begin{pmatrix} \hat{T}_1 \\ \hat{T}_2 \end{pmatrix}$$

$$= \begin{pmatrix} 1 & -1 \\ 0 & \tfrac{1}{2} \\ 0 & \tfrac{1}{2} \end{pmatrix} \begin{pmatrix} \hat{T}_1 \\ \hat{T}_2 \end{pmatrix}. \tag{66}$$

Notice that equation (66) is corresponding to equation (29) and the matrix H is seen to be

$$H = \begin{pmatrix} 1 & 0 & 0 \\ -1 & \tfrac{1}{2} & \tfrac{1}{2} \end{pmatrix}. \tag{67}$$

The orthogonal complement matrix C may be obtained by inspection:

$$C = \begin{pmatrix} 0 \\ 1 \\ -1 \end{pmatrix}. \tag{68}$$

Observe that the necessary condition $C^T H^T = 0$ is satisfied.

The force constraint equations in the form of equation (66) are then used to replace equation (60) in the dynamical analysis. The response of the system is shown in Fig. 4. Figure 5 shows the magnitudes of the constraint torques at the joints. These torques are needed to be supplied to the system to result in the desired motion. Observe that, indeed, the torque $\hat{T}_3$ is exactly one-half of the torque $\hat{T}_2$ as specified by equation (65) of the force constraints, and that the motion of the right end of the manipulator satisfies the specified motion described in equation (58).

5 Concluding Remarks

Dynamical equations derived based upon the classical theory, with or without the presence of undetermined multipliers, are unique if and only if the dynamical systems are free-from constraints other than configuration constraints. In this case, the constraint forces are internal reaction forces only, which can not be supplied to the systems by any other means. When motion constraints are imposed to the systems the dynamical equations are still valid, but not unique. It becomes "a" solution of the dynamical system, in which the constraint forces are restricted to a special form bound to the coefficient matrix of the constraint equations: even though, theoretically, there are infinite numbers of ways to supply constraint forces to the system to fulfill the motion constraints. As a result, for many applications such as the one shown in example 1, the restricted form of the constraint forces fails.

On the other hand, the undetermined force method, which may be viewed as a generalization of Kane's method, provides a more general form for formulating constraint forces and

Downloaded 03 May 2010 to 171.66.16.244. Redistribution subject to ASME license or copyright; see http://www.asme.org/terms/Terms_Use.cfm

dynamical equations. The method possesses several advantages. First, the method is applicable to systems subjected to both force and kinematics constraints which cannot be solved by using those classical methods, such as Lagrange multipliers, Kane's equations, etc. Second, the method provides additional freedom for preplanning the constraint forces before the dynamics analysis has been done. Recall that for $(m - q)$ motion constraints, it only requires that $(m - q)$ independent constraint forces be supplied. The method allows the specification of additional $(s - (m - q))$ constraints among the s constraint forces as illustrated in examples 1 and 2. Third, the method offers a mechanism to greatly reduce the computation burden for large mechanical systems through choosing a coefficient matrix with constant elements for the undetermined forces. In this case, we may first eliminate those configuration constraint forces from the analysis by using Lagrange's or Kane's methods such that the matrix C will depend on the motion constraint forces only. The undetermined force method then enables us to choose a set of motion constraint forces in which the coefficient matrix contains constant elements only, as illustrated in examples 1 and 2. Obviously, the matrix C needs to be evaluated only once. Recall that an orthogonal complement matrix C is needed for eliminating the constraint forces from the dynamic equations. If the coefficient matrix of the constraint forces involves time-dependent variables, which is very common when the undetermined multiplier method is used, the matrix C must be evaluated for each integration step. This can be a very inefficient computation for large systems.

Although the method is developed by using Kane's method, it can be shown that a similar result may be obtained by using other classical methods, e.g. Lagrange, Newton-Euler methods, etc. However, with Kane's method the generalized constraint forces may be conveniently evaluated. Also, generalized speeds and quasi-coordinate derivatives are readily accommodated and the equations may be developed in forms which are easily converted into numerical algorithms. The method is expected to be useful for analyses of mechanical systems with motion constraints, particularly for automated inverse dynamics analyses of large multibody systems. Such systems are commonly encouraged in human body, vehicle, robot, and spacecraft modeling.

Acknowledgment

I gratefully acknowledge the helpful suggestions of the reviewers.

References

Gear, C. W., and Petzold, L. R., 1984, "ODE Methods for the solution of Differential/Algebraic Systems," *SIAM Journal of Numerical Analysis*, Vol. 21, pp. 716–728.

Goldstein, H., 1980, *Classical Mechanics*, 2nd ed., Addison-Wesley Publishing Company.

Haug, E. J., Wehage, R. A., and Barman, N. C., 1981, "Dynamic Analysis and Design of Constrained Mechanical Systems," *ASME Journal of Mechanical Design*, Vol. 103, pp. 560–570.

Hemani, H., and Weimer, F. C., 1981, "Modeling of Nonholonomic Dynamic Systems with Applications," ASME JOURNAL OF APPLIED MECHANICS, Vol. 48, pp. 177–182.

Huston, R. L., Passerello, C. E., and Harlow, M. W., 1978, "Dynamics of Multi-Rigid-Body Systems," ASME JOURNAL OF APPLIED MECHANICS, Vol. 45, pp. 889–894.

Huston, R. L., and Passerello, C. E., 1979, "On Multi-Rigid-Body System Dynamics," *Computers and Structures*, Vol. 10, pp. 439–446.

Kamman, J. W., and Huston, R. L., 1984, "Dynamics of Constrained Multibody Systems," ASME JOURNAL OF APPLIED MECHANICS, Vol. 51, pp. 889–903.

Kane, T. R., 1961, "Dynamics of Nonholonomic Systems," ASME JOURNAL OF APPLIED MECHANICS, Vol. 28, pp. 574–578.

Kane, T. R., and Levinson, D. A., 1980, "Formulation of Equations of Motion for Complex Spacecraft," *Journal of Guidance and Control*, Vol. 3, pp. 99–112.

Kane, T. R., and Levinson, D. A., 1983, "Multibody Dynamics," ASME JOURNAL OF APPLIED MECHANICS, Vol. 50, pp. 1071–1078.

Kane, T. R., and Levinson, D. A., 1985, *Dynamics: Theory and Applications*, McGraw-Hill, New York, pp. 45–50.

Lawson, C. L., and Hanson, R. J., 1974, *Solving Least Squares Problems*, Prentice-Hall, Englewood Cliffs, N.J. pp. 9–22.

Lobdell, T. F., 1973, "Impact Response of the Human Thorax," *Proceedings of the Symposium on Human Impact Response Measurement and Simulation*, General Motors Research Laboratories, New York-Loden, Plenum Press, pp. 201–245.

Mani, N. K., Haug, E. J., and Atkinson, K. E., 1985, "Application of Singular Value Decomposition for Analysis of Mechanical Systems Dynamics," ASME *Journal of Mechanisms, Transmissions and Automation in Design*, Vol. 107, pp. 82–87.

Passerello, C. E., and Huston, R. L., 1973, "Another Look at Nonholonomic Systems," ASME JOURNAL OF APPLIED MECHANICS, Vol. 40, pp. 101–104.

Singh, R. P., and Likins, P. W., 1985, "Singular Value Decomposition for Constrained Dynamical Systems," ASME JOURNAL OF APPLIED MECHANICS, Vol. 52, pp. 943–948.

Viano, D. C., and Lau, I. V., 1988, "A Viscous Tolerance Criterion for Soft Tissue Injury Assessment," *Journal of Biomechanics*, Vol. 21, pp. 397–399.

Walton, Jr., W. C., and Steeves, E. C., 1969, "A New Matrix Theorem and Its Application for Establishing Independent Coordinates for Complex Dynamical Systems with Constraints," NASA Tech. Rep. TR R-326.

Wampler, C., Buffinton, K., and Shu-hui, J., 1985, "Formulation of Equations of Motion for Systems Subject to Constraints," ASME JOURNAL OF APPLIED MECHANICS, Vol. 52, pp. 465–470.

Wang, J. T., 1989, "Analytical Studies of Injury Criteria for the Thorax," ASME JOURNAL OF BIOMECHANICAL ENGINEERING, Vol. 111, pp. 128–135.

Wang, J. T., and Huston, R. L., 1987, "Kane's Equations with Undetermined Multipliers-Application to Constrained Multibody Systems," ASME JOURNAL OF APPLIED MECHANICS, Vol. 54, pp. 424–429.

Wang, J. T., and Huston, R. L., 1988, "Computational Methods in Constrained Multibody Dynamics: Matrix Formalisms," *Computers and Structures*, Vol. 29, No. 2, pp. 331–338.

Wittaker, E. T., 1937, *A Treatise on the Analytical Dynamics of Particles and Rigid Bodies*, Cambridge, London.

Downloaded 03 May 2010 to 171.66.16.244. Redistribution subject to ASME license or copyright; see http://www.asme.org/terms/Terms_Use.cfm

Optimization of Self-Acting Gas Bearings for Maximum Static Stiffness

Michel P. Robert
IBM General Products Division,
Mathematical Analysis and Simulation,
San Jose, CA 95193

The gap profile of a two-dimensional self-acting gas bearing is determined such that the static stiffness it can achieve is maximum. Three fundamental profiles are obtained according to the stiffness mode to be considered: normal, pitch, or roll. The optimization process takes place within the framework of the compressible lubrication theory among all the profiles having a given minimum film thickness. The method proposed here is based on the calculus of variations and uses a finite element technique coupled with an iterative mapping to converge to the final solution. As an example, the case of a square bearing is treated and the three fundamental gap profiles, along with their optimum characteristics, are plotted to illustrate the solutions.

1 Introduction

Very few examples of sliding bearing optimization can be found in the literature. The first and most famous one was investigated by Lord Rayleigh (1918) who found the one-dimensional step bearing which can carry the largest load. Five decades later, Maday (1968) extended the solution to a more general case: The optimum solution was found to be a tapered step. Finally, Rodhe and McAllister (1976) computed numerically the best gap profile for a two-dimensional incompressible gas bearing achieving maximum lift force. In all the above-mentioned examples, the common goal was to maximize the load developed by the bearing. Nevertheless, in many applications such a criterion is not essential: For instance, a gas bearing actuator with a high load capacity but a low stability will perform very poorly. Solving the eigenvalue problem associated with the time-dependent solution is beyond the scope of the present approach for which the optimization criterion is simplified to the static stiffness of the gas bearing. In other words, the problem consists of finding the gap profile which possess the best restoring performance, should a small rigid body perturbation of the pad occur. Furthermore, the search is limited to gap profiles having a given lower bound, which corresponds to a given clearance. Using a perturbation analysis on Reynolds equation, the effect of a small change in the film thickness can easily be derived. The corresponding restoring effect (force or moment) is then maximized via the process of calculus of variation, leading to a nonlinear inequality which the gap profile must satisfy.

Contributed by the Applied Mechanics Division of THE AMERICAN SOCIETY OF MECHANICAL ENGINEERS for presentation at the Winter Annual Meeting, Dallas, Texas, November 25-30, 1990.

Discussion on this paper should be addressed to the Technical Editor, Leon M. Keer, The Technological Institute, Northwestern University, Evanston, IL 60208, and will be accepted until two months after final publication of the paper itself in the JOURNAL OF APPLIED MECHANICS. Manuscript received and accepted by the ASME Mechanics Division, May 2, 1989.

Paper No. 90-WA/APM-18.

2 Mathematical Formulation

Let us define the gas bearing by its projected area Ω and by its profile $h(x, y)$. The pressure buildup $p(x, y)$ created by the motion of the flat runner beneath the slider is assumed to satisfy the Reynolds equation, written in a normalized form as:

$$R_0(P) = \nabla \cdot (H^3 P \nabla P - PH\Lambda) = 0 \text{ in } \Omega \text{ with } P = 1 \text{ on } \partial\Omega \quad (1)$$

where X, Y are the normalized coordinates x/L, y/L, respectively. L is a characteristic length of the domain Ω, and X is chosen to be parallel to the bearing number Λ defined as $6\mu_0 UL/p_0 h_0^2$ where $\mathbf{U}$ is the velocity of the flat runner and μ_0 is the gas viscosity. Also, P is the normalized pressure p/p_0, p_0 is the ambient pressure, H is the normalized film thickness h/h_0, and h_0 is the prescribed minimum of $h(x, y)$ over the domain Ω.

The normalized net force and moments (with respect to the coordinate axes) produced by the gas bearing are simply given by:

$$F = \int_\Omega [P(X, Y) - 1] dX dY$$

$$M^X = \int_\Omega [P(X, Y) - 1] Y dX dY$$

$$M^Y = \int_\Omega [P(X, Y) - 1] X dX dY. \quad (2)$$

Let us now perturb equation (1) with a small change in the film thickness H such that:

$$H = H_0 + \epsilon H_1. \quad (3)$$

We assume the pressure to be expressed as a regular expansion in ϵ

$$P = P_0 + \epsilon P_1 + O(\epsilon^2), \quad (4)$$

while the force and moments become

Copyright © 1990 by ASME
Downloaded 03 May 2010 to 171.66.16.244. Redistribution subject to ASME license or copyright; see http://www.asme.org/terms/Terms_Use.cfm

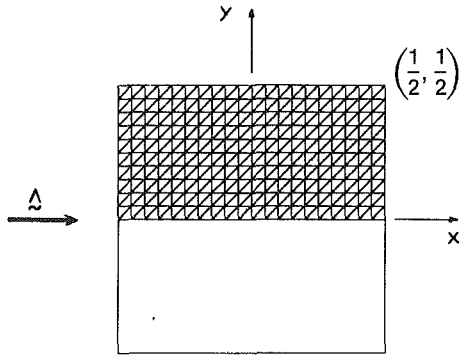


Fig. 1 Finite element discretization of the domain Ω with a uniform triangular mesh of 20 × 20 elements

$$F = F_0 + \epsilon F_1 + O(\epsilon^2) \tag{5}$$

$$M = M_0 + \epsilon M_1 + O(\epsilon^2). \tag{6}$$

Substituting expansions (3) and (4) into equation (1), the following results are obtained for the terms of $O(\epsilon)$:

$$R_1(P_1) = \nabla\cdot[H_0^3\nabla(P_0P_1) - P_1H_0\Lambda]$$

$$-\nabla\cdot(-3H_0^2H_1P_0\nabla P_0 + P_0H_1\Lambda) = 0 \text{ in } \Omega$$

$$P_1 = 0 \text{ on } \partial\Omega. \tag{7}$$

From equations (5) and (6), the restoring force and moments are given by:

$$F_1 = \int_\Omega P_1 dXdY, \tag{8}$$

$$M_1^X = \int_\Omega YP_1 dXdY, \tag{9}$$

$$M_1^Y = \int_\Omega XP_1 dXdY. \tag{10}$$

The various stiffness of the sliding bearing are defined accordingly as follows: (1) For the normal stiffness K_N, choose $H_1 = 1$, and therefore $K_N = -F_1$, (2) for the pitch stiffness K_P, choose $H_1 = X$, and therefore $K_P = -M_1^Y$, and (3) for the roll stiffness K_R, choose $H_1 = Y$, and therefore $K_R = -M_1^X$.

In a more compact form, the stiffness K can be written as:

$$K = \int_\Omega -H_1P_1 dXdY, \tag{11}$$

where H_1 is, respectively, 1, X or Y.

Thus, the optimization problem consists of finding the three different profiles H_0, larger than one, such that the quantity K is maximum for each case $H_1 = 1$, X or Y.

Using the Lagrange multiplier technique, integral (11) can be rewritten as:

$$K = \int_\Omega [-H_1P_1 + \lambda R_1(P_1) + \mu R_0(P_0)] dXdY, \tag{12}$$

where $\lambda(X, Y)$ and $\mu(X, Y)$ have been introduced to incorporate equations (1) and (7) into the optimization process. By choosing λ and μ to vanish on the boundary $\partial\Omega$, the stiffness K can be rewritten, after integration by parts, as follows:

$$K = \int_\Omega [-H_1P_1 + P_0P_1\nabla\cdot(H_0^3\nabla\lambda) + (P_0H_1 + P_1H_0)\Lambda\cdot\nabla\lambda$$

$$-3H_0^2H_1P_0\nabla P_0\cdot\nabla\lambda - H_0^3P_0\nabla P_0\cdot\nabla\mu$$

$$+P_0H_0\Lambda\cdot\nabla\mu] dXdY. \tag{13}$$

The Euler-Lagrange equations satisfied by λ and μ are

$$P_1\nabla\cdot(H_0^3\nabla\lambda) + H_0\Lambda\cdot\nabla\lambda - H_1 = 0 \text{ in } \Omega$$

$$\lambda = 0 \text{ on } \partial\Omega \tag{14}$$

$$P_0\nabla\cdot(H_0^3\nabla\mu) + H_0\Lambda\cdot\nabla\mu + P_1\nabla\cdot(H_0^3\nabla\lambda)$$

$$+H_1\Lambda\cdot\nabla\lambda + 3P_0\nabla\cdot(H_1H_0^2\nabla\lambda) = 0 \text{ in } \Omega$$

$$\mu = 0 \text{ on } \partial\Omega. \tag{15}$$

Furthermore, since K is maximum, the following condition must hold for any admissible variation δH_0 of the unknown profile

$$\delta H_0 \cdot Q \le 0, \tag{16}$$

where Q is defined as

$$Q = -3H_0^2[\nabla(P_0P_1)\cdot\nabla\lambda + P_0\nabla P_0\cdot\nabla\mu]$$

$$-6H_0(H_1P_0\nabla P_0\cdot\nabla\lambda)$$

$$+P_0\Lambda\cdot\nabla\mu + P_1\Lambda\cdot\nabla\lambda. \tag{17}$$

It can be deduced from inequality (16) that if $H_0 = 1$, then $Q \le 0$; on the other hand, if $H_0 > 1$, then $Q = 0$.

3 Numerical Solutions and Examples

The elliptic differential equations satisfied by the field variables P_0, P_1, λ, and μ are solved by standard finite element technique. The domain Ω is thus divided into a finite number of elements, chosen here to be triangles, and the unknowns become the values of the variable at the element vertices (or nodes). Furthermore, it is assumed in the present approach that the different fields vary linearly within each element (linear interpolation), and that the film thickness H_0 is constant throughout each element.

Since H_1 is known for each case ($H_1 = 1$ in the normal mode, $H_1 = X$ in the pitch mode, and $H_t = Y$ in the roll mode), the only unknown is in fact the gap profile H_0. The existence and uniqueness of an optimal solution for these problems have still to be derived and will not be treated in this paper. However, the typical example of a square gas bearing is presented to illustrate the adopted optimization process which consists of an iterative mapping on the gap profile eventually converging to a solution satisfying inequality (16).

Due to the symmetry of the problem (recall that Λ is parallel to the X-axis) the domain Ω can be reduced to its upper half portion corresponding to $0 \le Y \le 0.5$. Figure 1 shows the uniform triangular mesh for an 800 element discretization. On the axis of symmetry, $Y = 0$, the field variables must now satisfy the Neumann boundary conditions

$$\frac{\partial P_0}{\partial Y} = \frac{\partial P_1}{\partial Y} = \frac{\partial \lambda}{\partial Y} = \frac{\partial \mu}{\partial Y} = 0 \text{ at } Y = 0 \tag{18}$$

for the normal stiffness problem, while different boundary conditions apply in the roll and pitch modes:

$$\frac{\partial P_0}{\partial Y} = P_1 = \lambda = \frac{\partial \mu}{\partial Y} = 0 \text{ at } Y = 0. \tag{19}$$

The algorithm used in the following examples is given as follows (a superscript attached to a variable indicates the number of iterations at which the latter is computed).

- Step 1: Initialize the gap profile $H_0(i = 0)$; simply take $H_0^0 = 1$ everywhere in Ω.
- Step 2: Solve successively for the field variables P_0, P_1, λ, and μ according to equations (1), (7), (14), and (15), respectively, and compute the stiffness K according to equation (11). The numerical solver uses Newton's method with an analytical expression for the Jacobian matrix.
- Step 3: For each element of the domain Ω:
  (a) compute the quantity Q given by

Downloaded 03 May 2010 to 171.66.16.244. Redistribution subject to ASME license or copyright; see http://www.asme.org/terms/Terms_Use.cfm

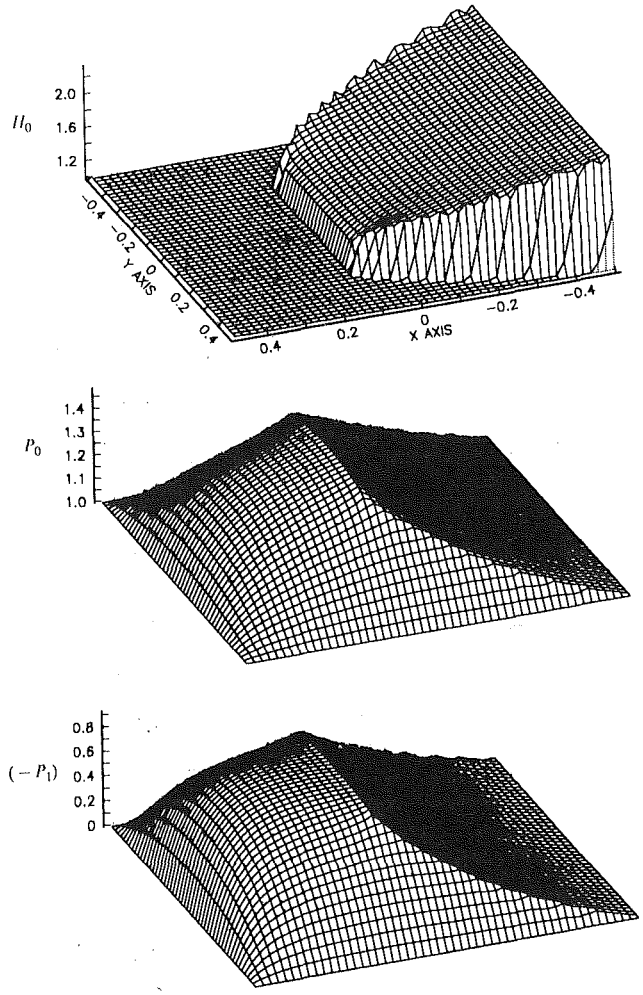


Fig. 2 Optimum gap profile H_0 in the normal mode ($H_1 = 1$) for a bearing number Λ of 10; corresponding pressure distributions P_0 and $(-P_1)$

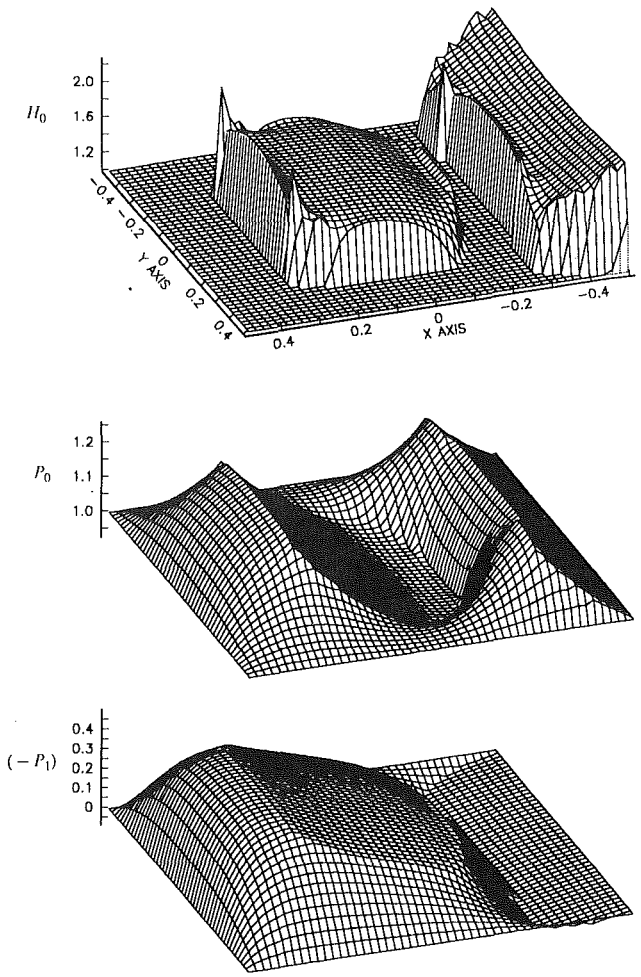


Fig. 3 Optimum gap profile H_0 in the pitch mode ($H_1 = X$) for a bearing number Λ of 10; corresponding pressure distributions P_0 and $(-P_1)$

$$\bar{Q}^i = \frac{\int_A Q^i dXdY}{\int_A dXdY}, \tag{20}$$

where Q^i is given by equation (17) and A represents the element being considered.

(b) map the profile H_0 according to:

$$H_0^{i+1} = (1 + \omega \bar{Q}^i) H_0^i, \tag{21}$$

where ω is a positive relaxation parameter introduced to accelerate the convergence.

(c) truncate H_0^{i+1} for values less than one.

- Step 4: Compute the norm of the change in H_0, defined as:

$$N(H_0^{i+1}) = \max_{\text{element}} |H_0^{i+1} - H_0^i| \tag{22}$$

and compare it to a given small number δ.

- Step 5: If $N(H_0^{i+1})$ is bigger than δ, then go back to Step 2 with $H_0^i = H_0^{i+1}$ and $i = i + 1$.
- Step 6:If $N(H_0^{i+1})$ is less than δ, then exit and print out the results.

A similar algorithm can be found in Robert and Hendriks (1989), where an homogenized externally pressurized gas bearing is optimized to achieve maximum load under the constraint of a given gas volume. Furthermore, the convergence of mapping equation (21) gave the same results as those obtained by Rhode and MacAllister (1976), by slightly modifying the definition of K in order to adopt the same optimization criterion (maximum lift force). In this case, the obtained solution perfectly matches the results previously published. Finally, each time mapping equation (21) is applied, the resulting stiffness computed with the new gap profile has increased. This means that the algorithm presented here is in fact a gradient method: The expression for Q in equation (17) was obtained through the derivative of K with respect to H_0.

Numerical Results for Optimum Normal Stiffness. In this case, H_1 is chosen to be one, and the optimum gap profile H_0 is illustrated in Fig. 2 when the bearing number Λ is 10 and for a 50×50 grid discretization. The convergence of the algorithm is quite fast (less than 300 iterations for $\delta = 10^{-5}$ and $\omega = 0.25$), and the solution is a two-dimensional step-like function very similar to the one found in Rhode and MacAllister (1976). The optimum characteristics of this profile are given as follows in normalized form:

$$\text{Load } F = \int_\Omega [P_0 - 1] dXdY = 0.197306 \tag{23}$$

$$\text{Stiffness } K_N = \int_\Omega -P_1 dXdY = 0.402159. \tag{24}$$

Figure 2 also shows the distribution of the first-order correction term in pressure $(-P_1)$ for which the integral over the domain Ω is maximized.

Numerical Results for Optimum Pitch Stiffness. In pitch

Downloaded 03 May 2010 to 171.66.16.244. Redistribution subject to ASME license or copyright; see http://www.asme.org/terms/Terms_Use.cfm

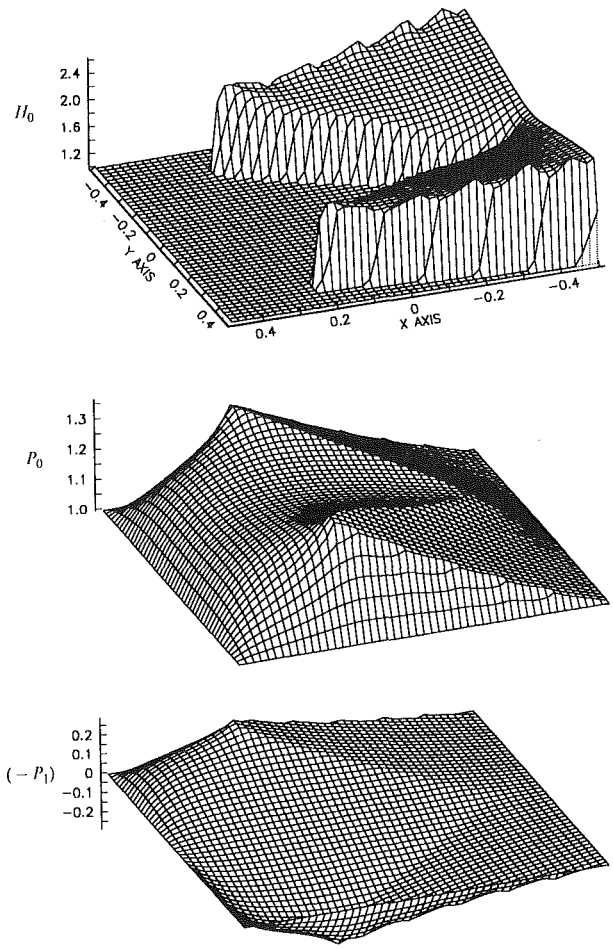


Fig. 4 Optimum gap profile H_0 in the roll mode ($H_1 = Y$) for a bearing number Λ of 10; corresponding pressure distributions P_0 and $(-P_1)$

mode, H_1, is chosen to be X, and the optimum profile H_0 is illustrated in Fig. 3 (bearing number Λ of 10 and grid discretization of 50×50). In this case, the solution is made of a tapered step-like function followed by a disjoint pocket in the center of the pad. The convergence of the optimization process was greatly accelerated by using an ω of 4.4, for which only 343 iterations where required ($\delta = 10^{-5}$). The four peaks located at the downstream corners of the gap profile are thought to be caused by numerical instability, and are not present when a coarse mesh (20×20) is used. The distribution of $(-P_1)$ for which the moment with respect to the Y-axis is maximized, is also presented in Fig. 3. The optimum characteristics of the solution are given next in normalized form.

$$\text{Load } F = \int_\Omega [P_0 - 1] dX dY = 0.070941 \tag{25}$$

$$\text{Stiffness } K_P = \int_\Omega - XP_1 dX dY = 0.374243 \times 10^{-1} \tag{26}$$

Numerical Results for Optimum Roll Stiffness. When H_1 is taken to be Y, the solution for the gap profile is illustrated in Fig. 4 corresponding to a bearing number Λ of 10 and a grid discretization of 50×50. The gap profile is composed of two adjacent step-like functions, each one being similar to the one obtained in the normal mode. Some convergence difficulties occurred when a constant ω is used in the iteration process: The profile H_0 tends to grow indefinitely at the tip of the steps. This phenomenon might be the sign of the existence of a local singularity for this problem, and could be linked to the peaks in the solution for the pitch mode. Nevertheless, a smoother profile can be obtained by using $\omega = |Q|$ in mapping equation (21), although Step 6 is satisfied only for a δ of 2×10^{-4} after 7000 iterations. In any case, the optimum characteristics of the bearing are very similar and are given as follows in normalized form:

$$\text{Load } F = \int_\Omega [P_0 - 1] dX dY = 0.163214 \tag{27}$$

$$\text{Stiffness } K_R = \int_\Omega - YP_1 dX dY = 0.245265 \times 10^{-1}. \tag{28}$$

Figure 4 also shows the distribution of the first-order correction term in pressure $(-P_1)$ for which the moment with respect to the X-axis is maximized.

4 Conclusions

An algorithm for maximizing the static stiffness of a two-dimensional gas bearing has been proposed within the framework of the compressible Reynolds equations. The canonical case of a square bearing has been solved successfully for the three fundamental modes of normal, pitch, and roll stiffness. This algorithm is directly applicable to more complicated geometries for which the results are believed to be similar to the ones presented in this paper. Furthermore, some slight modifications could be added to solve for the optimum gap distributions of more complicated problems such as journal bearings or thrust bearings. Finally, it gives the design engineer a convenient tool for improving the stability of sliding bearings, without solving the complete time-dependent problem.

Acknowledgments

The author would like to express his gratitude to F. Hendriks of the IBM T. J. Watson Research Center for his suggestions and helpful discussions concerning this article.

References

Lord Rayleigh, 1918, "Notes on the Theory of Lubrication," *Philosophical Magazine*, Vol. 35, pp. 1–12.

Maday, C. J., 1968, "The One-Dimensional Optimum Hydrodynamic Gas Slider Bearing," *ASME Journal of Lubrication Technology*, pp. 281–285.

Rodhe, S. M., and McAllister, G. T., 1976, "On the Optimization of Fluid Film Bearings," *Proc. R. Soc. London*, Vol. A351, pp. 481–497.

Robert, M. P., and Hendriks, F., 1990, "Gap Optimization and Homogenization of an Externally Pressurized Air Bearing," *STLE Tribology Trans.*, Vol. 33, No. 1, pp. 41–47.

Downloaded 03 May 2010 to 171.66.16.244. Redistribution subject to ASME license or copyright; see http://www.asme.org/terms/Terms_Use.cfm

Seth Lichter

Arie Dagan

William B. Underhill

Hassan Ayanle

Department of Aerospace and Mechanical Engineering, University of Arizona, Tucson, AZ 85721

Mixing in a Closed Room by the Action of Two Fans

The mixing induced by two constant flow rate fans, which vary periodically in direction, is studied as a function of the period of oscillation of the fans. The three-dimensional equations of motion are integrated to determine the particle trajectories. As first shown by Aref's work on a two-dimensional map, mixing may be greatly enhanced by unsteadiness. It is found that trajectories can be trapped in a restricted region by surfaces which function similarly to KAM tori in two dimensions. Results are presented for the largest Lyapunov exponent and the correlation dimension as a function of oscillation period. These results may be used to determine the conditions for good mixing.

1 Introduction

Aref (1984) has investigated the role of unsteadiness in Lagrangian mixing and illustrated his concept in a simple geometry. Two-dimensional mixing in a circle was induced by two point vortices of equal strength but switched on/off alternately. Both the rate at which the vortices were cycled on/off and their separation distance were varied. An initial square of several thousand particles was allowed to mix into the remainder of the circle by the action of the vortex "stirrers." Aref found mixing greatly enhanced by the proper choice of these two parameters. Qualitatively, the mixing was of two types: inefficient mixing, in which large areas were not close to any of the particles, and efficient chaotic mixing, in which almost the entire area of the circle was close to some particle. Crucial to efficient mixing was unsteadiness; two vortices remaining switched on would not induce chaotic particle trajectories, and mixing was inefficient.

Aref's (1984) idealized geometry had the advantage that the Lagrangian equations could be reduced to a map. The particle positions were then found by successive iterations of the map. Additionally, the flow field was modeled as a potential field, so that the two stirrers, when switched on, immediately altered the velocity field throughout the entire region. Khakhar et al. (1986) extended Aref's observations and related their chaotic diagnostics to quantities, such as line stretching, which are physically relevant in mixing.

The problem here, while inspired by his work, is different from that of Aref (1984) in that, rather than iterating a map, the Lagrangian differential equations of motion are integrated to find the particle positions. Second, the problem here is three-dimensional. Finally, while Aref quantified an intuitive, but subjective, consequence of mixing by measuring the area which appeared to be chaotic, in this paper, the effectiveness of mixing is given in terms of two chaotic diagnostics that directly measure the volume which is brought within the neighborhood of the particles and material line stretching.

The practical motivation for this work is optimizing mixing rates in clean rooms. Localized high (or low) concentrations might not be sampled by a fixed probe monitoring particle concentration; when mixed, however, a single probe measurement is indicative of the room's mean particle concentration. In contrast to a typical clean room, however, we consider, in this first paper, only a closed room with no inflow and outflow through the boundaries.

The paper is arranged as follows. In Section 2, we first discuss the underlying physics before presenting the formulation in Section 3. The implementation of the numerical code is discussed in Section 4. The results are presented and discussed in Section 5.

2 Modeling

Mixing in air is often accomplished by a blower or fan. A practical means to achieve the unsteadiness necessary for chaotic mixing is to consider those types of fans, in common usage, which oscillate to and fro in the horizontal plane. The fans, then, deliver a constant mass flow rate with an orientation which varies periodically in time.

Before attempting any mathematical model, let us first sketch the underlying physical phenomena controlling the flow field. For simplicity, consider a single fan with a fixed orientation in a closed room. The fan generates vorticity that is convected downstream and, in the closed room, ultimately dissipates or finds itself back at the fan. The fluid recirculating through the fan, then, possesses vorticity, which is increased by the action of the fan blades. This accretion of vorticity is limited by viscous dissipation which will, in the steady state, balance the generation of vorticity. So it can be expected that in the steady state and for moderately high Reynolds numbers, the vorticity

Contributed by the Applied Mechanics Division of THE AMERICAN SOCIETY OF MECHANICAL ENGINEERS for publication in the JOURNAL OF APPLIED MECHANICS.

Discussion on this paper should be addressed to the Technical Editor, Leon M. Keer, The Technological Institute, Northwestern University, Evanston, IL 60208, and will be accepted until two months after final publication of the paper itself in the JOURNAL OF APPLIED MECHANICS. Manuscript received by the ASME Applied Mechanics Division, Aug. 9, 1988; final revision, June 29, 1989.

Copyright © 1990 by ASME

Downloaded 03 May 2010 to 171.66.16.244. Redistribution subject to ASME license or copyright; see http://www.asme.org/terms/Terms_Use.cfm

distribution is highly concentrated in the jet and of much lower value in the bulk of the room volume.

The modeling may now be thought of as a singular perturbation. In the jet, where vorticity is large, the viscous model of the jet is used as the inner solution; the velocity profile is given by the steady-state viscous solution of a free turbulent jet (Schlichting, 1968). This profile is then matched to an inviscid outer solution that is due to a distribution of sinks whose strength is given by the entrainment along the jet. The limit of the outer solution along the jet axis is the viscous jet velocity profile. The limit of the inner solution at infinity is the irrotational velocity induced by the sink distribution.

Of course, it is not strictly correct to use the infinite jet to portray the jet in a closed room. However, only the case where the jet radius is small compared to the characteristic room size is considered.

The two components of the flow field, the viscous jet and the far field, can now be described in detail. In order to clarify the formulation, the problem of the oscillating fans in a room is approached by considering a fan of fixed orientation first (a) in an infinite domain, then (b) impinging on a wall, and then (c) in a closed room. Finally, two oscillating fans are placed in the room.

First consider a fan in an infinite domain. Using lifting surface theory, the vorticity of the fan blades is advected as the downwash (also called the slipstream or jet) of the fan (Durand, 1963). This downwash has a helical formation, but when its normal velocity is small compared to its angular velocity, the pattern of vorticity can be viewed more simply as a sequence of ring vortices. Under these assumptions, the jet region generated by the fan can be modeled as

$$\mathbf{u} = -\frac{1}{4\pi}\int_0^\infty \frac{\partial \Gamma}{\partial r}\sum_i \oint \frac{(\mathbf{x}-\mathbf{x}_i)\times d\mathbf{x}_i}{|\mathbf{x}-\mathbf{x}_i|^3}\,dr, \tag{1}$$

where Γ is the circulation along the fan blades; $\mathbf{x}_i = (r\cos\theta, r\sin\theta, iU\Delta t)$; (r, θ) are polar coordinates; the path for the line integral is $[0, 2\pi]$; and, anticipating the difference equations needed for the numerical computation, Δt is the time-step size. The sum in equation (1) can be approximated as

$$\mathbf{u} = -\frac{1}{4\pi}\int_0^l \frac{\partial \Gamma}{\partial r}\int_0^\infty \frac{1}{U\Delta t}\oint \frac{(\mathbf{x}-\mathbf{x}_1)\times d\mathbf{x}_1}{|\mathbf{x}-\mathbf{x}_1|^3}\,d\mu\,dr + \Theta(\Delta t)^2, \tag{2}$$

where $\mathbf{x}_1 = (r\cos\theta, r\sin\theta, \mu)$, U is the local velocity in the x_1-direction, and for $r > l$, the vorticity is considered negligible. A ring vortex is equivalent to a distribution of normal dipoles over the area, A, enclosed by the vortex (Lamb, 1945; Batchelor, 1970), so equation (2) can be rewritten as

$$\mathbf{u} = -\frac{1}{4\pi}\int_0^l \int_0^\infty \frac{\partial \Gamma}{\partial r}\frac{1}{U\Delta t}\frac{\partial}{\partial \mu}\oiint \nabla \frac{1}{|\mathbf{x}-\mathbf{x}_1|}\,dA\,d\mu\,dr, \tag{3}$$

where ∇ is the gradient operator. After integration by parts, the right-hand side describes a line distribution of sinks. Those sinks lying along the axis of the jet represent the entrainment velocity, and a sink located in the neighborhood of the fan represents the mass flux through the fan. The flow field outside the jet can be taken to be that due to the velocity induced by the sink distribution.

Consider now the problem of a jet impinging on a wall. It is desirable to use linear superposition; but, due to the nonlinearity of the vorticity equation, it appears inappropriate. However, considering the case in which the jet radius is small compared to the characteristic of the room, the vorticity is concentrated in the small volume of the jet, while the larger remaining volume has very little vorticity. So, linear superposition offers a reasonable approximation everywhere except in the interaction region of the jet itself.

It is known that since the ring vortex system is advected by the local velocity, the ring vortex radius will increase in the neighborhood of a wall as a result of the radial component advection. This suggests that the physical picture of the jet as a distribution of ring vortices that are distributed in the jet region, and which represent the viscous core of the jet even when the jet is enclosed in a room, can be maintained. In order to complete the picture, the sink distribution is limited in extent to the distance, L, between the fan and the wall. Additionally, a source distribution is placed at the wall in order to ensure no mass flux through the wall. The distribution will have the property that the total source strength will be of exactly the same magnitude as the total sink distribution.

Under these considerations, equation (3) is reduced to a finite integral over $(0, L)$

$$\begin{aligned}\mathbf{u} = {} & \frac{1}{4\pi}\int_0^l \frac{\partial \Gamma}{\partial r}\frac{1}{U\Delta t}\oiint \nabla \frac{dA}{|\mathbf{x}-\mathbf{x}_1|}\,dr\Big|_0 \\ & + \frac{1}{4\pi}\int_0^L \int_0^l \frac{\partial \Gamma}{\partial r}\frac{\partial}{\partial \mu}\left(\frac{1}{U\Delta t}\right)\oiint \nabla \frac{dA}{|\mathbf{x}-\mathbf{x}_1|}\,dr\,d\mu \\ & - \frac{1}{4\pi}\int_0^l \frac{\partial \Gamma}{\partial r}\frac{1}{U\Delta t}\oiint \Delta \frac{dA}{|\mathbf{x}-\mathbf{x}_1|}\,dr\Big|_L.\end{aligned} \tag{4}$$

In the far field, $|\mathbf{x}| \to \infty$,

$$\begin{aligned}\mathbf{u} = {} & \frac{Q_0}{4\pi}\nabla \frac{1}{\sqrt{x^2+r^2}} + \frac{1}{4\pi}\int_0^L q\nabla \frac{1}{\sqrt{(x-\lambda)^2+r^2}}\,d\lambda \\ & - \frac{Q_1}{4\pi}\nabla \frac{1}{\sqrt{(x-L)^2+r^2}},\end{aligned} \tag{5}$$

where, in both equations (4) and (5), the first expression describes the mass flux through the fan, the second is the entrainment function of the jet, and the source term guarantees zero normal velocity at the wall. In other words, the last integral guarantees the kinematic boundary condition at the wall. In practice, Q_0 would be specified as the strength of the fan; q is evaluated next as the entrainment function and

$$Q_0 + qL = Q_1. \tag{6}$$

Now, consider the fan enclosed in a room. The source distribution on the wall balances the sink distribution of the entraining jet, so the net flux into the room is zero. However, due to the presence of the other walls, image jet and source distributions must be placed outside the room. The placement of the images follows well-known procedures.

3 Formulation

We now proceed to the formal derivation of the governing equations. The flow inside the jet (the inner solution) can be represented by the velocity profile of a turbulent jet (Schlichting 1968),

$$u_s = \frac{3}{8\pi}\frac{K}{\epsilon_o x}\frac{1}{\left(1+\frac{1}{4}\beta^2\right)^2} \tag{7}$$

$$v_s = \frac{1}{4}\sqrt{\frac{3K}{\pi}}\frac{1}{x}\frac{\beta+\frac{1}{4}\beta^3}{\left(1+\frac{1}{4}\beta^2\right)^2} \tag{8}$$

where

$$K = 2\pi\int_0^\infty u_s^2\, r\, dr,$$

$$\beta = \frac{1}{4}\sqrt{\frac{3}{4}\frac{K}{\epsilon_0}}\frac{r}{x},$$

Downloaded 03 May 2010 to 171.66.16.244. Redistribution subject to ASME license or copyright; see http://www.asme.org/terms/Terms_Use.cfm

u_s and v_s are the axial and radial velocities of the jet, respectively, and from measurements, $\epsilon_0 = 0.0161\sqrt{K}$. It is worthwhile to notice that these components define the ring vortex distribution in any cross-section along the jet. The radial velocity can be easily verified as

$$\lim_{r\to\infty} v_s = -\frac{4\epsilon_0}{r}. \tag{9}$$

This velocity determines the entrainment of the jet. The sink distribution of the outer solution can be reduced after some calculation to

$$v_s = -\lim_{r\to 0}\frac{q}{4\pi}\int_0^L \frac{r\,d\lambda}{\left[(x-\lambda)^2+r^2\right]^{3/2}} = -\frac{q}{2\pi r}+\mathcal{O}(r^2). \tag{10}$$

By matching the inner solution to the outer solution,

$$q = 8\pi\epsilon_0. \tag{11}$$

The mass source distribution, q_1, can now be found by using the kinematic boundary condition where, for a wall at $x = L$,

$$\frac{1}{4\pi}\int\int \frac{q_1(x-L)\,d\tilde{y}_1 d\tilde{z}_1}{\left[(x-L)^2+(y-\tilde{y}_1)^2+(z-\tilde{z}_1)^2\right]^{3/2}} + u_0 = 0, \tag{12}$$

where u_0 is the normal velocity component on the wall that would result from Q_0 and q in an infinite domain at the wall location. The integral is evaluated for $x \to L$, yielding

$$q_1 = 2u_0(\tilde{y}_1,\tilde{z}_1), \tag{13}$$

where $\tilde{y}_1$, $\tilde{z}_1$ are in the plane of the wall. For the far-field solution, the contribution of all the sources of q_1 yields

$$Q_1 = \int\int q_1 d\tilde{y}_1 d\tilde{z}_1. \tag{14}$$

For an oscillating fan, it is necessary that the source and sink distributions move in order to coincide with the jet axis.

The method to solve this problem, then, is that the inner solution generates the outer solution. Higher-order approximations could be found to correct for the effect of the outer solution in the neighborhood of the inner solution. However, to lowest order, the inner and outer solutions can be described as

$$u_I = -\frac{Q_0}{4\pi}\frac{x}{(x^2+r^2)^{3/2}} + u_s - \frac{q}{4\pi}\left\{\frac{1}{\sqrt{(L-x)^2+r^2}} - \frac{1}{\sqrt{x+r^2}}\right\} + \frac{Q_1}{4\pi}\frac{L-x}{\left[(L-x)^2+r^2\right]^{3/2}} \tag{15}$$

$$v_I = -\frac{Q_0}{4\pi}\frac{r}{(x^2+r^2)^{3/2}} + \frac{v_s}{2}\left\{\frac{L-x}{\sqrt{(L-x)^2+r^2}} + \frac{x}{\sqrt{x^2+r^2}}\right\} + \frac{Q_1}{4\pi}\frac{r}{\left[(L-x)^2+r^2\right]^{3/2}}. \tag{16}$$

The first term on the right-hand side of equations (15) and (16) represents the velocity field due to a sink located at the fan. In equation (15), in the neighborhood of the jet, u_s dominates the third term, which describes the potential due to entrainment in the far field. Similar arguments apply to equation (16), for which the second term represents the flow due to entrainment. It is easy to verify that this term behaves asymptotically in the neighborhood of the jet as equation (7), while for the far field, $v_s \sim 1/r$, and this term is asymptotic to the potential flow distribution. The last term in both equations is due to the source distribution on the wall.

These equations are the basic unit flow used to generate the images. First, recall that for each fan, x is along the jet axis, r is the radial coordinate measured from the x-axis, and α is the angle that the jet makes with the X-axis. By a coordinate transformation, we must express this velocity in terms of the coordinates fixed to the room geometry, Fig. 1, where X is along the longest dimension of the room and Y is normal to both X and the vertical, Z. The dimensions of the room are (L, L_y, L_z). The two fans are located at (ξ_1, η_1, ζ_1) and (ξ_2, η_2, ζ_2). The volume flow rate through each fan is Q_0. The fans oscillate with frequency ω in the (X, Y)-plane, where α is the angle the fan makes with the X-axis.

Considering now only the fan located at (ξ_1, η_1, ζ_1), define

$$\mathbf{u}_H(X',Y',Z') = \mathbf{u}_I(X-\xi_1,Y-\eta_1,Z;\alpha) + \mathbf{u}_I(X+\xi_1,Y-\eta_1,Z;\pi-\alpha) + \mathbf{u}_I(X-\xi_1,Y+\eta_1,Z;\pi+\alpha) + \mathbf{u}_I(X-\xi_1,Y+\eta_1,Z;\pi-\alpha) \tag{17a}$$

$$\mathbf{u}_D(X'',Y'',Z'') = \mathbf{u}_H(X',Y',Z-\zeta_1) + \mathbf{u}_H(X',Y',Z+\zeta_1), \tag{17b}$$

where the coordinate involving α in equation (17a) sets the angle of the image jet with respect to the X-axis. Using these definitions, the final form for the distributions of images can be written simply as

$$\mathbf{u} = \sum_k\sum_m\sum_n U_D(X''-kL, Y''-mL_y, Z''-nL_z)$$

where k, m, and n take on all even values. A similar set of equations applies for the fan at (ξ_2, η_2, ζ_2).

To summarize, a jet in a closed room is approximated by using sink and source distributions for the far-field solution and the inner solution is described by the viscous solution of the jet. This model is physically acceptable for two jets operating in the same room (by the arguments given earlier) if the viscous regions of the jet are small.

4 Numerical Scheme

Due to the action of the fans, computation of the velocity field in the closed room requires substantial computer oper-

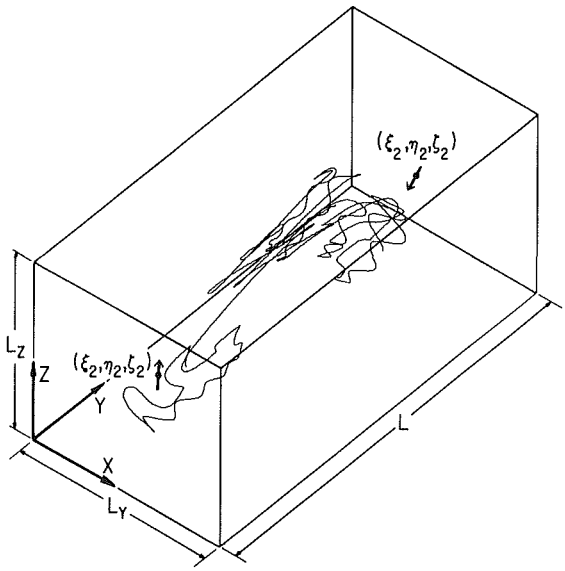


Fig. 1 The geometry and coordinate system used for the room, and the location of the fans

Downloaded 03 May 2010 to 171.66.16.244. Redistribution subject to ASME license or copyright; see http://www.asme.org/terms/Terms_Use.cfm

ations, $\mathcal{O}(N^3)$. It is therefore imperative to use a predictor method rather than a predictor corrector.

The Lagrangian system is written

$$\frac{d\mathbf{x}}{dt} = \mathbf{u}, \tag{18}$$

where $\mathbf{x} = (x, y, z)$ and $\mathbf{u} = (u, v, w)$. For computation, the velocity field is written in terms of the Lagrange interpolation polynomial (Isaacson and Keller, 1966)

$$\frac{dx}{dt} = \sum_{j=0.}^{u} u_j \prod_{k=0, k\neq j}^{n} \frac{t-t_k}{t_j-t_k} + R_n(t), \tag{19}$$

where the residual is given by

$$R_n(t) = \prod_{k=0}^{n} \frac{t-t_k}{(n+1)!} \frac{d^{(n+1)}}{dt^{(n+1)}} u(n+1)(\xi)$$

where $\min(x_0, x_1, \ldots, x_n) \leq \xi < \max(x_0, x_1, \ldots, x_n)$. Choosing $n = 3$ in the above scheme, the previously computed results for (u_0, u_1, u_2, u_3) are used to predict x_4; the velocity, u_4, is then computed at the new location, x_4; and the integration is carried further using (u_1, u_2, u_3, u_4) in order to compute x_5 and u_5, and so on.

As previously noted, $\mathcal{O}(N^3)$ operations are required. In order to speed up the computations, the time-step size is adjusted at each step according to the value of the residual at each step. However, since the residual expression requires solution by Newton-Raphson, the order of the residual is approximated as

$$R_n = \mathcal{O}\left(\Delta t^n \frac{d^n u}{dt^n}\right), \tag{20}$$

where the value of $d^n u/dt^n$ is approximated by Lagrange interpolation as

$$\frac{d^n}{dt^n} = \sum_{j=0}^{n} u_j \prod_{k=0, k\neq j}^{n} \frac{d^n}{dt^n} \frac{t-t_k}{t_j-t_k}.$$

This approximation, as an $(n-1)$ degree polynomial, results in a more restringent restriction of the time-step size. The norm of the residual compared to the maximum step size was limited to less than 10^{-3}

$$\Delta t^n \frac{\dfrac{d^n|u|}{dt^n}}{|x^{n+1}-x^n|} < 10^{-3}. \tag{21}$$

Using this criteria, however, we found, from testing the code in a case in which the particle paths should have formed closed loops, that when the value of $|u|$ was small, sometimes the error was unacceptably large. As a result, the final form for the step-size selection is

$$\Delta t = \min\left\{ |x^{n+1}(\Delta t) - x^n| < \delta, \frac{\Delta t^n \dfrac{d^n|u|}{dt^n}}{|x^{n+1}-x^n|} < \epsilon \right\}. \tag{22}$$

This expression, then, chooses Δt as the minimum of either the spatial step or the truncation error. The values of $\delta = \epsilon = 10^{-3}$ were found from a sensitivity check such that the truncation error was insensitive to changes in these values.

Approximately 6 seconds of CPU time on a Data General MV10000 were required to compute the velocity field for each time-step. The typical computational time varied as a function of ω, where for $\omega = 10$ about 500 time-steps were required for a particle to move a distance the order of the room length and for $\omega = 100$, 6000 time-steps were required. Unfortunately, as can be seen, for fans oscillating at large frequencies, ω, a great many time-steps are needed to resolve the sharp gradients produced.

5 Results

Particle trajectories and values of the correlation dimension and largest Lyapunov exponent are presented as a function of the nondimensional period

$$T = \frac{2\pi}{\omega} = \frac{8Q}{D^2 L \omega^*},$$

where $D = 0.1$ is the diameter of the fan, $Q = 0.1$ is the volume flow rate through the fan, L is the length of the room, and ω^* is the dimensional angular frequency of the fan oscillation. The fans are located at opposite ends of a room $[(\xi_1, \eta_1, \zeta_1) = (0.2, 0.5, 0.5), (\xi_2, \eta_2, \zeta_2) = (1.8, 0.5, 0.5)]$ of geometry $(L, L_y, L_z) = (2, 1, 1)$, Fig. 1. The fans oscillate through an angle of 0.17 rads in the X-Y plane. Results are presented for $10^{-2} < T < 10^4$, which extends over the range of practical interest.

5.1 Correlation Dimension. A direct measure of the volume in the neighborhood of mixed particles is obtained by measuring the correlation dimension of long, three-dimensional trajectories. It became evident that standard box-counting techniques would not converge without at least 500,000 points along the trajectory. Hence, a modified correlation integral method was implemented to reduce the number of points required to obtain the correlation dimension (Grassberger and Procaccia, 1983). The correlation integral method produces a more physical measure than the fractal (Hausdorff) dimension because it is weighted according to the concentration of points throughout the volume. Therefore, an inhomogeneous distribution of points will have a smaller correlation dimension that a homogeneous distribution of points occupying the same space. This is consistent with what is desired of a mixing measure, since a homogeneous distribution represents better mixedness.

Dimension measurements have traditionally been performed exclusively on volume-contracting dissipative flows, where trajectories ultimately become confined to attracting regions called attractors. In fact, the dimension measurement has been quite successful on strange attractors that contain bounded, yet chaotic, trajectories which diverge exponentially with time. These strange attractors have characteristic self-similar structures that reappear on finer and finer scales, thereby giving them the same dimensionality at all sufficiently small scales. Consequently, when the correlation integral $C(l)$ is plotted logarithmically, a straight line results which has a slope equal to the correlation dimension at small length scales.

Although volume-preserving Hamiltonian systems are not dissipative, it has been shown that the phase space consists of regular trajectories and regions of stochastic (chaotic) trajectories with regular trajectories separating the regions of stochasticity (Dombre et al., 1986). An intricate structure of regular trajectories gives rise to islands surrounded by stochastic regions. Furthermore, a self-similar island structure recurs on finer scales, thus allowing stochastic trajectories to only fill a finite portion of phase space. This suggests that dimension measurements may be used on flows in Hamiltonian systems, as well as in dissipative systems.

While our measurements are too crude to produce a flow that falls into the framework of analysis that predicts invariant KAM surfaces and the nested island structure, we observe some qualitatively similar structure that prevents some parts of the room from being visited by particle trajectories. Therefore, we believe that a standard measurement for volume filling, such as the correlation dimension, can be useful when used with care.

Due to the difficulty of calculating trajectories for many particles, we assume that one long trajectory fills the room in a way similar to many distinct particles. We realize that this is indeed not the case since particles can remain trapped in certain regions that depend on initial particle positions. Nevertheless, we found that this was unimportant for dimension

Downloaded 03 May 2010 to 171.66.16.244. Redistribution subject to ASME license or copyright; see http://www.asme.org/terms/Terms_Use.cfm

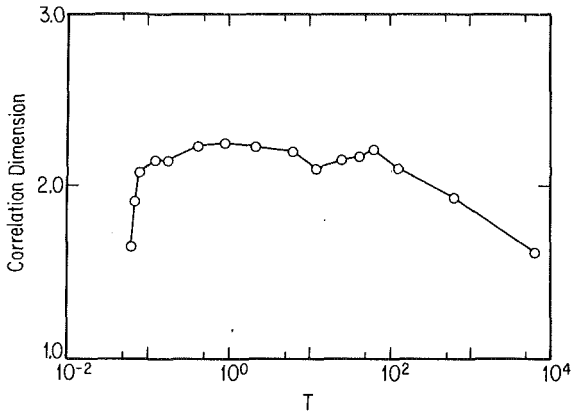


Fig. 2 Correlation dimension as a function of fan oscillation period, T

measurement because, due to symmetry, each trapping region was filled identically.

The correlation curves [ln $C(l)$ versus ln l] for the trajectories typically display two linear ranges with a transition range in between. The dimension measured in the upper range gives an indication of the amount of large-scale mixing that is occurring. Figure 2 shows that the dimension in the large-scale range is nearly constant and falls off only at large and small T. The small decrease near $T = 12$ and at large and small T appears to be the result of trajectories becoming more regular, thereby filling the volume inhomogeneously.

The small-scale linear range is bounded by $l = 2^{-5}$ and $l = 2^{-8}$. In this range of length scales, the dimension is approximately constant and is equal to about 1.1. This result can be predicted for any finite-length trajectory because boxes of size $l < 2^{-5}$ typically contain only one trajectory element. The trajectory is slightly greater than one-dimensional at these scales because some crossings (i.e., more than one element in a box) are inevitable.

5.2 Particle Trajectories. As mentioned previously, some of the features of flows in near-integrable systems can be observed of the particle trajectories presented here. In particular, separate regions of regular and stochastic motion are observed. Also, barriers that appear similar to KAM invariant surfaces prevent motion across certain surfaces, thereby isolating distinct stochastic regions of good local mixing. Therefore, in some of what follows, the well-understood Hamiltonian theory is used to aid, by analogy, the understanding of the particle dynamics. In addition, an argument based on the fluid motion also suggests that, due to the flow symmetry, regions of good mixing will be disconnected.

Consider the steady case, $T \to \infty$, and the axes of both fans aligned. Then, the midplanes $z = 0.5$ and $x = 1.0$ represent plane surfaces through which no streamlines pass. These planes are themselves limiting stream surfaces. For the cases presented here, T finite, these surfaces will continue to function as barriers to motion of the trajectories, until a sufficient perturbation is achieved (Fig. 3). For the smallest periods, the perturbations, though of high frequency, are small perturbations about a mean trajectory, and the trajectory is trapped in one-quarter of the room (Fig. 3(*a*)). As the period is increased, the trajectory is found throughout the lower half of the room (Fig. 3(*b*)). For a further increase in period, the trajectory penetrates through the horizontal midplane (Fig. 3(*c*)).

A similar effect was reported in the analysis of chaotic mixing in the Aref-blinking-vortex system (Khakhar et al., 1986). Their analysis revealed the existence of KAM curves that restrict the movement of particles into isolated chaotic regions. In fact, regions of good local mixing were practically isolated from one another at flow strengths where KAM curves had all been destroyed. The barriers separating these regions became evident when blobs of particles were released in different isolated regions of good mixing.

It appears that, in the present study, separatrix surfaces that divide the room into fourths become more tenuous as the period increases. The barrier that inhibits motion from the left to the right halves of the room, the $X = 1.0$ plane, disappears at an oscillation period of approximately 0.2, and the barrier that inhibits motion from the top to bottom halves disappears at $T = 1.1$. Assuming that the perturbation strength in the Hamiltonian increases with oscillation period, an analogy to dynamics of near-integrable Hamiltonian systems can help one understand the transition to global chaos within the closed room. Referring to a region of stochasticity that forms on either side of a separatrix as a resonance layer (Lichtenberg and Lieberman, 1983), stochastic resonance layers exist in the mixing room flow and nearly parallel the separatrices. Stochastic motion on a smaller scale exists in thin layers centered on the separatrices as well. The thickness of the resonance layers and the stochastic regions on the separatrices increases with increasing perturbation strength and leads to an overlap of the stochastic regions. This allows motion across the layers and the occurrence of motion throughout a larger portion of the room. The growth and overlap of the layers near the two separatrix surfaces apparently occurs at different rates, leading to the disappearance of the two barriers at different oscillation periods.

While the foregoing analysis helps to explain the general characteristics of the trajectories through transition to global chaos, it does not explain the trapping in the lower half of the room that sometimes occurs after transition. It was found that as the oscillation period increased, trapping became less common, but not entirely predictable. Therefore, it is reasonable to assume that the overlap of stochastic layers does not guarantee that the trajectories will cross the barriers, but increases the probability that they will.

5.3 Lyapunov Exponents. A common measure of the amount of mixing that is occurring in a system is based on the idea that good mixing will occur if material lines are rapidly stretched. In a closed region, divergence of trajectories due to stretching will cause particles to visit most parts of the volume on a large scale, while diffusion controls the rate of small-scale mixing. Therefore, the rate of material line stretching can be a good indication of the amount of mixing that will occur in a given time. The Lyapunov exponents are a convenient measure of the average rate of material line stretching.

Algorithms that allow the estimation of the non-negative part of the Lyapunov spectrum for a time series have been published (Wolf et al., 1985). A computer code based on the finite-evolution-time algorithm for the estimation of the largest positive exponent was developed and used on the mixing room data. Figure 4 shows that the Lyapunov exponent attains a maximum value when $T = 47$. Otherwise, the behavior for $T < 47$ resembles that of the exponents calculated for the Aref-blinking-vortex system. In particular, there is a general increase of the exponent with increasing period, interrupted by narrow regions of relatively poor stretching. Khakhar et al. (1986) associate these local minima with bifurcations that cause basic changes in the behavior of the system. Specifically, one of their local minima occurs at a flow strength where there is transition to global chaos. Likewise, the local minima of the exponent for the mixing room trajectories at $T \cong 0.2$ and $T \cong 1.1$ are associated with oscillation periods where trapping causes basic changes in the flow. In particular, the minimum at $T \cong 0.2$ marks the transition from trajectories typically filling only one corner of the room, Fig. 3(*a*)), to those filling one-half, Fig. 3(*b*)); for $T \gtrsim 1.1$, the trajectories fill the entire room (Fig. 3(*c*)).

Downloaded 03 May 2010 to 171.66.16.244. Redistribution subject to ASME license or copyright; see http://www.asme.org/terms/Terms_Use.cfm

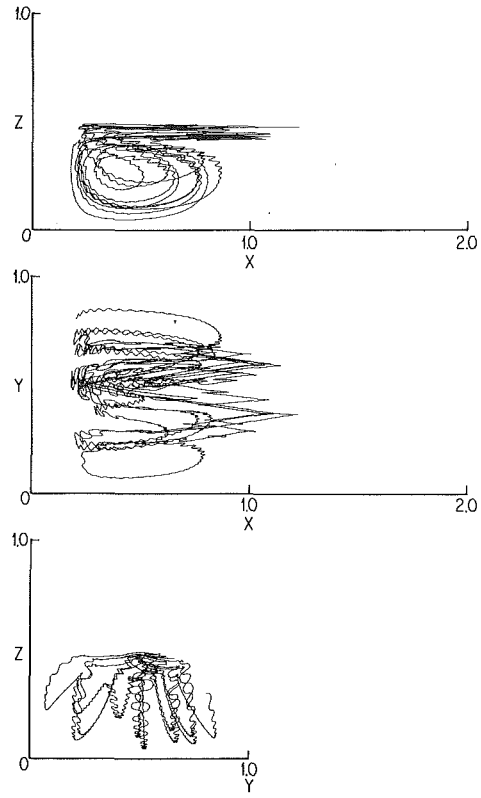


Fig. 3(*a*)

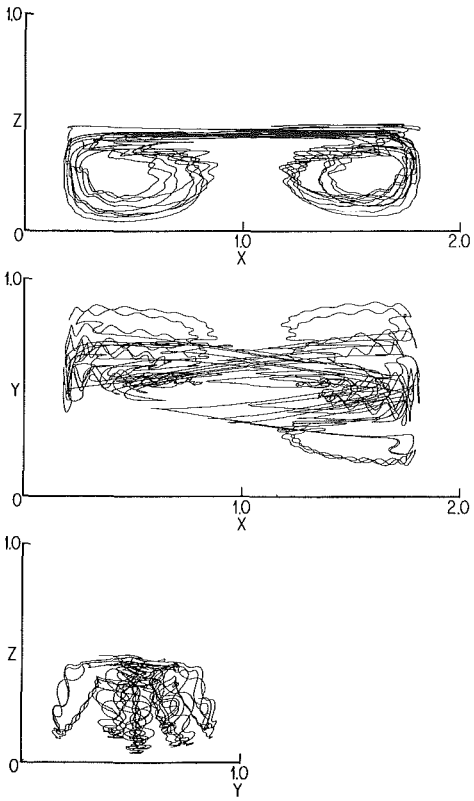


Fig. 3(*b*)

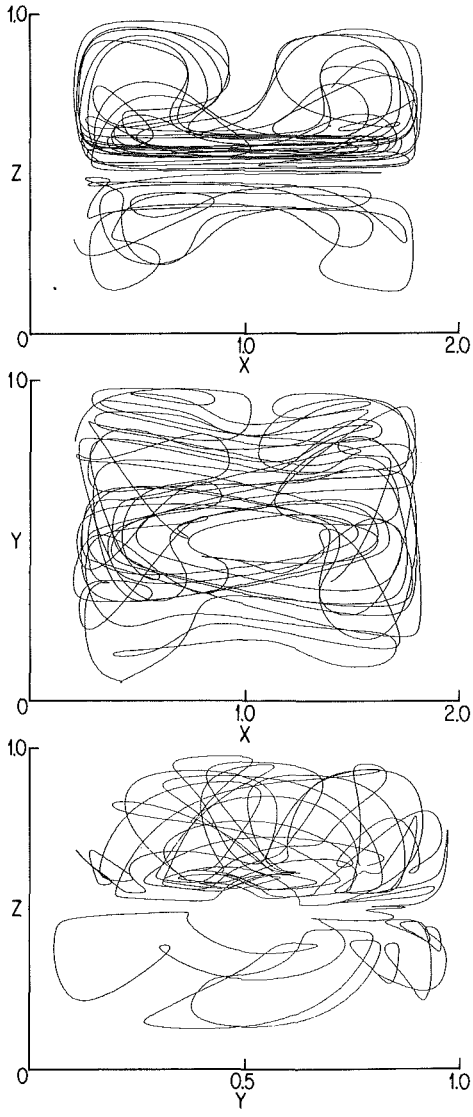


Fig. 3(*c*)

Fig. 3 Typical particle trajectories: (*a*) $T < 0.2$, with the particle trapped in one-quarter of the room; (*b*) $0.2 < T < 1.1$, with the trajectory filling the lower half of the room; (*c*) $T > 1.1$, for which the particle trajectory fills the entire volume

5.4 Discussion. Note that a simple dimensional argument would imply that mixing throughout the upper or lower half of the room would take place for those time scales, T_3 greater than that given by the characteristic length scale of the room, L, divided by the characteristic velocity, $4Q/\pi D^2$. This suggests good mixing for $T \geq 0.16$. This value is close to the numerical value noted above for which the trajectory typically fills the entire volume.

Though the curve presented in Fig. 4 is qualitatively similar to Khakhar et al.'s (1986) Fig. 14(*a*), the results here show some anomalously low values. The widths of the troughs at $T = 0.63$, 2.1, and 9.0 are narrow, however, indicating a sensitivity to initial conditions. This implies that in any real mixing process with a distribution of particles, these sharp troughs would not be significant (Bennetin et al., 1980).

For $T > 47$, the Lyapunov exponent falls off and at $T = \infty$ was found to be nearly zero, $L = 0.024$. This behavior is in contrast to that of the Aref-blinking-vortex system, where no single maximum was found and the exponent was found to continuously increase.

In conclusion, the mixing due to two unsteady fans was modeled by using the turbulent viscous similarity solution to generate the velocity field in a closed room. Both the Lyapunov exponents and correlation dimensions are useful for the evaluation of mixing processes. The correlation dimension gives a measure of the amount of volume filled by particles, while the

Downloaded 03 May 2010 to 171.66.16.244. Redistribution subject to ASME license or copyright; see http://www.asme.org/terms/Terms_Use.cfm

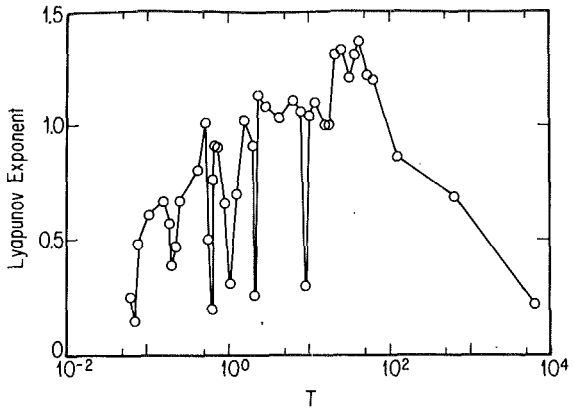


Fig. 4 Lyapunov exponent as a function of oscillation period, T. The typical trajectory is trapped in one corner of the room for $T < 0.2$ and moves throughout the entire volume for $T > 1.1$.

Lyapunov exponents give a measure of the rate of mixing due to the stretching of material lines. Hence, a large correlation dimension combined with a large Lyapunov exponent implies good mixing conditions. For a particular mixing process, the economic or energetic constraints will dictate how these measures should be weighted (Chien et al.,1986; Khakhar et al., 1986).

Acknowledgments

The authors thank George K. Batchelor, Andrew J. Bernoff, and Arne J. Pearlstein for several useful discussions. Rodney James helped significantly in some of the numerical coding. This work was supported by the Center for Microcontamination Control, University of Arizona.

References

Aref, H., 1984, "Stirring by Chaotic Advection," *J. Fluid Mech.*, Vol. 143, pp. 1–21.

Batchelor, G. K., 1970, *An Introduction to Fluid Dynamics*, Cambridge University Press, Cambridge, U.K.

Bennetin, G., Galgani, L., Giorgilla, A., and Strelcyn, J-M., 1980, "Lyapunov Characteristic Exponents for Smooth Dynamical Systems and for Hamiltonian Systems; A Method for Computing All of Them. Part 2: Numerical Application," *Meccanica*, Mar. 21–30.

Chien, W.-L., Rising, H., and Ottino, J.-M., 1986, "Laminar Mixing and Chaotic Mixing in Several Cavity Flows," *J. Fluid Mech.*, Vol. 170, pp. 355–377.

Dombre, T., Frisch, U., Greene, J. M., Hennon, M., Mehr, A., and Soward, A. M., 1986, "Chaotic Streamlines in the ABC Flows," *J. Fluid Mech.*, Vol. 167, pp. 353–391.

Durand, W. F., ed., 1963, *Aerodynamic Theory, A General Review of Progress*, Vol. 4, Dover Publications, New York.

Grassberger, P., and Procaccia, I., 1983, "Measuring the Strangeness of Strange Attractors," *Physica 9D*, pp. 189–208.

Isaacson, E., and Keller, H. B., 1966, *Analysis of Numerical Methods*, John Wiley and Sons, New York.

Khakhar, D. V., Rising, H., and Ottino, J. M., 1986, "Analysis of Chaotic Mixing in Two Model Systems," *J. Fluid Mech.*, Vol. 172, pp. 419–451.

Lamb, H., 1945, *Hydrodynamics*, Dover Publications, New York.

Lichtenberg, A. J., and Lieberman, M. A., 1983, *Regular and Stochastic Motion*, Springer-Verlag, New York.

Lieberman, M. A., and Tennyson, J. L., 1982, "Chaotic Motion Along Resonance Layers in Near-Integrable Hamiltonian Systems with Three or More Degrees of Freedom," in Non-Equilibrium Problems in Statistical Mechanics, Vol. 2, W. Horton, L. Reichl, and V. Szebebely, eds., John Wiley and Sons, New York.

Schlichting, H., 1968, *Boundary-Layer Theory*, 6th ed. McGraw-Hill, New York.

Wolf, A., Swift, J. B., Swinney, H. L., and Vastano, J. A., 1985, "Determining Lyapunov Exponents from a Time Series," *Physica 16D*, pp. 285–317.

Downloaded 03 May 2010 to 171.66.16.244. Redistribution subject to ASME license or copyright; see http://www.asme.org/terms/Terms_Use.cfm

The Meniscus Instability in Non-Newtonian Negative Squeeze Films

Hideo Koguchi
Associate Professor.

Toshio Yada
Professor.

Department of Mechanical Engineering,
Nagaoka University of Technology,
Kamitomioka, Nagaoka, 940-21, Japan

This paper treats an instability at the free surface of non-Newtonian (power-law) fluid films between two tilted plates in a negative squeeze motion. The meniscus instability in a fluid with the power-law constitutive equation was analyzed on the basis of the linear stability theory. In the analysis, a capillary number for the power-law fluid was newly defined and the relationship between the capillary number and the criterion for the instability of meniscus was theoretically deduced. In the experiment, a water solution of polyacrylamide (separan) whose viscosity obeys a power-law of the strain rate was used as a sample fluid, the meniscus instability in the fluid was examined by using a VTR and the wavelength of disturbances was measured. The theoretical criterion for the instability was in good agreement with experiments and the capillary number could rearrange well the experimental results for the disturbances.

1 Introduction

Problems on the instability for the free surface in a thin liquid film confined between two parallel plates or two rollers have been studied theoretically and experimentally so far: a flow within a Hele-Shaw cell (Saffman and Taylor, 1959; Park and Homsy, 1984; Saffman, 1986; Reinelt, 1987); the instability in roll-coating (Pearson, 1960; Greener and Middleman, 1975; Savage, 1982b; Savage, 1983c; Savage 1984d; Carter and Savage, 1987); rupture of the flow of viscous lubricant within a journal bearing (Savage, 1977a). Plates, rollers, or cylinders confining liquids in these investigations are stationary or move in parallel with respect to each other; contrastingly, there are few reports on the instability of meniscus in the case of boundaries moving in the normal direction on their own. Similar situations relate to the peeling of a pressure-sensitive adhesive tape (McEwan and Taylor, 1966), the breakup of thin oil film in journal bearing or thrust bearing in a squeeze motion (Tichy and Ku, 1988), and the formation for vein or striated patterns in glassy metals (Argon and Salama, 1979). But the papers were not to be the objects that deduced a relevant parameter for meniscus instability and an instability criterion for thin liquid film in a negative squeeze motion.

To study the instability of free surfaces in fluids under various situations it is necessary to extend the theory of meniscus instability constructed for Newtonian fluids into the fluids with another constitutive relation. It is known that many polymeric liquids bear approximately in a power-law of strain rate. The present work treats an analysis of the meniscus instability in power-law fluid films between two tilted plates in a negative squeeze motion.

When the plates move over a certain velocity, the free surface of the fluid is harmonically distorted (and consequently, the liquid remains of treelike patterns on the plates). The model for the analysis is analogous to the breakup of polymeric materials or of a viscous adhesive. The linearized perturbation method is applied to the analysis for yielding the criterion of instability. The analysis for Newtonian fluids presented in the previous paper (Koguchi, Okada, and Tamura, 1988) can now, in principle, be carried through for non-Newtonian fluids where the lubrication approximation can be properly applied.

In the present paper, a new capillary number (which is a function of the ratio of viscous force to surface tension, the size of the plate, the thickness of liquid film, and a power index of the fluid) is newly proposed in the analysis. The capillary number is defined by the moving velocity of meniscus in a similar manner to the one used so far in Newtonian fluids (Saffman and Taylor, 1959; Pearson, 1960; Park and Homsy, 1984; Saffman, 1986). The results of the theoretical analysis were compared with those of experiments on the wave number of disturbance with the capillary number. The best agreement for both results was obtained in the most unstable mode.

2 Analysis

2.1 Unperturbed Flow in a Thin non-Newtonian Liquid Film. Basic flow solutions for an unperturbed meniscus in a thin non-Newtonian liquid film between two tilted plates in a negative squeeze motion are deduced in this section. The so-

Contributed by the Applied Mechanics Division of THE AMERICAN SOCIETY OF MECHANICAL ENGINEERS for publication in the JOURNAL OF APPLIED MECHANICS.

Discussion on this paper should be addressed to the Technical Editor, Leon M. Keer, The Technological Institute, Northwestern University, Evanston, IL 60208, and will be accepted until two months after final publication of the paper itself in the JOURNAL OF APPLIED MECHANICS. Manuscript received by the ASME Applied Mechanics Division, Jan. 6, 1989; final revision, June 24, 1989.

Copyright © 1990 by ASME
Downloaded 03 May 2010 to 171.66.16.244. Redistribution subject to ASME license or copyright; see http://www.asme.org/terms/Terms_Use.cfm

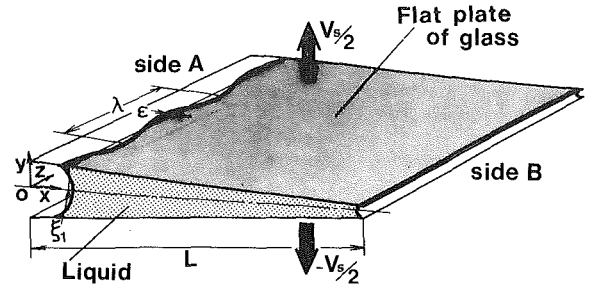


Fig. 1 Coordinate system for analysis and the schematic illustration of disturbances occurring on a free surface

lutions are applied to derive the criterion for meniscus instability.

The constitutive equation for a power-law fluid may be represented by

$$\sigma_{ij} = -p\delta_{ij} + 2\kappa\,\Theta e_{ij} \tag{1}$$

where σ_{ij} is the stress tensor, p the pressure, δ_{ij} the Kronecker delta, κ the pseudo-viscosity. The strain rate tensor e_{ij} and Θ are defined as follows, respectively,

$$e_{ij} = (u_{i,j} + u_{j,i})/2 \tag{2}$$

$$\Theta = |(e_{ij}:e_{ij})^{(n-1)/2}| \tag{3}$$

where u_i is the flow velocity and n the experimental viscometric constants.

The coordinate system for analysis is illustrated in Fig. 1. The origin of the coordinate system is placed at the middle point of the gap width and at the position of the meniscus at side A (see Fig. 1) at the beginning of movement. Rectangular axes are chosen such that y measures distance across the gap width while the x and z-axes are along the direction of fluid motion, i.e., the direction decreasing film thickness and across the width of the plates, respectively.

Disregarding all inertial terms postulates the motion equations as follows:

$$-p_{,j} + 2\kappa\,(\Theta e_{ij})_{,i} = 0. \tag{4}$$

The continuity equation is written as follows:

$$u_{i,i} = 0, \tag{5}$$

where u_i is the velocity vector with components (u, v, w) in the direction of x, y, and z-axes, respectively.

For simplicity of analysis, first neglecting the flow in the z-direction, and next estimating the magnitude of every flow rate in Θ by taking into account the sizes of the plates and the initial thickness h_0 ($h_0 \ll$ length L and width B of the plates) of the liquid film at side A, yields the following relations:

$$\frac{\partial u}{\partial y} \simeq \frac{LV_s}{h_0^2} \gg \frac{\partial u}{\partial x} \simeq \frac{V_s}{h_0} = \frac{\partial v}{\partial y} \simeq \frac{V_s}{h_0} \gg \frac{\partial v}{\partial x} \simeq \frac{V_s}{L}. \tag{6}$$

Whereupon, in experiments described later, $L = 60$ mm, $B = 100$ mm, $h_0 = 1.05 \sim 0.3$ mm and $V_s = 0.5 \sim 100$ mm/min. We assume that the shearing effects are deemed much more important than the elongation effects in this case. This allows us to adapt only the shear deformation rate $\partial u/\partial y$ in Θ:

$$\Theta = \left|\frac{\partial u}{\partial y}\right|^{n-1}. \tag{7}$$

Thus, the starting equations are

$$-\frac{\partial p}{\partial x} + \kappa\frac{\partial}{\partial y}\left(\left|\frac{\partial u}{\partial y}\right|^{n-1}\frac{\partial u}{\partial y}\right) = 0$$

$$-\frac{\partial p}{\partial y} = 0 \tag{8}$$

$$\frac{\partial u}{\partial x} + \frac{\partial v}{\partial y} = 0. \tag{9}$$

Integrating the first of equations (8) with respect to y under the boundary conditions $\partial u/\partial y = 0$ at $y = 0$ and $u = 0$ at $y = h/2$ and by taking into account the sign of velocity gradient of $\partial u/\partial y$ in $y > 0$ yields velocity u as follows:

$$u = \frac{n}{n+1}\left(\frac{\phi}{\kappa}\right)^{\frac{1}{n}}\left[\left(\frac{h}{2}\right)^{\frac{n+1}{n}} - y^{\frac{n+1}{n}}\right] \tag{10}$$

where $\phi = -dp/dx$ represents the pressure gradient in the x-direction and h is the thickness of liquid film. The thickness h is completely specified in terms of h_0, V_s and t as $h = h_0(1 + \alpha - x/L)$, where $\alpha = V_s t/h_0$ and t is the time elapsed from the beginning of displacement of the menisci.

Next, we deduce the pressure gradient ϕ and the velocity v from equations (9) and (10). Integrating equation (9) from 0 to $h/2$, with respect to y using equation (10) yields the following equation:

$$-V_s = \frac{d}{dx}\left\{\frac{2n}{2n+1}\left(\frac{\phi}{\kappa}\right)^{\frac{1}{n}}\left(\frac{h}{2}\right)^{\frac{2n+1}{n}}\right\}. \tag{11}$$

Integrating equation (11) with respect to x, and thus ϕ is obtained as follows:

$$\phi = \kappa\left(\frac{2n+1}{2n}\right)^{n}|\chi|^{n-1}\chi\left(\frac{2}{h}\right)^{2n+1} \tag{12}$$

where $\chi = C_1 - V_s x$ and C_1 is the integral constant determined from pressure boundary conditions taking account of curvatures of menisci.

Substituting equation (12) into (10), we obtain the velocity u:

$$u(x,y) = \frac{2n+1}{2(n+1)}\frac{2\chi}{h}\left\{\left(\frac{2y}{h}\right)^{\frac{n+1}{n}} - 1\right\} \tag{13}$$

Using equations (12) and (13), the average velocity of the flow in the x-direction is reduced to equation (14).

$$U = \frac{n}{2n+1}\left(\frac{\phi}{\kappa}\right)^{\frac{1}{n}}\left(\frac{h}{2}\right)^{\frac{n+1}{n}} \tag{14}$$

Integrating equation (9) with respect to y and substituting equation (13) into the result yields the following expression:

$$v(x,y) = \frac{2n+1}{n+1}\left(V_s + \frac{\chi h_0}{h L}\right)\frac{y}{h}\left\{\frac{n}{2n+1}\left(\frac{2y}{h}\right)^{\frac{n+1}{n}} - 1\right\} - \frac{\chi h_0}{h\,2L}\left(\frac{2y}{h}\right)^{\frac{2n+1}{n}}. \tag{15}$$

The pressure boundary condition for determining C_1 in χ existing in equations (12), (13), and (15) is derived from the force balance across the air-fluid interface. The equation of force balance is written as follows:

$$(p_a - p_2)n_i = -\sigma'_{ik}n_k + T(1/R_1 + 1/R_2)n_i \tag{16}$$

where p_a is atmospheric pressure, p_2 is the pressure of fluid, R_1 and R_2 are the radius of principal curvature of the free surface in the x-y section and the x-z section of liquid film, respectively, T is a surface tension, and n_i and n_k are the unit normal vectors to the free surface in fluid and $\sigma'_{ik} = 2\kappa\,\Theta\,e_{ik}$ ($i,k = 1,2,3$ or x,y,z).

The balance equations of the normal and tangential forces on the free surface in the x-y section of the liquid film, with no disturbance in the z-direction, can be derived readily from equation (16) as follows:

Downloaded 03 May 2010 to 171.66.16.244. Redistribution subject to ASME license or copyright; see http://www.asme.org/terms/Terms_Use.cfm

$$p_a - p_2 = -\sigma'_{11}n_1^2 - 2\sigma'_{12}n_1n_2 - \sigma'_{22}n_2^2 + \frac{T}{R_1} \quad (17)$$

$$(p_a - p_2)n_1(n_2 - \sqrt{1-n_1^2}) = -(\sigma'_{11}\sqrt{1-n_1^2} - \sigma'_{12}n_1)n_1 - (\sigma'_{12}\sqrt{1-n_1^2} - \sigma'_{22}n_1)n_2 + \frac{T}{R_1}n_1(n_2 - \sqrt{1-n_1^2}). \quad (18)$$

In very nonlinear fluids with small n, in the center of the gap where a pluglike flow exists, we can put $n_1 = 1$ and $n_2 = 0$, thus equations (17) and (18) yield the following equations:

$$p_a - p_2 = -\sigma'_{11} + \frac{T}{R_1} \quad (19)$$

$$\sigma'_{12} = 0. \quad (20)$$

Generally, we must solve iteratively equations (16) or (17) and (18) together with equations (4) and (5) under a suitable boundary condition to obtain the flow field around the free surface, and such calculations are very difficult to do. As a first step for an analysis, we consider that it is important to perform the analysis of the flow field under a simple assumption which neglects the stress σ'_{11}—because our main object is to deduce a relevant nondimensional parameter for stability analysis and to discuss a meniscus instability with the parameter. Also, when we assume to be able to extrapolate the solution (13) to the free surface, we can neglect the stress σ'_{11} around $y = 0$.

We consider that it is now possible to construct momentarily a free meniscus in the center portion of the gap with a constant radius of curvature, except near the plates where the shear stresses are large. Hence, when putting $1/R_1 = 2\beta/h$ (h is the thickness of the liquid film), $1/R_2 = 0$ and $p_2 = p_0$ into equation (16), the boundary conditions of the pressure in an unperturbed flow is written as follows:

$$p_0(\xi_1) = p_{\text{air}} - \frac{2\beta T}{h_1}$$

$$p_0(\xi_2) = p_{\text{air}} - \frac{2\beta T}{h_2}, \quad (21)$$

where p_0 represents the pressure in fluid, ξ_1 and ξ_2 are the positions of the meniscus at sides A and B (see Fig. 1), and h_1 and h_2 are the film thicknesses at ξ_1 and ξ_2, respectively. Here we consider the principle radius of curvature to be the film thickness multiplied by a factor $1/2\beta$. When β equals 1, the profile of meniscus is a semicircle.

The constant C_1 is determined at each position of the free surface by using equation (12) integrated with respect to x and equation (21). Thus, the influence of the curvature of the meniscus on the flow is taken into account through C_1.

2.2 Instability Analysis. An analysis for the growth of perturbations taking place at a free surface is presented in this section. The perturbations varying harmonically with wavelength λ, and amplitude ϵ is assumed to arise at the leading edge of the meniscus along the z-axis as shown in Fig. 1. The profile of the meniscus at side A in the x-z section of the liquid film may then be represented as follows:

$$s_1(\xi_1,z,t) = \xi_1(t) + \epsilon\, e^{\omega t}\cos kz, \quad (22)$$

where ξ_1 is the mean x-coordinate of free surface with the radius of curvature R_1 in the x-y section of the liquid film, t is the time, k is the wave number of the perturbation ($k = 2\pi/\lambda$), and ω is the amplification factor. We assume here that the pressure at the vicinity of perturbed meniscus is distributed as follows:

$$p(x,z,t) = p_0(x) + \epsilon\, g(x)e^{\omega t}\cos kz, \quad (23)$$

where $p_0(x)$ is the pressure distribution in the unperturbed flow, the range of x is $s_1 \leqq x \leqq s_2$, and s_2 is the position of meniscus at side B (see Fig. 1).

Furthermore, we consider the following velocity u, v, and w taking into account y-dependence of the velocity profile in order to be satisfied the perturbed momentum equations.

$$\begin{aligned} u(x,y,z,t) &= u_0(x,y) + u'(x,y,z,t) \\ &= u_0(1 + \epsilon F(x)e^{\omega t}\cos kz) \\ v(x,y) &= v_0(x,y) \\ w(x,y,z,t) &= w'(x,y,z,t) \\ &= u_0(x,y)\,\epsilon\, G(x)e^{\omega t}\sin kz \end{aligned} \quad (24)$$

where u_0 and v_0 are given in equations (13) and (15).

Substituting equations (24) into (5) and linearizing terms of order ϵ yields the following equations:

$$\frac{\partial u_0}{\partial x} + \frac{\partial v_0}{\partial y} = 0 \quad (25)$$

$$\frac{\partial u'}{\partial x} + \frac{\partial w'}{\partial z} = 0. \quad (26)$$

We can see that velocities u_0 and v_0 satisfy equation (25) in the process of their derivation. Substituting equations (24) into (26) and integrating the result with respect to y across the gap yields the relation between $F(x)$ and $G(x)$ as follows:

$$\frac{d}{dx}(\chi F) + \chi Gk = 0. \quad (27)$$

The perturbation assumed causes the rise of additional terms in the equations of motion and Θ. For simplicity of analysis, taking into account the most effective term $\partial w/\partial y$ alone on Θ, one obtains the following expressions for Θ and the motion:

$$\Theta^* = \left|\left\{\left(\frac{\partial u}{\partial y}\right)^2 + \left(\frac{\partial w}{\partial y}\right)^2\right\}^{\frac{n-1}{2}}\right| \quad (28)$$

$$-\frac{\partial p}{\partial x} + \kappa\frac{\partial}{\partial y}\left(\Theta^*\frac{\partial u}{\partial y}\right) = 0$$

$$-\frac{\partial p}{\partial z} + \kappa\frac{\partial}{\partial y}\left(\Theta^*\frac{\partial w}{\partial y}\right) = 0. \quad (29)$$

Substituting equations (24) into (28) and linearizing terms of order ϵ yields the following expression:

$$\Theta^* = \left|\frac{\partial u_0}{\partial y}\right|^{n-1}\{1 + \epsilon(n-1)F(x)e^{\omega t}\cos kz + \ldots.\}$$

$$= \left|\left\{\frac{2n+1}{n}\frac{2\chi}{h^2}\left(\frac{2y}{h}\right)^{\frac{1}{n}}\right\}\right|^{n-1} \times \{1 + \epsilon(n-1)F(x)e^{\omega t}\cos kz + \ldots.\}. \quad (30)$$

Substituting equations (23) and (24) into (29) and linearizing terms of order ϵ yields the following equations:
for nonperturbation term

$$-\frac{dp_0}{dx} + \kappa\frac{\partial}{\partial y}\left\{\left|\frac{\partial u_0}{\partial y}\right|^{n-1}\frac{\partial u_0}{\partial y}\right\} = 0, \text{ and} \quad (31)$$

for perturbation terms

$$-\frac{dg}{dx} + \kappa\frac{\partial}{\partial y}\left\{nF\left|\frac{\partial u_0}{\partial y}\right|^{n-1}\frac{\partial u_0}{\partial y}\right\} = 0$$

$$kg + \kappa\frac{\partial}{\partial y}\left\{G\left|\frac{\partial u_0}{\partial y}\right|^{n-1}\frac{\partial u_0}{\partial y}\right\} = 0 \quad (32)$$

Downloaded 03 May 2010 to 171.66.16.244. Redistribution subject to ASME license or copyright; see http://www.asme.org/terms/Terms_Use.cfm

We can obtain $F(x)$ and $G(x)$ from equation (32):

$$F(x) = \frac{h}{2n\,\kappa|\chi|^{n-1}\chi}\left(\frac{n}{2n+1}\frac{h^2}{2}\right)^n \frac{dg}{dx}$$

$$G(x) = -\frac{h}{2\,\kappa|\chi|^{n-1}\chi}\left(\frac{n}{2n+1}\frac{h_2}{2}\right)^n gk. \tag{33}$$

Substituting equations (33) into (27) yields the second-order ordinary differential equation for $g(x)$ as follows:

$$\frac{d}{dx}\left(\frac{h^{1+2n}}{|\chi|^{n-1}}\frac{dg}{dx}\right) - \frac{h^{1+2n}}{|\chi|^{n-1}} g\, nk^2 = 0\,. \tag{34}$$

Thus, we obtain the following equation:

$$\frac{d^2g}{dx^2} + \left\{(1+2n)\frac{1}{h}\frac{dh}{dx} + (1-n)\frac{1}{|\chi|}\frac{d|\chi|}{dx}\right\} \times \frac{dg}{dx} - nk^2 g = 0. \tag{35}$$

Equating n in equation (35) to 1 yields the equation for Newtonian fluid. Letting $\zeta = x - L(1+\alpha)$, one can solve equation (35) as follows:

$$g(x) = a_c \sum_{m=0}^{\infty} B_m \zeta^m, \text{ and } b_c\, \zeta^{-2n} \sum_{m=0}^{\infty} D_m \zeta^m, \tag{36}$$

where B_m and D_m are given by the following recurrence formula, respectively:

$$B_0 = 1,\ B_1 = 0$$

$$B_2 = \frac{nk^2}{2(2+2n)}$$

$$B_m = \frac{1}{m(m+2n)}\left[\frac{(m-1)(m+n)B_{m-1}}{C_1/V_s - L(1+\alpha)} + nk^2\left(B_{m-2} - \frac{B_{m-3}}{C_1/V_s - L(1+\alpha)}\right)\right]$$

$$D_0 = 1$$

$$D_1 = \frac{-2n(1-n)}{(1-2n)\{C_1/V_s - L(1+\alpha)\}}$$

$$D_2 = \frac{1}{2(2-2n)}\left[\frac{-2n(1-n)(2-n)}{\{C_1/V_s - L(1+\alpha)\}^2} + nk^2\right]$$

$$D_m = \frac{1}{m(m-2n)}\left[\frac{(m-1-2n)(m-n)B_{m-1}}{C_1/V_s - L(1+\alpha)} + nk^2\left(D_{m-2} - \frac{D_{m-3}}{C_1/V_s - L(1+\alpha)}\right)\right]. \tag{37}$$

We must choose a suitable function for the present problem from the solution equation (36): The variation of pressure by the perturbation decays with increase in the distance from the meniscus at side A. Hence, we obtain

$$g(x) = a_c \sum_{m=0}^{\infty} B_m \zeta^m\,. \tag{38}$$

The constant a_c in equation (38) can be determined from the boundary condition of pressure on the perturbed meniscus. Now, putting $1/R_1 = 2\beta/h_1(s_1)$, $1/R_2 = \epsilon k^2 e^{\omega t}\cos kz$, $p_2 = p_0 + \epsilon\, g(s_1)e^{\omega t}\cos kz$, $\sigma'_{ik} = 0$, $n_1 = 1$, $n_2 = n_3 = 0$ into equation (16), the pressure boundary condition is written as follows:

$$p_a - p_0(s_1) - \epsilon\, g(s_1)e^{\omega t}\cos kz = T\left(\frac{2\beta}{h(s_1)} + \epsilon\, k^2 e^{\omega t}\cos kz\right)\,. \tag{39}$$

Rearranging equation (39) by the Taylor development and linearizing and equating terms of order ϵ yields the following expression:

$$g(\xi_1) = -\frac{dp_0}{dx}\bigg|_{x=\xi_1} - T\left(\frac{2\beta h_0}{h^2(\xi_1)L} + k^2\right)\,. \tag{40}$$

The constant a_c in equation (38) is obtained from (40) with (12) as follows:

$$a_c = \frac{1}{I_1(\xi_1)}\left\{\kappa\left(\frac{2n+1}{2n}\right)^n |\chi_1|^n \chi \left(\frac{2}{h_1}\right)^{2n+1} - \frac{2\beta T h_0}{h_1^2 L} - k^2 T\right\} \tag{41}$$

where

$$\chi_1 = C_1 - V_s\xi_1$$

$$I_1(\xi_1) = \sum_{m=0}^{\infty} B_m\, \zeta_1^m$$

$$\zeta_1 = \xi_1 - L(1+\alpha)\,. \tag{42}$$

2.3 Neutral Stability Analysis. The stability criterion of perturbations arising at the leading edge of the meniscus is derived by following Chuoke, Van Meurs, and van der Poel, (1959), Pearson (1960), Savage (1984c), Carter and Savage, (1987), and Koguchi, Okada, and Tamura (1988). Whether or not the sign of ω in $\exp(\omega t)$ in equation (22) or (23) is plus or minus dominates the growth or decay of perturbations. The expression for ω can be derived from the kinematic condition for the perturbed meniscus. The average velocity of the meniscus at side A from equation (14) is given by

$$\frac{ds_1}{dt} = \frac{n}{2n+1}\left\{\left(\frac{h}{2}\right)^{\frac{n+1}{n}}\left(-\frac{1}{\kappa}\frac{dp}{dx}\right)^{\frac{1}{n}}\right\}\bigg|_{x=s_1}. \tag{43}$$

Substituting equations (22) and (23) into (43) yields the following equation:

$$\frac{d\xi_1}{dt} + \epsilon\,\omega e^{\omega t}\cos kz = \frac{n}{2n+1}\left(\frac{h}{2}\right)^{\frac{n+1}{n}}\bigg|_{x=\xi_1 + \epsilon e^{\omega t}\cos kz} \times \left(-\frac{1}{\kappa}\frac{dp_0}{dx} - \frac{\epsilon}{\kappa}\frac{dg}{dx}e^{\omega t}\cos kz\right)^{\frac{1}{n}}. \tag{44}$$

Equating terms of order ϵ in equation (44) yields the following expression:

$$\omega = \frac{n}{2n+1}\left[\frac{1}{n}\left(\frac{h}{2}\right)^{\frac{n+1}{n}}\left(-\frac{1}{\kappa}\frac{dp_0}{dx}\right)^{\frac{1-n}{n}}\left(-\frac{1}{\kappa}\frac{dg}{dx}\right)\bigg|_{x=\xi_1} + \frac{d}{dx}\left(\frac{h}{2}\right)^{\frac{n+1}{n}}\left(-\frac{1}{\kappa}\frac{dp_0}{dx}\right)^{\frac{1}{n}}\bigg|_{x=\xi_1}\right]. \tag{45}$$

Substituting equation (12) and the average velocity of unperturbed free surface $u_x = (C_1 - V_s\xi_1)/h_1$ into equation (45) gives the following equation:

Downloaded 03 May 2010 to 171.66.16.244. Redistribution subject to ASME license or copyright; see http://www.asme.org/terms/Terms_Use.cfm

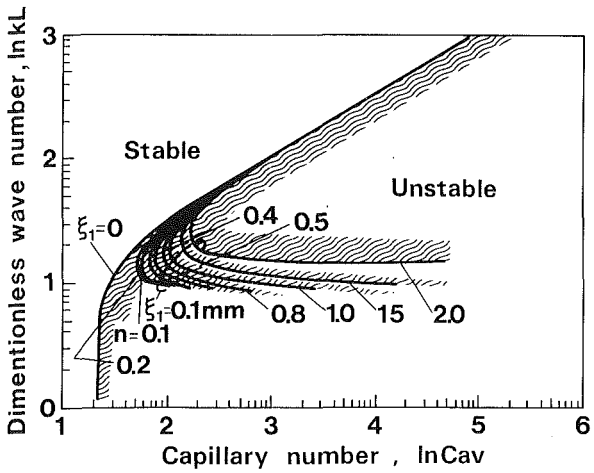


Fig. 2 The variation of neutral stability curves versus dimensionless wave number kL for various n at $\xi_1 = 0.0$ mm and 0.1 mm in the conditions $V_s = 1.0$ mm/min, $h_0 = 0.5$ mm, $L = 60.0$ mm, $\kappa = 14.0$ Pa·s^n, $T = 32.7$ mN/m, and $\beta = 1$

$$\omega = \left\{\frac{h_0(C_1 - V_s\xi_1)}{h_1{}^2 L} - \frac{V_s}{h_1}\right\} - \frac{1}{n}\frac{C_1 - V_s\xi_1}{h_1}\frac{I_2}{I_1} + \frac{12(C_1 - V_s\xi_1)}{Ca_v\, n\, h_1}\frac{I_2}{I_1}\left(k^2L^2 + \frac{2\beta h_0 L}{h_1{}^2}\right) = -\frac{u_x}{Ca_v L}\left\{12Ca_v\left(\frac{1}{n}\frac{I_2 L}{I_1} - \frac{h_0}{h_1} + \frac{V_s L}{u_x h_1}\right) - \frac{1}{n}\frac{I_2 L}{I_1}\left(\frac{2\beta h_0 L}{h_1{}^2} + k^2L^2\right)\right\} \tag{46}$$

where

$$I_2(\xi_1) = \sum_{m=1}^{\infty} mB_m\zeta_1{}^{m-1}\,. \tag{47}$$

We refer to Ca_v as a capillary number for power-law fluids and Ca_v is a new nondimensional number defined as follows:

$$Ca_v = \frac{\kappa\, u_x{}^n}{12\, T}\frac{L^2}{h_1{}^{n+1}}\left(\frac{2n+1}{2n}\right)^n 2^{2n+1}. \tag{48}$$

If n is equated to 1 and h_1 is a constant thickness, this capillary number is reduced to the one used in the study of fingering in Hele-Shaw cell by Homsy and Parks (1984), Tabelling, Zocchi, and Libchaber (1987), Reinelt (1987), Saffman (1986), and others.

The perturbation grows as time elapses in the case of $\omega > 0$. The demarcation between stable ($\omega < 0$) and unstable ($\omega > 0$) situations is given by $\omega = 0$. Thus, a neutral stability condition is obtained by arranging equation (46) with $\omega = 0$ as follows:

$$Ca_v = \frac{1}{12}\frac{\left(\frac{2\beta L h_0}{h_1{}^2} + k^2L^2\right)}{\left\{1 - \left(\frac{h_0}{h_1} - \frac{V_s}{u_x}\frac{L}{h_1}\right)\frac{n\, I_1(\xi_2)}{L\, I_2(\xi_2)}\right\}}\,. \tag{49}$$

It is necessary for the calculation of neutral stability curve during the movement of the free surface to obtain C_1, ξ_1, and ξ_2 at any time. As seen in equations (35) and (36), the solution for $g(x)$ has two neighbor singular points, and hence the calculation for I_1 and I_2 in equation (49) performed with the function $g(x)$ requires the exact values for C_1, ξ_1, and ξ_2. As mentioned previously, the equation for C_1 is given by integrating equation (12) with respect to x in the range from ξ_1 to ξ_2 and using (21) as follows:

$$2\beta T\left(\frac{1}{h_2} - \frac{1}{h_1}\right) = -\kappa\left(\frac{2n+1}{2n}\right)^n\left(\frac{2L}{h_0}\right)^{2n+1}\int_{\xi_2}^{\xi_1}\frac{|\chi|^{n-1}\chi}{\{L(1+\alpha) - x\}^{2n+1}}\,dx\,. \tag{50}$$

The x-coordinates ξ_1 and ξ_2 for the free surface in equation (50) are given by solving the following equations:

$$\frac{d\xi_1}{dt} = \frac{-V_s\xi_1 + C_1}{h_1}$$

$$\frac{d\xi_2}{dt} = \frac{-V_s\xi_2 + C_1}{h_2}\,. \tag{51}$$

The fourth Runge-Kutta-Gill formula was used in the calculation, and then V_sL was used as the initial value of C_1 by analogical inference to that of C_1 in Newtonian fluid. The calculation was carried out many times in order to obtain the accurate values for C_1, ξ_1, and ξ_2. For instance, the step size of time used was varied from 0.01 sec to 0.0001 sec in the case of $V_s = 1.0$ mm/min and $h_0 = 0.5$ mm and from 0.0005 sec to 0.000005 sec in the case of $V_s = 50$ mm/min and $h_0 = 0.5$ mm. We found, in these numerical calculations, that the free surfaces stopped moving at a distance though the plates were drawn apart. Also, although for different values of time step the distance was different even in the same numerical condition, the relationship between the displacement of free surface and the elapsed time was at least the same until ξ_1 approached to approximately 0.2 mm. We considered this to be due to numerical errors accumulated during the calculation.

Hence, we could only obtain the neutral stability curve after the immediate time of the movement. Figure 2 demonstrates an illustration of the neutral stability curves for several values of n at $\xi_1 = 0.0$ mm and 0.1 mm in the conditions of $h_0 = 0.5$ mm, $V_s = 1.0$ mm/min, $L = 60$ mm, $T = 32.7$ mN/m, $\kappa = 14.0$ Pa·s^n, and $\beta = 1$. The stability curves in $\xi_1 = 0.0$ mm do not vary even if the value of n changes.

We can deduce another important result on the neutral stability from equations (46) and (49) in a particular value of wavelength and elapsed time ($\lambda = \infty$, $t = 0$). As nI_1/LI_2 is very small at a long wavelength, and hence for $\omega > 0$,

$$Ca_v > \frac{\beta L h_0}{6h_1{}^2}\,. \tag{52}$$

This expression means that the free surface may become unstable when a given Ca_v is bigger than $\beta/12$ times of the inverse of the slope of plates, $h_0/(2L)$, at the time $t = 0$.

When β equals 1, the shape of meniscus is a semicircle in the x-y section of the liquid film. Hence, in a large radius of curvature, i.e., $\beta < 1$, this means that the meniscus instability may occur in a less value than one for $\beta = 1$. Since it is considered that the radius of curvature in very nonlinear fluids with a small n is larger than one half of the thickness, i.e., $\beta < 1$, the fluids with a larger n might have a ready tendency to be unstable.

We consider that the variation of calculated results for various values of β could be seen from the above, therefore the value of β is equated to 1 in the following calculation.

The variation of the neutral stability curves at $\xi_1 = 0.0$ mm for various plate length L is shown in Fig. 3 under the conditions $V_s = 1.0$ mm, $h_0 = 0.5$ mm, $\kappa = 14.0$ Pa·s^n, $n = 0.5$, and $T = 32.7$ mN/m. This figure illustrates the effect of the slope of the plates on the critical capillary number of the meniscus instability and reveals the validity of equation (52).

Of all perturbations, the one that dominates the breakup of the monolithic meniscus will have a wave number that maximizes ω and lies within the range of instability. We assume

Downloaded 03 May 2010 to 171.66.16.244. Redistribution subject to ASME license or copyright; see http://www.asme.org/terms/Terms_Use.cfm

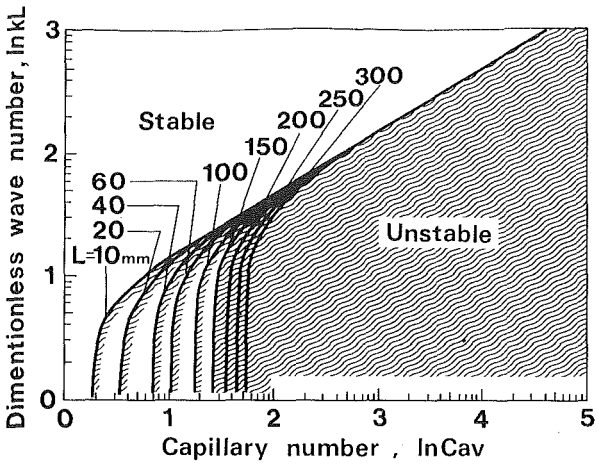


Fig. 3 The variation of neutral stability curves versus dimensionless wave number kL for various L in the conditions $V_s = 1.0$ mm, $h_0 = 0.5$ mm, $L = 60.0$ mm, $\kappa = 14.0 \text{Pa} \cdot s^n$, $n = 0.5$, $T = 32.7$ mN/m, and $\beta = 1$

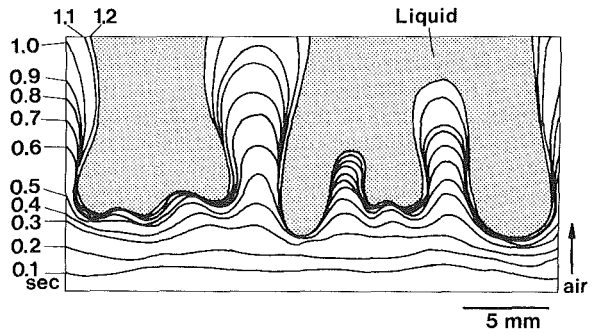


Fig. 4 The sketches of development of perturbations for the 4 percent water solution of separan at every 0.1 seconds in the experimental conditions $h_0 = 0.5$ mm and $V_s = 5$ mm/min

that this is the value of k that would be observed in practice. The relationship between the wave number and the capillary number Ca_v is derived by differentiating equation (46) with respect to k as follows:

$$Ca_v = \frac{1}{12}\left[k^2L^2 + \frac{2\beta Lh_0}{h_1^2} + \frac{2k^2L^2}{k\dfrac{d}{dk}\left\{\ln\dfrac{I_2(\xi_1)}{I_1(\xi_1)}\right\}}\right] . \quad (53)$$

Thus, the capillary number can be obtained in two ways, i.e., equations (48) and (53). Equation (48) is the definition of the capillary number including the moving velocity of the meniscus and the physical properties of the power-law fluid. As contrasted, the capillary number given by equation (53) is calculated from lengths concerned only with the experimental apparatus and the disturbances. We can thus theoretically obtain the capillary number Ca_v by substituting k, L, h_0, h_1, and ξ_1 or (V_s and time t) into equation (53). A comparison of the values of the capillary number obtained in both ways will be presented in the next section.

A simple relation on the wavelength of the disturbance is deduced from equation (53). The denominator in the third term of equation (53) is nearly equal to 1 in any larger values of k, hence,

$$\lambda = \frac{\pi L}{\sqrt{Ca_v}}$$

$$= \frac{\pi}{n}\left(\frac{n}{2(2n+1)}\right)^{\frac{n}{2}}\frac{6T h_1^{n+1}}{\kappa u_x^n} . \quad (54)$$

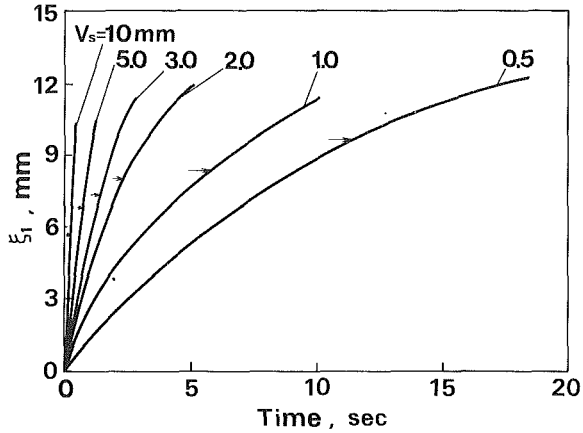


Fig. 5 The relations between elapsed time t and the position ξ_1 of free surface. The arrows indicate the position measured the wavelength.

When the mean propagating speed of free surface and the thickness of liquid film are known, we can roughly estimate the wavelength for disturbance with equation (54) and it can be known from (46) whether the free surface is stable or unstable.

3 Application to Experiments

Experimental results for power-law fluids obtained on the apparatus shown in the previous paper (Koguchi, Okada, and Tamura, 1988) are analyzed by using the foregoing solutions.

Tests were performed several times under the same experimental conditions for a water solution two percent and four percent of polyacrylamide (separan). The water solution is a typical power-law fluid and its rheological properties were determined from a log-log plot of shear stress versus shear strain. Typical values of the flow behavior index for the solutions were: for two percent solution, $\kappa = 14.0$ Pa$\cdot s^n$, $n = 0.26$, and for four percent solution, $\kappa = 44.0$ Pa$\cdot s^n$ and $n = 0.23$. Surface tensions measured by the Wilhelmy method were 32.7 mN/m for two percent solution and 28.3 mN/m for a four percent one, respectively. Experimental conditions for tension velocity V_s were $0.5 \sim 100$ mm/min and for initial thickness h_0 were 0.3, 0.5, 0.75 and 1.05 mm.

First, the growth of disturbances at the meniscus was precisely examined by using a VTR and the movement of the meniscus was traced with elapsed time. Figure 4 is an example of sketches at every 0.1 seconds for the four percent water solution under the experimental conditions $h_0 = 0.5$ mm and $V_s = 5$ mm/min. The free surface of meniscus is almost straight along the z-axis at the early time of the movement, although it is beginning to be harmonically distorted as time elapses. Air fingers advanced in more sharp and slender shapes in the power-law fluids than in the Newtonian ones.

Second, the average position of perturbed meniscus was measured from the VTR, since the mean velocity needed to calculate the capillary number on the basis of definition of equation (46). An example for the curves of ξ_1 versus the elapsed time t is shown in Fig. 5. The mean propagating velocity u_x at the position of the measurement of the wavelength (the position arrowed in Fig. 5) was obtained by approximating the curves with the least square method. In particular, the position for the measurement in four percent solution was nearer the edge of side A than that in the two percent one; however, the position was further than 3 mm in distance.

Finally, the wavelength of the first visible disturbances was compared with the capillary number in experiments and the theoretically predicted capillary number. The wavelength in experiments was measured from the sketches or by processing a digital image of the VTR. The capillary number in experi-

Downloaded 03 May 2010 to 171.66.16.244. Redistribution subject to ASME license or copyright; see http://www.asme.org/terms/Terms_Use.cfm

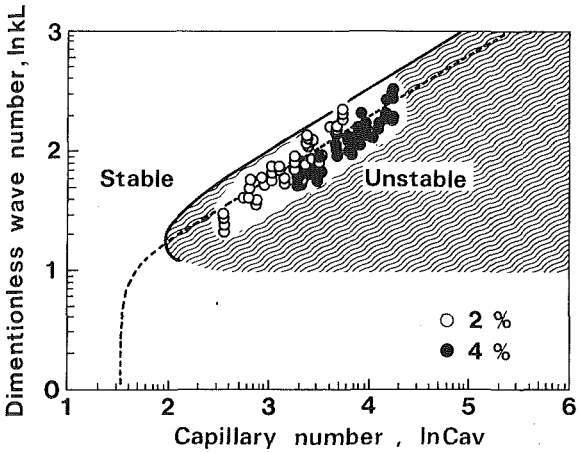


Fig. 6 The relation between the capillary number Ca_v and the dimensionless kL for the power-law fluids with different rheological properties. The solid line is the neutral stability curves at $\xi_1 = 0.1$ mm. The dotted line in the figure shows equation (53).

ments was then estimated with equation (48) at the position where the wavelength was measured.

The wave number and the capillary number in experiments are shown in Fig. 6 together with equations (49) and (53). As mentioned previously, since the curves theoretically calculated were only obtained at an immediate time of movement, thus the theory and the experiment could not be exactly compared with each other. We consider that the theoretical curves little shift except around the lower wave number in the unstable region, even if the meniscus propagates, in the same manner of the Newtonian fluid. This figure illustrates the results for power-law fluids with different rheological properties. Solid and dotted lines in this figure are plotted by the theoretical equations (49) and (53), respectively. It is found that there are no disturbances in the capillary number above the neutral stability curve equation (49) and the experimental values of the wave number are nearly on the curve for (53) corresponding to the most unstable mode. This means that the capillary number calculated by equations (48) and (53) is in good agreement.

4 Conclusion

In the present paper, the meniscus instability of a thin power-law fluid film confining between two tilted plates, which was separated with respect to each other perpendicularly to the plates, was studied theoretically and experimentally. An analysis of instability of the free surface in the fluid was conducted by using the linearized perturbation method. An analytical relationship between the instability criterion and the wave number was derived in a closed form for the capillary number Ca_v, which is a function of the ratio of surface tension to viscous force dependent on the rheological properties of the liquid, the dimension of the plate, and the thickness of liquid film. The results in various experimental conditions for tension speed V_s and thickness h_0 were compared with our theory. These results show the validity of the instability criterion. Better agreement of both results was obtained with the wave number which corresponds to the most unstable mode.

Acknowledgment

We were favored to have the assistance of Mr. K. Tamura who contributed his effort to the experimental work.

References

Argon, A. S., and Salama, M. M., 1977, "The Mechanism of Fracture in Glassy Materials Capable of Some Inelastic Deformation," *Materials Science and Engineering*, Vol. 23, pp. 219–230.

Carter, G. C., and Savage, M. D., 1987, "Ribbing in a Variable Speed Two-roll Coater," *Mathematical Engineering Industry*, Vol. 1, pp. 83–95.

Chuoke, R. L., Van Meurs, P., and van der Poel, C., 1958, "The Instability of Slow, Immiscible, Viscous Liquid-Liquid Displacements in Permeable Media," *Petroleum Transactions, AIME*, Vol. 216, pp. 188–194.

Greener, Y., and Middleman, S., 1975, "A Theory of Roll Coating of Viscous and Viscoelastic Fluids," *Polymer Engineering and Science*, Vol. 15, pp. 1–10.

Koguchi, H., Okada, M., and Tamura, K., 1988, "The Meniscus Instability of a Thin Liquid Film," ASME JOURNAL OF APPLIED MECHANICS, Vol. 110, pp. 975–980.

McEwan, A. D., and Taylor, G. I., 1966, "The Peeling of a Flexible Strip Attached by a Viscous Adhesive," *Journal of Fluid Mechanics*, Vol. 26, pp. 1–15.

Park, C. W., and Homsy, G. M., 1984, "Two-phase Displacement in Hele-Shaw Cells: Theory," *Journal of Fluid Mechanics*, Vol. 139, pp. 291–308.

Pearson, J., 1960, "The Instability of Uniform Viscous Flow Under Roller and Spreaders," *Journal of Fluid Mechanics*, Vol. 7, pp. 481–500.

Pitt, E., and Greiller, J., 1961, "The Flow of Thin Liquid Films Between Rollers," *Journal of Fluid Mechanics*, Vol. 11, pp. 33–50.

Reinelt, D. A., 1987, "Interface Conditions for Two-phase Displacement in Hele-Shaw Cells," *Journal of Fluid Mechanics*, Vol. 183, pp. 219–234.

Saffman, P. G., and Taylor, G. I., 1959, "The Penetration of a Fluid into a Porous Medium or Hele-Shaw Cell Containing a More Viscous Liquid," *Journal of Fluid Mechanics*, Vol. 245A, pp. 312–329.

Saffman, P. G., 1986, "Viscous Fingering in Hele-Shaw Cells," *Journal of Fluid Mechanics*, Vol. 173, pp. 73–94.

Savage, M. D., 1977a, "Cavitation in Lubrication. Part 1: On Boundary Conditions and Cavity-Fluid Interfaces. Part 2: Analysis of Wavy Interfaces," *Journal of Fluid Mechanics*, Vol. 80, pp. 743–767.

Savage, M. D., 1982b, "Mathematical Models for Coating Processes," *Journal of Fluid Mechanics*, Vol. 117, pp. 443–455.

Savage, M. D., 1983c, "Variable Speed Coating with Purely Viscous Non-Newtonian Fluids," *Journal of Applied Mathematics and Physics (ZAMP)*, Vol. 34, pp. 358–369.

Savage, M. D., 1984d, "Mathematical Model for the Onset of Ribbing," *American Institute of Chemical Engineers Journal*, Vol. 30, pp. 999–1002.

Tichy, J. A., and Ku, C. P., 1988, "A Thin Film Flow Rupture Model for Newtonian and Viscoelastic Fluids," *ASME Journal of Tribology*, Vol. 110, pp. 712–717.

Tabelling, P., Zocchi, G., and Libchaber, A., 1987, "An Experimental Study of the Saffman-Taylor Instability," *Journal of Fluid Mechanics*, Vol. 177, pp. 67–82.

Downloaded 03 May 2010 to 171.66.16.244. Redistribution subject to ASME license or copyright; see http://www.asme.org/terms/Terms_Use.cfm

Journal of Applied Mechanics

Brief Notes

A Brief Note is a short paper that presents a specific solution of technical interest in mechanics but which does not necessarily contain new general methods or results. A Brief Note should not exceed 1500 words *or equivalent* (a typical one-column figure or table is equivalent to 250 words; a one line equation to 30 words). Brief Notes will be subject to the usual review procedures prior to publication. After approval such Notes will be published as soon as possible. The Notes should be submitted to the Technical Editor of the JOURNAL OF APPLIED MECHANICS. Discussions on the Brief Notes should be addressed to the Editorial Department, ASME, United Engineering Center, 345 East 47th Street, New York, N. Y. 10017, or to the Technical Editor of the JOURNAL OF APPLIED MECHANICS. Discussions on Brief Notes appearing in this issue will be accepted until two months after publication. Readers who need more time to prepare a Discussion should request an extension of the deadline from the Editorial Department.

Cumulant Neglect Closure of Nonstationary Solutions of Stochastic System[1]

Marian Pawleta[2] and Leslaw Socha[2]

The comparison of the exact nonstationary solution of stochastic dynamic system with the corresponding one obtained by the cumulant closure technique is presented in this paper. The solutions of linear system with colored noise will be considered.

1 Introduction

The cumulant neglect closure technique is one of the most often used methods in the analysis of stochastic nonlinear dynamical systems. It has been applied by many authors, for example Wu and Lin (1984), Sun and Hsu (1987), and Banai and Brenig (1983). They have compared the exact stationary solution with the corresponding one obtained by the cumulant closure technique. In this paper we will compare the exact solution with the approximate one in the nonstationary case. We will consider linear systems with colored noise which have triangularizable matrices.

2 Analysis of Stationary Solutions

2.1 A Duffing Oscillator Under External Random Excitations. The first chosen case for investigation in this paper (Wu and Lin, 1984) was the Duffing oscillator described by equation:

$$\frac{d^2x}{dt^2}+\eta\frac{dx}{dt}+(x+\epsilon x^3)=\sqrt{\eta}F(t) \tag{1}$$

where η is a damping coefficient, $F(t)$ is a Gaussian white noise, and ϵ is a parameter representing the degree of nonlinearity.

The following accuracy of variation has been obtained for this system: 15 percent from Gaussian closure, 7 percent from neglecting the cumulants of fourth order, and 5 percent from neglecting the cumulants of sixth order.

2.2 A Nonlinear System Under a Random Parametric and Random External Excitations. The second chosen case for investigation (Wu and Lin, 1984) is the system described by equation:

$$\frac{d^2x}{dt^2}+(\alpha+\beta\cdot x^2)\frac{dx}{dt}+[1+F_1(t)]x=F_2(t), \tag{2}$$

where F_1,F_2 are independent Gaussian white noise processes, with spectral densities S_1, S_2, respectively, and α,β are small constants of the same order as the spectral density F_1.

The following accuracy of variation has been obtained for this system for $\alpha,\beta=0.1$, $S_1=0.3$: 6 percent from Gaussian closure, for $S_2>0.3$ and 0 percent from neglecting the cumulants of fourth order.

2.3 A Nonlinear Oscillator Under One Random External Excitation and Two Random Parametric Excitations. The third selected case for analysis is the Dimentberg example pictured by the equation:

$$\frac{d^2x}{dt^2}+2\alpha\frac{dx}{dt}[1+F_1(t)]+\beta_1\frac{dx}{dt}\left(x^2+\left(\frac{dx}{dt}\right)^2/\Omega^2\right)+\Omega^2x[1+F_2(t)]=F_3(t), \tag{3}$$

where α,β_1,Ω are constants and F_1,F_2,F_3 are Gaussian white noise processes with spectral densities S_1, S_2, S_3, respectively.

Similar to the previous cases, the following accuracy of variation has been obtained (Wu and Lin, 1984) for this system for $\alpha=0.5$, $\beta_1=1$, $S_1=S_2=0.1$—6 percent from Gaussian closure and 0 percent from neglecting the cumulants of fourth order.

This example has been analyzed by Sun and Hsu (1987) for a large range of parameters. They have found two regions in the parameter plane. These regions depend on bifurcation lines of approximate systems obtained by the cumulant neglect closure method. In one region, the cumulant neglect technique is invalid and gives faulty results. For the other region, the cumulant neglect method gives good approximate solution in most cases. The regions in parameters plane depend on the order of the cumulant neglect method.

2.4 Nonlinear Stochastic Differential Equation—Banai and Brenig's Example. Banai and Brenig (1983) have considered the nonlinear dynamical system described by stochastic differential equation:

$$dx=(ax-bx)dt+\sqrt{\alpha x^2+\beta x^{+1}}dW, \tag{4}$$

[1]This work is supported by the Central Program of Fundamental Research, Poland, CPBP.02.19.03.23.

[2]Institute of Transport, Silesian Technical University, 40-019 Katowice, ul. Krasinskiego 8, Poland.

Manuscript received by the ASME Applied Mechanics Division, June 6, 1988; final revision, May 9, 1989.

Copyright © 1990 by ASME
Downloaded 03 May 2010 to 171.66.16.244. Redistribution subject to ASME license or copyright; see http://www.asme.org/terms/Terms_Use.cfm

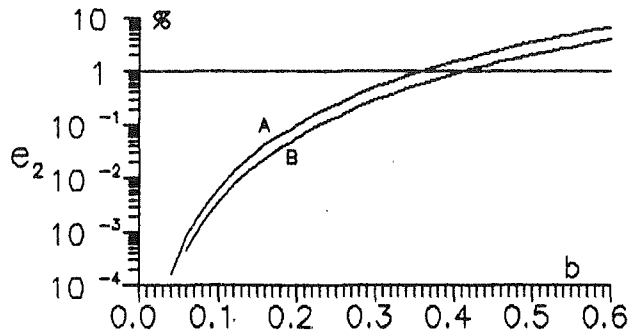


Fig. 1 Error of mean value versus parameter b

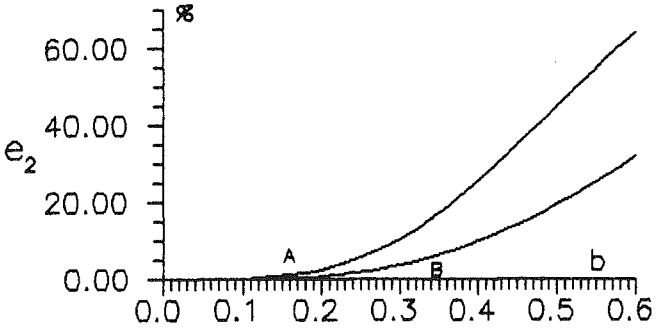


Fig. 2 Error of second moment versus parameter b

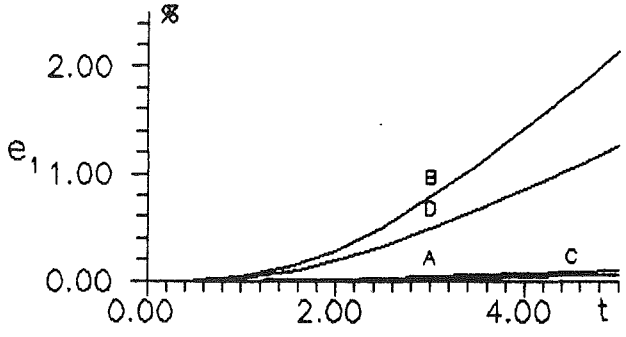


Fig. 3 Error of mean value versus time t

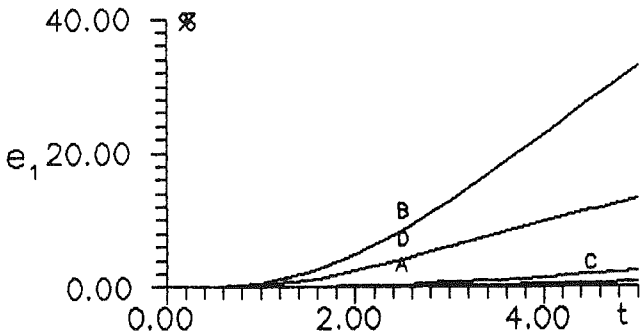


Fig. 4 Error of second moment versus time t

where $\gamma = 2, 3, 4, \ldots$, β, a, b are real parameters, and W is standard Wiener process.

The exact stationary solutions for sample values of this system are (Banai and Brenig, 1983): $x = 0$ for all values of parameters and $x = \sqrt{(-\alpha/\beta)}$ for parameters satisfying conditions:

$$\frac{\alpha}{\beta} = \frac{2a}{\beta - 2b} \text{ and } \alpha\beta < 0.$$

We can obtain the zero solution, and solution with any value of variance for $3\beta/4 - b = 0$ on the basis of the cumulant neglect technique. So, we can see that in this case the cumulant neglect technique gives us a different result from the exact one.

3 Analysis of Nonstationary Solutions

In this section we will study the cumulant neglect closure method for nonstationary solutions. First, we find the exact nonstationary solutions for one and two-dimensional systems, and next we apply the cumulant neglect closure to these systems. We compare the errors of approximation using the following measures:

$$e_1(t) = \frac{x_{\text{exact}}(t) - x_{\text{appr}}(t)}{x_{\text{exact}}(t)} \cdot 100 \text{ percent},$$

$$e_2 = \sup_{t \in [o,T]} \left| \frac{x_{\text{exact}}(t) - x_{\text{appr}}(t)}{x_{\text{exact}}(t)} \cdot 100 \text{ percent} \right| \quad (5)$$

where x_{exact} is an exact solution and x_{appr} is an approximate solution.

3.1 One-Dimensional Example With Colored Noise. Now we will consider the simplest case, i.e., a system described by a one-dimensional stochastic differential equation with a colored noise coefficient:

$$\frac{dx(t)}{dt} = -ax(t) + bx(t)\eta(t), \qquad x(t_o) = x_o, \quad (6)$$

where $\eta(t)$ is stationary Gaussian colored noise satisfying the filter stochastic differential equation:

$$d\eta = -\alpha\eta dt + \alpha d\xi, \qquad \eta(t_o) = \eta_o, \quad (7)$$

and parameters a, b, $\alpha > 0$ are real constants.

The exact solution of (6) is as follows:

$$x(t) = x_o \exp\left\{ -\int_{t_o}^{t} (a - b\eta(\tau))d\tau \right\}. \quad (8)$$

Since $\eta(t)$ is the Gaussian process, we can find the expectation and the variance of $x(t)$ in the form:

$$E[x(t)] = x_o \exp\left\{ -at + \frac{b^2}{2}\left[t - \frac{1}{\alpha} + \frac{1}{\alpha}\exp\{-\alpha t\} \right] \right\}, \quad (9)$$

$$E[x^2(t)] = x_o^2 \exp\left\{ -2at + 2b^2\left[t - \frac{1}{\alpha} + \frac{1}{\alpha}\exp\{-\alpha t\} \right] \right\}. \quad (10)$$

So the stationary solution (for parameters satisfying the stability conditions) is equal to zero. We obtain the same solution resulting from the cumulant neglect method.

The errors of the cumulant neglect technique for a nonstationary case are presented in Figs. 1-4.

In Figs. 1 and 2 "A" and "B" denote the errors of approximation of cumulant neglect closure of the second and fourth order, respectively. In Figs. 3 and 4 "A" and "C" denote the errors of approximation of the cumulant neglect closure of the second and fourth order, respectively, for parameters $a = 0.1$, $b = 0.2$, and "B" and "D" for parameters $a = 0.1$, $b = 0.44$.

3.2 Second-order System With Triangle Matrices. We can describe the second-order system with triangle matrices in the following form:

$$\frac{dx_1}{dt} = -ak_{10}(1 + K\eta)x_1, \qquad x_1(0) = x_{10},$$

$$\frac{dx_2}{dt} = -bk_{20}(1 + K\eta)x_2 + ak_{10}(1 + K\eta)x_1, \qquad x_2(0) = x_{20},$$

$$d\eta = -\alpha\eta dt + \alpha dW, \qquad \eta(0) = \eta_o, \quad (11)$$

where $\alpha, a, k_{10}, b, k_{20}, K$ are constant real parameters, $\alpha > 0$, η is colored noise, η_o is Gaussian random variable with zero ex-

Downloaded 03 May 2010 to 171.66.16.244. Redistribution subject to ASME license or copyright; see http://www.asme.org/terms/Terms_Use.cfm

pectation and variance equals to $\alpha/2$, and W is a standard Wiener process.

The solutions of (11) are as follows:

$$x_1(t) = x_{10}\exp\left(-\int_0^t ak_{10}(1+K\eta(s))ds\right),$$

$$x_2(t) = x_{20}\exp\left(-\int_0^t bk_{20}(1+K\eta(s))ds\right) +$$

$$+ x_{10}\int_0^t ak_{10}(1+K\eta(v))\cdot\exp\left(-\int_0^v ak_{10}(1+K\eta(s))ds\right.$$

$$\left.-\int_v^t bk_{20}(1+K\eta(s))ds\right)dv. \quad (12)$$

Using the method proposed by Willsky et al. (1975), we have obtained the expectation and variance of solutions in the form:

$$E[x_1(t)] = x_{10}\exp\left\{-ak_{10}t+\frac{1}{2}a^2k_{10}^2K^2(t-\alpha^{-1}+\alpha^{-1}e^{-\alpha t})\right\} \quad (13)$$

$$E[x_2(t)] = x_{20}\exp\left\{-bk_{20}t+\frac{1}{2}b^2k_{20}^2K^2(t-\alpha^{-1}+\alpha^{-1}e^{-\alpha t})\right\}$$

$$+ x_{10}\int_0^t\left(ak_{10}-\frac{1}{2}a^2k_{10}^2K^2(1-e^{-\alpha u})\right.$$

$$\left.-\frac{1}{2}abk_{10}k_{20}K^2(1-e^{-\alpha(t-u)})\right)\times\exp\left\{-ak_{10}u\right.$$

$$\left.-bk_{20}(t-u)+\frac{1}{2}a^2k_{10}^2K^2(u-\alpha^{-1}+\alpha^{-1}e^{-\alpha u})\right.$$

$$+\frac{1}{2}b^2k_{20}^2K^2(t-u-\alpha^{-1}+\alpha^{-1}e^{-\alpha(t-u)})$$

$$\left.+\frac{1}{2\alpha}abk_{10}k_{20}K^2(1-e^{-\alpha u}+e^{-\alpha t}-e^{-\alpha(t-u)})\right\}du \quad (14)$$

$$E[x_1^2] = x_{10}^2\exp\left\{-2ak_{10}t+2a^2k_{10}^2K^2\left(t-\frac{1}{\alpha}+\frac{1}{\alpha}e^{-\alpha t}\right)\right\} \quad (15)$$

$$E[x_2^2] = x_{20}^2\exp\left\{-2bk_{20}t+2b^2k_{20}^2K^2\left(t-\frac{1}{\alpha}+\frac{1}{\alpha}e^{-\alpha t}\right)\right\}$$

$$+2x_{10}x_{20}\int_0^t\left\{ak_{10}-\frac{1}{2}ak_{10}(ak_{10}\right.$$

$$\left.+bk_{20})K^2(1-e^{-\alpha v})-ak_{10}bk_{20}K^2(1-e^{-\alpha(t-v)})\right\}$$

$$\times\exp\left\{-(ak_{10}+bk_{20})v-2bk_{20}(t-v)+\frac{1}{2}(ak_{10}\right.$$

$$+bk_{20})^2K^2\left(v-\frac{1}{\alpha}+\frac{1}{\alpha}e^{-\alpha v}\right)+bk_{20}(ak_{10}$$

$$+bk_{20})K^2\frac{1}{\alpha}(1-e^{-\alpha v}+e^{-\alpha t}-e^{-\alpha(t-v)})$$

$$\left.+2b^2k_{20}^2K^2\left(t-v-\frac{1}{\alpha}+\frac{1}{\alpha}e^{-\alpha(t-v)}\right)\right\}dv$$

$$+2x_{10}^2\int_0^t\int_0^v\left\{\left[ak_{10}-a^2k_{10}^2K^2(e^{-\alpha(v-s)}-e^{-\alpha v})\right.\right.$$

$$-\frac{1}{2}ak_{10}K^2(ak_{10}+bk_{20})(1-e^{-\alpha(v-s)})$$

$$\left.\left.-ak_{10}bk_{20}K^2(1-e^{-\alpha(t-v)})\right]\right.$$

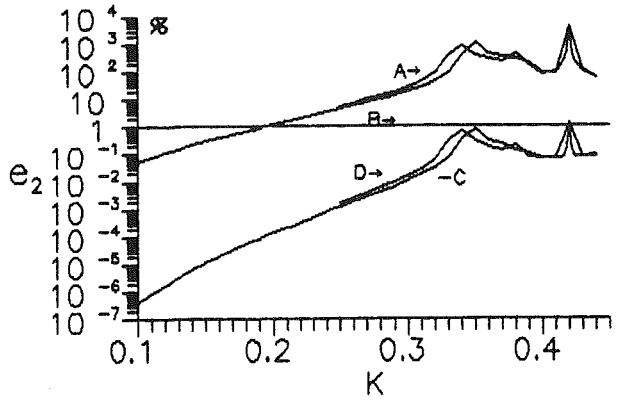


Fig. 5 Error of mean value versus parameter K

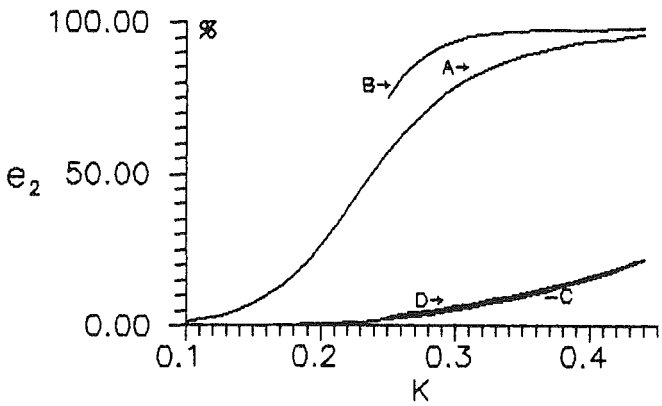


Fig. 6 Error of second moment versus parameter K

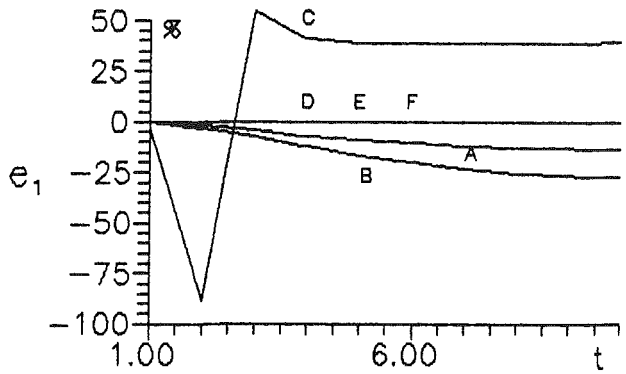


Fig. 7 Error of mean value versus time t

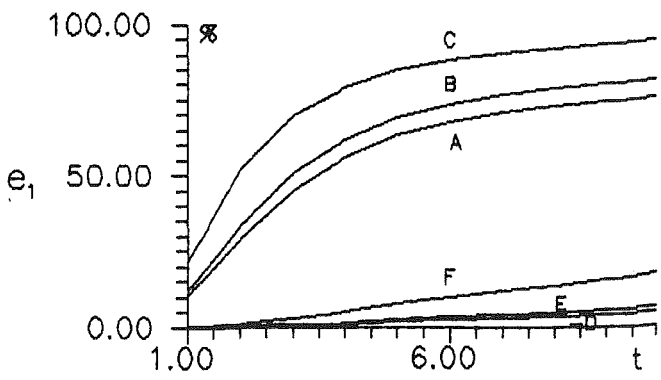


Fig. 8 Error of second moment versus time t

Downloaded 03 May 2010 to 171.66.16.244. Redistribution subject to ASME license or copyright; see http://www.asme.org/terms/Terms_Use.cfm

$$\times\left[ak_{10}-a^2k_{10}^2K^2(1-e^{-\alpha s})-\frac{1}{2}ak_{10}K^2(ak_{10}+bk_{20})\right.$$

$$\times(1-e^{-\alpha(v-s)})-ak_{10}bk_{20}K^2(e^{-\alpha(v-s)}-e^{-\alpha(t-s)})\Big]$$

$$+a^2k_{10}^2K^2\frac{\alpha}{2}\exp(-\alpha(v-s))\Big\}\times\exp\Big\{-2ak_{10}s$$

$$-(ak_{10}+bk_{20})(v-s)-2bk_{20}(t-v)$$

$$+2a^2k_{10}^2K^2\left(s-\frac{1}{\alpha}+\frac{1}{\alpha}e^{-\alpha s}\right)+2b^2k_{20}^2K^2\left(t-v\right.$$

$$\left.-\frac{1}{\alpha}+\frac{1}{\alpha}e^{-\alpha(t-v)}\right)+ak_{10}(ak_{10}$$

$$+bk_{20})K^2\frac{1}{\alpha}(1-e^{-\alpha s}+e^{-\alpha v}-e^{-\alpha(v-s)})$$

$$+2ak_{10}bk_{20}K^2\frac{1}{\alpha}(e^{-\alpha(v-s)}-e^{-\alpha v}+e^{-\alpha t}$$

$$-e^{-\alpha(t-s)})+\frac{1}{\alpha}(ak_{10}+bk_{20})^2K^2\left(v-s-\frac{1}{\alpha}\right.$$

$$\left.+\frac{1}{\alpha}e^{-\alpha(v-s)}\right)+(ak_{10}+bk_{20})bk_{20}K^2$$

$$\times\frac{1}{\alpha}(e^{-\alpha(t-s)}-e^{-\alpha(t-v)}+1-e^{-\alpha(v-s)})\Big\}dsdv. \qquad (16)$$

So the exact first and second moments of the stationary solutions are equal to zero. Using the cumulant neglect technique, we have obtained the same solution. The other solution obtained on the basis of the cumulant neglect technique for special values of parameters (for instance $2(ak_{10}+\alpha)=aK_{10}K\alpha$ for Gaussian closure), is as follows:

$$E[\eta]=0,\ E[\eta^2]=\alpha/2.$$

The other moments have the form of linear and/or quadratic functions of $E[x_1\eta]$. This solution differs from the exact one.

The errors of approximation of the cumulant neglect technique are given in Figs. 5–8. In Figs. 5 and 6, "A" and "C" denote the errors of approximation of the cumulant neglect closure of the second and fourth order, respectively, for parameters $a=0.1$, $b=0.5$, $k_{10}=k_{20}=1$, "B" and "D" for parameters $a=0.1$, $b=0.1$, $k_{10}=k_{20}=1$. In Figs. 7 and 8, "A" and "D" denote the errors of approximation of the cumulant neglect closure of second and fourth order, respectively, for parameters $a=0.1$, $b=0.5$, $k_{10}=k_{20}=1$, $K=0.29$, "B" and "E" for parameters $a=0.1$, $b=0.5$, $k_{10}=k_{20}=1$, $K=0.31$, and "C" and "F" for parameters $a=0.1$, $b=0.5$, $k_{10}=k_{20}=1$, $K=0.41$.

4 Conclusions

From the presented analysis one can learn that the cumulant neglect closure technique gives satisfying results for many values of parameters, but in some cases the obtained results are qualitatively different from the exact ones. This phenomenon occurred for the system of second order for mean values when this system was "on the stability border" but was not observed for the second-order moments of the solution. However, it is very important to study the stability regions of the considered system before using the cumulant neglect technique.

This fact has not as yet been admitted in the literature.

References

Banai, N., and Brenig, L., 1983, "A Non-Linear Stochastic Differential Equation: Exact Critical Statics and Dynamics," *Physica*, Vol. 119A, pp. 512–526.

Sun, J. Q., and Hsu, C. S., 1987, "Cumulant-Neglect Closure Method for Nonlinear Systems Under Random Excitations," ASME JOURNAL OF APPLIED MECHANICS, Vol. 54, pp. 649–655.

Willsky, A. S., Marcus, S. I., and Martin, D. N., 1975, "On the Stochastic Stability of Linear Systems Containing Colored Multiplicative Noise," *IEEE Trans. Automat. Control*, Vol. AC-20, pp. 711–713.

Wu, W. F., and Lin, Y. K., 1984, "Cumulant Neglect Closure for Non-Linear Oscillators under Random Parametric and External Excitations," *Int. J. Non-Linear Mechanics*, Vol. 19, pp. 349–362.

Flexural Waves in a Periodic Beam

Sen Yung Lee[3], Huei Yaw Ke,[4] and Ming Jang Kao[5]

The flexural wave propagation in the periodic beam can be interpreted as the superposition of two pairs of waves propagating in opposite directions. One of them forms an attenuated standing wave. The dispersion spectrum of the other pair of waves shows the band structure, consisting of stopping and passing bands. For the symmetry structure, the dispersion equation at the end points of Brillouin zone is uncoupled into two equations. Each of them corresponds to a standing wave which is either symmetric or antisymmetric about the midplane of the layers.

1 Introduction

The increasing interest of composites in structural applications has generated extensive research efforts in the area of dynamic behavior of periodic medium. For instance, the construction of various approximate continuum theories (Sun et al., 1968; Sve, 1971; Hegemier et al., 1974; Nayfeh, 1974), the application of Floquet theory (Lee et al., 1973; Kaul et al., 1982; Schoenberg, 1984), and the experimental verification (Kinra et al., 1983; Touratier, 1986). A quite interesting review on the theory and applications of waves in periodic structures can be found in two review papers (Elachi, 1976; Noor, 1988).

A general characteristic of the wave propagation through periodic structures is the existence of band structure in dispersion spectrum consisting of stopping and passing bands. This gives the periodic structure the characteristic of a mechanical filter, in which waves having frequency and wave number lying in the stopping bands are attenuated, while others are transmitted.

In this paper, as a preliminary study of the dynamic problem of a general periodic beam, we employ the Bernoulli-Euler beam theory to investigate the problem of free flexural wave propagation in a periodically segmented beam. The governing eigenvalue equation is a fourth-order ordinary differential equation with periodic, piecewise constant coefficients. The analysis and classification of the dynamic nature of the system is presented. For the symmetric problem which there exists one set of coordinate system to impart symmetry to the structure, the uncoupling of the dispersion equation at the ends of the Brillouin zones of the dispersion spectrum is examined in detail.

[3]Associate Professor, Department of Mechanical Engineering, National Cheng Kung University, Tainan, Taiwan.

[4]Institute of Aeronautics and Astronautics, National Cheng Kung University, Tainan, Taiwan.

[5]Chung Shan Institute of Science and Technology, Lung Tan, Taiwan.

Manuscript received by the ASME Applied Mechanics Division, August 15, 1988; final revision, May 17, 1989.

Downloaded 03 May 2010 to 171.66.16.244. Redistribution subject to ASME license or copyright; see http://www.asme.org/terms/Terms_Use.cfm

$$\times\left[ak_{10}-a^2k_{10}^2K^2(1-e^{-\alpha s})-\frac{1}{2}ak_{10}K^2(ak_{10}+bk_{20})\right.$$

$$\times(1-e^{-\alpha(v-s)})-ak_{10}bk_{20}K^2(e^{-\alpha(v-s)}-e^{-\alpha(t-s)})\Big]$$

$$+a^2k_{10}^2K^2\frac{\alpha}{2}\exp(-\alpha(v-s))\Big\}\times\exp\Big\{-2ak_{10}s$$

$$-(ak_{10}+bk_{20})(v-s)-2bk_{20}(t-v)$$

$$+2a^2k_{10}^2K^2\left(s-\frac{1}{\alpha}+\frac{1}{\alpha}e^{-\alpha s}\right)+2b^2k_{20}^2K^2\left(t-v\right.$$

$$\left.-\frac{1}{\alpha}+\frac{1}{\alpha}e^{-\alpha(t-v)}\right)+ak_{10}(ak_{10}$$

$$+bk_{20})K^2\frac{1}{\alpha}(1-e^{-\alpha s}+e^{-\alpha v}-e^{-\alpha(v-s)})$$

$$+2ak_{10}bk_{20}K^2\frac{1}{\alpha}(e^{-\alpha(v-s)}-e^{-\alpha v}+e^{-\alpha t}$$

$$-e^{-\alpha(t-s)})+\frac{1}{\alpha}(ak_{10}+bk_{20})^2K^2\left(v-s-\frac{1}{\alpha}\right.$$

$$\left.+\frac{1}{\alpha}e^{-\alpha(v-s)}\right)+(ak_{10}+bk_{20})bk_{20}K^2$$

$$\times\frac{1}{\alpha}(e^{-\alpha(t-s)}-e^{-\alpha(t-v)}+1-e^{-\alpha(v-s)})\Big\}dsdv. \qquad (16)$$

So the exact first and second moments of the stationary solutions are equal to zero. Using the cumulant neglect technique, we have obtained the same solution. The other solution obtained on the basis of the cumulant neglect technique for special values of parameters (for instance $2(ak_{10}+\alpha)=aK_{10}K\alpha$ for Gaussian closure), is as follows:

$$E[\eta]=0,\ E[\eta^2]=\alpha/2.$$

The other moments have the form of linear and/or quadratic functions of $E[x_1\eta]$. This solution differs from the exact one.

The errors of approximation of the cumulant neglect technique are given in Figs. 5–8. In Figs. 5 and 6, "A" and "C" denote the errors of approximation of the cumulant neglect closure of the second and fourth order, respectively, for parameters $a=0.1$, $b=0.5$, $k_{10}=k_{20}=1$, "B" and "D" for parameters $a=0.1$, $b=0.1$, $k_{10}=k_{20}=1$. In Figs. 7 and 8, "A" and "D" denote the errors of approximation of the cumulant neglect closure of second and fourth order, respectively, for parameters $a=0.1$, $b=0.5$, $k_{10}=k_{20}=1$, $K=0.29$, "B" and "E" for parameters $a=0.1$, $b=0.5$, $k_{10}=k_{20}=1$, $K=0.31$, and "C" and "F" for parameters $a=0.1$, $b=0.5$, $k_{10}=k_{20}=1$, $K=0.41$.

4 Conclusions

From the presented analysis one can learn that the cumulant neglect closure technique gives satisfying results for many values of parameters, but in some cases the obtained results are qualitatively different from the exact ones. This phenomenon occurred for the system of second order for mean values when this system was "on the stability border" but was not observed for the second-order moments of the solution. However, it is very important to study the stability regions of the considered system before using the cumulant neglect technique.

This fact has not as yet been admitted in the literature.

References

Banai, N., and Brenig, L., 1983, "A Non-Linear Stochastic Differential Equation: Exact Critical Statics and Dynamics," *Physica*, Vol. 119A, pp. 512–526.

Sun, J. Q., and Hsu, C. S., 1987, "Cumulant-Neglect Closure Method for Nonlinear Systems Under Random Excitations," ASME JOURNAL OF APPLIED MECHANICS, Vol. 54, pp. 649–655.

Willsky, A. S., Marcus, S. I., and Martin, D. N., 1975, "On the Stochastic Stability of Linear Systems Containing Colored Multiplicative Noise," *IEEE Trans. Automat. Control*, Vol. AC-20, pp. 711–713.

Wu, W. F., and Lin, Y. K., 1984, "Cumulant Neglect Closure for Non-Linear Oscillators under Random Parametric and External Excitations," *Int. J. Non-Linear Mechanics*, Vol. 19, pp. 349–362.

Flexural Waves in a Periodic Beam

Sen Yung Lee[3], Huei Yaw Ke,[4] and Ming Jang Kao[5]

The flexural wave propagation in the periodic beam can be interpreted as the superposition of two pairs of waves propagating in opposite directions. One of them forms an attenuated standing wave. The dispersion spectrum of the other pair of waves shows the band structure, consisting of stopping and passing bands. For the symmetry structure, the dispersion equation at the end points of Brillouin zone is uncoupled into two equations. Each of them corresponds to a standing wave which is either symmetric or antisymmetric about the midplane of the layers.

1 Introduction

The increasing interest of composites in structural applications has generated extensive research efforts in the area of dynamic behavior of periodic medium. For instance, the construction of various approximate continuum theories (Sun et al., 1968; Sve, 1971; Hegemier et al., 1974; Nayfeh, 1974), the application of Floquet theory (Lee et al., 1973; Kaul et al., 1982; Schoenberg, 1984), and the experimental verification (Kinra et al., 1983; Touratier, 1986). A quite interesting review on the theory and applications of waves in periodic structures can be found in two review papers (Elachi, 1976; Noor, 1988).

A general characteristic of the wave propagation through periodic structures is the existence of band structure in dispersion spectrum consisting of stopping and passing bands. This gives the periodic structure the characteristic of a mechanical filter, in which waves having frequency and wave number lying in the stopping bands are attenuated, while others are transmitted.

In this paper, as a preliminary study of the dynamic problem of a general periodic beam, we employ the Bernoulli-Euler beam theory to investigate the problem of free flexural wave propagation in a periodically segmented beam. The governing eigenvalue equation is a fourth-order ordinary differential equation with periodic, piecewise constant coefficients. The analysis and classification of the dynamic nature of the system is presented. For the symmetric problem which there exists one set of coordinate system to impart symmetry to the structure, the uncoupling of the dispersion equation at the ends of the Brillouin zones of the dispersion spectrum is examined in detail.

[3]Associate Professor, Department of Mechanical Engineering, National Cheng Kung University, Tainan, Taiwan.

[4]Institute of Aeronautics and Astronautics, National Cheng Kung University, Tainan, Taiwan.

[5]Chung Shan Institute of Science and Technology, Lung Tan, Taiwan.

Manuscript received by the ASME Applied Mechanics Division, August 15, 1988; final revision, May 17, 1989.

Copyright © 1990 by ASME
Downloaded 03 May 2010 to 171.66.16.244. Redistribution subject to ASME license or copyright; see http://www.asme.org/terms/Terms_Use.cfm

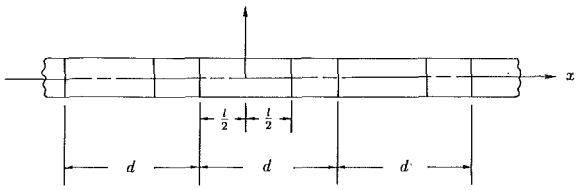


Fig. 1 Geometry of layered elastic beam

2 Governing Equations and Displacement Field

Consider a periodically segmented beam of infinite length as shown in Fig. 1. The one-dimensional domain along the length direction is the union of infinite number of cells with identical properties and has real minimal period d. Each cell consists of two layers. The two-phase composite is made up of two materials having different elastic properties and mass densities and each perfectly bonded at their interfaces.

For time-harmonic flexural wave with angular frequency ω, the flexural displacement $V(x)$ satisfies the eigenvalue problem,

$$V''''(x) - Q(x)V(x) = 0, \tag{1}$$

where accents indicate differentiation with respect to the variable x, and

$$Q(x) = \begin{cases} \alpha_1^4 = (\rho_1\omega^2)/(E_1 I), & x \in \left(-\frac{l}{2} + nd, \frac{l}{2} + nd\right) \\ \alpha_2^4 = (\rho_2\omega^2)/(E_2 I), & x \in \left(\frac{l}{2} + nd, (n+1)d - \frac{l}{2}\right) \end{cases} \tag{2}$$

where E_i, ρ_i, and α_i, $i = 1, 2$, represent the Young's modulus, mass per unit length, and the wave number of flexural waves of two different layers in one unit cell, respectively. I is the moment of inertia which is constant throughout the beam, l is the thickness of the first layer, and n is an integer. The function $Q(x)$ is sectionally constant. In the infinite domain, it is symmetric and periodic with period d, such that $Q(-x) = Q(x)$ and $Q(x+d) = Q(x)$. Being perfectly bonded elastic medium, the displacement, slope, bending moment, and shear force are required to be continuous at all the common interfaces.

We consider the general displacement field in the form

$$V(x) = AV_1(x) + BV_2(x) + CV_3(x) + DV_4(x), \quad x \in (-\infty, \infty)$$

$$= \begin{cases} AV_{11}(x) + BV_{21}(x) + CV_{31}(x) + DV_{41}(x), & x \in \left(-\frac{l}{2} + nd, \frac{l}{2} + nd\right) \\ AV_{12}(x) + BV_{22}(x) + CV_{32}(x) + DV_{42}(x), & x \in \left(\frac{l}{2} + nd, (n+1)d - \frac{l}{2}\right) \end{cases} \tag{3}$$

where V_{ij} represents the ith solution of the jth layer in one unit cell and satisfies the continuity condition at the interfaces. A, B, C, and D are four constants to be determined. For simplicity, the four fundamental solutions V_1, V_2, V_3, and V_4 are chosen such that they satisfy the following normalization condition at the origin of the coordinate system

$$\begin{bmatrix} V_1(0) & V_2(0) & V_3(0) & V_4(0) \\ V_1'(0) & V_2'(0) & V_3'(0) & V_4'(0) \\ V_1''(0) & V_2''(0) & V_3''(0) & V_4''(0) \\ V_1'''(0) & V_2'''(0) & V_3'''(0) & V_4'''(0) \end{bmatrix} = \begin{bmatrix} 1 & 0 & 0 & 0 \\ 0 & 1 & 0 & 0 \\ 0 & 0 & 1 & 0 \\ 0 & 0 & 0 & 1 \end{bmatrix}. \tag{4}$$

For instance, the solutions of the first and second layers of the first cell take the following form

$$V_{11}(x) = \frac{\cosh \alpha_1 x + \cos \alpha_1 x}{2}, V_{21}(x) = \frac{\sinh \alpha_1 x + \sin \alpha_1 x}{2\alpha_1},$$

$$V_{31}(x) = \frac{\cosh \alpha_1 x - \cos \alpha_1 x}{2\alpha_1^2},$$

$$V_{41}(x) = \frac{\sinh \alpha_1 x - \sin \alpha_1 x}{2\alpha_1^3}, \quad x \in \left(-\frac{l}{2}, \frac{l}{2}\right) \tag{5a}$$

and

$$\begin{bmatrix} V_{12}(x) \\ V_{22}(x) \\ V_{32}(x) \\ V_{42}(x) \end{bmatrix} = \begin{bmatrix} V_{11}\left(\frac{l}{2}\right) & V_{11}'\left(\frac{l}{2}\right) & \mu V_{11}''\left(\frac{l}{2}\right) & \mu V_{11}'''\left(\frac{l}{2}\right) \\ V_{21}\left(\frac{l}{2}\right) & V_{21}'\left(\frac{l}{2}\right) & \mu V_{21}''\left(\frac{l}{2}\right) & \mu V_{21}'''\left(\frac{l}{2}\right) \\ V_{31}\left(\frac{l}{2}\right) & V_{31}'\left(\frac{l}{2}\right) & \mu V_{31}''\left(\frac{l}{2}\right) & \mu V_{31}'''\left(\frac{l}{2}\right) \\ V_{41}\left(\frac{l}{2}\right) & V_{41}'\left(\frac{l}{2}\right) & \mu V_{41}''\left(\frac{l}{2}\right) & \mu V'''_{41}\left(\frac{l}{2}\right) \end{bmatrix} \begin{bmatrix} \tilde{V}_{12}\left(x - \frac{l}{2}\right) \\ \tilde{V}_{22}\left(x - \frac{l}{2}\right) \\ \tilde{V}_{32}\left(x - \frac{l}{2}\right) \\ \tilde{V}_{42}\left(x - \frac{l}{2}\right) \end{bmatrix}, x \in \left(\frac{l}{2}, d - \frac{l}{2}\right) \tag{5b}$$

where

$$\mu = \frac{E_1}{E_2},$$

$$\tilde{V}_{12}\left(x - \frac{l}{2}\right) = \frac{\cosh \alpha_2\left(x - \frac{l}{2}\right) + \cos \alpha_2\left(x - \frac{l}{2}\right)}{2},$$

$$\tilde{V}_{22}\left(x - \frac{l}{2}\right) = \frac{\sinh \alpha_2\left(x - \frac{l}{2}\right) + \sin \alpha_2\left(x - \frac{l}{2}\right)}{2\alpha_2},$$

Downloaded 03 May 2010 to 171.66.16.244. Redistribution subject to ASME license or copyright; see http://www.asme.org/terms/Terms_Use.cfm

$$\bar{V}_{32}\left(x-\frac{l}{2}\right)=\frac{\cosh\alpha_2\left(x-\frac{l}{2}\right)-\cos\alpha_2\left(x-\frac{l}{2}\right)}{2\alpha_2^2},$$

and

$$\bar{V}_{42}\left(x-\frac{l}{2}\right)=\frac{\sinh\alpha_2\left(x-\frac{l}{2}\right)-\sin\alpha_2\left(x-\frac{l}{2}\right)}{2\alpha_2^3}.$$

Since the coefficient of the governing equation (1), $Q(x)$, is periodic, the solutions in the second cell will be the linear combination of the base solutions in the first cell. After applying the normalization condition (4) and the continuity condition at $x=l/2$ and $x=d-l/2$, we can obtain the fundamental solutions of the second cell

$$\begin{bmatrix} V_1(x+d)\\ V_2(x+d)\\ V_3(x+d)\\ V_4(x+d)\end{bmatrix}=\begin{bmatrix} V_1(d) & V_1'(d) & V_1''(d) & V_1'''(d)\\ V_2(d) & V_2'(d) & V_2''(d) & V_2'''(d)\\ V_3(d) & V_3'(d) & V_3''(d) & V_3'''(d)\\ V_4(d) & V_4'(d) & V_4''(d) & V_4'''(d)\end{bmatrix}\begin{bmatrix} V_1(x)\\ V_2(x)\\ V_3(x)\\ V_4(x)\end{bmatrix}. \tag{6}$$

3 Quasi-Periodic Condition

For a periodically segmented beam, according to the Floquet theorem, the displacement, slope, bending moment, and shear force are quasi-period from cell to cell. It follows

$$\begin{aligned} V(x+nd)&=\sigma V(x+(n-1)d),\\ V'(x+nd)&=\sigma V'(x+(n-1)d),\\ V''(x+nd)&=\sigma V''(x+(n-1)d),\\ V'''(x+nd)&=\sigma V'''(x+(n-1)d),\end{aligned} \tag{7}$$

where σ may be real or complex number. Taking $n=1$, $x=0$ and using the normalization condition (4), we obtain a system of linear homogeneous equations. For the existence of nontrivial solutions, the determinant of the coefficients must vanish. This yields the characteristic σ-equation

$$\sigma^4+p\sigma^3+q\sigma^2+r\sigma+t=0. \tag{8}$$

From equations (4), (5), and (7) it can be shown that

$$\begin{aligned} p&=r,\\ t&=1,\end{aligned} \tag{9}$$

where

$$p=-[V_1(d)+V_2'(d)+V_3''(d)+V_4'''(d)],$$

$$q=\begin{vmatrix} V_1(d) & V_2(d)\\ V_1'(d) & V_2'(d)\end{vmatrix}+\begin{vmatrix} V_1(d) & V_3(d)\\ V_1''(d) & V_3''(d)\end{vmatrix}+\begin{vmatrix} V_1(d) & V_4(d)\\ V_1'''(d) & V_4'''(d)\end{vmatrix}+\begin{vmatrix} V_2'(d) & V_3'(d)\\ V_2''(d) & V_3''(d)\end{vmatrix}+\begin{vmatrix} V_2'(d) & V_4'(d)\\ V_2'''(d) & V_4'''(d)\end{vmatrix}+\begin{vmatrix} V_3''(d) & V_4''(d)\\ V_3'''(d) & V_4'''(d)\end{vmatrix}. \tag{10}$$

As a result, the characteristic σ-equation can be factorized into the product form

$$(\sigma^2+H_1\sigma+1)(\sigma^2+H_2\sigma+1)=0, \tag{11}$$

where H_1 and H_2 are

$$H_{1,2}=\frac{p\pm\sqrt{p^2-4(q-2)}}{2}. \tag{12}$$

If σ_1, σ_2 and σ_3, σ_4 are the roots of equations $\sigma^2+H_1\sigma+1=0$ and $\sigma^2+H_2\sigma+1=0$, respectively, then

$$\sigma_{1,2}=\frac{-H_1\pm\sqrt{H_1^2-4}}{2}, \tag{13}$$

$$\sigma_{3,4}=\frac{-H_2\pm\sqrt{H_2^2-4}}{2}. \tag{14}$$

If we define

$$Y_j(x)=e^{i\lambda_j x}V(x)\,|_{\sigma=\sigma_j},\quad j=1,2,3,4, \tag{15}$$

where λ_j is a Floquet wave number, then $Y_j(x)$ is a periodic function with period d, provided

$$\sigma_j=e^{i\lambda_j d}. \tag{16}$$

Because $\sigma_1\sigma_2=1$ and $\sigma_3\sigma_4=1$, hence $\lambda_2=-\lambda_1+m\pi/d$ and $\lambda_4=-\lambda_3+n\pi/d$, where m and n are integer numbers. Without loss of generality, we can select $m=n=0$ here. The general displacement field thus takes the following familiar form (Brillouin, 1953)

$$V(x)=C_1Y_1(x)e^{i\lambda_1 x}+C_2Y_2(x)e^{-i\lambda_1 x}+C_3Y_3(x)e^{i\lambda_3 x}+C_4Y_4(x)e^{-i\lambda_3 x}, \tag{17}$$

where C_1, C_2, C_3, and C_4 are four constants to be determined. This solution is a superposition of two pairs of waves propagated (or attenuated) in opposite directions. This is clearly seen if we retain the $e^{i\omega t}$ factor. If these two pair of waves attenuate from cell to cell, then the waves will be finally stopped after certain cells. The frequency intervals in which both pairs of waves attenuate are known as stopping bands. On the other hand, the frequency intervals in which any one pair of waves propagate are known as passing bands.

From equations (5), (6), and (10) it can be shown that, in the dynamic case ($\omega\neq 0$),

$$p^2-4(q-2)>0, \tag{18}$$

and

$$H_2<-2. \tag{19}$$

Hence, σ_3 and σ_4 are two distinct, positive real numbers. It follows from equation (16) that λ_3 is entirely imaginary. Therefore, there always exists one pair of standing waves attenuated in opposite directions. The characteristic of the other pair of waves will thus be determined by function H_1, which may be greater than, equal to, or less than 2 in absolute value.

If $|H_1|<2$, then it follows from equations (13) and (16) that the second pair of waves propagate in opposite directions. Hence, the frequency intervals which correspond to $|H_1|<2$ are passing bands.

If $H_1>2$ (or $H_1<-2$), then from equations (13) and (16) it follows that the second pair of waves form a standing wave with amplitude attenuating in both directions. Hence, the frequency intervals those correspond to $|H_1|>2$ are stopping bands.

In case $H_1=-2$ (or $H_1=2$), both σ_1 and σ_2 are equal to unity (or -1). If the group velocity $\partial\omega/\partial R_e\lambda$ is equal to zero, where $R_e\lambda$ represents the real part of Floquet wave number λ, then the waves form a standing wave with period d (or double

Downloaded 03 May 2010 to 171.66.16.244. Redistribution subject to ASME license or copyright; see http://www.asme.org/terms/Terms_Use.cfm

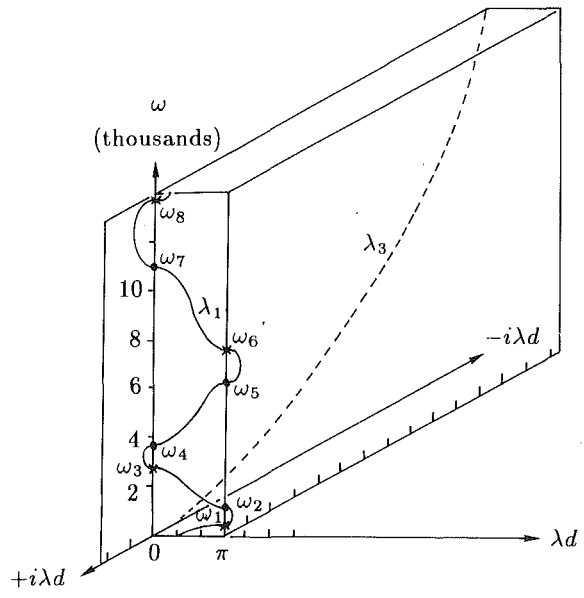


Fig. 2 Dispersion spectrum in Brillouin reduced zone scheme

period $2d$). On the other hand, if the group velocity is not equal to zero, the waves will propagate in both directions. An interesting discussion on this specific problem can be found in Brillouin's book (1953).

Figure 2 is the dispersion spectrum in reduced Brillouin zone scheme with the material and geometry parameters given as follows:

	Young's modulus	mass density
Aluminum	$E_1 = 6.8947 \times 10^{10}$ N/m^2	2698.4 kg/m^3
Plumbum	$E_2 = 1.3789 \times 10^{11}$ N/m^2	11342. kg/m^3

cross-section area $A = 7.74 \times 10^{-4}$ m^2, moment of inertia $I = 4.16 \times 10^{-8}$ m^4, period of the structure $d = 0.254$ m, and thickness of the first layer $l = 0.1524$ m. Since $\lambda_1 = -\lambda_2$ and $\lambda_3 = -\lambda_4$, in this figure only two curves those correspond to λ_1 and λ_3 are presented. The dashed line and real line correspond to λ_3 and λ_1, respectively. From equations (13), (14), and (16), we realize that λ_3 and λ_1 are dominated by H_2 and H_1, respectively. For the branch λ_3, it stands for a pair of attenuated standing waves in all the frequency domain. For the branch λ_1, the frequency intervals between ω_{2n-1} and ω_{2n}, which correspond to the case $|H_1| < 2$, are stopping bands and the other frequency intervals are passing bands. On the right and left end points of Brillouin zones, H_1 is equal to -2 and 2, respectively. It can be observed that the dispersion spectrum for the branch λ_1 is similar to that of the dynamic systems governed by the second-order ordinary differential equation with periodic coefficients (Kaul et al., 1982; Lee et al., 1973), and the existence of passing bands and stopping bands is also a characteristic of flexural waves in periodic beams.

4 Decomposition of the Dispersion Equation

If there exists one set of a coordinate system which imparts symmetry to the structure, then the coefficient function of the governing equation (1), $Q(x)$, is an even function. If follows that $V_1(x)$, $V_3(x)$, $V_2'(x)$, $V_4'(x)$, $V_1''(x)$, $V_3''(x)$, $V_2'''(x)$, $V_4'''(x)$ are even functions and $V_2(x)$, $V_4(x)$, $V_1'(x)$, $V_3'(x)$, $V_2''(x)$, $V_4''(x)$, $V_1'''(x)$, $V_3'''(x)$ are odd functions.

In this case, the dispersion equation at the end points of Brillouin zones can be uncoupled into two equations. If we set $\sigma = 1$ in equation (8), then the dispersion equation, which corresponds to the left end points of the reduced Brillouin zone of Fig. 2, is uncoupled into

$$V_1'\left(\frac{d}{2}\right) V_3'''\left(\frac{d}{2}\right) - V_1'''\left(\frac{d}{2}\right) V_3'\left(\frac{d}{2}\right) = 0, \tag{20}$$

$$V_2\left(\frac{d}{2}\right) V_4''\left(\frac{d}{2}\right) - V_2''\left(\frac{d}{2}\right) V_4\left(\frac{d}{2}\right) = 0. \tag{21}$$

Similarly, if we set $\sigma = -1$ in equation (8), then the dispersion equation which corresponding to the right end point of the reduced Brillouin zone of Fig. 2, is uncoupled into

$$V_1\left(\frac{d}{2}\right) V_3''\left(\frac{d}{2}\right) - V_1''\left(\frac{d}{2}\right) V_3\left(\frac{d}{2}\right) = 0, \tag{22}$$

$$V_2'\left(\frac{d}{2}\right) V_4'''\left(\frac{d}{2}\right) - V_2'''\left(\frac{d}{2}\right) V_4'\left(\frac{d}{2}\right) = 0. \tag{23}$$

The significance of this uncouping can be explained. For symmetric motion the displacement field, equation (3), is the combination of two even functions

$$V(x) = AV_1(x) + CV_3(x).$$

By setting $n = 1$, $\sigma = 1$ and $x = -d/2$ in equation (7), and realizing that $V_1(x)$, $V_3(x)$, $V_1''(x)$, $V_3''(x)$ are even functions and $V_1'(x)$, $V_3'(x)$, $V_1'''(x)$, $V_3'''(x)$ are odd functions, we can obtain two linear independent equations. For the existence of nontrivial solutions, the determinant of the coefficients vanishes. It yields equation (20). Hence, equation (20) is the dispersion equation for a symmetric standing wave with period d and adjacent cells vibrate in the same phase. Similarly, we can show that equation (21) is the dispersion equation for an antisymmetric standing wave with period d and adjacent cells vibrate in the same phase, while equations (22) and (23) govern symmetric and antisymmetric standing wave with double period $2d$ and adjacent cells vibrate in counter phase, respectively. In the special case that both equations (20) and (21) are equal to zero, the stopping band vanishes and the group velocity is not equal to zero. So does for the case that both equations (22) and (23) are equal to zero. For instance, the flexural waves can propagate freely in a homogeneous beam at any frequency and it can be easily shown that equation (20) is equal to equation (21), and equation (22) is equal to equation (23). The other example also can be found if we change the material and/or geometry parameters.

On both ends of Brillouin zone of Fig. 2, the marks "." and "×" are used to indicate the symmetric and antisymmetric vibration mode, respectively.

5 Conclusions

The flexural waves propagation in the periodic beam is considered as the superposition of two pairs of waves propagating in opposite directions. One of them forms a standing wave with amplitude attenuating. The dispersion spectrum of the other pair of waves is shown to take the band structure, consisting of stopping and passing bands. Hence, the justification of the dynamic nature of the system is mainly dominated by a simple function H_1, equation (12). For symmetric structure, the dispersion equation, which corresponds to the end points of Brillouin zone of the dispersion spectrum, is uncoupled into two equations. Each of them corresponds to a standing wave which is either symmetric or antisymmetric about the midplane of the layers.

Acknowledgment

The support of the National Science Council of Taiwan, R.O.C. is gratefully acknowledged.

References

Brillouin, L., 1953, *Wave Propagation in Periodic Structures*, Dover, New York.

Elachi, C., 1976, "Waves in Active and Passive Periodic Structures: A review," *Proc. of the IEEE*, Vol. 64, pp. 1666–1698.

Downloaded 03 May 2010 to 171.66.16.244. Redistribution subject to ASME license or copyright; see http://www.asme.org/terms/Terms_Use.cfm

Hegemier, G. A., and Bache, T. C., 1974, "A General Continuum Theory with Microstructure for Wave Propagation in Elastic Laminated Composite," ASME JOURNAL OF APPLIED MECHANICS, Vol. 41, pp. 101–105.

Ince, E. L., 1956, *Ordinary Differential Equations*, Dover, New York.

Kaul, R. K., and Lee, C. S., 1982, "Free Torsional Vibrations of a Hollow Cylidner with Laminated Periodic Structure," *Int. J. Solids Structures*, Vol. 18, pp. 297–314.

Kinra, V. K., and Ker, E. L., 1983, "An Experimental Investigation of Pass Bands and Stop Bands in Two Periodic Particulate Composites," *Int. J. Solids Structures*, Vol. 19, pp. 393–410.

Kittel, CC., 1963, *Introduction to Solid State Physics*, 5th ed. John Wiley and Sons, New York.

Lee, E. H., and Yang, W. H., 1973, "On Waves in Composite Materials With Periodic Structures," *SIAM J. Appl. Math.*, Vol. 25, pp. 492–499.

Magnus, W., and Winkler, S., 1979, *Hill's Equation*, Dover, New York.

Nayfeh, A. H., 1974, "Time-harmonic Waves Propagating Normal to the Layers of Multilayered Periodic Media," ASME JOURNAL OF APPLIED MECHANICS, Vol. 41, pp. 92–96.

Noor, A. K., 1988, "Continuum Modeling for the Repetitive Lattice Structures," ASME *Appl. Mech. Rev.*, Vol. 41, pp. 285–296.

Schoenberg, M., 1984, "Wave Propagation in Alternating Solid and Fluid Layers," *Wave Motion*, Vol. 6, pp. 303–320.

Sun, C. T., Achenbach, J. D., and Herrmann, G., 1968, "Continuum Theory for a Laminated Medium," ASME JOURNAL OF APPLIED MECHANICS, Vol. 35, pp. 467–475.

Sve, C., 1971, "Time-harmonic Waves Traveling Obliquely in a Periodically Laminated Medium," ASME JOURNAL OF APPLIED MECHANICS, Vol. 38, pp. 477–482.

Touratier, M., 1986, "Floquet Waves in a Body With Slender Periodic Structures," *Wave Motion*, Vol. 8, pp. 485–495.

The Effect of Wall Motions on the Governing Equations of Contained Fluids

Roger Ohayon[6] and Carlos A. Felippa[7]

The equations of motion for an acoustic fluid enclosed in a moving or flexible container are studied. It is shown that the determination of the reference state must account for the surface-integrated effect of the wall motions. The governing equation of transient motions about this state in the displacement potential does not generally reduce to the classical wave equation unless special adjustments are made. The results are relevant to finite elements formulations based on the displacement potential.

1 Problem Description

The results presented in this Note were obtained in the course of a wider study by Felippa and Ohayon (1989) of variational methods for transient motions and vibrations of acoustic fluids held in flexible and/or moving containers. These partial results merit special attention on two counts. First, they extend the classical dynamic equations of acoustic fluids to include wall motions as well as the static limit in a consistent manner. Second, they are relevant to finite element implementations that have not accounted for the correction terms described herein. Computations that are particularly affected by these corrections involve liquid masses subject to prescribe dynamic motions, such as tanks and reservoirs under seismic ground motion excitations, and rocket fuel tanks under launch conditions.

The general problem is as follows. A container (the structure) is totally or partly filled with a compressible, homogeneous liquid or gas (the fluid). Although the container is generally flexible, the rigid-but-moving container case is not excluded. The fluid is modeled as an acoustic medium (the linearly compressible generalization of an ideal fluid). We consider dynamic motions about a static reference state, which will be determined as part of the study.

If the container is rigid and fixed, the reference state is well known: the static equilibrium solution in which the pressure is equal to the hydrostatic pressure, and the displacements may be taken as zero. The acoustic motions about this position are governed by the homogeneous wave equation in the displacement potential. But if the container walls move, we show that a correction term that depends on the mean boundary motion appears. The reference state is affected, and the resulting transient vibration problem is no longer given by the classical wave equation unless special adjustments are made.

A boundary integral term representing the mean container motion was introduced by Aganovic (1981) for the surface wave problem of an incompressible fluid posed in terms of the velocity potential. Ohayon (1987) considered similar terms in the displacement potential formulation. The general forms presented in this Note for a compressible fluid are believed to be new.

2 The Acoustic Fluid

The three-dimensional volume occupied by the fluid is denoted by V. This volume is assumed to be simply connected. The fluid boundary S consists generally of two portions

$$S{:}S_d \cup S_p. \tag{1}$$

S_d is the interface with the container at which the normal displacement d_n is prescribed (or found as part of the coupled fluid structure problem) whereas S_p is the "free surface" at which the pressure p is prescribed (or found as part of the "slosh" problem). If the fluid is fully enclosed by the container, as is necessarily the case for a gas, then S_p is missing and $S \equiv S_d$. The domain is referred to a Cartesian coordinate system (x_1, x_2, x_3) grouped in vector $\mathbf{x}$.

The fluid is under a body force field $\mathbf{b}$ which is assumed to be the gradient of a *time-independent* potential $\beta(\mathbf{x})$, i.e., $\mathbf{b} = \nabla\beta$. All displacements are taken to be infinitesimal and thus the fluid density ρ is invariant.

We consider three states or configurations: *original*, from which displacements, pressures and forces are measured, *current*, where the fluid is in dynamic equilibrium at time t, and *reference*, which is obtained in the static equilibrium limit of slow motions. *Transient* motions are the difference between current and reference states. It should be noted that in many situations the original configuration is not physically attainable. Table 1 summarizes the notation used in relation to these states.

Field Equations. The governing equations of the acoustic fluid are the momentum, state, and continuity equations. They are stated as follows for the current configuration, and specialized to the reference configuration later. The momentum (balance) equation expresses Newton's second law for a fluid particle:

$$\rho\ddot{\mathbf{d}}^t = -\nabla p^t + \mathbf{b} = -\nabla p^t + \nabla\beta. \tag{2}$$

The continuity equation may be combined with the linearized equation of state to produce the *constitutive equation* that expresses the small compressibility of a liquid:

$$p^t = -K\nabla\mathbf{d}^t = -\rho c^2 \nabla\mathbf{d}^t, \tag{3}$$

where K is the bulk modulus and $c = \sqrt{K/\rho}$ the fluid sound speed. If the fluid is incompressible, K, $c \to \infty$. This relation is also applicable to nonlinear elastic fluids such as gases undergoing small excursions from the reference state, if the constitutive equation is linearized there so that $K = \rho_0(dp/d\rho)_0$.

[6]Office National D'Études et de Recherches Aérospatiales, BP 72, 92322 Chalillon, France.

[7]Department of Aerospace Engineering Sciences and Center for Space Structures and Controls, University of Colorado, Boulder, CO 80309-0429, Mem. ASME.

Manuscript received and accepted by the ASME Applied Mechanics Division, Nov. 8, 1988.

Downloaded 03 May 2010 to 171.66.16.244. Redistribution subject to ASME license or copyright; see http://www.asme.org/terms/Terms_Use.cfm

Hegemier, G. A., and Bache, T. C., 1974, "A General Continuum Theory with Microstructure for Wave Propagation in Elastic Laminated Composite," ASME JOURNAL OF APPLIED MECHANICS, Vol. 41, pp. 101–105.

Ince, E. L., 1956, *Ordinary Differential Equations*, Dover, New York.

Kaul, R. K., and Lee, C. S., 1982, "Free Torsional Vibrations of a Hollow Cylidner with Laminated Periodic Structure," *Int. J. Solids Structures*, Vol. 18, pp. 297–314.

Kinra, V. K., and Ker, E. L., 1983, "An Experimental Investigation of Pass Bands and Stop Bands in Two Periodic Particulate Composites," *Int. J. Solids Structures*, Vol. 19, pp. 393–410.

Kittel, CC., 1963, *Introduction to Solid State Physics*, 5th ed. John Wiley and Sons, New York.

Lee, E. H., and Yang, W. H., 1973, "On Waves in Composite Materials With Periodic Structures," *SIAM J. Appl. Math.*, Vol. 25, pp. 492–499.

Magnus, W., and Winkler, S., 1979, *Hill's Equation*, Dover, New York.

Nayfeh, A. H., 1974, "Time-harmonic Waves Propagating Normal to the Layers of Multilayered Periodic Media," ASME JOURNAL OF APPLIED MECHANICS, Vol. 41, pp. 92–96.

Noor, A. K., 1988, "Continuum Modeling for the Repetitive Lattice Structures," ASME *Appl. Mech. Rev.*, Vol. 41, pp. 285–296.

Schoenberg, M., 1984, "Wave Propagation in Alternating Solid and Fluid Layers," *Wave Motion*, Vol. 6, pp. 303–320.

Sun, C. T., Achenbach, J. D., and Herrmann, G., 1968, "Continuum Theory for a Laminated Medium," ASME JOURNAL OF APPLIED MECHANICS, Vol. 35, pp. 467–475.

Sve, C., 1971, "Time-harmonic Waves Traveling Obliquely in a Periodically Laminated Medium," ASME JOURNAL OF APPLIED MECHANICS, Vol. 38, pp. 477–482.

Touratier, M., 1986, "Floquet Waves in a Body With Slender Periodic Structures," *Wave Motion*, Vol. 8, pp. 485–495.

The Effect of Wall Motions on the Governing Equations of Contained Fluids

Roger Ohayon[6] and Carlos A. Felippa[7]

The equations of motion for an acoustic fluid enclosed in a moving or flexible container are studied. It is shown that the determination of the reference state must account for the surface-integrated effect of the wall motions. The governing equation of transient motions about this state in the displacement potential does not generally reduce to the classical wave equation unless special adjustments are made. The results are relevant to finite elements formulations based on the displacement potential.

1 Problem Description

The results presented in this Note were obtained in the course of a wider study by Felippa and Ohayon (1989) of variational methods for transient motions and vibrations of acoustic fluids held in flexible and/or moving containers. These partial results merit special attention on two counts. First, they extend the classical dynamic equations of acoustic fluids to include wall motions as well as the static limit in a consistent manner. Second, they are relevant to finite element implementations that have not accounted for the correction terms described herein. Computations that are particularly affected by these corrections involve liquid masses subject to prescribe dynamic motions, such as tanks and reservoirs under seismic ground motion excitations, and rocket fuel tanks under launch conditions.

The general problem is as follows. A container (the structure) is totally or partly filled with a compressible, homogeneous liquid or gas (the fluid). Although the container is generally flexible, the rigid-but-moving container case is not excluded. The fluid is modeled as an acoustic medium (the linearly compressible generalization of an ideal fluid). We consider dynamic motions about a static reference state, which will be determined as part of the study.

If the container is rigid and fixed, the reference state is well known: the static equilibrium solution in which the pressure is equal to the hydrostatic pressure, and the displacements may be taken as zero. The acoustic motions about this position are governed by the homogeneous wave equation in the displacement potential. But if the container walls move, we show that a correction term that depends on the mean boundary motion appears. The reference state is affected, and the resulting transient vibration problem is no longer given by the classical wave equation unless special adjustments are made.

A boundary integral term representing the mean container motion was introduced by Aganovic (1981) for the surface wave problem of an incompressible fluid posed in terms of the velocity potential. Ohayon (1987) considered similar terms in the displacement potential formulation. The general forms presented in this Note for a compressible fluid are believed to be new.

2 The Acoustic Fluid

The three-dimensional volume occupied by the fluid is denoted by V. This volume is assumed to be simply connected. The fluid boundary S consists generally of two portions

$$S{:}S_d \cup S_p. \tag{1}$$

S_d is the interface with the container at which the normal displacement d_n is prescribed (or found as part of the coupled fluid structure problem) whereas S_p is the "free surface" at which the pressure p is prescribed (or found as part of the "slosh" problem). If the fluid is fully enclosed by the container, as is necessarily the case for a gas, then S_p is missing and $S \equiv S_d$. The domain is referred to a Cartesian coordinate system (x_1, x_2, x_3) grouped in vector $\mathbf{x}$.

The fluid is under a body force field $\mathbf{b}$ which is assumed to be the gradient of a *time-independent* potential $\beta(\mathbf{x})$, i.e., $\mathbf{b} = \nabla\beta$. All displacements are taken to be infinitesimal and thus the fluid density ρ is invariant.

We consider three states or configurations: *original*, from which displacements, pressures and forces are measured, *current*, where the fluid is in dynamic equilibrium at time t, and *reference*, which is obtained in the static equilibrium limit of slow motions. *Transient* motions are the difference between current and reference states. It should be noted that in many situations the original configuration is not physically attainable. Table 1 summarizes the notation used in relation to these states.

Field Equations. The governing equations of the acoustic fluid are the momentum, state, and continuity equations. They are stated as follows for the current configuration, and specialized to the reference configuration later. The momentum (balance) equation expresses Newton's second law for a fluid particle:

$$\rho\ddot{\mathbf{d}}^t = -\nabla p^t + \mathbf{b} = -\nabla p^t + \nabla\beta. \tag{2}$$

The continuity equation may be combined with the linearized equation of state to produce the *constitutive equation* that expresses the small compressibility of a liquid:

$$p^t = -K\nabla\mathbf{d}^t = -\rho c^2 \nabla\mathbf{d}^t, \tag{3}$$

where K is the bulk modulus and $c = \sqrt{K/\rho}$ the fluid sound speed. If the fluid is incompressible, K, $c \to \infty$. This relation is also applicable to nonlinear elastic fluids such as gases undergoing small excursions from the reference state, if the constitutive equation is linearized there so that $K = \rho_0(dp/d\rho)_0$.

[6]Office National D'Études et de Recherches Aérospatiales, BP 72, 92322 Chalillon, France.

[7]Department of Aerospace Engineering Sciences and Center for Space Structures and Controls, University of Colorado, Boulder, CO 80309-0429, Mem. ASME.

Manuscript received and accepted by the ASME Applied Mechanics Division, Nov. 8, 1988.

Copyright © 1990 by ASME
Downloaded 03 May 2010 to 171.66.16.244. Redistribution subject to ASME license or copyright; see http://www.asme.org/terms/Terms_Use.cfm

Table 1 Notation for fluid states

Quantities	Domain	Original	Reference	Current	Transient
Displacements	V	$\mathbf{0}$	$\mathbf{d}^0$	$\mathbf{d}^t$	$\mathbf{d}=\mathbf{d}^t-\mathbf{d}^0$
Velocities	V	$\mathbf{0}$	$\dot{\mathbf{d}}^0$	$\dot{\mathbf{d}}^t$	$\dot{\mathbf{d}}=\dot{\mathbf{d}}^t-\dot{\mathbf{d}}^0$
Boundary displacements*	S	0	d_n^0	d_n^t	$d_n=d_n^t-d_n^0$
Displacement potential	V	$\mathbf{0}$	ψ^0	ψ^t	$\psi=\psi^t-\psi^0$
Pressures	V	0	p^0	p^t	$p=p^t-p^0$
Body forces	V	$\mathbf{0}$	$\mathbf{b}=\nabla\beta$	$\mathbf{b}=\nabla\beta$	
Density	V	ρ	ρ	ρ	

*Positive along outward normal

The boundary conditions are

$$d_n^t=\tilde{d}_n^t \text{ on } S_d,\quad p^t=\tilde{p}^t \text{ on } S_p, \tag{4}$$

where $\tilde{d}_n^t$ is either prescribed or comes from the solution of an auxiliary problem as in fluid-structure interaction, and $\tilde{p}$ may be either prescribed or a function of d_n and $\mathbf{b}$, as in the surface wave ("slosh") problem.

3 The Reference State

Taking the curl of both sides of (2) yields

$$\mathbf{curl}\ \ddot{\mathbf{d}}^t=\mathbf{0}. \tag{5}$$

The general integral of this equation for a simply connected domain is

$$\mathbf{d}^t=\nabla\psi^t+\mathbf{a}+\mathbf{b}t, \tag{6}$$

where $\psi^t=\psi^t(\mathbf{x},t)$ is the displacement potential, $\mathbf{a}=\mathbf{a}(\mathbf{x})$ and $\mathbf{b}=\mathbf{b}(\mathbf{x})$ are time-independent vector functions, and t denotes the time. If accelerationless motions (for example, rigid body motions) are precluded by the boundary conditions, $\mathbf{a}$ and $\mathbf{b}$ vanish. Replacing $\ddot{\mathbf{d}}^t=\nabla\ddot{\psi}^t$ into the momentum equation (2) we get

$$\nabla p^t=-\rho\nabla\ddot{\psi}^t+\nabla\beta, \tag{7}$$

which spatially integrated gives

$$p^t=-\rho\ddot{\psi}^t+\beta+C(t), \tag{8}$$

where the scalar $C(t)$ is not spatially dependent. Next, integrate the constitutive equation (3) over V and apply the divergence theorem to $\nabla\mathbf{d}$:

$$(p^t)_V+(\rho c^2\nabla\mathbf{d}^t)_V=(p^t)_V+[\rho c^2 d_n^t]_S=0. \tag{9}$$

Inserting p^t from (8) into equation (9) furnishes a condition on $C(t)$, giving

$$C(t)=-\frac{\rho c^2}{v}[d_n^t]_S+\frac{\rho}{v}(\ddot{\psi}^t)V-\frac{1}{v}(\beta)V$$

$$=-\frac{\rho c^2}{v}[d_n^t]_S+\rho\bar{\ddot{\psi}}^t-\bar{\beta}, \tag{10}$$

where $v=(1)_V$ is the fluid volume and $\bar{f}=(f)_V/v$ denotes the volume average of a function f defined over V. Substituting $C(t)$ into (9) we get

$$p^t=-(\rho(\ddot{\psi}^t-\bar{\ddot{\psi}}^t)+(\beta-\bar{\beta})-\frac{\rho c^2}{v}[d_n^t]_S. \tag{11}$$

In the static limit the inertia terms may be neglected and we recover the reference solution

$$p^0=(\beta-\bar{\beta})-\frac{\rho c^2}{v}[d_n^0]_S. \tag{12}$$

For an incompressible fluid, $[d_n]_S=0$ but $c\to\infty$; thus it would be incorrect to conclude that $p^0=\beta-\bar{\beta}$. To illustrate this point, consider a rigid cylindrical container of cross-section area A, filled with liquid up to height $H=H_1+H_2$. The origin of the Cartesian system (x_1, x_2, x_3) is placed at H_2 below the free surface, with $x_1\equiv x$ upwards and normal to that surface (see Fig. 1). The body force is the gravity field $\mathbf{b}=(-\rho g,0,0)$; thus $\beta=-\rho g x+B$, B being an arbitrary constant.

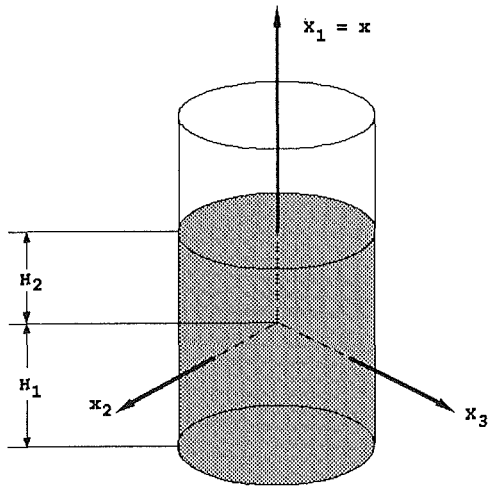


Fig. 1 Cylindrical fluid container in gravity field

In passing from the original configuration under zero body force to the reference configuration under gravity, the free surface moves downwards by the amount

$$d_n|_{x=H_2}=\eta^0=-\frac{\rho g H^2}{2K}=-\frac{gH^2}{2c^2}. \tag{13}$$

Evaluation of (12) gives

$$p^0=\rho g\left(x-\frac{1}{2}(H_2-H_1)\right)+B-B$$

$$+\frac{\rho c^2 A\eta^0}{AH}=\rho g(H_2-x), \tag{14}$$

which is the correct hydrostatic pressure if $\delta\ll H$. If one passes to the incompressible limit, $c\to\infty$ and $\delta\to 0$, but $c^2\delta$ remains fixed and equal to $gH^2/2$. Note that substracting $\bar{\beta}$ eliminates B. The associated displacement field is easily calculated to be

$$\mathbf{d}^0=\begin{Bmatrix} d_1^0\\ d_2^0\\ d_3^0\end{Bmatrix}=\begin{Bmatrix} -\frac{g}{2c^2}[H^2-(x-H_2)^2]0\\ 0\\ 0\end{Bmatrix}+\mathbf{d}_{rot}^0, \tag{15}$$

where $\mathbf{d}_{rot}^0$ is an arbitrary divergence-free rotational motion that satisfies the boundary conditions.

4 Transient Motions

Substracting the constitutive relations at the current and reference states we get

$$p=-\rho c^2\nabla^2\psi=\rho c^2 s, \tag{16}$$

where $s=-\nabla^2\psi$ is the condensation. Subtracting (12) from (11) yields

Downloaded 03 May 2010 to 171.66.16.244. Redistribution subject to ASME license or copyright; see http://www.asme.org/terms/Terms_Use.cfm

$$p = -\rho(\ddot{\psi} - \ddot{\bar{\psi}}) - \frac{\rho c^2}{v}[d_n]_S. \tag{17}$$

On equating (16) and (17) we get modified forms of the wave equation that account either for nonzero mean boundary surface motions,

$$s = \nabla^2\psi = \frac{\ddot{\psi} - \ddot{\bar{\psi}}}{c^2} + \frac{1}{v}[d_n]_S, \tag{18}$$

or nonzero mean dilatation,

$$c^2(\nabla^2\psi - \overline{\nabla^2\psi}) = c^2(\nabla^2\psi + \bar{s}) = \ddot{\psi} - \ddot{\bar{\psi}}. \tag{19}$$

The second form follows from $-v\bar{s} = [d_n]_S$, which is a consequence of the divergence theorem. For an incompressible fluid, $c \to \infty$ and $\bar{s} = [d_n]_S = 0$, and from either form one recovers the Laplace equation $\nabla^2\psi = 0$.

Adjusting the Displacement Potential. If the transient displacement potential is modified by a function of time:

$$\psi = \hat{\psi} + P(t), \tag{20}$$

where $\hat{\psi}$ is the potential of (6)–(19), we may chose $P(t)$ so that $c^2\ddot{\bar{\psi}} = \overline{\nabla^2\psi} = -\bar{s}$ for any t. ($P(t)$ may be found by integrating $c^2\ddot{\bar{\psi}} - \nabla^2\psi$ twice in time.) We then recover the classical wave equation

$$c^2\nabla^2\psi = \ddot{\psi}. \tag{21}$$

If this adjustment has been made, $C(t)$ vanishes and (17) reduces to

$$p = -\rho\ddot{\psi}. \tag{22}$$

As an example, consider again the container of Fig. 1 in which $H_1 = 0$ for convenience. At $t \le 0$, the container is in the reference state of rest. At $t \ge 0$, it is subjected to a prescribed constant velocity motion of the bottom surface,

$$\tilde{d}_n(t)\Big|_{x=0} = -\alpha t, \quad t \ge 0, \tag{23}$$

positive upwards for $\alpha > 0$. The unknown free surface vertical displacement is $\eta(t)$, also positive upwards. As all quantities become independent of x_2 and x_3, the governing equation is one-dimensional:

$$\psi'' = \frac{\ddot{\psi} - \ddot{\bar{\psi}}}{c^2} + \frac{1}{H}(-\alpha t + \eta), \tag{24}$$

where primes denote derivatives with respect to $x_1 \equiv x$. The solution for $0 \le t \le H/c$ is

$$\eta = 0, \ \psi(x,t) = \begin{cases} \alpha t x + \dfrac{\alpha}{2c}x^2 + P(t), & x \le ct, \\ P(t) - \dfrac{1}{2}\alpha c t^2, & x \ge ct. \end{cases} \tag{25}$$

The adjustment condition gives $P(t) = -1/2\ \alpha c t^2$, and consequently $\psi = 0$ for $x \ge ct$. Hence, for finite c we have $\psi'' = c^2\ddot{\psi}$. If $c \to \infty$, the solution approaches the rigid body motion $\eta = \alpha t$.

5 References

Aganovic, I., 1981, "On a Spectral Problem in Hydroelasticity," *Journal de Mécanique*, Vol. 20, pp. 409–414.

Felippa, C. A., and Ohayon, R., 1989, "Treatment of Coupled Fluid-Structure Interaction Problems by a Mixed Variational Principle," *Proceedings of the 7th International Conference in Finite Element Methods in Fluids*, UAH Press, University of Alabama, Huntsville, Ala., pp. 555–563.

Ohayon, R., 1987, "Fluid-structure modal analysis. New Symmetric Continuum-Based Formulations. Finite Element Applications," *Proceedings International Conference on Numerical Methods in Engineering: Theory and Applications, NUMETA 87*, Contribution T46, M. Nijhoff Pubs., Dordrecht.

Steady Axial Motions of Strings

T. J. Healey[8] and J. N. Papadopoulos[9]

1 Introduction

Consider the planar motion of a closed loop of inextensible, homogeneous chain or string in the absence of external forces. A classical, but virtually forgotten, result states that the loop can occupy any fixed, spatial configuration (satisfying the length constraint), with each particle moving tangentially at the same constant speed (cf. Routh, 1884). In other words, the string flows steadily as though it were enclosed in a frictionless tube. The cowboy's lariat lends credence to the theory, and more careful experimental evidence was obtained over a century ago (cf. Aitken, 1876).

In this short Note we establish two generalizations of the classical result, which do not appear to be well known, and we discuss the existence of a preferred shape. In Section 2 we show that the arbitrary configuration of the chain need not be planar—any closed space curve of the appropriate length will do. Furthermore, we obtain a similar class of solutions for extensible, nonlinearly elastic strings, where the length is now a function of speed. In Section 3 we employ a minimum energy criterion to show that one specific motion within this class—a circular configuration rotating rigidly about its major axis of inertia—is preferred over the others.

2 Formulation and Axial Solutions

Consider a closed loop of homogeneous string in some fixed natural (tension-free) state of length L. We identify a material point of the string by its arclength coordinate s in that configuration. Let $\mathbf{r}(s, t)$ denote the position vector of point s at time t, as measured from the origin O of some fixed frame of reference (cf. Fig. 1). In the absence of body forces, the principle of balance of linear momentum takes the well-known local form

$$(T\mathbf{r}_s/|\mathbf{r}_s|)_s = \rho\mathbf{r}_{tt}, \tag{1}$$

where $T(s, t)$ is the tension at (s, t), $\rho > 0$ is the uniform mass per unit length of string in the natural state, $(\ )_s \equiv \partial(\ )/\partial s$, and $|\mathbf{a}|$ denotes the length of the vector $\mathbf{a}$.

We require all solutions of (1) to satisfy $\mathbf{r}(s + L, t) \equiv \mathbf{r}(s, t)$, which insures that the deformed configuration of the chain is also a closed loop. If the string is inextensible, we supplement (1) with the constraint

$$|\mathbf{r}_s| = 1, \tag{2}$$

and require $T(s + L, t) \equiv T(s, t)$. For an elastic string, we assume the existence of a continuously differentiable function $\hat{T}:(0, \infty) \to \mathbb{R}$ such that

$$T(s,t) = \hat{T}(|\mathbf{r}_s(s,t)|). \tag{3}$$

We make the physically reasonable assumption that the tangent modulus of elasticity is always positive, i.e., $\hat{T}' > 0$. Since the reference configuration is a natural state, it follows that $T(1) = 0$.

Let $\mathfrak{s}(s, t)$ denote the arclength coordinate of the material point in the current configuration that occupies coordinate s in the reference state. An *axial* motion is characterized by an invariant spatial configuration, i.e.,

$$\mathbf{r} = \mathbf{p}(\mathfrak{s}), \tag{4}$$

[8]Assistant Professor, Department of Theoretical and Applied Mechanics, Ithaca, NY 14853.

[9]Assistant Professor, Department of Mechanical Engineering, Northern Illinois University, Dekalb, IL 60115.

Manuscript received and accepted by the ASME Applied Mechanics Division, May 19, 1989.

Downloaded 03 May 2010 to 171.66.16.244. Redistribution subject to ASME license or copyright; see http://www.asme.org/terms/Terms_Use.cfm

$$p = -\rho(\ddot{\psi} - \ddot{\bar{\psi}}) - \frac{\rho c^2}{v}[d_n]_S. \tag{17}$$

On equating (16) and (17) we get modified forms of the wave equation that account either for nonzero mean boundary surface motions,

$$s = \nabla^2\psi = \frac{\ddot{\psi} - \ddot{\bar{\psi}}}{c^2} + \frac{1}{v}[d_n]_S, \tag{18}$$

or nonzero mean dilatation,

$$c^2(\nabla^2\psi - \overline{\nabla^2\psi}) = c^2(\nabla^2\psi + \bar{s}) = \ddot{\psi} - \ddot{\bar{\psi}}. \tag{19}$$

The second form follows from $-v\bar{s} = [d_n]_S$, which is a consequence of the divergence theorem. For an incompressible fluid, $c \to \infty$ and $\bar{s} = [d_n]_S = 0$, and from either form one recovers the Laplace equation $\nabla^2\psi = 0$.

Adjusting the Displacement Potential. If the transient displacement potential is modified by a function of time:

$$\psi = \hat{\psi} + P(t), \tag{20}$$

where $\hat{\psi}$ is the potential of (6)–(19), we may chose $P(t)$ so that $c^2\ddot{\bar{\psi}} = \overline{\nabla^2\psi} = -\bar{s}$ for any t. ($P(t)$ may be found by integrating $c^2\ddot{\bar{\psi}} - \nabla^2\psi$ twice in time.) We then recover the classical wave equation

$$c^2\nabla^2\psi = \ddot{\psi}. \tag{21}$$

If this adjustment has been made, $C(t)$ vanishes and (17) reduces to

$$p = -\rho\ddot{\psi}. \tag{22}$$

As an example, consider again the container of Fig. 1 in which $H_1 = 0$ for convenience. At $t \le 0$, the container is in the reference state of rest. At $t \ge 0$, it is subjected to a prescribed constant velocity motion of the bottom surface,

$$\tilde{d}_n(t)\Big|_{x=0} = -\alpha t, \quad t \ge 0, \tag{23}$$

positive upwards for $\alpha > 0$. The unknown free surface vertical displacement is $\eta(t)$, also positive upwards. As all quantities become independent of x_2 and x_3, the governing equation is one-dimensional:

$$\psi'' = \frac{\ddot{\psi} - \ddot{\bar{\psi}}}{c^2} + \frac{1}{H}(-\alpha t + \eta), \tag{24}$$

where primes denote derivatives with respect to $x_1 \equiv x$. The solution for $0 \le t \le H/c$ is

$$\eta = 0, \ \psi(x,t) = \begin{cases} \alpha t x + \dfrac{\alpha}{2c}x^2 + P(t), & x \le ct, \\ P(t) - \dfrac{1}{2}\alpha c t^2, & x \ge ct. \end{cases} \tag{25}$$

The adjustment condition gives $P(t) = -1/2\ \alpha c t^2$, and consequently $\psi = 0$ for $x \ge ct$. Hence, for finite c we have $\psi'' = c^2\ddot{\psi}$. If $c \to \infty$, the solution approaches the rigid body motion $\eta = \alpha t$.

5 References

Aganovic, I., 1981, "On a Spectral Problem in Hydroelasticity," *Journal de Mécanique*, Vol. 20, pp. 409–414.

Felippa, C. A., and Ohayon, R., 1989, "Treatment of Coupled Fluid-Structure Interaction Problems by a Mixed Variational Principle," *Proceedings of the 7th International Conference in Finite Element Methods in Fluids*, UAH Press, University of Alabama, Huntsville, Ala., pp. 555–563.

Ohayon, R., 1987, "Fluid-structure modal analysis. New Symmetric Continuum-Based Formulations. Finite Element Applications," *Proceedings International Conference on Numerical Methods in Engineering: Theory and Applications, NUMETA 87*, Contribution T46, M. Nijhoff Pubs., Dordrecht.

Steady Axial Motions of Strings

T. J. Healey[8] and J. N. Papadopoulos[9]

1 Introduction

Consider the planar motion of a closed loop of inextensible, homogeneous chain or string in the absence of external forces. A classical, but virtually forgotten, result states that the loop can occupy any fixed, spatial configuration (satisfying the length constraint), with each particle moving tangentially at the same constant speed (cf. Routh, 1884). In other words, the string flows steadily as though it were enclosed in a frictionless tube. The cowboy's lariat lends credence to the theory, and more careful experimental evidence was obtained over a century ago (cf. Aitken, 1876).

In this short Note we establish two generalizations of the classical result, which do not appear to be well known, and we discuss the existence of a preferred shape. In Section 2 we show that the arbitrary configuration of the chain need not be planar—any closed space curve of the appropriate length will do. Furthermore, we obtain a similar class of solutions for extensible, nonlinearly elastic strings, where the length is now a function of speed. In Section 3 we employ a minimum energy criterion to show that one specific motion within this class—a circular configuration rotating rigidly about its major axis of inertia—is preferred over the others.

2 Formulation and Axial Solutions

Consider a closed loop of homogeneous string in some fixed natural (tension-free) state of length L. We identify a material point of the string by its arclength coordinate s in that configuration. Let $\mathbf{r}(s, t)$ denote the position vector of point s at time t, as measured from the origin O of some fixed frame of reference (cf. Fig. 1). In the absence of body forces, the principle of balance of linear momentum takes the well-known local form

$$(T\mathbf{r}_s/|\mathbf{r}_s|)_s = \rho\mathbf{r}_{tt}, \tag{1}$$

where $T(s, t)$ is the tension at (s, t), $\rho > 0$ is the uniform mass per unit length of string in the natural state, $(\ )_s \equiv \partial(\ )/\partial s$, and $|\mathbf{a}|$ denotes the length of the vector $\mathbf{a}$.

We require all solutions of (1) to satisfy $\mathbf{r}(s + L, t) \equiv \mathbf{r}(s, t)$, which insures that the deformed configuration of the chain is also a closed loop. If the string is inextensible, we supplement (1) with the constraint

$$|\mathbf{r}_s| = 1, \tag{2}$$

and require $T(s + L, t) \equiv T(s, t)$. For an elastic string, we assume the existence of a continuously differentiable function $\hat{T}:(0, \infty) \to \mathbb{R}$ such that

$$T(s,t) = \hat{T}(|\mathbf{r}_s(s,t)|). \tag{3}$$

We make the physically reasonable assumption that the tangent modulus of elasticity is always positive, i.e., $\hat{T}' > 0$. Since the reference configuration is a natural state, it follows that $T(1) = 0$.

Let $\mathfrak{s}(s, t)$ denote the arclength coordinate of the material point in the current configuration that occupies coordinate s in the reference state. An *axial* motion is characterized by an invariant spatial configuration, i.e.,

$$\mathbf{r} = \mathbf{p}(\mathfrak{s}), \tag{4}$$

[8]Assistant Professor, Department of Theoretical and Applied Mechanics, Ithaca, NY 14853.

[9]Assistant Professor, Department of Mechanical Engineering, Northern Illinois University, Dekalb, IL 60115.

Manuscript received and accepted by the ASME Applied Mechanics Division, May 19, 1989.

Copyright © 1990 by ASME

Downloaded 03 May 2010 to 171.66.16.244. Redistribution subject to ASME license or copyright; see http://www.asme.org/terms/Terms_Use.cfm

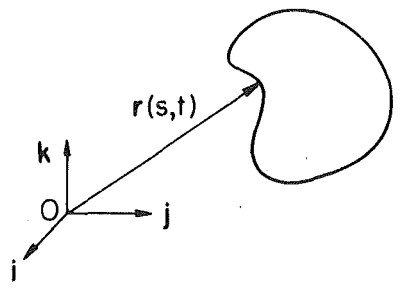


Fig. 1 Current configuration of a loop of string

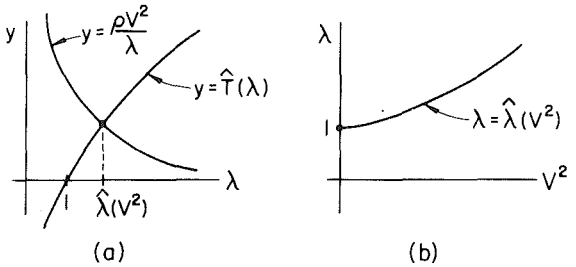


Fig. 2 Graphical solution of equation (8) for a typical nonlinearity elastic string

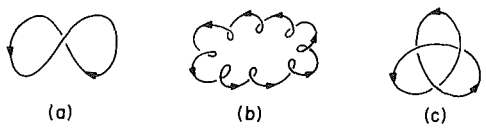


Fig. 3 Three examples of self-equilibrated axial motion

where $\mathbf{p}$ is a continuously differentiable, vector-valued function whose image is a closed-space curve, without self-intersection and of total (unspecified) length l. Since the argument of $\mathbf{p}$ is arclength, we have

$$|\mathbf{p}'| \equiv 1. \tag{5}$$

In addition, we assume that $\mathbf{p}'$ is piecewise continuously differentiable (i.e., $\mathbf{p}''$ is bounded and possesses at most a finite number of discontinuities). We seek *steady* axial solutions of equation (1), i.e.,

$$\mathbf{r}(s,t) = \mathbf{p}(\lambda s + vt), \tag{6}$$

where $\lambda > 0$ and $v \neq 0$ are parameters. By virtue of equations (4)–(6), we have

$$|\mathbf{r}_s(s,t)| \equiv \lambda, \text{ and } |\mathbf{r}_t(s,t)| \equiv |v|, \tag{7}$$

i.e., λ is the uniform stretch and v the constant speed of each material point in the string.

The substitution of (4) and (6) into (1) yields

$$T_s\mathbf{p}' + T\lambda\mathbf{p}'' = \rho v^2\mathbf{p}''.$$

Since the unit tangent vector $\mathbf{p}'$ is never parallel to the normal vector $\mathbf{p}''$, it follows that T is independent of s. Moreover, if $\mathbf{p}''$ is not the zero vector, then

$$T\lambda = \rho v^2. \tag{8}$$

If $\mathbf{p}''$ vanishes on an open set (a segment of the wire is straight) or at an isolated point, or if $\mathbf{p}''$ has an isolated discontinuity, then the integral form of (1) applied to an appropriate free body readily demonstrates the validity of (8).

For an inextensible string, $\lambda \equiv 1$. Thus, a solution of (1) and (2) is

$$T \equiv \rho v^2, \quad \mathbf{r}(s,t) = \mathbf{p}(s + vt). \tag{9}$$

Clearly, $l \equiv L$ insures that $\mathbf{r}$ is L-periodic in s. For an extensible elastic string, we can solve equations (3), (7), and (8) for λ as a unique function of v^2, denoted $\lambda = \hat{\lambda}(v^2)$, where $\hat{\lambda}:[0, \infty) \to [1, \infty)$ is monotonically increasing (cf. Fig. 2). Hence,

$$\mathbf{r}(s,t) = \mathbf{p}(\hat{\lambda}(v^2)s + vt) \tag{10}$$

is a solution of equations (1) and (3). In this case, $l \equiv \hat{\lambda}(v^2)L$ insures the L-periodicity of $\mathbf{r}(\cdot, t)$. Note that the length of an elastic loop increases with increasing values of v^2. For example, a linearly elastic string, characterized by $\hat{T}(\nu) \equiv k(\nu - 1)$, $k > 0$, yields

$$l = [1 + (1 + 4\rho v^2/k)^{1/2}]L/2.$$

Note that equations (9) and (10) are characterized by an *unspecified* vector-valued function $\mathbf{p}$, which is reminiscent of D'Alembert's solution of the linear wave equation. It is amusing to envision some of the conceivable configurations of the moving string, which follow from the ambiguity inherent in our solutions. Perhaps the first thing that comes to mind is the planar, circular state alluded to in Section 1. However, any simple closed curve (topologically equivalent to the ring) of the appropriate length is a valid configuration, two examples of which are depicted in Figs. 3(*a*) and (*b*). The string could even be tied in a loose knot (without self-contact), as shown in Fig. 3(*c*).

3 A Preferred Shape

It is natural to wonder which (if any) of the uncountably many axial motions are most likely to occur from the standpoint of minimum energy. A straightforward calculation shows that the total angular momentum of the string, while undergoing any motion of the form (9) or (10), is a constant that depends upon the shape $\mathbf{p}$. Accordingly, we wish to identify the shape(s) requiring the least energy, given that the total angular momentum is a prescribed constant. However, we find it simpler to address the following (equivalent) dual problem: Identify those motions of the form (9) or (10) that maximize a specified component of the angular momentum, given that the total energy of the string is constant. This criterion implies that a planar, circular configuration rotating rigidly about its major axis of inertia is preferred, as we now show.

We first discuss an inextensible chain. Let $\mathbf{i}, \mathbf{j}, \mathbf{k}$ denote the usual unit vectors associated with rectangular Cartesian coordinates. Without loss of generality, we seek to maximize the component of the total angular momentum along $\mathbf{k}$:

$$H(\mathbf{p},v) \equiv \mathbf{k} \cdot \int_0^L \mathbf{r} \times \mathbf{r}_t \rho ds = \rho v \int_0^L \mathbf{k} \cdot (\mathbf{p} \times \mathbf{p}')ds, \tag{11}$$

where we have made use of equation (9). The total energy comprises the kinetic energy

$$T = (1/2)\int_0^L |\mathbf{r}_t|^2 \rho ds = (\rho v^2/2)\int_0^L |\mathbf{p}'|^2 ds = \rho L v^2/2,$$

which is a constant if and only if v is a constant, say $v = v_o$.

We wish to show that H has an absolute maximum at the circular configuration

$$\mathbf{r} = \mathbf{p}_o(\circ) \equiv (L/2\pi)[\cos(2\pi\circ/L)\mathbf{i} + \sin(2\pi\circ/L)\mathbf{j}], \tag{12}$$

for all configurations of the form (9), where $\circ = s + v_o t$ and $v_o \neq 0$. Let $x(\zeta)\mathbf{i} + y(\zeta)\mathbf{j} + z(\zeta)\mathbf{k} \equiv \mathbf{p}(\zeta L/2\pi)$, where $\zeta \equiv 2\pi\circ/L$. Then by equation (11), we have

$$I(\mathbf{p}) \equiv [H(\mathbf{p}_o,v_o) - H(\mathbf{p},v_o)]/2\rho v_o$$

$$= L^2/4\pi - (1/2)\int_0^{2\pi} (xy' - yx')d\zeta. \tag{13}$$

The first term on the right side of (13) is the area enclosed by a circle of circumference L. If $z' \equiv 0$, then the subtracted integral term represents the area of the region bounded by the simple, closed curve $x\mathbf{i} + y\mathbf{j}$, $0 \leq \zeta < 2\pi$. In that case, we conclude that

$$I(\mathbf{p}) > 0 \text{ for all } \mathbf{p} \neq \mathbf{p}_o, \tag{14}$$

Downloaded 03 May 2010 to 171.66.16.244. Redistribution subject to ASME license or copyright; see http://www.asme.org/terms/Terms_Use.cfm

by virtue of the celebrated "isoperimetric inequality" (which states that the area enclosed by a planar, simple, closed curve of fixed length, is a maximum when the perimeter is a circle).

If $z' \not\equiv 0$, then the projected curve $x\mathbf{i} + y\mathbf{j}$, $0 \le \zeta < 2\pi$, is closed, but need not be simple, and its length is less than L. Consequently, the isoperimetric inequality is not directly applicable. Nonetheless, we can establish (14) in a manner similar to Hurwicz's proof of the isoperimetric inequality (cf. Courant and Hilbert (1953)). In view of equations (5) and (13), it follows that

$$I(\mathbf{p}) \equiv (1/2)\int_0^{2\pi} [(x')^2 + (y')^2 + (z')^2 - xy' + x'y]d\zeta. \quad (15)$$

Under the conditions imposed upon $\mathbf{p}$ (cf., Section 2), we have the Fourier series representations

$$x(\zeta) = \sum_{n=1}^{\infty} [a_n \cos(n\zeta) + b_n \sin(n\zeta)]$$

and

$$y(\zeta) = \sum_{n=1}^{\infty} [c_n \cos(n\zeta) + d_n \sin(n\zeta)], \quad (16)$$

the substitution of which into (15) yields

$$I(\mathbf{p}) = (\pi/2)\sum_{n=1}^{\infty} [(na_n - d_n)^2 + (nb_n + c_n)^2 + (n^2 - 1)(c_n^2 + d_n^2)] + (1/2)\int_0^{2\pi} (z')^2 d\zeta. \quad (17)$$

Clearly, $I(\mathbf{p}) \ge 0$, with equality holding only if

$$a_n = b_n = c_n = d_n = 0 \text{ for } n = 2,3, \ldots,$$
$$d_1 = a_1, c_1 = -b_1, \text{ and}$$
$$z' \equiv 0 \quad (18)$$

i.e., only if $\mathbf{p} = \mathbf{p}_o$.

For an elastic string, we seek to maximize equation (11) for $\mathbf{p}$ of the form of equation (10). Here the total energy comprises the kinetic and potential energies:

$$E \equiv \int_0^L [|\mathbf{r}_t|^2 \rho/2 + W(|\mathbf{r}_s|)]ds = \int_0^L [|\mathbf{p}'|^2 \rho v^2/2 + W(\hat{\lambda}(v^2))]ds = \rho L v^2/2 + L W(\hat{\lambda}(v^2)),$$

where we have used equation (10), and where $W(\eta) \equiv \int \hat{T}(\eta)d\eta$ is the free energy density. Again, we conclude that the total energy is constant if and only if v is constant, i.e., $v = v_o$.

In this case, we want to show that H has an absolute maximum at the circular configuration

$$\mathbf{r} = \mathbf{p}_o(\delta) \equiv (l/2\pi)[\cos(2\pi\delta/l)\mathbf{i} + \sin(2\pi\delta/l)\mathbf{j}], \quad (19)$$

for all motions of the form (10), where $\delta = \hat{\lambda}(v_o^2)s + v_o t$, $v_o \neq 0$ and $l = \hat{\lambda}(v_o^2)L$. Let $x(\zeta)\mathbf{i} + y(\zeta)\mathbf{j} + z(\zeta)\mathbf{k} \equiv \mathbf{p}(\zeta l/2\pi)$, where $\zeta \equiv 2\pi\delta/l$, and define

$$I(\mathbf{p}) \equiv \hat{\lambda}(v_o^2)[H(\mathbf{p}_o, v_o) - H(\mathbf{p}, v_o)]/2\rho v_o.$$

We then have

$$I(\mathbf{p}) = l^2/4\pi - (1/2)\int_0^{2\pi} (xy' - yx')d\zeta,$$

and the required calculations from here are identical to equations (14)–(18) (with l in place of L). Hence, we conclude that equation (14) holds for all $\mathbf{p}$ of the form (10), i.e., the same result is true for elastic strings.

Final Remarks

The restricted calculations of Section 3 suggest that the rigid, circular motion $\mathbf{p}_o$, given by equation (12) or equation (19), is stable. If we seek minimizers of the total energy within a general class of motions, under the constraint of constant angular momentum, then a necessary condition for an extremum is that the motion be *rigid* (cf., Healey, 1990). The only axial motion that is rigid is the circular state $\mathbf{p}_o$. This result and the calculations of Section 3 suggest that the uncountably many noncircular motions $\mathbf{p} \neq \mathbf{p}_o$ (cf. equations (9) and (10)) are unstable in the presence of small dissipation. It can be shown that $\mathbf{p}_o$ is unconditionally stable (for all speeds $v_o \neq 0$) for inextensible chains and for sufficiently stiff elastic strings. On the other hand, for a class of soft elastic materials, $\mathbf{p}_o$ is stable only for sufficiently small speeds, above which bifurcation to other rigidly rotating shapes occurs (cf. Healey, 1990).

Acknowledgment

The work of T. J. Healey was supported by the U.S. Air Force Office of Scientific Research, Grant No. AFOSR-88-0222 and URI Contract No. F49620-87-C-0011.

References

1 Aitken, J., 1876, "Experiments Illustrating Rigidity Produced by Centrifugal Force," *Proc. Phil Soc.*, Glasgow, Vol. 14, pp. 99–106.

2 Courant, R., and Hilbert, D., 1953, *Methods of Mathematical Physics*, John Wiley and Sons, New York, Chapter 2, Section 10.1.

3 Healey, T. J., 1990, "Stability and Bifurcation of Rotating Nonlinearly Elastic Loops," to appear in *Q. Appl. Math.*

4 Routh, E. J., 1884, *Dynamics of a System of Rigid Bodies*, Part 2, 4th ed., MacMillan and Co., London, Sections 522–524.

Use of Statical Indentation Laws in the Impact Analysis of Composite Laminated Plates and Shells

H. J. Lin[10] and Y. J. Lee[10]

Introduction

This note examines the impact response of laminated plate and cylindrical shells. It is well known that one of the weakness of advanced fiber-reinforced composites is their relatively poor resistance to impact loading. Therefore, the impact analysis of composite laminates is one of the major research in recent years. Tan and Sun (1982, 1985), and Caprino et al. (1984) investigated the impact response of plate. Most previous works on impact response analysis are restricted to plate. Impact response analysis on a shell is scarce. Here, we study the curvature effect on impact response of laminates using the static indentation laws.

In the literature, impact loading is often regarded as a given function. However, the loading between the projectile and the target in the real contact is an unknown quantity to be determined. The Hertz (1881) contact law has been used in the impact analysis of isotropic materials by many authors. Due to the microscopically inhomogeneous and macroscopically anisotropic properties of composites, the contact behavior becomes much more complicated. Thus Hertz contact law might not be adequate in the analysis of contact formulation between the projectile and laminates. Using the static indentation test to establish the contact law has been conducted by Tan and Sun (1982, 1985) and has been shown that it is a good simulation to the real contact of composite laminated plate. Therefore, same procedures are used to investigate the curvature effect on the impact response in this work.

[10]Institute of Naval Architecture, National Taiwan University, Taipei, Taiwan.

Contributed by the ASME Applied Mechanics Division, January 16, 1989; final revision, August 4, 1989.

Downloaded 03 May 2010 to 171.66.16.244. Redistribution subject to ASME license or copyright; see http://www.asme.org/terms/Terms_Use.cfm

by virtue of the celebrated "isoperimetric inequality" (which states that the area enclosed by a planar, simple, closed curve of fixed length, is a maximum when the perimeter is a circle).

If $z' \not\equiv 0$, then the projected curve $x\mathbf{i} + y\mathbf{j}$, $0 \le \zeta < 2\pi$, is closed, but need not be simple, and its length is less than L. Consequently, the isoperimetric inequality is not directly applicable. Nonetheless, we can establish (14) in a manner similar to Hurwicz's proof of the isoperimetric inequality (cf. Courant and Hilbert (1953)). In view of equations (5) and (13), it follows that

$$I(\mathbf{p}) \equiv (1/2)\int_0^{2\pi} [(x')^2 + (y')^2 + (z')^2 - xy' + x'y]d\zeta. \quad (15)$$

Under the conditions imposed upon $\mathbf{p}$ (cf., Section 2), we have the Fourier series representations

$$x(\zeta) = \sum_{n=1}^{\infty} [a_n \cos(n\zeta) + b_n \sin(n\zeta)]$$

and

$$y(\zeta) = \sum_{n=1}^{\infty} [c_n \cos(n\zeta) + d_n \sin(n\zeta)], \quad (16)$$

the substitution of which into (15) yields

$$I(\mathbf{p}) = (\pi/2)\sum_{n=1}^{\infty} [(na_n - d_n)^2 + (nb_n + c_n)^2 + (n^2 - 1)(c_n^2 + d_n^2)] + (1/2)\int_0^{2\pi} (z')^2 d\zeta. \quad (17)$$

Clearly, $I(\mathbf{p}) \ge 0$, with equality holding only if

$$a_n = b_n = c_n = d_n = 0 \text{ for } n = 2,3, \ldots,$$
$$d_1 = a_1, c_1 = -b_1, \text{ and}$$
$$z' \equiv 0 \quad (18)$$

i.e., only if $\mathbf{p} = \mathbf{p}_o$.

For an elastic string, we seek to maximize equation (11) for $\mathbf{p}$ of the form of equation (10). Here the total energy comprises the kinetic and potential energies:

$$E \equiv \int_0^L [|\mathbf{r}_t|^2 \rho/2 + W(|\mathbf{r}_s|)]ds$$
$$= \int_0^L [|\mathbf{p}'|^2 \rho v^2/2 + W(\hat{\lambda}(v^2))]ds = \rho L v^2/2 + LW(\hat{\lambda}(v^2)),$$

where we have used equation (10), and where $W(\eta) \equiv \int \hat{T}(\eta)d\eta$ is the free energy density. Again, we conclude that the total energy is constant if and only if v is constant, i.e., $v = v_o$.

In this case, we want to show that H has an absolute maximum at the circular configuration

$$\mathbf{r} = \mathbf{p}_o(\delta) \equiv (l/2\pi)[\cos(2\pi\delta/l)\mathbf{i} + \sin(2\pi\delta/l)\mathbf{j}], \quad (19)$$

for all motions of the form (10), where $\delta = \hat{\lambda}(v_o^2)s + v_o t$, $v_o \neq 0$ and $l = \hat{\lambda}(v_o^2)L$. Let $x(\zeta)\mathbf{i} + y(\zeta)\mathbf{j} + z(\zeta)\mathbf{k} \equiv \mathbf{p}(\zeta l/2\pi)$, where $\zeta \equiv 2\pi\delta/l$, and define

$$I(\mathbf{p}) \equiv \hat{\lambda}(v_o^2)[H(\mathbf{p}_o, v_o) - H(\mathbf{p}, v_o)]/2\rho v_o.$$

We then have

$$I(\mathbf{p}) = l^2/4\pi - (1/2)\int_0^{2\pi} (xy' - yx')d\zeta,$$

and the required calculations from here are identical to equations (14)–(18) (with l in place of L). Hence, we conclude that equation (14) holds for all $\mathbf{p}$ of the form (10), i.e., the same result is true for elastic strings.

Final Remarks

The restricted calculations of Section 3 suggest that the rigid, circular motion $\mathbf{p}_o$, given by equation (12) or equation (19), is stable. If we seek minimizers of the total energy within a general class of motions, under the constraint of constant angular momentum, then a necessary condition for an extremum is that the motion be *rigid* (cf., Healey, 1990). The only axial motion that is rigid is the circular state $\mathbf{p}_o$. This result and the calculations of Section 3 suggest that the uncountably many noncircular motions $\mathbf{p} \neq \mathbf{p}_o$ (cf. equations (9) and (10)) are unstable in the presence of small dissipation. It can be shown that $\mathbf{p}_o$ is unconditionally stable (for all speeds $v_o \neq 0$) for inextensible chains and for sufficiently stiff elastic strings. On the other hand, for a class of soft elastic materials, $\mathbf{p}_o$ is stable only for sufficiently small speeds, above which bifurcation to other rigidly rotating shapes occurs (cf. Healey, 1990).

Acknowledgment

The work of T. J. Healey was supported by the U.S. Air Force Office of Scientific Research, Grant No. AFOSR-88-0222 and URI Contract No. F49620-87-C-0011.

References

1 Aitken, J., 1876, "Experiments Illustrating Rigidity Produced by Centrifugal Force," *Proc. Phil Soc.*, Glasgow, Vol. 14, pp. 99–106.

2 Courant, R., and Hilbert, D., 1953, *Methods of Mathematical Physics*, John Wiley and Sons, New York, Chapter 2, Section 10.1.

3 Healey, T. J., 1990, "Stability and Bifurcation of Rotating Nonlinearly Elastic Loops," to appear in *Q. Appl. Math.*

4 Routh, E. J., 1884, *Dynamics of a System of Rigid Bodies*, Part 2, 4th ed., MacMillan and Co., London, Sections 522–524.

Use of Statical Indentation Laws in the Impact Analysis of Composite Laminated Plates and Shells

H. J. Lin[10] and Y. J. Lee[10]

Introduction

This note examines the impact response of laminated plate and cylindrical shells. It is well known that one of the weakness of advanced fiber-reinforced composites is their relatively poor resistance to impact loading. Therefore, the impact analysis of composite laminates is one of the major research in recent years. Tan and Sun (1982, 1985), and Caprino et al. (1984) investigated the impact response of plate. Most previous works on impact response analysis are restricted to plate. Impact response analysis on a shell is scarce. Here, we study the curvature effect on impact response of laminates using the static indentation laws.

In the literature, impact loading is often regarded as a given function. However, the loading between the projectile and the target in the real contact is an unknown quantity to be determined. The Hertz (1881) contact law has been used in the impact analysis of isotropic materials by many authors. Due to the microscopically inhomogeneous and macroscopically anisotropic properties of composites, the contact behavior becomes much more complicated. Thus Hertz contact law might not be adequate in the analysis of contact formulation between the projectile and laminates. Using the static indentation test to establish the contact law has been conducted by Tan and Sun (1982, 1985) and has been shown that it is a good simulation to the real contact of composite laminated plate. Therefore, same procedures are used to investigate the curvature effect on the impact response in this work.

[10]Institute of Naval Architecture, National Taiwan University, Taipei, Taiwan.

Contributed by the ASME Applied Mechanics Division, January 16, 1989; final revision, August 4, 1989.

Copyright © 1990 by ASME
Downloaded 03 May 2010 to 171.66.16.244. Redistribution subject to ASME license or copyright; see http://www.asme.org/terms/Terms_Use.cfm

Table 1 Contact coefficients in loading, unloading, and reloading laws

CONTACT COEFF.	PLATE	CYLINDRICAL SHELL	
	$[0^\circ_5/90^\circ_5/0^\circ_5]$	$[0^\circ_5/90^\circ_5/0^\circ_5]^*$	$[0^\circ_5/90^\circ_5/0^\circ_5]^\#$
K	0.0837	0.0611	0.0682
n	1.5	1.5	1.5
q	1.4121	1.6056	1.7319
S_p	0.4331	0.6583	
α_p	4.4828	12.5225	
S_f	0.2702	0.3054	

Unit of contact force : Kg
Unit of indentation : 0.001 mm

Static Indentation Laws

The laminating sequence of $[0^\circ_5/90^\circ_5/0^\circ_5]$ Graphite/Epoxy laminate is used. Two groups of cylindrical shells are considered. Specimens denoted by the superscript * are the cylindrical shells curved in 0-deg direction, those denoted by # represent the curvature in 90-deg direction. Thus one group of plate specimens, $[0^\circ_5/90^\circ_5/0^\circ_5]$, and two groups of shell specimens, $[0^\circ_5/90^\circ_5/0^\circ_5]^*$ and $[0^\circ_5/90^\circ_5/0^\circ_5]^\#$, are applied in the present static indentation test. The mechanical properties of Graphite/Epoxy ply are given as:

$E_1 = 108.07$ GPa $E_2 = 8.44$ GPa $\nu_{12} = 0.28$
$G_{12} = G_{13} = G_{23} = 3.32$ GPa $\rho = 2.50$ kg/m^2 $t = 1.65$ mm

where E_1 and E_2 are the longitudinal (fiber direction) and transverse Young's moduli, G_{12}, G_{13}, and G_{23} are the in-plane and transverse shear moduli, ν_{12} is the longitudinal Poisson's ratio, ρ is the mass density per unit area, and t is the thickness of laminate.

To neglect the large deflection of beam specimen, a small specimen with dimension 30×30 mm was used in the indentation test. The nose diameter of the indentor is 12.7 mm. According to the test results, the contact law is given as follows:

Loading Curve

$$F = K\,\alpha^n \tag{1}$$

Unloading Curve

$$F = F'_m\,[(\alpha - \alpha_o)\,/\,(\alpha_m - \alpha_o)]^q \tag{2}$$

$$F'_m = F_m - \Delta F \tag{3}$$

$$\alpha_o = S_p\,(\alpha_m - \alpha_p) \tag{4}$$

$$\Delta F = S_f\,(\alpha_m - \alpha_p) \tag{5}$$

Reloading Curve

$$F = F_m\,[(\alpha - \alpha_o)\,/\,(\alpha_m - \alpha_o)]^{1.5} \tag{6}$$

F and α are the contact force and indentation, respectively. K and n in equation (1) are two contact coefficients to be determined from the experimental results along with the least-square curve fitting. F_m and α_m in equations (2)–(6) are the contact force and indentation at which unloading begins, ΔF is the force jump during the unloading process, and α_o denotes the permanent indentation in an unloading cycle. Test results are presented in Table 1. The power index of $n = 1.5$ fits the loading curves very well. In Table 1, we can see that the contact coefficient K of the cylindrical shell is less than that of plate by about 20 percent owing to less contact area of the cylindrical shell under the same indentation. Because the "softer" specimen provides larger contact coefficient k due to its larger contact area, the value of k of $[0^\circ_5/90^\circ_5/0^\circ_5]^\#$ is thus larger than that of $[0^\circ_5/90^\circ_5/0^\circ_5]^*$ by about eight percent.

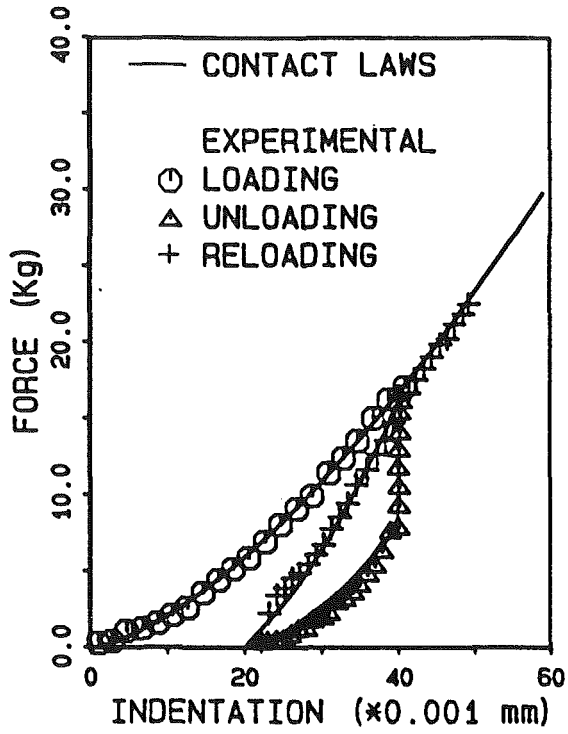


Fig. 1 Typical loading, unloading, and reloading curve of a cylindrical shell

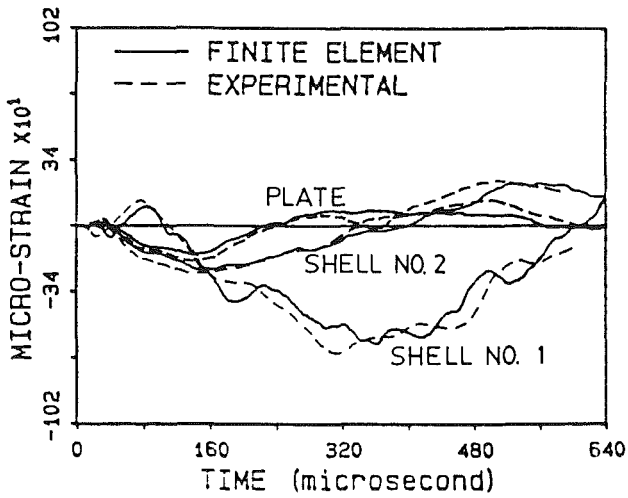


Fig. 2 Strain response histories of plate and cylindrical shells

From equation (2), we can observe that the unloading load is a complicated function of F'_m, ΔF, α, α_m, α_o, and q. Fortunately, a linear relationship between them was found (equations (4) and (5)). The typical loading, unloading, and reloading curve of the cylindrical shell are shown in Fig. 1. Since the fiber reaction has a component in the loading direction, cylindrical shells have smaller force jump and larger critical permanent indentation, α_p. It can be seen that the contact laws fit very well with the experimental results.

Results and Discussion

The Graphite/Epoxy Structures of one plate and two cylindrical shells with dimensions of $149 \times 149 \times 1.65$ mm were used as the impact target. The laminating sequence of $[0^\circ_5/90^\circ_5/0^\circ_5]$ is applied to the plate and cylindrical shells. The 0-deg direction was arranged in the positive x-axis. Two cylindrical shells with radii of 125 mm curved in the y and x-axis are named shell

Downloaded 03 May 2010 to 171.66.16.244. Redistribution subject to ASME license or copyright; see http://www.asme.org/terms/Terms_Use.cfm

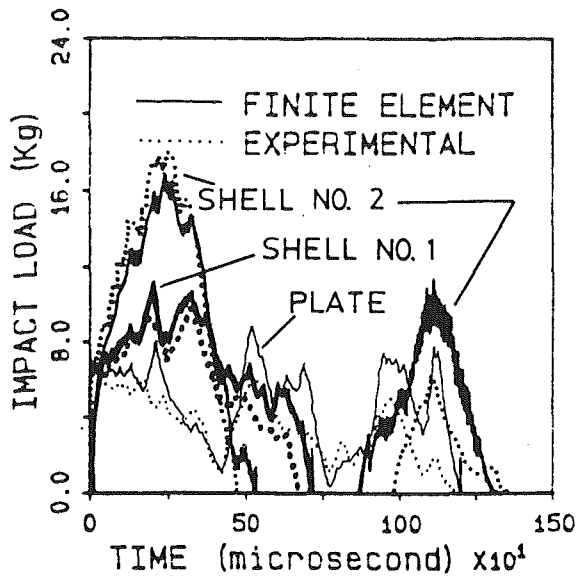


Fig. 3 Impact force histories of plate and cylindrical shells

no. 1 ($[0_5^\circ/90_5^\circ/0_5^\circ]^\#$) and shell no. 2 ($[0_5^\circ/90_5^\circ/0_5^\circ]^*$), respectively. A strain gage was placed on the back face (rear to the impact face) along the x-axis and was 40 mm apart from the impact node. An H.P. 5183U digitizing oscilloscope and a Kyowa DCV 230v high-rate strain gage amplifier were used to capture the strain response. The impact-force transducer of Model 200A5 marketed by PCB Piezotronics, Inc. was used also to record the impact force history. The targets were hung with three strings at the center and corners to achieve the free boundary condition. The mass of impactor with a nose diameter of 12.7 mm and target were 0.03887 kg and 0.05563 kg. Four strings were used to keep the balance of the impactor. The impact velocity of 1.704 m/s was produced. A quarter region of the target was modeled by 36 (6×6) shell elements due to the symmetry of geometry and material. The Newmark time integration method with time-steps of 1.0 microseconds and eight iterations in each time-step were used.

Figure 2 shows the strain response histories of plate and cylindrical shells. The dash and solid line represent the experimental and numerical results, respectively. It can be seen that the finite element and experimental results are in good agreement. It is well known that the shell has larger bending rigidity compared with that of the plate, while the larger magnitude of strain response of cylindrical shells is observed in Fig. 2 (shell no. 1 > shell no. 2 > plate). It can be explained from the results of Fig. 3 that the more the lateral rigidity the higher the impact load is produced. Since the stress wave induced after the impact occurs, the oscillating phenomenon of impact force is observed in Fig. 3. Figure 3 also shows the multiple contact of shell no. 2 and different contact duration. Therefore, we may conclude that the larger lateral rigidity (i.e., curvature effect) of the target induces a larger impact force, shorter contact duration, and multiple contact in the free end boundary condition of the target. Although the finite element results of impact loading do not match very well with the experimental results, it is evident that the finite element analysis does predict the strain response, contact duration, and the multiple contact phenomenon of experiment.

Acknowledgments

This work was supported by the National Science Council, Republic of China, under Grant no. NSC78-0405-E002-11. The authors would like to express their sincere appreciation to Prof. C. T. Sun (Purdue University), for his valuable discussions and the idea for this research.

References

Caprino, G., Crivelli, I., and Dillio, A., 1984, "Composite Materials Response Under Low-Velocity Impact," *Composite Structures*, Vol. 2, pp. 261–271.

Hertz, H., 1881, "Uber die Beruhrung fester Elastischer Korper," *Journal Reine Angle Math, Crelle*, Vol. 92, p. 155.

Tan, T. M., and Sun, C. T., 1982, "Wave Propagation in the Graphite/Epoxy Laminates due to Impact," Report No. NASA-CR-168057.

Tan, T. M., and Sun, C. T., 1985, "Use of Statical Indentation Laws in the Impact Analysis of Laminated Composite Plates," ASME JOURNAL OF APPLIED MECHANICS, Vol. 52, pp. 6–12.

The Effective Thermal Conductivity of a Packing of Spheres

A. Jagota[11] and C. Y. Hui[12]

The anisotropic effective thermal conductivity of a random packing of spheres is derived. The conductivity is closely related to the fabric *tensor of the theory of granular materials. The derivation involves a mean temperature field assumption which is shown to render the model an upper bound. Closed-form expressions for the conductivity are obtained in the isotropic and axisymmetric cases.*

1 Introduction

This Note presents a model for the effective anisotropic thermal conductivity of a random packing of spherical particles. The determination of effective properties of composite materials is a classical problem and a review of the literature for transport properties may be found in Hale (1976) and McCullough (1985). Our concern is with dense random packings of spheres in a medium whose conductivity can be neglected. Each sphere is assumed to be in contact with other spheres and transport is through these contacts. The contacts are assumed to be small compared with the dimensions of the sphere so that, microscopically, the gradients in the temperature are localized near the contact. Batchelor and O'Brien (1977) have considered the isotropic case of this problem in detail. Hadley (1986) and Nozad et al. (1985) have employed their results and compared them to experiment.

2 Macroscopic Flux and Effective Conductivity

Consider a representative volume in the sense of Hill (1963) and Batchelor (1970). A direct definition of macroscopic flux J_i is the surface average of microscopic flux j_i on an arbitrary plane cut with normal n_i:

$$J_i n_i = \frac{1}{S}\int_S j_k n_k dS \tag{1}$$

$$J_i = \frac{1}{S}\int_S j_i dS \tag{2}$$

where S is the area of the cut section[13] (Fig. 1). The average flux $\bar{J}$ transmitted through the plane is

$$\bar{J} = \frac{1}{S}\int_S j_i n_i dS = \frac{1}{S}\sum_{q=1}^{N^p}\int_{S^p} j_i n_i dS. \tag{3}$$

[11]Central R&D, E. I. Du Pont de Nemours and Co., Wilmington, DE 19880. Assoc. Mem. ASME.

[12]Department of Theoretical and Applied Mechanics, Cornell University, Ithaca, NY 14853.

[13]It follows from the definition of the representative volume that the surface average is equal to a volume average.

Contributed by the Applied Mechanics Division of THE AMERICAN SOCIETY OF MECHANICAL ENGINEERS. Manuscript received, Apr. 10, 1989; final revision, June 28, 1989.

Downloaded 03 May 2010 to 171.66.16.244. Redistribution subject to ASME license or copyright; see http://www.asme.org/terms/Terms_Use.cfm

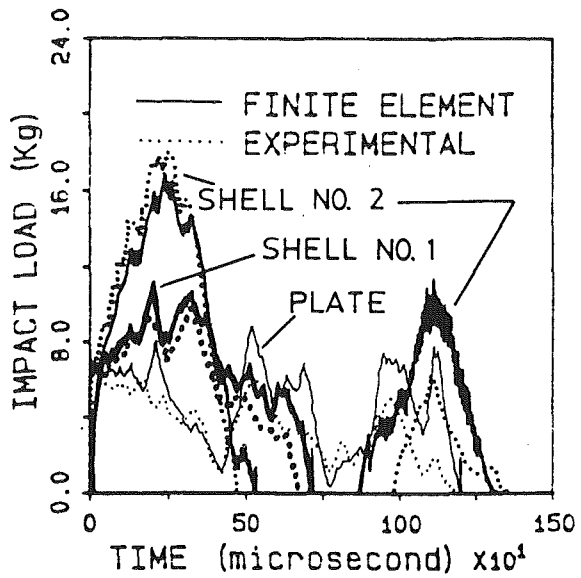


Fig. 3 Impact force histories of plate and cylindrical shells

no. 1 ($[0_5^g/90_5^g/0_5^g]^{\#}$) and shell no. 2 ($[0_5^g/90_5^g/0_5^g]^*$), respectively. A strain gage was placed on the back face (rear to the impact face) along the x-axis and was 40 mm apart from the impact node. An H.P. 5183U digitizing oscilloscope and a Kyowa DCV 230v high-rate strain gage amplifier were used to capture the strain response. The impact-force transducer of Model 200A5 marketed by PCB Piezotronics, Inc. was used also to record the impact force history. The targets were hung with three strings at the center and corners to achieve the free boundary condition. The mass of impactor with a nose diameter of 12.7 mm and target were 0.03887 kg and 0.05563 kg. Four strings were used to keep the balance of the impactor. The impact velocity of 1.704 m/s was produced. A quarter region of the target was modeled by 36 (6×6) shell elements due to the symmetry of geometry and material. The Newmark time integration method with time-steps of 1.0 microseconds and eight iterations in each time-step were used.

Figure 2 shows the strain response histories of plate and cylindrical shells. The dash and solid line represent the experimental and numerical results, respectively. It can be seen that the finite element and experimental results are in good agreement. It is well known that the shell has larger bending rigidity compared with that of the plate, while the larger magnitude of strain response of cylindrical shells is observed in Fig. 2 (shell no. 1 > shell no. 2 > plate). It can be explained from the results of Fig. 3 that the more the lateral rigidity the higher the impact load is produced. Since the stress wave induced after the impact occurs, the oscillating phenomenon of impact force is observed in Fig. 3. Figure 3 also shows the multiple contact of shell no. 2 and different contact duration. Therefore, we may conclude that the larger lateral rigidity (i.e., curvature effect) of the target induces a larger impact force, shorter contact duration, and multiple contact in the free end boundary condition of the target. Although the finite element results of impact loading do not match very well with the experimental results, it is evident that the finite element analysis does predict the strain response, contact duration, and the multiple contact phenomenon of experiment.

Acknowledgments

This work was supported by the National Science Council, Republic of China, under Grant no. NSC78-0405-E002-11. The authors would like to express their sincere appreciation to Prof. C. T. Sun (Purdue University), for his valuable discussions and the idea for this research.

References

Caprino, G., Crivelli, I., and Dillio, A., 1984, "Composite Materials Response Under Low-Velocity Impact," *Composite Structures*, Vol. 2, pp. 261-271.

Hertz, H., 1881, "Uber die Beruhrung fester Elastischer Korper," *Journal Reine Angle Math, Crelle*, Vol. 92, p. 155.

Tan, T. M., and Sun, C. T., 1982, "Wave Propagation in the Graphite/Epoxy Laminates due to Impact," Report No. NASA-CR-168057.

Tan, T. M., and Sun, C. T., 1985, "Use of Statical Indentation Laws in the Impact Analysis of Laminated Composite Plates," ASME JOURNAL OF APPLIED MECHANICS, Vol. 52, pp. 6-12.

The Effective Thermal Conductivity of a Packing of Spheres

A. Jagota[11] and C. Y. Hui[12]

The anisotropic effective thermal conductivity of a random packing of spheres is derived. The conductivity is closely related to the fabric *tensor of the theory of granular materials. The derivation involves a mean temperature field assumption which is shown to render the model an upper bound. Closed-form expressions for the conductivity are obtained in the isotropic and axisymmetric cases.*

1 Introduction

This Note presents a model for the effective anisotropic thermal conductivity of a random packing of spherical particles. The determination of effective properties of composite materials is a classical problem and a review of the literature for transport properties may be found in Hale (1976) and McCullough (1985). Our concern is with dense random packings of spheres in a medium whose conductivity can be neglected. Each sphere is assumed to be in contact with other spheres and transport is through these contacts. The contacts are assumed to be small compared with the dimensions of the sphere so that, microscopically, the gradients in the temperature are localized near the contact. Batchelor and O'Brien (1977) have considered the isotropic case of this problem in detail. Hadley (1986) and Nozad et al. (1985) have employed their results and compared them to experiment.

2 Macroscopic Flux and Effective Conductivity

Consider a representative volume in the sense of Hill (1963) and Batchelor (1970). A direct definition of macroscopic flux J_i is the surface average of microscopic flux j_i on an arbitrary plane cut with normal n_i:

$$J_i n_i = \frac{1}{S}\int_S j_k n_k dS \tag{1}$$

$$J_i = \frac{1}{S}\int_S j_i dS \tag{2}$$

where S is the area of the cut section[13] (Fig. 1). The average flux $\bar{J}$ transmitted through the plane is

$$\bar{J} = \frac{1}{S}\int_S j_i n_i dS = \frac{1}{S}\sum_{q=1}^{N^p}\int_{S^p} j_i n_i dS. \tag{3}$$

[11]Central R&D, E. I. Du Pont de Nemours and Co., Wilmington, DE 19880. Assoc. Mem. ASME.

[12]Department of Theoretical and Applied Mechanics, Cornell University, Ithaca, NY 14853.

[13]It follows from the definition of the representative volume that the surface average is equal to a volume average.

Contributed by the Applied Mechanics Division of THE AMERICAN SOCIETY OF MECHANICAL ENGINEERS. Manuscript received, Apr. 10, 1989; final revision, June 28, 1989.

Copyright © 1990 by ASME
Downloaded 03 May 2010 to 171.66.16.244. Redistribution subject to ASME license or copyright; see http://www.asme.org/terms/Terms_Use.cfm

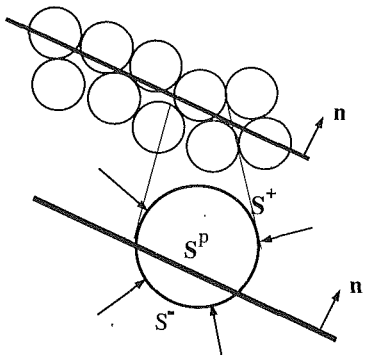


Fig. 1 The representative packing of spheres is cut by a plane. The macroscopic flux is defined in terms of the integral of microscopic flux on this cut.

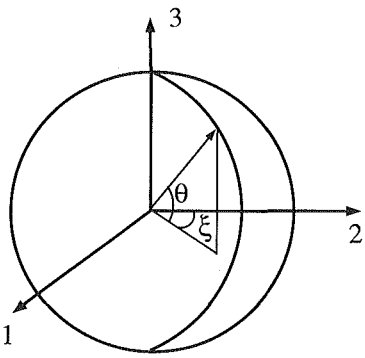


Fig. 2 Spherical coordinate system used to represent the orientation of contact normals. Axis "3" is the axis of symmetry.

Here, N^p is the number of particles cut by the plane and S^p is the exposed circular cross-sectional area of each of the particles. Each particle has contacts on the positive and negative sides of the cut plane. The total flux through the negative side of the cut is equal to the integral of flux over the surfaces of the spheres submerged in the negative half space, S^-:

$$\int_{S^p} j_i n_i dS = \int_{S^-} j_i n_i dS. \tag{4}$$

Since all transport is through the contacts, equation (3) reduces to

$$\overline{J} = \frac{1}{S}\sum_{i=1}^{N^s} \hat{J} \tag{5}$$

where N^s is the number of contacts in S^- that belong to particles cut by the plane and $\hat{J}$ is the flux through each of these contacts. Let an orientation distribution function $A(\beta)$ be defined so that $\overline{N}\,A(\beta)d\beta$ is the number of contacts per unit volume with normal β oriented in a solid angle $d\beta$ centered at β. $\overline{N}$ is the average number of contacts per unit volume, i.e.,

$$\overline{N} = \rho n^c / 2V^o, \tag{6}$$

where n^c is the coordination number, ρ is the volume fraction of spheres, and V^o is the particle volume. The number of contacts contributing to $\overline{J}$ at a fixed β_i is (Jagota et al., 1988)

$$S4R\beta_i n_i \overline{N}\, A(\beta)d\beta. \tag{7}$$

The total flux $\overline{J}$ is obtained by multiplying this expression by $\hat{J}$, integrating over all solid angles for which $\beta_i n_i > 0$, and dividing by S,

$$\overline{J} = \left[\overline{N}\int A(\beta)4R\hat{J}\,\beta_i d\beta\right] n_i. \tag{8}$$

Since the flux on the positive side of the cut is the negative of the flux on the negative side of the cut, we can remove the restriction $\beta_i n_i > 0$ on equation (8) and divide it by a factor of two to obtain

$$\overline{J} = \left[\overline{N}\int A(\beta)2R\hat{J}\beta_i d\beta\right] n_i. \tag{9}$$

Since $\overline{J} = J_i n_i$,

$$J_i = \overline{N}\int A(\beta)2R\hat{J}\beta_i d\beta. \tag{10}$$

This expression can also be derived from a volume average definition of macroscopic flux.

If the contact radius is small compared to the particle radius, the temperature in a sphere is uniform except near a contact, and the flux through a contact depends only on the temperature difference across it. This may be modeled as the problem of heat flow between two half spaces connected through a circular contact. The solution to this problem can be found in Carslaw and Jaeger (1959, article 8.2) and Lamb (1945, article 102).[14] If $\Delta\Phi$ is the temperature difference between points far from the contact on either side, then

$$\hat{J} = -4Rkr\Delta\Phi/2R. \tag{11}$$

We now use the mean field assumption that the temperature difference between sphere centers for any two spheres in contact is given by the macroscopic temperature gradient. This assumption, which is true for regular packings, does not imply that the temperature gradient is microscopically uniform. As a consequence of this assumption, the temperature difference across a contact depends only on its orientation:

$$\Delta\Phi/2R = \Phi_{,i}\,\beta_i. \tag{12}$$

Using equations (11) and (12) in (10),

$$J_i = \left[-\frac{3}{\pi R}\rho n^c k\int A(\beta)\, r\,\beta_i\beta_j d\beta\right]\Phi_{,j}. \tag{13}$$

Hence, the effective anisotropic conductivity is

$$K_{ij} = \frac{3}{\pi R}\rho n^c k\int A(\beta)\, r\,\beta_i\beta_j d\beta. \tag{14}$$

If the contact radius is not a function of orientation, the anisotropy depends only on the orientation distribution function

$$K_{ij} = \frac{3}{\pi R}\rho n^c kr\, F_{ij} \tag{15}$$

$$F_{ij} = \int A(\beta)\beta_i\beta_j d\beta \tag{16}$$

where F_{ij} is the fabric tensor (Oda, Nemat-Nasser, and Mehrabadi, 1982) which is used often to describe the mechanical state of a granular material. This equivalence between the effective conductivity and the fabric offers a direct means for its measurement.

3 Bounding Properties

We now show that the effective conductivity obtained using the mean field assumption is an upper bound. The variational principles of Hashin and Shtrikman (1962) and Biot (1970) state that among all temperature fields which satisfy the boundary conditions on the representative volume V, the true field maximizes the integral $\frac{1}{V}\int_V j_i\phi_{,i}\,dV$. Evaluating this integral over all N^p spheres in V (with N^c contacts each, N^c being different for each sphere), we obtain after an integration by parts

[14]It is interesting to note that the corresponding problem in two dimensions; the problem of heat flow between two half planes connected through a contact length, has no solution. For any finite flux $\hat{J}$, the temperature is unbounded in regions far from the contact (Lamb 1945, article 66).

Downloaded 03 May 2010 to 171.66.16.244. Redistribution subject to ASME license or copyright; see http://www.asme.org/terms/Terms_Use.cfm

$$\frac{1}{V}\int_V j_i\phi_{,i}dV = \frac{1}{V}\sum_{q=1}^{N^p}\int_{V^p} j_i\phi_{,i}dV = \frac{1}{V}\sum_{q=1}^{N^p}\sum_{t=1}^{N^c}\hat{J}\phi$$

$$= \frac{1}{V}\sum_{q=1}^{N^p}\sum_{t=1}^{N^c}\hat{J}(\phi - \phi^o) \tag{17}$$

where ϕ is the temperature at the contact, and ϕ^o is the temperature at the center of the sphere. Since each contact is shared by two particles, the double summation can be replaced by a single one, i.e.,

$$\frac{1}{V}\int_V j_i\phi_{,i}\,dV = \frac{1}{V}\sum_{q=1}^{N}\hat{J}\Delta\phi \tag{18}$$

where $\Delta\phi$ is the temperature difference between sphere centers. Since the integral must be maximized,

$$\frac{1}{V}\int_V j_i\phi_{,i}dV = \frac{1}{V}\sum_{q=1}^{N}\hat{J}\Delta\phi \geq \frac{1}{V}\sum_{q=1}^{N}\hat{J}^*\Delta\phi^* \tag{19}$$

where ϕ^* is any other temperature field that satisfies the boundary conditions and $\hat{J}^*$ are the corresponding contact fluxes. The left-hand side of equation (19) is $-\Phi_{,i}K^t_{ij}\Phi_{,j}$ where K^t_{ij} is the "true" conductivity of the packing.

We now use equations (12) and (11) in equation (19) to obtain

$$\Phi_{,i}\,K^t_{ij}\Phi_{,j} \leq \Phi_{,i}\left[\overline{N}\int A(\beta)L\eta\beta_i\beta_j d\beta\right]\Phi_{,j}. \tag{20}$$

In this sense, the conductivity predicted by equation (14) is an upper bound on the "true" conductivity. In principal coordinates, each element is individually an upper bound.

4 Isotropic and Axisymmetric Cases

The integral over orientation can be solved for the isotropic case (Batchelor and O'Brien, 1977) and the conductivity K is:

$$K = \frac{1}{\pi R}\rho n^c k r. \tag{21}$$

Consider now the case of a packing which possesses an axis of symmetry. We choose spherical coordinates so that the axis of symmetry is "3" (Fig. 2). The unit vector β_i is

$$\beta = \cos\theta\sin\xi e_1 + \cos\theta\cos\xi e_2 + \sin\theta e_3 \tag{22}$$

and

$$d\beta = \cos\theta d\theta d\xi. \tag{23}$$

Because the contacts are uniformly distributed in the ξ-direction, the orientation distribution function is

$$A(\beta) = A(\xi,\theta) = B(\theta)/2\pi. \tag{24}$$

Then, equation (14) becomes

$$K_{ij} = \frac{3}{\pi R}\rho n^c k\int_{-1}^{+1} d(\sin\theta)B(\theta)r\,\frac{1}{2\pi}\int_0^{2\pi}\beta_i\beta_j d\xi. \tag{25}$$

The inner integrals over ξ can be evaluated and the results are

$$K_{33} = \frac{3}{\pi R}\rho n^c k\int_{-1}^{+1} B(\theta)r\sin^2\theta d(\sin\theta) \tag{26}$$

$$K_{11} = K_{22} = \frac{3}{\pi R}\rho n^c k\int_{-1}^{+1} B(\theta)r\,\frac{\cos^2\theta}{2}\,d(\sin\theta). \tag{27}$$

References

Batchelor, G. K., 1970, "The stress system in a suspension of force free particles," *Journal of Fluid Mechanics*, Vol. 41, pp. 545–570.

Batchelor, G. K., and O'Brien, R. W., 1977, "Thermal or electrical conduction through a granular material," *Proceedings of the Royal Society, London*, Vol. A355, pp. 313–333.

Biot, M. A., 1970, *Variational Principles in Heat Transfer*, Clarendon Press, Oxford, U.K.

Carslaw, H. S., Jaeger, J. C., 1959, *Conduction of Heat in Solids*, 2nd ed., Clarendon Press, Oxford, U.K.

Hadley, G. R., 1986, "Thermal conductivity of packed metal powders," *International Journal of Heat and Mass Transfer*, Vol. 29, pp. 909–920.

Hale, D. K., 1976, "The physical properties of composite materials," *Journal of Materials Science*, Vol. 11, pp. 2105–2141.

Hashin, Z., and Shtrikman, S., 1962, "A variational approach to the theory of the effective magnetic permeability of multiphase materials," *Journal of Applied Physics*, Vol. 33, pp. 3125–3131.

Hill, R., 1963, "Elastic properties of reinforced solids: some theoretical principles," *Journal of the Mechanics and Physics of Solids*, Vol. 11, pp. 357–372.

Jagota, A., Dawson, P. R., and Jenkins, J. T., 1988, "An anisotropic continuum model for the sintering and compaction of powder packings," *Mechanics of Materials*, Vol. 11, pp. 357–372.

Lamb, H., 1945, *Hydrodynamics*, 6th ed., Dover Publications, New York.

McCullough, R. L., 1985, "Generalized combining rules for predicting transport properties of composite materials," *Composite Science and Technology*, Vol. 22, pp. 3–21.

Nozad, I., Carbonell, R. G., and Whitaker, S., 1985, "Heat conduction in multiphase systems—I, Theory and experiment for two phase systems," *Chem. Eng. Sci.*, Vol. 40, pp. 843–856.

Oda, M., Nemat-Nasser, S., and Mehrabadi, M. M., 1982, "A statistical study of fabric in random assembly of spherical granules," *International Journal for Numerical and Analytical Methods in Geomechanics*, Vol. 6, pp. 77–94.

Vertical Ground Motion Induced by a Blast Wave

Frederick Reyes Norwood[15]

1 Introduction

The title problem is of particular interest for the study of seismic signals arising from explosions. Much of the previous work has focused on the acoustic wave traveling through air (Glasstone, 1977), but there are references which deal with the steady-state seismic analysis of moving line loads (Cole and Huth, 1985; Sackman 1961). Cinelli and Fugelso (1959) evaluate the equations found in Sneddon (1951) for stresses and displacements in an elastic half space and find the steady-state response to a blast wave. These steady-state analyses do not capture the observed transient phenomena. Hence, an improved theoretical understanding of the transient seismic motion induced by a blast wave in air is still needed. For the accidental explosion at Pepcon (Reed, 1988), Henderson, Nev., on May 4, 1988, seismic signals of the ground motion were recorded at locations in Las Vegas, several kilometers from the blast, at a depth of 5 meters. The record showed an upward velocity precursor ahead of the blast wave front. This upward movement ahead of the blast wave is opposite to the direction of the applied load (the blast wave) and therefore has been considered anomalous. This precursor can induce motion to a structure in the neighborhood of the blast wave front. Thus, a structure may be affected by the seismic motion induced at its foundation, followed immediately by a blast wave. In the present work, to analyze this phenomenon, a simple model of a two-dimensional blast wave was used, assuming a uniform blast wave speed, to derive an analytic solution for the transient problem in terms of integrals with singular kernels. It will be shown that this model predicts the upward velocity precursor. Hence, the anomality will be explained.

2 Statement of the Problem

In the rectangular Cartesian coordinate system shown in Fig. 1, consider the problem of a uniformly moving blast wave. For notation and solution technique, refer to Norwood (1975) where this problem has been solved in general terms. The solution to the current problem, in transform space, may be found from the canonical problem A in Norwood (1975) by identifying the load

[15]Sandia National Laboratories, Albuquerque, NM 87185. Mem. ASME.

Manuscript received and accepted by the ASME Applied Mechanics Division, Mar. 20, 1989.

Downloaded 03 May 2010 to 171.66.16.244. Redistribution subject to ASME license or copyright; see http://www.asme.org/terms/Terms_Use.cfm

$$\frac{1}{V}\int_V j_i\phi_{,i}dV = \frac{1}{V}\sum_{q=1}^{N^p}\int_{V^p} j_i\phi_{,i}dV = \frac{1}{V}\sum_{q=1}^{N^p}\sum_{t=1}^{N^c}\hat{J}\phi$$

$$= \frac{1}{V}\sum_{q=1}^{N^p}\sum_{t=1}^{N^c}\hat{J}(\phi - \phi^o) \tag{17}$$

where ϕ is the temperature at the contact, and ϕ^o is the temperature at the center of the sphere. Since each contact is shared by two particles, the double summation can be replaced by a single one, i.e.,

$$\frac{1}{V}\int_V j_i\phi_{,i}\,dV = \frac{1}{V}\sum_{q=1}^{N}\hat{J}\Delta\phi \tag{18}$$

where $\Delta\phi$ is the temperature difference between sphere centers. Since the integral must be maximized,

$$\frac{1}{V}\int_V j_i\phi_{,i}dV = \frac{1}{V}\sum_{q=1}^{N}\hat{J}\Delta\phi \geq \frac{1}{V}\sum_{q=1}^{N}\hat{J}^*\Delta\phi^* \tag{19}$$

where ϕ^* is any other temperature field that satisfies the boundary conditions and $\hat{J}^*$ are the corresponding contact fluxes. The left-hand side of equation (19) is $-\Phi_{,i}K^t_{ij}\Phi_{,j}$ where K^t_{ij} is the "true" conductivity of the packing.

We now use equations (12) and (11) in equation (19) to obtain

$$\Phi_{,i}\,K^t_{ij}\Phi_{,j} \leq \Phi_{,i}\left[\overline{N}\int A(\beta)L\eta\beta_i\beta_j d\beta\right]\Phi_{,j}. \tag{20}$$

In this sense, the conductivity predicted by equation (14) is an upper bound on the "true" conductivity. In principal coordinates, each element is individually an upper bound.

4 Isotropic and Axisymmetric Cases

The integral over orientation can be solved for the isotropic case (Batchelor and O'Brien, 1977) and the conductivity K is:

$$K = \frac{1}{\pi R}\rho n^c k r. \tag{21}$$

Consider now the case of a packing which possesses an axis of symmetry. We choose spherical coordinates so that the axis of symmetry is "3" (Fig. 2). The unit vector β_i is

$$\beta = \cos\theta\sin\xi e_1 + \cos\theta\cos\xi e_2 + \sin\theta e_3 \tag{22}$$

and

$$d\beta = \cos\theta d\theta d\xi. \tag{23}$$

Because the contacts are uniformly distributed in the ξ-direction, the orientation distribution function is

$$A(\beta) = A(\xi,\theta) = B(\theta)/2\pi. \tag{24}$$

Then, equation (14) becomes

$$K_{ij} = \frac{3}{\pi R}\rho n^c k\int_{-1}^{+1} d(\sin\theta)B(\theta)r\,\frac{1}{2\pi}\int_0^{2\pi}\beta_i\beta_j d\xi. \tag{25}$$

The inner integrals over ξ can be evaluated and the results are

$$K_{33} = \frac{3}{\pi R}\rho n^c k\int_{-1}^{+1} B(\theta)r\sin^2\theta d(\sin\theta) \tag{26}$$

$$K_{11} = K_{22} = \frac{3}{\pi R}\rho n^c k\int_{-1}^{+1} B(\theta)r\,\frac{\cos^2\theta}{2}\,d(\sin\theta). \tag{27}$$

References

Batchelor, G. K., 1970, "The stress system in a suspension of force free particles," *Journal of Fluid Mechanics*, Vol. 41, pp. 545–570.

Batchelor, G. K., and O'Brien, R. W., 1977, "Thermal or electrical conduction through a granular material," *Proceedings of the Royal Society, London*, Vol. A355, pp. 313–333.

Biot, M. A., 1970, *Variational Principles in Heat Transfer*, Clarendon Press, Oxford, U.K.

Carslaw, H. S., Jaeger, J. C., 1959, *Conduction of Heat in Solids*, 2nd ed., Clarendon Press, Oxford, U.K.

Hadley, G. R., 1986, "Thermal conductivity of packed metal powders," *International Journal of Heat and Mass Transfer*, Vol. 29, pp. 909–920.

Hale, D. K., 1976, "The physical properties of composite materials," *Journal of Materials Science*, Vol. 11, pp. 2105–2141.

Hashin, Z., and Shtrikman, S., 1962, "A variational approach to the theory of the effective magnetic permeability of multiphase materials," *Journal of Applied Physics*, Vol. 33, pp. 3125–3131.

Hill, R., 1963, "Elastic properties of reinforced solids: some theoretical principles," *Journal of the Mechanics and Physics of Solids*, Vol. 11, pp. 357–372.

Jagota, A., Dawson, P. R., and Jenkins, J. T., 1988, "An anisotropic continuum model for the sintering and compaction of powder packings," *Mechanics of Materials*, Vol. 11, pp. 357–372.

Lamb, H., 1945, *Hydrodynamics*, 6th ed., Dover Publications, New York.

McCullough, R. L., 1985, "Generalized combining rules for predicting transport properties of composite materials," *Composite Science and Technology*, Vol. 22, pp. 3–21.

Nozad, I., Carbonell, R. G., and Whitaker, S., 1985, "Heat conduction in multiphase systems—I, Theory and experiment for two phase systems," *Chem. Eng. Sci.*, Vol. 40, pp. 843–856.

Oda, M., Nemat-Nasser, S., and Mehrabadi, M. M., 1982, "A statistical study of fabric in random assembly of spherical granules," *International Journal for Numerical and Analytical Methods in Geomechanics*, Vol. 6, pp. 77–94.

Vertical Ground Motion Induced by a Blast Wave

Frederick Reyes Norwood[15]

1 Introduction

The title problem is of particular interest for the study of seismic signals arising from explosions. Much of the previous work has focused on the acoustic wave traveling through air (Glasstone, 1977), but there are references which deal with the steady-state seismic analysis of moving line loads (Cole and Huth, 1985; Sackman 1961). Cinelli and Fugelso (1959) evaluate the equations found in Sneddon (1951) for stresses and displacements in an elastic half space and find the steady-state response to a blast wave. These steady-state analyses do not capture the observed transient phenomena. Hence, an improved theoretical understanding of the transient seismic motion induced by a blast wave in air is still needed. For the accidental explosion at Pepcon (Reed, 1988), Henderson, Nev., on May 4, 1988, seismic signals of the ground motion were recorded at locations in Las Vegas, several kilometers from the blast, at a depth of 5 meters. The record showed an upward velocity precursor ahead of the blast wave front. This upward movement ahead of the blast wave is opposite to the direction of the applied load (the blast wave) and therefore has been considered anomalous. This precursor can induce motion to a structure in the neighborhood of the blast wave front. Thus, a structure may be affected by the seismic motion induced at its foundation, followed immediately by a blast wave. In the present work, to analyze this phenomenon, a simple model of a two-dimensional blast wave was used, assuming a uniform blast wave speed, to derive an analytic solution for the transient problem in terms of integrals with singular kernels. It will be shown that this model predicts the upward velocity precursor. Hence, the anomality will be explained.

2 Statement of the Problem

In the rectangular Cartesian coordinate system shown in Fig. 1, consider the problem of a uniformly moving blast wave. For notation and solution technique, refer to Norwood (1975) where this problem has been solved in general terms. The solution to the current problem, in transform space, may be found from the canonical problem A in Norwood (1975) by identifying the load

[15]Sandia National Laboratories, Albuquerque, NM 87185. Mem. ASME.

Manuscript received and accepted by the ASME Applied Mechanics Division, Mar. 20, 1989.

Copyright © 1990 by ASME
Downloaded 03 May 2010 to 171.66.16.244. Redistribution subject to ASME license or copyright; see http://www.asme.org/terms/Terms_Use.cfm

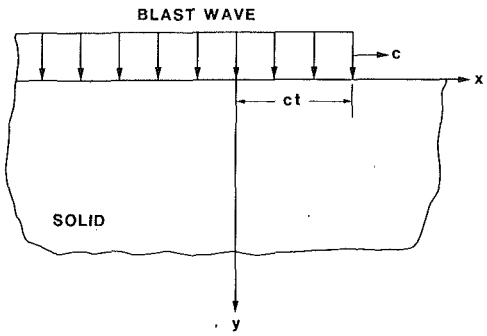


Fig. 1 Geometry of the problem

$$g(x,t) = F\{H(-x)H(t) + H(t-x/c)H(x)\} \tag{1}$$

where F is a constant and $H(t)$ is the Heaviside unit function.

Using the notation of Norwood (1975), it may be shown that the double transform of g is given by

$$\tilde{g}^L(k,p) = \frac{F}{p^2}\left\{-\frac{1}{k} + \frac{1}{k-1/c}\right\} \quad \Re ep>0,\ 0<\Re ek<1/c, \tag{2}$$

with the indicated strip of analyticity in the k-plane; p and k are transform variables.

The potentials ϕ and ψ are related to the displacements $\mathbf{U} = \mathbf{U}_1 + \mathbf{U}_2$ through $\mathbf{U}_1 = \nabla\phi$ and $\mathbf{U}_2 = \nabla \times \psi$. The vertical component of velocity, in transform space is given by

$$\tilde{v}^L = \tilde{v}_1^L + \tilde{v}_2^L = -p^2\{\eta_1\tilde{\phi}^L - k\tilde{\psi}^L\} \tag{3}$$

where, from Norwood (1975),

$$\tilde{\phi}^L(k,y,p) = A(k,p)e^{-p\eta_1(k)y},\ \tilde{\psi}^L(k,y,p) = C(k,p)e^{-p\eta_2(k)y}, \tag{4}$$

$$p^2A(k,p)R(k) = \tilde{g}^L(k,p)(a_2^2-2k^2),\ p^2C(k,p)R(k) = -2k\eta_1\tilde{g}^L(k,p), \tag{5}$$

$$R(k) = (a_2^2-2k^2)^2 + 4k^2\eta_1(k)\eta_2(k), \tag{6}$$

$$a_ic_i = 1,\ \eta_i(k) = (a_i^2-k^2)^{1/2},\ \Re e\eta_i \geq 0,\ i=1,2. \tag{7}$$

$$\rho c_1^2 = \lambda + 2\mu,\ \rho c_2^2 = \mu, \tag{8}$$

λ and μ are the Lamé constants and ρ is the material density. No summation is implied by the repeated indices in the first of equations (7).

3 Transform Inversion

The details of the transform inversion follow closely the plan and outline of Norwood (1973). For the present case, there are singularities in the k-plane located at $k = 0$, $k = 1/c$, $k = 1/c_R$, where c_R is the Rayleigh speed. The inversion of the transform in x for the dilatational contribution may be written as:

$$\tilde{v}_1(x,y,p) = -\frac{F}{p}\frac{1}{2\pi i}\int_C \frac{\eta_1(k)(a_2^2-2k^2)}{R(k)}\left\{-\frac{1}{k} + \frac{1}{k-1/c}\right\}e^{-p[kx+\eta_1(k)y]}dk \tag{9}$$

where C is a path within the strip of analyticity. The evaluation of the integral is performed by Cagniard's technique (Norwood, 1973, 1975). When $y = 0$, Cagniard's path collapses to the real k-axis, the points $k = 1/c$ and $k = 1/c_R$ give residue contributions, and there result principal value integrals. In this short Note, to explain the anomality noted in the introduction, the case $y > 0$ will be considered. For $y > 0$, and an arbitrary value of x, one finds

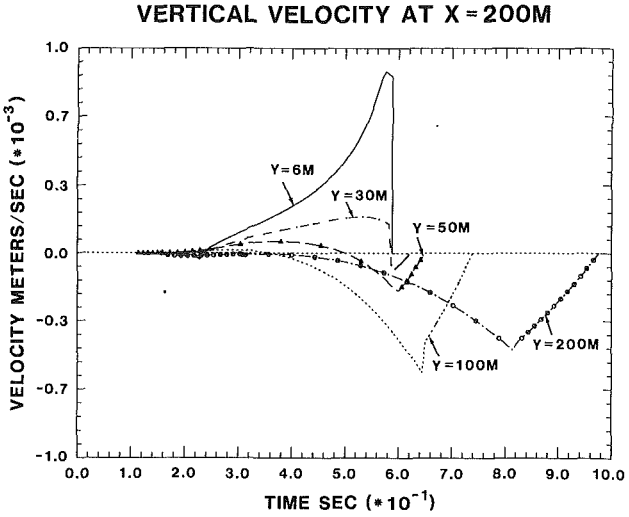


Fig. 2 Velocity histories at 200 m for various depths

$$\tilde{v}_1(x,y,p) = -\frac{F}{p}\mathcal{L}\{S(x,y,t)\chi_1(x,y,t)\}, \tag{10}$$

where $\mathcal{L}$ represents the Laplace transform operator,

$$S(x,y,t) = \Re e\frac{\eta_1^2(k_1)(a_2^2-2k_1^2)}{\pi R(k_1)(t^2-a_1^2r^2)^{1/2}}\frac{1}{k_1(ck_1-1)}, \tag{11}$$

$$\chi_j(x,y,t) = H(t-a_jr), \quad j=1,2 \quad r^2 = x^2+y^2, \tag{12}$$

$$k_j(x,y,t) = [tx + iy(t^2-a_j^2r^2)^{1/2}]/r^2,\ j=1,2. \tag{13}$$

Thus, by the convolution theorem, the dilatational contribution may be written as

$$v_1(x,y,t) = -F\chi_1(x,y,t)\int_{a_1r}^t S(x,y,\tau)d\tau. \tag{14}$$

The integrand has a removable square root singularity at $t = a_1r$. However, at $k_1 = 1/c$, the singularity may not be removed. This singularity will play a role in the present work in the limit as the surface is approached from the interior of the half plane. The shear contribution is given by

$$v_2(x,y,t) = 2F\chi_2(x,y,t)\int_{a_2r}^t Q(x,y,\tau)d\tau + 2F\chi_3(x,y,t)\int_{t_h}^t K(x,y,\tau)d\tau + 2F\chi_2(x,y,t)\int_{t_h}^{a_2r} K(x,y,\tau)d\tau,$$

where

$$Q(x,y,t) = \Re e\frac{G(k_2)}{(t^2-a_2^2r^2)^{1/2}},$$

$$K(x,y,t) = \Re e\frac{G(k_3)}{i(a_2^2r^2-t^2)^{1/2}},$$

$$G(k) = \frac{\eta_1(k)\eta_2^2(k)}{\pi R(k)(kc-1)},$$

$$k_3(x,y,t) = [tx - y(a_2^2r^2-t_2)^{1/2}]/r^2,$$

$$\chi_3(x,y,t) = H(t-t_h) - \chi_2(x,y,t),$$

$$t_h = a_1x + y(a_2^2-a_1^2)^{1/2}. \tag{15}$$

The total vertical displacement $v = v_1 + v_2$ was evaluated numerically, with the following values: $\mu F = 400$ Pa, $c = 340$

Downloaded 03 May 2010 to 171.66.16.244. Redistribution subject to ASME license or copyright; see http://www.asme.org/terms/Terms_Use.cfm

m/sec, ρ = 1800 kg/m^3, c_1 = 1800 m/sec, and c_2 = 900 m/sec.[16] The results are shown in Fig. 2 for a fixed horizontal distance of 200 m and various depths; velocity is taken as positive upwards. The curves for depths of 200 m, 100 m, 50 m, and 30 m are plotted for time $t \le r\,(1/c + 1/c_2 - 1/c_1)$. In these curves, $t = r/c$ is the time when the curves change direction. For the depth of 6 m, response was calculated to $t = r/c$, the limit of the numerical solution resulting from the nonremovable singularity at $k_1 = 1/c$; the path C in equation (9) used to derive the current results passes close to the pole at $k_1 = 1/c$. These results show that there is no upward velocity precursor at a depth of 200 m. However, as the depth decreases, this is not the case. The velocity precursor for 6 m and 30 m resembles the recorded signal for the accidental explosion at Pepcon, which showed a .1 sec rise time and a sudden drop at the arrival of the blast wave. Clearly, the anomalous precursor results from seismic signals which propagate within the geologic medium faster than the surface blast front.

4 References

Cinelli, G., and Fugelso, L. E., 1959, "Theoretical Study of Ground Motion Produced by Nuclear Blasts," Mechs. Res. Div. American Machine and Foundry Company, Report under Contract AF 29 (601)-1190 with AF SWC.

Cole, J., and Huth, J., 1958, "Stresses Produced in a Half Plane by Moving Loads," ASME JOURNAL OF APPLIED MECHANICS, Vol. 25, pp. 433-436.

Glasstone, S., and Dolan, P. J., 1977, The Effects of Nuclear Weapons, U.S. Department of Defense and the Energy R&D Administration, Washington, D.C.

Norwood, F. R., 1975, "Transient Response of an Elastic Plate to Loads with Finite Characteristic Dimensions," *Int. J. Solids Structures*, Vol. 11, pp. 33-51.

Norwood, F. R., 1973, "Similarity Solutions in Plane Elastodynamics," *Int. J. Solids Structures*, Vol. 9, pp. 798-803.

Reed, J. W., 1988, "Analysis of the Accidental Explosion at Pepcon, Henderson, Nevada, May 4, 1988," Report SAND88-2902 UC-70, Sandia National Laboratories, Albuquerque, N. M., printed Nov. 1988.

Sackman, J. L., 1961, "Uniformly Moving Load on a Layered Half Plane," *J. Engrg. Mechs. Div.*, ASCE, Aug., pp. 75-89.

Sneddon, I. N., 1951, *Fourier Transforms*, McGraw-Hill, New York.

The Rolling Motion of an Expanding and Contracting Cylinder

E. V. Wilms[17,19] and H. Cohen[18,19]

Introduction

Nonlinear resonance has been discussed by a number of authors (e.g., Heinbockel and Struble, 1963; Kane and Kahn, 1968; Srinivasan and Sankar, 1974; Minorsky, 1962) for a system consisting of an extensible pendulum as shown in Fig. 1.

The system consists of a particle of mass m attached to a spring of constant k. δ is the elongation and r is the unstretched length. The potential energy is

$$V = \frac{1}{2}k\delta^2 + mg(r - (r+\delta)\cos\theta). \tag{1}$$

The kinetic energy is

$$T = \frac{1}{2}m(\dot{\delta}^2 + (r+\delta)^2\dot{\theta}^2). \tag{2}$$

Kane and Kahn have carried out an analysis which shows that under certain conditions, the θ motion grows and the motion becomes entirely pendulumlike. The θ oscillation then decreases and the δ motion becomes predominant. This motion repeats itself periodically.

In the present work we show that an elastic cylinder rolling on a curved surface of radius R has the same governing equations as the system shown in Fig. 1, and hence the same type of behavior.

We then modify the system by allowing the cylinder to roll on a flat surface. It is shown that the governing equations are the same as for the system in Fig. 1 if gravity is neglected for the pendulum.

Cylinder Rolling on a Curved Surface

The thin elastic cylinder of radius $r + \delta$ rolls on curved surface as shown in Fig. 2. r is the underformed radius and δ is the deformation. The cylinder undergoes elastic deformation in such a way that its shape remains circular. The cylinder remains circular if we neglect deformation due to bending. There are two degrees of freedom, θ and δ. The normal and tangential components of the velocity of point P on the cylinder are:

$$v_{Pn} = \dot{\delta} - (r+\delta)\omega\sin\phi - \dot{\delta}\cos\phi, \tag{3a}$$

$$v_{Pt} = (R - r - \delta)\dot{\theta} - (r+\delta)\,\omega\cos\phi + \dot{\delta}\sin\phi. \tag{3b}$$

In equations (3), ω is the angular velocity of the cylinder,

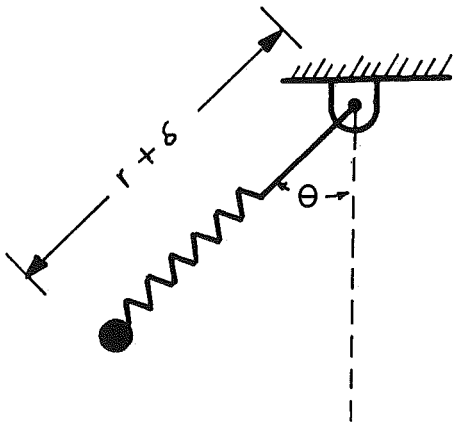


Fig. 1 An extensible pendulum

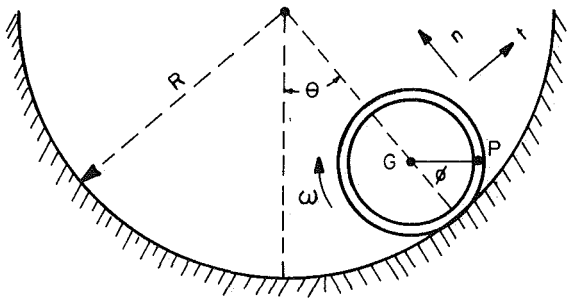


Fig. 2 A cylinder rolling on a curved surface

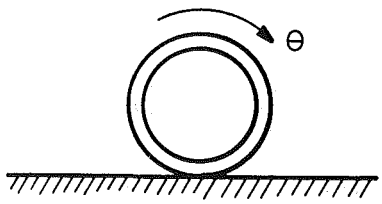


Fig. 3 A cylinder on a flat surface

[16]These values are representative of the alluvium in the neighborhood of the measurement reported in Reed (1988).

[17]Associate Professor.

[18]Distinguished Professor and Dean of Science.

[19]Department of Civil Engineering, University of Manitoba, Winnipeg, Manitoba, Canada, R3T 2N2.

Manuscript contributed by the ASME Applied Mechanics Division, June 15, 1989; final revision, Oct. 16, 1989.

Downloaded 03 May 2010 to 171.66.16.244. Redistribution subject to ASME license or copyright; see http://www.asme.org/terms/Terms_Use.cfm

m/sec, ρ = 1800 kg/m^3, c_1 = 1800 m/sec, and c_2 = 900 m/sec.[16] The results are shown in Fig. 2 for a fixed horizontal distance of 200 m and various depths; velocity is taken as positive upwards. The curves for depths of 200 m, 100 m, 50 m, and 30 m are plotted for time $t \le r\,(1/c + 1/c_2 - 1/c_1)$. In these curves, $t = r/c$ is the time when the curves change direction. For the depth of 6 m, response was calculated to $t = r/c$, the limit of the numerical solution resulting from the nonremovable singularity at $k_1 = 1/c$; the path C in equation (9) used to derive the current results passes close to the pole at $k_1 = 1/c$. These results show that there is no upward velocity precursor at a depth of 200 m. However, as the depth decreases, this is not the case. The velocity precursor for 6 m and 30 m resembles the recorded signal for the accidental explosion at Pepcon, which showed a .1 sec rise time and a sudden drop at the arrival of the blast wave. Clearly, the anomalous precursor results from seismic signals which propagate within the geologic medium faster than the surface blast front.

4 References

Cinelli, G., and Fugelso, L. E., 1959, "Theoretical Study of Ground Motion Produced by Nuclear Blasts," Mechs. Res. Div. American Machine and Foundry Company, Report under Contract AF 29 (601)-1190 with AF SWC.

Cole, J., and Huth, J., 1958, "Stresses Produced in a Half Plane by Moving Loads," ASME Journal of Applied Mechanics, Vol. 25, pp. 433-436.

Glasstone, S., and Dolan, P. J., 1977, The Effects of Nuclear Weapons, U.S. Department of Defense and the Energy R&D Administration, Washington, D.C.

Norwood, F. R., 1975, "Transient Response of an Elastic Plate to Loads with Finite Characteristic Dimensions," *Int. J. Solids Structures*, Vol. 11, pp. 33-51.

Norwood, F. R., 1973, "Similarity Solutions in Plane Elastodynamics," *Int. J. Solids Structures*, Vol. 9, pp. 798-803.

Reed, J. W., 1988, "Analysis of the Accidental Explosion at Pepcon, Henderson, Nevada, May 4, 1988," Report SAND88-2902 UC-70, Sandia National Laboratories, Albuquerque, N. M., printed Nov. 1988.

Sackman, J. L., 1961, "Uniformly Moving Load on a Layered Half Plane," *J. Engrg. Mechs. Div.*, ASCE, Aug., pp. 75-89.

Sneddon, I. N., 1951, *Fourier Transforms*, McGraw-Hill, New York.

The Rolling Motion of an Expanding and Contracting Cylinder

E. V. Wilms[17,19] and H. Cohen[18,19]

Introduction

Nonlinear resonance has been discussed by a number of authors (e.g., Heinbockel and Struble, 1963; Kane and Kahn, 1968; Srinivasan and Sankar, 1974; Minorsky, 1962) for a system consisting of an extensible pendulum as shown in Fig. 1.

The system consists of a particle of mass m attached to a spring of constant k. δ is the elongation and r is the unstretched length. The potential energy is

$$V = \frac{1}{2}k\delta^2 + mg(r - (r+\delta)\cos\theta). \tag{1}$$

The kinetic energy is

$$T = \frac{1}{2}m(\dot{\delta}^2 + (r+\delta)^2\dot{\theta}^2). \tag{2}$$

Kane and Kahn have carried out an analysis which shows that under certain conditions, the θ motion grows and the motion becomes entirely pendulumlike. The θ oscillation then decreases and the δ motion becomes predominant. This motion repeats itself periodically.

In the present work we show that an elastic cylinder rolling on a curved surface of radius R has the same governing equations as the system shown in Fig. 1, and hence the same type of behavior.

We then modify the system by allowing the cylinder to roll on a flat surface. It is shown that the governing equations are the same as for the system in Fig. 1 if gravity is neglected for the pendulum.

Cylinder Rolling on a Curved Surface

The thin elastic cylinder of radius $r + \delta$ rolls on curved surface as shown in Fig. 2. r is the underformed radius and δ is the deformation. The cylinder undergoes elastic deformation in such a way that its shape remains circular. The cylinder remains circular if we neglect deformation due to bending. There are two degrees of freedom, θ and δ. The normal and tangential components of the velocity of point P on the cylinder are:

$$v_{Pn} = \dot{\delta} - (r+\delta)\omega\sin\phi - \dot{\delta}\cos\phi, \tag{3a}$$

$$v_{Pt} = (R - r - \delta)\dot{\theta} - (r+\delta)\,\omega\cos\phi + \dot{\delta}\sin\phi. \tag{3b}$$

In equations (3), ω is the angular velocity of the cylinder,

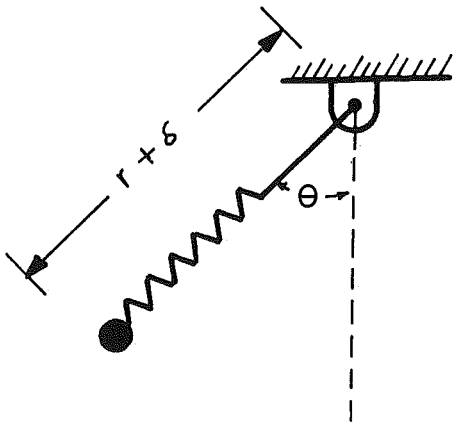


Fig. 1 An extensible pendulum

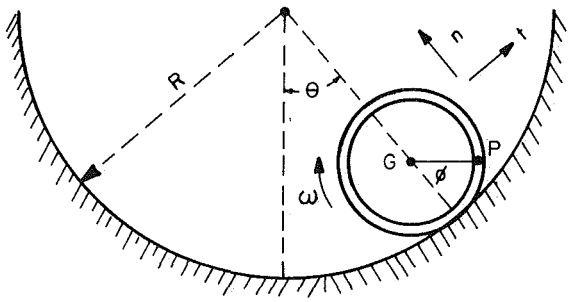


Fig. 2 A cylinder rolling on a curved surface

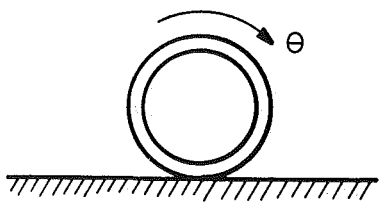


Fig. 3 A cylinder on a flat surface

[16]These values are representative of the alluvium in the neighborhood of the measurement reported in Reed (1988).

[17]Associate Professor.

[18]Distinguished Professor and Dean of Science.

[19]Department of Civil Engineering, University of Manitoba, Winnipeg, Manitoba, Canada, R3T 2N2.

Manuscript contributed by the ASME Applied Mechanics Division, June 15, 1989; final revision, Oct. 16, 1989.

Copyright © 1990 by ASME
Downloaded 03 May 2010 to 171.66.16.244. Redistribution subject to ASME license or copyright; see http://www.asme.org/terms/Terms_Use.cfm

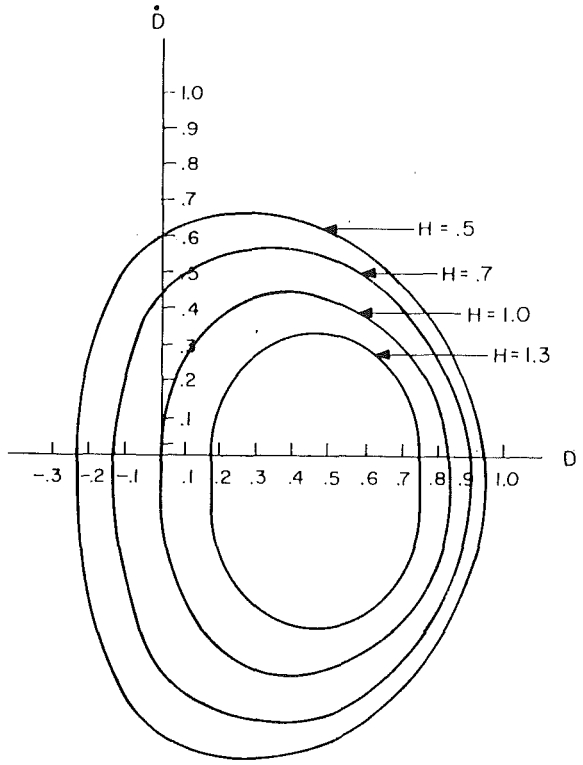


Fig. 4 The phase plane

and ϕ defines the point P on the cylinder. The total kinetic energy is:

$$T=\frac{1}{2}\int v_p^2 dm=\frac{1}{2}\frac{m}{2\pi}\int_0^{2\pi} v_p^2 d\phi. \tag{4}$$

m is the mass of the cylinder. From a consideration of point G, we have:

$$(R-r-\delta)\dot{\theta}=(r+\delta)\omega. \tag{5}$$

Equations (3), (4) and (5) then yield:

$$T=m(\dot{\delta}^2+(R-r-\delta)^2\dot{\theta}^2). \tag{6}$$

Here we have used the fact that

$$\int_0^{2\pi}\cos\phi\, d\phi=\int_0^{2\pi}\sin\phi\, d\phi=0.$$

The potential energy is

$$V=\frac{1}{2}k\delta^2+mg(R-r-(R-r-\delta)\cos\theta). \tag{7}$$

Letting $\delta=-\delta$, we see that equations (6) and (7) have a form which is identical to equations (1) and (2). Hence, the motion is identical to that which has been discussed by Kane and Kahn (1968) for the system shown in Fig. 1.

Cylinder Rolling on a Flat Surface

The kinetic energy may be found in the same way as for the rolling cylinder on a curved surface.

We have:

$$T=m\{(r+\delta)^2\dot{\theta}^2+\dot{\delta}^2\}. \tag{8}$$

$$V=\frac{1}{2}k\delta^2+mg\delta.$$

Since the Lagrangian $L = T - V$ is cyclic in θ, Lagrange's equation corresponding to θ yields:

$$h=\dot{\theta}(r+\delta)^2. \tag{10}$$

Here h is a constant. Since the total energy remains constant, equations (8), (9), and (10) yield:

$$e=mh^2(r+\delta)^{-2}+m\dot{\delta}^2+\frac{k}{2}\delta^2+mg\delta. \tag{11}$$

Here, e is the total energy.

If we make the substitution $\delta' = \delta + \frac{mg}{k}$, equation (11) may be written:

$$e'=mh^2(r'+\delta')^{-2}+m\dot{\delta}^2+\frac{k}{2}\delta'^2, \tag{12}$$

$$\text{where } r'=r-\frac{mg}{k},\ e'=e+\frac{m^2g^2}{2k}.$$

We note that this is identical in form to the total energy of the system in Fig. 1, if gravity is neglected for the pendulum. (In this case equations (1) and (2) yield an equation identical in form to equation (12), if Lagrange's equation is used as was done to obtain equation (10).) If a suitable nondimensionalization is carried out, equation (12) may be written:

$$\dot{D}^2=E-H^2(R+D)^{-2}-D^2, \tag{13}$$

where $\dot{D}$, E, H, R, and D are proportional to $\dot{\delta}'$, e', h, r', and δ', respectively. Equation (13) is plotted in the phase plane for $E = R = 1$ and varying values of H (Fig. 4).

We note that when H is sufficiently large, D the deflection remains positive. These cases correspond to a high rate of rolling for which the cylinder is in a constant state of tension.

We note that when $R = 0$, equation (13) may be integrated to yield:

$$D^2=\left(\frac{E^2}{4}-H^2\right)^{1/2}\cos 2t+\frac{E}{2}. \tag{14}$$

Here we have used the initial condition $\dot{D} = 0$, when $t = 0$. If we refer to Fig. 1, this case corresponds to a pendulum of zero unstretched length. $R = 0$ is an idealized situation which, in the case of the pendulum, can actually be realized by the construction of a suitable device.

References

Heinbockel, J. H., and Struble, R. A., 1963, "Resonant Oscillations of an Extensible Pendulum," *Journal of Applied Mathematics and Physics*, (*ZAMP*), Vol. 14, No. 3, pp. 262–269.

Kane, T. R., and Kahn, M. E., 1968, "On a Class of Two-Degree-of-Freedom Oscillations," ASME JOURNAL OF APPLIED MECHANICS, Vol. 35, pp. 547–552.

Srinivasan, P., and Sankar, T. S., 1974, "Autoparametric Self-Excitation of a Pendulum Type Elastic Oscillator," *Journal of Sound and Vibration*, Vol. 35, pp. 549–557.

Minorsky, N., 1962, *Nonlinear Oscillations*, Van Nostrand, Princeton, N.J., p. 506.

Downloaded 03 May 2010 to 171.66.16.244. Redistribution subject to ASME license or copyright; see http://www.asme.org/terms/Terms_Use.cfm

Journal of Applied Mechanics

Discussion

A Note on Microbuckling in Unidirectional Fibrous Composites[1]

T. W. Shield.[2] The analysis presented in this note agrees with the results of Chung and Testa (1969), who presented an analysis of periodic fibers. Their results agree exactly with the results of Minahen and Knauss in the limit of $h_2/\lambda \to \infty$, where h_2 is the spacing between fibers and λ the buckled wavelength. After finding the corresponding equations to (16) and (17) of Minahen and Knauss, Chung and Testa solve for the value of λ that minimizes the buckling load (strain). This value of strain is then the critical strain, which only depends on the modulus ratio, E_f/E_m, and the Poisson's ratio of the substrate, ν_m. The condition for a minimum is strain is

$$\frac{\partial \epsilon_0}{\partial \rho} = 0, \qquad (A)$$

whose solution is $\rho_c = \dfrac{2\pi h}{\lambda_c}$, where λ_c is the critical wavelength and h the fiber thickness. Then (16) or (18) can be used to find the critical value of ϵ_0.

For the bonded case, (16) can be solved for $-\epsilon_0$ as

$$-\epsilon_0 = \frac{\rho^3 + a\rho^2 + 12b\rho + 4a}{12\rho} \qquad (B)$$

where

$$a = \frac{12\mu}{(3 - \nu_m)(1 + \nu_m)},$$

$$b = \frac{2\mu(1 - \nu_m)}{(3 - \nu_m)(1 + \nu_m)},$$

and $\mu = E_m/E_f$. Substitution of (B) into (A) and rearranging yields the condition for a minimum in strain,

$$2\rho^3 + a\rho^2 - 4a = 0. \qquad (C)$$

This equation agrees with equation (34) of Chung and Testa if the quadratic term in ρ is neglected. The solution to (C), ρ_c, when substituted into (B) gives the critical strain for buckling to occur in the bonded case.

Similarly, for the unbonded case we rewrite (18) as

$$-\epsilon_0 = \frac{\rho^3 + \mu}{12\rho}. \qquad (D)$$

Applying (A) and solving for ρ_c gives

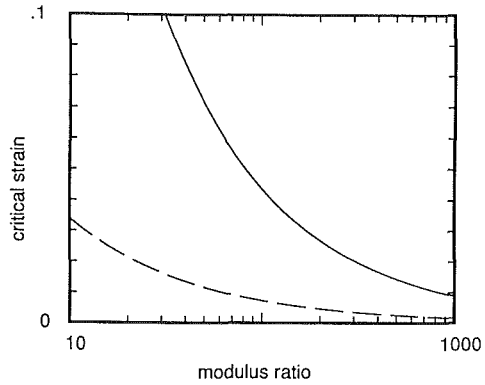


Fig. 1 The critical strain for buckling to occur versus the modulus ratio E_f/E_m, for a substrate with $\nu_m = 0.5$. The solid curve is the bonded case and the dashed curve is the unbonded case.

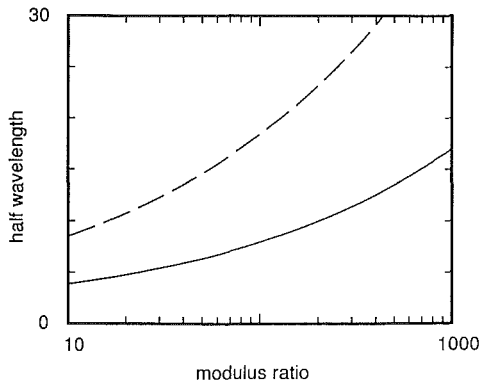


Fig. 2 The half wavelength, $\lambda_c/2$, of the buckled fiber versus the modulus ratio E_f/E_m, for a substrate with $\nu_m = 0.5$. The solid curve is the bonded case and the dashed curve is the unbonded case.

$$\rho_c = (\mu/2)^{1/3}. \qquad (E)$$

Substitution of (E) into (D) gives the value of the critical strain for the unbonded case.

Figures 1 and 2 show the values of the critical stain and critical half wavelength versus the modulus ratio E_f/E_m, for the case of an incompressible substrate, $\nu_m = 0.5$. The solid curves are the bonded case and the dashed curves are the unbonded case. These results still agree with the conclusions presented in the note that the unbonded configuration buckles at a much lower strain than the bonded case.

Reference

Chung, W-Y. and Testa, R. B., 1969, "The Elastic Stability of Fibers in a Composite Plate," *J. Composite Materials*, Vol. 3, pp. 58-80.

[1]By T. M. Minahen and W. G. Knauss, published in the Dec. 1989 issue of the ASME JOURNAL OF APPLIED MECHANICS, Vol. 56, pp. 983-985.

[2]Division of Engineering, Brown University, Providence, RI 02912. Assoc. Mem. ASME.

Copyright © 1990 by ASME
Downloaded 03 May 2010 to 171.66.16.244. Redistribution subject to ASME license or copyright; see http://www.asme.org/terms/Terms_Use.cfm

Discussion of Thin-Walled Open-Profile Bars[3]

Yoshiaki Goto,[4] Wai-Fah Chen,[5] and Fumio Nishino.[6]
This paper yields incorrect and misleading information on the buckling theory of thin-walled bars. In a recent paper (Goto and Chen, 1989), we showed the validity of the Wagner hypothesis and pointed out the problems associated with Ojalvo's derivation. In this discussion, we will provide a supplementary explanation to show more specifically why Ojalvo's theory is incorrect.

First, we will show that Ojalvo's criticism of our formulation of the finite displacement theory of thin-walled beams is incorrect. He objected to the equilibrium equations (3.22) and (3.23) of Washizu (1968) and hence the use of pseudo-stress, i.e., the second Piola-Kirchhoff stress tensor, in our variational formulation. In fact, identical equilibrium equations can be written using either the pseudo or the actual stress, although the expressions are different because of the difference in the definitions of the two stresses. With a proper transformation, it is not difficult to show that the two different expressions of equilibrium equations agree with each other. Thus, Ojalvo's statement that the equilibrium equations written by the pseudo-stress have no basis in a conventional understanding of statics is not correct. Beam theory (Goto et al., 1985) under the conditions of finite displacements and finite strains precisely considers this difference between the pseudo-stress and the actual stress. For the equilibrium equations obtained by variational calculus, all the pseudo-stress resultants are transformed to the actual stress resultants. The validity of these equilibrium equations is also confirmed by the equilibrium approach in the referenced paper. Furthermore, under the assumption of small strains, the actual stress can be approximated well by the second Piola-Kirchhoff stress tensor. For almost all engineering structures, strains are negligibly small compared with unity, even in the case where structures have undergone extremely large displacements. Thus, the procedure adopted by Nishino et al. (1973, 1979) and Hasegawa et al. (1985) is also valid and there is no problem in these theories. These three theories lead naturally to Wagner's K term.

Next, we will proceed to demonstrate that Ojalvo's theory simply results from some mistakes and inconsistencies in his derivation.

For buckling under uniform compression, we have explained in some detail the problems associated with Ojalvo's theory (Goto and Chen, 1989). So here we only discuss his other theory for bars with a longitudinal plane of symmetry.

Ojalvo presented an expression for the external potential in equation (12) where the following equation is used to represent the curvature of the centroidal line about the x-axis:

$$-v_c'' = -[\theta(u'' + y_o\theta'') + y_o(\theta')^2/2]. \tag{20}$$

We will show in what follows that equation (20) is incorrect. Ojalvo derived the x-component of the relative rotation of the centroidal line as $-\theta(u'' + y_o\theta'')dz$, assuming that the η-component of the incremental displacement at the shear center is zero at the instant of buckling. This gives the first term of the right-hand side of equation (20). However, this assumption has no good justification and is generally inadequate. A correct procedure to obtain this curvature will be shown later.

The other mistake found in Ojalvo's derivation is the second term in the right-hand side of equation (20). This term, as seen from Figs. 4 and 6, corresponds to a component of the curvature due to the centroidal displacement in the η- direction caused by the rotation about the shear center. Ojalvo calculated this component of the curvature about the ξ- axis by the equation

$$-[\hat{v}_c(z+dz) - \hat{v}_c(z)]/dz^2 = -y_o(\theta')^2/2, \tag{21}$$

where $\hat{v}_c(z)$ is the centroidal displacement in the direction of the η- axis at z. However, the use of equation (21) to calculate the curvature is incorrect. In lieu of equation (21), the curvature, which is the second derivative of displacement $\hat{v}_c$, should be calculated by

$$-\{[\hat{v}_c(z+dz) - \hat{v}_c(z)]/dz - [\hat{v}_c(z) - \hat{v}_c(z-dz)]/dz\}/dz = -y_o(\theta')^2. \tag{22}$$

Here, we shall show a correct procedure to calculate $-v_c''$. Since v_c can be expressed in the form $v_c = v + y_o(1 - \cos\theta)$, the curvature $-v_c''$ is given as follows up to the second order in terms of the torsional angle:

$$-v_c'' = -v'' - y_o(\theta')^2 - y_o\theta\,\theta''. \tag{23}$$

v'' in equation (23) should be determined from the condition that the bending moment M_x remains constant at the instant of buckling. The curvature $-v''$ so determined is given by $u'\theta' - (1/2)\beta_x(\theta')^2$ (Goto and Chen, 1989). Finally, $-v_c''$, which should be used in equation (12), is expressed as

$$-v_c'' = u'\theta' - (1/2)(\beta_x + 2y_o)(\theta')^2 - y_o\theta\,\theta''. \tag{24}$$

References

Goto, Y., and Chen, W. F., 1989, "On the Validity of Wagner Hypothesis," *International Journal of Solids and Structures*, Vol. 25, No. 6, pp. 621–634.

Nishino, F., and Hasegawa, A., 1979, "Thin-Walled Members," *Journal of Faculty of Engineering*, University of Tokyo, B-Vol. 35, pp. 109–190.

Author's Closure

The criticisms voiced in the Goto, Chen, and Nishino Discussion may be separated into three categories: (1) It is believed that our expression for curvature about the x-axis, $-[\theta(u'' + y_o\,\theta'') + (\theta')^2\,y_o/2]$, used with the virtual work theorem for the singular purpose of evaluating the potential of external loads, is incorrect, (2) exception is taken to our remarks concerning the Washizu virtual work principle (theorem) and stationary potential energy principle (theorem), both for finite displacements. We believe these to be false theorems, and (3) exception is taken to our assertion that the Wagner effect has no place in a rational theory of bars.

As to the first criticism, the discussers object because the part $-\theta(u'' + y_o\,\theta'')$ is written without consideration of a certain η component of the shear center displacement. Such η component does not enter because $u'' + y_o\,\theta''$ is a curvature of the centroid line about the η-axis which, when multiplied by $-\theta$, gives the component of the curvature about the x-axis.

With regard to the remainder of the first criticism, we emphatically disassociate ourselves from equation (21) which is inaccurately attributed to us. Equation (22), suggested instead by the discussers, fails because it ignores that η is not a fixed direction such as y. The part of our analysis which yields x-axis curvature $(\theta')^2\,y_o/2$ is valid up to an approximation which ignores terms of higher order than those which are quadratic in displacements u, θ, and /or their derivatives.

Criticism voiced with respect to our statements concerning the Washizu theorems are unresponsive. We object to the Washizu theorems because they are derived without regard for Newtonian laws for statics. If we are correct, there can be no mathematical transformation of the type alluded to which can cure an infirmity in the physics of the problem. We doubt the

[3]By M. Ojalvo and published in the Sept. 1989 issue of the ASME JOURNAL OF APPLIED MECHANICS, Vol. 56, pp. 633–638.

[4]Department of Civil Engineering, Nagoya Institute of Technology, Gokisocho, Showaku, Nagoya 466, Japan.

[5]School of Civil Engineering, Purdue University, West Lafayette, IN 47907.

[6]Department of Civil Engineering, University of Tokyo, Bunkyo-Ku, Tokyo 113, Japan.

Copyright © 1990 by ASME
Downloaded 03 May 2010 to 171.66.16.244. Redistribution subject to ASME license or copyright; see http://www.asme.org/terms/Terms_Use.cfm

Journal of Applied Mechanics

Book Reviews

Non-Linear Oscillations, 2nd ed., by Peter Hagedorn. Clarendon Press, Oxford, 1988. 308 pages. Price: $39.95.

REVIEWED BY P. D. SPANOS[1]

The book covers most of the traditional topics of nonlinear oscillations. The treatment is clear and reflects a strong flavor of applicability to engineering problems.

Chapter 1 covers free and forced oscillations in damped and undamped single degree-of-freedom nonlinear systems. The basic ideas are presented by studying the simple pendulum motion. Concepts such as "phase space," "perturbation method," "harmonic balance," and "equivalent linearization" are introduced in a rather applied format.

Chapter 2 starts with the concept of Liapounov stability. Methods for investigating stability are discussed. The rest of the chapter is devoted to concepts of bifurcation theory. The Poincare map is introduced and applied to the analysis of bifurcation of equilibria and Hopf bifurcation. This last part constitutes the major update from the first edition of the book, reflecting the emerging importance of these topics.

Chapter 3 treates self-excited oscillations. Perturbation methods and equivalent linearization methods reappear in this chapter and are applied to specific problems. Self-excited oscillations of multi-degree-of-freedom systems are briefly discussed.

Chapter 4 deals with Hamiltonian systems and canonical perturbations.

The last chapter consists of an introduction to the theory of optimal control. The Pontryagin maximum principle is presented, and methods introduced in the previous chapters are applied to several problems.

Collectively, the topics of the book are grouped in a manner emphasizing the kind of oscillations involved and the underlying physical process. This feature makes the book appealing for developing a traditional perspective of nonlinear phenomena in engineering. In this context it is understandable that a discussion of modern concepts such as "strange attractors" is not included. Somewhat surprisingly, even concepts of traditional singular perturbation analysis are not included.

Overall, the book could serve as a textbook for a graduate level course in nonlinear vibrations, and as a reference for researchers in the field. Further, the numerous exercises with solutions appended at the end of the book, make it quite suitable for an introductory self-study of the subject of nonlinear oscillations.

[1]Brown School of Engineering, Rice University, Houston, TX 77251.

Rock Rheology, N. Cristescu. Kluwer Academic Publishers, Dordrecht, The Netherlands, 1989. 336 pages.

REVIEWED BY L. S. COSTIN[2]

Rock Rheology was apparently intended to be a general text for the advanced rock mechanics student. I do not think it adequately fulfills that role, primarily because it is not a general review of the subject but an extensive review of the author's own work on the subject. However, the book would be a good supplementary text because it discusses several important concepts regarding time-dependent deformation of rock that are not discussed in much detail in other more general rock mechanics texts. In addition, the bibliography provides an excellent compendium of resource material on the subject.

The book is composed of three main sections. The first describes the time-dependent behavior of rock as interpreted from experimental data. The focus of the book is in the second section, which deals with the development of elastic-viscoplastic constitutive models to describe the behavior of rock. The final section presents some applications of the constitutive theories to practical problems.

The author's discussion of rock behavior in the first three chapters is quite thorough and is amply illustrated by the use of experimental data taken from many sources. The main problem in the discussion is that most of the data presented are from tests on salt, which is not really representative of the brittle deformation mechanisms associated with most rocks. Even at moderate temperatures and pressures, salt deforms in creep primarily by dislocation motion similar to the deformation of metallic materials. Most other rocks deform by brittle mechanisms, such as microcracking. Thus, many of the phenomena pointed out as being characteristic of rock, are really quite peculiar to salt. It is interesting to note that the author stresses that the constitutive theory should be based on the principal mechanism of rock deformation, time-dependent nucleation, and growth of microcracks; but the experimental evidence for the effect of this mechanism comes from a material in which the mechanism is of secondary importance. However, even with this discrepancy, the author does manage to discuss the important concepts involved in time-dependent deformation, especially with regard to what important features need to be considered in the development of constitutive models.

[2]Geomechanics Analysis and Testing Division 6314, Sandia National Laboratories, Albuquerque, NM 87185.

Copyright © 1990 by ASME
Downloaded 03 May 2010 to 171.66.16.244. Redistribution subject to ASME license or copyright; see http://www.asme.org/terms/Terms_Use.cfm